

Tom Proulx *Editor*

Rotating Machinery, Structural Health Monitoring, Shock and Vibration, Volume 5

Proceedings of the 29th IMAC,
A Conference on Structural Dynamics, 2011



Conference Proceedings of the Society for Experimental Mechanics Series

For other titles published in this series, go to
www.springer.com/series/8922

Tom Proulx
Editor

Rotating Machinery, Structural Health Monitoring, Shock and Vibration, Volume 5

Proceedings of the 29th IMAC, A Conference
on Structural Dynamics, 2011

Editor

Tom Proulx
Society for Experimental Mechanics, Inc.
7 School Street
Bethel, CT 06801-1405
USA
tom@sem1.com

ISSN 2191-5644 e-ISSN 2191-5652
ISBN 978-1-4419-9427-1 e-ISBN 978-1-4419-9428-8
DOI 10.1007/978-1-4419-9428-8
Springer New York Dordrecht Heidelberg London

Library of Congress Control Number: 2011923651

© The Society for Experimental Mechanics, Inc. 2011

All rights reserved. This work may not be translated or copied in whole or in part without the written permission of the publisher (Springer Science+Business Media, LLC, 233 Spring Street, New York, NY 10013, USA), except for brief excerpts in connection with reviews or scholarly analysis. Use in connection with any form of information storage and retrieval, electronic adaptation, computer software, or by similar or dissimilar methodology now known or hereafter developed is forbidden.

The use in this publication of trade names, trademarks, service marks, and similar terms, even if they are not identified as such, is not to be taken as an expression of opinion as to whether or not they are subject to proprietary rights.

Printed on acid-free paper

Springer is part of Springer Science+Business Media (www.springer.com)

Preface

Rotating Machinery, Structural Health Monitoring, and Shock and Vibration Topics represents one of six clusters of technical papers presented at the 29th IMAC, A Conference and Exposition on Structural Dynamics, 2011 organized by the Society for Experimental Mechanics, and held in Jacksonville, Florida, January 31 - February 3, 2011. The full proceedings also include volumes on Advanced Aerospace Applications; Modal Analysis, Linking Models and Experiments, Civil Structures; and Sensors, Instrumentation, and Special Topics.

Each collection presents early findings from experimental and computational investigations on an important area within Structural Dynamics. The current volume on *Rotating Machinery, Structural Health Monitoring, and Shock and Vibration* includes studies on Random Vibrations, Wind Turbine Blade Sensing and Health Monitoring, Rotating Machinery, Machinery Condition Monitoring and Diagnostics, Structural Health Monitoring, Shock and Vibration, Acoustics, and Damage Detection.

Condition monitoring, diagnostics and damage detection are a series of related topics of increasing importance. Structural Health Monitoring (SHM) has been an evolving technology for a number of years. Machinery monitoring and non-destructive testing topics have been active areas in IMAC and other forums. With the development of more powerful computational capability and miniaturized sensors, SHM schemes are being explored that can be designed into the structure, providing a comprehensive health evaluation.

The organizers would like to thank the authors, presenters, session organizers and session chairs for their participation in this track.

Bethel, Connecticut

Dr. Thomas Proulx
Society for Experimental Mechanics, Inc

Contents

1	Development of Pretest Planning Methodologies for Load Dependent Ritz Vectors	1
	G.C. Khoury, D.C. Zimmerman, University of Houston	
2	Spectral Analysis Methodology for Acoustical and Mechanical Measurements Relative to Hydraulic Turbine's Generator	15
	F. Lafleur, S. Bélanger, E. Coutu, A. Merkouf, Institut de Recherche d'Hydro-Québec, IREQ	
3	Transverse Vibrations of Tapered Materially Inhomogeneous Axially Loaded Shafts	25
	A.J. Mazzei, Jr., Kettering University; R.A. Scott, University of Michigan	
4	Converting a Driven Base Vibration Test to a Fixed Base Modal Analysis	37
	R.L. Mayes, Sandia National Laboratories; M.S. Allen, University of Wisconsin-Madison	
5	Model Form Error of Alternate Modeling Strategies: Shell Type Wind Turbine Blades	53
	K.L. Van Buren, S. Atamturktur, Clemson University	
6	Operational Modal Analysis of Operating Wind Turbines: Application to Measured Data	65
	S. Chauhan, D. Tcherniak, Bruel and Kjaer Sound and Vibration Measurement A/S; J. Basurko, O. Salgado, I. Urresti, Ikerlan-IK4; C.E. Carcangiu, M. Rossetti, Alstom Wind	
7	Amplitude Dependent Crack Characterization of Growing Fatigue Cracks	83
	A.U. Rehman, K. Worden, J.A. Rongong, University of Sheffield	
8	Utilization of Localized Panel Resonant Behavior in Wind Turbine Blades	93
	D.T. Griffith, Sandia National Laboratories	
9	Random Vibration – History and Overview	105
	T.L. Paez, Thomas Paez Consulting	
10	Reduction of Vibration Transmission in String Trimmers	129
	P. Rajbhandary, J. Leifer, B.J. Weems, Trinity University	

11	Insight Into Strong Motion Behavior of Large Concrete Structures Based on Low Level Response Monitoring in the Field	139
	N. von Gersdorff, Southern California Edison Company; Z. Duron, Harvey Mudd College; V. Chiarito, ERDC/WES	
12	Stability Monitoring of Burning Structures Based on Fire-induced Vibration Monitoring	149
	Z.H. Duron, Harvey Mudd College	
13	Application of Energy Methods in Mechanical Shock to Study Base Excited Nonlinear System Response	157
	J.E. Alexander, BAE Systems, US Combat Systems	
14	Experimental Assessment of Gear Meshing Excitation Propagation Throughout Multi Megawatt Gearboxes	177
	J. Helsen, Katholieke Universiteit Leuven; F. Vanhollebeke, B. Marrant, Hansen Transmissions International nv; D. Berckmans, D. Vandepitte, W. Desmet, Katholieke Universiteit Leuven	
15	An Advanced Numerical Model of Gear Tooth Loading From Backlash and Profile Errors	191
	A. Sommer, J. Meagher, X. Wu, California Polytechnic State University	
16	A Differential Planetary Gear Model With Backlash and Teeth Damage	203
	X. Wu, J. Meagher, A. Sommer, California Polytechnic State University	
17	Determination of Wind Turbine Operating Deflection Shapes Using Full-field 3D Point-tracking	217
	C. Warren, C. Niezrecki, P. Avitabile, University of Massachusetts Lowell	
18	Dynamic Performance and Integrity Assessment of an Electricity Transmission Tower	227
	E.P. Carden, J.R. Maguire, Lloyd's Register EMEA	
19	Operational Modal Analysis of Resiliently Mounted Marine Diesel Generator/Alternator	237
	H. Clarke, J. Stainsby, E.P. Carden, Lloyd's Register EMEA	
20	Eigenvalues and Nonlinear Behaviour of Levitron®	245
	E. Bonisoli, C. Delprete, M. Silvestri, Politecnico di Torino	
21	Optical Measurements and Operational Modal Analysis on a Large Wind Turbine: Lessons Learned	257
	M. Ozbek, D.J. Rixen, Delft University of Technology	
22	Operational Damage Detection of Turbine Rotors Using Integrated Blade Sensors	277
	S.R. Dana, D.E. Adams, Purdue University	

23	Uncertainty Assessment in Structural Damage Diagnosis S. Sankararaman, S. Mahadevan, Vanderbilt University	287
24	A Framework for Embedded Load Estimation From Structural Response of Wind Turbines A.V. Hernandez, R.A. Swartz, Michigan Technological University; A.T. Zimmerman, University of Michigan	295
25	A Review of Gearbox Condition Monitoring Based on Vibration Analysis Techniques Diagnostics and Prognostics A.S. Sait, Y.I. Sharaf-Eldeen, Florida Institute of Technology	307
26	Experimental Results of Wind Turbine Operational Monitoring With Structural and Aerodynamic Measurements J.R. White, Sandia National Laboratories; D.E. Adams, Purdue University	325
27	Torsional Response of Structure with Mass Eccentricity H. Wu, Edith Cowan University	333
28	Examination of a Feeling of Pulse Control Method for Cruiser-type Motorcycle N. Tsujiuchi, T. Koizumi, T. Tonomura, Doshisha University	341
29	Seeding Cracks Using a Fatigue Tester for Accelerated Gear Tooth Breaking N.G. Nenadic, J.A. Wodenscheck, M.G. Thurston, Rochester Institute of Technology; D.G. Lewicki, NASA Glenn Research Center	349
30	Operational Modal Analysis of a Rectangular Plate Using Noncontact Acoustic Excitation Y.F. Xu, W.D. Zhu, University of Maryland, Baltimore County	359
31	Algorithm Hybridization for Automated Modal Identification and Structural Health Monitoring C. Rainieri, G. Fabbrocino, University of Molise	375
32	Fiber Optic Sensor Installation for Monitoring of 4 Span Model Bridge in UCF I.B. Kwon, M. Malekzadeh, Q. Ma, H. Gokce, T.K. Terrell, A. Fedotov, F.N. Catbas, University of Central Florida	383
33	A Model of Uncertainty Quantification in the Estimation of Noise-contaminated Transmissibility Measurements for System Identification Z. Mao, M. Todd, University of California, San Diego	389
34	A Modified Whiteness Test for Damage Detection Using Kalman Filter Innovations D. Bernal, Y. Bulut, Northeastern University	399
35	Vibration Reduction of an Atomic Force Microscope in the Point of the Mechanical Design C. Kim, J. Jung, J. Jeong, K. Park, Gwangju Institute of Science and Technology	405

- 36 Modal Analysis and SHM Investigation of CX-100 Wind Turbine Blade** 413
K. Deines, New Mexico State University; T. Marinone, University of Massachusetts Lowell; R. Schultz, Michigan Technological University; K. Farinholt, G. Park, Los Alamos National Laboratory
- 37 Model-based Diagnostics and Fault Assessment of Induction Motors With Incipient Faults** 439
M. Nakhaeinejad, J. Choi, M.D. Bryant, The University of Texas at Austin
- 38 Use of the Cepstrum to Remove Selected Discrete Frequency Components From a Time Signal** 451
R.B. Randall, N. Sawalhi, University of New South Wales
- 39 A Review of Signal Processing and Analysis Tools for Comprehensive Rotating Machinery Diagnostics** 463
T. Reilly, Data Physics Corporation
- 40 Simple Tools for Simulating Structural Response to Underwater Explosions** 481
F.A. Costanzo, Naval Surface Warfare Center Carderock Division, UERD
- 41 Using Vibration Signatures Analysis to Detect Cavitation in Centrifugal Pumps** 499
S.N. Ganeriwala, V. Kanakasabai, SpectraQuest, Inc.
- 42 Modes Indicate Cracks in Wind Tubine Blades** 509
S.N. Ganeriwala, V. Kanakasabai, SpectraQuest, Inc.; M. Richardson, Vibrant Technology, Inc.
- 43 Estimating Shock Severity** 515
H.A. Gaberson, Consultant
- 44 Progress in Shock and Vibration Technology Over 80 Symposia** 533
H.C. Pusey, SAVIAC Manager of Technical Services
- 45 Rationale for Navy Shipboard Shock & Vibration (S&V) Requirements** 545
J.E. Howell, III, Naval Surface Warfare Center, Carderock Division
- 46 Deformation and Vibration Measurement and Data Evaluation on Large Structures Employing Optical Measurement Techniques** 547
H. Berger, M. Klein, GOM Gesellschaft für Optische Messtechnik mbH

Development of Pretest Planning Methodologies for Load Dependent Ritz Vectors

George C. Khoury
Graduate Research Assistant
Department of Mechanical Engineering
University of Houston
Houston, TX 77204-4792, USA

David C. Zimmerman
Professor
Department of Mechanical Engineering
University of Houston
Houston, TX 77204-4792, USA

ABSTRACT

Load dependent Ritz vectors have been found to be suitable alternatives to mode shape vectors for structural vibration analysis. While much research has focused on how to best set-up and perform modal property identification, there has been no investigation on such pretest planning for Ritz vectors. Pre-test planning is a vital part of successful vibration tests, especially when dealing with large complex structures. In such cases, it is common that a limited number of sensors and actuators must be placed in a configuration to obtain the most important dynamic information. In this study, previously developed modal sensor placement techniques were utilized to determine Ritz vector sensor sets for the NASA eight-bay truss structure. The techniques used were the eigenvector product, kinetic energy product, and effective independence. The Modal Assurance Criteria was employed to determine how well each technique performed. Since Ritz vectors are subject to change due to the excitation locations, the paper also investigated the effect of various loading configurations on the Ritz vector sensor placement results. Finally, Ritz vectors and mode shapes were combined in an effort to verify that a single sensor set could be used to identify both sets of basis vectors.

Introduction

Pre-test planning is an integral part of successful structural dynamic testing. When dealing with large complex structures, typically a limited number of sensors and actuators must be placed in a configuration to obtain the most important dynamic information. Since sensor and actuator locations strongly influence structural testing, it is important that the selected locations be optimized. Optimal sensor placement methods tend to utilize information obtained from the baseline finite element model (FEM). Although much research has been performed in this area for mode shape vectors [1-3], there has been no investigation on such pre-test planning for Ritz vectors. The motivation for this paper is to apply sensor placement techniques to optimize the information obtained during experimental Ritz vector testing.

Load dependent Ritz vectors have been found to be suitable alternatives to mode shape vectors for structural vibration analysis. The Ritz vector analysis is a computational method that allows accurate dynamic analyses to be obtained at a reduced computational cost [4]. Ritz vectors have several advantages over traditional mode shapes. (1) They automatically include the static correction term. (2) Once a system realization is obtained, Ritz vectors are less computationally expensive to extract. (3) All Ritz vectors generated by a load will be excited by that load. (4) Each Ritz vector describes behavior across a range of frequencies, so fewer Ritz vectors than mode shapes are typically needed to achieve the same level of accuracy in transient response prediction and model reduction. (5) Because the Ritz vector extraction process depends on the solution of linear algebraic equations instead of an eigensolution, Ritz vectors may be less sensitive to noise than measured mode shapes. An important step in the advancement of Ritz vector applications was the development of a method to extract Ritz vectors from dynamic testing data by Cao and Zimmerman [5], which was further refined by Boxoen and Zimmerman [6].

The sensor placement techniques presented in this paper were previously developed to perform the same function for mode shape vectors, but can be extended for use with any basis vector. The Eigenvector product uses the basis vector product from the reduced FEM to identify possible sensor or actuator locations [2]. The kinetic energy product uses the modal kinetic energy calculated utilizing the FEM mass matrix and target modes to place sensors or actuators at points of maximum kinetic energy [1, 2]. Finally, the Effective Independence is a more elaborate sensor placement method that attempts to maintain the linear independence of the basis vectors, by maximizing the determinant of the Fisher information matrix, as candidate sensor locations are eliminated [1-3].

The techniques above were used to find sensor placement locations for mode shapes, Ritz vectors, as well as a combination of both basis vectors. The NASA eight-bay truss model was used as the analytical test-bed. The Modal Assurance Criteria (MAC) was utilized to compare the sensor placement results and obtain a representation of how well each technique performed. Section 2 presents a detailed look into the Ritz vector extraction method. Section 3 details the sensor placement techniques used. The numerical studies and results are presented in section 4. Finally, the concluding remarks are given in section 5.

1 Ritz Vector Analysis

The dynamic equilibrium equation for a discrete n -degree-of-freedom (DOF) structure can be expressed as

$$\mathbf{M} \ddot{\underline{x}}(t) + \mathbf{C} \dot{\underline{x}}(t) + \mathbf{K} \underline{x}(t) = \underline{f} u(t) \quad (1)$$

where \mathbf{M} , \mathbf{C} , and \mathbf{K} are the $(n \times n)$ mass, damping and stiffness matrices, respectively, $\underline{x}(t)$ is the $(n \times 1)$ position vector, \underline{f} is the $(n \times 1)$ force influence vector, and $u(t)$ is the scalar force input signal. The over-dots represent differentiation with respect to time.

The first Ritz vector, representing the deflection of the structure under a unit static load [4], is found from the solution of

$$\mathbf{K} \underline{v}_1^* = \underline{f}, \quad (2)$$

where \underline{v}_1^* is the non-normalized Ritz vector. Although Wilson [4] mass-normalized the Ritz vectors, it was found that in experimental identifications it is more appropriate that the Ritz vectors be unit-normalized as the mass matrix is unknown [5, 6]. The first Ritz vector is unit-normalized as

$$\underline{v}_1 = \frac{\underline{v}_1^*}{\sqrt{(\underline{v}_1^*)^T \underline{v}_1^*}}. \quad (3)$$

The subsequent Ritz vectors are found from the solution of

$$\mathbf{K} \underline{v}_i^* = \mathbf{M} \underline{v}_{i-1}. \quad (4)$$

Each Ritz vector is orthogonalized using a Gram-Schmidt orthogonalization process

$$\hat{\underline{v}}_i = \underline{v}_i^* - \sum_{j=1}^{i-1} c_j \underline{v}_j \quad (5)$$

where

$$c_j = \underline{v}_j^T \underline{v}_i^*. \quad (6)$$

After each Ritz vector is orthogonalized, it is unit-normalized

$$\underline{v}_i = \frac{\hat{\underline{v}}_i}{\sqrt{\hat{\underline{v}}_i^T \hat{\underline{v}}_i}}. \quad (7)$$

2 Sensor Placement Techniques

2.1 Vector Product (VP)

This technique is generally referred to as the Eigenvector Product technique [2]. In this study the technique is referred to as the Vector Product as it is used with basis vectors other than mode shapes. The basis vectors found from the finite element model (FEM) can be used to identify possible sensor or actuator locations. The shapes of interest are chosen as shown below

$$\Phi = \begin{bmatrix} \phi_{11} & \phi_{12} & \dots & \phi_{1m} \\ \vdots & \vdots & & \vdots \\ \phi_{n1} & \phi_{n2} & & \phi_{nm} \end{bmatrix}, \quad (8)$$

where Φ is the set of mode shapes, Ritz vectors or a combination of both. The VP is calculated by multiplying the Φ components, such that

$$VP_i = \phi_{i1}\phi_{i2} \dots \phi_{im}, \quad (9)$$

where subscript i corresponds to the degree-of-freedom (DOF) of interest. The total set of vector products, \underline{VP} , is sorted so that the maximum values are found. A high value of VP_i corresponds to nodes with high displacement and thus a candidate location. Vector product will exclude node point DOFs of any vector as VP_i will give a value of zero.

2.2 Kinetic Energy Product (KE)

The KE product can be used for sensor placement identification [1, 2]. The technique uses the assumption that maximum observability will occur by placing sensors at locations with maximum kinetic energy. Using the FEM basis vectors, the kinetic energy is found as follows

$$ke_{im} = \phi_{im} \sum_{j=1}^n \mathbf{M}_{ij} \phi_{jm}, \quad (10)$$

where i corresponds to the DOF of interest, m is the target basis vector, and n corresponds to the total number of DOFs in the system. The total kinetic energy matrix is as follows

$$\mathbf{ke} = \begin{bmatrix} ke_{11} & ke_{12} & \dots & ke_{1m} \\ \vdots & \vdots & & \vdots \\ ke_{n1} & ke_{n2} & & ke_{nm} \end{bmatrix}. \quad (11)$$

Finally, the KE product is found by multiplying the \mathbf{ke} components

$$KE_i = ke_{i1}ke_{i2} \dots ke_{im}, \quad (12)$$

so that the total KE product, \underline{KE} , can be sorted from highest to lowest. As with VP, a high value of KE_i corresponds to a candidate location. The KE product will also negate node points associated with a single shape since the product will be zero at that DOF. The mass weighting inherent to the KE product causes the sensor and actuator placement to be dependent on the finite element discretization, such that there is a bias against areas with fine mesh sizes (and thus small masses).

2.3 Effective Independence (EI)

Effective independence was developed as a technique to select sensor locations for large space structures [1]. The candidate sensor sets are ranked according to their contribution to the linear independence of the target basis vectors. The first step is to find the Fisher information matrix

$$\mathbf{A}_o = \sum_{i=1}^n \phi^i \phi^{iT}, \quad (13)$$

where ϕ^i is the i^{th} row of the target basis vector and n is the total number candidate sensor locations in the system. Equation 13 demonstrates that information can be added to or subtracted from the Fisher information matrix with the inclusion or exclusion of DOFs. The number of DOFs in the sensor set can be reduced by eliminating locations that do not contribute to the independence of the target basis vectors.

The analysis starts by solving the eigenvalue equation for \mathbf{A}_o .

$$[\mathbf{A}_o - \lambda_j \mathbf{I}] \underline{\Psi}_j = 0, \quad j = 1, 2, \dots, m \quad (14)$$

where m is the total number of basis vectors in the system, and $\underline{\Psi}_j$ are orthogonal vectors resulting in the relations

$$\underline{\Psi}_j^T \mathbf{A}_o \underline{\Psi}_j = \lambda_j \quad \text{and} \quad \underline{\Psi}_j^T \underline{\Psi}_j = 1. \quad (15)$$

The EI coefficients of the candidate sensors are computed as

$$\mathbf{G} = [\Phi \Psi] \otimes [\Phi \Psi], \quad (16)$$

where the symbol \otimes represents term-by-term matrix multiplication, and $\Psi = [\underline{\Psi}_1, \underline{\Psi}_2, \dots, \underline{\Psi}_m]$. Next, Eq. (16) is post-multiplied by the inverse of the matrix of eigenvalues,

$$\mathbf{F}_E = \mathbf{G} \lambda^{-1}, \quad (17)$$

where \mathbf{F}_E represents the fractional eigenvalue distribution, and $\lambda = \text{diag}([\lambda_1, \lambda_2, \dots, \lambda_m])$. Finally, the terms within each row of \mathbf{F}_E are added to obtain

$$\underline{\text{EI}} = \begin{bmatrix} \sum \mathbf{F}_{E1} \\ \sum \mathbf{F}_{E2} \\ \vdots \\ \sum \mathbf{F}_{En} \end{bmatrix}. \quad (18)$$

Alternatively, $\underline{\text{EI}}$ can be found using the following formulation

$$\underline{\text{EI}} = \text{diag}(\Phi [\Phi^T \Phi]^{-1} \Phi^T). \quad (19)$$

The values of $\underline{\text{EI}}$ will range from 0 to 1, with a value of 0 indicating that the DOF does not contribute to the observability of the system. The smallest value of the $\underline{\text{EI}}$ vector is removed and the above process is repeated iteratively until the desired number of sensors is found.

3 Numerical Study

3.1 Test Bed Description

A sensor placement analysis was performed to compare the various placement techniques utilizing mode shapes, Ritz vectors, and a combination of both basis vectors. The analysis was based on the eight-bay hybrid-scaled truss structure designed for research in dynamic scale model ground testing of large space structures at the NASA Langley Research Center [7]. The truss was cantilevered at one end and each truss member was modeled as a rod element. Concentrated masses were attached at each node to represent joint and instrumentation mass properties. The structure was modeled as an undamped 96-DOF structure. The model is shown in [figure 1](#).

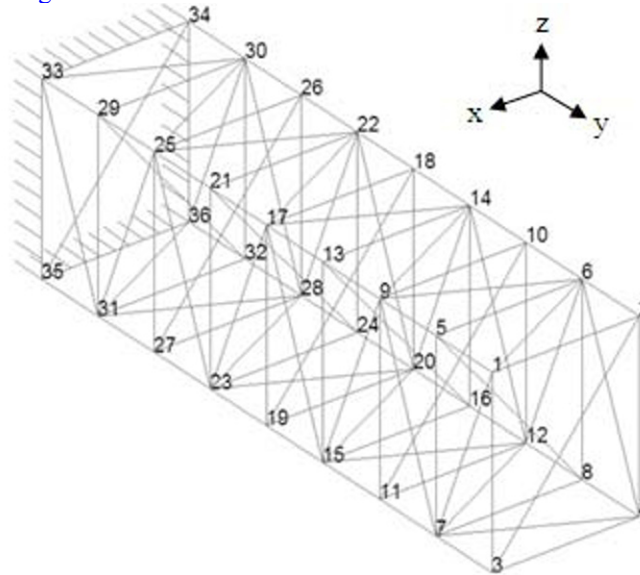


Figure 1: NASA Eight-bay Truss

From the above figure it can be seen that the first 32 nodes are unconstrained in the x-, y-, and z-directions. The last four nodes are constrained in all three directions. Using the supplied mass and stiffness matrices, the mode shapes and Ritz vectors were calculated. It was assumed that the first five mode shapes and Ritz vectors were the target shapes to be identified.

3.2 Mode Shape Sensor Placement

Using the first five full mode shapes from the FEM model, 15 sensor locations were found using the three placement techniques. The results are shown in [figure 2](#).

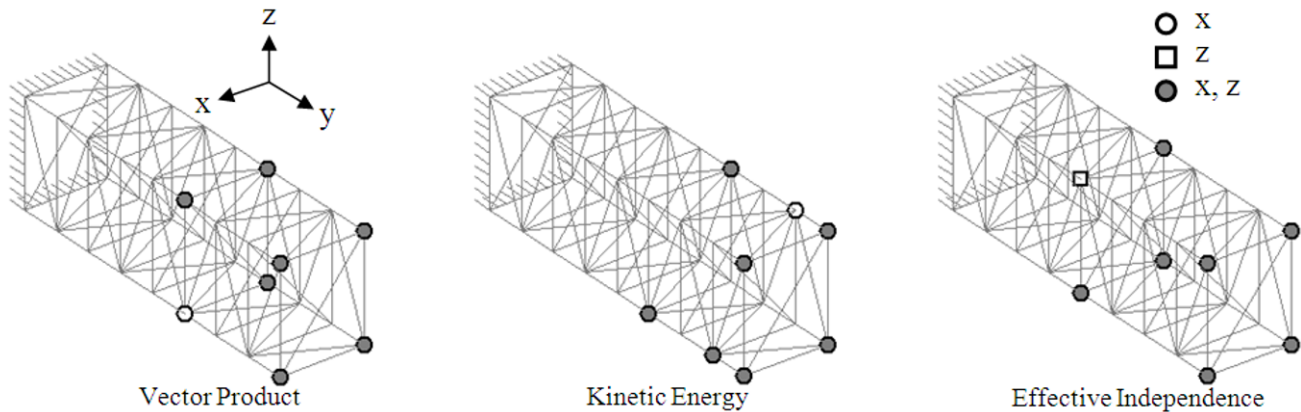


Figure 2: Sensor Locations using Mode Shapes

The reduced mode shapes were found by selecting the modal data from the sensor location DOFs. The modal assurance criteria (MAC) of the first five reduced mode shapes were compared, as shown in [figure 3](#) below.

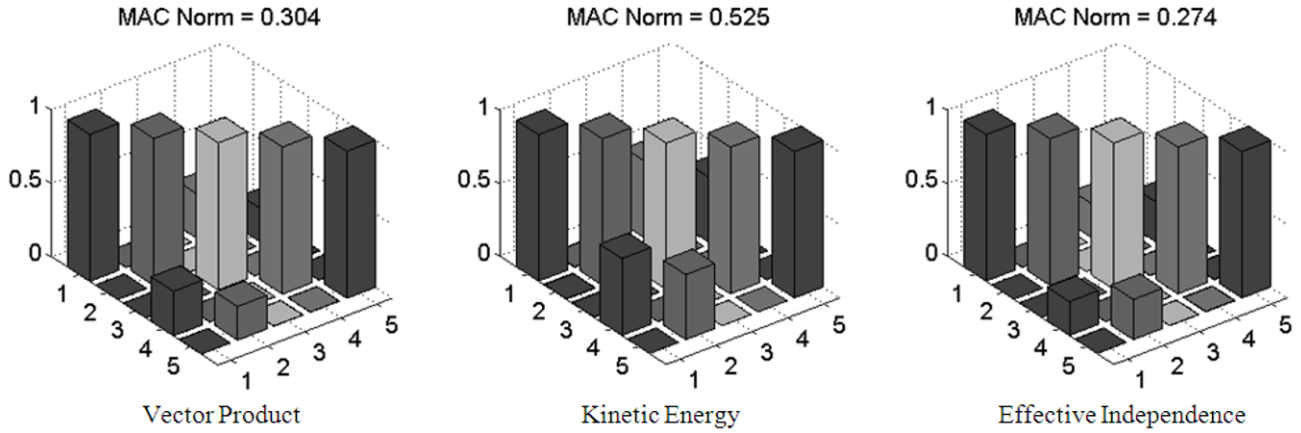


Figure 3: MAC of Identified Mode Shapes

As can be seen in the MAC plots, the VP and EI gave similar results. KE gave slightly worse results than the other two placement techniques. The MAC norm values above each plot show the norm of the off-diagonal values of the MAC matrix.

3.3 Ritz Vector Sensor Placement

For all Ritz vector sensor placement cases the force was placed in the x- and z-directions located at node 1 with an angle, θ , measured from the x-axis, as shown in [figure 4](#).

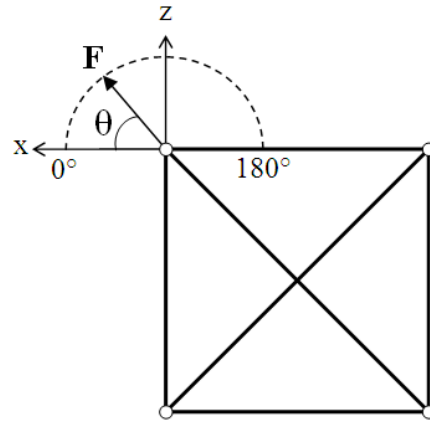


Figure 4: Eight-Bay Truss Force Application

For the first case, a force was placed at node 1 with a 45 degree angle. Using the first five Ritz vectors from the FEM model, 15 sensor locations were found using the three placement techniques. The sensor placement results are shown in [figure 5](#).

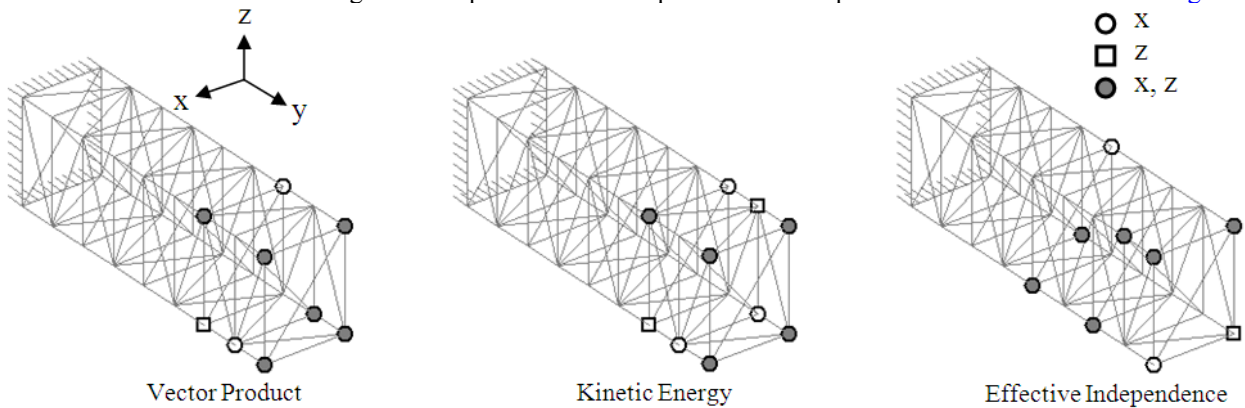


Figure 5: Sensor Locations using Ritz Vectors (Force at node 1, 45 degrees)

Figure 6 shows the MAC plots of the above sensor placement results.

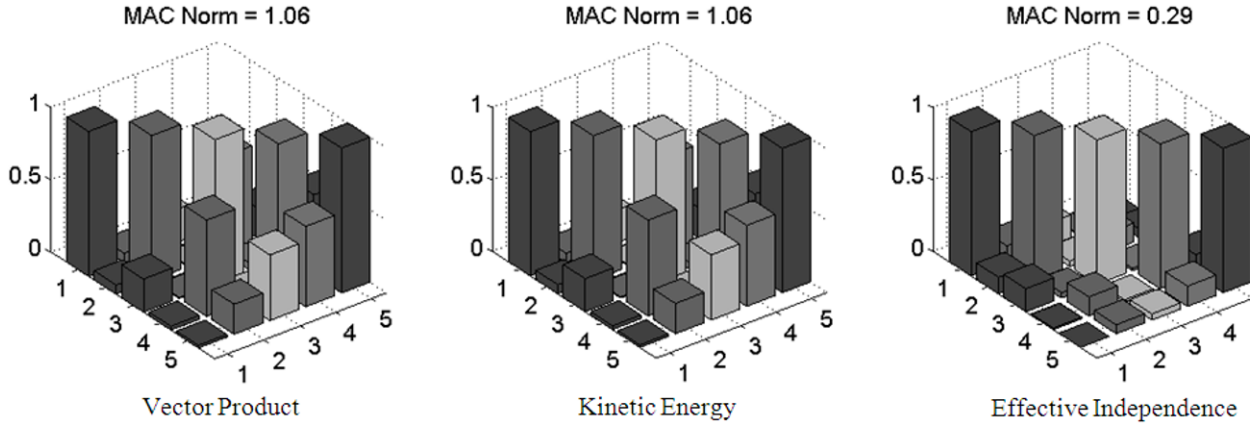


Figure 6: MAC of Identified Ritz Vectors (Force at node 1, 45 degrees)

The VP and KE gave nearly identical results since the sensor placements were very similar. EI gave the best results of the three.

Since Ritz vectors are subject to the force locations and direction, an optimization process can be performed to improve the MAC results. In this case, a sub-optimal solution was found by changing the x- and z-direction force magnitudes at node 1 by varying the force angle on the x-axis from 0 to 180 degrees. The results are shown in figure 7.

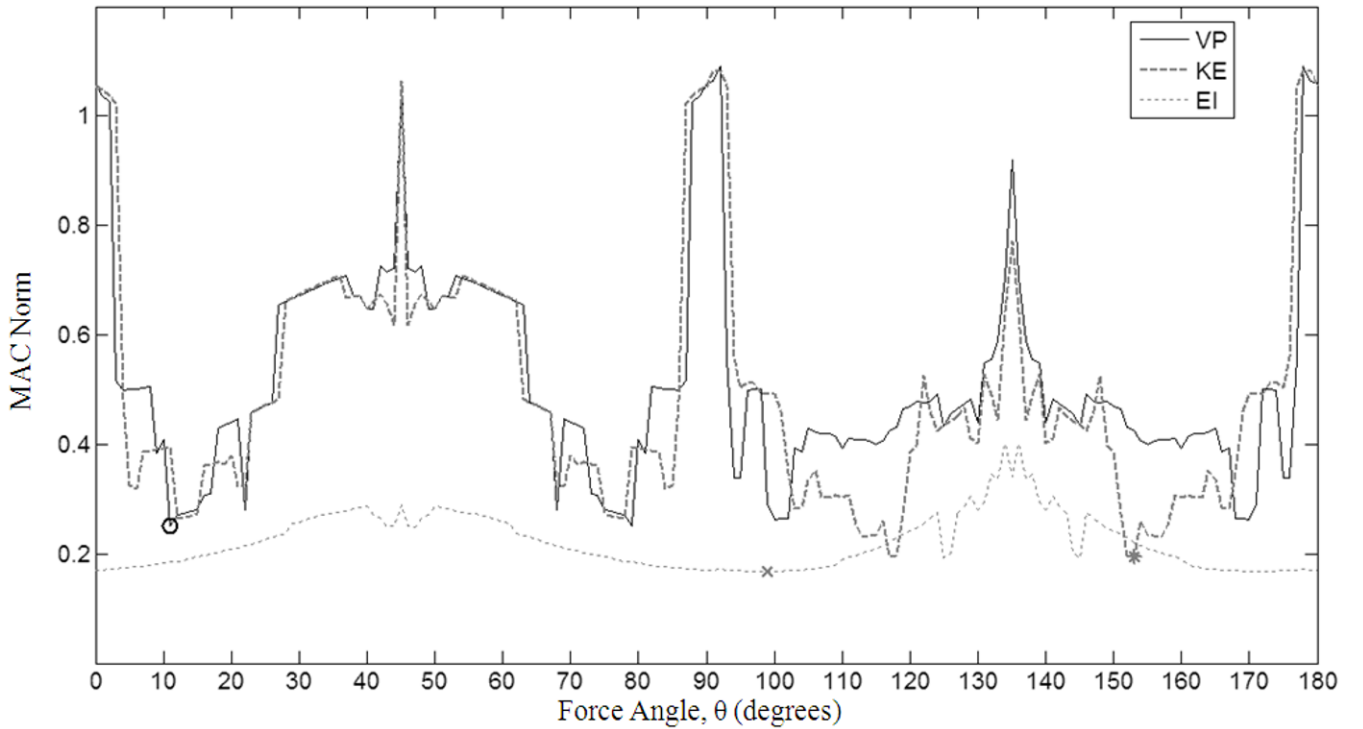


Figure 7: MAC Norm Range for Ritz Vectors

In Figure 7, o, *, and x identify the minimum MAC norm for VP, KE, and EI, respectively. The figure shows clearly that EI gave the best MAC results in most cases, while VP tended to give the worst. When the forces were completely in the x- or z-directions, the VP and KE MAC results were at their worst. Although one would expect symmetry about 90 degrees, the complex lacing pattern creates motion in multiple axes for a force purely aligned in one axis. Note that the MAC norm plots are symmetric about 45 and 135 degrees from 0 to 90 and 90 to 180 degrees, respectively. This plot repeats every 180

degrees. It's apparent that the force selection for case 1 above does not give good MAC results compared to other force directions.

From the MAC norm results from [figure 7](#), a sensor set was found in an attempt to obtain better MAC results. The force was selected at node 1 with an angle of 75 degrees from the x-axis. This selection was made as it nears the minimum for all three placement techniques and would allow for slight alignment error in an experimental test. The first five Ritz vectors from the FEM model were used to find 15 sensor locations. The sensor locations and MAC results are shown in [figures 8 and 9](#) respectively.

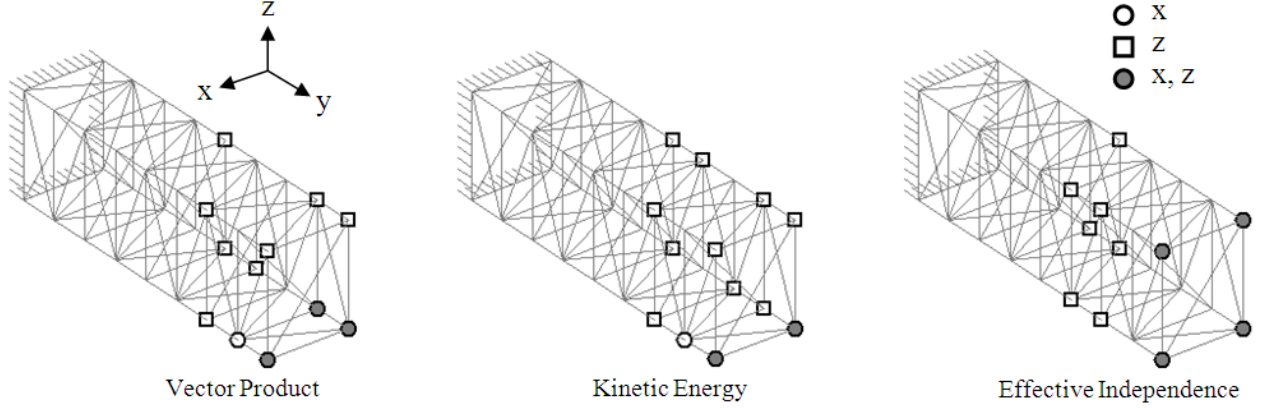


Figure 8: Sensor Locations using Ritz Vectors (Force at node 1, 75 degrees)

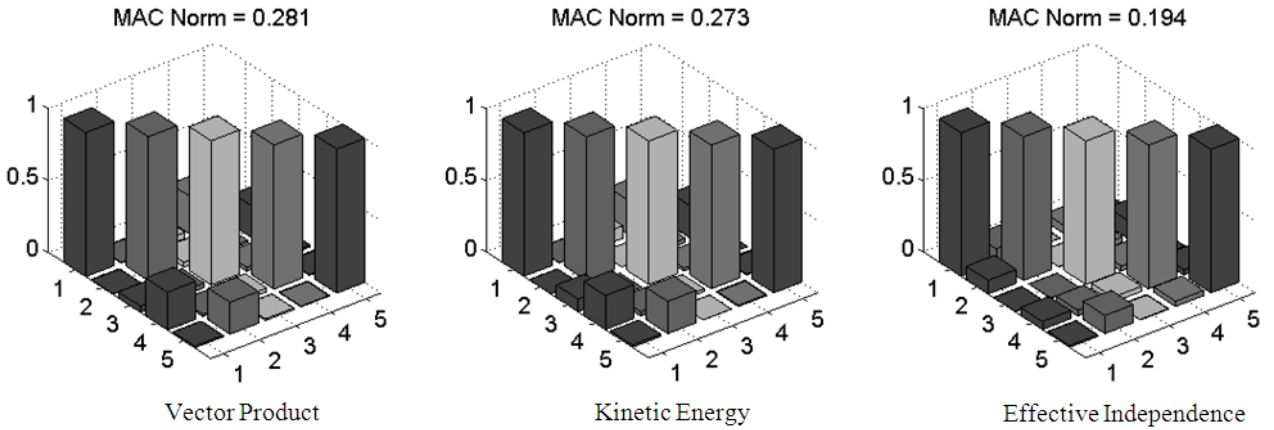


Figure 9: MAC of Identified Ritz Vectors (Force at node 1, 75 degrees)

Comparing the sensor placements for cases 1 and 2 in [figures 5 and 8](#) shows that the force placed at 75 degrees located more sensors in the z-direction, due to the increased force in that axis. [Figure 9](#) shows greatly improved MAC results for the VP and KE methods, while EI was improved slightly.

3.4 Combination Sensor Placement

Sensor placement locations using a mode shape and Ritz vector combination was examined. The aim of combining the two shapes was to determine whether a single sensor set could be used to accurately find both basis vectors experimentally. In this study, the first five mode shapes and first five Ritz vectors were concatenated to a single matrix. The three sensor placements algorithms were then performed using this ten column shape matrix. Because some Ritz vectors could resemble mode shapes, a second procedure was to perform a singular value decomposition (SVD) of the ten column matrix and retain the first number of columns containing 95% of the singular value information. As with the Ritz vectors alone, an optimization process was applied to improve the MAC results. The sub-optimal solution was found by varying the force angle on the x-axis from 0 to 180 degrees as before. The MAC for the reduced mode shapes and Ritz vectors were found separately and then normalized together. [Figure 10](#) shows the MAC norm plots for both cases.

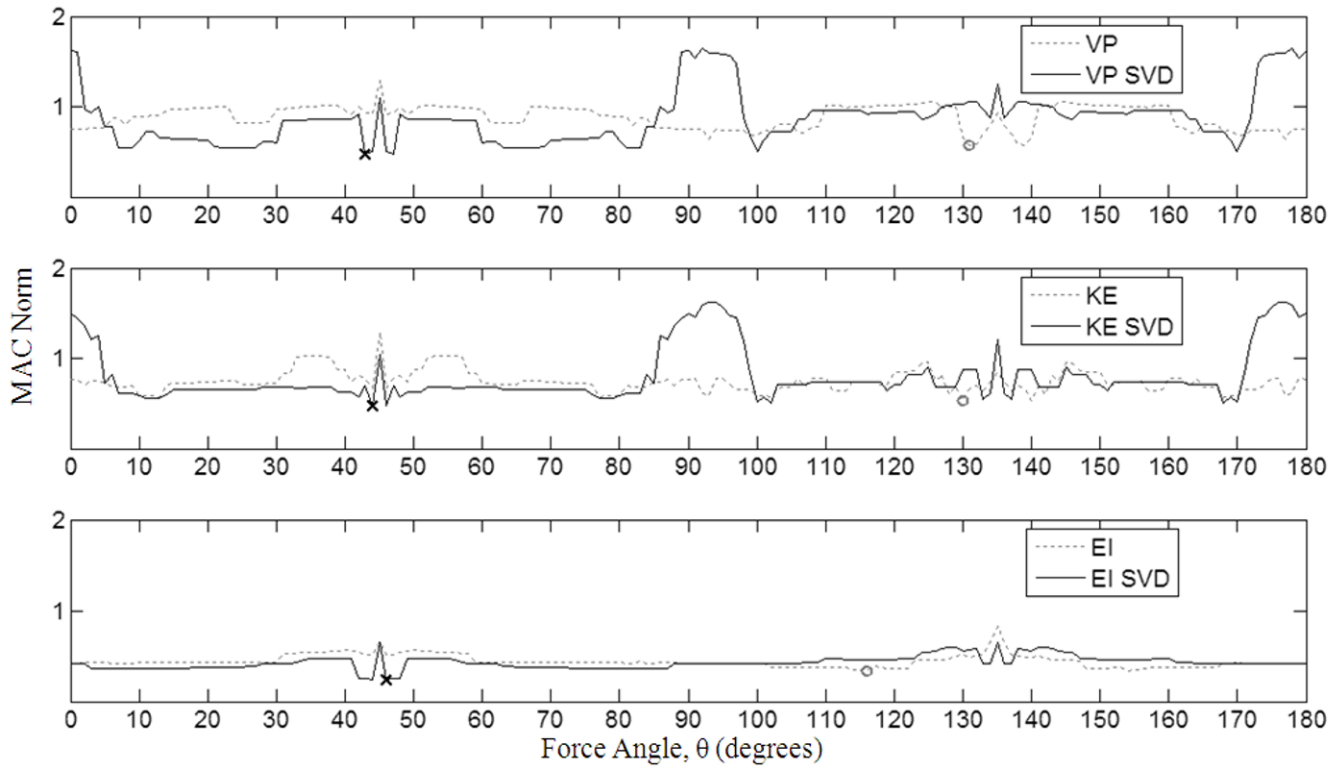


Figure 10: MAC Norm Range for Mode Shapes and Ritz Vectors

The x and o symbols in [figure 10](#) represent the minimum MAC norm values for the SVD and non-SVD cases, respectively. There are a few items to note from [figure 10](#). First, there is no clear-cut choice between the SVD and non-SVD approach. Therefore, it is recommended to calculate both the SVD and non-SVD and make a selection on a case-by-case basis. Secondly, as with the Ritz vectors alone, the VP tends to give the worst results, while EI gives the best.

Using a force at node 1 with a 75 degree angle, sensor sets were found for the mode shape and Ritz vector combination. For comparison purposes, both the SVD and non-SVD cases were considered. [Figures 11](#) and [12](#) show the sensor location results for the non-SVD and SVD cases, respectively.

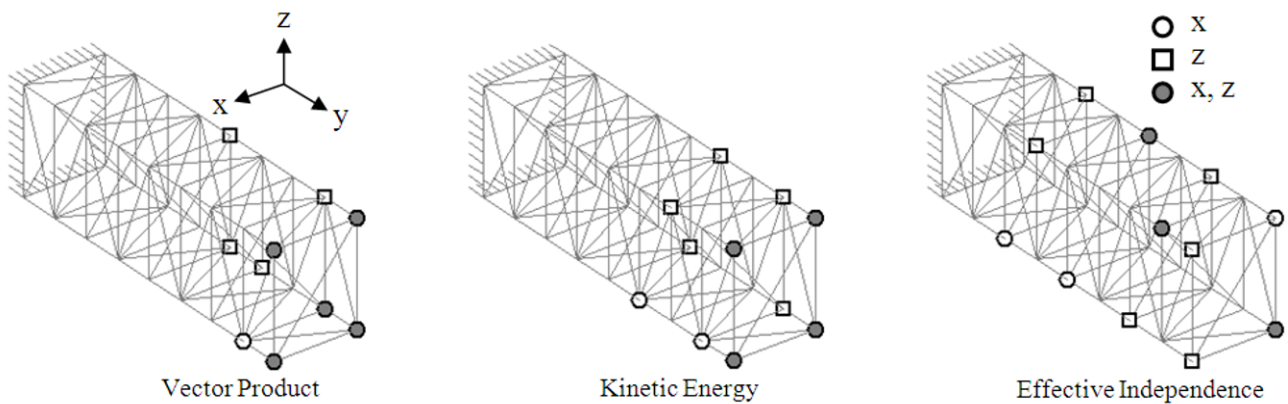


Figure 11: Non-SVD Sensor Locations using Mode Shapes and Ritz Vectors (Force at node 1, 75 degrees)

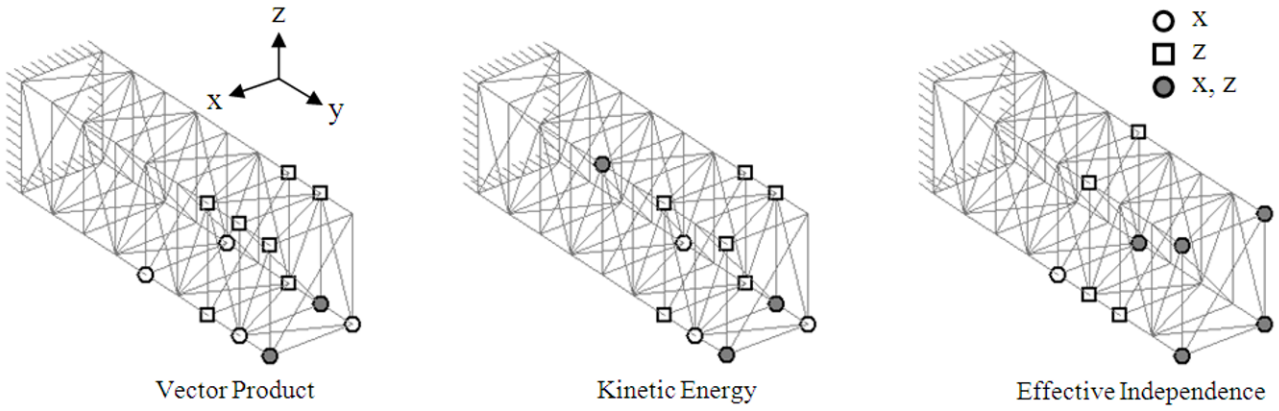


Figure 12: SVD Sensor Locations using Mode Shapes and Ritz Vectors (Force at node 1, 75 degrees)

Comparing the non-SVD and SVD placement results from figures 11 and 12 above shows that for the selected force the SVD spatially spread out the sensors for VP and KE, but grouped the sensors closer together for EI. The MAC was found for mode shapes and Ritz vectors separately for all three sensor placement techniques. The mode shape MAC results are shown in figures 13 to 15.

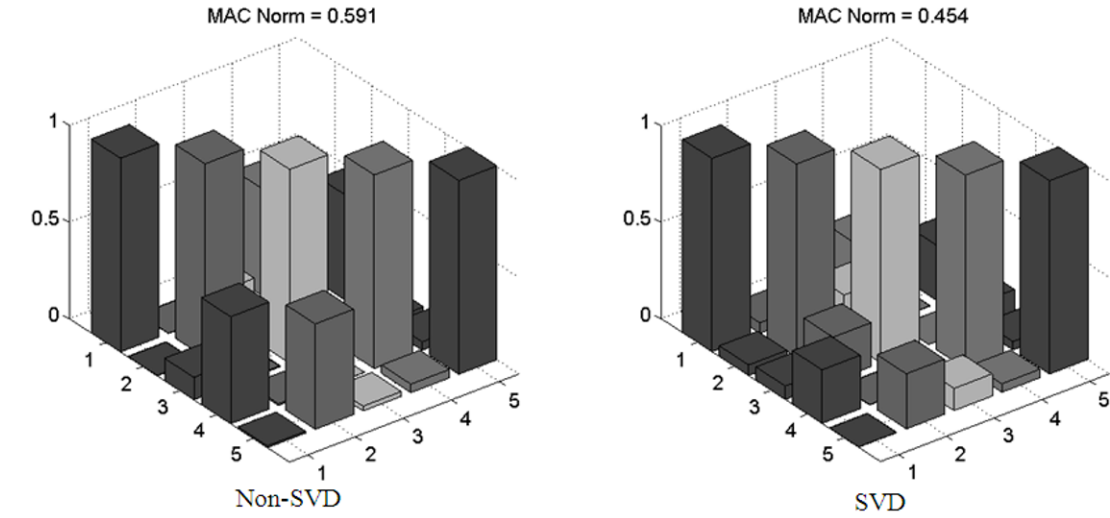


Figure 13: MAC of Identified Mode Shapes using Vector Product (Force at node 1, 75 degrees)

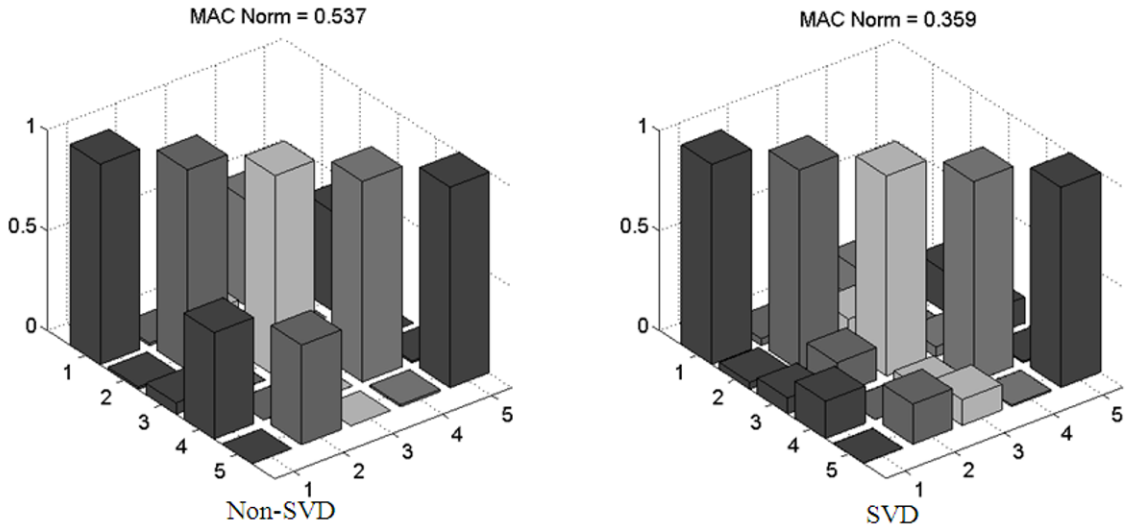


Figure 14: MAC of Identified Mode Shapes using Kinetic Energy (Force at node 1, 75 degrees)

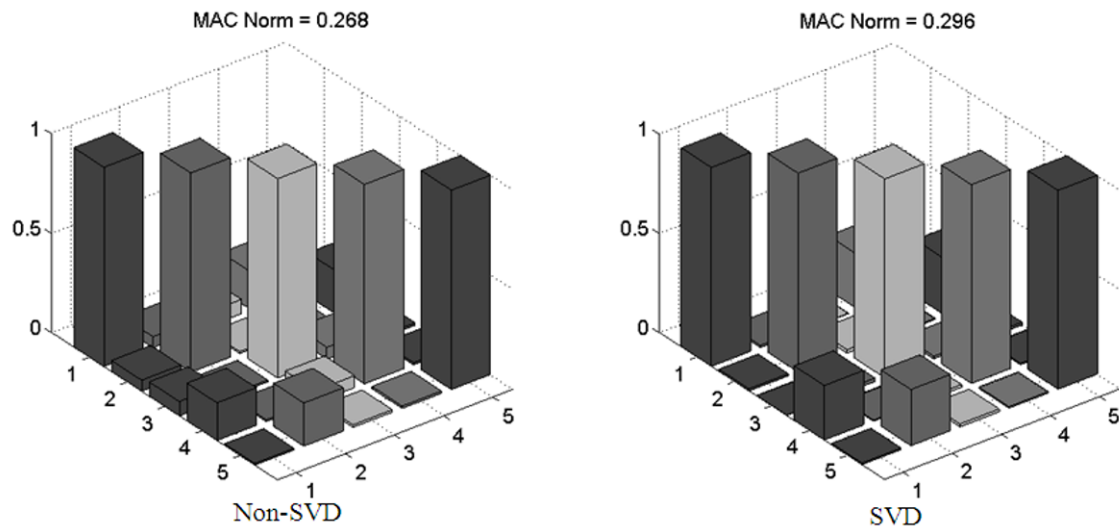


Figure 15: MAC of Identified Mode Shapes using Effective Independence (Force at node 1, 75 degrees)

The mode shape MAC figures above show that mode shapes improved significantly with SVD for VP and KE, while EI gave slightly worse results. It is important to note that the results for EI only changed slightly and still gave better results than the other two methods. The MAC results were generally not as good when compared to the mode shapes calculated alone in [figure 3](#), although the difference is not great. This indicates that combining the mode shapes with Ritz vectors still gave acceptable mode shape results. The only outlier was the KE case with SVD, where the results for the combined basis vectors improved over the mode shapes alone. The improvement may be due to greater spatial distribution of the sensor placement for KE that the combination basis vectors offer. It should also be noted that the results in section 4.2 for KE were not very good.

The MAC was found for the Ritz vectors as shown in [figures 16 through 18](#) below.

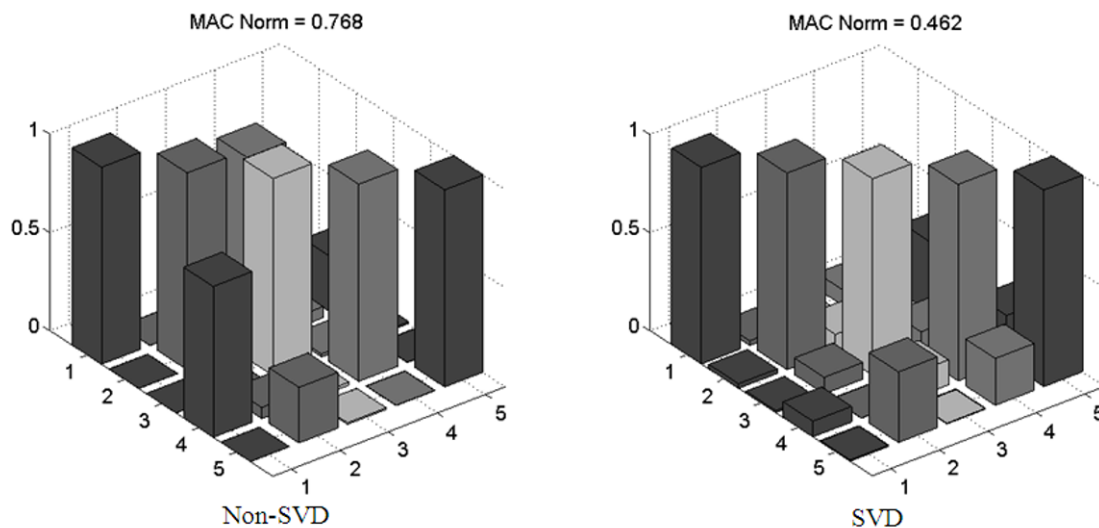


Figure 16: MAC of Identified Ritz Vectors using Vector Product (Force at node 1, 75 degrees)

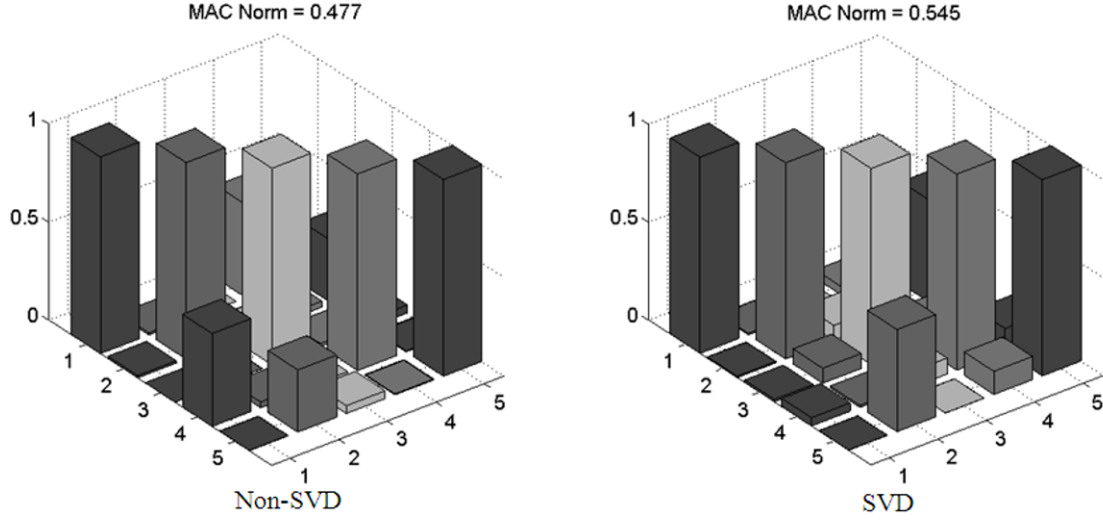


Figure 17: MAC of Identified Ritz Vectors using Kinetic Energy (Force at node 1, 75 degrees)

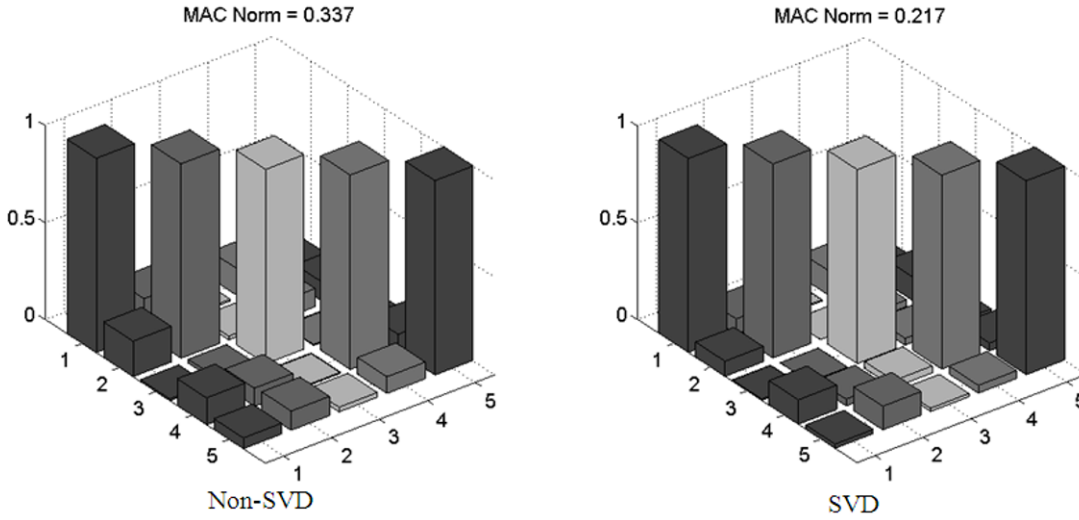


Figure 18: MAC of Identified Ritz Vectors using Effective Independence (Force at node 1, 75 degrees)

The Ritz vector MAC plots above show that the VP and EI methods improved using the SVD. KE did worsen in terms of the MAC norm, but it is important to note that the MAC went from having coupling between two sets of Ritz vectors (1 and 4, 2 and 5) to one set (2 and 5) using the SVD procedure. Again, EI gave the best results of the three techniques. When comparing the MAC results for Ritz vectors alone with the 75 degree force angle, as shown in [figure 9](#), it can be easily deduced that the results deteriorate when the combination basis vectors were used. In the case of EI, the difference between the combination basis vectors and the Ritz vectors alone was negligible. However, as with the mode shape results, the combination basis vectors still gave acceptable Ritz vector results

4 Conclusion

Pre-test planning is an important aspect of structural dynamic analyses. This study aimed at investigating sensor placement utilizing Ritz vectors for the NASA eight-bay truss. Three techniques developed for mode shape analysis in previous studies were utilized: the Vector Product (VP), the Kinetic Energy Product (KE), and Effective Independence (EI). The three techniques were used to find 15 sensor locations for mode shapes, Ritz vectors, and a combination of both. The results showed that VP, KE, and EI successfully identified sensor locations and gave good MAC results for Ritz vectors. Varying the force direction and location was found to change the Ritz vectors, affecting the sensor sets and in turn changing the MAC results. The off-diagonal norms of the MAC plots were used in an optimization process to select a force that would optimize

the results. Generally, the sensor placement for VP and KE gave similar Modal Assurance Criteria (MAC) results, although KE was slightly better in some cases. As was expected, EI gave the best MAC results and therefore the best sensor location results. In an effort to determine if a single sensor set could be used to find both mode shapes and Ritz vectors, the basis vectors were combined and used with the three sensor placement techniques. The results showed that although the basis vectors deteriorated slightly when combined, a single sensor set could identify both mode shapes and Ritz vectors with reasonable accuracy.

5 References

- [1] Kammer, D.C., "Sensor Placement for On-Orbit Modal Identification and Correlation of Large Space Structures," *Journal of Guidance, Control, and Dynamics*, Volume 15 Issue 2, pp.251-259, 1991.
- [2] Larson, C.B., Zimmerman, D.C., and Marek, E.L., "A Comparison of Modal Test Planning Techniques: Excitation and Sensor Placement Using the NASA 8-Bay Truss," *Proceedings of the 12th International Modal Analysis Conference*, pp. 205-211, 1994.
- [3] Yap, K.C. and Zimmerman, D.C., "Optimal Sensor Placement for Dynamic Model Correlation," *Proceedings of the 18th International Modal Analysis Conference*, Volume 4062 Issue 2, pp. 607-612, 2000.
- [4] Wilson, E.L., Yuan, M.W. and Dicken, J.M., "Dynamic Analysis by Direct Superposition of Ritz Vectors," *Earthquake Engineering and Structural Dynamics*, Volume 10 Issue 6, pp. 813-821, 1982.
- [5] Cao, T. and Zimmerman, D.C., "Procedure to Extract Ritz Vectors from Dynamic Testing Data," *ASCE Journal of Structural Engineering*, Volume 125 Issue 12, pp. 1393-1400, 1999.
- [6] Boxoen, T. and Zimmerman, D.C., "Advances in Experimental Ritz Vector Identification," *ASCE Journal of Structural Engineering*, Volume 129 Issue 8, pp. 1131-1140, 2003.
- [7] Kashangaki, T.A.L., "Ground Vibration Tests of a High Fidelity Truss for Verification of On Orbit Damage Location Techniques," *NASA-LaRC Technical Memorandum 107626*, 1992.

SPECTRAL ANALYSIS METHODOLOGY FOR ACOUSTICAL AND MECHANICAL MEASUREMENTS RELATIVE TO HYDRAULIC TURBINE'S GENERATOR

Lafleur F., Bélanger S., Coutu E., and Merkouf A.

Institut de Recherche d'Hydro-Québec, IREQ
1800 Boul-Lionel-Boulet
Varennnes, Québec
Canada, J3X 1S1

ABSTRACT

This paper presents a spectral analysis methodology for acoustical and mechanical measurements performed on hydraulic turbine's generator in the context of power increase diagnostic. The purpose of this analysis is to link the different excitation frequencies to the electromagnetic or mechanical sources. A multidisciplinary team was necessary to provide the necessary inputs and the specific workload for this analysis.

This methodology included a number of activities such as:

- Choice of measurements points and sensors (microphones, accelerometers, strain gages);
- Input of the generator's electromagnetic frequency analysis;
- Input of the rotor and stator's Finite Element Analysis (FEA) modes;
- Knowledge of the hydraulic turbine's generator operating frequencies;
- Measurement and recording of the different time based signals and computing their respective FFTs;
- Identifying peaks in the frequency domain from different mechanical signals;
- And several analyses that leads to identifying excitation sources and frequencies.

The methodology will be presented along with an example of an analysis performed on specific mechanical signals.

INTRODUCTION

In the context of a study of existing generators' power increase, full instrumentation was installed on high-power hydro-generators (> 60 MW). The main goal of this project is to assess the thermal limits of the stator in relation to the increase in power [1,2]. The mechanical limits are also accessed using vibration measurements performed on the generator's rotor and stator. The vibration measurements, combined with other mechanical measurements such as thermal dilatation of the stator, stress measurements on the rotor, and acoustic measurements, allow us to identify the forces acting on both structures. This paper will present the spectral methodology used in this project and will show preliminary results.

ALTERNATOR CHARACTERISTICS

A newly refurbished hydraulic power generator was instrumented and monitored. [Figure 1](#) shows the generator's rotor and stator during refurbishing. [Table 1](#) shows the generator's characteristics.

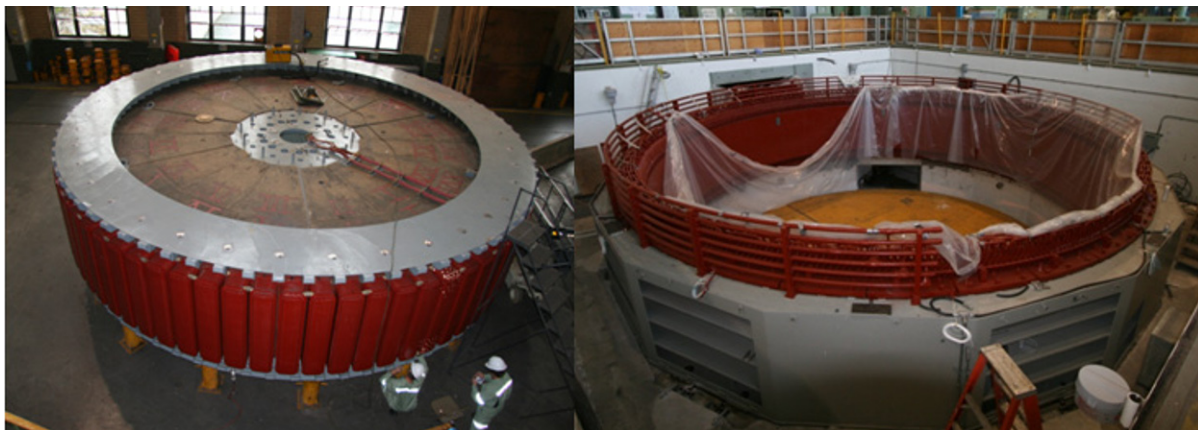


Figure 1: Rotor and stator of the hydraulic generator

Generator's characteristics	
Total power (Winter/Summer)	(75/65) MVA
Power factor	0,85
Real Power (Winter/Summer)	(64/55) MW
Rotation speed	94,7 rpm, 1,58 Hz
Number of poles on the rotor	76
Number of slots on the stator	396
Rotor External diameter	9,08 m
Stator Internal diameter	9,11 m
Gap	12,7 mm
Rotor height	1,6 m

Table 1: Generator characteristics

DESCRIPTION OF MEASUREMENTS

Performance measurements

Generator performance measurements were taken for several operating conditions, namely: Speed No Load (SNL), 0%, 70%, 85% and 100% of the nominal summer power specifications (55 MW).

Acoustical and Mechanical measurements

The mechanical measurements performed on the generator's rotor and stator include sound pressure level, vibration and stress for each of the abovementioned operating condition. Acoustic measurements were performed at 8 different locations on the alternator floor. These measurements were used to evaluate the overall noise level for monitoring the working environment and machinery by non-contact sensing. Frequency analyses (FFT 0-2 kHz and 0-10kHz) were also performed to correlate the acoustic signals to the operating conditions.

Mechanical (vibration and strain gages) instrumentation was installed on the rotor and stator. The rotor instrumentation includes 3 accelerometers installed in the axial, radial, and tangential directions and 16 strain gages (one per cross arm, with their position optimized by finite-element analysis and previous measurements) (Figure 2). The signals coming from the rotor instrumentation were transferred to the acquisition system by RF transmission. The stator's instrumentation allows for acceleration measurements (radial and tangential) of the stator core and stator frame (Figure 3). These mechanical measurements, combined with a thorough frequency analysis, were used to investigate the results obtained during different operating conditions.



Figure 2: Rotor instrumentation

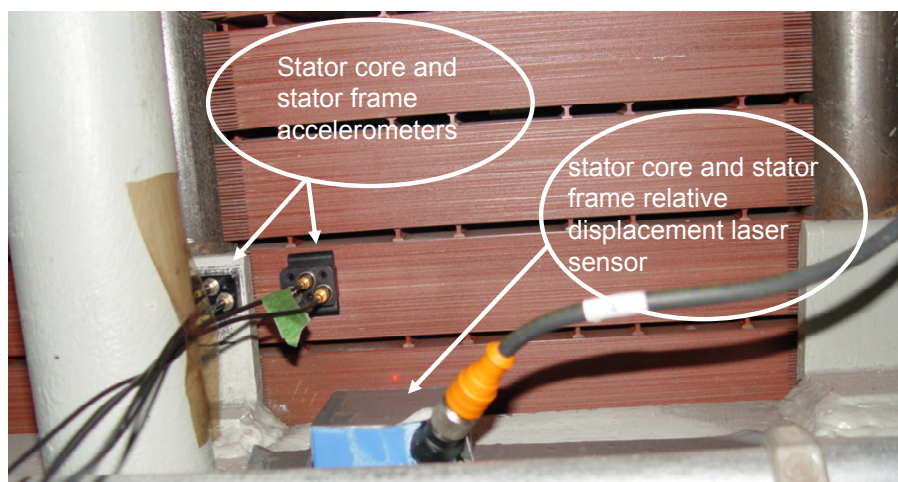


Figure 3: Stator instrumentation

SPECTRAL ANALYSIS METHODOLOGY

A spectral analysis methodology was developed for the various mechanical signals. [Figure 4](#) presents the various steps of this methodology in the form of a logical diagram. The analysis allows the identification of the hydro generator excitation sources using the different sensor inputs (accelerometers, strain gages and microphones). This methodology consists of several steps and has two key goals that can be found at the bottom line of the logical diagram of [figure 4](#). The first goal is to determine the source of the various frequencies detected by comparing those with the spectral contents coming from the stator and rotor. The second goal is to ensure the follow-up of the evolution of a spectral component on a particular signal for the various operating conditions. There are two types of inputs for this analysis which can be found at the top line of the logical diagram ([figure 4](#)). Firstly, the output generated by the various sensors is recorded as a time based signal. These signals, representing acceleration and stress endured by the generator rotor and stator, are analyzed in the frequency domain using a FFT transformation over a frequency range of 0-2kHz. We also use other types of data sets which allow us to identify the excitation frequencies and their causes. These data sets include the knowledge of the operational and mechanical characteristics of the hydraulic generator, the FEA and analytical analysis of the rotor/stator and electromagnetic simulations of the system. These data set allows the identification of the synchronous frequency, the vibration modes and the electromagnetic excitation. These are then compared to the peaks found in the frequency domain of the different mechanical signals. There are three types of comparison which can be made:

- For a specific sensor and a specific operating condition to find the equivalent peaks from the mechanical signal and excitation frequencies.
- Between the peaks of different sensors for the same operating condition to find the common excitation frequencies.
- For a specific sensor and a specific and different operating condition to follow the evolution of one or more excitation peak.

The logical diagram of [figure 4](#) shows the overall process performed during this analysis. Each box of the logic diagram is an action on the input data or on the intermediate results that helps achieve the two key goals described above.

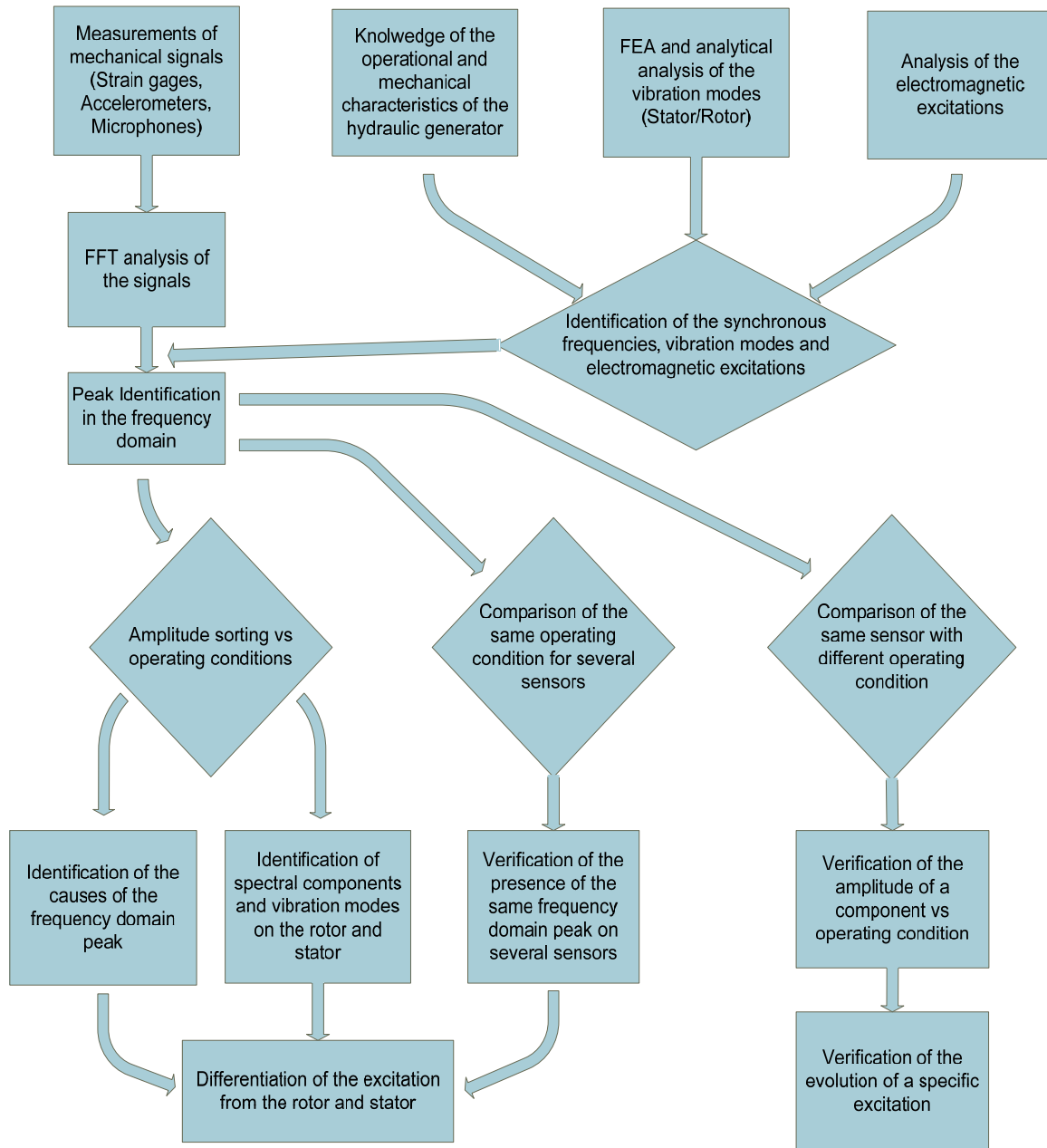


Figure 4: Spectral analysis methodology

TYPICAL SPECTRAL ANALYSIS RESULTS

The typical results of the analysis show that the signals coming off the rotor and the stator have different spectral contents. Figure 5 and 6 respectively show the spectra of the generator's rotor and the stator radial acceleration with an aim of comparing the frequencies content in each signal (the amplitude of the graphs is adjusted to the maximum of each signal). The vibration content of the stator consists principally of harmonics of the even multiple of the electric fundamental frequency (120 Hz, 240 Hz...). Table 2 presents a list of the rotor's main frequencies of vibration as well as their associated causes.

Figure 7 presents the stress spectrum measured on a cross arm of the generator's rotor. We notice that the maximum stress is reached at a frequency of 94.8 Hz, which is similar to the rotor radial acceleration. Another stress peak is reached at a frequency of 1.58 Hz, which corresponds to the actual rotor rotational speed. The stress level at the rotation speed of the rotor (1.58 Hz) is also comparable with the one at the principal frequency, which corresponds to the actual rotor rotational speed.

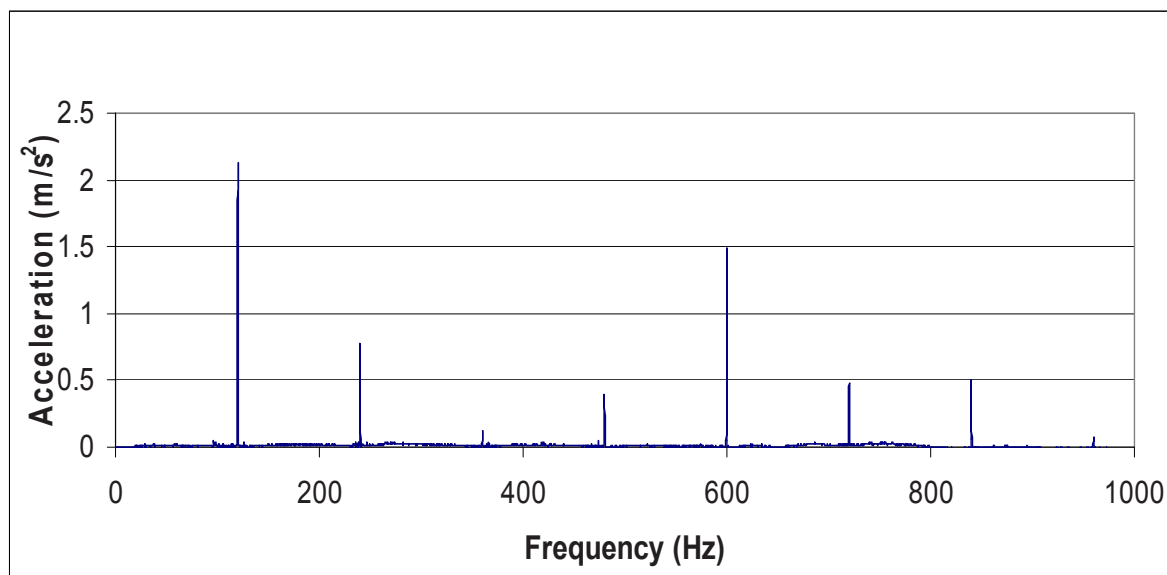


Figure 5: Radial acceleration spectrum of the stator

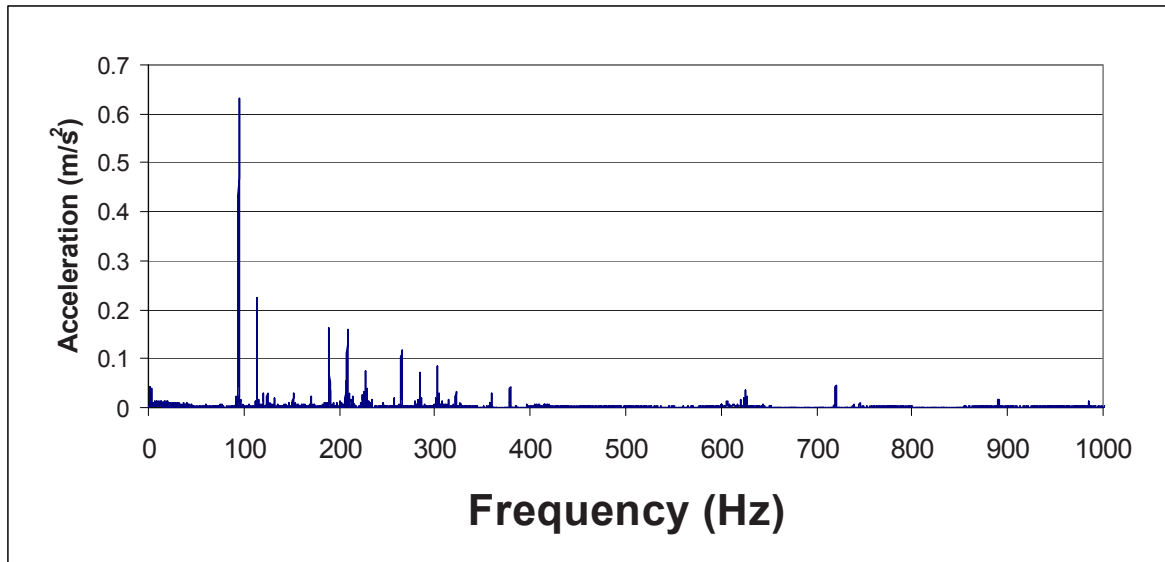


Figure 6: Radial acceleration spectrum of the rotor

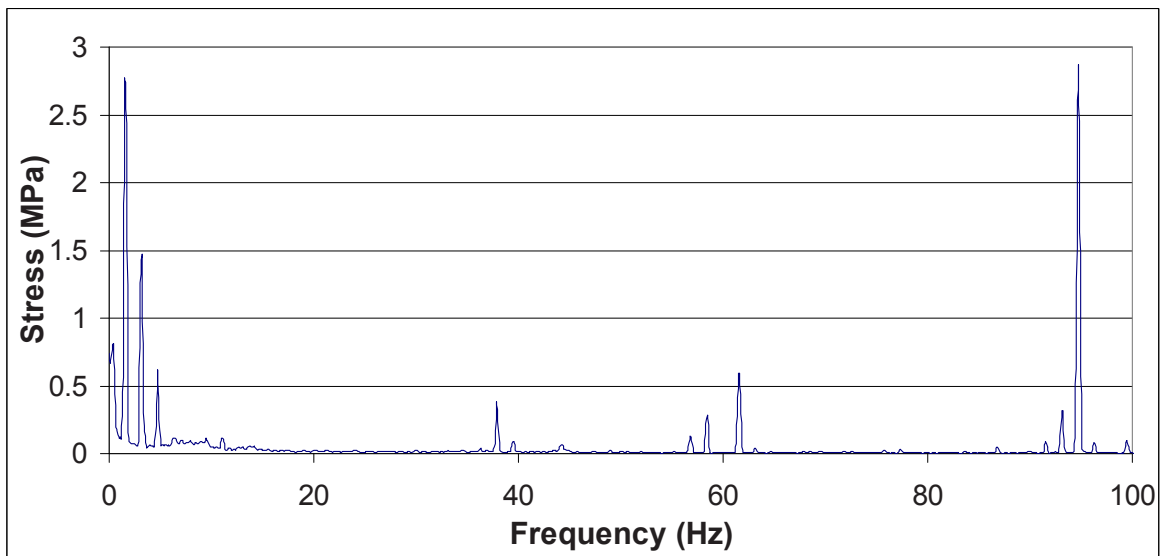


Figure 7: Strain gage spectrum of the rotor cross arm

Frequency (Hz)	Associated causes
94.8	Magneto motive force harmonic Rotation frequency harmonic
113.7	Magneto motive force harmonic Blade passing frequency harmonic
189.5	Magneto motive force harmonic Blade passing frequency harmonic
208.4	Blade passing frequency harmonic
265.2	Magneto motive force harmonic Blade passing frequency harmonic
303.2	Magneto motive force harmonic Blade passing frequency harmonic
227.4	Magneto motive force harmonic Blade passing frequency harmonic
1250.3	Magneto motive force harmonic
284.1	Magneto motive force harmonic
206.8	Rotation frequency harmonic
720.0	harmonics of the even multiple of the electric fundamental frequency
378.9	Rotation frequency harmonic
1.58	Rotation frequency harmonic
191.0	Coincidence with a mode of the rotor (analytical calculation)
625.2	Slot passing frequency

Table 2: Main rotor vibration frequencies and their associated causes

The end result obtained from the study of the frequency versus the operating condition evolution is used in the diagnosis of power increase. The spectral analysis methodology allows us to compare the amplitude of the major spectral components or principal excitations variation against the operating condition for the stator (figure 8) and rotor (figure 9). We notice that the various excitation components do not respond in the same manner when subjected to a power increase. For this type of analysis, we look at the tendency (rising, stable or falling) of a particular excitation according to the increase in power. The tendency informs us on the types of extrapolation of the levels of excitation according to the increase of power beyond the nominal output. The tendency cues us that a specific excitation might rise or fall when the generator's power is increased beyond its nominal output, which helps us determine the main mechanical limiting factors.

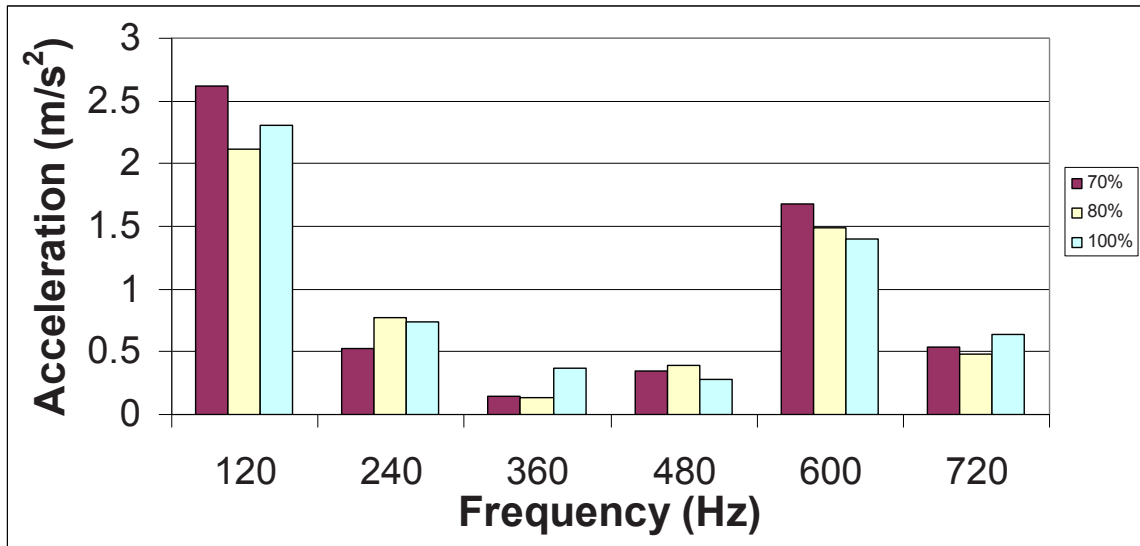


Figure 8 : Acceleration level at the stator vs. operating condition

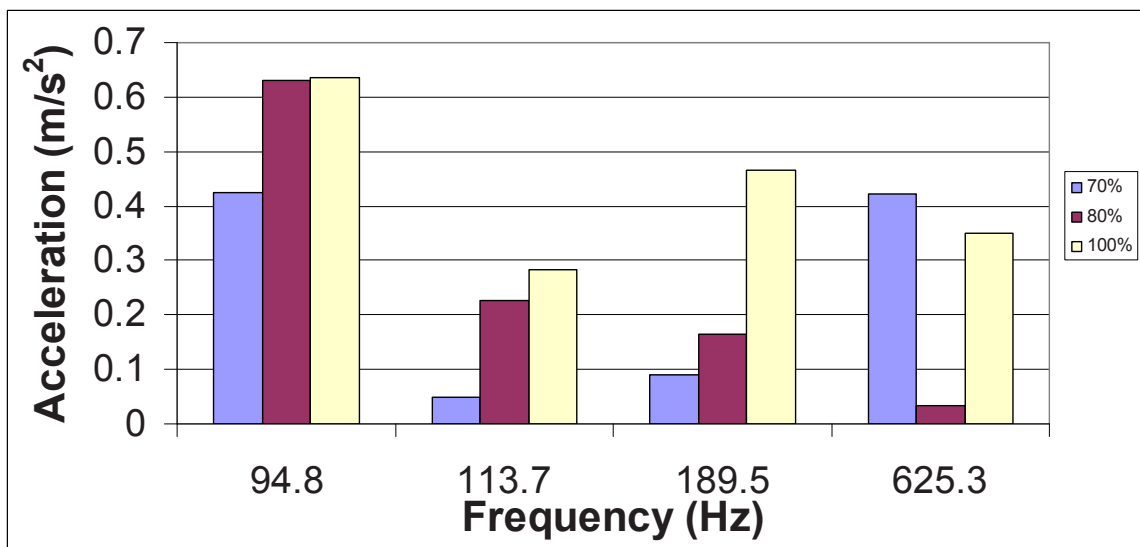


Figure 9 : Acceleration level at the rotor vs. operating condition

CONCLUSION

A spectral methodology analysis of the mechanical signals (accelerometers, strain gauges, microphones) was applied to the diagnostic of power increase of hydroelectric generators. This methodology allows us to better understand the excitation forces on the various parts of the generator. The methodology also allows the understanding of the evolution of a particular excitation in relation to the operating conditions. The complete analysis of the data obtained will enable us to refine the analysis methodology and to obtain a more complete mechanical diagnostic in the power increase of hydro generator.

ACKNOWLEDGMENTS

The authors acknowledge the technical staff of the Hydro-Québec research institute (IREQ) for the quality of their work. This team includes Luc Martell and Mathieu Soares.

REFERENCES

- [1] C. Hudon, M. Chaaban, J. Leduc and D.N. Nguyen, Use of distributed Temperature Measurements to Explain a Generator Winding Faillure, CIGRE 2005, Lausanne, 6 pages.
- [2] F. Lafleur, S. Bélanger, L. Marcouiller and A. Merkouf, Acoustic and mechanical measurements of an hydraulic turbine's generator in relation to power levels and excitation forces, IMAC 2009, Jacksonville, FL, 7 pages.

Transverse vibrations of tapered materially inhomogeneous axially loaded shafts

Arnaldo J. Mazzei, Jr.

*Department of Mechanical Engineering
C. S. Mott Engineering and Science Center
Kettering University
1700 University Avenue
Flint MI, 48504, USA*

Richard A. Scott

*Department of Mechanical Engineering
University of Michigan
G044 W. E. Lay Automotive Laboratory
1231 Beal Avenue
Ann Arbor MI, 48109, USA*

ABSTRACT

Shafts loaded by axial compressive constant forces constitute an area of considerable technical importance. The transverse vibration of such shafts is the subject of the current work. Occasionally the shafts are tapered and of interest is the effect of employing functionally graded materials (FGM), with properties varying in the axial direction, on the buckling load and lowest natural frequency. The shaft cross section is circular and two types of taper are treated, namely, linear and sinusoidal. All shafts have the same volume and length and are subjected to a constant axial force below the static buckling load. Euler-Bernoulli theory is used with the axial force handled by a buckling type model. The problems that arise are computationally challenging but an efficient strategy employing MAPLE®'s two-point boundary value solver has been developed. Typical results for a linear tapered pin-pin shaft where one end radius is twice the other, and the FGM model varies in a power law fashion with material properties increasing in the direction of increasing area, include doubling of the buckling load and first bending frequency increase of approximately 43%, when compared to a homogeneous tapered shaft. For the same material and boundary conditions, a sinusoidal shaft, with mid-radius twice the value of the end ones, increases the buckling load by about 118% and the first frequency by 26%, when compared to a homogeneous sinusoidal shaft.

NOMENCLATURE

A ,	area of the shaft cross section (A_0 initial value)
a, m, n, λ ,	real arbitrary constants
E ,	Young's modulus (E_0, E_t, E_b , Young's modulus values for different non-homogenous materials)
F ,	axial compressive force acting on the shaft
f ,	external transverse force per unit length acting on the shaft
f_1, f_2, f_3, f_4 ,	non-dimensional functions for material / geometrical properties
F_1, F_2 ,	non-dimensional parameters ($F_1 = \frac{F}{\rho_0 A_0 L^2 \Omega_0^2}$, $F_2 = \frac{f}{\rho_0 A_0 L \Omega_0^2}$)
I ,	area moment of inertia of the shaft cross section (I_0 initial value)
K_1 ,	non-dimensional stiffness ($K_1 = \frac{E_0 I_0}{\rho_0 A_0 L^4 \Omega_0^2}$)

L ,	length of shaft
R ,	cylindrical shaft radius
R_1, R_2 ,	conical shaft radii
$R_{midspan}$,	sinusoidal shaft radius at mid-length
R_0 ,	sinusoidal shaft end radius
$S(\xi)$,	non-dimensional spatial function
s ,	numerical parameter ($\sqrt{3/\alpha^2 + \alpha + 1}$)
s_1 ,	numerical parameter ($\sqrt{2\pi/(\beta^2\pi + 2\pi + 8\beta)}$)
t ,	time
w ,	shaft displacement in the y direction
xyz ,	inertial reference system (coordinates x, y, z)
Y ,	non-dimensional shaft displacement in the y direction
α ,	numerical parameter (R_1/R_2)
β ,	numerical parameter ($R_{midspan}/R_0$)
γ_1, γ_2 ,	numerical parameters ($\gamma_1 = E_b/E_t, \gamma_2 = \rho_b/\rho_t$)
ν ,	non-dimensional frequency
ν ,	Poisson's ratio
ρ ,	mass density (ρ_0, ρ_t, ρ_b , density values for different non-homogenous materials)
ξ ,	non-dimensional spatial coordinate
τ ,	non-dimensional time
Ω ,	frequency of the shaft
Ω_0 ,	reference frequency – first bending frequency of a pin-pin homogeneous shaft

INTRODUCTION

This work is concerned with the buckling and transverse vibration of tapered shafts, both homogeneous and non-homogeneous. The non-homogeneity is modeled by the use of functionally graded materials (FGM) with material properties varying in the axial direction. A brief, by no means exhaustive, survey of previous work will now be given.

There is a considerable body of research on the buckling of homogeneous tapered shafts, motivated, in part, by the search for the “strongest column” (i.e., for a given volume and length, what is the maximum buckling load?). See Lee et al. [1] for numerous references on this. Buckling of variable cross-section columns was also treated by, for example, Darbandi et al. [2], Totry et al. [3] and Rahai and Kazemi [4]. The latter pointed out that tapered shapes are widely used in buildings, bridges, bearings etc.

Work on buckling of structures made of functionally graded materials has also been done. See, for example, Naei et al. [5].

Transverse vibrations of tapered shafts have received attention. See, for example, the works of Kim et al. [6] and Elishakoff (references [7] and [8]). In the latter work, the flexural stiffness is frequently taken to be a polynomial function of the axial coordinate and analytical solutions were found.

Here two types of taper are treated, namely, linear and sinusoidal. All shafts are assumed to have the same volume and length. They are subjected to a constant axial force. Two FGM models are used. A basic goal is the determination of the effects of the FGM on the lowest bending frequency.

The underlying mechanical modeling is Euler-Bernoulli theory with the axial force entering by a buckling type approach. The governing equations are partial differential equations with coefficients that vary in a complex fashion. In general analytic solutions cannot be found and numerical methods must be used. Rather than developing a finite element, or finite difference scheme, here a strategy is employed for obtaining results using MAPLE[®]'s two-point boundary value solver. The boundary conditions are taken to be pin-pin.

MODELING

The equation of motion for a shaft in bending under axial load can be derived via a Newton-Euler approach applied to a differential element of the beam (see Figure 1, which shows the underlying variables).

(A detailed derivation focusing on a rotating shaft under axial loading and bending is given by the authors in a previous work [9].) The equation, based on Euler-Bernoulli theory, is given below. The axial force (here compressive: F) enters by a buckling modeling type approach (details can be found in reference [10]).

$$\frac{\partial^2}{\partial x^2} \left(EI \frac{\partial^2 w}{\partial x^2} \right) + F \frac{\partial^2 w}{\partial x^2} + \rho A \frac{\partial^2 w}{\partial t^2} = f$$

(1)

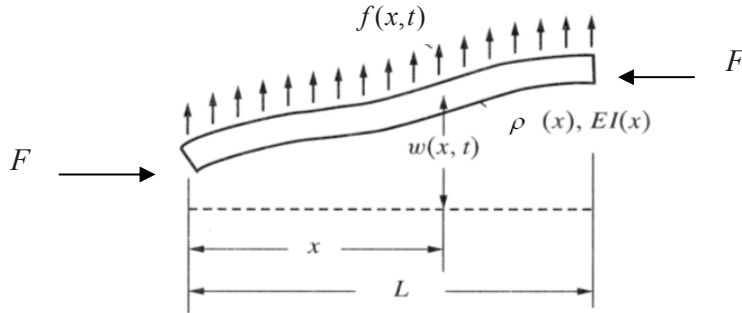


Figure 1 – Beam configuration element

No assumption was made for the material type in the derivation of equation (1). Thus, it can be either a homogeneous or non-homogeneous material. Here both types are considered. The non-homogeneous materials utilized are Functionally Graded Materials (FGM, see, for example, reference [11]).

Here an exploration is made on the joint use of tapering and non-homogeneous materials. Circumstances may dictate the use, and shape, of tapers. Here two types are considered: conical (linear) and sinusoidal following a model of Lee et al. [1]. All shafts are assumed to have the same volume and length. For the linear taper the volume assumption leads to the following relations for the cross-sectional areas and area moments of inertia:

$$A(x) = A_0 s^2 \left[\alpha + (1 - \alpha) \frac{x}{L} \right]^2, \quad I(x) = I_0 s^4 \left[\alpha + (1 - \alpha) \frac{x}{L} \right]^4 \quad (2)$$

where α is the ratio between the smallest to the largest radius of the shaft: $\alpha = R_1/R_2$ and $s = \sqrt{3/(\alpha^2 + \alpha + 1)}$.

For the sinusoidal case the relations are:

$$A(x) = A_0 s_1^2 \left[1 + \beta \sin(\pi \frac{x}{L}) \right]^2, \quad I(x) = I_0 s_1^4 \left[1 + \beta \sin(\pi \frac{x}{L}) \right]^4 \quad (3)$$

where $\beta = R_{midspan}/R_0$ is the ratio between the mid-span radius to one end radius (radii end values are the same), and $s_1 = \sqrt{2\pi/(\beta^2\pi + 2\pi + 8\beta)}$.

Next, two types of FGM are considered.

FGM I

For this model, as done by Chiu and Erdogan [12], the material is assumed to be isotropic and non-homogeneous with properties given by:

$$E(x) = E_0 \left(a \frac{x}{L} + 1 \right)^m, \quad \rho(x) = \rho_0 \left(a \frac{x}{L} + 1 \right)^n \quad (4)$$

where a , m and n are arbitrary real constants with $a > -1$. E_0 and ρ_0 are the Young's modulus and mass density at $x = 0$.

A non-dimensional version of equation (1) is developed next. By taking $\tau = \Omega_0 t$, $\nu = \Omega/\Omega_0$, $\xi = x/L$, $Y = w/L$,

$I(x) = I_0 s^4 [\alpha + (1 - \alpha)\xi]^4 = I_0 f_2(\xi)$, $A(x) = A_0 s^2 [\alpha + (1 - \alpha)\xi]^2 = A_0 f_4(\xi)$, $E(x) = E_0 (a\xi + 1)^m = E_0 f_1(\xi)$, $\rho(x) = \rho_0 (a\xi + 1)^n = \rho_0 f_3(\xi)$ and substituting into equation (1), one obtains, for the linear taper case:

$$\left(\frac{E_0 I_0}{\rho_0 A_0 L^4 \Omega_0^2} \right) \frac{\partial^2}{\partial \xi^2} (f_1(\xi) f_2(\xi) \frac{\partial^2 Y}{\partial \xi^2}) + \left(\frac{F}{\rho_0 A_0 L^2 \Omega_0^2} \right) \frac{\partial^2 Y}{\partial \xi^2} + f_3(\xi) f_4(\xi) \frac{\partial^2 Y}{\partial \tau^2} = \frac{f}{\rho_0 A_0 L \Omega_0^2} \quad (5)$$

where Ω_0 is a reference frequency (first bending frequency of a pin-pin cylindrical shaft).

Alternatively, one can take $I(x) = I_0 s_1^4 [1 + \beta \sin(\pi \xi)]^4 = I_0 f_2(\xi)$ and $A(x) = A_0 s_1^2 [1 + \beta \sin(\pi \xi)]^2 = A_0 f_4(\xi)$. This allows equation (5) to be used for the sinusoidal taper case.

In equation (5), seeking vibration frequencies, one can assume $Y(\xi, \tau) = S(\xi)\sin(\nu\tau)$ and harmonic external forcing $f = f \sin(\nu\tau)$. This leads to:

$$K_1 \frac{\partial^2}{\partial \xi^2} (f_1(\xi)f_2(\xi) \frac{\partial^2 S(\xi)}{\partial \xi^2}) + F_1 \frac{\partial^2 S(\xi)}{\partial \xi^2} - \nu^2 f_3(\xi)f_4(\xi)S(\xi) = F_2 \quad (6)$$

where $K_1 = \frac{E_0 I_0}{\rho_0 A_0 L^4 \Omega_0^2}$, $F_1 = \frac{F}{\rho_0 A_0 L^2 \Omega_0^2}$ and $F_2 = \frac{f}{\rho_0 A_0 L \Omega_0^2}$.

Given the properties of the FGM and equations (2), i.e., $f_1(\xi)$, $f_3(\xi)$, $f_2(\xi)$ and $f_4(\xi)$, numerical solutions for equation (6) can, in principle, be obtained.

FGM I is taken to be a composite made from aluminum and silicon carbide. The properties of the material are given in Table 1 and are taken from reference [12].

Aluminum / Silicon Carbide	
E_0 (GPa)	105.197
ρ_0 (kg/m ³)	2710.000
a	1.14568
m	1.00000
n	0.17611
ν	0.33

Table 1 – Material properties for Al / SiC FGM

FGM II

The second FGM model utilized assumes a composition derived from a mixture of two materials, with the material variation given by a power-law gradient (see, for instance, reference [13]). The material properties are given by:

$$E(x) = E_b + (E_t - E_b) \left(\frac{x}{L} \right)^\lambda, \quad \rho(x) = \rho_b + (\rho_t - \rho_b) \left(\frac{x}{L} \right)^\lambda \quad (7)$$

where λ is a positive constant describing the volume fraction, which can be determined experimentally ([13]). The subscripts b and t refer to the value of the parameter at $x = 0$ and $x = L$, respectively. These values are the ones for the “pure” materials involved in the composition of the FGM and are obtained from tables or manufacturer’s specifications. Here, the FGM is taken to be a mixture of aluminum and steel.

Taking $E_b = \gamma_1 E_t$ and $\rho_b = \gamma_2 \rho_t$, one can write:

$$E(x) = E_t \left[\gamma_1 + (1 - \gamma_1) \xi^\lambda \right], \quad \rho(x) = \rho_t \left[\gamma_2 + (1 - \gamma_2) \xi^\lambda \right] \quad (8)$$

Equation (6) can still be used with the following modifications:

$$f_1(\xi) = [\gamma_1 + (1 - \gamma_1)\xi^\lambda], f_3(\xi) = [\gamma_2 + (1 - \gamma_2)\xi^\lambda], K_1 = \frac{E_t I_0}{\rho_t A_0 L^4 \Omega_0^2}, F_1 = \frac{F}{\rho_t A_0 L^2 \Omega_0^2} \text{ and } F_2 = \frac{f}{\rho_t A_0 L \Omega_0^2}.$$

(9)

NUMERICAL RESULTS

The numerical values used in the simulations are: $L = 0.896$ m, $R = 0.034950$ m. Aluminum properties are: $E = 0.71\text{E}11$ N/m² and $\rho = 2710$ Kg/m³; and steel properties are: $E = 2.10\text{E}11$ N/m² and $\rho = 7850$ Kg/m³. The exact value of the first bending frequency of a homogeneous aluminum shaft with these dimensions can be calculated from (see, for example, reference [10]): $\Omega_0 = \frac{\pi^2}{L^2} \sqrt{\frac{EI}{\rho A}} \cong 175$ Hz.

The FGMs utilized are Aluminum / Silicon Carbide (AlSiC – FGM I) and Aluminum / Steel (AlSt – FGM II, $E_b = E_{\text{Aluminum}}$, $\rho_b = \rho_{\text{Aluminum}}$).

Buckling load

The value of the axial load F used must be less than the static buckling load, which can be found from the equation

$$K_1 \frac{\partial^2}{\partial \xi^2} (f_1(\xi) f_2(\xi) \frac{\partial^2 S(\xi)}{\partial \xi^2}) + F_1 \frac{\partial^2 S(\xi)}{\partial \xi^2} = F_2$$

(10)

subjected to pin-pin conditions and with $F_2 = 0$.

Equation (10) does not in general possess an analytic solution. Here, rather than generating a finite element, or finite difference solution, use is made of MAPLE[®]'s two-point boundary value solver as follows. Assigning a value for the external load F_2 , the problem is solved for various compressive loads and, observing the shaft deflection, one can infer the critical load by noting when an abrupt change in the sign of the deflection occurs.

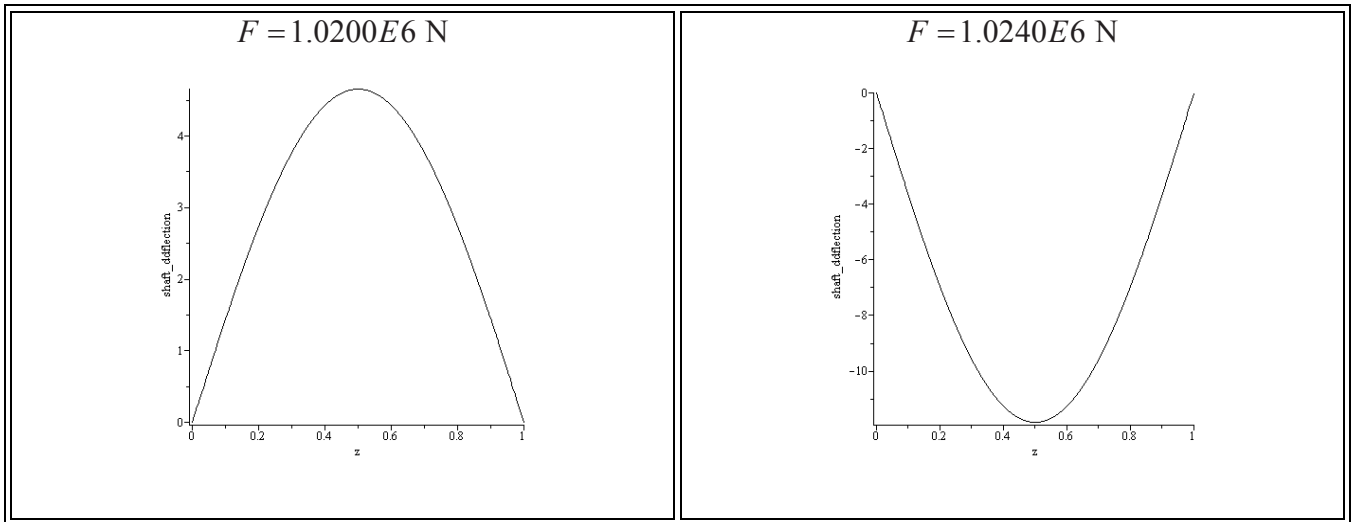


Figure 2 – Aluminum shaft static deflection for increasing compressive loads

Figure 2 shows the results for a homogenous cylindrical pin-pin aluminum shaft. The critical load is approximately $1.0240E6$ N. This result is in very good agreement with the theoretical Euler's critical load for this problem ($P_{crit} = EI\pi^2/L^2 = 1.0229E10^6$ N), which lends confidence to the numerical approach.

In the case of non-homogeneous materials and conical shafts, two distinct situations are possible. The material properties can increase or decrease in the direction of increasing cross-sectional area. Here this is controlled by the parameter α and two cases are investigated, namely $\alpha = 0.5$ (area increasing in the direction of increasing material properties) and $\alpha = 2.0$ (area decreasing).

Utilizing the procedure described above for cylindrical and conical shafts, made of both homogeneous and non-homogeneous materials, the critical loads were calculated and are given in Table 2.

	Homogeneous Shaft (Al)		FGM I shaft (AlSiC)		FGM II shaft (AlSt)	
	Cylindrical	Conical	Cylindrical	Conical	Cylindrical	Conical
$P_{crit} (\alpha = 0.5)$	1.02E6 N	7.52E5 N	2.33E6 N	1.53E6 N	1.93E6 N	1.20E6 N
$P_{crit} (\alpha = 2.0)$	1.02E6 N	7.52E5 N	2.33E6 N	1.90E6 N	1.93E6 N	1.64E6 N

Table 2 – Critical loads for homogeneous and non-homogeneous cylindrical and conical shafts

The table shows that in all cases the use of a linear taper decreases the buckling load, a non-beneficial result. If conical tapers are mandated the user should be aware of this. For non-homogeneous materials, the table shows that in the case $\alpha = 2.0$, the use of the FGM is beneficial in that the decrease in the buckling load is considerably less when compared to the homogeneous case.

Note that for cylindrical shafts, the use of AlSiC increases the load by approximately 128% when compared to pure aluminum. For AlSt the increase is about 89%. For conical shafts, the AlSiC leads to an increase of approximately 103% and the AlSt leads to an increase of about 60%.

Next the case of non-homogeneous materials and sinusoidal shafts is considered. Equation (10) is utilized with the appropriate area moment of inertia function ($f_2(\xi) = s_1^4 [1 + \beta \sin(\pi\xi)]^4$). The parameter β controls the sinusoidal profile of the shaft and here, as an example, it is taken to be 1. This gives a shaft with a mid-radius that is twice the size of the end radii.

Using the above procedure the critical loads were calculated and are shown in Table 3.

	Homogeneous Shaft (Al)		FGM I shaft (AlSiC)		FGM II shaft (AlSt)	
	Cylindrical	Sinusoidal	Cylindrical	Sinusoidal	Cylindrical	Sinusoidal
$P_{crit} (\beta = 1)$	1.02E6 N	1.32E6 N	2.33E6 N	2.88E6 N	1.93E6 N	2.29E6 N

Table 3 – Critical loads for homogeneous and non-homogeneous cylindrical and sinusoidal shafts

Note that for pure aluminum, the sinusoidal shaft increases the buckling load by 29% when compared to the cylindrical shaft.

For the non-homogeneous materials results are as follows. For AlSiC, the sinusoidal shaft gives an increase of 24% on the critical load when compared to the cylindrical shaft. Similarly, for the AlSt the increase is 19%. Also, the use of an AlSiC sinusoidal shaft in place of a pure aluminum sinusoidal shaft can lead to an increase in the load of about 118%. In the case of AlSt this increase can be about 73%.

These are all beneficial results and demonstrate that both changes in profile and material can drastically improve the critical buckling load.

Frequencies

Next the influences of the FGM, and shaft profiles, on the first bending frequency are investigated. In the subsequent numerical simulations, the values for the compressive load are chosen to be 80% of the smallest value.

Equation (6), with $F_2 = 0$, has to be solved subjected to pin-pin boundary conditions. This again, in general, does not have analytic solutions. The following numerical strategy is employed based on MAPLE[®]'s two-point boundary value solver and by assigning a value to the forcing function F_2 . By varying the frequency ν and observing the mid-span deflection, the resonant frequency can be found on noting where an abrupt change (positive to negative) occurs.

For a pure aluminum cylindrical shaft, an analytical solution involving the frequency ν can be found using MAPLE[®]. Figure 3 shows a plot of the mid-span deflection, as a function of the frequency ν , clearly showing a resonance at $\nu = 0.65$.

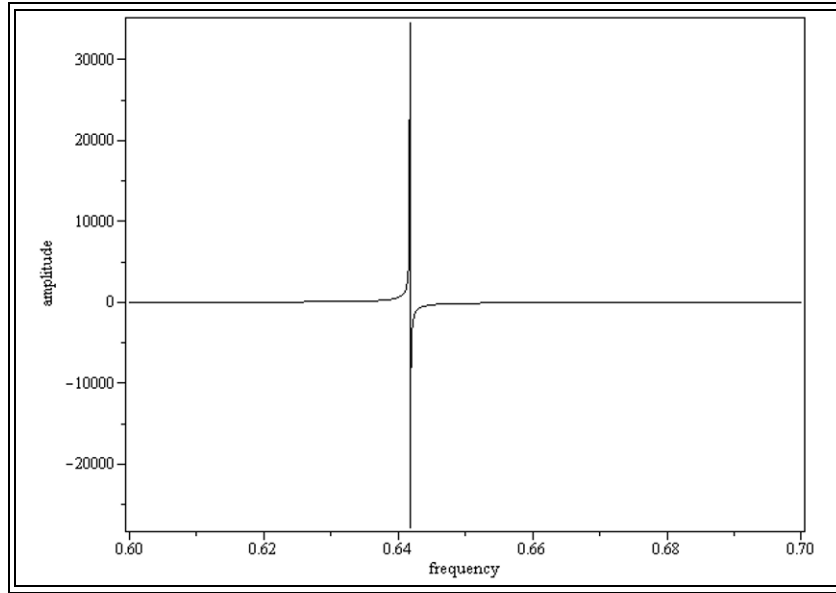


Figure 3 – Shaft deflections at mid-span as a function of ν

In the following the numerical method described above is tested against this value. Assuming a value of 1 for the external forcing and varying ν , the resultant deflections are plotted and investigated. Figure 4 shows these deflections for two distinct values of the frequency (close to the resonant value estimated above).

Note that the figure confirms the value 0.65 as the resonant frequency, lending confidence to the procedure.

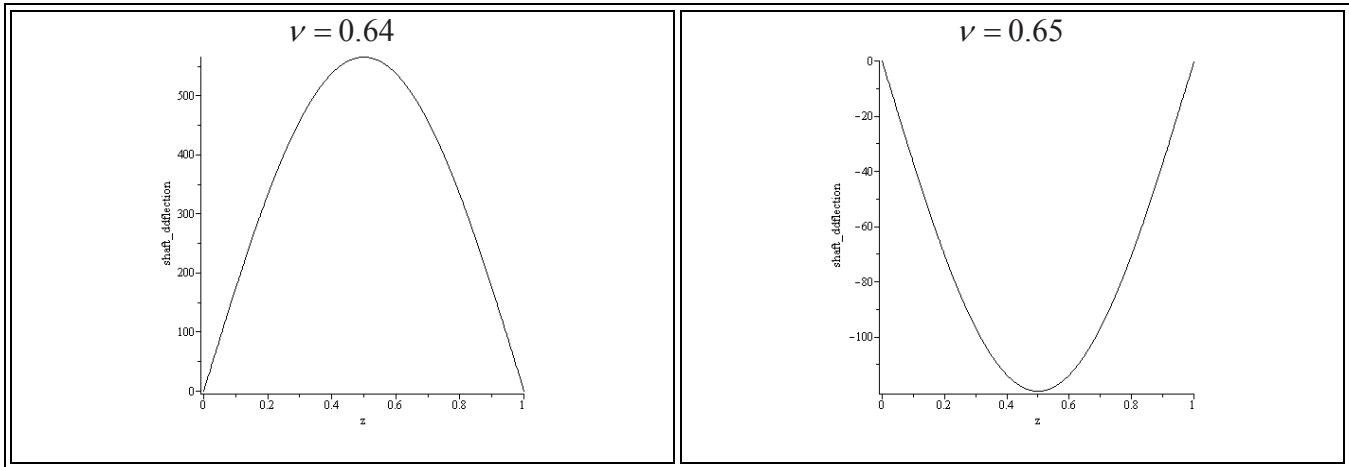
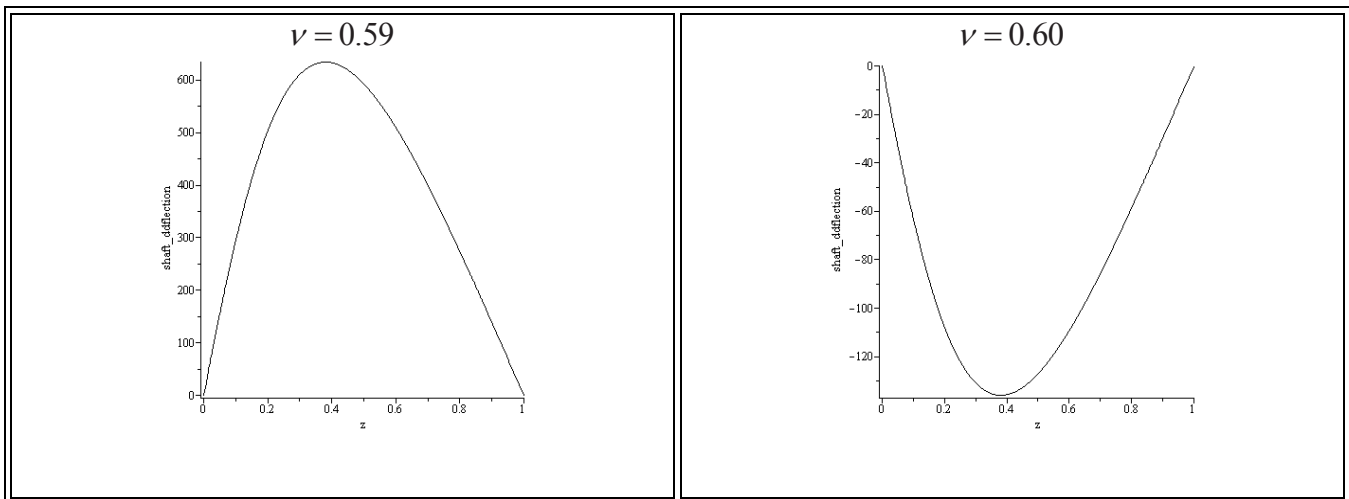


Figure 4 – Aluminum cylindrical shaft deflections for $\nu = 0.64$ and 0.65 respectively

For the conical shafts the two values of the parameter α were used and, for instance, [Figure 5](#) shows the deflections for the conical AlSiC shaft for $\alpha = 0.5$. Resonance is seen around $\nu = 0.60$.



[Figure 5](#) – Aluminum silicon carbide conical shaft deflections for $\nu = 0.59$ and 0.60 respectively

Proceeding in this fashion, resonance values were calculated and the results can be seen in [Table 4](#).

	Homogeneous Shaft (Al)		FGM I shaft (AlSiC)		FGM II shaft (AlSt)	
	Cylindrical	Conical	Cylindrical	Conical	Cylindrical	Conical
ν ($\alpha=0.5$)	0.65	0.42	1.01	0.60	0.71	0.42
Resonance Frequency $= \nu \Omega_0$ ($\Omega_0 = 175\text{Hz}$)	113.75 Hz	73.50 Hz	176.75 Hz	105.00 Hz	124.25 Hz	73.50 Hz
ν ($\alpha=2.0$)	0.65	0.42	1.01	0.84	0.71	0.63
Resonance Frequency $= \nu \Omega_0$ ($\Omega_0 = 175\text{Hz}$)	113.75 Hz	73.50 Hz	176.75 Hz	147.00 Hz	124.25 Hz	110.25 Hz

Table 4 – Linear taper summary results for shaft resonant frequencies as a function of shaft profile and material

Note that the cylindrical AlSiC shaft increases the frequency by about 55% when compared to the aluminum one. The AlSt gives an increase of about 9%.

For the conical shafts where the area increases in the direction of increasing material properties, the AlSiC increases the frequency by about 43% while the AlSt practically does not change it. In the case of area decreasing in the direction of increasing material properties, the AlSiC gives an increase of 100% while the AlSt shows an increase of about 50%.

The results demonstrate that the FGM can lead to increases in the frequency and can be beneficial for shaft applications, under compressive loads, that require this goal.

The procedure given above was also utilized for obtaining the frequencies of the sinusoidal shafts (with $f_2(\xi) = s_1^4 [1 + \beta \sin(\pi\xi)]^4$ and $f_4(\xi) = s_1^2 [1 + \beta \sin(\pi\xi)]^2$ in equation (6)). The results can be seen in [Table 5](#).

	Homogeneous Shaft (Al)		FGM I shaft (AlSiC)		FGM II shaft (AlSt)	
	Cylindrical	Sinusoidal	Cylindrical	Sinusoidal	Cylindrical	Sinusoidal
ν	0.65	0.92	1.01	1.16	0.71	0.80
Resonance Frequency $= \nu \Omega_0$ ($\Omega_0 = 175\text{Hz}$) ($\beta = 1$)	113.75 Hz	161.00 Hz	176.75 Hz	203.00 Hz	124.25 Hz	140.00 Hz

Table 5 – Sinusoidal taper summary results for shaft resonant frequencies as a function of shaft profile and material

Comparing the homogeneous shafts, note that the sinusoidal one increases the first bending frequency by 42%.

In the case of the non-homogeneous shafts, the AISiC sinusoidal one increases the frequency by 15% and the AISt by 13%.

Here, the use of an AISiC sinusoidal shaft in place of an aluminum sinusoidal shaft can lead to an increase in the first frequency of about 26%. On the other hand, the use of AISt decreases the frequency by 13%.

With exception of the AISt, the remainder results are all very beneficial and, again, demonstrate the usefulness of changes in profile and material with the objective of frequency increase.

CONCLUSIONS

It is seen that the use of FGM can be very useful for shaft applications, either cylindrical or tapered, where the shaft is under compressive loads.

For cylindrical shafts, for the case studied, the use of an AISiC shaft increases the critical buckling load by approximately 128% when compared to a pure aluminum one. For an AISt shaft the increase is about 89%.

For conical shafts, the AISiC leads to an increase of approximately 103% and the AISt leads to an increase of about 60%, when the material properties are increasing with increasing cross-sectional area. For the case where the material properties are decreasing, the increase in the critical load is about 153% and 118 % for the AISiC and AISt, respectively.

In the case of sinusoidal shafts made of aluminum, it was shown that increases in the buckling load of the order of 29% are possible when compared to cylindrical shafts. AISiC sinusoidal shafts show an increase of 24% on the load, whereas AISt shafts show about 19%.

The use of an AISiC sinusoidal shaft in place of a pure aluminum shaft can lead to an increase in the load of about 118%. In the case of AISt this increase can be about 73%.

Regarding the first bending frequency, the cylindrical AISiC shaft leads to a frequency increase of 55% when compared to the aluminum one. The AISt gives a frequency increase of about 9%.

For conical shafts where the area increases in the direction of increasing material properties, the AISiC allows for a frequency increase of 43% while the AISt practically gives no change. In the case of area decreasing in the direction of increasing material properties, the AISiC allows for a frequency increase of 100% while the AISt shows an increase of about 50%.

In the case of homogeneous sinusoidal shafts, the sinusoidal profile gives an increase in the first bending frequency of about 42%.

For non-homogeneous sinusoidal shafts, the AISiC one increases the frequency by 15% and the AISt by 13%. The use of an AISiC sinusoidal shaft in place of an aluminum one leads to an increase in the first frequency of 26%. However, the use of AISt decreases the frequency by 13%.

With the majority of the results showing beneficial trends, it is seen that, for shaft under axial compressive loads, the use of FGM with tapering can lead to improvements in terms of increases both in critical buckling loads and first bending frequencies.

REFERENCES

- [1] Lee, B. K., Carr, A. J., Lee, T. E. and Kim, I. J., Buckling Loads of Columns with Constant Volume, *Journal of Sound and Vibration*, 2006, **294** (1 - 2), 381 - 387.
- [2] Darbandi, S. M., Firouz-Abadi, R. D. and Haddadpour, H., Buckling of Variable Section Columns under Axial Loading, *Journal of Engineering Mechanics*, 2010, **136** (4), 472 - 476.

- [3] **Totry, E. M., Altus, E. and Proskura, A.**, Buckling of Non-Uniform Beams by a Direct Functional Perturbation Method, *Probabilistic Engineering Mechanics*, 2007, **22** (1), 88 - 99.
- [4] **Rahai, A. R. and Kazemi, S.**, Buckling Analysis of Non-Prismatic Columns Based on Modified Vibration Modes, *Communications in Nonlinear Science and Numerical Simulation*, 2008, **13** (8), 1721 - 1735.
- [5] **Naei, M. H., Masoumi, A. and Shamekhi, A.**, Buckling Analysis of Circular Functionally Graded Material Plate Having Variable Thickness under Uniform Compression by Finite Element Method, *Journal of Mechanical Engineering Science*, 2007, **221** (11).
- [6] **Kim, W., Argento, A. and Scott, R. A.**, Free Vibration of a Rotating Tapered Composite Timoshenko Shaft, *Journal of Sound and Vibration*, 1999, **226** (1), 125 - 147.
- [7] **Elishakoff, I. and Rollet, O.**, New Closed-Form Solutions for Buckling of a Variable Stiffness Column by Mathematica, *Journal of Sound and Vibration*, 1999, **224** (1), 172 - 182.
- [8] **Elishakoff, I.**, *Eigenvalues of Inhomogeneous Structures: Unusual Closed-Form Solutions*, CRC Press, Boca Raton, FL, 2005.
- [9] **Mazzei Jr., A. J. and Scott, R. A.**, 2008, Bending Frequency Alteration of Rotating Shafts, *International Modal Analysis Conference - IMAC*, Orlando, FL.
- [10] **Weaver Jr., W., Timoshenko, S. P. and Young, D. H.**, *Vibration Problems in Engineering*, 5th, John Wiley and Sons, 1990.
- [11] **Miyamoto, Y., Kaysser, W. A., Rabin, B. H., Kawasaki, A. and Ford, R. G.**, *Functionally Graded Materials: Design, Processing and Applications*, 1st, Springer, 1999.
- [12] **Chiu, T.-C. and Erdogan, F.**, One-Dimensional Wave Propagation in a Functionally Graded Elastic Medium, *Journal of Sound and Vibration*, 1999, **222** (3), 453-487.
- [13] **Li, X.-F.**, A Unified Approach for Analyzing Static and Dynamic Behaviors of Functionally Graded Timoshenko and Euler-Bernoulli Beams, *Journal of Sound and Vibration*, 2008, **318** (4-5), 1210 - 1229.

Converting a Driven Base Vibration Test to a Fixed Base Modal Analysis

Randy L. Mayes
Experimental Mechanics, NDE and Model Validation Department
Sandia National Laboratories*
P.O. Box 5800 - MS0557
Albuquerque, NM, 87185
rlmayes@sandia.gov

Matthew S. Allen
Assistant Professor
Department of Engineering Physics
University of Wisconsin-Madison
535 Engineering Research Building
1500 Engineering Drive
Madison, WI 53706
msallen@engr.wisc.edu

Nomenclature

a	acceleration
dof	degree of freedom
H	Frequency response function
f	Applied force
FRF	Frequency Response Function
q	Generalized coordinate
\mathbf{R}	Reduction matrix applying the constraint to equations of motion
Φ_c	The mode shape matrix of the bare table at dof to be constrained
ζ	Modal damping ratio
ω	Angular frequency (radians/second)
Ψ	Mass normalized real mode shapes
Subscripts	
c	degree of freedom at locations to be constrained
f	dof at free locations
t	dof at tip of the slip table
s	dof at the classic shaker input location on the slip table
i	any other dof not including t or s

*Sandia is a multiprogram laboratory operated by Sandia Corporation, a Lockheed Martin Company, for the U.S. Department of Energy under Contract DE-AC04-94AL85000.

1) Abstract

Qualification vibration tests are routinely performed on prototype hardware. Model validation cannot generally be done from the qualification vibration test because of multiple uncertainties, particularly the uncertainty of the boundary condition. These uncertainties can have a dramatic effect on the modal parameters extracted from the data. It would be valuable if one could extract a modal model of the test article with a known boundary condition from the qualification vibration test. This work addresses an attempt to extract fixed base modes on a 1.2 meter tall test article in a random vibration test on a 1.07 meter long slip table. The slip table was supported by an oil film on a granite block and driven by a 111,000 Newton shaker, hereinafter denoted as the big shaker. This approach requires obtaining dominant characteristic shapes of the bare table. A vibration test on the full system is performed. The characteristic table generalized coordinates are constrained to zero to obtain fixed base results. Results determined the first three fixed base bending mode frequencies excited by the shaker within four percent. A stick-slip nonlinearity in the shaker system had a negative effect on the final damping ratios producing large errors. An alternative approach to extracting the modal parameters directly from transmissibilities proved to be more accurate. Even after accounting for distortion due to the Hann window, it appears that dissipation physics in the bare shaker table provide additional damping beyond the true fixed base damping.

2) Motivation

Motivation for obtaining modal parameters for model validation from tests on flexible vibration tables flows from three driving concerns. First, executing a modal test in conjunction with a vibration test would save considerable time in that there would be no time lost in moving the object between facilities, and some duplication would be eliminated in tear down and setup. Second, because only one setup is required, handling is decreased thus reducing risk of damage to delicate test articles. Finally, since damping tends to be nonlinear and vary with response amplitude, damping could be extracted at operational levels, instead of just the low level usually imparted in modal tests. Typically, damping is higher at operational levels than at traditional modal test levels, which is favorable from a qualification perspective.

However, obtaining modal parameters for model validation from qualification tests is not trivial. Two primary difficulties are: 1. to determine the modal parameters, including modal mass, from data for which no force measure exists; and 2. to account for the dynamic effects of the vibration table so that the modal parameters can be related to the finite element model. In previous work Mayes and Bridgers [1] and Allen et al [2] showed that fixed base results can be approximated from modal tests on flexible fixtures. Mayes and Bridgers reviewed earlier work and then extracted a single fixed base mode from a prototype flexible shaker table random vibration test of a beam. Allen et al. extracted several fixed base modes for a beam, with the beam mounted on a flexible plate in a free-free modal test. Both papers apply a method extended from the authors' earlier work in experimental substructuring to constrain the table motion in analysis after the modal test is performed. Instead of applying classical physical degree of freedom constraints, modal constraints are utilized, which avoids significant ill conditioning of the matrices in either frequency based or modal based data. The method has a smaller number of constraints that is based on a number of table modes to be constrained rather than a large number of physical degrees of freedom to be constrained. This work attempts to apply the method to a production vibration system instead of research hardware to see if there are any logistical obstacles. It also considers generalized coordinates other than the modal coordinates.

This present work attempts to extract fixed base modes from a random vibration test on a production shaker system at Sandia National Laboratories. A shaker capable of 111,000 Newtons drives a 1.07 m long by 0.91 m wide magnesium slip table which is supported by a granite block. Oil forced from a pump lubricates the interface between the slip table and the granite block. A test article that is 1.2 m tall is utilized to attempt to provide some overturning moment to the slip table.

The theoretical approach will be reviewed in section 3, with a new extension to obtaining characteristic table shapes. Section 4 is focused on the method to obtain a "truth" model utilizing a seismic mass modal test of the test article with some analytical corrections to obtain fixed base results. The characterization of the shaker table shapes is addressed in section 5. In this method, a portable shaker (hereinafter denoted as the tip shaker) is brought in and applied at the tip of the shaker table when the test article is mounted to the table, and this is addressed in section 6. The actual random vibration test is covered in section 7. Section 8 covers the analysis to provide the fixed base results. Uncertainty quantification for the process is addressed in section 9, and conclusions follow.

3) Review of Theory and Modal Constraints

Crowley, et al. presented the original structural modification using FRFs (sometimes called SMURF) [3], and it is repeated here as the basis for this method. The FRF matrix equations can be partitioned as

$$\begin{Bmatrix} a_f \\ a_c \end{Bmatrix} = \begin{bmatrix} H_{ff} & H_{fc} \\ H_{cf} & H_{cc} \end{bmatrix} \begin{Bmatrix} f_f \\ f_c \end{Bmatrix} \quad (1)$$

where a is acceleration, H is a frequency response function and f is force. The subscripts associated with partitioning are f for free dof and c for dof which will be constrained mathematically at a later time.

Only a few (perhaps just one) columns of equation (1) are measured, therefore the other columns must be reproduced from the modal parameters extracted from the measured columns. This method is limited by the effects of modal truncation.

By constraining a_c to zero, equation (1) can be rearranged

$$\{a_f\} = [H_{ff} - H_{fc}H_{cc}^{-1}H_{cf}] \{f_f\} \quad (2)$$

However, H_{cc} is usually poorly conditioned on inversion and gives uncertain results. Poor results are probably the reason why this constraint theory has not been more popular. By reducing the physical c dof in equation (2) to the modal coordinates of the table, the conditioning is much improved. Equation (3), which utilizes modal connection dofs, can be much more robust and is given by

$$\{a_f\} = [H_{ff} - H_{fc}\Phi_c^{T+}[\Phi_c^+H_{cc}\Phi_c^{T+}]^{-1}\Phi_c^+H_{cf}] \{f_f\} \quad (3)$$

where Φ_c is the mode shape matrix of the flexible table without a test article, and the superscript $+$ indicates the pseudo-inverse.

This procedure can also be performed using the modes of the system rather than measured FRFs. An equivalent modal approach begins with the equations of motion based on modes extracted from the full system modal test on the shaker table as

$$[\omega_n^2]\{q\} - \omega^2[I]\{q\} = \Psi^T\{f\} \quad (4)$$

where ω_n represents the circular natural frequencies from the system modal test, q represents the modal coordinates, f is the vector of forces and Ψ provides the mass normalized mode shapes. A constraint for the table degrees of freedom can be written as

$$\{x_c\} = \{0\} \quad (5)$$

or using the modal substitution, then

$$\Psi_c\{q\} = \{0\}. \quad (6)$$

Using modal constraints (which are weaker than physical dof constraints) produces

$$\Phi_c^+\Psi_c\{q\} = \{0\} \quad (7)$$

where Φ_c comes from the previously characterized mode shapes of the bare table. This projects the constraint onto the vector space of the bare table shapes, which has the advantage of producing a least squares fit through any experimental modal analysis errors. After the constraint is applied, the eigenvalue problem is solved again to estimate the fixed base modes. The number of final modes will be reduced from the original number of modes in eqn (4) by the number of constraints. As a practical consideration, any significant dynamics of the table which are active in the full system test need to be constrained. Modes of the table that are not active are ignored. In the authors' experience, it can actually be detrimental to the results to include them in the constraint mode shapes, Φ_c , particularly if there are no test article modes that exercise these inactive table modes.

A new approach to obtaining Φ_c is addressed in this paper. Φ_c is not required to be the mode shape matrix of the bare table, but should have characteristic shapes which span the motion of the table in the actual random vibration test. An alternative way to obtain Φ_c is to extract all the mass normalized modes excited during the actual random vibration test, and then perform a singular value decomposition on the table partition of the mode shapes associated with subscript c DOF. Then one would identify an appropriate set of the left singular vectors that are most active in the given mode shapes and constrain their motion to zero. The logistical advantage of this approach is that it does not require a modal test of the bare table in advance (although the proper placement of sensors to obtain a well conditioned Φ_c might still require such a test).

In order to extract mass normalized mode shapes from the full system modal test, we require accelerance FRFs. The authors chose to approach this by attempting to estimate the shaker force. We cannot easily measure the shaker force, but an estimate of the shaker force can be inferred using reciprocity. Reciprocal FRFs can be written as

$$H_{st} = H_{ts} \quad (8)$$

where H is the accelerance FRF and subscript s represents the shaker location and subscript t represents the tip of the table farthest from the shaker. Now the relation of the acceleration at the tip due to the force at the shaker is

$$a_t = H_{ts} f_s \quad (9)$$

which can be rewritten to determine the shaker force, if a and H are known, as

$$f_s = a_t / H_{ts} \quad (10).$$

Substituting (8) into (10) gives

$$f_s = a_t / H_{st} \quad (11).$$

Define location i as any location of interest. Then

$$H_{is} = a_i / f_s \quad (12)$$

and substitute (11) into (12) to estimate any accelerance FRF as

$$H_{is} = H_{st} a_i / a_t \quad (13)$$

where a_i/a_t is simply the transmissibility to the tip accelerometer which is usually collected in a random vibration test for any response of interest. Theoretically, it does not have to be an accelerometer at the tip of the table; it may be anywhere; but practically, an accelerometer at the tip of the shaker table farthest from the shaker input force is well conditioned in that it has the fewest anti-resonances of any location on the table. For this reason, this is often the location of the control accelerometer in random vibration tests.

4) Seismic Mass Truth Test

In order to evaluate the accuracy of the fixed base modes of the test article, a truth model was needed. Test hardware was devised which is basically a nylon beam with a base and some stiffening flanges as shown in Figure 1. The test article was mounted on a 14,500 kg steel mass. The top surface of this mass can be seen in the figure. The mass was supported on air springs. The article was tested in this configuration. The frequencies and damping of the modes from the SMAC algorithm [4] are given in Table 1. Although this was a massive boundary condition, it was not truly fixed base. Eqns (4 & 7) were applied to estimate the fixed base frequencies, using only the six rigid body modes of the seismic mass in the Φ_c matrix.

The fixed base modes and corresponding damping are also listed in the latter columns of the table. The rigid body modes on the seismic mass are not listed here, but had frequencies from 0.9 to 2.3 Hz. The rigid body modes were extracted with step sine testing and the elastic modes were extracted with impact or shaker testing. Long time blocks were required to get accurate damping since the damping is light. The results from the analytical fixed based columns are used as the best estimate for truth for the remainder of this work. The seismic mass elastic modal frequencies started at about 250 Hz. It was assumed that they have negligible effect on the listed modes.

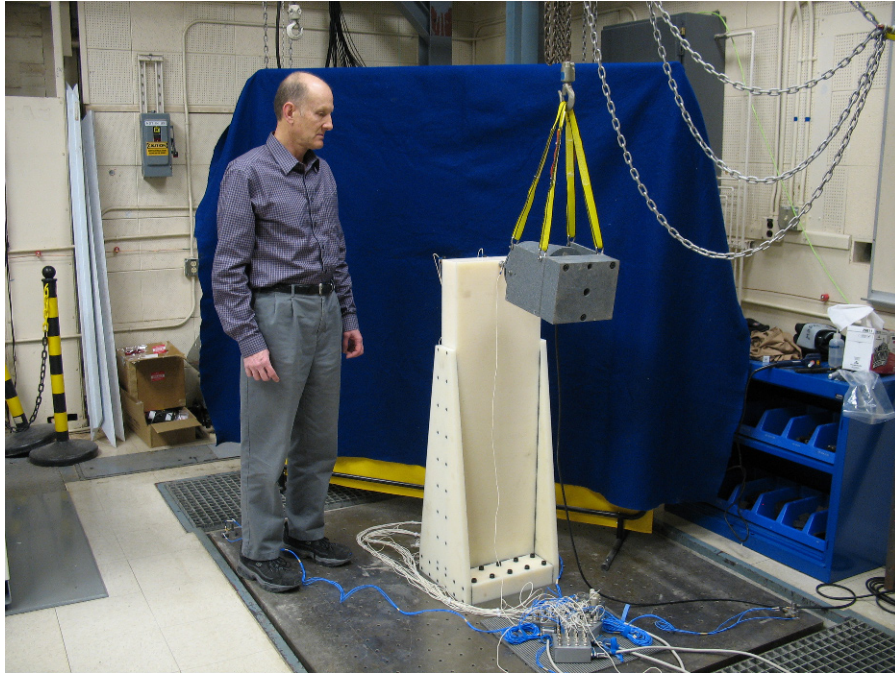


Figure 1 - Test Article on Seismic Mass

Table 1- Truth Test Results

Mode #	Seismic Mass Test		Analytical Fixed Base		Mode Description
	Frequency Hz	% Modal Damping	Frequency Hz	% Modal Damping	
1	38.77	0.22	38.54	0.22	First bend soft direction
2	91.78	0.20	91.13	0.19	First bend stiff direction
3	134.0	0.20	134.0	0.20	First torsion
4	164.2	0.25	164.0	0.24	2nd bend soft direction
5	342.7	0.25	342.3	0.25	2nd torsion
6	396.5	0.32	394.8	0.32	3rd bend soft direction

5) Characterization of Shaker Table

The shaker characterization accelerometers were triaxial gages placed at the four corners of the table and four points mid-side between the corners (similar to Figure 5 but without the test article). The characterization of the shaker table in the axial direction (direction of the standard shaker force input) indicated only two significant modes up to 1000 Hz. The higher frequency mode had the same shape as the classical first elastic mode of a rod with the free end of the slip table out of phase with the armature around 900 Hz. However this analysis was only performed to 500 Hz, so this mode was neglected. The lowest mode was a nearly rigid body mode of the table and armature bouncing back and forth on the flexures of the armature at about 8 Hz. However the damping in this mode was nonlinear, being much higher at lower force input levels and decreasing with higher force input levels as can be seen in Figure 2. This is not a serious problem for frequency and shape analysis as long as the mode shape can be extracted, which was possible for either of the higher levels. The table mode shapes, Φ_c , are used in the constraint of eqn (7), but the damping is not used. However the nonlinear damping *is* an issue for calculating final damping from the full system test and will be discussed extensively in section 6.

The characterization of the table in the lateral direction yielded only very highly damped modes which were neglected since they were not excited in the full system test.

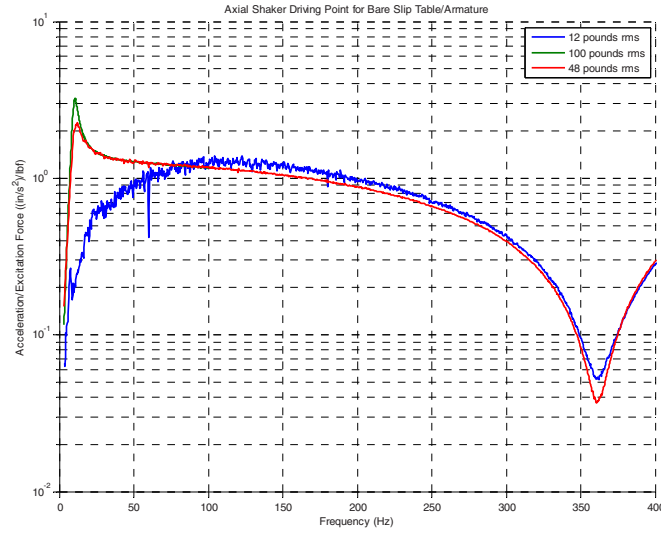


Figure 2 - Bare Table Axial Driving Point FRF at Multiple Force Levels

The characterization of the vertical direction yielded some interesting surprises. As can be seen from the blue line in [Figure 3](#) below, there were many vertical modes of the table. At first it appeared to be a daunting task to extract all the vertical modes, but these were only important *if* they were significant in the full system test. To be extracted with accuracy from the full system test they must also have reasonable amplitude in the drive point FRF from which scaling is derived.

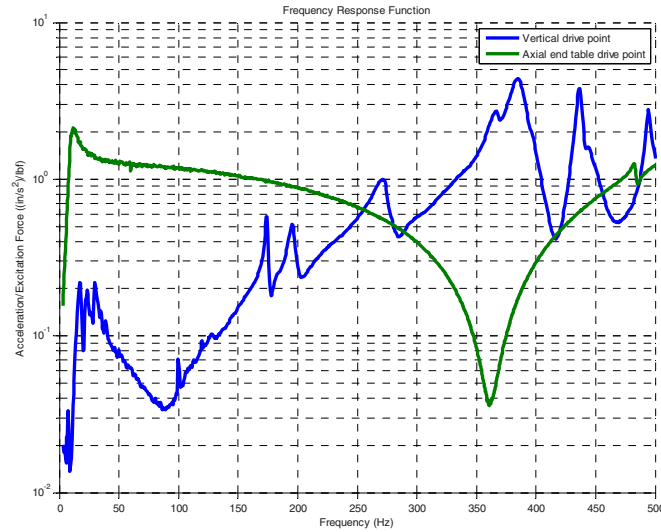


Figure 3 - Bare Table Drive Point FRFs

As can be seen in [Figure 4](#), the green drive point FRF from the tip shaker had almost no visible response due to the vertical modes of the plate that are seen in [Figure 3](#). Only the first lateral rigid body mode and three bending modes of the test article were strongly evident based on modal extractions associated with the four dominant resonances in the green curve. If there was no drive point response for any of the vertical modes then their associated shapes could not be scaled accurately, and they could not be used in the fixed base analysis. In [Figure 4](#) it can be seen from the vertical response of the blue curve that there were many modes in the system. However their response amplitude was very low, except for the four highest peaks, modes that were driven by the test article. As a result, only one table mode was utilized for the Φ_c matrix - the axial rigid body mode near 8 Hz. This was not anticipated at the outset of the project.

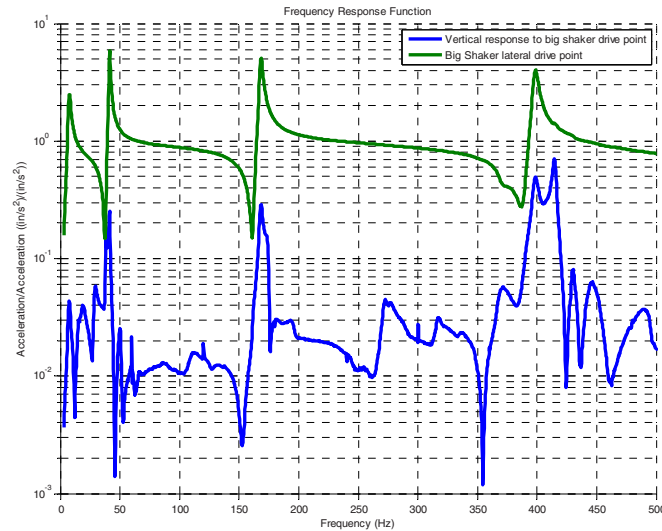
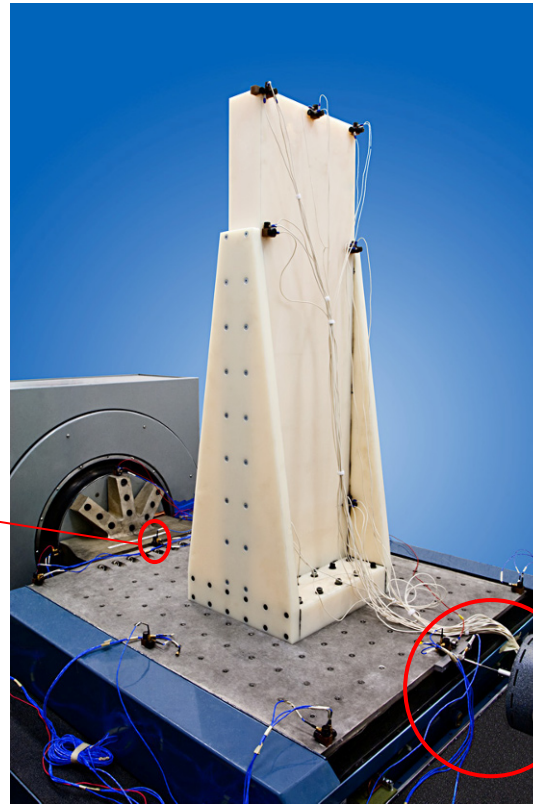


Figure 4 - Tip Shaker FRFs

6) Tip Shaker Testing

To obtain accelerance FRFs for eqn (13) a reciprocity FRF had to be measured with a shaker applied at the tip of the table and a response ideally located near the armature of the actual vibration table forcing shaker. Logistically the accelerometer could not be placed inside the armature, so a location on the slip table next to the connector to the shaker was chosen. The setup can be seen in Figure 5 where the MB50 modal shaker is attached at the tip of the table and the reciprocity accelerometer is circled. A significant difficulty with the process was encountered in measuring the reciprocity FRF. Eqn (13) is based on the assumption that the reciprocity FRF is linear and representative for all excitation levels. In Figure 6 the modulus of this FRF is plotted for various shaker input levels. Some of the plots are for random inputs and some for step sine inputs. The MB50 shaker had to be changed out for a MB250 shaker to achieve the higher level inputs. As can be seen, the response was not linear, but changed with amplitude. The worst nonlinearity was in the low frequency region, and even with an 890 Newton (200 pound) peak force sine input, it did not appear to have converged to a consistent damping at the lowest resonance. With higher force, the damping in the first resonance decreases. During sine testing the table acceleration time histories had discontinuities at the maximum and minimum amplitude of the sine wave, indicating that the table was sticking at the end of every stroke. This was most evident at lower force levels and had less effect as force level was increased. The armature, table and test article weighed about 180 kg (400 pounds), so even at the highest force level attempted, the rigid body response was only about 0.5 g. The stiction is apparently high enough that it has an appreciable nonlinear effect at the force input levels that were available with the tip shakers. When the actual random vibration test was run, an analytical reciprocity FRF was developed by fitting the magenta curve (for the first mode) and the cyan curve for three other modes. Note that the damping ratio in the first mode of the magenta curve was about 15 percent, which will be important later. Although the only process requirement for the tip shaker was to obtain the reciprocity FRF, all the accelerometers were attached and available, so a modal test was performed with the tip shaker. Results will be given in Section 8.1, and then analytically modified to provide fixed base estimates. One significant observation that can be taken from Figure 6 is that only four modes are really active at the higher levels in the direction of the force input.

Reciprocity
Accelerometer



MB50 Tip Shaker
and Force Gage

Figure 5 - Tip Shaker Test Setup

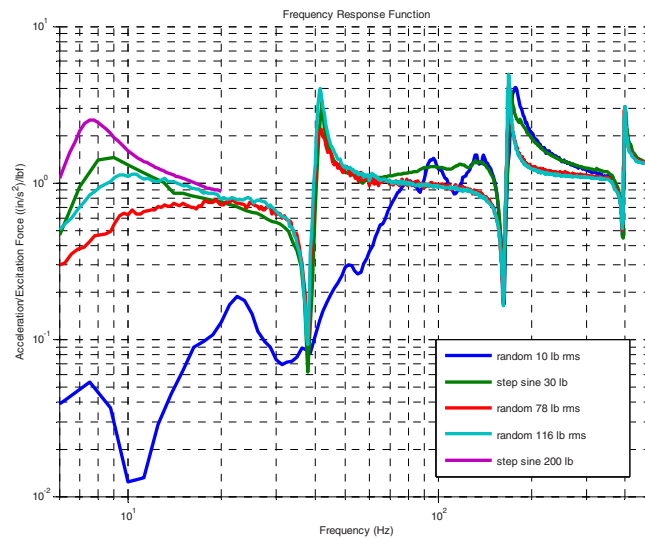


Figure 6 - Demonstration of Nonlinearity in Reciprocity FRF with Test Article on Table

7) Full Level Random Vibration Test

After the tip shaker was removed, a random vibration test to 500 Hz was performed with a flat random input measured at an accelerometer on the tip of the table. The level was $0.001 \text{ g}^2/\text{Hz}$. Another test was performed at -6dB down, and the transmissibility of an accelerometer at the top of the beam is shown in [Figure 7](#) for both levels. At these levels, there appears to be very little nonlinearity in the data, indicating that the stick slip phenomenon has been mostly overcome. In the very first resonance, the full level data has slightly lower damping (0.9% vs. 1.2%), but elsewhere it overlays.

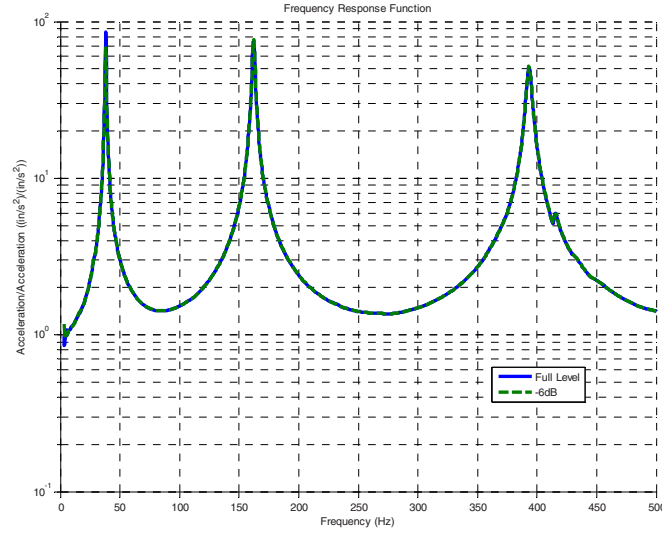


Figure 7 - Transmissibilities of the Top of the Beam at .001 g²/Hz and Down 6dB

8) Fixed Base Analysis

8.1) Full System Modal Analysis based on FRFs from Tip Shaker

The first full system mode was extracted from a 200 pound force step sine test (magenta line in Figure 6). All higher frequency modes were extracted from a 105 pound rms 500 Hz random vibration test. Both these tests utilized a 250 pound force tip shaker, and modes were extracted with the SMAC algorithm [4]. The Φ_c utilized only the first axial rigid body mode of the shaker. Results are shown in Table 2 with the % error relative to the truth fixed base results. Only the most active modes of the test article are included up to 400 Hz. First, second and third bending mode shapes are shown in Figure 8. The damping of each mode is found utilizing the diagonals of the final damping matrix determined from

$$\{\zeta_{new}\} = \text{diag}(\Psi_{new}^T \mathbf{R}^T [2\zeta\omega_n] \mathbf{R} \Psi_{new}) / [2\omega_{new}] \quad (14)$$

where $\{\zeta_{new}\}$ is the new vector of damping ratios, $[2\zeta\omega_n]$ is the diagonal damping matrix from the unconstrained modes, Ψ_{new} is the new eigenvector matrix, and $[2\omega_{new}]$ is the diagonal matrix with twice the new natural frequencies. \mathbf{R} is the reduction matrix which applies the constraint to eqn (4) with $\{q_c\}$ providing the new reduced number of constrained DOF as

$$\{q\} = \mathbf{R}\{q_c\}. \quad (15)$$

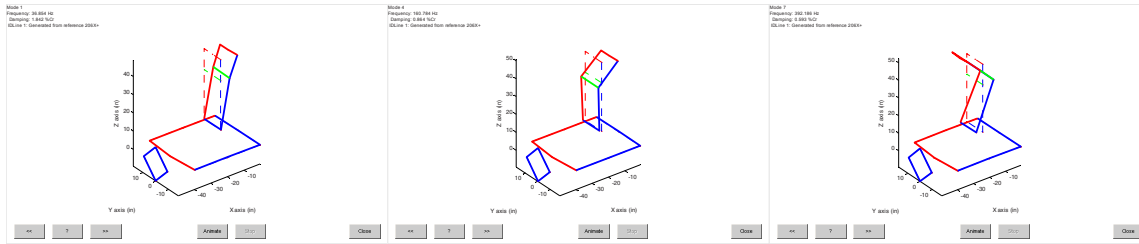


Figure 8 - Fixed Base Bending Mode Shapes

Table 2 - Fixed Base Results from Tip Shaker (Real Modes Assumption)

Frequency-Hz	Frequency Error	Damping %	Damping Error
37.7	-2.1%	2.4	1090%
161.7	-1.4%	0.8	320%
392.7	-0.5%	0.6	188%

The rigid body mode that was at 8 Hz has been constrained away. The first bending mode, which was at 41.3 Hz in the unconstrained test has been reduced about 10% in the analytical fixed base result. The fixed base frequency errors are not too bad, but the damping errors are very large. In section 9.1 it will be shown that the Hann window affects the first mode adding about 0.4% damping, but it has less than 0.1% effect on the other modes. The final damping ratio is a linear combination of the initial unconstrained damping ratios. If one recalls that the damping ratio for the first rigid body axial mode is nearly 15% due to stiction in the table, it is apparent that this high damping is propagated to the other frequencies in eqn (14). So this error is almost entirely due to energy dissipation associated with the table physics, not the test article. This error would be reduced if a more powerful tip shaker was used.

8.2) Full System Modal Analysis Combining Transmissibilities from Large Shaker Table Shaker with Reciprocity FRF from Smaller Tip Shaker and a Single Table Mode Shape Constraint

After running a random vibration test with the big shaker and obtaining transmissibilities, the analytically reproduced reciprocity FRF from the above tip shaker testing was applied to the transmissibilities from eqn (13) and the SMAC algorithm [4] was used to extract the modal parameters of the vibration table test. Then a single mode shape was used in Φ_c to fix the base using the constraint from eqn (7). Results are given using a real mode analysis in Table 3.

Table 3 - Fixed Base Results from Big Shaker (Real Modes Assumption)

Frequency-Hz	Frequency Error	Damping %	Damping Error
36.9	-4.2%	1.8	818%
160.8	-2.0%	0.9	360%
392	-0.7%	0.6	188%

Frequency errors are slightly worse with the large shaker and the real mode analysis. Damping estimates are still bad, although the first mode improves slightly. The large shaker provides enough force at the high level to overcome a bit more of the stiction reducing the quality factor in the transmissibility for the first bending mode, but the high damping of the first rigid body mode is still the same in the driving point FRF created from the low level reciprocity FRF from the tip shaker.

8.3) Full System Modal Analysis Combining Transmissibilities from Large Shaker Table Shaker with Reciprocity FRF from Smaller Tip Shaker and Singular Vector Shape Constraints

Utilizing the same FRF data as in section 8.2, Φ_c was determined utilizing the singular value decomposition of the subscript c partition of the mode shapes. As many modes as possible were fit; every mode was kept which yielded a positive drive point mode shape. The complex mode indicator function from these fits is shown in Figure 9.

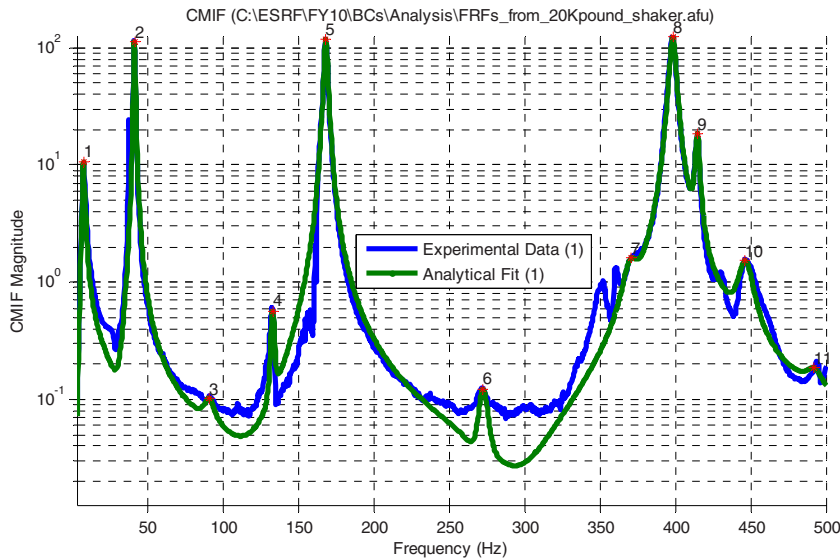


Figure 9 - CMIF of Modal Parameter Fit with Big Shaker Data - Analysis (Green) vs Exp Data (Blue)

Results using a single shape for Φ_c and a real mode analysis were almost exactly the same as in Table 3. However when a second singular vector was added to Φ_c , slightly more accurate results for the first mode were obtained as shown in Table 4. These results deteriorated if any of modes 6,7,9 or 10 from the CMIF were left out, which each had considerable table motion. Modes 3 and 4 could be left out and did not deteriorate the results. Modes 3 and 4 are test article torsion and out of axis bending modes that are very weakly excited. When a third shape was added to Φ_c , the result was poor for the first mode, with a frequency error of 22 percent.

Table 4 - Fixed Base Results from Big Shaker and Two Singular Vectors (Real Modes Assumption)

Frequency-Hz	Frequency Error	Damping %	Damping Error
39.4	+2.1%	1.7	773%
161.5	-1.5%	0.9	360%
392.2	-0.7%	0.6	188%

The singular values associated with Φ_c , are shown in Figure 10. One value is dominant, but there is no clear knee in the curve to determine how many shapes are significant. When looking at the shapes, the first shape looked like the rigid body axial shape. The second shape was a combination of pitch and vertical motion, somewhat similar to the shape seen in the mode at 270 Hz which was extremely weak in the data. The third shape did not look like any physical mode that might be exercised in the table, and its addition caused large errors.

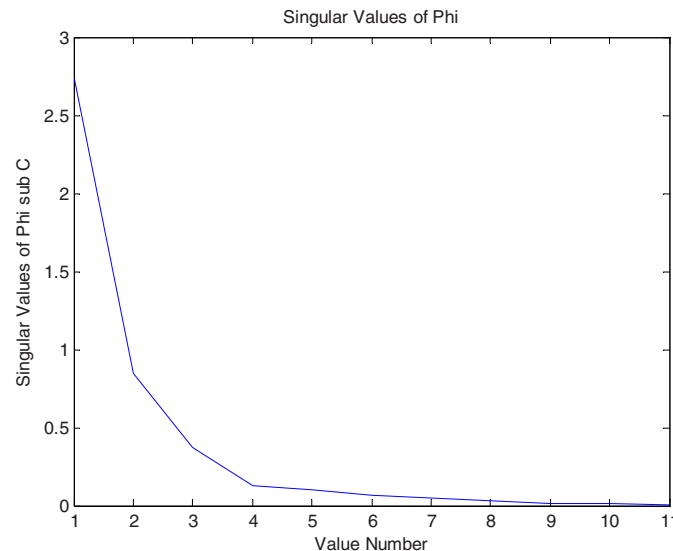


Figure 10 - Singular Values of Phi

8.4) Transmissibility Method

It has been shown previously by Carne and Belliveau [5,6] that if the vibration table is rigid and has motion only in the direction of the force input, one can generate acceleration to force frequency response functions (FRFs) from the transmissibilities by subtracting one from the transmissibilities that are in line with the shaking motion. The resulting FRFs have a fixed dof associated with the acceleration in the denominator of the transmissibility. This does not fix the table motion at any point other than the tip accelerometer location. In contrast, the modal constraint approach developed here is applicable even if the table moves in multiple directions and has multiple significant flexible modes. However, the system here is rigid up to 500 Hz and the table moves mostly in the tip accelerometer direction. The full level random data were analyzed, and modal parameters were extracted with SMAC [4]. Results are given in Table 5 which are the most accurate results in this work. This method has the advantage that no characterization of the table motion is required. It also does not require the reciprocity FRF measurement. For this application it worked better for multiple reasons. First, the table is rigid in this bandwidth. Second, there is negligible motion of the table in the vertical or lateral directions of the actual test. If there had been out of axis motion or elastic axial motion, this method cannot correct for those motions. Third, it does not have the damping error for the rigid body mode associated with the low level tip reciprocity FRF. Only the damping from

Table 5 - Transmissibility Method Results from Big Shaker

Frequency-Hz	Frequency Error	Damping %	Damping Error
38.0	-1.3%	0.9	409%
162.1	-1.2%	0.7	280%
393.3	-0.4%	0.6	188%

the shaker at the high level at which it was excited is present, plus the effect of the Hann window. As will be shown later, about 0.4 % of the first mode damping and 0.1% of the second mode damping are due to the Hann window. Roughly 0.3% of the damping is apparently coming from the shaker table bearings or oil film.

8.5) Discussion of Results

In the frequency band examined, this shaker and slip table have only one major table mode at about 8 Hz, so that is the only significant motion that had to be constrained to obtain fixed base results. Although there were many vertical modes of the table, they are not strongly active in the test. For this reason, the transmissibility method worked very well for this data.

The tip shaker method worked reasonably well for fixed-base frequency estimates, but because there was so much low frequency damping in the reciprocity FRF, this damping was imposed upon the big shaker test, causing large damping errors. The reciprocity FRF was nonlinear with forcing level, so a much larger tip shaker would have been required to get the table up to the response levels that were possible with the large shaker in order to get a reciprocity FRF with accurate damping in the resonances.

The results of two methods were compared, one which used the modes of the bare table as constraints and another which used the SVD of the observed table motion. The SVD method improved the frequencies slightly, but the main advantage of this method is that it avoids the requirement of the table modal test, except for knowing how to place the accelerometers on the table to adequately capture table motion. A similar approach might be to use the table partition of the active table mode shapes from Ψ as Φ_c .

One guiding rule for choosing the number of shapes in Φ_c is that one wants to constrain away only table modes, not the test article modes. For this reason there need to be at least as many modes that are dominated by the shaker table dynamics, when testing the test article on the table, as there are constraint shapes in Φ_c .

Some damping is added to the results due to damping in the shaker table. In the best results from Table 5, even after removing the damping added by the Hann window, there is still about 0.3 percent damping that appears to be added by the shaker/slip table system. With test articles that have higher damping than the lightly damped system analyzed here, this may not be a big issue.

9) Uncertainty Quantification

9.1) Uncertainty Quantification Associated with Damping

There was some distortion that affected the damping due to the Hann window that was applied to the random vibration data. Much of the data were acquired with a 4096 block size with Hann window, so the effect was analyzed for this block size. An analytical FRF for a single dof system was generated for frequencies at [.01 .05 .1 .2 .3 .4 .5 .6 .7 .8 .9] times the Nyquist frequency and with 0.1 percent critical damping. These FRFs were excited by a random force input, with a block size three times 4096. Then just the last third of the data were used to calculate FRFs with a Hann window on the force and acceleration time histories. Using the last third of the data mitigated the effects of transients. The FRFs were created with 100 averages. Then the FRFs were fit in the SMAC modal analysis package to estimate the frequency and damping values. This was repeated for five sets of data and the results of the damping added by the Hann window are plotted in Figure 11 below. The damping ratio is drastically over estimated at a frequency that is 0.01 times the Nyquist frequency, and it has significant scatter even with 100 averages. But by the time one reaches 0.05 times the Nyquist frequency the effect is less than 0.5 percent and by 0.2 times the Nyquist, the effect is less than 0.1 percent of actual added damping, which is on the order of uncertainty in modal parameter damping estimators. Based on this, the damping associated with the Hann window for the first mode extracted in the random vibration testing (near 38 Hz) would be about 0.4 percent and for the second mode (near 162 Hz) it would be less than 0.1 percent. Based on the damping estimates in Table 5, this indicates that there is

additional damping beyond the truth measurements on the order of 0.3 percent that is due to other sources in the shaker/slip table system.

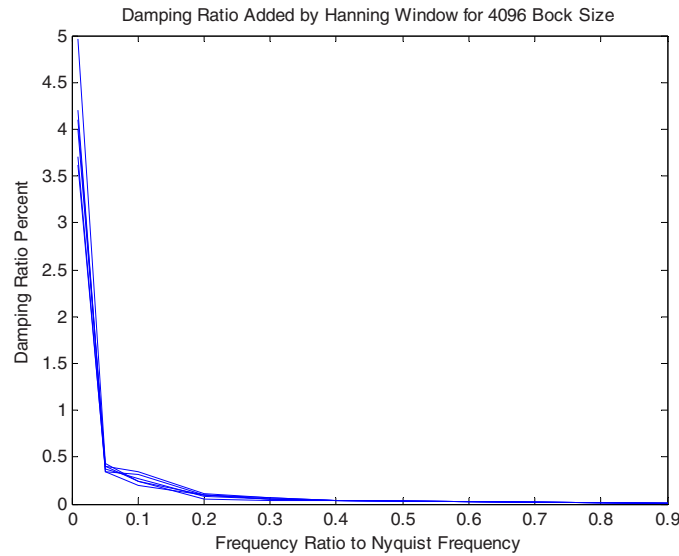


Figure 11 - Damping Ratio Due to Hann Window for 4096 Block Size

9.2) Uncertainty Quantification Associated with Mode Shape

The effect of mode shape scaling was investigated. For the Φ_c matrix the scaling has no effect. The matrix just needs to be invertible, i.e. have a low condition number. This method was implemented with real modes, and it was noticed that the real mode fit for the first mode of the system at 8 Hz did not fit very well. That mode had considerable damping, nearly 15 percent. The mode was fit with complex modes and then approximated from the complex amplitude with a real mode. This basically increased the amplitude of that mode shape. This slightly reduced the errors in frequency by the reciprocity FRF method (previous Table 3) as shown in Table 6. This indicated that relative error between the scaling of table modes and test article modes create some uncertainty.

Table 6 - Reciprocity FRF Fixed Base Results from Big Shaker Refining First Mode Fit

Frequency-Hz	Frequency Error
37.4	-2.9%
161.6	-1.5%
392.6	-0.4%

A simple sensitivity study was performed addressing the relationship of the first rigid body mode shape scale to the first elastic mode shape scale. If the scale of the first full system rigid body mode (8 Hz) that was extracted was increased by 10 percent, it caused the first fixed base modal frequency to increase by two percent. If the first elastic bending mode shape scaling was increased by 10 percent, the first fixed base bending modal frequency decreased by two percent.

One question is "How does one know, without a truth model, whether these constraint methods have worked?" From these efforts, one can tell when the constraint has *not* worked if there is significant motion in the table mode shape response. A good example of this comes from a vertical mode of the table shown below. This mode is somewhat weakly excited, but there is clearly significant table motion, as one can see by comparing the table deformed motion (solid line) with the table undeformed motion (dotted line) in the left mode shape of Figure 12. The right mode shape shows the first bending mode where the table motion has been constrained by the method.

In this work, the well excited first through third modes in the direction of the shaker motion were constrained fairly well by the method in all analyses for the purpose of modal frequency analysis. Also, in all analyses, modes that were not well excited were not constrained well. In this case, these poorly excited modes included lateral bending, torsion and vertical modes.

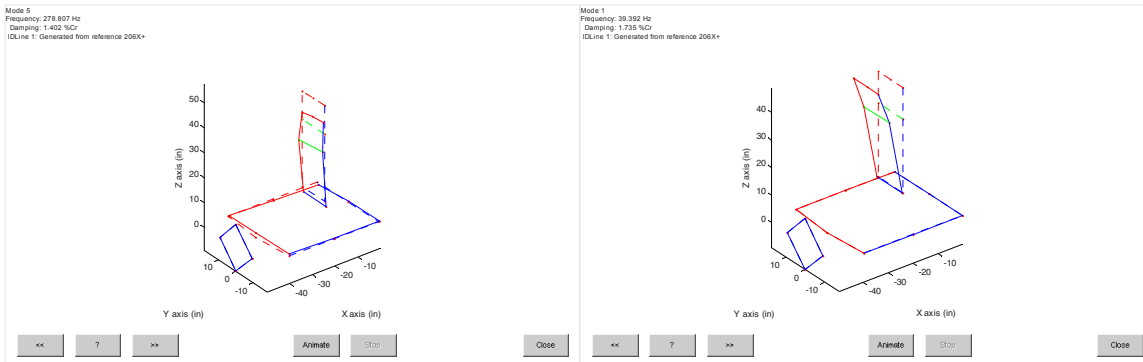


Figure 12 - Base Motion Not Well Constrained in a Vertical Mode (Left) vs Well Constrained in a Bending Mode (Right)

10) Conclusions

This work investigated the estimation of fixed base modal parameters from random vibration data on a medium sized shaker and slip table by two methods. One method extracts modes during the random vibration test utilizing a previously estimated reciprocity FRF and a tip shaker, and then applies constraints through generalized coordinates associated with the table motion. For this application, the frequencies of the major modes were estimated with various modifications to within about four percent in the worst case. The damping estimates were poor for reasons given below. The second method is based on the transmissibilities of the various accelerometers to a reference accelerometer at the tip of the table. For this hardware the transmissibility method gave frequencies within 1.5% of the true fixed base modes and better damping estimates.

For this application, the only significant motion observed in the slip table was one rigid body lateral mode. Hence, only the rigid body lateral motion of the table needed to be constrained to accurately estimate fixed base frequency results for the well excited bending modes up to 500 Hz. Since only one rigid body mode was active, the transmissibility method actually worked even better. If any other modes had to be constrained, the transmissibility method cannot correct for additional motions. The modes that were strongly excited in the random vibration test were easily constrained at the base, while weakly excited modes were not well constrained. Slightly better results for the constraint were obtained when two shapes from the singular value decomposition of the table partition of the full system mode shapes were used in the constraint. The SVD method did not require a modal test of the shaker and bare table as the mode shape constraint method does.

The method of obtaining a force through the reciprocity FRF suffered because the shaker system (particularly the energy dissipation) was nonlinear, and the small tip shaker force levels engaged much higher damping at low levels than at the higher levels of interest. Since the full level vibration test had much higher response levels, and consequently lower damping, the only way to overcome this problem and continue use of the reciprocity FRF would be to excite with a more forceful tip shaker, if determination of the damping is important.

Using the transmissibility method, it appeared that the damping was greatly reduced in the full level random vibration test which was performed at much higher levels than the tip shaker vibration tests. However, even there, additional damping was experienced by the full system than for the seismic mass truth test. This indicates that some damping is introduced to the system by energy dissipation physics associated with the table and shaker. Here it was on the order of 0.3 percent after the effects of the Hann window were removed. However, because the test article damping was so low, a 0.3 percent damping ratio error was on the order of 100 percent more damping than the truth test.

The transmissibility method actually gave better frequency and damping results. This method acquires the data at the high levels of the vibration test. At these high levels the stiction is much less, so the apparent damping is lower. Nominally, one would expect exactly the same frequency result as with the previous method utilizing the single rigid body mode for a constraint. Perhaps the extra stiction pollutes the mode shape estimates slightly in the other method. If any other modes of the table had been active, this method cannot constrain the base motion for those cases.

The guiding rule for the number of constraints in this approach is that there must be at least as many table modes that are obvious in the data as generalized characteristic DOF in the constraint to remove them. As shown from the driving point FRF in Figure 4 and the full system modal analysis, only one table mode shows up strongly in the full system data. Many

table modes exist in the frequency band, particularly in the vertical direction, but only the axial rigid body mode was really significant up to 500 Hz.

Uncertainty quantification studies showed that the scaling on the modes in Φ_c was unimportant, but incorrect scaling of the mode shapes from the full system shaker test could cause errors.

A combination of using the damping results from transmissibility analysis and the frequency and mode shape results from the constrained tip shaker analyses may provide the best results for future work. This limits the damping errors and maintains the capability to remove effects of multiple table motions in frequency and shape analyses.

References

- 1 Mayes, Randy L. and Bridgers, L. Daniel, "Extracting Fixed Base Modal Models from Vibration Tests on Flexible Tables", *Proceedings of the 27th International Modal Analysis Conference*, Orlando, FL, February 2009, paper 67.
- 2 Allen, Matthew S., Gindlin, Harrison M. and Mayes, Randall L., "Experimental Modal Substructuring to Extract Fixed-Base Modes from a Substructure Attached to a Flexible Fixture", *Proceedings of the 28th International Modal Analysis Conference*, Jacksonville, FL, February 2010, paper 164.
- 3 Crowley, John R., Klosterman, Albert L., Rocklin, G. Thomas and Vold, Havard, "Direct Structural Modification Using Frequency Response Functions", *Proceedings of the Second International Modal Analysis Conference*, Orlando, Florida, February 1984, pp. 58-65.
- 4 Hensley, Daniel P., and Mayes, Randall L., "Extending SMAC to Multiple References", *Proceedings of the 24th International Modal Analysis Conference*, pp.220-230, February 2006.
- 5 Carne, Thomas G., Martinez, David R. and Nord, Arlo R., "A Comparison of Fixed-Base and Driven Base Modal Testing of an Electronics Package", *Proceedings of the Seventh International Modal Analysis Conference*, Las Vegas, Nevada, February 1989, pp. 672-679.
- 6 Beliveau, J.G., Vigneron, F.R. and Soucy, Y., and Draissey, S., "Modal Parameter Estimation from Base Excitation", *Journal of Sound and Vibration*, Vol. 107, January 1986, pp. 435-449.

Model Form Error of Alternate Modeling Strategies: Shell Type Wind Turbine Blades

Kendra Lu Van Buren¹ and Sez Atamturktur²
Civil Engineering Department, Clemson University, Clemson, SC 29634

ABSTRACT: In the U.S. there is a need for the Wind Energy sector to reduce maintenance costs and increase the continuous availability of wind turbines to compete with other forms of energy. In this respect, reliable modeling and simulation techniques play an indispensable role in allowing a better understanding of wind turbine blade vibrations. The purpose of this paper is to quantify the degrading effects of simplifications to the material cross section of a finite element (FE) model of a Suzlon S88-2.1 MW wind turbine blade. First, a code verification study with ANSYS Shell281 elements is performed to verify the element type selection. Next, a three-dimensional model of the blade is developed using NuMAD, pre-processing software and analyzed in ANSYS, FE modeling software. A solution verification study is performed to identify the mesh size that will yield converged solutions with manageable demands on computational resources. Five constitutive models are developed by incrementally simplifying the cross section of the blade. The most sophisticated model is idealized as the baseline to create synthetic experimental data, utilizing orthotropic materials and a composite cross section, in comparison to the least involved model which has an isotropic, smeared cross section. This manuscript explores the extent to which errors are increased as the model is simplified in order to reduce the number of input calibration parameters and computation time. Considering the baseline, the model form errors associated with the four models of lesser sophistication are estimated. The estimates of model form error conveniently quantify the effects of simplifications to the entire domain of a FE model wind turbine blade. Model form error will help to identify the tradeoffs between varying levels of sophistication in the physics, and will thus aid in future attempts to develop dependable FE models of shell type wind turbine blades.

KEYWORDS: Wind Turbines, Wind Turbine Blades, Finite Element Model, Model Form Error

1. INTRODUCTION

To address the nation's energy security and carbon footprint concerns, the U.S. Department of Energy (DOE) is aiming to promote the installed wind capacity with a target of meeting 20% of the nation's energy needs by 2030 [1]. Reliance on wind energy has been steadily increasing, bringing the installed capacity to 17 GW in the U.S. at the end of 2007 [2]. However, the U.S. needs 305 GW of installed wind power to meet 20% of the nation's energy by 2030 [1]. This demand requires a significant shift in reliance to wind energy, where the burgeoning industry is facing severe engineering problems due to premature failures of wind turbines. The wind turbine design criteria adapted in the U.S. is driven by the European wind industry and is not representative of the dynamic environmental conditions that typically occur in the U.S. wind corridor [3]. As a result, although today's wind turbines are designed for a life span of 20 years in the U.S., wind turbines typically fail on

¹ Doctoral Student, Mailing: Clemson University, Civil Engineering Department, 110 Lowry Hall, Box 340911, Clemson, South Carolina 29634-0911, U.S.A. Phone: 864-656-3003. Fax: 864-656-2670. E-mail: klvan@clemson.edu.

² Assistant Professor, Mailing: Clemson University, Civil Engineering Department, 110 Lowry Hall, Box 340911, Clemson, South Carolina 29634-0911, U.S.A. Phone: 864-656-3003. Fax: 864-656-2670. E-mail: sez@clemson.edu.

average 2.6 times per year within the first 10 years of their life span [4]. Achieving the DOE's 2030 target will only be possible if these premature failures can be prevented.

As part of the 2030 target, the DOE is also aiming to reduce the operation and maintenance costs by 40% [1]. Wind turbine unavailability (number of occurrences \times length of downtime) is attributed to three major causes: the gearbox, the generator, and the rotor blades [5]. The DOE targeted the turbine rotor and blades as the main opportunity for advancement of next generation wind turbines [1]. Furthermore, the blades are of particular importance because they produce all of the energy and are the key components in the load transfer within a wind turbine system ([6], [7], [8], and [9]). The current trend is toward larger turbines due to the increased potential for power output [2]. Larger wind turbine blades with new designs and concepts will only create more complexities in vibration characteristics. Therefore, in order to accommodate new and innovative wind turbine blades, modeling and simulation of vibration induced failures will increasingly gain importance to validate their design.

The purpose of this paper is to explore the effects of simplifications to a FE model of a 44-meter Suzlon S88-2.1 MW Type AE-42E wind turbine blade. First, a code verification study is performed, in which closed form solutions are used to ensure that ANSYS Shell281 elements converge to the calculated results. FE models are then developed using NuMAD, preprocessing software developed at Sandia National Laboratories (SNL), with a representative geometry of the Suzlon S88-2.1 MW wind turbine blade, developed from in-field measurements. The baseline model is developed, using orthotropic materials and a composite cross-section with bi-axial layers. Four additional models with less sophistication are subsequently developed, in which the sophistication of the cross section is reduced. A solution verification study is performed to determine the appropriate mesh size for the FE models. Synthetic experimental data for the displacement of the blade is developed and compared to simulations from the four less sophisticated models. Gaussian Process Model for Simulation Analysis (GPMSA), a MATLAB code developed at Los Alamos National Laboratory is utilized to represent model form error of the displacement of the four less sophisticated models with respect to the baseline model. This study will help to quantify the effects of simplifying the cross section of a FE model wind turbine blade by comparing the computation time and model form error for each model. With reduced computation cost and calibration parameters, simplified models have the potential to be implemented into complex simulations and to reduce the time necessary for model development.



Figure 1: Blade Failure in a Storm

2. REVIEW OF PERTINENT LITERATURE

Significant steps in wind turbine blade design were taken in 1984 when the National Renewable Energy Laboratory (NREL), formerly the Solar Energy Research Institute began a joint effort with Airfoils, Incorporated to develop wind turbine blades [10]. Airfoils used for wind turbine blades were originally based off those used for airplanes even though the design requirements for an airplane airfoil differ significantly from those for wind turbine blades [11]. These design requirements have since spurred the onset of several wind turbine blade innovations. In 2002, SNL formerly began the Blade System Design Study (BSDS), which incorporates the aerodynamics, structural, and manufacturing aspects of design, instead of letting individual design factors control [8]. In addition to modifying the airfoil shape, studies have also proposed other innovations such as adding microtabs [12] and the use of dihedrals, sweep, and winglets [13]. For the successful development of these new design concepts, accurate modeling and simulation of the turbine blades are emphasized to be crucial [6]. The simulation models of wind turbine blades offer a faster and more economical alternative to building and testing blades for each concept. This, however, introduces a new paradigm of how to create accurate models with high confidence in the results without extensive experiments or fidelity to data.

In 2005, a code verification of shell elements was investigated in its application to predicting the torsional response of wind turbine blades [14]. At the time this study was performed, it was typical for shell element formulations to utilize nodes at the exterior surface. Hollow cylinders were developed and modeled using three FE model configurations in ANSYS: shell elements with nodes on the exterior surface, shell elements with nodes at mid thickness, and solid elements. In the response

to bending loads, all three formulations had acceptable error in bending stress. However, as shown in Figure 2, shell elements with exterior nodes produced inaccurate results in response to torsional loads, with diverging error as the mesh was refined. The results from this study also show that solid elements are the most accurate in response to bending, converging faster and closer to the closed form solution, while shell elements with nodes at mid section need a finer mesh to converge. Despite this, solid elements are considerably more intensive to model than shell elements and are computationally more expensive even though the mesh converges more quickly. In addition, the finding that modeling shell elements with nodes on the exterior surface is a limitation of FE analysis could be a possible explanation for why previous studies were not capable of accurately accounting for the stress stiffening of wind turbine blades (see [15] and [16]).

In 2010, the tradeoffs of using a 2-dimensional beam property extraction technique versus a 3-dimensional modeling for model wind turbine blades is investigated [9].

While 2-dimensional section analyses can be appropriate for preliminary design, the authors suggest that 3-dimensional models are necessary for more detailed investigations of blades. Their study used experimental

data available for the BSDS blade, developed at SNL, and found that the 3-D FE model had a 20% difference in the mass, while the 2-D model had 16.8% difference. This is likely due to uncertainty in the manufacturing process resulting when extra material, such as glue, is used in the fabrication process. While these results are promising, it should be noted that one of the design goals of the BSDS at SNL is to reduce the weight of the blades [8].

Similar to the aforementioned study, the present paper will focus on simplifications to the FE model of a wind turbine blade, but with respect to the sophistication of the cross section. The error introduced by simplifications to the cross section can be represented by the discrepancy in the model, as previously defined [17]:

$$y_{\text{obs}}(x) = y_{\text{sim}}(x, \theta) + \delta(x) + \varepsilon^{\text{Test}} \quad (1)$$

where $y_{\text{obs}}(x)$ are the physical or observed measurements, $y_{\text{sim}}(x, \theta)$ are the model predictions, $\delta(x)$ is the discrepancy term, and $\varepsilon^{\text{Test}}$ is the measurement error. In the above equation, x represents factors that can be controlled during an experiment, also known as the control parameters. Likewise, θ represents the calibration parameters, which are parameters that are input or observed during experimentation. Calibration parameters have inherent variability, which is represented as a range of values with a zero mean, Gaussian distribution. The discrepancy term provides a representation of the disagreement between prediction and measurement for all possible values of control parameter settings. Model form error is the discrepancy that exists when there is no uncertainty in the calibration parameters input to the model. The GPMSA software package developed at LANL utilizes this procedure, and will be used later in this study to quantify model form error (refer to [17] for more a more detailed explanation).

3. VERIFICATION AND MODEL DEVELOPMENT

Verification is the process of identifying sources of numerical uncertainty due to programming mistakes, deficient implementations of algorithms and models, and the spatial and temporal discretization of continuous equations. There are two main verification activities performed in this study: code verification and solution verification. Code verification activities quantify the error produced from potential errors in the computer code by comparing closed form solutions to simulated results. Solution verification activities use mesh refinement studies to quantify the error produced at different levels of discretization of the model on a computational mesh. Code and solution verification activities are necessary for the

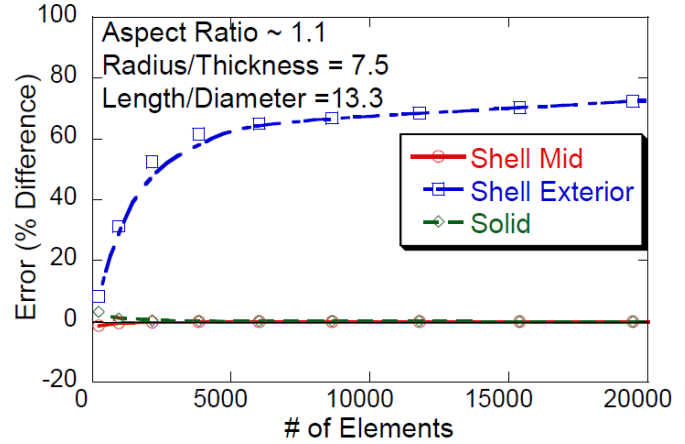


Figure 2: Mesh Refinement Study by Laird et al., with permission

credibility of the FE model, and should be performed on aspects that have significant influence on the accuracy of the solutions.

Code Verification with ANSYS

The FE models used in this study utilize Shell281 elements in ANSYS version 12, which were chosen because they have an improved formulation in response from previous studies. The first step to creating the FE model is to verify the use of these shell elements by performing code verification studies in ANSYS. This is done by comparing the results of a closed form solution to the numerical solution produced in ANSYS. Successful code verification studies occur when the numerical solution converges to the calculated solution as the mesh is refined. Any discrepancy that may be produced will quantify the numerical error from using ANSYS Shell281 elements. Significant error with a sufficiently discretized model is an indication that different element types should be utilized.

For this study, three scenarios were investigated in the code verification study: response to bending loads, response to torsional loads, and modal analysis. The first two scenarios were chosen to verify that the issues that arose from a previous code verification study [13] were resolved with the new ANSYS Shell281 elements. The verification of the modal analysis was also demonstrated because a modal analysis is one of the most typical dynamic characterizations ([18], [19], and [20]).

The first scenario involved a hollow cantilevered cylinder with bending loads applied to it. The closed form solution for bending stress is:

$$\sigma = \frac{Mc}{I} \quad (2)$$

where σ = maximum normal stress due to bending, M = bending moment, C = greatest distance from neutral axis, and I = cross sectional moment of inertia [21]. The solution was evaluated at the mid section of the shell, to avoid any membrane-bending coupling that occurs at the edge of shell layers. Figure 3 shows the result of the mesh convergence in bending.

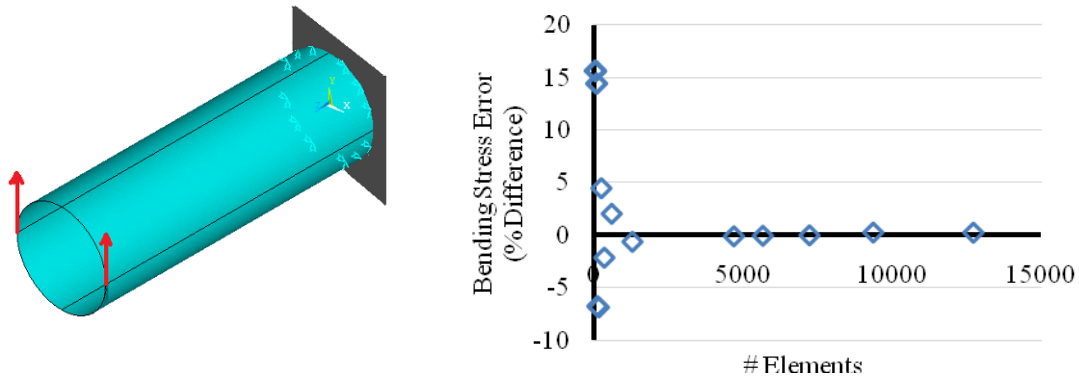


Figure 3: FE model setup for bending loads (left) and mesh refinement error (right)

The second scenario involved a hollow cantilevered cylinder with torsion loads applied to it. The closed form solution to shear stress from torsional loads is:

$$\tau = \frac{Tr}{J} \quad (2)$$

where τ = maximum shear stress due to torsion, T = applied torque, r = outer radius, and J = polar moment of inertia [21]. The solution was evaluated at the outer layer of the shell. Figure 4 plots the result of the mesh convergence for the code verification in torsion. The mesh converges nicely, showing that the Shell281 elements in ANSYS resolve the issues brought up in the past.

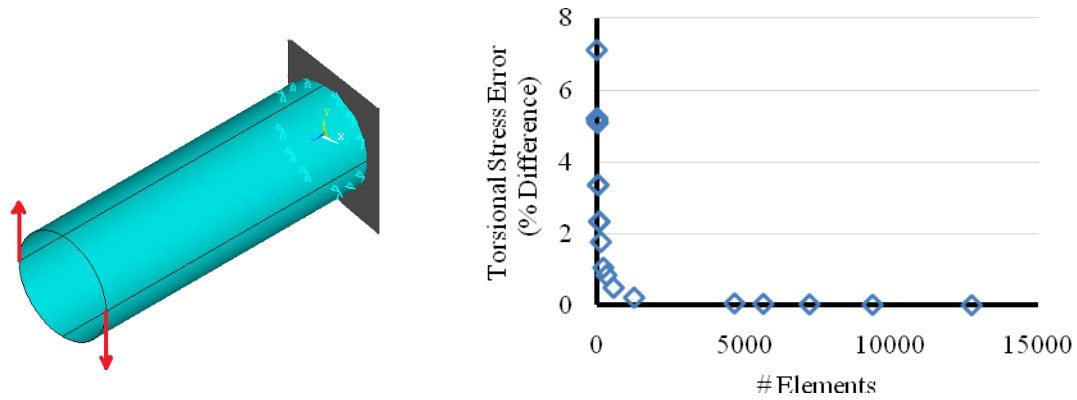


Figure 4: FE model setup for torsional loads (left) and mesh refinement error (right)

The last scenario involved a simply supported hollow cylinder without axial constraint. The purpose was to assess how reliably the modal frequencies were evaluated using Shell281 elements in ANSYS. Equations can be obtained to evaluate the closed form solutions for natural frequencies [22]. The results of the mesh refinement study for bending frequency and torsional frequency are shown in Figure 5.

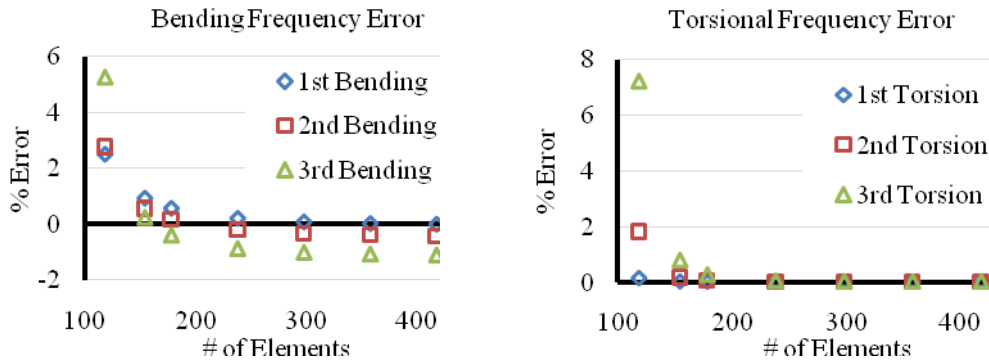


Figure 5: Mesh Refinement of the Bending (left) and Torsional (right) Frequencies of a Hollow Cylinder

From these code verification activities, it is demonstrated that there is enough evidence to support that ANSYS Shell281 elements perform acceptably. Verifying every aspect of a code is not possible for more complex engineering problems, however code verification activities strive to remove any reason to doubt the ability of the software that is implemented.

Model Development with NuMAD

NuMAD, pre-processing software developed at SNL, was utilized to create the three-dimensional FE model. The blade used herein is 44 meters long and has a representative geometry of a Suzlon S88-2.1 MW Type AE-42E wind turbine blade. The input blade dimensions were approximated from on site measurements, as shown in Figure 8, of the Suzlon wind turbine blade in Texas.

Available NREL airfoil profiles were approximated from the measurements in the absence of design airfoils for the cross sections. This ensured that the cross sections would have realistic dimensions. The material makeup of the blade was modeled using

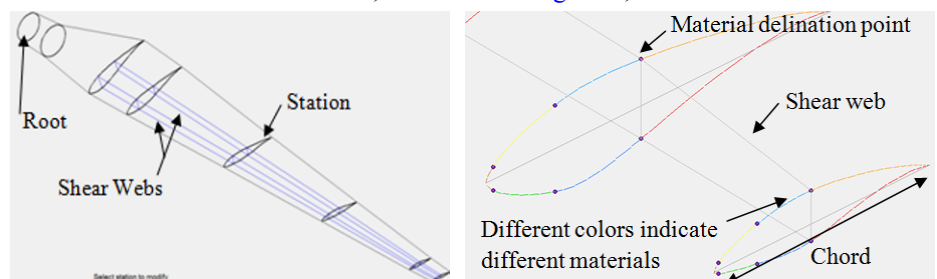


Figure 6: Wind Turbine Blade Development in NuMAD

material lay-ups similar to that of the CX-100 wind turbine blade, developed at SNL [23]. Using these material lay-ups, a baseline FE model was created, in which the cross-section was modeled using orthotropic materials and a composite lay-up with bi-axial layers. Isotropic and orthotropic materials can be input into NuMAD, which can in turn be used to create composite layers of specific thickness. The blade is modeled by defining different cross sections of the blade at a specific distance from the root, hereby known as a station, as shown in Figure 7. The airfoil, twist of station, chord length, and distance from the root of the blade are specified at each station. The stations are then divided into material sections, and different composite layers can be assigned to each material section. The internal structure of the shear web is modeled by connecting delineation points through the airfoil cross sections of the blade. In order for a blade to be modeled with considerable detail,



Figure 8: Measuring the Wind Turbine Blade



Figure 7: Suzlon Blade Interior with Shear Web

several stations with different material lay-ups are needed. Nine stations are used to define the Suzlon S88-2.1 MW blade. In the absence of a thorough investigation of the material layup, the shear web is idealized as having a constant thickness, with the height changing as the blade tapers. Five sections are defined and represented in Figure 9 with different colors: the root, the spar of the blade, the trailing edge, the leading edge, and the internal shear web that is not shown.

Basic assumptions were established to simplify the cross section. To assume a uni-axial composite from a bi-axial composite, all of the materials were assumed to have no rotation, effectively creating a cross-section with all of the composite layers oriented in the same direction. To assume an isotropic cross-section, the Young's Modulus used in the x- direction was assumed for the y- and z- directions. To convert from a composite to a smeared cross section, the rule of mixtures for composites [24] was applied, which is a method for computing a characteristic Young's Modulus, Shear Modulus, Poisson's ratio, density, and thickness for a composite, so that only one layer is needed to model the cross section.

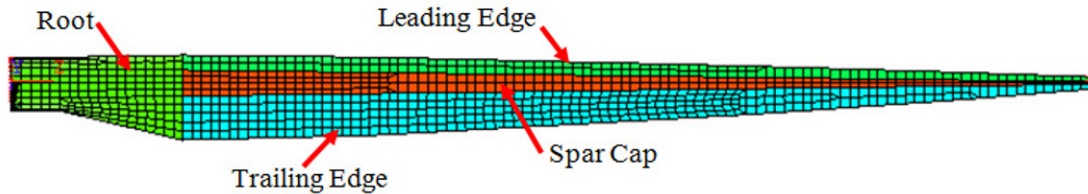


Figure 9: ANSYS model showing different sections of the blade

Subsequent FE models of the Suzlon blade with incrementally simplified cross sections were created by applying these assumptions. First, the bi-axial layers of the baseline blade were rotated so that all of the layers in the cross section were oriented in the same direction, creating uni-axial layers for the Blade 1 model. This reduced the number of calibration parameters, because the angle by which layers are rotated is now uniform, and no longer needs to be defined. From Blade 2, the rule of mixtures for composites was applied, resulting in a uniform cross section for each material section to define Blade 3. Blade 2 can also be simplified by defining the composite layers with isotropic material properties, by eliminating the Young's Modulus in the y- and z- directions. This reduces the number of calibration parameters because fewer values are needed to define the material properties. Blade 4 is created by applying the rule of mixtures to the Blade 3 model, resulting in a uniform cross section defined with isotropic properties. The resulting FE models are summarized in Table 1. The number of calibration parameters is calculated based on the material properties, and the number of materials used in each model, and is also reported in Table 1. The blade numbering of the FE models reflects the reduction in the number of calibration parameters associated with each model.

FE Model	Material Properties	Lay-Up	Layer Orientations	Number of Parameters
Baseline	Orthotropic	Composite	Bi-Axial	90
Blade 1	Orthotropic	Composite	Uni-Axial	81
Blade 2	Orthotropic	Smeared	N/A	45
Blade 3	Isotropic	Composite	N/A	36
Blade 4	Isotropic	Smeared	N/A	20

Table 1: FE Models Developed in ANSYS

Solution Verification with ANSYS

A solution verification study is performed by refining the mesh of the FE model to assure solution accuracy. A proper mesh refinement should yield a solution that converges to an asymptote, meaning that further refining the mesh will not affect the results.

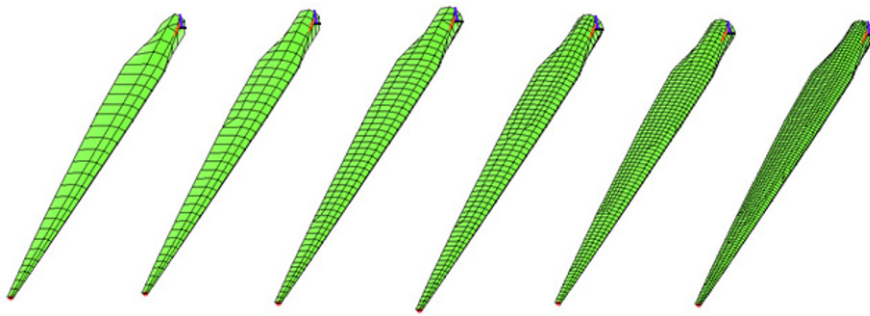


Figure 10: Six Representative Mesh Refinements in ANSYS

For the purpose of this study, the mesh convergence study was performed using static and modal analysis simulations in ANSYS. Static and modal analysis simulations were chosen since they constitute two common experiments practiced today on wind turbine blades. The modal analysis observed the convergence of four of the modes. The static analysis observed the stress produced at the root of the blade and the tip displacement of the blade due

to four point loads on the blade.

Figure 10 shows six of the forty meshes used to perform the mesh refinement study in ANSYS. The coarsest mesh is shown on the left with 62 elements, and the finest on the right, with 10,663 elements, and intermediate levels of mesh discretizations in between.

The mesh convergence of the first natural frequency for the five FE models is plotted in Figure 11. The mesh refinement for the modal analysis and static analysis were compared, and the mesh size chosen for the final FE model consisted of 2152 elements and is highlighted with the vertical black line in Figure 11. Table 2 reports the error of the four simplified FE models when compared to the baseline FE model as the reference solution. Together, the first two flapwise modes and first two edgewise modes are reported.

From the results in Table 2, the step of rotating the composite layers from the baseline model to the Blade 1 model produces a significant amount of deviation in each of the modes. This is especially true for the flapwise modes, in which the average percent error from the baseline FE model was -45.40% as compared to the edgewise modes, in which the average percent error was 1.59%. The next simplification, in which the layers in the Blade 1 model were smeared to develop the Blade 2 model, appears to create compensating errors, which allows Blade 2 to potentially perform better than Blade 1. Compensating errors occur when the error introduced past the first simplification accounts for the original error incurred, resulting in an overall smaller error. This is noticeable in the first and second flapwise modes, where the error for Blade 2 is significantly less than the error for Blade 1.

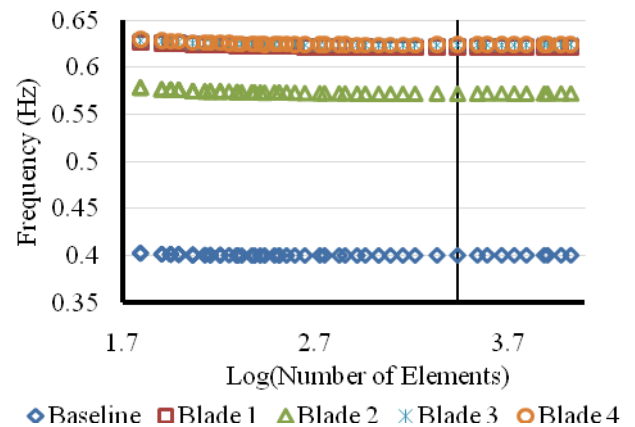


Figure 11: Mesh Convergence for Mode 1

FE Model	Computation time in ANSYS	Mode 1 – 1 st Flap	Mode 2 – 1 st Edge	Mode 3 – 2 nd Flap	Mode 5 – 2 nd Edge
Baseline	25 sec.	--	--	--	--
Blade 1	25 sec.	-55.31%	5.86%	-51.63%	-2.69%
Blade 2	21 sec.	-42.96%	13.40%	1.83%	46.86%
Blade 3	25 sec.	-55.94%	5.49%	-49.99%	-0.02%
Blade 4	19 sec.	-55.99%	5.54%	-50.24%	0.02%

Table 2: Percent Error of the Simplified FE Models under Modal Analysis

The errors for blades 3 and 4, which are the isotropic models, are comparable. Unlike when the FE models were Orthotropic, this result can be attributed to the ability of the rule of mixtures to produce a cross section with comparable properties to its composite counterpart. In addition, the computation time necessary in ANSYS is also reported. Blades 2 and 4, which both utilized smeared cross sections, effectively decrease the computation necessary to run the simulation.

The mesh convergence of the root stress and tip displacement for the five FE models is plotted in Figure 12. These figures confirm the asymptotic convergence of the FE models with increasing mesh refinement.

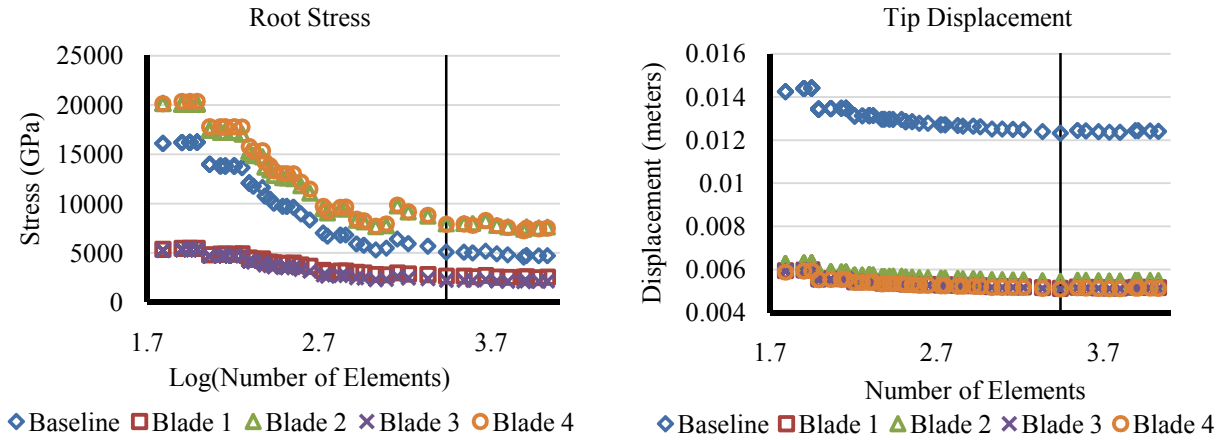


Figure 12: Mesh Convergence of the Root Stress (Left) and Tip Displacement (Right)

Table 3 shows the error, for the five simplified FE models when compared to the baseline FE model as the reference solution of the results for the static analysis.

FE Model	Computation time in ANSYS	Tip Displacement	Root Stress
Baseline	22 sec.	--	--
Blade 1	23 sec.	58.40%	50.52%
Blade 2	13 sec.	55.81%	-53.90%
Blade 3	22 sec.	58.69%	57.89%
Blade 4	13 sec.	58.70%	-55.40%

Table 3: Percent Error of the Simplified FE Models under Static Analysis

The results from Table 3 show a consistent percent error for all of the simplified FE models in both the tip displacement and stress at the root, except that blades 2 and 4, which utilized smeared cross sections, produce a negative stress error. This signifies that the root stress prediction for the smeared models increased when compared to the baseline model, whereas root stress for the composite models decreased. In terms of tip displacement, blades 2 and 4, which have smeared cross sections, produce comparable results to blades 1 and 3, which both use composite, uni-axial layers. Unlike when the modal analysis was performed, the computation in ANSYS varies significantly for the static analysis. Notably, the smeared FE models require 44% less computation time to be analyzed than the baseline blade model. This, combined with the decreased number

of calibration parameters needed to define those models, make FE models that utilize smeared cross sections of wind turbine blades potentially attractive to implement. The differences associated with each model with respect to the baseline model will be discussed further in the next section, in which model form error is developed.

4. INFERRING MODEL FORM ERROR

The ability of the alternate blade models to accurately predict the results from the “baseline” model is limited with respect to the sophistication of the physics in the FE models, exhibited through model form error, which must be bias corrected. Discrepancy is not quantified as a single value, but rather as a range of values. Thus, the bias correction results in a range of

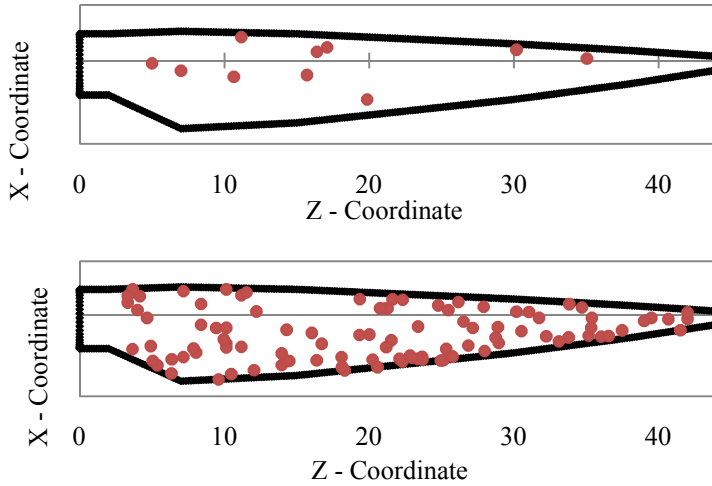


Figure 13: Blade Profile with Observed Data Points (Top) and Simulated Data Points (Bottom)

values for the prediction range of the calibrated simulator models. To investigate model form error in this study, the simulations for the baseline model are used to generate synthetic experimental data, and the simulations from the blade models with lower sophistication are calibrated with respect to this synthetic experimental data. It will be assumed that the calibration parameters in the FE models are known with certainty, such that the discrepancy that will be quantified is due to the inadequacies with respect to the sophistication of the physics in the model. This is an important assumption, because it means that the error in the blade models is attributed to model form error and experimental variability, and that the errors due to uncertainty in the parameters have already been accounted for. While this study is meant to be a proof of concept for model form error, it should be noted that a thorough

sensitivity analysis and parametric study of the calibration parameters should be carried out. However, in the absence of experimental data, the values chosen for the calibration parameters are based off the assumptions discussed in the model development section of this paper.

This study uses the Gaussian Process Model for Simulation Analysis (GPMSA) developed at Los Alamos National Laboratory, to infer model form error. In the way implemented herein, GPMSA has two functions: (1) to create a fast running surrogate model of the relationship developed from the simulation inputs and outputs, and (2) to create a difference model between the simulation and experimental results. The synthetic experimental data is generated by applying a concentrated point load to ten randomly chosen points on the blade, as shown in the top blade of [Figure 13](#). The control parameters used to measure these points are the x and z coordinates, which are the parameters that can be changed to obtain results at different locations for the same type of experiment. In this study, all possible values of x and z represent the entire domain of applicability, which forms the profile of the blade. Using the synthetic experimental data from the baseline FE model and the simulation data of the four FE blade models with lower sophistication, four surrogate models are trained to represent model form error in GPMSA.

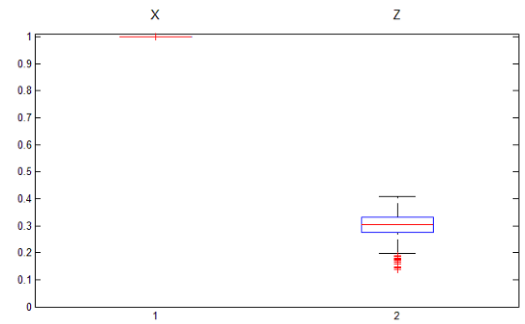


Figure 13: Sensitivity Analysis of the GPM for the Blade 4 model

Because the parametric uncertainty of the calibration parameters is assumed to be zero, the only uncertainty taken into account is experimental variability, which is assumed to be 0.01%. The GPMSA software trains a surrogate model from the simulated data and experimental variability. Although several levels of sophistication were removed from the baseline

model to develop the four blade models, the initial step of rotating the bi-axial layers to create a composite blade with layers oriented in the same direction, from the baseline blade to Blade 1 appears to have the most effect on the errors produced in the less sophisticated blade models. For illustrative purposes, Blade 4 will be used to report the results from GPMSA since

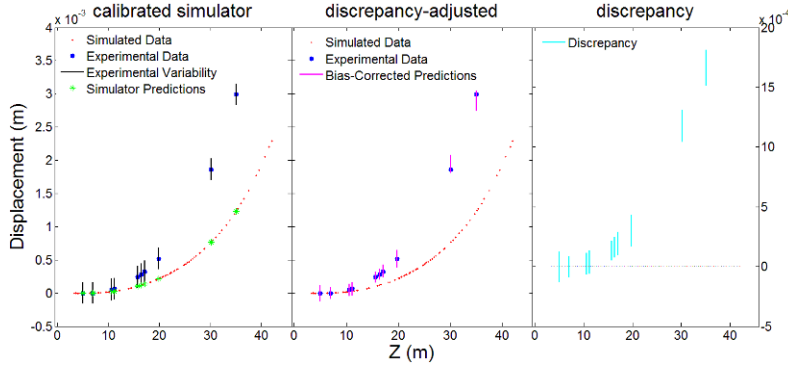


Figure 14: Calibrated Predictions (left), Bias-Corrected Predictions (Middle), and Discrepancy (Right) for Blade 4

the results for the other three blades produce a comparable discrepancy when plotted. As shown in Figure 14 for the Blade 4 model, a sensitivity analysis shows that the trained surrogate model is more sensitive to the z-coordinate of where the concentrated point load is applied rather than the x- coordinate.

Figure 15 shows the results of the trained surrogate model for Blade 4. First, the surrogate model is trained to fit the simulated data, as shown in the left plot. Next, the surrogate model is bias corrected so that the predictions at the locations of the synthetic experiments converge to the experimental variability. The results of the bias corrections are represented by the error bars in the second plot of Figure 15. Although the predictions are not perfectly aligned with the experimental variability of the first subplot, the surrogate model is accurate because the experimental measurements fall within the range of values for the bias corrected predictions. The difference between the mean of the simulator predictions before and after being bias corrected is shown in the far right plot of Figure 16. This difference is known as the discrepancy at experimental locations, and is the amount of error that is associated with the less sophisticated blade model when compared to the baseline.

In addition to the experimental locations, the surrogate models in GPMSA can also be used to predict displacement values over the entire domain of applicability, as shown in Figure 17. This predictive capability is more comprehensive when compared to just the ten locations shown in Figure 15. The volume between the surface of bias corrected predictions and calibrated predictions is highlighted and used to quantify model form error. The values for the volume associated with each blade model are reported in Table

4. The volumes are then normalized to unity as a comparison between all four models. Blade 2 has the smallest value, representing the blade model with lowest discrepancy, and subsequently, lowest model form error. This comes as expected, as shown in the mean discrepancy plot of Figure 16. This result can come from a variety of possibilities. First, it is possible that when multiple simplifications are made from the baseline model, the error introduced past the first simplification compensates for an earlier simplification. Thus, although the model form error is expected to increase as the number of simplifications increases, the simplified model instead compensates for the original error and provides the lower model form error. It is also possible that the assumptions applied to simplify the models were too crude to produce FE models with calibration parameters comparable to each other. The strong assumption that the calibration parameters were known with certainty could be explored in later studies by developing models when experimental data is

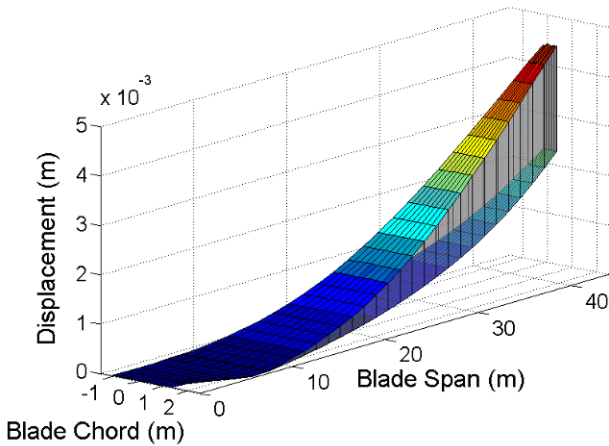


Figure 15: Bias-Corrected Predictions (top) and Calibrated Predictions (bottom)

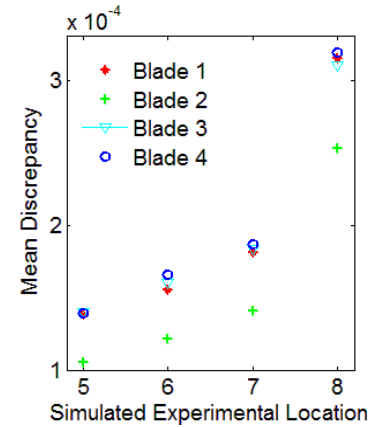


Figure 16: Mean Discrepancy at four of the ten experimental locations

available rather than synthesized.

FE Model	Volume (m ³)	Normalized Volume
Blade 1	0.02194	0.9881
Blade 2	0.02017	0.9083
Blade 3	0.02221	1.0000
Blade 4	0.02218	0.9985

Table 4: Model Form Error of the Blade Models

5. CONCLUSIONS

The model form errors associated with simplifications to a FE model of a 44-meter Suzlon S88-2.1 MW Type AE-42E wind turbine blade were investigated in this study. Surrogate models developed using GPMSA were utilized to compare the model form errors, and were effective in developing predictions over the entire domain of applicability, rather than at just the locations of synthetic experimental data. The initial simplification of rotating composite layers to develop a material cross section with composite layers oriented in the same direction appears to have the greatest affect on the discrepancy produced in the subsequent FE models. However, compensating effects of errors still need to be accounted for, because they can make it appear that a less sophisticated model has less discrepancy than one model with a higher level of sophistication. To further explore model form error, future studies could incorporate experimental data into their analyses to reduce the need for assumptions, and to further quantify the predictive abilities of simplified FE models.

6. REFERENCES

- ¹ U.S. Department of Energy, “20% Wind Energy by 2030 – Increasing Wind Energy’s Contribution to U.S. Electricity Supply,” DOE/GO-102008-2567, 2008.
- ² Ashwill, T.D., “Materials and Innovations for Large Blade Structures: Research Opportunities in Wind Energy Technology,” *50th AIAA Structures, Structural Dynamics, & Materials Conference*, Palm Springs, CA, 2009, AIAA-2009-2407.
- ³ Kelley, N., Shirazi, M., Jager, D., Wilde, S., Adams, J., Buhl, M., Sullivan, P., and Patton, E., “Laminar Low-Level Jet Project Interim Report,” NREL Technical Report NREL-TP-500-34593, 2004.
- ⁴ Echavarria, E., Hahn, B., van Bussel, G.J.W., and Tomiyama, T., “Reliability of Wind Turbine Technology Through Time,” *Journal of Solar Energy Engineering*. Vol 130, No. 3, pp. 031005, 2008.
- ⁵ Hill, R.R., Stinebaugh, J.A., Briand, D., Benjamin, A.S., and Lindsay, J., “Wind Turbine Reliability: A Database and Analysis Approach,” Sandia National Laboratories Report SAND2008-0983, 2008.
- ⁶ Ashwill T., and Laird, D., “Concepts to Facilitate Very Large Blades,” *45th AIAA Aerospace Sciences Meeting and Exhibit*, Reno, NV, 2007, AIAA-2007-817.
- ⁷ Ashwill, T., “Blade Technology Innovations for Utility-Scale Turbines,” Sandia National Laboratories Technical Report, Report # SAND2006-4941C.
- ⁸ Paquette, J.A., and Veers, P.S., “Increased Strength in Wind Turbine Blades through Innovative Structural Design,” *European Wind Energy Conference*, 2007, Milan, Italy.
- ⁹ Resor B, Paquette J, Laird D, Griffith DT, “An Evaluation of Wind Turbine Blade Cross Section Analysis Techniques,” *AIAA/ASME/ASCE/AHS/ASC Structures, Structural Dynamics, and Materials Conference*, April 2010, Orlando, FL, USA.

- ¹⁰ Tangler, J.L., and Somers, D.M., “NREL Airfoil Families for HAWTs,” *American Wind Energy Association Windpower Conference*, 1995, Washington, DC, USA.
- ¹¹ Somers, D.M., “Design and Experimental Results for the S805 Airfoil,” NREL Technical Report, Report NREL/SR-440-6917, 1988.
- ¹² Nakafuji, D.T., van Dam, C.P., Smith, R.L., and Collins, S.D., “Active Load Control for Airfoils using Microtabs,” *Journal of Solar Energy Engineering*, Vol. 123, No. 4, pp 282-290, 2001.
- ¹³ Chattot, J., “Effects of Blade Tip Modifications on Wind Turbine Performance using Vortex Model,” *Computers and Fluids*, Vol. 38, No. 7, pp. 1405-1410, 2009.
- ¹⁴ Laird DL, Montoya FC, and Malcolm DJ, “Finite Element Modeling of Wind Turbine Blades,”” *43rd AIAA Aerospace Sciences Meeting and Exhibit*, January 2005, Reno, NV, USA.
- ¹⁵ Bechly, M.E., and Clausen, P.D., “Structural Design of a Composite Wind Turbine Blade Using Finite Element Analysis,” *Computers and Structures*, Vol. 63, No. 3, pp. 639-646, 1997.
- ¹⁶ Jensen, F.M., Galzon, B.G., Ankersen, J., and Stang, H., “Structural testing and numerical simulation of a 34 m composite wind turbine blade,” *Composite Structures*, Vol. 76 Issues 1-2, pp 52-61, 2006.
- ¹⁷ Kennedy, M., and O’Hagan, A., “Predicting the Output from a Complex Computer Code when Fast Approximations are Available,” *Biometrika*, Volume 87, No. 1, pp. 1-13, 2000.
- ¹⁸ Higdon, D., Gattiker, J., Williams, B., and Rightley, M., “Computer Model Calibration Using High-Dimensional Output,” *Journal of the American Statistical Association*, Vol. 103, No. 482, pp. 570-583, 2008.
- ¹⁹ White J.R., Adams D.E., and Rumsey M.A., “Modal Analysis of CX-100 Rotor Blade and Micon 65/13 Wind Turbine,” *28th International Modal Analysis Conference*, February 2010, Jacksonville, FL, USA.
- ²⁰ Griffith, D.T., and Carnes, T.G., “Experimental Modal Analysis of 9-meter Research-sized Wind Turbine Blades,” *28th International Modal Analysis Conference*, February 2010, Jacksonville, FL, USA.
- ²¹ Griffith, D.T., Carne, T.G., and Paquette, J.A., “Modal Testing for Validation of Blade Models,” *Wind Engineering*, Vol. 32, No. 2, pp. 91-102, 2008.
- ²² Hibbeler, R.C., **Mechanics of Materials**, Pearson Prentice Hall, Upper Saddle River, New Jersey, 2005.
- ²³ Blevins, D.R., **Formulas for Natural Frequency and Mode Shapes**, Krieger Publishing Company, Malabar, Florida, 1993.
- ²⁴ Berry, D., and Ashwill, T., “Design of 9-meter Carbon-Fiberglass Prototype Blades: CX-100 and TX-100,” *Technical Report SAND-2007-0201*, Sandia National Laboratories, Albuquerque, New Mexico, 2007.
- ²⁵ Tsai, S.W., and Hahn, H.T., **Introduction to Composite Materials**, Technomic Publishing Co., Westport, CT, 1980.

7. ACKNOWLEDGEMENTS

The authors wish to express their gratitude to Mark Mollineaux, Ph.D student at Stanford University in civil engineering for his contribution to the code verification study. The authors are also grateful to Jean-Paul Cane, of Rope Partner, Inc. for providing the measurements and photos of the Suzlon wind turbine blade.

Operational Modal Analysis of Operating Wind Turbines: Application to Measured Data

S. Chauhan⁺, D. Tcherniak⁺, Jon Basurko[#], Oscar Salgado[#], Iker Urresti[#]
Carlo E. Carcangiu[‡], Michele Rossetti[‡]

⁺ Bruel & Kjaer Sound and Vibration Measurement A/S
Skodsborgvej 307, DK-2850, Naerum, Denmark

[‡] Alstom Wind, Spain

[#] Ikerlan-IK4, Spain

Email: schauhan@bksv.com

ABSTRACT

Previous works by the authors have shown that though Operational Modal Analysis (OMA) techniques are suitable for global dynamic analysis of a wind turbine under parked conditions, there are several issues in their application to operational wind turbines. These issues including time varying nature of the structure, presence of harmonic content in the loading (due to rotor rotation), considerable aerodynamic damping etc. prevent straightforward application of OMA to operational wind turbines. The authors have further proposed a strategy to combat these issues and modify OMA methodology to tune it for operational wind turbines. A successful implementation of this strategy was employed and demonstrated to work satisfactorily on simulated vibration response data for a 3MW wind turbine.

Work presented in the current paper is an extension of the previous work and describes the details of the measurement campaign aimed at identifying modal parameters of ALSTOM's ECO 100 wind turbine. Since measuring on an operational wind turbine is a challenging job in itself, the paper also describes measurement planning and execution phases. The paper illustrates various key aspects related to practical measurements on an actual wind turbine and underlines the importance of proper planning and experiment design. The importance of a priori knowledge provided by finite element model based simulations is also underlined.

1. INTRODUCTION

Current focus of designing bigger and efficient wind turbines to meet the growing energy demands has put several challenges in front of wind turbine designers and manufacturers. A thorough understanding of wind turbine dynamics is necessary to meet these requirements. In this regard, use of Operational Modal Analysis (OMA), as a tool to understand wind turbine dynamics based on measured data, seems very promising.

Work presented in this paper builds on the studies showcased in [1-3]. While application of OMA is quite straight forward in case of parked wind turbines [4], several challenges are posed in case of operational wind turbines. Study [1] discussed the applicability limits of OMA to operational wind turbines. This work showed, based on analytical and simulation studies, that presence of considerable aeroelastic effects and rotational components in the excitation along with time varying nature of wind turbine structure restricts application of OMA to operational wind turbines as they stretch the basic OMA assumptions.

It is shown that since a wind turbine structure consists of several substructures that move with respect to each other (yawing of nacelle, pitching of blades, rotor rotation etc), the assumption regarding time invariance of the structure is not valid anymore. Additionally, it is further observed that aeroelastic forces exciting an operational wind turbine are characterized with prominent peaks which are accompanied with thick tails, there by not fulfilling the OMA requirement that excitation forces should have uniform broadband spectra. These forces are also found to be quite correlated at the rotational frequency and its harmonics. This nature of excitation forces also results in violation of basic OMA assumptions. This work was carried forward in [2] by combining the knowledge gained on the basis of these investigations and the recommendations that have been suggested to perform OMA on operational wind turbines.

In [2] it is shown by means of simulated data, how the above mentioned challenges can be overcome and OMA can be applied to operational wind turbines using careful planning and techniques such as multi-blade coordinate (MBC) transformation. The feasibility of OMA approach for understanding dynamics of operational wind turbines was shown by means of simulations on a model of ALSTOM WIND ECO 100 wind turbine; a 3 MW turbine.

Work presented in this paper is in continuation of the work presented in [2] and focuses on the experiment phase of the overall OMA campaign on ECO 100 turbine installed in La Collada, Tarragona, Spain. It is important to note that overall goal of this ongoing project is to utilize the strategies (formulated and consolidated by means of simulated data in [2]) to perform OMA on data acquired on ECO 100 turbine in operation for its dynamic characterization.

The paper is organized as follows. Section 2 describes the main motivation behind the project and lays down the goals and objectives for the two campaigns, short term and long term, in which the project is split. Section 3 discusses the design of the measurement campaigns, including test set up planning keeping in view the goals of the project, understanding gained from simulation based studies and limitations of OMA. The instrumentation and data acquisition phase is described in section 4. Main goal of this section is to not only provide the details of instrumentation and test layouts for short term and long term campaigns, but also share practical issues and challenges during this task and measures taken to overcome the same. Following this some preliminary results are presented and finally conclusions are drawn.

2. OBJECTIVES

The main motivation of this project is to obtain a reliable dynamic model of the wind turbine. Typically there exist several numeric models (such as aeroelastic models, finite element models etc) of a wind turbine to characterize its dynamics. However, it is imperative from dynamics point of view to validate these models by means of experimentation in order to prove and improve their reliability. Based on its suitability and applicability on large real-life structures and its ability to characterize the dynamics of large structures, Operational Modal Analysis (OMA) is chosen as a technique for experiment based characterization of wind turbine dynamics. The choice of OMA as a preferred technique for this task was validated by means of a pre study whose results are already published in [2].

The objectives of this project can be viewed from three different perspectives;

- **Structural:** To get an understanding of the dynamic behavior of the wind turbine and the interaction between the main structural elements (systems and subsystems) of the turbine (i.e. tower, drive train, rotor and main frame) with other mechanical and electrical subsystems (i.e. generator, transformer, gearbox and inverter). This understanding is expected to aid in the overall design process of these structural elements by means of verification of existing design and redesigning if necessary. Yet another objective in this respect is to correlate the experimentally identified system with FE/Multibody analysis based simulations.
- **Controls:** Use the OMA based system identification for better controller design by using results from system identification and extracting linear models from real experiments and compare them with linear models extracted from the simulations. This is important since control performance is dependent on accuracy of these linear models and hence it's important to validate these models for achieving optimal control [5].
- **Mechanical:** Validation of models of drive train and elastic mounts of mechanical components (gearbox and generator).

To accomplish the goals and objectives of characterizing the dynamics of wind turbine structure and substructures under the variety of operational conditions, it is decided to carry out the project in two stages; a *long term campaign* and a *short term campaign*.

The aim of the *long term campaign* is to experimentally determine the modes of the main structural components of the wind turbine; i.e. estimation of tower modes, rotor modes, drive train mode and mainframe modes for a number of operational working points that collectively represent the complete operational conditions of the wind turbine. Since this requires data acquisition for a long period of time (that is deemed sufficient in order to ensure that data corresponding to various

operational conditions is acquired), this campaign is termed long term campaign. In addition to the above mentioned modes, the gearbox and generator modes are also required to be estimated when turbine is operating at nominal power and when it's operating at 1/3 of nominal power. On the other hand, the *short term campaign* is aimed at identification of modes of other mechanical and electrical subsystems (transformer and electrical cabinets) and understanding their interaction with nacelle and mainframe. The details of these campaigns, keeping in view the overall objectives of the project, are provided in the next section, which describes the design and planning of experiments pertaining to the two campaigns.

3. DESIGN OF EXPERIMENTS

The results of the long term campaign are to be presented in the form of a Campbell diagram [6] which is a representation of wind turbine dynamics in its operating regime, typically given in terms of varying wind speeds. Thus, to characterize the dynamics of the operational turbine, operational working points are chosen in the wind speed range of 3 m/s to 25 m/s in steps of 2 m/s. For the short term campaign, aimed at identification of modes of other mechanical and electrical subsystems, the identification procedure is independent of turbine operating conditions. The modes of interest (for both campaigns) are listed in [Table 1](#).

While designing an experiment of this kind, one has to keep in mind the practical constraints which play a significant role in terms of what is measurable and what is not. One of the foremost practical issues associated with this experimental campaign is that measurement on the turbine blades is quite difficult. From the observability point of view, it would have been ideal to instrument the three blades at various sections (along the length) as that would have significantly enhanced the chances of observing and estimating the rotor modes. However, in this project, this was not a possibility as only a limited section of the blades was approachable for sensor instrumentation and that too would have required special arrangements with regards to measured data transfer and synchronization. However it was expected that the rotor-related modes will affect dynamics of the tower and nacelle, thus these modes can be detected from the tower and nacelle measurements. This supposition was partly confirmed by OMA performed on simulated data: the rotor modes were found in tower measurements, although it was comparatively difficult to distinguish and classify them.

Significance of simulation studies in test planning is further underlined by the fact that the simulations provide considerable aid in choosing the sensor locations so as to observe all the modes of interest.

Large size of the turbine also makes it important to plan the placement of various data acquisition systems. There are other considerations as well, with regards to the data acquisition system, which are important from test planning perspective. A measurement campaign along the lines of this project puts the following requirements on the design of data acquisition system; a high quality data acquisition system that

- can continuously acquire data for a long period of time (several months),
- can be used as a distributed and synchronized system,
- can support a large number of measurement channels,
- can support auxiliary channels (such as wind speed, yaw angle, tacho signals etc), and
- can be remotely monitored and operated.

Since the measurement system is a distributed system, placement of data acquisition front ends plays an important role in optimizing the required cable length and also effective management of the cables, thus aiding in minimizing the workload related to wind turbine instrumentation.

The demands of a robust data acquisition system also emerge from the need of long term campaign. Since the project aims at characterizing the dynamics of an operational turbine under various operating conditions, it is necessary that the data is acquired over a long period of time. This requires data acquisition system to be remotely monitored, capable of automatic operation and needs of emergency backup in case of power shutdowns. These points are also taken into consideration while planning the measurement phase. It is further decided, keeping in view these requirements that the duration of long term campaign is 3 months from August, 2010 to October, 2010. The choice of this period is governed by the fact that the site at which the wind turbine prototype is installed is expected to experience sufficient wind during this timeframe, and that three months time period should suffice in terms of capturing all the operational modes of the turbine.

Table 1: Modes to be identified

	Systems and Subsystems	Modes	Abbreviations
Main Structural Components	Tower Dominated Modes	1 st Fore Aft Mode	T1FA
		2 nd Fore Aft Mode	T2FA
		1 st Side to Side Mode	T1SS
		2 nd Side to Side Mode	T2SS
		Torsional Mode	T1T
	Drive Train Dominated Modes	1 st Drive Train Mode	DT1
	Rotor Dominated Modes	1 st Collective In Plane Mode	I1C
		2 nd Collective In Plane Mode	I2C
		1 st Collective Out of Plane Mode	O1C
		2 nd Collective Out of Plane Mode	O2C
		1 st Forward and Backward In Plane Whirling Modes	I1FW, I1BW (when parked: I1Vert, I1Hor)
		2 nd Forward and Backward In Plane Whirling Modes	I2FW, I2BW (when parked: I2Vert, I2Hor)
		1 st Forward and Backward Out of Plane Whirling Modes	O1FW, O1BW (when parked: O1Yaw, O1Tilt)
		2 nd Forward and Backward Out of Plane Whirling Mode	O2FW, O2BW (when parked: O2Yaw, O2Tilt)
	Main Frame	Fore Aft Bending Mode	
		Side to Side Bending Mode	
		Torsional Mode	
	Nacelle	Fore Aft Bending Mode	
		Side to Side Bending Mode	
		Torsional Mode	
Other Mechanical and Electrical Components	Transformer	3 first modes (3 principal axes of inertia)	
	Electrical Cabinets	3 first modes (3 principal axes of inertia)	
	Generator	3 first modes (3 principal axes of inertia)	
		Vertical Mode	
	Gearbox	3 first modes (3 principal axes of inertia)	
		Vertical Mode	

4. INSTRUMENTATION AND MEASUREMENTS

The measurements are performed on ALSTOM ECO 100 prototype located in La Collada, Tarragona, Spain (Fig. 1). ECO 100 is a three bladed turbine with a rated power output of 3 MW and has rotor diameter of 100.8 m [7].



Figure 1: The ECO 100 Wind Turbine

4.1 Control Signals

As previously stated, the project is run in two stages aiming at different set of objectives. Since the project comprises of two separate measurement campaigns, the choice of locations where acceleration signals are to be measured differ in case of long term and short term campaigns. However, there are several control signals that are to be measured in case of both campaigns. These control signals are required in order to define the turbine operating conditions or status, as one of the project objectives requires measurement of turbine dynamic characteristics under various operating conditions. The control signals measured in this project are: wind direction, wind speed, converter torque, torque reference, yaw angle, low speed shaft rotation, high speed shaft rotation, pitch angle and active power. While all of these signals help in characterizing the operating conditions of the turbine, they also serve a very useful purpose of classifying the vast amount of data collected during the project. At this point, it is important to realize that the combined time span of both campaigns is close to 3.5 months during which the acquisition system will be continuously acquiring data. Hence an effective means of classifying this data is paramount to thoroughly exploit the acquired data for dynamic analysis. Further, yaw angle signal is also used for coordinate transformation in order to correctly align the nacelle and the tower when the turbine is yawing, as explained in section 3.5.

4.2 Data Acquisition System and Transducers

Keeping in view the demands of the project and based on the criterion listed in previous section, four Bruel & Kjaer PULSE IDA Frontends (Type 3560) are used. These frontends are capable of being configured for functioning as a distributed system by means of a synchronization cable. An important reason for choosing this particular type of frontends is the need to have a wide dynamic range so as to cover all the possible vibration levels during the entire measurement campaign. The frontends are also capable of handling the auxiliary signals coming from the control system of the turbine.

Fig. 2 shows the location of Frontends in the turbine during the measurement phase. Two frontends are placed in the tower and other two are placed in the nacelle. The two frontends in the tower, with 6 channels each, are located at 24m and 62m level platforms and are only used for tower acceleration measurements during long term campaign. These are not utilized in the short term campaign during which data is acquired by means of two frontends in the nacelle only.

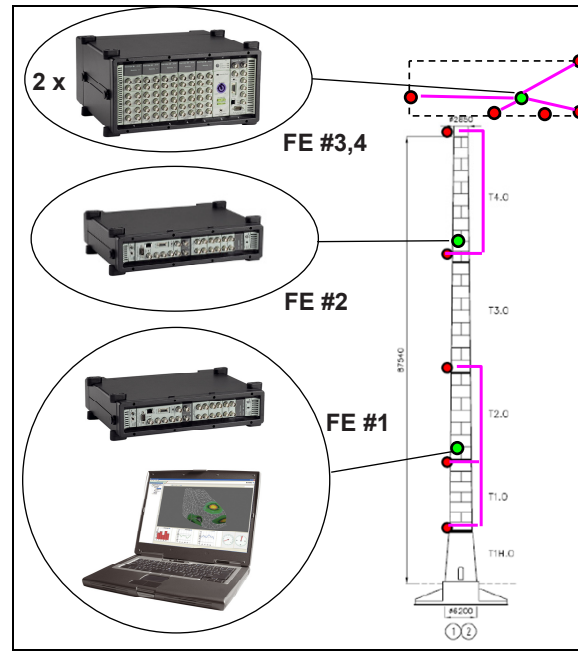


Figure 2: Frontend Locations

Since the nacelle is capable of yawing about the tower during operation, special care has to be taken with regards to cable handling since the data acquisition system is distributed in the tower and the nacelle. This requires ascertaining proper length of various cables (synchronization cables, data cables etc.) so that cable coiling due to yaw is avoided.

The modal frequencies of interest, for the wind turbine structure, are expected to be below 50 Hz, and the expected vibration magnitude is below 2g. Based on these considerations, Bruel & Kjaer DC accelerometers Type 4575 are chosen as they are very sensitive and have suitable measurement and frequency range. An optical tachoprobe (B&K Type MM-0360) is also used to precisely measure the low shaft RPM.

4.3 Softwares

Data acquisition software used in this project is Bruel & Kjaer PULSE Data Recorder Type 7780. Apart from the data acquisition software, remote monitoring software is also used to monitor the system for variety of reasons including restarting of acquisition software, rebooting the computer, downloading the measured data etc.

Once the measurement campaign is over, the data will be analyzed with PULSE OMA Type 7760 to estimate modal parameters for dynamic characterization of the turbine.

4.4 Short Term Measurement Campaign

The main goal of the short term campaign is to identify the modal parameters of various mechanical and electrical subsystems and understand their dynamics in terms of their interaction with nacelle mainframe. This campaign also serves a secondary purpose of providing a check for the performance of the data acquisition purpose before the start of the long term campaign. The structures instrumented in this campaign are nacelle mainframe, transformer, convertor and control cabinets. During this campaign, acceleration measurements are taken at 20 locations, with nacelle frame instrumented most heavily (14 locations, 38 channels, including central and frontal mainframe, see Fig. 3).

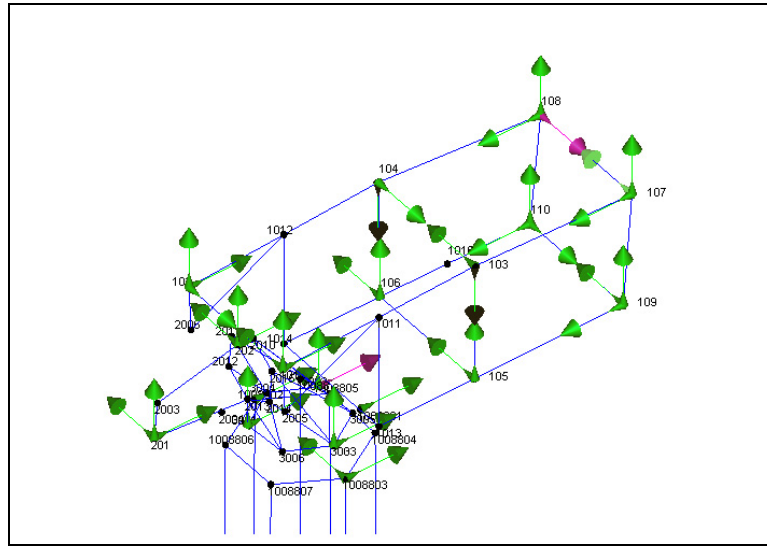


Figure 3: Nacelle Mainframe Instrumentation for Short Term Campaign

The instrumentation set up on transformer and electrical cabinets consists of two measurement points each primarily on the big diagonal of the structures and acceleration is measured in all three principal directions.

4.5 Long Term Measurement Campaign

In the long term campaign, spanning over 3 months, the tower is also instrumented along with the gearbox and the generator, in addition to the nacelle, which is also instrumented in case of short term campaign.

Instrumentation on the tower is shown in Figure 4. The measurement locations are indicated in the Fig. 4(a) by red circles. While choosing these locations, the convenience of sensor mounting and other practicalities are taken in consideration. Thus these locations are chosen such that there are platforms available nearby. The chosen levels are at an height of 12, 24, 42, 62 and 90 m. There are two accelerometers mounted as shown in Figure 4(c) at the all the levels except the top level (at 90 m) where 4 sensors are mounted in the configuration shown in Figure 4(b). The chosen configuration is primarily aimed at identification of tower bending modes. The two extra sensors on the tower top are placed to capture the tower torsion. Thus in total the tower is instrumented at 5 levels (11 locations) using 12 accelerometers.

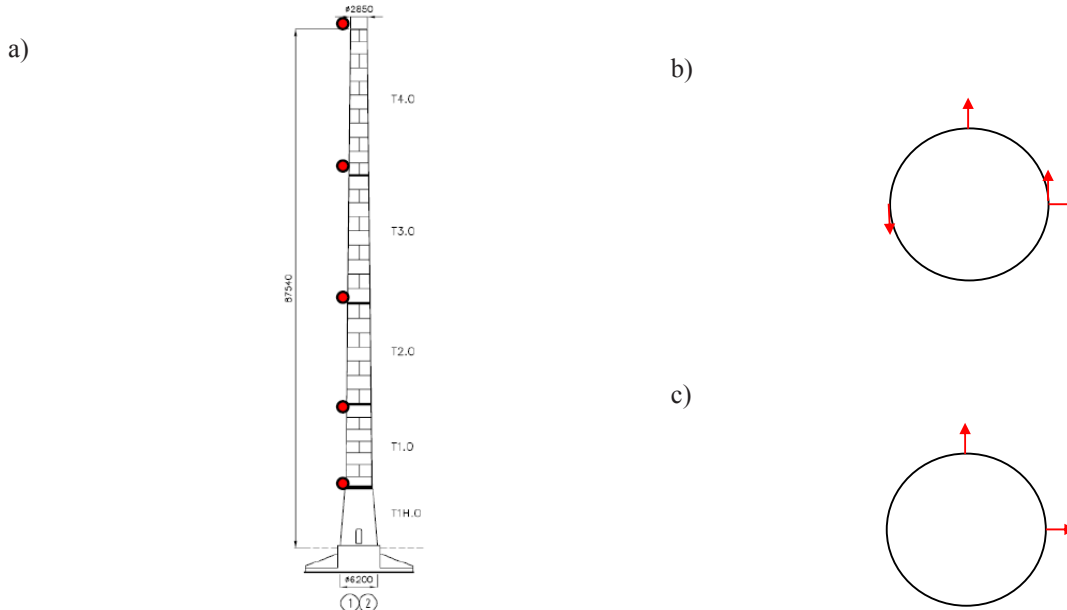


Figure 4: Tower Instrumentation for Long Term Campaign

In case of gearbox and generator, 3 locations each are selected and acceleration is measured in all three directions at these locations.

The fact that a wind turbine is a complex structure, which involves rotational movement of various substructures with respect to each other, necessitates careful defining of various coordinate systems and the relation amongst them in order to understand the dynamics of the overall system and the interactions between individual subsystems. In context of this project, motion of tower-nacelle subsystem is of particular importance. This is due to the fact that proper designing of various coordinate systems will ensure correct visualization of estimated mode shapes, which is very necessary for correct understanding and nomenclature of the identified modes.

The relative motion of the tower-nacelle subsystems is due to the yawing of the nacelle about the top of the tower; this rotation being defined by the yaw angle. Accelerometers mounted on the tower measure the tower vibration w.r.t. ground coordinate system (GCS) and along the axes of GCS; while accelerometers mounted on the nacelle measure accelerations w.r.t. GCS but along the axis of the nacelle. In order to analyze the two subsystems together, it is necessary to describe them in the same coordinate system before analyzing them. Thus it is necessary to take yaw into account.

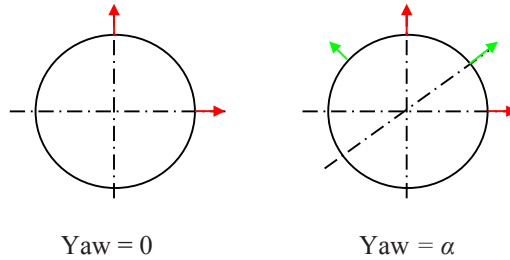


Figure 5: Yaw angle illustration

In the current project it is the tower accelerations that are transformed into the local coordinate system (LCS) of the nacelle. In Figure 5, the red arrows represent the physical accelerometers on the tower. As yaw changes, the acceleration signals are transformed so that they are in the coordinate system defined by the green arrows. This is mathematically equivalent to performing simple rotation using Eqn. 1. These new “virtual” accelerations signals are to be used as input for OMA.

$$\begin{aligned} x_1(t) &= x_0(t) \cos \alpha + y_0(t) \sin \alpha \\ y_1(t) &= -x_0(t) \sin \alpha + y_0(t) \cos \alpha \end{aligned} \quad (1)$$

4.6 Data Acquisition

During the course of the entire project, data is acquired at a sampling rate of 256 Hz. Duration of each measurement is 15 minutes. As mentioned earlier, each recording file contains (meta) data channel with wind speed and direction, yaw angle, state of the wind turbine, etc. Using the metadata, a recording database was created. Querying such a database, one can quickly find datasets satisfying the required parameters, e.g. mean wind speed, RPM, production state, etc.

5. PRELIMINARY RESULTS

Since the measurements are still in the progress at the moment of writing the paper, only preliminary results will be discussed in this section.

As mentioned before, one of the main challenges of this project was mode identification based on incomplete datasets (no information about blade acceleration is available). The approach taken in this project is to use the general knowledge about wind turbine dynamics [8] combined with the results of simulations using commercial aeroelastic code. The latest, however, models the wind turbine in a quite simplistic way, for example, the tower is modeled without torsional stiffness; the nacelle is modeled just as a point mass. Trial operational modal analysis using incomplete datasets from the simulations showed that some important modes cannot be observed or identified. This required us to create another finite element model in order to better simulate the details of the nacelle and tower dynamics.

The model of the ALSTOM ECO100 wind turbine was developed using ANSYS software in IKERLAN. The model includes the main structural and inertial components. The tower, blades, low speed shaft and rear frame were modeled as beam elements. Geometry, stiffness and mass properties for the tower and blades were taken from the blades and tower suppliers. The stiffness of the beam elements of the rear frame were updated using an existing shell elements model, so that the main structural mode shapes and frequencies are better correlated.

Heavy components as the central mainframe, front mainframe and hub were modeled using superelements, which were previously calculated from 3D FE models. Gearbox casing was also modeled as a superelement. Some other components as

the generator, electric cabinets and converter were also included as rigid boxes with concentrated mass properties. Elastic connections between components and bearings were modeled using 6 DOF spring elements.


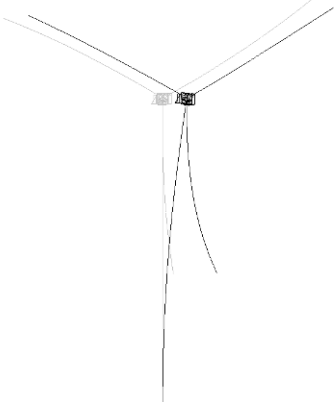
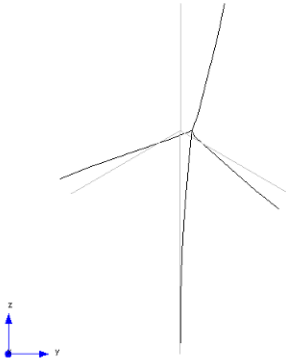
As discussed in [1, 2], the dynamics of a wind turbine while operating is quite rich and complicated. Therefore it was decided to start with a simpler parked case. Also to start with, a dataset is chosen with a steady in strength and direction moderate wind (8 m/s); the wind turbine is not yawing, and the pitch of all blades is 84° thus creating least aerodynamic forces acting on the blades. During the observed 15 minutes the rotor is slowly rotating (just few full revolutions during the recording period).




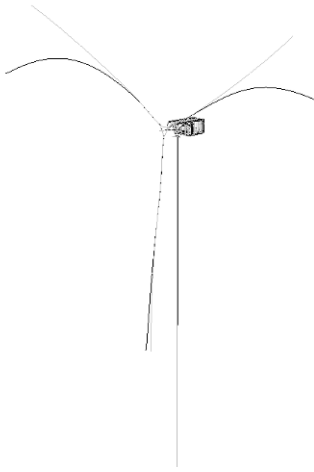
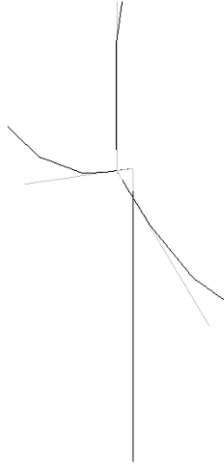

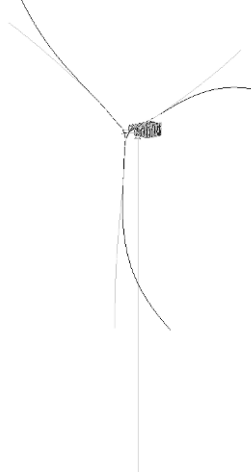
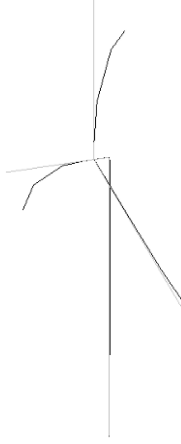
The obtained acceleration data is preprocessed according to (1) in order to take into account the yaw (i.e. the mutual orientation of the tower and the nacelle). Bruel and Kjaer PULSE Operational Modal Analysis Type 7760 is used for data analysis and SSI UPC algorithm with enabled Crystal Clear SSI option is chosen for modal parameter estimation [9].

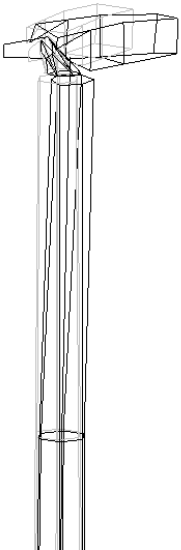
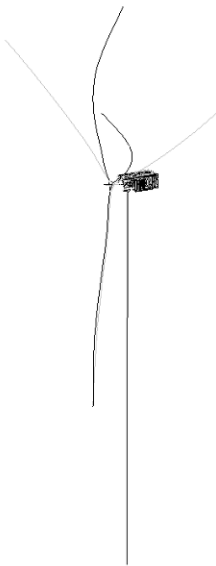
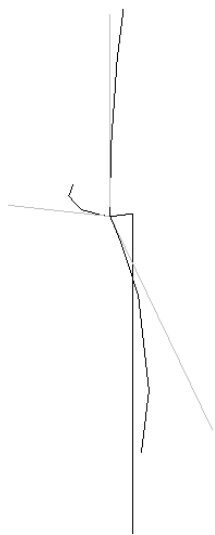
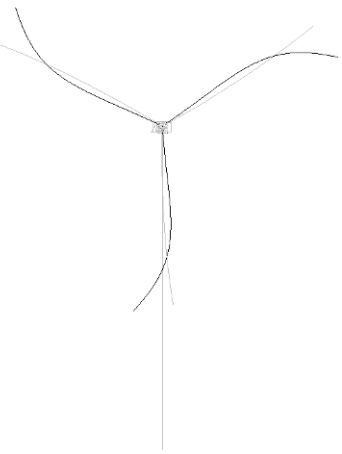
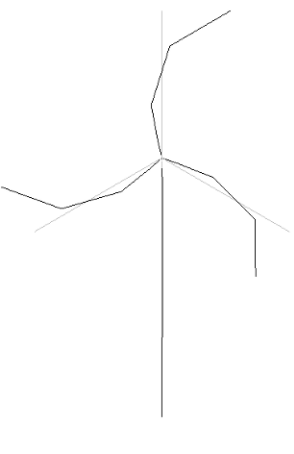
Table 2 compares the mode shapes obtained using three different techniques: OMA on experimental data, eigenmodes obtained using ANSYS eigenvalue solver and OMA on simulated data [2]. The table demonstrates how the similarity in mode shapes is used for naming the experimentally obtained mode shapes (see also comments placed in the table).


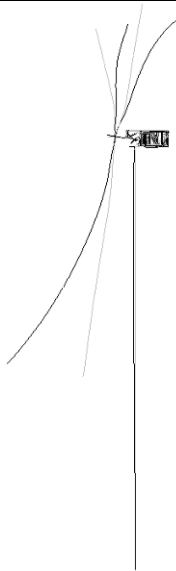
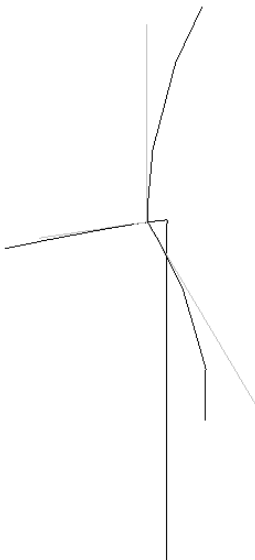
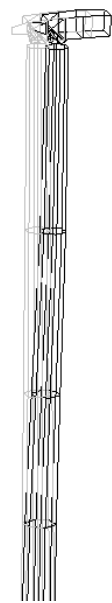
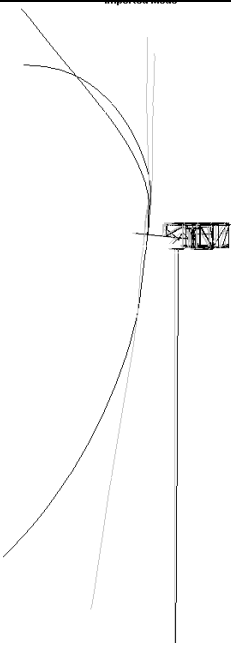
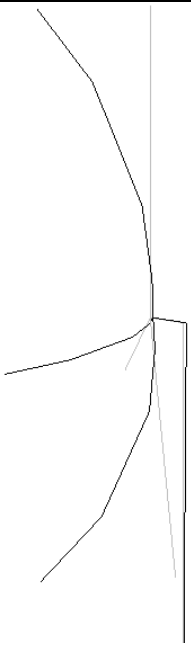
Based on this study it can be said that the technique generally works but there are still difficulties with naming some modes, e.g. mode number 4 which seemingly belongs to in-plane family but it is difficult to tell if this is a vertical (I1Vert) or horizontal (I1Hor) mode.



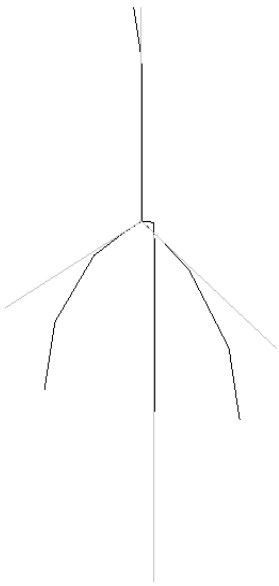

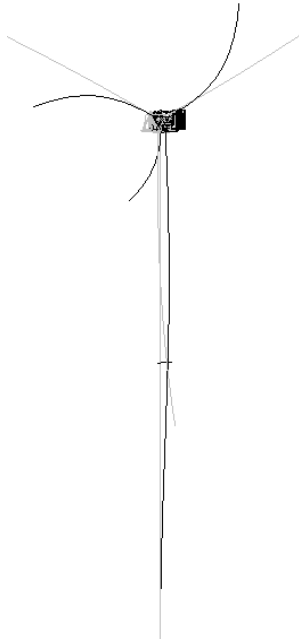
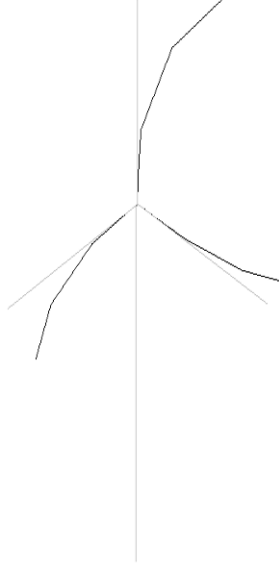
Table 2: Mode Shape Comparison

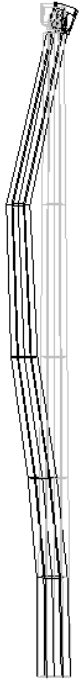


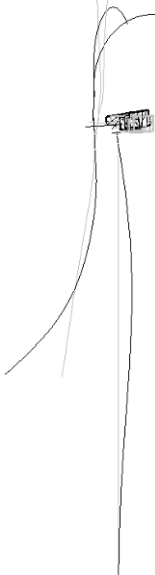
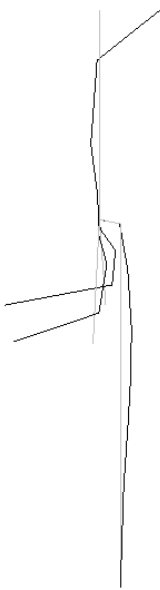
#	Mode name	Mode shapes obtained using		
		OMA on experimental data	ANSYS eigenvalue solver	OMA on simulated data
1	T1SS	 <p>This mode has much higher damping comparing to T1FA which is probably due to higher aerodynamic resistance of the nacelle and blades (pitch is 86°)</p>		 <p>The mode was found using frequency domain decomposition OMA algorithm (FDD) [9].</p>

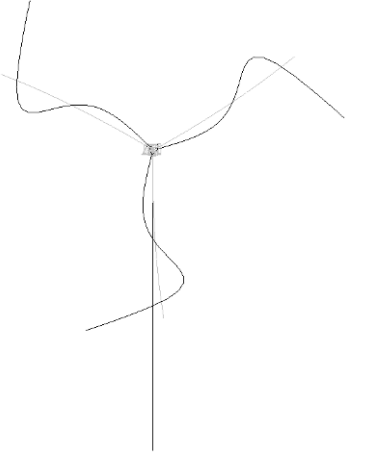

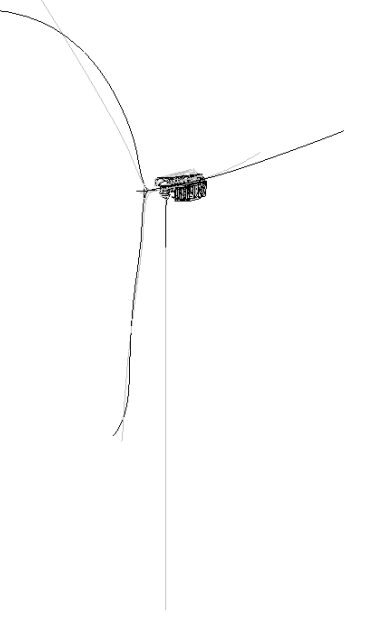
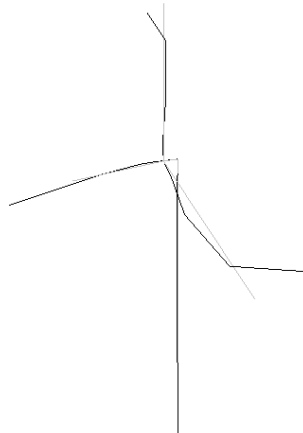
2	T1FA			
3	I1Vert	<p>Not found so far. Probable reason is that this mode is heavily damped due to the blades aerodynamics</p>	 <p>In contrast to I1Hor, this mode does not have tower side-to-side component but rather has for-aft one due to designed rotor 5° tilt.</p>	
4	I1Hor	 <p>Not certain, this can also be I1Vert. More likely this is I1Hor due to tower side-to-side motion</p>		

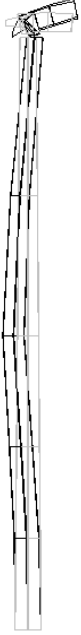
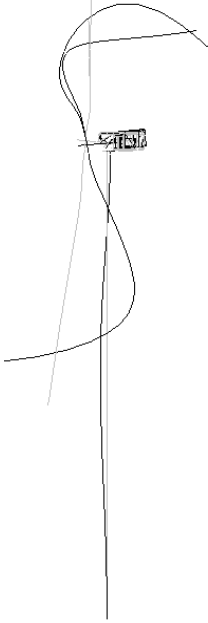

5	O1Yaw	 <p>This mode can be identified due to a torsional component in the tower motion</p>		
6	I1C	Not found so far. Probable reason is that this mode is heavily damped due to the blades aerodynamics		

7	O1Tilt	 <p>The mode can be identified by second tower bending component in fore-aft direction</p>		
8	O1C	 <p>This mode can be identified by tower fore-aft motion</p>		

9	I2Vert	 <p>The mode can be identified by second tower fore-aft component and nacelle tilt</p>	 <p>The tower displacement is exaggerated and blades cut out. The inset at the bottom shows blades' deformation</p>	
10	I2Hor	 <p>The mode can be recognized by second tower side-to-side motion and nacelle yaw. This mode is antisymmetric to I2Vert</p>	 <p>Tower motion exaggerated, the blades are cut off.</p>	

11	T2SS	 <p data-bbox="327 888 715 1035">This mode has a higher damping compare to T2FA which is probably due to higher aerodynamic resistance of the nacelle and the fully pitched blades</p>	 <p data-bbox="737 888 1114 1008">Due to blades' curvature and rotor plane inclination, this mode is coupled with T2FA which has almost the same frequency.</p>	<p data-bbox="1145 184 1382 268">Not found. Probably because of the higher damping.</p>
12	T2FA		 <p data-bbox="737 1707 1109 1917">Note, the tower and blades have comparable magnitude in contrast to e.g. I2Vert where the tower displacement had to be exaggerated in order to notice its deformation with respect to the blades</p>	

13	I2C	<p>Not identified. Probably, not observable using tower and nacelle instrumentation. In FEM, we cannot see any tower and nacelle motion associated with this mode (very little Fore-Aft motion)</p>		<p>This mode is located higher in frequency range.</p>
14	O2Yaw	 <p>The mode is characterized by significant torsional motion of the tower and the nacelle</p>		 <p>The nacelle and tower torsion is not modeled. Thus one cannot observe these two motions which are important for identification. ANSYS-based FEM which takes into account tower torsion and nacelle deformations is used instead.</p>

15	O2Tilt	 <p data-bbox="331 856 703 947">This mode involves the tilt of the nacelle and tower fore-aft bending mode</p>		
----	--------	---	--	---

6. CONCLUDING REMARKS

Experimental dynamic characterization of an operational wind turbine is a challenging task from both instrumentation and algorithmic points of view. This paper describes the measurement phase and preliminary results for ALSTOM's ECO 100 wind turbine prototype. The main aim of the project is to perform experimental dynamic characterization of the operational wind turbine using Operational Modal Analysis. Since measurements form a key part of the project, the paper shows how the planning and design of experiments are done in order to achieve the objectives of the project.

The preliminary results, corresponding to a simple case (parked wind turbine), are shown. It is observed that the main problem lies in observability and identification of rotor-related modes due to unavailability of acceleration data from the blades. The paper shows how this limitation can be dealt with the aid of mode shapes obtained from FEM based simulations.

The project described in this paper is currently running and its successful completion is expected to not only achieve the objectives mentioned in the paper but also provide a framework for carrying out OMA based dynamic characterization of wind turbines.

REFERENCES

- [1] Tcherniak, D., Chauhan, S., Hansen M.H., *Applicability Limits of Operational Modal Analysis to Operational Wind Turbines*, Proceedings of International Modal Analysis Conference, Jacksonville (FL), USA, Feb. 2010.
- [2] Tcherniak, D., Chauhan, S., Rossetti, M., Font, I., Basurko, J., Salgado, O., *Output-only Modal Analysis on Operating Wind Turbines: Application to Simulated Data*, Proceedings of European Wind Energy Conference, Warsaw, Poland, April, 2010.
- [3] Chauhan S, Tcherniak, D., Hansen M.H., *Dynamic Characterization of Operational Wind Turbines using Operational Modal Analysis*, Proceedings of China Wind Power 2010, Beijing, China, Oct. 2010.
- [4] Chauhan, S., Hansen, M.H., Tcherniak, D., *Application of Operational Modal Analysis and Blind Source Separation /Independent Component Analysis Techniques to Wind Turbines*, Proceedings of XXVII International Modal Analysis Conference, Orlando (FL), USA, Feb. 2009.

- [5] Font, I., Kanev, S., Tcherniak, D., Rossetti, M., *System Identification Methods on Alstom ECO 100 Wind Turbine*, Proceedings of 3rd Torque conference, Heraklion, Crete, Greece, June, 2010.
- [6] Burton, T., Sharpe, D., Jenkins, N., Bossanyi, E., *Wind Energy Handbook*, John Wiley & Sons, Chichester, U.K., 2001.
- [7] ECO 100 Platform, http://www.power.alstom.com/_eLibrary/presentation/upload_99947.pdf
- [8] Hansen, M.H., *Aeroelastic Instability Problems for Wind Turbines*, *Wind Energy*, Vol. 10, pp. 551-577, 2007.
- [9] Operational Modal Analysis – Type 7760, <http://www.bksv.com/doc/bp1889.pdf>

Amplitude Dependent Crack Characterization of Growing Fatigue Cracks

A.U. Rehman, K. Worden, J. A. Rongong
Dynamics Research Group

University of Sheffield, Mappin Street, Sheffield S1 3JD, United Kingdom

ABSTRACT

The presence of a crack in repeating structures, like gas turbine blade sets, causes local variation in the stiffness that affects the overall mechanical behaviour of the system. Crack characterization is essential to understand the effects on the dynamic response of the whole system. This paper introduces an approach for amplitude dependent crack characterisation considering fatigue crack growth. A test rig is established and a dog-bone type specimen is considered for this experimental work. Cracks are introduced into the specimen through fatigue loads at resonant frequencies. The dynamics of the cracked specimen are obtained by measuring the frequency response functions (FRFs). Different vibration amplitude settings are considered to investigate the nonlinear behaviour of breathing cracks on the FRFs. Natural frequency and modal damping ratios are measured for flexural and torsional vibration modes; these exercise the cracks in different directions. A comparison of output responses is made between crack-free and cracked specimens. Test samples are fatigued and tested repeatedly to analyze the cracks of various depths. Experimental results are then compared with FE simulations.

1. INTRODUCTION

Mechanical vibrations are a significant source of possible failures of rotating machines, specifically gas turbines operating in both power generation and the aerospace industries. Gas turbine blades have always been vulnerable to the severe dynamic loads experienced in operations that include engine order excitations along with nominally random vibrations. This dynamic effect extrapolates itself if some abnormality is developed inside the operating system e.g crack initialization in the blade. The structural integrity of a blade (and hence the turbine itself) and its life are highly dependent on the crack initiation and propagation. The presence of a crack in a repeating structure such as turbomachinery blading, has a significant effect on the modal characteristics (natural frequencies, mode shapes and modal damping values) obtained. Changes in the modal characteristics may not be same for each mode as they depend on the size and location of the crack. Crack characterization is, therefore, essential to understand the effects on the dynamic response of the whole system [1, 2]. Crack initiation and propagation result in drops in the natural frequencies. The stress is a minimum for a particular mode of vibration at the modal nodes (points with zero displacements). Any damage or crack of a given size may result in a very lesser shift in the natural frequency as compared to the damage or crack of the same size located in the region of high stress [1]. Different approaches have been addressed in the past regarding the selection of the modes of interest for a vibration analysis [3, 4, 5]. Some suggested the lower vibrations modes to be best suited [3], whereas others explained the advantages of higher modes [5].

Nonlinear resonance ultrasound spectroscopy has been successfully applied for crack characterization in materials such as rocks, bones, composite materials and metal structures by various researchers in the past [6, 7, 8]. Varying input excitations result in the shift of resonant frequency peaks and the cracks are characterized by the value of slope obtained from the peaks of FRFs obtained for increasing excitation levels [6]. According to the linear theory of vibration, natural frequencies of a system should be independent of the amplitude of the input vibrations. In practice, an increase in the vibration amplitude results in the decrease of natural frequencies, indicating the presence of nonlinearity in the system [9]. It is now well established that the presence of fatigue damage or a crack in an operating structure also leads to the presence of nonlinearity in the system. A small crack produces a nonlinear stress-strain relationship which can be highlighted by an increase in the dynamic strain. This increase in the dynamic strain is accomplished by the increasing the excitation amplitude [6, 10, 11]. Indication of a crack is significantly highlighted in nonlinear effects as compared to linear ones (propagation, velocity, attenuation, elastic modulus).

As far as the modelling of cracks in finite element analysis is concerned, different techniques were used in the past, keeping focus on the type of crack to be modelled i.e open crack or breathing crack. Reduction in stiffness of selected elements at crack locations by decreasing elastic modulus, defining a pinned joint at a crack location by rotational spring

and simple material removal at crack location are some of the methods of representing an open crack in the beam structure. For breathing cracks, bilinear stiffness models have been used for the opening and closing of a crack [12]. Reduction in the natural frequency, due to the presence of damage in the system, can also be achieved by attaching a mass. This approach is quite useful for those structures where it is not possible to damage the structure and then detect it [13].

In this study, the shift in the FRF as a function of increasing excitation levels is considered to characterize the cracks of different depths in a bending and a torsion mode of a dog-bone specimen. Besides this, drops in the natural frequencies due to the crack propagation itself are also studied by carrying out a modal analysis of the dog-bone specimen. Participation factors are calculated for different modes and a selection criterion is addressed to choose the modes of interest for the characterization of cracks. This is accomplished by obtaining a relationship between:

- i- Frequency and varying crack length/fixed excitation levels
- ii- Frequency and varying excitation levels/ fixed crack lengths.

Experimental and numerical natural frequencies are then compared for the bending and torsion mode for varying excitation levels.

2. FE MODEL OF THE DOG-BONE SPECIMEN AND LOCATION OF CRACK

The dog-bone specimen was modelled accurately in ANSYS. Specimen is 200 x 100 mm in size with 3.03mm thickness. The dog-bone specimen was meshed with a 3-D 20-node structural solid element. The total number of elements along the thickness of the model was set to be three; 16 along the width of the specimen and 23 along the specimen neck width. The reason for choosing the higher number of elements in the neck region was to model the cracks of various depths precisely, without disturbing the mesh density of the model. This resulted in 2495 elements for the whole of the dog-bone FE model. The material assigned to this FE model was steel ($E = 200\text{GPa}$, $\nu = 0.3$). The dog-bone specimen was constrained in all degrees of freedom from one end, as shown in Figure 1.

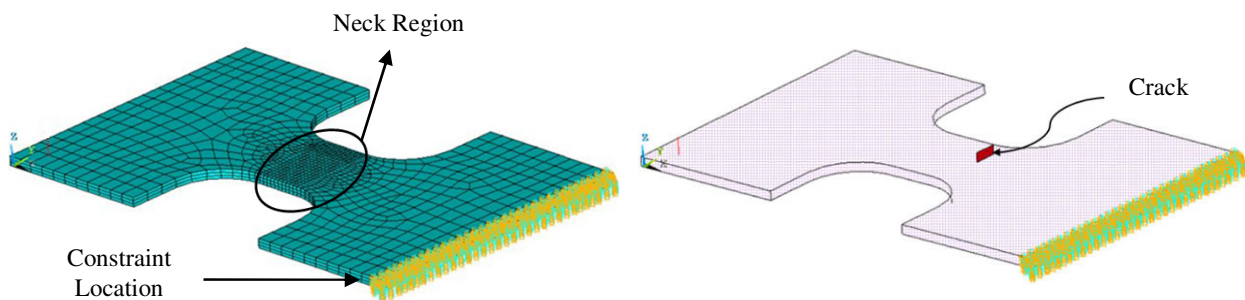


Fig. 1 FE Model of the Dog-Bone Specimen with crack location

Three different techniques have been suggested for representing cracks in simple models in [2]. These included simple material removal at the crack location, periodic reduction in the modulus of elasticity 'E' and attaching a lumped mass. As far as the material removal method is concerned, it is a simple subtraction of material up to the required depth at a desired location. Whereas periodic reduction in modulus of elasticity requires the 'E' value to be divided on the number of elements at crack location in accordance with the crack depth considered. The modulus is set at a very low value (near to zero) at the blade edge and incrementally increases up to the actual value for the blade at the crack tip. In the lumped mass method for simulation of the crack, a very small mass is attached. For the FE Model of the dog-bone specimen, crack was modelled by the two separate surfaces resting on each other with no material removal between them, as shown in Figure 1. This represented a hair-line crack which was identical to the actual crack which appeared inside the dog-bone specimen during the experimentation. Location of the crack was also kept the same in the FE model for an accurate comparison between the experimental and finite element results. Seven different scenarios were considered:

- i. Model without crack
- ii. Model with 1.5mm crack
- iii. Model with 2.5mm crack
- iv. Model with 5.0mm crack
- v. Model with 9.0mm crack
- vi. Model with 19.0mm crack
- vii. Model with 26.0mm crack

3. MODAL ANALYSIS OF THE DOG-BONE SPECIMEN

A modal analysis determines the vibration characteristics (natural frequencies and mode shapes) of a component. Modes, inherent properties of a structure, are determined by the mass, damping, stiffness (material properties) and boundary conditions of the structure. Each mode is uniquely defined by its modal parameters which include modal or resonant frequency, modal damping and a mode shape. Modes of a structure are highly dependent on any change in its material properties or boundary conditions. The presence of cracks of various depths can result in the alteration of the modal parameters and to investigate this, modal properties of the dog-bone specimen were obtained by carrying out its modal analysis. The first five natural frequencies were obtained and compared for the model without crack and having cracks of various depths (Table 1). It is clear that increase in the crack depth resulted in the dropping of natural frequencies due to loss of stiffness, but the extent of this frequency drop was different for different modes. Amongst the first five modes, mode-4 (swaying) indicated a 19.568% decrease in the natural frequency when compared with the dog-bone specimen model without crack and with crack of 9.0mm depth. Increase in the crack depth from zero to 9mm resulted in 30% decrease in the ' r ' term of the moment of inertia (I). This indicated a cubic drop in ' I ' and hence the natural frequency of the swaying mode decreased significantly as compared with the other modes. The torsion mode indicated the second highest decrease in the natural frequency because of the reason mentioned above. Besides this, mode-5 (3rd bending) indicated the least drop in the natural frequency for the same comparison. Natural frequencies for the dog-bone specimen having cracks of 19.0mm and 26.0mm were also obtained but not included in Table 1. As the crack depth was increased from 9.0mm to 19mm and then to 26.0mm, the swaying mode indicated a huge amount of decrease in its natural frequency. Besides this, for the 19.0mm crack, mode swapping occurred between mode 3 (2nd bending) and mode 4 (swaying) which replaced the order for 19.0mm crack. For the 26.0mm crack, mode swapping occurred once again and this time mode 2 (torsion) and mode 3 (swaying) replaced the orders and mode 2 became swaying and mode 3 became torsion. The first five mode shapes for the specimen without crack and with a crack of 9.0mm depth are shown in Figures 3 and 4 respectively. The effect of the presence of a crack is significant for the torsion and swaying modes, as indicated by the sudden change of contour at the crack location.

Table 1 First five natural frequencies for the dog-bone specimen

Mode Number & Type	Without Crack	1.5mm Crack	2.5mm Crack	5.0mm Crack	9.0mm Crack	Percentage Difference
1(1 st Bending)	93.953	93.871	93.741	93.152	91.785	-2.3075%
2(Torsion)	269.67	269.35	269.10	266.52	260.27	-3.4835%
3(2 nd Bending)	661.87	661.47	660.80	657.83	650.99	-1.6443%
4(Swaying)	1159.86	1150.67	1134.07	1065.67	932.90	-19.568%
5(3 rd Bending)	1429.83	1429.55	1429.03	1426.35	1419.90	-0.6951%

The effective modal mass and the participation factor for a particular mode provides a means of judging the importance in terms of the possibility of being excited. They are calculated for each mode in global translation and rotation directions and their values are based on a unit displacement spectrum. The high value of effective modal mass and participation factor in a given direction indicates that the mode will be readily excited by the forces in that direction. On the other hand, modes with low modal mass and PF values cannot be easily excited. In order to investigate the ability of different modes to be excited with increasing crack depths, participation factors in the vertical displacement direction (along z axis as shown in Figure 1) were obtained for first five modes of the dog-bone specimen without crack and with cracks of various depths. Participation factors for the specimen having crack depths up to 9.0mm are shown in Table 2.

Table 2 Participation factors for first five modes of the dog-bone specimen

Mode Number	Without Crack	1.5mm Crack	2.5mm Crack	5.0mm Crack	9.0mm Crack	Percentage Difference
1(1 st Bending)	0.3889	0.3889	0.3888	0.3885	0.3876	-0.3368%
2(Torsion)	0.49e-5	0.26e-4	0.94e-4	0.57e-3	0.17e-2	34262.14%
3(2 nd Bending)	0.2298	0.2299	0.2301	0.2307	0.2321	0.9789%
4(Swaying)	0.81e-10	0.78e-10	0.66e-10	0.33e-10	0.15e-10	-81.481%
5(3 rd Bending)	-0.1240	-0.1240	-0.1240	-0.1244	-0.1256	1.3552%

As the crack depth was increased from no crack to a 9.0mm crack (and then to 19.0mm and 26.0mm), the ability of mode 2 (torsion) to excite increased tremendously in the z direction. Mode 4 (swaying) indicated a very much lower participation factor in the z direction but high participation factors in the x and y directions (swaying plane). The maximum values for the participation factors obtained in the x and y directions were 0.3292 and 0.0768 respectively. Bending modes 1, 3 and 5 indicated stability as the crack depth was increased.

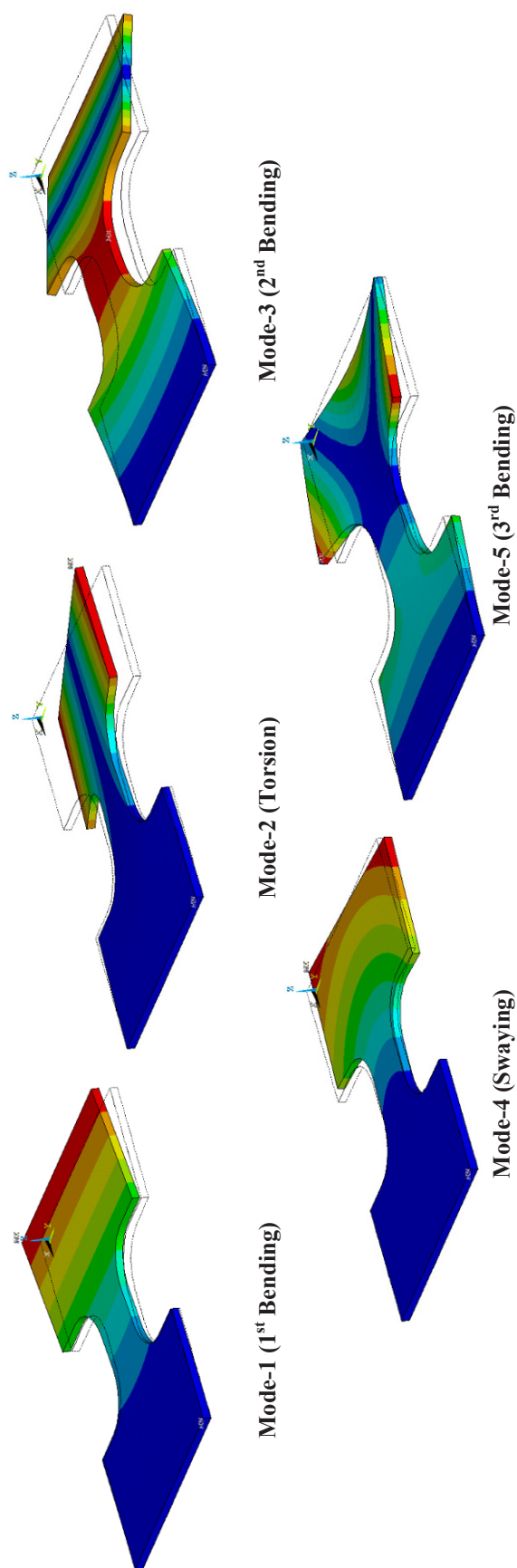


Fig. 3 First five mode shapes of the dog-bone specimen without crack

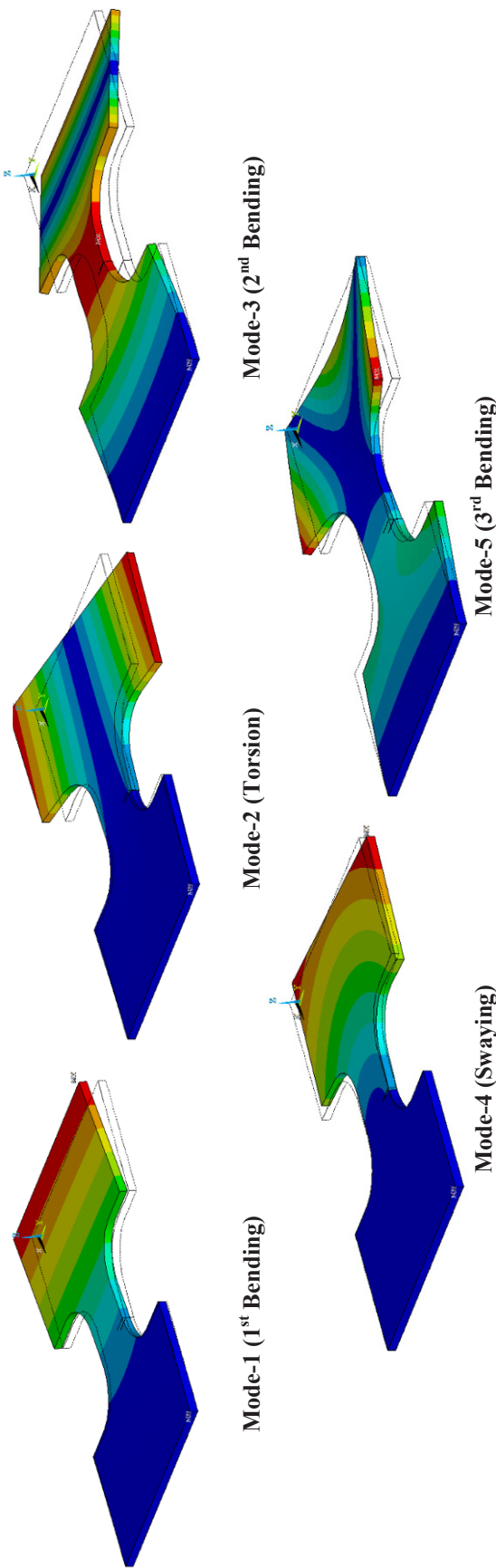


Fig. 4 First five mode shapes of the dog-bone specimen with 9.0mm crack

4. SELECTION OF BENDING AND TORSION MODE

Selection of the bending and torsion modes for the detailed analysis of the dog-bone specimen with and without cracks of various depths was based on the participation factors obtained for the first five mode shapes. Mode 1 (bending) was selected as it indicated the highest participation factor and mode-2 (torsion) was selected as it showed significant increase in its excitability as the crack depth was increased. Besides this, the crack in the dog-bone specimen behaved in different combinations of mode-I (opening), II (sliding) and III (tearing) (three modes by which loads can operate on a crack) considering the bending and torsion mode. Figure 5 shows exaggerated views of the bending mode and torsion mode of the dog-bone specimen with a crack of 9.0mm depth. In the bending mode, the crack appears to behave in all the three crack opening modes; whereas in the torsion mode, the crack is primarily exhibiting mode-III behaviour. So an overall estimation of crack behaviour in all three operating modes was obtained by considering bending and torsion modes of the dog-bone specimen.

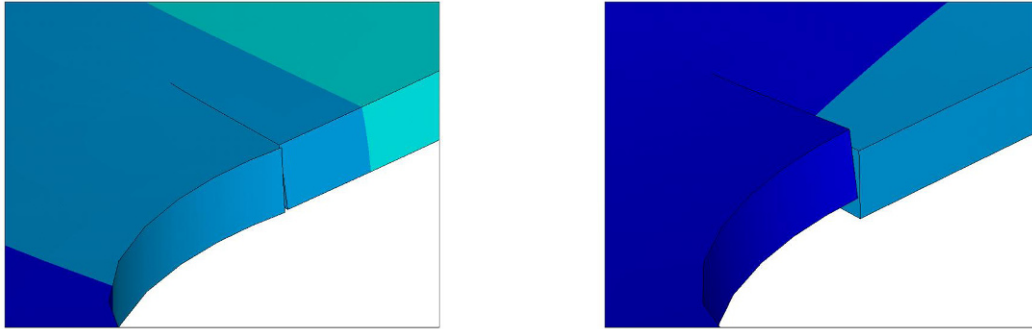


Fig. 5 Bending and torsion modes indicating crack behaviour in Mode-I, II and III

5. EXPERIMENTAL SETUP

The dog-bone specimen is shown in Figure 6. The material selected for the dog-bone specimen was medium carbon steel. The purpose of selecting the dog-bone shape was to force the crack to initiate near the curve. The width of the neck is 30mm ($1/3^{\text{rd}}$ of the total width of the specimen). An experimental rig was set up to test the dog-bone specimens. Siglab was used to obtain the experimental data. The specimen was held in the horizontal plane in a cantilever position with a force transducer underneath. The response was measured at the specimen edge using a laser vibrometer. Due to noise issues, the specimen was clamped in a horizontal cantilever position with a supporting heavy block of steel hanging freely from the test stand, as shown in Figure 6.

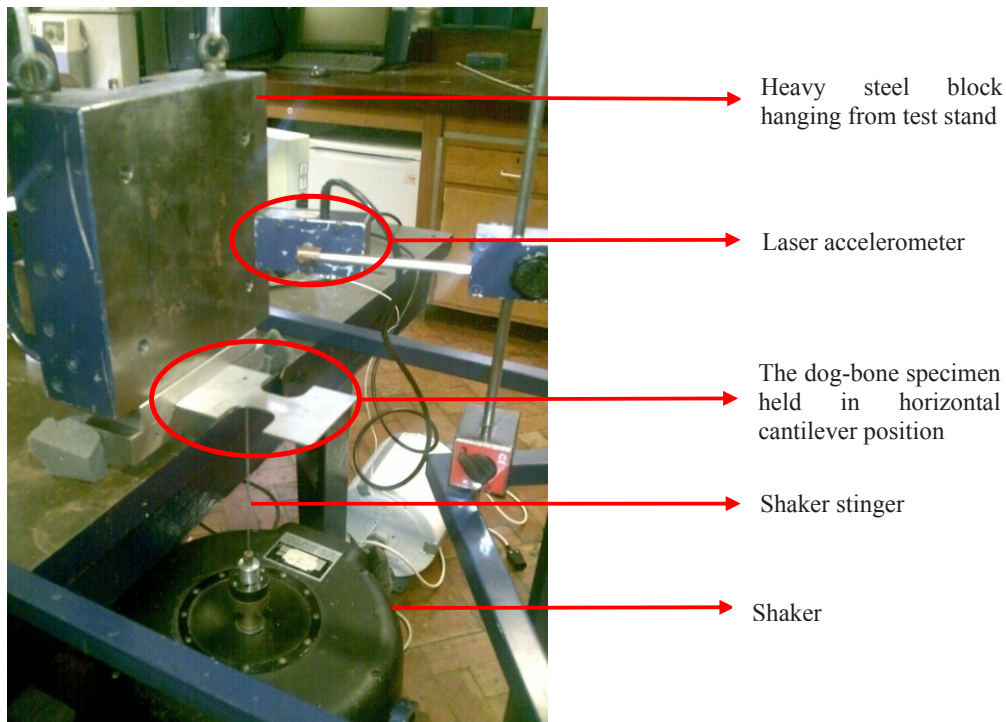


Fig. 6 Test rig

6. CRACK INCLUSION AND EXCITATION LEVELS

The dog-bone specimen was tested under random excitation to obtain the frequency response function (FRF). The frequency range of 0-500Hz was selected; a total of three resonant peaks can be seen in Figure 7. The second peak refers to the bending mode that occurs at 93.125Hz and the third peak indicates the torsion mode occurring at 271.87Hz. The first peak at 5Hz reflects the motion of the steel block hanging from the test stand and is ignored. In order to induce a crack in the dog-bone specimen, a 0.1mm notch was made. This was done to force the crack to grow at the desired location instead of generating surface cracks on the top and bottom surfaces of the specimen without having a notch. The bending mode of the dog-bone specimen was then excited with a 6mm peak-to-peak amplitude until a crack appeared at the notch location. The dog-bone specimen was then fatigued and tested repeatedly to analyze the cracks of various depths. Different levels of excitation were considered to test the dog-bone specimen without crack and with cracks of various depths. The range of the excitation levels was from 0.1mm/0.04V to 1.0mm/0.40V in ten equally-spaced steps. The swept sine measurement technique was used to obtain the FRFs with varying excitation levels and crack depths.

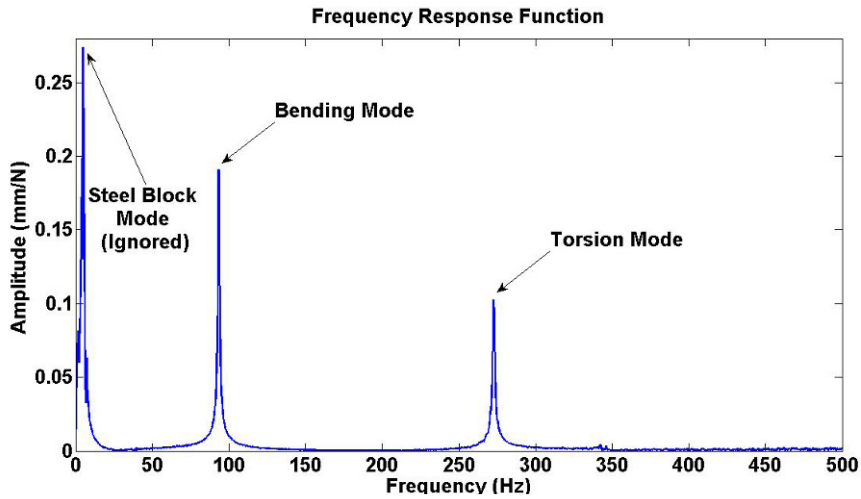


Fig. 7 Frequency response function of the dog-bone specimen

7. FRFS OBTAINED FOR BENDING MODE WITH VARYING EXCITATION LEVELS

The dog-bone specimen was tested for the flexural (bending) mode. Different scenarios were considered which included the specimen without crack and with cracks of various depths. FRFs for different excitation levels (EL), ranging from 0.1mm/0.04V to 1.0mm/0.4V, were then obtained. In this test, displacements were controlled and force was allowed to vary during the test. FRFs for the specimen without crack and with crack of 5.0mm depth are shown in Figure 8. For the specimen without crack, the natural frequency for 0.1mm/0.04V EL was 92.83 Hz and for 1.0mm/0.4V, natural frequency was 92.53 Hz, indicating a 0.323 % decrease. It is quite obvious from the plot that the extent of this decrease greater for the first three levels of excitations (0.1mm/0.04V, 0.2mm/0.08 and 0.3mm/0.12V EL) as compared with the rest of the excitation levels. For the specimen with 5.0mm crack, at the low level of excitation (0.1mm/0.04V), the frequency was 91.86 Hz and for the high level of excitation (1.0mm/0.40V), the frequency lowered to 91.38 Hz. This indicated almost a 0.522 % decrease in the frequency. The FRFs obtained for the dog-bone specimen having 5.0mm crack were approximately equally spaced, indicating uniformity in the response. The value of coherence was in the range of 0.98-1 for this particular test.

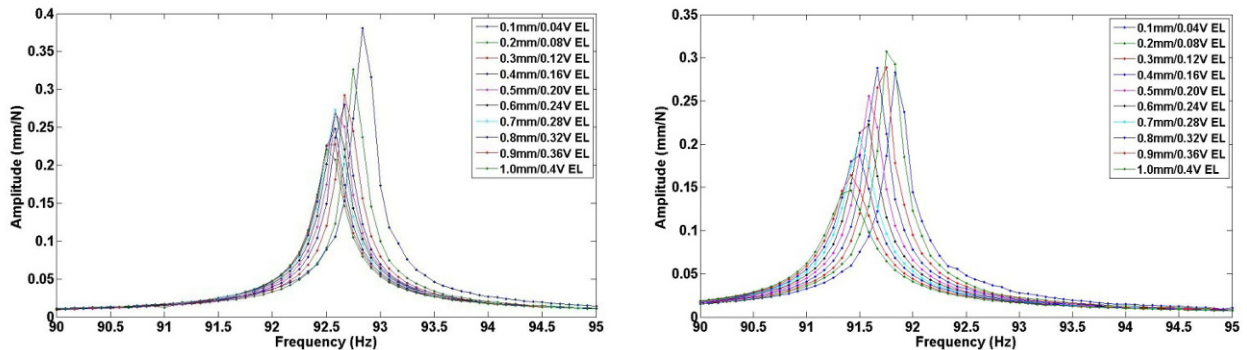


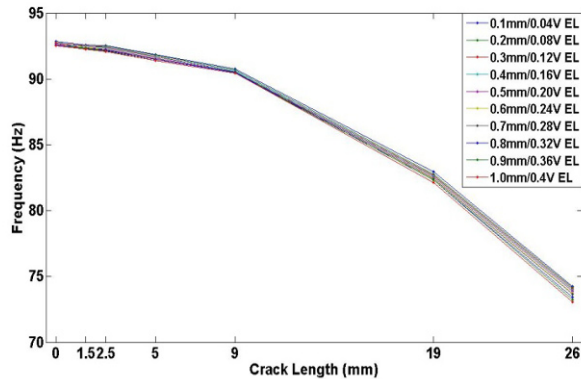
Fig. 8 FRFs for specimen without crack and 5.0 mm crack (varying excitation levels)

The frequency and coherence ranges and the percentage decrease in the natural frequency for the dog-bone specimen, both without crack and having 1.5, 2.5, 5.0, 9.0, 19.0 and 26.0mm cracks, considering different excitation levels for the bending mode are summarized in Table 3. Most of the experimental test iterations resulted in a coherence range of 0.975-1 except for the test involving the specimen without crack where the coherence value dropped to 0.83. This drop in the coherence value occurred for 0.1mm/0.04V and 0.2mm and 0.08V excitation levels, indicating poor signal-to-noise ratio for low excitation levels.

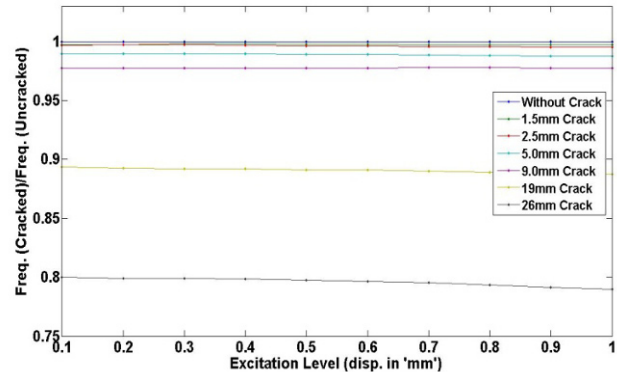
Table 3 Frequency and coherence range for different excitation levels

Specimen	Frequency (Hz)		%age decrease	Coherence Range
	0.1mm/0.04V	1.0mm/0.40V		
Without Crack	92.83	92.53	0.323	0.83-1
1.5mm Crack	92.55	92.25	0.324	0.975-1
2.5mm Crack	92.54	92.08	0.497	0.98-1
5.0mm Crack	91.86	91.38	0.522	0.98-1
9.0mm Crack	90.75	90.45	0.330	0.99-1
19.0mm Crack	82.97	82.14	1.00	0.965-1
26.0mm Crack	74.25	73.07	1.63	0.992-1

It is evident from Table 3 that the natural frequencies of the dog-bone specimen were not independent of the input excitation amplitude. In order to investigate the frequency trend for varying crack length with fixed excitation level, the drop in the frequencies due to crack propagation is plotted in Figure 9. Each line represents a different excitation level. The frequency drop occurred as the level of excitation was increased. The overall trend for this frequency drop across the whole range of different crack lengths is quite similar for varying levels of excitations. Besides this, increasing the crack depth resulted in a higher value of percentage decrease for the natural frequency for a given range of excitation level. This is indicated by the narrow lines for the small crack lengths, which then become widened as the crack propagates deep into the dog-bone specimen in Figure 9a. When the excitation level was varied from 0.1mm/0.04V to 1.0mm/0.4V for a fixed crack length, the frequency patterns obtained are shown in Figure 9b. Frequencies for the cracked specimen were normalized by the frequencies obtained for the specimen without crack. Different horizontal lines represent varying crack depths. For the whole range of excitation levels, a drop in the natural frequency occurs and the extent of this drop is quite significant for larger crack depths as compared to smaller ones. Figures 4a and 4b truly depict the nonlinear behaviour of the system under variable excitation inputs. Increasing crack depth resulted in greater interfacial motion of the crack faces, indicating larger signs of friction among them and as a result, the natural frequency drop increases with cracks of greater depths for given excitation levels.



a- Frequency Vs varying crack length/fixed excitation level



b- Frequency Vs varying excitation level /fixed crack length

Fig. 9 Frequency trends for increasing crack lengths and excitation levels

8. FRFS OBTAINED FOR TORSION MODE WITH VARYING EXCITATION LEVELS

The dog-bone specimen was then tested for the torsion mode. Different scenarios were considered which included the specimen without crack and specimen with cracks of various depths. Frequency response functions for different excitation levels (EL), ranging from 0.1mm/0.04V to 0.6mm/0.24V, were then obtained. The level of excitation was lowered in the torsion mode, as compared to the bending mode due to some difficulties in controlling the displacements at higher excitation levels. FRFs for the specimen without crack and having a 5.0mm crack are shown in Figure 10.

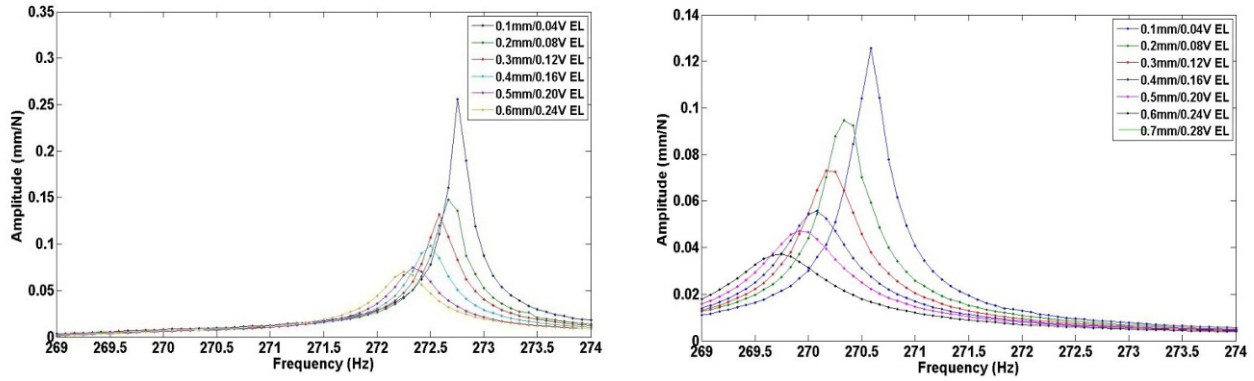


Fig. 10 FRFs for specimen without crack and 5.0 mm crack (varying excitation levels)

For the specimen without crack, the frequency for 0.1mm/0.04V EL was 272.80 Hz and for 0.6mm/0.24V, the frequency obtained was 272.30 Hz, indicating a 0.22 % decrease. It is clear from the plot that the extent of this decrease is quite uniform through the whole range of varying excitation levels. Displacements were controlled and force was allowed to vary in the torsion mode in a similar fashion as in the case of the bending mode. For most of the excitation levels, the coherence values lie near 1, which indicates high quality/confidence in the FRF measurement. Only for first level of excitation (0.1mm/0.04V), does the coherence value drop to 0.9. This occurred due to the low signal-to-noise ratio for the low level of excitation. In the case of the specimen with 5.0mm crack, it was found that for the excitation level of 0.1mm/0.04V, the frequency was 270.60 Hz and for the excitation level of 0.6mm/0.24V, the frequency was 269.73 Hz; this shows a 0.321 % decrease in the natural frequency. The value for coherence was in the range of 0.99-1, indicating an acceptable level of accuracy, except for 0.1mm/0.04V excitation level when the value of coherence dropped to 0.92 due to poor signal-to-noise ratio. The frequency and coherence ranges and the percentage decrease in the natural frequency for the dog-bone specimen, without crack and having 1.5, 2.5 and 5.0mm cracks, considering different excitation levels for the torsion mode are summarized in Table 4. FRFs for the crack lengths greater than 5mm showed odd behaviour because of difficulties in controlling the displacements in torsion mode; results for the 9mm, 19mm and 26mm cracks are not shown here. Once again, like the bending mode, the natural frequencies indicated their dependence on the amplitude of the input.

Table 4 Frequency and coherence range for different excitation levels

Specimen	Frequency (Hz)		%age decrease	Coherence Range
	0.1mm/0.04V	1.0mm/0.40V		
Without Crack	272.80	270.30	0.22	0.9-1
1.5mm Crack	271.42	270.70	0.265	0.9-1
2.5mm Crack	271.26	270.50	0.354	0.91-1
5.0mm Crack	270.60	269.73	0.321	0.99-1

Frequency trends for varying crack depths with fixed excitation levels are shown in Figure 11a. A similar type of behaviour was obtained for the torsion mode as in the case of the bending mode. The important thing to note here is the similarity in frequency trends for varying excitation levels. The frequency decreased with the increase in excitation level. In addition to this, increase in the crack depth indicated a large decrease in the natural frequency considering a given range of excitation levels. This is also evident from the narrow band of frequency lines for the specimen without crack which tries becomes widened as the crack depth was increased to 5.0mm. For varying excitation levels (from 0.1mm/0.04V to 0.6mm/0.24V) and fixed crack length, frequency trend comparison is shown in Figure 11b. Trends for the frequency changes are quite similar to those discussed earlier for bending mode.

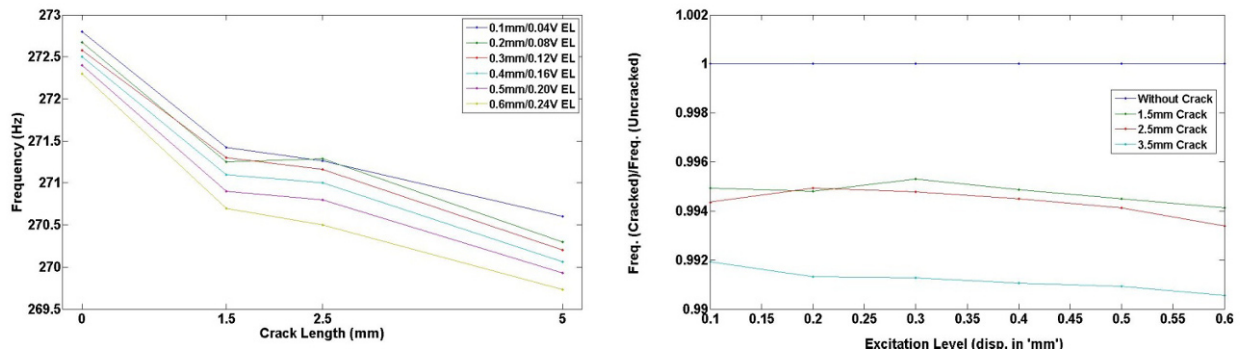


Fig. 11 Frequency trends a- fixed EL/varying CL b- fixed CL/varying EL

9. COMPARISON OF EXPERIMENTAL AND NUMERICAL RESULTS

Experimental natural frequencies of the dog-bone specimen, without crack and with cracks of various depths, were then compared with the numerical natural frequencies. The first two modes (bending and torsion) were considered for this comparison, as shown in Table 5. For both the modes, the experimental and numerical frequencies were a little offset from each other and never crossed. This indicated a consistent trend over the increasing crack depth. But the difference between the results of two techniques increased for torsion mode for the cracks having greater depths. These mismatches in the natural frequencies can be attributed to inaccuracies in the experimental setup.

Table 5 Comparison of experimental and numerical results

Crack Depth	Bending Mode Frequency (Hz)			Torsion Mode Frequency (Hz)		
	<i>Experimental</i>	<i>Numerical</i>	<i>%age Diff.</i>	<i>Experimental</i>	<i>Numerical</i>	<i>%age Diff.</i>
No Crack	93.125	93.953	0.889	271.87	269.668	-0.809
1.5mm	92.550	93.871	1.427	270.70	269.351	-0.498
2.5mm	92.187	93.741	1.685	271.15	269.101	-0.755
5.0mm	91.901	93.152	1.361	270.65	266.516	-1.527
9.0mm	90.625	91.785	1.280	268.75	260.274	-3.153

10. CONCLUSIONS

Crack characterization for the bending and torsion mode of a dog-bone specimen was addressed in this paper. This was accomplished by considering different crack depths and increasing the excitation levels of vibration input. As the crack propagated deeper into the specimen, the slope obtained from the peaks of the FRFs at different levels of input excitation increased. This indicated higher nonlinearity level in the specimen with a larger crack. Cracks of increasing depths produced a nonlinear stress-strain relationship which was indicated in the form of FRF peak shifting (decrease in the natural frequency) with the increasing excitation levels. Besides this, the ability of a particular mode to be excited in a particular direction depends largely on the direction of its modal displacement vector. Increase in the crack depth resulted in the alteration of the ability of various modes for being excited due to the changes in their modal displacement vectors. Comparison of experimental and numerical natural frequencies for the bending and torsion mode indicated a good correlation. Crack characterization by obtaining the amplitude dependent FRFs and utilization of participation factor to select the modes of interest helped understanding the dynamics of the dog-bone system.

REFERENCES

- [1] Salawu, O.S., Detection of structural damage through changes in frequency: a review, *Engineering Structures*, Vol. 19, No. 9, pp. 718-723, 1997.
- [2] Rehman, A.U., Rongong, J. A. and Worden, K., Detection of Damage in Repeating Structures, *Proceedings of the ASME Turbo Expo 2010: Power for Land, Sea and Air, GT 2010*, June 14-18, 2010, Glasgow, UK.
- [3] Slastan, J., and Pietrzko, S., Changes of RC-beam modal parameters due to cracks. In: (1st edn.), *Proceedings, 11th International Modal Analysis Conference*, Kissimmee, Florida 1 (1993), pp. 70–76.
- [4] Begg, R. D., Mackenzie, A.C., Dodds, C.J. and Loland, O., Structural integrity monitoring using digital processing of vibration signals. In: (1st edn), *Proceedings, 8th Offshore Technology Conference*, Houston, Texas 2 (1994).
- [5] Salawu, O.S., Identification of damage-sensitive vibration modes. In: *Vibration and Noise '95*, *Proceedings of the International Conference on Vibration and Noise* (April 25–27 1995).
- [6] Cheong, Young-Moo, Alam, M. K. and Kim, CheolGi, Nonlinear parameters for a diagnosis of micro-scale cracks using a nonlinear resonant ultrasound spectroscopy (NRUS), *Review of quantitative non-destructive evaluation* Vol. 29, 2010 American institute of physics 978-0-7354-0/10.
- [7] Meo, M., Ploimeno, U. and Zumpano, G., Detecting damage in composite material using nonlinear elastic wave spectroscopy methods, *Appl compos mater* (2008) 15:115-126, DOI 10.1007/s10443-008-9061-7.
- [8] Muller, M., Sutin, A., Guyer, R. and Johnson, P.A., Nonlinear resonant ultrasound spectroscopy (NRUS) applied to damage assessment in bone, *J. Acoust. Soc. Am.* 118 (6), 2005.
- [9] Pany, C. and Rao, G. V., Calculation of nonlinear fundamental frequency of a cantilever beam using nonlinear stiffness, *Journal of sound and vibration* (2002) 256(4), 787-790.
- [10] Johnson, P. A., *The New Wave in Acoustic Testing*, *Materials World*, The J. Inst. Materials, 7, pp. 544 –546 (1999).

- [11] Abeele, V., Carmeliet, J. and Johnson, P. A., Nonlinear Elastic Wave Spectroscopy (NEWS) Techniques to Discern Material Damage, Part II: Single-Mode Nonlinear Resonance Acoustic Spectroscopy, *Research in Nondestructive Evaluation*, 12, pp. 31– 42 (2000).
- [12] Friswell, M. I., Penny, J. E. T., *Crack Modeling for Structural Health Monitoring*, *Journal of Structural Health Monitoring (SHM)* Vol 1(2): 0139-148 [1475-9217 (200210) 1:2; 139-148; 10.1106/145792102028836].
- [13] Papatheou, E., Manson, G., Barthorpe, R. J., Worden, K., *The use of pseudo-faults for novelty detection in SHM*, *Journal of Sound and Vibration*, Volume 329, Issue 12, 7 June 2010, Pages 2349-2366.

Utilization of Localized Panel Resonant Behavior in Wind Turbine Blades

D. Todd Griffith
Analytical Structural Dynamics Department
Sandia National Laboratories*
Albuquerque, NM 87185-0557

ABSTRACT

The shear webs and laminates of core panels of wind turbine blades must be designed to avoid panel buckling while minimizing blade weight. Typically, buckling resistance is evaluated by consideration of the load-deflection behavior of a blade using finite element analysis (FEA) or full-scale static loading of a blade to failure under a simulated extreme loading condition. This paper examines an alternative means for evaluating blade buckling resistance using non-destructive modal tests or FEA. In addition, panel resonances can be utilized for structural health monitoring by observing changes in the modal parameters of these panel resonances, which are only active in a portion of the blade that is susceptible to failure. Additionally, panel resonances are considered for updating of panel laminate model parameters by correlation with test data. During blade modal tests conducted at Sandia Labs, a series of panel modes with increasing complexity was observed. This paper reports on the findings of these tests, describes potential ways to utilize panel resonances for blade evaluation, health monitoring, and design, and reports recent numerical results to evaluate panel resonances for use in blade structural health assessment.

I. Introduction

A structural analysis or test demonstrating the buckling resistance of a wind turbine blade under an extreme loading condition is required by wind turbine certification standards. Typically, linear static buckling analysis is performed in the design phase and a full-scale test is performed for validation. Many times the full-scale test load is applied until the blade fails. In this work, we consider the blade structural dynamics as an indicator of buckling resistance using localized blade panel resonances. Experimental modal analysis, or modal testing, is a non-destructive method for measuring the resonant response of a structure [1]. Likewise, resonant behavior (including localized resonance) can be predicted using FEA. The potential exists to evaluate buckling resistance without the need to test a blade to failure.

Along these same lines of thought, observation of panel resonances during a modal test may be used to improve the fidelity of a blade model by calibrating panel laminate models. An improved model would also provide a means to more accurately evaluate the blade design drivers, such as buckling resistance, using analysis. Furthermore, because blades often fail in the panels near maximum chord, real time observations of panel modes in operation would provide a means to evaluate structural health in key regions of the blade most susceptible to failure.

Now the wind turbine blade architecture is discussed, in particular as it relates to the focus of this work. A composite shell with spar caps forms the airfoil shape of a blade and reinforcing shear webs are placed inside the blade to stiffen the blade in the flap-wise direction. The spar caps are dimensioned and the shear webs are placed so as to add stiffness to unsupported panel regions and reduce panel dimensions. To better understand this construction, note [Figure 1](#) which shows a representative wind turbine blade cross section. At each span-wise blade station, a designer seeks to minimize the blade weight while maximizing stiffness and strength. Key decisions that impact both blade weight and buckling resistance are related to the design of the shear webs. The number of shear webs, their dimensions, and locations must be considered in the structural optimization. For example, a designer seeks to minimize the number and length of shear webs in order to reduce weight and manufacturing complexity. However, having fewer shear webs results in longer unsupported panel lengths, which may compromise buckling resistance without thickening of the panels. The segments of the airfoil between the two shear webs are called the spar caps and are composed of thick fiber/resin laminates. Buckling is not typically a concern in the spar cap. However, the panels located fore and aft of the spar caps are principally composed of much less stiff core materials (foam or balsa) to minimize weight. Central to work going forward is noting that the resonant frequencies of modes localized

* Sandia National Laboratories is a multi-program laboratory operated by Sandia Corporation, a wholly owned subsidiary of Lockheed Martin Corporation, for the U.S. Department of Energy's National Nuclear Security Administration under contract DE-AC04-94AL85000.

in the blade panels depend on geometry, material selection, and material placement in much the same way as panels designed using conventional static buckling analysis.

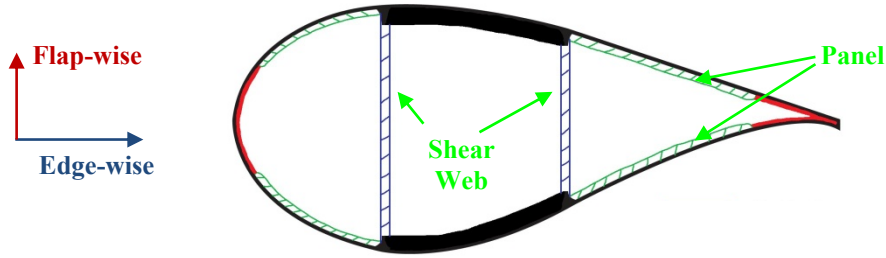


Figure 1. Representative Wind Turbine Blade Cross-section

With regard to a modal test, traditionally only low-order bending modes have been considered for validation of a blade structural model. As has been demonstrated, panel resonances can be predicted from FEA and compared with measurements from a modal test akin to the way the bending modes have traditionally been used. Additionally, structural damage tends to be a localized phenomenon. The use of global resonant responses, such as the bending or torsional modes, may not be a reliable indicator of damage. The use of blade panel modes is envisioned as an improved structural dynamics based indicator of damage as these modes are more dependent on local mechanics, and they are present in regions of the blade where damage usually occurs.

This paper presents ongoing research on the utilization of panel resonances, for blade buckling evaluation, structural health monitoring, and blade model validation, that builds upon previously published work in Reference 2. This paper reviews the work of Reference 2 and presents new results on the assessment of panel resonances for structural health assessment. The paper reviews experimental observations of panel resonances in blade modal tests. Prior work also demonstrated that high-fidelity FEA can predict panel resonances [2]. Thereafter, the prediction of panel resonances is utilized in FEA studies to quantify the sensitivity of the modal parameters to simulated damage in the core panels.

II. Experimental Observations

A program has been underway at Sandia Labs for several years to evaluate innovative structural mechanics concepts for wind turbine blades. The most recent set of “9-meter” research-sized blades have been evaluated with static, fatigue, and modal tests. Modal test results for the BSDS (Blade System Design Study) blade are the focus of this paper. Modal tests of the BSDS blade have been presented in prior work [3,4,5,6,7,8]. These papers focused on global bending and twisting blade modes for structural model validation and, in particular, experimental techniques for quantifying and reducing uncertainty in the modal parameters. The current work is focused on localized panel resonances.

A. BSDS Free Boundary Condition Modal Test

Figure 2 shows the modal test setup for the free boundary condition modal test of the BSDS blade. The free boundary condition was approximated using soft bungee cords supporting the blade at two span-wise locations.

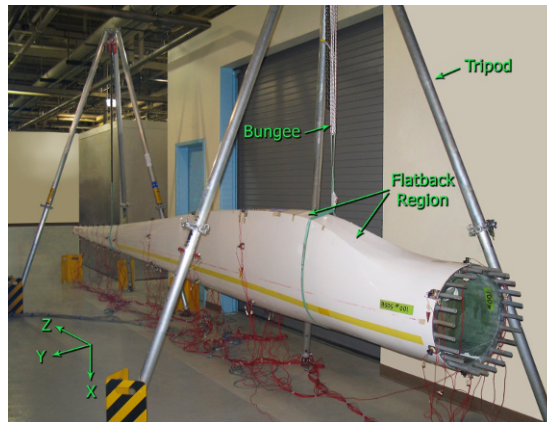


Figure 2. BSDS Free Boundary Condition Modal Test

The instrumentation layout is shown in Figure 3. The instrumentation was placed about the perimeter at each station and no sensors were placed on the internal shear web, which was located approximately along the z-axis as indicated in Figure 3. We chose not to mount accelerometers near the shear web in order to observe the panel resonances. Additionally, accelerometers were placed on both sides of the blade for the first 6 stations starting from the root end. At each location noted in the figure, sensor measurements were made in the flap-wise and edge-wise directions. Note that the blue markers indicate corresponding sensors on the opposite side of the blade.

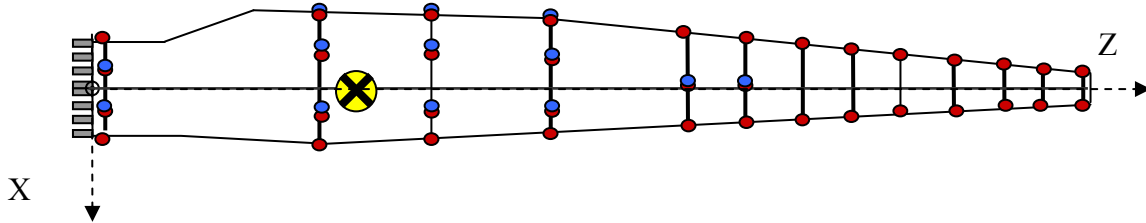


Figure 3. Instrumentation Layout for Free Boundary Condition BSDS Wind Turbine Blade Modal Test

The natural frequencies obtained from modal tests of two nominally identical BSDS blades with a free boundary condition (as shown in Figure 2) are given in Table 1. It should be noted that BSDS 001 had a shear web which was located slightly closer to the root. Only the low-order bending modes and panel modes are listed. Note that the first panel mode, the 4th lowest frequency mode, occurs at a relatively low frequency of 22 Hz. Clearly, there are some small differences between the two blades.

Table 1. Modal Parameters for BSDS Free Boundary Condition Modal Tests

<i>Mode Description</i>	Freq (Hz)	
	<i>BSDS 001</i>	<i>BSDS 004</i>
1st Flap-wise	5.4	5.3
2nd Flap-wise	13.5	13.5
1st Edge-wise	16.5	17.2
Panel Mode #1	21.4	22.3
Panel Mode #2	49.7	51.4

The mode shape plot for the first panel mode is shown in Figure 4. The first panel mode was well-excited with limited coupling with other modes. It shows a symmetric shape as the aft panel on each side of the blade is either moving outward or inward in unison. Note that there are no nodal crossings between the 2nd and 6th stations of the instrumentation, which were instrumented specifically to measure panel resonance. The higher frequency panel modes were more difficult to determine visually from these tests by inspection of the mode shapes. Nodal crossings were used to determine the second and third panel modes. The second panel mode shape has similar features to the first panel model although it is highly coupled with the first torsional mode. This mode has a nodal crossing between the 2nd and 3rd stations of the instrumentation layout. A third panel mode was identified in these tests at 70 Hz. This mode demonstrated high coupling with other modes and has a nodal crossing between the 3rd and 4th stations of the instrumentation layout.

These appear to be three modes in a series of panel modes as the complexity in the shape of these modes increases with frequency in a fashion similar to a family of modes for a plate structure.

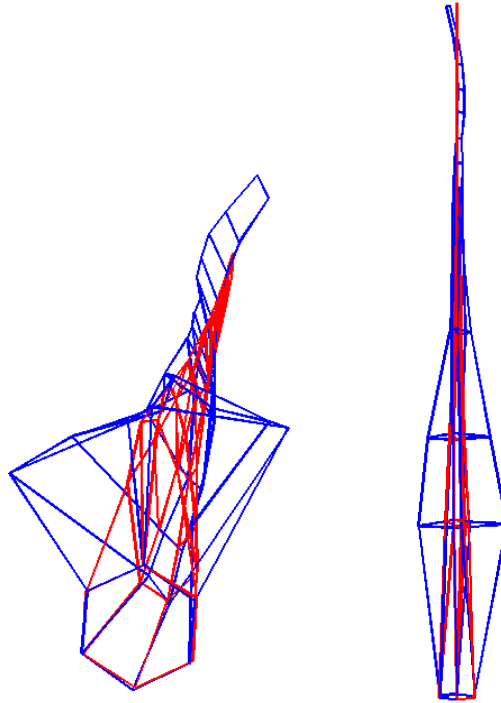


Figure 4. Principal Panel Mode (22 Hz), Isometric View (left) and Top View (right)

The measurement of panel resonances was not the primary objective of the free boundary condition modal tests as the principal goal was to provide validation data for the global bending and torsional modes. Although some aspects of the instrumentation design and test execution could have been improved for measurement of panel resonances, these preliminary test results provide some key observations that have motivated the subsequent work. These include:

- (1) Panel resonances are relatively low frequency modes,
- (2) A series of panel resonances of increasing complexity are present, and
- (3) Panel resonances are present in a section of the structure that is important for buckling design considerations and which is also susceptible to damage.

Some natural questions which we have investigated [2] and seek to further investigate include the ability to predict panel resonances in high-fidelity finite element models and their potential uses for blade evaluation, structural health monitoring, and design.

B. BSDS Seismic-Mass-on-Airbags Boundary Condition Modal Test

A second series of modal tests was performed on the BSDS blade. The new test was devised to validate BSDS structural models, particularly in the root region. A root boundary condition consisting of a seismic-mass-on-airbags was utilized in this test to provide a boundary condition that could be accurately characterized for inclusion in the structural analysis. This approach is very important to eliminate error in the boundary condition, which has a large effect on the modal parameters. In addition, this boundary condition provides a service-type boundary condition because the root region of the blade is strained and the seismic mass can move as dictated by the dynamics of the boundary condition. The boundary condition is modeled with a simple mass-damper-spring model. A full description of the test and validation results is reported in References 7 and 8. A photo of the test concept is shown in [Figure 5](#).

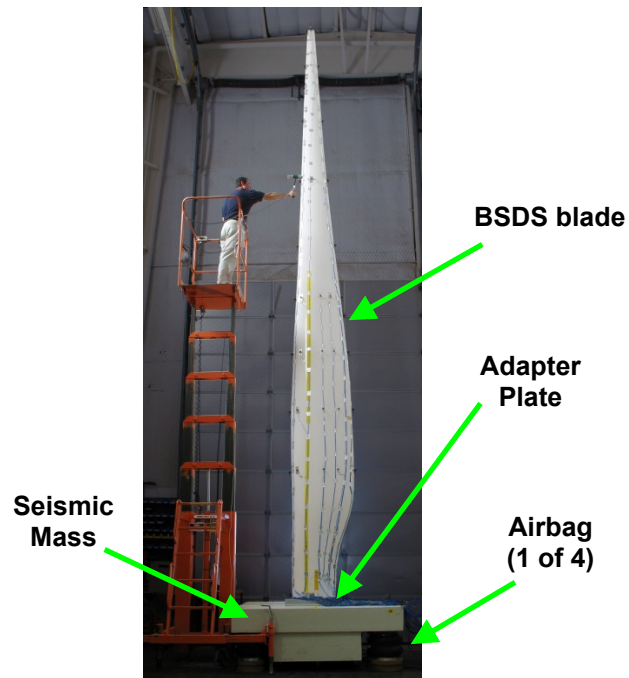


Figure 5. Photo of BSDS Blade Being Modal Tested with Seismic Mass on Airbags Boundary Condition

The instrumentation layout for this test is shown in Figure 6. This instrumentation setup was similar to the prior test; however, fewer span-wise stations were needed with more sensors placed on the panel regions (red dots, uniaxial accelerometers at the 60, 90, 120, and 150 inch span-wise locations) as compared to the previous test. In summary, less instrumentation was needed outboard on the blade as the bending modes were well-characterized in the previous free boundary condition modal test. However, this setup was a significant improvement for spatial characterization of the mode shapes of the panel resonances.

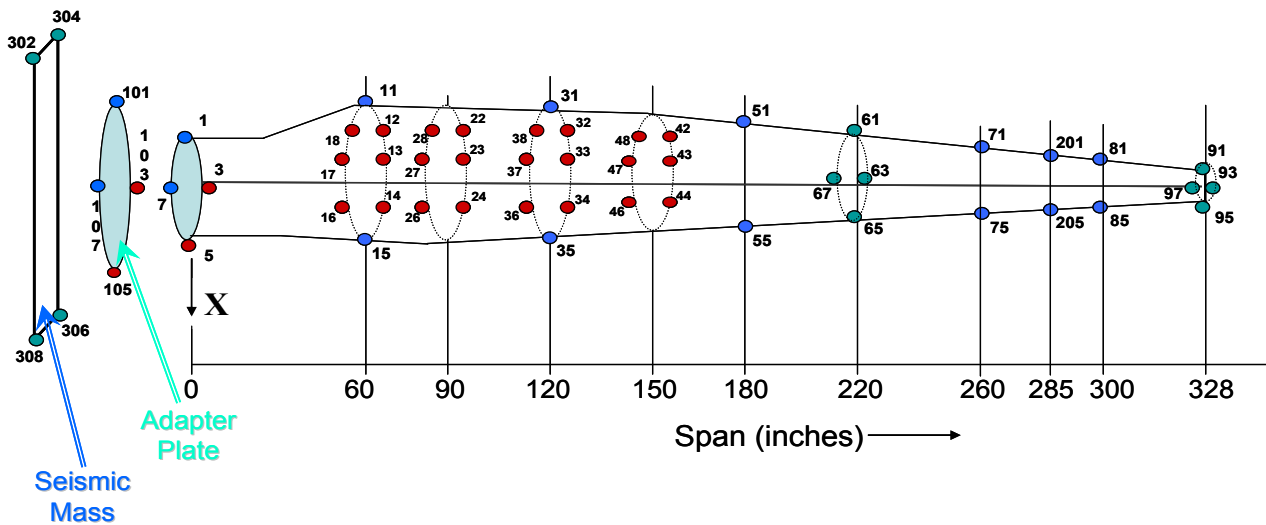


Figure 6. Instrumentation Layout with Seismic Mass on Airbags Boundary Condition

Figure 7 shows how the blade panel resonances were excited in these tests. Excitation at the panel easily provides the best excitation; however, panel resonances were also easily extracted from data sets with impacts along the span even with impact at the blade tip.



Figure 7. Impact Excitation of Blade Panel

Table 2 provides a partial list of modes for the BSDS blade tested with the seismic-mass-on-airbags boundary condition. The five lowest frequency modes are all bending modes. The first panel mode is at 27 Hz, and is strongly coupled with the 28 Hz fourth flap-wise bending mode. With the improved instrumentation setup, a number of other panel modes were identified. A second panel mode was found at 35 Hz, with node crossing at the middle of the instrumented panel between the 90 and 120 inch span-wise stations. Again, the panel resonances were measured at four stations (60, 90, 120, and 150 inches). An additional panel mode, which resembled Panel Mode #2, was found at 73 Hz. Although the shape was the same, this mode included a significant edge-wise bending component of the flatback. A third panel mode in the series was found at 92 Hz. This mode had two node crossings, between the first and second, and between the third and fourth stations.

Table 2. Modes of BSDS with Seismic Mass on Airbags Boundary Condition

<i>Mode Description</i>	Freq (Hz)	Node Crossing Location
	<i>BSDS 004</i>	
1st Flap-wise	4.0	
2nd Flap-wise	9.3	
1st Edge-wise	10.2	
3rd Flap-wise	17.5	
2nd Edge-wise	21.8	
<i>Panel Mode #1</i>	27.4	None observed
4th Flap-wise	28.4	
<i>Panel Mode #2</i>	35.0	Between 90 and 120 inches
<i>Panel Mode #2(edge)</i>	73.8	Between 90 and 120 inches
<i>Panel Mode #3</i>	92.0	Between 60 and 90, and between 120 and 150 inches

The mode shapes for the panel resonances were determined more easily visually due to the improved spatial resolution of the panel instrumentation for this test as indicated in Figures 8 and 9. The lowest frequency panel mode, which is highly coupled with the fourth flap-wise bending mode, is plotted in Figure 8. The second and third panel modes are plotted in Figure 9. From these plots, nodal crossings can be observed, and the complexity of the panel resonant shapes can be seen to increase as is the case for modes of a plate structure.

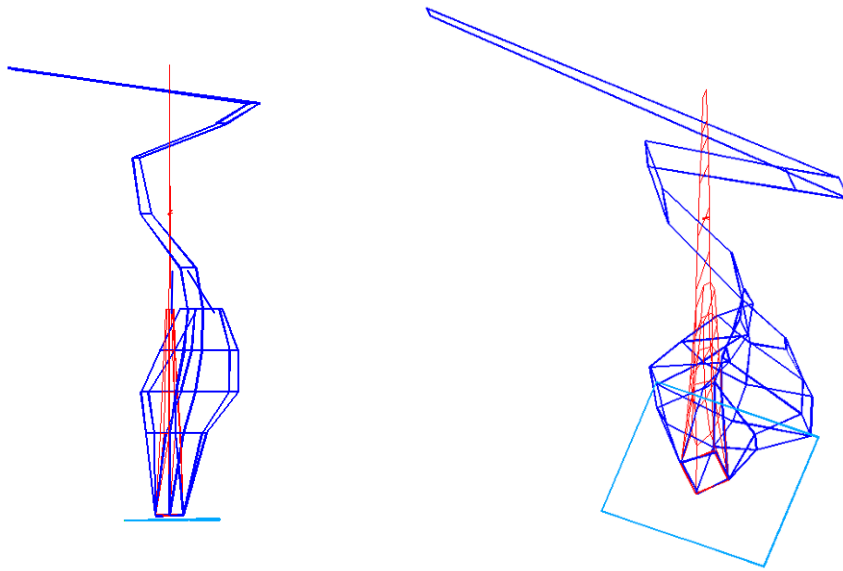


Figure 8. Mode Shape Plot of Panel Mode #1 (27 Hz)

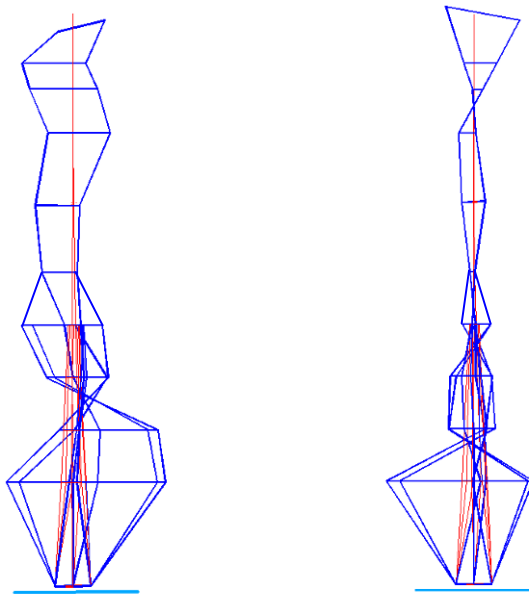


Figure 9. Mode Shape Plots of Panel Mode #2 (left, 35 Hz) and # 3 (right, 92 Hz)

III. Utilization of Panel Resonance Behavior for Design and Evaluation

Panel resonances are envisioned for use in the following: (1) evaluation of buckling resistance of a panel section of a blade, (2) as a metric or feature for structural health monitoring of blades, and (3) for use in validation of blade panel laminate models. Each of these potential uses of blade panel resonances is discussed in this section.

A. Buckling Resistance

Based on laboratory and field studies, blades have a tendency to fail in the panels. As a result, designers must carefully design panel sections to avoid buckling failure. Full-scale tests to failure may be necessary to validate the buckling predictions. Panel resonances, which can be measured during modal tests or predicted by FEA, are proposed as an indicator of blade buckling resistance. The advantage, if this approach proves viable, is that buckling evaluation could be performed non-destructively with a modal test as the magnitude of the resonant frequency may indicate the buckling capacity of the

panel. Additionally, panel modes could also be considered to provide a preliminary test evaluation before a full-scale static test is conducted. Buckling of the shear web is also an important consideration in blade design. Measurement of localized resonance of the shear web can also be considered in this discussion.

Central to these ideas is noting that the resonant frequencies of modes localized in the blade panels depend on geometry, material selection, and material placement in much the same way as panels designed using conventional static buckling analysis.

Optimization has also been considered to improve buckling resistance. In Reference 9, the effect of fiber orientation of panel laminates is studied to improve buckling resistance with significant improvements to the critical buckling load. Considering the above argument, increasing the frequency of panel resonances in design iterations is also expected to improve buckling resistance.

B. Structural Health Monitoring

Blade panel resonances provide a feature to use for real-time health monitoring. While global modes may provide an indication of damage or deterioration, it is difficult to understand in advance which global mode is an indicator of damage and to what extent damage must be present before the global modes show deviation due to damage. However, local modes will provide an indication of damage in the section of the blade in which they are active.

Panel resonances could be monitored throughout the lifetime of a blade from fabrication through operation. Some initial ideas for in-situ monitoring and sensor selection are suggested. Traditional approaches using accelerometer and strain sensors, similar to the approach of these modal tests, are viable. It is expected that as few as a single accelerometer could be used to continuously monitor panel resonances; with aid in placement by a modal test or FEA prediction. A key question with any in-situ sensing approach will be having sufficient excitation of panel resonances during operation. These modal tests demonstrate that excitation need not be localized in the panels to excite these modes. However, additional study would be needed for specific turbine blades to determine if localized excitation devices may be required.

Digital Image Correlation (DIC) [10] and photogrammetry [11] are being considered for deformation measurements for wind turbine blades. These techniques provide non-contacting measurement approaches, and could be considered for laboratory as well as periodic, full-field techniques for monitoring of panel resonances.

C. Laminate Model Validation

Global bending and torsional modes provide a great deal of information for blade model validation. The level of model validity they provide ensures that beam-type representations of the blade are adequate. Panel resonances are considered for further refinement (higher-level validation) of blade models to ensure accurate prediction of localized effects for strength or buckling analysis. Measured panel resonances can be used for either blade calibration or validation to improve existing blade model validation methodology [5]. Likely, use of blade panel resonances will be very important for better predictive models that will allow increased design authority. A more thorough modeling and simulation based approach can reduce blade development costs and result in more reliable designs.

IV. Numerical Results for Blade Structural Health Assessment

A high-fidelity finite element model of the BSDS blade was used to quantify the effect of simulated damage in the blade core panel. The following sections detail the methodology used to simulate damage and the numerical results of these calculations.

A. FEA Simulation of Damage

The objective of this numerical study was to compare the relative sensitivities of the natural frequencies of the global blade bending and twisting modes with those of the localized panel modes. A damaged area of size approximately 6 inches by 6 inches was chosen for the analysis, as shown in Figure 10. Damage was simulated in a panel on only one side of the blade near maximum chord and approximately centered along the chord-wise direction in the blade panel between the spar cap and trailing edge. A shear delamination failure was chosen as the damage mechanism. It was desired to simulate a realistic type of damage with modest extent of damage; although the damage mechanism and size of the damage area were chosen somewhat arbitrarily. The goal was not to replicate an observed damage, but rather to perform a comparative study of one type of damage on the modal parameters. The “shear delamination failure” was simulated by zeroing the values of the Moduli of Rigidity and Poisson’s Ratio for the fiber layers in the skin of the panel. The upper surface coating, balsa core material, and fiber layers on the interior surface of the laminate were not affected. The approach was similar to that taken in Reference 12.

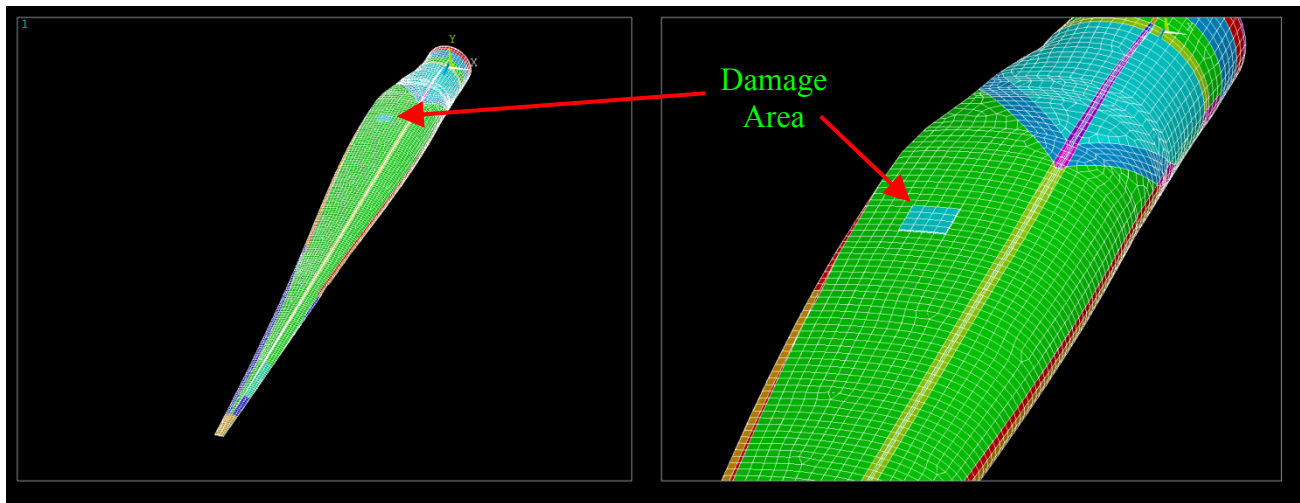


Figure 10. Finite Element Models of Blade (left) and Closeup Showing Damaged Area (right)

B. Numerical Results and Discussion

Two cases of shear delamination failure were simulated: (1) a nominal case in which no longitudinal or transverse Moduli were affected, and (2) a case in which the Moduli of Elasticity were reduced in value by 90%. First, the blade model with nominal “undamaged” properties was solved for the normal modes of vibration using ANSYS. Then, each of the two damaged cases was solved. The percent change in the modal frequency of each of the first 16 modes was computed and is plotted in Figure 11. The first mode in which significant motion in the panel is predicted is mode 9. Modes 1 through 8 are dominated by global bending and torsional motions. Modes 9 and higher have significant motion in the panels, with increasing levels of panel resonance shape complexity and coupling with global bending/twisting modes at higher frequencies.

The results of Figure 11 indicate that for both damage cases the natural frequencies of the panel resonances are significantly more sensitive to damage than the low frequency bending modes. Compared to the fundamental mode of the blade, the modes with significant panel motions are 10-20 times, and in some instances 50 times, more sensitive to the simulated damage. These initial studies are promising for the use of panel resonances in structural dynamics based damage detection.

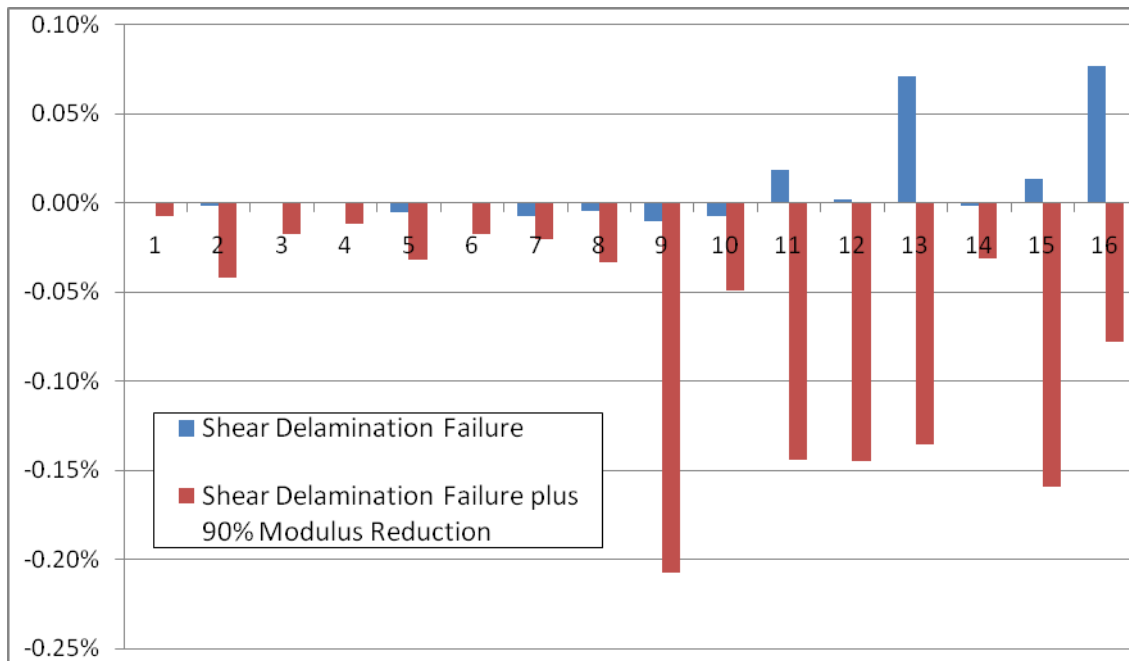


Figure 11. Percent Change in Modal Frequencies of First 16 Blade Modes

V. Conclusions

This paper addressed localized panel resonance behavior in wind turbine blades. Experimental results from modal tests were presented to demonstrate the presence of these localized modes in blades. A series of panel resonances were observed with increasing complexity similar to a series of plate modes. These modes were active in a region of the blade that is susceptible to buckling failure. The hope is that these fundamental observations of the panel resonances and their characteristics provides new knowledge regarding blade dynamics and will lead to new methods for blade evaluation, health monitoring, and design.

A number of uses of panel resonances were proposed. These include non-destructive evaluation of buckling resistance, structural health monitoring, and blade panel laminate validation. Resonant frequencies of modes localized in the blade panels depend on geometry, material selection, and material placement in much the same way as panels designed using conventional static buckling analysis. Panel resonances are active in parts of the blade susceptible to failure, and panel resonances may provide a higher level of model validation. These uses and benefits of panel resonances are the motivation for this ongoing research.

In the earlier reported work, FEA was performed to investigate the ability to predict these modes. It was found that FEA also predicts a series of localized panel resonances similar to those measured in the modal tests. The ability to predict panel resonances demonstrates that panel resonances have potential uses in both experimental and analytical methods.

Numerical studies to evaluate the use of panel resonances for structural health monitoring indicate the panel resonant frequencies are significantly more sensitive to damage in the core panels than low-order bending modes. Knowledge of the characteristics of the panel modes can guide a health monitoring strategy as panel resonances occur in a series which can all be monitored to identify and locate damage in the core panels.

Acknowledgements

Joshua Paquette of the Sandia Wind Energy Department is acknowledged for providing the high-fidelity finite element model of the BSDS blade.

References

- [1] Ewins, D.J., *Modal Testing: Theory, Practice and Application*, 2nd ed. Research Studies Press, Ltd, 2000.
- [2] Griffith, D.T., Paquette, J.A., "Panel Resonant Behavior of Wind Turbine Blades," 51th AIAA Structures, Structural Dynamics, and Materials Conference, April 12-15, 2010, Orlando, FL, AIAA-2010-2741.
- [3] Griffith, D.T., and Carne, T.G., "Experimental Modal Analysis of 9-meter Research-sized Wind Turbine Blades," 28th International Modal Analysis Conference, February 2010, Orlando, FL, USA.

- [4] Griffith, D. T. and Carne, T.G., "Experimental Uncertainty Quantification of Modal Test Data," *25th International Modal Analysis Conference*, February 2007, Orlando, FL, USA.
- [5] Griffith, D.T., Paquette, J.A., and Carne, T.G., "Development of Validated Blade Structural Models," *46th AIAA Aerospace Sciences Meeting and Exhibit*, 7-10 January 2008, Reno, NV, USA, AIAA 2008-1297.
- [6] Carne, T.G., Griffith, D.T. and, Casias, M.E., "Support Conditions for Free Boundary-Condition Modal Testing," *25th International Modal Analysis Conference*, February 2007, Orlando, FL, USA.
- [7] Griffith, D.T., Hunter, P.S., Kelton, D.W., Carne, T.G., and Paquette, J.A., "Boundary Condition Considerations for Validation of Wind Turbine Blade Structural Models," *Society for Experimental Mechanics Annual Conference*, June 2009, Albuquerque, NM, USA.
- [8] Griffith, D.T., "Structural Dynamics Analysis and Model Validation of Wind Turbine Structures," *50th AIAA Structures, Structural Dynamics, and Materials Conference*, May 4-7, 2009, Palm Springs, CA, AIAA-2009-2408.
- [9] *Mechanical Response of Composites*, Computational Methods in Applied Sciences Book Series, Volume 10, Chapter 12, "On Buckling Optimization of a Wind Turbine Blade," Lund, E. and Johansen, L.S., Springer Netherlands, 2008, pgs. 243-260.
- [10] Helfrick, M., Niezrecki, C., and Avitabile, P., "Optical Noncontacting Vibration Measurement of Rotating Turbine Blades," *27th International Modal Analysis Conference*, Orlando, FL, February 2009.
- [11] Paulsen, U., Erne, T., Sanow, W., and Schmidt, T., "Wind Turbine Operational and Emergency Stop Measurements Using Point Tracking Videogrammetry," *Society for Experimental Mechanics Annual Conference*, June 2009, Albuquerque, NM, USA.
- [12] Zonghong, X., Ruibo, B., and Lei, Z., "Damage Prediction of a Composite Laminate Under Quasi-Static Indentation Force," *2nd International Conference on Computer Engineering and Technology*, April 2010, Chendu, China.

Random Vibration – History and Overview

Thomas L. Paez
Thomas Paez Consulting
175 Iron King
Durango, Colorado 81301

Abstract

The history of the mathematical theory of random vibration started in 1905 with the publication by Einstein of his paper, “On the Movement of Small Particles Suspended in a Stationary Liquid Demanded by the Molecular Kinetic Theory of Heat.” He developed an approach to random vibration that is no longer widely used, but he showed the potential for mathematical treatment of random vibration. Many others joined the effort to develop methods for random vibration analysis. In 1930 Weiner formally defined spectral density, and in so doing, opened the way for the current approach to random vibration analysis. In 1958 Crandall organized a workshop at MIT to introduce the theory and practice of random vibration to engineers. The historical work of these researchers, and many others, is discussed in this paper.

1.0 Introduction

Random vibrations are the oscillations of mechanical systems excited by environments that vary randomly in time and, perhaps, space. Practically all real physical systems are subjected to random dynamic environments, and many systems will fail due to the effects of these exposures. Mathematical and experimental studies of random vibrations are pursued to explain observed phenomena, to predict the characteristics of system responses, to aid in the design of mechanical systems, and to demonstrate the survivability of physical systems.

Random vibrations have been studied in a mathematical framework since about the turn of the previous century. Albert Einstein (1905) performed the first mathematical analysis that could be considered a random vibration analysis when he modeled the Brownian movement of particles suspended in a liquid medium. (This is the same year in which his results on the photoelectric effect, for which he received the 1921 Nobel prize in physics, and his results on special relativity were published.) Numerous studies whose results would later be used to explain the random vibration of mechanical systems were carried out in the decades to follow, and in 1930 Norbert Weiner formally defined the spectral density of a stationary random process, i.e., a random process in a temporal steady state. Spectral density is the de-facto fundamental quantitative descriptor of stationary random processes in use today. But it was not until the 1950's that the subject of random vibrations of mechanical systems would be addressed directly, with the approach in use, today. A comprehensive theory of random vibrations was needed to accurately predict structural response to jet engine noise and missile launch-induced environments. In 1958 Steven Crandall organized a special summer program at the Massachusetts Institute of Technology to address problems in the various areas of random vibrations of mechanical systems. Specifically, the papers covered topics such as analysis of random vibrations and design for random environments, random vibration testing, and the analysis of data from random environments. The history of these contributions to the theory and practice of random vibrations from the time of Einstein to 1958, and the years immediately following, are described. The historical presentation is chronological, to the extent possible, and some limited mathematics are included.

Texts are available for those seeking an introduction or a more advanced presentation of the mathematics of random vibrations. Some of these are the texts by Crandall (1958,1963); Crandall and Mark (1963); Robson (1964); Lin (1967); Elishakoff (1983); Nigam (1983); Newland (1993); Bolotin (1984); Augusti, Baratta and Casciati (1984); Ibrahim (1985); Yang (1986); Schueller and Shinozuka (1987); Roberts and Spanos (1990); Ghanem and Spanos (1991), Soong and Grigoriu (1993); Wirsching, Paez, and Ortiz (1995); and Bendat and Piersol (2000). Historical developments in the theory of stochastic processes (The term “stochastic” is used interchangeably with “random.”) are included in Gnedenko (1997), and Feller (1971).

This paper will focus mainly on the description of historical developments in random vibration analysis. Section 2 summarizes Einstein's description of Brownian motion as a diffusion process and other early researchers' random vibration modeling efforts. Section 3 summarizes the development of spectral density, the fundamental descriptor of stationary random

processes, and traces some preliminary thoughts on the subject back to 1889. Analysis of the random vibrations of mechanical systems, as practiced today, started in the 1950's, and the beginnings of the analytical developments are covered in Section 4. Some of the works from Crandall's 1958 workshop are discussed. Examples are provided throughout the paper.

2.0 Einstein's Era

Around the turn of the previous century, Einstein (1905) constructed a framework for analyzing the Brownian movement - the random oscillation of particles suspended in a fluid medium and excited by the molecular motion associated with the kinetic theory of matter. Brownian movement had been recognized about a century earlier during observations of microscopic particles of pollen immersed in a liquid medium; it is characterized by the erratic movement of the pollen particles. The particle motion characteristics depend on the mass and geometry of the particle and the physical characteristics (such as viscosity and temperature) of the fluid medium.

Because the problem Einstein solved yields the probabilistic description of the motion of a mass attached via a viscous damper to a fixed boundary and excited with white noise (a random excitation with frequencies covering a broad band), his development can be thought of as the first solution to a random vibration problem and the dawning of the era of random vibration analysis.

In his solution of the problem of Brownian movement Einstein did not use a direct formulation that writes and analyzes the differential equation governing motion of the system. (The direct approach would eventually become the one most commonly used for random vibration analysis.) However, for reference, the governing equation is

$$m\ddot{X} + c\dot{X} = W(t) \quad t \geq 0, X(0) = 0, \dot{X}(0) = 0 \quad (1)$$

where $\{X(t), t \geq 0\}$ is the one-dimensional particle displacement response random process, m is particle mass, c is the damping that ties the mass to an inertial frame, $\{W(t), -\infty < t < \infty\}$ is the white noise excitation random process, and dots denote differentiation (in a sense appropriate for a random process) with respect to time. The white noise excitation random process has the constant spectral density $S_{WW}(\omega) = S_{WW}, -\infty < \omega < \infty$. (Spectral density defines the mean square signal content of a random source as a function of frequency. The spectral density defined here is two-sided because it is defined for positive and negative frequencies. The definition of spectral density, along with some examples, and some ideas underlying random processes and their notations are provided in the following section.) The system of Eq. (1) is shown schematically in Figure 1. The white noise random process is a source with mean square signal content that is uniformly distributed over the entire range of frequencies (up to infinity, in theory).

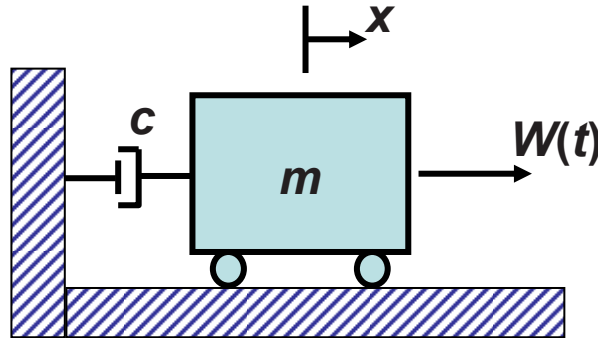


Figure 1. Schematic of the system considered by Einstein in his solution of the Brownian movement problem/random vibration analysis.

With a very intuitive discussion, Einstein developed the diffusion construct for analyzing the random vibration of mechanical systems. This framework models diffusion of a particle (rigid mass) under the influence of applied impacts. In the application he considered, the impacts arose from the motions of the molecular constituents in the fluid surrounding the particle. The paper Einstein wrote has two parts. The first part uses the idea of osmotic pressure and equilibrium of a sphere moving in a fluid medium to derive the coefficient of diffusion of such a particle. He showed that the coefficient of diffusion can be modeled as $D = (RT/N)(1/6\pi\eta r)$, where R is the universal gas constant, T is absolute temperature, N is Avagadro's number,

c_f is the coefficient of viscosity of the fluid, and r is the radius of the sphere. The coefficient of diffusion governs the rate at which particles will spread throughout a fluid in an equilibrium condition.

The second part of Einstein's paper considered particle diffusion in one dimension. He defined a time interval τ that is short compared to an interval of visual observation but long enough that particle movements executed in two consecutive intervals are independent. He assumed that during the time τ the x coordinate of an individual particle will increase by a random amount Δ (positive or negative). The quantity Δ is a random variable with symmetric PDF $f_\Delta(\alpha)$, $-\infty < \alpha < \infty$. (Einstein neither used the term "random variable" nor "probability density function" because the terminology was not yet established, however, these are what he described.) He then specified that the PDF of the x coordinate of a particle after time t , i.e., the PDF of a random variable $X(t)$ in the random process $\{X(t), t \geq 0\}$, is $f_X(t)(x)$, $t \geq 0, -\infty < x < \infty$, and wrote the relation

$$dx \cdot f_X(t+\tau)(x) = dx \cdot \int_{-\infty}^{\infty} f_X(t)(x+\alpha) f_\Delta(\alpha) d\alpha \quad t \geq 0, -\infty < x < \infty \quad (2)$$

This equation states that the probability of finding the x coordinate of a particle in the interval $(x, x+dx]$ at time $t+\tau$ (left side) equals the "sum" of probabilities that the particle starts in the interval $(x+\alpha, x+\alpha+d\alpha]$ at time t , and moves a distance $-\alpha$ during the time increment τ (right side). He expanded $f_X(t+\tau)(x)$ in a Taylor's series in τ , and $f_X(t)(x+\alpha)$ in a Taylor's series in α and substituted the series into Eq. (2). He simplified the integral on the right hand side and noted that because of the symmetry of $f_\Delta(\alpha)$, only the odd numbered terms are non-zero. The term $f_X(t)(x)$ occurs on both sides and the two terms cancel. He retained only the linear term in τ on the left hand side, arguing the permissibility of this approximation because of the small magnitude of τ . He set the integral in the third term on the right hand side (the first non-zero term) to the coefficient of diffusion.

$$D = \frac{1}{\tau} \int_{-\infty}^{\infty} \frac{\alpha^2}{2} f_\Delta(\alpha) d\alpha \quad (3)$$

And he eliminated the remainder of the terms on the right hand side, arguing that they are small relative to the term retained. The result he obtained is

$$\frac{\partial f_X(t)(x)}{\partial t} = D \frac{\partial^2 f_X(t)(x)}{\partial x^2} \quad t \geq 0, -\infty < x < \infty \quad (4)$$

He pointed out that this is the equation governing diffusion of a particle in a liquid medium with coefficient of diffusion D .

Einstein specified as the initial condition

$$f_X(0)(x) = \delta(x) \quad -\infty < x < \infty \quad (5)$$

where $\delta(x)$, $-\infty < x < \infty$, is the Dirac delta function. (The Dirac delta function was not actually defined until later, so Einstein described an initial condition with this character, but not using the terminology. The Dirac delta function is a "distribution," a function described by its behavior under an integral. Its integral is one, $\int_{-\infty}^{\infty} \delta(x) dx = 1$, and it has "small" values away from the origin, $\delta(x) = 0, x \neq 0$. In the application written above, it indicates certainty that the system starts with zero displacement.) Under these conditions, the solution to Eq. (4) is

$$f_X(t)(x) = \frac{1}{\sqrt{4\pi D}} \frac{1}{\sqrt{t}} \exp\left(-\frac{x^2}{4Dt}\right) \quad t \geq 0, -\infty < x < \infty \quad (6)$$

The displacement response random process has a normal (Gaussian) distribution with mean zero and variance $2Dt$. (This also equals the mean square, or mean of the square of $X(t)$, because the random process has zero-mean.) The displacement of a particle in Brownian motion has a variance that increases linearly with time. Its root-mean-square (RMS) departure from the origin increases at a rate of \sqrt{t} . Increases in the coefficient of diffusion, D , imply increased response variance at a given time. D increases linearly with temperature of the medium, and decreases as the inverse of coefficient of viscosity and particle size. Einstein pointed out, and it was confirmed later, by more accurate analyses, that this result is not accurate for times that are small compared to (m/c) . Nevertheless, Eq. (6) stands as the first solution of a random vibration problem.

The diffusion coefficient is related to the parameters of Eq.(1) via $D = S_{WW}/2c^2$ when S_{WW} has units of $lb^2/(rad/sec)$. Figure 2 shows five marginal PDFs (i.e., PDFs of single random variables) of response at normalized times $\tau = 2Dt = 0.1, 1, 4, 7, 10$. The normalized time versus x plane also shows the plus and minus one times the standard deviation curves, $\pm\sqrt{\tau}$. The plots clearly indicate the effects of the uniformly increasing variance. As time increases the standard deviation – and, thus, the width – of each normal PDF increases, and the peak of the PDF decreases. We reiterate the important fact that Einstein's analysis, summarized here, was the first random vibration analysis of a discrete mechanical system.

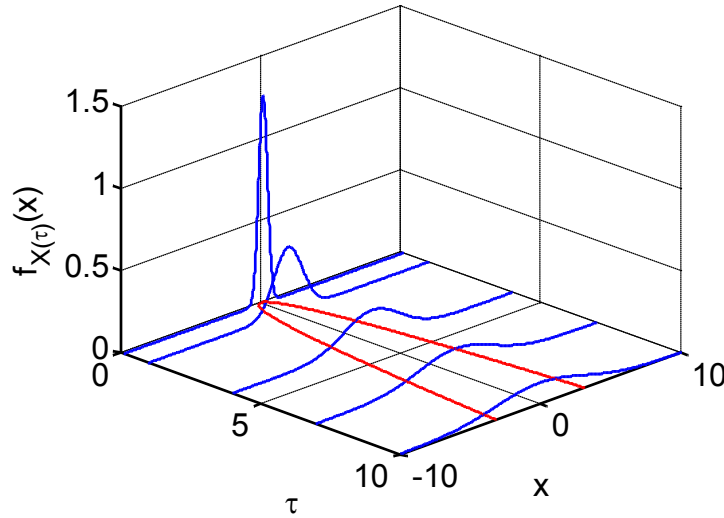


Figure 2. Marginal PDFs of some normal distributions of the displacement response of a particle in Brownian motion for normalized times $\tau = 2Dt = 0.1, 1, 4, 7, 10$.

Einstein augmented his initial study with further investigations (all reprinted in Einstein, 1956, and written during the period of 1905 through 1908). He considered, among other things, extensions to his original development and the problem of molecular parameter identification.

A sample time history drawn from a random source (a random process) is known as a realization of the random process. For example, consider Figures 3a, 3b and 3c. The first of these shows a realization of a band-limited white noise force. It has signal content up to a maximum frequency of 50 Hz, a spectral density of $1lb^2/Hz$, and, therefore, a mean square of $50lb^2$. The second shows the corresponding realization of displacement response random process of a rigid particle with mass $m=1 lb\text{-}sec^2/in$ attached via a viscous damper with constant $c=0.1 lb\text{-}sec/in$ to an inertial frame. The third shows the corresponding realization of the velocity response random process. All the plots have a time increment of $\Delta t = 0.01 sec$.

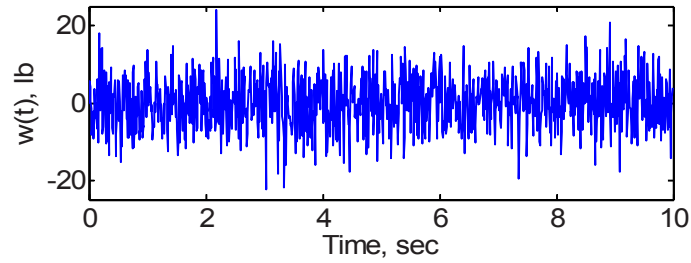


Figure 3a. Realization of a band-limited white noise excitation.

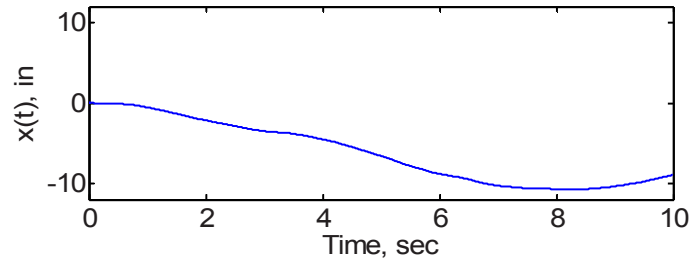


Figure 3b. Realization of displacement response of the system shown in Figure 1 to the excitation shown above.

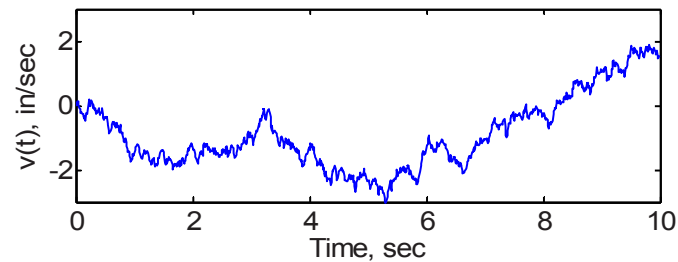


Figure 3c. Realization of velocity response of the system shown in Figure 1 to the excitation shown above.

Smoluchowski (1916) and Furth (1917) independently generalized Einstein's analysis and performed Brownian motion experiments to verify the predictions of the theory. Smoluchowski was first to write a form of the diffusion equation (later known as Fokker-Planck equation) for systems in which a displacement-related force restrains the mass. He wrote the diffusion equation governing the PDF of the response of a single-degree-of-freedom (SDF) system connected to a fixed boundary via a linear spring and viscous damper. A schematic of such a system is shown in Figure 4. But the equation that he developed, and its solution, govern only the response of an over-damped SDF system, i.e., a system with relatively high damping – one that executes a non-oscillatory response in free vibrations caused by non-zero initial conditions. The over-damped solution is less interesting to structural dynamicists than the lightly damped one because most practical structural dynamic systems are lightly damped.

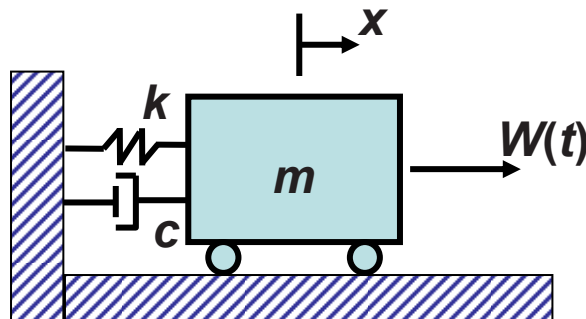


Figure 4. Schematic of the system considered by Smoluchowski in his random vibration analysis.

The limitation on the Fokker-Planck equation would later be overcome (Wang, Uhlenbeck, 1945), but in the short term Ornstein (1919) developed a method for assessing the displacement and velocity response PDFs for the linear SDF system. Ornstein's solution was summarized in detail in the 1930 paper by Uhlenbeck and Ornstein. The method involves direct consideration of the response based on its governing equation of motion.

$$m\ddot{X} + c\dot{X} + kX = W(t) \quad t \geq 0, X(0) = 0, \dot{X}(0) = 0 \quad (7)$$

where the parameters and variables have the same meanings as defined following Eq. (1), and k is the SDF system stiffness. Their first step was to mathematically characterize the white noise excitation. They required that the random process have zero mean, $E[W(t)] = 0, -\infty < t < \infty$, and a second order average, known now as the autocorrelation function, with the following behavior.

$$E[W(t_1)W(t_2)] = R_{WW}(t_1, t_2) = 2\pi S_{WW}\delta(t_2 - t_1) \quad -\infty < t_1, t_2 < \infty \quad (8)$$

where $\delta(\tau), -\infty < \tau < \infty$, is Dirac's unit delta function. This terminology was still not used in 1930, but it does, effectively, describe the characteristics Ornstein specified. The requirement of Eq. (8) indicates that the average of the product of the excitation at times t_1 and t_2 is zero for $t_1 \neq t_2$, and effectively, infinite for $t_1 = t_2$. The important implication is that mean square displacement response to such an excitation is finite.

Any measure of the response of the system governed by Eq. (7) (or any linear system) can be expressed with a convolution integral. The displacement response is

$$X(t) = \int_0^t h(t-\tau)W(\tau)d\tau \quad t \geq 0 \quad (9)$$

where $h(t), t \geq 0$, is the impulse response function relating the system excitation to the response measure of interest. In this case, the *impulse response function* is the displacement response following application of the unit delta function excitation, and is given by

$$h(t) = \frac{1}{m\omega_d} e^{-\zeta\omega_n t} \sin(\omega_d t) \quad t \geq 0 \quad (10)$$

where $\omega_n = \sqrt{k/m}$ is the natural frequency of the SDF system, the approximate frequency, in radians/sec, at which the system responds in free vibration, $\zeta = c/2\sqrt{km}$ is the (unitless) system damping factor (or, critical damping ratio), an indicator of the rate at which energy is dissipated in the system, and $\omega_d = \omega_n\sqrt{1-\zeta^2}$ is the damped natural frequency, the actual frequency at which the damped SDF system responds. The expected value of the response is zero. Uhlenbeck and Ornstein wrote the expression for the square of the convolution integral, Eq. (9), and computed the expectation to obtain the mean square displacement response.

$$E[X^2(t)] = \sigma_X^2(t) = \frac{\pi S_{WW}}{2\zeta\omega_n^3 m^2} \left\{ 1 - e^{-2\zeta\omega_n t} \left[1 + \frac{2\zeta^2}{(1-\zeta^2)} \sin^2(\omega_d t) + \frac{\zeta}{\sqrt{1-\zeta^2}} \sin(2\omega_d t) \right] \right\} \quad t \geq 0 \quad (11)$$

This equation establishes the growth of displacement response mean square with time for a linear SDF system. They went on to show that certain conditions on the random excitation yield a response that is Gaussian distributed.

Figure 5 shows a sequence of Gaussian, displacement response PDFs in normalized coordinates for a damping factor of $\zeta = 0.05$. Normalized time is $\tau = \omega_n t$. The normalized displacement is $\xi = x/\sigma_X(\infty)$, where $\sigma_X^2(\infty) = \pi S_{WW}/2\zeta\omega_n^3 m^2$, i.e., the displacement divided by the root-mean-square (RMS) response as $t \rightarrow \infty$. The normalized PDFs governing the displacement response at normalized times $\tau = 1, 10, 20, 30, 40, 50$, are plotted.

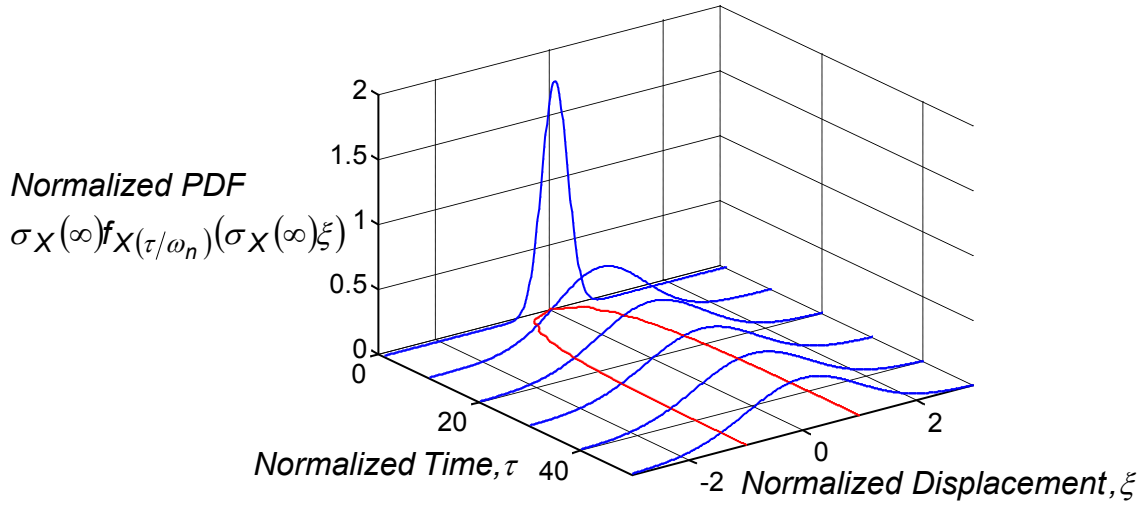


Figure 5. Marginal PDFs of some normal distributions of the displacement response of a linear SDF system excited by white noise, for normalized times $\tau = 1, 10, 20, 30, 40, 50$, as a function of the normalized displacements $\xi = x / \sigma_X(\infty)$.

This work of Uhlenbeck and Ornstein is extraordinarily important because it is the first treatment of random vibration for the under-damped case pertinent to structural dynamics. Further, it is the first analysis of response characteristics that directly uses the convolution integral representation of the response, which is the approach that is used most frequently today for random vibration analyses.

Many other studies were performed and papers written to advance the theory of random vibrations during the following years.

It is understandable that the collection of papers summarized in this section on the Brownian motion of particles, including particles that respond to input in an oscillatory fashion, may not have spurred the imagination of structural dynamics researchers interested in the motions of large-scale structures. However, some of the papers involving structures like beams, written more than two decades prior to the time in the 1950's when widespread interest grew in random vibration of mechanical systems, might have served as an impetus to practical random vibration investigations. It appears, though, that those papers were not widely known by structural dynamics researchers, and some of the earliest and strongest motivations for random vibrations research, namely the effects caused by jet noise and missile launch environments, did not yet exist. It appears that among those who participated in early random vibrations research, only Lyon (1956) referred to a 1931 paper by Van Lear and Uhlenbeck (1931). For their part, Van Lear and Uhlenbeck refer to even earlier investigations into the random vibration of structural systems. Ornstein (1927) wrote a paper on the random vibration of an elastic string, and Hodijk (1928) wrote a paper on the random vibration of an elastic rod. Still, these three papers cannot really be considered part of the literature that inspired the popular development of random vibrations of mechanical systems.

Planck (1927) and Fokker (1913) used a different approach to obtain the diffusion problem formulation and solution for Brownian motion. They started with the discrete space/discrete time framework of the random walk to characterize the dynamic motion of a particle in Brownian motion. Figure 6 shows a particle on the real line. During this simple random walk a particle starts at the origin at time $t = 0$, and moves at each step with probability $p = 1/2$, one step to the right, and with probability $q = 1/2$ one step to the left. They specified the time duration of each step as Δt , and the length of each step as Δx , so that the times under consideration are $t = j\Delta t, j = 0, 1, 2, \dots$, and the displacements under consideration are $x = k\Delta x, k = 0, \pm 1, \dots, \pm j$.

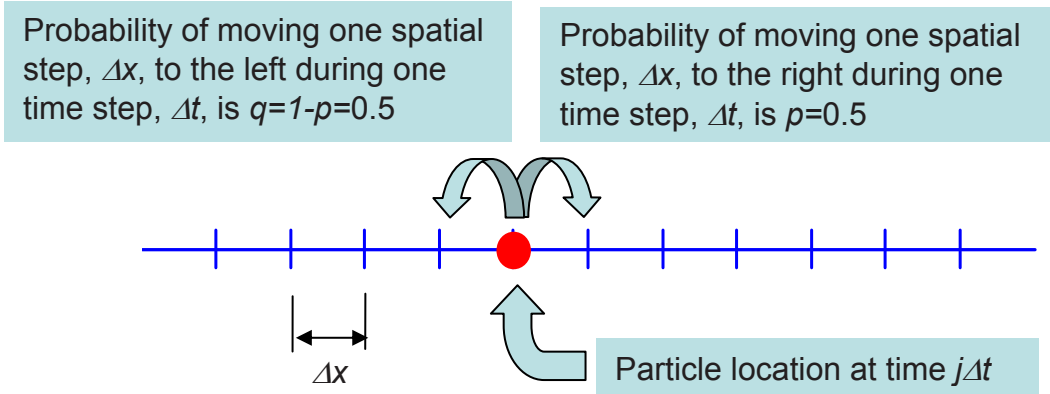


Figure 6. The schematic idea that forms the basis for the derivation of the diffusion model from a discrete time/discrete space foundation – the random walk.

Let the notation $f_X(t)(x) = f_X(j\Delta t)(k\Delta x)$, $j = 0, 1, 2, \dots, k = 0, \pm 1, \pm 2, \dots, \pm j$, denote the probability that at time $t = j\Delta t$, following j impacts, the particle lies at the location $x = k\Delta x$, k steps to the right of the origin (k can be positive or negative). If i equals the total number of steps to the right and $j - i$ the total number of steps to the left, then it must be that $k = i - (j - i) = 2i - j$ because k represents the net number of steps to the right. This can be solved for i , and because $x = k\Delta x$, $i = \frac{1}{2}(k + j) = \frac{1}{2}\left(\frac{x}{\Delta x} + j\right)$. Because each step in the random process involves a random binary movement, the probability distribution of the discrete location of the particle is binomial (see Ang and Tang, 1975), and Planck and Fokker wrote

$$\begin{aligned} P\left(\frac{X(t)}{\Delta x} = k\right) &= \binom{j}{\frac{1}{2}(j+k)} \left(\frac{1}{2}\right)^{\frac{1}{2}(j+k)} \left(\frac{1}{2}\right)^{\frac{1}{2}(j-k)} \\ &= \binom{j}{\frac{1}{2}(j+k)} \left(\frac{1}{2}\right)^j = P(X(t) = k\Delta x) \quad j = 0, 1, 2, \dots, k = 0, \pm 1, \dots, \pm j \end{aligned} \quad (12)$$

where the notation $\binom{j}{r} = \frac{j!}{r!(j-r)!}$ refers to the binomial coefficient. Based on this, the expected value of $X(t)$ is zero, $E[X(t)] = 0$, and its variance is $V[X(t)] = (\Delta x)^2 j$.

The law of total probability indicates that the chance that the particle lies at the point $x = k\Delta x$ at time $t + \Delta t$, i.e., $X(t + \Delta t) = k\Delta x$, can be decomposed into two parts: the chance that the particle lies at the point $(k-1)\Delta x = x - \Delta x$ at time t times the chance that it moves one step to the right between t and $t + \Delta t$, plus the chance that the particle lies at the point $(k+1)\Delta x = x + \Delta x$ at time t times the chance that it moves one step to the left between t and $t + \Delta t$. This is

$$f_X(t+\Delta t)(x) = \left(\frac{1}{2}\right) f_X(t)(x - \Delta x) + \left(\frac{1}{2}\right) f_X(t)(x + \Delta x) \quad (13)$$

This difference equation governs motion of the particle, subject to the initial condition

$$f_X(0)(x) = \begin{cases} 1 & x = 0 \\ 0 & x \neq 0 \end{cases} \quad (14)$$

Planck and Fokker subtracted $f_X(t)(x)$ from both sides of Eq. (13) then divided the left side of the result by Δt and the right side by a scaled version of Δt to obtain

$$\frac{f_X(t+\Delta t)(x) - f_X(t)(x)}{\Delta t} = \frac{1}{2} \frac{(\Delta x)^2}{\Delta t} \left(\frac{\left(\frac{1}{2}\right)f_X(t)(x-\Delta x) - f_X(t)(x) + \left(\frac{1}{2}\right)f_X(t)(x+\Delta x)}{(\Delta x)^2} \right) \quad (15)$$

Next, they let $\frac{(\Delta x)^2}{2\Delta t} = D$, a diffusion coefficient, and took the limit at $\Delta t \rightarrow 0$ to obtain a continuous equation governing the PDF of the displacement response.

$$\frac{\partial f_X}{\partial t} = D \frac{\partial^2 f_X}{\partial x^2} \quad t \geq 0, -\infty < x < \infty \quad (16)$$

with initial condition $f_X(0)(x) = \delta(x), -\infty < x < \infty$. This is, of course, identical to the equation developed by Einstein, except that the present mathematical development has its origins in a scenario remote from physical diffusion.

Planck and Fokker could have stopped at this point and simply solved Eq. (16) for the PDF governing response, but instead they noted that the probability distribution of the response is already given, in its discrete form, by Eq. (12). The DeMoivre-Laplace Theorem (see Papoulis, 2002) holds that as the number of trials, j in Eq. (12), increases the binomial distribution approaches a normal distribution with the same mean and variance. Note that the mean and variance of $X(t)$ were shown to be $E[X(t)] = 0$ and $V[X(t)] = (\Delta x)^2 j$, therefore, because of the definition given in the previous paragraph, $(\Delta x)^2 = 2(\Delta t)D$, and the variance approaches $2Dt$. The PDF of the response is the same as that given in Eq. (6), but the result was derived from a completely different perspective. Among other things, it is interesting to note here that the random response is the accumulated result of numerous transitions, none of which is governed by a normal distribution.

This discrete formulation was extended to cover several other cases including the one in which the particle experiences a drift caused by a constant force superimposed over the oscillatory force, and the one in which the particle is harmonically bound. A summary of much of the early work is given by Kac (1947).

Many special cases of the Fokker-Planck equation (written in its fully general form in Lin, 1967) have been developed over the years, and work in this area continues. Kolmogorov (1931) is credited with having greatly generalized the ideas of the Fokker-Planck equation. (Gnedenko, 1997, states that in the 1931 paper cited above, Kolmogorov started the “construction of the general theory of stochastic processes.”) Also, among many other things, Wang and Uhlenbeck (1945) systematized the development of a Fokker-Planck equation for a system governed by specific equations.

3.0 The Development of Spectral Density

It is unlikely that the mathematical theory of random vibrations of mechanical systems would have become as popular and practically useful as it is today, had it not been for the development of spectral density by Norbert Wiener (1930) and those who preceded him. Spectral density (also known as mean square spectral density, power spectral density, and by other descriptive names) is the fundamental characteristic of a weakly stationary random process. It describes the distribution in the frequency domain of the mean square signal content of a stationary random process.

Here is what the terms in the previous paragraph mean, qualitatively, and why spectral density is essential to random vibration analysis. First, an alternate way of thinking about random processes (alternate to the sequence-of-random-variables description, provided in the previous section) is to consider a random process to be an infinite ensemble (collection) of signals. Frequently, almost all the signals in the ensemble look alike, in a general sense, but, in detail, they all differ. For example, finite duration segments of two signals from the ensemble of a single random process are shown in Figure 7. They look alike in their general random character, but they differ in their details. When practically all of the signals in the ensemble of a random process are in a random steady state from the infinite past to the infinite future, the random process is stationary. (Precisely what is meant by the phrase “random steady state” will be described in a moment. Of course, no real signal maintains a steady state from the infinite past to the infinite future. In a practical sense, if signals from a random source maintain a steady state for a “long time,” then the source is considered stationary.) The notation $\{X(t), -\infty < t < \infty\}$ indicates a random process defined at times in $(-\infty, \infty)$. With the current interpretation this might be thought of as a collection of signals $x_j(t), j = 1, 2, \dots, -\infty < t < \infty$. Each signal $x_j(t)$ is a realization of the random process $\{X(t), -\infty < t < \infty\}$.

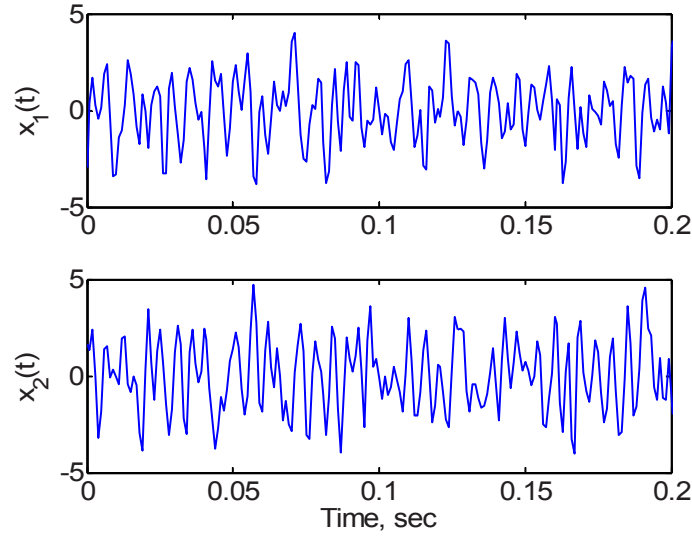


Figure 7. Segments of two realizations from a single random process.

Second, the stock in trade of structural dynamic analysts and experimentalists is frequency domain analysis of structures and their characteristics via Fourier expansion. Frequency domain analysis often reveals the modal characteristics of structural behavior. The modal frequencies of a mechanical system are the frequencies at which motion is amplified in structural response, and the mode shapes of the system are the shapes the mechanical system naturally assumes when it responds at specific modal frequencies. For any excitation, it is useful to know the frequencies of substantial signal content because this information indicates the frequencies where substantial response might be excited in a structure. For any response, it is useful to know the frequencies of substantial signal content because these frequencies indicate where the excitation has at least some signal content, and the response amplified the input signal content. When the input and response are finite duration and deterministic, direct Fourier analysis can be used to answer these questions about excitation and response signal content. But when a source is a random process the ensemble of the random process contains an infinite collection of signals, and further, each one has infinite duration. Infinite duration signals do not have Fourier transforms in a traditional sense. Spectral density considers signal content in a mean square sense, and in so doing enables characterization of the signal content of an infinite collection of random process realizations, each of which has infinite duration.

Wiener started the process of defining the spectral density (in strict terminology, the autospectral density, for reasons that will be seen below) by defining a related function – the autocorrelation function. It is

$$R_{XX}(\tau) = E[X(t)X(t+\tau)] = \lim_{T \rightarrow \infty} \frac{1}{2T} \int_{-T}^T x(t)x(t+\tau)dt \quad -\infty < \tau < \infty \quad (17)$$

where $x(t)$, $-\infty < t < \infty$, is a realization of the random process $\{X(t), -\infty < t < \infty\}$. Equation (17) defines the autocorrelation function in terms of a temporal average. With this definition, it is assumed that the random process realization chosen to perform the time averaging computation in Eq. (17) is representative of practically all the other realizations in the random process. (When one arbitrarily chosen stationary random process realization can be used in the above formula to define a valid autocorrelation function, the random process is said to be ergodic. See Lin, 1967.) Wiener could have defined the autocorrelation function in terms of an average over all j of products like $x_j(t)x_j(t+\tau)$ across the ensemble of the random process, but did not do so. An assertion of the formula in Eq. (17) is that the average presented is a function of τ only. When this assertion is correct for the random process, and when the mean of the random process is constant over all time, then the random process is weakly stationary, and maintains the random steady state mentioned above. (The term “weak” used to describe stationarity refers to a random steady state that is characterized exclusively in terms of the mean and autocorrelation functions.) The function defined in Eq. (17) is referred to as the autocorrelation function because it defines the correlation of one random variable in the process, $X(t)$, to another random variable in the same random process, $X(t+\tau)$. Finally, the autocorrelation function is a symmetric function in τ , and it can be shown to be non-negative definite.

When a random process is weakly stationary the spectral density exists; it was defined by Wiener as the Fourier transform of the autocorrelation function.

$$S_{XX}(\omega) = \frac{1}{2\pi} \int_{-\infty}^{\infty} R_{XX}(\tau) e^{-i\omega\tau} d\tau \quad -\infty < \omega < \infty \quad (18)$$

Because of the characteristics of the autocorrelation function, mentioned above, the spectral density is symmetric and non-negative. Equation (18) is called a two-sided spectral density because it is defined for negative as well as positive frequencies. (As mentioned earlier, negative frequencies are to be interpreted in the sense that harmonic functions are defined for negative arguments.) Among many other things, Wiener showed that the autocorrelation function can be recovered from the spectral density via inverse Fourier transformation.

$$R_{XX}(\tau) = \int_{-\infty}^{\infty} S_{XX}(\omega) e^{i\omega\tau} d\omega \quad -\infty < \tau < \infty \quad (19)$$

Because, from Eq. (17), $R_{XX}(\tau) = E[X(t)X(t+\tau)]$, the mean square of the random process is the constant $\sigma_X^2 = R_{XX}(0)$. Therefore, evaluation of Eq. (19) at $\tau = 0$ gives the mean square of the random process $\{X(t), -\infty < t < \infty\}$. This is

$$R_{XX}(0) = \int_{-\infty}^{\infty} S_{XX}(\omega) d\omega \quad (20)$$

As Wiener pointed out, Eq. (20) shows that the mean square of a random process is the area under the spectral density curve, and it is clear that the integral of the spectral density over a portion of the frequency axis yields the part of the mean square of the random process due to contributions over that frequency range.

The function defined in Eq. (18) is, in strict terms, an autospectral density because it is the Fourier transform of the autocorrelation function, and because it is the frequency domain characterization of the mean square behavior of a random process.

In his 1930 paper defining spectral density, Wiener attributed the fundamental idea underlying spectral density to Schuster (1899, 1900, 1905). He wrote: "The germs of the generalized harmonic analysis of this paper are already in the work of Schuster, but only the germs. To make the Schuster theory assume a form suitable for extension and generalization, a radical recasting is necessary."

However, some of the ideas underlying spectral density preceded Schuster's 1899 paper. Rayleigh (1889) introduced the idea that a random process has an autocorrelation, and, in a footnote, he gave an excellent example of how and why it exists. He did not define the autocorrelation via an equation, though. In the same paper he showed how an energy spectrum can be defined as a frequency domain description of a stationary random process. He recognized the difficulty in writing the Fourier transform of a signal that extends from minus infinity to infinity, and he multiplied the time-domain signal by a symmetric, exponential lag weighting to make the Fourier transform well-defined. He did not hint at the possibility that the autocorrelation might be related to the spectral density, but he certainly introduced the idea that a spectral representation can be developed for a stationary source.

Schuster wrote another paper (1894) that discusses the idea of a spectral representation for random signals. His topic was the characterization of light, but, as Rayleigh had done earlier, he suggested that random sources can be described in terms of their energy spectra, and that energy over limited ranges of frequency represent the content of signal components. In his 1894 paper, Schuster appears not to have accommodated the problem of growth of the Fourier transform magnitude of a stationary signal as greater duration signals are represented. But in a later paper Schuster (1897) indicated that the modulus of the Fourier transform of a segment of stationary random signal taken on the interval $(t, t+T)$ increases as the square root of T when the signal has no periodic components. Still, he did not apply the correction in his spectral characterization in the 1897 paper. It was not until later that Schuster (1905) inserted the correction into his definition of the *periodogram*. The expression he developed did not take the limit as $T \rightarrow \infty$, but it is still the earliest definition of a quantity that is very similar to the spectral density in use today.

The first mathematical definition of the autocorrelation function appears to have been written by Taylor (1920). In a paper that considered the diffusion of heat in fluids in turbulent motion, he defined a random process that proceeds in discrete, temporal steps. He defined the correlation between random variables in the process at adjacent steps and inferred a correlation structure for the process.

To understand in a practical and intuitive sense the meaning of spectral density, consider the schematic of Figure 8. It indicates that every real signal, like the one shown at left in the figure, can be filtered into a finite number of components. A sequence of idealized filter gain functions is shown in the second column. The filters are non-overlapping, band-pass, equal width, and vary from low to high frequency, top to bottom. Some components of the signal at left are shown by the third column of signals. The signals vary from the lowest frequency component at the top to the highest frequency component at the bottom. The mean square value of each signal can be estimated by squaring a long-duration segment of each component and computing the average. The mean square values of the signal components are plotted as a function of band-pass filter center frequencies in the fourth column of figures. Finally, the mean square values of the signal components are divided by the effective filter bandwidths to obtain the estimate of spectral density of the random source from which the measured signal arose. Of course, the units of the spectral density are the units of the measured signal squared per unit of frequency (usually Hz). This is how spectral density is related to random source. The explanation is meant only to be a rough description of the meaning of spectral density. Issues like the filter type, shape and widths, and the measured signal duration are all important. Even so, a physical implementation of the process described here was used to estimate the spectral density of measured sources into the 1960's and 1970's. Miles (1954) mentions the need to obtain a spectral density estimate from experimentally measured signals, in order to perform random vibration analyses, and suggests a method like the one outlined here. A paper by Rona (1958) describes the process, shown graphically, here, for estimation of spectral density of mechanical system motions.

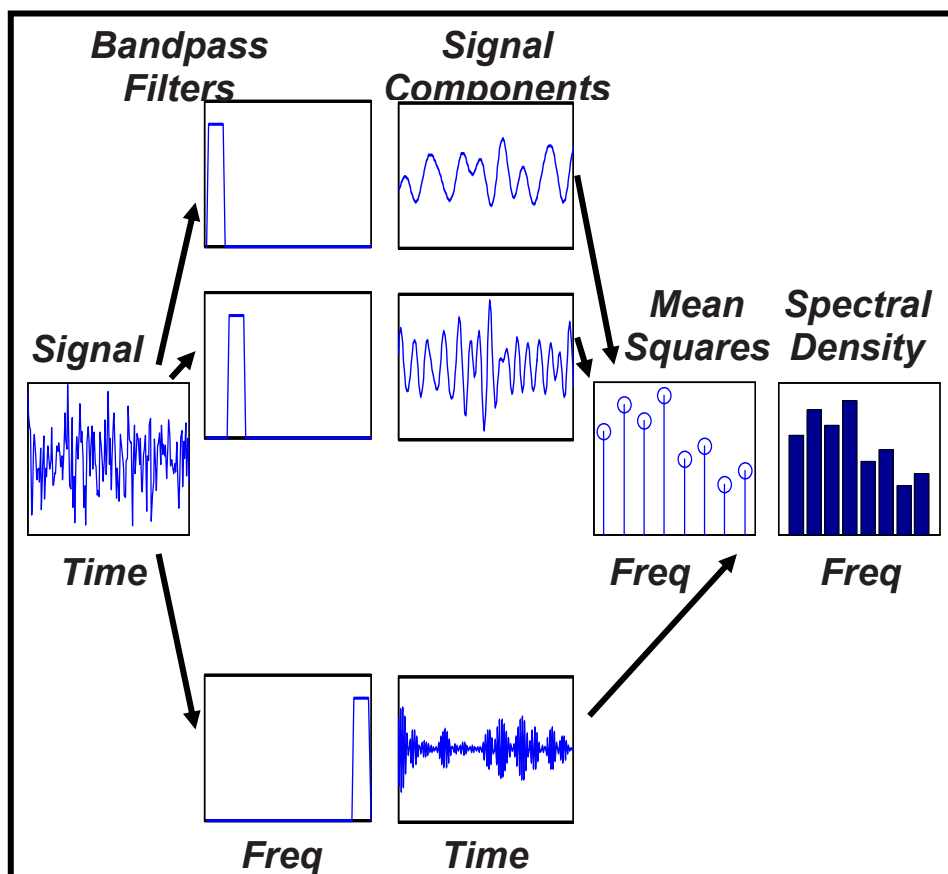


Figure 8. Schematic describing the meaning of spectral density.

A random process known as an ideal white noise is one whose two-sided spectral density is finite and constant on $(-\infty, \infty)$. Indeed, the excitation characteristics described mathematically by Uhlenbeck and Ornstein (1930) imply a white noise excitation, though not in those words. Even prior to that description, the assumptions made by Einstein (1905) in his early development of a Fokker-Planck equation imply an assumption of white noise-type excitation.

It was stated following Eq. (20) that the area under the spectral density curve is the mean square of a zero-mean random process; therefore, an ideal white noise has infinite mean square. In spite of this, the ideal white noise model is important because some measures of the mean square response of stable linear systems to white noise are finite. For example, the mean square displacement and velocity responses of force-excited, fixed-base, linear structures to a white noise excitation are finite. For this reason, the white noise excitation model is used even today to perform relatively simple, yet accurate, analyses. Part of modern analyses is the development of the relation between the spectral density of a random excitation and the spectral density of the response it excites. In view of this, an understanding of the history of random vibrations requires knowledge of the origins of input/output spectral density relations.

Wiener pursued this topic in his 1930 paper. He did so in a far-ranging section entitled “Spectra and Integration in Function Space.” Without writing the formula, he stated the relation that is most fundamental to the modern practice of random vibrations of linear mechanical systems. He stated the result for a white noise excitation in three ways; here are two of them. First, he wrote, “the spectral density of [random linear system response] is half the square of the modulus of the Fourier transform of [the system impulse response function].” Later, “if a linear resonator is stimulated by a uniformly haphazard sequence of impulses, each frequency responds with an amplitude proportional to that which it would have if stimulated by an impulse of that frequency and of unit energy.” The excitation he is referring to is a type of white noise. (See discussions of shot noise in Papoulis, 2002.) The Fourier transform of the system impulse response function is the system frequency response function (FRF). The *FRF of a linear system* is the coefficient of proportionality relating magnitude and phase of a harmonic response component to magnitude and phase of a harmonic input component. That is, $H(\omega)$ is the FRF in the relation

$$X(\omega) = H(\omega)Q(\omega) \quad -\infty < \omega < \infty \quad (21)$$

where $Q(\omega) = \int_{-\infty}^{\infty} q(t)e^{-i\omega t} dt, -\infty < \omega < \infty$, is the Fourier transform of a system excitation, and

$X(\omega) = \int_{-\infty}^{\infty} x(t)e^{-i\omega t} dt, -\infty < \omega < \infty$, is the Fourier transform of a linear system response.

When $\{W(t), -\infty < t < \infty\}$ is a zero-mean, ideal white noise random process with spectral density $S_{WW}(\omega) = S_{WW} = \text{constant}, -\infty < \omega < \infty$, Wiener’s statement is

$$S_{XX}(\omega) = |H(\omega)|^2 S_{WW} \quad -\infty < \omega < \infty \quad (22)$$

where $S_{XX}(\omega), -\infty < \omega < \infty$, is the spectral density of the response random process $\{X(t), -\infty < t < \infty\}$. For example, when a linear, single-degree-of-freedom (SDF) system with mass, $m = 1.0 \text{ lb-sec}^2/\text{in}$, damping factor, $\zeta = 0.05$, and natural frequency $\omega_n = 2\pi \text{ rad/sec}$, is excited by a zero-mean, ideal white noise with spectral density $S_{WW} = 1 \text{ lb}^2/\text{Hz}$, the displacement response spectral density is

$$S_{XX}(\omega) = \frac{1}{m^2 \left((\omega_n^2 - \omega^2)^2 + (2\zeta\omega_n\omega)^2 \right)} = \frac{1}{\left(((2\pi)^2 - \omega^2)^2 + (0.1(2\pi)\omega)^2 \right)} \quad -\infty < \omega < \infty \quad (23)$$

because

$$H(\omega) = \frac{1}{m(\omega_n^2 - \omega^2 + 2i\zeta\omega_n\omega)} \quad -\infty < \omega < \infty \quad (24)$$

This response spectral density is graphed in Figure 9.

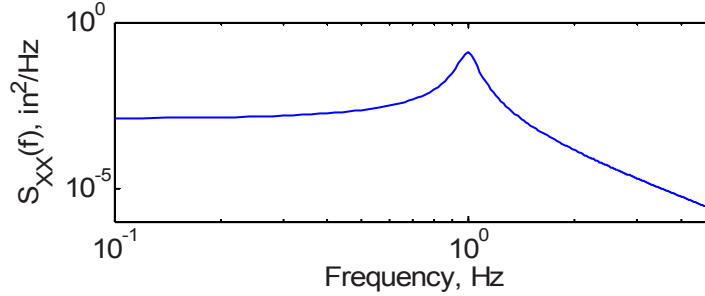


Figure 9. Spectral density of the response of an SDF system.

It appears that Carson (1925) had previously defined the input/output relation for spectral densities in work Wiener was not aware of. Carson was motivated by a need to describe the effects of noise on an electrical communications system. He defined what he called the *energy spectrum of random interference*, as the modulus squared of the Fourier transform of a finite duration segment of a random process realization, divided by the duration of the segment. This quantity is essentially the same as Shuster's (1905) definition of the periodogram, and, as Schuster, Carson failed to take the limit as $T \rightarrow \infty$. But Carson wrote the expression for the mean square response of a linear system to the random excitation in terms of the energy spectrum. Essentially, he wrote Eq. (22), but he wrote it in terms of the linear system impedance, the inverse of the system FRF. A few years later, Carson (1931) modified the definition of what he now called the *energy-frequency spectrum* by taking the limit as $T \rightarrow \infty$. He re-wrote the input/output spectral density relations for a linear system in the 1931 paper, and, in addition, proposed several shot noise-type models (see Lin, 1967) for the electrical noise.

Wiener went much further in his 1930 paper and defined what is now known as the cross-spectral density. He called it coherency, and used it to define frequency domain relations among random processes in a quadratic mean sense. He developed the cross-spectral density in terms of cross-correlations between random processes. Consider a collection of M zero-mean, stationary, ergodic random processes $\{X_m(t), -\infty < t < \infty\}, m = 1, \dots, M$. Each random process consists of an infinite collection of realizations, and one of the realizations in any of the random processes is representative of practically all the other realizations in the random process. The signals $x_m(t), m = 1, \dots, M, -\infty < t < \infty$, are realizations, one from each of the M random processes, respectively. He defined a function, one that we now call the cross-correlation function between a pair of random processes $\{X_j(t), -\infty < t < \infty\}, j \in (1, \dots, M)$, and $\{X_k(t), -\infty < t < \infty\}, k \in (1, \dots, M)$, as

$$R_{X_j X_k}(\tau) = \lim_{T \rightarrow \infty} \frac{1}{2T} \int_{-T}^T x_j(t) x_k(t + \tau) dt \quad j, k \in (1, 2, \dots, M), -\infty < \tau < \infty \quad (25)$$

Normally we consider $j \neq k$. Wiener defined the cross-spectral density as the Fourier transform of the cross-correlation function.

$$S_{X_j X_k}(\omega) = \frac{1}{2\pi} \int_{-\infty}^{\infty} R_{X_j X_k}(\tau) e^{-i\omega\tau} d\tau \quad j, k \in (1, 2, \dots, M), -\infty < \omega < \infty \quad (26)$$

He described many of the characteristics of the cross-spectral density, and noted that the matrix of all the cross-spectral densities of the random processes $\{X_m(t), -\infty < t < \infty\}, m = 1, \dots, M$, namely,

$$\mathbf{S}_{\mathbf{X}\mathbf{X}}(\omega) = \begin{bmatrix} S_{X_1X_1}(\omega) & S_{X_1X_2}(\omega) & \cdots & S_{X_1X_M}(\omega) \\ S_{X_2X_1}(\omega) & S_{X_2X_2}(\omega) & \cdots & S_{X_2X_M}(\omega) \\ \vdots & \vdots & \ddots & \vdots \\ S_{X_MX_1}(\omega) & S_{X_MX_2}(\omega) & \cdots & S_{X_MX_M}(\omega) \end{bmatrix} \quad -\infty < \omega < \infty \quad (27)$$

“determines the spectra of all possible linear combinations of [the random processes].”

He noted that the cross-spectral density matrix is Hermetian (i.e., $S_{X_jX_k}(\omega) = S_{X_kX_j}^*(\omega)$), and that every cross-spectral density matrix can be diagonalized. He pointed out that this makes it easy to generate correlated random processes starting with completely uncorrelated random processes – a fact that has been rediscovered many times. This is important, for example, in the laboratory-experimental generation of coherent, stationary random signals for multi-axis testing. (See Smallwood, 1982a, and 1982b.)

The use of the cross-spectral density to define the coefficient of coherency is useful and interesting, but the most important use for the cross-spectral density involves the estimation of the FRF. It appears that this is one very important application that Wiener did not explicitly include in his 1930 paper. The frequency domain input/output relation for a linear system, Eq. (21), above, can be used to develop a relation among the excitation autospectral density, $S_{QQ}(\omega)$, $-\infty < \omega < \infty$, the cross-spectral density between the response and the excitation, $S_{XQ}(\omega)$, $-\infty < \omega < \infty$, and the FRF, $H(\omega)$, $-\infty < \omega < \infty$, of the linear system.

$$S_{XQ}(\omega) = H(\omega)S_{QQ}(\omega) \quad -\infty < \omega < \infty \quad (28)$$

When the auto- and cross-spectral densities in the equation are estimated, the FRF can be inferred. Wiener did suggest methods for estimating auto- and cross-spectral densities, though they are not the approaches used in the current digital age. Details on this sort of estimation can be obtained in any text that discusses random signal analysis, for example, Bendat and Piersol, 2000, or Wirsching, Paez, and Ortiz, 1995.

It would be inappropriate to end this section without noting that the spectral density was independently defined in 1934 by Khintchine. He also defined the autospectral density as in Eq. (18), and in honor of his work, and, of course, that of Wiener, Eqs. (18) and (19) are usually known as the Wiener-Khintchine relations. In fact, many papers and texts, especially those written in Russia, acknowledge Khintchine as the person who developed spectral density.

The history presented here is, by no means, comprehensive. The texts listed at the end of the Introduction and a paper by Paez (2006) include much more detail.

4.0 The Popularization of Random Vibration of Mechanical Systems

The modern field of random vibrations of mechanical systems and probabilistic structural dynamics, in general, has gained importance as the awareness that real mechanical environments are stochastic has broadened. Today random vibration analyses are performed frequently and in practical settings, usually within the framework of a commercial finite element code. Commercial finite element codes include, in general, rather limited capabilities to perform probabilistic structural dynamic analyses, at least without much pre- and post-processing. The most common analyses are those wherein the auto- (and, perhaps, cross-) spectral densities of stationary excitation random processes are specified, and response auto- and cross-spectral densities are computed. Some of the developments that led to the formulas that have been implemented are summarized below.

Steven Crandall is normally credited as the person (in the United States) who made the topic of random vibrations of mechanical systems accessible to practicing engineers. He organized a summer program at the Massachusetts Institute of Technology devoted to presentations on the fundamental topics in random vibrations. The presentations are published in Crandall (1958), and cover analysis of and design for random vibrations, testing, data analysis, spectral density estimation, and other topics. Chapters 1, 2, and 4, in the proceedings present an introduction to random vibrations on a most elementary level. Because of their historical significance, and, in particular, the historical significance of Chapter 4, those three chapters will be summarized first. Next, some papers whose publication actually preceded the MIT summer program will be

discussed. These papers contain some of the earliest modern efforts to develop methods for the analysis of random vibration of mechanical systems. Then we will return briefly to one of the papers from the proceedings of the summer program.

The first chapter in the program proceedings by Crandall (1958a), entitled “Mechanical Vibrations with Deterministic Excitations,” develops, very briefly, the ideas of impulse response function and frequency response function, and it uses these to write expressions for the responses of linear systems in terms of the convolution integral and its Fourier transform. The time-domain expression for scalar, transient response, $x(t), t \geq 0$, is

$$x(t) = \int_0^t q(\tau)h(t-\tau)d\tau \quad t \geq 0 \quad (29)$$

where $q(t), t \geq 0$, is the scalar excitation to the system, and $h(t), t \geq 0$, is the system unit impulse response function. Equation (29) is the same as the convolution integral of Eq. (9). When there is a single excitation and a single response, then the functions $x(t), q(t), h(t)$ are scalar. The equation can be written for any measure of response, for example, displacement, velocity or acceleration. The excitation can be any quantity of interest, for example, force or imposed motion. The impulse response function is the response of the system at the location where $x(t), t \geq 0$, is measured to a unit-impulse excitation (a unit delta function) applied at the location where $q(t), t \geq 0$, is applied. Crandall’s development and explanation of Eq. (29) was very intuitive.

When the excitation to the system is applied starting at time less than zero, perhaps at $t \rightarrow (-\infty)$, then the lower limit on the integral in Eq. (29) can be changed to $(-\infty)$ and the upper limit can be changed to ∞ . The Fourier transform of the resulting expression can be taken to obtain the frequency-domain equivalent to the convolution integral. It is

$$X(\omega) = H(\omega)Q(\omega) \quad -\infty < \omega < \infty \quad (30)$$

where $X(\omega), -\infty < \omega < \infty$, $H(\omega), -\infty < \omega < \infty$, and $Q(\omega), -\infty < \omega < \infty$, are, respectively, the Fourier transforms of $x(t), -\infty < t < \infty$, $h(t), t \geq 0$, and $q(t), -\infty < t < \infty$, defined

$$\begin{aligned} X(\omega) &= \int_{-\infty}^{\infty} x(t)e^{-i\omega t} dt \quad -\infty < \omega < \infty \\ H(\omega) &= \int_0^{\infty} h(t)e^{-i\omega t} dt \quad -\infty < \omega < \infty \\ Q(\omega) &= \int_{-\infty}^{\infty} q(t)e^{-i\omega t} dt \quad -\infty < \omega < \infty \end{aligned} \quad (31)$$

The function $H(\omega), -\infty < \omega < \infty$, is called the *frequency response function* (FRF) of the system, and it is the fundamental descriptor of linear system behavior in the frequency domain. It is the factor by which a harmonic excitation can be multiplied to obtain the harmonic response of a linear system at a single point. Its magnitude is the scale factor between input and response amplitudes, and its phase is the phase difference between input and response. Crandall’s derivation of Eq. (30) was also very intuitive. He developed Eqs. (29) and (30) because they form the basis for the fundamental input/output relations for linear random vibrations.

The second chapter in the program proceedings was written by Siebert (1958), and is entitled “The Description of Random Processes.” It provides an introductory discussion of the ideas of probability, random processes, moments, correlation functions and spectral density. It seeks to establish a motivation for describing structural dynamic excitations and responses as random processes.

Chapter 4 in Crandall (1958b), entitled “Statistical Properties of Response to Random Vibration,” starts with the expression of linear system response in terms of the convolution integral and its Fourier transform, Eqs. (29) and (30). He proceeds to develop the single-input/single-output relations for randomly excited linear systems in terms of integrals involving

autocorrelation and impulse response functions, and autospectral densities and frequency response functions. Specifically, he derived the expression for the response autocorrelation function $R_{XX}(\tau)$, $-\infty < \tau < \infty$, of the scalar, stationary random process $\{X(t), -\infty < t < \infty\}$.

$$R_{XX}(\tau) = \int_{-\infty}^{\infty} d\tau_1 \int_{-\infty}^{\infty} d\tau_2 h(\tau_1) h(\tau_2) R_{QQ}(\tau + \tau_2 - \tau_1) \quad -\infty < \tau < \infty \quad (32)$$

where $R_{QQ}(\tau)$, $-\infty < \tau < \infty$, is the autocorrelation function of the stationary excitation random process $\{Q(t), -\infty < t < \infty\}$. Intuitive interpretation of Eq. (32) is difficult, except, perhaps, to note that $R_{XX}(0) = \sigma_X^2$, is the mean square of the response random process when the means of the excitation and response are zero.

In the same chapter, Crandall also derived the expression for response spectral density $S_{XX}(\omega)$, $-\infty < \omega < \infty$, of the stationary random process $\{X(t), -\infty < t < \infty\}$. It is obtained through Fourier transformation of Eq. (32).

$$S_{XX}(\omega) = |H(\omega)|^2 S_{QQ}(\omega) \quad -\infty < \omega < \infty \quad (33)$$

where $S_{QQ}(\omega)$, $-\infty < \omega < \infty$, is the autospectral density of the stationary, excitation random process. Equation (33) describes the distribution of the mean square of the response of a randomly excited system in the frequency domain. It is much easier to visualize than Eq. (32), and is, Crandall said, the “central result” of random vibrations. Using the inverse Fourier transform, Crandall next wrote the expression for the response autocorrelation function as

$$R_{XX}(\tau) = \int_{-\infty}^{\infty} |H(\omega)|^2 S_{QQ}(\omega) e^{i\omega\tau} d\omega \quad -\infty < \tau < \infty \quad (34)$$

When evaluated at $\tau = 0$, it shows that the response mean square is strongly influenced by structural system modes, the frequencies where the greatest amplifications occur in the frequency response function, $H(\omega)$, $-\infty < \omega < \infty$, and the mean square distribution of signal content in the stationary excitation. The expression is

$$R_{XX}(0) = \sigma_X^2 = \int_{-\infty}^{\infty} |H(\omega)|^2 S_{QQ}(\omega) d\omega \quad (35)$$

Following these developments, Crandall discussed the probability distribution of response in the Gaussian excitation case. He developed expressions for the response of a single-degree-of-freedom (SDF) system to ideal white noise, and he discussed how these results might be applied in the practical case where the excitation is not ideal white, but only relatively constant in the vicinity of the natural frequency of a lightly damped structure.

The developments of researchers who investigated the random vibration responses of linear systems, several years before Crandall’s workshop, are, in some cases, much more detailed and complex. Some of those developments will be summarized in a moment. But this seems to indicate that Crandall sought to keep his developments and results simple and clear, and he certainly accomplished that goal.

The result in Eq. (33) is, in a practical sense, the most important result in linear random vibrations because it is the formula applied in the vast majority of practical analyses. Indeed, practitioners seeking to characterize the random vibration response of systems which they are willing to approximate as linear use the formulas in the following way. Consider a mechanical system that has been either experimentally or analytically evaluated, and whose frequency response function relating acceleration response at one location to force excitation at another location has the modulus shown in [Figure 10](#). The system motion may involve multiple modes, but the displayed FRF indicates that three of them are dominant – the ones at 821, 1381, and 1706 Hz. Suppose that an analyst or designer wishes to characterize the response motion via its spectral density to the excitation whose spectral density is specified by the curve of [Figure 11](#). She or he would compute the product of the curves in [Figures 10](#) and [11](#) to obtain the approximate spectral density of the response shown in [Figure 12](#). Many features of the

response character can be inferred from its spectral density, but perhaps most important, is the fact that its RMS value is approximately 22 g. (This is the square root of the area under the response spectral density curve.) The RMS value of the excitation is approximately 181 lb. As Crandall explained, if the acceleration excitation is normally distributed with zero mean, then the response at each time is a normally distributed random variable with zero mean and standard deviation 22 g.

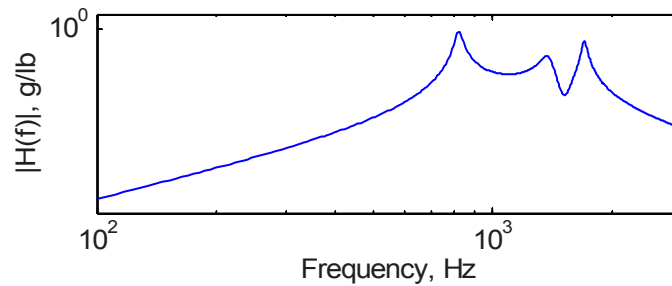


Figure 10. Modulus of the FRF of acceleration response on a system to a force excitation.

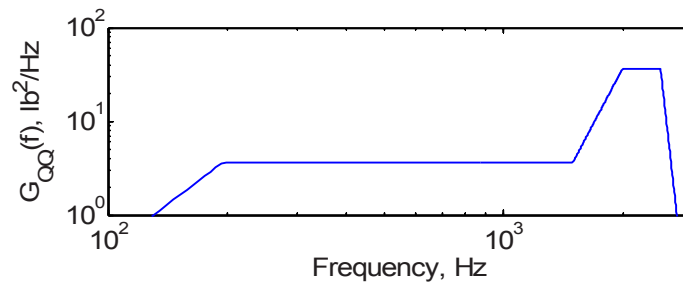


Figure 11. Spectral density of the system excitation.

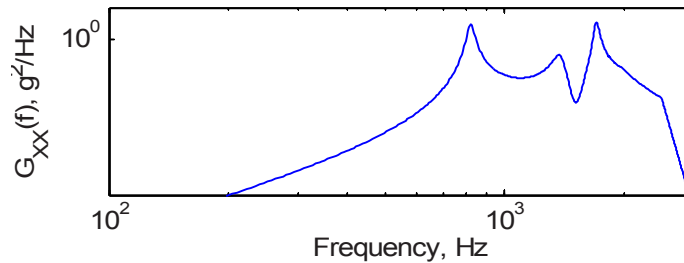


Figure 12. Spectral density of the acceleration response of the system.

Because Crandall's is one of the earliest popular works on the subject of random vibrations of mechanical systems, it is important to note the references he provides as the sources for his work. He cites Davenport and Root (1956) for ideas in random processes, but more importantly, he cites Lanning and Battin (1956) for ideas in the response of linear systems to random excitation. Their book arose from a set of lecture notes on random processes in the field of automatic control, first offered at MIT in 1951. They devote an entire chapter to the subject of "Analysis of Effects of Time-Invariant Linear Systems on Stationary Random Processes." In that chapter, they express the autocorrelation function and autospectral density of the response of a linear system to a stationary random excitation, and this is apparently the source of Crandall's corresponding expressions. They also refer to the idea of filtering of random processes and mention the relation of that activity to the analysis of system response. However, Lanning and Battin do not explicitly cite the source for their approach to the development of the input/output spectral density relation for randomly excited linear systems.

The reference to filtering by Lanning and Battin is interesting in view of the fact that Siebert (1958), in the chapter mentioned above, also briefly develops the input/output spectral density relation for randomly excited linear systems, and he references an early source for that development as James, Nichols and Phillips (1947). Their text is written on the subject of servomechanisms. The input/output spectral density relations are developed in a chapter entitled "Statistical Properties of Time-Variable Data." It was written by Phillips (1947) with reference to the input/output relations for servomechanisms, and with much reference to the terminology of signal filtering. Though the equations relating the spectral density of a stationary, white noise random input to the spectral density of the output of a linear system had appeared several years earlier, no reference is made by Phillips to any other derivation.

Another early development of the input/output spectral density relation for linear systems excited by ideal white noise is the one given by Wang and Uhlenbeck (1945). That paper was not written with reference to mechanical systems in particular, but with reference to linear systems, in general. In it, the authors focus most of their attention on finding the probability distributions of the solutions to white noise excited, first and second order linear differential equations, and systems of second order linear equations using the Fokker-Planck equation approach. However, they did write the input/output spectral density relation for a first order linear system and for a second order linear system excited by white noise. The first order linear system they considered is a massless particle connected to a fixed boundary via a spring and damper, and excited by white noise. They did not write the relations in a general way using FRF or impedance, and they did not discuss the implications of the expressions for interpreting signal content of the response mean square. Nevertheless, the relations are presented, perhaps, for the first time since Wiener wrote them. Whether or not they independently rediscovered the input/output spectral density relation is not clear, but their footnotes and comments on other parts of the work of Wiener appear not to credit him with the idea.

Many papers on the subject of random vibrations of mechanical systems were written prior to the publication of the proceedings of Crandall's MIT summer program. Among those was a paper by Y. C. Fung (1953), though it was not referenced by Crandall. It is a development that appears in the mechanical systems literature of the input/output spectral density relation for randomly excited linear systems. His paper on the structural dynamics of aeronautical systems used the relation between the spectral density of an excitation force and the spectral density of a system response to express the mean square value of the response. (Instead of using the FRF, he used system impedance.) The equation is

$$\sigma_X^2 = \int_{-\infty}^{\infty} \frac{S_{QQ}(\omega)}{|Z(\omega)|^2} d\omega \quad (36)$$

where $Z(\omega) = 1/H(\omega)$, $-\infty < \omega < \infty$, is the impedance of a linear system. The complex impedance of a linear system at a given frequency is the quantity by which a harmonic component of the input must be divided in order to obtain the harmonic component of the response. Fung did not separately express the spectral density input/output relation, as in Eq. (33), but he clearly opened the door to future developments in the area. Further, though he only wrote the relation for a simple system, he noted "The preceding relation holds for a much wider class of dynamic systems than that represented by" the equation for an SDF system. "It holds for higher order linear differential equations, linear integral equations, or linear integral-differential equations under mild restrictions." Equation (36) appears to be the first occurrence of the formula in a paper on structural dynamics. In the paper Fung referenced Liepmann (1952) who applied random process concepts to the study of aeronautical buffeting.

Fung used the work of Housner (1947) to express an envelope on the response of a structural dynamic system. Housner's work is interesting in its own right because he considers earthquakes to be sequences of random pulses that are time-varying. In his paper Housner developed a means for analyzing earthquakes based on averages of their Fourier transform magnitudes. Specifically, he showed that the sample mean of the square of the Fourier transform modulus (the estimate of spectral density, when averaged) of ten earthquakes is nearly constant in the frequency range [0.5,5] Hz. However, he did not generalize the idea, or speculate on its meaning relative to limiting arguments on the number of signals averaged. Nor did Housner refer to the quantity he was estimating as a spectral density.

Fung's 1953 paper led to another contribution (Fung, 1955). In the latter paper he developed – in an extraordinarily direct and intuitive manner – results far beyond any that had previously been presented, and that were not used until much later. The objective of his main development was to obtain the formula for the expected value of the n^{th} power of the nonstationary random response of a linear structure given information on the character of a nonstationary random excitation. He accomplished this, and much more, in the paper. The paper covered many other subjects useful in random vibrations including the simplification of random vibration problems using normal mode analysis, analysis of bending moments, and applications to structural design, including extreme value considerations.

The subject of structural fatigue was and remains one of great importance in structural dynamics. Among many other sources, it is strongly motivated by the response of structural components in the presence of a rapidly varying pressure field of the sort that arises in connection with aerodynamic turbulence. Of course, developments were starting to take place in the field of jet propulsion during the early to mid 1950's. Miles (1954) wrote perhaps the first paper that considered the subject of random fatigue of structural components in mechanical systems. His paper started with the assumption that many lightly damped structures can be approximated as SDF systems (an assumption essential to his mode of analysis). He expressed the response

spectral density and noted that, as far as displacement and stress responses are concerned, the spectral density approximately equals the one that would be excited in a system by a white noise excitation with spectral density equal to the actual input spectral density at the natural frequency of the SDF system. Specifically, if the excitation random process is zero-mean and stationary, with spectral density $S_{QQ}(\omega)$, $-\infty < \omega < \infty$, and if the SDF system has FRF $H(\omega)$, $-\infty < \omega < \infty$, then the response spectral density is given by Eq. (33). Miles' approximation states that the response spectral density can be approximated by

$$S_{XX}(\omega) = |H(\omega)|^2 S_{QQ}(\omega_n) \quad -\infty < \omega < \infty \quad (37)$$

where ω_n is the natural frequency of the SDF system. For example, when an SDF system with natural frequency $\omega_n = 2\pi \text{ rad/sec}$, and damping factor $\zeta = 0.05$, is excited by an input with the spectral density shown in Figure 13, its displacement response is a random process with the spectral density shown in Figure 13. The response spectral density is the product of the modulus squared of the FRF (also shown) and the input spectral density. Miles' approximation to the response spectral density is the product of the white noise spectral density with magnitude $S_{QQ}(\omega_n)$ and the modulus squared of the FRF, both shown in Figure 13. The RMS value of the response is the square root of the area under the response spectral density curve. In this case the exact value is 0.312 in, and the value that comes from the approximation is 0.297 in. For this example, the approximation yields accuracy of about five percent. (Of course, in individual cases, the approximation may be better or worse.) Miles' paper may be better known for this intermediate result than for its final result involving fatigue analysis.

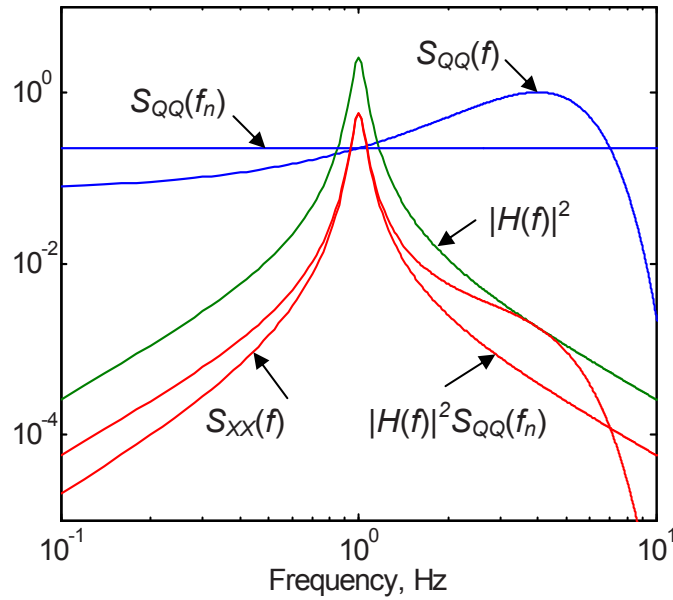


Figure 13. Graphic showing the meaning of Miles' approximation to the response spectral density.

The response spectral density approximation that Miles defined is so attractive that it has gained widespread acceptance, and is in use in many applications. For example, NASA uses it in combination with finite element models and a load combination scheme to establish an approximation for the overall load on a system. (See, for example, Himmelblau, et al., 2001, Ferebee, 2000, and NASA, 2002.)

Thomson and Barton (1957) wrote a paper that extended the approximation of Miles. They pointed out that through modal analysis the equations of motion of a complex linear structure can be reduced to a set of equations that have the form of the equation governing motion of an SDF system. These simple equations can be evaluated individually, then the mean square responses in the modes can be synthesized to approximate the mean square response at a point on the system. Their modal assumption is that the response at a location \mathbf{r} on a complex system $\mathbf{x}(\mathbf{r}, t)$, $\mathbf{r} \in \mathbf{V}$, $-\infty < t < \infty$, can be expressed as a series

$$x(\mathbf{r}, t) = \sum_k \xi_k(t) \phi_k(\mathbf{r}) \quad \mathbf{r} \in V, -\infty < t < \infty \quad (38)$$

where $\phi_k(\mathbf{r}), k = 1, 2, \dots, \mathbf{r} \in V$, are the mode shapes of the system, i.e., the shapes the system assumes when response is harmonic and occurs at the modal frequencies $\omega_k, k = 1, 2, \dots$, and $\xi_k(t), k = 1, 2, \dots, -\infty < t < \infty$, are the modal coordinates of the system, i.e., the amplitudes of the responses in the individual modes. When a system is excited by a single excitation $q(t), -\infty < t < \infty$, then response in the k^{th} mode is governed by

$$\ddot{\xi}_k + 2\zeta_k \omega_k \dot{\xi}_k + \omega_k^2 \xi_k = \phi_k(\mathbf{r}_{in}) q(t) \quad k = 1, 2, \dots, -\infty < t < \infty \quad (39)$$

where $\zeta_k, k = 1, 2, \dots$, are the modal damping factors, and \mathbf{r}_{in} is the location on the continuous structure where the excitation is applied. Based on this equation, when the actual input is a stationary random process, an approximation to the mean square response in each mode can be established using Miles' approximation. This is the approximation that Thomson and Barton made to obtain the overall mean square response at a point on the complex linear structure. When the excitation random process applied at the point \mathbf{r}_{in} has zero-mean, and is stationary with spectral density $S_{QQ}(\omega), -\infty < \omega < \infty$, then the approximate mean square response of the system at location \mathbf{r} is (when the response achieves a stationary state) given by

$$\sigma_{X(\mathbf{r})}^2 = \sum_k \frac{\pi \phi_k^2(\mathbf{r}_{in}) \phi_k^2(\mathbf{r}) S_{QQ}(\omega_k)}{2\zeta_k \omega_k^3} \quad \mathbf{r} \in V \quad (40)$$

Development of this approximation includes the assumption that the correlation between pairs of modal responses is zero.

Another paper in Crandall's 1958 *Random Vibration* volume was written by Rona (1958) and is titled "Instrumentation for Random Vibration." The paper considers both issues of experimental instrumentation and the estimation of spectral density. He discussed several types of accelerometer, and described how analog-to-digital conversion of measured signals is performed. He also discussed the possibility of digital signal analysis, but pointed out that it was not in general use at the time. He described what was, at the time of that writing, the technique used for estimation of spectral density. In essence, his description is the one given by Figure 8 in Section 3. He referenced Blackman and Tukey (1958) for the spectral density estimation technique.

Hardware implementations of the approach he described were used to estimate spectral densities of stationary random sources in the laboratory and the field, through at least the mid-1960's. The input signals were, of course, analog. The filters were band-pass filters, and were used in banks of 40 to 80. Spectral density estimates were frequently obtained up to 1000 to 2000 Hz. Mean square values of signal components were obtained in two ways. First, the filtered signals might be run through a full-wave rectifier. The means of the resulting signals could be computed, and from this, the RMS values of the filtered signal components inferred. These quantities could be squared to obtain estimates of the component mean squares. A second method involved the squaring of the filtered signal components using an analog squarer, then the averaging of the resulting signals to obtain the component mean squares. Finally, the mean square of each signal component was scaled by the factor $1/(BW)$ (the inverse of the effective bandwidth of the band-pass filters) to obtain the analog estimate of spectral density.

Rona's paper presented an early discussion (one of many) on the subject of test instrumentation, random signal analysis, and random vibration test control. Through the years, it is likely that as much time, effort and funding has gone to the performance of laboratory and field random vibration testing and analysis as has gone into the development of analytical techniques. The reason is simple; those burdened with the requirement to assure that actual systems that are capable of being tested are robust and reliable have tended to trust the results of physical experiments over analytical predictions, or in addition to analytical predictions.

The papers discussed in this section form a part of the legacy of the modern development of the theory of random vibrations. During the 1960's and beyond the study of random vibrations of mechanical systems flourished, and many papers dealing with the subject were published. Even the briefest summary of the topics covered in random vibration studies during the past

50 years would require a substantial discussion and admit an enormous bibliography. For those reasons, the papers summarized here stand out, forming the starting point of the modern theory of random vibrations.

6.0 Conclusion

The history of the mathematical theory of random vibration of mechanical systems spans the previous century, starting with the work of Einstein, continuing through the work of Wiener, and on to its introduction to the American engineering community by Crandall. Work in random vibration continues to the present. This paper briefly presents some developments in that history through the year 1958.

References

- Ang, A., Tang, W., (1975), *Probability Concepts in Engineering Planning and Design, Volume 1 – Basic Principles*, John Wiley and Sons, New York.
- Augusti, G., Baratta, A., and Casciati, F., (1984), *Probability Methods in Structural Engineering*, Chapman and Hall, New York.
- Bendat, J., Piersol, A., (2000), *Random Data: Analysis and Measurement Procedures*, 3rd Ed., Wiley-Interscience, New York.
- Blackman, R. B., Tukey, J. W., (1958), "Measurements of Power Spectra from the Viewpoint of Communication Engineering," *Bell Syst. Tech. Journ.*, Jan.-March.
- Bolotin, V., (1984), *Random Vibration of Elastic Systems*, Martinus Nijhoff, The Hague, The Netherlands.
- Carson, J. R., (1925), "Selective Circuits and Static Interference," *Bell System Technical Journal*, pp. 265-279.
- Carson, J. R., (1931), "The Statistical Energy-Frequency Spectrum of Random Disturbances," *Bell System Technical Journal*, pp. 374-381.
- Crandall, S., (Ed.), (1958), *Random Vibration*, Technology Press of MIT and John Wiley and Sons, New York.
- Crandall, S., (1958a), "Mechanical Vibrations with Deterministic Excitations," Chapter 1 in *Random Vibration*, S. Crandall, Ed. (1958).
- Crandall, S., (1958b), "Statistical Properties of Response to Random Vibration," Chapter 4 in *Random Vibration*, S. Crandall, Ed. (1958).
- Crandall, S., (Ed.), (1963), *Random Vibration*, MIT Press, Cambridge, MA.
- Crandall, S., Mark, W., (1963), *Random Vibration in Mechanical Systems*, Academic, New York.
- Davenport, W. B., Root, W. L., (1956), *Random Signals and Noise*, McGraw-Hill Book Co., NY.
- Einstein, A., (1905), "On the Movement of Small Particles Suspended in a Stationary Liquid Demanded by the Molecular Kinetic Theory of Heat," *Annalen der Physik*, V. 17, p. 549. Also, reprinted in Einstein (1956).
- Einstein, A., (1956), *Investigations on the Theory of the Brownian Movement*, Dover Publications, New York, Edited by R. Furth.
- Elishakoff, I., (1983), *Probabilistic Methods in the Theory of Structures*, Wiley, New York.
- Feller, W., (1971), *An Introduction to Probability Theory and Its Applications*, John Wiley and Sons, New York.
- Ferebee, R., (2000), "Loads Combination Research at Marshall Space Flight Center," Marshall Space Flight Center, Marshall Space Flight Center, Alabama, Report No. NASA/TM-2000-210331.
- Fokker, A., (1913), Dissertation, Leiden.
- Fung, Y., (1953), "Statistical Aspects of Dynamic Loads," *Journal of the Aeronautical Sciences*, Vol. 20, pp. 317-330.
- Fung, Y., (1955), "The Analysis of Dynamic Stresses in Aircraft Structures During Landing as Nonstationary Random Processes," *J. Appl. Mech.*, Vol. 2, pp. 449-457.
- Furth, R., (1917), *Ann. D. Physik*, V. 53, 177.
- Ghanem, R. G., Spanos, P. D., (1991), *Stochastic finite Elements: A Spectral Approach*, Springer-Verlag, New York.
- Gnedenko, B., (1997), *Theory of Probability*, 6th Ed., Gordon and Breach Science Publishers, UK.
- Himmelblau, H., Kern, D. L., Manning, J. E., Piersol, A. G., Rubin, S., (2001), "Dynamic Environmental Criteria," NASA Technical Handbook, NASA-HDBK-7005.
- Housner, G., (1947), "Characteristics of Strong Motion Earthquakes," *Bull. Seism. Soc. Amer.*, Vol. 37, pp. 19-31.
- Houdijk, A., (1928), *Archives Néerlandaises des Sciences Exactes et Naturelles*, Series III A, 11, p. 212.
- Ibrahim, R., (1985), *Parametric Random Vibration*, Wiley, New York.
- James, H., Nichols, N., Phillips, R., (Eds.) (1947), *Theory of Servomechanisms*, Radiation Laboratory Series, Vol. 25, MIT, McGraw-Hill, New York.
- Kac, M., (1947), "Random Walk and the Theory of Brownian Motion," *American Mathematical Monthly*, V. 54, No. 7. Reprinted in Wax (1954).
- Khintchine, A., (1934), "Korrelations Theorie der Stationären Stochastischen Prozesse," *Math. Ann.*, 109, 604-615.
- Kolmogorov, A. N., (1931), "On Analytical Methods in the Theory of Probability," *Math. Ann.*, Vol. 104, pp. 415-458.
- Laning, J. H., Battin, R. H., (1956), *Random Processes in Automatic Control*, McGraw-Hill, New York.

- Liepmann, H., (1952), "On the Application of Statistical Concepts to the Buffeting Problem," *Journal of the Aeronautical Sciences*, Vol. 19, No. 12, p. 793. Also, *An Approach to the Buffeting Problem from Turbulence Considerations*, Report No. SM-13940, Douglas Aircraft Company, Inc., 1951.
- Lin, Y., (1967), *Probabilistic Theory of Structural Dynamics*, McGraw-Hill, New York. Republished in 1976 by Krieger, Huntington, New York.
- Lyon, R. H., (1956), "Response of Strings to Random Noise Fields," *The Journal of the Acoustical Society of America*, V. 28, No. 3, pp. 391-398.
- Miles, J. W., (1954), "On Structural Fatigue Under Random Loading," *Journal of the Aeronautical Sciences*, V. 21, pp. 753-762.
- NASA, (2002), "Payload Flight Equipment Requirements and Guidelines for Safety-Critical Structures," International Space Station Program, NASA, No. SSP 52005 Revision C.
- Newland, D., (1993), *Random Vibrations, Spectral and Wavelet Analysis*, Longman, New York.
- Nigam, N., (1983), *Introduction to Random Vibrations*, MIT Press, Cambridge, MA.
- Ornstein, L., (1919), *Proc. Acad. Amst.*, Vol. 21, No. 96.
- Ornstein, L. S., (1927), *Zeits. F. Physik*, 41, p. 848.
- Paez, T., (2006), "The History of Random Vibrations through 1958," *Mechanical Systems and Signal Processing*, V. 20, pp. 1783-1818.
- Papoulis, A., (2002), *Probability, Random Variables and Stochastic Processes*, 4th Ed., McGraw-Hill, New York.
- Phillips, R., (1947), "Statistical Properties of Time Variable Data," Chapter 6 in James, Nichols and Phillips (1947).
- Planck, M., (1927), *Berl. Ber.*, p. 324.
- Lord Rayleigh, (1889), "On the Character of the Complete Radiation at a Given Temperature," *Philosophical Magazine*, V. 27, pp. 460-469.
- Roberts, J., Spanos, P., (1990), *Random Vibration and Statistical Linearization*, Wiley, New York.
- Robson, J., (1964), *An Introduction to Random Vibration*, Elsevier, New York.
- Rona, T., (1958), "Instrumentation for Random Vibration," Chapter 7 in *Random Vibration*, S. Crandall, Ed. (1958).
- Schueller, G., Shinozuka, M., (1987), (Eds.), (1987), *Stochastic Methods in Structural Dynamics*, Martinus Nijhoff, Boston.
- Schuster, A., (1894), "On Interference Phenomena," *Philosophical Magazine*, V. 37, pp. 509-545.
- Schuster, A., (1897), "On Lunar and Solar Periodicities of Earthquakes," *Proceedings of the Royal Society of London*, V. 61, pp. 455-465.
- Schuster, A., (1899), "The Periodogram of Magnetic Declination," *Camb. Phil. Trans.*, 18, 108.
- Schuster, A., (1900), "The Periodogram of Magnetic Declination," *Trans. Camb. Phil. Soc.*, 107-135.
- Schuster, A., (1905), "The Periodogram and Its Optical Analogy," *Proceedings of the Royal Society*, V. 77, pp. 136-140.
- Siebert, W. M., (1958), "The Description of Random Processes," Chapter 2 in *Random Vibration*, S. Crandall, Ed. (1958).
- Smallwood, D., (1982a), "Random Vibration Testing of a Single Test Item with a Multiple Input Control System," *Proceedings of the IES Annual Meeting*, IES.
- Smallwood, D., (1982b), "Random Vibration Control System for Testing a Single Test Item with Multiple Inputs," *Advances in Dynamic Analysis and Testing*, SAE Publication SP-529, Paper No. 821482.
- v. Smoluchowski, M., (1916), *Phys. Zeits.*, 17, p. 557.
- Soong, T., Grigoriu, M., (1993), *Random Vibration of Mechanical and Structural Systems*, Prentice-Hall, Englewood Cliffs, NJ.
- Taylor, G. I., (1920), "Diffusion by Continuous Movements," *Proceedings of the London Mathematical Society*, V. 20, pp. 196-212.
- Thomson, W. T., Barton, M. V., (1957), "The Response of Mechanical Systems to Random Excitations," *Journal of Applied Mechanics*, V. 24, pp. 248-251.
- Uhlenbeck, G., Ornstein, L., (1930), "On the Theory of the Brownian Motion," *Physical Review*, V. 36, pp. 823-841. Reprinted in Wax (1954).
- Van Lear, G. A., Uhlenbeck, G. E., (1931), "The Brownian Motion of Strings and Elastic Rods," *Physical Review*, V. 38, pp. 1583-1598.
- Wang, M., Uhlenbeck, G., (1945), "On the Theory of Brownian Motion II," *Reviews of Modern Physics*, V. 17, Nos. 2 and 3, pp. 323-342. Reprinted in Wax (1954).
- Wax, N. (ed.), (1954), *Selected Papers on Noise and Stochastic Processes*, Dover Publications, New York.
- Wiener, N., (1930), "Generalized Harmonic Analysis," *Acta Mathematica*, V. 55, No. 118.
- Wirsching, P., Paez, T., Ortiz, K., (1995), *Random Vibrations: Theory and Practice*, Wiley, New York.
- Yang, C., (1986), *Random Vibration of Structures*, Wiley, New York.

Reduction of Vibration Transmission in String Trimmers

Paurakh Rajbhandary, Undergraduate Research Assistant
Jack Leifer, PhD, PE, Associate Professor of Engineering Science
Bryan J. Weems, Undergraduate Research Assistant
Department of Engineering Science
Trinity University, One Trinity Place, San Antonio, TX 78212

ABSTRACT

It has been well documented that over long periods of time, people who regularly operate hand tools powered by small internal-combustion engines can become affected by a debilitating set of clinically irreversible effects, collectively referred to as hand-arm vibration syndrome (HAVS). Although HAVS cannot be cured, the onset of the disorder can be delayed or, in fact, prevented, by restricting either the duration of the exposure, and/or the magnitude of the vibration transmitted from the tool to an operator's hands and arms (per ANSI and similar standards). In this paper, we've evaluated an approach for reducing the magnitude of transmitted vibration at the engine-side grip of one commercial- and one consumer-grade string trimmer. The ultimate goal of this work is to develop a set of simple, passive retrofits for these tools that will reduce the likelihood of HAVS in full-time grounds-maintenance workers. The idea for this work stems from a stated need of Goodwill Industries of San Antonio, our NPA (non-profit agency) collaborator over the past several years. Based on this preliminary work, we've found that grips incorporating half-inch rubber studs placed at areal densities of either 25/in² or 12/in² significantly reduce the RMS vibration transmitted to the hand and arm at all frequencies (including the low frequency components known to be most harmful).

I. Introduction

Hand-arm Vibration Syndrome (HAVS) is an irreversible condition that affects individuals who are exposed to certain levels of vibration from equipment powered by internal combustion engines on a long-term basis. The recent survey by Pelmeier and Wasserman states that HAVS may arise after long-term exposure to all types and sizes of vibrating, hand-operated tools, including jack hammers, impact wrenches, orthodontic grinders, floor polishers, chain saws, and string trimmers. [1] Symptoms of HAVS include blanching of the fingers, tingling and numbness, and are generally more prevalent in cold weather. While HAVS cannot generally be cured, its onset and severity can be controlled through the combined approach of reducing both the magnitude and/or the duration of the exposure to the vibrations generated by the tools. Such an approach has been well documented by a variety of standards, including ISO 5349-1 and ANSI S2.70. [2,3] Therefore, for workers whose jobs require them to operate such tools for many hours per day, the only practical method of limiting the onset of HAVS is to reduce the amplitude of the vibration transmitted through the tools into their hands and arms.

The objective of this on-going study is to quantify the effect that various padding materials have on reducing the magnitude of transmitted vibration in string trimmers, with the ultimate goal of retrofitting these types of tools to decrease the likelihood of HAVS in full-time grounds-maintenance workers. Referring to the photograph shown in [Fig. 1](#), string trimmers are generally held in two locations so they can be maneuvered as they are used. The handgrip located at the top of the shaft, adjacent to the engine, is supported by the same hand that also actuates the throttle control. The loop-shaped handle is located further down the shaft, and allows the orientation of the string-trimmer to be changed by simply changing grip position on the handle. In order to passively reduce transmitted vibration, padding materials can be introduced in a variety of ways: (1) as a replacement for the manufacturer's handgrip (held by the operator's hand below the engine); (2) as a wrap applied over the loop-



Fig. 1 A typical string trimmer is supported by a grip adjacent to the engine (left) and a loop-shaped handle (right) located further down the shaft [4]

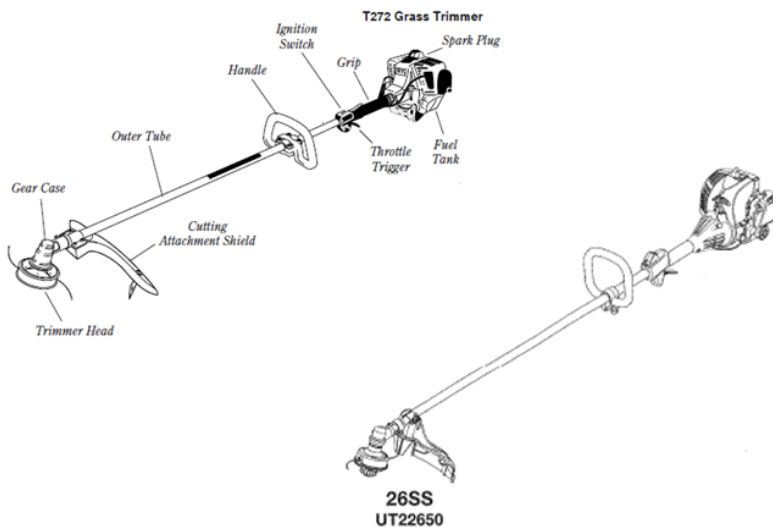


Fig. 2 Schematic of Shindaiwa (top) and Homelite (bottom) string trimmers used in this study. [5,6]

shaped handle; and (3) as a wrap installed between the loop-shaped handle and the shaft of the tool. In this study, we concentrated on evaluating materials that could replace the manufacturer's engine-side handgrip.

II. Materials and Methods

(a) Accelerometers and DAQ Boards. In order to measure all three components of generated vibration simultaneously, two similar Piezotronics U339B01 triaxial ICP accelerometers were used for various experiments in this study. The accelerometers each had a resolution of 0.002g between 1 Hz and 2 kHz, and nominal sensitivities in the x, y and z directions of 90.9 mV/g, 89.1 mV/g, and 90.9 mV/g (SN 2988) and 99.1 mV/g, 93.9 mV/g, and 71.6 mV/g (SN 3198). Both accelerometers were interfaced to an Iotech Wavebook516 16-bit Data Acquisition System equipped with an eight-channel WBK14 expansion module specifically designed for ICP accelerometers.

(b) String Trimmers. While every engine and chassis combination produces a unique vibration signature, the general effects of the vibration mitigation approaches evaluated herein are likely applicable to a whole range of string trimmers and other similar hand-held power tools. In order to test this hypothesis, measurements were taken on two different string trimmers. (1) The Shindaiwa T272 (Fig. 2) is intended for the commercial market. Equipped with a 1.4 hp 2-stroke engine, the dry weight of the unit is approximately 14.7 pounds. (2) The Homelite 26SS (Fig. 2) is lighter (weighs only 10 lbs), and is intended for the home (consumer) market. Its two-stroke engine is slightly smaller than that of the Shindaiwa. It is apparent from the schematics that both string trimmers have essentially the same layout - each one has an engine that is mounted atop a straight shaft, and the engine on each unit is started with a typical pull-starter. Engine speed is controlled by a throttle mounted on the shaft immediately adjacent to a padded grip, and a loop-type handle that extends normal to the string trimmer is mounted on each shaft about a foot below the grip/throttle combination. In both cases, the handle is mounted using a sleeve fit, and tightness against the shaft is controlled by one (Homelite) or four (Shindaiwa) bolts.

(c) Passive Damping Materials. The use of elastomeric materials to reduce transmitted vibration must be considered carefully, as the increased perception of user comfort offered by padded handles and grips does not always indicate a decreased risk for HAVS. As described by ISO 5349-1 [2], daily vibration exposure, $A(8)$, is a parameter that considers episode duration along with a weighted RMS acceleration magnitude (a_{hw}) as follows:

$$a_{hv} = \sqrt{a_{hw x}^2 + a_{hw y}^2 + a_{hw z}^2} \quad (1)$$

and

$$A(8) = \sqrt{\frac{1}{8} \sum_{i=1}^n a_{hvi}^2 T_i} \quad (2)$$

where a_{hv} in Eq. 1 simply represents the magnitude of the RMS values of the weighted acceleration components calculated in each direction (with respect to a basicentric coordinate system), and $A(8)$ in Eq. 2 represents the RMS value of each individual exposure (of duration T_i) normalized to an 8-hour workday. Note that ISO 5349-1 has established a frequency-weighting factor scheme that considers the relative effect that each frequency component has on hand injury. It has been found that low frequency components are most injurious, therefore the highest relative weightings (between 0.873 and 1.00) are concentrated between frequency components centered from 8 Hz - 16 Hz.

Researchers such as Ko have found that elastomeric wraps can reduce $A(8)$ by nearly 50%. [7] However, others sources warn that wraps may not be effective at the vibration frequencies that contribute most to the daily exposure levels (i.e. at low frequencies), and may in fact cause $A(8)$ vibration exposure to increase. [8] Rather than evaluate flat elastomeric materials (e.g. santoprene, closed-cell neoprene) that have been studied previously, we chose to test the effectiveness of the studded rubber mats shown in Fig. 3. The base of each mat was approximately 3/32 inch thick, and the studs were distributed uniformly at an aerial density of 25 studs/in² over the mat surface in its as-purchased condition. Although the stud diameter (0.125 inch) was the same on both

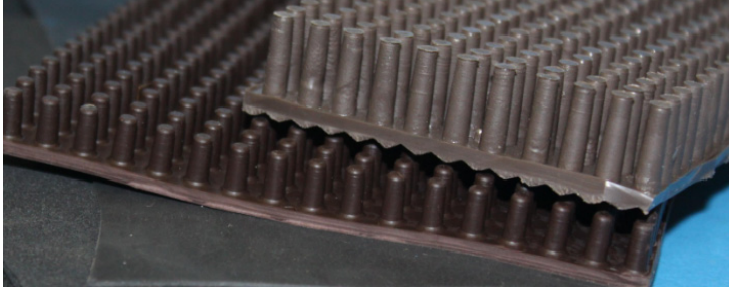


Fig. 3 Studded rubber mats used as wraps in the attenuation tests. The studs on the bottom mat were 0.25 in long, the studs the top mat were 0.50 inch long.

mats pictured, stud length was 0.25 inch and 0.50 inch, respectively, on the lower and upper mats shown in Fig. 3. The mats with the 0.5 inch studs were sourced from two different suppliers, and were referred to respectively (based on their physical behavior) as “stiff and compliant” in the test section, below. Studded mats were chosen because it was proposed that this particular material configuration would provide both damping and compliance characteristics that would reduce vibration transmission in both the radial (along the studs) and transverse directions. This hypothesis is

based in part on the work of Andersson, who implemented a “vibration damping handle” consisting of both damping and compliant elements that effectively reduced measured vibration between approximately 5 – 1500 Hz. [9]

III. Experimental

In all cases, a single accelerometer was used and aligned with a basicentric coordinate system (as suggested by ISO 5349-1) defined by the shaft axis, radius (line directed from the shaft axis to its surface), and tangent (normal to both the radial and axial components). For each experiment, the accelerometer was attached to the string trimmer using cyanoacrylate adhesive (superglue) and standard glue-mounting studs that were provided with the accelerometers. In order to ensure a flat, stable mounting surface for the accelerometer glue stud, a flat was milled into the surface of the elastomeric material under evaluation (Fig. 4a). In cases where milling a flat into a curved surface was not practical (e.g. on the bare shaft of the string trimmer), a custom aluminum adapter was used to couple between the flat glue stud and curved surface (Fig 4b).

Early in the testing sequence, it was noted that both the magnitude and frequency content of the measurements were dependent on a variety of parameters including engine speed, human factors such as hand pressure and position, and string trimmer orientation. In order to reduce the effect of these variables, initial measurements were performed on a string trimmer suspended horizontally in a “free-free” orientation approximated by two

bungee cords separated by approximately 35 inches (Fig. 5). In order to ensure that the bungee cords did not move during the testing sequence, small pieces of masking tape were used to lightly secure their position against the string trimmer's shaft.

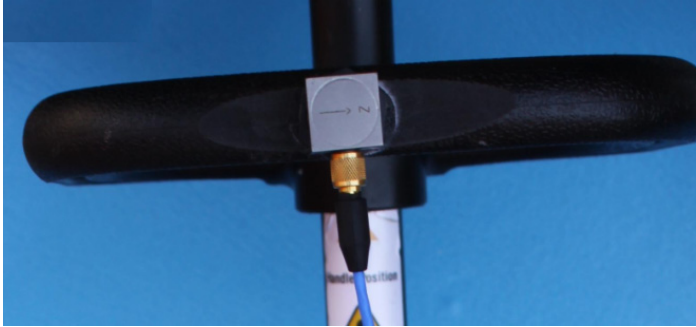


Fig. 4a Accelerometer mounted on handle, aligned with a basicentric coordinate system. Note the flat milled into the surface of the handle facilitates a secure coupling

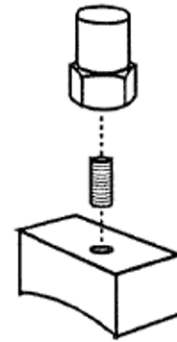


Fig. 4b Schematic representation of an adapter that allows a flat accelerometer to be mounted to a contoured surface (adapted from ISO 5439-2) [2]



Fig. 5 Free-free suspension approach for string trimmer baseline test. The Shindaiwa trimmer is shown here.

(a) Baseline Test. To obtain the baseline frequency content in each of the basicentric coordinate directions, the loop handle was removed from the each string trimmer, and the accelerometer (SN 2988) was installed in its place. This was done by gluing an adapter (Fig. 4b) to the shaft, and attaching the accelerometer to the adapter using the threaded stud. This accelerometer was located exactly 4 inches below the lower end of the manufacturer's grip. Surface acceleration components were measured at both an unthrottled (idle) and throttled condition. Note that to obtain a throttled measurement, the string trimmer throttle was carefully squeezed by hand without disturbing the hanging free-free support. Acceleration components were measured at this point using the method provided for triaxial measurement in the ISO 5349-2 standard. [2] For both the throttled and unthrottled conditions, data were taken for 5.0 seconds at a sampling frequency of 5000 Hz. Conversion to the frequency domain was accomplished within MatLAB using a fast-fourier transformation algorithm, and typical spectra obtained for each accelerometer channel are shown in Fig. 6 (for the Homelite trimmer only). Note that most of the content in each coordinate direction is concentrated below 500 Hz; furthermore, the vibration amplitude for the throttled condition increased by about an order of magnitude over that obtained for the unthrottled condition. The data presented in Fig. 6 are a typical example of the measurements obtained, and clearly show that string trimmers generate significant vibrations in all three of the basicentric coordinate directions.

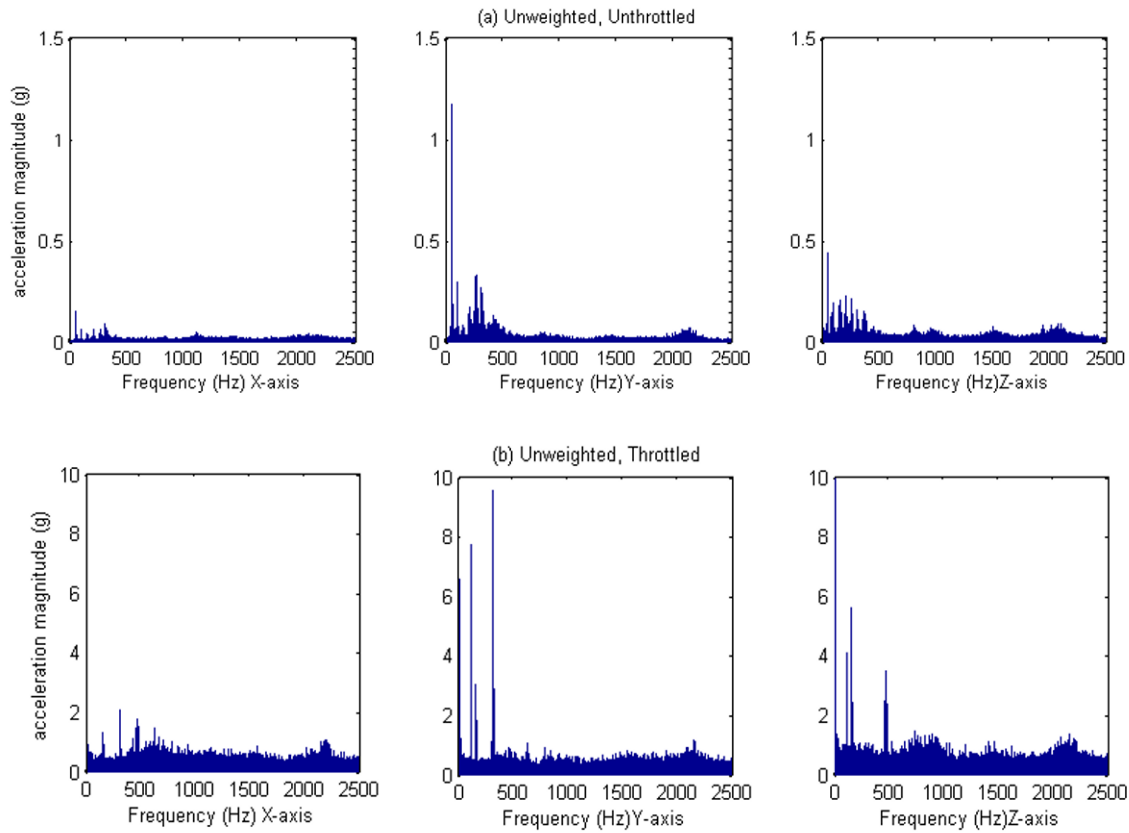


Fig. 6 Baseline frequency domain plots of acceleration components taken by the fixed accelerometer (SN 2988) for the (a) unthrottled and (b) throttled conditions using the Homelite string trimmer

Since Eq. 2 (above) uses acceleration magnitude to calculate $A(8)$; the remainder of the measurements presented herein will report the RMS magnitudes of both the unweighted and weighted acceleration signals rather than the component data.

(b) Grip Test. As mentioned previously, a string trimmer is typically supported in two locations: at the loop handle (held by the operator's left hand in Fig. 1), and at the padded area of the shaft (grip; held by the operator's right hand in Fig. 1). At the grip location, the shaft of the string trimmer is covered with a soft padded material that differs from model to model. The function of the padding is to both reduce the vibrations transmitted to the hand and arm of the operator, and to also protect the thin throttle cable that controls engine speed. The padded grip area on the Shindaiwa is located between the throttle and the engine (Fig. 5); the material used for the grip on the Homelite string trimmer, pictured in Fig. 7, is somewhat thicker. In order to determine whether the magnitude of the transmitted vibration at the grip could be reduced significantly via passive means, the studded mats shown in Fig. 3 were used to fabricate a variety of grips.



Fig. 7 The grip area of the Homelite string trimmer

For each of the tests performed, the accelerometer (SN 3198) was attached directly to the shaft or the padding (using cyanoacrylate) so that it was positioned directly under the operator's right hand, and aligned with the basicentric coordinate system defined by the shaft of the string trimmer. To ensure that the influence of the hand-arm coupling

was included in the measurement, the operator gripped the accelerometer and the shaft simultaneously with his or her right hand, in an adaptation of the “moulded hand-held adaptor” approach discussed in the ISO 5349-2 standard. [2] The operator’s left hand held the loop handle, allowing the string trimmer to be supported during testing in its typical operating position (although no grass was cut during the tests).

For the two trimmers evaluated, each of the test grips was installed in turn after the manufacturers’ grip was removed. The studded material used for each test grip was measured and cut to size (using the original manufacturer’s grip as a template), and glued directly to the shaft using cyanoacrylate ([Fig. 8](#), left).

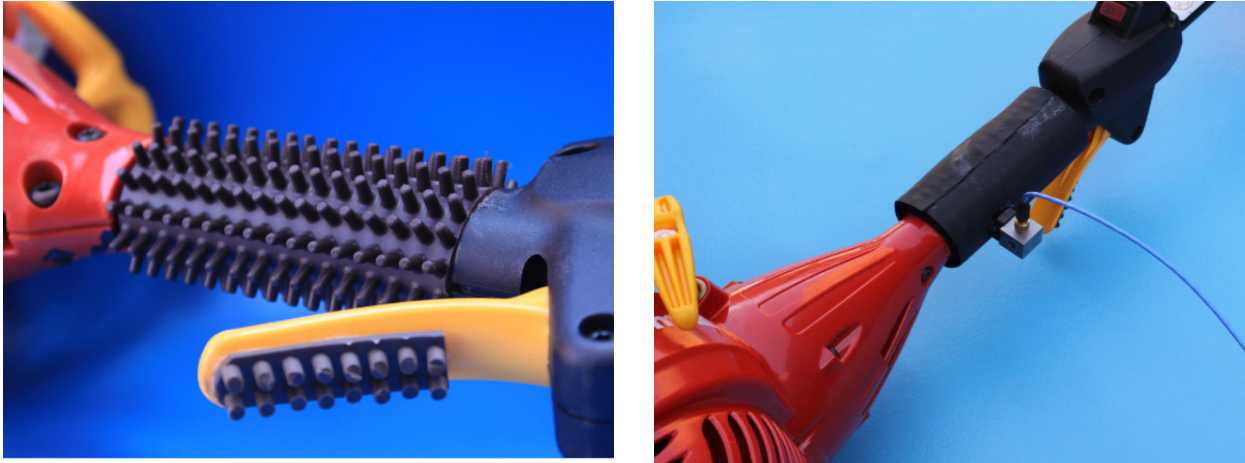


Fig. 8 Quarter-inch studded material is glued directly to the shaft of the Homelite trimmer (left), and then covered with a very thin layer of rubber to facilitate the accelerometer (right). To increase operator comfort, studded material was also installed on the throttle actuator.

Test	Material	Comments
1	Manufacturer’s Grip	-
2	Bare shaft	Used as baseline measurement
3	0.5” studded	Stiff material
4	0.5” studded	Stiff material – half density (every other stud removed)
5	0.25” studded	–
6	0.5” studded	Compliant material
7	0.5” studded	Compliant material - half density

To ensure comfort (and to provide an appropriate surface for accelerometer mounting), a thin layer of sheet rubber was glued to the top of the studs ([Fig. 8](#), right). For each grip material tested, ten measurements were performed using each string trimmer (five throttled and five unthrottled). A summary of the grip conditions tested is contained in [Table 1](#), and results are presented in [Figs. 9-12](#). For each of the tests performed, the measurement period was set to 20 seconds and a sampling frequency of 5000 Hz was used. In all cases, the error bars shown represent +/- 1 standard deviation over the five samples taken for each measurement.

The following general observations can be made based on the data shown in [Figs. 9-12](#):

- The Homelite (consumer model) string trimmer generally transmits more vibration to an operator’s hand and arm than the Shindaiwa (commercial) string trimmer.
- When gripped as shown in [Fig. 1](#), the surface accelerations generated by a throttled string trimmer increase by about an order of magnitude over those generated by a string trimmer operating in an idled (unthrottled) condition. This result conforms to that obtained for the frequency-domain data shown in [Figs. 6a](#) and [6b](#) for the Homelite string trimmer suspended in a free-free condition.
- The Homelite manufacturer’s grip (condition #2) provides some protection against transmitted vibration when compared with the bare shaft (condition #1) for both the throttled and unthrottled conditions.

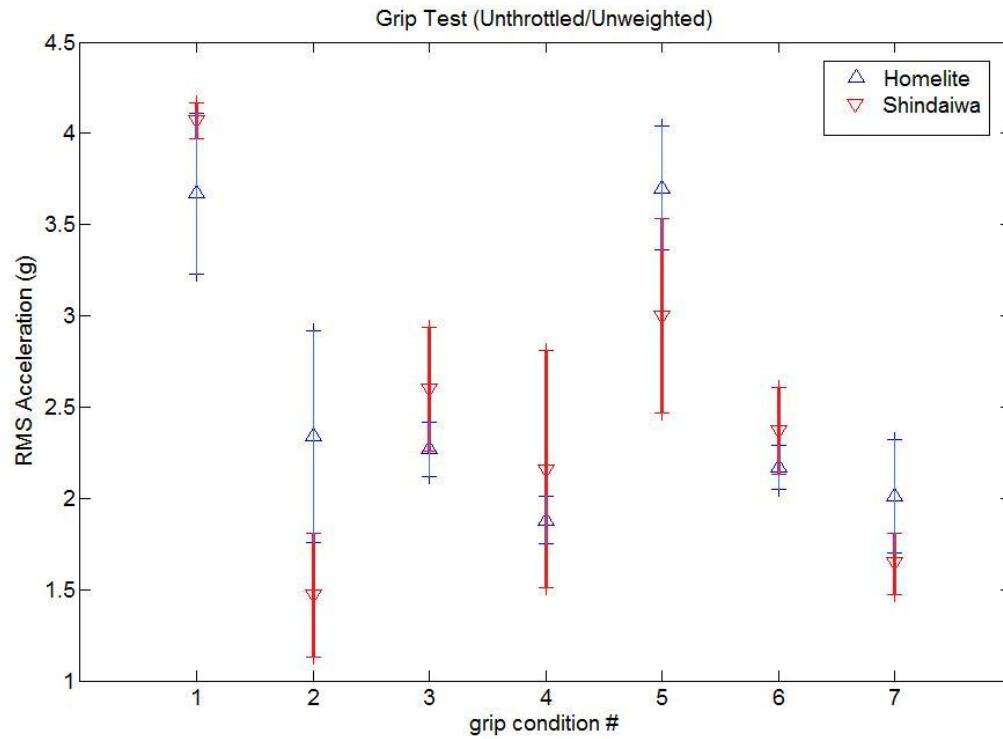


Fig. 9 Performance of various grips under unthrottled engine conditions (unweighted)

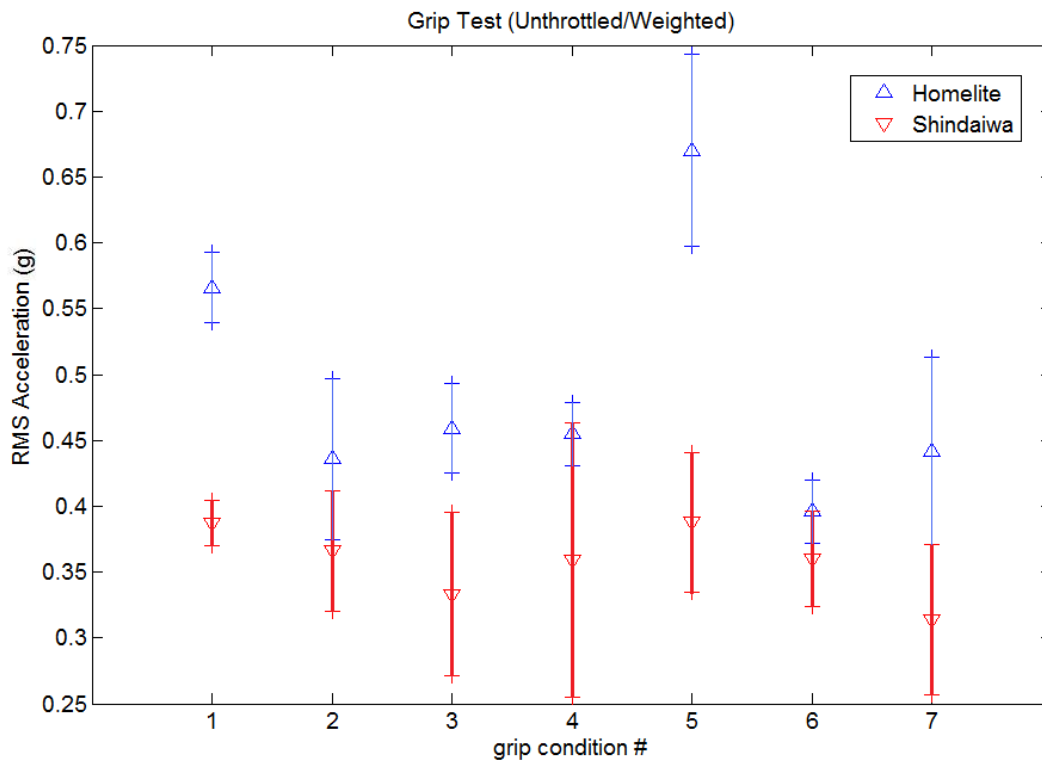


Fig. 10 Performance of various grips under unthrottled engine conditions (weighted)

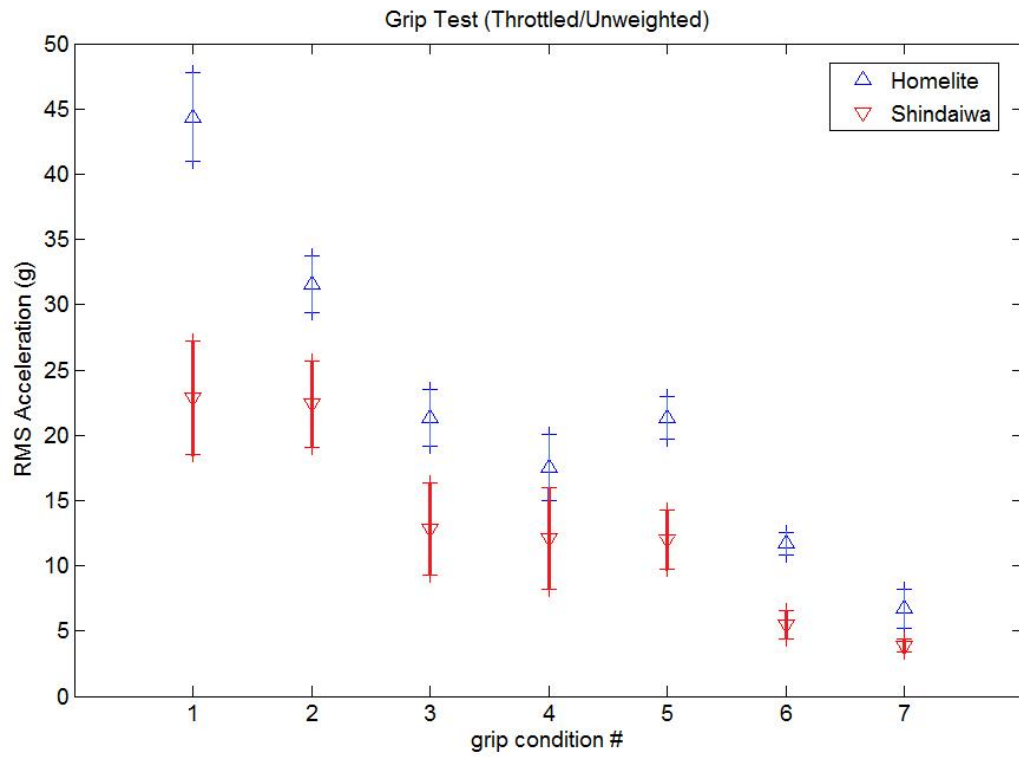


Fig. 11 Performance of various grips under throttled engine conditions (unweighted)

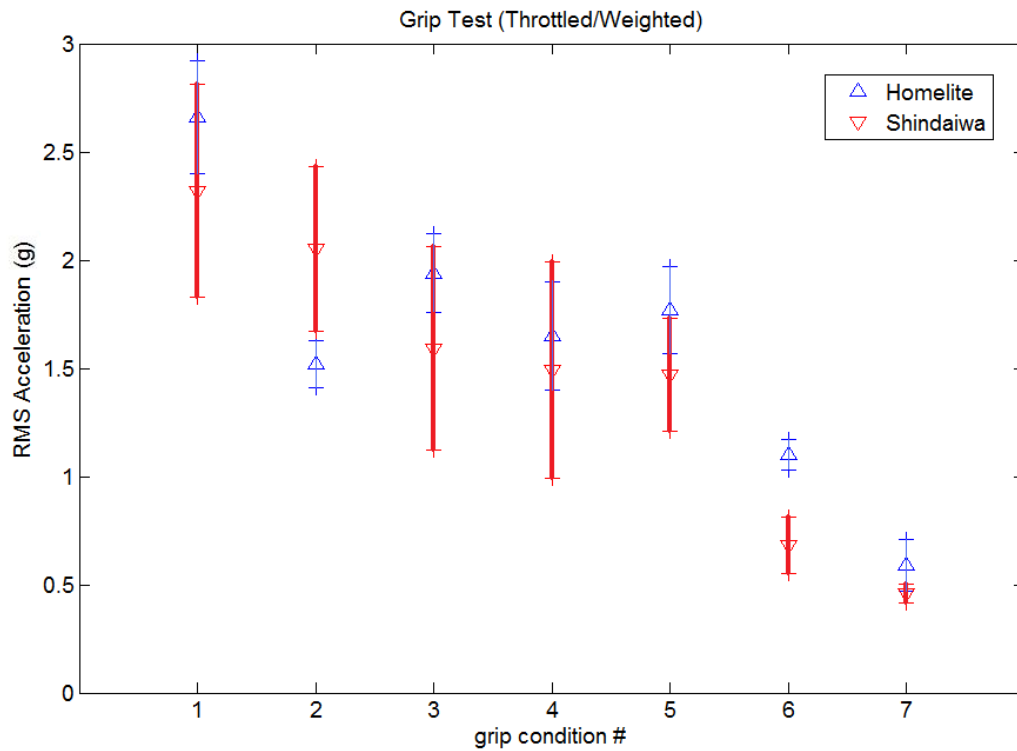


Fig. 12 Performance of various grips under throttled engine conditions (weighted)

- When the data are weighted to only consider the transmission of harmful frequencies, the Shindaiwa manufacturer's grip (condition #2) does not seem to offer additional protection over the bare shaft (condition #1).
- During idling periods (Figs. 9 and 10), none of the studded grips seem to offer any advantage over the manufacturers' respective grips.
- Based on the throttled, unweighted data (Fig. 11), all of the studded grips (conditions 3 – 7) perform better than either of the manufacturers' grips by reducing the amount of perceived vibration. However, as mentioned previously, a perceived increase in comfort may not reduce HAVS injury potential.
- When the throttled data are weighted so that only the harmful frequencies are taken into consideration, only the grips fabricated from the more compliant, half-inch studded material seem to be effective at lowering the vibration transmitted to the hand.

V. Discussion

The compliant mats with half-inch studs are clearly effective at significantly reducing the dose of harmful, low-frequency vibrations transmitted to a string-trimmer operator's hand and arm in both the Homelite and Shindaiwa units evaluated herein. However, neither the material parameters nor the stud geometries were optimized, and parametric studies are underway that specifically evaluate the effects of stud length, areal density, and material parameters on vibration transmission. All of the studded materials used for this study were purchased at a wholesale restaurant supply shop, hence exact material parameters can only be obtained through careful testing. One approach that we are currently using to characterize these materials is modal testing using a frequency- and amplitude-controlled shaker.

Other factors to be considered when developing vibration-reduction approaches for string trimmers include the following:

- While the more compliant half-inch studded mats seemed to be most effective at reducing transmitted vibration, the resulting grip diameter was more awkward to hold and maneuver than the manufacturers' grips. Installing a smaller diameter shaft prior to incorporating the studded wrap may allow the development of an effective anti-vibration grip whose overall diameter is not larger than the diameter of the original manufacturers' grip.
- As part of this work, extensive measurements of the vibrations transmitted through the loop handles of each respective string trimmer were performed. Although not reported here, we found some correlation between transmitted vibration and the tightness of the handle/trimmer shaft interface. We believe that in addition to monitoring screw tightness (as an indication of handle-shaft contact force), studded materials similar to those used for the grip can be incorporated between the handle sleeve and the string trimmer shaft in order to further reduce transmitted vibration. However, in order to accommodate such a modification, either the diameter of the trimmer shaft will need to be reduced, or the handle sleeve will need to be modified to accommodate the larger diameter presented by the wrapped shaft.
- Just as the studded materials proved effective when incorporated as wraps at the engine-side grip location, it is likely that such materials will be similarly effective when incorporated as loop-handle wraps. Experiments to confirm this are currently under way.

IV. Conclusions

Based on the work reported herein, the following results can be reported:

- Regardless of the support configuration (free-free or held at the two grip locations), both the commercial- and consumer-oriented string trimmers produce high-amplitude vibrations. A significant portion of the vibration is produced at the low frequencies considered to be most harmful.
- We have shown that studded materials incorporating both damping and compliant elements can reduce the amplitude of transmitted vibrations at the engine-side grip of string trimmers, including the low-frequency components.
- The effectiveness of the grip material seems to depend on compliance (vibration attenuation increases with compliance) and stud length (vibration attenuation increases with stud length). Parametric studies are currently under way that will confirm these preliminary findings.

Acknowledgements

The authors are grateful for support from Trinity University's Howard Hughes Medical Institute (HHMI) program, as well as the Trinity University Office of Academic Affairs. We also appreciate the participation of Goodwill Industries of San Antonio, TX.

References

- [1] Pelmear, P.L., and Wasserman, D.E., *Hand-Arm Vibration*, 2nd ed. Beverly Farms, MA: OEM Press, 1998.
- [2] *Mechanical Vibration – Measurement and Evaluation of Human Exposure to Hand-Transmitted Vibration*. ISO 5349, 2001.
- [3] *Guide for the Measurement and Evaluation of Human Exposure to Vibration Transmitted to the Hand*. ANSI S2.70-2006.
- [4] Yeo, D. R., http://en.wikipedia.org/wiki/File:Man_weedeating.jpg, accessed 11 OCT 2010.
- [5] Shindaiwa Owner's/Operator's Manual. http://www.shindaiwa.com/_docs/oms/trimmers/t272.pdf, accessed 13 JUL 2010.
- [6] Homelite Operator's Manual: 26cc Trimmers. Homelite Consumer Products, Inc., Anderson, SC, 19 OCT 2009.
- [7] Ko Ying Hao, *Investigation of Elastomeric Pad Attenuation of Hand-Transmitted Vibration*, MS Thesis, Universiti Sains Malaysia, 2008.
- [8] *EU Guide to Good Practice on Hand-Arm Vibration*, <http://www.fosterohs.com/links.htm>, accessed 25 OCT 2010.
- [9] Andersson, E.R., "Design and Testing of a Vibration Attenuating Handle," *International Journal of Industrial Ergonomics*, vol 6, 1990, pp. 119-125.

Insight into Strong Motion Behavior of Large Concrete Structures

Based on Low Level Response Monitoring in the Field

Nick von Gersdorff¹ and Zee Duron² and Vincent Chiarito³

Abstract

The inability to induce strong motion excitation levels in structures is often cited as a limiting factor in evaluating the seismic performance of large concrete dams. The advent of modern computational tools that provide advanced non-linear analysis capabilities for these structures contributes to the view held by many analysts that low-level response monitoring does not contribute meaningful insights to overall dam performance. Recent experiences with low-level monitoring of two large concrete dams suggest that this may not be entirely true. Results from field tests are discussed in which the ambient testing technique was used to design follow-on forced vibration tests on a large concrete gravity dam and that formed the basis for the evaluation of predicted seismic response behavior of a large multiple concrete arch dam. An overview of the field test procedures employed is described, and sample response measurements are also presented. Details of the time and frequency domain analysis techniques employed are presented and results from each test are interpreted in the context of seismic performance. Recommendations for standardizing field monitoring procedures are provided.

Introduction

Field monitoring techniques aimed at understanding the dynamic response behavior of large civil structures can assist in the evaluation of a structure's capacity to perform under a wide range of loading conditions. The most commonly used field procedures for evaluating the dynamic characteristics of large structures involve the use of large eccentric mass vibrators, also known as shakers, that produce sinusoidal excitations, the use of large impact devices that are capable of delivering short duration high amplitude pulses, and even devices that create explosive like loading conditions. The use of these and other devices capable of producing forced response behavior – whether sinusoidal, transient, or random – in the structure are generally well accepted and reported in the literature.

The forced vibration test at Folsom Dam, a large gravity dam, required extensive planning. To help facilitate the test, preliminary results were obtained using the ambient test technique – a technique that relies on ambient or naturally occurring environmental conditions at the site to produce measurable structural response behavior.

A problem exists in the use of shakers when they cannot be directly attached to the structure. Gem Lake Dam is a thin multiple arch dam and its crest is too narrow to safely install a shaker. In this instance an alternative field monitoring technique must be employed that is capable of extracting the desired dynamic response characteristics, but does so without the advantage of large excitation devices and large load magnitudes. Measurable and accurate dynamic response information can be extracted from just the ambient testing technique.

Experience with the ambient technique applied to large civil structures can be traced to the early days of full-scale dynamic testing in which “people power” was used to excite responses in a tall building. Since then, advances in computer and instrumentation technologies have contributed to the development of the ambient test technique. Ambient testing has been conducted on large concrete dams, buildings, and even on large launch vehicles, and while results have often compared well with numerical model results (Ref [1]), the technique is not widely accepted or perhaps well understood in the engineering community.

Recent experiences with ambient testing on large concrete dams have shown excellent agreement can be achieved with forced vibration test results. Recently conducted tests at Big Creek Dam No. 7 (Ref [2]) indicate a match between ambient and

¹ Engineer, Dam Safety Group, Southern California Edison Company, San Dimas, California 91773

² Professor of Engineering, Harvey Mudd College, Claremont, California 91711

³ Research Engineer, ERDC/WES, Vicksburg, Mississippi 39180

forced vibration results to within 6%. Comparisons of corresponding response shapes have also indicated very good agreement. If these comparisons can be reproduced on other large civil infrastructure, perhaps the ambient technique will gain acceptance. Nonetheless, reported experiences at Big Creek Dam No. 7 and at San Vicente Dam (Ref [3]) suggest that it is a viable option for identifying dynamic response behavior in dams.

Folsom Dam Ambient Survey

The ambient survey results were used to plan the forced vibration tests and provide an appropriate context for interpreting measured forced response behavior.

Folsom Dam, located approximately 23 miles northeast of Sacramento, CA, was constructed in 1956 by the U.S. Army Corps of Engineers and is now operated by the U.S. Bureau of Reclamation. The dam crest is 1,400 ft long and 36 ft wide, and the maximum height and base width are 340 ft and 270 ft, respectively. The dam consists of 28 monoliths, 50 ft wide each, constructed in 5-ft lifts and founded in hard granodiorite rock (Ref [4]). Monoliths 1 through 11 are referred to as the right gravity section, Monoliths 12 through 20 as the spillway section, and Monoliths 21 through 28 as the left gravity section (Figure 1). For the most part measurement locations along the crest and inside the dam were placed at the center of each monolith.

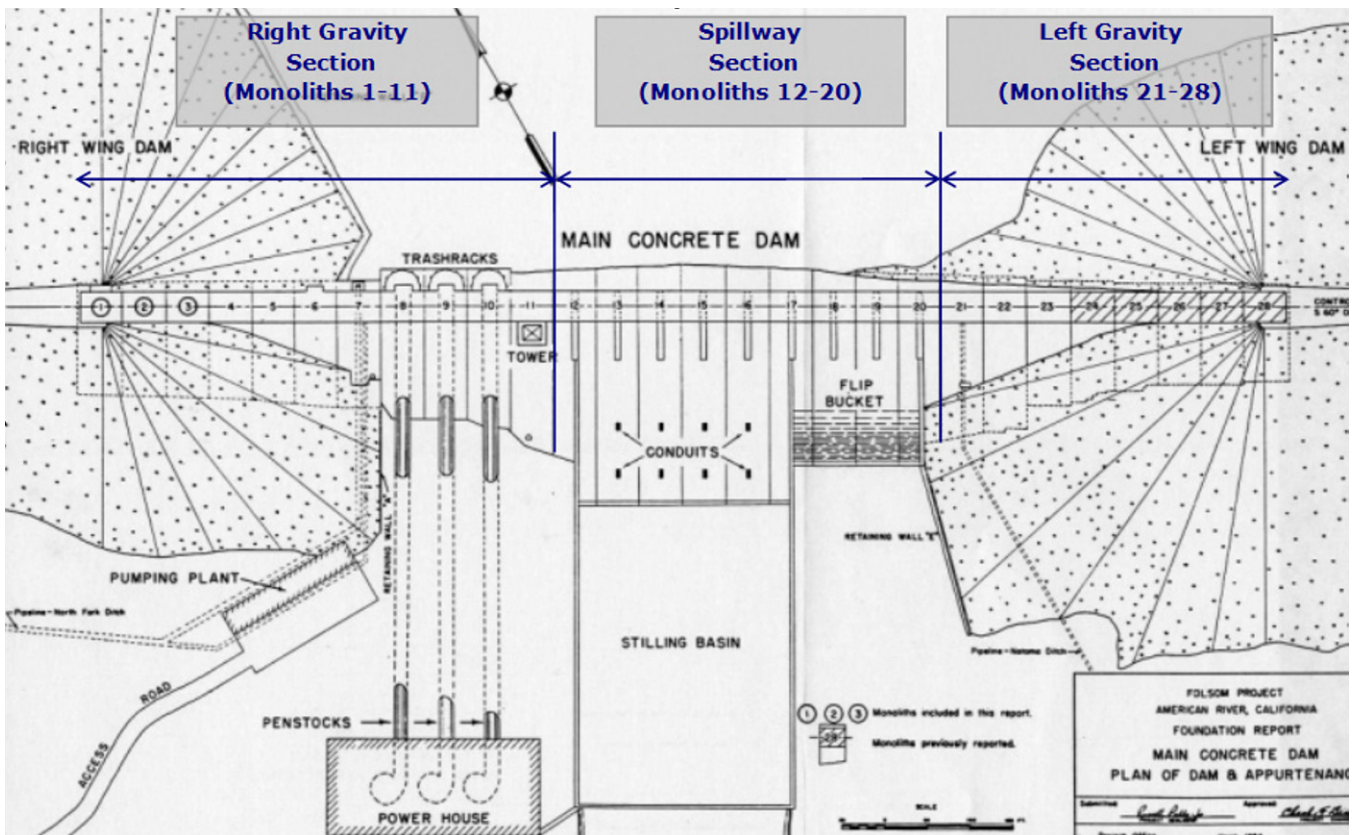


Figure 1. Plan view of Folsom Dam

A preliminary ambient survey was conducted at Folsom Dam in March 2004. It consisted of 16 tests at 73 monitored locations in the dam, on the adjacent foundation, and on the left embankment. Ambient hydrodynamic pressure responses were also acquired behind Monoliths 14 and 21 (Ref [5]).

Ambient vibration responses on the dam and on the adjacent foundation were acquired using Q-Flex accelerometers (models QA-700, QA-750) manufactured by Honeywell. The unit is particularly effective because of its high signal-to-noise ratio, which helps ensure data quality for low response levels.

Hydrodynamic pressure responses in the reservoir were acquired using a hydrophone instrument array. The array consists of eight solid-state hydrophones spaced 50 ft apart along an 800-ft-long Kevlar reinforced cable. Hydrophone sensitivity averaged 0.7 V/psi.

Responses were acquired digitally using a National Instruments Model 6036E data acquisition card installed in a laptop computer. A *MATLAB*-based software package, **ISHAKE**, developed for the tests at Folsom Dam, provided capability for data acquisition, writing and storing data files, and shaker control.

Analyses of measured responses indicated near-monolithic behavior in the dam below 10 Hz in which the fundamental response shapes along the crest of the dam were identified as shown in Figure 2. The near-monolithic response character observed in the dam suggested that a single vibrator (shaker) attached to the crest on Monolith 11 could yield similar behavior. Furthermore, since ambient responses indicated that individual monolith response behavior appeared above 10 Hz, an attempt could be made to capture relative joint motion during the forced vibration tests.

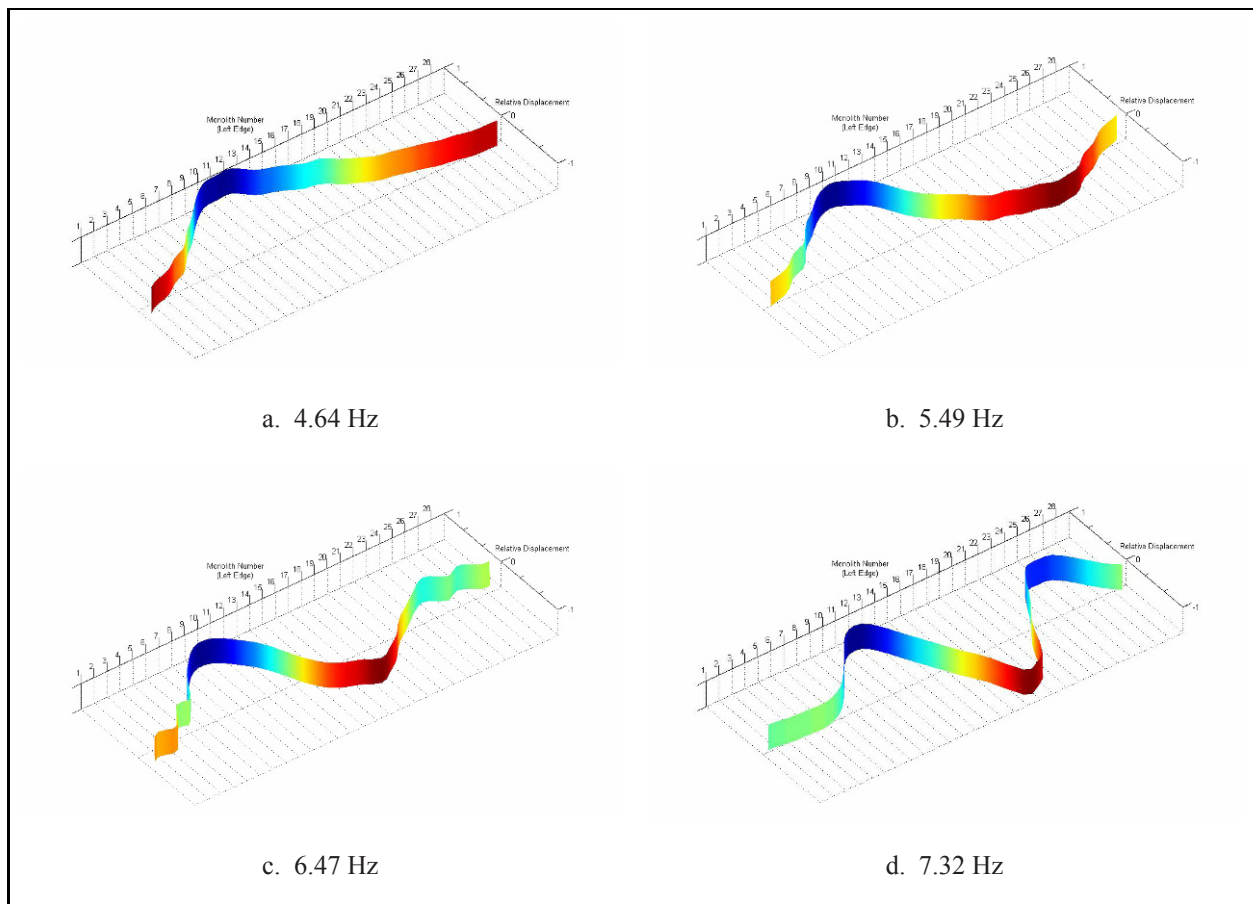


Figure 2. Fundamental response behavior indicated from preliminary ambient survey

Evidence of foundation flexibility effects was also observed at the base of Monolith 12 from ambient responses acquired in the vertical direction at the heel and toe of the monolith. Based on this, an attempt could be made to further characterize foundation flexibility effects by placing the shaker inside a monolith in order to excite vertical responses at the heel and toe. Ambient measurements of hydrodynamic pressure responses in the reservoir indicated strong resonant behavior. This offered confidence to attempt extraction of reservoir frequency response behavior from forced response measurements of pressure.

As seen in [Table 3](#) (Ref [6]), the ambient results matched the forced vibration results very closely. The ambient results provided confidence in our choice of shaker location and ensured that major resonance frequencies would be accurately captured.

Table 3 Comparison of Measured Ambient and Forced Resonances at Folsom Dam	
Resonant Frequency, Hz	
Ambient Vibration Survey	Forced Vibration Tests
4.64	4.65
5.49	5.46
6.47	6.24
7.32	7.16
8.18	8.00
8.91	8.87

Description of Gem Lake Dam

Gem Lake Dam is a concrete multiple arch dam located on Rush Creek, on the eastern slope of the Sierra Nevada mountain range in Mono County, California. The dam is 80 ft tall at its maximum height with sixteen complete arches and two partial arches at the ends. The crest is at an elevation of 9057.5 ft above sea level and its overall length is 688 ft. The dam was completed in 1916, and in 1924 concrete was placed against the intrados of the original arches in a concentric arch ring shape with the intention of compensating for the rapid freeze/thaw deterioration of the lower parts (to within 30 ft of the crest) of the arches. In 1966 and again in 1977, the entire upstream dam face was covered with a 3-inch layer of reinforced, high strength gunite. In 2007, the entire upstream face was covered with a geomembrane liner which proved effective in waterproofing the dam and significantly reducing leakage through the face. A picture of Gem Lake Dam is included in [Figure 3](#).



Figure 3. Upstream face (with geomembrane liner) of Gem Lake Dam.

Gem Lake Field Test Procedure and Measurement Layout

The objective of the field tests at Gem Lake Dam was to measure dynamic response characteristics of the entire dam. This test objective would require the development of an innovative procedure that could both excite and acquire responses on each of the 18 arches in the dam. In selecting the appropriate field test procedure for evaluating the dynamic characteristics of Gem Lake Dam, forced vibration testing with an eccentric mass vibrator attached to the dam crest was considered. Since the dam crest is actually a cantilevered walkway less than 4 ft in width, attaching a vibrator with a base plate dimension of 3 ft by 5 ft was judged to be impractical and unsafe. Impact testing was also considered in which a calibrated hammer is used to induce transient responses in the dam. However, the length of the dam and the 18 arch configuration would most likely have resulted in localized behavior instead of the desired global response along the entire length of the dam. The development and frequency analysis of a numerical model of Gem Lake Dam provided important insights into the expected dynamic behavior of the structure that ultimately led to the innovative field test procedure employed. A frequency analysis of the numerical model led to the realization that individual arches as well as groups of arches could be excited apart from the overall resonant behavior in the dam. A successful field test procedure, therefore, would allow individual arch, as well as group or clustered arch responses in the dam to be identified across a relatively broad frequency range.

Ambient testing was selected as the basis for developing a field test procedure that allowed practical monitoring of each arch, the use of both global (dam) and local (arch) reference measurement locations, and whose responses could be interpreted in the context of individual arch, clustered arch, and overall dam response behavior. The ability of ambient testing to provide credible evidence of dynamic response behavior relies on the use of reference measurements that act as inputs to the remaining measurement locations in the structure. This allows spectral responses to be computed based on relative behavior between measurement locations and any reference location in the dam. At Gem Lake Dam, the ability to extract individual arch response and to use individual arch characteristics to provide an overview of the entire dam behavior required the use of two types of reference measurements. The first reference measurement was of the usual type, selected at three locations in the dam where large response magnitudes could be expected – a global reference measurement. The second type consisted of a single reference measurement on each arch, at the same relative location – a local reference measurement.

A total of 13 accelerometers were used to conduct the ambient survey – three reference accelerometers placed on Arches 3, 7, and 12, and ten accelerometers used to capture random responses on Arches 1-16. Arches 17 and 18 were judged to be sufficiently more rigid compared to the other arches, contributing more as boundary conditions than as flexible contributors to dam response, and were not monitored. Testing was completed over a 3-day period in late July and early August, 2009 – which for such a large structure, demonstrates the ability of the field test procedure to provide complete coverage in a reasonable time frame. The measurement layout for each arch is shown in [Figure 4](#), where each location around the arch is labeled a-k and oriented radially.

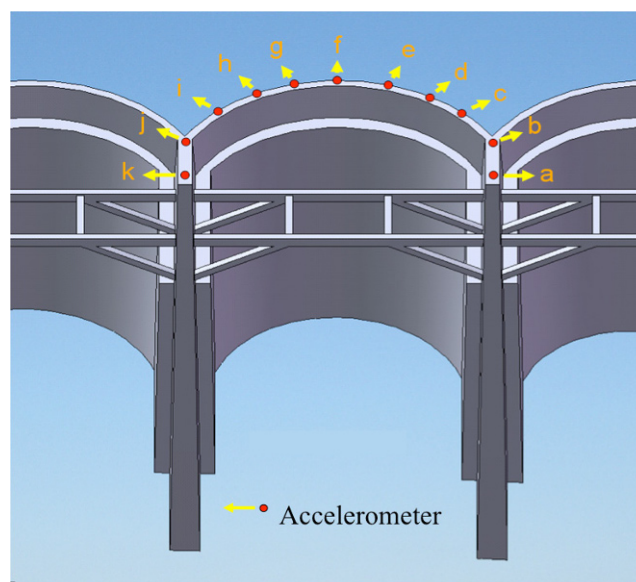


Figure 4. Measurement layout at Gem Lake Dam.

Ambient vibrations in the dam crest were acquired using Q-Flex Model QA-700 and QA-750 current output accelerometers manufactured by Honeywell. Accelerometers were mounted on plates supported by three thumbscrews, placed on the concrete surface, and leveled using a bubble level to ensure a planar orientation in the radial direction at each measurement location. No adhesives or permanent mounting of the accelerometer plates was necessary for installation. Threshold levels to $1 \mu\text{g}$ can be accurately measured, and the current output of these sensors allows extended cable lengths to be used throughout the dam without loss of signal quality. Accelerometer sensitivities ranged from 10.7 V/g to 12.3 V/g .

Analog signals from each accelerometer were band-pass filtered using a 2-pole high-pass Butterworth with cutoff at 1 Hz , and a 4-pole low-pass Butterworth with cutoff at 30 Hz . Amplification gains were set at 100 for crest measurements, and at 10 for buttresses measurements. These signals were then digitized at a sample rate of 2500 samples per second (sps) and time histories were acquired over a 10-minute interval to achieve satisfactory signal quality.

Sample Response Measurements

Response measurements of accelerations acquired on the crest during ambient monitoring periods showed response envelopes typical of expected random behavior. Even with the low-pass filtering at 30 Hz , the high sampling rate of 2500 sps contributes to the elevated noise levels and higher than normally acquired frequency content since the filter is not ideal. However, overall signal quality is considered to be high. Sample time histories are shown in [Figure 5](#). (Ref [7])

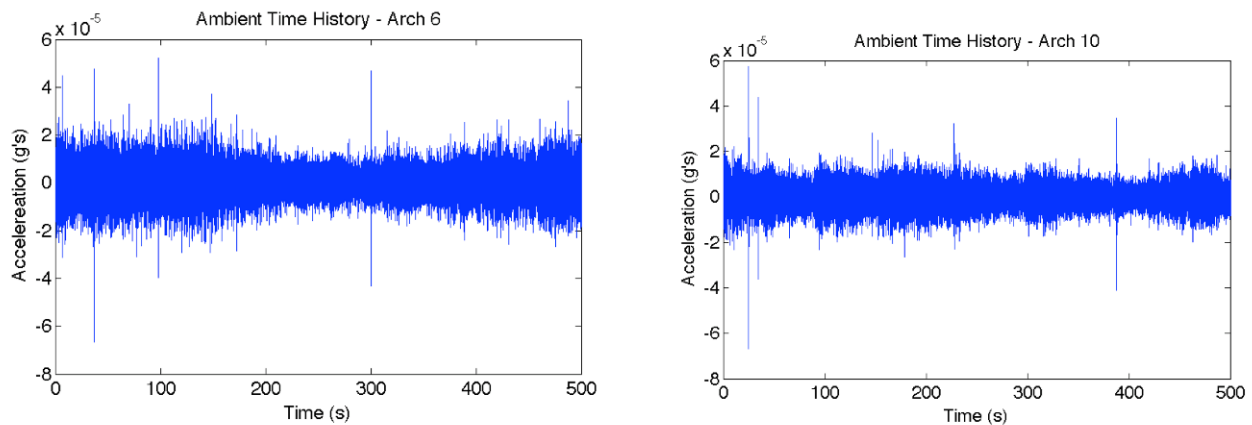


Figure 5. Sample time histories at Arches 6 and 10.

A combined analysis approach was used to identify local arch and global behavior in the entire dam. Fast Fourier transform (FFT) analysis was used to compute estimates of power spectral density (PSD), frequency response (FRF) magnitude and phase, and coherence. Maximum entropy method (MEM) analysis was also used to compute estimates of power spectral density. FRF-based estimates were used to evaluate the effectiveness of using the global references at Arches 3, 7, and 12 to identify overall dam behavior, and also provided response shape information for each arch. The identification of individual arch resonances and the ability to identify global (overall) resonances benefited from the use of the MEM-based spectral estimates.

Based on these comparisons, it was determined that the global reference measurements placed at Arches 3, 7, and 12 produced estimates with high coherence only for those arches in the vicinity of each reference location, and could not be used to identify response behavior across the entire dam. For instance, good coherence with the reference at Arch 7 was observed out to Arch 11, and dropped off quickly beyond.

The spectral estimates in each arch computed using the local reference for each arch provided significantly better coherence indicators. Sample frequency response function magnitude, phase, and coherence estimates computed from ambient responses are discussed below.

Spectral estimates across the dam suggest no measurable response behavior below 10 Hz. Coherence levels exceed 0.6 (the level above which confidence in estimates exists) over a 5 Hz band between 10-15 Hz, and in narrow bands beyond. Spectral estimates from the smaller arches near the ends of the dam show elevated coherence levels above 20 Hz, suggesting that broad-band ambient excitations exist that are capable of inducing dynamic response in these smaller, stiffer arches. The corresponding phase response is consistent with the relative absence of dynamic response below 10 Hz (jagged, near zero phase), followed by a nearly 180 degree shift in the vicinity of 15 Hz – indicative of classic 2nd order response behavior – followed by regions of transition that approach similar phase shifts. Phase responses that approach 180 degree shifts, but that fall short of the full 180 degree shift, are typically encountered in the testing of large civil structures and are indicative of damping or energy absorption mechanisms associated with radiation damping in adjacent foundation or at boundaries along the dam-foundation, dam-reservoir, and foundation-reservoir interfaces.

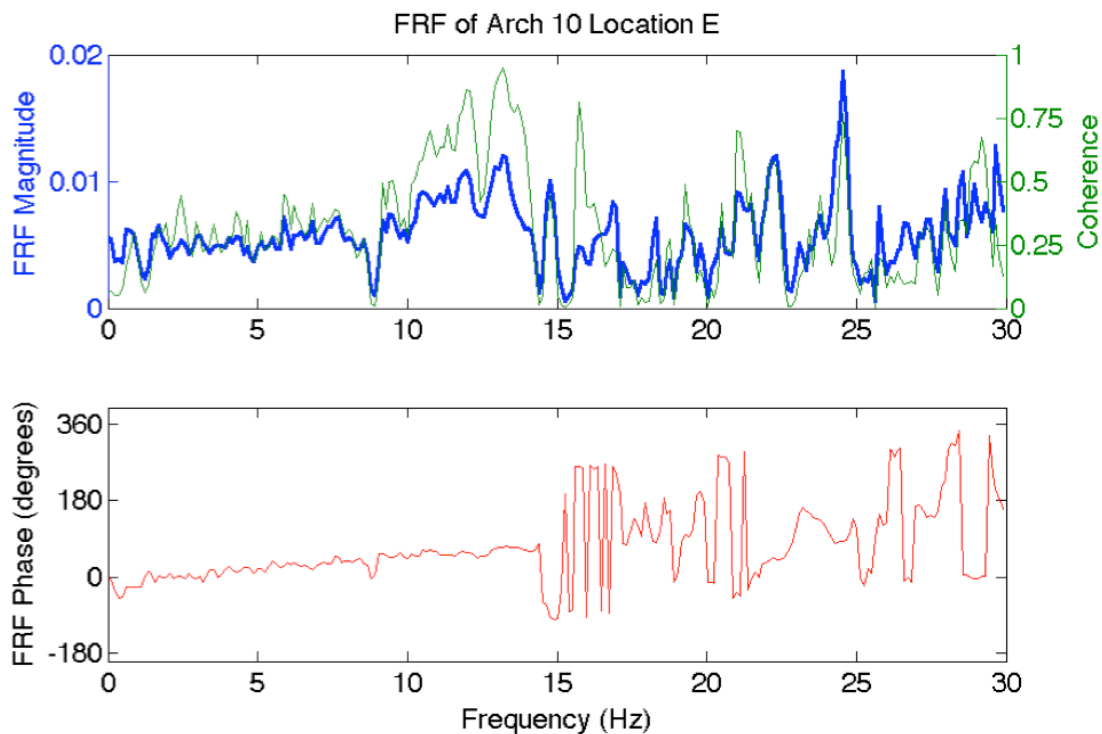


Figure 6. Spectral estimates at location E (See [Figure 2](#)) on Arch 10.

The spectral estimates in Arch 10 ([Figure 6](#)), in the tallest section of the dam, indicate elevated frequency response behavior below 15 Hz as compared to the responses in Arches 2 and 6. Coherence levels are also relatively higher, and coupled with the smooth phase response below 15 Hz, the data and corresponding spectral estimates in this arch are considered among the best observed in the dam. Excellent phase transitions are observed in Arch 10 above 20 Hz, which are probably influenced by the adjoining arches and buttresses in this section of the dam.

MEM-based estimates of power spectral density are shown in [Figure 7](#) at the same location (E) in Arch 10. The overall spectral character for each of these estimates is similar – each contains a number of resonant peaks, elevated responses over certain frequency bands, and relatively lower responses levels below 10 Hz. The MEM estimates reveal more spectral detail, particularly below 10 Hz, as compared to the FFT-based results in [Figure 4](#). This added detail can be leveraged by assembling MEM-based spectra in each arch to provide indication of dynamic behavior everywhere in the dam.

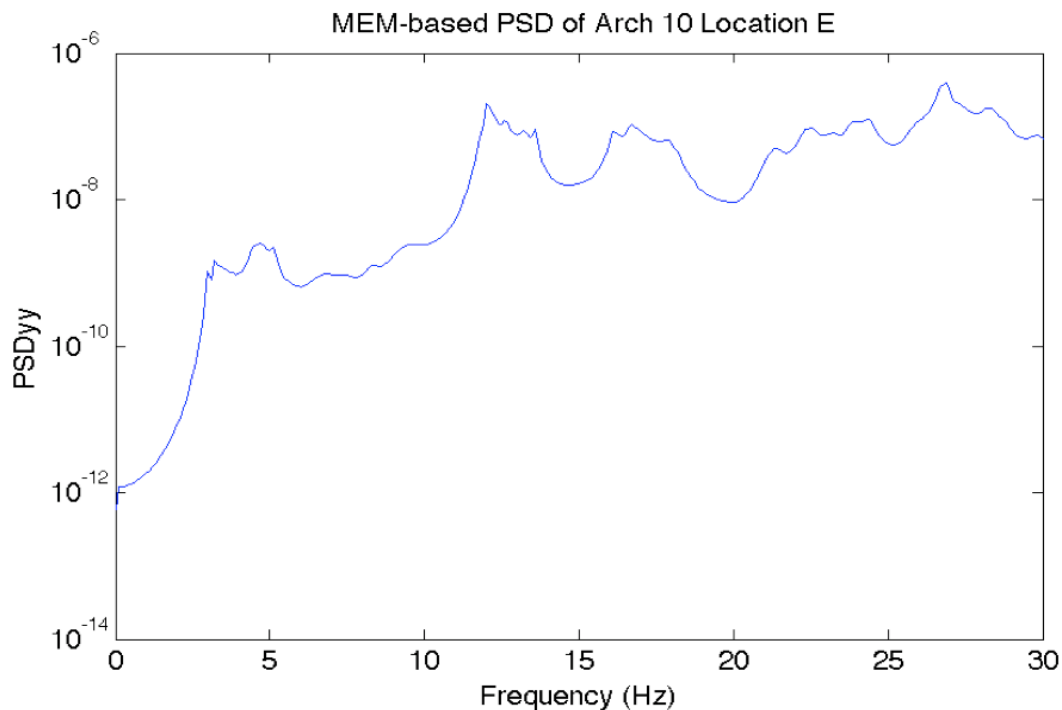


Figure 7. MEM-based spectral estimates at Arch 10.

Recommendations for Standardizing Ambient Test Procedure

Ambient testing of large civil infrastructure has not gained wide acceptance, particularly since excitation levels are characterized as low-level and not of the type typically associated with significant loading events such as earthquakes. Acceptance of the technique is complicated by the inability to characterize the “input” or excitation source, and for its reliance on “output” or response measurements only. When considered alongside the type of mathematical analyses that are required, the technique has not gained support outside of the traditional applications in aerospace where it is routinely employed.

Advances in computer and instrumentation technologies have enhanced the performance of sensors capable of capturing low-level response behavior, and magnitudes as low as a few micro-g’s of acceleration can now be measured with reliability. Furthermore, computational capabilities facilitate the analysis of large data sets which often result during ambient monitoring. These large data sets are used to reduce the dependency on sophisticated mathematical techniques that enhance the information extracted from response measurements. Techniques such as ensemble and block averaging, windowing, and time domain modifications to ambient responses are capable of producing spectral descriptions of characteristic system behavior with quantifiable confidence.

The examples presented illustrate the benefit that can be derived from ambient induced responses, and also highlight the accuracy and confidence with which extracted dynamic response behavior can be viewed. Standardized test procedures and guidelines for the selection and operation of sensors and signal conditioning circuitry, as well as guidelines for subsequent data processing techniques should be developed. These standards and guidelines will propel the industry’s understanding and confidence in the technique and in the application to large civil infrastructure.

References

- [1] W. E. Daniell, C. A. Taylor, "Effective Ambient Vibration Testing for Validating Numerical Models of Concrete Dams," *Journal of Earthquake Engineering and Structural Dynamics*, Vol. 28, No. 11, pp. 1327-1344, 1999.
- [2] Florian Scheulen, Elizabeth Ellis, Z.H. Duron, "Experimental and Finite Element Studies of the Forced Vibration Response of Big Creek Dam No. 7," submitted to Southern California Edison, October 2009.
- [3] Z. H. Duron et. al, "Ambient and Forced Vibration Survey of San Vicente Dam," submitted to Montgomery Watson Harza (MWH) and the San Diego County Water Authority (SDWCA), October 2007.
- [4] Hall, R. L., Woodson, S. C., and Nau, J. M. (1989). "Seismic stability evaluation of Folsom Dam and Reservoir Project; Report 3, Concrete gravity dam," Technical Report GL-87-14, U.S. Army Engineer Waterways Experiment Station, Vicksburg, MS.
- [5] Duron, Z. H., Flynn, E., von Gersdorff, N., Cho, A., and Chiarito, V. P. (2004). "Ambient vibration survey of Folsom Dam." Report prepared for U.S. Army Engineer Research and Development Center, Geotechnical and Structures Laboratory, by Engineering Department, Harvey Mudd College, Claremont, CA.
- [6] Z. H. Duron et. al, "Dynamic Testing and Numerical Correlation Studies for Folsom Dam," US Army Corps of Engineer Report, Engineer Research and Development Center (ERDC), Vicksburg, Mississippi, Report No. A966644, September 2005.
- [7] E. Ellis, Z.H. Duron, N. von Gersdorff, M. Knarr, "Dynamic Characterization of a Large Multiple-Arch Dam" presented at the USSD 30th Annual Meeting and Conference, Sacramento, California, April 2010

Stability Monitoring of Burning Structures Based on Fire-induced Vibration Monitoring

Ziyad H. Duron, Professor of Engineering, Harvey Mudd College, 301 Platt Blvd, Claremont, California 91711

Abstract

Monitoring stability loss in burning structures can provide firefighters with valuable information during operations. A fire-induced vibration based monitoring technique, developed under previously funded research and development efforts and in collaboration with the Building Fire Research Laboratory (BFRL) and the National Institute of Standards and Technology (NIST), has been field demonstrated in over 30 full-scale burn tests. The technique relies on the interpretation of characteristic response behavior induced in a burning structure that can be associated with changing structural conditions and stability loss. An overview of the important aspects necessary for a practical implementation in the field is presented.

Background

The Building Fire Research Laboratory (BFRL) at the National Institute of Standards and Technology (NIST) has funded fundamental research in the area of structural collapse for the purpose of improving firefighter safety over the past decade. Details of the origins of a vibrations-based approach to structural stability monitoring, of the theoretical background that assists the interpretation of observational evidence of stability loss, and of results from numerous full-scale burn tests in which structures have been burned to collapse are reported in References [1,2].

Motivation for the continued development of the monitoring approach intensifies with each firefighter injury or fatality associated with structural collapse¹. In recent history, no single event has drawn more attention to the technology and methodology of modern firefighting techniques than the collapse of the World Trade Center Towers. The collapse of those structures and the corresponding loss of life revealed vulnerability in the absence of real-time health monitoring that may have informed firefighters of the weakening structural conditions around them. Since September 11, 2001, communications and coordination among support agencies during firefighting operations have benefited from advances in computer and information technologies, and it is not uncommon to have a centralized firefighting command with access to media, police and emergency agency information feeds to aid in deployment, safety, and tactical decision making during operations. The fact remains, however, while audio communications and some video tracking have greatly advantaged modern firefighting techniques, virtually no information is currently available from the structures themselves. In the absence of structural response information, firefighters continue to have no real basis for monitoring changing conditions in a structure under fire and continue to rely on “field-learned” heuristics.

Improved understanding and use of observed structural behavior can inform firefighting operations and lead to a practical and reliable collapse monitoring technique in the field. If successful, the field procedures could be extended to other weakened or damaged structures – independent of the fire or other event of hazard that might have induced the damaged state of the structure.

Considerations for a Practical Field Monitoring Approach

Fire-induced vibration based structural health monitoring relies on a fire’s ability to supply sufficient spectral energy to excite a structure’s natural characteristic motions. The idea that fire can induce measureable characteristic behavior in a burning building has been at the heart of a research and development effort that has resulted in the design and development of fire-sensor technologies, and that has been demonstrated in over 30 full-scale burn tests. Testing has been conducted on a large warehouse, single family homes, and strip mall structures made of wood, steel and masonry. Through these experiences, a large database of measured fire-induced responses has been collected and analyzed for trends that track observable evidence of stability loss leading to ultimate collapse.

¹ According to the U.S. Fire Administration Firefighter Fatality Database (http://www.usfa.dhs.gov/applications/ffmem/tally_report_results.jsp), three hundred sixty-two firefighters died in collapsed structure incidents during the four year period between 2001 and 2005.

System stability theory provides an invaluable context for the interpretation and understanding of the measured field trends by allowing the investigation of system performance to be conducted apart from an exact knowledge of the loading, or excitation, provided. In fact, much can be learned about a system's stability from examination of response measurements alone if the responses are "constructed" of that system's true characteristic behavior. The effectiveness of the current fire-induced vibration approach lies in the use of fire-sensor technologies that capture structural response in the form of combined random and transient behavior that can be prepared for trend extraction. The accompanying algorithmic development has evolved into a field-ready tool that allows visual inspection of the measured responses and – more importantly – of the stability indicators used to track the structure's performance as it burns.

A practical field approach will result if these algorithms produce near real-time indicators of impending stability loss and that contribute to improved firefighter safety.

The advent of wireless, mem, and micro-computer technologies provides tools sufficient for the design and development of a wireless field-ready stability monitoring tool for burning buildings. Using the documented performance of the original wired approach as a benchmark (Ref [2]), a wireless system has been developed to reproduce the same stability indicators of the wired system. Burn tests on simple wood frame structures have produced results that indicate the practicality of the wireless system in a manner consistent with both observed and wired system behavior.

A practical field approach will result if instrumentation is available that can be easily attached to a burning building, can transmit reliable and characteristic information, and that differentiates between fire-induced structural response and firefighter induced behavior.

Practical Insights from Full-Scale Burn Tests

The interpretation of fire-induced vibration responses is complicated by the fact that fire, when allowed to develop into a significant loading event, becomes a random-like and broad-band (spectral) excitation. These random and broad-band excitations produce structural responses with similar signal characteristics which can be difficult to analyze under real-time and often stressful situations in the field. Additional complications stem from a structure's inherent redundancy and its tendency to "redistribute" loads and to create new load paths during burn. The problem of interpreting measured structural response under burn conditions becomes even more complex when one considers that structures actually exhibit periods of increased strength or stability at times, which can provide a false sense of "safe operations conditions" in the field.

Broad-band Response Behavior

The complex nature of measured fire-induced vibrations is perhaps best demonstrated through the monitoring of a "simple" wood frame structure. Shown in Figure 1 is a frame constructed using 2x6 wood members and loaded at the center of the top cross-beam with approximately 350lbs. The connections are nailed metal "L" brackets, and the columns are secured in quick-setting concrete at the base. Fire loading is applied at one of the top corner connections using the torches shown in the figure, and the resulting fire-induced response shown was acquired on the left vertical column member during burn. The test was actually conducted over a time sufficient for total collapse of the top cross-beam which is characterized by the large spike seen in the measured response near 1200 secs.

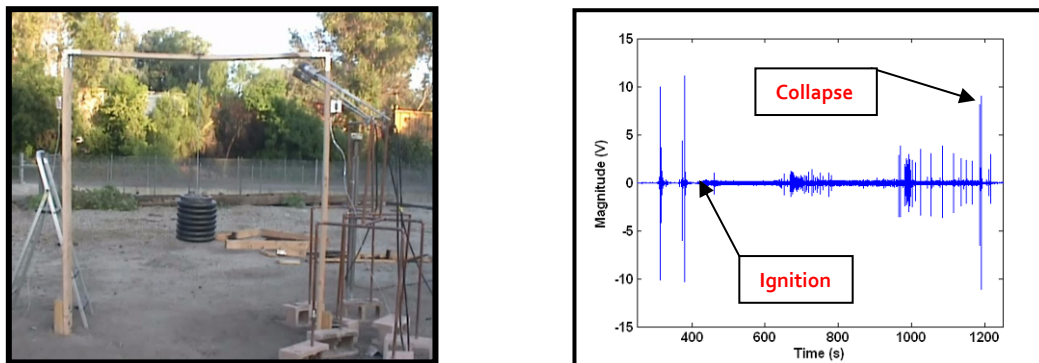


Figure 1 - Burn test on a simple wood frame and corresponding response.

The time of ignition (i.e. the start of the fire-induced portion of this test) is indicated on the measured response, and the subsequent behavior is dominated by both random-like and transient characteristics. The random nature of the response stems from the broad-band spectral energy of the fire loading, and the transient nature (i.e. spikes) results from the changing conditions in the structure itself. In fact, there is a clear transition that occurs in the measured response in the time approaching 1000 secs where “mostly” random behavior turns into “mostly” transient responses leading to ultimate collapse. In terms of well-known systems engineering, the wood frame structure and its response are clearly showing time-varying behavior. The transient spikes are believed to be associated with stick and slip movements of the nails being pulled out of the connection as collapse nears.

The question remains – “What characteristics in this response are the ones that most closely track the changes that indicate stability loss and that can be used to indicate early warning of impending collapse?”

Broad-band Spectral Trends

Time-varying behavior results when elements that make up the inherent properties or characteristics of a system change during operation. For example, a rocket’s resonant frequencies will change throughout flight as a result of changing fuel mass during burn. A burning structure is somewhat different in that while mass is certainly lost, stiffness is also changing which has an overall effect of altering the frequency range where trends that correlate to stability loss can be observed.

In the early stages of the research, frequency trends that tracked stability loss were thought to coincide or fall within a structure’s fundamental resonant frequency range – a range that for most structures falls well below 50 Hz. However, numerous tests on large civil structures have shown weak correlation between damaged states and changes in resonant frequencies (Ref [3]). This weak correlation was also observed in the various full-scale burn tests conducted during the early stages of this effort.

A breakthrough was achieved when it was realized that the broad-band nature of the fire produced similarly broad-band response behavior that was predominately associated with motions at the structural connections. Time-frequency analyses of measured fire-induced responses over much broader frequency ranges revealed trends that actually tracked observable and impending collapse mechanisms during burn. As an example, the corresponding time-frequency analysis result from the simple wood frame test (Figure 1) is shown in Figure 2.

The result shown in Figure 2 was obtained using a series of digital band-pass filters to analyze the measured response in Figure 1. The contour plot shows filter “outputs” over a 400 Hz frequency range where a number of frequency trends are observed.

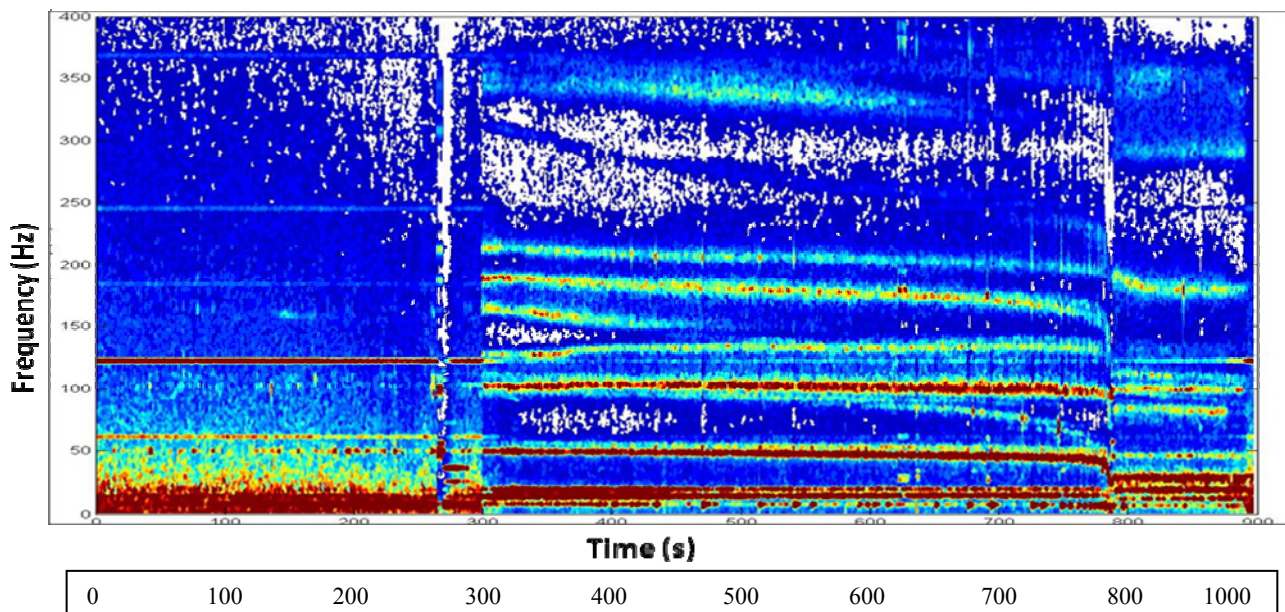


Figure 2 - Time-Frequency analysis of fire-induced vibration response. (Vertical axis is Hz, Horizontal axis is seconds).

As indicated in Figure 2, ignition occurs near 300 secs, and observable frequency shifts are seen in the frequency bands above 25 Hz. For the simple wood frame structure, resonant frequencies were known to be below 25Hz, and the contour plot shows apparent uniform (i.e. unchanging) frequency response during burn in this frequency band. However, as shown in the time-frequency analysis, significant and changing frequency content is captured above 50 Hz, and the higher frequencies – those above 150 Hz - seem to indicate the largest and most visible shifts. It is important to note that this finding is not limited to the results from this simple wood frame test, and in fact has been observed in responses acquired from burn tests on full-scale structures. In addition, this result does not suggest that frequencies below 50 Hz do not exhibit similar trends – rather, it demonstrates that important trend information is available at higher frequencies. As a result, new algorithms were developed to produce stability indicators based on these higher frequency trends, and modifications were made to the fire-sensor in order to provide better high frequency information.

Application to Wood Trusses

Two demonstration burn tests were conducted in collaboration with WTCA at the Iowa Fire Service Training Field. Diagrams of the structures designed and built by WTCA are shown in Figure 3, which were used to conduct demonstration burns aimed at comparing truss performance against joist performance.

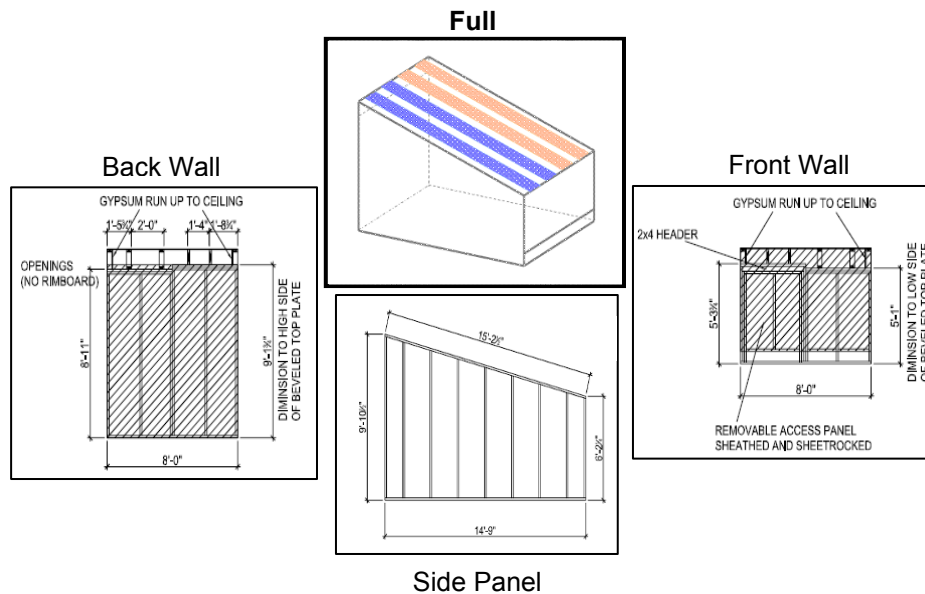


Figure 3 - Structural drawing developed by WTCA for demonstration burns.

Pictures of the structure instrumented with fire-sensors, and in the early stages of the burn are shown in Figure 4. Although not evident from either the drawing or the pictures, the right side of the roof is supported by wood trusses, and the left side of the roof is supported by joists. Oriented strand board (OSB) was used as exterior sheathing and in the roof diaphragm, and roof loads were applied to achieve equivalent stress levels in both trusses and joists.



Figure 4 - WTCA burn test. Fire-sensors are shown installed and protected using aluminum wrapping.

Sample fire-induced vibration responses acquired during the test are shown in Figure 5, and as can be seen, the responses are characterized by random-like and transient behavior.

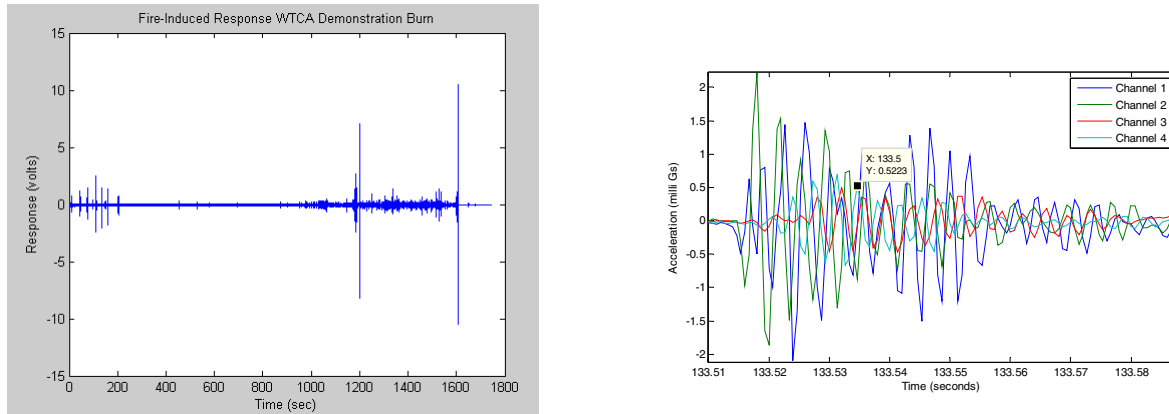


Figure 5 - Sample time histories of fire-induced vibration responses acquired during the WTCA burn demonstrations.

A close-up of the response behavior (right, Figure 5) reveals the decaying sinusoidal character of the transient portions in the signals associated with both truss and joist behavior². The high signal-to-noise ratio and quality exhibited in these responses provides evidence of the fire-sensor's ability to capture transient events during burn even for this relatively lightweight structure³. A corresponding time-frequency analysis conducted on one of these responses is shown in Figure 6.

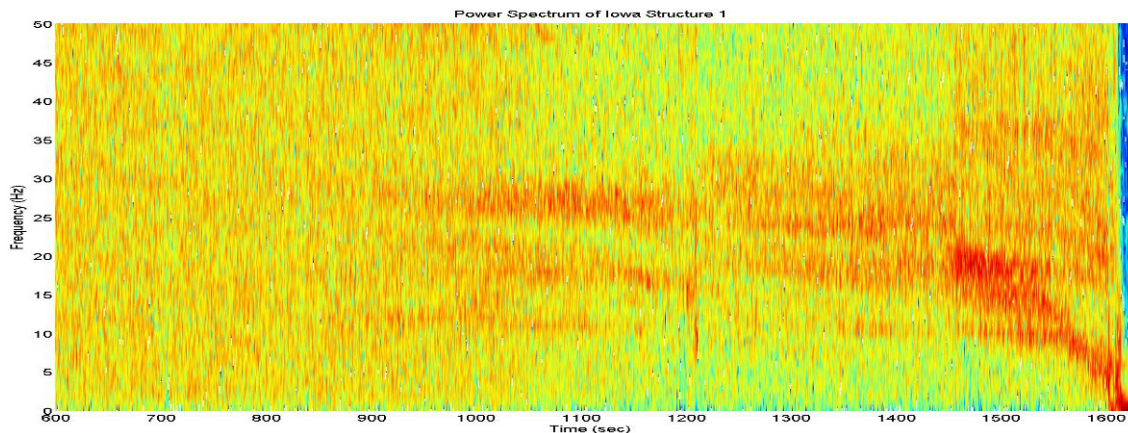


Figure 6 - Time-frequency analysis of measured response during WTCA burn tests.

Although changes in frequency (i.e. frequency trends) are observed, the result is judged to be “too noisy” and does not provide sufficiently clear indication of stability loss. Better indicators are obtained using impulse tracking and instantaneous frequency, as shown in Figures 7 and 8.

² Four fire-sensors were installed during this test. Two sensors (front/back) across the truss portion of the structure, and two sensors (front/back) across the joist portion.

³ Transients in measured structural response typically result from movements of large, heavily loaded structural members; however, these transients demonstrate the fire-sensor's ability to capture behavior associated with relative motions across the end connections in the structure since there are no large members present.

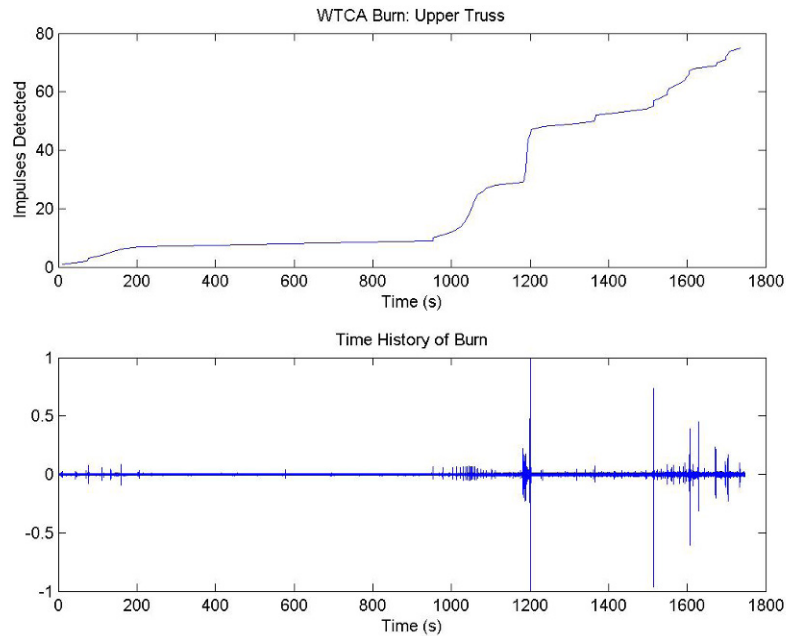


Figure 7 - Stability indicator for WTCA burn tests based on impulse tracking.

The significance of the indicator in Figure 7 rests with the strong correlation between step-like changes in the index and the presence of transient peaks in the fire-induced response (bottom response in Figure 7 above). The jump in indicator value at 1000 secs signals a transition from a “non-changing” period (prior to 1000 secs) to a period of “elevated response”. The result shown is based on fire-sensor response across the truss supported portion of the structure, and could be used to provide indication of early warning in the context of irreversible changes in the structure. Additional insights into truss and joist performance are obtained from stability indicators that track instantaneous frequency.

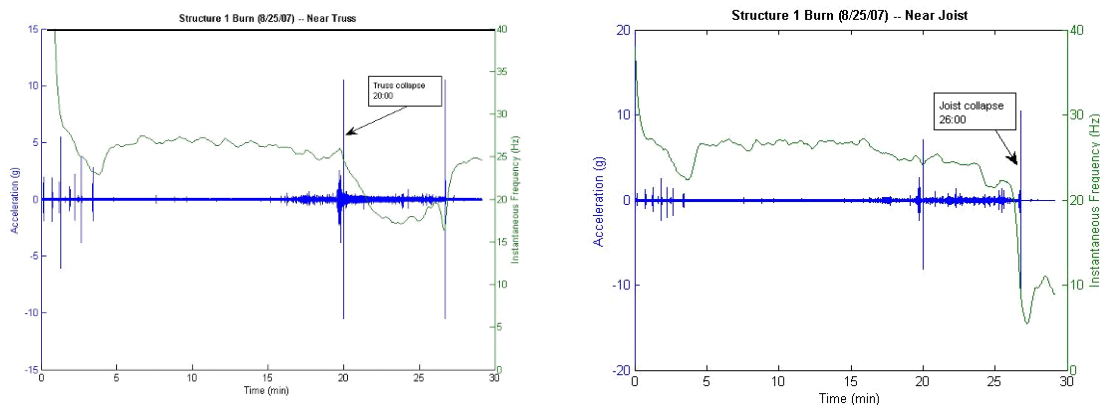


Figure 8 - Stability indicators for truss (left) and joist (right) performance during WTCA burns.

The results shown in Figure 8 indicate periods during the burn when “unchanging” conditions exist in both truss (left, Figure 8) and joist (right, Figure 8) response (i.e. between 5-15 mins into the burn). Beyond 15 mins, however, conditions begin to change in the truss and ultimately collapse is observed near 20 mins – whereas, the joist indicator enters a period of irreversible decline after 15 mins leading to collapse at 26 mins. Based on these results and for this particular test, the joist indicator provided additional early warning of changing conditions over the truss indicator. The significance of these results is that responses were actually acquired on the exterior walls of the structure and were not made directly on either the trusses or joists, and that for both structural support systems, indication of changing conditions leading to ultimate collapse is observed.

The overall quality in the stability indicators (impulse tracking and instantaneous frequency in this case) and the excellent correlation with the observed collapse during burn demonstrate once again that information can be extracted from fire-induced vibration responses to evaluate impending collapse in a burning structure.

Development of a Real-Time Structural Stability Sensor System (RTS4)

The Real Time Structural Stability Sensor System (RTS4) is a tool designed to assist firefighters in critical situations by accessing structural information that would otherwise be unavailable. The system is designed to enhance a firefighter's ability to assess and to evaluate the structural condition of a burning structure. The current RTS4 system is a base station and a network of sensors. The Base Station is a laptop connected to a wireless radio, which pulls information from the network and packages it into useful information via a Windows-based Graphical User Interface (GUI). The fire-sensors are designed to acquire fire-induced vibration responses and to compute stability indicators that track changes in structural stability. The design facilitates the digital acquisition of fire-induced structural response and the computation of stability indicators that are streamed in real-time over an ad-hoc wireless network. A picture of the prototype RTS4 system complete with base station and two fire-sensors is shown in [Figure 9](#).



Figure 9 - RTS4 prototype system.

Fire-induced vibrations are acquired using an accelerometer selected for its ability to accurately sense low-level random and transient motions typical of structures subjected to fire. The accelerometer output is sent to a microprocessor with built-in digital signal processing capability and to a secure digital (SD) memory card for storage. The use of a Blackfin processing unit allows the handling of complex numeric tasks in near real-time sufficient for the field application. A subset of the stability indicators previously investigated and reported in Refs [1, 2] has been implemented in the current wireless design. The Blackfin's computational results are then sent to a XBEE PRO providing a wireless transmission capability to a base station.

Implications for Future Work

A wireless real-time structural stability sensor system (RTS4) has been developed that can be used to track changes in structural stability in burning structures. The system consists of fire-sensors capable of sensing fire-induced vibrations, and that can be attached directly to the exterior of the burning building. Stability indicators are computed using a powerful micro processor inside the fire-sensor unit which can be transmitted to a base-station for visual display. System operation has been verified in bench tests of cantilevered beam and vibrating platform response behavior. System performance in the field during a series of full-scale demonstration burns has been completed. Data from those tests are currently under evaluation, and the performance of the wireless systems will be evaluated. Researchers also plan to deliver RTS4 units to fire departments and to BFRL/NIST for further evaluation which should lead to practical improvements over the current design.

References

1. Z.H. Duron, et.al, "Early Warning Capabilities for Firefighters: Testing of Collapse Prediction Technologies," NIST GCR 03-846, February 2003.
2. Z.H. Duron, et.al, "Fire Induced Vibration Monitoring for Building Collapse: Final Report," NIST GCR 06-885, October 2005.
3. S.W. Doebling, C.R. Farrar, et.al, "Damage Identification and Health Monitoring of Structural and Mechanical Systems from Changes in their Vibration Characteristics: A Literature Review", Los Alamos National Laboratory Report, LA-13070-MS, May 1996.

Application of Energy Methods in Mechanical Shock to Study Base Excited Nonlinear System Response

J. Edward Alexander
BAE Systems, US Combat Systems
4800 East River Road
Minneapolis, MN 55421
ed.alexander@baesystems.com

Abstract

The paper describes a structural dynamic analysis of a notional ground combat vehicle instrumentation display rack. The rack was subjected to hypothetical base accelerations typical for vehicle mobility loads, but not actual data. The rack concept was used as a surrogate to study the accuracy of an approach using an acceleration time-history synthesized to be compatible with a prescribed shock response spectrum (SRS). The SRS was determined from an original (given) acceleration-time history. Both the original and the synthesized time histories were applied to a simple lumped mass six degree-of-freedom (6DOF) model of the display rack. The rack was modeled with both linear and nonlinear shock mounts. Comparisons of displacements were made using the original and synthesized time histories at five different system frequencies. At certain system frequencies there was good agreement, poor agreement at other frequencies. Evolving energy methods in mechanical shock were used to explore the root cause of the frequency based variability in the system response. Input energy spectra were generated for each time history and compared to the maximum energies from the 6 DOF model at each system frequency.

INTRODUCTION

Numerous authors have studied the methods to synthesize an input base acceleration time history to be compatible with a prescribed shock response spectrum (SRS) for modeling structural dynamic systems (Scanlan and Sachs [1], Gasparini and Vanmarcke [2], Alexander [3]). My past research [3] has been to use the shock response spectrum (SRS) from a prescribed acceleration signal to synthesize an artificial acceleration time history that has the same SRS. Past studies have shown that valid results can often be obtained for a linear MDOF model, but if nonlinearities are introduced, the results from the synthesized acceleration-time history can under predict, or over predict, the response depending on the characteristics of the synthesized time-history and the nonlinearity. The objective of this study was to apply evolving energy methods in shock (Uang and Bertero [4], Edwards [5]) to determine if information can be gleaned from energy comparisons to understand why nonlinear model results do not match at certain frequencies.

PART I - Synthesis of Acceleration Time Histories and Transient Results

1A – Base Accelerations

A notional base acceleration time history was developed to be generally consistent with what would be expected in a tracked combat vehicle subjected to mobility loads. This given, or prescribed, acceleration signal is termed “*Sim6m*” (Figure 1). The maximum amplitude and duration of *sim6m* is 1297.4 in/sec² and 2.0 seconds, respectively. The shock response spectrum (SRS) of *Sim6m* is plotted in Figure 2 as the magenta curve labeled “*target SRS*.”

A second acceleration signal termed “New2” with a similar peak amplitude ($1,417.6 \text{ in/sec}^2$) and the same duration is plotted in Figure 3. *New2* is an acceleration time history that was synthesized to not only have a similar peak and duration as *Sim6m*, but also the same SRS. The SRS of *New2*, shown as the blue curve in Figure 2, matches that of *Sim6m* within 2.5% averaged over all frequencies.

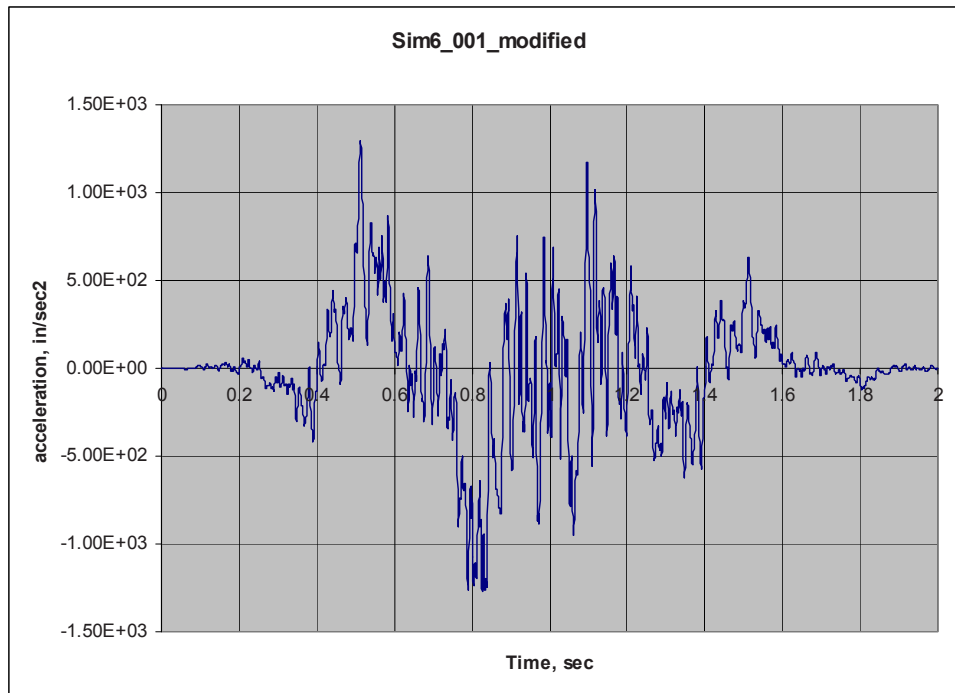


Figure 1 – Acceleration-Time Signal of *Sim6m*

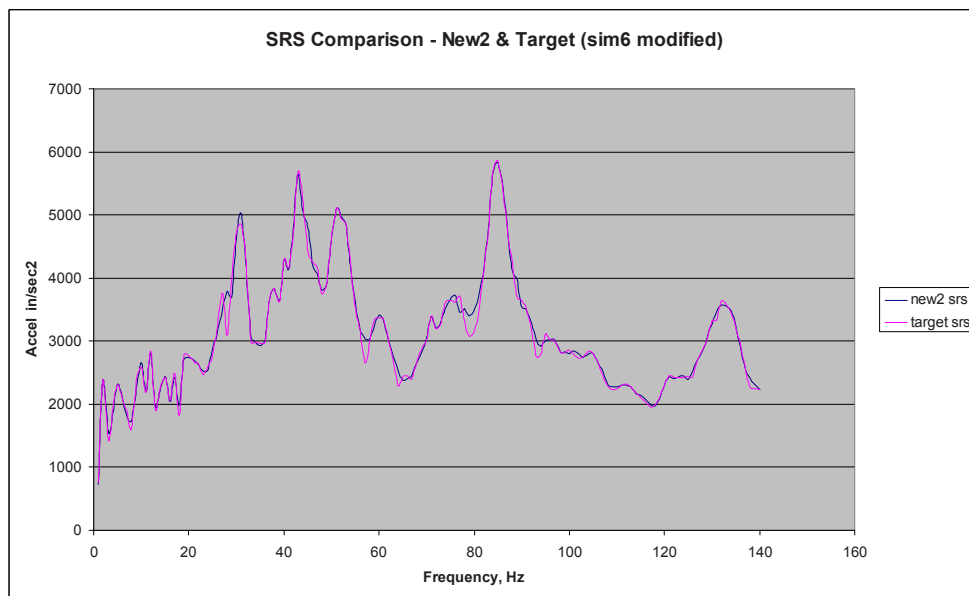


Figure 2 – SRS of *Sim6m* and *New2* (0 damping)

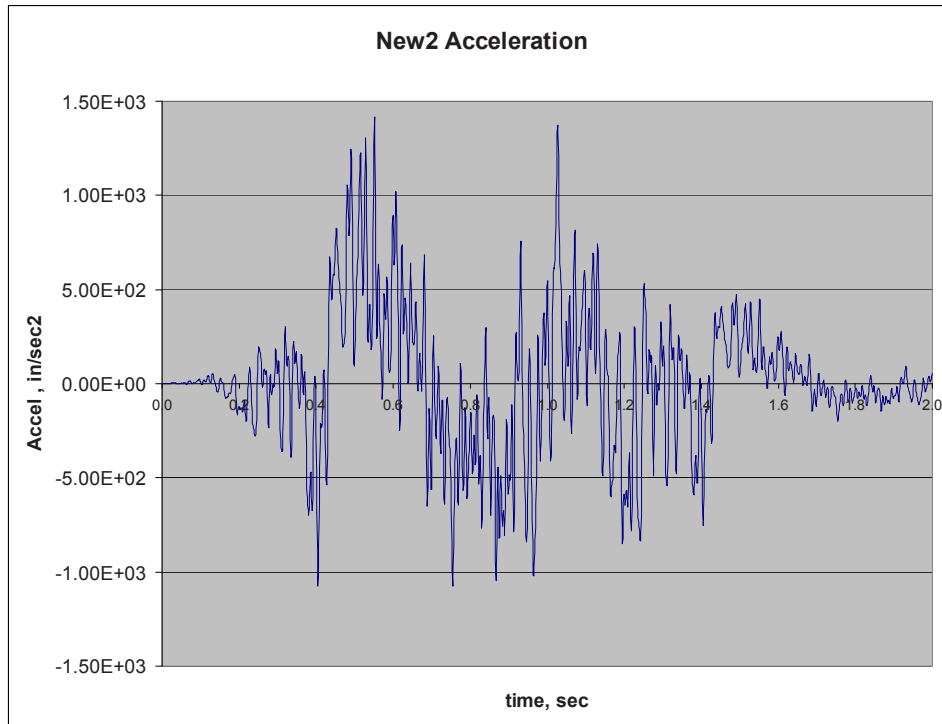


Figure 3 - Acceleration-Time Signal of New2

The approach used to synthesize *New2* is the summation of sinusoids of differing amplitudes and random phase angles. The overall rise and decay is governed by an envelope function, $E(t)$.

$$\ddot{u}_b(t) = E(t) \sum_{n=1}^N A_n \sin(\omega_n t + \phi_n) \quad (1)$$

Using (1) it is possible, by iteration of A_n at each frequency n , to synthesize a base acceleration time history $\ddot{u}_b(t)$ that is compatible with a prescribed SRS. It is noted, however, that while the synthesized acceleration $\ddot{u}_b(t)$ will be compatible with the SRS, it will not be unique. This approach to synthesize an acceleration-time history to match a prescribed SRS is described in more detail in References [1], [2] and [3].

IB – Surrogate 6 DOF Model

A conceptual ground combat vehicle instrumentation display rack, [Figure 4](#), was used as a surrogate for this study. The solid model was approximated with a 6 DOF (three translations, three rotations) three mass model shown in [Figure 5](#). The comparative results from the original *Sim6* and synthesized *New2* base accelerations were determined based on the response of the 6 DOF model.

The three lumped masses are connected via beams of stiffness EI . The lumped masses on the ends are connected to the base via shock mounts. Both linear and nonlinear shock mounts are included to study linear and nonlinear system behaviors. The six degrees of freedom correspond to three vertical translations and three in-plane rotations of each of the masses, $u_i(t)$ and $\theta_i(t)$ respectively. Relative translations, defined in [Figure 5](#), are the difference between the absolute translations of each mass and the motion of the base. Excitation to the model comes from base accelerations *Sim6m* and *New2*.

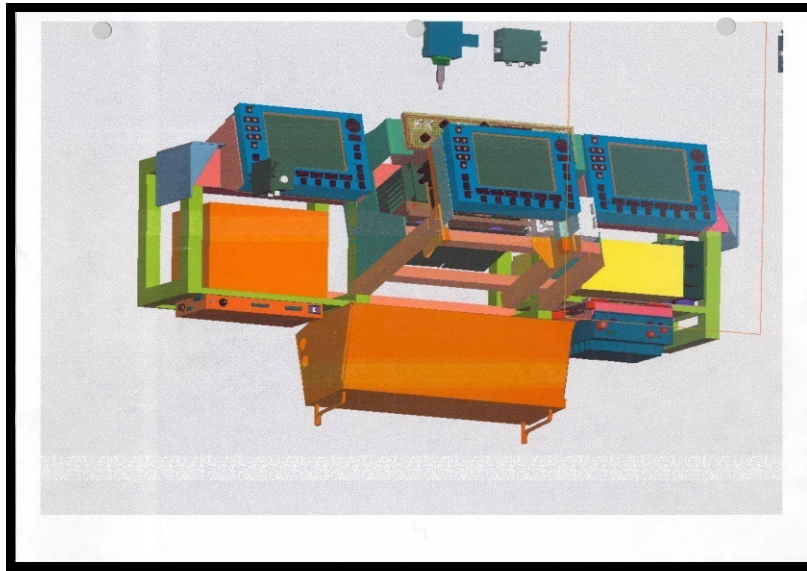


Figure 4 – Ground Combat Vehicle Instrumentation Display Rack Solid Model

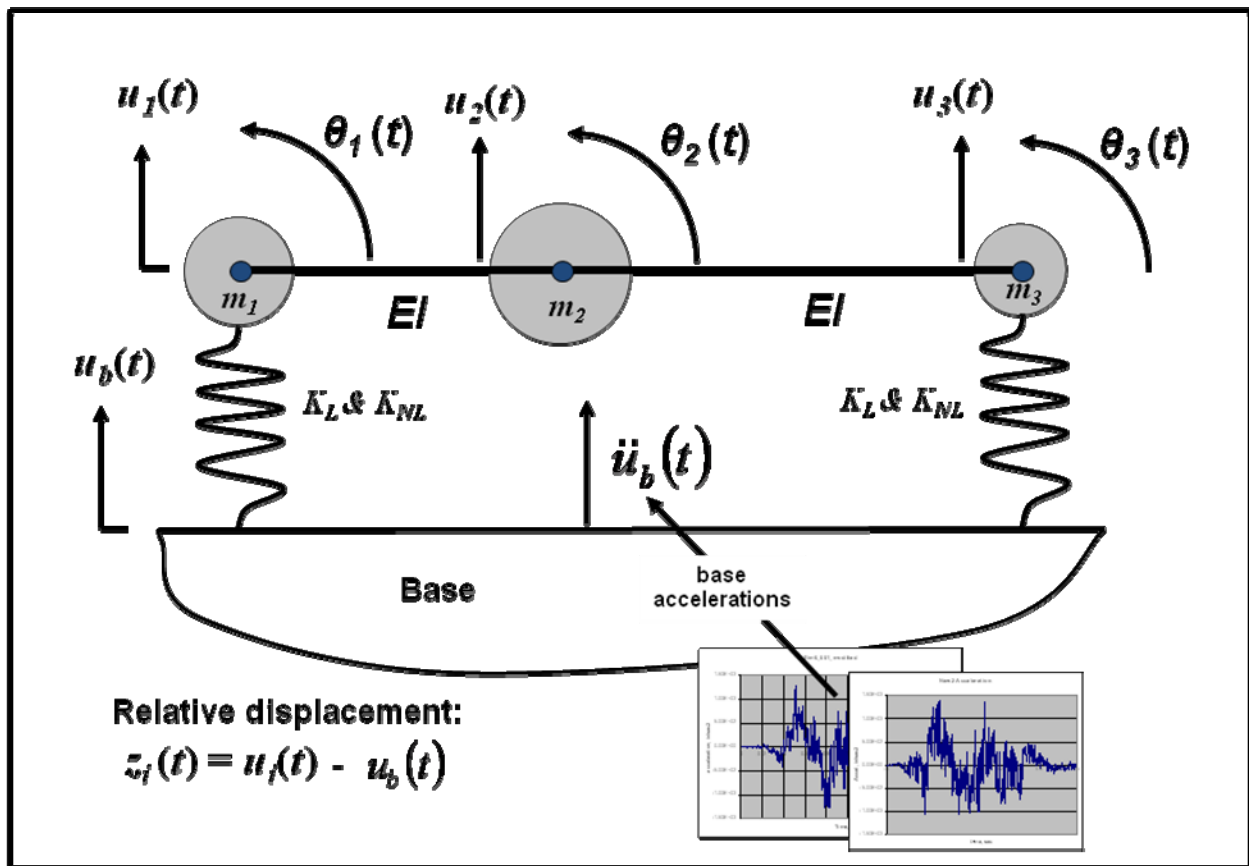


Figure 5 – 6 DOF Model of Instrumentation Display Rack with Linear and Nonlinear Shock Mounts

The values for the masses, rotational inertias, EI , beam lengths, and shock mount stiffness were approximated from display rack solid model. Six equations of motions were formulated by placing each of the three masses in

translational and rotational dynamic equilibrium, resulting in six equations. Arranging equations in matrix form results in the following equation of motion for the linear system.

$$\begin{bmatrix} [m] & 0 \\ 0 & [J] \end{bmatrix} \begin{Bmatrix} \ddot{z} \\ \ddot{\theta} \end{Bmatrix} + \begin{bmatrix} k_{zz} & k_{z\theta} \\ k_{z\theta} & k_{\theta\theta} \end{bmatrix} \begin{Bmatrix} z \\ \theta \end{Bmatrix} = - \begin{bmatrix} [m] & 0 \\ 0 & [J] \end{bmatrix} \begin{Bmatrix} 1 \\ 0 \end{Bmatrix} \ddot{u}_b(t) \quad (2)$$

$$[m] = \begin{bmatrix} m_1 & 0 & 0 \\ 0 & m_2 & 0 \\ 0 & 0 & m_3 \end{bmatrix} \quad [J] = \begin{bmatrix} J_1 & 0 & 0 \\ 0 & J_2 & 0 \\ 0 & 0 & J_3 \end{bmatrix} \quad k_{ij} = f(EI, L_a, L_b, K_L)$$

IC – Linear Model Modal Extraction

A modal extraction of the linear model was performed to determine the frequencies, mode shaped, participation factors and modal masses of the system. The modal properties of the system for each of the six modes are given in [Tables 1 and 2](#) and the first three mode shapes are shown graphically in [Figure 6](#). It is evident from the modal properties that the system response is heavily dominated by the first mode, which has 94% of the mass and largest participation factor. The three translational displacements for mode 1 are in phase based on the mode shapes, where mass 1 has the largest displacement and mass 3 the smallest. Mode 2 is a “teeter-totter” type mode shape where masses 1 and 3 are out of phase and mass 2 is generally in a null position. Mode 3, with negligible modal mass and a significantly higher frequency, is the only mode with bending of the beam connecting the masses.

Modes	1	2	3	4	5	6
Frequency, <i>HZ</i>	4.7967	6.2921	42.4688	93.9889	158.9739	198.6559
Participation Factors	1.3994	-0.3648	-0.0129	-0.0010	-0.0009	0.0001
Modal Mass <i>lb-sec²/in</i>	1.9584 *	0.1331	0.0002	0	0	0

Table 1 – Modal Properties of Linear System

Mode	1	2	3	4	5	6
Z_1	0.8538	0.5511	-0.4649	0.0078	-0.2644	0.4527
Z_2	0.6586	-0.2339	0.4938	0.1521	0.4658	-0.1808
Z_3	0.4174	-1.1213	-0.4521	-0.3576	-0.6604	-0.2659
Θ_1	-0.0058	-0.0238	0.0450	0.0594	-0.0489	0.0565
Θ_2	-0.0061	-0.0236	0.0056	-0.0501	0.0329	0.0661
Θ_3	-0.0065	-0.0235	-0.0494	0.0478	0.0388	0.0121

Table 2 – Mode Shapes of Linear System

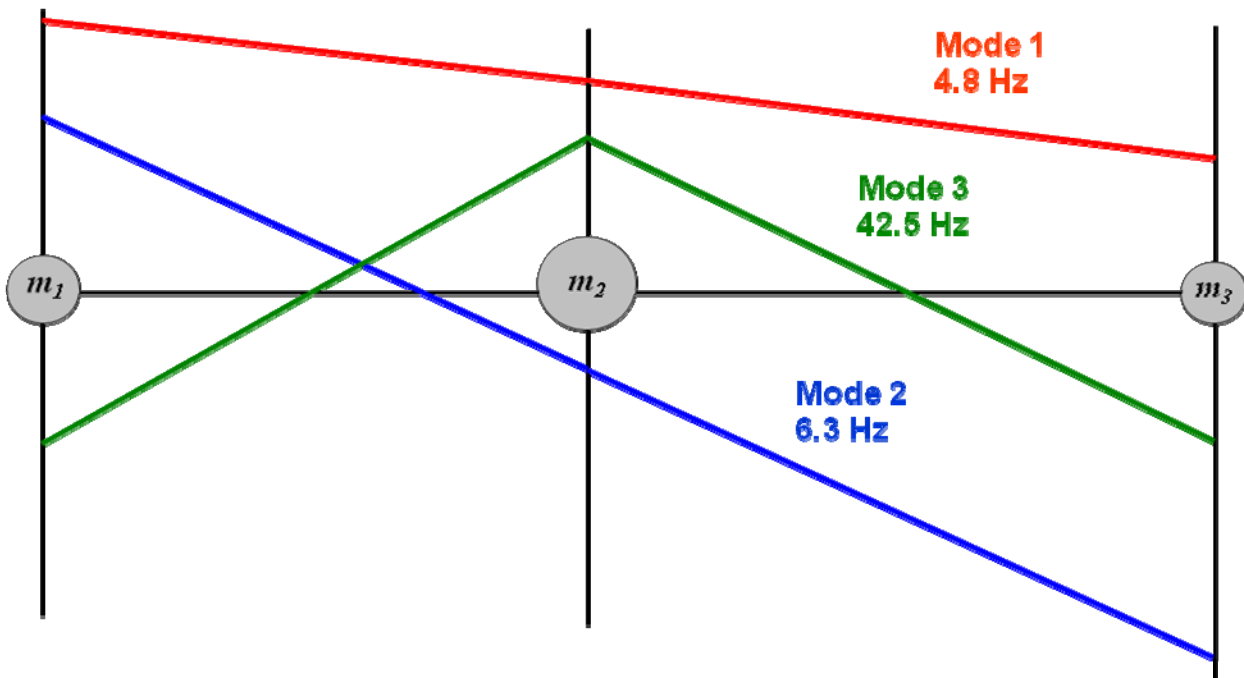


Figure 6 – Mode Shapes for First Three Modes

ID – Linear Model Transient Analysis

A transient analysis of the linear version of the 6 DOF model was performed. The model was exercised using both *Sim6m* and *New2* base accelerations. The relative displacements are plotted in Figures 7 and 8, respectively. As expected from the modal properties, mode 1 highly dominated. As shown in the figures, the displacements were all in-phase as expected, with mass 1 having the largest displacement and mass 3 the lowest. The frequency of vibration from the transient analysis corresponds to the mode 1 frequency determined from the modal extraction.

Another significant finding is that the magnitudes of the displacements resulting from the two base accelerations are close. This result was expected given model linearity and that the two base accelerations had the same SRS, similar shapes, close peak magnitudes and identical durations. Table 3 lists the numerical values for the translation and rotations of the three masses. In all cases, the response of the linear model to *Sim6m* base acceleration is slightly higher than from those resulting from the *New2* base acceleration. The overall averaged ratio of displacements (translational and rotational) resulting from the *New2:Sim6m* base input is 91.5%.

As a check on the analytical model formulated from the equations of motion described in Section 1B, an ABAQUS finite element models was also developed as a check. While there are small differences between the analytical and finite element model maximum displacements, the agreement is close enough to ensure correct derivation of the analytical model. Results from both the analytical model and the ABAQUS model are included in Table 3.

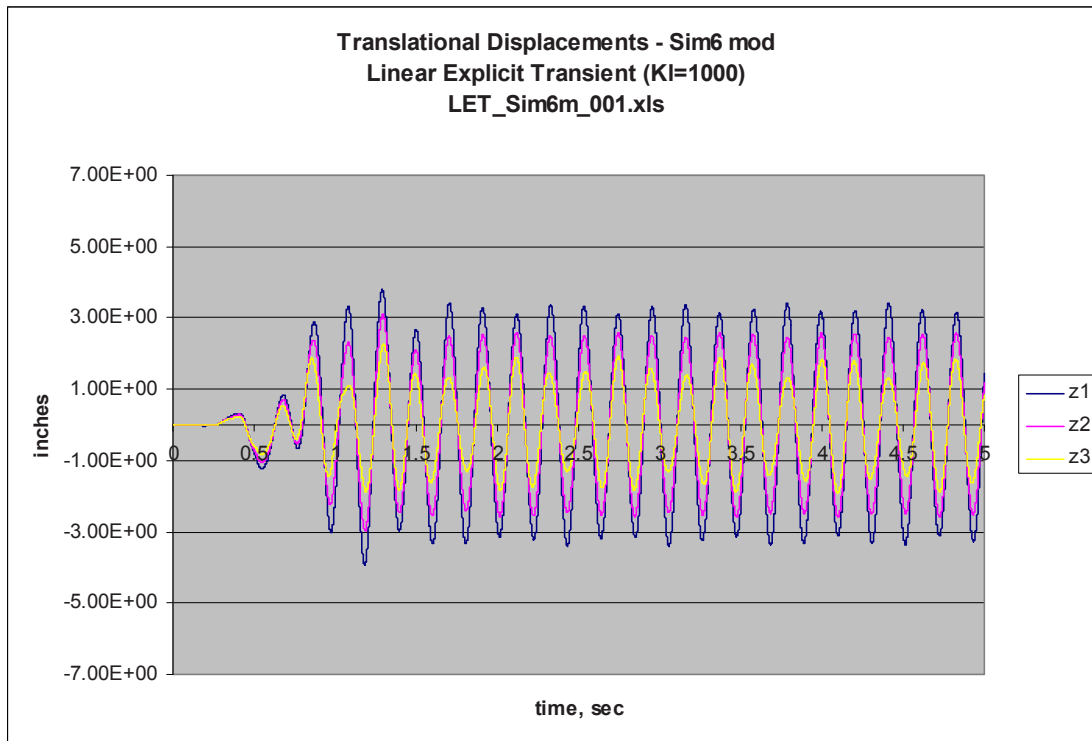


Figure 7 – Relative Displacements Resulting from *Sim6m* Base Acceleration, Linear Model

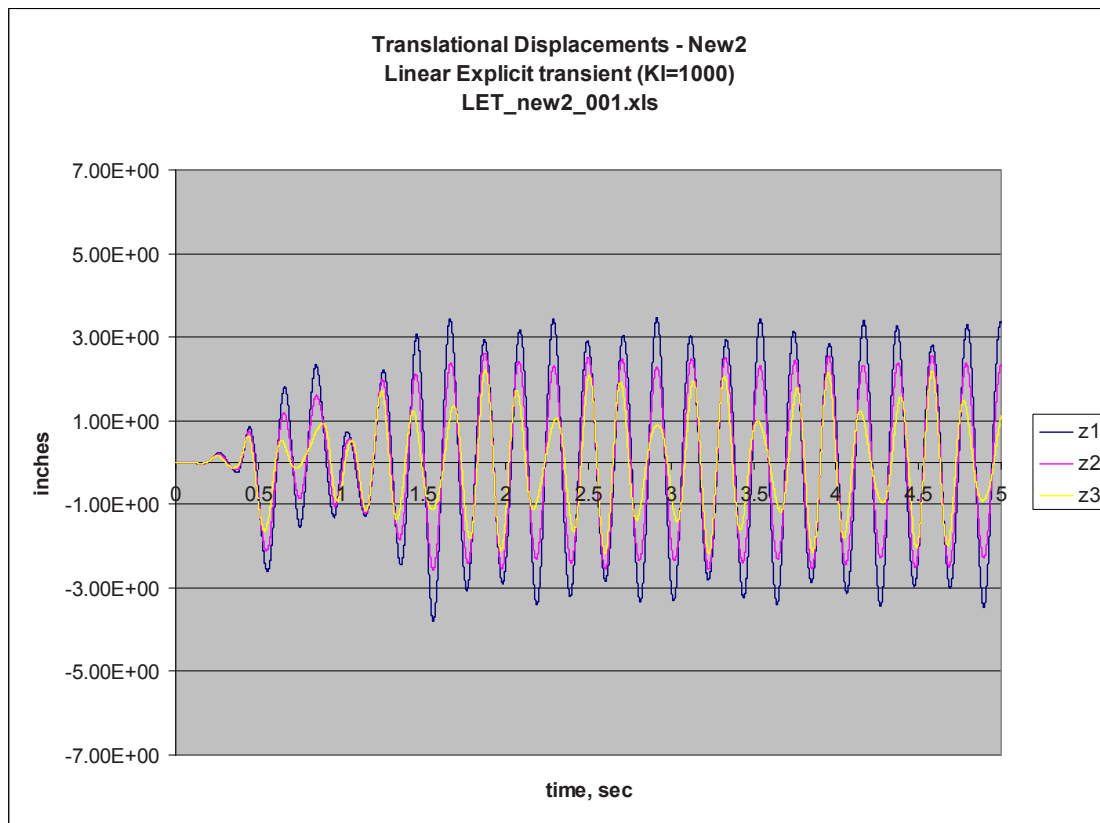


Figure 8 – Relative Displacements Resulting from *New2* Base Acceleration, Linear Model

Translations, in	<i>Sim6mod</i> acceleration ("original")	<i>New2</i> acceleration (synthesized from SRS of <i>Sim6mod</i>)	Ratio: <i>New2</i> / <i>Sim6mod</i>
$z_1(t)_{\max}$ - JEA	3.931	3.790	0.964
$z_1(t)_{\max}$ - ABAQUS	3.613	3.391	0.939
$z_2(t)_{\max}$ - JEA	3.090	2.621	0.848
$z_2(t)_{\max}$ - ABAQUS	3.116	2.854	0.916
$z_3(t)_{\max}$ - JEA	2.254	2.218	0.984
$z_3(t)_{\max}$ - ABAQUS	2.538	2.181	0.859
Rotations, rad			
$\theta_1(t)_{\max}$ - ABAQUS	0.0246	0.0222	0.902
$\theta_2(t)_{\max}$ - ABAQUS	0.0258	0.0235	0.911
$\theta_3(t)_{\max}$ - ABAQUS	0.0274	0.0251	0.916

Ave Ratio = 0.915

**Table 3 – Maximum Relative Displacements from
Sim6m and *New2* Base Excitation, Linear Model**

IE – Nonlinear Model Transient Analysis

The base accelerations, *Sim6m* and *New2*, were next applied to a nonlinear version of the 6 DOF rack model. The nonlinearity corresponds to the force-displacement curve for the shock isolators that roughly correspond to a “Barry” isolator originally included in the conceptual design of the rack. [Figure 9](#) is a plot of the shock isolator force-displacement relationship. The nonlinear isolator was used for both of the springs in the model. The resulting displacements from *Sim6m* and *New2* base accelerations are shown in [Figures 10](#) and [11](#), respectively. The tabular comparison of results is listed in [Table 4](#).

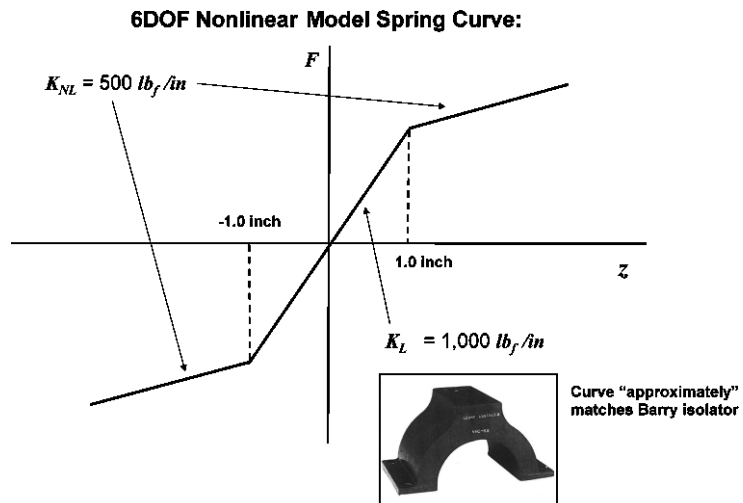


Figure 9 – Nonlinear Shock Isolator Force-Displacement Relationship

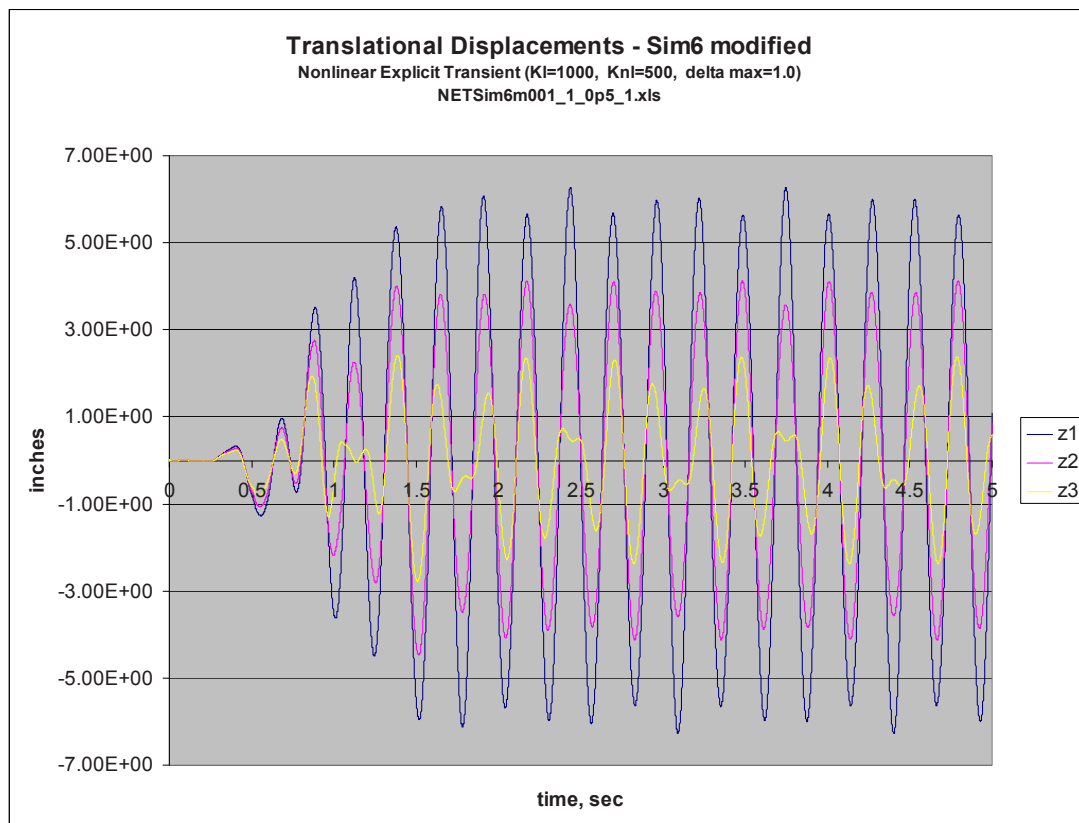


Figure 10 – Relative Displacements Resulting from *Sim6m* Base Acceleration, Nonlinear Model

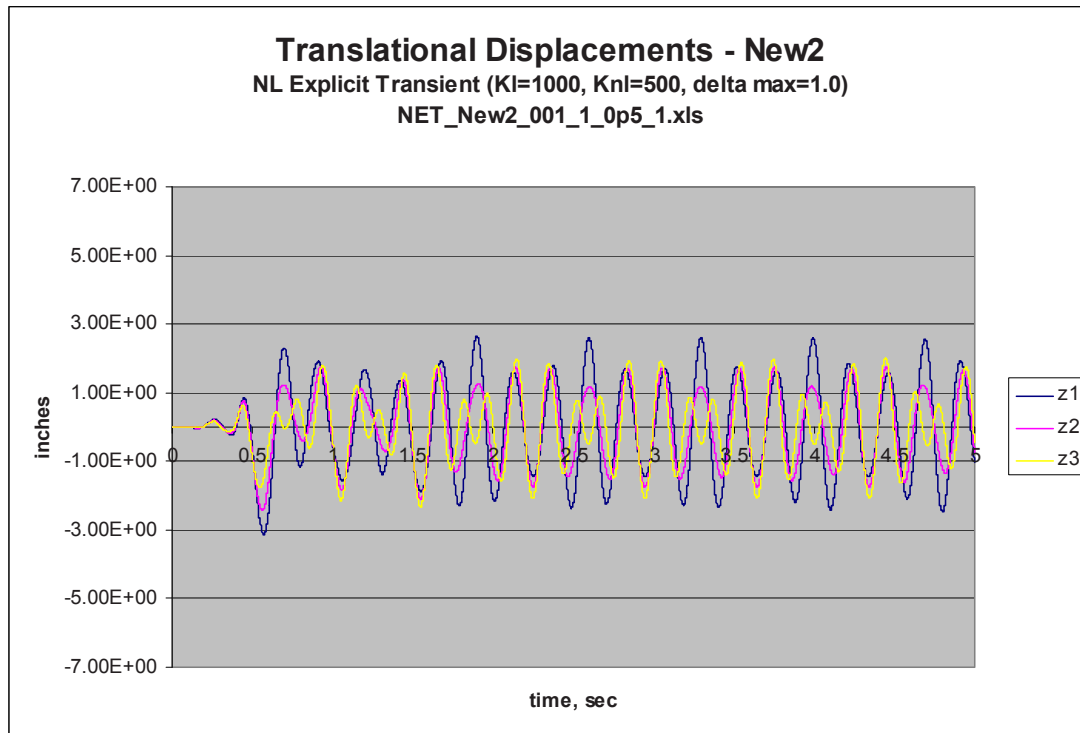


Figure 11 – Relative Displacements Resulting from New2 Base Acceleration, Nonlinear Model

Nonlinear Model Displacements

$K_l = 1,000 \text{ lb}_f/\text{in}$ ($-1.0 < Z < 1.0$)

$K_{nl} = 500 \text{ lb}_f/\text{in}$ $Z > \text{ABS} (+/- 1.0)$

(Estimated freq = 3.96 HZ)

Translations, in	Sim6 modified acceleration ("original")	New2 acceleration (synthesized from SRS of Sim6 mod)	Ratio: New2/Sim6m results	Poor correlation
$ z_1(t) _{\max}$ JEA	6.277	3.148	0.502	
- ABAQUS	5.581	3.114	0.563	
$ z_2(t) _{\max}$ JEA	4.480	2.437	0.544	
ABAQUS	4.633	2.438	0.526	
$ z_3(t) _{\max}$ JEA	2.776	2.331	0.840	
ABAQUS	3.481	1.766	0.507	
Rotations, rad				
$ \theta_1(t) _{\max}$ JEA	.0819			
ABAQUS	.0318	.0222	0.698	
$ \theta_2(t) _{\max}$ JEA	.0821			
ABAQUS	.0330	.0235	0.712	
$ \theta_3(t) _{\max}$ JEA	.0837			
ABAQUS	.0351	.0251	0.715	

Ave Ratio = 0.623

**Table 4 – Maximum Relative Displacements from
Sim6m and New2 Base Excitation, Nonlinear Model**

IF – Comparison of Linear and Nonlinear Model Results

Unlike the linear model case, significant differences in the displacements from the nonlinear model resulting from *Sim6m* and *New2* base accelerations applied to the nonlinear model was not expected. The peak translations increased by 45% and decreased by 10% from the linear to nonlinear model for *Sim6m* and *New2* base accelerations, respectively. As such, on the average, the maximum translations from the *New2* base acceleration were only 58% of those resulting from *Sim6m*, (71% for rotations). The increase in displacements from the linear to the nonlinear model for the *Sim6m* base acceleration was expected, since the nonlinear spring curve represents a “softer,” more flexible spring. It follows that the displacements should increase for the same input. This was not the case for the *New2* base acceleration applied to the nonlinear model. Not only did the displacements not increase, but in fact decreased by 10% from the linear to the nonlinear model. Given the similarities of the two base accelerations including the same SRS, and the rather “mild” nonlinearity of the spring curve, this difference in the response of the nonlinear system to the two base accelerations is a surprise. As before, the results of the analytical model were checked with the ABAQUS model.

PART II – Energy Considerations

Given the unexpected result for the nonlinear model, it was decided to apply evolving energy methods for mechanical shock being advocated by Sandia to this example to see if explanations can be gleaned from total system energies during the shock transient. A brief overview of the development of the energy equation for a single degree of freedom system, [Figure 12](#), subjected to a base acceleration is included herein. Two formulations are possible; one for relative energies and another for absolute energies. For this study, the relative energy formulation is used. A more detailed development of both is included in Reference [4].

IIA –Relative Energy Equation

[Figure 12](#) is a schematic of a damped SDOF system subject to a base acceleration $\ddot{u}_b(t)$. The equation of motion for this system is given by (3) where $z(t)$ is a relative coordinate defined to be the difference between the motion of the mass coordinate relative to the base coordinate.

$$\begin{aligned} m\ddot{z}(t) + c\dot{z}(t) + kz(t) &= 0 \\ z(t) &= u(t) - u_b(t) \end{aligned} \tag{3}$$

Taking the second derivative of $z(t)$ and substituting for the absolute acceleration of the mass in (3) results in the equation of motion in terms of the relative coordinate (4). Note that the base acceleration appears on the right hand side in the term $-m\ddot{u}_b(t)$ as a forcing term.

$$m\ddot{z}(t) + c\dot{z}(t) + kz(t) = -m\ddot{u}_b(t) \tag{4}$$

Integrating (4) with respect to z yields (5) which has unit of energy.

$$\int m\ddot{z}(t)dz + \int c\dot{z}(t)dz + \int kz(t)dz = -\int m\ddot{u}_b(t)dz \tag{5}$$

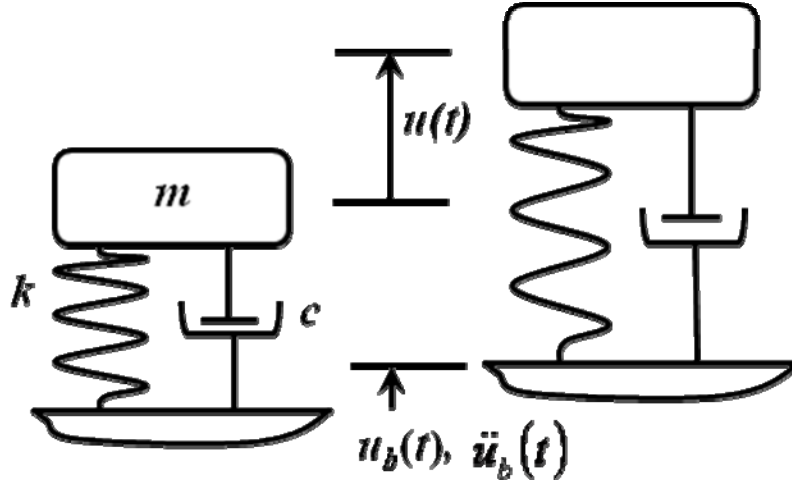


Figure 12 – Damped Single DOF Oscillator Subject to Base Motion

After some math (see Reference [4] for details), the relative energy equation is given by (6).

$$\frac{1}{2}m\dot{z}(t)^2 + \int c\dot{z}(t)^2 dt + \int kz(t)dz = -\int m\ddot{u}_b(t)dz \quad (6)$$

Term by term descriptions of (6) indicated that:

relative kinetic energy + damped energy + absorbed energy = relative input energy

This indicates that the total system energy (kinetic, damped, and absorbed) is equal to the input energy. The terms of (6) were programmed into a central difference numerical integration routine. The expressions programmed in the numerical integration program are indicated in equations (8) - (11). The time corresponding to the $(n+1)$ time step in the numerical integration scheme is given by (7).

$$t = t^{n+1} = (n+1)\Delta t \quad (7)$$

Terms in Numerical Integration Program

Relative kinetic energy: $\frac{1}{2}m\dot{z}(t)^2 \Rightarrow \frac{1}{2}m(\dot{z}^{n+1})^2 \quad (8)$

Damped energy: $\int c\dot{z}(t)^2 dt \Rightarrow \sum_{i=0}^n c(\dot{z}^{i+1})^2 \Delta t \quad (9)$

Absorbed energy: $\int kz(t)dz \Rightarrow \frac{1}{2}k(z^{n+1})^2 \quad (10)$

Input Energy: $-\int m\ddot{u}_b(t)dz = -\int m\ddot{u}_b(t)\dot{z}(t)dt \Rightarrow -m\Delta t \sum_{i=1}^n (\ddot{u}_b^{i+1})(\dot{z}^{i+1}) \quad (11)$

IIB - Energy Response Spectra

Equation (11) was used to determine total input energy per unit mass from each of the two base accelerations used in this study; *Sim6m* and *New2*. The numerical integration procedure was run over all frequencies of interest and a “Relative Energy Response Spectrum” (RERS) was constructed by plotting the maximum system input energy at each frequency. Figure 13 is a plot of the ERS for both base accelerations. It is noted that for the two frequencies of interest for the linear and nonlinear 6 DOF systems, 4.8 Hz and 3.96 Hz, respectively, the RERS for both *Sim6m* and *New2* are quite close. Had the ERS for *New2* been considerably lower than that of *Sim6m* at the nonlinear system frequency, it would have been a clear indication why the nonlinear 6 DOF system response was significantly lower. This, however, is not the case as the energy spectral values are relatively close.

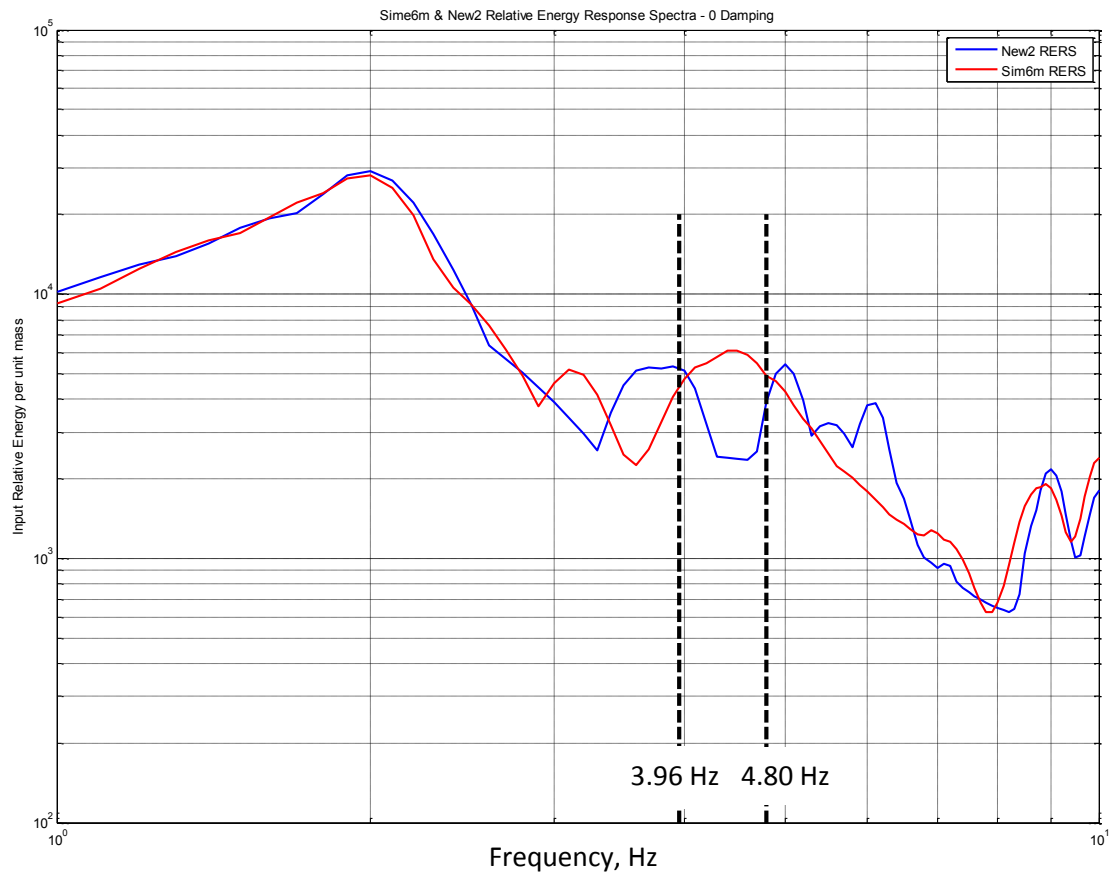


Figure 13 – Relative Energy Response Spectra for *Sim6m* and *New2* Base Accelerations

IIC – Six DOF Model Energies

An addition piece of information available is the maximum energy determined directly from the 6 DOF model. Given that there is no damping or any other energy dissipation in the model, for each oscillation of the system, the maximum energy reverses between all kinetic energy (KE) at maximum velocity to all strain energy at maximum displacement. The total KE based on relative velocities for the linear system is plotted in Figure 14 for both base accelerations. Since the RERS represents the total input energy per unit mass, the maximum 6 DOF energy based on KE is divided by the system mass to compare with the RERS. The total KE is calculated from (12) includes from all translations and rotations. The total KE/unit mass is determined from (13) where the total mass of the system is $2.0917 \text{ lb}_f \text{sec}^2/\text{in}$.

$$Total\ KE = \sum_{i=1}^3 \left(\frac{1}{2} M_i \dot{z}_i^2 + \frac{1}{2} I_i \omega_i^2 \right) \quad (12)$$

$$\frac{KE_{\max}}{unit\ mass} = \frac{Total\ KE_{\max}}{Total\ mass} \quad (13)$$

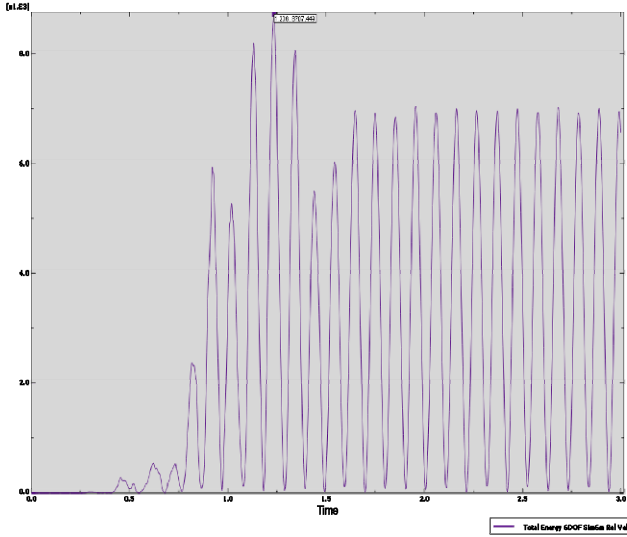
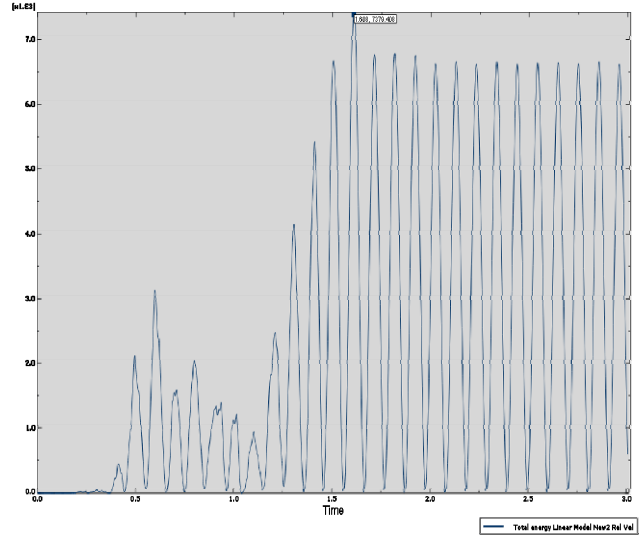
KE from *Sim6m* AccelerationKE from *New2* Acceleration

Figure 14 – 6 DOF Linear Model Total Kinetic Energies from Relative Velocities

$$Max\ KE\ from\ Sim6m = 8,707/2.0917 = 4,163\ in^2/sec^2$$

$$Max\ KE\ from\ New2 = 7,379/2.0917 = 3,528\ in^2/sec^2$$

The maximum numerical values for the linear 6 DOF model corresponding to Figure 14 are given above. The corresponding values for the nonlinear model were determined with the same procedure.

IID – Comparison of 6 DOF Model energies with Relative Energy Response Spectra

The maximum relative energies from the 6 DOF model were determined using the above procedure and plotted on the graph for relative energy response spectra, Figure 14. For the linear system (4.8 Hz) the energies from the 6 DOF model was reasonably close to not only the respective energy response spectra for both *Sim6m* and *New2*, but also close to each other (4163 and 3528, respectively). This is consistent with the prior findings that the displacements resulting from the two base accelerations were reasonably close. Note that the ratio of the 6 DOF maximum energies for $KE(New2)/KE(Sim6m) = 0.847$. The KE_{\max} ratio can be estimated from the maximum displacements assuming sinusoidal behavior (which appears to be a good approximation from the linear model results of Figures 7 and 8) using (14).

$$\frac{KE_{\max}^{New2}}{KE_{\max}^{Sim6m}} \cong \sum_{i=1}^3 \frac{\frac{1}{2} M_i (\omega z_{i\max}^{New2})^2}{\frac{1}{2} M_i (\omega z_{i\max}^{Sim6m})^2} = \frac{(z_1^2 + 1.516z_2^2 + 0.671z_3^2)^{New2}}{(z_1^2 + 1.516z_2^2 + 0.671z_3^2)^{Sim6m}} = 0.842 \quad (14)$$

Similar to these results for the linear model, the maximum kinetic energy ratio determined directly from the nonlinear 6 DOF model was close to that estimated from (14). The ratio $KE(New2)/KE(Sim6m) = 0.225$ was determined directly from the nonlinear 6 DOF model results. The same ratio estimated from maximum displacements using (14) is 0.295. The agreement is reasonably good, but not as close as was the case for the linear model, perhaps due to deviations from pure sinusoidal motion shown in [Figures 10 and 11](#), especially for Z_3 .

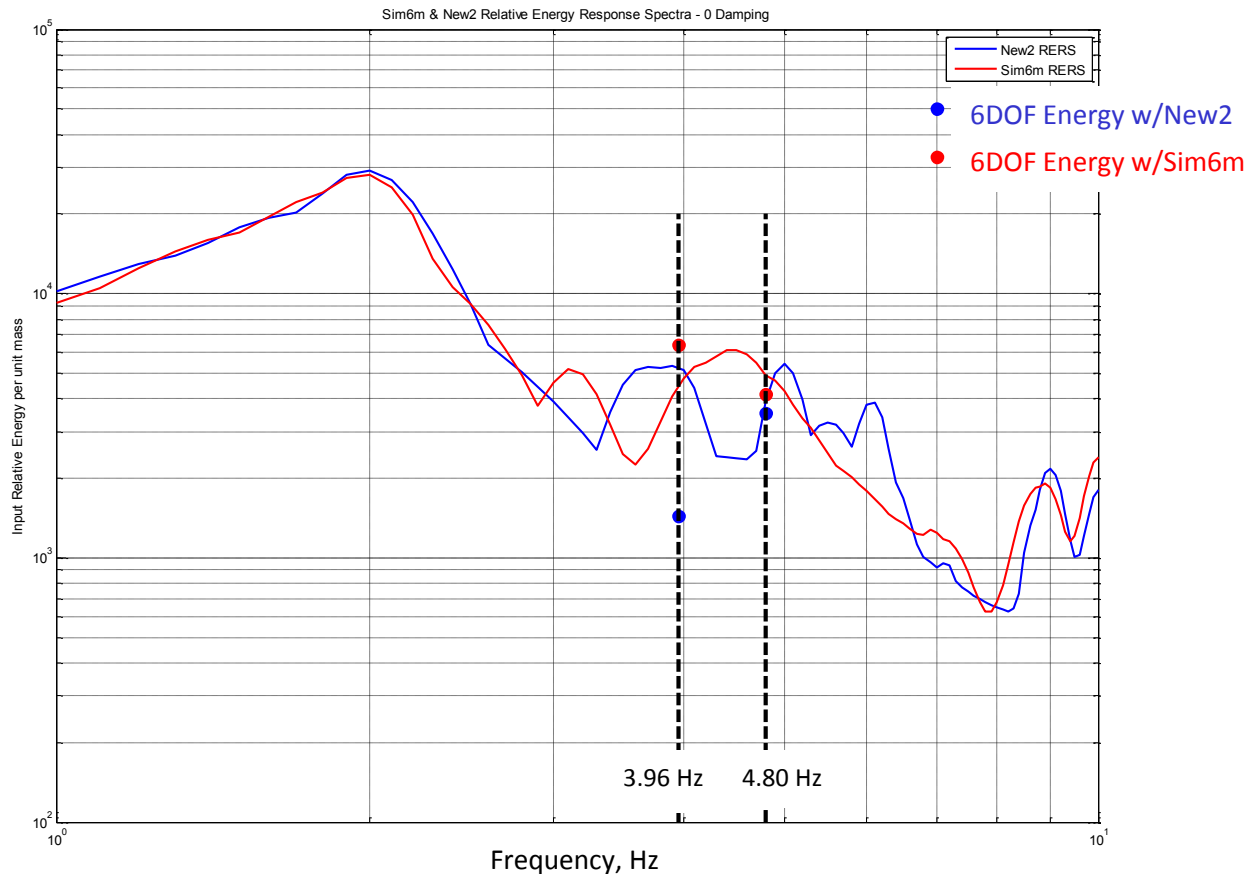


Figure 15 – Relative Energy Response Spectra for *Sim6m* and *New2* Base Accelerations with Max Energies from 6 DOF Linear and Nonlinear Models (0 Damping)

The poor nonlinear model results correlation from the two base accelerations motivated curiosity to investigate other nonlinear model frequencies. Three other frequencies were evaluated by adjustments in the nonlinear force-displacement curve for the shock mounts. The additional frequencies evaluated were 2.17 Hz, 3.05 Hz and 3.29 Hz. Comparison of model maximum displacements resulting from *Sim6m* and *New2* base accelerations at these frequencies were improved from those of the prior 3.96 Hz nonlinear system. In addition, there is improved agreement between the maximum energies from the 6 DOF model and the Relative Energy Response Spectra. [Figure 16](#) includes the maximum energies determined from the 6 DOF model at the additional three frequencies.

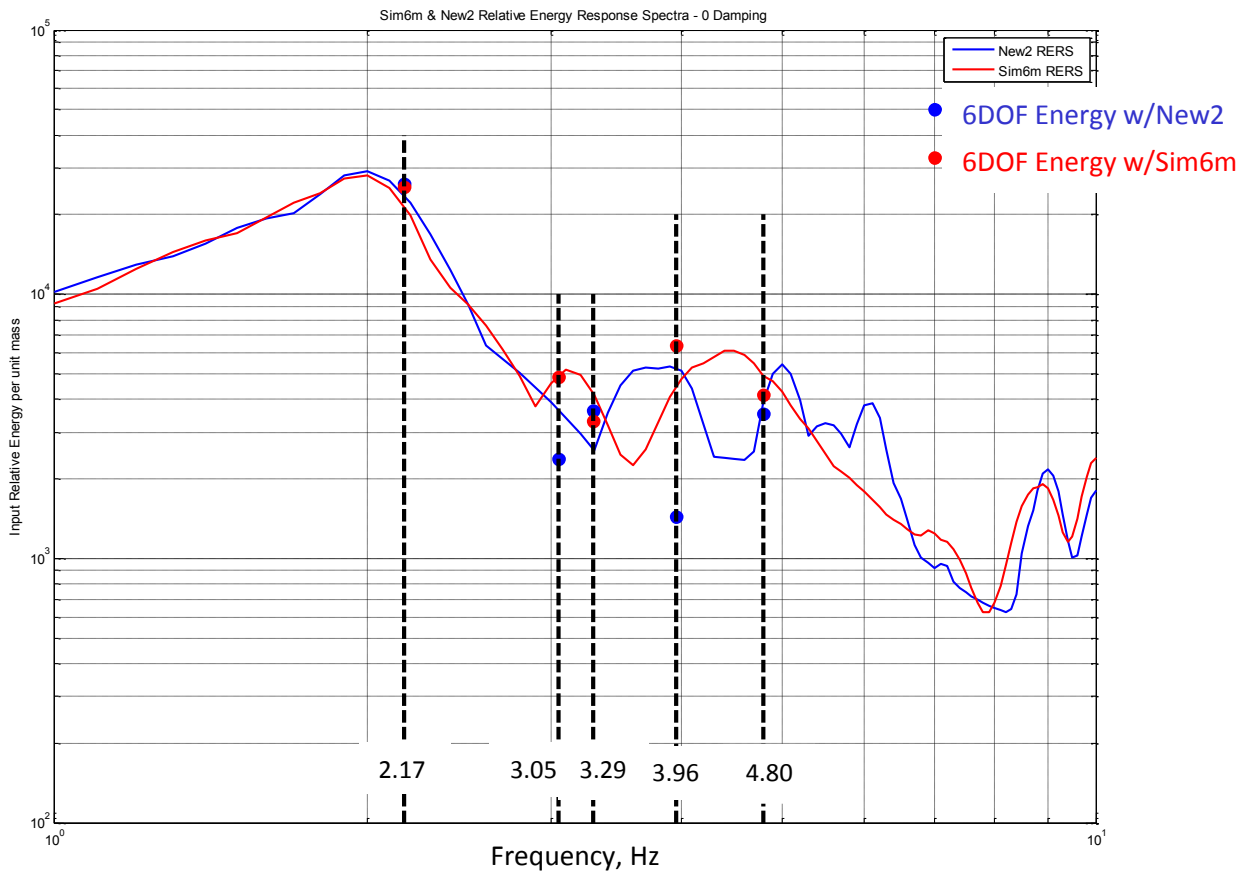


Figure 16 – Relative Energy Response Spectra (RERS) for *Sim6m* and *New2* Base Accelerations with Max Energies from Five 6 DOF Models (0 Damping)

PART III – Summary of Results

The results for the five 6 DOF model frequencies are summarized in [Table 5](#) & [6](#) and [Figure 17](#). The results are presented in terms of the ratio of the response from the *New2* base acceleration to those of the *Sim6m* base acceleration. [Table 5](#) is a tabulation of the ratio ($6DOF KE_{max} / RERS$) resulting from both base accelerations at each frequency evaluated.

One motivation to consider energies in this study was to determine if the *RERS*, which is model independent, could be used to consistently predict the maximum energy of the nonlinear 6 DOF model at specific frequencies. Results were mixed as indicated by [Table 5](#). Of the five frequencies considered, the best agreement between the *RERS* and 6 DOF model energies were at 2.17 Hz and 4.80 Hz, the former a nonlinear model and the latter a linear model. At 2.17 Hz, the agreement is quite good. At 4.80 Hz (linear model), the ratios were also reasonably good. However, at other frequencies the correlations were not as close. For the nonlinear model at 3.96 HZ the ratio was 0.271 for the *New2* base acceleration, which was the poorest correlation.

6 DOF Model Frequency HZ	2.17	3.05	3.29	3.96	4.80 (linear)
$\left(\frac{6DOF KE_{max}}{RERS}\right)_{Sim6m}$	1.165	0.972	0.780	1.408	0.844
$\left(\frac{6DOF KE_{max}}{RERS}\right)_{New2}$	1.095	0.658	1.387	0.271	0.912

Table 5 – Ratio of 6 DOF Model KE_{max} to $RERS$ at 5 Frequencies Evaluated

Table 6 lists the ratio of the maximum displacements of the model for *New2* and *Sim6m* base accelerations at the respective frequencies, average over the three masses. The trend for displacement ratios generally followed those of the energy ratios of Table 5. The agreements were good for the highest, lowest and middle frequency (2.17, 3.29, and 4.80 respectively). As was evident from Figures 10 & 11 and Table 4, the correlation was the poorest for the nonlinear model at 3.96 Hz. The differences in displacements were consistent with the differences in the maximum kinetic energies of the model for the two base accelerations.

6 DOF Model Frequency HZ	2.17	3.05	3.29	3.96	4.80 (linear)
$ave\left\{\frac{ z_i^{max} _{New2}}{ z_i^{max} _{Sim6m}}\right\}$	1.021	0.732	1.031	0.532	0.905

Table 6 – Average of the Ratio of Maximum Displacements for *New2* & *Sim6m* at Model Frequencies

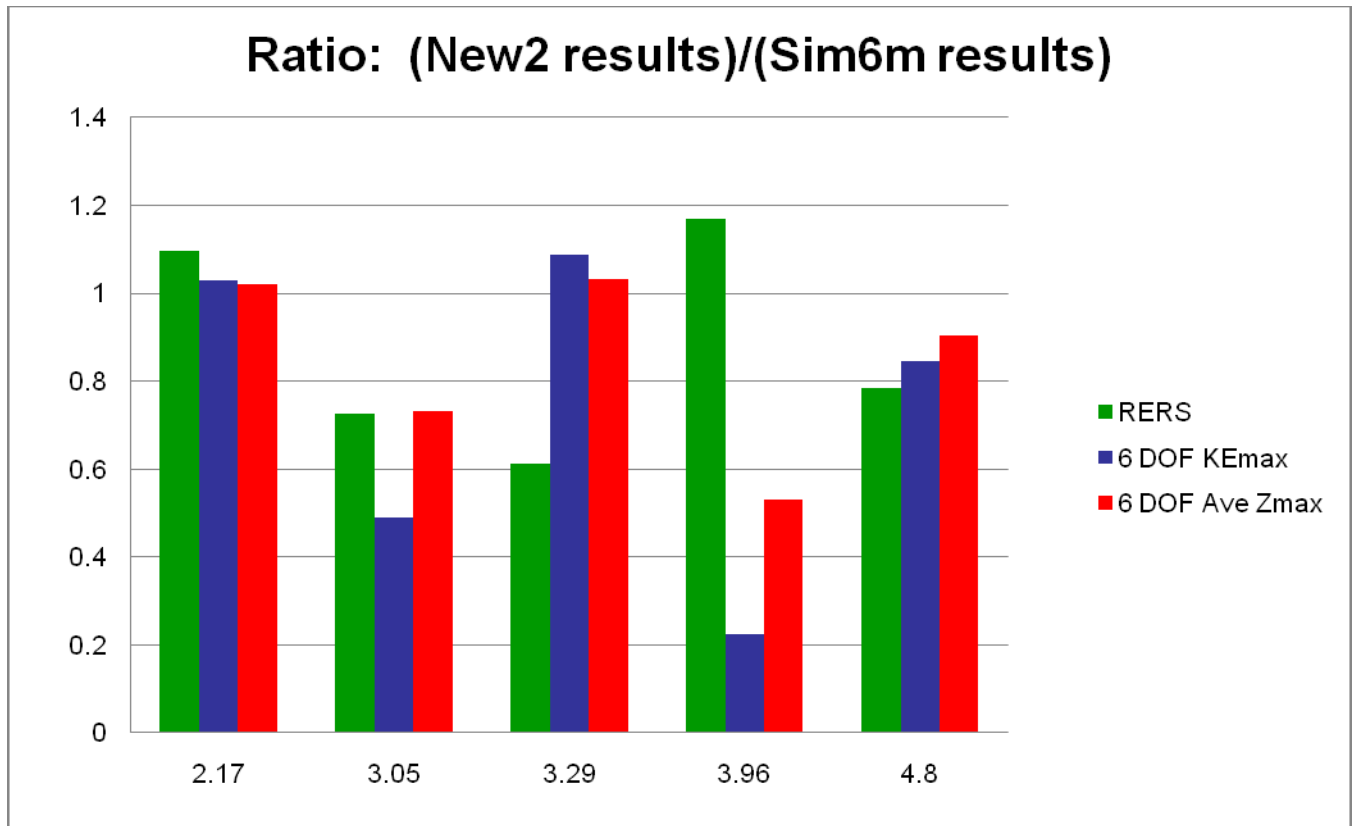


Figure 17 – Ratio of *New2:Sim6m* Results for Five 6 DOF Model Frequencies

Figure 17 shows similar results ratios for comparisons of RERS, max 6DOF model kinetic energy, and averages of maximum model relative displacements resulting from each base acceleration. As before, the most inconsistent results occurred at 3.96 Hz (nonlinear system). At that frequency, the *RERS* of *New2* was approximately 15% higher than that of *Sim6m*, but the maximum 6 DOF model energy resulting from *New2* was only 20% of the corresponding value from *Sim6m*.

PART IV – Conclusions and Recommendations

Both base acceleration time histories used in this study were quite similar. Each had similar wave forms, peak values that were reasonably close, identical durations and nearly identical shock response spectra. When applied to a linear MDOF model, the results from both agreed reasonably well in terms of both maximum displacements and maximum relative energies determined from the model, as well as correlation to the relative energy response spectra at the frequency of the model. When the force-displacement curves of the model shock isolators changed from linear to nonlinear, the results were inconsistent depending on model frequency. At certain nonlinear frequencies, the correlation of results was good; at other nonlinear system frequencies the correlations were poor, especially at 3.96 Hz. The reasons for this inconsistency are not clear, at least to the author.

The root cause for the mixed results begs for further investigation. One parameter to further explore is the dependency of results on system nonlinearity. Evaluation linear 6 DOF models at the same nonlinear system frequencies used in this study may be helpful to determine if system nonlinearity is a root cause for inconsistent results. Also, evaluation of the 6 DOF model (both linear and nonlinear versions) at higher frequencies may help determine if frequency dependency exists. Finally, the model evaluated in this study had no damping. Evaluation of a model with modest amount of damping appropriate for a mechanical system, perhaps 5%, might help determine if damping has a stabilizing effect.

Part V - Acknowledgement

The review and comments of this study from Mr. Tim Edwards, Sandia National Laboratories and the Matlab energy spectra m-files received from Mr. David Smallwood, Consultant, were most helpful and greatly appreciated.

PART VI - References

- [1] Scanlan, R. H. and Sachs, K., "Earthquake Time Histories and Response Spectra," *Journal of Engineering Mechanics Division, Proceedings ASCE*, (August 1974)
- [2] Gasparini, D. and Vanmarcke, E. H., "Simulated Earthquake Motions Compatible with Prescribed Response Spectra," Publication No. R76-4, Dept. of Civil Engineering, M.I.T., (January 1976)
- [3] Alexander, J. E., "Structural Analysis of a Nonlinear System Given a Shock Response Spectrum Input," *SAVIAC Proceedings of the 69th Shock and Vibration Symposium*, 1998, Unlimited Volume
- [4] Uang, C. M. and Bertero, V. V., "Evaluation of Seismic Energy in Structures," *Earthquake Engineering and Structural Dynamics*, 1990, Vol. 19, 77-90
- [5] Edwards, T. S., "Using Work and Energy to Characterize Mechanical Shock," accepted for publication in *Shock and Vibration*

Experimental assessment of gear meshing excitation propagation throughout multi megawatt gearboxes

Jan Helsen, Frederik Vanhollebeke, Ben Marrant, Dries Berckmans, Dirk Vandepitte, Wim Desmet

Abstract Gearboxes consisting of both planetary and helical gear stages are increasingly used in helicopters, wind turbines and vehicles. A requirement for reliable gearbox design calculations is sufficient insight in internal gearbox dynamics. Excitation frequencies and excitation levels play an important role. Main objective of this work is to investigate the influence of internal gear meshing excitation on the overall gearbox dynamics. Experiments are conducted on a dynamic 13.2MW test facility on which two multi-megawatt wind turbine gearboxes are placed back to back. A dedicated dynamic load case representing realistic drive train excitation is applied and the role of the meshing orders in spreading this excitation over a broader frequency range is determined by means of waterfall spectra from measurement signals of bearing displacement sensors, torque sensors, encoders and accelerometers throughout the gearbox. Moreover the propagation of the meshing excitation throughout the gearbox is of interest. Relating the orders to the corresponding excitation source allows the definition of order influence regions within the gearbox. These insights will be used to prove the need for accurate gear mesh order excitation representation within the corresponding flexible multibody simulation model. Moreover the meshing order influence regions offer the opportunity to tune order excitation to the gearbox modal properties and reduce vibration levels.

Jan Helsen, Dries Berckmans, Dirk Vandepitte, Wim Desmet
K.U.Leuven Department of Mechanical Engineering Division PMA, Celestijnenlaan 300B 3001
Heverlee, Belgium, e-mail: jan.helsen@mech.kuleuven.be

Frederik Vanhollebeke, Ben Marrant
Hansen Transmissions International nv, De Villermontstraat 9 2550 Kontich, Belgium e-mail: fvanhollebeke@hansentransmissions.com

1 Introduction

Gearboxes consisting of both planetary and helical gear stages are increasingly used in helicopters, wind turbines and vehicles. Guaranteeing reliable and cost-effective gearboxes requires expert insight in internal dynamics during operation. Excitation frequencies and excitation levels play an important role. This work focuses on wind turbine gearboxes. Main objective is to investigate the interaction between the external and internal gearbox excitation and its influence on the overall gearbox dynamics.

To get insights in the gearbox dynamics detailed measurements were performed. To overcome issues concerning test repeatability experienced in field testing, test-rig testing is suggested for experimental investigation. Tests are performed on a dynamic test-rig with a nominal power of 13.2 MW and a peak power capacity of 16.8MW on which two wind turbine gearboxes are placed in a back-to-back configuration. In order to be representative, dedicated dynamic load cases, which represent specific dynamics on the gearbox in a wind turbine are realized on the test-rig. Figure ?? shows the correlation between the real wind turbine configuration and the controlled back-to-back test set-up. The left side of the back-to-back gearbox test rig represents the 'wind & rotor' and is composed of an electrical machine (motor 1), an optional speed reducer (3:1 gearbox)(*) and a wind turbine gearbox (gearbox 1). The right side represents the 'grid & generator' and is composed of an electrical machine (motor 2) and an optional speed reducer. Analogous to the operation of a wind turbine, the 'wind' side of the test rig is speed controlled, whereas the 'generator' side is torque controlled. In between, the test gearbox (gearbox 2) is driven at a certain time varying speed by the 'wind' and loaded with a certain time varying torque by the 'generator' and thus experiences test conditions very similar to wind turbine behavior.

The investigated gearbox consists of one planetary and two helical gear stages. The planetary system consists of a cage planet carrier (PC) with three identical equally spaced planets. The planet ring is fixed. All gear contacts between the planets, ring and sun are helically shaped. The helical part of the gearbox consists of two stages. On the low speed shaft (LSS) the slow wheel is pressed. This is in contact with the teeth on the intermediate shaft (ISS). On the intermediate shaft a high speed wheel is mounted, which establishes contact with the teeth on the high speed shaft (HSS).

2 Gearbox dynamics

2.1 *External gearbox excitation at gearbox input and output*

External excitation sources for the wind turbine are loads at the rotor hub and torque at the generator side. In addition there is excitation from the sea waves in case of an offshore turbine. For the rotor hub, mainly drive train torque and speed are de-

termining for the design of the gearbox. The torque and speed vary and thus result in various possible dynamic effects. In addition, the torque on the gearbox at the generator side can also be influenced by events occurring in the electricity grid. Furthermore, loads change in combination with rotational speed fluctuations. These simultaneous variations define the dynamic loading of the gearbox.[?] Most of these 'external excitations' have a low frequency content. Figures ?? and ?? show an equivalent load case containing the most important external dynamic excitations for a traditional wind turbine. From this figure it is clear that external excitations are in a lower frequency range.

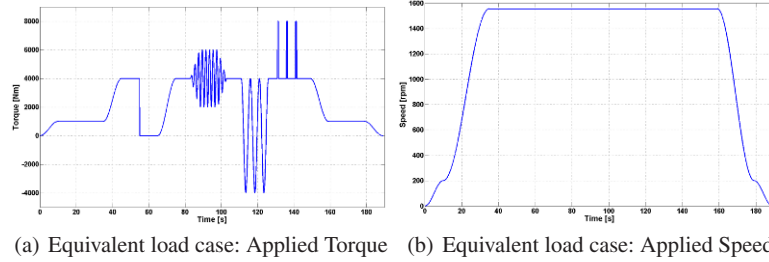


Fig. 1 Equivalent load case containing the important external gearbox excitations

2.2 Gear mesh excitation

Internal gearbox excitation on the other hand originates from periodic excitation due to gear meshing. Flexibility of the gear teeth and gear body causes the gear meshing forces to be non constant, which results in gear related vibrations and noise. This gear excitation of two flexible gears is caused by a combination of several phenomena. The first is the excitation originating from the change in tooth meshing stiffness over the line of action due to a change in contact location on the tooth flank.[?][?] A second influence on the gear contact forces is gear body compliance. A last effect is backlash. A variable to describe the influence of flexibility and related excitation is the gear transmission error, which can be defined as the difference between the actual position of the driven gear and the position that the driven gear would occupy if it were rigid and perfect.[?] The excitation at the gear mesh frequency is a result of the once per tooth variation of the transmission error in a gear mesh. For a parallel gear system, the gear mesh frequency equals:

$$f_{gm} = z \cdot n_{gear} \quad (1)$$

with z the number of teeth of the gear and n_{gear} its rotational speed (in Hz). For a planetary gear system with a fixed ring wheel, the gear mesh frequency equals:

$$f_{gm} = z_{rw} \cdot n_{carrier} \quad (2)$$

with z_{rw} the number of teeth of the ring wheel and $n_{carrier}$ the rotational speed of the planet carrier (in Hz).

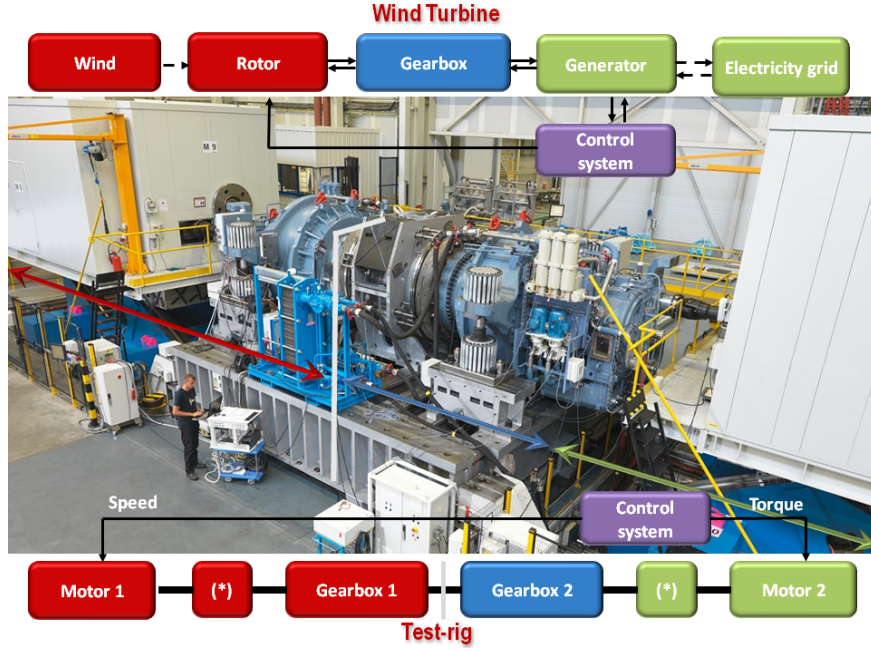


Fig. 2 The concept of the back-to-back gearbox test rig is based on the vision that it is possible to transform wind turbine behavior into test rig conditions. The gearboxes in this photo are gearboxes for the REpower 6M turbine. This photo is only used for clarification of the test-rig concept. Measurement results from other gearboxes were used for the research in this paper.

2.3 Gearbox modal behaviour

In general, the modes of a full gearbox system differ from the ones of the stand alone gearbox components, such as single helical stages or single planetary stages.[?] Therefore the full gearbox should be measured and modelled. The modes of the full gearbox consisting of both planetary and helical stages without any structural flexibilities, can be classified in three categories: *Planetary modes*, *Helical modes* and *Global modes*. These modes are found for a model where all structural components are considered rigid. Flexibility is only situated in gear meshes and bearings. In *Planetary modes*, the mode shape is mainly manifested in the planetary stage,

whereas for *Helical modes*, the mode shapes are predominantly manifested in the helical gear stages of the gearbox. The *global modes*, on the other hand, are manifested in both the planetary gear stages and the helical gear stages of the gearbox. On the other hand in case structural flexibilities, such as planet carrier, LSS, ISS, HSS and housing, are introduced in the model significant coupling occurs between the overall gearbox modes and the modes of the different structural components[?][?]. Previous investigation on structural flexibility modeling[?] showed, that the influence of flexibility is characterized by two frequency ranges. The first range is defined for frequencies well below the first structural component eigenfrequency. In this frequency range a significant gear system eigenfrequency decrease and no coupling between the structural component modal behavior and the overall gearbox modal behavior are found. In the second frequency range coupling between the modes of the structural component and the overall gearbox modes occurs. Previous work suggests the use of frequency response functions throughout the finite element model of the structural component to determine the frequency range where coupling occurs for each structural component.[?] This results in the definition of frequency ranges of influence for the different gearbox structural components, shown in Figure ???. To show the need for insights in the excitation mechanisms throughout the

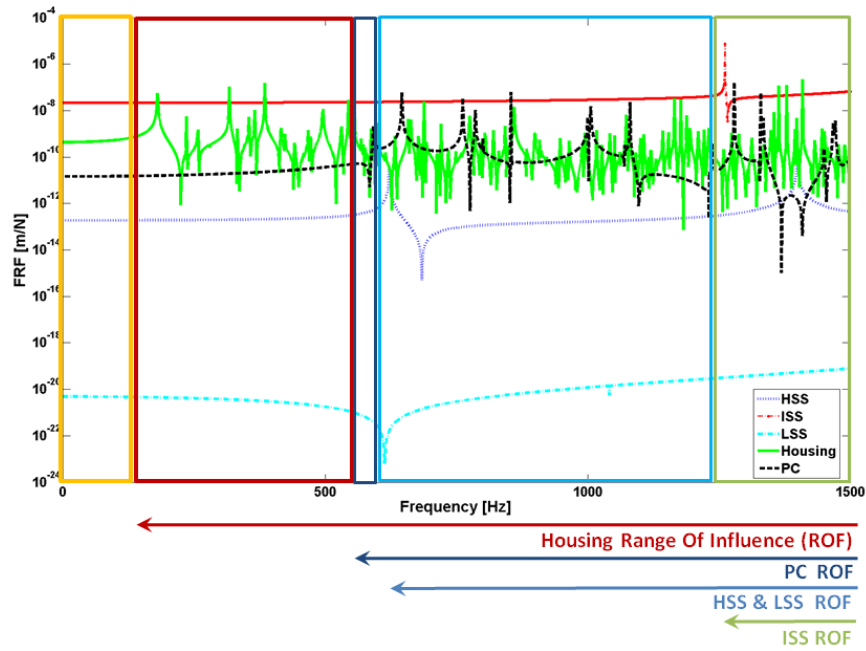


Fig. 3 FRFs defining the frequency ranges of influence for the different gearbox structural components.

gearbox and corresponding frequency ranges of influence first the characteristics of

the gearbox modal behaviour are discussed. Mainly interaction between the overall gearbox modes and structural component modes and corresponding frequency ranges of influence are of interest. Given certain modes are only important for the gearbox designer if they are excited under operating conditions the frequency ranges of excitation during operation will be determined. Excitation amplitudes on different locations in the gearbox are determined by means of an order tracking on measured sensor signals throughout the gearbox. This allows to determine the role of the meshing orders in spreading the low frequency external excitation over a broader frequency range during turbine operation. Moreover the propagation of this excitation throughout the gearbox is determined by comparing excitation amplitudes for different gearbox locations. Relating the orders to the corresponding excitation source allows the definition of order influence regions within the gearbox.

3 Approach

3.1 General approach

To prove the influence of the internal gearbox excitation an order tracking algorithm is used. To facilitate a straight forward tracking of the meshing orders a more straight forward load case is used. In this work the applied load case is a speed run-up from 95rpm to 1700rpm at a torque of 11605Nm. Goal is to determine the amplitude of the order excitation signal for the orders of the different gear meshes. To increase the quality of the estimates multiple sensors and sensors of different type are used to characterize the orders of each gear mesh: 55 acceleration signals, 28 displacement signals and 6 torque signals. Moreover to assess the propagation capability of each order the order tracking will be performed at locations all over the gearbox. This results in a sensor set-up as schematically represented in Figure ?? . Moreover 4 encoders register rotation of LSS,IMS,HSS and planet carrier.

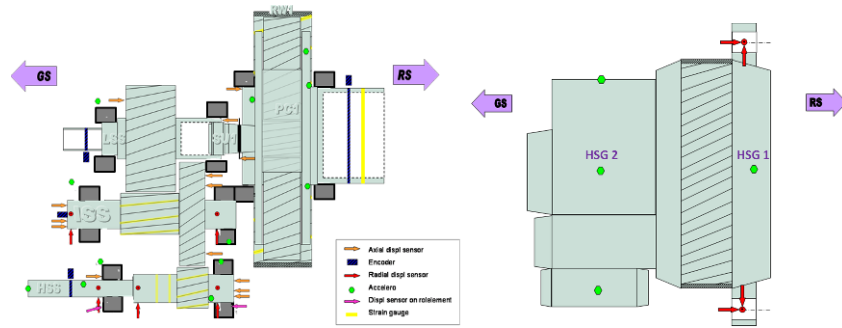


Fig. 4 Sensor types and placement for the measurements performed on the investigated gearbox. GS: Generator Side, RS: Rotor Side

3.2 Ordertracking technique

The analysis of vibrations of rotating machinery is commonly performed through the use of order tracking techniques. An order is defined as a time varying phasor rotating at an instantaneous frequency related to the rotational frequency of a reference shaft of the machine. The latter is derived from a tachometer signal on this reference shaft. Given the frequency dependent characteristics of most rotating machinery, the amplitude and the phase of the orders will normally change as the periodic loading changes speed. A single order k is characterized by Equation ??, with t time, $A_k(t)$ the amplitude of the order as a function of time, ϕ_k the phase angle of order k and $f(t)$ the instantaneous frequency of the primary order as a function of time. Parameter k can be positive for representing positive frequencies, zero for the DC offset and negative for negative frequencies. Gear stage measurement signals contain multiple orders, which is mathematically described by a summation of time varying phasors, as shown in Equation ??.

$$x_k(t) = A_k(t) \sin(2\pi f(t)t + \phi_k) \quad (3)$$

$$x(t) = \sum_{k=-\infty}^{\infty} A_k(t) \sin(2\pi f_k(t)t + \phi_k) \quad (4)$$

In this work the order tracking algorithm is used to extract the amplitudes $A_k(t)$ of the different orders present in the measurement signals throughout the gearbox. Nonetheless this amplitude determination will not be exact, since the amplitude varying property of the orders inherently causes errors as all order tracking techniques consider the amplitude of an order to be semi-constant over the analysis period used to estimate the amplitude and the phase of the order.[?] To minimize this effect the speed run-up is performed as slow as possible. The Time Varying Discrete Fourier Transform (TVDFFT) order tracking algorithm with compensation is used since it combines a good computational efficiency with the ability to minimize leakage errors.[?, ?, ?, ?]

4 Speed run-up testing to assess meshing order propagation throughout the gear stages

4.1 Set-up

The load case used for the order tracking is a HSS speed run-up from 0 to nominal rpm at a torque of 11605Nm. Due to hardware limitations and the long duration of the performed run-ups, sensor data was only available at a sampling rate of 2000Hz. This implies that order information could only be tracked up to 1000Hz. Therefore

not the full time signal will be used in the amplitude determination calculations. For sake of brevity orders originating from the planetary stage gear meshing between planets and ring and planets and sun will be referred to as *Low Speed Stage Orders*, whereas orders related to gear mesh excitation between the low speed gear and the intermediate speed gear are indicated by the term *Intermediate Speed Stage Orders*. Orders originating from gear meshing between intermediate speed gear and high speed gear will be referred to by the name *High Speed Stage Orders*. For sake of brevity not all results of all tracked sensors are discussed. Moreover only the results for the planet carrier and high speed shaft are discussed since results for the low and intermediate speed shaft are similar. All discussed sensor signals are accelerations unless specified otherwise. Absolute vibration amplitudes are not shown due to confidentiality reasons.

4.2 Planet carrier excitation

4.2.1 Excitation originating from Low Speed Stage Orders

In a first step, it is assessed whether the *Low Speed Stage Orders* are visible in the spectrum and consequently exciting the planet carrier. This is quantitatively assessed by ordertracking of the amplitude of the *Low Speed Stage Orders*. These orders are related to the gear meshing excitation originating from planet-ring and planet-sun gear contacts. Since this meshing is occurring in the investigated stage these order excitations are expected to be present. The resulting maximum amplitudes for the 10 first Low Speed Stage Orders are shown in Figure ???. The maximum amplitude

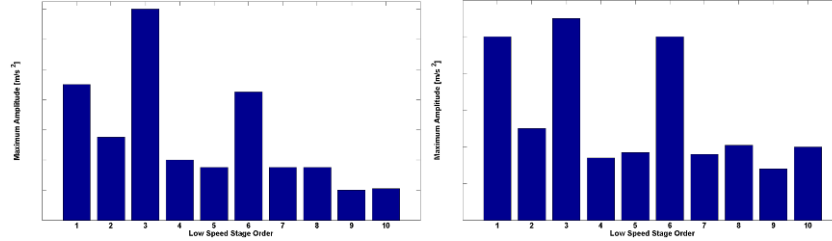


Fig. 5 Comparison of the maximum order amplitudes for the first 10 Low Speed Stage Orders as tracked in the signal of axial (left)/radial (right) signal of one of the three accelerometers at the front of the planet carrier.

is used since the interest of this work is in proving the presence of meshing order excitation in the gearbox structural components. Comparison of the left and right subfigure shows that maximum vibration amplitudes differ for the different planet carrier degrees of freedom, since not all modeshapes have equal displacement in all degrees of freedom. Moreover not only the lowest meshing orders contribute signif-

icantly by exciting resonances, but also higher meshing orders of planetary stage. These higher orders excite at frequencies above the wind turbine excitation range. Nevertheless the excitation frequency spectrum is not high enough in frequency to excite the planet carrier flexibility.

4.2.2 Excitation originating from *Medium Speed Stage Orders*

Furthermore excitation of the planet carrier originating from the *Medium Speed Stage Orders* is determined. Figure ?? compares the maximum amplitudes for the axial and radial degree of freedom for the planet carrier vibrations originating from the *Medium Speed Stage Orders*. The first three and the eighth meshing order clearly

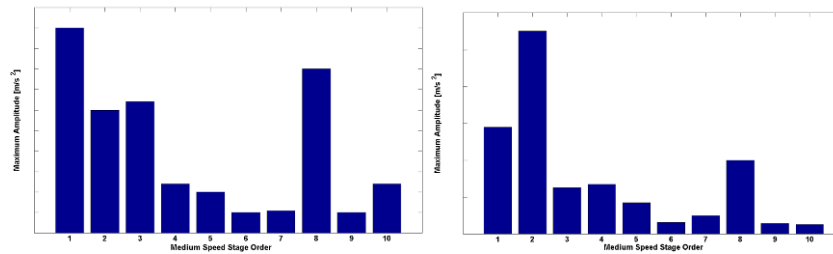


Fig. 6 Comparison of the maximum order amplitudes for the first 10 Medium Speed Stage Orders as tracked in the signal of axial (left)/radial (right) signal of one of the three accelerometers at the front of the planet carrier.

show the most significant planet carrier excitation. This indicates the propagation of the meshing order excitation of the first helical gear stage to the planetary part of the gearbox. This implies that in addition to the *Global* and *Helical Modes*, also planetary modes can be excited by the first helical gear stage. Moreover due to the higher rotation speed of the first helical gear stage higher frequencies up to approximately 1000Hz can be excited by the first ten meshing orders of the first helical gear stage. This excitation is clearly within the ranges of influence of the different structural flexibilities shown in Figure ?. However only the low speed helical stage meshing orders with an order number of five and higher can excite above 500Hz. Figure ? shows strongly reduced vibration levels for these higher order excitation levels in comparison with the first five Medium Speed Stage Order excitation levels, indicating that either these orders are exciting less or that no resonance with significant influence on the dynamic behaviour is excited. Furthermore when comparing excitation levels for the higher orders of Figure ? to those for the Low Speed Stage shown in Figure ? it is shown that these higher order excitations are significantly less, except for the eight *Medium Speed Stage Order*. This could indicate that excitation frequency and gearbox resonance could be close and clearly shows that the eight order is exciting the planetary system significantly. Therefore it can be con-

cluded that the *Medium Speed Stage Orders* are found to propagate to the planetary stage. Given that these orders can excite higher frequency ranges both planet carrier and gearbox housing structural flexibility, including planetary ring flexibility are potentially excited. Therefore, it is advised, that overall gearbox modal behaviour and planet carrier and housing modal behaviour should be tailored to avoid resonance excitation by the *Medium Speed Stage Orders*.

4.2.3 Excitation originating from *High Speed Stage Orders*

A similar approach can be used to assess the propagation of the high speed helical stage orders to planet carrier. However since sensor data was only available at a sampling rate of 2000Hz, order information could only be tracked up to 1000Hz, limiting the tracking times for the *High Speed Stage Orders*. Due to the limited time signals no strong conclusions will be drawn based on the data. For the first two *High Speed Stage Orders* however signals are significantly long and it was found that the *High Speed Stage Orders* are present in the planet carrier and that amplitudes are of the order of magnitude of the second and third *Medium Speed Stage Orders*.

4.3 High speed shaft excitation

For the investigation of the HSS structural flexibility the accelerometer placed at the rear HSS bearing was used.

4.3.1 Excitation originating from *Low Speed Stage Orders*

Figure ?? shows maximum *Low Speed Stage Order* amplitudes measured at the HSS. From this figure it is clear that the first order is dominant, whereas all higher orders have significantly smaller amplitudes. Nonetheless are these orders present in the HSS signal, implying full propagation of Low Speed Stage excitation throughout the full gearbox. This indicates the need for a full gearbox model consisting of all gear stages.

4.3.2 Excitation originating from *Medium Speed Stage Orders*

For the *Medium Speed Stage Orders* the maximum amplitudes in axial and radial degree of freedom are shown in Figure ?. The first five meshing orders show dominant response. Nevertheless all ten *Medium Speed Stage Orders* are present in the response signals indicating excitation of the HSS. Furthermore comparison of Figures ?? and shows that all responses related to the *Medium Speed Stage Orders* are lower than those related to the first *Low Speed Stage Order*. This emphasizes the

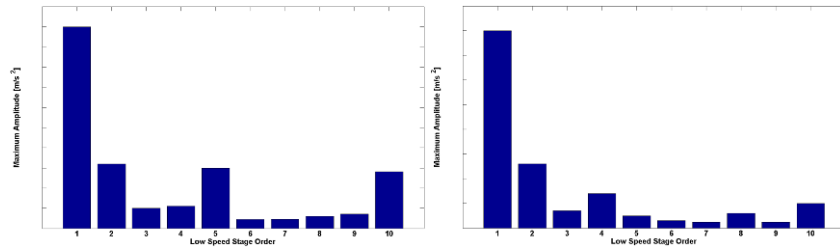


Fig. 7 Comparison of the maximum order amplitudes for the first 10 Low Speed Stage Orders as tracked in the signal of axial (left)/radial (right) accelerometer at the rear high speed shaft bearing

propagation of the order excitation throughout the full gearbox system. Therefore it can be concluded that for the investigated gearbox orders propagate throughout the full gearbox system resulting in equal *Order Influence Regions*, which span the full gearbox.

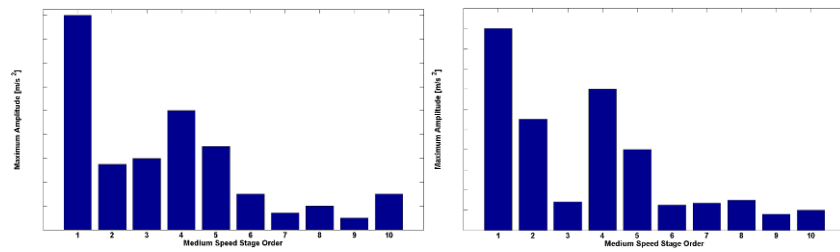


Fig. 8 Comparison of the maximum order amplitudes for the first 10 Medium Speed Stage Orders as tracked in the signal of axial (left)/radial (right) accelerometer at the rear high speed shaft bearing

4.3.3 Excitation originating from *High Speed Stage Orders*

Since the HSS is part of the High Speed Helical stage the *High Speed Stage Orders* are clearly present in the response amplitudes for the HSS accelerometer signals.

5 Conclusions

The modal behaviour of gearboxes consisting of planetary and helical gear units is primarily concentrated in the respective gearbox subsystems, which results in the definition of Planetary and Helical Modes. In addition however Global Modes are

present, which are characterized by modal deformation in both planetary and helical gear stages. Given this concentration of the modal behaviour in the respective subsystems, it was investigated whether excitation was also primarily limited to the subsystems. The determination of excitation amplitudes by means of ordertracking on several sensors spread out over the full gearbox showed however that all meshing orders fully propagate throughout the gearbox. In addition it was shown that in general lower orders excite more significant than higher orders. Furthermore frequency ranges of influence were discussed for the different gearbox structural components. In such frequency regions overall gearbox modal behaviour couples with structural component modal behaviour. However these frequency ranges of influence are at frequencies far above the frequency range of the excitation applied at the gearbox input and output. To prove the need for structural flexibility, it was shown that the gear meshing orders spread out the low frequency external excitation, in this case a very slow run-up, over a broader frequency range into the ranges of influence of the different structural components. This was shown by several significant responses at higher orders, indicating the excitation of a higher frequency resonance. Since this order excitation behaviour is of significant influence on gearbox dynamics an accurate representation of the gear meshing order amplitudes in gearbox models is necessary.

Acknowledgements

This research was performed in the framework of a research project supported by the Institute for the Promotion of Innovation by Science and Technology in Flanders (IWT Vlaanderen).

References

1. D. Qin, J. Wang, T.C. Lim, Flexible multibody dynamic modeling of a horizontal wind turbine drive train system, *J. of Mechanical Design*, 131(11)(2009) 114501-1 114501-8
2. J. Helsen, D. Vandepitte, W. Desmet, Flexible modelling of wind turbine gearboxes with special focus on shaft flexibilities, *Proc. 10th International Conference on Recent Advances in Structural Dynamics (RASD) 2010*, Southampton
3. J. Helsen, F. Vanhollebeke, D. Vandepitte, W. Desmet, Optimized implementation of flexibility in wind turbine gearbox multibody model for model updating on dynamic test-rig, *Proc. 1st joint International Conference on Multibody System Dynamics (IMSD) 2010*, Lappeenranta Finland
4. S.L. Harris, *Dynamic loads on the teeth of spur gears*, Institute of Mechanical Engineers 1954
5. R.G. Parker, S.M. Vijayakar, T. Imajo, Non-linear dynamic response of a spur gear pair: modelling and experimental comparisons, *J Sound Vib*, 237(3) (2000) 435-455
6. J. D. Smith, *Modelling the dynamics of misaligned helical gears with loss of contact*, Institute of Mechanical Engineers 1998

7. A.Heege, J.Betran, Y.Radovic: Fatigue load computation of wind turbine gearboxes by coupled finite element, multibody system and aerodynamic loads, *Wind Energ*, 10 (2007) 395-413 DOI 10.1002/we.226
8. D. Berckmans, Tools for the synthesis of traffic noise sources, PhD. dissertation Katholieke Universiteit Leuven, Department of Mechanical Engineering, Leuven, Belgium, 2010
9. J. Blough, A survey of DSP methods for rotating machinery analysis, what is needed, what is available? *J. Sound Vib* 262(3)(2003) 707720.
10. J. Blough, Improving the analysis of operating data on rotating automotive components, Ph.D. dissertation University of Cincinnati, Dept.of Mechanical, Industrial, and Nuclear Engineering, Cincinnati, USA, 1998
11. J. Blough, Development and analysis of time variant discrete fourier transform order tracking, *Mechanical Systems and Signal Processing* 17(6)(2003) 11851199

An Advanced Numerical Model of Gear Tooth Loading from Backlash and Profile Errors

Andrew Sommer, Jim Meagher, Xi Wu

Department of Mechanical Engineering, California Polytechnic State University, San Luis Obispo, CA.
93407-0358

ABSTRACT

This study demonstrates the early transient dynamic loading on teeth within a fixed-axis gear transmission arising from backlash and geometric manufacturing errors by utilizing a non-linear multi-body dynamics software model. Selection of the non-linear contact parameters such as the stiffness, force exponent, damping, and friction coefficients are presented for a practical transmission. Backlash between gear teeth which is essential to provide better lubrication on tooth surfaces and to eliminate interference is included as a defect and a necessary part of transmission design. Torsional vibration is shown to cause teeth separation and double-sided impacts in unloaded and lightly loaded gearing drives. Vibration and impact force distinctions between backlash and combinations of transmission errors are demonstrated under different initial velocities and load conditions. Additionally, the loading dynamics of a crank-slider mechanism with two-stage gear driving train is analyzed. The backlash and manufacturing errors in the first stage of the gear train are distinct from those of the second stage. By analyzing the signal at a location between the two stages, the mutually affected impact forces are observed from different gear pairs, a phenomenon not observed from single pair of gears.

Keywords: Vibration health monitoring, Malfunction Diagnostics, Contact Mechanics, Gear train, Simulation, multi-body kinematic model.

1. Introduction

Gear trains with different designs play very important roles in automobiles, helicopters, wind turbines, and other modern industries. Excessive loading on the gear teeth may arise due to the combination of gear backlash and teeth defects. Without vibration health monitoring to ensure proper operation performance will degrade.

Dubowsky and Freudenstein [1, 2] developed a theoretical model to investigate the dynamic response of a mechanical system with clearance. Based on this research, Azar and Crossley [3] explored the dynamic behaviors of the engaged gearing systems with gear backlash, time-varying stiffness and damping of the gear teeth. Compared with above investigations, Yang and Sun [4] developed a more realistic dynamic model for a spur gear system with backlash. By taking the involute tooth profile into consideration, they were able to account for material compliance, energy dissipation, time-varying mesh stiffness and damping due to the contact teeth-pair alternating between one and two during the gear engagement. In order to accurately simulate the gear dynamic behavior, the gear mesh stiffness between meshing gear pairs should include at least two factors: local Hertzian deformation and tooth bending. Even though the authors only considered the Hertzian contact stiffness, the dynamic simulations for free vibration, constant load operation and sinusoidal excitation presented insightful results.

Two notable review papers that discuss the numerical modeling of gear dynamics are by Özgüven and Houser in 1988 [5] and by Parey and Tandon in 2003 [6]. Özgüven categorized the models as dynamic factor models, models with tooth compliance, models for gear dynamics, those for rotor dynamics, and those for torsional vibration. The listed goals for the studies included reliability, life, stress, loading, noise, and vibratory motion. Curiously, condition monitoring was not included. Early work modeled the meshing stiffness as either an average or piecewise linear variation. Parey and Tandon's review concentrated mostly on the modeling of defects but includes an extensive compilation of various lumped parameter models. Dalpiaz etc. [7] investigated a gear pair with a fatigue crack and discussed the effectiveness and sensitivity of the time-synchronous average (TSA) analysis, cyclostationary analysis, and traditional cepstrum analysis on the basis of

experiment. Parey etc. [8] developed a six DOF nonlinear model for a pair of spur gears on two shafts, calculated the Hertzian stiffness for the tooth surface contact, and implemented the empirical mode decomposition (EMD) method to simulate the different defect widths. Many authors [9, 10, 11, 12] utilized different methods of estimating time-varying stiffness in order to get practical dynamic simulation results. Meagher and Wu etc. [13] presented three different dynamic system modeling strategies currently being used by researchers to identify diagnostic indicators of gear health: a strength of materials based lumped parameter model, non-linear quasi-static finite element modeling, and rigid multi-body kinematic modeling with nonlinear contact stiffness. This research contrasts these methods of modeling gear dynamics by comparing their predicted stiffness cycle and its effect on dynamic response. Data from experiments are shown for the high contact ratio pair.

Previous research shows that the signal patterns due to the combination of backlash, time-varying gear mesh stiffness, and the involute profile errors, are very complicated and highly depend on gear train design and configurations. In other words, the signals from a specific gearing system are difficult to interpret until a series of modeling, testing and data processing work are carried out. However, it is not realistic to experimentally test each type of gear train for the specific fault patterns. To solve this issue, a virtual experiment method based on multi-body dynamics and nonlinear contact mechanics simulation is presented. Ebrahimi and Eberhard [14] used multi-body dynamics software to model gear mesh stiffness using a rigid-elastic model. Hertzian contact at the gear interface is used to represent gear elasticity as a compromise over fully elastic models; thereby reducing computational effort. Kong and Meagher etc. [15] modeled a large industrial gearbox used in a 12 m³ electric mining shovel. The nonlinear contact mechanics is analyzed to predict the bearing support force variation and gear tooth loading of ideal gears and gears with defects using multi-body dynamics software. No gear backlash was considered. In this study, the authors demonstrate the importance of accurate geometric modeling of gear tooth involutes, and realistic center distance separation on the transient response of ideal and defective gears. The highly nonlinear character of loading and geometry requires special attention to Hertzian contact modeling. Once modeled accurately, double sided tooth impacts and associated loading can be determined as well as superposition of effects at a shaft intermediate to sets of gears.

2. One-stage Gear Train and Discussions

2.1. Multi-body kinematic model of a One-stage Gear Train

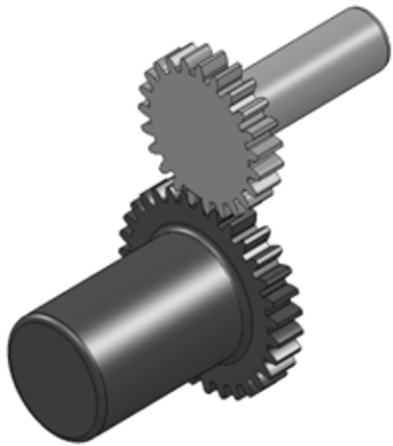


Fig.1 A pair of meshing gears

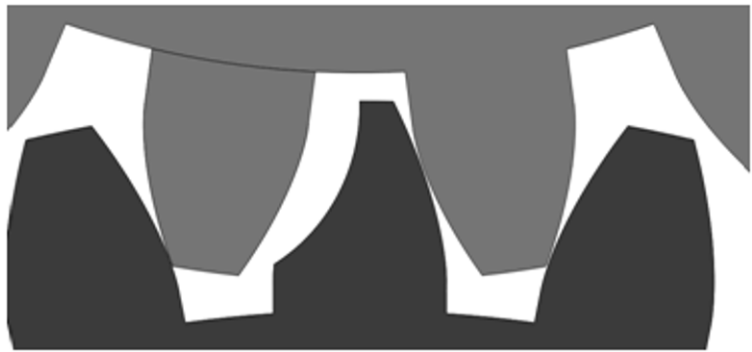


Fig.2 Eccentric pinion tooth with chipped gear

A rigid-elastic model [17] of a pair of meshing gears is shown in Fig.1. Fig.2 shows the eccentric pinion tooth with chipped gear. The gear bodies are rigid but the contact surfaces between the gears are modeled as deformable flex-bodies. The nonlinear contact force, $F = K(d)^e - cv$, is composed of an elastic and damping portion [16], d is the penetration depth. The damping force, cv , is proportional to impact velocity, v . The stiffness coefficient, K , is taken to be the average value of stiffness over one tooth mesh cycle. The force exponent, e , was determined from trial simulations. The damping coefficient generally takes a numeric value between 0.1% - 1% of K . The determination of force exponents however is not obvious and must be based on experience.

The MSC.ADAMS IMPACT algorithm was chosen as the contact force model because of its robustness in numerical integration. The restitution model is extremely sensitive to the duration of the contact event, and is best suited for impulse type simulations. It is not ideal for time histories that include a large number of contact events in which the force vector is not known beforehand. The stiffness parameter is reasonable for this lightly loaded steel gear pair, and was determined via a trial and error method. The response of interest occurs over a very short time interval, around one hundred milliseconds. Because the damping force in meshing gears is such a small percentage of K , its affect on the simulation results is not significant. Therefore, the damping coefficient is kept as near to zero as possible to simplify the numerical solver routine. Penetration depth is defined here as the depth at which the damping force becomes active. Similarly, modification of this value does not have a significant effect on response of either gear. The geometric gear pair parameters and MSC.ADAMS contact parameters are shown in Table 1.

Table 1. Geometric Parameters and Simulation Contact Force.

Algorithm		MSC.ADAMS IMPACT
Stiffness		2e7 [lb _f /in]
Force Exponent		2.2
Damping		2e-2 [% stiffness]
Penetration		1e-7 [in]
Diametral Pitch	P_d	10 [teeth/in]
Pressure Angle	Φ	20 [deg]
Face Width	F	0.5 [in]
Pinion	p	23 [teeth]
Gear	g	31 [teeth]
Backlash	B	0.004 [in]

The eccentric tooth is generated by rotating the involute profile along the base circle of the pinion by a very small, arbitrary angle that does not cause mesh interference. Similarly, the chipped gear is created by removing a reasonable amount of mass from a single tooth. From the defined gear backlash, the center distance of the gear pair is calculated as 2.705 in [18].

2.2 Simulation results and discussions

Combined with gear profile errors, backlash may cause loss of contact between gear teeth. This may induce consecutive single-sided and/or double-sided impacts and generate large impact forces and large vibration. R_p and R_g are the radii of the base circles of pinion and gear, respectively. The relative displacement between the two mating teeth profiles along the line of action is represented as, $S = R_g\theta_g - R_p\theta_p$. Obviously, when S is bigger than the gear backlash B , there is contact between pinion and gear. For a simple spur set this equation should be true at all times, $-B \leq R_g\theta_g - R_p\theta_p \leq B$.

Fig.3 shows relative displacement S along the line of action with pinion initial velocity $\omega_{\text{input}} = 100$ rad/s for a perfect meshing pair and for a pair with eccentric tooth on the pinion. It is interesting to notice that the back collision takes place during the separation of the gears. Successive double-sided impacts are observed on the alternating surfaces of the meshing pair. The early motion of Fig.3 is outside $\pm B$ because of the penetration required by the impact force algorithm. As time increases, penetration decreases and the period between impacts increase for both perfect gear and eccentric gear pairs.

Furthermore, since each point on this plot determines a precise orientation of the mating teeth of each gear, the geometric condition of the eccentric pinion tooth causes an interesting result. More "oscillations" have occurred in the same amount of time. This can be explained by considering that the tooth itself is larger, and therefore it has less space to move within the backlash band of $2B$. Upon startup the eccentric tooth will contact with the mating tooth earlier than it would with perfect geometry.

Fig.4 illustrates the angular velocity of the gear for both a perfect gear pair and a chipped gear pair with a pinion initial velocity and constant applied torques. As contact with the gear occurs, the pinion and gear velocities both change rapidly.

These large magnitudes, which occur for the first 20 ms, are due to the pinion's initial velocity. This transient response dies out quickly, and only the effects of the constant applied torques are observed. Both pinion and gear experience single-sided impacts, shown in Fig.4.

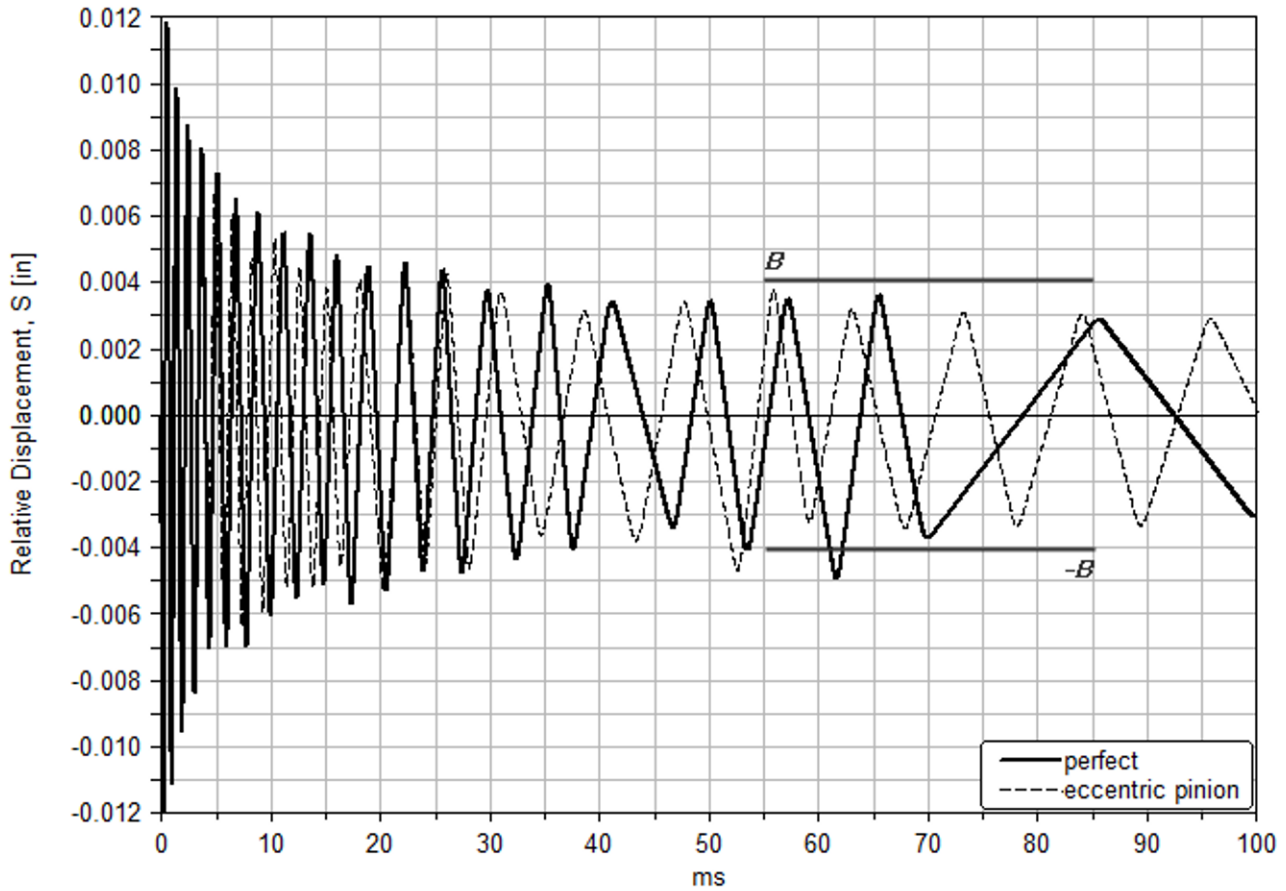


Fig.3 Relative displacement S along the line of action with pinion initial velocity $\omega_{\text{input}} = 100$ rad/s

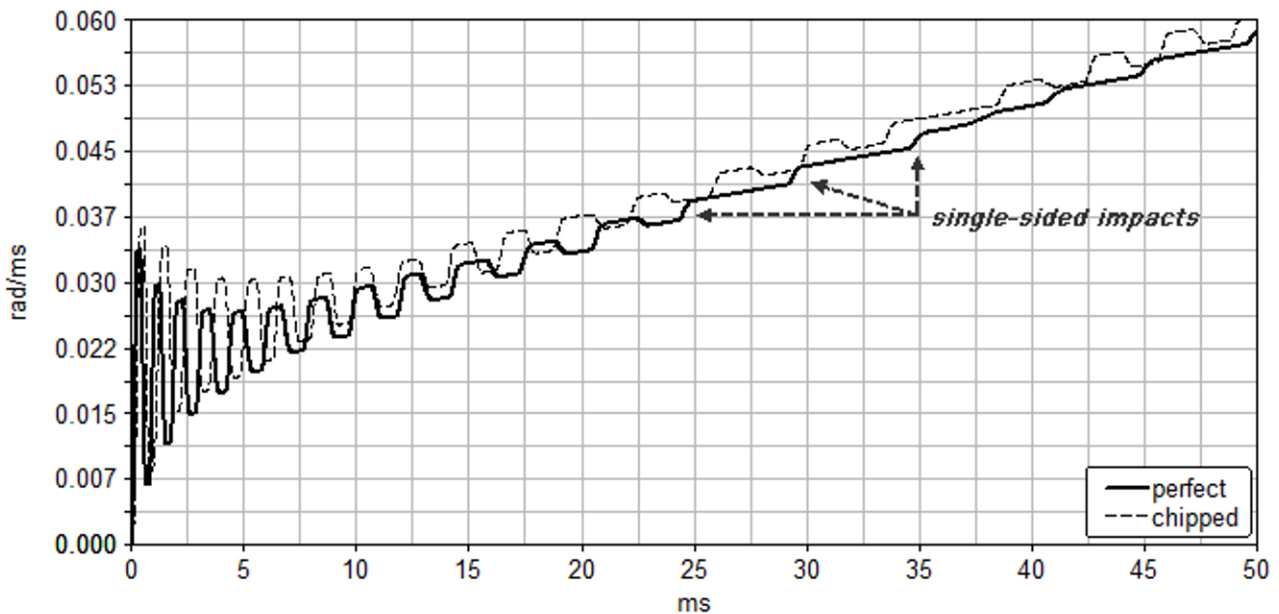


Fig.4 Angular velocity of the pinion with initial velocity 100 rad/s; 3 lbf-in torque applied to pinion; -3 lbf-in torque applied to gear.

The effect on the number of impacts is the opposite of that seen with the eccentric tooth presented in Fig.3. It takes a little longer for the pinion to contact the gear because the gear's involute profile has been modified. Close inspection shows that the chipped gear case has less direction changes than the perfect case, and hence less impact events. This is a clear representation of double-sided impacts.

3. Crank-Slider Mechanism with Two-stage Gear Train

3.1. Multi-body kinematic model of crank-slider mechanism with two-stage gear train

In order to investigate how the interaction of backlash and manufacturing errors affects the dynamic behaviors and contact forces of a more complicated gearing system, a crank-slider mechanism with two-stage gear train is studied. The gear design parameters and simulation parameters are shown in Table 3 and Table 4, respectively. Fig.5 and Fig.6 show the two-stage gear train and crank-slider mechanism respectively.

Table 3. Gear Design parameters

Modules m [mm/tooth]	$m_1=4; m_2=5$
Number of teeth	$Z_a=17; Z_b=60;$ $Z_c=19; Z_d=72$
Standard Pitch circle diameter d (mm)	$d_a=68; d_b=240;$ $d_c=95; d_d=360$
Total gear ratio	13.375
Pressure angle	20°

Table 4. Simulation parameters

Backlashes [mm]	$B_1 = 0.05; B_2 = 0.08$
Material properties	$E = 2.07 \times 10^{11} \text{ Pa};$ $\nu = 0.29;$ $\rho = 7801 \text{ kg/m}^3$
Force exponent	2.2
Penetration	10^{-7} mm
Stiffness	$2 \times 10^7 \text{ N/mm}$

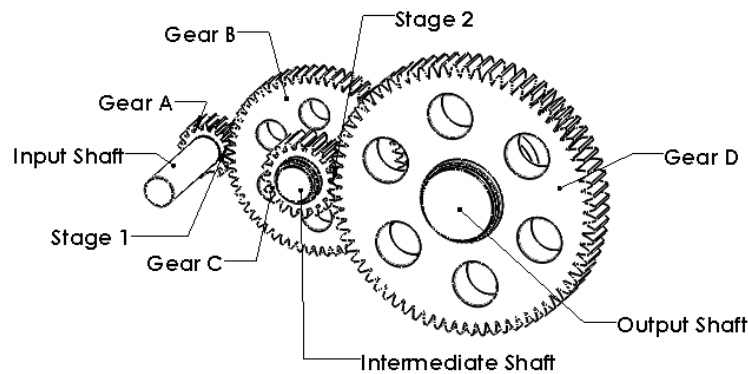


Fig.5 Two-stage gear train

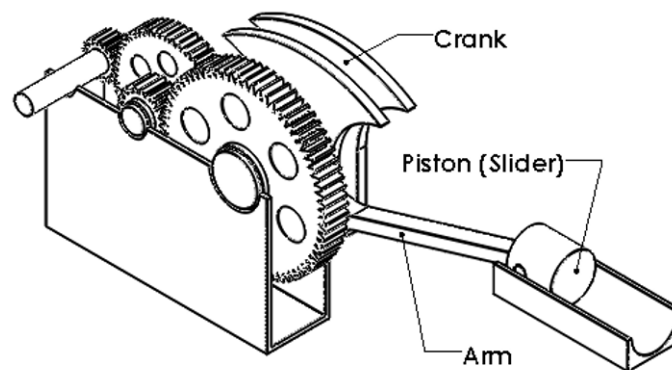


Fig.6 Crank-Slider Mechanism

3.2 Free Vibration Simulation Results and Discussion

The "perfect" waveform represented in Fig.7 is the response of all four gears with perfect geometry and prescribed backlash. The "chipped" curve is the response of an input pinion with a chipped tooth, all other gears are perfect. The coordinate orientation is such that a force *from the pinion to the gear* is considered positive. This simulation emulates the machine operating at steady-state conditions and suddenly losing power. The system is given an initial velocity on each shaft that corresponds to its rotary speed under operating conditions.

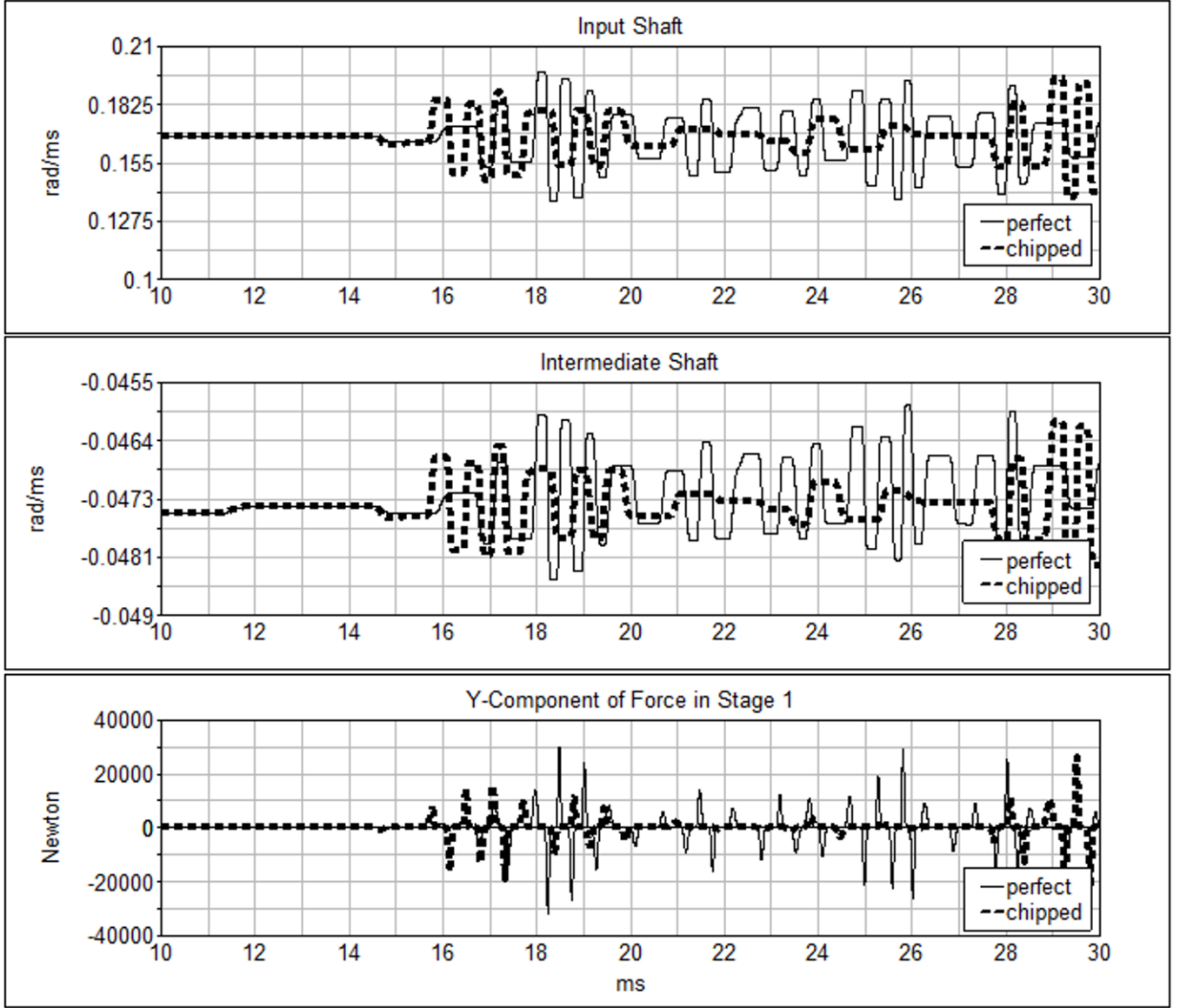


Fig.7 Free vibration response with input shaft, 167.5 rad/s; intermediate shaft, -73.5 rad/s; output shaft, 12.5 rad/s.

From the top two plots of Fig.7, the initial position of the gears is such that neither stage is in contact at the beginning of the simulation. Therefore, all three shafts are rotating without any impacts until Gear C touches Gear D at approximately 12 ms. Gear B touches Gear A around 15 ms, causing the contacts in Stage 1 to increase in frequency for the next 20 ms. The response of the intermediate shaft is due to a superposition of the impact in Stage 1 and Stage 2. The angular velocity of the intermediate shaft is shown to be combination of the other two shafts' angular velocities.

Double-sided impacts are clearly evident in the Y-Component of Force in Stage 1. For the chipped pinion case the impact force occurs at an earlier time. This can be explained in part through the reduction in inertia. The mass moment of inertia of the perfect input pinion is $I_{zz} = 1.06 \times 10^{-3} \text{ kg-m}^2$, while the chipped tooth pinion is $I_{zz} = 1.04 \times 10^{-3} \text{ kg-m}^2$. This is a reduction of

1.76%. The chipped pinion will experience a larger acceleration for a given impact force. The teeth neighboring the chipped tooth will contact the mating gear sooner than it would with the standard inertia.

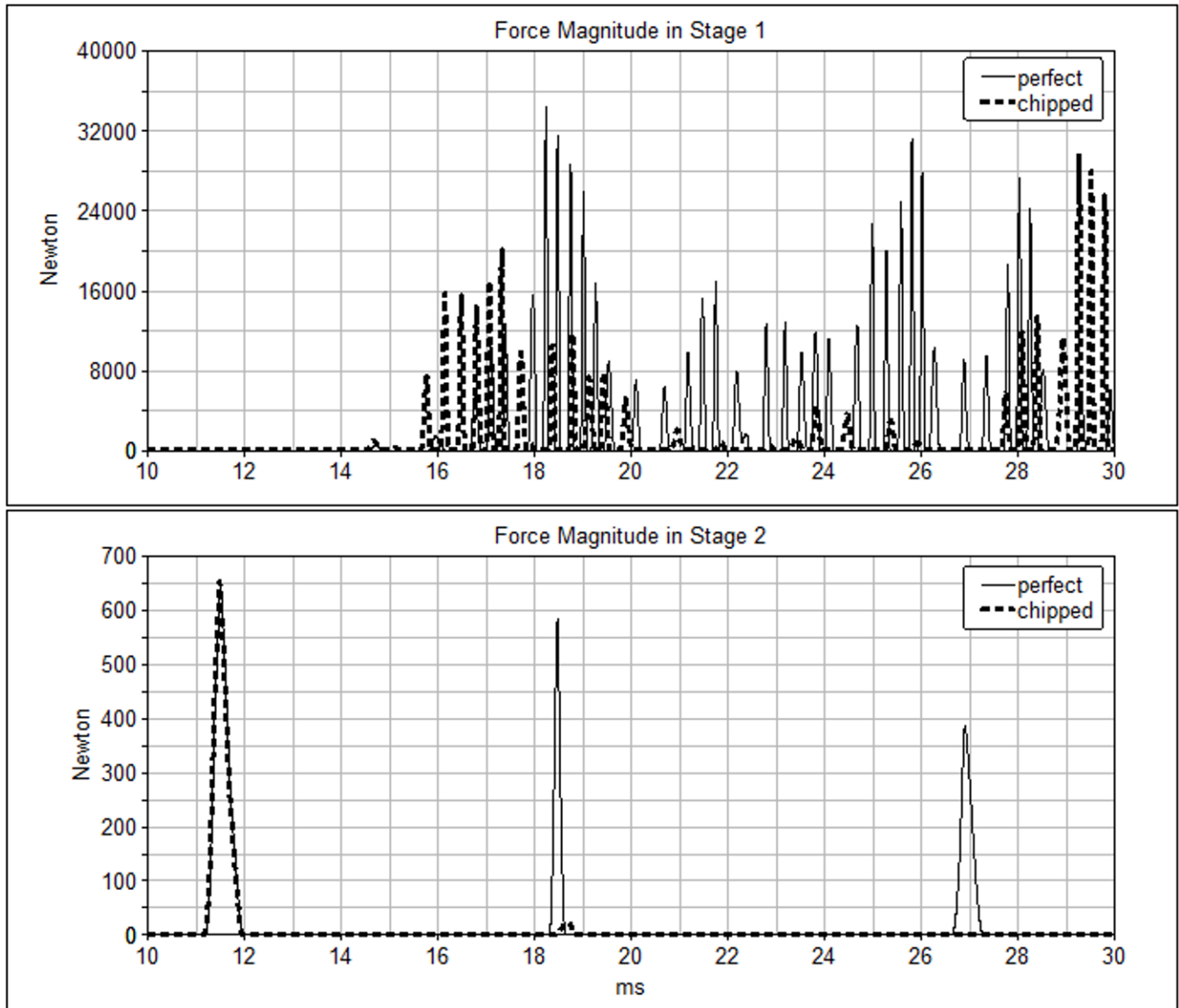


Fig.8 Comparison of the force magnitudes of Stage 1 and Stage 2 with the initial conditions: input shaft, 167.5 rad/s; intermediate shaft, -73.5 rad/s; output shaft, 12.5 rad/s.

The force response in Stage 2 is depicted in Fig.8. The first and second contacts occur at nearly the same time for both the perfect and chipped cases. With perfect mesh geometry, Gear D experiences three single-sided impacts for $10 \leq t \leq 30$ ms. With a chipped pinion tooth, Gear D only experiences two single-sided impacts during the same interval.

An impact occurs in Stage 2 before Stage 1, at first this may seem counter-intuitive. The initial velocities given to each shaft are based upon their rated operating speed. The bearings are modeled as frictionless, constraining all degrees of freedom except for rotation in the normal plane. The relative velocity on the pitch circle of Gear C and Gear D is slightly larger than between Gear A and Gear B. For initial conditions in which the relative velocity between Gear A and Gear B is larger than between Gear C and Gear D, the opposite would occur.

The system is modeled as the interaction of three rigid bodies. The first is the input shaft and Gear A. The second is Gear B, the Intermediate Shaft, and Gear C. The third is Gear D, the Output Shaft, and the Crank. The third body has an inertial mass at least one order of magnitude larger than the other two bodies. Its velocity changes more slowly than for the other

two bodies, due to inertia effects. The small delay between responses around 18.5 ms can be attributed to the chipped tooth. Because the tooth is missing the force response in Stage 2 is slightly delayed.

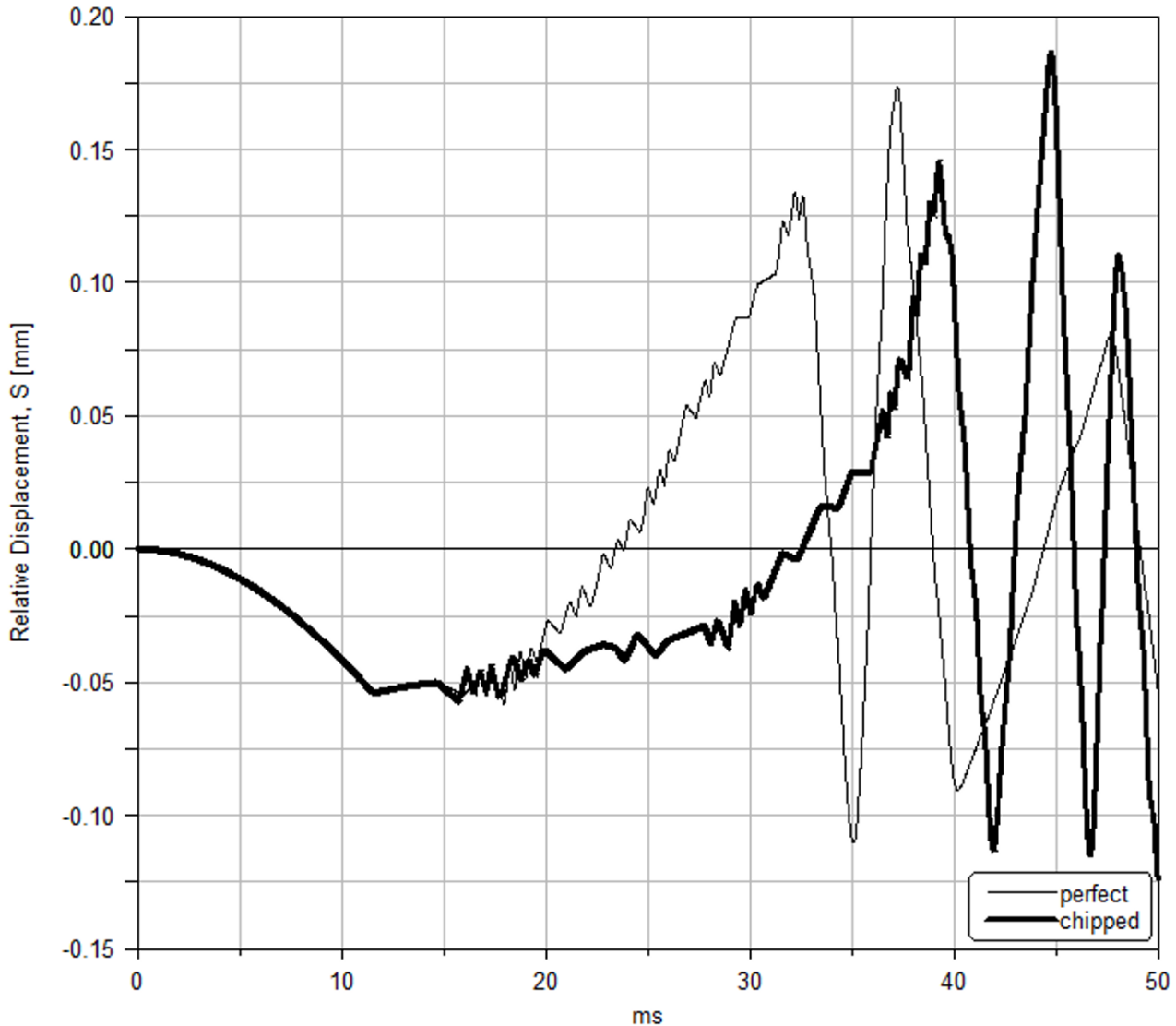


Fig.9 Relative displacement S along the line of action on stage 2 with the initial conditions: input shaft, 167.5 rad/s; intermediate shaft, -73.5 rad/s; output shaft, 12.5 rad/s.

Fig.9 shows the relative displacement between Gear C and Gear D in Stage 2. Any point on this plot defines the position for both Gear C and Gear D for any give time. The contacts in the first stage directly effect the position of Gear C. Due to the interaction of Gear A and Gear B, Gear C oscillates back and forth as it moves between teeth of Gear D. The quantity $S = R_g \theta_g - R_p \theta_p$ for the second stage appears as a jagged line. These small peaks correspond directly to the Force in Stage 1, shown previously in Fig.8. Once Gear C makes contact with Gear D the response becomes smoother. The effect is still there, but the speed of Gear D is now changing more rapidly and these smaller position changes are more difficult to distinguish. For the case with a chipped tooth on the input pinion, the entire curve is shifted forward in time. Although the impacts in Stage 1 occur earlier, the overall effect in Stage 2 is delayed. The missing tooth causes Stage 1 to become more excited, as a result it takes longer for the contact in Stage 2 to occur.

3.3 Forced Vibration Simulation Results and Discussions

A step torque of the form $T(1 - e^{t/\tau})$ is applied to the input shaft with amplitude of 149.123 N-m at 100 ms. to simulate an accelerating condition.

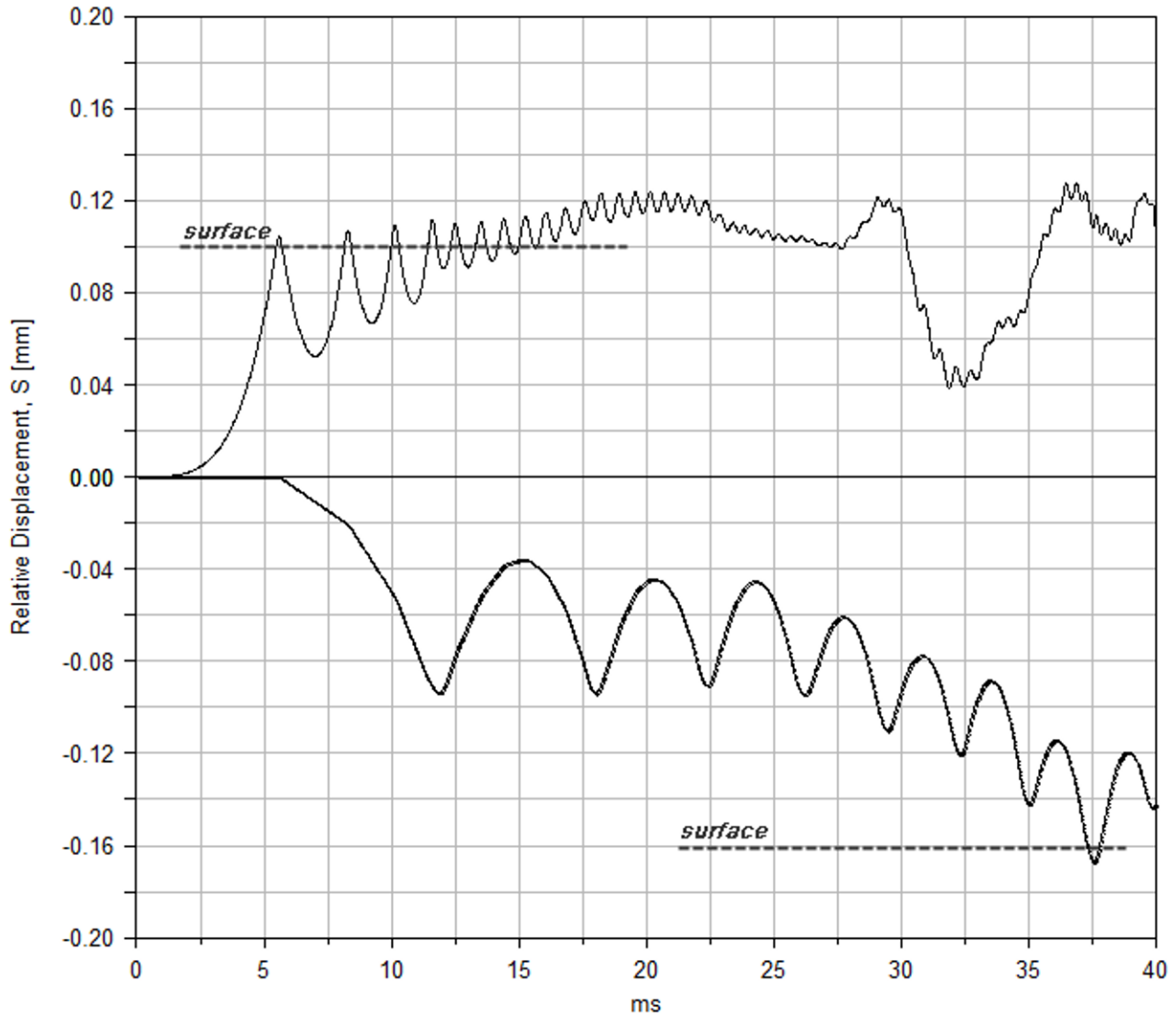


Fig.10 Comparison of relative displacements S along the line of action on stage 1 and stage 2 with step input torque 149.123 N-m

From Fig.10, the gears in each mesh come to an equilibrium position in which they remain in contact. This must be true for the system to be transmitting power. The driving teeth approach the "surface" of the driven teeth, oscillating with less amplitude as time increases. The decrease in oscillation amplitude is most notable in Stage 1. The quantity $S = R_g\theta_g - R_p\theta_p$ waveforms approach the "surfaces" indicated.

From Fig.11, the impacts in both stages increase in magnitude with time, and also occur at increasingly shorter intervals. The force in Stage 2 is larger because Gear D is being driven, effectively by the torque on the Input Shaft. The large inertia of this third rigid body must be overcome solely with the force from Gear C to Gear D in Stage 2. The Stage 2 impacts carry the energy accumulated in the Stage 1, and therefore have a larger amplitude.

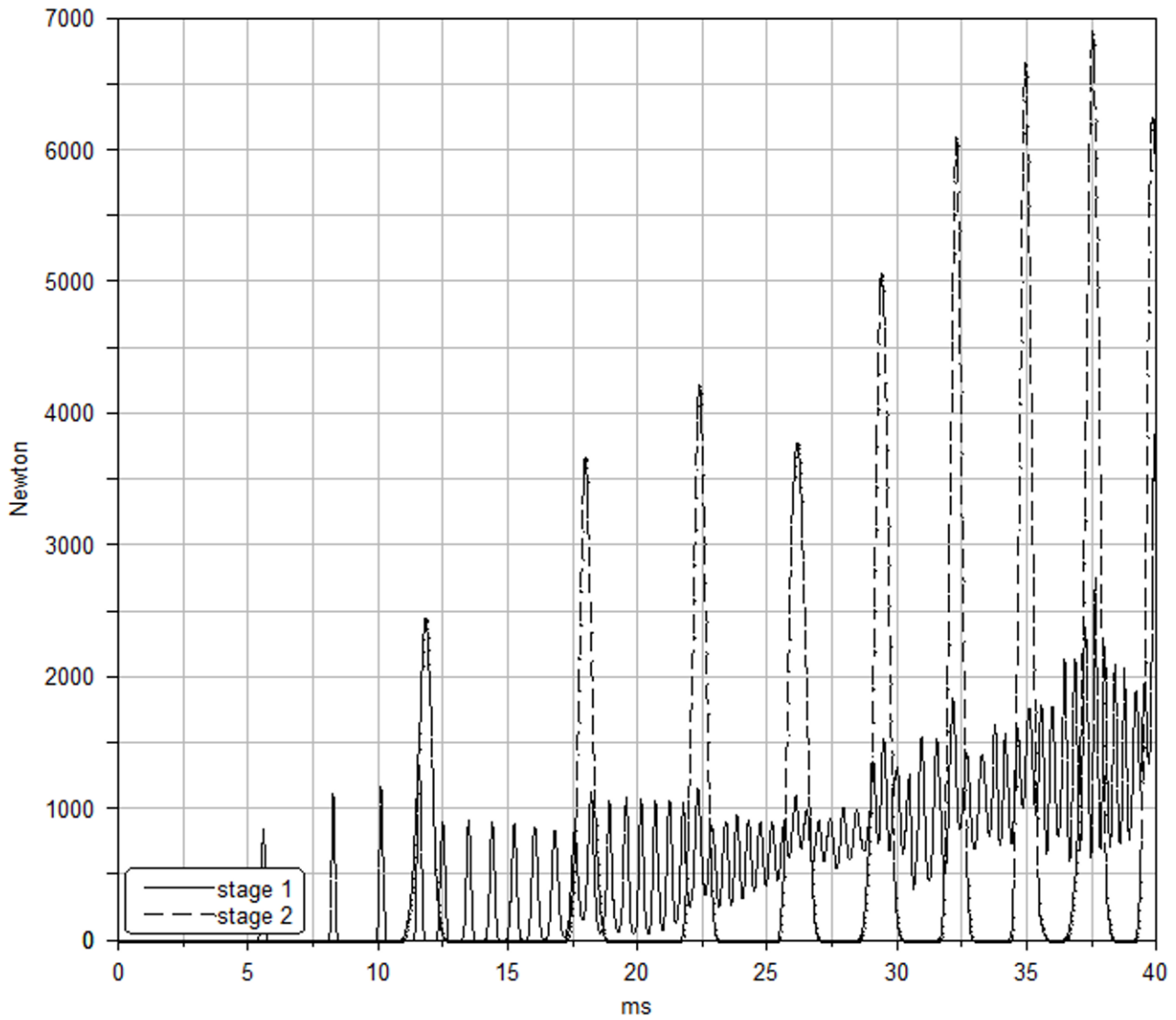


Fig.11 Comparison of the force magnitudes on stage 1 and stage 2 with step input torque 149.123 N-m

4. Conclusions

A non-linear multi-body dynamic software model has been developed for a fixed-axis transmission and a crank-slider mechanism to demonstrate the effects of dynamic loading on gear teeth. The stiffness, force exponent, damping, and friction coefficients for the MSC.IMPACT force algorithm are derived for a practical transmission. Single-sided impacts are observed in a spur pair when the pinion is given an initial velocity, and torques of equal magnitude but opposite direction are applied to each gear. The dynamic behavior of the intermediate shaft of a two stage crank-slider mechanism is shown to be a superposition of the impact forces acting in each mesh. The geometric error of a chipped tooth on the pinion gear of this mechanism causes a delay in the contact forces in the second stage. A realistic driving step torque creates impact forces which increase in both magnitude and frequency as the crank accelerates to its operating speed.

5. Acknowledgement

The authors acknowledge the Donald E. Bently Center for Engineering Innovation at California Polytechnic State University San Luis Obispo for support of this work.

REFERENCES

1. Dubowsky, S. and Freudenstein, F., "Dynamic Analysis of Mechanical Systems With Clearances, Part 1: Formulation of Dynamic Model", *ASME Journal of Engineering for Industry*, Vol. 93, Feb. 1971, pp. 305-309.
2. Dubowsky, S. and Freudenstein, F., "Dynamic Analysis of Mechanical Systems With Clearances, Part 2: Dynamic Response", *ASME Journal of Engineering for Industry*, Vol. 93, Feb. 1971, pp. 310-316.
3. Azar, R. C., and Crossley, F. R. E., "Digital Simulation of Impact Phenomenon in Spur Gear Systems", *ASME Journal of Engineering for Industry*, Vol. 99, Aug. 1977, pp. 792-798.
4. Yang D.C.H. and Sun Z.S., "A Rotary Model for Spur Gear Dynamics", Transactions of the ASME, *Journal of Mechanisms, Transmissions and Automation in Design*, Vol. 107, Dec. 1985, pp. 529-535.
5. Özgüven H.N. and Houser D.R., "Mathematical Models used in Gear Dynamics – A Review", *Journal of Sound and Vibration*, 121(3), 1988, pp. 383-411.
6. Parey, A. and Tandon, N., "Spur Gear Dynamic Models Including Defects: A Review", *The Shock and Vibration Digest*, Vol. 35, No. 6, Nov. 2003; pp. 465-478.
7. G. Dalpiaz, A. Rivola and R. Rubini, "Effectiveness and Sensitivity of Vibration Processing Techniques for Local Fault Detection in Gears", *Mechanical Systems and Signal Processing*, Vol. 14(3), 2000, pp. 387-412.
8. Parey, M. El Badaoui, F. Guillet, N. Tandon, "Dynamic modeling of spur gear pair and application of empirical mode decomposition-based statistical analysis for early detection of localized tooth defect", *Journal of Sound and Vibration* Vol. 294, 2006, pp. 547–561.
9. Saeed Ebrahimi and Peter Eberhard, "Rigid-elastic modeling of meshing gear wheels in multi-body systems", *Multi-body System Dynamics* Vol. 16, 2006, pp. 55–67.
10. Tahar Fakhfakh, Fakher Chaari and Mohamed Haddar, "Numerical and experimental analysis of a gear system with teeth defects", *The International Journal of Advanced Manufacturing Technology*, Vol. 25, 2005, pp. 542–550.
11. I. Ciglaric and A. Kidric, "Computer-aided derivation of the optimal mathematical models to study gear-pair dynamic by using genetic programming", *Structural and Multidisciplinary Optimization*, Vol 32, 2006, pp. 153–160.
12. M. Pimsarn and K. Kazerounian, "Pseudo-interference stiffness estimation, a highly efficient numerical method for force evaluation in contact problems", *Engineering with Computers*, Vol.19, 2003, pp. 85–91.
13. Meagher, J., Wu, X., Kong, D., Lee, C., "A Comparison of Gear Mesh Stiffness Modeling Strategies", *IMAC XXVIII a Conference on Structural Dynamics*, Society for Experimental Mechanics, Jacksonville, Florida USA, February 1 –4, 2010.
14. Ebrahimi S. and Eberhard P., "Rigid-elastic modeling of meshing gear wheels in multi-body systems", *Multi-body System Dynamics*, Vol. 16, 2006, pp. 55–71.
15. Kong, D., Meagher, J., Xu, C., Wu, X., Wu, Y., "Nonlinear Contact Analysis of Gear Teeth for Malfunction Diagnostics", *IMAC XXVI a Conference on Structural Dynamics*, Society for Experimental Mechanics, Orlando, Florida USA, February 4 –7, 2008.
16. MSC Inc., *MSC ADAMS reference manual*.
17. Machinery's Handbook 28th Larger Print Edition.
18. Raymond J. Drago, *Fundamentals of Gear Design*, 1988.

A Differential Planetary Gear Model with Backlash and Teeth Damage

Xi Wu, Jim Meagher, Andrew Sommer

Department of Mechanical Engineering, California Polytechnic State University, San Luis Obispo, CA.
93407-0358

ABSTRACT

Planetary gear trains can be more compact and efficient as power transmissions than fixed axis gear trains but are also more complicated and less understood in terms of vibration health monitoring. A practical differential planetary gear train, which combines two inputs and one output, is studied using multi-body dynamics software. Backlash between the sun gear and planet gears are precisely specified to avoid teeth interference and undercut. In order to calculate accurate impact forces, an impact model is chosen. Tooth geometry errors are created on the sun gear. Constraints and contact forces to the model are applied as close as possible to real operating conditions. Torsional vibration induced by backlash and tooth geometry errors is shown to cause teeth separation and double-sided impacts in unloaded and lightly loaded gearing drives. Planetary gears with only backlash errors are compared to those containing both backlash and tooth defects under different kinematic and loading conditions. Time domain results show that the dynamic responses due to the combination of backlash and tooth defects depend on the interaction of many components of the differential planetary system.

Keywords: Vibration health monitoring, Contact Forces, Planetary Gear, Backlash, Chipped Tooth, Multi-body kinematic model.

1. Introduction

The planetary gear train is widely used in transmission design of automobiles, helicopters and aircraft engines due to the numerous advantages over traditional fixed-axis gear transmissions. Since the load being transmitted is shared between several planets, torque capability is significantly increased. One notable advantage of a planetary gear is its distinctive combination of both compactness and magnificent power transmission efficiencies. Despite the above advantages, however, the complicated dynamic forces existing among sun, planet and ring gears are difficult to analyze for the main sources of the vibration. Reasonably simulating the practical dynamic force between single-mating-gear pair still remains as an important topic. Needless to say, it is even more challenging to realistically model a planetary gear train with multiple meshing stages. As a result, the dynamic analyses of planetary gear trains have received far less attention than fixed-axis gear trains.

The earliest review papers that discuss the numerical modeling of gear dynamics focus on spur gears: Özgüven and Houser in 1988 [1] and by Parey and Tandon in 2003 [2]. The models had a limited number of degrees of freedom and most commonly did not include tooth defects. Tooth meshing stiffness was characterized as either an average or piecewise linear variation instead of the highly nonlinear Hertzian contact. Parey and Tandon's review did include spur gear defects. Parey etc. [3] developed a six DOF nonlinear model for a pair of spur gears on two shafts, calculated the Hertzian stiffness for the tooth surface contact, and implemented the empirical mode decomposition (EMD) method to simulate the different defect widths. The above research is based on fix-axis gears.

Lin and Parker [4] analytically investigate the parametric instability of planetary gears induced by gear mesh stiffness variation. The authors use rectangular waveforms with different contact ratios and mesh phasing to simulate the gear mesh stiffnesses existing between sun-planet and planet-ring gear mating pairs. Instability boundaries are directly associated with meshing parameters in the vibration modes. The authors also demonstrate some numerical simulation results about the teeth separation caused by parametric instability and strong impact in the system response. Lin and Parker [5] derive a theoretical model and carefully identify the important characteristics of the natural frequencies and vibration modes for planetary gears. The model uses three planar degrees of freedom for each component of the planetary gears and takes gyroscopic effects and time-varying gear mesh stiffnesses into consideration. The authors do comprehensive investigations about the distinctive

characteristics of each type of mode. Based on the model of reference [5], Guo and Parker [6] extended the two-dimensional lumped-parameter model by incorporating the factors of teeth separation, back-side contact, tooth wedging, and bearing clearances. By scrutinizing the dynamic response of an example planetary gear, the authors investigate the nonlinear tooth wedging behavior often observed on a wind turbine planetary gear train. More research about dynamic behavior of planetary gears can be found in reference [7, 8]. Unfortunately, the majority of current papers about planetary gears does not include the interactive effects of backlash and gear teeth damage.

Although simplified model for even a one-stage gear train involves sophisticated mathematics, it cannot accurately simulate the gear train's practical dynamic behavior even for an ideal system by simply assuming time-varying gear mesh stiffness as square waveforms. The impact forces between the mating pairs are very sensitive to the geometric profile of gear tooth and the gear backlash which must be carefully designed. Geometric simplifications can be overcome by combining CAD models with ADAMS. Kong and Meagher etc. [9] modeled the nonlinear contact mechanics of large gearbox in that way but backlash was not included.

In this study, a practical differential planetary gear train, which combines two inputs and one output, is studied using multi-body dynamics software. The backlash between the sun gear and planet gears are carefully designed and calculated to avoid teeth interference and undercut. Tooth profile errors are introduced for comparison to ideal gears. The nonlinear contact mechanics model of the meshing teeth is built by careful calculation and selection of the contact simulation parameters such as the stiffness, force exponent, and damping and friction coefficients. Planetary gears with only backlash errors are compared to those containing both backlash and tooth defects under different kinematic and loading conditions. Time domain results will show that the dynamic responses due to the combination of backlash and tooth defects depend on the interaction of many components of the differential planetary system.

2. Modeling a differential planetary gear train with backlash and teeth damage

The differential planetary gear chosen for study has two inputs and one output [11,12, 13]. The transmission schematic and CAD model are shown in Fig.1(a), and Fig.1(b), respectively. The profile of the "chipped" sun gear tooth is shown in Fig.2. Geometric parameters of the planetary gear train are shown in Table 1.

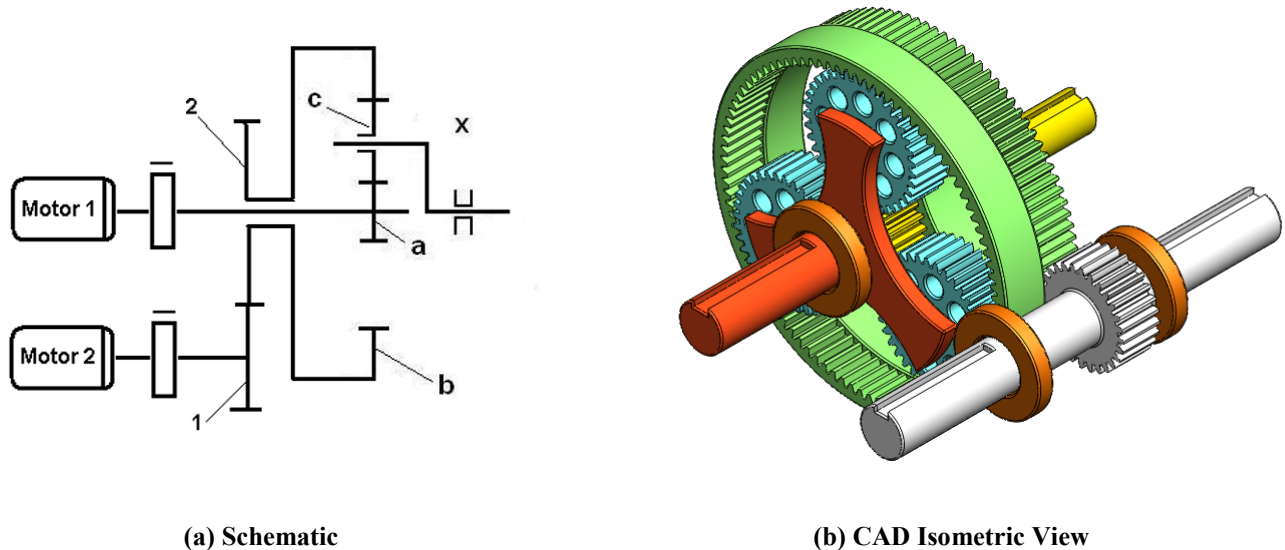


Fig.1 A differential planetary gear with two inputs and one output



Fig.2 Chipped tooth profile

Table 1. Planetary gear design and simulation parameters

Module m (mm)	$m = 2$	Backlashes (mm)	$B_1 = 0.04; B_2 = 0.03$
Number of teeth	$Z_a=20; Z_b = 94;$ $Z_c= 37; Z_1 =28; Z_2 =98$	Material properties	$E = 2.07 \times 10^{11} \text{ Pa};$ $\nu = 0.29;$ $\rho = 7801 \text{ kg/m}^3$
Standard Pitch circle diameter d (mm)	$d_a = 40; d_b = 188;$ $d_c=74; d_1 =56; d_2 = 196$	Force exponent	2.2
Gear Ratios	5.7; 1.213	Penetration	10^{-7} (mm)
Pressure angle	20°	Stiffness	$2 \times 10^7 \text{ (N/mm)}$

Combined with gear profile errors, the backlash may cause the loss of contact between gear teeth. This may induce large impact forces associated with consecutive single-sided and/or double-sided impacts. The contact surfaces between the gears are modeled as deformable flex-bodies. The nonlinear contact force, $= K(d)^e - cv$, is composed of an elastic and damping portion [10]. d is the penetration depth. The damping force, cv , is proportional to impact velocity, v . The stiffness coefficient, K , is taken to be the average value of stiffness over one tooth mesh cycle. The force exponent, e , was determined from trial simulations. The damping coefficient generally takes a numeric value between 0.1%-1% of K . The determination of force exponents however is not obvious and must be based on experience.

The MSC.ADAMS IMPACT algorithm was chosen as the contact force model because of its robustness in numerical integration. The restitution model is extremely sensitive to the duration of the contact event, and is best suited for impulse type simulations. It is not ideal for time histories that include a large number of contact events in which the force vector is not known beforehand. The stiffness parameter is reasonable for this lightly loaded steel gear pair, and was determined via a trial and error method. The response of interest occurs over a very short time interval, around one hundred milliseconds. Because the damping force in meshing gears is such a small percentage of K , its affect on the simulation results is not significant. Therefore, the damping coefficient is kept as near to zero as possible to simplify the numerical solver routine. Penetration depth is defined here as the depth at which the damping force becomes active. Similarly, modification of this value does not have a significant effect on response of either gear. The MSC.ADAMS contact parameters are shown in [Table 1](#). For ease of comparison, the dynamic conditions of each figure are shown in [Table 2](#).

Table 2. Dynamic Conditions Depicted in Figures

Fig. No.	Simulation Parameters
3, 4, 5	$\omega_{x0} = 100$ rad/sec <i>initial</i> angular velocity applied to the carrier, fixed ring
6,7	$\omega_{x0} = 100$ rad/sec <i>initial</i> angular velocity applied to the carrier, free ring
8, 9,10	$\omega_1 = 102.1$ rad/sec <i>constant</i> angular velocity applied to the sun, fixed ring
11, 12, 13(a)	$T_1 = 70.518$ N-m step torque applied to the sun, fixed ring
13(b), 14	$T_1 = 70.518$ N-m step torque applied to the sun, $T_2 = 67.935$ N-m applied to gear 1

3. Dynamic response and discussion of a planetary gear with the ring gear fixed

When ring gear b and gear 1 are fixed, an initial angular velocity $\omega_{x0} = 100$ rad/sec is applied on the carrier x. The carrier and sun gear are rotating in the same direction. By inspection of Fig.3, the planets must be rotating in the opposite direction of both the sun and carrier. The responses of the planet gears are nearly identical. This is expected because their axes are moving with the rotating carrier, and therefore make contact with both the sun and ring at nearly the same instant.

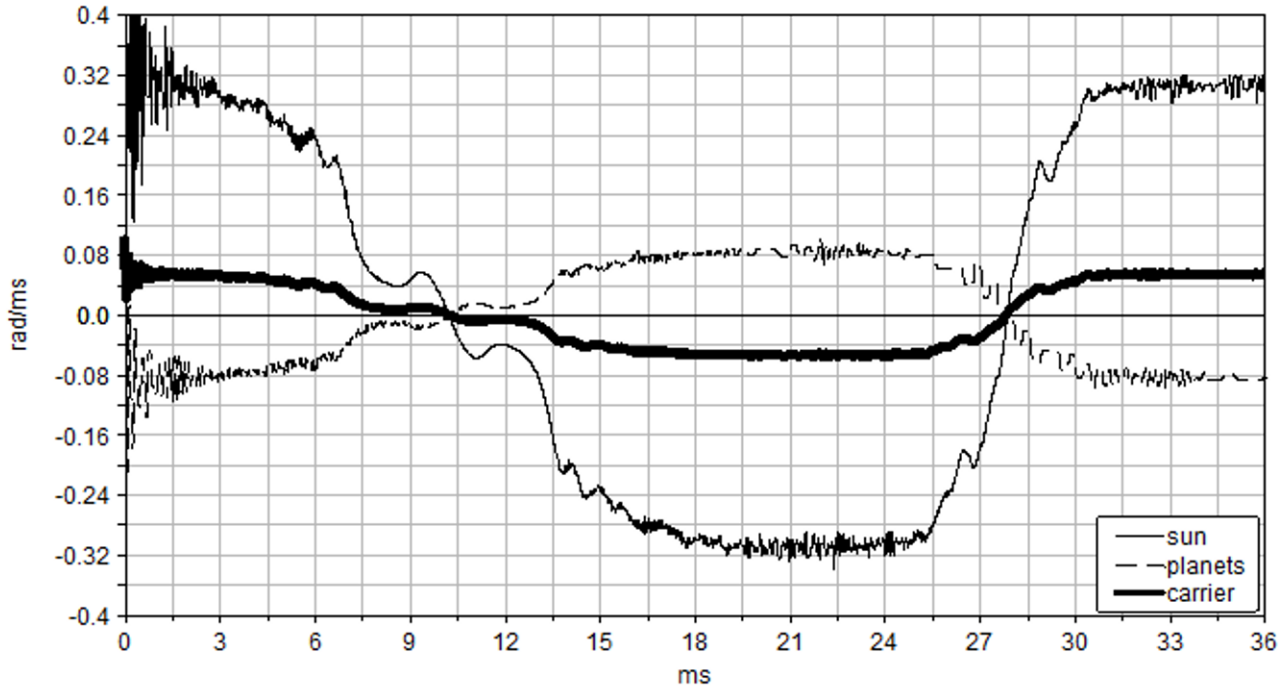


Fig.3 Angular velocity vs. time, when *initial* angular velocity $\omega_{x0} = 100$ rad/sec is applied to the carrier

Consider the situation in Fig.4 when two or more planets experience nearly identical forces. This occurs when they are both in contact with a given element, either the sun or ring, and are "sharing" the load. Each planet gear is given an arbitrary designation of either 1, 2, or 3, respectively. Between 5 and 15ms planet 1 is the only planet in contact with the sun, therefore both planet1 and planet 3 are traveling within their respective backlash. During this same interval, planet1 is not in contact with the ring. The MSC.ADAMS simulation model includes six contact forces: three on the sun gear from each planet, and three on the ring gear from each planet. At any instant in time, no force or any combination of all six forces are potentially active. Due to the small damping prescribed in the contact force, this pattern will completely die out after a significant amount of time has passed. The pattern enclosed shown between 0 and 30 ms continuously repeats with slightly less magnitude on each repetition.

A *near equilibrium position* is utilized in all presented simulations. First, consider the situation when the transmission is in an exactly symmetrical position. The front and right planes of the sun and ring would be coincident, and their top planes parallel. Each of the three planets would be in the exact center of the backlash space of the sun and ring meshes. In this position the response of each planet gear would be identical, and contact would occur at the exact same instant. The

symmetrical position is deliberately avoided. The sun, planets, and ring begin within the backlash space, but slightly displaced from the perfect center. In this way contact occurs on each element at different times, and the interesting force response of Fig.4 are observed. This *near equilibrium position* creates the difference in contact force magnitudes, which is driving the behavior of the planetary transmission. The *near equilibrium position* is utilized in all simulations presented in this investigation.

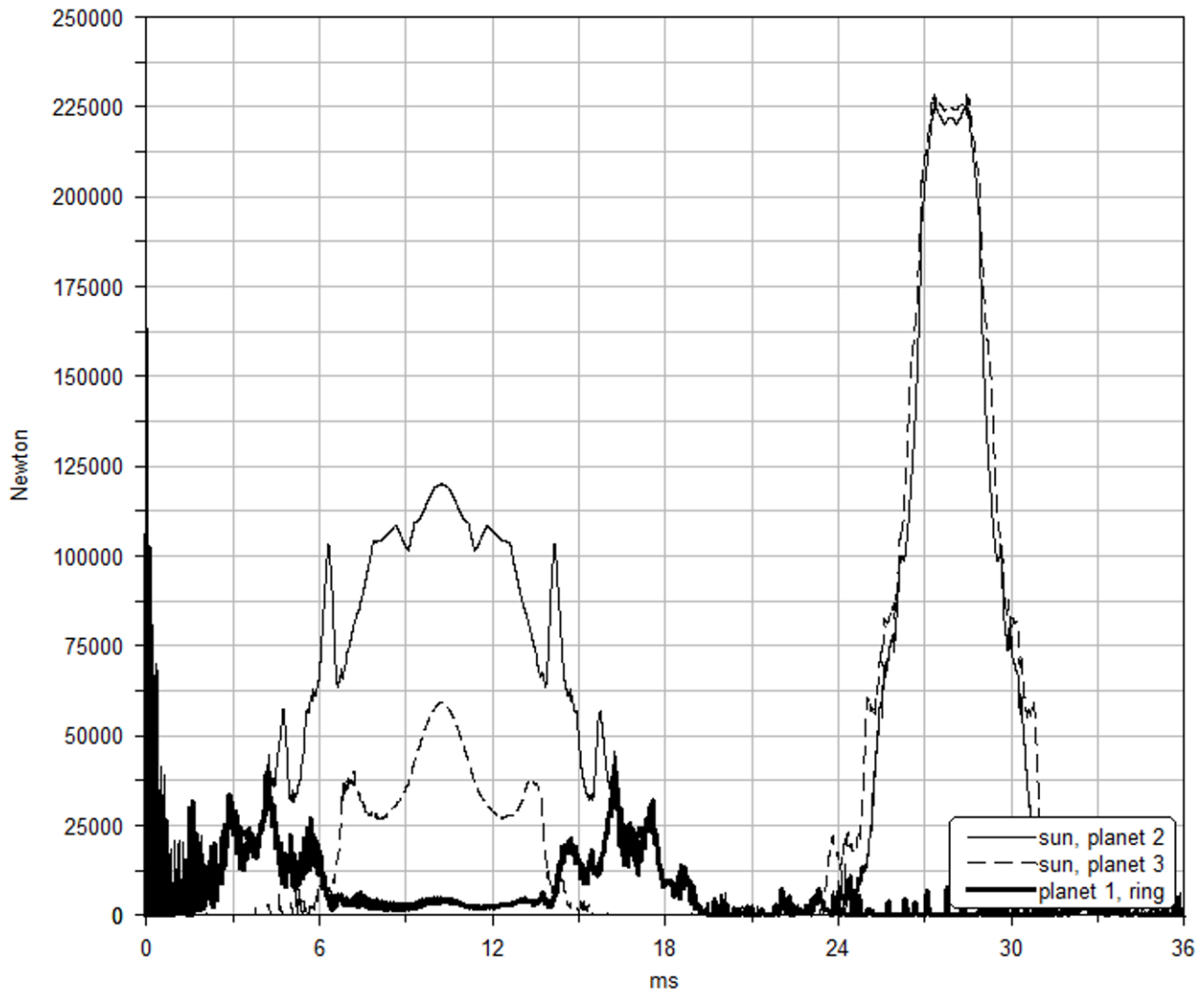


Fig.4 Contact forces vs. time, when *initial* angular velocity $\omega_{x0} = 100$ rad/sec is applied to the carrier

4. Dynamic response and discussion of a planetary gear with free ring gear

This discussion is an extension of the free vibration explored in section 3. Both the ring gear and gear 1 are now unconstrained and allowed to rotate freely. The initial velocity of the carrier is now transferred into all of the transmission elements, instead of only the sun and planets. Due to the ring gear's relatively large mass moment of inertia, the introduction of its rotation causes some interesting phenomena.

The results of this more complicated free vibration are counter-intuitive. The elements no longer oscillate with the same frequency with respect to the equilibrium position. The system returns to this position at 93 ms, instead of the quicker period of 20ms shown in Fig.3. The sun, planets, and carrier have the same period of 27 ms because their rotations are coupled together. Similarly, a rotation of gear1 must cause a rotation of the ring gear, and they are coupled together with the longer period of 93ms. Fig.5 depicts the relatively large system period of 93 ms.

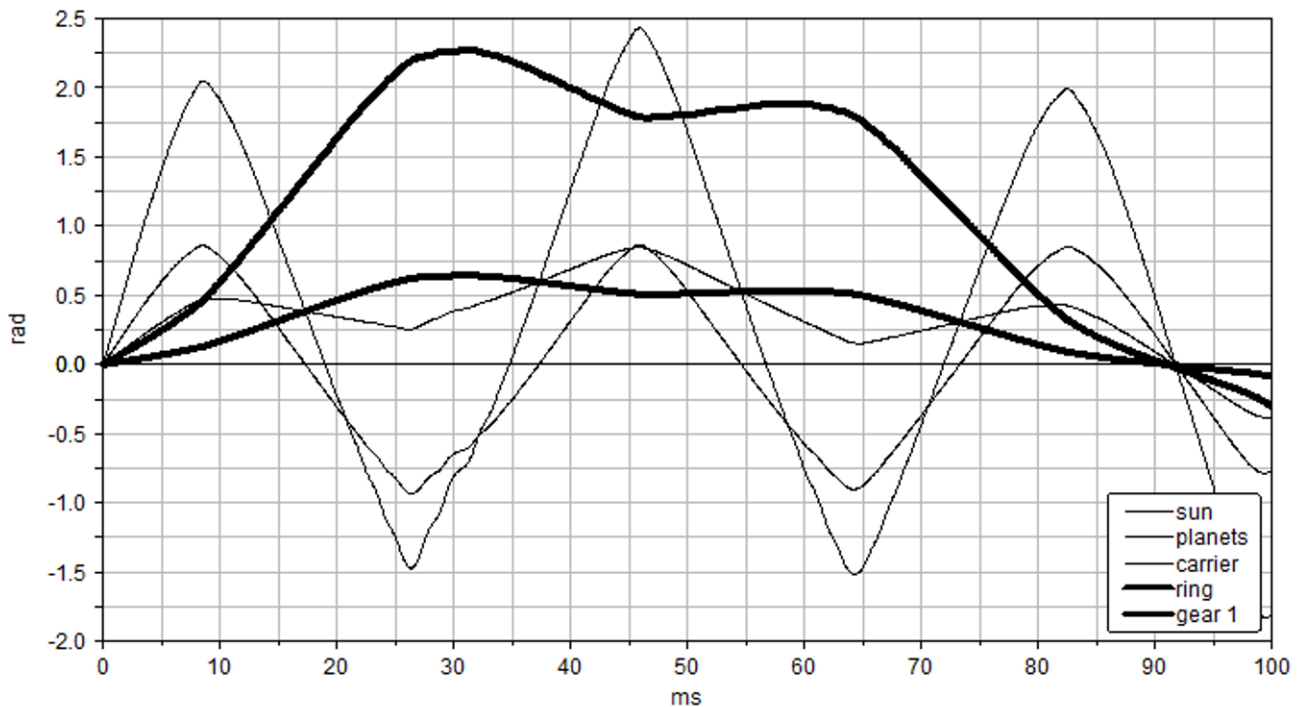


Fig.5 Angular displacement vs. time, when *initial* angular velocity $\omega_{x0} = 100$ rad/sec is applied to the carrier

Significantly more vibration occurs when an element reverses direction, shown in Fig.6. This is because of the "time lag" caused by the various interplay of inertias. In section 3 when the sun makes contact with a planet, the planet in turn makes contact with the ring which is a fixed rigid body. In this configuration when the sun makes contact with a planet, the planet in turn makes contact with the ring, which in turn makes contact with gear 1, which is freely rotating. Because no fixed element is present, only the gear inertias are contributing to the change in angular velocity. Between 25 and 35 ms the sun makes contact with various planets, and its inertia makes a more significant change in the planet's rotation than if the ring was fixed. The end result is this larger "settling time" as the sun reaches its new angular velocity at 35 ms.

The magnitude of the contact force between dynamic elements is shown in Fig.7. A comparison with the analogous plot shown in Fig.4 yields some important conclusions. The repeating symmetry of section 3 is not observed. The first significant impact, occurs faster than it does in the fixed ring configuration. The interval in which the impact takes place has decreased. For example, the sun and planet 2 are in contact for 20 ms in section 3, but now only remain in contact for 15 ms. This can be explained by again considering that the inertias of all components are now interacting. When the sun makes contact with planet 2 the rotation of the ring and gear1 are ultimately effected, and therefore the time in which these two elements are in contact is less than if the ring and gear1 were fixed. The general shape of the curve is the same, only the impact duration has changed.

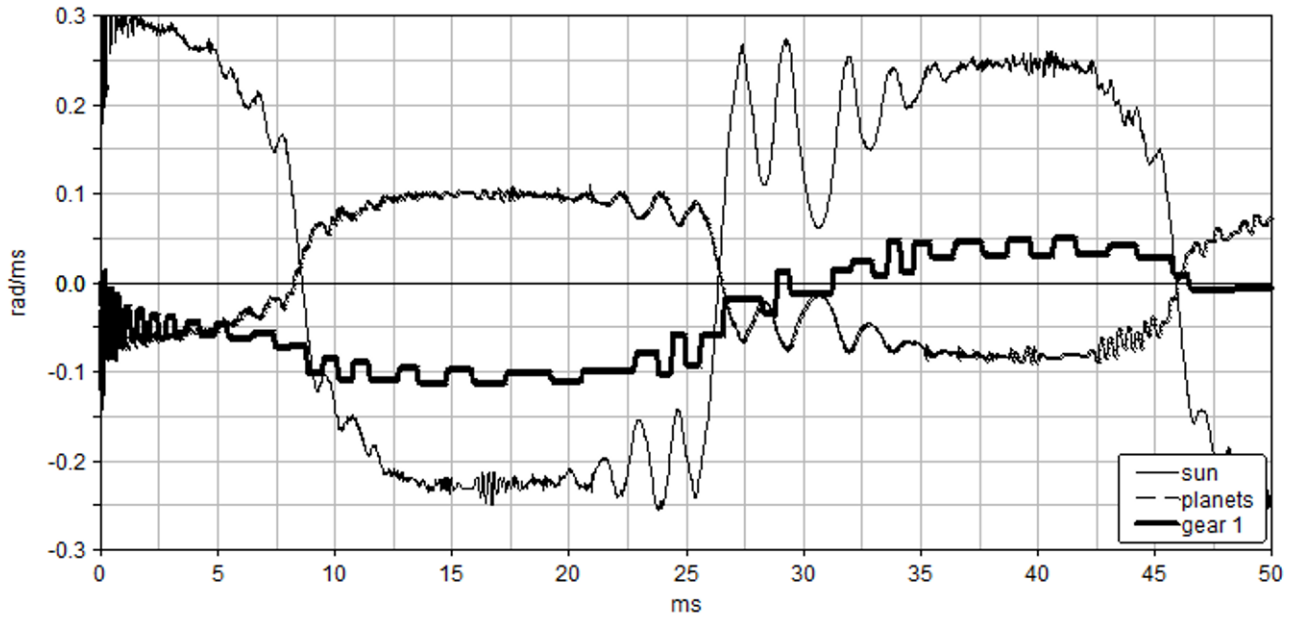


Fig.6 Angular velocity vs. time, when *initial* angular velocity $\omega_{x0} = 100$ rad/sec is applied to the carrier

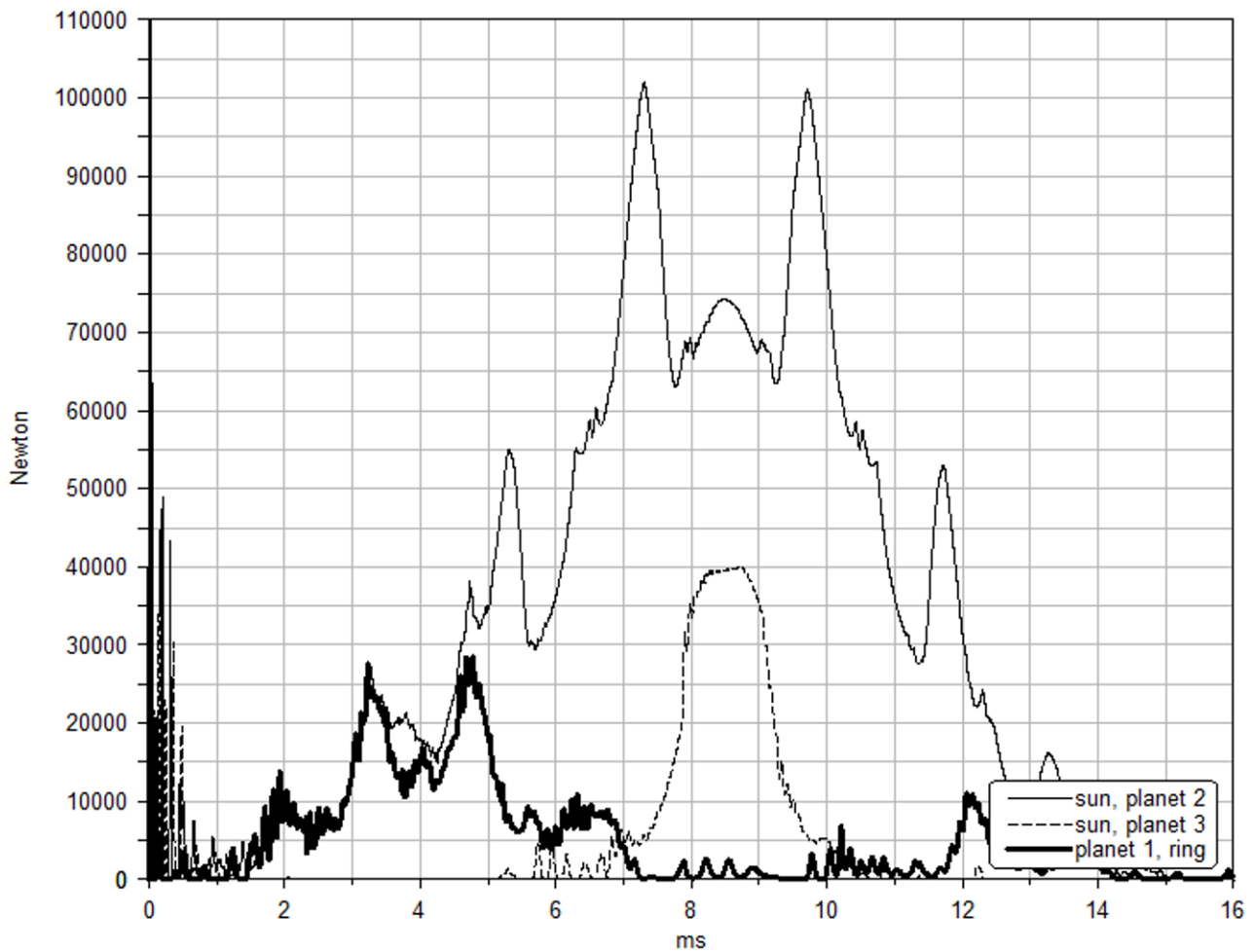


Fig.7 Contact forces vs. time, when *initial* angular velocity $\omega_{x0} = 100$ rad/sec is applied to the carrier

5. Dynamic response and discussion of a planetary gear with constant velocity from sun gear

The ring gear is fixed and the sun gear is being driven by Motor 1, which is assumed to have a constant angular speed of 975 rpm = 102.1 rad/sec. Fig.8 is the magnitude of each gear's angular velocity. Obviously, the planet gears must be rotating in a direction opposite that of the sun and carrier. For the first few milliseconds it is observed that the angular velocities change rapidly, and converge to an average speed based on the gear ratios. The planets have a much smaller rotary inertia relative to the carrier assembly. Since the planets experience forces from the sun and internal ring, it follows that their angular velocities should change with a larger magnitude. These "oscillations" die out rather quickly because the system is being driven by a kinematic motion constraint. In other words, the sun will have a constant velocity regardless of any force it experiences. This loading assumption essentially "forces" the other elements to reach steady-state very quickly.

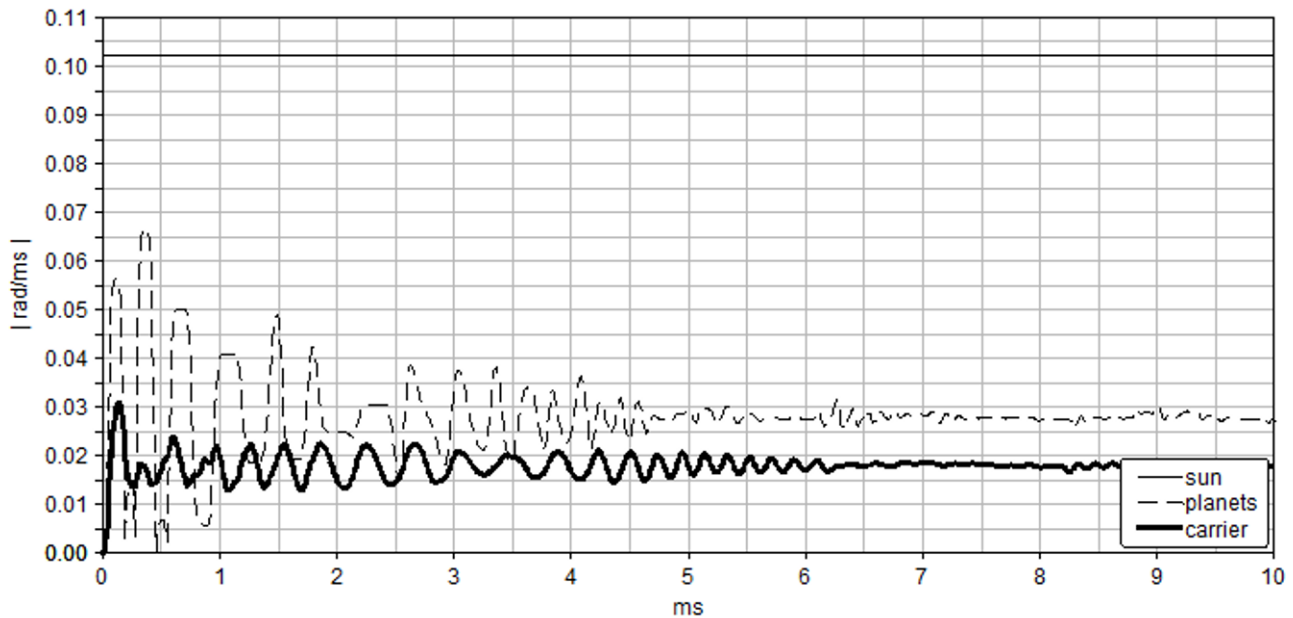


Fig.8 Angular velocities vs. time, when *constant* angular velocity $\omega_1 = 102.1$ rad/sec is applied to the sun

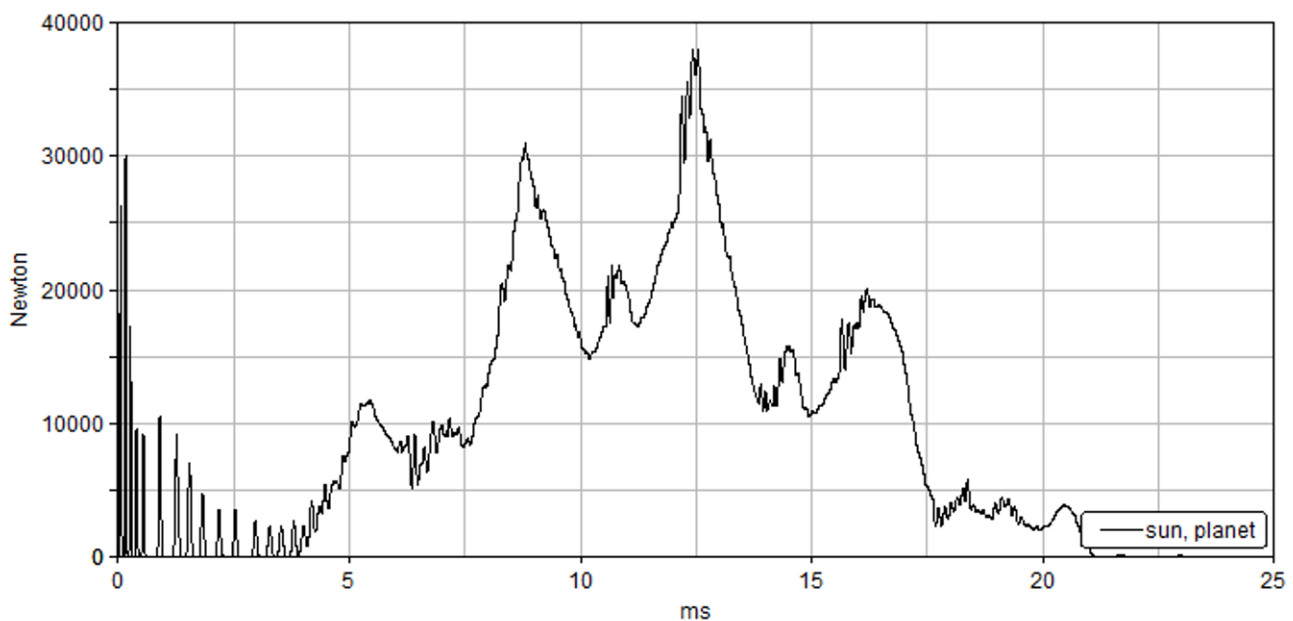


Fig.9 Sun-planet contact force vs. time, when *constant* angular velocity $\omega_1 = 102.1$ rad/sec is applied to the sun gear

The sun and planet 1 share an interesting force history shown in Fig.9. The large peaks can be attributed to the configuration in which the sun is in contact with only one planet. The smaller peaks include "load sharing" between the other two planet gears. The force between the sun this planet is reduced when the sun is in contact with the other planet gears. The peaks and troughs of this plot are due to the rapidly changing contact ratio on the sun.

Consideration of a sun gear with a "chipped" tooth is depicted in Fig.10. This planet gear is in mesh with the chipped area of the sun. In the first millisecond, fewer impacts have occurred because of the damaged tooth. It takes longer for the gears to make contact because geometry is simply missing. The magnitude of the velocity change has also increased, particularly between 1 and 3 ms. This is because the planet gear has more room to move in the backlash due to the gap created by the missing tooth. An impact causes a change in acceleration, which is allowed to propagate further because of the gap. The response of the gears become nearly identical after 10 ms because the chipped tooth has moved through the mesh.

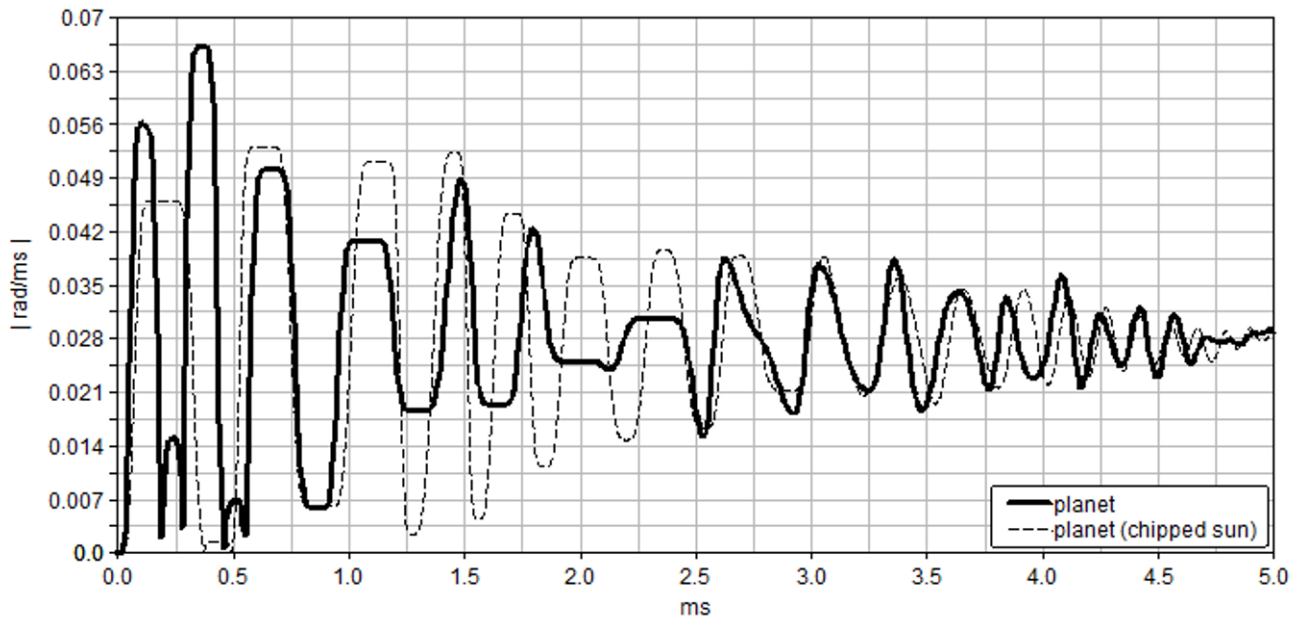


Fig.10 Angular velocities vs. time, when constant angular velocity $\omega_1 = 102.1$ rad/sec is applied to the sun

6. Dynamic response and discussion of a planetary gear with a step torque applied to the sun gear

With the ring gear fixed, a step input torque with the magnitude of 70.518 N-m is applied on the sun gear over 100 ms. A step torque of the form $T(1 - e^{-t/\tau})$ is applied to represent a typical electric motor characteristic curve. The torque magnitude and time constant is calculated using the rated torque and rated speed.

Compare the contact force magnitude of Fig.11 with the analogous plot of Fig.9. The first significantly large magnitude response occurs at 9 ms for the constant input speed section 5, while the same magnitude here begins at 25 ms. This delay is due the dynamic nature of torque. A torque applied to a body will not instantaneously cause motion, instead it causes an angular acceleration. This acceleration works against the inertia of the sun, causing the response to occur later than the constant speed case. The smaller peaks and troughs are again due to the rapidly changing contact ratio on the sun. The largest peaks occur when this planet is the only planet gear in contact with the sun.

The chipped sun experiences fewer impact events than the standard sun, shown in Fig.12. This is because an entire tooth is missing and it takes longer for the gears to contact. The magnitude of the velocity changes for the chipped sun are larger. This is because the torque has had more time to accelerate the sun before contact is made. This larger velocity change corresponds to a larger force magnitude. The chipped tooth causes the sun to experience more harsh start-up conditions. These oscillations die out quickly as the torque continues to accelerate the system, and the contact between gear teeth becomes constant on one side only. Velocity changes from positive to negative, like those shown here, represent double sided impacts.

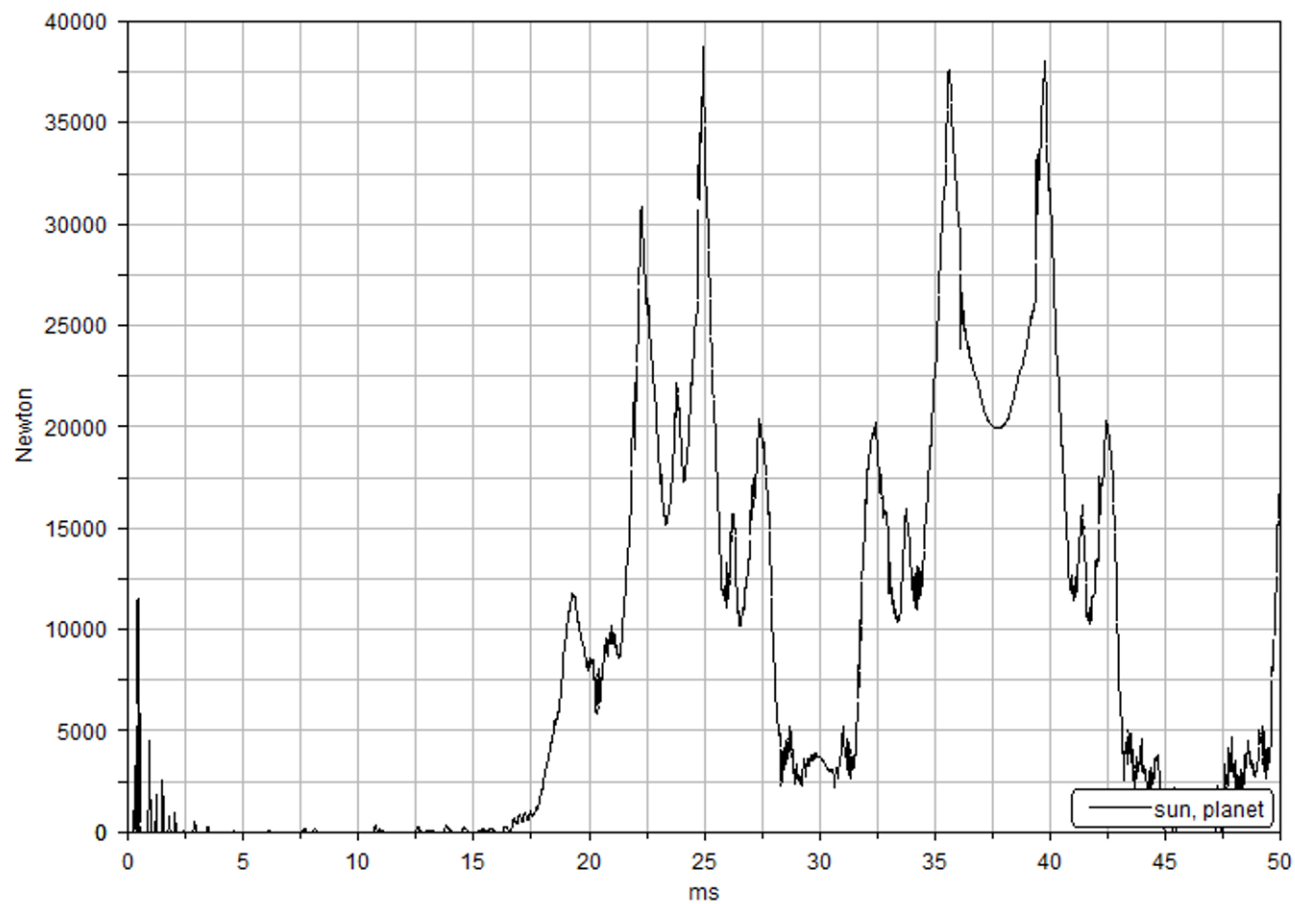


Fig.11. Sun-planet contact force vs. time, when the torque $T_1 = 70.518 \text{ N}\cdot\text{m}$ is applied to the sun gear

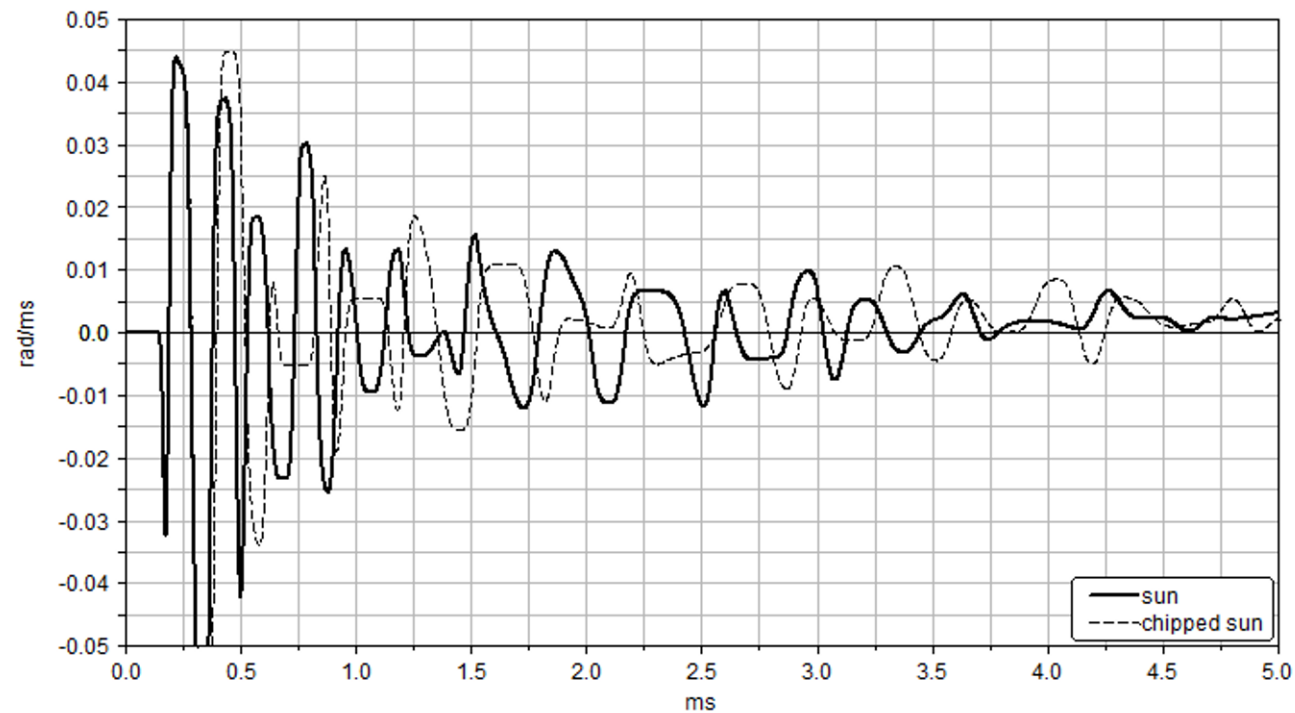
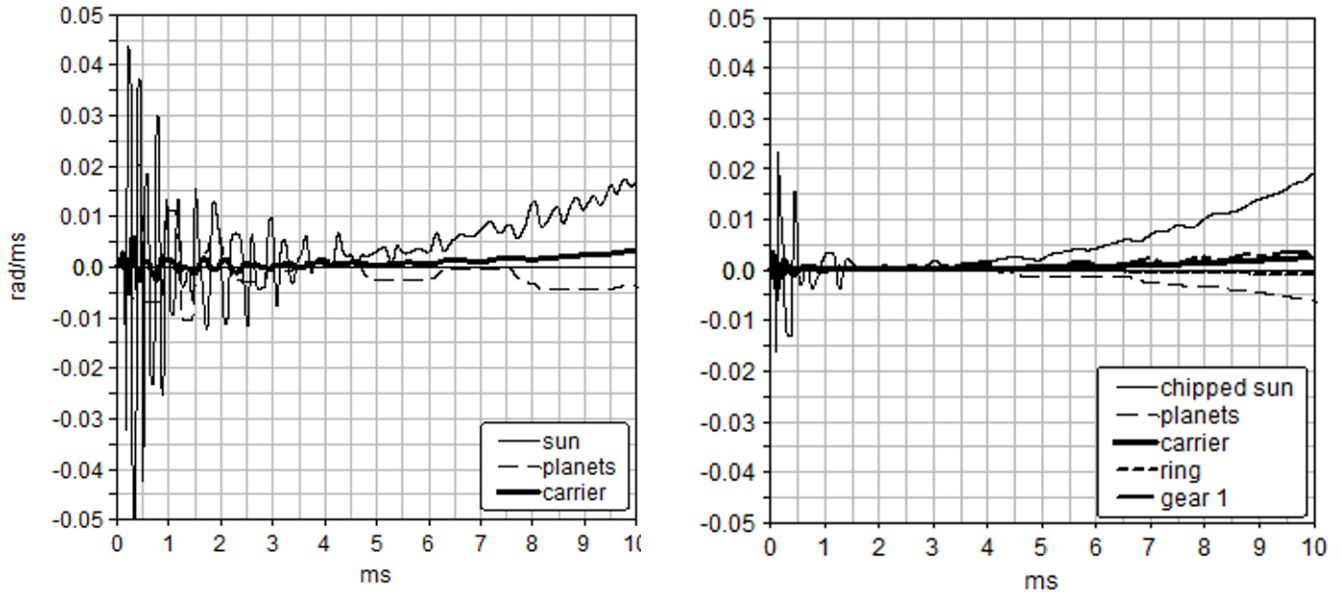


Fig.12 Sun angular velocity vs. time, when the torque $T_1 = 70.518 \text{ N}\cdot\text{m}$ is applied to the sun gear

7. Dynamic response and discussion of a planetary gear with a step torque applied to both sun gear and gear 1

The system is operating as a differential transmission, with both Motor 1 and Motor 2 in operating in the same direction. A step torque of the form $T(1 - e^{-t/\tau})$ is applied to represent a typical electric motor characteristic curve. The torque magnitude and time constant is calculated using the rated torque and rated speed, which are 70.518 N-m and 67.935 N-m on the sun and gear 1, respectively.



(a) Ring gear fixed, $T_1 = 70.518$ N-m

(b) $T_1 = 70.518$ N-m, $T_2 = 67.935$ N-m

Fig.13 Angular velocity with applied step torques

With the ring gear fixed as in Fig.13(a), the sun gear closely follows the input torque curve. The planets dissipate energy from the sun input to the carrier output. The planets must get the carrier inertia moving from rest. The sun, having the smallest inertia, oscillates with the largest amplitude of any gear. The amplitude of the sun gear's velocity change is decreased with the system operating as a differential transmission, shown in Fig.13(b). The rotation of the ring causes the planets to move in the same direction as the applied torque on the sun. This makes the angular velocity of the sun more smooth when compared to the simple planetary configuration of the fixed ring. This effect is also seen in the other gears. The detrimental effects of the chipped tooth on the sun gear is lessened with the system operating in the differential mode.

The gear 1 and ring mesh has a smaller prescribed backlash than the meshes between the sun and planets. Therefore, contact occurs between these two gears before the sun and planets. A clear succession of contacts is observed. First gear 1 contacts the ring, the ring contacts a planet, and the planet contacts the sun. The interval from 3.5 ms to 4.5 ms in Fig.14 clearly shows this progression. The planet gears are potentially in contact with both the sun and ring. The contact between gear 1 and the ring directly affects the magnitude of the force between the planet and ring, shown as the smaller peak at 7.5 ms. The response of planet gear is a superposition of impact forces between its sun mesh and ring mesh.

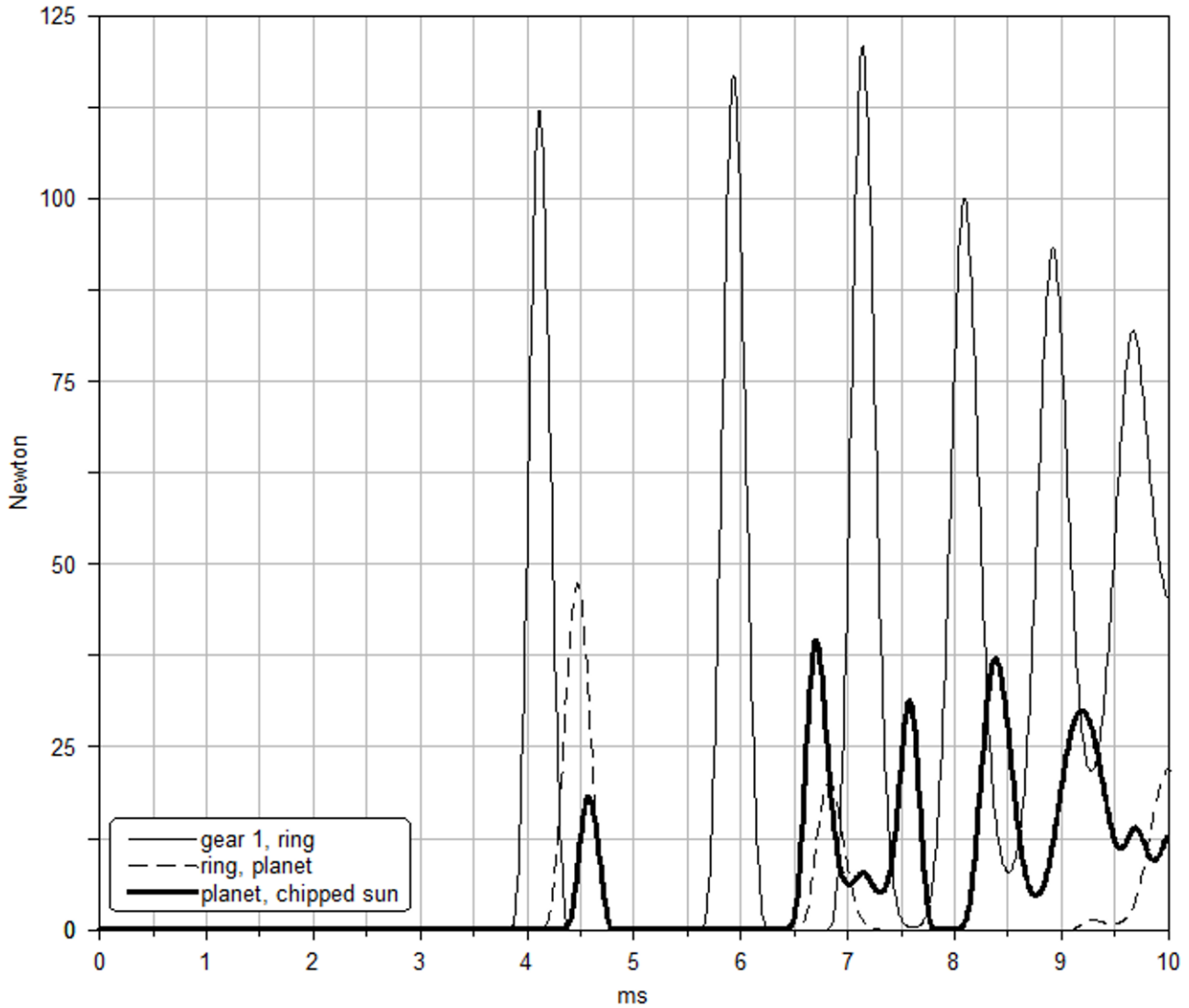


Fig.14 Angular velocity when torque $T_1 = 70.518$ N-m is applied to the sun gear and $T_2 = 67.935$ N-m is applied to gear

8. Conclusions

A practical differential planetary gear train which combines two inputs and one output has been analyzed using a non-linear multi-body dynamics software model. To avoid interference and undercut the backlash between the sun/planet and planet/ring meshes are precisely specified. When the transmission operates with a fixed ring gear and undergoes free vibration from a *near equilibrium position*, six contact forces are potentially active. The magnitude of the contact force between each element is shown to depend on the rapidly changing contact ratios of each gear. For free vibration and a freely rotating ring, the duration of the contact event between gears decreases. When compared to the perfect mesh geometry, a planet in mesh with the chipped tooth of the sun causes its angular velocity to change with a larger magnitude. Step torques of the form $T(1 - e^{-t/\tau})$ applied in opposite directions to each input closely models the constraints and loading conditions of realistic operation. The transient response of this differential mode is shown to be significantly less destructive to the sun gear. The interactions of many components of this differential planetary transmission contribute to the complicated transient behavior observed in the time domain.

9. Acknowledgement

The authors acknowledge the Donald E. Bently Center for Engineering Innovation at California Polytechnic State University San Luis Obispo for support of this work.

REFERENCES

1. Özgüven H.N. and Houser D.R., “Mathematical Models used in Gear Dynamics – A Review”, *Journal of Sound and Vibration*, 121(3), 1988, pp. 383-411.
2. Parey, A. and Tandon, N., “Spur Gear Dynamic Models Including Defects: A Review”, *The Shock and Vibration Digest*, Vol. 35, No. 6, Nov. 2003; pp. 465-478.
3. Parey, M. El Badaoui, F. Guillet, N. Tandon, “Dynamic modeling of spur gear pair and application of empirical mode decomposition-based statistical analysis for early detection of localized tooth defect”, *Journal of Sound and Vibration* Vol. 294, 2006, pp. 547–561.
4. J. Lin and R. G. Parker, “Parametric Instability of Planetary Gears under Mesh Stiffness Variation”, *Journal of Sound and Vibration*, 2002, vol. 249, pp. 129-145.
5. J. Lin and R. G. Parker, “Analytical Characterization of the Unique Properties of Planetary Gear Free Vibration”, *ASME Journal of Vibration and Acoustics*, vol. 121, July 1999, pp. 316-321.
6. Yi Guo and R. G. Parker, “Dynamic Modeling and Analysis of a Spur Planetary Gear Involving Tooth Wedging and Bearing Clearance Nonlinearity”, *European Journal of Mechanics A/Solids*, 2010, vol. 29, pp. 1022-1033.
7. R. G. Parker and X. Wu, “Vibration Modes of Planetary Gears with Unequally Spaced Planets and an Elastic Ring Gear”, *Journal of Sound and Vibration*, 2010, vol. 329, pp. 2265-2275.
8. Yichao Guo and R. G. Parker, “Purely Rotational Model and Vibration Modes of Compound Planetary Gears”, *Mechanism and Machine Theory*, 2010, vol. 45, pp. 365–377.
9. Kong, D., Meagher, J., Xu, C., Wu, X., Wu, Y., “Nonlinear Contact Analysis of Gear Teeth for Malfunction Diagnostics”, *IMAC XXVI a Conference on Structural Dynamics*, Society for Experimental Mechanics, Orlando, Florida USA, February 4 –7, 2008.
10. MSC Inc., *MSC ADAMS reference manual*.
11. Raymond J. Drago, “Fundamentals of Gear Design”, 1988.
12. Huamin Li, Guixian Li, “Gear Mechanism Design and Application”, 2007 (in Chinese).
13. Zengang Rao, “Planetary Gear Transmission Design”, 2003 (in Chinese).

Determination of Wind Turbine Operating Deflection Shapes Using Full-field 3D Point-tracking

Chris Warren, Chris Niezrecki, Peter Avitabile
Structural Dynamics and Acoustic Systems Laboratory
University of Massachusetts Lowell
One University Avenue
Lowell, Massachusetts 01854

ABSTRACT

The ability to collect operating data at a high number of points to monitor the structural dynamics of rotating structures will lead to a better physical understanding of these structures during operation. Today, however, structural dynamic measurements are typically obtained while the structure is in a static configuration. Differences are likely to exist in the structural dynamic behavior when comparing statically performed tests and the measurements while taken during operation. In order to evaluate a rotating system while in operation, slip-rings are typically used during testing with measurements made at only a few discrete points. Slip-ring configurations can be difficult to instrument, suffer from measurement noise, and the attached sensors can obscure the true dynamic response due to mass loading and aerodynamic effects. In past work, stereophotogrammetry techniques have been shown to measure the in- and out-of-plane motion of rotating structures. To extend these prior efforts, a 46 inch (1.17 m) diameter wind turbine was mounted to a commercial fan motor so controlled rotating conditions could be created in a laboratory environment. Displacements in three dimensions at dozens of measurement points were determined using 3D point-tracking while the turbine was spun at multiple speeds. Operating deflection shapes extracted from these data were compared to other rotating tests and to a static (non-rotating) modal test. The test results indicate a correlation between conventional static and optically measured mode shapes, however some spectral differences exist between the data sets and may be due to the changes in the structural boundary conditions present during operation at different speeds.

INTRODUCTION

Since the early 1980s, full-field, image-based measurement techniques have been developing as valid methods to determine shape, displacement, and strain in static and quasi-static applications. Recently, however, stereophotogrammetry has been exploited to measure high-speed dynamic events. Digital image correlation (DIC) and three-dimensional point tracking (3DPT) are robust and have a wide dynamic range that is not strongly affected by rigid body motions nor ambient vibrations. Even if the cameras are moving relative to each other, methods exist to compensate for this motion, provided stationary reference points remain in the field of view throughout the test [1]. Alternatively, as long as the positions of the cameras are precisely known, new calibration information for each synchronized image pair can be generated. This extends the use of high-speed stereophotogrammetry to applications in which both camera fields of view are constantly changing. Based on this principle, the dual laser tracker digital image correlation (DLTDIC) system developed at Sandia National Laboratory was shown to successfully acquire time-space-position-information (TPSI) of translating and rotating objects [2,3]. Additionally, the authors of this paper have shown that DIC and 3DPT provide measurements that are consistent with those measured by using a laser Doppler vibrometer and accelerometers [4] and that highly-accurate mode shapes can be determined using DIC & 3DPT [5].

In light of the recent advances in wind turbine size and the desire for improved rotor performance, the demand for viable techniques to measure rotating structures in operation has become more important. “The U.S. wind industry broke all previous records by installing close to 10,000 megawatts of new generating capacity in 2009... The total installed capacity in the U.S. is now over 35,000 MW. In 2009, 38 manufacturing facilities were brought online, announced or expanded” [6]. Even more recently, Ken Salazar, United States Secretary of the Interior, approved the Cape Wind Project by signing the first

off-shore wind farm lease in US waters [7]. This provides a clear indication that the need to measure these types of structures will increase in the years to come.

Additionally, rotorcraft blades are currently replaced on a schedule established by a statistically determined lifespan rather than the condition of the blades. By taking this approach, functional blades may be replaced long before their potential service lives have ended. Developing non-contacting, full-field measurement approaches may improve physical understanding and significantly lower costs by allowing engineers to adopt condition based maintenance instead of scheduled based maintenance.

Past work has shown that three-dimensional point tracking can be used to measure the time domain response of large rotating wind turbines while in operation using high speed cameras (measured at 20–30 times the rotational frequency) [8]. Digital image correlation has also been used with a phase-stepping approach to measure the out-of-plane motion of a desk fan [9]. Although measurements have been made on “wind turbines” at both ends of the size spectrum, the validity of these experiments remains to be verified by a simultaneous measurement from a collocated sensor.

A series of experiments were designed and performed to extend previous research [10] that focused on demonstrating the potential of stereophotogrammetry in measuring a rotating structure. A small wind turbine rotor was selected due to the relatively high flexibility associated with slender structures. Furthermore, the ability to spin the rotor using a commercial fan motor allowed for the simulation of rotating conditions in a controlled laboratory environment. Photos of the turbine while in the manufacturer’s configuration (driving a motor for power generation) and in the experimental setup (being driven by motor) can be seen in Figure 1. Collocated 3DPT and accelerometer measurements were compared for points at the tips of each of the three blades while the turbine was spinning. 3DPT was performed using the commercially available software package PONTOSTM [11]. To provide a reference in the non-rotating state, a modal survey was performed to determine the mode shapes in the frequency range of interest.

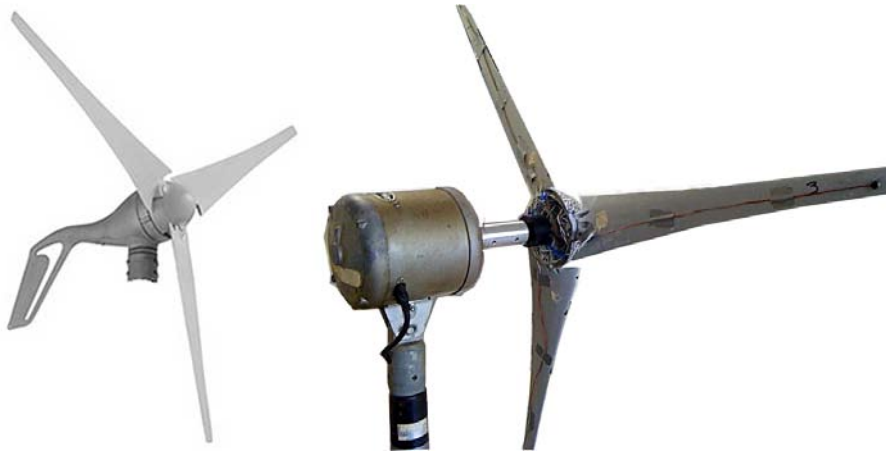


Figure 1: (a) Southwest Windpower Airbreeze wind turbine with generator [12,13].
(b) Airbreeze wind turbine mounted to the commercial fan motor with a 3 channel slip ring.

TESTING OF THE ROTATING TURBINE

For tests herein, a pair of 3.6 Mpixel cameras operating at 500 frames per second (FPS) was used to monitor the 46 inch (1.17m) diameter Southwest Windpower Air Breeze wind turbine as it was being driven by the electric motor at rotational speeds of approximately 4.1 and 9.7 Hz (246 and 582 rpm). The measurement yields approximately 50-100 images per revolution, equivalent to about one image every 3.6 to 7.2 degrees. Frame rates of this speed were necessary because high-frequency, out-of-plane vibrations were of interest.

A separate data acquisition system was synchronized with the 3D point-tracking system and measured accelerometer outputs via a slip ring. Frequency domain comparisons were made to evaluate the performance of the image-based system in making out-of-plane measurements of a rotating structure. Once the 3D point-tracking system was shown to provide spectra comparable to the reference accelerometers, operating deflection shapes were extracted and compared to the mode shapes obtained during the stationary testing.

COMPARISON OF 3D POINT-TRACKING AND ACCELEROMETERS

To establish a reference to which the 3D point-tracking measurements could be compared, three accelerometers were mounted to the rotor, one at the tip of each blade. Figure 2 shows an accelerometer mounted at the tip of one of the turbine blades in the out-of-plane direction. The precise rotating speed of each test was determined by performing a peak-pick of the linear spectrum of the in-plane displacement of a 3DPT measurement point at a blade tip. Figure 3a shows a sample set of in-plane time outputs of the points at the tips of the 3 blades from the 9.7 Hz test. Each oscillation is 120° out of phase with the other two, and the amplitudes are all nominally equal, as expected for a 3-bladed structure. Figure 3b shows the magnitude of the linear spectrum for Blade 1 and the peak value obtained.



Figure 2: Accelerometer mounted to turbine blade #1.

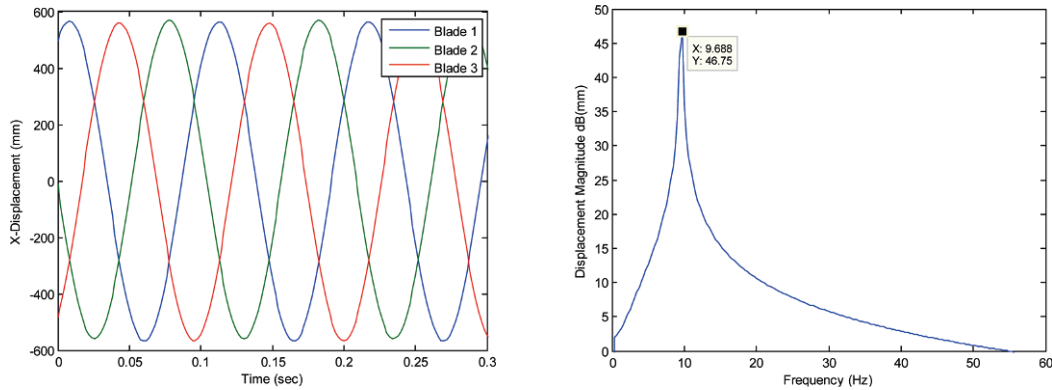


Figure 3: (a) Typical rotating 3D point-tracking results for blade tips, x-displacement (9.688 Hz rotating speed).
(b) Linear spectrum for an in-plane measurement (9.688 Hz rotating speed).

To maintain a consistent coordinate system from test to test with the 3D point-tracking system, the xy-plane was determined by calculating the best-fit plane through all measurement points on the rotor, with the z-axis defined by the vector about which the rotor turns. Figure 4a displays the time response of the 3 blade tips in the z-direction (out-of-plane) measured by the 3D point-tracking system. The main rotating component is clearly visible in the displacement time data, but there is also high-frequency content as well. As with the in-plane measurement, there is a clear 120° phase between the three time traces. The synchronized, collocated accelerometer measurement for the first blade is displayed in Figure 4b. In the accelerometer signal, the beating observed is an indication of at least two significant signal components at closely spaced yet independent frequencies.

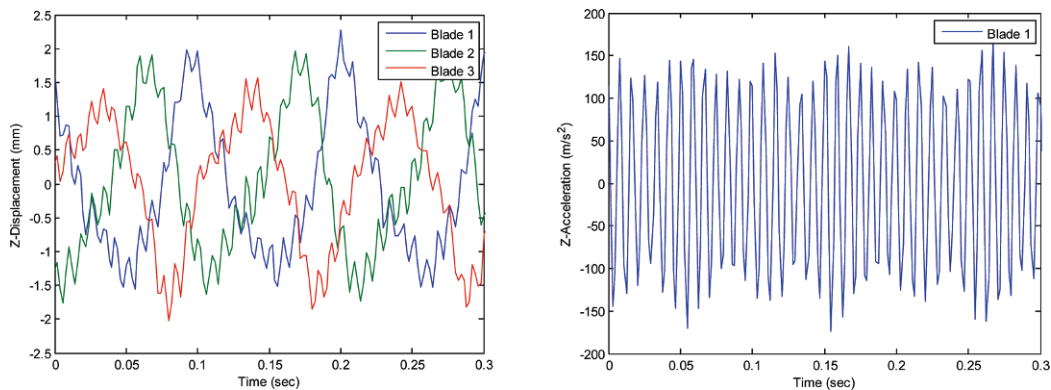


Figure 4: (a) Blades 1-3 3DPT results, z-displacement (9.688 Hz rotating speed).
(b) Blade 1, synchronized accelerometer measurement.

Once the time domain data was acquired, a flattop window was applied and FFTs were calculated to compare the 3D point tracking and accelerometer data in the frequency domain. Flattop windows were applied to reduce the effects of leakage while reporting the amplitude of response more accurately. Frequency-based comparisons were made to avoid the errors associated with numerical differentiation and integration of time data that are caused by bias, quantization error, etc. Furthermore, conversion from acceleration to displacement in the frequency domain requires a simple division by a factor of ω^2 at each spectral line in the digital frequency spectrum. Figure 5a displays an overlay of auto-power spectra from typical measurements at the tip of one of the blades using 3D point-tracking and an accelerometer for the 9.688 Hz test. Three isolines are also plotted to provide reference in the decibel scale for their corresponding un-scaled values.

Inspection of Figure 5a indicates that the initial results are fairly consistent but differences are apparent at lower frequencies and for low levels of displacement. The accelerometer is reporting significantly lower amplitudes of response than the 3DPT system, on the order of 30 dB at one of the peaks. Known issues that must be considered are: the cross-axis sensitivity of the accelerometers; noise from the slip ring; the noise floor of the optical system; and the useful ranges of both sensors (i.e. poor sensitivity for accelerometers at low frequencies and for optical systems at high frequencies). Additionally, a slight misalignment of the coordinate system when transforming the 3DPT measurements could account for some level of variation in the reported displacements. These discrepancies have not been addressed and are left as the subject of future work. Figure 5b depicts an enlarged view of the 90-150 Hz band, where the two measurements are very consistent. This band is of particular interest because a cluster of non-harmonic peaks were consistently reported here and will be discussed in the next section.

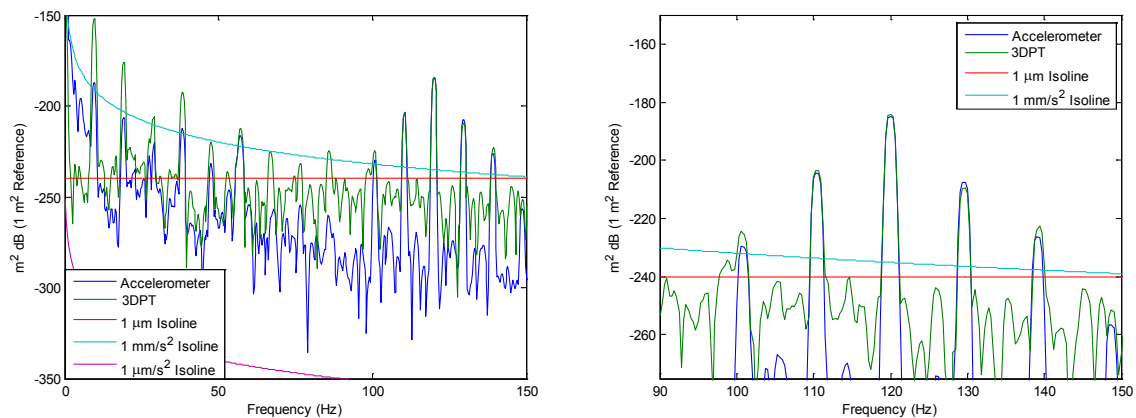


Figure 5: (a) 9.688 Hz rotating speed auto-power spectra overlay.
(b) 9.688 Hz rotating speed auto-power spectra overlay (zoomed).

MODAL TEST OF THE TURBINE (NON-ROTATING)

Once operating data was acquired on the rotating turbine, the dominant response was observed to consistently occur in the 90-150 Hz band regardless of rotating speed. A single shaker, 1D scanning laser Doppler vibrometer (SLDV) test was run with a bandwidth of 0-256 Hz. The shaker was mounted to the rear of the fan motor, which can be seen in Figure 6. Table 1 lists the natural frequencies and auto-MAC for the modes in frequency band of interest [14,15]. High off-diagonal terms are indicators of high correlation between modes due to spatial aliasing resulting from unmeasured portions of the structure. The intent of this paper is not to identify the differences between those modes but to compare the results of the similar modes of the different tests [16].

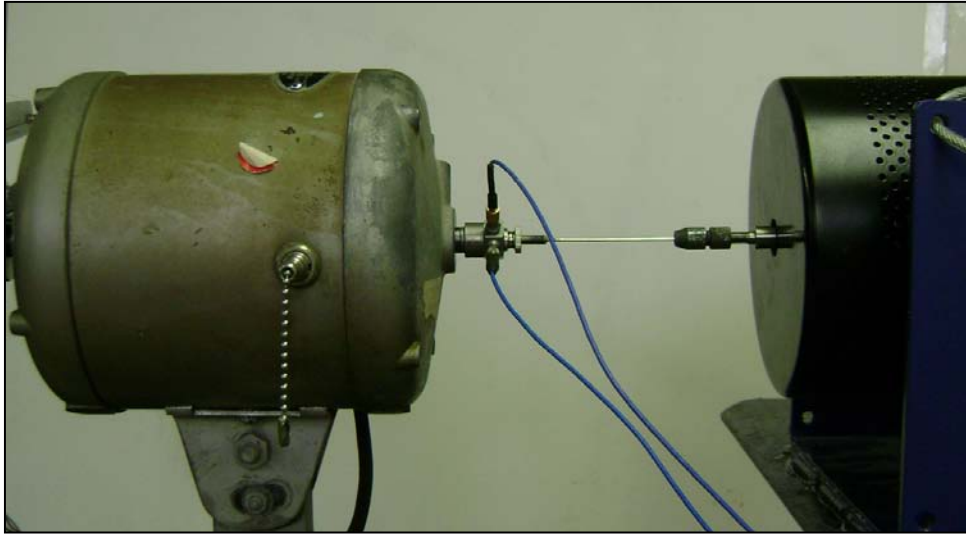


Figure 6: Shaker mount for the subsequent single-shaker, 1D SLDV turbine test.

Table 1: Natural Frequencies and Auto-MAC for the Single-shaker, 1D SLDV Test (Reported as %)

Mode #	-	14	15	16	17	18	19	20
-	<i>Freq (Hz)</i>	<i>103.855</i>	<i>109.153</i>	<i>119.922</i>	<i>124.117</i>	<i>139.72</i>	<i>154.327</i>	<i>158.424</i>
14	<i>103.855</i>	100	92.9	42.1	18.1	24.7	26	24.5
15	<i>109.153</i>	92.9	100	28.8	33.2	42.1	17.3	14
16	<i>119.922</i>	42.1	28.8	100	0.3	0.3	49.2	41.1
17	<i>124.117</i>	18.1	33.2	0.3	100	74.3	1.6	0.1
18	<i>139.72</i>	24.7	42.1	0.3	74.3	100	0	0.9
19	<i>154.327</i>	26	17.3	49.2	1.6	0	100	95.6
20	<i>158.424</i>	24.5	14	41.1	0.1	0.9	95.6	100

OPERATING DEFLECTION SHAPES OF THE ROTATING TURBINE

All the measurements previously shown represent a single point on the structure. However, a significant advantage of 3DPT is that all measurements are collected simultaneously as long as the corresponding targets remain in the field of view. This enables the determination of operating deflection shapes (ODSs) at many points from a few seconds worth of data. Cross-power spectra for roughly 55 locations on the turbine were calculated relative to the 3DPT measurement point at the tip of blade 1. Figures 7a and 7b display the summation of the cross-power spectra for the 4.063 and 9.688 Hz tests, respectively. The vertical dashed lines indicate harmonics of the rotating frequency for each test.

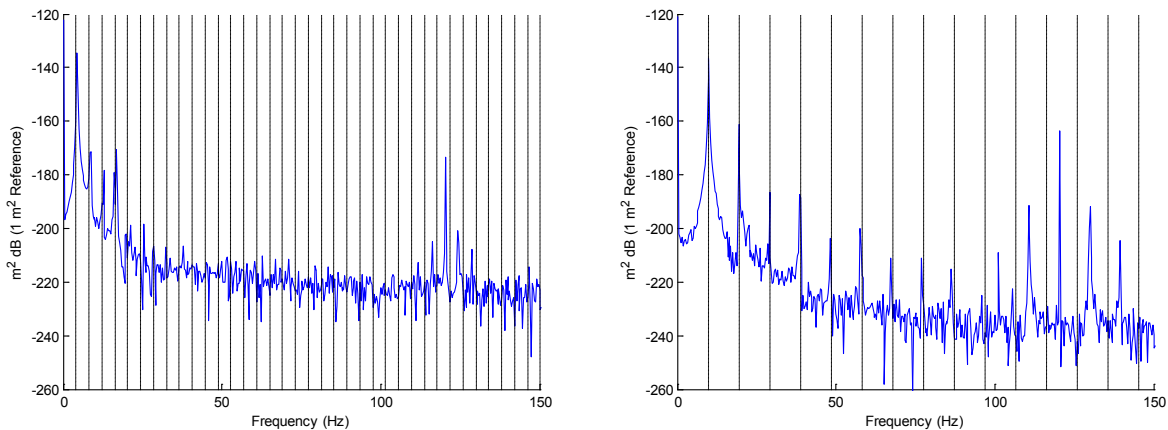


Figure 7: (a) Summation of cross-power spectra for the rotating 4.063 Hz test.
(b) Summation of the cross-power spectra for the rotating 9.688 Hz test.

As noted before, the 90-150 Hz band is of particular interest because non-harmonic peaks consistently appear in this frequency range, regardless of rotation speed. Figures 8a and 8b show enlarged views of this band with arrows indicating the peaks at which operating deflection shapes were extracted using LMS PolyMAX [17,18]. These frequencies are referred to as comparison pairs 1, 2, 3, 4, and 5 for the 4.063 Hz rotating test and 1, 2, 3, 4, 5, and 6 for the 9.688 Hz rotating test. Only the shapes at these frequencies are used in this comparison because those occurring at the harmonics exhibited little or no flexible motion.

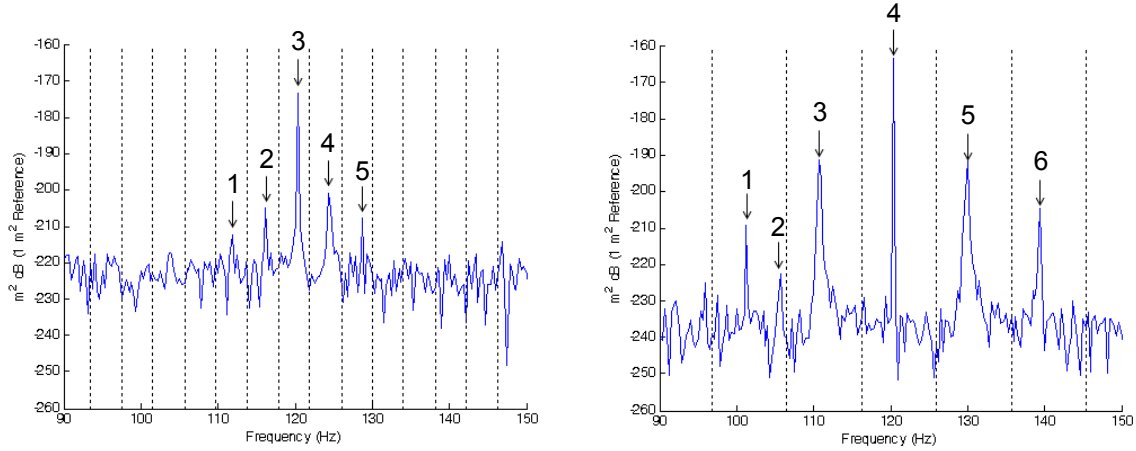


Figure 8: (a) Summation of cross-power spectra for the rotating 4.063 Hz test (zoomed-in).
(b) Summation of cross-power spectra for the rotating 9.688 Hz test (zoomed-in).

The modal test described was performed in preparation to provide a reference set of shapes to which the operating deflection shapes in the 90-150 Hz band could be compared. Table 2 lists the MAC matrices comparing the ODSs from the two rotating tests to the mode shapes obtained from the 1D SLDV test and to each other. Tables 3 and 4 list auto-MACs for the ODSs of the tests at 9.688 and 4.063 Hz, respectively. In all three tables, values over 50% are in bold to highlight pairs of shapes with high levels of correlation. Keep in mind that operating shapes are the result of a linear combination of all the modes of a structure. An ODS may strongly resemble one or may loosely resemble multiple mode shapes, depending on the contribution each mode shape [19]. Some shapes can be seen to correlate well to some modes in particular, but generally, the ODSs obtained from both rotating tests do not exhibit single-mode behavior. The highest MAC value for either test when compared to the 1D SLDV modal test is 83.7%. This trend is reasonable as the modes in this band are closely spaced.

Perhaps more interesting than the comparison to the mode shapes are the changes of the ODSs observed as a result of a varied operating speed. Table 5 lists pairs of shapes from the two tests that show high levels of correlation. The shape pairs are also displayed in Figures 9-10. The most consistent shape from test to test was by far the ODS that appeared at 120.31 Hz in both the 9.688 and 4.063 Hz tests. The MAC value between the two shapes is 96.6%, indicating that the two shapes are extremely similar. Two more shape pairs were observed, but the frequency at which they occurred increased with the rotation speed of the rotor. Previous research has shown analytically that due to centrifugal and gyroscopic forces imparted on the rotating body, a structure's natural frequencies will be higher when rotating compared to when at rest [20-22]. While the second and third ODS pairs have MAC values of at least 87.4%, the frequencies for the 9.688 Hz test were on average 10% higher than those for the 4.063 Hz test. These increases in frequency follow the trend shown before in past studies, but the pair of highly correlated shapes at 120 Hz in both tests contradicts this. This phenomenon certainly should be investigated in future work, but the current results show great potential for the measurement of rotating structures.

Table 3: MAC Matrices Comparing 1D SLDV Mode Shapes with ODSs from Both Rotating Tests

			9.688Hz Rotating Operating Deflection Shapes						4.063Hz Rotating Operating Deflection Shapes				
Mode #	-		1	2	3	4	5	6	1	2	3	4	5
-	Freq (Hz)		101.246	105.602	110.795	120.313	129.894	139.389	111.904	116.259	120.313	124.442	128.756
1D SLDV	14	103.855	36.6	23.7	83.7	0.7	25	59.5	48.1	14.6	7	45	60.2
	15	109.153	39.2	15.3	72.8	1.4	9.7	59.1	44	4	5	60.7	58.4
	16	119.922	12.1	20.9	29.5	35	68.6	5.4	9.4	72.6	59.6	10.7	12.7
	17	124.117	6.1	1	6.5	0.3	12.1	27	6.1	16.8	0.3	50.7	23.8
	18	139.72	2.3	0.2	11.1	2.9	13.3	22.8	9.1	11.6	0.7	80	28.7
	19	154.327	3.5	13	16.6	3.3	54	18.1	9.5	32.1	20	3.7	18.4
	20	158.424	3.7	13.1	17.5	0	61.5	23.9	15	35.4	10.3	0.4	23.5
	1	111.904	16.2	6.7	35.3	6.2	14.3	61.3					
	2	116.259	5.8	17.6	13.8	25.6	86.9	0					
	3	120.313	1.1	6.7	1.6	96.6	22.1	7.1					
4.063Hz Rotating Operating Deflection Shapes	4	124.442	8.1	4.5	24.2	14.8	1.5	24.1					
	5	128.756	14.8	5.4	43.6	4.3	11.5	87.3					

Table 4: 9.688 Hz Rotating Test Auto-MAC Matrix

Freq (Hz)	101.246	105.602	110.795	120.313	129.894	139.389
101.246	100	3.7	33.8	0.2	12.7	22.4
105.602	3.7	100	28.7	0	18.5	6
110.795	33.8	28.7	100	0.4	22	45.3
120.313	0.2	0	0.4	100	2.1	17.7
129.894	12.7	18.5	22	2.1	100	9.5
139.389	22.4	6	45.3	17.7	9.5	100

Table 5: 4.063 Hz Rotating Test Auto-MAC Matrix

Freq (Hz)	111.904	116.259	120.313	124.442	128.756
111.904	100	6.6	4.7	9	65.7
116.259	6.6	100	30.6	1.3	3.5
120.313	4.7	30.6	100	11.8	3.9
124.442	9	1.3	11.8	100	19.8
128.756	65.7	3.5	3.9	19.8	100

Table 5: ODS Pairs for the 9.688 and 4.063 Hz Rotating Tests

Shape Pair #	9.688 Hz ODS #	Frequency	4.063 Hz ODS #	Frequency	Diff.	MAC
1	4	120.31 Hz	3	120.31 Hz	0.00%	96.6
2	5	129.89 Hz	2	116.26 Hz	11.73%	89.7
3	6	139.39 Hz	5	128.76 Hz	8.26%	87.4

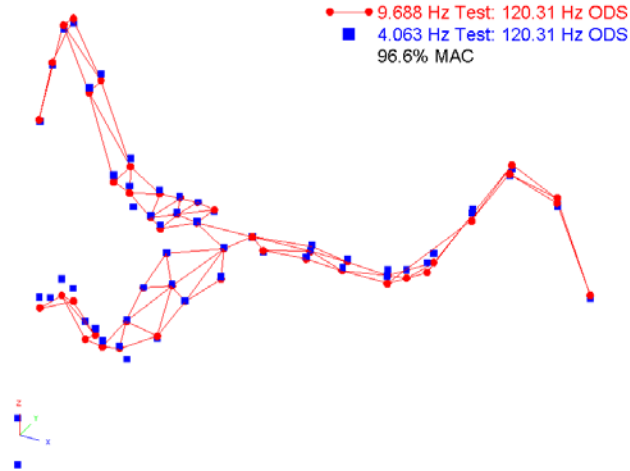
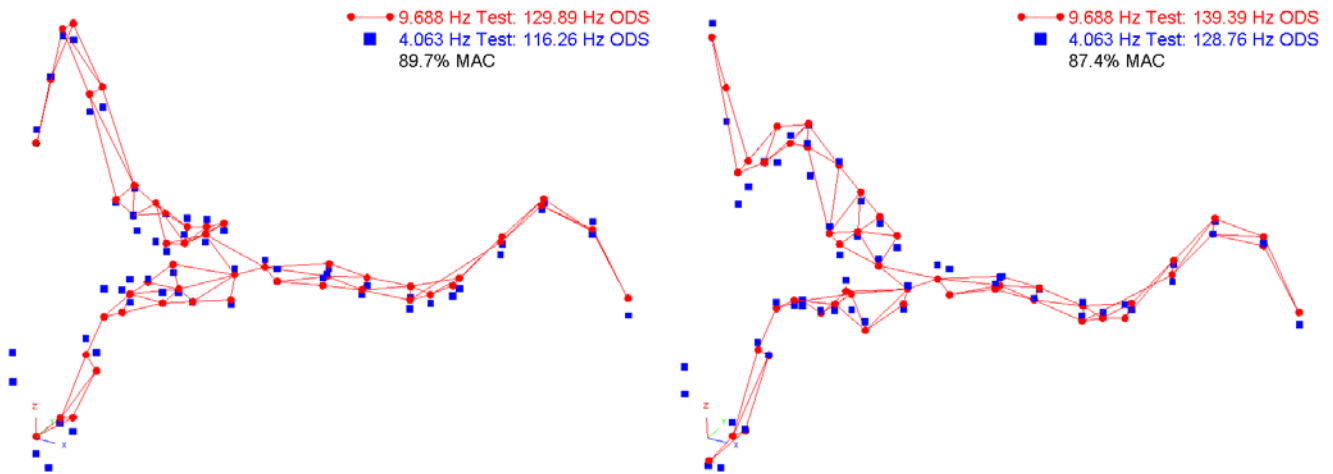


Figure 9: ODS pair #1 for the 9.688 Hz (ODS # 4) and 4.063 Hz (ODS # 3) tests.

Figure 10: (a) ODS pair #2 for the 9.688 Hz (ODS # 5) and 4.063 Hz (ODS # 2) tests.
(b) ODS pair #3 for the 9.688 Hz (ODS # 6) and 4.063 Hz (ODS # 5) tests.

EXPERIMENTAL CONSIDERATIONS

For all results presented, no rigid body corrections were performed. Rigid body correction algorithms exist as part of commercial DIC and 3DPT software packages (including PONTOS™) currently available on the market, so their use and effects should be evaluated in subsequent studies. Additionally, the images used as references when calculating the relative displacements were taken once the rotating turbine had nominally reached steady state. In the future, images taken while the structure is at rest should be used to minimize the deviation of the calculated reference plane.

Presently, the primary limiting factors of these image-based techniques are camera resolution, light sensitivity/reflection, and computer memory. The relationship between the spatial resolution and the number of pixels in the camera array is linear, so

higher resolution cameras will lower the effective noise floor for a given field of view, allowing for the measurement of smaller levels of vibrations. Future development of better cameras with more pixel resolution is critical if the low displacements associated with high-frequency phenomenon are to be effectively measured. These high-frequency signals also require short shutter times and faster frame rates, resulting in the acquisition of many, many images that require significant amounts of memory. The reduction of shutter times is made possible by more light-sensitive cameras, but the large number of images can only be accommodated by more on-board memory for the camera and hard drive space. As a reference, each rotating test presented required approximately 2.5 gigabytes worth of data, so the amount of memory space required is very large. Additionally, much of the time required to process the data is spent moving and loading the images.

CONCLUSIONS

Stereophotogrammetry techniques were shown to be consistent with accelerometer measurements for a three-bladed rotor/turbine tested while rotating. 3D point-tracking allows for the measurement of the full-field motion of the rotating blade at numerous points, without contact. In the tests, roughly 50-60 data points were tracked, but the number of points could be increased very easily, especially if DIC were to be used.

The results presented in this work demonstrate that 3D point-tracking can be used to obtain operating deflection shapes (ODSs) of a small wind turbine while rotating at various frequencies. ODSs that were extracted from the rotating tests provide a clear picture of how the turbine is behaving while in operation. Similar shapes were observed in each data set, but in some cases at very different frequencies. However, the shape that correlated the best was extracted at the same spectral line. Because of this inconsistency, similar tests on a simpler rotating structure should be conducted. While there seems to be an indication of inertial stiffening due to the rotor spinning, firm conclusions cannot be drawn at this point. Additional measurements need to be made to further validate these preliminary findings.

ACKNOWLEDGEMENTS

The authors gratefully appreciate the financial support for this work provided by the U.S. Army Research Office Nanomanufacturing of Multifunctional Sensors Ref. Award Number: W911NF-07-2-0081 and the National Science Foundation under Grant No. 0900534, entitled "Dynamic Stress-Strain Prediction of Vibrating Structures in Operation". Any opinions, findings, and conclusions or recommendations expressed in this material are those of the authors and do not necessarily reflect the views of the National Science Foundation or Army Research Office. The authors would also like to thank Tim Schmidt of Trillion Quality Systems for providing insight and equipment necessary to conduct the measurements.

REFERENCES

- [1] Miller, Timothy J., Hubert W. Schreier, and Phillip L. Reu, "High-speed DIC Data Analysis from a Shaking Camera System," Proceedings of the 2007 SEM Annual Conference and Exposition on Experimental and Applied Mechanics. June 3-6, 2007. Springfield, MA.
- [2] Miller, Timothy J., Hubert W. Schreir, Michael T. Valley, and Timothy L. Brown, "Extending Digital Image Correlation to Moving Field of View Application: A Feasibility Study," Proceedings of the XIth Society of Experimental Mechanics International Congress and Exposition. June 2-5, 2008. Orlando, FL.
- [3] Miller, Timothy J., Edward F. Romero, Hubert W. Schreir, and Michael T. Valley, "Extending Digital Image Correlation to Moving Field of View Application: Error Assessment Using Outdoor Centrifuge," Proceedings of the SEM Annual Conference. June 1-4, 2009. Albuquerque, NM.
- [4] Warren, Chris, Pawan Pingle, Chris Niezrecki, & Peter Avitabile, "Comparison of Image Based, Laser, and Accelerometer Measurements," Proceedings of the IMAC-XXVIII, February 1-4, 2010, Jacksonville, Florida USA.
- [5] Warren, Chris, Chris Niezrecki, & Peter Avitabile, "FRF Measurements and Mode Shapes Determined Using Optically-based 3D Point-tracking," to be published in the Proceedings of the IMAC-XXIX, January 31 – February 3, 2011, Jacksonville, FL USA.
- [6] *American Wind Energy Association (AWEA) 2009 Year End Market Report*. (January 2010). Retrieved from: http://www.areadevelopment.com/article_pdf/id19734_AWEA.pdf
- [7] *Cape Wind™: Energy for Life*, World Wide Web, <http://www.capewind.org>, Accessed October 24, 2010.

- [8] Paulsen, U. S., Erne, O., Moeller, T., Sanow, G., Schmidt, T., "Wind Turbine Operational and Emergency Stop Measurements Using Point Tracking Videogrammetry," Proceedings of the 2009 SEM Annual Conference and Exposition, Albuquerque, NM, June 4, 2009.
- [9] Helfrick, Mark., Chris Niezrecki, & Peter Avitabile, "3D Digital Image Correlation Methods for Full-Field Vibration Measurement." Proceedings of the IMAC-XXVI, February 2008, Orlando, FL USA.
- [10] Warren, Chris, Chris Niezrecki, and Peter Avitabile. "Effects of Shaker Test Set Up on Measured Natural Frequencies and Mode Shapes." Proceedings of IMAC XXVIII. February 1-4, 2010. Jacksonville, Florida, USA.
- [11] PONTOS – GOM mbH, Mittelweg 7-8, 38106 Braunschweig, Germany.
- [12] Camping Gear Depot, *Southwest Windpower Air Breeze Wind Turbine Marine*, Image retrieved from <http://www.campinggeardepot.com/> Accessed October 24, 2010.
- [13] Southwest Windpower, *Southwest Windpower: Air X and Air Breeze small wind generators for remote homes, sailboats, offshore platforms and more*,
- [14] Allemang, R.J. and Brown, D.L., "A Correlation Coefficient for Modal Vector Analysis," First International Modal Analysis Conference, Orlando, Florida, November 1982, 110-116.
- [15] Allemang, Randall J. "The Modal Assurance Criterion – Twenty Years of Use and Abuse." Sound and Vibration Magazine. August 2003. 14-21.
- [16] Warren, Chris and Peter Avitabile. "Effects of Shaker Test Set Up on Measured Natural Frequencies and Mode Shapes." Proceedings of IMAC XXVIII. February 1-4, 2010. Jacksonville, Florida, USA.
- [17] PolyMAX, Leuven Measurement Systems, Leuven, Belgium.
- [18] LMS Test.Lab, Leuven Measurement Systems, Leuven, Belgium.
- [19] Richardson, Marc *Is It a Mode Shape, or an Operating Deflection Shape?* Sound and Vibration Magazine, March 1997.
- [20] Bir, Gunjit S., and Karl Stol, "Operating Modes of a Teetered-Rotor Wind Turbine," Proceedings of the International Modal Analysis Conference – IMAC, Vol.2 (1999) 1586-1596.
- [21] Ortiz, Jose L., and Gunjit S. Bir, "Verification of New MSC.ADAMS Linearization Capability for Wind Turbine Applications," Proceedings of the 44th AIAA Aerospace Sciences Meeting and Exhibit. January 9-12, 2006. Reno, Nevada.
- [22] Bir, Gunjit, *Coupled Modal Dynamics of a Large Wind Turbine Blade*, #143, Oral Presentation. IMAC XXVIII. February 1-4, 2010. Jacksonville, Florida, USA.

Dynamic Performance and Integrity Assessment of an Electricity Transmission Tower

E. Peter Carden*, John R. Maguire
Lloyd's Register EMEA, 71 Fenchurch St. London EC3M 4BS, UK.
*Corresponding Author: Peter.Carden@lr.org

Abstract

As part of a programme of structural integrity assessment, an electricity transmission tower was instrumented with an anemometer, strain gauges, thermocouples and accelerometers and its performance monitored for one year. The monitoring system emailed statistics of wind, strain, temperature and acceleration data daily together with modal parameters automatically identified with operational modal analysis. Extremely large diurnal changes in the natural frequencies of the tower were observed with the first mode varying between approximately 0.8 Hz and 3.0 Hz and the second mode varying between approximately 2.8 Hz and 6.0 Hz. Unexpected bending of the leg members was also observed. The diurnal changes in modal parameters and bending strains of the leg members were correlated with temperature. The changes in the performance of the tower were investigated numerically through analysis of the changes in tension of the conductors due to temperature and a finite element model of the tower. The bending strains induced in the legs were large enough to be important in the integrity assessment. The measured dynamic performance of the tower implies that a structural health monitoring paradigm based on modal parameter changes must be able to account for large shifts due to environmental variability.

Introduction

As infrastructure ages towards and past its design life, it is prudent to undertake residual life and integrity assessments of these valuable assets. Suitable general methodologies for the integrity assessment will differ depending on the type of infrastructure and site and structure specific issues. For example the approaches taken for the residual life assessment of a ship unloader in [2] may be compared with that for electricity pylons in [1].

As part of a programme of structural integrity assessment conducted by the authors, an electricity transmission tower was instrumented and monitored for approximately one year. One of the motivating factors in monitoring this particular tower was to understand the wind load loading actually experienced by the tower and compare this with old and modern wind codes and nearby weather station records. Understanding of wind loading has increased substantially since the 1950s and this is reflected in modern wind loading codes. However, the dynamic performance of the tower during the monitoring period was found to very different to that which was expected and this is the focus of this paper.

Full scale monitoring and analytical studies of overhead tower transmission towers have been undertaken before. Results from the monitoring of a 96 m tall overhead transmission tower are described in [3], where the primary interest was in understanding the local wind loading in a mountainous area. Identification of the modes of the structure was conducted using two methods at two different times. Unusual variations in the modes of the structure were not identified or described, though with such a limited number of estimates this is not surprising. In a companion paper [4] to [3], the finite element modelling of towers is described. The natural frequencies of the towers were predicted to be insensitive to the mean wind force. The effects of other environmental variables were not considered and no large changes in the modes of the towers were predicted.

The importance of the gust response factors used in design, which are dependent on the natural frequencies of the structures under design, are highlighted in [5]. A 52 m high free standing lattice tower was instrumented and monitored. The lowest natural frequency was identified and quoted as a single value. No variation in the modes of the structure with changes in environmental factors was identified or discussed.

The effect of soil-structure interaction in an analytical study on a 32.86 m tall overhead transmission tower in [6] was found to be negligible on the lower natural frequencies of the tower. This effect was described as being expected as the relevant design factor of a transmission line tower foundation is the overturning moment arising from the action of wind. As a consequence, footings designed for this type of tower and load result in low tension and compression stresses on the soil and consequently very small settlements. Large changes in the natural frequencies due to other environmental variables were not predicted.

In [7] the influence of design methods in assessing the effects on wind loading of a transmission tower of approximately 44 m height were investigated. The influence of the first two modes was found to be important in terms of fatigue life but the values of the first two natural frequencies were assumed to be constant for the life of the structure.

In [1] a series of laser vibrometer measurements were taken on a selection of towers in a single line to assist in a residual life assessment. Modes were identified between approximately 1.2 Hz to 2.2 Hz and 4 Hz to 6 Hz. A correlation exercise was carried out, relating conductor span length to measured frequency which indicated that, in general, as the mass carried (conductor length) increased then the natural frequency decreased, as would normally be expected. Only a single set of measurements were made and so the influence of environmental factors was not identified.

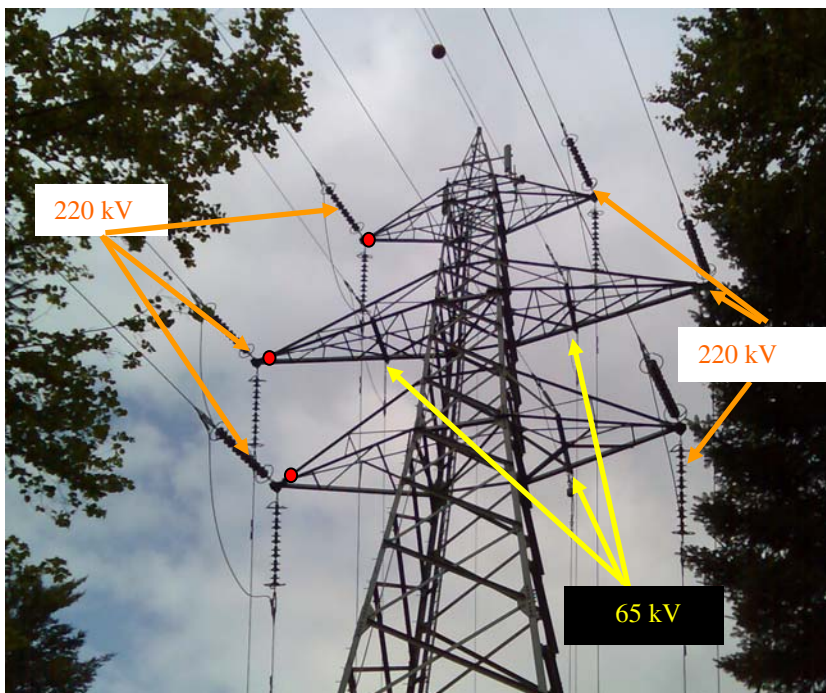


Figure 1. Red circles indicate position of the accelerometers.

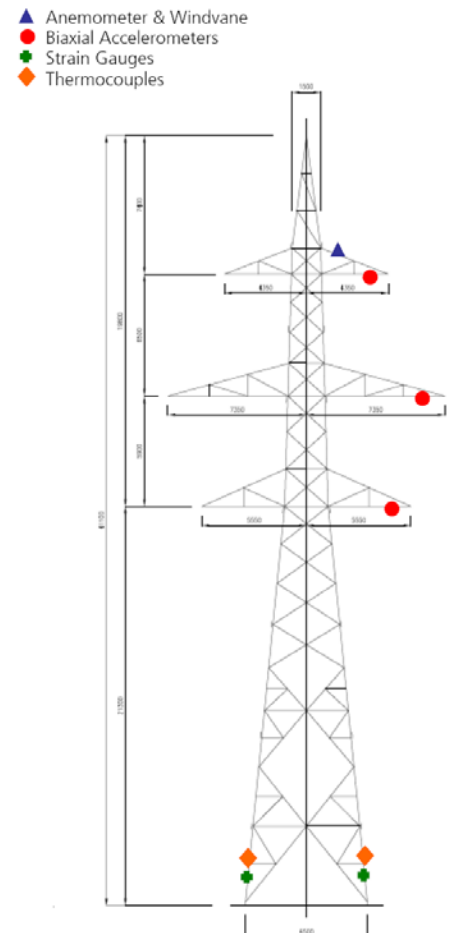


Figure 2. Position and type of sensors on the tower.

Large variations in natural frequencies of large structures have been reported but only relatively recently; diurnal changes of the order of 20 % were identified in the first two modes of a 183 m chimney in [8] and in the second

mode of a 335 m bridge main span in [9]. The identification of these variations has been made possible with the advent of on-line modal identification with powerful operational modal analysis algorithms and these techniques have been applied to the overhead transmission tower which is the subject of this paper.

Overhead transmission tower and monitoring system

The transmission tower instrumented in this study was part of a line that was originally constructed in the 1950s with two 220 kV circuits. Approximately 6 years ago a third circuit, of 65 kV, was added (Figure 1). The 41m tall tower is situated on top of a ridge in an orographically complicated area between plains and mountains. Wind from the north of tower blows up the ridge which gains approximately 200 m of height in approximately 230 m. The conductors span 260 m south and 305 m north and are both attached to the tower at an angle of approximately 12 degrees in the horizontal plane. Telecommunication equipment was installed on the top of the tower which may be seen in Figure 1. The tower was instrumented with strain gauges, biaxial accelerometers (in the horizontal plane), an anemometer and thermocouples in the locations shown in Figure 2.

The monitoring system was programmed to email a summary of the data collected daily in the form of a Microsoft Excel attachment to an email via a mobile phone network. The summary data included modal parameters, which were computed on-line by the data acquisition system with the method described in the next section.

Modal parameter extraction

Mathematically, structural systems may be recast from continuous second order differential equations governing their behaviour into discrete state space equations. Stochastic Subspace Identification (SSI) is an efficient method for identifying the state space matrices from measured response data. The natural frequencies, damping parameters and mode shapes may then be extracted from these state space matrices. The major advantages of taking this approach are that it is quick and non-iterative and therefore does not suffer from convergence problems. Fundamental proofs and discussions of numerical stability are described in [10] while a succinct, though thorough, step-by-step procedure with an example application is provided in [11].

There are various subtypes of SSI available. Covariance-driven SSI was used in the monitoring system described herein. The advantage of using covariance-driven SSI as opposed to data-driven SSI is that the data reduction is far less memory intensive. The data-driven subspace projection utilises a QR decomposition of the data Hankel matrix and for large data sets this becomes very memory demanding. Covariance-driven SSI requires the formation of the Toeplitz matrix of the covariance of the measured output and is far less memory demanding. For on-line real time monitoring this yields a substantial advantage.

Covariance-driven SSI requires the formation of a Toeplitz matrix of covariances, T , see [10 & 11] for further details. T_i is singular value decomposed according to Equation (1) and this implies the choosing of the order of the system, n . The subscript i in T_i refers to the number of lags of the covariances used.

$$T_i = USV^T = \begin{pmatrix} U_1 & U_2 \end{pmatrix} \begin{pmatrix} S_1 & 0 \\ 0 & S_2 \end{pmatrix} \begin{pmatrix} V_1^T \\ V_2^T \end{pmatrix} \rightarrow U_1 S_1 V_2^T \quad (1)$$

In theory the number of non-zero singular values will equal the order of the system, n . In equation (1) the singular value matrix is broken into S_1 and S_2 . With perfect numerical accuracy and absolutely clean data, S_1 would be comprised of a diagonal of n non-zero entries and S_2 would be comprised of all zeros. In such a case, T_i would decompose to $U_1 S_1 V_1^T$. However, in practice this will not happen. On rare occasions, with very good quality data and with some luck, there is a dramatic drop in the singular values which marks the order of the system. All too often this step down in magnitude of value is not present and it is up to the analyst's skill and experience to choose the correct order. Once an order is chosen, the extended observability matrix may be calculated as in Equation (2).

$$O_{i,n} = U_1 S_1^{1/2} \quad (2)$$

The dynamic matrix A may be calculated in a least squares manner by making use of the shift structure of the observability matrix (Equation 3). The eigenvalues of this dynamic matrix are the poles of the system and thus yield

the natural frequencies and damping estimates while the eigenvectors may be converted to the mode shape vectors. Details may be found in [4].

$$A = \underline{O_{i,n}^\dagger} \overline{O_{i,n}} \quad (3)$$

where $\underline{O_{i,n}}$ is equal to $O_{i,n}$ without the last L (number of channels) rows and $\overline{O_{i,n}}$ is equal to $O_{i,n}$ without the first L rows.

The construction of a stability diagram has proven invaluable in helping the analyst in choosing the correct order of the system and in distinguishing between true modal parameters and mathematical chimera. The stability diagram is formed by choosing a range of values for n and extracting the modal parameters from the dynamic matrix for each of these values. The analyst defines rules by which modal parameters may be considered stable between two different assumed orders. Figure 3 is an example of a stability diagram from data recorded on the transmission tower after the application of a 10 Hz digital lowpass filter. The rules used to define a pole as being stable between successive orders were:

- variation in the natural frequency of less than 1 %
- variation in damping of less than 5 %.
- variation in modal assurance criterion less than 2 %.

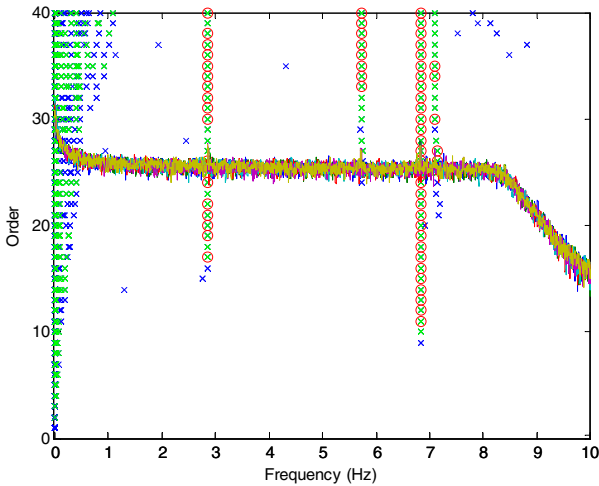


Figure 3 Typical stability diagram from the transmission tower. The Auto PSDs are under laid as solid lines. Red circles indicate stable poles while green and blue crosses indicate unstable poles.

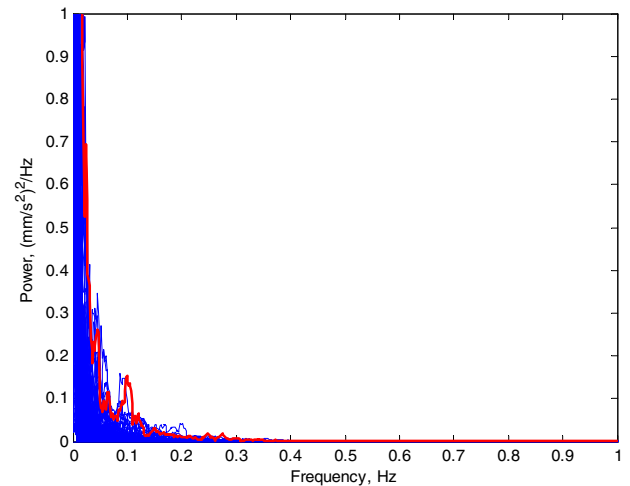


Figure 4. Power Spectral Densities (PSDs) of wind speeds recorded in 10 minute periods between May and November 2009. The maximum wind speed during this time is highlighted in red; it had a 10 minute mean speed of 8.9 m/s and maximum 1 sec gust speed of 18.5 m/s. The y-axis has been cut short to show some detail in the sub 0.3 Hz range.

A large number of unstable poles below approximately 1 Hz may be seen in Figure 3 coincident with curving of the auto power spectral densities. This structure at the low end of the frequency spectrum was not an artefact of the accelerometer performance but was due to the energy in the wind loading. Figure 4 shows a compilation of power spectral densities of the wind speeds recorded by the anemometer, which shows that the energy imparted by the wind was concentrated in the first few tenths of a hertz.

The columns of red circles in Figure 3 indicate the identification of a mode. Although the stability diagram in Figure 3 was reasonably clear, not all the data provided such clear identifications. This may be seen in Figure 5 where a compilation of identification for each 10 minute period over the course of a week is shown. In an attempt to clean up the pattern of natural frequency shifts seen in Figure 5, the identified poles were ranked in terms of energy off-line after the raw monitoring data had been collected from the transmission tower DAQ.

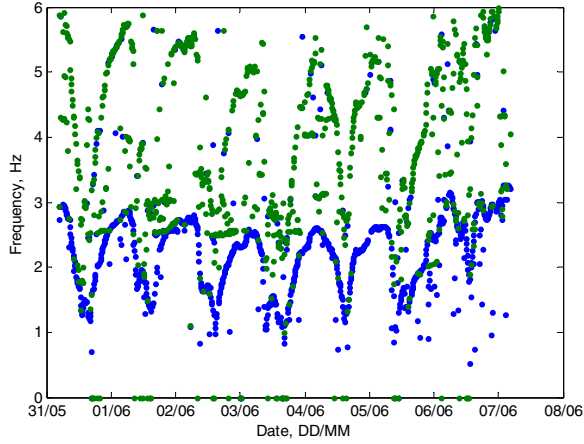


Figure 5. Identified natural frequencies of the transmission tower. First mode in blue and second mode in green. Modes are poorly identified at times when there is little excitation.

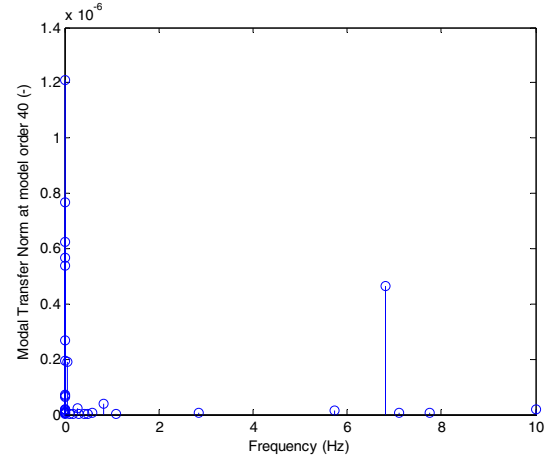


Figure 6. Modal Transfer Norm calculated for the poles at order 40 in the stability diagram in Figure 3.

To rank the identified poles in terms of energy an alternative calculation of the dynamic matrix, A , to that in equation (3) was developed.

The dynamic matrix, A , may be calculated using a total least squares approach [10] through a singular value decomposition as in Equations 4, 5 and 6.

$$svd(\underline{O}_{i,n} \quad \overline{O}_{i,n}) = USV^T \quad (4)$$

$$V = \begin{pmatrix} \overset{n}{\longleftrightarrow} V_{11} & \overset{n}{\longleftrightarrow} V_{12} \\ V_{21} & V_{22} \end{pmatrix} \begin{matrix} \updownarrow n \\ \updownarrow n \end{matrix} \quad (5)$$

$$A = -V_{12}(V_{22})^\dagger \quad (6)$$

In practice, there is little difference in the results calculated by Equation 3 and 6. However, we have modified the second approach by making use of a truncated total least squares solution [12]. A choice is made as to the number, k , of the highest energy poles to be identified and Equation 5 is modified to Equation 7 with the change in partition of the right singular vectors. The dynamic matrix, A , is then estimated in the same way as Equation 6.

$$V = \begin{pmatrix} \overset{k}{\longleftrightarrow} V_{11} & \overset{2n-k}{\longleftrightarrow} V_{12} \\ V_{21} & V_{22} \end{pmatrix} \begin{matrix} \updownarrow n \\ \updownarrow n \end{matrix} \quad (7)$$

An additional advantage of neglecting the $n-k$ lower energy poles is that a more stable solution for the k poles is achieved by removing stabilities associated with division by small singular values [12]. The authors' experience on other structures has shown this to be reliable in identifying the highest excited modes consistently.

When applying this alternative identification algorithm on the tower it was found that the highest energy poles were not those of the lowest modes of the structure. This may be seen in Figure 6 where the relative energy for each pole had been calculated using the modal transfer norm [13]. The stable mode of the structure at 2.7 Hz

seen in Figure 3 had the lowest energy poles and the stable mode at 5.7 Hz had the third lowest energy poles identified at the order of 40.

Despite the inability to clean Figure 5 based on energy content, the pattern of variation in natural frequencies can still be distinguished.

Monitoring system results

The temperature measured on two of the legs of the tower over the first week of June is shown in Figure 7, which corresponds with the period shown in Figure 5. A diurnal pattern may be seen in both figures with lower natural frequencies corresponding to higher temperatures. This pattern held over the entire monitoring period. The first mode of tower varied between approximately 0.8 Hz and 3.0 Hz and the second mode varied between approximately 2.8 Hz and 6.0 Hz.

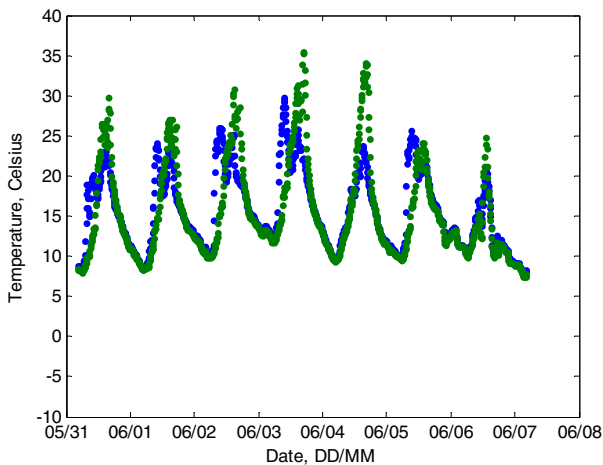


Figure 7. Temperature measured on two legs of the tower during the first week of June 2009.

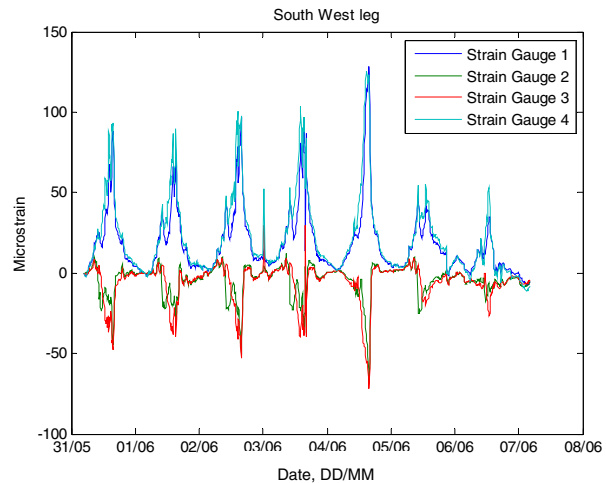


Figure 8. Mean 10 minute strain measurements on the south west leg of the tower.

Figure 8 shows the 10 minute mean strains in the south west leg over the same period as Figure 3 and 7. A strain gauge was installed on each leg of the two angles joined to form each leg of the tower with + shaped cross-sections. A diurnal pattern is again seen with two gauges going into tension and two into compression with higher temperatures. The pattern of strain indicated that the legs were undergoing bending. The stresses induced by the bending were of the order of 30 % of the stresses predicted by the design wind and self weight load. The other legs also showed the same diurnal pattern of bending strains. However, the bending stress maxima did not, in general, occur at the same time in each leg with differences of the order of half an hour being observed. It may be noted that Figure 7 shows that the maximum temperatures also did not coincide on the legs. The bending indicated that the legs were not behaving as members of an ideal truss structure.

Figure 9 shows the temperature data recorded over the last week of January 2010 and Figure 10 shows the natural frequency estimates during this period. The first mode may be seen clearly in Figure 10, although the second mode is less distinct. There are a larger number of spurious identifications in Figure 10 compared to Figure 5. The wind was relatively light during the last week of January compared to the first week of June. The correlation between temperature increases and natural frequency is also seen in Figures 9 and 10.

Figure 11 shows the relationship between temperature and the first natural frequency identified for both the January and the June data. Although there is noise present in the plot from spurious identifications, a reasonably linear relationship between temperature and natural frequency may be discerned for each set of data. The natural frequencies identified in January are generally lower than those that would be expected if the linear pattern seen in the June data was extrapolated to the lower temperatures. A likely reason for this is the extra mass due to the

snow and ice loading on the tower and conductors. Figure 12 shows a photograph of one of the legs of the tower in early December after the first heavy snow fall of the winter.

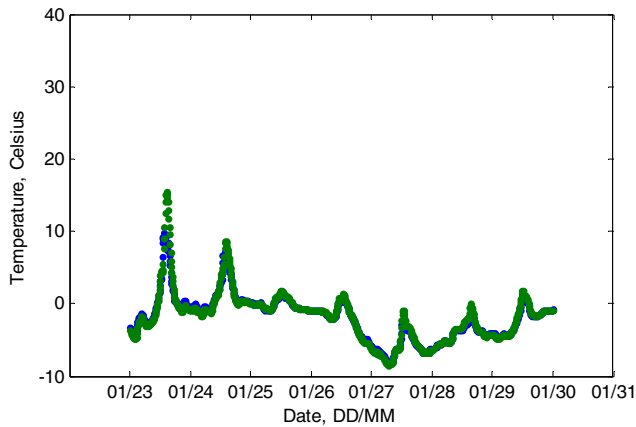


Figure 9. Temperature measured on two legs of the tower during the last week in January 2010.

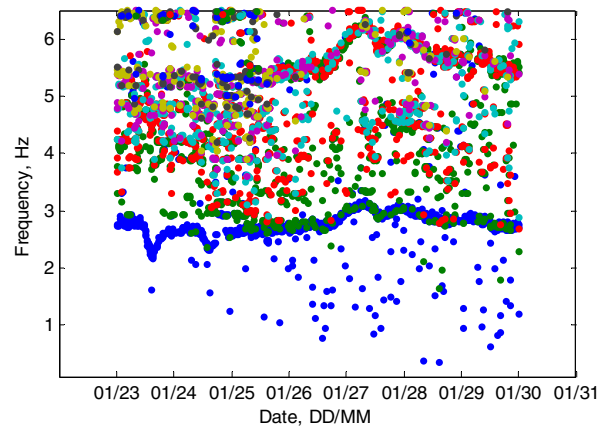


Figure 10. Identified natural frequencies of the transmission tower. Modes are poorly identified at times when there is little excitation and there are a large number of spurious identifications.

Modelling of the tower

A finite element (FE) model of the tower was built in ANSYS to help investigate the unusual observed behaviour of the tower. The literature suggested that changes in tension in the conductors due to wind loading [4] and soil-structure interaction [6] would have little effect on the dynamic behaviour. An examination was made as to the effect of a rise in temperature on the increase in length of the conductors, thereby changing their sag, tension and effective stiffness.

3D beam elements were used to model each angle member. Isolators and the telecommunication frame and equipment were modelled as lump mass elements at the points of their attachment. Forces applied by the conductors were estimated using the method described in [14]. It would have been beneficial to have measured the conductor tensions directly and any future monitoring program should consider this. Three static analyses were executed with the model:

- 1) no conductor loads;
- 2) conductors loads with a zero change in temperature;
- 3) conductors loads with a +60 °C change in temperature.

The self weight of the pylon (first load case) was fairly evenly spread over the four legs of the pylon with a relatively small amount of bending in each leg. The change in conductor tensions due to temperature change resulted in differences in the load sharing in the legs but in all three load cases the local bending of the legs was small compared to the axial strains for all legs. The FE model was not able to capture the effects of bending in the legs through only changes in the loads from the conductors.

Four modal analyses were conducted with the FE model. As an initial simplifying assumption, half the masses of each of the conductors were applied as point loads at the points of attachment of the isolators in each case. The conductors were modelled as beam elements with negligible mass and moduli of elasticity equal to the equivalent tangent moduli estimated using the methods in [14]. The four load cases chosen were:

- 1) conductors with zero moduli of elasticity;
- 2) conductors with tangent moduli of elasticity equivalent to 0 °C temperature change;
- 3) conductors with tangent moduli of elasticity equivalent to +60 °C change in temperature;
- 4) conductors with moduli of elasticity equal to the cable moduli of elasticity.

The fourth load case, conductors with moduli of elasticity equal to the cable moduli of elasticity, is unrealistic but was used as a limit case to investigate the sensitivity of the natural frequencies of the model to changes in cable stiffness.

The natural frequencies of the first two modes are given in Table 1 and the mode shapes in Figure 13. The mode shapes did not differ significantly in form across the four variations of conductor moduli with the first mode being transverse bending with respect to the line of the conductors and the second mode being bending in-line with the conductors. Increasing the stiffness of the conductors has the effect of increasing the difference in natural frequency of the first two modes. Increasing stiffness has a greater effect on increasing the natural frequency of the second mode than the first mode. The finite element model predicted an operational variation in the first natural frequency of the tower of the order of hundredths of a hertz and a variation in the natural frequency of the second mode of the tower of the order of tenths of a hertz.

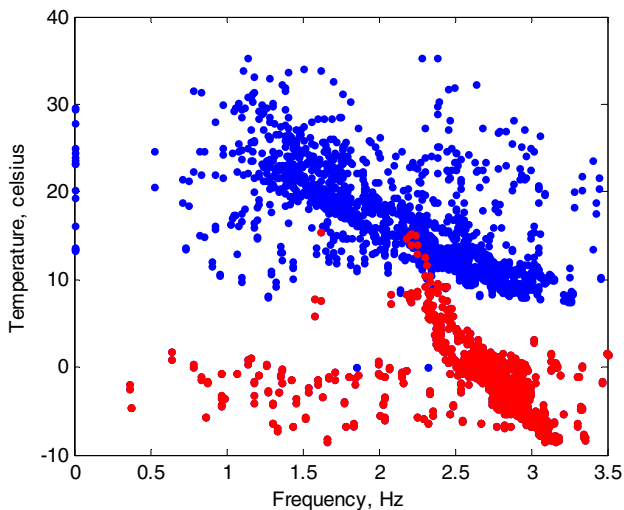


Figure 11. First natural frequency variation with temperature. The blue dots show the identification in the first week of June from Figure 5. The red dots show the identification in the last week of January from Figure 5.



Figure 12. Photograph of one of the tower legs in December after the first heavy snow fall of the winter.

The effect of change in temperature on the conductors' tension and effective stiffness does not account wholly for the changes in bending strains in the legs and shifts in natural frequencies which were observed to correlate with changes in temperature. The effects of temperature induced strains in the lattice structure may provide an explanation for the observed behaviour but this has not been investigated to date.

Conclusion

Extremely large diurnal changes in the natural frequencies of the tower were observed with the first mode varying between approximately 0.8 Hz and 3.0 Hz and the second mode varying between approximately 2.8 Hz and 6.0 Hz. However, the practical effects on the dynamic response of the tower to wind were not considered to be of major significance due to the majority of the energy in the wind being below a few tenths of a hertz. The bending

strains induced in the leg members were correlated with the temperature changes and the natural frequency shifts and show that the tower is deviating substantially from the behaviour of an ideal truss structure. The stresses induced by the bending were of the order of 30 % of the design stresses calculated from the design wind and self weight load.

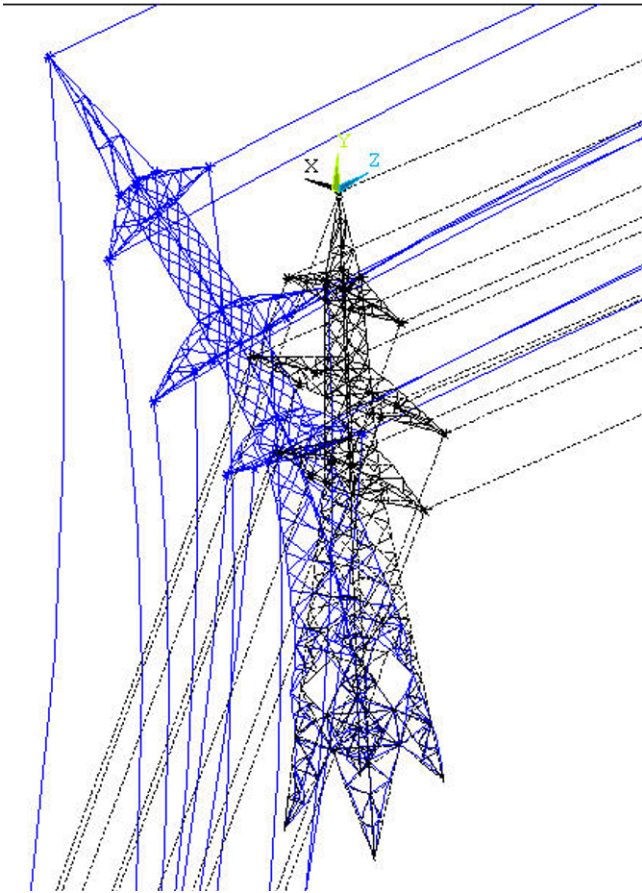


Figure 13a. First mode shape, bending transverse to the conductors

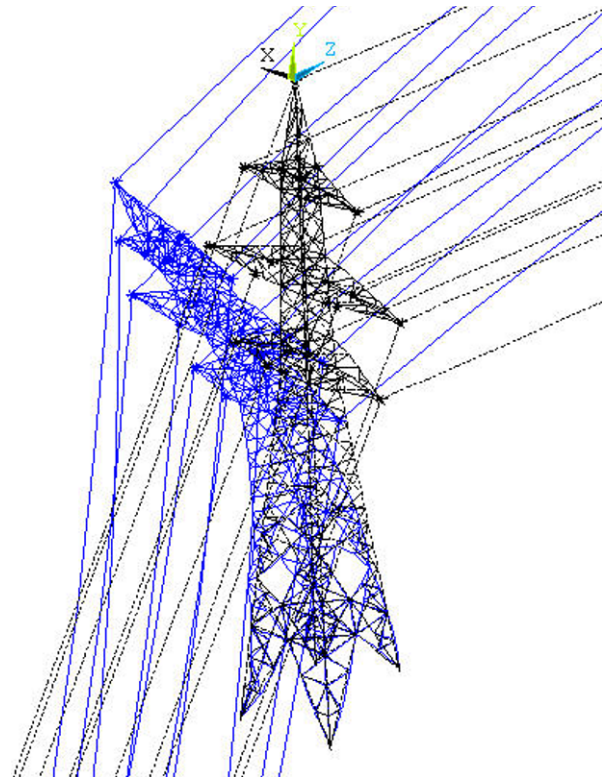


Figure 13b. Second mode shape, bending inline with the conductors

Natural frequency with no conductor stiffness (Hz)	Natural frequency with conductor stiffness at +60 °C temperature change (Hz)	Natural frequency with conductor stiffness at 0 °C temperature change (Hz)	Natural frequency with conductor with original cable moduli (Hz)
1.92	1.93	1.94	2.05
2.02	2.18	2.30	3.48

Table 1. Finite element predicted natural frequencies of Pylon 128

The changes in the performance of the tower were investigated numerically through analysis of the changes in tension of the conductors due to temperature and a finite element model of the tower. However, the effect of changing tension in the conductors could not alone explain the bending strains or shifts in natural frequencies. The bending strains induced in the legs were large enough to be important in the integrity assessment. The measured dynamic performance of the tower implies that a structural health monitoring paradigm based on modal parameter changes must be able to account for large shifts due to environmental variability.

References

- 1 Maguire John R., Residual life assessment of electricity pylons – a case study, *Key Engineering Materials Vols. 413-414* (2009) pp 219-228
- 2 Maguire John R., Risk-based residual life assessment – a case study, *Key Engineering Materials Vols. 245-246* (2003) pp 359-366
- 3 Y. Momomura, H. Marukawa , T. Okamura , E. Hongo, T. Ohkuma Full-scale measurements of wind-induced vibration of a transmission line system in a mountainous area, *Journal of Wind Engineering and Industrial Aerodynamics* 72 (1997) 241 252.
- 4 H. Yasui, H. Marukawa, Y. Momomura, T. Ohkuma Analytical study on wind-induced vibration of power transmission towers, *Journal of Wind Engineering and Industrial Aerodynamics* 83 (1999) 431}441.
- 5 P. Harikrishna, J. Shanmugasundaram, S. Gomathinayagam, N. Lakshmanan, 'Analytical and experimental studies on the gust response of a 52 m tall steel lattice tower under wind loading *Computers and Structures* 70 (1999) 149 -160
- 6 Ronaldo C. Battista, Rosângela S. Rodrigues, Michèle S. Pfeil Dynamic behavior and stability of transmission line towers under wind forces *Journal of Wind Engineering and Industrial Aerodynamics* 91 (2003) 1051–1067
- 7 A.M. Loredou-Souza, A.G. Davenport The influence of the design methodology in the response of transmission towers to wind loading *Journal of Wind Engineering and Industrial Aerodynamics* 91 (2003) 995–1005
- 8 Brownjohn J.M.W., Carden E.P., Goddard C.R. and Oudin, G. (2010) Real time performance monitoring of tuned mass damper system for a 183m reinforced concrete chimney. *Journal of Wind Engineering and Industrial Aerodynamics* Vol. 8, No. 3, March, pp. 169-179.
- 9 Brownjohn, J. M. W. and Carden, P. (2008) Real-time operation modal analysis of Tamar Bridge. 26th International Modal Analysis Conference (IMAC XXVI), Orlando, Florida, USA, 4-7 February.
- 10 Van Overschee P, De Moor B, Subspace Identification for Linear Systems, 1996 Kluwer Academic Publishers, USA, pp254
- 11 Peeters B, De Roeck G, Reference-Based Stochastic Subspace Identification For Output-Only Modal Analysis, *Mechanical Systems and Signal Processing* (1999) 13(6), 855-878
- 12 R. D. Fierro, G. H. Golub, P. C. Hansen, And D. P. O'leary Regularization By Truncated Total Least Squares *Siam Journal of Scientific Computing* Vol. 18, No. 4, pp. 1223-1241, July 1997.
- 13 E. Reyndars, G. De Roeck, Reference-based combined deterministic–stochastic subspace identification for experimental and operational modal analysis, *Mechanical Systems and Signal Processing* 22(3) (2008) 617-637
- 14 Karoumi R., Some modelling aspects in the nonlinear finite element analysis of cable supported bridges, *Computers and Structures*, 71, pp.397 – 412, 1999

Operational modal analysis of resiliently mounted marine diesel generator/alternator

Hayden Clarke*, Joe Stainsby, E. Peter Carden
Lloyd's Register EMEA, 71 Fenchurch St. London EC3M 4BS, UK

*Corresponding Author: Hayden.Clarke@lr.org

Abstract

Excitation from diesel engines can cause fatigue failures of the engine or mounting structure and potentially cause high vibration levels to surrounding ship structures. Understanding the causes of cracking in an alternator set requires knowledge of its vibration modes and their effects on the structure. Cracks in the alternator casing and bed plate on identical resiliently mounted marine units on two separate sister ships were investigated. Operational modal analysis (OMA) was an effective tool in assessing the alternator set vibration characteristics. Measurements were taken under ambient excitation conditions, during startup and shutdown and while running at a range of operational power levels. Difficulties in establishing modes solely from single speed or ambient excitation measurements were encountered due to high engine and surrounding alternator set harmonic excitation. Despite short time records the startup and shutdown of the engines provided the most effective data for identifying mode shapes. Several rigid body and non-rigid body modes were identified between 5 Hz and 180 Hz. A high level of correlation was established between alternator sets. Modes were identified that corresponded with engine harmonics and their shapes provided insight into the crack failure mechanisms on the alternator casing and bedplate.

Introduction

The authors carried out a technical investigation onboard a ship in March 2010. The purpose of the attendance was to investigate the cause of cracks found in the alternator air filter/separator housings of four auxiliary generating sets and additionally, two cracks in the bed frame of one set.

As a result of the findings of the inspections and measurements, a similar investigation was undertaken on the sister vessel.

Auxiliary electrical power is provided on each vessel by seven generating sets. Each comprises a 6 cylinder in-line engine rated to deliver 370 kW at 1,800 rpm, coupled to a synchronous alternator rated at 416 kVa at 60 Hz. The typical operating load for each of the generating sets varies between 150 kW and 200 kW. All the generating sets are arranged in one machinery space.

The engine and alternator are directly coupled and are mounted on a common bed frame which is supported on 6 flexible mountings. The bed frames are constructed of heavy gauge steel "U" section beams 300 mm high and 100 mm deep, welded together to form a rectangle some 2.4 metres long and 920 mm wide. Transverse members support the alternator mounting feet.

The alternator casings are constructed of thin gauge steel plate bolted together at flanged connections. Cable entry to the terminals is at the top centre of the alternator. A single stage air filter/separator mounted in an aluminium casing is bolted to each of the alternators.

Background

During inspections on vessel 1 it was noted that the alternator casing of four sets had cracked at the upper corners at the bolted flanged connection to the filter/separator housings, [Figure 1](#). Additionally, it was noted that the bed frame of 1 generating set had cracked in two places, [Figure 2](#).

A subsequent inspection carried out on the sister vessel, vessel 2, revealed one generating set, was affected by cracking of the alternator casing, in a similar location at the upper corners at the bolted flanged connection to the filter/separator housing. There were no visible cracks on the generating set bed frames.



Fig. 1 Auxiliary generating set no. 1, separator housing vertical crack, port forward corner



Fig. 2 Bed frame crack, starboard aft corner, transverse frame weld

The operating hours of the affected generating sets varied between 2,188 and 4,242. It is worth noting that a set with 7,600 service hours was undamaged.

Scope of investigation

The aim of the investigation was to carry out visual inspections, static measurements, and measure operational vibration amplitudes on and adjacent to the generating sets in order to establish the vibration characteristics and the effectiveness of the flexible mounts.

In addition, OMA of selected generating sets was carried out to establish the mode shapes and natural frequencies of both the alternator casing and the bed frame/engine.

Vibration measurements

Measurements were carried out using 16 Wilcoxon type 793-35 uni-axial velocity transducers.

Measurements were taken on and adjacent to four generating sets on vessel 1 and two sets on vessel 2. Sets onboard vessel 1 and vessel 2 with cracking damage were selected. Additionally, on both vessels a common set, set 3, was selected because there was no cracking damage. The flexible mounting installation had been established on both undamaged sets and was noted as being generally satisfactory with an even distribution of heights and thus suitable for comparative measurement. On the sets where damage was found, the installation of the flexible mounting was outside the manufacturers recommended limits.

The transducers were arranged in several different arrays in order to collect the optimum data for a range of different operating conditions. Results from two of these arrays, [Figures 3 and 4](#), were then utilised for OMA, which concentrated on the cracked local area of the alternator casings and the global vibration of the bed frames.

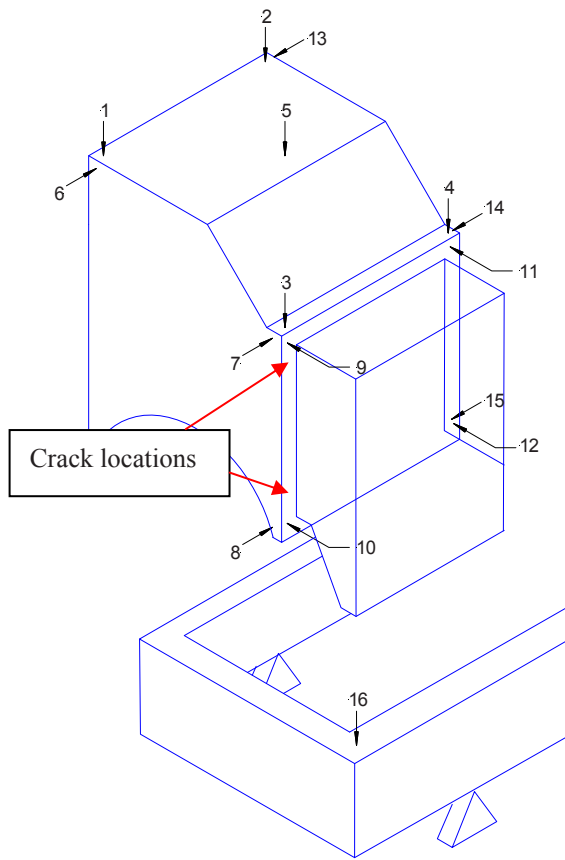


Fig. 3 Velocity transducer array 1, alternator casing vibration

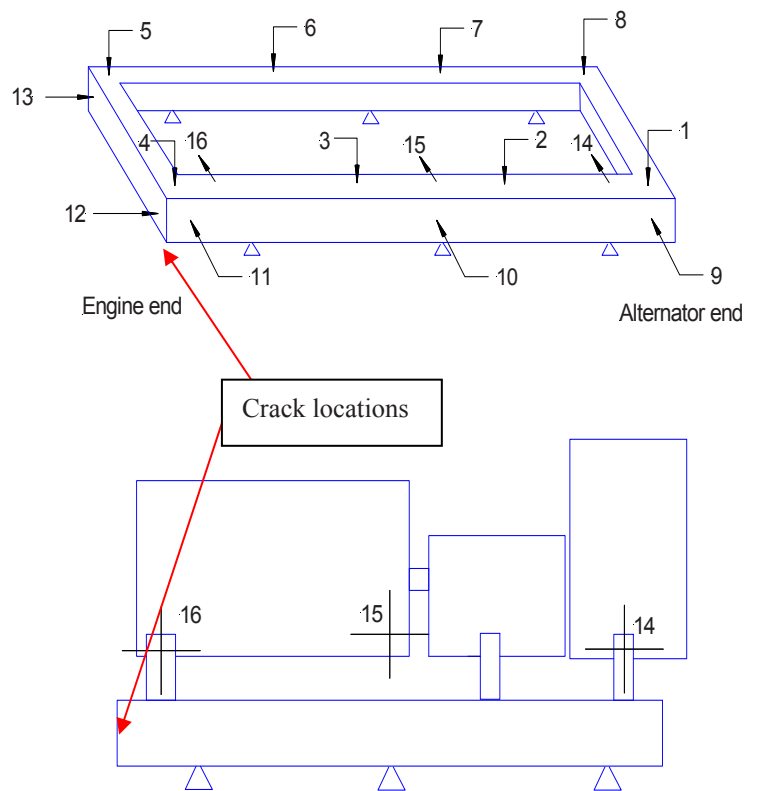


Fig. 4 Velocity transducer array 2, alternator bed frame vibration

OMA was carried out on the vibration data from four of the generating sets, two from each vessel. The analysis was carried out from several trials on each set:

- | | |
|--|-------------------------------------|
| • Engine in shutdown condition: | 10 minute recording |
| • Engine in running no load condition: | 2 minute recording |
| • Engine running at 100 kW load: | 2 minute recording |
| • Engine startup: | approximately 5.5 seconds recording |
| • Engine shutdown: | approximately 16 seconds recording |

The engine startup and shutdown trials were limited to the time taken for the engine speed to increase from zero rpm to idle speed or vice versa.

Modal analysis extraction

Stochastic Subspace Identification (SSI) was used to identify the state space matrices from measured response data. The natural frequencies, damping parameters and mode shapes were then established. Fundamental proofs and discussions of numerical stability are described in [1] while a thorough step-by-step procedure with an example application is provided in [2].

Stability diagrams were created to help establish true modal parameters. The analyst defines rules by which modal parameters may be considered stable between two different assumed orders. Detailed information regarding the use of stability diagrams is provided in [3]. Figure 5 is an example of a stability diagram from data recorded during the shutdown of a generating set. The rules used to define a pole as being stable between successive orders were:

- Variation in the natural frequency of less than 1%
- Variation in damping of less than 10%
- Variation in modal assurance criterion less than 2%

The data from the engine in the running condition proved to be difficult to analyse. Modes with natural frequencies removed from the $\frac{1}{2}$ engine speed harmonics, 15 Hz intervals, were identified as well as false modes at the engine harmonics. The engine harmonic modes were easily isolated due to the very low damping values, approximately 0.1 to 0.3%. However any true modes within approximately 2.5 Hz of a harmonic were often masked by the high excitation from the engine.

The baseline measurements with the engine shutdown relied on the ambient excitation to excite the modes. However, at all times at least two other generating sets were operating in the engine room which provided the majority of the excitation therefore providing similar problems of identifying true modes at frequencies close to $\frac{1}{2}$ engine speed harmonics.

The most effective OMA results were obtained from the engine startup and shutdown measurements due to a sweep of the frequency range as the engine traversed its speed range. In particular the engine shutdown measurements were deemed more reliable due to the longer time taken for the engine speed to decrease from 1800rpm to zero rpm (16 seconds).

As a result the engine shutdown and startup analyses were used to identify modes between 5 and 180 Hz. Results of the baseline and engine operating trials were used to help verify that those modes already identified were indeed true modes.

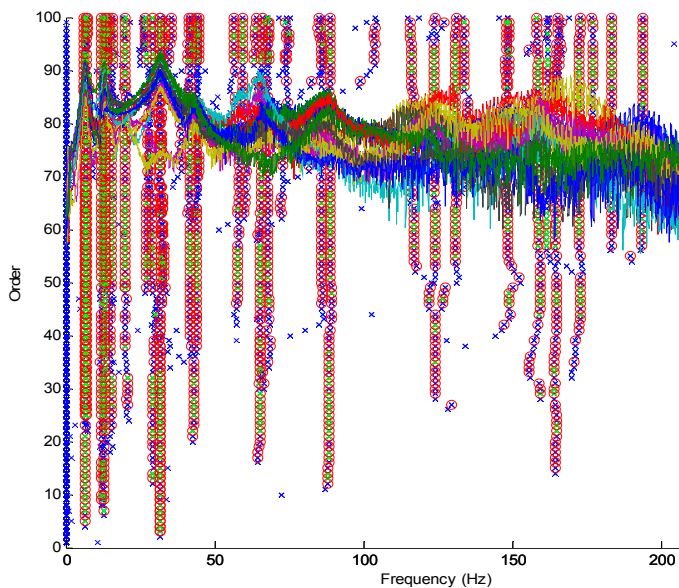


Fig. 5 Example stability diagram from the shutdown of a generating set. The Auto PSDs are under laid as solid lines. Red circles indicate stable poles while green and blue crosses indicate unstable pole

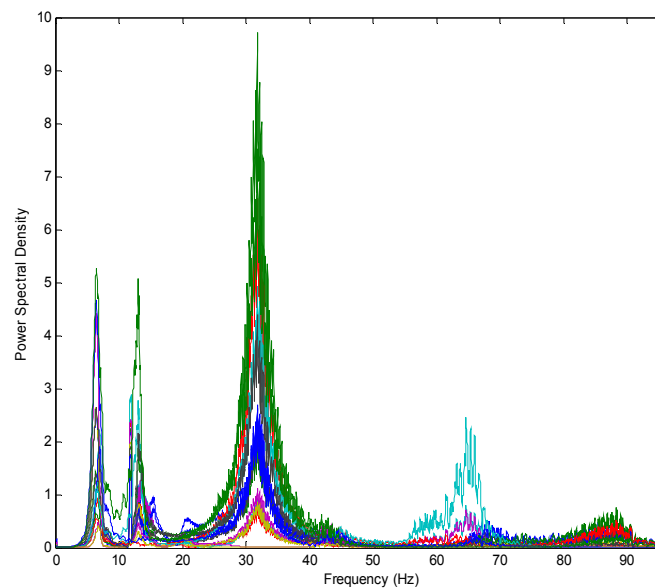


Fig. 6 Power Spectral Densities (PSDs) from the shutdown of a generating set. Several natural frequencies are evident with the strongest being at approximately 32 Hz. The frequency range is limited to 100 Hz for more detail

A large number of modes were identified on each set from the engine shutdown as shown in [Figure 5](#) by the columns of stable poles (red circles). Many more modes are identified by the criteria than were considered true modes. In addition to the SSI method and establishing meaningful criteria, true modes were verified by:

- Inspection of PSDs for all trials, [Figure 6](#).
- Spectrograms of startup and shutdown sequences, [Figure 7](#).
- Complexity of mode shapes, [Figure 8](#).

Modes were eliminated if the PSD or spectrograms illustrated harmonic excitation in combination with a damping ratio of <1%. Additionally many modes were identified that were close in natural frequency. Inspection of their mode shapes often revealed mode identification was repeated and therefore the most stable was selected from the stability diagrams.

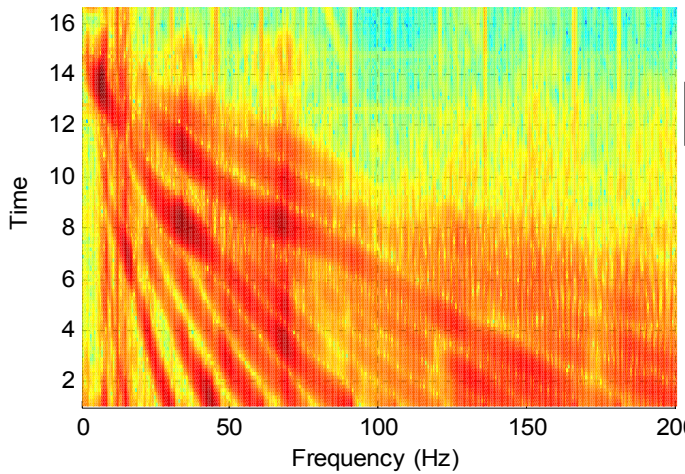


Fig. 7 Example spectrogram of one vibration transducer during a generating set shutdown. The red regions indicate higher amplitudes and clearly show the harmonics of the engine as it shuts down. Strong natural frequencies are evident at approximately 7 Hz, 13 Hz, 33 Hz and 67 Hz.

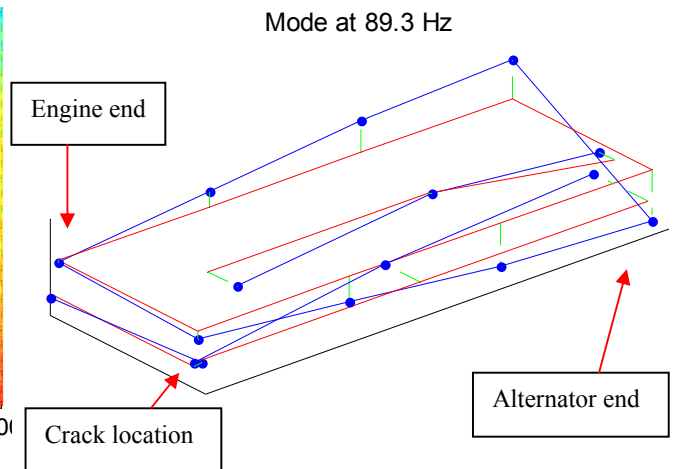


Fig. 8 Example mode shape at 89.3 Hz of a generator bed frame. The mode shape shows a non-rigid body motion with twisting of the bed frame at the alternator end.

In most cases the engine startup and shutdown OMA analysis identified the same true modes though some modes identified from the shutdown were not identified from the startup. Also the shutdown analyses revealed repeat modes at close natural frequencies with more regularity. The modes identified in the two trials for the same generating set generally determined the natural frequencies to be within 1.5% and the damping ratios up to 3% different. The inaccuracies in the analyses between the two trials and the difficulty in determining between closely spaced modes can be attributed to the short measurement periods.

Though all data was used to aid in the determination of a mode the natural frequencies and damping were taken as the mean of those calculated during the startup and shutdown tests on the respective generating sets. The natural frequency and damping ratio was determined directly from the shutdown analysis if the mode was not identified from the startup analysis but was considered to be a true mode.

Alternator casing OMA results

Modal analysis was carried out for the alternator casing for data recorded on vessel 1, sets 1 and 2 and vessel 2 on sets 3 and 4. The identified modes are presented in [Table 1](#) along with the approximate calculated damping.

The vibration modes identified were found to be typical for three of the sets. Slightly different mode shapes were present on vessel 2, Set 4. The main differences were in the first 2 rigid body modes. The first mode was a transverse rocking motion as opposed to the diagonal rocking of the other sets. The second mode was a diagonal rocking mode as opposed to an end to end pitching motion.

The analysis has identified up to 13 different vibration mode natural frequencies between 6.2 Hz and 163.6 Hz. Modes are identified at or very close to the $\frac{1}{2}$, 1st, $1\frac{1}{2}$, 2nd, 3rd (firing frequency), 4th and $5\frac{1}{2}$ harmonic of the generator set rotation at 15, 30, 45, 60, 90, 120 and 165 Hz respectively. The modes at 33 Hz and below are considered to be rigid body modes. The calculated damping varies between a minimum of 1.1% and a maximum of 8.8%.

Alternator Casing Modes – Transducer Array 1								
Mode number	Vessel 1				Vessel 2			
	Set 1		Set 2		Set 3		Set 4	
	Frequency (Hz)	Damping (%)	Frequency (Hz)	Damping (%)	Frequency (Hz)	Damping (%)	Frequency (Hz)	Damping (%)
1	7.3	3.7	6.7	5.1	6.2	8.8	6.8	7.0
2	7.9	5.6	7.7	7.4	6.9	5.8	7.8	5.2
3	13.7	3.9	13.4	3.9	13.0	4.2	14.0	4.0
4	15.4	3.8	16.7	6.3	15.5	7.3	16.3	4.8
5	21.5	5.0	22.4	5.6	20.0	4.3	21.2	3.6
6	27.9	3.9	26.9	4.0	27.6	4.4	27.9	2.3
7	33.6	4.6	32.6	4.2	31.4	5.3	33.5	3.9
8	-	-	44.8	2.6	42.2	2.4	43.3	2.1
9	-	-	55.9	3.3	55.4	3.1	-	-
10	67.5	2.0	67.0	2.1	66.6	2.1	69.6	2.9
11	88.8	2.4	89.5	1.1	84.1	3.0	90.7	1.8
12	115.5	2.3	-	-	117.6	3.1	114.4	1.8
13	167.6	1.4	166.1	1.3	163.6	1.2	170.1	1.8

Table 1 Modal analysis, alternator casing vibration, array 1

Engine bed frame OMA results

For array 2, where the transducers were located on the bed frame and engine, the modes identified are presented in Table 2.

The analysis identified 11 different vibration modes at a range of natural frequencies between 6.5 Hz and 163.2 Hz. Modes are identified at or very close to the $\frac{1}{2}$, 1st, 2nd, 3rd (firing frequency), 4th and 5 $\frac{1}{2}$ harmonic of the generator set rotation at 15, 30, 60, 90, 120 and 165 Hz respectively. The modes at 33 Hz and below are considered to be rigid body modes. The calculated damping varies between a minimum of 1.0% and a maximum of 10%.

Alternator Bed Frame Modes – Transducer Array 2								
Mode number	Vessel 1				Vessel 2			
	Set 1		Set 2		Set 3		Set 4	
	Frequency (Hz)	Damping (%)	Frequency (Hz)	Damping (%)	Frequency (Hz)	Damping (%)	Frequency (Hz)	Damping (%)
1	6.5	6.6	6.8	6.3	7.3	5.4	7.0	8.3
2	7.2	6.2	7.9	5.4	8.1	9.2	7.8	10.0
3	13.1	3.6	13.9	3.7	13.5	3.2	14.2	3.9
4	13.5	7.7	14.4	4.9	14.0	5.4	15.6	5.4
5	32.0	5.7	33.2	5.7	33.0	4.3	33.8	5.2
6	65.8	3.0	68.0	2.4	63.7	2.7	66.9	2.9
7	88.7	4.2	90.4	2.6	90.5	3.0	87.7	2.0
8	-	-	-	-	-	-	114.0	3.6
9	123.9	1.9	127.9	2.0	123.3	2.5	124.7	2.9
10	158.0	2.0	155.4	1.9	147.3	2.2	157.1	2.6
11	165.0	1.5	165.1	1.0	163.2	1.6	164.0	1.4

Table 2 Modal analysis, bed frame vibration, array 2

Discussion

The results of analysis for alternator casing and bed frames indicate that there is good correlation between the two in the rigid body modes as expected.

The greatest vibration amplitudes of the bed frame and alternator casing at low alternator loads were typically at 30 Hz (engine rotating frequency) while at higher loads the 90 Hz (firing order) component was the highest. At loads above approximately 150 kW the narrow band vibration amplitudes at both these frequencies exceed the Lloyd's Register's guideline values for reciprocating machinery. This is likely to be a result of vibration modes with natural frequencies close to the principal excitation frequencies.

The bed frame mode 7, at 88 to 90 Hz, which is consistent with the engine firing frequency, results in a transverse twisting motion at the alternator end of the bed frame. This motion results in high vibration amplitudes at the alternator. This is consistent with the identified modes of the alternator casings at approximately 89 to 90 Hz, and is likely to be the most significant contributory cause of the cracking damage.

Given that the alternator casings have similar vibration modes with only small variations in natural frequencies it is probable that other contributory factors are causal to the damage. Uncertainties in casing assembly practice and power cable stiffness and entry location were identified.

The twisting motion of the bed frame results in vibration nodes at the corners of the engine end of the bed frame. The corresponding increased vibratory stress at these nodes may result in the development of fatigue cracks. However, the common mode shape and the absence of a wider bed frame cracking problem suggest that increased vibratory stress is not necessarily the primary cause of the damage and that other contributory factors must be considered. This includes the uncertainty in the welding and weld dressing process which might result in subsurface defects or reduced strength which, in regions of high stress would facilitate the propagation of fatigue cracks more readily.

The measured wide range in the flexible mounting heights and a corresponding variation in load distribution between mountings did not significantly affect the bed frame vibration mode shapes or natural frequencies.

Conclusions

OMA proved to be an effective tool in determining the vibration characteristics of a resiliently mounted diesel engine. However, the modes can be difficult to identify while the generator is running or when other engines are running in the vicinity. The best results were obtained from the engine on startup and shutdown measurements. In particular the engine shutdown measurements proved the most important due to the longer run down time from idle speed to zero rpm.

Despite providing the best results the small time record of both the startup and shutdown did reduce the accuracy of the modal parameters and considerable thought into qualifying certain identified modes was required. It is possible that some existing modes may not have been identified.

OMA identified up to 13 alternator casing modes and up to 11 bed frame modes. The correlation between the four generating sets analysed was satisfactory given the individual installation variations that each set had. There were some modes that were identified on certain generating sets that were not identified on others. In this regard further research into eliminating the risk associated with the incorrect identification or exclusion of modes is required.

References

1. Van Overschee P, De Moor B, Subspace Identification for Linear Systems, 1996 Kluwer Academic Publishers, USA, pp254
2. Peeters B, De Roeck G, Reference-Based Stochastic Subspace Identification For Output-Only Modal Analysis, Mechanical Systems and Signal Processing (1999) 13(6), 855-878
3. Van der Auweraer H, Peeters B, Discriminationg Physical Poles in High Order Systems: Use and Atomation of the Stabilization Diagram, Instrumentation and Measurement Technology Conference, Como, Italy, 18-20 May 2004

Eigenvalues and Nonlinear Behaviour of Levitron®

Elvio Bonisoli, Cristiana Delprete and Marco Silvestri
Politecnico di Torino, Corso Duca degli Abruzzi, 24 - 10129, Torino, Italy

ABSTRACT

When the floating magnetic spin called Levitron® was presented on market, it caught the attention of how a spinning top could trick the famous Earnshaw's theorem of magnetic levitation instability. Although it is well known that gyroscopic effect stabilizes the rotor of this magnetic top, consistent analytical models and exhaustive explanations about limit conditions on its stability are not completely presented. Some dynamic properties, such as physical masses and magnetic limits, angular speed ranges and geometrical subspace, where the stability may be reached, need nonlinear models and/or modal approaches to identify the different behaviour.

The paper presents an exhaustive magneto-rotordynamic model that allows to obtain the nonlinear equations of motion of all rigid body modes of the spinning top. The mechanical model is coupled to a nonlinear magneto-static model that is able to predict nonlinear phenomena in the surrounding subspace. The linearized model provides the natural frequencies that characterize the planar vibrations of the rotor, the precession motion of its axis and its floating vertical behaviour. The model allows to evaluate rotation speed conditions to assure the levitation stability. The parametric eigenvalues and eigenmodes analysis demonstrates the levitation limits and underlines possible industrial application as a flywheel energy storage system. High nonlinear effects are presented through coupling three-dimensional displacements, and nonlinear behaviour is predicted. In order to experimentally identify the complex dynamic behaviour of the rotor, an experimental test bench is presented and some tests are discussed.

NOMENCLATURE

A_0, B_0, C_0, \dots	Taylor coefficients
B_r, M	residual magnetic induction of the base magnet and magnetization of the spin volume
L	Lagrangian function of a dynamical system
Q_i	generalized force applied to the i -th generalized coordinate
V	magnetic volume of the spin
G	constant of gravity
e, i, π	respectively Nepero number, imaginary operator, pi-greco
l_g	distance between centre of gravity and magnetic volume centre of the spin
m, I_P, I_T	mass, polar and transversal inertia of the spin
q_i, \dot{q}_i	i -th generalized coordinate displacement and velocity
r, η	complex translational and rotational spin coordinates
s, σ, λ	respectively eigenvalue, decay rate, natural frequency
t	time
ρ	density of material
$\omega, \omega_{\min}, \omega_{\max}$	respectively spin speed, minimum and maximum speed stability limits
$x, y, z, \psi, \chi, \varphi$	spin displacement and rotational degrees of freedom
$\mathbf{B}, B_x, B_y, B_z$	magnetic induction vector and its components
$\mathbf{M}, \mathbf{K}, \mathbf{G}$	respectively mass, stiffness and gyroscopic matrices
\mathbf{q}	planar vector coordinate

INTRODUCTION

When Levitron® entered the market, immediately attracted the attention of many scientists and especially the experts in the field of magnetic levitation. Attention was focused on finding the best explanation of how a spinning top could violate the famous theorem of Earnshaw [1].

Although it is well known that gyroscopic effect stabilizes the rotordynamic behaviour of Levitron® system, consistent analytical models and exhaustive explanations about limit conditions on the system stability are not completely presented.

One of the earliest and most cited paper is published by Berry in 1996 [2]. He first expressed a theory based on this type of magnetic levitation. Facing the fact of how the force proportional to the gradient of the magnetic field can be in balance with the weight force of the spinning top, he defined the vertical stability range for a magnet with disk-shaped base, the admissible range for the mass of the top, the rotational speed range where it is possible to find a stable behaviour, and finally the stability conditions in the horizontal plane. The Berry's publication has covered all the main points of the Levitron® analysis that many other authors have also expanded.

In 1999 Gov, Shtrikman and Thomas [3] describe the problem with a more dynamical approach and define the stability field along the vertical axis in terms of spin speed. They define a range of variation for the top mass depending on the size of the magnetic base and, therefore, depending on the magnetic repulsive force. In other papers [4, 5] they supply the expressions of the minimum speed precession that depends on the transversal and the polar moments of inertia of the top; furthermore they also fail to describe what is the maximum height reached by the top with a more physical-magnetic approach.

A short time later Genta, Delprete and Rondano publish a paper in which, by means of a nonlinear rotordynamic model and without introducing any simplification, they obtain the equations of motion of all the rigid body modes of the top [6]. Computing the natural frequencies that characterize the translational vibrations of the rotor in the horizontal direction and the motion of precession of its axis, they obtain the spin speed conditions to assure the stability of the levitation. Furthermore they present some results obtained by numerical integration of the equations of motion.

In 2004 the publication of San Miguel [7] arrives at results similar to those of the Italian research group. He shows the results of three different methods to integrate the equations of motion obtained by a mechanical approach.

In 2005 the publication of Bonisoli, Delprete and Vigliani [8] is presented to take into account a nonlinear magnetic model based on the analogy of the equivalent solenoids. They revisit the Genta, Delprete, Rondano paper [6], presenting a nonlinear and a linearized analyses that allow to describe the physical causes corresponding to the existence of two spin speed thresholds of the system stability; they perform some numerical simulation to underline the limits of the linearized analysis. They also present the numerical results for the nonlinear model in which the dynamic behaviour is influenced by the coupling between different mode shapes.

Finally in 2008, De Grève, Versèlèl, and Lobryl present a Levitron® made by recycled materials and a finite element model for the analysis of stability [9].

After this chronological state of art on the most significant improvement on the argument, it has to be noted that excluding the paper by Bonisoli, Delprete and Vigliani [8], all other authors have considered a uniform magnetic field or a magnetic field linearized at the levitation point, and then have obtained the rotordynamic equations arbitrarily uncoupling the behaviour of planar and vertical degrees of freedom. Differently, in [8] a complete analysis is shown without any dynamic or magnetic field simplification, but the geometrical stability and the spin speed ranges are not deeply investigated.

In the present paper a nonlinear and a linearized analyses are presented, in order to deeply analyze stability properties, modal linearized dynamic behaviour and nonlinear properties. The possibility to compute the solutions by means of time-numerical integration for any point in the space and to estimate the magneto-static force intensity by means of a nonlinear magnetic model based on the analogy of the equivalent solenoids, allows to calculate the top trajectories in the space. Subsequently, the nonlinear equations of motion are linearized and, with a dynamical analysis of the system eigenvalues, the stability conditions, both vertical and horizontal, are determined. A spectral analysis of the computed time histories is then presented and together with experimental measurements, the complex nonlinear dynamic nature of the Levitron® is discussed.

THEORY

In Figure 1 a simplified sketch of Levitron® and its equivalent model are shown. The spinning top possesses a main magnetic disk of rare-earth material with vertical magnetization; some additional rings of different paramagnetic or diamagnetic materials are used as calibrated weights in order to adjust the floating height produced through the magnetic base with vertical magnetization and in repulsive configuration.

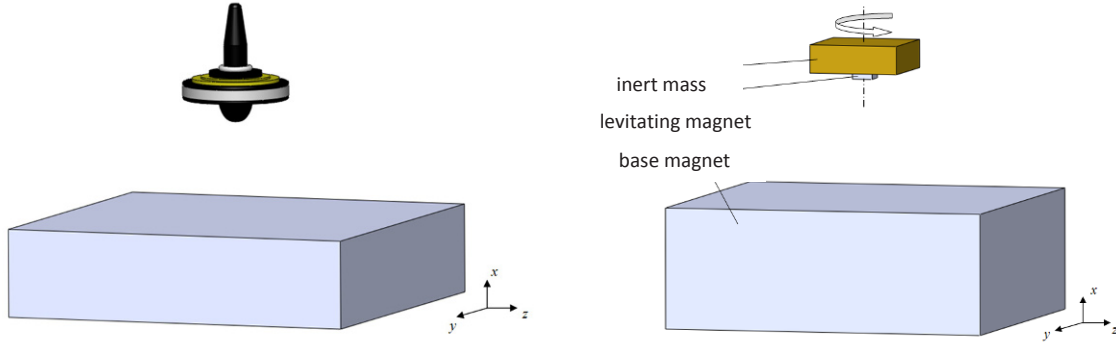


Figure 1 – Model used: from actual rotor (left) to a rotor with inert mass and levitate magnet with parallelepiped square shape (right).

To describe the rotordynamic behaviour of the spinning top, the mathematical model of [8] is used and, with a Lagrangian approach, a system of n differential equations is defined:

$$\frac{d}{dt} \left(\frac{\partial L}{\partial \dot{q}_i} \right) - \frac{\partial L}{\partial q_i} = Q_i \quad (1)$$

where q_i , \dot{q}_i and Q_i are respectively the i -th generalized coordinate, velocity and force.

By developing, without any simplification, the equations of motion (1) of the 6 degrees of freedom, the following nonlinear system is obtained:

$$\left\{ \begin{array}{l} m \ddot{x} = -M V \left(\cos(\psi) \cos(\chi) \frac{\partial B_x}{\partial x} + \sin(\chi) \frac{\partial B_y}{\partial x} - \sin(\psi) \cos(\chi) \frac{\partial B_z}{\partial x} \right) - m g \\ m \ddot{y} = -M V \left(\cos(\psi) \cos(\chi) \frac{\partial B_x}{\partial y} + \sin(\chi) \frac{\partial B_y}{\partial y} - \sin(\psi) \cos(\chi) \frac{\partial B_z}{\partial y} \right) \\ m \ddot{z} = -M V \left(\cos(\psi) \cos(\chi) \frac{\partial B_x}{\partial z} + \sin(\chi) \frac{\partial B_y}{\partial z} - \sin(\psi) \cos(\chi) \frac{\partial B_z}{\partial z} \right) \\ \left(I_T \cos(\psi)^2 + I_P \sin(\chi)^2 \right) \ddot{\psi} + I_P \sin(\chi) \ddot{\phi} + I_P \cos(\chi) \dot{\phi} \dot{\chi} + 2 \sin(\chi) \cos(\chi) \dot{\chi} \dot{\psi} (I_P - I_T) = \\ = M V \left(\sin(\psi) \cos(\chi) B_x + \cos(\psi) \cos(\chi) B_z \right) - m g I_g \sin(\psi) \cos(\chi) \\ I_T \ddot{\chi} + \sin(\chi) \cos(\chi) \dot{\psi}^2 (I_T - I_P) - I_P \dot{\psi} \dot{\phi} \cos(\chi) = \\ M V \left(\cos(\psi) \sin(\chi) B_x - \cos(\chi) B_y - \sin(\psi) \sin(\chi) B_z \right) - m g I_g \cos(\psi) \sin(\chi) \\ I_P \ddot{\phi} + I_P \sin(\chi) \ddot{\psi} + I_P \cos(\chi) \dot{\chi} \dot{\psi} = 0 \end{array} \right. \quad (2)$$

Thanks to the polynomial formulation of the magnetic induction field and its gradients by Bonisoli and Vigliani [10], it is possible to linearize the equations of motion with respect the equilibrium point (the marked degrees of freedom are referred to the equilibrium position of the spinning top, e.g. $\bar{x} = x - x_{eq}$), where the gravity force mg is equal to the magnetic repulsive force of the magnetic base. The linearized system so obtained is:

$$\begin{cases} m \ddot{\bar{x}} + \frac{MVB_r}{4\pi} 2A_2 \bar{x} = 0 \\ m \ddot{\bar{y}} + \frac{MVB_r}{4\pi} 2B_0 \bar{y} + \frac{MVB_r}{4\pi} D_0 \bar{\chi} = 0 \\ m \ddot{\bar{z}} + \frac{MVB_r}{4\pi} 2C_0 \bar{z} - \frac{MVB_r}{4\pi} E_0 \bar{\psi} = 0 \\ I_T \ddot{\bar{\psi}} + I_P \omega \dot{\bar{\chi}} + \left(mg I_g - \frac{MVB_r}{4\pi} A_0 \right) \bar{\psi} - \frac{MVB_r}{4\pi} E_0 \bar{z} = 0 \\ I_T \ddot{\bar{\chi}} + I_P \omega \dot{\bar{\psi}} + \left(mg I_g - \frac{MVB_r}{4\pi} A_0 \right) \bar{\chi} + \frac{MVB_r}{4\pi} D_0 \bar{y} = 0 \\ I_P \ddot{\bar{\phi}} = 0 \end{cases} \quad (3)$$

The first and the last equations of system (3) can be studied separately by the others. This possibility highlights the uncoupling between the vertical behaviour (in x direction) and the planar behaviour described by the four central equations. The planar behaviour can be studied by using the following complex translational and rotational coordinates:

$$\bar{r} = \bar{y} + i\bar{z} \quad , \quad \bar{\eta} = \bar{\chi} - i\bar{\psi} \quad (4)$$

By introducing the vector coordinate:

$$\mathbf{q} = \begin{Bmatrix} \bar{r} \\ \bar{\eta} \end{Bmatrix} \quad (5)$$

it is possible to define the system (3) in matrix form:

$$\mathbf{M} \ddot{\mathbf{q}} - i\omega \mathbf{G} \dot{\mathbf{q}} + \mathbf{K} \mathbf{q} = 0 \quad (6)$$

with:

$$\mathbf{M} = \begin{bmatrix} m & 0 \\ 0 & I_T \end{bmatrix}, \quad \mathbf{K} = \begin{bmatrix} \frac{MVB_r}{4\pi} 2B_0 & \frac{MVB_r}{4\pi} D_0 \\ \frac{MVB_r}{4\pi} D_0 & mg I_g - \frac{MVB_r}{4\pi} A_0 \end{bmatrix}, \quad \mathbf{G} = \begin{bmatrix} 0 & 0 \\ 0 & I_P \end{bmatrix} \quad (7)$$

where A_0 , B_0 and D_0 are three of the Taylor's coefficients used in the polynomial formulation of the magnetic field.

The magnetic field components are:

$$B_x \cong \frac{B_r}{4\pi} (A_0 + A_1 \bar{x}) \quad , \quad B_y \cong \frac{B_r}{4\pi} D_0 \bar{y} \quad , \quad B_z \cong \frac{B_r}{4\pi} D_0 \bar{z} \quad (8)$$

and their corresponding derivatives are:

$$\begin{aligned}
\frac{\partial B_x}{\partial x} &\cong \frac{B_r}{4\pi} (A_1 + 2A_2\bar{x}) , \quad \frac{\partial B_y}{\partial y} \cong \frac{B_r}{4\pi} (D_0 + D_1\bar{x}) , \quad \frac{\partial B_x}{\partial y} = \frac{\partial B_y}{\partial x} \cong \frac{B_r}{4\pi} 2B_0\bar{y} = \frac{B_r}{4\pi} D_1\bar{y} \\
\frac{\partial B_x}{\partial z} = \frac{\partial B_z}{\partial x} &\cong \frac{B_r}{4\pi} 2B_0\bar{z} = \frac{B_r}{4\pi} D_1\bar{z} , \quad \frac{\partial B_z}{\partial z} \cong \frac{B_r}{4\pi} (D_0 + D_1\bar{x}) , \quad \frac{\partial B_y}{\partial z} = \frac{\partial B_z}{\partial y} \cong 0
\end{aligned} \tag{9}$$

The trend of the Taylor's coefficients is shown in [Figure 2](#), where the origin of the x axis is located at the centre of gravity of the magnetic base.

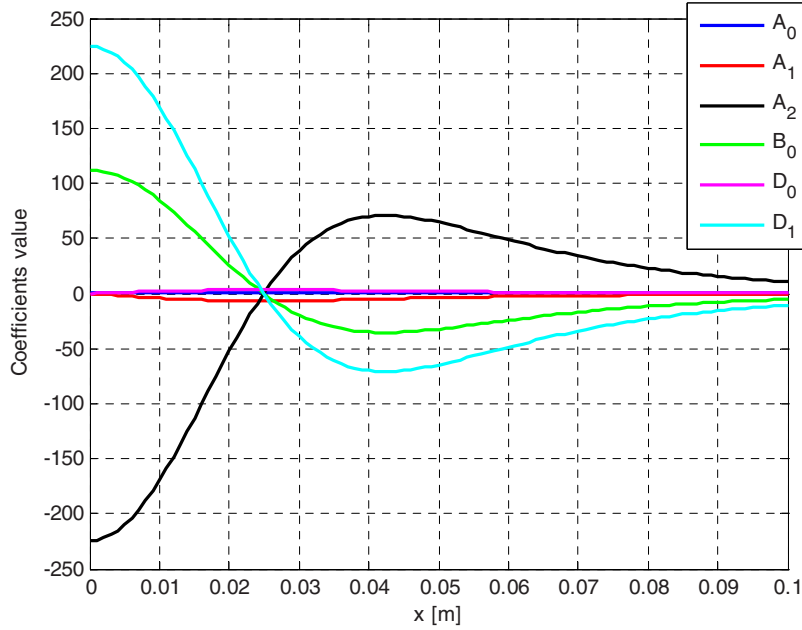


Figure 2 – Taylor's coefficients.

By assuming the classical approach of rotordynamics, the solutions have form as:

$$\bar{r}(t) = r_0 e^{st} , \quad \bar{\eta} = \eta_0 e^{st} \tag{10}$$

where s is the eigenvalue:

$$s = \sigma \pm i \lambda \tag{11}$$

with σ the decay rate and λ the natural frequency.

PLANAR STABILITY

To make easier the numerical solution of the volume integrals to compute the magnetic force and torque [10], the magnetic base and the levitating magnet have been chosen with parallelepiped square shape. This choice, especially for the levitating magnet is concerned, does not change the qualitatively dynamic behaviour.

The configuration under investigation has:

- parallelepiped magnetic base 30×80×80 mm ($x \times y \times z$ dimensions); it is uniformly magnetized with a residual magnetic induction $B_r = 1.13$ T (NdFeB magnet presupposed);

- parallelepiped levitating magnet $2 \times 5 \times 5$ mm ($x \times y \times z$ dimensions); it is uniformly magnetized with a residual magnetic induction $B_r = 1.13$ T (NdFeB magnet presupposed, density $\rho = 7300$ kg/m³);
- parallelepiped inert mass $7 \times 22 \times 22$ mm ($x \times y \times z$ dimensions) with density $\rho = 8580$ kg/m³ (brass).

It is possible to demonstrate that the system is stable in the horizontal plane if the spin speed of the spinning top is included between a lower limit value and an upper limit value ($\omega_{\min} = 98$ rad/s and $\omega_{\max} = 241$ rad/s for the investigated configuration). In Figure 3 the Campbell's diagram is shown; the root locus is reported in Figure 4.

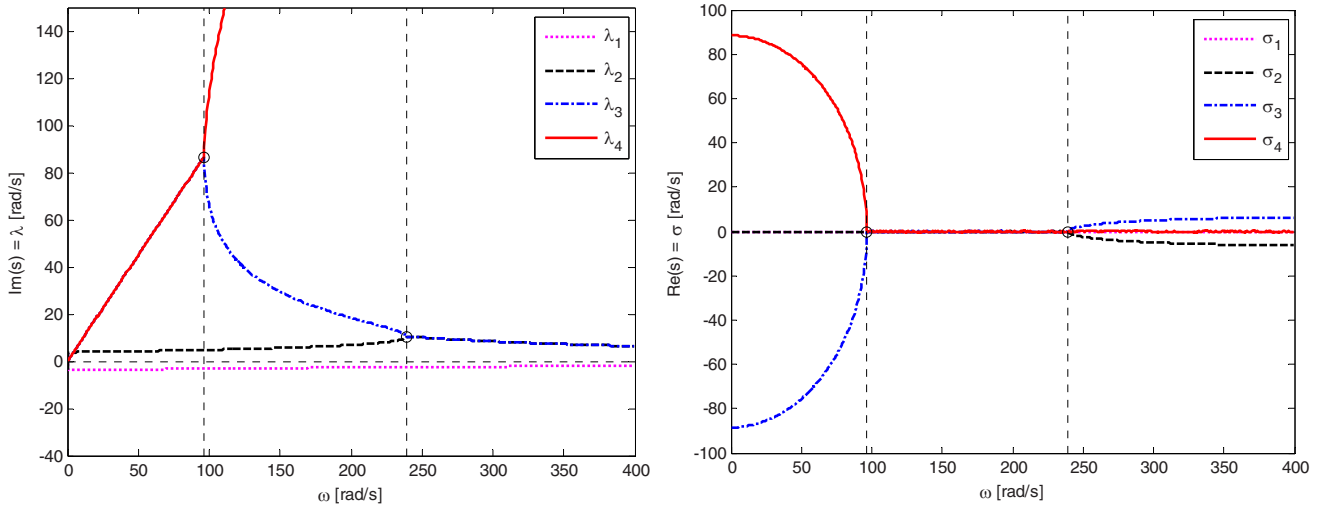


Figure 3 – Campbell's diagram (left) and decay rate $\sigma = \Re(s)$ versus spin speed ω (right).

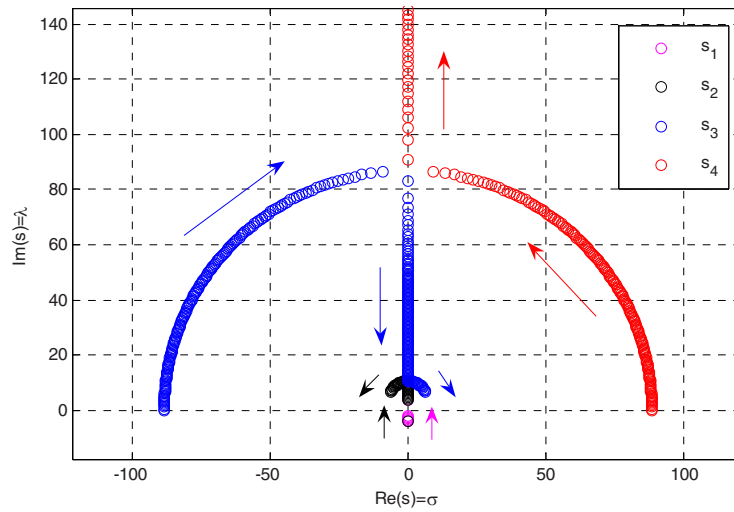


Figure 4 – Root locus.

In the Campbell's diagram (Fig. 3), the rotor's stability range is included between ω_{\min} and ω_{\max} where the four natural frequencies are distinct; before and after the stability range there is only a couple of natural frequencies. In the decay rate diagram, the stability range is the only region of the diagram where the decay rates are equal to zero.

The eigenvalues s form arcs of circular orbit in the complex plane (Fig. 4). On the root locus some arrows are drawn to show the eigenvalues directions when the spin speed increases. The stability exists when the real part of all eigenvalues is equal to zero (or minor than zero, if some dissipative term is taken into account).

VERTICAL STABILITY

The first equation of the linearized system (3) can be studied separately by the others. It represents a magnet-pendulum system and its solution is an oscillatory behaviour around the equilibrium height x_{eq} ($x_{eq} = 26.9$ mm for the investigated configuration), with fundamental harmonic equal to:

$$\omega_x = \sqrt{\frac{MVB_r}{2\pi} A_2} \quad (12)$$

The sign of the Taylor's coefficient A_2 is linked to the second derivative of the magnetic field \mathbf{B} and then with the vertical stability, according to Earnshaw [1, 11]:

$$\frac{\partial^2 B_x}{\partial x^2} \cong \frac{B_r}{2\pi} A_2 \quad (13)$$

Generally if a particle $P = (x_0, y_0, z_0)$ is located in a field of static forces $\mathbf{F}(x, y, z)$, the resultant of the forces operating on the particle is $\mathbf{F}(x_0, y_0, z_0)$. Because P is a condition of stable equilibrium, the following conditions must be verified:

$$\mathbf{F}(x_0, y_0, z_0) = 0, \quad \nabla \cdot \mathbf{F}(x_0, y_0, z_0) < 0 \quad (14)$$

In the x direction it has to be:

$$\frac{\partial F_x}{\partial x} < 0. \quad (15)$$

If a magnetic force is defined as:

$$\mathbf{F} = -\nabla U = -\nabla(\mathbf{M} \cdot \mathbf{B}) \quad (16)$$

and taking into account the (15), to obtain a stable equilibrium condition in x direction it has to be:

$$\frac{\partial^2 B_x}{\partial x^2} \cong \frac{B_r}{2\pi} A_2 > 0 \quad (17)$$

The vertical stability is then assured where the Taylor's coefficient A_2 is positive. For a vertical position lower than x_{min} ($x_{min} = 24.9$ mm for the investigated configuration), A_2 is negative and the vertical stability does not exist; if the vertical position is higher than x_{min} , A_2 is positive and the vertical stability exists (Figure 5).

In addition to the lower limit x_{min} , the vertical stability also has an upper limit x_{max} which is determined by analyzing the stiffness matrix (7) of the system, thought as the stiffness matrix of the equivalent system sketched in Figure 6.

By neglecting the gyroscopic effect, the equivalent system corresponds to the linearized system whose generalized coordinates are the complex coordinates (4); m_{TR} and k_{TR} are the mass and the stiffness related to the complex translation, m_{ROT} and k_{ROT} the mass and the stiffness related to the complex rotation, and k_C the coupling stiffness between complex translation and rotation. The stiffness matrix is:

$$\mathbf{K} = \begin{bmatrix} k_{TR} + k_C & -k_C \\ -k_C & k_C + k_{ROT} \end{bmatrix} = \begin{bmatrix} \frac{MVB_r}{4\pi} 2B_0 & \frac{MVB_r}{4\pi} D_0 \\ \frac{MVB_r}{4\pi} D_0 & mg l_g - \frac{MVB_r}{4\pi} A_0 \end{bmatrix} \quad (18)$$

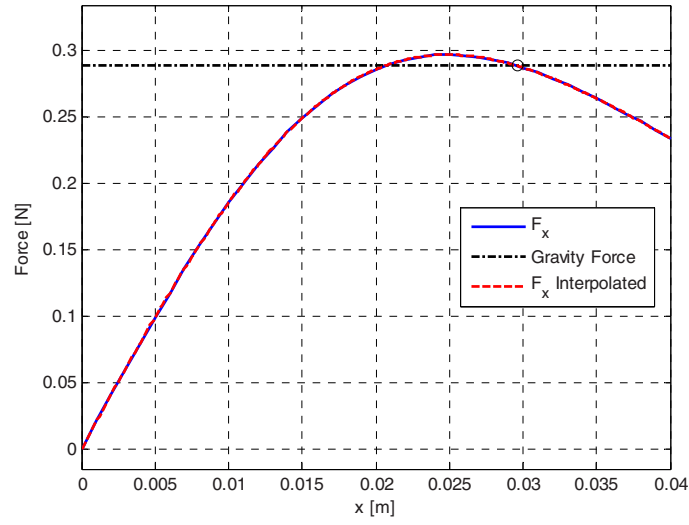


Figure 5 – Vertical equilibrium of the spinning top.

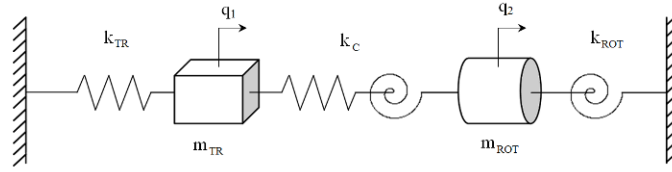


Figure 6 – Equivalent system with 2 complex degrees of freedom for the stability investigation.

To investigate the static stability of the system, the sign of the two eigenvalues of matrix (18) is studied. The eigenvalues visualization with Gershgorin's circles in the Argand's plane is reported in [Figure 7](#). By increasing the levitation height (indicated by the direction of the black arrows in [Figure 7](#)), the two real eigenvalues vary their values: the first eigenvalue s_1 varies remaining always negative (corresponding to an unstable translational mode that is stabilized through gyroscopic effect), while the second eigenvalue s_2 varies from positive values (corresponding to stable precession mode) to negative values (corresponding to another unstable mode). The transition limit for the sign of s_2 corresponds to the upper limit x_{\max} of the vertical stability ($x_{\max} = 31.4$ mm for the investigated configuration).

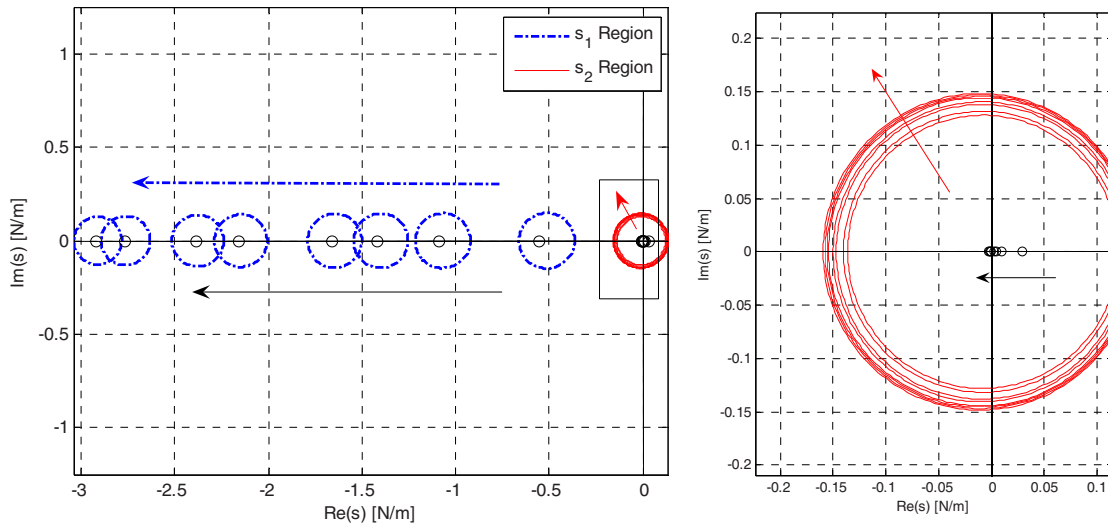


Figure 7 – Root locus of the stability of the spinning top.

TRAJECTORIES ANALYSIS: NUMERICAL AND EXPERIMENTAL INVESTIGATION

The nonlinear equations of motion (2) have been implemented in a numerical model, in Simulink® environment, and have been numerically integrated with a variable step solver (ode45). Starting from the initial conditions of the rotor and the simulation time chosen, each numerical simulation provides the trend of the coordinates of the centre of gravity of the levitating magnet: on a single three-dimensional diagram the spatial trajectory of the magnet is obtained.

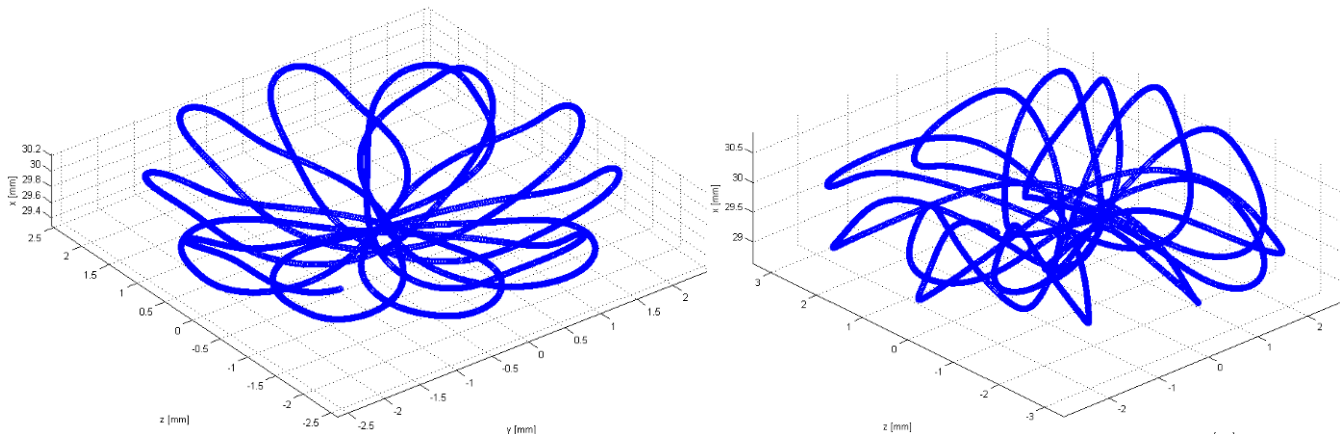


Figure 8 – Numerical trajectories of the spinning top starting from non-zero initial condition without vertical perturbation (left) and with vertical perturbation (right).

Figure 8 (left) shows the trajectory of the rotor obtained with the initial conditions: $x_0 = x_{eq} = 29.6$ mm, $\dot{y}_0 = 10$ mm/s, $\dot{\varphi}_0 = 167$ rad/s (where $\dot{\varphi}_0 = \omega$, average value of the spin speed within the range of stability visible on the Campbell's diagram) and simulation time $T = 10$ s. Looking at the trajectory it can be imagined that the spinning top swings from one extreme to the other drawing a “flower” shape. The edge effects, with intensity greater than the magnetic force in the middle, increases the vertical component (x direction) of the centre of gravity when the spinning top is far away from the centre of the “flower” (which also corresponds to the centre of the base magnet). This effect leads to fold up the “petals” of the flower.

By varying the initial conditions, the trajectory of the centre of gravity of the levitating magnet can become more complex than that with “flower” shape and therefore its domain can take a form other than a “bowl”. Figure 8 (right) shows the trajectory corresponding to an initial condition with $x_0 \neq x_{eq}$ (in particular $x_0 = x_{eq} - 1 = 28.6$ mm) which presents an increase in the oscillations of the vertical component. This increase is due to the magneto-static force, that allows the levitation and is similar to the elastic force of a nonlinear spring [10, 12, 13], that is greater than the case with initial condition $x_0 = x_{eq}$.

The trajectories of the spinning top have been experimentally investigated using a test bench and a video analysis developed with dedicated Matlab® programs. To record the information about the coordinates x , y and z as a function of time without synchronizing two digital cameras filming the rotor from two different perspectives, it was used a shooting set up with two mirrors that allows to have on the same frame of a unique digital camera, the three coordinates in function of time.

In Figure 9 (left) the sketch of the video system is reported while in Figure 9 (right) one of the frames acquired by the digital video camera is visible. In the top view and in the profile view of the spinning top, a visual contrast black and white was used to highlight the contour of the rotor, so as to increase the definition of the contours of the spinning top to determine its correct centre of gravity in each frame.

Figure 10 shows the experimental trajectories detected. In the yz plane is reported the filmed “flower” shape. The correspondence between the experimental trajectory and the trajectory computed by numerical integration of the equations of motion confirms the goodness of the analytical-numerical model developed.

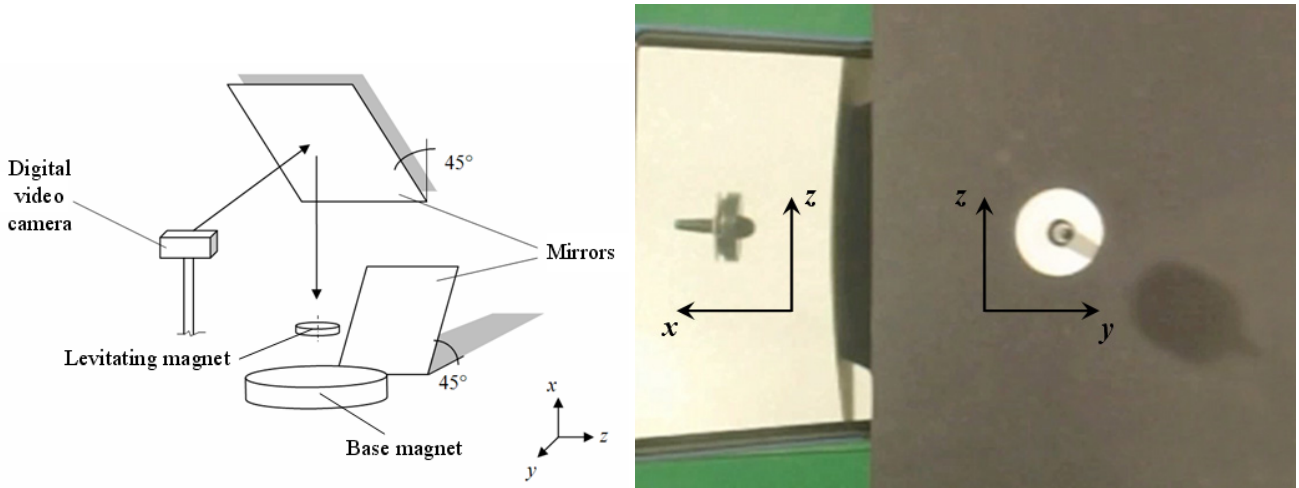


Figure 9 – Experimental test bench (left) and frame acquired through the digital video camera (right).

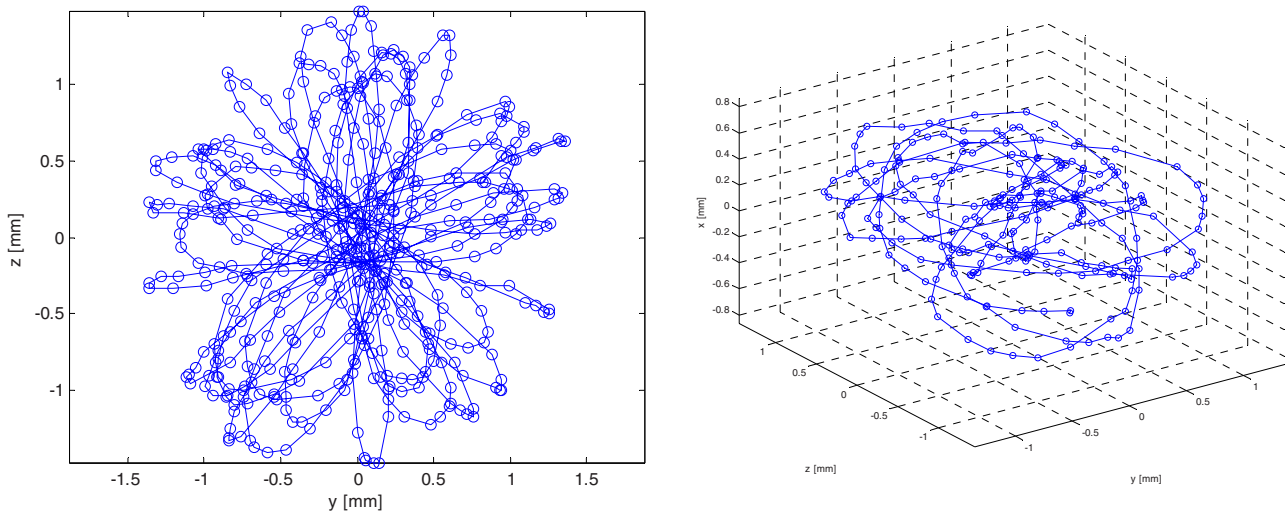


Figure 10 – Experimental trajectories of the spinning top starting from non-zero initial condition without vertical perturbation (left) and with vertical perturbation (right).

It was also carried out an analysis of the frequency content of the experimental measurements to show more information on the Levitron® that the time domain analysis cannot reveal. One of this information is the coupling between various degrees of freedom of the system, which confirms its nonlinear behaviour. To calculate the frequency response an Hamming windowing function was used.

Figure 11 shows the frequency response function (FRF) and the power spectrum density (PSD) related to x coordinate (above) and z coordinate (below); the y coordinate is almost identical to the z and, so, it is omitted. In Figure 11 (above) the main harmonic $\omega_{1,x}$ and the next super-harmonic $2\omega_{1,x}$ are identified; the harmonic ω_2 is thought to be referred to as the sub-harmonic $\lambda_{2/3}$, it appears individually but also added or subtracted to the main harmonic and to its super-harmonic. In Figure 11 (below) the main harmonic $\omega_{1,z}$ is visible together with the values of the first three natural frequencies λ_1 , λ_2 and λ_3 of the Campbell's diagram of Figure 3 (left); the main harmonic $\omega_{1,z}$ coincides with the value of the second natural frequency λ_2 . Another important characteristic of nonlinearity which demonstrates the coupling between the vertical behaviour and the planar behaviour of the spinning top is the presence of the main harmonic primary $\omega_{1,x}$ which is coupled with the $\omega_{1,z}$ and the λ_3 .

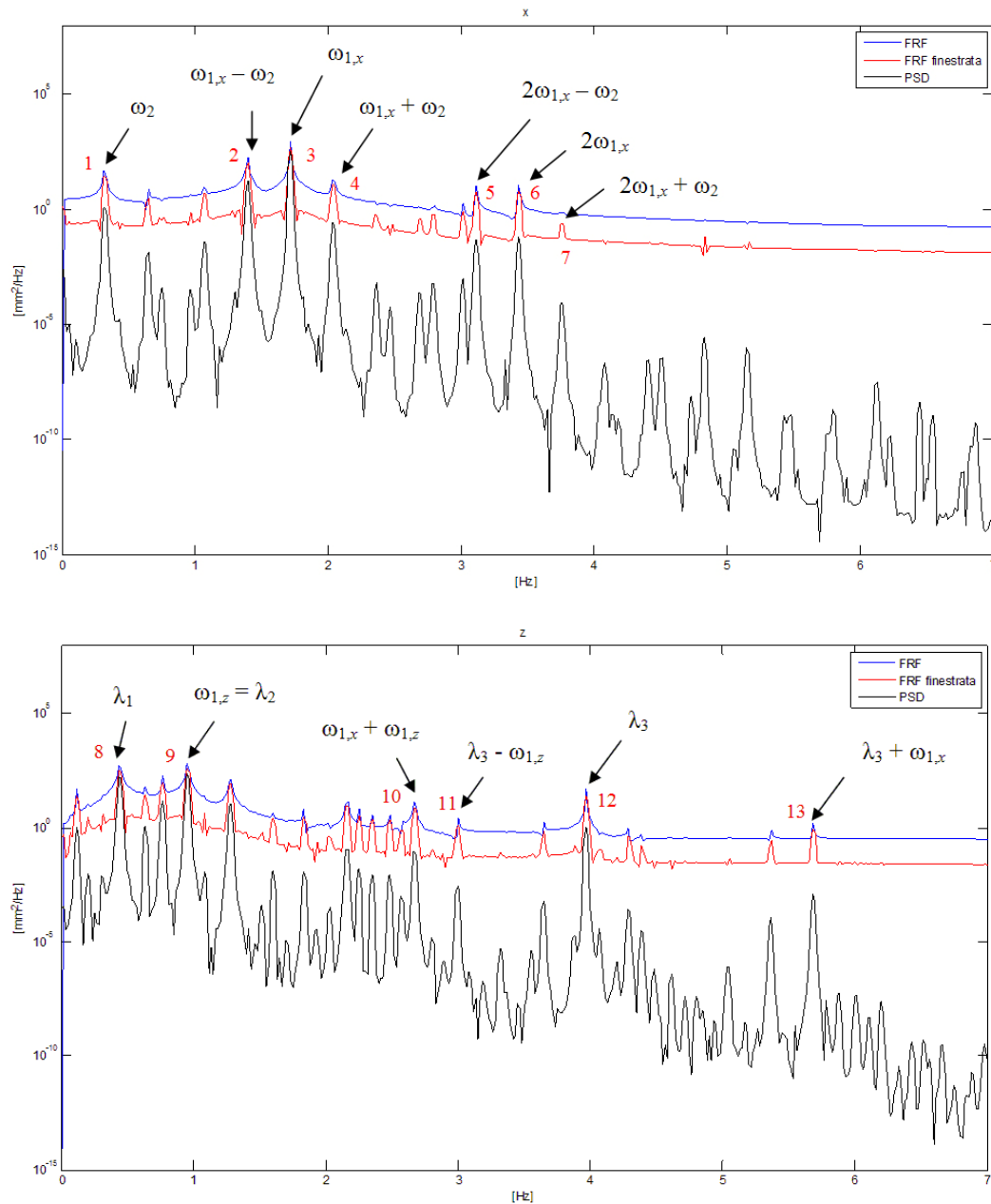


Figure 11 – Experimental frequency response functions of vertical (above) and in plane (below) displacements.

CONCLUSIONS

The paper reports a study of the equations of motion of Levitron® that allows, using a single mathematical model, to describe the full nonlinear behaviour of the spinning top. The modelization developed does not resort to any simplification with regard to the system dynamics and the representation of the magnetic field that surrounds the rotor. In particular, the mathematical representation of the magnetic field is based on a robust model based on the analogy of the equivalent solenoids.

Thanks to the presented modelization it is possible to describe the complete dynamic behaviour of the rotor, and to highlight the presence of stability fields related to the spin speed and to the vertical level of levitation of the spinning top.

By means of the numerical integration of the equations of motion, the spatial trajectories of the spinning top have been computed; these trajectories have been validated by comparison with the experimental trajectories

measured on a test bench which, despite its simplicity, has proven effective to validate, at least qualitatively, the analytical-numerical model developed.

The analysis of the frequency content of the experimental measures has highlighted the strong features of coupling between the planar degrees of freedom and the vertical degree of freedom of the system; the frequency values determined by the numerical solution of the linearized system are also found again.

The modelization and the numerical programs developed to solve the equations of motion represent, in the authors opinion, a useful tool for further investigation on the Levitron® and for the sensitivity investigation of different geometric configurations and magnetic properties of the system.

BIBLIOGRAPHY

- [1] Earnshaw S., On the nature of the molecular forces which regulate the constitution of the luminiferous ether, *Trans. Cambridge Philos. Soc.*, 7(116), 1842, pp. 97-112.
- [2] Berry M.V., The Levitron™: an adiabatic trap for spins, *Proceedings Royal Society London*, 452, 1996, pp. 1207-1220
- [3] Gov S., Shtrikman S., Thomas H., On the dynamical stability of the hovering magnetic top, *Physica D*, 126, 1999, pp. 214-224.
- [4] Flanders P., Gov S., Shtrikman S., Thomas H., On the spinning motion of the hovering magnetic top, *Physica D*, 126, 1999, pp. 225-235.
- [5] Gov S., Shtrikman S., How high can the U-CAS fly?, *arXiv:physics/9902002 v1*, 31 Jan, 1999, pp. 1-20.
- [6] Genta G., Delprete C., Rondano D., Gyroscopic stabilization of passive magnetic levitation, *Meccanica*, 34, 1999, pp. 411-424
- [7] San Miguel A., Numerical integration for the dynamics of the heavy magnetic top, *Physics A*, 335, 2005, pp. 235-244.
- [8] Bonisoli E., Delprete C., Vigliani A., Dinamica magneto-elastica del Levitron, 17th AIMETA Congress of Theoretical and Applied Mechanics, Firenze, Italy, 11-15 September, 2005, pp. 1-13.
- [9] De Grève Z., Versèlèl C., Lobryl J., Using Perturbation Force Analysis for the Design of a Levitron® : an Application of Magnetic Levitation, Excerpt from the Proceedings of the COMSOL Conference 2008 Hannover, 2008, pp. 1-7.
- [10] Bonisoli E., Vigliani A., Static behaviour of magneto-elastic forces, 16th AIMETA Congress of Theoretical and Applied Mechanics, Ferrara, Italy, 9-12 September 2003, (full text in CD Rom).
- [11] Bassani R., Earnshaw (1805-1888) and passive magnetic levitation, *Meccanica*, 41, 2006, pp. 375-389.
- [12] Bonisoli E., Delprete C., Vigliani A., Modello e analisi della stabilità di una sospensione magnetica passiva, XVII Congresso AIMETA, Firenze, Italy, 11-15 September 2005, (full text in CD Rom).
- [13] Bonisoli E., Vigliani A., Passive elasto-magnetic suspensions: nonlinear models and experimental outcomes, *Mechanics Research Communications*, 34, 2007, pp. 385-394.

Optical Measurements and Operational Modal Analysis on a Large Wind Turbine: Lessons Learned

Muammer Ozbek^{a,*}, Daniel J.Rixen^a

^a, Delft University of Technology, Faculty of Mechanical Engineering, Mekelweg 2, 2628CD, Delft, the Netherlands

1. Introduction

Wind turbines have very specific characteristics and challenging operation conditions. Since they are designed and optimized to provide maximum power production for changing wind speeds and directions, they are expected to adapt to the rapidly varying physical conditions and other extreme environmental factors. Depending on their types and sizes, wind turbines are usually intended to be operational for wind speeds between 5 and 25 m/sec. In order reach this goal, most of the turbines utilize active pitch control mechanisms where the angle of the blade (pitch angle) is changed as a function of wind speed. Similarly, the whole rotor is rotated towards the effective wind direction by using the yaw mechanism.

The ability of the turbine structure to adapt to the changes plays a crucial role in ensuring the maximum energy production and the safety of the turbine during extreme wind conditions. However, this on the other hand, makes it more difficult to investigate the structure from the dynamic analysis point of view. Some important prerequisites such as time invariant system and steady state random excitation assumptions are not always satisfied easily. These assumptions form the basics of almost all types of the system identification methods and their violation causes at least a large scatter in the extracted system parameters (eigenfrequencies, damping ratios and mode shapes). Besides, different from most civil engineering structures the identified damping ratio is not purely structural but aero-elastic which is a combination of both structural and aerodynamic damping and primarily dependent on the wind speed.

Therefore, all of these factors should be taken into account during different steps of the structural investigation such as measurement, data analysis and evaluation of the results. This paper aims at discussing the effects of these and other similar factors on the identified system properties by presenting the results of infield tests performed on a 2.5 MW wind turbine.

2. Test turbine

The tests presented in this paper were conducted on a pitch controlled, variable speed Nordex N80 wind turbine located at the ECN (Energy Research Center of the Netherlands) wind turbine test site in Wieringermeer, the Netherlands. Detailed information about the facilities of the test site can be found through the related website (1).

The turbine has a rated power of 2.5 MW, a rotor diameter and a tower height of both 80 meters. Detailed information about the technical properties of the wind turbine can be obtained through the website of the manufacturer (2).

3. Measurement Systems

Within the scope of the work, three different measurement systems were utilized to monitor the dynamic behavior of the structure. Several data sets were recorded both when the turbine was in operation and at parked conditions. The first 2 groups of measurements were taken by using optical measurement techniques which were based on laser interferometry and photogrammetry.

An important advantage of the optical measurement techniques is that no additional preparations such as cable installations for power and data transfer are required inside the blade. However, some reflective markers should be placed on the structure. These markers are made up of a retro-reflective material that is 1000 times more reflective than the background blade material. Since the markers are in the form of very thin stickers (with a diameter of 400mm) they do not have any effect on the aerodynamic performance of the blades. A total of 55 markers were placed on the turbine (11 markers for each blade and 22 markers on the tower). The distribution of the markers throughout the structure can be seen in [Figure 1](#).



Figure 1 Distribution of the markers throughout the turbine.

The laser interferometry measurements were taken by using a Polytec OFV 505 laser head and OFV 5000 controller with VD 06 velocity decoder. These systems were located in the field at a distance of 200 meters from the turbine. An SLR (Super Long Range) lens which enables an increased measurement range up to 300 meters was also required to take measurements from this distance. The utilized LDV and reflection of the laser beam from the marker on the blade can be seen in [Figure 2](#) and [Figure 3](#), respectively.



Figure 2 Laser Doppler vibrometer

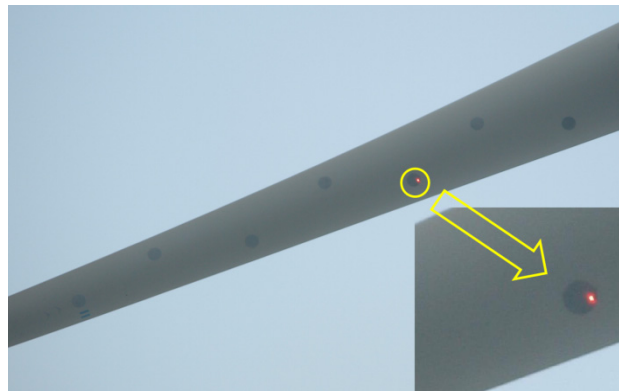


Figure 3 Reflection of the laser beam from the blade.

Since it is very difficult to keep the laser on the same marker while the turbine is rotating, LDV was only used for standstill measurements. A more detailed description of these measurements and the corresponding data analyses can be found in (3).

The second measurement technique was based on photogrammetry which is a proven technology based on determination of the 3D coordinates of the points on an object by using two or more images taken from different positions. Although the several applications of photogrammetric measurements are currently in use and demonstrated to provide very accurate measurements for a wide variety of disciplines, its use is usually limited to small measurement volumes and experiments that are performed in laboratories or similar controllable environments. Within this small measurement volume it can be efficiently used for different purposes such as;

- 3D shape determination, modeling and reverse engineering (4), (5), (6)
- Static or dynamic deformation measurements (7),(8),(9), (10), (11), (12), (13) ,(14),(15)
- Modal analysis and system identification (16), (17), (18), (19), (20), (21)

This technology was for the first time applied on a MW scale wind turbine within the scope of this work. The 3D dynamic response of the rotor was captured at 33 different locations

simultaneously by using 4 CCD (charge coupled device) cameras while the turbine was rotating. The response data obtained from the tower markers are not presented or used in this article since tower measurements were interrupted each time a blade passed in front of it.

The utilized photogrammetric measurement setup can be seen in Figure 4. Initial results show that the deformations on the turbine can be measured with an average accuracy of ± 25 mm from a measurement distance of 220 m. Preliminary analyses of the measurements also show that some of the important turbine modes can be identified from photogrammetric measurement data. More detailed information about these measurements and the corresponding data analyses can be found in (22) and (23).

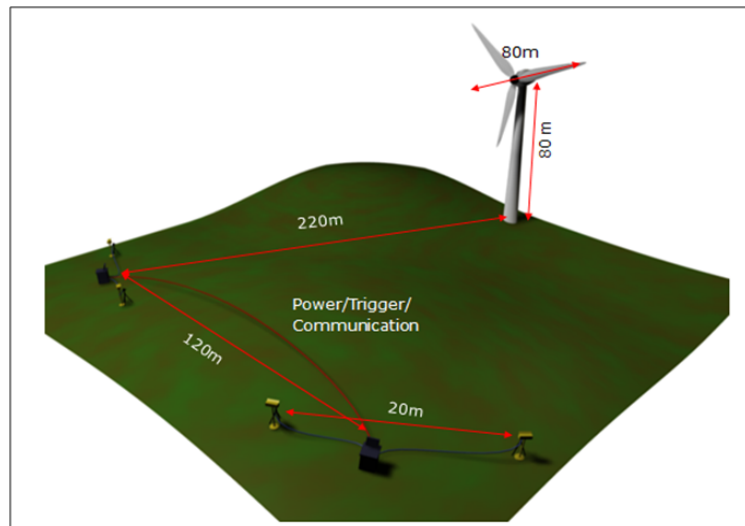


Figure 4 Photogrammetric measurement setup.

A third system, which has already been installed in the turbine to monitor the wind loading on the structure, consists of 6 strain gauges placed at the root region of the three blades (2 strain gauges per blade) and 2 strain gauges located at the tower base. These strain gauges are used to monitor the flapwise and edgewise vibration of the blade and the tower and have a sampling frequency of 32 Hz. The strain gauge data used in this work was provided by ECN turbine monitoring program. Table 1 summarizes the main features of measurements taken by these 3 different measurement systems.

Measurement type	f_s [Hz]	Parked turbine	Rotating turbine	Measurement blocks
Strain gauge	32	X	X	continuous
Photogrammetry	28	-	X	21 secs
Laser Doppler vibrometer	1280	X	-	294 secs

Table 1 Main features of the measurements

4. Factors Affecting the Identified System Parameters

Before presenting the results of the measurements and data analyses, the factors which affect the identified system parameters are briefly discussed below.

4.1. Measurement Accuracy

The first step in extracting the dynamic properties of a system is ensuring a reliable and accurate measurement of its response. High noise to signal ratios or other physical factors limiting the accuracy of the measurements may cause an inherent problem for the rest of the analyses and have a negative effect on the results which are generally very difficult to detect and eliminate.

The strain gauges installed in the turbine are used as a part of a long term health monitoring program and checked regularly. Therefore, the data acquired from these sensors were considered to be accurate enough and mostly used as a reference measurement in this work.

Provided that the signal quality is high, laser Doppler vibrometers have very high accuracies (in micron scale). The laser measurements mentioned in this paper were taken on the special locations where retro-reflective markers were placed. As mentioned before, the advantage of this material is that it is 1000 times more reflective than the background blade material and it reflects the light directly back to its source. During the tests the signal level was continuously checked and verified to be within acceptable range.

However, photogrammetric measurements were performed as a feasibility study aiming at testing whether they can be used for monitoring large turbines or not. Photogrammetry was applied for the very first time on a MW scale turbine within the scope of this work. Therefore, the measurement accuracy has not been verified for such a large measurement volume before (please see [Figure 4](#)). Since the conventional methods used to estimate the accuracy of the small scale photogrammetric measurements were not appropriate to be applied for the field tests, all the critical pre or post-processing operations and the corresponding error estimation analyses have been done by using the measurements themselves i.e. by verifying the consistency of the data recorded. [Figure 5](#) shows a typical flapwise direction tip marker displacement measured by photogrammetry.

An important point that should be paid attention to was the synchronization of the different measurement systems having different sampling frequencies and data acquisition systems. The data recorded by the LDV (sampling frequency 1280 Hz) photogrammetric measurement system (sampling frequency 28 Hz) and the strain gauges were later synchronized by using a GPS clock. The estimated accuracy of the absolute time recorded by these GPS systems was in the range of 10 milliseconds. Considering the fact that the sampling frequency of the strain gauges were 32 Hz and that the dominant frequencies that were expected to be identified were mainly lower than 5 Hz, this accuracy can be said to be sufficient.

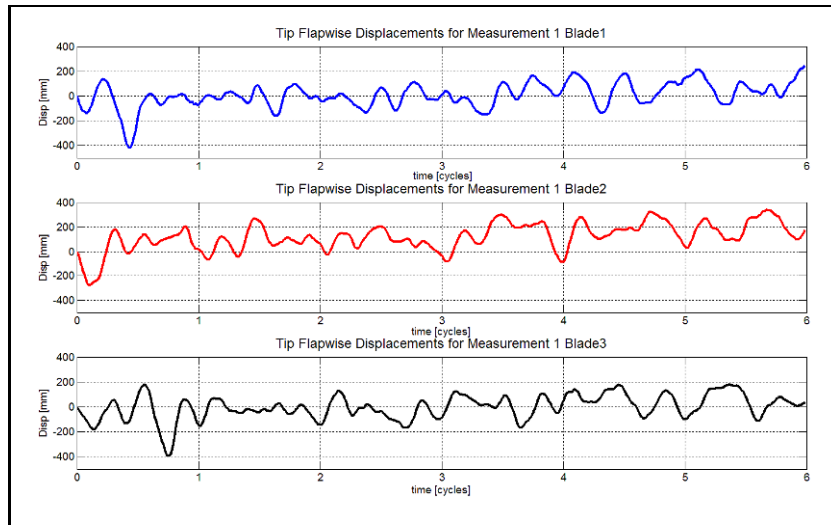


Figure 5 Tip marker displacement measurements in flapwise direction (measurement 1).

Initial analyses of the measurements revealed that the deformation of the turbine can be measured with an average accuracy of ± 25 mm from a distance of 220 meters. It was also found that this error, in fact, consists of 2 different parts, namely the random and the systematic error parts. The random error is in range of ± 5 mm and can be corrected by using higher resolution cameras.

Systematic errors were investigated further in frequency domain to find the underlying reasons. The 3D frequency distribution of the calculated measurement errors is displayed in [Figure 6](#). The frequencies, normalized with respect to the rotational frequency, are displayed along the X-axis. The Y-axis represents the marker number. The numbering of the markers was depicted in [Figure 7](#). The Z-axis represents the amplitude of the Fourier transform. As can be seen from [Figure 6](#), the systematic error also has two important components mainly caused by different physical factors having different frequencies and patterns.

A dominant 1P component where P denotes the rotational frequency of the rotor is determined for markers 1 and 2. These 2 markers are placed on curved surfaces close to the root of the blade. The measurement errors calculated for these markers are expected to be mainly related to the reflection quality and marker orientation varying during the rotation. A variation in the reflection quality appears once per cycle when the marker passes through the problematic region. The 1P component of the measurement error can easily be eliminated by using a spatial filter based on the expected deformation modes (for example based on simple beam theory).

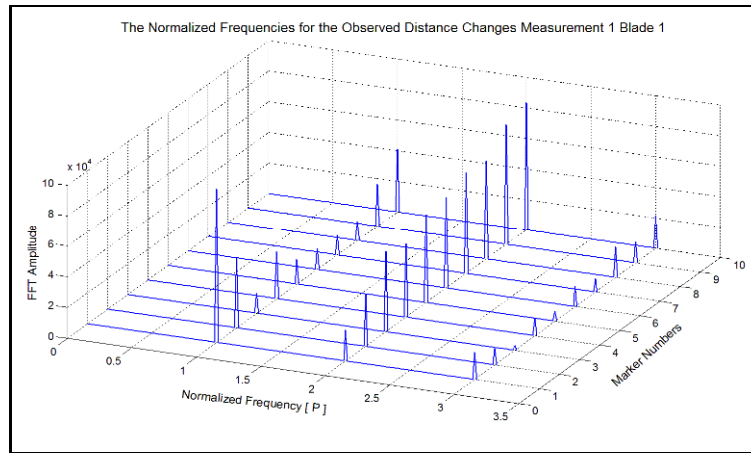


Figure 6 3D Frequency distribution of the systematic measurement error.

Similarly, a measurement error of $2P$ is likely to occur when the tracked marker passes through the regions where the view and reflection angles approach to the limit values. During the rotation, the markers move on a circular path, which should be fully captured in each one of the 2D images analyzed. For the outermost markers, the horizontal and the vertical view angles approach to critical values twice a cycle. As the distance from the center of rotation increases, the contribution of $2P$ component gradually becomes more important, probably because those markers are closer to the boundaries of the field of view where calibration errors and artifacts due to projection on the plane of rotation become more dominant. Unfortunately, the $2P$ components exhibit a spatial distribution along the blade that is similar to the expected deformation. Therefore, the $2P$ component of the error cannot be easily eliminated by using simple filters and constitutes the major part of the error. The maximum value of the $2P$ part can reach ± 30 mm and is experienced by the outermost marker. This error can be reduced further by using more sophisticated camera calibration techniques and data comparison algorithms.

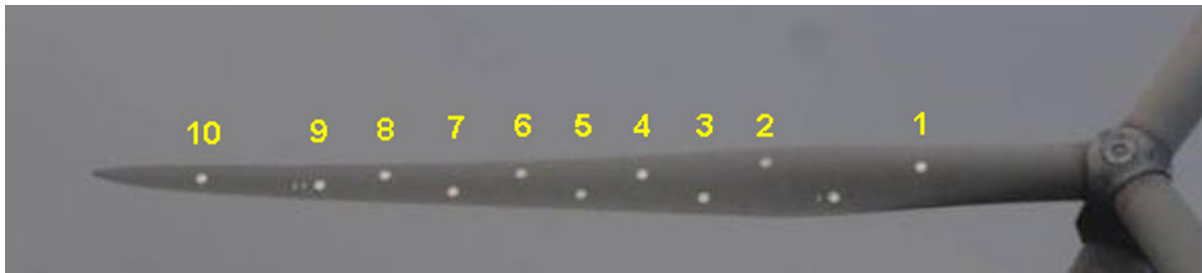


Figure 7 The locations and corresponding labeling of the markers used in error estimation.

The overall measurement error is the summation of random and systematic errors. Its maximum value can reach up to 35 mm and experienced by the outermost marker. As getting closer to the center of rotation it linearly decreases. Depending on the results of these analyses the average measurement error can be reported as ± 25 mm. Although such an amount of error corresponds to approximately 10 % of the measured deformation amplitudes (shown in [Figure 5](#)), it is only effective within a narrow frequency range. Therefore, it is not expected to have a negative effect on the identification of important turbine modes.

4.2. Measurement Duration

Due to their sizes and specific operation conditions, wind turbines cannot be tested dynamically by using standard experimental modal analysis tools. Although there have been some attempts to excite the turbine (at parked condition) by measurable excitation forces (24), (25), as the dimensions of the turbines increased the application of this method became impractical because of the large amplitudes of forces required to excite these structures efficiently.

Several researchers also tried to excite a specific turbine mode by applying a harmonic force at its frequency. Simulations and feasibility tests showed that a harmonic force at the desired frequency can be generated by continuously changing blade pitch angles and generator torque or by installing a special rotating mass system on the nacelle. However, the field tests performed on large scale wind turbines showed that it is not possible to achieve the required pitch amplitudes to excite the modes with high modal frequency or high damping ratio due to the limited capacity of electrical pitch actuators. On the other hand, significant energy transfer between the modes having similar frequencies but different damping ratios (especially longitudinal and lateral tower modes) has been observed. The authors concluded that since the excited turbine vibrations are not pure modal vibrations, the estimated damping cannot be considered as the actual modal damping (26),(27).

Therefore, dynamic testing of the turbines can only be performed by using the methods utilizing the response measurements only. Several types of these methods are currently in use and proven to provide very valuable information on the dynamic properties of the structures. However, these methods are based on some important assumptions such as time invariant system and stationary random excitation which are not always satisfied easily.

Besides, these identification algorithms are mainly based on the correlations established between different response signals (28),(29),(30). Although in theory the calculation of the correlation function is founded on the use of infinite time series, for systems with low modal damping ratios, it was demonstrated to produce satisfactory results even with finite length short time series (30). However, if the system analyzed has high damping ratios, much longer response data should be used to generate correlation functions that enable to detect these high damping modes. The length of the data series is usually expressed in terms of the number of cycles of the lowest frequency included in the measurement block. Since for a rotating wind turbine, most of the modes have relatively high damping ratios (due to aerodynamic coupling), long time series are needed to calculate the required correlation functions.

Carne and James, in a very recent article (31) reviewed the history and development of NExT (Natural Excitation Technique - a well known output only modal analysis method) by presenting the outcomes of the landmark tests performed on wind turbines. The results of the tests and analyses summarized in the article show that the appropriate measurement duration is directly related to the expected damping ratios. The authors tested the efficiency of the method by using an analytical model. For this purpose, they generated data series of 82 seconds (40 cycles of the lowest frequency) to compute correlation functions and compared the extracted system parameters with the real known values. Since the damping ratios were relatively low (maximum 0.6 %) such a short duration enabled correlation functions to represent the system response

accurately. However, the authors needed measurement durations of 30 minutes (900 cycles of the lowest frequency) to test a rotating VAWT (vertical axis wind turbine) which has a maximum aeroelastic damping ratio of 7 %.

Similarly Hansen et al. (27) performed comprehensive measurements and analyses on a 2.75 MW turbine. The researchers utilized data blocks with durations varying between 1 and 3 hours. The data series recorded at different locations on the tower and main shaft were analyzed by using Stochastic Subspace identification which does not require the use correlation functions but the time domain response measurements. However, it was again not possible to extract the symmetric and whirling flapwise modes which have been known to have high aeroelastic damping. The authors conclude that this situation might be caused due to the fact that these modes have too high aerodynamic damping to be identified from the response to turbulence excitation.

Therefore, it is a common application to use data series which include at least 500 cycles. A recent work aiming at evaluating how the reliability of the estimated system parameters changes as a function of the measurement duration can be found in (32). In this work, the authors apply two different system identification algorithms (SSI-Stochastic Subspace Identification and LSCE-Least Square Complex Exponential) to analyze a simulation data and compare the results of the identification with the known real values. The utilized SSI method is the same as the one which Hansen et al. used in their research study (27). Similarly, LSCE is based on NExT which was developed and used by Carne and James. Figure 8 shows an example of how estimated damping ratio changes with the measurement duration. The authors report that the required number of cycles of the lowest frequency can be as high as 1000 (especially for LSCE) while for a lightly damped system 200 cycles can provide quite satisfactory results.

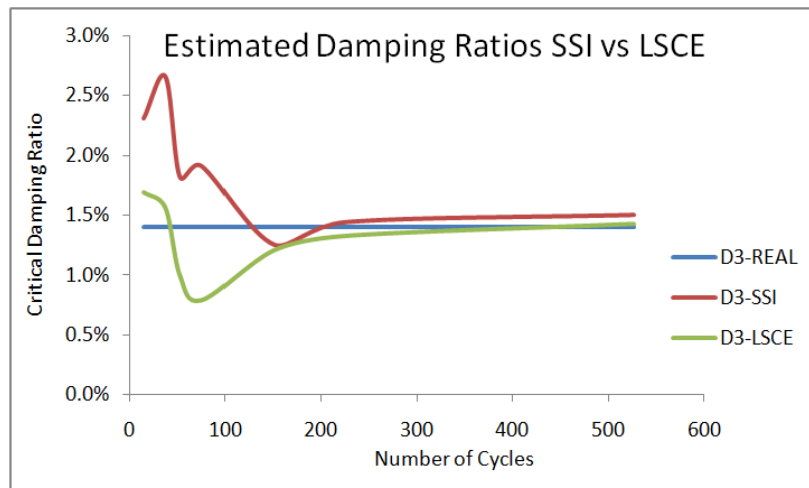


Figure 8 Change of estimated damping value as a function of measurement duration.

For wind turbines where low frequency vibrations dominate the overall response, such a limitation requires minimum measurement durations around 30 minutes or longer. It has to be noted that high damping modes are still not guaranteed to be extracted unless they have a

significant participation in the overall signal. The eigenfrequencies are relatively easier to be determined but corresponding damping ratios require long measurement durations to be used in the identification process.

4.3 Changing Wind Speed and Direction

The difficulty in acquiring data series with sufficient length is not in measuring or storing the data but finding a suitable period where the blade pitch angle, the wind speed, rotor speed or dominant wind direction (more critical for the tests performed at parked turbines) remains unchanged. Hansen, et al. reported that about 3 months of measurements were scanned to find 1–3 h long periods of low standard deviations of wind and rotor speeds to improve the assumption of a time-invariant system in the SSI analysis.

The wind speed and direction changing during the measurements is an important issue to be considered for the tests performed both on rotating and parked turbines. The tests conducted at the parked condition also provide very useful information for tuning and validating numerical models. Since these tests are done at parked condition during very low wind speed periods the identified system parameters are assumed to be mainly structural and not affected by the aerodynamic factors. However, even very low wind speeds may have an effect on the extracted dynamic properties, especially on damping ratios. James, et al. (29) reported that a drag phenomenon similar to that experienced by a flat plate oscillating normal to a strong wind can cause some changes in the estimated damping ratios and showed that a 1.2 % (in terms of critical damping ratio) damping increase can be seen for the first flapwise modes of a VAWT due to the above mentioned aero-drag effects.

The changing wind direction is another important factor affecting the results of the tests performed on parked wind turbines. Since the turbine is kept in a fixed orientation at parked condition, the instantaneous wind direction directly affects the excitation direction. The relative angle between the wind direction and the turbine can be used to check how the effective excitation direction changes during the measurements. The change in this angle also affects the aerodynamic damping component by causing a different aerodynamic coupling between the structure and the air flow.

4.4 Insufficient Excitation Level

This problem is also more critical for the tests applied on parked turbines. Besides the unexpected scatter in damping due to the drag phenomenon mentioned above, some wind loading is needed to excite the turbine to be tested. If the wind speed is very low, the level of the ambient excitation may not be sufficient to excite the turbine modes and unstable results can be obtained

4.5 High Amplitudes of Harmonics

As mentioned before an important assumption of OMA (Operational Modal Analysis) is steady state random excitation. Although turbulence is close to being random, the resulting excitation from the aerodynamic forces will contain significant components on all P-harmonics (the harmonics of turbine rotational frequency P) on the rotor frame and on the 1P, 3P, 6P, etc.

harmonics in the fixed frame. Depending on the operating conditions (wind speed and rotor speed) these frequencies may coincide with the eigenfrequencies of the system and affect the estimated system parameters. Several researchers performing measurements on wind turbines report that they had to discard some of their measurements and analyses since several P harmonics coincide with the real turbine modes (27). Such a problem can be solved by two different ways. Vibration data measured at a different rotational speed can be used for the identification. Although such a solution would separate the previously coinciding real eigenfrequency and the P harmonics, it is not always easy to find the required measurement period because of the reasons mentioned above.

As a second alternative, Mohanty and Rixen (33), (34) proposed a modified version of OMA which was extended to identify modal parameters in the presence of harmonic excitations even with frequencies close to the eigenfrequencies of the system.

5. Identified System Parameters

This section presents the results of the infield tests performed on the 2.5 MW – 80 meter diameter - wind turbine whose technical properties were given in the previous sections. The main features of the utilized measurement systems, tests durations, and sampling frequencies are summarized in [Table 1](#).

The acquired dynamic response was then analyzed by using LSCE (Least Square Complex Exponential) method which is in theory based on NExT (Natural Excitation Method) explained before. It should be noted that in order to protect the interests of the turbine manufacturer, the frequencies mentioned in this work were normalized and not given explicitly.

5.1. Operational Modal Analysis of the Parked Turbine

The measurements and analysis results summarized in this section was obtained using the measurements from the strain gauges installed in the turbine and the LDV (laser Doppler vibrometer). Several laser measurements were performed both on the tower and the blades. [Figure 9](#) shows the PSD (Power Spectral Density) graph calculated from the laser measurements taken on the tower. Although there are 2 different tower modes having almost the same frequencies, the clear peak shown in the figure represents the longitudinal tower frequency because the instantaneous orientation of the laser was almost the same as the longitudinal tower vibration while the data series were being acquired.

The obtained data series were also processed by using LSCE method. The lateral tower vibration could not be identified. The average damping ratios were calculated as 0.3% with minimum and maximum values of 0.1% and 0.5%, respectively. The turbine was observed to be yawing slowly during the measurement which produced the maximum damping ratio of 0.5 %. Therefore, it is thought to be caused by the drag phenomenon mentioned above whereas the minimum damping of 0.1 % is believed to be due to insufficient excitation and very low wind speed experienced during the test. Since the damping value is very low, the measurement duration of 294 sec (approximately 100 cycles) was long enough to identify tower and several

other turbine modes. Longitudinal and lateral tower modes have very close frequencies and damping ratios when the turbine is at parked condition, but as the turbine starts rotating the damping of the longitudinal tower mode observed is significantly greater than the damping of lateral tower mode.

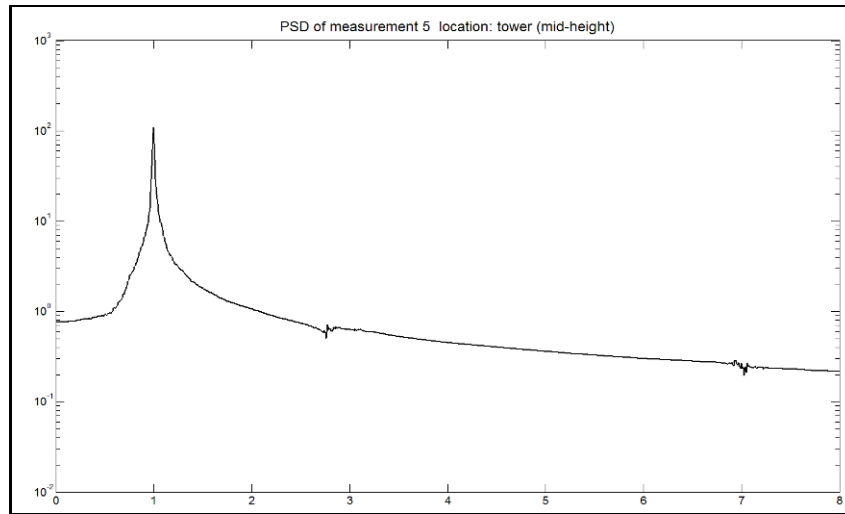


Figure 9 PSD of laser measurements taken on the tower (longitudinal direction)

The tower frequencies were also identified by using the data obtained from the strain gauges. The turbine was tested at 3 different pitch angle configurations. At parked conditions, the controller of the turbine was keeping the pitch angles at 90, 110 or 180 degrees. The 180 degree orientation represents the case where the blade flapwise vibration corresponds to out of plane direction motion. Similarly, at the 90 degree orientation edgewise blade modes represent out of plane vibration. Besides the 3 different pitch angle configuration, since the turbine was kept at a fixed angle, the relative direction between the effective wind direction and turbine orientation was changing which resulted at different aerodynamic coupling between the wind loads and the structure. The identified damping parameters were observed to be dependent on the pitch angle and the relative angle between the turbine and wind direction which supports the idea that the aerodynamic coupling has a strong influence on the identified results. The measurements performed on the parked turbine by using the tower strain gauges and the acquired results are summarized in Table 2. The abbreviations TF, TD and PTMB1 stand for **Tower Frequency**, **Tower Damping** and **Parked Turbine Measurement Block1**, respectively. Similarly, LON and LAT are used to refer the **Longitudinal** and **Lateral** direction strain gauge signals. The results displayed in the table are calculated by using 3 different signal groups. The signal used in the analysis is shown in parenthesis. (LON) or (LAT) groups were calculated by using one strain gauge measurements whereas (LON-LAT) group contains two signals together.

It can easily be seen that tower frequencies change slightly depending on the pitch angle. Measurement blocks 1, 2, 3 and 7 having very close pitch angles produce very close longitudinal tower frequencies varying between 0.9991 and 1.0006. The slight difference can be attributed to measurement noise, physical factors changing during the long measurement blocks or round off errors. The only frequency which is thought to be related to lateral tower mode is **1.0119**. A

frequency appearing in lateral vibration direction does not need to be caused by lateral tower mode. Since the vibration paths of longitudinal and lateral tower modes are not exactly vertical to each other, high amplitude longitudinal vibration can also be dominant in lateral direction. As the pitch angle decreases to 110 degrees, the longitudinal tower mode slightly increases to 1.0017 (PTMB5) and 1.0023 (PTMB6). A further decrease to 93 degrees results in a slightly larger longitudinal frequency of 1.0049 for PTMB4. The same tendency was also observed in LDV measurements; the longitudinal tower frequency changed from 1.0009 to 1.0040 when the pitch angle was changed from 180 to 90.

On the other hand damping is observed to be affected from aerodynamic coupling and excitation direction. The drag phenomenon mentioned several times in the article is thought to cause an unexpected damping increase in the lateral tower mode. 0.0086 is approximately 3 times larger than the damping ratio expected for this wind speed. The results presented in [Table 2](#) conflicts with what is reported in literature because longitudinal tower mode are usually believed to have higher frequencies than the lateral tower mode at parked condition. However, there is not a unique pitch angle configuration for a parked turbine. For a rotating turbine, a certain wind speed approximately corresponds to a specific pitch angle; besides this, the relative angle between the turbine and wind direction is always small due to active yawing. However, there is not a unique configuration of relative angle, pitch angle or wind speed for a parked turbine. Therefore, more measurements and data analyses are needed to validate this observation.

Name	Duration	Relative Angle	Pitch Angle	Wind Speed	TF(LON)	TD(LON)	TF(LAT)	TD (LAT)	TF(LON-LAT)	TD(LON-LAT)
PTMB1	2800	-110	178	5.30	1.000	0.0046	1.0119	0.0086	-	-
PTMB2	2100	-100/-110	178	4.50	1.0003	0.0030	-	-	1.0000	0.003
PTMB3	4650	-10 / -20	178	5.10	0.9991	0.0030	-	-	0.9985	0.001
PTMB4	3700	-110	93	3.75	1.0049	0.0011	1.0035	0.0050	-	-
PTMB5	2808	changes a lot	110	1.50	-	-	-	-	1.0017	0.002
PTMB6	4860	changes a lot	110	1.55	1.0023	0.0020	1.0009	0.0030	1.0009	0.003
PTMB7	468	-110	180	5.20	1.0006	0.0032	0.9959	0.0044	1.0009	0.003

Table 2 Longitudinal and lateral tower frequencies and damping ratios extracted from tower strain gauges

LDV measurements were also taken at several locations on the blade and the obtained results were compared with those acquired from the strain gauges installed in the blades. [Table 3](#) shows the frequencies identified from blade vibration data measured on a parked turbine.

Frequency (normalized with respect to the tower frequency)	S _o	S _i	L
1.0	X	X	X
2.6	X	X	X
2.8	X	x	X
3.2	X	x	X
5.3		X	X
5.4		X	X
6.7	X	X	X
7.1	X	X	X
8.7	X		X
9.1	X		X
17.9	X		X

Table 3 frequencies identified for parked turbine blade vibrations data (normalized wrt. tower frequency)

As performed in tower measurements, the obtained data were analyzed in different signal combinations. The abbreviations S_o, S_i refer to the 6 strain gauges placed out of plane direction and in plane directions, respectively. Similarly L represents the laser measurements.

As can be seen from [Table 3](#), some of the frequencies are detectable either from in-plane strains or from out of plane strains only but not from both of them at the same time. However, some frequencies are detectable both from in-plane and out of plane strain signals. Laser signals are able to detect all the frequencies displayed in [Table 3](#). Therefore it can be concluded that laser signals can be used together with both in-plane and out of plane signals.

[Table 4](#) shows the system parameters calculated from the signals explained above. Signals 2, 4, 6 are used as out of plane direction strain gauges whereas signals 1, 3, 5 represent in-plane direction strain gauges. Signal 7 is used for laser measurements.

It can be noticed from [Table 4](#) that even if the estimated damping ratios slightly change depending on the time series analyzed, the value obtained by using LDV and one strain gauge is always very close to those calculated from other signal combinations. This proves that LDV measurements are always consistent with strain gauge measurements and the results found are almost the same.

Although more measurements and analyses are required for the final conclusion the normalized frequencies of 2.6, 2.8 and 3.2 may be related to the first yaw, first tilt and first symmetric flapwise modes, respectively. The normalized frequencies of 5.3 and 5.4 are mainly related to the first vertical edgewise and first horizontal edgewise modes, respectively. The identified frequencies and damping values are consistent with those reported for the edgewise modes in the literature. The normalized frequencies of 6.7 and 7.1 are believed to correspond to the second tilt and the second yawing modes. However the identified damping values are again lower than those reported in the literature.

Nor. frequency	Measurement	Reference	Damping	Nor. frequency	Measurement	Reference	Damping
1.0	4	123456	0.007	1.0	7	123456	0.002
1.0	4	57	0.006	1.0	7	17	0.003
1.0	4	67	0.006	1.0	7	27	0.003
2.6	4	123456	0.012	2.6	6	123456	0.008
2.6	4	57	0.011	2.6	6	17	0.008
2.6	4	67	0.013	2.6	6	27	0.009
2.8	5	123456	0.020	2.8	7	123456	0.010
2.8	5	37	0.020	2.8	7	17	0.009
2.8	5	47	0.020	2.8	7	27	0.012
3.2	4	123456	0.010	3.2	7	123456	0.020
3.2	4	57	0.010	3.2	7	17	0.019
3.2	4	67	0.010	3.2	7	27	0.019
5.3	4	135	0.004	5.3	7	135	0.006
5.3	4	57	0.005	5.3	7	17	0.007
5.4	3	135	0.006	5.4	5	135	0.007
5.4	3	57	0.008	5.4	5	37	0.005
6.7	2	123456	0.007	6.7	4	123456	0.004
6.7	2	17	0.008	6.7	4	57	0.004
6.7	2	27	0.008	6.7	4	67	0.004
7.1	2	123456	0.003	7.1	4	123456	0.007
7.1	2	17	0.003	7.1	4	57	0.007
7.1	2	27	0.003	7.1	4	67	0.007
8.7	2	246	0.005	8.7	3	246	0.006
8.7	2	27	0.005	8.7	3	27	0.006
9.1	4	246	0.004	9.1	7	246	0.004
9.1	4	67	0.004	9.1	7	27	0.004
17.9	4	246	0.006	17.9	6	246	0.004
17.9	4	67	0.006	17.9	6	27	0.004

Table 4 frequencies (normalized wrt. tower frequency) and damping ratios identified from standstill measurements

5.2 Operational Modal Analysis of the Rotating Turbine

The in-operation vibration data of the turbine was measured by using both the strain data recorded by the gauges and the photogrammetric measurement systems. Due to the technical limitations of the sensors each photographic measurement block consists of 6 cycles of rotation. As mentioned before, it is almost impossible to get stable and reliable identification results by using such short measurement duration. However, the P harmonics dominating the overall response and some important turbine modes can be seen from the PSD plots of the recorded vibration data. [Figure 9](#)[Figure 10](#) and [Figure 11](#) show the PSD graphs of the edgewise and flapwise direction blade vibration data, respectively. These figures are presented to provide a 3D frequency distribution which also includes the information related to the measurement location. The X-axis represents the normalized frequencies identified from the analyzed data; the Y-axis corresponds to the marker number (defined in [Figure 7](#)) and the Z-axis represents the computed PSD amplitude. The 1P and 2P components, and first edgewise mode can be recognized from [Figure 10](#).

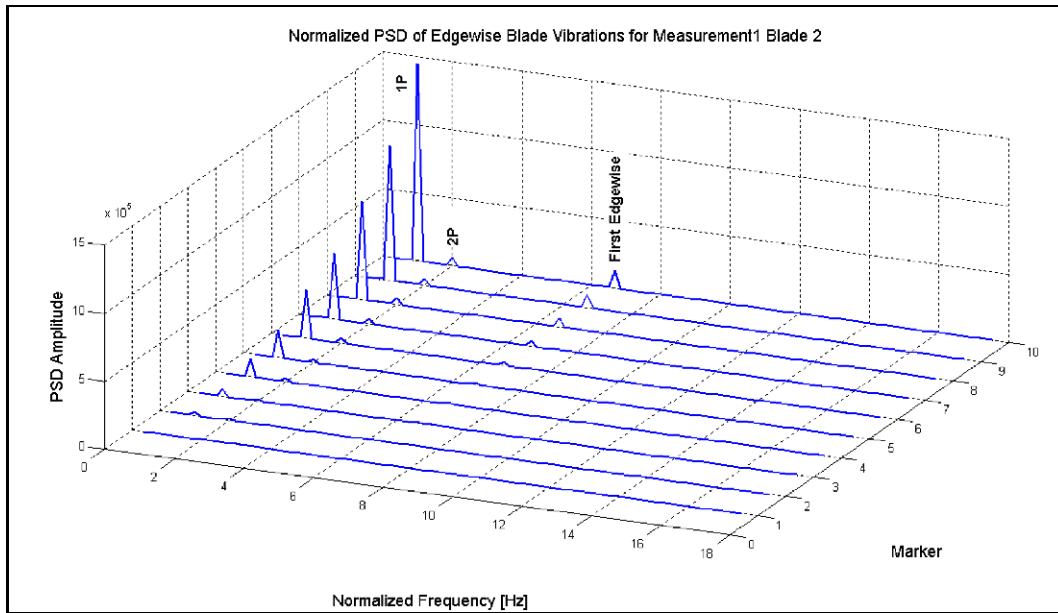


Figure 10 Normalized PSD of edgewise blade vibration for measurement 1 Blade 2.

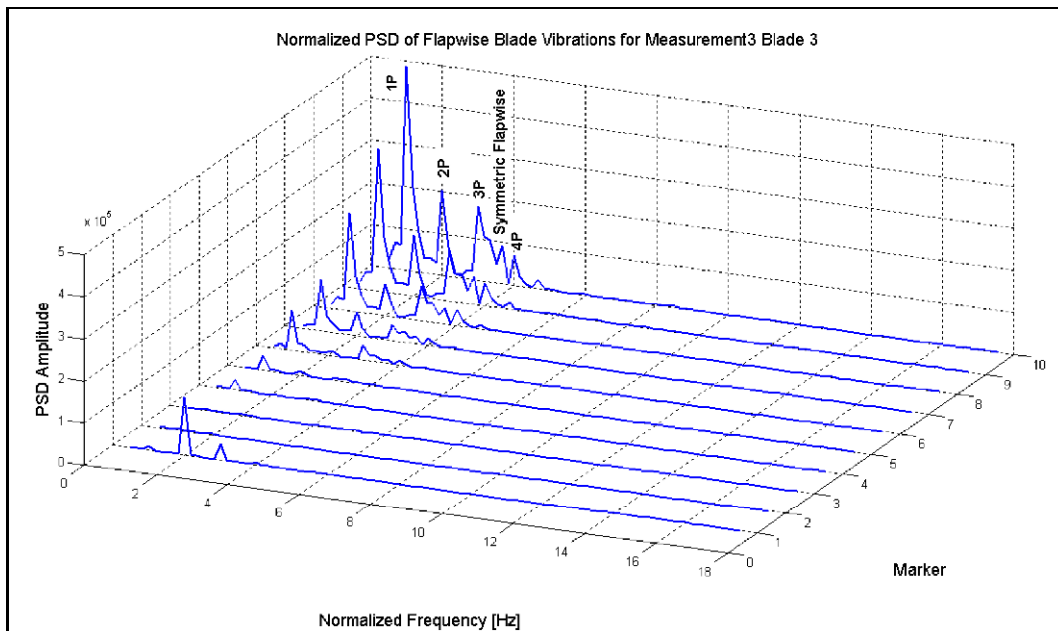


Figure 11 Normalized PSD of flapwise blade vibration for measurement 3 Blade 3.

As can be seen from [Figure 11](#), flapwise vibration data enables more frequencies to be identified. The integer multiples of rotation frequency up to 4P can be detected from the corresponding PSD graph. The contribution of these P components in the overall motion is consistent with those reported by several researchers (35). Besides these P components, first flapwise mode can also be seen in [Figure 11](#). Since the response is mainly dominated by the

integer multiples of rotational frequency (P components) the other turbine modes which have relatively weaker participations in the overall response and which can also exhibit significant damping cannot be identified easily from PSD plots only. However, several system identification methods enable weaker frequencies to be detected. A more detailed investigation (22) of the measured turbine response carried out by utilizing these identification methods showed that the second edgewise, second and third flapwise modes of the blades can also be identified. However, further analyses and measurements are needed for validation of observability of these high frequency modes from photogrammetric measurements (23).

The in-operation response data was also recorded by the strain gauges installed in the blades. Unfortunately, symmetric, FW (forward whirling) or BW (backward whirling) flapwise modes could not be identified from the short measurement durations available. A possible explanation can be that the correlation function based identification methods need very long measurement durations to detect high damping modes. However, it is believed that measurement and analysis of longer data series will enable these high damping modes to be detected too. On the other hand, the 2 tower modes having relatively lower damping ratios could be detected by strain gauge data.

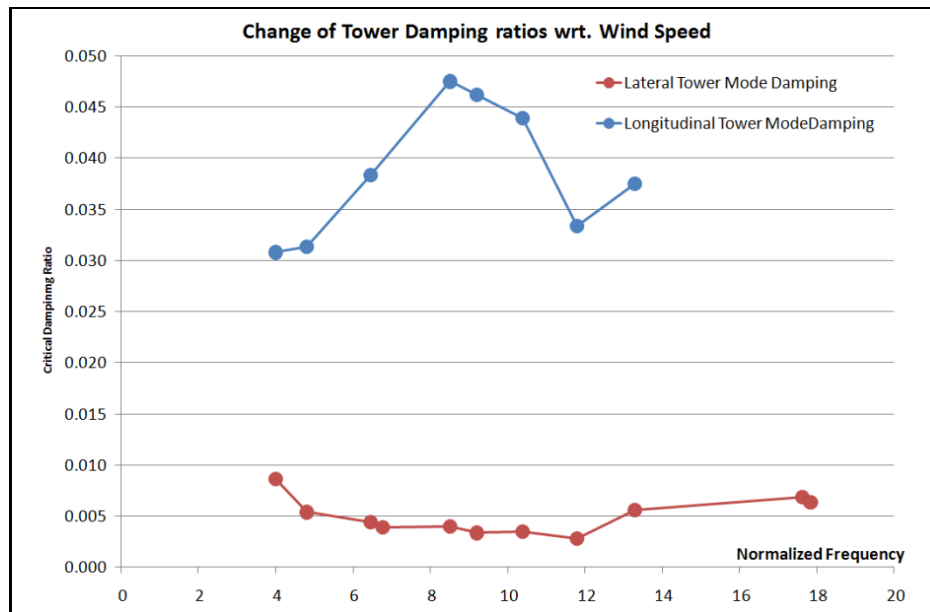


Figure 12 Change of tower damping ratios wrt. wind speed

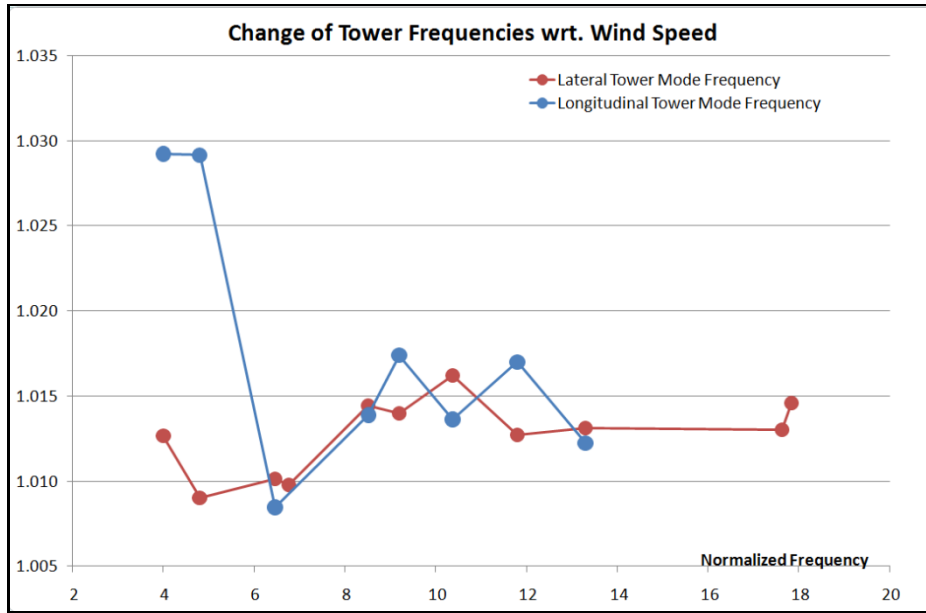


Figure 13 Change of tower frequencies wrt. wind speed

Figure 12 and Figure 13 show the change of aeroelastic damping ratios and eigenfrequencies of the longitudinal and lateral tower modes, respectively.

6. Conclusion

Wind turbines have very specific characteristics and challenging operating conditions. In order to be able to obtain reliable and stable identification results, several factors should be taken into account.

Selection of a suitable low noise ratio data series, ensuring sufficient data length, checking the changes at excitation levels, are some of the important steps that should be paid attention before starting the measurements. Even if all the procedure is followed very precisely, significant scatter can be encountered. Besides, the used identification systems can have some sensitivity or the prerequisites of the analyses tools might not be satisfied.

Although the appropriate data is analyzed by utilizing suitable algorithms the desired information can have much weaker contribution in the overall motion. Therefore, the whole identification procedure should be considered as an iterative operation and necessary attention should be always paid to verify the internal consistency of the results.

Acknowledgements

This research project was partly funded by the We@Sea research program, financed by the Dutch Ministry of Economical Affairs.

The authors would like to thank ECN (Energy Research Center of the Netherlands) for providing the tests turbine and other technical equipment.

The authors also acknowledge the extensive contribution of Pieter Schuer (GOM mbH), Wim Cuypers (GOM mbH), Theo W. Verbruggen (ECN) and Hans J. P. Verhoef (ECN) in organizing and performing the field tests.

Bibliography

1. [Online] ECN Energy Research Center of the Netherlands. <http://www.ecn.nl/units/wind/wind-turbine-testing/>.
2. [Online] Nordex Wind Enerfy. <http://www.nordex-online.com/en/products-services/wind-turbines/n80-25-mw/>.
3. *Remote monitoring of wind turbine dynamics by laser interferometry:Phase1*. **Ozbek, M, Rixen, D.J. and Verbruggen, T.W.** Orlando,Florida : IMAC International Modal Analysis Conference, 2009.
4. *Experimental modal analysis: Efficient geometry model creation using optical techniques*. **Pauwels, S., Debille, J., Komrower, J., Lau, J.** 2 104-113, s.l. : Journal of the IEST, 2006, Vol. 49.
5. *FEM modeling of structures based on close range digital photogrammetry*. **Armesto, J., Lubowiecka, I., Ordóñez, C., Rial, F.I.** 5 559-569, s.l. : Automation in Construction, 2009, Vol. 18.
6. *In-vacuum photogrammetry of a 10-meter solar sail* . **Meyer, C.G., Jones, T.W., Lunsford, C.B., Pappa, R.S.** s.l. : Collection of Technical Papers - AIAA/ASME/ASCE/AHS/ASC Structures, Structural Dynamics and Materials Conference, 2005. AIAA-2005-1889.
7. *Full-field dynamic displacement and strain measurement - Specific examples using advanced 3D image correlation photogrammetry: Part II* . **Schmidt, T., Tyson, J., Galanulis, K.** 4 22-26, s.l. : Experimental Techniques, 2003, Vol. 27.
8. *Full-field dynamic displacement and strain measurement using advanced 3D image correlation photogrammetry: Part I* . **Schmidt, T., Tyson, J., Galanulis, K.** 3 47-50, s.l. : Experimental Techniques, 2003, Vol. 27.
9. *Full-field dynamic deformation and strain measurements using high-speed digital cameras*. **Schmidt, T., Tyson, J., Galanulis, K., Revilock, D., Melis, M.** s.l. : Proceedings of SPIE - The International Society for Optical Engineering, 2005.
10. *Repair and strengthening of reinforced concrete structures using CFRPs* . **Haritos, N., Hira, A., Mendis, P., Perera, U.** 1 1-9, s.l. : Advances in Structural Engineering, 2006, Vol. 9.
11. *Structural dynamics experimental activities in ultralightweight and inflatable space structures*. **Pappa, R.S., Lassiter, J.O., Ross, B.P.** 1 15-23, s.l. : Journal of Spacecraft and Rockets, 2003, Vol. 40.
12. *Out-of-plane deformation measurements of an aluminium plate during quasi-static perforation using structured light and close-range photogrammetry*. **Grytten, F., Fagerholt, E., Auestad, T., Førre, B., Børvik, T.** 17 5752-5773, s.l. : International Journal of Solids and Structures 44 (17), pp. 5752-5773 , 2007, Vol. 44.
13. *Flexible videogrammetric technique for three-dimensional structural vibration measurement*. **Chang, C.C., Ji, Y.F.** . 6, s.l. : ASCE Journal of Engineering Mechanics , 2007, Vol. 133. ISSN 0733-9399.
14. *From photogrammetry, computer vision to structural response measurement*. **Chang, C.C.** s.l. : Proceedings of SPIE - The International Society for Optical Engineering, 2007. 652903 .
15. *Aeroelastic behavior of inflatable wings: Wind tunnel and flight testing* . **Simpson, A., Smith, S.W., Jacob, J.** s.l. : ollection of Technical Papers - 45th AIAA Aerospace Sciences Meeting 18, 2007.

16. *Identification of structural dynamic behavior for continuous system based on videogrammetric technique*. **Ji, Y., Chang, C.C.** s.l. : Proceedings of SPIE - The International Society for Optical Engineering, 2006. 61731I .
17. *Photogrammetry and videogrammetry methods for solar sails and other gossamer structures*. **Black, J.T., Pappa, R.S.** s.l. : Collection of Technical Papers - AIAA/ASME/ASCE/AHS/ASC Structures, Structural Dynamics and Materials Conference , 2004.
18. *Dot-Projection Photogrammetry and Videogrammetry of Gossamer Space Structures*. **Pappa, R.S., Black, J.T., Blandino, J.R., Jones, T.W., Danehy, P.M., Dorrington, A.A.** 6 858-867, s.l. : Journal of Spacecraft and Rockets 40 (6), pp. 858-867 , 2003, Vol. 40.
19. *3D digital image correlation methods for full field vibration measurement*. **Helfrick, M., et al.** Orlando, Florida : the 26th IMAC, International Modal Analysis Conference Proceedings, 2008.
20. *Optical non-contacting vibration measurement of rotating turbine blades*. **Helfrick, M., Niezrecki, C and Avitabile, P.** Orlando, Florida : the 27th IMAC, International Modal Analysis Conference Proceedings, 2009.
21. *Applications of digital image correlation and dynamic photogrammetry for rotating and non-rotating structures*. **Warren, C., Niezrecki, C. and Avitabile, P.** Stanford, CA : the 7th international workshop on structural health monitoring, 2009.
22. *Identification of the Dynamics of Large Wind Turbines by Using Photogrammetry*. **Ozbek, M., Meng, F., Rixen, D. J. and van Tooren, M. J. L.** Jacksonville, Florida, U.S.A : 28thIMAC, International Modal Analysis Conference Proceedings, 2010.
23. *Feasibility of monitoring large wind turbines using photogrammetry*. **Ozbek, Muammer, et al.** s.l. : Energy, 2010. 10.1016/j.energy.2010.09.008.
24. *Modal testing of a very flexible 110 m wind turbine structure*. **Carne, T.G., Lauffer, J.P. and Gomez, A.J.** Kissimmee, Florida, USA : Proceedings of the Sixth International Modal Analysis Conference, 1988.
25. *Experimental modal analysis of a 750 kW wind turbine for structural model validation*. **Molenaar D. P.** Reno, Nevada : 41st Aerospace Sciences Meeting and Exhibit, 2003. AIAA-2003-1047.
26. *A method for determination of damping for edgewise blade vibrations*. **Thomsen K, Petersen JT, Nim E, Øye S, Petersen B.** 3: 233–246, s.l. : Wind Energy, 2000.
27. *Two methods for estimating aeroelastic damping of operational wind turbine modes from experiments*. **Hansen M. H., Thomsen K., Fuglsang P.** 9: 179-191., s.l. : Wind Energy, 2006.
28. *Modal testing using natural excitation*. **James, G.H., Carne, T.G. and Lauffer, J.P.** San Diego, California, USA : Proceedings of the 10th International Modal Analysis Conference, 1992.
29. **James G.H., Carne T.G., Lauffer J.P.** *The natural excitation technique (NExT) for modal parameter extraction from operating wind turbines*. s.l. : Sandia National Laboratories, 1993. SAND92-1666.
30. *Damping measurements using operational data*. **James GH, Carne TG, Veers P.S.** 118 190–193, s.l. : ASME Journal of Solar Energy Engineering, 1996.
31. *The inception of OMA in the development of modal testing technology for wind turbines*. **Carne, T.G. and G.H., James.** s.l. : Mechanica I Systems and Signal Processing, 2010, Vol. 24.
32. *Comparison of System Identification Techniques for Predicting Dynamic Properties of Large Scale Wind Turbines by Using the Simulated Time Response*. **Meng, F., Ozbek, M., Rixen, D., Tooren M.J.L.** Jacksonville : IMAC International Modal Analysis Conference, 2010.
33. *Operational modal analysis in the presence of harmonic excitation*. **Mohanty, P., Rixen, D.J.** 270 93–109, s.l. : Journal of Sound and Vibration, 2004.
34. *Modified SSTD method to account for harmonic excitations during operational modal analysis*. **Mohanty, P., Rixen. D.J.** 12 1247-1255, s.l. : Mechanism and Machine Theory, 2004, Vol. 39.

Operational Damage Detection of Turbine Rotors using Integrated Blade Sensors

S. R. Dana and D. E. Adams

Department of Mechanical Engineering, Purdue University, West Lafayette, IN 47907-2031

NOMENCLATURE

DIC = Digital Image Correlation

ABSTRACT

Predictive maintenance of wind turbines could provide an estimated 81% reduction in cost when compared to reactive maintenance, the current industry standard. The ability to identify damage using wind turbine operating data is necessary for a predictive maintenance approach. To identify such damage, strain measurements were performed on a Whisper 100 blade using a Trilion DIC System with flap-wise applied loading masses to establish a static strain field. This measurement revealed that the root section exhibited the largest strains as anticipated. A crack was then machined in the blade surface to simulate structural damage. Modal analysis techniques were used to detect a downward shift in natural frequency of the rotor assembly due to the damage; however, this small frequency shift would not be useful for damage detection using operating data. To amplify the sensitivity to localized damage that was simulated in the root of the blade, the Modal Assurance Criterion was calculated and revealed several modes that were most sensitive to the damage. Operational data was synchronously averaged and a Discrete Fourier Transform was applied to identify the forced response spectrum. It was shown that for a given wind speed, changes existed in the linear spectra between the healthy rotor and damaged rotor sets.

1 INTRODUCTION

The following work was performed to develop new approaches for operational blade health monitoring to reduce the occurrence of failure and develop updated maintenance scheduling. This work was conducted using an instrumented small-scale wind turbine with a 2m rotor diameter in a laboratory setting.

1.1 Background & Motivation

Wind turbine blades account for 7% of unforeseen malfunctions or failure and wind turbine reliability issues [1]. While this percentage is not particularly high relative to other subsystems like the gearbox and bearings, turbine blades account for 15-20% of the total turbine cost. Blade damage is also the most expensive damage to repair and also has the longest repair time [2]. Additionally, blade failure leads to secondary component damage in the entire system if prompt repair action is not taken resulting in greater monetary losses [3]. Overall, predictive maintenance of rotors and other turbine subsystems can significantly reduce the cost of wind farm maintenance when compared to the current reactive maintenances approach. The ability to continuously monitor blades during operation has benefits both in terms of wind farm output (by identifying changes in the blade set point to maximize energy capture) and blade health (by identifying damage that can be repaired early or blade damage that will necessitate blade replacement to avoid the loss of other turbine subsystems). The detection of damage in operational blades is a form of condition monitoring, and operational modal analysis one methodology for acquiring and processing data from the blade to estimate dynamic properties for use in damage detection. Wind is a highly stochastic excitation and was once believed to be an ideal excitation for operational modal analysis; however, the aeroelastic phenomena due to rotor rotation present challenges for operational modal analysis because these phenomena are nonlinear and time-varying in nature over the rotation of the blade [4].

1.2 Previous Works

Damage detection methods have successfully been applied to wind turbines in offline testing. For example, acoustic emission sensors have been used to detect the initiation and propagation of cracks in blades, but the effectiveness of this method requires that the sensor location be relatively close to the damage location [5]. Critical areas, such as the root and blade tip, are generally instrumented to facilitate the application of acoustic emission techniques. Fiber Bragg grating strain gauges are installed along the entire span of rotor blades, are immune to electromagnetic interference, and are lightweight; however, they lack the durability of other packaged sensor devices [6]. Digital image correlation techniques have been used to determine real-time blade displacement and the global structural integrity by comparing operational video frames with a baseline image [7]. Modal analysis can be applied to this data to determine the natural frequencies but the effectiveness of this method is yet to be determined. Capacitive accelerometers have also been implemented on utility scale wind turbines for measuring the dynamic response of the blades [8]. The ability to measure both static and dynamic acceleration was shown to provide a means for estimating the deflection of the blade as well as the variations in wind loads acting upon the blade. Modal impact testing of blades is commonly used to estimate the modal frequencies and modal deflection shapes in non-rotating blades [9-10]. Many other researchers have focused on the use of vibration response measurements that are acquired from wind turbine rotor blades for the purpose of detecting and monitoring the growth of damage in the blades. For example, various algorithms for detecting damage in wind turbine blades were tested by measuring and processing data using piezoceramic sensor patches [11-12]. However, the effects of operational loading on damage detection were not analyzed in these studies. In the present paper, the nature of the operational loading acting on a horizontal axis wind turbine rotor is used to explore operational damage detection methods when a mechanical change is introduced into one of the three rotor blades.

1.3 Experimental Apparatus

A laboratory test apparatus was used in this study. This apparatus enables control of the wind state and wind turbine including rotor pitch, yaw, and longitudinal position relative to the wind source in addition to full measurement of the rotor response using integrated blade sensors. The apparatus uses a Whisper 100™ 2 meter rotor diameter wind turbine, which is manufactured by Southwest Windpower and is pictured in [Figure 1](#). Wind is produced using four 7.5 hp belt-driven, axial fans (each with 48 in blade diameter). A quasi-laminar flow state is developed by forcing the generated airflow through a stabilizing honeycomb core containing 0.25 inch polycarbonate cells.

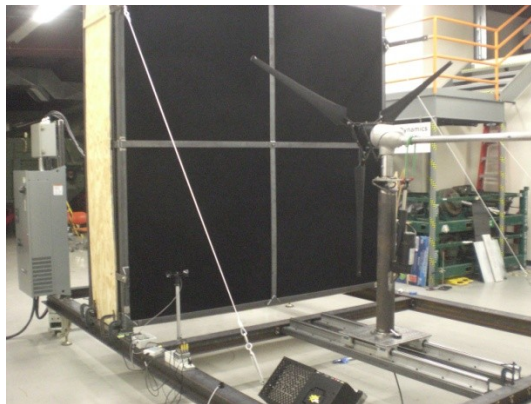


Fig. 1 Two meter diameter wind turbine experimental test apparatus developed for generating wind and measuring dynamic response of rotor blades.

Each turbine blade was instrumented with one triaxial, DC coupled accelerometer manufactured by Silicone Designs (model 2460-050, 80 mV/g nominal sensitivity) and one uniaxial AC coupled accelerometer manufactured by PCB Piezotronics (model 333B32, 100 mV/g nominal sensitivity). The triaxial and uniaxial accelerometers were attached on the low-pressure side of the blade at a distance 14 in and 15 in, respectively, from the blade tips (refer to [Figure 2 \(a\)](#)). Operational data was acquired from these accelerometers using a battery powered National Instruments™ c-DAQ-9172 chassis, which was mounted on the rotor hub. Data was streamed wirelessly from the rotating hub via a Gefen® wireless USB 2.0 extender. Wind speed data was simultaneously acquired from a WMS-21 wind speed transducer that was manufactured by Omega Engineering using a National Instruments USB-9162 carrier. [Figure 2 \(b\)](#) shows a close-up view of the nacelle of the wind turbine that has been fitted with a fixture to hold the data acquisition and wireless transmission hardware. The fixture was designed to position this instrumentation symmetrically around the hub to avoid excessive imbalance forces during operation; however, responses due to imbalance in the rotor are still observed in the experimental data.

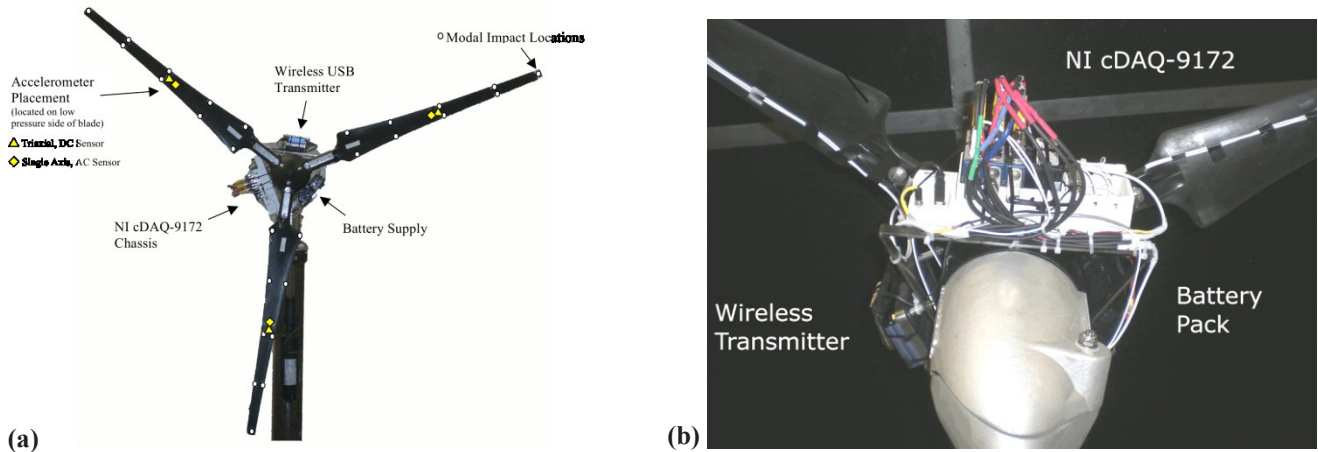


Fig. 2 Whisper 100 wind turbine. (a) Details of accelerometer placement, input and output measurement degrees of freedom and data acquisition hardware. (b) Close up view of nacelle showing data acquisition system, onboard batteries and wireless extender mounted symmetrically around the rotor hub.

2 EXPERIMENTAL TESTING

Three sets of experiments were conducted to introduce a mechanical fault into the blade and to explore methods for operational damage identification. A static loading strain study was performed to identify localized areas of strain. The results dictated where the fault should be positioned and how it should be oriented. With the fault introduced, modal impact testing and operational forced response testing were conducted. Static and operational datasets that were recorded for the healthy rotor were used to analyze the datasets that were acquired after the fault was introduced.

2.1 Static Loading and Digital Image Correlation

To determine how damage should be introduced into the blade, one blade from the Whisper 100 was selected to undergo static loading to identify strain concentrations using a Trillion Digital Image Correlation system. The selected blade was first painted with a random speckle pattern. The digital image correlation system was then used to track small changes in the speckles before and after loading was applied to render the static strain field (Figure 3 (a) and (b)). To apply the load, the blade was cantilevered to a rigid post and loading masses were applied to a surface contact hook that was mounted with pressure adhesive on the low-pressure side of the blade at mid-span (Figure 3 (b)). The mid-span loading location was chosen based on prior work that indicated this region experiences the highest wind loading in operation [8]. The digital image correlation cameras were positioned over the cantilevered blade to track the blade deflection as loading masses were added. A mass of 0.5 kg was initially attached and then increased in steps of 0.5 kg to a final mass of 2.5 kg. Images were collected for each incremental increase in load. The initial testing revealed that the root of the blade exhibited the highest strain concentration. This strain field also indicated the orientation of the strain made a 45 degree angle with respect to the span direction (further discussed in Section 3.1). This information was used to machine a crack, which is shown in Figure 3 (c), on the low-pressure side of the blade surface to preserve the calibrated paint pattern for further static testing. The blade was returned to the cantilever mount and the same incremental loads were applied.



Fig. 3 Static load testing using a DIC system used to locate and track local strain concentrations. (a) Trillion DIC cameras on precision mount. (b) Example of static loading at blade mid-span. (c) Machined crack at identified strain concentration.

2.2 Free Response Modal Testing

After the blade strain study was completed, the damage blade was returned to the turbine for a multi-reference modal impact test using the same measurement degrees of freedom that were used in a previous impact test of the undamaged turbine. For both tests, there were 12 reference channels of data that were acquired using an Agilent E8401A VXI mainframe that was paired with an E1432A module, which sampled at 51.2 kHz. These 12 channels consisted of the three triaxial and uniaxial accelerometers that were described earlier. A PCB Piezotronics modally tuned hammer (model 086C01, nominal sensitivity 50 mV/lbf) was used to apply and measure the impulsive forces in the transverse direction at each point that is indicated on [Figure 2 \(a\)](#) that are labeled ‘Modal Impact Locations’. The modal test grid consisted of 27 impact points that followed the outline of the blade. A threshold force window was applied to the force time history to minimize the noise on the force data. After applying 5 modal impacts at each location and measuring both the impact force and response time histories corresponding to these impacts, the single input-multiple output frequency response functions were estimated for the 5 averages using the H1 algorithm to minimize noise on the response measurements. Ordinary coherence functions were also estimated to determine the quality of fit of the linear frequency response function models.

2.3 Operational Testing

A final experiment was performed to gather operational data, which was acquired using National Instruments™ LabVIEW SignalExpress® software. Operational data from the blade mounted accelerometers was acquired from 16 inches downwind from the honeycomb core that is pictured in [Figure 1](#). Data was taken at two constant fan speeds: 15 and 20 Hz. The duration of these measurements was set to approximately 60 sec to ensure a sufficient time period for the observed perturbations in the wind speed to produce dynamic responses in the turbine rotor blades.

3 DATA ANALYSIS

The digital image correlation test results were used to generate static strain fields for each of the mass loading stages. The modal impact data that was collected after the machined fault was introduced was analyzed and compared to healthy rotor modal data to characterize any changes in the free dynamic response of the rotor and the modal assurance criterion between the undamaged and damaged data to determine modes of vibration that were sensitive to damage. Then the forced response data was analyzed using these free response characteristics to identify the blade crack. A preliminary analysis of the operational data is described in the paper, but the conference presentation will describe the crack detection results that were obtained using the operating data.

3.1 Blade Strain Field

The results of the first static loading test revealed high levels of localized strain in the root of the blade at the leading edge. Additionally, this strain field also revealed the orientation of the principal strain along the blade surface due to the static load. Based on the baseline strain field results, it was determined that a crack should be introduced in this area and direction to simulate the natural degradation of the blade. [Figure 4 \(a\)](#) and [\(b\)](#) show some of the results of the static loading tests. The baseline blade reached a maximum major strain of 0.182% in the blade root. Likewise, the faulty blade test revealed similar strain concentrations with a major strain of 0.315%, which was nearly twice the baseline strain level.

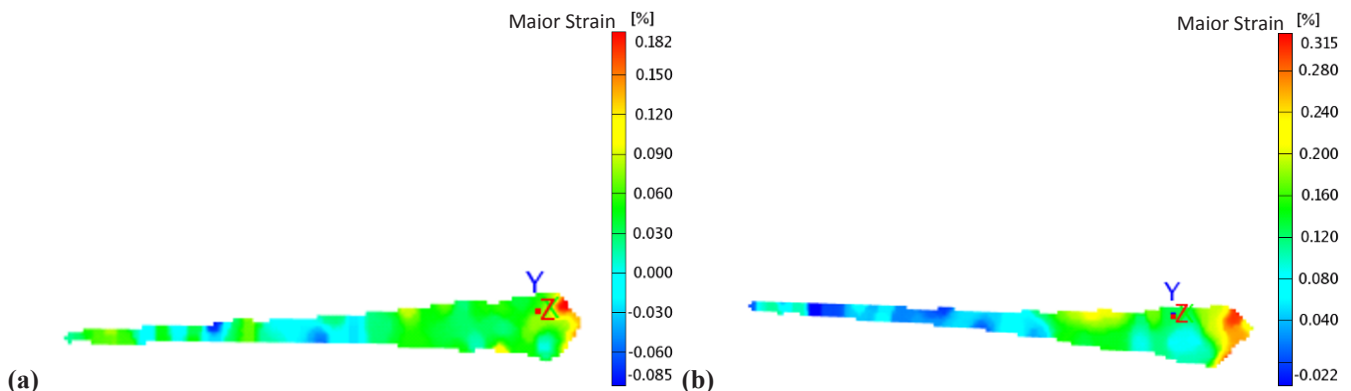


Fig. 4 Static loading strain fields in percentage of major strain generated from digital image correlation testing. (a) Baseline strain field with 2.5 kg mass at blade mid-span. (b) Faulty blade strain field with 2.5kg mass at blade mid-span.

3.2 Modal Characteristics

The free dynamic response characteristics were identified by analyzing the modal impact test data that was acquired as described in the free response modal testing section. Previous modal impact testing of the baseline rotor revealed repeated modes of vibration or highly coupled modes due to the symmetric nature of the turbine and the highly compliant stiffness of the blades. It should also be noted that the damped natural frequencies for this rotor are relatively high compared to a typical utility scale wind turbine blade such as the one tested in [10]. In order to identify the strongly coupled modes of vibration, the multiple input, multiple output frequency response function data was analyzed using the Complex Mode Indication Function, or CMIF [13]. The CMIF was analyzed in Matlab® by performing the singular value decomposition of the normal matrix that was produced using the matrix of frequency response function data, $[H(j\omega)]$, for the modal impact tests:

$$[H(j\omega)]_{27 \times 12}^H [H(j\omega)]_{27 \times 12} = [V(j\omega)]_{12 \times 12} [CMIF(j\omega)]_{12 \times 12} [V(j\omega)]_{12 \times 12}^H \quad (1)$$

In Eq. (1), the CMIF is equivalent to the singular value of the normal matrix as a function of frequency. The left singular vectors contained in the columns of $[V(j\omega)]$ are the modal participation factors associated with the frequency response functions. Each peak in the CMIF corresponds to a mode of vibration, not including peaks formed due to crossing of the singular values in the CMIF plot. This calculation was carried out for both baseline and faulty rotor sets. Figure 5 shows a side by side comparison of the corresponding baseline and faulty CMIF plots. As is evident from Figure 5, there was virtually no change in the resonant frequencies of the turbine. Several of these modes of vibration are degenerate with repeated roots and this result was consistent across both data sets. One of the more dominant modes was identified at 9.4 Hz for which there were 3 roots corresponding to this single mode of vibration; consequently, there were 3 modal deflection shapes associated with this mode of vibration. To form the modal deflection shapes $\{\psi\}$, the following equation was adapted from [13], which is derived by comparing the modal decomposition of the frequency response function matrix to the singular value decomposition given in Eq. (1):

$$\{\psi_{9.4 Hz}\}_{27 \times 1} = [H(j9.4)]_{27 \times 12} \{v(j9.4)\}_{12 \times 1} \quad (2)$$

where $\{v(j9.4)\}$ is the left singular vector from Eq. (1) corresponding to the singular value at the peak near 9.4 Hz in Figure 5.

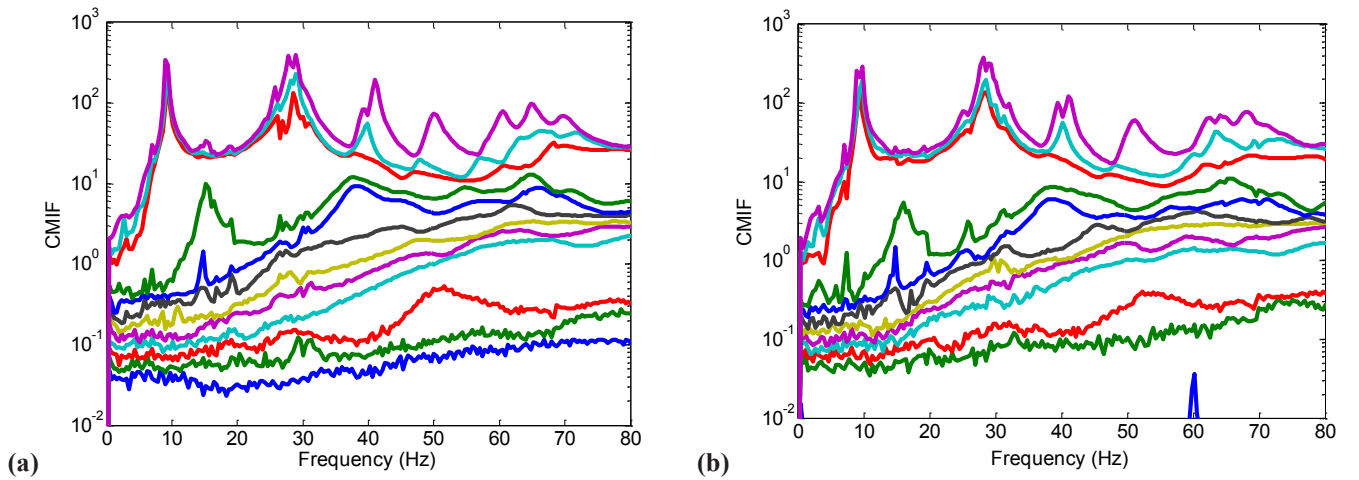


Fig. 5 CMIF used to identify repeated roots and damped natural frequencies of the wind turbine rotor system. (a) Healthy system. (b) Faulty system.

Table 1 below provides a summary of the damped natural frequencies represented by each peak and multiple peaks found in the CMIF plot. Figure 6 shows the three modal deflection shapes associated with the damped natural frequency near 9.4 Hz (3 roots). These deflection shapes illustrate the phase difference between blades in the modal deflections for the case of a repeated root. Figures 6 (a) and (b) exhibit bending in phase while the third blade bends out of phase. Figure 6 (c) exhibits symmetric bending in which all three blades move in phase. This mode shape is often called an umbrella mode. It is believed this mode of vibration is largely associated with asymmetric loading that is experienced during operation.

Table 1 Summary of Turbine Modes

ω_d (Hz)	Description
2.7 (2 roots)	1 st bending – Two blades in phase and the third blade out of phase w/ hub rocking
5.5	Asymmetric bending w/ one blade in 1 st bending + torsion and other blades bending w/ hub rocking
7.0	Pseudo-repeated root of 5.5 Hz modal deflection shape w/ different phase
9.4 (3 roots)	1 st bending – Two roots w/ asymmetric and one root w/ symmetric blade motion, no rocking of hub
15.2 (2 roots)	1 st bending – Two blades bend in phase and the third blade bends out of phase, no rocking of hub
19.1 (2 roots)	2 nd bending – One root w/ asymmetric and one root w/ symmetric blade motion, 2 nd bending of blades
25.8, 27.7, 28.9	2 nd bending – Two blades bend in phase and the third blade is out of phase, 2 nd bending of blades
30.8	2 nd bending – Three blades w/ symmetric motion in phase undergoing 2 nd bending
39.1	2 nd bending – Two blades w/ asymmetric motion in phase in 2 nd bending, third blade torsion
41.0	2 nd bending – Two blades w/ asymmetric motion in phase in 2 nd bending, third blade torsion

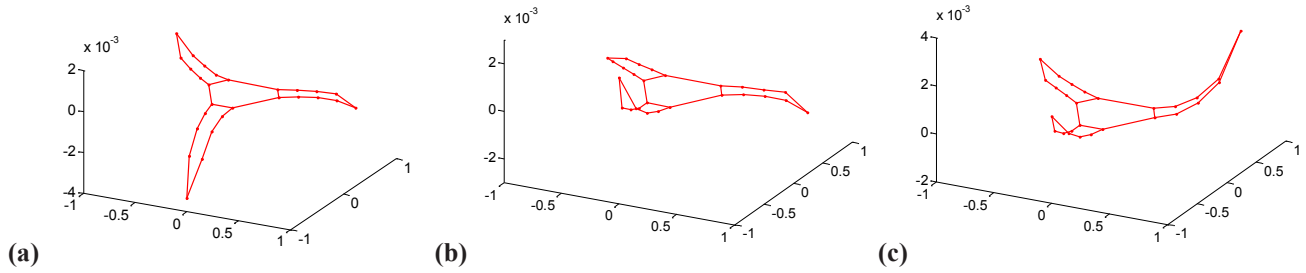


Fig. 6 Deflection shapes for modes of vibration near 9.4 Hz showing phase difference between repeated roots.
 (a) Asymmetric bending. (b) Asymmetric bending of second root. (c) Symmetric bending of third root.

3.3 MAC Study

A negligible change in natural frequencies was measured due to the machined crack; therefore, an alternative approach to identify damage using modal deflection shapes was pursued. The method that was used was the Modal Assurance Criterion. The MAC provides a measure of consistency between modal vectors and can be used to determine deflection shapes, which are comprised of modal vectors, which are sensitive to perturbations in blade properties. The MAC can be written as follows:

$$MAC_{crdr} = \frac{\left| \{\psi_{cr}\}^H \{\psi_{dr}\} \right|^2}{\{\psi_{cr}\}^H \{\psi_{cr}\} \{\psi_{dr}\} \{\psi_{dr}\}^H} \quad (3)$$

where ψ is the modal vector and subscripts cr and dr refer to the rows and columns, respectively, of the r th mode. The MAC also provides a means of determining the degree of consistency between different sets of modal vectors from the same system. In this study, modal vectors from the baseline turbine can be evaluated against the turbine containing the blade fault. The cross MAC between two different sets of modal vectors corresponding to the same structure and impact locations offers insight into modes that are most sensitive to the simulated damage. In this case, the modal vectors for the first six modes that dominate the response in the CMIF plot were used to perform the calculation. Figure 7 show the results of the MAC calculation as a 3-D bar plot. Figures 7 (a) and (b) show the MAC for the baseline (healthy) and faulty turbine, respectively. Numbers 1 through 6 represent the mode and the axis numbered 0 through 1 represents the correlation between the modal vectors. It can be seen that unity is reached along the diagonal for all modes in (a) and (b). This result is expected because the dot product of a modal vector with itself when normalized by the length squared is 1 as indicated in Eq. (3). However,

when the modal vectors from the baseline system are crossed with the faulty system, several modes on the diagonal do not approach unity. This result indicates that the fault has affected the modal properties of the blade. Furthermore, these results indicate that modes 2 and 3 were the most sensitive to the presence of the fault in the blade that was machined. Finally, these results also indicate that the off-diagonal entries in the MAC (compare (a) and (b)) could be used to avoid the need for comparing a historical baseline record from the healthy turbine with the turbine whose health is in question. This capability would allow this method to be applied to turbines for which a baseline record is not available assuming the coupling among modes for all blades share the pattern that is evident in [Figures 6 \(a\) and \(b\)](#).

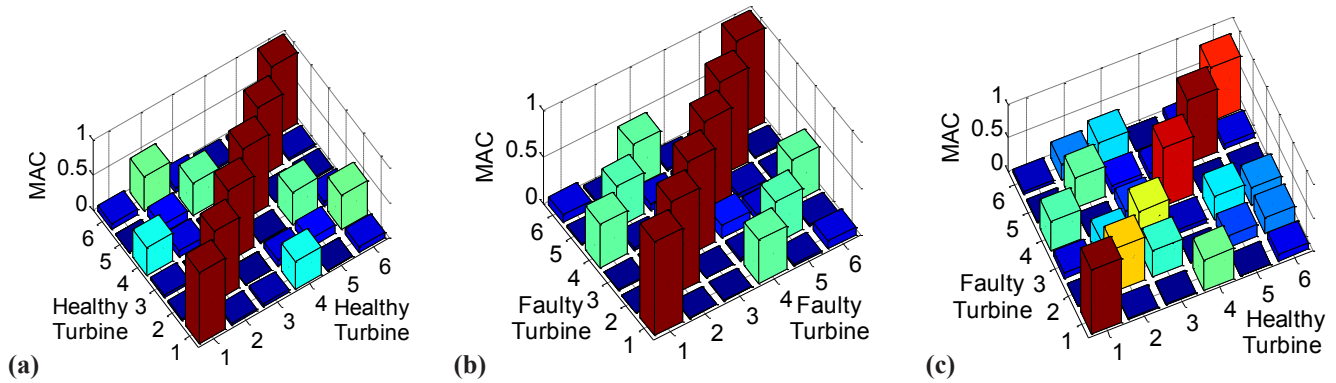


Fig. 7 Modal Assurance Criterion. (a) Turbine with baseline (healthy) rotor blades. (b) Turbine with one faulty rotor blade. (c) Cross MAC result between healthy turbine and faulty turbine.

3.4 Operational Data

The two sets of operational data comprised of 12 acceleration measurements were collected at different steady-state fan speeds. [Figure 8](#) below illustrates the DC acceleration measurements in the span, lead-lag and flap directions for blade 3. It is evident from the figures that the span and lead-lag accelerations have a low frequency sinusoidal characteristic related to oscillations in gravitational loading of the rotors by $+1$ to $-1g$ as they operate through one revolution. [Figure 8 \(b\)](#) reveals an increase in rotor imbalance that is evident in the loss of a clear sinusoidal pattern in the span direction as the rotational speed increases. Such a characteristic might be indicative of drive train mounting issues in an actual turbine but is related to the imbalance from the instrumentation package in this small-scale turbine. For this experiment, the flap direction is of most interest due to the machined fault in the blade root. It is hypothesized that bending modes will be most sensitive to this fault because the flap direction corresponds to bending of the blade on the root. It can be seen in [Figure 8](#) that the flap direction exhibits a multi-frequency response that is associated with higher frequency structural blade dynamics.

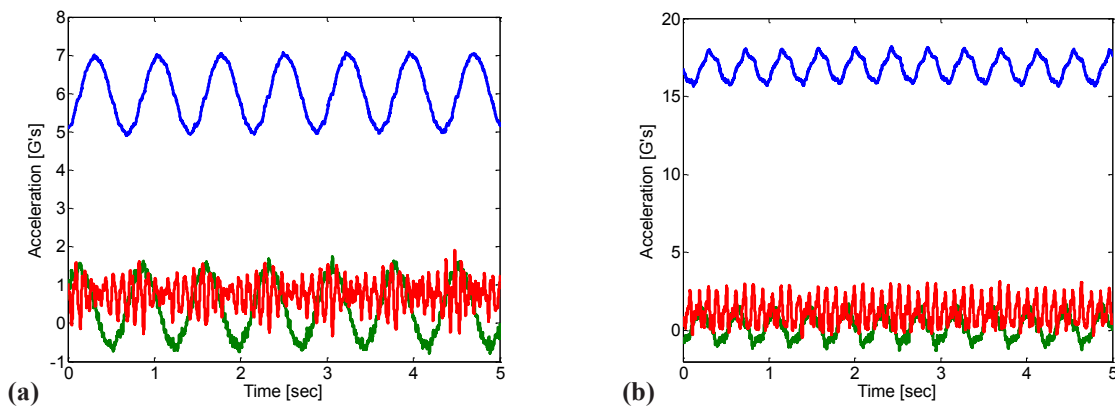


Fig. 8 Operational DC acceleration measurements of blade 3 in the span (blue), lead-lag (green), and flap (red) directions. (a) 15 Hz steady state fan speed. (b) 20 Hz steady state fan speed.

The linear spectra for each steady-state operational speed were calculated to better understand the operational dynamic response of the blades. These spectra were calculated by using 30 synchronous averages with a blocksize equal to the period of blade rotation for the flap direction and by summing the DC and AC accelerations for each blade. No signal processing

window was used to avoid the effects of the window and because this type of cyclic averaging reduces the effects of leakage. Figure 9 shows the resulting averaged linear spectra. The flap direction acceleration exhibited the highest dynamic components as was expected based on the time histories shown in Figure 8. The 15 Hz fan speed linear spectra resembles the FRFs that were obtained using the CMIF. There are two clear groupings near 9 Hz and 28 Hz. The CMIF plot shares this characteristic. The cluster of peaks near 28 Hz is lost at higher rotational speeds implying that the forcing function at this frequency does not excite these modes to the same extent as the forcing function for the lower fan speed.

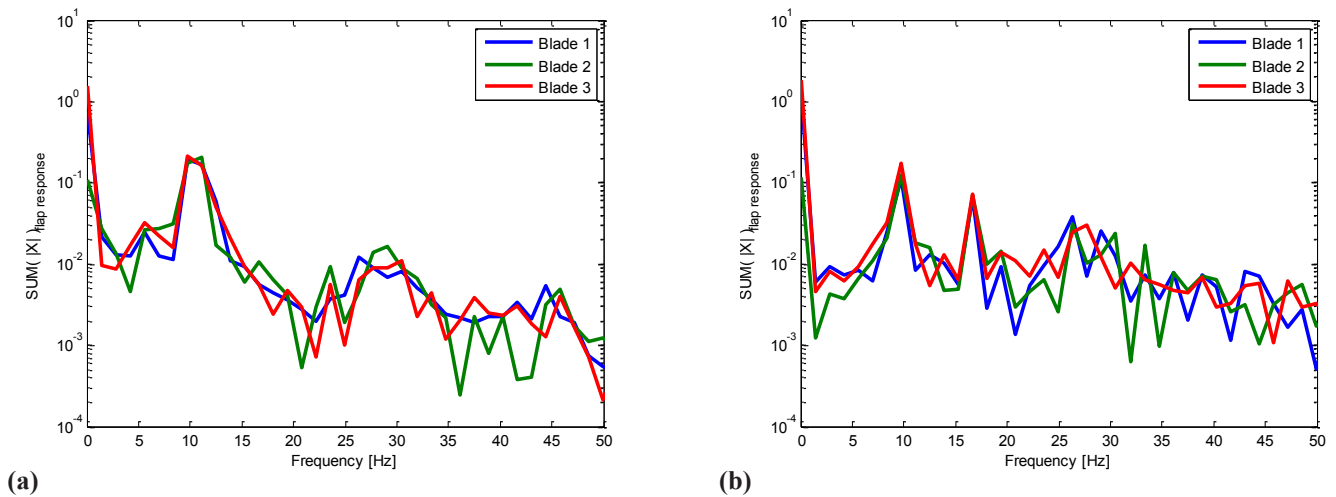


Fig. 9 Magnitude of synchronously averaged flap acceleration for each blade. (a) 15 Hz steady state fan speed. (b) 20 Hz steady state fan speed.

To further understand the forced response the linear spectrum was plotted for blade 3, the damaged blade, and compared with the healthy spectrum for the same blade. Figure 10 shows a comparison of the forced response spectra for the healthy and faulty turbines. Figure 10 (a) is the spectra for blade 3, the blade with known damage. It can be seen from the plot that near 9.4 Hz, indicated with an arrow, all of the spectral lines come together in direction pairs (i.e. flap with flap, etc). Notably, the lead-lag spectra, green lines, do not meet. For two of the measurement directions to come together and the third to be significantly different suggests i) the measurement is repeatable and ii) any changes in the measurement are significant. For the case at hand this suggests the lead-lag direction has detected a change in the rotor blade with known damage. Figure 10 (b) highlights the difference in magnitude of the DC acceleration for all lead-lag measurement channels of the healthy and faulty turbine. Note the difference in blade 3, red lines, is far more appreciable when compared with blades 1 and 2. The calculated percent difference of the change in magnitude of the DC acceleration between blade 1 and 3 is 193.4% and 156% between blades 2 and 3. The second arrow in Figure 10 (a) marks another area of interest in the spectra. Here the spectra sets converge near 38 Hz but with opposite magnitudes. This may also be suggestive of a change in the rotor system. Statistical analysis of this data and more data sets can be used to confirm these traits found in the forced response spectra.

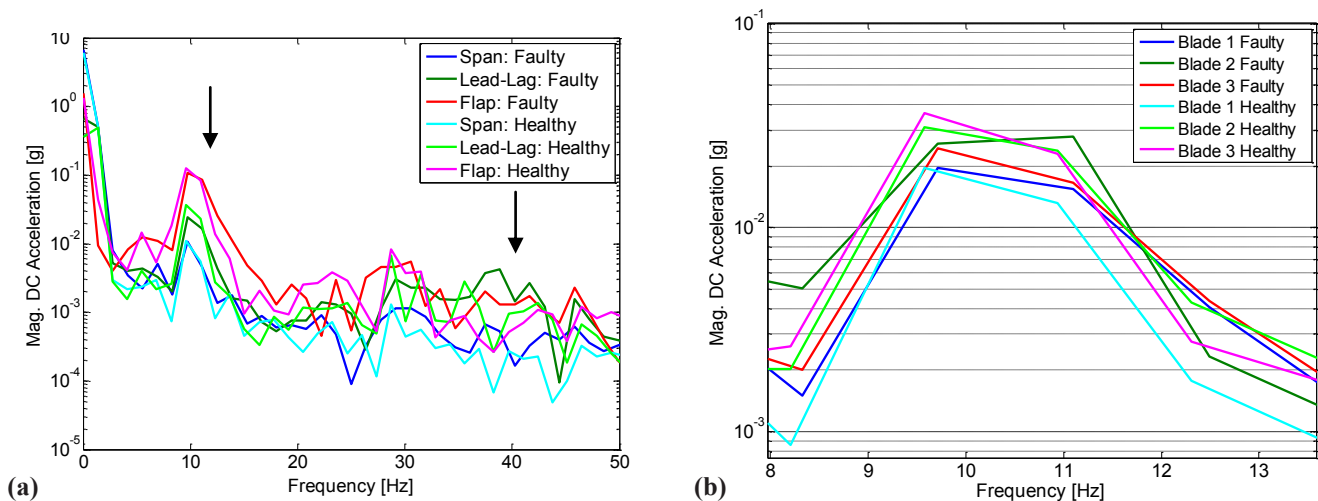


Fig. 10 Linear spectra comparison of the healthy and faulty turbines. (a) Blade 3 linear spectra. Arrows indicate areas of interest for damage identification. (b) Lead-lag spectra for all blades near first area of interest.

4 FUTURE WORK

Statistical analysis of the operational data will be used to confirm the traits in the linear spectra that are suggestive of damage in the rotor. Additional damage detection techniques will also be considered such as operational deflection shapes and modal filtering.

5 CONCLUSIONS

A 2 meter diameter Whisper 100 wind turbine was analyzed using modal analysis techniques to identify blade damage. Digital image correlation was used to establish static strain fields when flap-wise loading masses were applied to reveal strain concentrations in the blade root. A crack was then machined in the blade surface to simulate structural damage. Modal analysis techniques revealed a small downward shift in natural frequency of the rotor assembly. The Modal Assurance Criterion was calculated and revealed several modes that were most sensitive to the damage. Operational data was synchronously averaged and a Discrete Fourier Transform was applied to identify the forced response spectrum. It was shown that for a given wind speed the lead-lag direction has significant deviation from the baseline spectrum after damage while the spectra for the span and flap directions remained identical. Statistical analysis can be used to identify the repeatability of these changes.

6 ACKNOWLEDGEMENTS

The authors gratefully acknowledge Joseph Yutzy at Purdue Center for Systems Integrity for his assistance in conducting operational experiments.

REFERENCES

1. Hahn, B., Durstewitz, M., and Rohrig, K., "Wind Energy (Reliability of Wind Turbines Experiences of 15 Years with 1,500 W)," ed J Peinke *et al*, Springer, Berlin, pp. 329–332, 2007.
2. Flemming, M. L. and Troels, S., "New lightning qualification test procedure for large wind turbine blades," Int. Conf. Lightning and Static Electricity, Blackpool, UK, pp. 36.1–10, 2003.
3. Rosenbloom, E., "A Problem with Wind Power," www.aweo.org, 2006.
4. Tcherniak, D., Shauhan, S., and Hansen, M. H., "Applicability Limits of Operational Modal Analysis to Operational Wind Turbines," Proc. of IMAC-XXVIII, Jacksonville, FL, 2010.
5. Beattie, A. G., "Acoustic Emission Monitoring of a Wind Turbine Blade during a Fatigue Test," Prof. of AIAA, paper number 958, pp. 10, 1997.
6. Zayas, J. R., Roach, D. P., Rumsey, M. A., Allan, W. R., and Horslev, D. A., "Low-Cost Fiber Bragg Grating Interrogation System for in situ Assessment of Structures," Proc. of SPIE, Vol. 6529 (2), pp. 65293C.1–65293C.12, 2007.

7. Van Hemelrijck, D., Smits, A., and Philippidis, T. P., "Study of the Behaviour of a Glass Fibre Reinforced Epoxy Composite System used for Wind Turbine Rotor Blades under Biaxial Load Conditions," Proc. of Eur. Wind Energy Conf. Exhibition 2006, Athens, Greece, 2006.
8. White, J., Adams, D., Rumsey, M., and Zayas, J., "Measurement of Operational Loading and Deflection with a Smart Turbine Rotor Blade," Windpower, Chicago, IL, 2009.
9. White, J. R., Adams, D. E., Rumsey, M. A., "Modal Analysis of CX-100 Rotor Blade and Micon 65/13 Wind Turbine," Proc. of IMAC-XXVIII, Jacksonville, FL, 2010.
10. Larsen, G. C., Hansen, M. H., Baumgart, A., and Carlen, I., "Modal Analysis of Wind Turbine Blades," Riso-R-1181 (EN).
11. Ghoshal, A., Dundaresan, M. J., Shulz, M. J., and Pai, P. F., "Structural Health Monitoring Techniques for Wind Turbine Blades," Journal of Wind Engineering and Industrial Aerodynamics, pp. 85, 2000.
12. Luczak, M., Peeters, B., Dohler, M., Mevel, L., Ostachowicz, W., Malinowski, P., Wandowski, T., and Branner, K., "Damage Detection in Wind Turbine Blade Panels Using Three Different SHM Techniques," Proc. of IMAC-XXVIII, Jacksonville, FL, 2010.
13. Shih, C. Y., Tsuei, Y. G., Allemang, R. J., and Brown, D. L., "Complex Mode Indication Function and Its Applications to Spatial Domain Parameter Estimation," Proc. of IMAC-VII, Las Vegas, NV, 1989.

Uncertainty Assessment in Structural Damage Diagnosis

Shankar Sankararaman and Sankaran Mahadevan

Department of Civil and Environmental Engineering
Box 1831-B, Vanderbilt University, Nashville, TN – 37235
United States of America

ABSTRACT

This paper develops methods for the quantification of uncertainty in each of the three steps of damage diagnosis (detection, localization and quantification), in the context of continuous online monitoring. A model-based approach is used for diagnosis. Sources of uncertainty include physical variability, measurement uncertainty and model errors. Damage detection is based on residuals between nominal and damaged system-level responses, using statistical hypothesis testing whose uncertainty can be captured easily. Localization is based on the comparison of damage signatures derived from the system model. Both classical statistics-based methods and Bayesian statistics-based methods are investigated to quantify the uncertainty in all the three steps of diagnosis, i.e. detection, localization, and quantification. While classical statistics-based methods use the concept of least squares-based optimization, Bayesian methods make use of likelihood function and Bayes theorem. The uncertainties in damage detection, isolation and quantification are combined to quantify the overall uncertainty in diagnosis. The proposed methods are illustrated using two types of example problems, a structural frame and a hydraulic actuation system.

1. INTRODUCTION

Damage diagnosis consists of three major steps – damage detection, damage localization (or isolation), and damage quantification. Practical applications often consist of multi-level, multi-domain systems, where only a few response quantities are monitored but the number of prospective damage candidates is very high. In such cases, it is almost impossible to achieve precise damage diagnosis. Further, the model inputs, physical parameters, sensor measurements, the model form, etc. may all be uncertain and hence render the results of diagnosis uncertain. The quantification of uncertainty in damage diagnosis is an essential step to guide decision-making with respect to operations, maintenance, and risk management.

The uncertainty in detection [1] has been previously addressed by non-destructive evaluation (NDE) techniques through the quantity probability of detection (POD). In such POD calculations, nominally identical damage is introduced in a number of nominally identical specimens, and the number of successful detections is used to calculate the probability of detection. However, such an approach is only applicable to offline testing and not directly applicable to real time diagnosis [2].

System identification techniques have been pursued by several researchers for the purpose of damage isolation and quantification. Fundamentally, these methods could be viewed as statistical calibration problems where the model parameters are calibrated and the uncertainty in calibration can be expressed through confidence bounds in the parameter estimation. Several studies have investigated classical statistics-based methods [e.g. 3] and Bayesian methods [4, 5] for uncertainty quantification in system identification and structural health monitoring. These methods involve estimating all the system parameters simultaneously; this makes the computation time-consuming and thus not suitable for online diagnosis. System identification-based methods also combine damage isolation and damage quantification into one procedure; the individual contributions from different stages of diagnosis (detection, localization, and quantification) to the overall uncertainty in diagnosis are not separated. This paper presents two different approaches – based on classical and Bayesian statistics - to quantify the uncertainty in the three steps of diagnosis, and thereby the overall uncertainty in diagnosis. The scope of the paper is currently limited to single faults and multiple fault scenarios will be considered in future.

Damage detection is based on statistical hypothesis testing of the residuals, i.e. the difference between the model predictions and system measurements. In classical hypothesis testing [6], the choice of the significance level of testing is used to calculate the uncertainty in detection. In the Bayesian hypothesis testing-based approach, the likelihoods of two scenarios, i.e. “no fault” and “fault” are calculated and the uncertainty in the detection is quantified.

Damage isolation is first done qualitatively based on cause-effect relationships between model parameters and measurements, and this helps to isolate a prospective set of candidate damage parameters. In the classical statistics-based approach, a heuristic measure based on the least squares corresponding to each candidate damage parameter is used to quantify the uncertainty in damage isolation. In the Bayesian statistics-based approach, the probability of a particular parameter being faulty is calculated directly.

Damage quantification is based on least squares approach or likelihood maximization. The uncertainty in damage quantification is calculated using statistical confidence intervals in the classical statistics-based approach, and using Bayesian inference in the Bayesian approach. Note that the latter approach directly calculates the probability distribution of the damage parameter while the former approach only gives a measure of uncertainty.

The overall uncertainty in diagnosis is calculated by combining the uncertainties in the three stages of diagnosis using the principle of total probability, and the overall probability distribution of the damage parameter is calculated. The methods for uncertainty quantification in damage detection, localization and quantification are developed in the Sections 2-4. The proposed methods are illustrated using two different kinds of systems, a structural frame (Section 5) and a hydraulic actuator (Section 6).

2. UNCERTAINTY IN DAMAGE DETECTION

Detection is based on comparison between healthy system response (predicted by the model) and the observed system response. ‘Significant’ deviation of y from the expected performance indicates the presence of damage. The difference, i.e the residuals $r(t)$ are averaged over a moving window and the mean (μ) is subjected to a hypothesis test at a chosen significance level α , as follows:

$$H_0: \mu = 0 \text{ (No damage)} \quad (1)$$

$$H_1: \mu \neq 0 \text{ (Damage)} \quad (2)$$

The null hypothesis (H_0) in Eq. 1 states that the residuals are not significantly different from zero (no damage) while the alternate hypothesis (H_1) in Eq. 2 states that the residuals are significantly different from zero (damage).

Classical Statistics-based Approach

The uncertainty in detection is calculated as the probability that the damage is true after having detected a fault. This is established using the choice of the significance level α in hypothesis test. The probabilities of different types of errors in hypothesis testing are well established in literature. The error of rejecting a correct null hypothesis is known as Type-I error while the error of not rejecting a false null hypothesis is known as Type-II error. The probability of Type-I error is equal to α and the probability of Type-II error is denoted by β . Suppose that the residuals calculated from the system have been subjected to statistical hypothesis testing at significance level α and damage has been detected. Hence, the hypothesis H_0 has been rejected. The confidence in damage detection can be calculated as the probability that the actual state of the system is H_1 , subject to having rejected the hypothesis H_0 . This probability is equal to $(1 - \alpha)$ and is denoted as P_d .

Bayesian Statistics-based Approach

In this method, residuals are assumed to be normally distributed, i.e. $r \sim N(\mu, \sigma^2)$, and the probability distribution of the mean μ is continuously updated with measurements. Let the prior distribution be $N(\rho, \tau^2)$. If no additional information is available, Migon and Gamerman [7] suggest $\rho = 0$ and $\tau^2 = \sigma^2$. Then the posterior distribution of μ can be calculated to be normal with mean and variance as follows:

$$\text{Posterior Mean of } \mu = \frac{\frac{\rho}{\tau^2} + \frac{r_1 + r_2 \dots + r_n}{\sigma^2}}{\frac{1}{\tau^2} + \frac{n}{\sigma^2}} \quad (3)$$

$$\text{Posterior Variance of } \mu = \left(\frac{1}{\tau^2} + \frac{n}{\sigma^2} \right)^{-1} \quad (4)$$

Damage detection can be achieved through the use of Bayes factor which is defined as the ratio of likelihood of the two scenarios: “damage” and “no damage” as follows:

$$B = \frac{P(D|H_1)}{P(D|H_0)} \quad (5)$$

In Eq. 5, D refers to the data on the residuals obtained during health monitoring. Jiang and Mahadevan [5] derived the expression for the (natural) logarithm of Bayes factor.

$$\log B = -\frac{1}{2} \log(n+1) + \frac{n^2 R^2}{2(n+1)\sigma^2} \quad (6)$$

In Eq. 6, R stands for the mean of the observed residuals, i.e. $R = (r_1 + r_2 + r_3 \dots + r_n) / n$. If the Bayes factor B is greater than 1, it implies that the data favors the hypothesis H_1 , and hence suggests that there is damage. The confidence in damage detection, i.e. the probability that the fault is true can be calculated as $P(H_1|D)$ and is equal to $B/B+1$ if the prior probabilities for $P(H_0)$ and $P(H_1)$ are chosen to be equal.

This metric gives a direct measure of the probability of damage and hence is easy to compute and interpret in comparison with the classical statistics-based metric. Further, the probabilities $P(H_0)$ and $P(H_1)$ can be updated continuously with measurements and thereby helps in tracking the uncertainty with acquisition of more measurements.

3. UNCERTAINTY IN DAMAGE LOCALIZATION

Damage localization is based on the comparison between damage signatures calculated from the system model and the symbols calculated from the system measurements. First, the system model is used to derive cause-effect relationships between the model parameters (that correspond to damage parameters) and model outputs (that correspond to system measurements). These cause-effect relationships, collectively called as the damage signatures, describe the qualitative changes in the 0th and 1st derivatives of a system output as a result of a change in a system parameter. There are several ways to obtain these signatures; for example, by using finite difference with the system model to calculate approximate derivatives. This paper uses a bond graph-based methodology to derive the damage signatures; this method is qualitative and hence, can aid in rapid online damage localization of damage parameters [6, 8].

However, practical engineering systems usually have a large number of parameters that could become faulty, but only a small set of measurements. It may be difficult to exclusively isolate one particular damage parameter if several candidates have the same set of damage signatures. Instead, a set of prospective candidate damage parameters, θ_i ($i = 1$ to m) may be suggested by the isolation procedure. This section associates a measure of uncertainty to each of the candidate damage parameters.

Classical Statistics-based Approach

The uncertainty in damage localization is calculated using a heuristic least squares-based metric. Consider a particular damage parameter θ and let \hat{y} and y denote the model prediction and sensor measurements respectively. Suppose that the fault was detected at t_f and consider N further measurements. Then a least square estimate of the damage parameter θ can be calculated by minimizing Eq. 7.

$$S(\theta) = \sum_{t=t_f}^{t_f+N} (\hat{y}(\theta) - y)^T (\hat{y}(\theta) - y) \quad (7)$$

Let the least square estimate be $\hat{\theta}$ and $S(\hat{\theta})$ the corresponding least squares value. Then the probability that θ is the true damage parameter can be heuristically said to be inversely proportional to $S(\hat{\theta})$ and the constant of proportionality by considering all prospective damage parameters and equating the total probability to unity.

Bayesian Statistics-based Approach

The Bayesian approach directly calculates the probability that a given damage parameter is faulty and provides an exact measure of uncertainty as against a heuristic measure provided by the classical statistics-based approach. Let A denote the event that θ_i is the true damage parameter. The proposed metric calculates the probability of event A after observing the data (D). A prior probability P_i' is first assumed (a suitable initial assumption would be $1/m$ as any of the candidate damage parameters is equally likely to be the damage parameter) and then updated to calculate a posterior probability P_i'' based on the following likelihood function.

$$P(D|A) = P(D | \theta_i \text{ is the true damage parameter}) = L(\theta_i) \quad (8)$$

This probability is the likelihood of event A , denoted by $L(\theta_i)$. The calculation of this probability is explained in the following paragraphs.

Let \hat{y} represents the model prediction. Let B denote the event that q_i is the value of the damage parameter θ_i . Thus, for a given x and t , \hat{y} depends on the value of θ_i .

$$\hat{y} = f(x, t; q_i) \quad (9)$$

Assume that damage has been detected at time ' t_f ', when the value q_i of the parameter θ_i changes to an unknown value. Let measurements continue to be available after damage detection and y denote the measurements available (for example, pressure, velocity, etc.) at any time instant from t_f to $t_f + N$. The standard deviation of these measurements can be monitored until damage is detected and the covariance matrix (Σ) of the residuals can be calculated. Then the likelihood function corresponding to event $A \cap B$ (i.e. the probability of observing the data conditioned on (i) event A , i.e. θ_i is the true damage parameter and (ii) event B , i.e. the true damaged value is q_i can be calculated by assuming an appropriate distribution (normal, below) for the residuals:

$$P(D|A \cap B) = L(\theta_i, q_i) \propto \prod_{t=t_f}^{t_f+N} \exp[-(\hat{y}(q_i) - y)^T \Sigma (\hat{y}(q_i) - y)] \quad (10)$$

Note that y and \hat{y} are column vectors of length n , and the covariance matrix Σ is of size n , where n is the number of measured quantities. Hence, the right hand side of Eq. 10 is a scalar.

The joint likelihood $L(\theta_i, q_i)$ in Eq. 10 can be used in Bayesian inference to update P_i . Let $f'(q_i | \theta_i)$ denote the probability density function (PDF) of the damage value q_i conditioned on event A . The posterior probabilities P_i'' and $f''(q_i | \theta_i)$ can be calculated based on Bayes theorem. While the former indicates the uncertainty in damage localization, the latter indicates the uncertainty in damage quantification. Section 4 focuses on the latter topic and the choice of prior and the estimation of the posterior $f''(q_i | \theta_i)$ is discussed in detail in Section 4. This section deals only with the estimation of P_i'' . It can be proved that

$$P_i'' \propto P(D|A)P_i' \propto P_i' \int L(\theta_i, q_i) f'(q_i | \theta_i) dq_i \quad (11)$$

Note that there is proportionality constant in Eq. 11. This constant can be evaluated by imposing the constraint that the sum of all P_i s should be equal to unity. These probabilities can be continuously updated with the acquisition of measurements.

4. UNCERTAINTY IN DAMAGE QUANTIFICATION

This section calculates the uncertainty in the damage quantification stage. The classical statistics-based approach calculates statistical confidence intervals on the damage parameter while the Bayesian statistics-based approach directly calculates the probability distribution of the damage parameter.

Classical Statistics-based Approach

A least squares estimate for θ was obtained in Section 3, and the least squares error was estimated as $S(\hat{\theta})$ by minimizing Eq. 7. To calculate the confidence bounds on θ , the first step is to assign bounds on the squared error $S(\theta)$ as shown in Eq. 12.

The values of θ that correspond to this error define the confidence bounds on θ :

$$S(\theta) \leq S(\hat{\theta}) \left\{ 1 + \frac{p}{n-p} F_{p, N-p}^\alpha \right\} \quad (12)$$

In Eq. 12, N denotes the number of observations over which the least squares error was estimated and p denotes the length of the vector θ . In this case of single fault assumption, $p = 1$. $F_{p,N-p}^\alpha$ denotes the F-statistic, with estimation (numerator) degrees of freedom p and residual (denominator) degrees of freedom $N - p$ at significance level α .

For example, $\alpha = 0.05$ would yield a 95% confidence interval for the damage parameter whose bounds would be approximate estimates of values that correspond to cumulative probabilities of 0.025 and 0.975 of the ‘true’ value. By repeating this procedure for different values of α , it is possible to obtain the entire an approximation to the cumulative probability distribution of the damage parameter.

Bayesian Statistics-based Approach

This section calculates the uncertainty in q_i , the value of the damage parameter θ_i . A maximum likelihood estimate \hat{q}_i of the damage value can be obtained easily by maximizing the RHS of Eq. 10. The likelihood function calculated in Eq. 10 can be used in Bayes theorem and the entire probability distribution of the value q_i of the damage parameter θ_i can be calculated as:

$$f''(q_i|\theta_i) = \frac{L(\theta_i, q_i)f'(q_i|\theta_i)}{\int L(\theta_i, q_i)f'(q_i|\theta_i) dq_i} \quad (13)$$

In Eq. 23, $f'(q_i|\theta_i)$ is the prior density function and represents the knowledge about q_i . As there is no ‘‘prior’’ knowledge about the damage value before the damage quantification, a uniform distribution may be assumed for the prior distribution to begin with. Then, this distribution can be updated continuously with acquisition of more measurements. This paper uses advanced numerical integration [9] to calculate the denominator in Eq. 13. The probability distribution of the value q_i of the damage parameter θ_i can be calculated, and updated continuously with acquisition of more measurements.

5. OVERALL UNCERTAINTY IN DIAGNOSIS

The probability distribution calculated in the previous section is conditioned on two events: damage detection and localization being correct. This section develops the method to obtain the unconditional distribution of the damage parameter, i.e. overall uncertainty in diagnosis.

Let P_d denote the confidence in damage detection, as calculated in Section 2. This is equal to the probability that there is damage. Let P_i denote the confidence in isolation, as calculated in Section 3. This is equal to the probability that the damage is in θ , given that there is damage. The unconditional distribution of θ can be calculated as:

$$F_\theta(\theta) = (1-P_d) * F_{\theta}(\theta_{\text{healthy}}) + P_d * (1-P_i) * F_{\theta}(\theta_{\text{healthy}}) + P_d * P_i * F_{\theta}(\theta|\text{Damage is true, Damage is in } \theta) \quad (14)$$

The expression in Eq. 14 quantifies the overall uncertainty in the diagnosis procedure, by calculating the unconditional cumulative distribution of the damage parameter. Further, the corresponding probability density function can also be calculated by differentiating the expression in Eq. 14. The following sections illustrate the proposed methods through two numerical examples, a structural frame and a hydraulic actuation system.

6. ILLUSTRATION USING STRUCTURAL FRAME

Consider the two story frame discussed in Moustafa et al. [8]. This system has 6 parameters, $m_1, m_2, k_1, k_2, D_1, D_2$. The inputs to the system are forces at the two levels and the measured outputs are the accelerations at the two levels. The masses of the first and second floors are assumed not to change. Hence, there are only 4 parameters that could be affected by damage. Using the damage signatures (cause-effect relationships between the model parameters and measurements), it is possible to identify the floor that is damaged, and hence the prospective damage parameters are the stiffness and damping of that particular floor.

The value of k_1 is reduced to 80% at 5 seconds. This means a change from 30700 N/m to 24560 N/m. Sensor noise is simulated by adding Gaussian white noise to the measurements.

Damage detection is done through hypothesis testing, as explained in Section 2. A moving window is used to calculate the mean of the residuals and this mean is tested to detect damage. While classical statistics-based hypothesis testing detects

damage with 95% confidence, the Bayesian method facilitates easy quantification and updating of uncertainty from a 61% confidence at 5 seconds to 99.98% confidence at 5.05 seconds.

Following damage detection, three consecutive sets of measurements are assumed to be available. The qualitative damage localization results suggest that either k_I or D_I could be faulty. The heuristic measures of uncertainty using classical statistics-based methods yield 98% and 2% probabilities for k_I and D_I to be faulty, considering the 3 sets of measurements. The uncertainty in localization of k_I , using the Bayes method, is calculated for the I set as 99% , and updated using Bayes theorem for the following two sets to 100% and 100%.

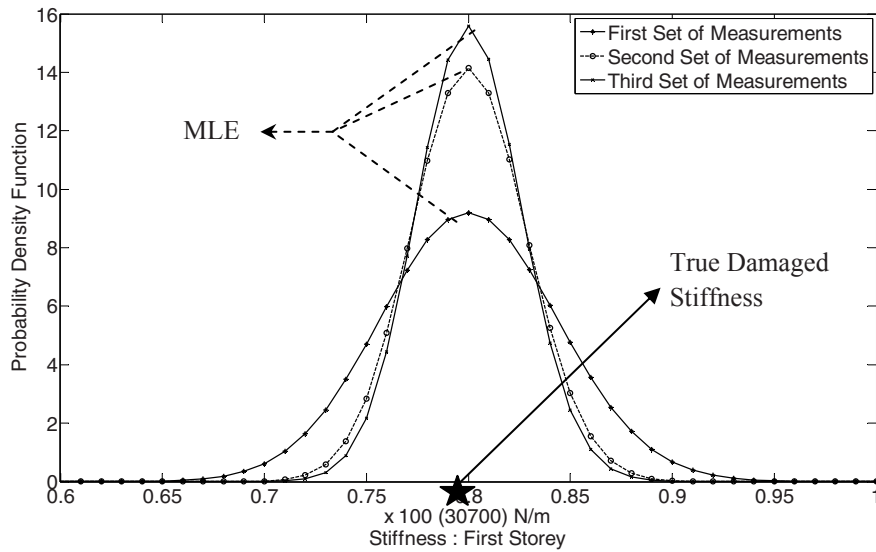


Fig. 1. PDF of k_I

Damage quantification using the classical statistics procedure yields a 90% confidence interval of (24509 N/m, 24612 N/m). This can be repeated for multiple confidence intervals and the approximation to the cumulative distribution function can be calculated. The Bayesian approach directly calculates the cumulative distribution function as explained in Section 4. The overall uncertainty in diagnosis can be calculated as in Section 5 and the corresponding PDF is shown in Fig. 1. From Fig. 1, it can be seen that (i) the maximum likelihood estimate (MLE) of k_I matches closely with the true damage value, and (ii) the uncertainty in the estimate of k_I decreases with acquisition of more measurements.

The above diagnosis procedure was also extended to five-story frames, where qualitative localization is able to isolate to the floor of damage accurately. Different damage scenarios were considered for the five-story frame, and these were detected and isolated (localized) satisfactorily with the proposed method. The damage was quantified with high accuracy. Uncertainty quantification associated with each of these three processes was also successful and both classical statistics-based and Bayesian methods were investigated. The easy extension to multi-story frames clearly indicates that this diagnosis methodology is applicable to practical structures.

7. HYDRAULIC ACTUATION SYSTEM

The developed approach for structural health monitoring is now illustrated for a hydraulic actuation system. The Pump-Actuator-Load system shown in Fig. 2 is modeled using bond graphs to aid in damage isolation. The system is described and studied in detail by Sankararaman et al. [10] and only the data and results pertaining to diagnosis uncertainty quantification are provided in this section.

Six different fault candidates are considered and five measurements are made from the system. Several faults were introduced in the system at $t = 150$ seconds and were diagnosed successfully. Measurements are collected at the rate of 2/sec. The uncertainties in damage detection, isolation and quantification were also quantified. One sample fault diagnosis example is discussed below.

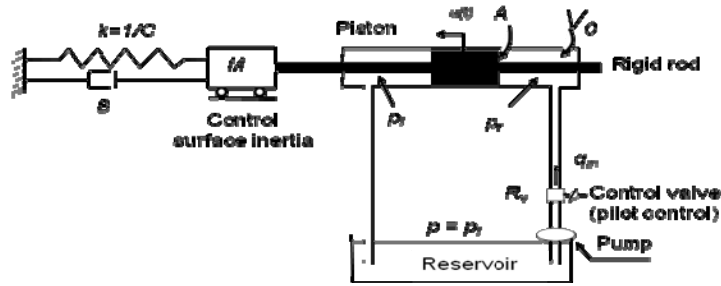


Fig. 2 Actuation System

The value of C , the load compliance, is suddenly doubled at 150 seconds. Similar to the previous section, measurements with noise are simulated by adding Gaussian white noise to the signals.

Damage detection is done through hypothesis testing, as explained in Section 2. A moving window is used to calculate the mean of the residuals and this mean is tested to detect damage. While classical statistics-based hypothesis testing detects damage with 95% confidence, the Bayesian method facilitates easy quantification and updating of uncertainty from a 52% confidence at 150 seconds to 99.1% confidence at 152 seconds.

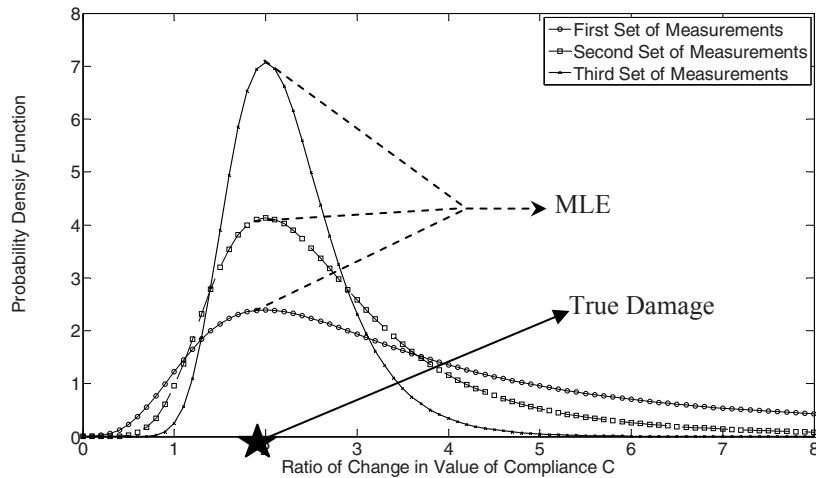


Fig. 3. PDF of Ratio of Increase in C

Following damage detection, three consecutive sets of measurements are assumed to be available. The qualitative damage localization results suggest that either C or B could be faulty. The heuristic measures of uncertainty using classical statistics-based methods yield 99.9% and 0.1% probabilities for C and B to be faulty, considering the 3 sets of measurements. The uncertainty in localization of C , using the Bayes method, is calculated for the I set as 99.9% , and updated using Bayes theorem for the following two sets to 100% and 100%.

Damage quantification using the classical statistics procedure yields a 90% confidence interval of (1.93, 2.06 N/m) for the ratio of increase. This can be repeated for multiple confidence intervals and the approximation to the cumulative distribution function can be calculated. The Bayesian approach directly calculates the cumulative distribution function as explained in Section 4. The overall uncertainty in diagnosis can be calculated as in Section 5 and the corresponding PDF is shown in Fig. 3. From Fig. 3, it can be observed that (i) the maximum likelihood estimate (MLE) of damage is reasonably equal to the true damage value, and (ii) the uncertainty associated with the PDF decreases with acquisition of more measurements.

8. SUMMARY

This paper developed methods to quantify the uncertainty in the three steps of damage diagnosis, i.e. damage detection, damage localization, and damage quantification. Classical statistics-based methods and Bayesian methods were investigated

for this purpose. Damage detection was based on statistical hypothesis testing. While the classical hypothesis testing procedure calculated the uncertainty in detection based on the significance level of testing, the Bayesian hypothesis testing procedure calculated the likelihood of “no damage” scenario to “damage” scenario, thereby providing a robust Bayesian metric to assess the confidence in detection. The uncertainty in localization was quantified using heuristic measures in the classical statistics-based approach while the Bayesian method directly quantified the probability that a given damage parameter is faulty. The uncertainty in damage quantification was expressed in statistical confidence intervals in the classical statistics-based approach while the Bayesian method gives the entire probability distribution of the damage parameter. Finally, the uncertainties in the three different steps were combined to determine the PDF of the damage parameter as a measure of the overall uncertainty in diagnosis. While the two methods are fundamentally different and hence, it may not be correct to compare the results from the two methods, it is evidently seen that the Bayesian method is easy to implement and interpret. Further, the Bayesian method also facilitates easy updating of uncertainty with acquisition of measurements. The scope of this paper was limited to single faults only; in realistic problems, several faults may occur in the system. This will be considered in future work.

9. ACKNOWLEDGEMENT

This study was partly supported by funds from the U. S. Air Force Research Laboratory through subcontract to General Dynamics Information Technology (Contract No. USAF-0060-43-0001, Project Monitor: Mark Derriso). The support is gratefully acknowledged.

10. REFERENCES

- [1] Achenbach, J.D. Quantitative nondestructive evaluation, International Journal of Solids and Structures, Volume 37, Issues 1-2, January 2000, Pages 13-27, ISSN 0020-7683, DOI: 10.1016/S0020-7683(99)00074-8.
- [2] Guratzsch, R. Sensor placement optimization under uncertainty for structural health monitoring systems of hot aerospace structures. Ph.D. Dissertation, Vanderbilt University, Nashville, TN. 2007.
- [3] Dalai, M., Weyer, E., and Campi M.C. Parametric Identification of Nonlinear Systems : Guaranteed Confidence Regions. Proceedings of the 44th IEEE Conference on Decision and Control, and the European Control Conference 2005 Seville, Spain, December 12-15, 2005.
- [4] Beck J.L, Au S.K, and Vanik M.V. Monitoring structural health using a probabilistic measure. *Computer-Aided Civil and Infrastructure Engineering* 2001; **16**:1–11.
- [5] Jiang, X., and Mahadevan, S. Bayesian Wavelet Methodology for Structural Damage Detection. *Struct. Control Health Monit.* 2008; **15**:974–991.
- [6] Sankararaman, S., and Mahadevan, S. Uncertainty Quantification in Structural Damage Diagnosis. doi: 10.1002/stc.400 Published Online May, 2010.
- [7] Migon H.S, and Gamerman D. Statistical Inference: An Integrated Approach. Arnold: London, 1999.
- [8] Moustafa, A., Mahadevan, S., Daigle, M., Biswas, G. Structural and Sensor Damage Identification using the Bond Graph Approach. J. International Association of Structural Control and Health Monitoring. Published Online Jul. 2008.
- [9] McKeeman, M.W. Algorithm 145: Adaptive numerical integration by Simpson's rule. *Commun. ACM*, Vol. 5, No. 12, Aug. 1962.
- [10] Sankararaman, S., Bartram, G., Biswas, G., and Mahadevan, S. 2009. Bond Graph Method for Hierarchical Multi-Domain Systems Diagnosis. In the Proceedings of 7th International Workshop on Structural Health Monitoring, Stanford, CA. Sept. 9-11, 2009.

A Framework for Embedded Load Estimation from Structural Response of Wind Turbines

Antonio V. Hernandez, Ph.D. Pre-Candidate, Department of Civil and Environmental Engineering,
Michigan Technological University, 1400 Townsend Dr., Houghton, MI 49931

R. Andrew Swartz, Assistant Professor, Department of Civil and Environmental Engineering, Michigan
Technological University, 1400 Townsend Dr., Houghton, MI 49931

Andrew T. Zimmerman, Post-Doctorate Fellow, Department of Civil and Environmental Engineering,
University of Michigan, 2350 Hayward Ave, Ann Arbor, MI 48109

Abstract The international push in the development of energy that is sustainable in the long term is driving technological improvements in the area of wind-generated energy. Pushing the limits of current knowledge, turbines now feature increasingly slender towers, larger gear boxes, and significantly longer blades in search of greater capacities and improved efficiency. In addition, siting concerns are leading planners to build these structures in increasingly challenging environments where they are subject to harsh and poorly characterized loadings (particularly in off-shore applications where wind and wave interactions are poorly understood). Future safe and economical designs require accurate characterization of design loads, however direct measurement of wind loads on turbines can be problematic due to the disturbance caused by the wind's interaction with the turbine blades. This paper presents a novel means of estimating wind loading from the dynamic response of the turbine tower to these loads. A model of the structure is derived using the assumed modes method and then updated using dynamically collected acceleration data where the input-output relationships are established and input loading spectra estimated. The method relies on reduced-order modal space models making it suitable for real-time operation or embedment in a low-cost autonomous (perhaps wireless) monitoring system. Results derived for a full scale structure under lateral seismic loading are presented.

Introduction

Renewable energy sources are garnering considerable attention in light of growing concerns regarding the finite supply of traditional fossil fuels, not to mention the environmental and geopolitical impacts that result from their use. Impediments to increased usage and acceptance of renewable resources in critical energy infrastructure systems are based largely on political, economic, environmental, and reliability concerns [1-3]. In the US, Federal subsidies have helped to increase renewable energy's share of the total energy capacity from 81,321 million kWh in 2000 to 125,422 million kWh (over 10% of the total installed capacity) in 2008 [4] and helped to make these energy sources economically competitive with legacy energy technologies (even after accounting for Federal subsidies that are provided to those industries) [4, 5]. The fastest growing renewable energy technology at this time is wind power [4]. Wind power represents approximately 60% of the installed non-hydro renewable energy capacity in the US and 50% of the growth in energy capacity in the US over all energy sources [4, 6]. While the sector's current growth rate is encouraging, continued growth and acceptance of wind power faces significant barriers. Installation and maintenance costs are critical for wind turbine structures, particularly given their relative novelty and the large number necessary to replace a single traditional power plant (e.g., coal, natural gas, or nuclear) [7] as well as the expected downtime individual turbines will experience during periods of low wind or maintenance [1, 8]. Poorly characterized (random) design loads and the use of novel composite materials can lead to overly conservative designs that erode profitability and consequently, attractiveness. Unknown operational state (condition) and overly frequent maintenance and inspections coupled with the high cost of generator downtime will also lead to reduced profitability [1]. To address design concerns as well as concerns regarding operational maintenance (including structural health monitoring) the National Renewable Energy Lab (NREL) has identified load characterization as one of the most pressing research needs to help ensure the future of the nascent wind power industry [9]. Previous extensive work characterizing loads for ships [10] and oil drilling platforms [11] has tended to focus on wave loads, as these structures tend to be shorter and less exposed to wind loading than

are turbine towers [12, 13]. Additional field data to characterize the interactions between these loads will be critical in the development of turbines in off-shore [9, 14] and other extreme environments.

The most straightforward approach to characterize stochastic loadings on structures is through direct measurement campaigns in the field; however, direct measurement of wind loads acting on wind turbines is complicated by the fact that wind flow is disturbed during its interaction with the turbine blades [8, 15]. The typical megawatt capacity horizontal axis wind turbine (HAWT) in service today is designed with an active yaw system that keeps the turbine blades facing into the wind during operation [8]. This practice results in improved safety and performance for the turbine, however wind measurement instrumentation mounted to the tower or the nacelle is only able to measure the profile of the wind after it has been disturbed by its interaction with the turbine blades, during which energy and frequency content of the wind is altered [15]. Ideally, wind measurements would be collected from an external measurement tower located upwind from the wind turbine. However, the construction of a single dedicated measurement tower to obtain undisturbed wind measurements at appropriate heights above ground represents an unwelcome expenditure for wind energy producers.

To overcome these limitations, this study proposes a load estimation framework to extract input loadings from the measured dynamic response of the turbine tower itself. Load estimation from dynamic response has its origin in both small-scale and large-scale applications [16]. Observer based methods have been used to estimate loads on rotating machines [17, 18]. Similar methods have been used successfully in the control community to estimate characteristics of unwanted disturbance loads [19-21] in order to improve controller performance; however, these methods rely on the availability of a known, controllable input source. Load estimation from vibrations of passive systems using black-box, system identification techniques was first developed for the aerospace domain [22]. Load estimation from structural response was later adapted for civil engineering structures in applications that include stochastic bridge loading [23], crowd induced loading of sports stadiums [24], wind loads on roofs [25, 26], lattice domes [27], shells [28], towers [29-31], tall buildings [31], and wind turbine blades [32]. Naturally, all of these methods rely on a model of the system in question. It has been clearly demonstrated that a highly accurate estimate of loading can be found using a high-order model based on the finite element method (FEM) [25, 27, 28], however, such a large model is very impractical to embed within a wireless sensor network due to its computational complexity and memory requirements. Methods based on non-mechanistic system identification techniques, such as autoregressive time-series models [29] and state-space realizations [30, 31], have shown promise due to their relatively low computational demand and, when coupled with the Kalman filter [31, 33], these models can be autonomously updated to account for modeling error, as well as behavioral changes due to the environment, changes in usage, or even damage. However these models, constructed using totally data-driven methods, will not be able to distinguish between persistent input harmonics, and dynamics inherent to the structure to be modeled [34]. This limitation means that persistent wave dynamics (in offshore turbines) may appear as part of the model. In addition, the ability of these models to represent desired subsystems of the structure (*e.g.*, a single blade, or the tower and nacelle) is greatly limited due to the coupling of the complete system.

To overcome these limitations, it is proposed to develop a low-order, modal-domain, mechanistic model that can be used for autonomous load estimation of wind turbine structures using wireless sensor networks. This framework includes a model updating step to limit the estimation errors due to modeling error or variations in time of the dynamic behavior of the structure (*e.g.*, due to environmental effects). The model of the structure is mechanistic and derived in the modal domain to reject the inclusion of spurious modes that may appear due to sensor noise, mathematical artifacts of a system identification algorithm, or unknown and persistent input harmonics. The theoretical background behind this study is presented in the following section. After the theoretical background is a description of the experimental setup. Results and discussion follow.

Theory

This study seeks to develop a novel, robust, and highly-accurate framework for estimating lateral loading on wind turbines from measurements made of the dynamic response of the tower itself. The framework is developed to utilize low-order, autonomously updatable, mechanistic models that may be suitable for embedded execution in low-cost wireless sensor networks. Models are to be autonomously updated to eliminate the effects of errors arising from differences between design and as-built conditions, as well as those due to environmental changes. Mechanistic models are necessary to restrict the autonomous system identification algorithm to physically meaningful model parameters. This study presents a novel load estimation framework that utilizes a low-order, mechanistic model based on the assumed modes method (AMM), that is capable of describing multi-input, multi-output (MIMO) systems, and can describe either the turbine structure in its entirety, or into its constituent components (*i.e.*, tower, blades, nacelle, *etc.*). To minimize errors inherent in the inverse estimation problem, that model is autonomously updated from operational data within a low-cost wireless sensor network via a parallel simulated annealing search algorithm that minimizes the difference between modal properties realized from the AMM model,

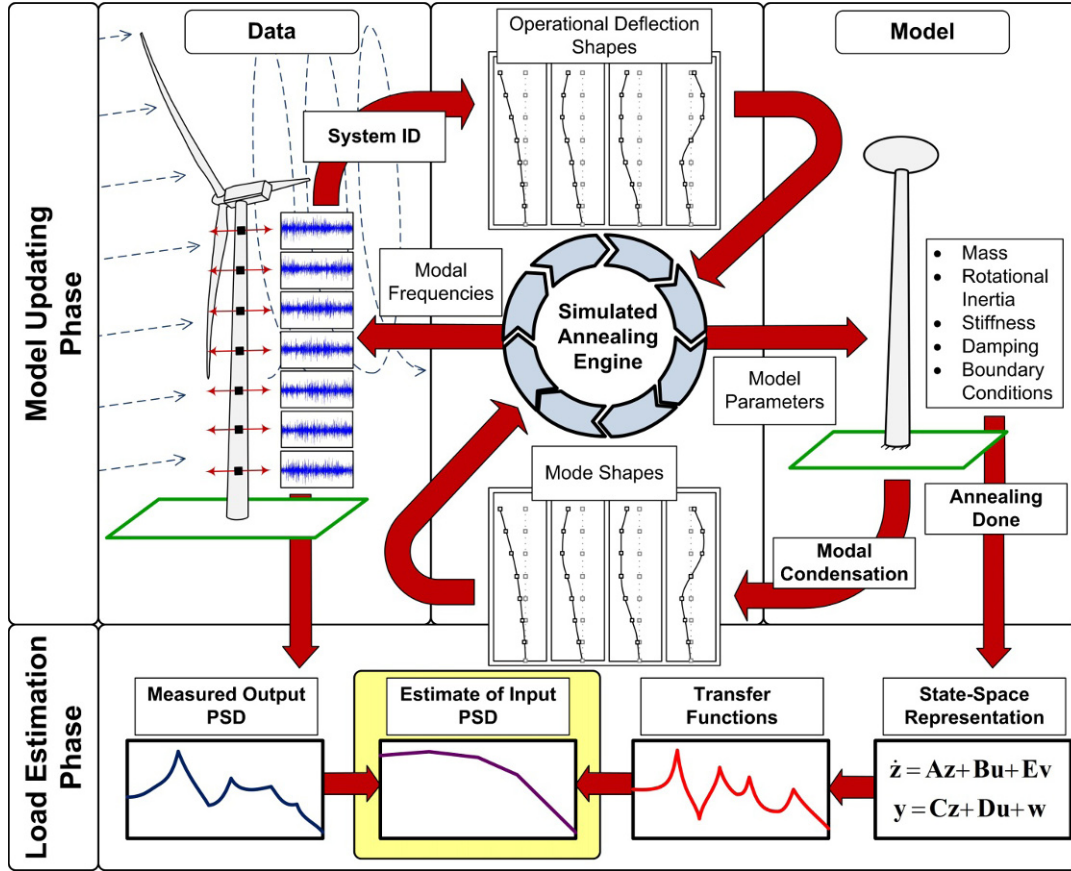


Fig. 1. Summary of proposed load estimation framework including the model updating phase and load estimation phase

and estimates of modal properties derived from operational data using a parallel frequency domain decomposition (FDD) algorithm. The updated model, that maps inputs of interest to sensor outputs, is then inverted to identify input spectra from the known outputs. One key component of this method is the fact that it employs a mechanistic model that is constrained by available information regarding the physics of the turbine structure, a fact that greatly enhances the autonomy of the model updating step. A second key aspect of this framework is the use of algorithms with low data transfer demand to allow it to scale to large sensor networks without exhausting available wireless communication bandwidth. Figure 1 depicts a high-level summary of the proposed framework.

Modeling Using the Assumed Modes Method

Fusing the results of a system identification approach with a mechanistic model will generate useful restrictions on the form of the system identification model that are consistent with the physical system under consideration. To achieve this fusion, the input estimate is based on a mechanistic model of the structure built using the assumed modes method (AMM). The AMM is a spatially-continuous, energy-based method for estimating modal properties (eigenvalues and eigenvectors) of distributed mass/stiffness structures and is closely related to the Rayleigh-Ritz method [35, 36]. The method assumes a solution of a boundary-value problem of a conservative system in the form:

$$y(x, t) = \sum_{i=1}^n \phi_i(x) q_i(t) \quad (1)$$

where $q_i(t)$ are generalized coordinates and $\phi_i(x)$ are a set of orthogonal trial functions that fit the geometric boundary conditions of the structure (though not necessarily the natural boundary conditions). The trial functions are differentiable and complete, with an infinite set of trial functions ($n = \infty$) leading to an exact solution to the boundary value problem [35],

while a finite set of trial functions will yield an approximate solution. Kinetic energy, $T(t)$, and potential energy, $U(t)$, may then be expressed by taking the partial derivative with respect to x :

$$T(t) = \frac{1}{2} \sum_{i=1}^n \sum_{j=1}^n m_{ij} \dot{q}_i(t) \dot{q}_j(t) \quad U(t) = \frac{1}{2} \sum_{i=1}^n \sum_{j=1}^n k_{ij} q_i(t) q_j(t) \quad (2)$$

where m_{ij} and k_{ij} are consistent mass and stiffness matrices respectively based on the respective mass and stiffness distributions of the assumed trial functions [35]. These expressions for kinetic and potential energy simplify Lagrange's equation for conservative systems, reducing it to the matrix form:

$$[\mathbf{m}]\{\ddot{\mathbf{q}}(t)\} + [\mathbf{k}]\{\mathbf{q}(t)\} = \{\mathbf{0}\} \quad (3)$$

whose eigen-solution consists of eigenvalues, $\lambda_r = \omega_r^2$, where ω_r is the r^{th} natural frequency of the system (regardless of coordinates), and eigenvalues, ψ_r , are related to the mode shapes of the system through a simple change of basis operation from the space defined by the assumed trial functions, to generalized coordinates [36]. Consistent mass and stiffness matrices, \mathbf{m} and \mathbf{k} , may be derived as:

$$m_{ij} = \int_0^L \rho A(x) \phi_i(x) \phi_j(x) dx + M(x) \phi_i(L+e) \phi_j(L+e) + J \frac{d\phi_i(L)}{dx} \frac{d\phi_j(L)}{dx} \quad (4)$$

$$k_{ij} = \int_0^L EI(x) \frac{d^2 \phi_i(x)}{dx^2} \frac{d^2 \phi_j(x)}{dx^2} dx$$

where ρ is the density of the tower material, A is the cross-sectional area (and can vary with height), M is the mass of the nacelle assembly, J is the rotational stiffness of the nacelle, E is the modulus of elasticity of the tower material, and I is the moment of inertia of the tower cross section (also variable by height)

The advantages of using the AMM in this context are fourfold. First, estimated modal frequencies are limited to sets that are consistent with the known physics of the structure. That is to say that the model based on the AMM will only incorporate identified modes that are consistent with the mechanistic model eliminating spurious apparent modes arising from mathematical artifacts, electronic filter imperfections, or persistent input harmonics. Second, the AMM is based on a very small order modal-domain model, the solution to which is many orders of magnitude easier to obtain than that generated using a spatial-domain FEM model. This computational demand reduction is vital for any process proposed for embedment in low-cost wireless networks. Third, the AMM takes in physical parameters of the system as its inputs and yields modal frequencies and mode shapes based on those parameters. By updating the estimates of these parameters, a match between mode shapes and modal frequencies identified from collected data can be found. Finally, dynamics of specific structural subsystems may be isolated through decomposition of the model to estimate input spectra for the entire structure, or just certain components. In this way, changes in the structure (or its model) due to environmental factors, usage changes, degradation, or modeling error can be realized without allowing the model (through unsupervised system identification or adaptive filtering) to incorporate physically unrealizable modal features.

The assumed modes method yields a set of eigenvalues and eigenvectors that, together with some basic assumptions about the mass distribution within the turbine, can be used to produce a state-space model of the structural dynamics of the turbine. State-space models inherently support MIMO system dynamics. A sufficiently dense network of output sensors is required to characterize the inputs of interest. A single-input, multiple-output (SIMO) state-space mode of the structure is assembled using the mass and matrix of modal frequencies, $\mathbf{\Omega}$, and mode shape matrix, $\mathbf{\Phi}$, returned from the model updating engine based on:

$$\begin{aligned} \dot{\mathbf{z}}(t) &= \mathbf{A}\mathbf{z}(t) + \mathbf{B}u(t) \\ \mathbf{z}(t) &= [\mathbf{v}(t)^T \quad \dot{\mathbf{v}}(t)^T]^T \\ \mathbf{y}(t) &= \mathbf{C}\mathbf{z}(t) + \mathbf{D}u(t) \end{aligned} \quad (5)$$

where \mathbf{v} is the vector of lateral tower displacements, \mathbf{A} is the state matrix, \mathbf{B} is the input matrix, \mathbf{C} is the output matrix, and is the direct feed-through term:

$$\mathbf{A} = \begin{bmatrix} [\mathbf{0}] & [\mathbf{I}] \\ [-\mathbf{M}^{-1}\mathbf{K}] & [-\mathbf{M}^{-1}\mathbf{C}_d] \end{bmatrix}, \mathbf{B} = \begin{bmatrix} [\mathbf{0}] \\ [\mathbf{M}^{-1}\mathbf{T}] \end{bmatrix} \quad (6)$$

$$[\mathbf{M}^{-1}\mathbf{K}] = [\Phi][\Omega][\Phi]^{-1}, [\mathbf{M}^{-1}\mathbf{C}_d] = a_1 + a_2[\mathbf{M}^{-1}\mathbf{K}]$$

and the parameters a_1 and a_2 are constants calculated using an estimate of (Rayleigh) damping for the structure. To simplify the input matrix, the distributed mass is assumed to be negligible with respect to the influence of ground motion on the response of the structure; therefore \mathbf{T} is taken to be $[0 \ \cdots \ 0 \ 1]^T$. For acceleration sensors, the matrices \mathbf{C} is the bottom half of the \mathbf{A} matrix and \mathbf{D} is the ones vector. The state-space model yields the i^{th} term of the transfer matrix form via:

$$H_i(j\omega) = \mathbf{C}_i(j\omega\mathbf{I}_{2n} - \mathbf{A})^{-1}\mathbf{B} + D_i \quad (7)$$

that can be used to generate estimate input spectra the standard input/output relationship:

$$Y_i(j\omega) = H_i(j\omega)U(j\omega) \quad (8)$$

Simulated Annealing Model Updating

A key component of this proposed framework is the development of an automated model updating algorithm for the wind turbine structure. Because it is desired to collect operational data to estimate inputs under a broad range of conditions that will cause variations in the dynamic behavior of the turbine structure, it is not sufficient to perform a single model update operation (that might easily be performed manually) to rectify the design model to the as-built model. Instead, to account for environmental variations (or even damage), near-continuous updating of the model is desired. Obviously, frequent and continuous model updating on a large number of turbine structures must be automated. To accomplish this task, it is necessary to search a space of model parameters and minimize the error between the model and observed data. This study uses a model updating engine based on simulated annealing to keep the inverse model tuned to the real-time dynamic behavior of the structure.

Global optimization searches can be computationally intensive, a problem in low-cost wireless sensor networks, because individual sensor nodes lack significant computational power and memory compared with a typical desktop personal computer (PC). However, within a wireless sensor network, there exists significant distributed computing power [37]. Thusly, an optimization algorithm that can take advantage of the distributed computing resources and work in a parallel manner is necessary [38, 39]. Simulated annealing is capable of converging to a global minimum despite the presence of multiple local minima and has been demonstrated to parallelize well [40]. Simulated annealing is a mathematical analog for the process by which physical materials converge to an optimal energy state as they cool [41, 42]. The algorithm treats search parameters as random variables, making assignments to these variables and calculating objective function values that result. The algorithm makes many assignments to these variables, sometimes retaining the set that minimizes the objective function, but also randomly retaining non-optimal sets to avoid convergence to local minima [42]. The process is repeated iteratively. The “temperature” of the search determines the probability that sub-optimal sets of realizations are retained. As the temperature is slowly reduced, the number of sub-optimal realizations accepted by the algorithm is reduced until the global minimum is realized, resulting in the model parameters that yield dynamic behavior that matches the data collected.

Experimental Methods

A computational validation study is undertaken for a representative wind turbine structure undergoing simulated base excitations on a shaking table. The structure is a 65 kW wind turbine tested at the Network for Earthquake Engineering Simulation (NEES) facility at the University of California, San Diego (UCSD). The structure was manufactured by the Nordtank Corporation and donated for seismic testing using the 7.6 by 12.2 m outdoor shaking table at UCSD [43]. The tower of the structure is approximately 22 m high with a rotor diameter of approximately 16 m. The tower is composed of three sections with hollow circular cross sections with diameters that decrease with height. These sections are joined via

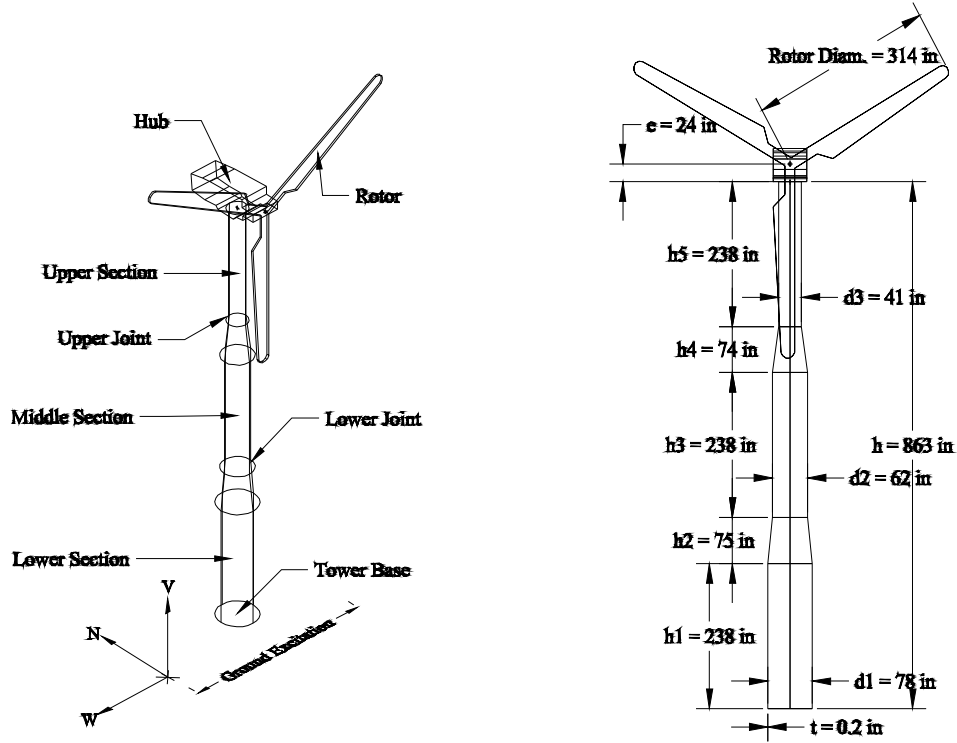


Fig. 2. Wind turbine structure and dimensions

tapered sections, see Figure 2. The structure is excited laterally at the base. Wireless smart sensors are installed along the height of the tower to collect and record acceleration data from the response of the structure to the base excitation. An additional sensor measures base acceleration and stores it as the input to the system (for validation of the load estimation procedure). Traditional cable-based sensors are installed in parallel for validation of the wireless data. Analysis of the data, model updating, and load estimation are performed offline.

Sixteen physical parameters are identified for updating using the simulated annealing algorithm and used to build the AMM model of the structure. These parameters consist of material properties, including modulus of elasticity (E) and density (ρ), section properties including the cross-sectional area of each tower section (A_1, A_2, A_3) and moments of inertia for each section (I_1, I_2, I_3), and structural dimensions, including tower section heights (L_1, L_2, L_3 , and L_4), total tower height (L), tip mass (M), tip mass eccentricity (e), and rotational inertia of the tip mass (J). Expressing the kinetic and potential energy of the structure in terms of these parameters and the assumed basis functions (Equation 4), the consistent mass and stiffness matrix terms are expressed in terms of the height along the tower and integrated over each section of the tower. The contributions from each section is integrated and added to form the mass and stiffness matrix terms.

These sixteen physical parameters represent the modeling degrees of freedom allotted to the simulated annealing algorithm. The simulated annealing search algorithm makes random assignments to the set of physical parameter producing \mathbf{m} and \mathbf{k} matrices according to Equation 4. Random assignments to well-known quantities (e.g., length values and section properties) are afforded relatively small variability to keep the model updating process well behaved and reduce convergence times. The solution of the eigen-problem in Equation 3 produces eigenvalues that are the square of the modal frequencies of the realized model, and eigenvectors that become mode shapes with a change of basis transformation into generalized coordinates. Operational deflection shapes can be extracted from the collected data at the modal frequency of the model via a parallelizable frequency domain decomposition (FDD) algorithm [44]. The distance between the mode shape of the model and the data-driven operational deflection shape (using the modal assurance criterion as a measure) is then used as part of the objective function that determines the fitness of the model to data. In addition, under the assumption that the noise, though colored, does provide some excitation within the spectral vicinity of the modal resonant frequencies, and that most sensors are not be placed at nodes of the modes of interest of the structure, it is further assumed that the measured outputs with exhibit peaks in their spectra consistent with resonance. A measure of the “peakness” of a frequency in the measured output (relative to its surrounding frequencies) is also included in the objective function. Finally, an *a priori* estimate of the first

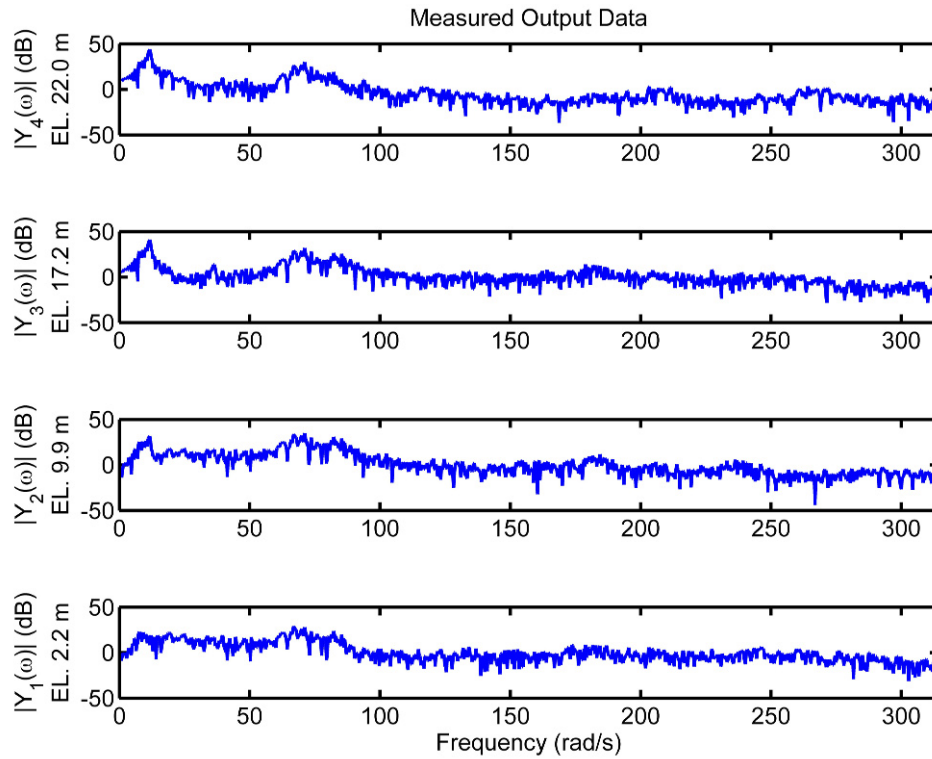


Fig. 3. Representative measured output accelerations at four heights on the tower

modal frequency of the structure (as determined from its design parameters) is included as a third term of the objective function under the assumption that computation of the fundamental resonant frequency of the turbine is well within the abilities of the design engineer. To accommodate minor variations in this frequency (*e.g.*, due to environment factors), this value is not locked, but realizations that produce large variations from the computed frequency are penalized according to the size of the variation.

Results

Data collected from the turbine tower as the structure was shaken was used to update the AMM model of the structure using the simulated annealing model updating engine. Updated model properties match reasonably well to the anticipated values taken from the design of the turbine (Table 1). Modal frequencies for the first three flexural modes were identified at 10.7, 84.8, and 195 rad/s and later confirmed through a subsequent modal identification study using the measured based loading signal. Figure 3 presents output acceleration measurements made at multiple points along the tower height. The transfer functions obtained from the state space model derived from Equations 5-6 for the physical properties returned by the simulated annealing model updating algorithm are depicted in Figure 4. The input estimate constructed from the individual tower measurements and the identified transfer function is presented in Figure 5. As can be seen in Figure 5, significant spurious spectral energy was present in the input signal in the vicinity of 69.1 rad/s. This peak is also clearly present in the recorded output signal. The mechanistic model does not allow for two closely spaced flexural modes within this region, and correctly rejects this apparent mode. Figure 6 depicts data-driven operational deflection shapes derived from the colored input driven output data overlaid with the mode shapes derived from the AMM model.

Table 1. Key model parameters as updated by the simulated annealing model updating engine.

Parameter	E (GPa)	ρ (kg/m ³)	L (m)	M (kg)	J (kg*m ²)	e (m)
Design Value [43]	200	7850	21.9	4300	--	0.7
Annealed Value	201.7	7955	21.1	4881	5861	0.49

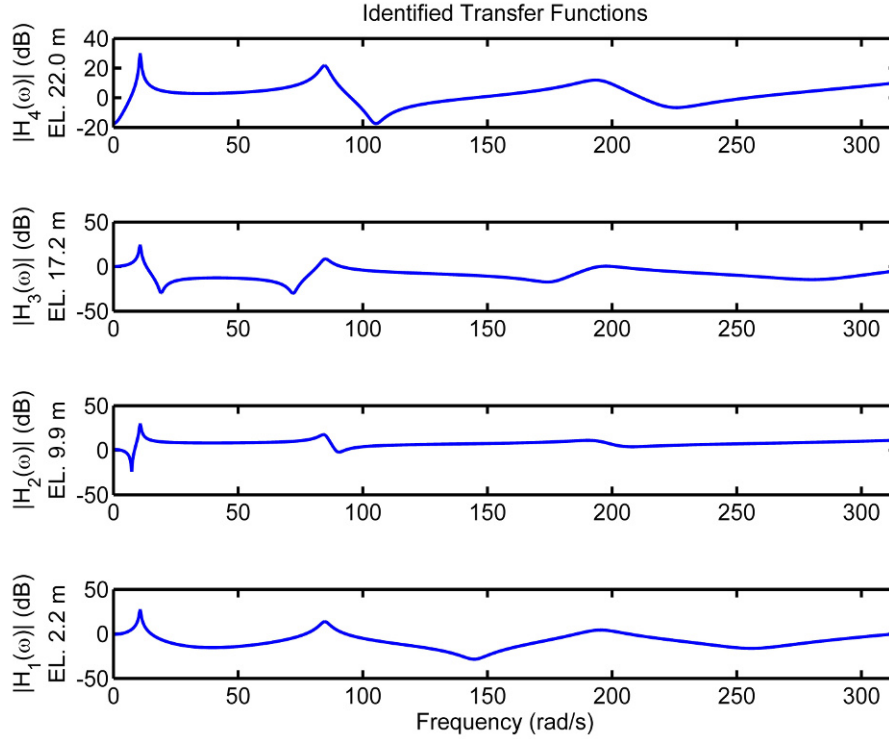


Fig. 4. Representative identified transfer functions at four heights on the tower

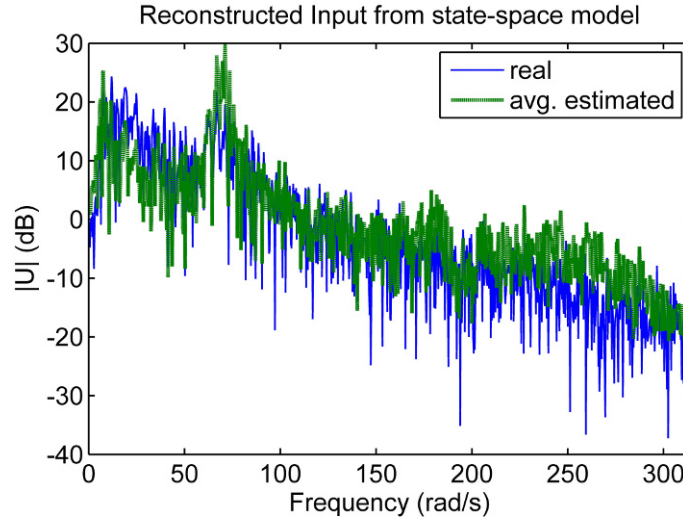


Fig. 5. Estimated input spectra reconstructed from multiple measured outputs and plotted against the measured spectra for validation

Despite the distortions in the operational deflection shapes, the algorithm selects the correct modal frequencies. In this figure, the peaks present in the output signal associated with the flexural modes of the tower have been removed, leaving an estimate of the input signal that still includes both the persistent harmonics the input signal as well as harmonics associated with the blades. Through use of the mechanistic model, the automated model updating algorithm was able to avoid characterizing these dynamics as part of the tower dynamics (as would a data-driven system identification algorithm), instead correctly preserving them as part of the input.

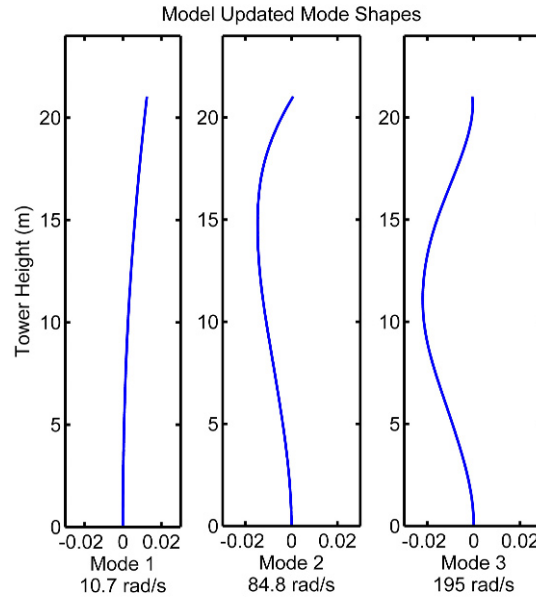


Fig. 6. Spatially continuous mode shapes identified by the assumed modes method model using the simulated annealing algorithm model updating engine

Conclusions

This study presents an application of a load estimation framework for use in wind turbine structures to estimate *in-situ* dynamic loads that may inform future turbine designs, improve control algorithms, estimate fatigue life expended, or form the basis of structural health monitoring algorithms. In the proposed framework the measured dynamic response is used as a starting point to estimate unknown input forces. A model of the structure is developed, inverted, and used to estimate the desired input. The framework uses model updating to account for model uncertainty and time variation in the dynamic behavior of the system in order to reduce errors in the inverse model. The framework also employs a modal domain, mechanistic model to constrain the form of the model and reject spurious modes. The framework was applied to a 65 kW wind turbine subjected to base accelerations simulating seismic excitation. The algorithm was demonstrated to be effective in estimating the input spectra of the ground motion applied. The algorithm successfully discriminated between peaks in the output spectra associated with the dynamics of the turbine tower and peaks in the output spectra associated with persistent harmonics in the input acceleration and did so without knowledge of the input signal.

Further work is necessary in developing the proposed algorithm before widespread adoption is recommended. The current implementation of the algorithm is reliant upon an *a priori* estimate of the first modal frequency of the structure. While this estimate is not unreasonable to compute, elimination of the need for this estimate is desired. In addition, the current algorithm is limited to flexural modes in a single direction. Because the structure was only excited unidirectionally, experimental validation of the framework's ability to handle out-of-plane flexure or even torsional modes will be validated using input/output data generated by a finite element model based on the updated structural properties found in this study. Finally, a demonstration of embedded operation of the load estimation framework within an autonomous system is required to demonstrate its efficacy within a memory and power limited wireless sensor network. Tradeoffs between model size, convergence time (in the model updating engine), and estimation accuracy must be explored and characterized using the limited resources available to wireless smart sensors.

Acknowledgements

The authors would like to express their gratitude to Prof. Jerome P. Lynch of the University of Michigan, Ann Arbor, MI, and Ian Prowell of UC, San Diego for their generous support of work on this project.

References

- [1] Valentine, S.V., *A STEP toward understanding wind power development policy barriers in advanced economies*. Renewable and Sustainable Energy Reviews, **14**(9): p. 2796-2807. 2010.
- [2] Cabooter, Y., L. Dewilde, and M. Langie. *An inventory of locations suitable for wind energy in Flanders region*. in *1999 European Wind Energy Conference*. Nice, France. 1999.
- [3] InterAcademy Council, *Lighting the Way: Toward a Sustainable Energy Future*. IAC: Amsterdam, The Netherlands. 2007.
- [4] US Department of Energy (DOE), *2008 Renewable Energy Data Book*, in *Energy Efficiency & Renewable Energy*. US Department of Energy: Washington DC. 2009.
- [5] US Department of Energy (DOE), *Wind Energy Multiyear Program Plan for 2007-2012*. U.S. Department of Energy: Washington D. C. 2006.
- [6] National Renewable Energy Lab (NREL), *Wind Power Today 2010*. U.S. Department of Energy, Office of Scientific and Technical Information: Oak Ridge, TN. 2010.
- [7] Morthorst, P.E., *Wind Energy - The Facts, Volume 2, Costs and Prices*. European Wind Energy Association: Brussels, Belgium. 2004.
- [8] Hau, E., *Wind Turbines: Fundamentals, Technologies, Applications, and Economics*, Berlin, Germany: Springer. 2006.
- [9] Butterfield, S., S. Sheng, and F. Oyague. *Wind energy's new role in supplying the world's energy: what role will structural health monitoring play?* in *Proceedings of the 7th Annual Workshop on Structural Health Monitoring*. Stanford, CA. 2009.
- [10] Haddara, M.R. and C.G. Soares, *Wind loads on marine structures*. Marine Structures, **12**(3): p. 199-209. 1999.
- [11] Lighthill, J., *Fundamentals concerning wave loading on offshore structures*. Journal of Fluid Mechanics, **173**: p. 667-681. 1986.
- [12] Musial, W., S. Butterfield, and A. Boone. *Feasibility of floating platform systems for wind turbines*. in *Proceedings of the 23rd ASME Wind Energy Symposium*. Reno, NV. 2004.
- [13] Faltinsen, O.M., *Sea Loads on Ships and Offshore Structures*, Cambridge, UK: Cambridge University Press. 1990.
- [14] Butterfield, S., W. Musial, J. Jonkman, and P. Sclavounos. *Proceeding of the Engineering Challenges for Floating Offshore Wind Turbines*. in *2005 Copenhagen Offshore Wind Conference*. Copenhagen, Denmark. 2005.
- [15] Medici, D. and P.H. Alfredsson, *Measurements on a wind turbine wake: 3D effects and bluff body vortex shedding*. Wind Energy, **9**(3): p. 219-236. 2006.
- [16] Stevens, K.K. *Force identification problems: an overview*. in *Proceedings of the 1987 SEM Spring Conference on Experimental Mechanics*. Houston, TX. 1987.
- [17] Gibson, A.O. and J.L. Stein. *Linear observer based approach for estimating spindle bearing loads*. Atlanta, GA, USA: ASME. 1996.
- [18] Kim, D.-H., K.-S. Hong, and K. Yi, *Driving load estimation with the use of an estimated turbine torque*. JSME International Journal, Series C: Mechanical Systems, Machine Elements and Manufacturing, **49**(1): p. 163-171. 2006.
- [19] Abidi, K., A. Sabanovic, and S. Yesilyurt. *Sliding mode control based disturbance compensation and external force estimation for a piezoelectric actuator*. in *Proceedings of the 8th IEEE International Workshop on Advanced Motion Control*. Piscataway, NJ, USA: IEEE. 2004.
- [20] Ronkanen, P., P. Kallio, and H.N. Koivo. *Simultaneous actuation and force estimation using piezoelectric actuators*. in *Proceedings of the IEEE International Conference on Mechatronics and Automation*. Piscataway, NJ, USA: IEEE. 2007.
- [21] Nurung, S., K.C. Magsino, and I. Nilkhamhang. *Force estimation using piezoelectric actuator with adaptive control*. in *Proceedings of the 6th International Conference on Electrical Engineering/Electronics, Computer, Telecommunications and Information Technology (ECTI-CON)*. Piscataway, NJ, USA: IEEE. 2009.
- [22] Liu, J.-J., C.-K. Ma, I.-C. Kung, and D.-C. Lin, *Input force estimation of a cantilever plate by using a system identification technique*. Computer Methods in Applied Mechanics and Engineering, **190**(11-12): p. 1309-22. 2000.
- [23] Yu, L. and T.H.T. Chan, *Recent research on identification of moving loads on bridges*. Journal of Sound and Vibration, **305**(1-2): p. 3-21. 2007.
- [24] Ellis, B.R. and J.D. Littler, *Response of cantilever grandstands to crowd loads. Part 2: load estimation*. Proceedings of the Institution of Civil Engineers. Structures and Buildings, **157**(5): p. 297-307. 2004.
- [25] Uematsu, Y., M. Yamada, and A. Sasaki, *Wind-induced dynamic response and resultant load estimation for a flat long-span roof*. Journal of Wind Engineering and Industrial Aerodynamics, **65**(1-3): p. 155-166. 1996.
- [26] Uematsu, Y., K. Watanabe, A. Sasaki, M. Yamada, and T. Hongo, *Wind-induced dynamic response and resultant load estimation of a circular flat roof*. Journal of Wind Engineering and Industrial Aerodynamics, **83**(1-3): p. 251-261. 1999.

- [27] Uematsu, Y., O. Kuribara, M. Yamada, A. Sasaki, and T. Hongo, *Wind-induced dynamic behavior and its load estimation of a single-layer latticed dome with a long span*. Journal of Wind Engineering and Industrial Aerodynamics, **89**(14-15): p. 1671-1687. 2001.
- [28] Li, Y.-Q. and Y. Tamura, *Equivalent static wind load estimation in wind-resistant design of single-layer reticulated shells*. Wind and Structures, **8**(6): p. 443-54. 2005.
- [29] Ma, C.K., J.M. Chang, and D.C. Lin, *Input forces estimation of beam structures by an inverse method*. Journal of Sound and Vibration, **259**(2): p. 387-407. 2003.
- [30] Law, S.S., J.Q. Bu, and X.Q. Zhu, *Time-varying wind load identification from structural responses*. Engineering Structures, **27**(10): p. 1586-1598. 2005.
- [31] Hwang, J.-S., A. Kareem, and W.-J. Kim, *Estimation of modal loads using structural response*. Journal of Sound and Vibration, **326**(3-5): p. 522-539. 2009.
- [32] White, J.R., D.E. Adams, and M.A. Rumsey. *Operational load estimation of a smart wind turbine rotor blade*. in *Proceedings of the SPIE 7295 - Health Monitoring of Structural and Biological Systems 2009*. San Diego, CA: SPIE - The International Society for Optical Engineering. 2009.
- [33] Liu, J.-J., C.-K. Ma, I.C. Kung, and D.-C. Lin, *Input force estimation of a cantilever plate by using a system identification technique*. Computer Methods in Applied Mechanics and Engineering, **190**(11-12): p. 1309-1322. 2000.
- [34] Åström, K.J. and P. Eykhoff, *System identification--A survey*. Automatica, **7**(2): p. 123-162. 1971.
- [35] Merovitch, L., *Elements of Vibration Analysis*. 2nd ed, New York, NY: McGraw-Hill. 1986.
- [36] Ginsberg, J.H., *Mechanical and Structural Vibrations : Theory and Applications*, New York, NY: Wiley. 2001.
- [37] Straser, E. and A.S. Kiremidjian, *Modular, Wireless Damage Monitoring System for Structures*. John A. Blume Earthquake Engineering Center: Stanford, CA. 1998.
- [38] Culler, D.E. *Wireless Sensor Networks - Where Parallel and Distributed Processing Meets the Real World*. in *Parallel and Distributed Processing Symposium, 2005. Proceedings. 19th IEEE International*. 2005.
- [39] Lynch, J.P. and K.J. Loh, *A summary review of wireless sensors and sensor networks for structural health monitoring*. The Shock and Vibration Digest, **38**(2): p. 91-128. 2006.
- [40] Zimmerman, A.T. and J.P. Lynch, *A parallel simulated annealing architecture for model updating in wireless sensor networks*. IEEE Sensors Journal, IEEE, **9**(11): p. 1503-1510. 2009.
- [41] Metropolis, N., A. Rosebluth, M. Rosebluth, A. Teller, and E. Teller, *Equation of state calculations by fast computing machines*. Journal Chemical Physics, **21**: p. 1087-1092. 1953.
- [42] Kirkpatrick, S., C.D. Gelatt, Jr., and M.P. Vecchi, *Optimization by simulated annealing*. Science, **220**: p. 671-680. 1983.
- [43] Prowell, I., M. Veletzos, A. Elgamal, and J. Restrepo, *Experimental and numerical seismic response of a 65 kW wind turbine*. Journal of Earthquake Engineering, **13**(8): p. 1172-1190. 2009.
- [44] Zimmerman, A.T. and J.P. Lynch. *Data driven model updating using wireless sensor networks*. in *Proceedings of the 3rd Annual ANCRiSST Workshop*. Lake Tahoe, CA. 2006.

A Review of Gearbox Condition Monitoring Based on vibration Analysis Techniques Diagnostics and Prognostics

Abdulrahman S. Sait
asait@my.fit.edu

Yahya I. Sharaf-Eldeen
eldeen@fit.edu

Department of Mechanical and Aerospace Engineering
Florida Institute of Technology
Melbourne, FL 32901

ABSTRACT

This paper provides a review of the literature on condition monitoring of a gearbox. The progress and changes over the past 30 years in failure detection techniques of rotating machinery including helicopter transmission are reviewed. Vibration Analysis techniques, indicators and parameters used in condition monitoring are arranged in a historical perspective. The use of vibration-based analysis damage detection techniques is classified and discussed in details. The capability of each technique to sense failure and damage in rotary equipments is addressed. These diagnostics techniques in gearbox condition monitoring are organized and regrouped in this review paper in a better approach so they can be easily recognized.

Keywords: Condition monitoring; rotating machinery; gearbox; transmission; vibration-based; time-statistical; RAW; RMS; crest factor; energy ratio; energy operator; kurtosis; enveloping; demodulation; TSA; FM0; residual signal; NA4; NA4*; difference signal; FM4; FM4*; M6A; M6A*; M8A; M8A*; Band-Pass Mesh Signal; NB4; NB4*; Time-Frequency; Short-Time Fourier Transform; Winger-Ville Distribution; Wavelet Transform; NP4.

1. Introduction

Over the past 30 years, many researches have been extensively studied and focused on failure and damage detection techniques in mechanical equipments. Fault can take place at any time on rotating machinery which lead to harmful results or delays in production. It is important to detect any problems at an early stage to stay away from unexpected breakdown. Therefore, condition monitoring process was involved to detect such problems in rotating machinery in order to have an early notice of damages and to avoid unexpected failure. Condition monitoring system minimizes machines downtime. It also saves money and time in maintenance by recognizing the damaged elements without calling for shutdown or inspection.

The field of condition monitoring of rotating machinery is wide. There are hundreds of researches have been extensively studied and focused on failure and damage detection in mechanical equipments. These researches and works, have many different techniques and approaches applied to all rotating machinery in order to detect any damage way before it happens. The main goal of these techniques is to minimize the cost and time in machines repairs and also to enhance the ways of detecting failures. Since the techniques in condition monitoring in rotating machinery where started long time ago, many approaches have been improved in damage detection and diagnostics field. Some of these approaches have a basic failure detection process such as oil debris analysis techniques. On the other hand, most of the recent work are focused on more advanced techniques such as angular motion analysis, vibration-based analysis, model-based analysis and mathematical

modeling. This paper focuses on Vibration-Based Analysis techniques. Vibration-Based Analysis techniques are classified into two main groups and they are discussed in details in the following sections.

2. Vibration-Based Analysis

Vibration analysis is the most common and popular technique used in the field of condition monitoring of rotating machinery and it is also called feature extraction techniques. Most of the recent work are focused on vibration based techniques. In these techniques, accelerometers are used to acquire vibration signals that come from a defective part in a machinery system. Vibration-based techniques can be divided into two main different processing groups. These two main processing group are: Time-Statistical Analysis and Time-Frequency Analysis. Furthermore, each one of these processing groups are also divided into subgroups as shown in [figure 1](#) below. Each individual technique is explained and addressed in details below.

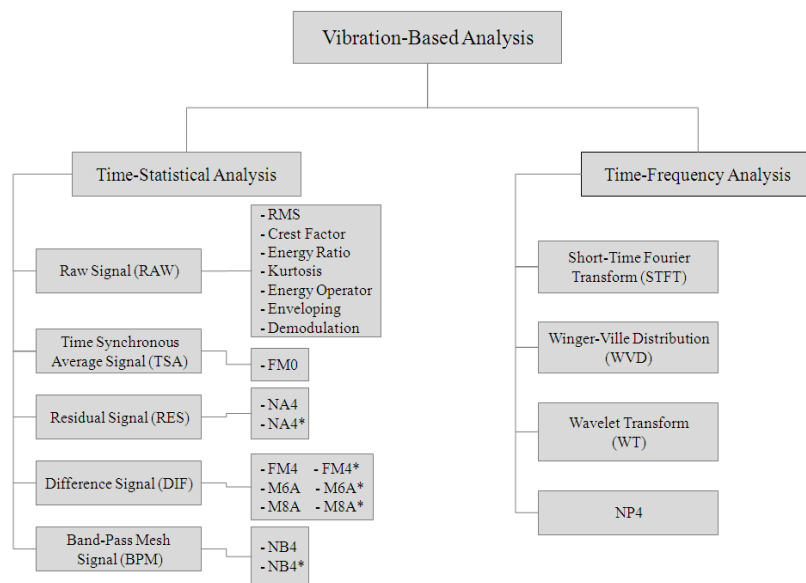


Fig.1 Classification of Vibration-Based Analysis Techniques and Parameters

2.1. Time-Statistical Analysis

Time-statistical analysis is one of the traditional methods used in rotating machinery failure detection and condition monitoring. This type of traditional analysis is typically based on some statistical measurement of vibration energy [1]. There are five different processing subgroups fall in this category of analysis: Raw Signal, Time Synchronous Average Signal, Residual Signal, Difference Signal, and Band-Pass Mesh Signal. [Figure 2](#) below shows the processing flow for feature extraction techniques.

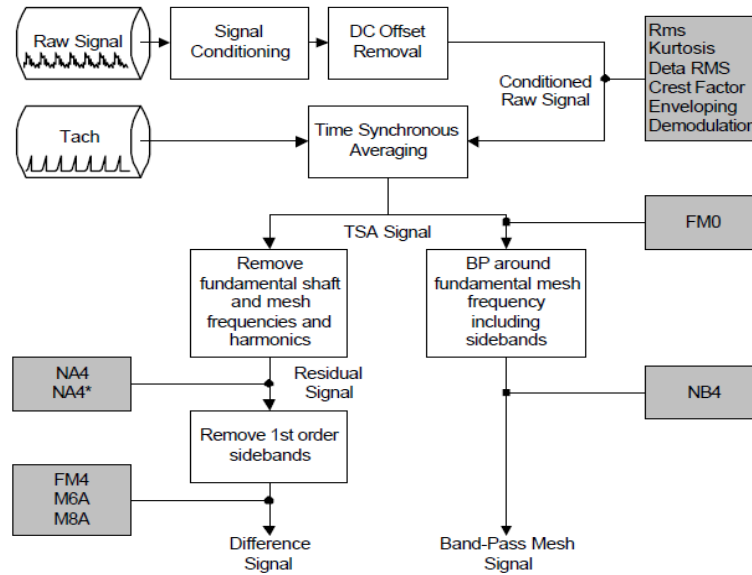


Fig.2 Processing Flow for Feature Extraction Techniques [2]

2.1.1. Raw Signal (RAW)

The RAW preprocessing indicates elements that are computed from the raw or trained signal collected by the sensor. Training the signal or eliminating the mean of the signal is the only preprocessing required for these elements. Training the signal can be done by multiplying all the data points by a calibration constant that is based on the accelerometer used. There are seven techniques fall in this subgroup: Root Mean Squared, Crest Factor, Energy Ratio, Kurtosis, Energy Operator, Enveloping and Demodulation [2].

2.1.1.1. Root Mean Squared (RMS)

The is the simplest method in detecting and measuring defects in the time domain. It is good for tracking the general noise level. It is also very useful for detecting unbalanced rotating elements. The root mean squared, also is called a quadratic mean, is a statistical measure of the magnitude of a varying quantity. RMS was initially developed to describe a temperature of a resistor subjected to sine wave alternative current. "The root mean squared value of vibration signal is a time analysis feature that is the measure of the power continent in the vibration signature." [2] It is very useful in sinusoidal waves. The RMS for a sine wave can be defined to be 0.707 times the amplitude of the signal [3]. RMS can be defined as the square root of the average of the sum of the squares of the signal samples [4, 5].

$$RMS = \sqrt{\frac{1}{N} \left[\sum_{i=1}^N (x_i)^2 \right]} \quad (1)$$

where,

x the original sample time signal

N the number of samples taken

i the sample index

The Delta RMS is the change between the present and the previous RMS values [2].

2.1.1.2. Crest Factor (CF)

This method gives better measurements than RMS in detecting defects in rotating machinery. "It is used to detect changes in the signal pattern due to impulsive vibration sources such as tooth damage in a gearbox or a defect in the outer race of a bearing." The crest factor can be defined as the ratio of the positive peak value of the input signal x to the RMS level. The value of the crest factor is affected by the numbers of peaks in the time series signal. Crest factor can be calculated to be between 2 and 6 in normal operation. However, any value higher than 6 is usually related to machinery problems [2]. A signal that has a less number of high amplitude peaks can generate a larger crest factor value as the numerator increases (high amplitude peaks), as the denominator decreases (few peaks means lower RMS) [6].

$$CF = \frac{\text{Peak level}}{\text{RMS}} = \frac{x_{0-pk}}{\text{RMS}} \quad (2)$$

where,

pk the sample index for the maximum positive peak of the signal

x_{0-pk} the value of x at pk

Crest Factor (CF) is a normalized measurement of the amplitude of the signal and is calculated to increase even when a small number of high amplitude peaks, such as a signal resulted from local tooth damage, occurs [5].

2.1.1.3. Energy Ratio (ER)

This is a useful technique for detecting heavy uniform wear [3]. It can be defined as the ratio of the RMS of the difference signal (d) and the RMS of the signal of the regular meshing component (r) [5].

$$ER = \frac{\text{RMS}_d}{\text{RMS}_r} \quad (3)$$

The energy in the regular component signal (r) is compared to the energy in the difference signal (d). The theory in this technique is that the energy moves from the regular signal to the difference signal [6].

2.1.1.4. Kurtosis

This technique provides a measure of the size of the tails of distribution. It can be used as an indicator of major peaks in a signal [2]. The kurtosis can be defined as the fourth normalized moment of the signal. The fourth moment is normalized by the square of the variance [3]. It is useful measurement of the peakedness of a signal [5]. "As gear wears or breaks, this feature should signal error due to the increased level of vibration." [7] Simply, it can be said that kurtosis is a statistical measure of the number of amplitude of peaks in a signal. when there are more peaks in a signal, kurtosis value become larger. A signal of Gaussian noise has a kurtosis value close to 3. A gearbox in a good condition is associated with a Gaussian distribution and have a kurtosis around 3. It should be noted that researchers subtract 3 from the calculated value and they end up with a value of near zero for a healthy gearbox [8]. Kurtosis equation is given by

$$\text{Kurtosis} = \frac{N \sum_{i=1}^N (x_i - \bar{x})^4}{\left[\sum_{i=1}^N (x_i - \bar{x})^2 \right]^2} \quad (4)$$

where,

- x the signal
- \bar{x} mean value of the signal
- i the index of data points in time record
- N the total number of data points in time record

2.1.1.5. Energy Operator (EO)

The Energy Operator can be simply calculated by making the input signal of each point squared, and then subtracting the product of the point before and after from squared signal as follows

$$x_i^2 - (x_{i-1} * x_{i+1}) \quad (5)$$

"For the end points, the data is looped around." The Energy Operator is calculated by taking the normalized kurtosis of the resultant signal [9].

2.1.1.6. Enveloping

Enveloping is a useful technique in monitoring high frequency response of rotating elements faults such as bearing and gear. An impact is generated when there is a fault on the inner or outer race of the bearing. Also, a damaged gear tooth produces impact when meshing with the other gear [10]. "Impacts in time domain generate many harmonics excite resonance to very high frequency in frequency domain". [Figure 3](#) below shows the vibration and fault frequencies caused by amplitude modulation. The red curve shows the envelope that is caused by impacts of the defected elements. The enveloping technique can be applied by extracting the frequency of the envelope, and then the damaged part of the bearing or gearbox can be detected [11].

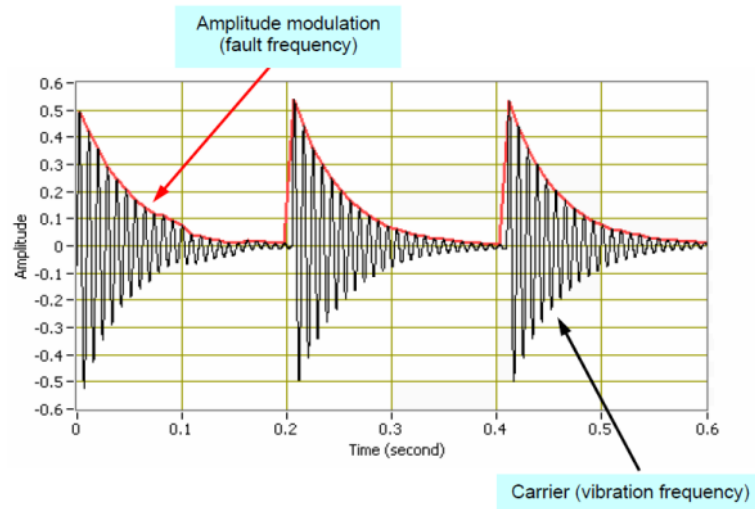


Fig.3 Envelope frequency caused by amplitude modulation [11]

The impact or impulse has a short duration compared to the interval between the pulse. The impact also excites a resonance in a mechanical system at a higher frequency than the vibration produced by the other elements in the system. the enveloping analysis has been extensively used in many applications. It has provided successful results in the early stage of damage detection in bearings. Furthermore, this technique helps finding the actual cause of bearing failure by analyzing the actual frequencies of the faulty rolling element bearing [2].

2.1.1.7. Demodulation

Demodulation techniques is functional in detecting and identifying the amplitude modulation factors stimulated by gear damage in the region of a single gear mesh frequency (GMF) and sometimes double gear mesh frequency (2GMF). Demodulation is different from enveloping techniques that is in demodulation techniques, the combined effect over a range of frequencies can be distinguish. demodulation technique can be applied by first high-pass filtering the raw data at 85 percent of the gear mesh frequency. Then, by low-pass filtering the raw data at 115 percent of the gear mesh frequency. The actual gear mesh frequency can be acquired by investigating the power spectral density of the filtered signal [2].

2.1.2. Time Synchronous Average Signal (TSA)

Time synchronous averaging is a signal averaging process and used to "extract repetitive signal from additive noise". TSA can be applied by dividing the raw signal into equal segments and averaged together. "before the signal is segmented based on the synchronous signal, the number of data points in the series is increased by means of interpolation. When Enough number of averages are taken, the random noise is canceled" [2]. Background noise can be removed using TSA analysis [12]. TSA can also be used to remove the periodic actions that are not synchronous with the monitored gears [13]. FM0 is the best technique would fall in this subgroup.

2.1.2.1. FM0

FM0 parameter was first proposed by Stewart in 1977. FM0 is a strong sign of major faults in a gear meshing [14]. However, it is not a good sign for minor tooth damage. FM0 is used for detecting major changes in the gear meshing pattern by comparing the maximum peak-to-peak amplitude of the signal to the sum of the amplitudes of the meshing frequencies and their harmonics. FM0 value increases when heavy wear occurs. This is because the peak-to-peak frequency stay constant and the gear meshing frequency shrinks [7]. FM0 equation is given as

$$FM0 = \frac{PP_x}{\sum_{n=0}^H P_n} \quad (6)$$

where,

- PP_x the maximum peak-to-peak amplitude of signal x
- P_n the amplitude of n th harmonics
- H the total number of harmonics in frequency rang

2.1.3. Residual Signal (RES)

RES analysis can be applied by removing the shaft components and the gear meshing frequency with their harmonics in order to calculate the residual signal that contains the time synchronous averaged signal. The two techniques fall in this subgroup are: NA4 and NA4*.

2.1.3.1. NA4

The NA4 parameter was initially found by Zakrajsek, Townsend and Decker in 1993 at the NASA Lewis Research Center. NA4 is useful technique for detecting the onset of fault and the continuing development of damage in mechanical equipments [15]. Because FM4, which will be discussed later in this paper, was less sensitive in detecting damages, two changes were made to it in order to develop the NA4 parameter. These two changes made the NA4 a better indicator and more sensitive in detecting faults. The first change is that the difference signals were used to compute the FM4. On the other hand, the residual signals were used to compute the NA4. These residual signals have the first order sidebands which were removed from the difference signals. The second change is that the FM4 is the ration of the kurtosis of a data to the square of the variance of the same data record. However, the NA4 is the ration of the kurtosis of a data record to the square of the average variance which is the mean value of the variance of all previous data records in the run ensemble [1]. NA4 equation is given as

$$NA4 = \frac{N \sum_{i=1}^N (r_i - \bar{r})^4}{\left\{ \frac{1}{M} \sum_{j=1}^M \left[\sum_{i=1}^N (r_{ij} - \bar{r}_j)^2 \right] \right\}^2} \quad (7)$$

Where,

- r the residual signal
- \bar{r} the mean value of residual signal

N	the total number of data points in time record
M	the number of current time record in run ensemble
i	the index of data points in time record
j	the index of time record in run ensemble

2.1.3.2. NA4*

NA4* was developed by Decker, Handschuh and Zakrajsek in 1994 to be an enhanced version of NA4 [15]. "As damage grows from localized to distributed, the variance of kurtosis increases dramatically. Since the kurtosis is normalized by the variance, this result in the kurtosis decreasing to normal values even with damage present. To counter this effect, NA4* was developed" [3]. In NA4 analysis technique, the kurtosis of a data record is normalized by the squared average variance for the run ensemble. However, in NA4* analysis technique, the kurtosis of a data record is normalized by the squared variance for a healthy gearbox. NA4* is given as

$$NA4^* = \frac{N \sum_{i=1}^N (r_i - \bar{r})^4}{(M_2)^2} \quad (8)$$

where,

r	the residual signal
\bar{r}	the mean value of residual signal
N	the total number of data points in time record
M_2	the variance of the residual signal for a healthy gearbox
i	the index of data points in time record

The variance value in a damaged gearbox is greater than the one in a healthy gearbox. The variance for a healthy gearbox can be estimated by selecting a less number of data records in order to guarantee "a statistically significant sample size." The residual signal and the mean and standard deviation of the variances are calculated in order to make the decision that is based on the upper limit L , which is given by

$$L = \bar{x} + \frac{Z}{\sqrt{n}} \sigma \quad (9)$$

where,

\bar{x}	the mean value of previous variances
Z	the value of a normal distribution
n	the number of samples, $n \geq 30$
σ	the standard deviation of previous variances

The judgment can be made based on the variance value. For instance, when the current variance value goes over the limit L , then it is considered that the gearbox is not healthy any more [16]. This modification makes NA4* more sensitive than NA4 in detecting a growth of damage in gearbox.

2.1.4. Difference Signal (DIF)

In the operation of a gearbox, the shaft frequency and its harmonics, the primary gear meshing frequency and the first order sidebands and its harmonics are the main elements of the regular gear meshing signal. The preprocessing technique is initially applied by removing that regular gear meshing signal from the time synchronous average (TSA) signal. The actual processing technique can be applied by removing only the sidebands of the primary gear meshing frequencies from the residual signals which resulted from the elimination of the shaft and primary gear meshing frequencies and harmonics [2]. Techniques would fall in this subgroup are: FM4, FM4*, M6A, M6A*, M8A and M8A*.

2.1.4.1. FM4

FM4 was initially developed by Stewart in 1977. It was calculated to detect faults only for limited number of gears. FM4 is defined as the ratio of the kurtosis and the square of the variance of the difference signal. It is given as

$$FM4 = \frac{N \sum_{i=1}^N (d_i - \bar{d})^4}{\left[\sum_{i=1}^N (d_i - \bar{d})^2 \right]^2} \quad (10)$$

where,

- d the difference signal
- \bar{d} the mean value of difference signal
- i the index of data points in time record
- N the total number of data points in time record

Like NA4, FM4 is nondimensional and will have approximate value of three if the difference signal is purely Gaussian. When damage grows up, the peaks in the difference signal increase which affect the kurtosis value to go over three [14].

2.1.4.2. FM4*

FM4* parameter has a similar calculations that are done in the parameter NA4* which was discussed earlier in this paper. "The diagnostic parameter FM4* is an addition of the run ensemble averaging, and also a statistical limitation of the growth of the square of the variance". The calculation of the numerator of FM4* stays the same as the numerator in FM4. However, "the denominator has the averaging effect of NA4*, and also determine if the current variance is of sufficient probability to be contained in the previous samples" [3].

2.1.4.3. M6A

M6A was initially proposed by Martin in 1989. It was calculated to detect surface damage on mechanical components. The theory applied in M6A is the same as the one applied in FM4. Both M6A and FM4 parameters are applied to the difference signal. However, M6A is expected to be "more sensitive to peak in the difference signal". This is because M6A uses the sixth moment normalized by the variance to the third power [17]. M6A is given as

$$M6A = \frac{N^2 \sum_{i=1}^N (d_i - \bar{d})^6}{\left[\sum_{i=1}^N (d_i - \bar{d})^2 \right]^3} \quad (11)$$

where,

- d the difference signal
- \bar{d} the mean value of difference signal
- i the index of data points in time record
- N the total number of data points in time record

2.1.4.4. M6A*

M6A* parameter has a similar calculations that are done in the parameter NA4* and FM4* which were discussed earlier in this paper. "The diagnostic parameter M6A* is an addition of the run ensemble averaging, and also a statistical limitation of the growth of the square of the variance". The calculation of the numerator of M6A* stays the same as the numerator in FM4. However, "the denominator has the averaging effect of NA4* and FM4*, and also determine if the current variance is of sufficient probability to be contained in the previous samples." [3, 4]

2.1.4.5. M8A

Like M6A, M8A was initially proposed by Martin in 1989. It was calculated to detect surface damage on mechanical components in a better way than M6A. The theory applied in M8A is the same as the one applied in FM4 and M6A. M8A, M6A and FM4 parameters are applied to the difference signal. However, M8A is expected to be more sensitive than M6A and FM4 to peak in the difference signal. This is because M8A "uses the eight moment normalized by the variance to the fourth power." [17] M8A is given as

$$M8A = \frac{N^3 \sum_{i=1}^N (d_i - \bar{d})^8}{\left[\sum_{i=1}^N (d_i - \bar{d})^2 \right]^4} \quad (12)$$

where,

- d the difference signal
- \bar{d} the mean value of difference signal
- i the index of data points in time record
- N the total number of data points in time record

2.1.4.6. M8A*

M8A* parameter has a similar calculations that are done in the parameter NA4*, FM4* and M6A* which were discussed earlier in this paper. "The diagnostic parameter M8A* is an addition of the run ensemble averaging, and also a statistical limitation of the growth of the square of the variance". The calculation of the numerator of M8A* stays the same as the numerator in FM4. However, "the denominator has the averaging effect of NA4*, FM4* and M6A*, and also determine if the current variance is of sufficient probability to be contained in the previous samples" [3, 4].

2.1.5. Band-Pass Mesh Signal (BPM)

The Band-pass mesh signal technique is applied by band-pass filtering the TSA signal around the primary gear meshing frequency. Then, the Hilbert transform is applied to the filtered signal which generates a complex time series of real and imaginary parts. Techniques fall in this subgroup are: NB4 and NB4*

2.1.5.1. NB4

The NB4 parameter was initially found by Zakrajsek, Handschuh and Decker in 1994 to be used as a useful technique for localized tooth damage. NB4 and NA4 are similar and have the same technique of analysis and exact way of calculation by using quasi normalized kurtosis. However, NB4 and NA4 have only one difference that is the residual signal is used in NA4 analysis while the envelope of the band-passed segment of the time synchronous averaged signal is used in NB4 Analysis [18]. NB4 is defined as the fourth statistical moment of the envelope signal divided by the current run time averaged variance of the envelope signal which is raised to the power two. NB4 is given as

$$NB4 = \frac{N \sum_{i=1}^N (E_i - \bar{E})^4}{\left\{ \frac{1}{M} \sum_{j=1}^M \left[\sum_{i=1}^N (E_{ij} - \bar{E}_j)^2 \right] \right\}^2} \quad (13)$$

Where,

- E the envelope signal
- \bar{E} the mean value of envelope signal
- N the total number of data points in time record
- M the number of current time record in run ensemble
- i the index of data points in time record
- j the index of time record in run ensemble

The theory behind NB4 is that when there is a few damage on gear teeth, a transient load fluctuations are created. These transient load fluctuations are different from the ones that are created by healthy gear teeth, and it can be recognized by using

the envelope signal. To calculate NB4, the envelope signal first has to be calculated using the Hilbert transform which given as

$$E(t) = \sqrt{(A(t))^2 + H[A(t)]^2} \quad (14)$$

where,

$E(t)$	the envelope of the band-passed signal
$A(t)$	the band-passed signal
$H[A(t)]$	the Hilbert transform of the band-passed signal

The Hilbert transform generates a complex time signal with two parts: real and imaginary. The real part is the band-passed signal and the imaginary part is the Hilbert transform of the signal. "The envelope of the band-passed signal is the magnitude of the complex signal or the analytical signal which is $|A(t) + iH[A(t)]|$ " [2, 19].

2.1.5.2. NB4*

NB4* parameter has a similar calculations that are done in the parameter NA4*, FM4*, M6A* and M8A* which were discussed earlier in this paper. "The diagnostic parameter NB4* is an addition of the run ensemble averaging, and also a statistical limitation of the growth of the square of the variance". The calculation of the numerator of NB4* stays the same as the numerator in FM4. However, "the denominator has the averaging effect of NA4*, FM4*, M6A* and M8A*", and also determine if the current variance is of sufficient probability to be contained in the previous samples." [3, 4, and 20]

2.2. Time-Frequency Analysis

Time-frequency analysis has become a popular and useful technique for gear fault detection. It was recognized that gear faults can generate a sharp transients in the vibration signals of gearboxes. Therefore, the exploration of time-frequency features started in the late 1980s [21]. The vibration signature from a gearbox consists of three significant components: "a sinusoidal component due to time varying loading, a broad-band impulsive component due to impact, and random noise." [5] The sinusoidal component dominates in a healthy gearbox. on the other hand, the sinusoidal component shows signs of modulation and reduction in amplitude [22, 23]. In addition to that, "both the broad-band impulsive component and the random noise become more prevalent." [24] The trend displayed by the sinusoidal components are more observable in the frequency domain while the trends displayed by the broad-band impulsive components are more observable in the time domain. Therefore, to capture these trends, time-frequency analysis is considered as a proper technique [25]. There are four different processing subgroups fall in this category of analysis: Short-Time Fourier transform, Winger-Ville distribution, Wavelet transform, and NP4.

2.2.1. Short-Time Fourier Transform (STFT)

The short-time Fourier transform can be considered as a typical time-frequency analysis technique. It useful technique for detecting gear faults by studying the energy distribution signal over a time-frequency domain [26]. The frequency domain of

the signal $x(t)$ can be studied by multiplying that signal by a window function $h(t)$. The squared magnitude of the short-time Fourier transform $|X(\omega)|^2$ gives the spectrogram. The spectrogram $P_{sp}(t, \omega)$ calculates the energy density range of the signal as function of time [27], and given as

$$P_{sp}(t, \omega) = |X_t(\omega)|^2 = \left| \frac{1}{\sqrt{2\pi}} \int e^{-j\omega\tau} x(\tau) h(\tau-t) d\tau \right|^2 \quad (15)$$

2.2.2. Winger-Ville Distribution (WVD)

Different from STFT, WVD can be obtained by taking the "sum of the product of the signal before time t , $x(t - 1/2\tau)$ and the reversed signal after time t , $x(t + 1/2\tau)$. The reversal of the signal after time t ensures that at time t , the point being multiplied are equidistant in time from t , specifically $\pm \frac{1}{2}\tau$ " [5]. Thus the WVD is given as

$$\frac{1}{2\tau} W(t, \tau) = \frac{1}{2\pi} \int x^*(t - 1/2\tau) x(t + 1/2\tau) e^{j\tau\omega} d\tau \quad (16)$$

The winger-Ville distribution (WVD) was first developed in the quantum correction for the thermodynamics equilibrium by Winger in 1932 [28]. Later, WVD was applied to signal processing by Ville in 1948 [29]. In the 1990s, more focus and research were applied to WVD in the field of gearbox damage detection analysis and diagnostics[30]. A great improvement was made by Forrester who applied the WVD analysis to investigate the averaged vibration signals of a faulty gearbox. Forrester found an incredible use of this technique in damage detection. The damage can be purely identified by a visual inspection of the different patterns in the WVD plots which are generated by different types of faults [31-34]. In [figure 4](#) below, the WVD plot illustrates the disturbance at a shaft angle of 100° as a result of a fault in a helicopter gearbox [35].

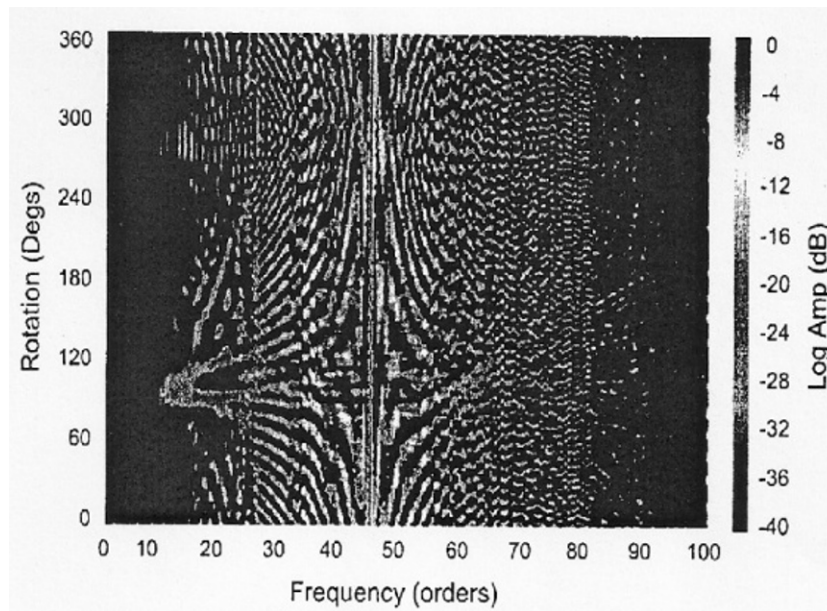


Fig.4 WVD plot of helicopter gearbox with cracked pinion gear [35]

In the early 1990s, McFadden continued the same great work by applying the properties of the continuous and discrete signals on WVD. He showed that the effect of the cross-terms can be minimized by using the sliding weighted functions to

the WVD [36-38]. The work done by Choy, Huang, Zakrajsek, Handschuh, and Townsend at NASA Glen Research Center concluded that "the WVD provided vital information regarding the location and severity of gear tooth damage." [39]

2.2.3. Wavelet Transform (WT)

The investigation of wavelet transform (WT) analysis was started in the mid 1980's. WT was found to be a powerful technique for analysis of gearbox vibration signals. WT is a time-frequency analysis technique and has similar characteristics to WVD. However, WT differs from Fourier transform in the way that it "uses a new class of real and complex nonstationary basis function, termed wavelets, which can be independently dilate and shifted as a function of time". This technique has two advantages. The first advantage is that the time and frequency are independent which makes WT useful for describing the local behavior of the signals. The second advantage is that the frequency of the signal can be analyzed without losing the essential information of the time-domain.

Wavelet transform analysis can be applied by "convolving a signal with time shifted and dilated versions of a nonstationary wavelet basis function" [5]. To perform this analysis, the function $\psi_\lambda(t)$ is first defined as a wavelet, where λ belongs to some set of indices Φ . The basis Ψ is then given as

$$\Psi = \{\psi_\lambda | \lambda \in \Phi\} \quad (17)$$

Once the basis was chosen, the signal x is then signified as an arrangement of wavelets. The wavelet signal is given as

$$x = \sum_{\lambda} c_{\lambda} \psi_{\lambda} \quad (18)$$

Where the coefficient c is given as

$$c = \{c_{\lambda} | \lambda \in \Phi\} \quad (19)$$

In the process of continuous wavelet transform (CWT) which is a non orthogonal process, the coefficients c_{λ} are required to be computed over all time and frequency. However, in the process of discrete wavelet transform (DWT) which is an orthogonal process, the "dilation and position of the wavelets are chosen to be powers of two.

In 1993, Newland introduced both compact and smooth wavelets [40]. In 1995, Wang and McFadden performed a nice analysis for a transmission fault detection and they compared between the compact and smooth wavelets. Both compact and smooth wavelet were used with the DWT to analyze the vibration signal of a helicopter gearbox. It was found that smooth wavelet was a little better to damage detection than compact wavelet. However, Wang and McFadden reported that the nonorthogonal CWT used with a Gaussian was more efficient than the orthogonal DWT used with either compact or smooth wavelets [41, 42].

2.2.4. NP4

NP4 was initially found by Polyshchuk, Choy, and Braun in 2000. It was developed to be a novel technique in gear damage detection derived from WVD. "The novelty of the NP4 parameter is in application of the previously defined statistical parameter called kurtosis to the WVD data and its interpretation for gear fault detection". The calculation of NP4 does not required a comparison between a faulty and a healthy gear's signals. This makes NP4 a useful method for detecting the damage without tracing the vibration history of the gear. NP4 can be defined as the normalized kurtosis of the signal power P [43, 44]. NP4 is given as

$$NP4 = \frac{N \sum_{i=1}^N (P_i - \bar{P})^4}{\left[\sum_{i=1}^N (P_i - \bar{P})^2 \right]^2} \quad (20)$$

where,

- P the instantaneous signal power calculated using the WVD
- \bar{P} the mean value of the signal power
- i the index of data points in time signal
- N the total number of data points in time signal

3. Closure

The progress and changes over the past 30 years in failure detection techniques of rotating machinery were reviewed. Vibration Analysis techniques, indicators and parameters used in condition monitoring were arranged in a historical perspective. Also, they were organized and regrouped in a better way so they can be easily understood. The capability of each individual technique to sense the failure and detect the damage in rotary equipments was discussed in details. Many of these approaches and techniques have shown successful progress in detecting the damages. However, improvement in this field of analysis is still needed. Therefore, new techniques for damage detection will be investigated and the research will be continued.

Acknowledgment

The authors would like to thank the Royal Commission for Jubail & Yanbu and Yanbu Industrial College (YIC) in Saudi Arabia for their support of this work.

References

- [1] Zakrajsek, J.J.: "An Investigation of Gear Mesh Failure Prediction Techniques," NASA TM-102340, AVSCOM TM 89-C-005, November 1989.
- [2] Lebold, M.; McClintic, K.; Campbell, R.; Byington, C.; Maynard, K.: "Review of Vibration Analysis Methods for Gearbox Diagnostics and Prognostics," Proceeding of the 54th Meeting of the Society for Machinery Failure Prevention Technology, Virginia Beach, VA, pp. 623-634, May 1-4, 2000.
- [3] Decker, Harry J.: "Crack Detection for Aerospace Quality Spur Gears," NASA TM-2002-211492, ARL-TR-2682, Prepared for the 58th Annual Forum and Technology Display, by the American Helicopter Society, Montreal, Canada, June 11-13, 2002.
- [4] Decker, H.J.; and Lewicki, D.G.: "Spiral Bevel Pinion Crack Detection in a Helicopter Gearbox," in Proceeding of the American Helicopter Society 59th Annual Forum, Phoenix, AZ, pp. 1222-1232, 2003.
- [5] Samuel, Paul D.; and Pines, Darryl J.: "A Review of Vibration-Based Techniques for Helicopter Transmission Diagnostics," Journal of Sound and Vibration. vol. 282, no 1-2, pp. 475-508, April 6, 2005.
- [6] Swansson, N.S.: "Application of Vibration Signal Analysis Techniques to Signal Monitoring," in: Conference on Friction and Wear in Engineering, Institute of Engineering, Barton, Australia, pp. 262-267, 1980.
- [7] Zakrajsek, J.J.: NASA Technical Memorandum 102340, Lewis Research Center, Cleveland, OH.
- [8] Miller, Irwin,; and Freund, J.E.: "Probability and Statistics for Engineering," 3rd Edition, Prentice-Hall, Inc., New Jersey, p.74, 1985.
- [9] Ma, J.: "Energy Operator and Other Demodulation Approaches to Gear Defect Detection," Proceeding of 49th Meeting of the Society of Mechanical Failure Prevention Technology, Virginia Beach, VA, pp. 127-140, April 1995.
- [10] Spectra Quest Tech Note, "Analyzing Gearbox Degradation Using Time-Frequency Signature Analysis," March 2006.
- [11] Spectra Quest Tech Note, "Rotating Machinery Fault Diagnosis Techniques-Enveloping and Cepstrum Analyses," October 2006.
- [12] Wang, Wilson Q.: "Rotary Machinery Health Condition Monitoring Fault Diagnosis and Prognosis," Thesis, University of Waterloo, Waterloo, Ontario, Canada, 2002.
- [13] McFadden, P.: "A Technique for Calculating the Time Domain Averages of Vibration of the Individual Planet Gear and the Sun Gear in an Epicyclic Gearbox," Journal of Sound and Vibration, vol. 144, no.1, pp. 163-172, 1991.
- [14] Stewart, R.T.: "Some Useful Analysis Techniques for Gearbox Diagnostics," Technical Report MHM/R/10/77, Machine Health Monitoring Group, Institute of Sound and Vibration Research, University of Southampton, July 1977.
- [15] Zakrajsek, J.J.; Townsend, D.P.; and Decker, H.J.: "An Analysis of Gear Fault Detection Methods as Applied to Pitting Fatigue Failure Data," Technical Report NASA TM-105950, A VSCOM TR-92-C-035, NASA and the US Army Aviation System Command, Prepared for the 47th Meeting of The System Engineering Approach to Mechanical Failure Prevention, January 1993.

- [16] Decker, H.J.; Handschuh, R.F.; and Zakrajsek, J.J.: "An Enhancement to the NA4 Gear Vibration Diagnostic Parameter," Technical Report NASA TM-106553, ARL-TR-398, NASA and the US Army Research Laboratory, July 1994.
- [17] Martin, H.R.: "Statistical Moment Analysis As a Mean of surface Damage Detection," Proceeding of the 7th International Model Analysis Conference, Society of Experimental Mechanics, Schenectady, NY, pp. 1016-1021, 1989.
- [18] Zakrajsek, J.J.: "A Review of transmission Research at NASA Lewis Research Center," Technical Report NASA TM-106746, ARL-TR-599, NASA and the US Army Research Laboratory, December 1994.
- [19] Zakrajsek, J.J.; Handschuh, R.F.; Lewicki, D.G.; and Decker, H.J.: "Detecting gear Tooth fracture in a High Contact Ratio Face Gear Mesh," Proceeding of the 49th Meeting of the Mechanical Failure Prevention Group, Virginia Beach, VA, April 18-20, 1995.
- [20] Zakrajsek, J.J.: "Transmission Diagnostics Research at NASA Lewis Research Laboratory," Technical Report NASA TM-106901, ARL-TR-748, NASA and the US Army Research Laboratory, April 1994.
- [21] Forrester, B.D.: "Use of the Wigner-Ville Distribution in Helicopter Transmission Fault Detection," Proceeding of the Australian Symposium on Signal Processing and Applications-ASSP 89, Adelaide, Australia, pp.78-82, 1989.
- [22] McFadden, P.D.: "Detecting Fatigue Crack in Gears by Amplitude and Phase Demodulation of the Meshing Vibration," Journal of Vibration, Acoustic, Stress, and Reliability in Design, vol. 108, pp. 165-170, 1986.
- [23] Brennan, M.; Chen, M.H.; and Reynolds, A.G.: "Use of Vibration Measurements to Detect Local Tooth Defects in Gears," Journal of Sound and Vibration, vol. 31, pp. 12-17, November 1997.
- [24] Larder, B.: "An Analysis of HUMS Vibration Diagnostics Capabilities," Proceeding of the American Helicopter Society 53rd Annual Forum, pp. 1308-1315, Virginia Beach, VA, 1997.
- [25] Samuel, P.D.; Pines, D.J.; and Lewicki, D.G.: "A Comparison of Stationary and Non-Stationary Transforms for Detecting Faults in Helicopter Gearboxes," Journal of the American Helicopter Society, vol. 45, pp. 125-136, February 2000.
- [26] Wang, W.; and McFadden P.: "Early Detection of Gear failure by Vibration Analysis – I, Calculation of the Time – Frequency Distribution," Mechanical System and Signal Processing, vol. 7, no. 3, pp. 193-203, 1993.
- [27] Cohen L.: Time-Frequency Analysis, Prentice-Hall, Inc., New York, 1995.
- [28] Winger E.P.: "On the Quantum Correction for the Thermodynamics Equilibrium," Physics Review, vol. 40, pp. 745-759. 1932.
- [29] Ville, J.: "Theorie ef Applications de la Naotion de Signal Analytique," Cables et Transmission, vol. 2A, pp. 61-74, 1948.
- [30] Staszewski, W.J.; Worden, K.; and Tomlinson, G.R.: "Time-Frequency Analysis in Gearbox Fault Detection Using The Winger-Ville Distribution and Patter Recognition," Mechanical System and Signal Processing, vol. 11, no. 5, pp. 673-692, 1997.
- [31] Forrester B.D.: "Use of the Winger Ville Distribution in Helicopter Transmission fault Detection," Proceedings of the Australian Symposium on Signal Processing and Applications-ASSPA 89, Adelaide, Australia, April 17-19, 1989.

- [32] Forrester B.D.: "Analysis of Gear Vibration in the Time-Frequency Domain," Proceedings of the 44th Meeting of the Society of Mechanical Failures Prevention Group (MFPT) of the Vibration Institute, Virginia Beach, Virginia, pp. 225-239, April 3-5, 1989.
- [33] Forrester B.D.: "Time –Frequency Analysis of helicopter Transmission Vibration," Technical Report 108, Aeronautical Research Laboratory, ARL Propulsion, Melbourne, Australia, 1990.
- [34] Forrester B.D.: "Time –Frequency Analysis in Machine Fault Detection," Time –Frequency Signal Analysis, B. Boashash Edition, Longman Cheshire, Melbourne, Australia, 1992.
- [35] Blunt, D.M.; and Forrester B.D.: "Health Monitoring of Blackhawk and Seahawk Main Transmission Using Vibration Analysis," Proceedings of the 6th Australian Aeronautical Conference, 2nd Pacific Conference on Aerospace Science and technology, Melbourne, Australia, 1995.
- [36] McFadden P.D.; and Wang, W.J.: "Time-Frequency Domain Analysis of Vibration Signatures for Machinery Diagnostics (I) Introduction to the Winger-Ville Distribution," Technical Report OUEL 1859, Department of Engineering Science, Oxford University, 1990.
- [37] McFadden P.D.; and Wang, W.J.: "Time-Frequency Domain Analysis of Vibration Signatures for Machinery Diagnostics (II) The Weighted Winger-Ville Distribution," Technical Report OUEL 1891, Department of Engineering Science, Oxford University, 1991.
- [38] McFadden P.D.; and Wang, W.J.: "Analysis of Gear Vibration Signatures by the Weighted Winger-Ville Distribution," Proceedings of the 5th International Conference on Vibration in Rotating Machinery, Institution of Mechanical Engineers, University of Bath, Bath, UK, pp. 387-393, 1992.
- [39] Choy, F.K.; Huang S.; Zakrajsek, J.J.; Handschuh, R.F.; and Townsend D.P.: "Analysis of the Effects of Surface Pitting and Wear on the Vibrations of Gear Transmission System," Technical Report NASA TM-106678, ARL-TR-520, NASA and the US Army Research Laboratory, July 1994.
- [40] Newland, D.E.: "An Introduction to Random Vibration, Spectral, and Wavelet Analysis," 3rd Edition, Longman Essex, 1993.
- [41] Wang, W.J.; and McFadden P.D.: "Application of Orthogonal Wavelets to Early Gear Damage Detection," Mechanical System and Signal Processing, vol. 9, no. 5, pp. 497-507, 1995.
- [42] Wang, W.J.; and McFadden P.D.: "Application of Wavelets to Gear Vibration Signals for Fault Detection," Journal of Sound and Vibration, vol. 192, no. 5, pp. 927-939, 1996.
- [43] Polyshchuk, V.V.; Choy, F.K.; and Braun, M.J.: "New Gear-Fault-Detection Parameter by Use of Joint Time-Frequency Distribution," Journal of Propulsion and Power, vol. 16, no. 2, pp. 340-346, 2000.
- [44] Polyshchuk, V.V.; Choy, F.K.; and Braun, M.J.: "Gear Fault Detection with Time-Frequency Based Parameter NP4," International Journal of Rotating Machinery, vol. 8, no. 1, pp. 57-70, 2002.

Experimental Results of Wind Turbine Operational Monitoring with Structural and Aerodynamic Measurements

J. R. White¹ and D. E. Adams²

¹Wind and Water Power Technologies, Sandia National Laboratories, Albuquerque, New Mexico 87123

²School of Mechanical Engineering, Purdue University, West Lafayette, IN 47907-2031

NOMENCLATURE

DOE	=	Department of Energy, Energy Efficiency and Renewable Energy Office
Flap-wise	=	Direction of rotor blade oriented from high-pressure to low-pressure side of the airfoil
Lead-lag	=	Direction of rotor blade oriented from lead-edge to trailing-edge along the chord of the airfoil
Span	=	Direction of rotor blade oriented from root to tip along the length of the rotor blade
SNL	=	Sandia National Laboratories Wind and Water Power Technologies Department

ABSTRACT

At the end of 2009, 1.8% of the electricity utilized in the U.S. was produced by wind turbines, which are projected to eventually supply 20% or more to the U.S. electrical grid. As the percentage of wind energy increases, energy supply stability will become increasingly tied to the availability and reliability of turbines. To improve availability and reliability, adaptive wind turbines and wind farms are envisioned that can estimate the applied forces, state of structural health, and adapt their operational states to increase performance and minimize damage accumulation. A critical component of the adaptive wind turbine will be operational monitoring approaches that can estimate the applied forces and state of damage from inference algorithms applied to rotor-based measurements. Sandia National Laboratories has been working to embed structural and aerodynamic measurements and inference algorithms in operational rotors. In this paper the results of the DOE/SNL Sensor Blade 1 experiment will be presented in which a turbine rotor was instrumented with an array of accelerometers, foil strain gages, Fiber-Bragg strain sensors, fiber optic temperature sensors, hot-film sensors, pressure taps, and a five-hole Pitot tube. The data was GPS time-synchronized and correlated with reference measurements of the in-flow, rotor azimuth, hub strain, and tower strain. Inference algorithms were applied to the measurements to estimate rotor deflection and applied forces. The results were used to evaluate the accuracy and latency of the different operational monitoring approaches and measurement types.

1 INTRODUCTION

The motion of an operating wind turbine rotor is a combination of quasi-steady, deterministic, and stochastic components. The decomposition of the motion into these components is useful when applied to controls, structural health monitoring, and turbine design. For example, the deterministic components could be used to develop algorithms for individual blade pitch and structural health monitoring because the turbine response can be predicted from the inflow. Stochastic decomposition is useful for active load control in which the aerodynamic forces cannot be predicted a priori and therefore a real-time local observer and control device is required. Lastly, an estimate of the steady loads and rotor deflections can be used to monitor the tower clearance and potentially

lead to lighter, less expensive rotor blade designs. Previous efforts have focused on developing the individual modeling and signal processing tools to decompose this motion into its components. In this paper all of these tools will be combined and applied to simulated and experimental data. At the time of this publication the Sensored Rotor 2 experiment, a fully instrumented and time synchronized rotor, was not yet operational and, therefore, the results will not be presented.

1.1 Previous Work

Smart turbines are envisioned that could be used to estimate operational loading, detect damage, and actively adapt to short time constant wind conditions [1,2]. Given these performance objectives, smart rotor blades must incorporate health monitoring techniques that estimate the operational state of the rotor, detect damage, and transmit this information to an active control mechanism in the blade. The information generated through monitoring can also be useful to the turbine operator and designer for maintenance planning and design validation and improvement.

Fritzen [3] provided a review of load estimation research that has been performed on offshore horizontal axis wind turbines. The work focused on estimating wave and wind loads that were applied to the turbine tower and a lumped parameter idealization of the tower-top, but this analysis did not include the flexibility and inertial forces of the rotating components. A state observer was developed from a state-space model approach and used with structural measurements to estimate the applied forces. Some of the methods were demonstrated on a simplified laboratory tower structure and in computational models. A review of force reconstruction methods, which were not restricted to wind turbines, was also provided. The concept of creating a smart rotor blade with embedded sensors to perform load estimation was not discussed by Fritzen, nor was the use of accelerometers with both static and dynamic measurement capabilities in the rotating reference frame of the blade. White [4,5] proposed the use of modal filtering and operational displacement tracking of wind turbine rotor blades for load estimation. These methods will be described in more detail in subsequent chapters. Accurate load estimates allowed for the estimation of fluctuating loads and as inputs to an active control system.

Additional explanation and development of the following methods and results can be found in White [6].

1.2 Sensored Rotor Blade

The US Department of Energy, Energy Efficiency and Renewable Energy Office has funded Sandia National Laboratories Wind and Water Power Technologies department to design, fabricate, operate, and test-to-failure a rotor blade embedded with promising sensing technologies to serve the next generation needs in controls, active load control turbines, blade design, and structural health monitoring / condition monitoring. An experimental 9 m CX-100 rotor blade was fabricated by TPI composites during which several project partners collaborated to install fiber optic strain and temperature, strain gage, accelerometer, and resistive temperature detector sensors. The blade was shipped to the USDA-ARS / SNL wind rotor testing facility in Bushland, TX where it was ground tested and then operated on a Micon 65/13M wind turbine. The experimental data and model that was generated were used for all of the following results.

2 APPROACH

Wind loading and turbine response are a summation of quasi-steady, deterministic, and stochastic processes. Therefore, approaches are needed to decompose the total process into these separate components.

2.1 Quasi-Steady Decomposition

The wind is assumed to have a mean flow component that has constant speed, direction, and profile across the swept area of the turbine, which changes at frequencies less than 0.1 Hz. In other words, the change of the mean flow is assumed to occur over time periods longer than 10 seconds with insignificant derivatives in time. To estimate the deflection of the rotor blade from the mean wind flow using inertial measurements, the centripetal

acceleration vector can be used as a reference to estimate the local blade elastic deflection and slope as presented in [6]:

$$\hat{u}_s \left(z, \frac{\partial u_s}{\partial z} \right) = \{ f(L, z) \}_{1 \times (n-3)} [g(L, z_i)]_{(n-3) \times m}^+ \left\{ \frac{\partial u_s}{\partial z} \right\}_{z_i} \Big|_{m \times 1} \quad (1)$$

where \hat{u}_s is the estimated deflection, $f(L, z)$ is the polynomial estimator function, $g(L, z_i)$ is the slope condition function, and $\frac{\partial u_s}{\partial z}$ is the elastic slope estimated from the accelerometer. This quasi-steady estimator relates the elastic deformation slope measured by the accelerometer to the continuous elastic deflection along the rotor blade.

2.2 Deterministic Decomposition

Components in the wind such as vertical wind shear are assumed to produce a deterministic force and response that behave sinusoidally as a function of the rotor azimuth and the mean wind speed. These components can be extracted using order analysis, which uses rotational sampling and averaging to extract the deterministic components from a combined quasi-steady, deterministic, and stochastic process. For example, in Figure 1a the force applied to the rotor blade in a dynamic simulation is shown in black as a function of rotor azimuth angle and the rotationally sampled and averaged force is shown in white. The details of the simulation model are given in White [6]. An example output from this rotational sampling procedure is shown in Figure 1b. These results show that the applied force has a quasi-steady component of approximately 150 N, a deterministic sinusoid with a maximum near 20 degrees and a minimum near 200 degrees, and a random stochastic distribution about the summation of the quasi-steady and deterministic forces.

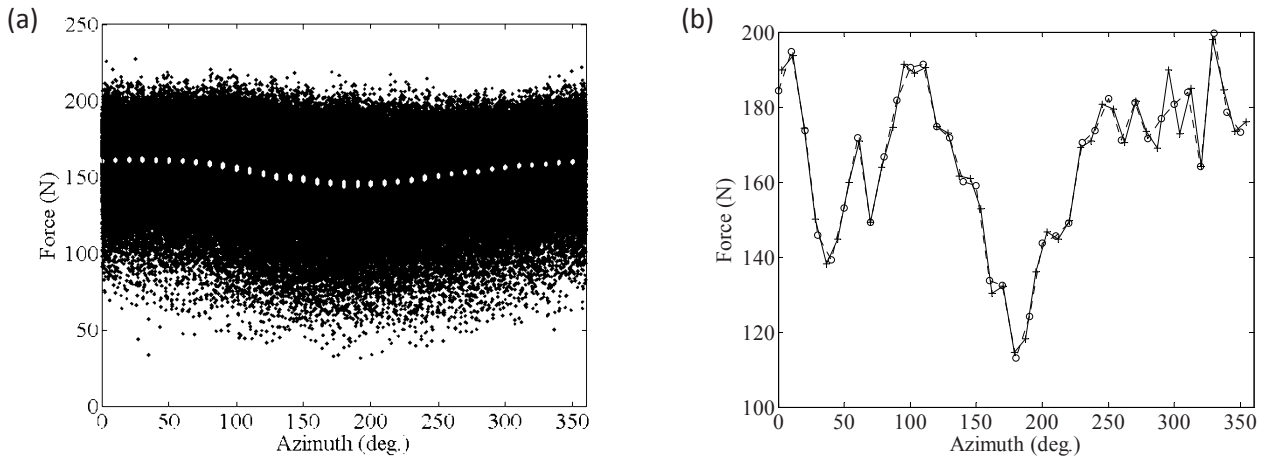


Figure 1: (a) Flap-wise force for 8 m/s turbulent wind as a function of wrapped azimuth angle for time-sample (black) and inverse Fourier transform of rotationally-sampled-averaged data (white dot). (b) Flap-wise force for 8 m/s, turbulent wind illustrating time sampling (+) and rotational sampling (o).

In Figure 2 a Fourier transform of the time-sampled and rotationally sampled and average data are shown. These results show that order analysis can better extract the harmonic components of the process and, unlike a Power Spectrum Density function, are able to retain the phase information that is equally as useful as the magnitude of the spectrum.

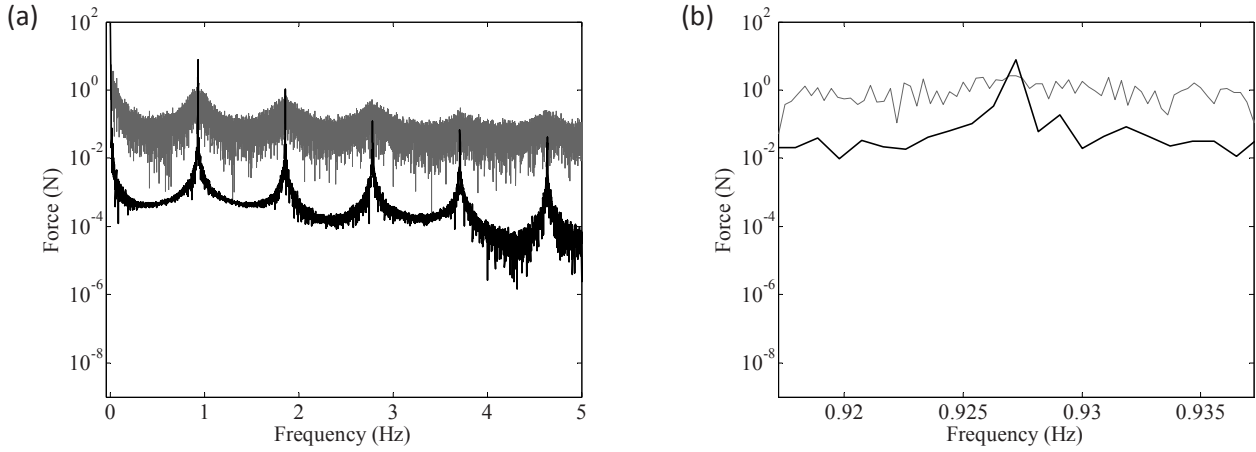


Figure 2: (a) Fourier transform of flap-wise force for 8 m/s, turbulent wind at tip of blade for un-windowed time-sampled (gray) and rotationally-sampled-averaged (black). (b) View of first harmonic Fourier transform of flap-wise force for 8 m/s, turbulent wind at tip of blade for un-windowed time-sampled (gray) and rotationally-sampled-averaged (black).

2.3 Stochastic Decomposition

The stochastic process that remains after the quasi-steady and deterministic components are extracted is random in that the input and the response can only be represented by probability density functions; however, it is assumed here that the structure behaves linearly and that the dynamic motion is a summation of the individual modal contributions. Therefore, a modal filter is used to project the physical measurements into estimates of the modal coordinate contributions. In the modal domain the contribution of each mode shape is estimated by a time-dependent modal coefficient defined by:

$$u_d(z, t) = \sum_{r=1}^{\infty} U_r(z) \eta_r(t) \quad (2)$$

where u is the dynamic response of the structure, U_r is the basis set of mode shape functions, and η is the modal contribution coefficient. The basis set of functions can be any set of functions; however, the set of functions must be able to sufficiently span the space of the motion. Mode shapes are typically used because they a) represent the theoretical minimum set of functions to sufficiently span the space of motions within the frequency range of the active dynamics and b) mode shapes can be used to decouple the modal contributions of one mode from all other modes.

3 RESULTS

In the following section each of the approaches was applied to the simulation of the CX-100 rotor blades on the Micon 65/13M turbine. The simulation was performed in MSC.ADAMS© in turbulent wind conditions at 8, 10, and 14 m/s IEC Class B turbulent wind with 0.2 power law vertical wind shear. The experimental data was acquired in 8 m/s IEC Class B turbulent wind conditions and, wherever possible, the Sensor Blade 1 project data was used. In the near future results of these approaches applied to the Sensored Rotor 2 experiment will be published.

3.1 Quasi-Steady Decomposition

The elastic deformation slope was simulated and measured using the centripetal acceleration as a reference. In Figure 3a the deformation slope along the rotor blade as a function of simulated wind speeds is shown. The experimentally measured slope at 6.5 m is also shown above and below the slope predicted by 8 m/s. These results showed that the deformation slope increased along the rotor blade, was continuous, and had reasonable agreement with the experimental data.

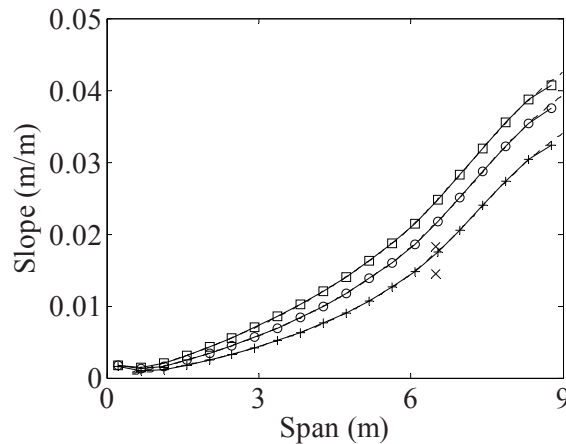


Figure 3: Slope of average deflection (dashed) compared to estimate from sensor rotation (solid) for 8 m/s (plus), 10 m/s (circle), and 14 m/s (square). Slope estimates from the operational rotor blade at 6.5 m (x).

A one hour average was used in the previous results for the deformation slope. To implement the deflection estimation algorithm in real-time, the data was low-pass filtered at 0.1 Hz as shown in Figure 4a. The simulated and estimated tip deflection were compared in Figure 4 for two different embodiments of the static deflection estimator. These results showed that the tip deflection estimate matched well with the actual tip deflection in the simulated data with a maximum difference of 3 mm for deflection on the order of 100-150 mm.

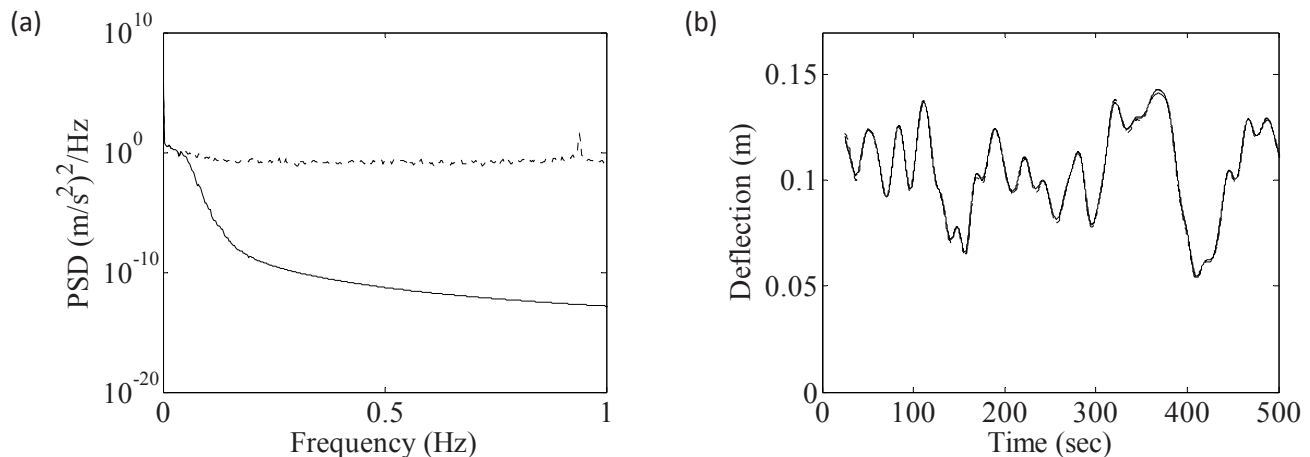


Figure 4: (a) Power spectral density of flap-wise acceleration before and after low-pass filtering. (b) 8 m/s tip deflection for simulated deflection (dotted), second order estimator with 3.6 m and 8.55 m sensor placement (solid), and third order estimator with 3.65 m, 6.55 m, and 8.25 m sensor placement (dashed).

3.2 Deterministic Decomposition

Order analysis was applied to the simulated data to extract the deterministic components of the turbine operation. In Figure 5, the results of the extraction are shown for the different wind speed cases for a once-per-revolution oscillation, as a function of magnitude and phase along the rotor blade span. The results show that the deflection increases with wind speed and that the peak of the oscillation approaches zero degrees azimuth with wind speed. Additionally, the three rotor blades are always phased 120 degrees apart because they all exhibit the same pattern and the azimuth angle is defined relative to Blade 1 vertically up. In Figure 6 the operational deflection shapes are shown for once (as detailed in Figure 5), twice, and three times per revolution where the black shading indicates that the blade is in downwind deflection and the white shading indicates that the blade is in upwind deflection. These surfaces represent the swept oscillation path of all of the rotor blades. For example, in Figure 6a when blade 1 is at the peak of downwind deflection (slightly clockwise of vertical), the other two blades are 120 degrees ahead and behind of the blade 1.

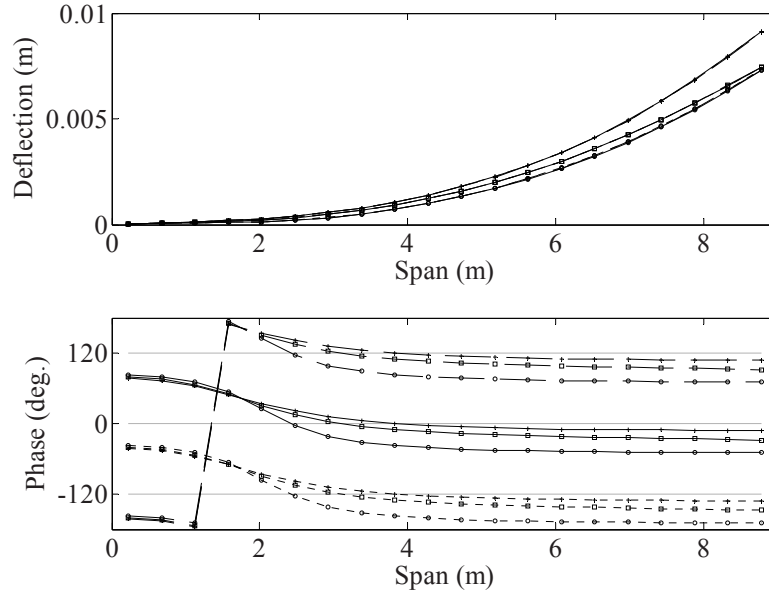


Figure 5: Once per revolution flap-wise deflection magnitude and phase along rotor blades 1 (solid), 2 (dashed), and 3 (dotted) for 8 m/s (+), 10 m/s (square), and 14 m/s (circle) (turbulent wind cases).

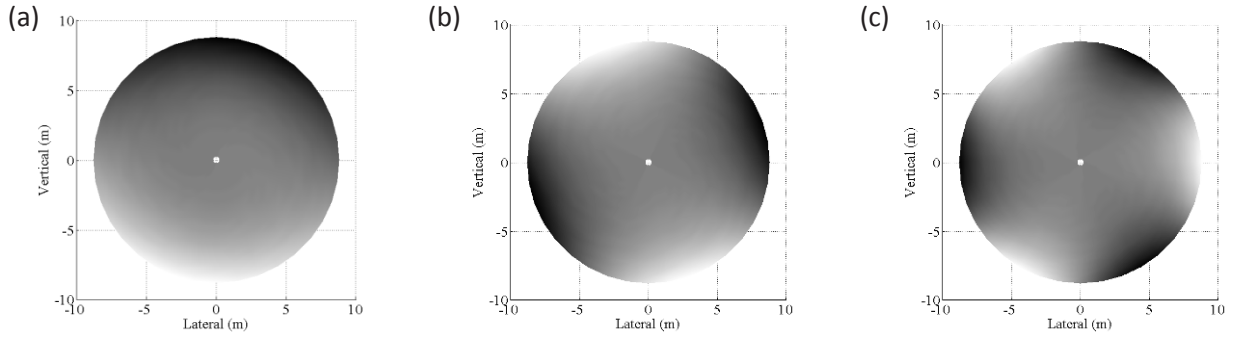


Figure 6: Operational deflection shapes for 8 m/s turbulent wind for (a) once, (b) twice, and (c) three times per revolution.

3.3 Stochastic Decomposition

To decompose the random stochastic process, a modal filter was used with the static mode shapes of the turbine as the basis set of functions. The simulated turbine measurements were projected onto the mode shape functions to estimate the modal contribution coefficients. The results shown in Figure 7 show the modal coefficients as a function of wind speed. The distribution across the coefficients and the existence of tails on both sides of the coefficients indicates that the mode shape basis set of functions are sufficient to span the space and decompose the stochastic process. Furthermore, modes 3 – 10 account for the majority of the modal projection. Interestingly, in modes 3 – 5 (first torsion, first anti-symmetric flap modes) an increasing in wind speed results in a reduction in the modal coefficients. This result indicates that increasing wind speed appears to dampen out the random oscillations from these modes.

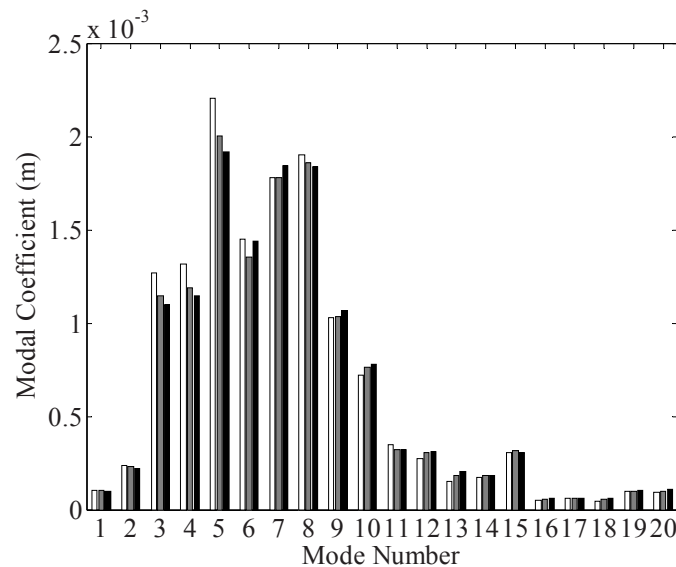


Figure 7: Deflection modal coefficients for 8 m/s (white), 10 m/s (gray), and 14 m/s (black).

4 SUMMARY

Methods were presented from previous works to decompose the combined quasi-steady, deterministic, and stochastic components of the turbine in operation. A static deflection estimator based on accelerometer rotation relative to centripetal acceleration was shown by simulation and experiment to accurately estimate the elastic deformation slope and deflection. Order analysis was shown to extract the deterministic sinusoidal forces and responses of turbine operation. A modal filter was shown to decompose the random stochastic process which remained after the quasi-steady and deterministic components were extracted. The static mode shapes used in the modal filter basis functions were also shown to span the space of the motions. These results showed that the methods and tools developed by SNL for operational monitoring of a horizontal axis wind turbine are capable of decomposing the total process into quasi-steady, deterministic, and stochastic components.

5 ACKNOWLEDGEMENTS

The results presented in this work were made possible by the US Department of Energy Sandia National Laboratories Sensors Task performed by the Wind and Water Power Technologies Department. The experimental results were made possible with help from B. Neal and A. Holman of the US Department of Agriculture Conservation and Production Research Laboratory.

REFERENCES

1. Butterfield, S.. "Condition Monitoring Thoughts." National Renewable Energy Laboratory (2006).
2. Berg, D.. "Selected Topics in Wind Turbine Blade Technology." Sandia National Laboratories (2007).
3. Fritzen, C., Kremer, P. and Klinkov, M. "Structural Health Monitoring of Offshore Wind Energy Plants." 4th European Workshop on Structural Health Monitoring (2008).
4. White, J., Adams, D., Rumsey, M., van Dam, J., and Hughes, S.. "Impact Loading and Damage Detection in a Carbon Composite TX-100 Wind Turbine Blade." 46th AIAA Aerospace Sciences Meeting and Exhibit (2008).
5. White, J., Adams, D., Rumsey, M. and Paquette, J.. "Estimation of Wind Turbine Blade Operational Loading and Deflection with Inertial Measurements." 47th AIAA Aerospace Sciences Meeting and Exhibit (2009).
6. White, J. "Operational Monitoring of Horizontal Axis Wind Turbines with Inertial Measurements." Doctoral Dissertation Purdue University (2010).

Torsional Response of Structure with Mass Eccentricity

Dr. Helen Wu

Edith Cowan University, 270 Joondalup Dr. Perth, WA 6027, Australia

h.wu@ecu.edu.au

ABSTRACT

Base isolation is found effective in reducing torsional response of structures with mass eccentricity when subjected to earthquakes. In this study, dynamic characteristics of an eccentric five-storey benchmark model, isolated with laminated rubber bearings (LRB) and lead core rubber bearings (LCRB), were examined using a shaker table and four different ground motions. The earthquake-resistant performance of LRB and LCRB isolators was evaluated. It was observed that both transverse and torsional responses were significantly reduced with the addition of an LRB or LCRB isolated system regardless of ground motion input. However, the LRB was identified to be more effective than LCRB in reducing relative torsional angle, model relative displacements, accelerations and angular accelerations, and therefore, provided a better protection of the superstructure and its contents.

1 Introduction

Ground motions produced by severe earthquakes are often quite damaging to structures and their contents. Conventional earthquake-resistant designs often focus on the strengthening of structures to resist such disturbances and avoid structural collapse, whilst little attention is given to the prevention of damage. Using such design approaches, it is almost impossible to construct completely ‘earthquake-proof’ structures that are both reasonable in cost and aesthetically acceptable.

Seismic isolation of the building structure is an efficient design scheme that can successfully reduce earthquake loading to improve safety and reduce building damage [1-2]. A seismically isolated structure can have a fundamental frequency considerably lower than the fundamental frequency of the same structure built without isolation and also lower than the usual predominant frequencies of a typical earthquake [3]. This is achieved by mounting the structure on a set of isolators that provide low horizontal stiffness, thereby shifting the fundamental frequency of the structure to a much lower value. As a result, most deformations occur within the isolation level, allowing the superstructure to remain essentially undeformed and able to move like a rigid body. This technique prevents damage to the structural and nonstructural components of the building [1].

However, a real world structure is usually eccentric, meaning its centre of stiffness is offset from its centre of mass. Some structures are inherently eccentric, due to an asymmetric floor plan (usually dictated by the needs of the building occupancy) leading to an asymmetric layout of the structural members, or may be eccentric due to the location of stairwells and lift-shafts, etc. When a transverse mode is coupled to a rotational mode, arising from the eccentricity, the torsional component of seismic responses will be amplified if certain conditions are met.

Up to now, studies of the seismic behaviour of asymmetric structures, especially using shaker table tests, have been very limited. As a result, understanding of the role and effectiveness of rubber bearings in protecting eccentric structures has remained limited. Consequently, experimental studies on the response of eccentric structural systems with base isolators will provide valuable insight to this technique. Well-conducted experimentation will provide data for analysis and design of such structures isolated with rubber bearings. This paper describes a series of shaker table tests designed to evaluate the seismic performance of an eccentric five-storey building model subjected to various simulated earthquake inputs. The effectiveness of two rubber isolation systems against torsional response is investigated in detail to assist further development of new and effective isolation systems for asymmetric structures.

2 Experimental Studies

Five-storey benchmark building model

In order to encourage international collaborative research in the area of motion control of building structures, the International Association for Structural Control (IASC) formed a Building Group in 1996 with the aim of devising a few international benchmark building models. The brief was to choose a few benchmark models for both analytical and experimental research in the field of structural control. A five-storey benchmark model designed by Samali [4] was one of many adopted by IASC for benchmark studies. This benchmark model will allow researchers, all over the world, to test their control algorithms on the same model possessing identical properties. This will allow direct comparison of results among researchers with obvious benefits.

The experimental benchmark building model, having dimensions of 1.5m x 1.0m x 3m, offers the flexibility needed to model and test various building configurations. The eccentric model was created by adding a total of 350 kg mass to one side of a symmetrical concentric steel frame weighing 1200 kg, as shown in Figure 1. The additional 350 kg mass consisted of 140 steel disks equally distributed on the front side of each floor. This produces an eccentricity of $0.125L$, where L is the width of the floor. This level of eccentricity is regarded as moderate eccentricity.

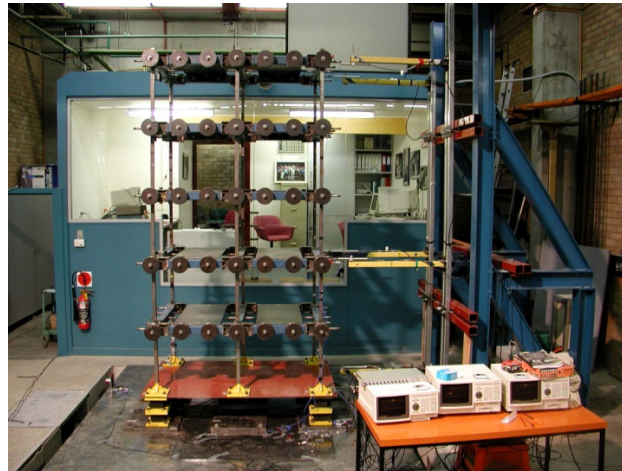


Fig. 1 Eccentric five-storey building model with isolators

Characteristics of rubber bearing isolators

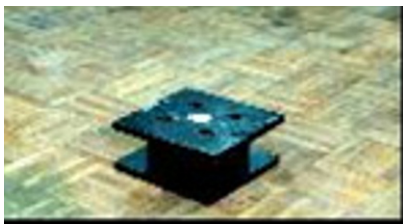


Fig. 2 Photo of an individual lead core rubber bearing

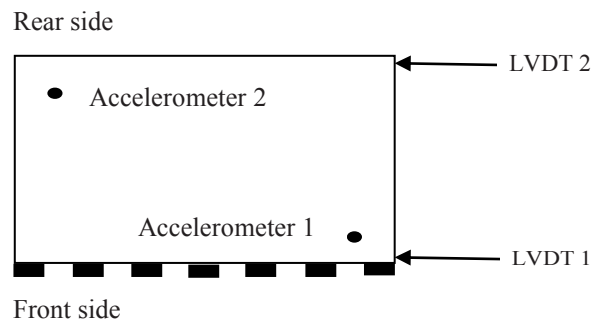


Fig. 3 Location of accelerometers and LVDTs in plan

The laminated rubber bearings (LRB) used in this study consisted of 25 thin rubber sheets with a sheet thickness of 2.2 mm and 25 thin layered steel plates each 1.8 mm thick. The rubber sheets were vulcanized and bonded under pressure and

heat so as to alternate with each thin steel plate. The effect achieved by including the inner steel plates is to control the shape factor of each elastomeric rubber layer, so as to prevent lateral bulging, achieving a vertical stiffness approximately 500 times the lateral stiffness of 220 kN/m. This ensures a large vertical load carrying capacity. Horizontal flexibility is provided through shear deformation of the individual rubber sheets. The overall dimensions of the laminated bearing used for the experiment were 120 x 120 x 100mm. Two thick mounting steel plates (200 x 200 x 20 mm) were bonded to the bottom and top surfaces of each laminated bearings so as to provide for connection fixings to the shaker table and to the superstructure, as shown in [Figure 1](#).

The configuration and dimensions of lead core rubber bearings (LCRB) ([Figure 2](#)) were the same as LRB but a lead plug with a diameter of 30 mm was inserted into a machined hole at the center of each bearing. In addition to the elastomeric characteristics of the LRB type, a further energy dissipation mechanism can be achieved with the LCRB due to the plastic deformation of the lead plug. A lead rubber bearing also provides initial rigidity under lateral service loads, such as during wind loads, due to the high stiffness prior to yielding of the lead plug. In that arrangement, however, the energy dissipation mechanism is activated only after the lead plug has yielded. Lead rubber bearings also provide a greater restoring effect to re-centre the isolators at their original locations after normal service loads.

Shaker table testing

Tests were carried out using the unidirectional shaker table facility at University of Technology, Sydney. The plan dimensions of the table are 3m x 3m. The table allows movement in a horizontal direction operated by a hydraulic actuator with a maximum acceleration of 2.5g (bare table), with a maximum stroke and piston velocity of +/-100mm and 550 mm/s respectively. As shown in [Figure 3](#), two accelerometer and two LVDT (linear variable displacement transducer) measurement locations were utilized for each survey measurement level. Two accelerometers and two LVDTs were located at each of the rubber bearing level, the 2nd and the 5th floor levels respectively. A further accelerometer and LVDT combination was installed on the shaker table to measure the table response.

A total of 14 channels of data were therefore recorded using two YOKOGAWA Analyzers. The shaker table was driven in the longitudinal direction of the five-storey model. To determine a suitable input excitation to the table, motion records from four earthquakes were used: El Centro (1994), Hachinohe (1968), 50%-intensity Kobe (1995) and Northridge (1994). Measured maximum accelerations on the shaker table were 0.42g, 0.23g, 0.41g and 0.45g representing the above four earthquakes respectively. To maintain dynamic similitude, each record was compressed in time by a factor of 3 to ensure the first mode frequency of the model was consistent with dominant frequency of the earthquake record. That is, the dominant frequencies of the simulated earthquakes were increased by a factor of 3.

The shaker table tests were conducted using both fixed-base and base-isolated structures, with the experimental set-up for the LRB-isolated five-storey benchmark model on the shaker table shown in [Figure 1](#).

3 Results and discussion

The effectiveness of the base isolation systems was evaluated by comparing the structural transverse and torsional responses of the two models – isolated and non-isolated – for each load case. This was determined by measuring the variation in maximum relative displacement with floor height in the direction of shaker for each model. For the non-isolated model this was defined as the floor displacement relative to the shaker table, and for the isolated model as displacement relative to the base of column pads.

These results are shown in [Figure 4](#). It can be seen that relative displacement increases with the floor height, as expected. A comparison of maximum relative displacements between front side and rear sides of the models reveals larger values for the front than the rear, attributable to a higher mass distribution on the front side. Time histories of relative displacement at 5th floor level due to El Centro earthquake are shown in [Figure 5](#). Clearly, both LRB and LCRB isolators are effective in reducing the relative movements of the model in both displacement amplitude and time. However, LRB isolator is the superior isolator. The smaller improvement to earthquake response achieved by the LCRB-isolated model is attributable to its non-linear stiffness characteristic, where high initial stiffness is maintained until the elastic limit of the lead core is reached; however the superior damping effects of the LCRB isolator are visible in the diminished time effects.

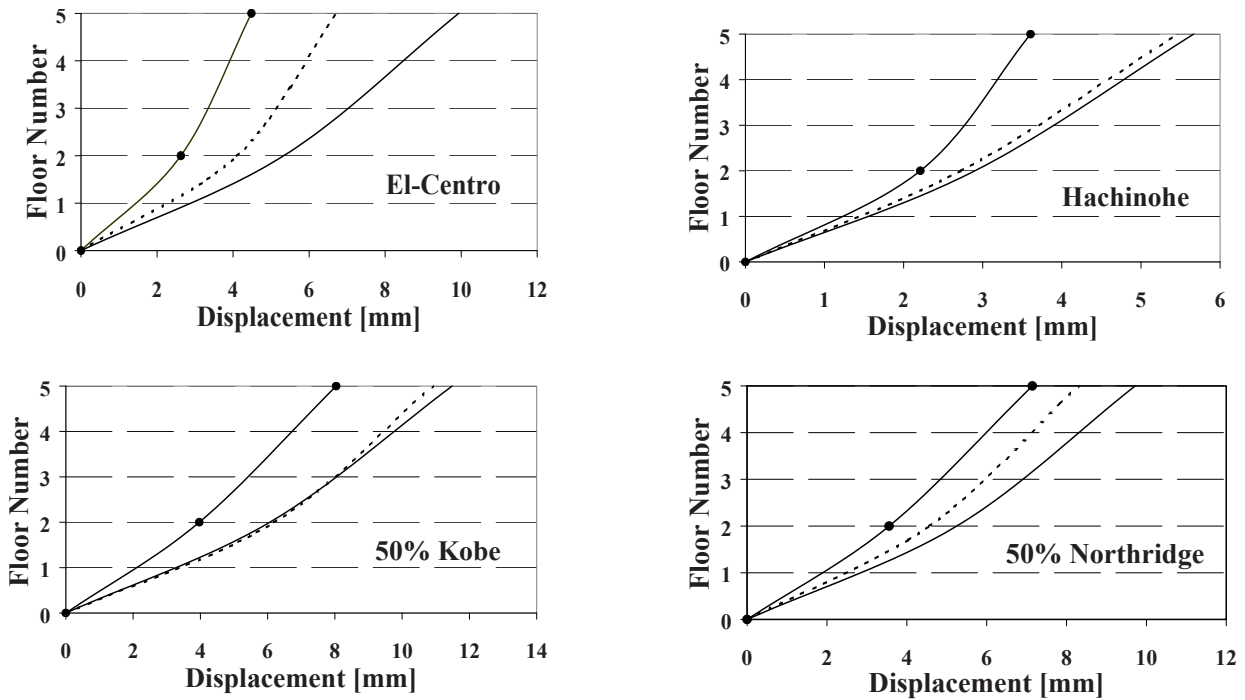


Fig. 4 Variation of maximum relative displacement with floor height, — Bareframe; ---- LCRB isolated; —●— LRB isolated

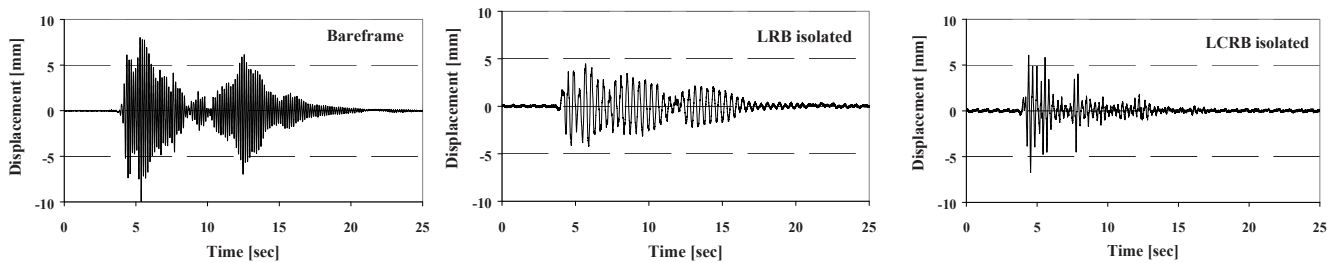


Fig. 5 Time histories of relative displacement on level 5 under El Centro earthquake

Considering Figure 4 further, it is apparent that the high initial stiffness of the LCRB isolator appears to have provided little control of relative displacement for the lower intensity load case of Hachinohe, but also for 50% Kobe where loads were comparable with El-Centro. This may indicate a difference in the frequency content of Hachinohe, however in all cases the improved damping characteristics of the LCRB isolator would be evident in more rapid decay of oscillation in the building structure.

Torsional angle was used to characterize the torsional behaviour of the model. This is simply defined as the rotational angle of movement of the rigid floor diaphragm of the model.

Relative torsional angle is defined as the difference in torsional angle between the fifth floor and the base (isolation level), which characterizes the torsional deformation within the building model. Variation of maximum relative torsional angle with floor height for each case is presented in Figure 6. It is clear that a significant reduction in model torsional angle can be obtained when either LCRB or LRB isolators are installed. The isolated models behave more like a rigid body than does the bareframe. In the isolated case, rubber bearings absorb most of the total torsional component, resulting in only a small torsional component of energy being transmitted into the building. Moreover, the effectiveness of LCRB is almost as good as that of LRB. The capacity of isolators to reduce torsional damage is achieved by ensuring the fundamental horizontal frequency of the isolator is far lower than the dominant frequencies generated by earthquakes.

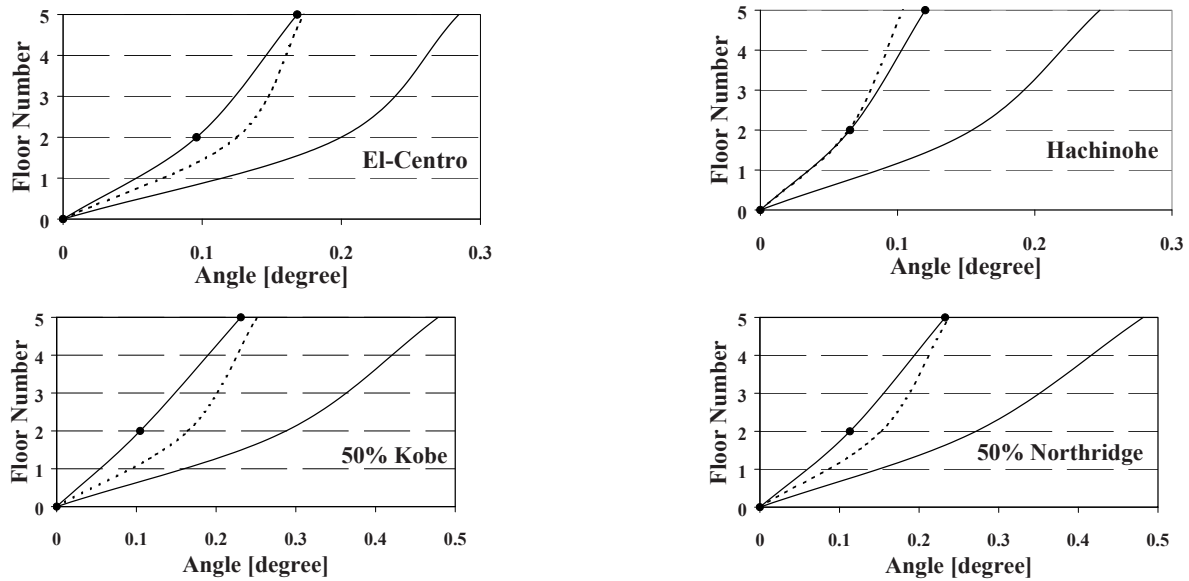


Fig. 6 Variation of relative torsional angle with floor height, — Bareframe; ---- LCRB isolated; —●— LRB isolated

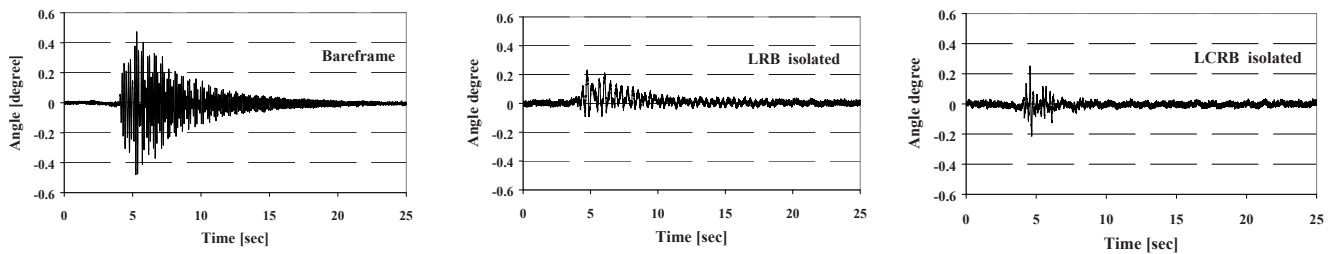


Fig. 7 Time histories of model torsional angle under Kobe earthquake

Time histories of the model torsional angle for the fifth floor under 50% intensity Kobe earthquake are depicted in Figure 7. Maximum torsional angle for the bareframe reaches a maximum of 0.48 degrees compared with 0.23 and 0.25 degrees for LRB and LCRB isolated models respectively. In addition, decay of the torsional angle vibration effects is considerably faster for the isolated models than it is in the bareframe.

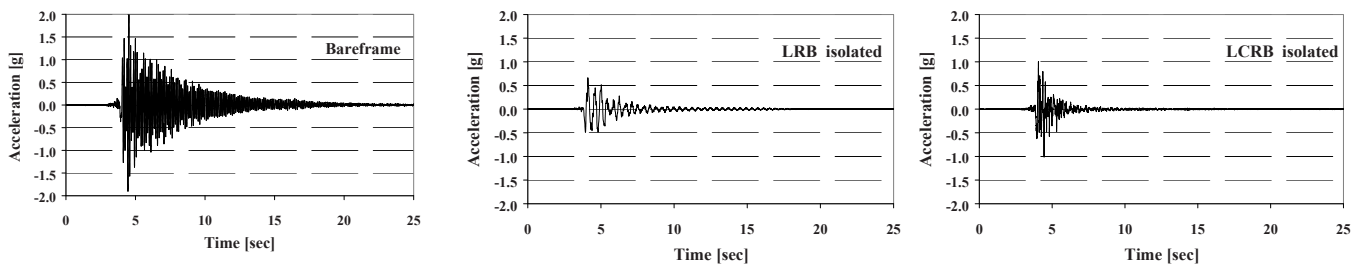


Fig. 8 Time histories of acceleration at the rear of fifth floor under Northridge earthquake

Time histories of model acceleration at the back of fifth floor subjected to 50% intensity Northridge earthquake are plotted in Figure 8, and the full test data are presented in Table 1. Maximum angular accelerations of base floor (rubber bearing), second and fifth floors of bareframe, LRB and LCRB isolated models under the four earthquakes are summarized in Table 2. Angular accelerations of both LRB and LCRB isolated models show considerably lower outcomes for all earthquakes and floor levels, compared with that of bareframe. For instance, maximum angular acceleration on fifth floor of bareframe under

Hachinohe earthquake amounts to 16.7 rad/sec^2 , while those of LRB and LCRB isolated models are only 3.56 and 5.36 rad/sec^2 respectively. It is also clear that LRB is more effective in reducing angular acceleration than LCRB.

In considering the LRB and LCRB characteristics it must be emphasized that LCRB is stiffer at low deflections and therefore more stable than LRB under normal working loads such as wind. This is an outcome of the presence of a rigid lead core. For situations where stability of the structure is of concern, such as with increased height, the use of LCRB over LRB may be preferred.

Table 1. Maximum accelerations [g]

El Centro earthquake			
	Bare	LRB	LCRB
Front		0.46	0.77
Back		0.52	0.61
Front	1.21	0.53	0.82
Back	0.77	0.49	0.65
Front	2.07	0.60	1.35
Back	1.15	0.54	0.83
Hachinohe earthquake			
	Bare	LRB	LCRB
Front		0.31	0.71
Back		0.30	0.50
Front	0.63	0.34	0.60
Back	0.61	0.33	0.39
Front	1.04	0.40	1.04
Back	1.08	0.40	0.76

50% Kobe earthquake				
		Bare	LRB	LCRB
Base	Front		0.64	1.30
	Back		0.60	1.13
2 nd	Front	1.38	0.68	1.40
	Back	1.42	0.66	1.01
5 th	Front	2.26	0.91	2.21
	Back	2.43	0.82	1.72
50% Northridge earthquake				
		Bare	LRB	LCRB
Base	Front		0.70	0.88
	Back		0.51	0.65
2 nd	Front	1.24	0.70	1.15
	Back	1.00	0.54	0.78
5 th	Front	1.87	0.79	1.77
	Back	1.99	0.66	1.00

Table 2. Maximum angular accelerations [$\text{rad} / \text{sec}^2$]

El Centro earthquake			
	Bare	LRB	LCRB
Base		5.60	5.32
2 nd floor	11.3	5.46	9.24
5 th floor	17.2	5.88	13.7
Hachinohe earthquake			
	Bare	LRB	LCRB
Base		2.66	4.51
2 nd floor	8.71	2.94	4.72
5 th floor	16.7	3.56	5.36
50% Kobe earthquake			
	Bare	LRB	LCRB
Base		5.04	8.26
2 nd floor	17.7	5.6	12.18
5 th floor	30.2	6.72	16.80
50% Northridge earthquake			
	Bare	LRB	LCRB
Base		4.76	13.16
2 nd floor	17.3	4.06	13.30
5 th floor	28.2	5.32	24.36

Table 3. Absolute deformation (mm) and torsional angle (degree) of rubber bearings

Earth-quake	Base isolator	Absolute deformation of rubber bearing (mm)		Absolute torsional angle of rubber bearing (degree)
		Front side	Rear side	
El Centro	LRB	17.54	18.16	0.374
	LCRB	13.33	12.89	0.109
Hachinohe	LRB	18.06	16.62	0.254
	LCRB	14.02	13.77	0.078
50% Kobe	LRB	26.26	23.27	0.468
	LCRB	17.16	16.15	0.118
50% Northridge	LRB	35.26	34.38	0.402
	LCRB	23.60	22.71	0.085

Absolute deformation and torsional angle of rubber bearings are presented in Table 3. In comparing LRB and LCRB, a larger absolute rubber deformation and torsional angle of the model isolated by LRB are seen which is related to smaller torsional stiffness of the LRB. The results also show that LCRB is more stable than LRB due to the presence of a rigid lead core. Therefore, when stability of the structure is of concern the use of LCRB over LRB is recommended.

4 Conclusions

In this study, a series of shaker table tests were conducted on non-isolated model, LRB-isolated and LCRB-isolated eccentric models. The objective of the tests was to evaluate the benefit to building structures of the incorporation of LRB and LCRB isolators to mitigate against torsional damage under strong ground motions. Both LRB and LCRB have been shown to reduce torsional deformation, relative displacement, acceleration and angular acceleration within the model structures. Important differences between the two isolator types were identified. The LRB was found to be similar to LCRB in protecting torsional deformation of the model but was more effective than LCRB in reducing model relative displacement. LCRB rendered a smaller torsional angle and absolute deformation of the base isolation system, a more stable structural system. Therefore, base isolation can greatly reduce torsional as well as translational response of building structures.

Acknowledgement

Author is grateful for Prof. Bijan Samali at University of Technology Sydney for his valuable advice.

References

- 1 Skinne R. I, Robinson W. H, and McVerry G. H, “*Introduction to seismic isolation*”, (John Wiley & Sons. 1993).
- 2 D.J. Dowrick: *Earthquake Resistant Design and Risk Reduction*. John Wiley & Sons, Inc. (2009)
- 3 Kelly J. M, “New applications and R&D for isolated civil buildings in the united states”, in *Proceedings of the international post-smart conference seminar*, Taormina, Sicily, Italy, p69-86, August 25-27, 1997.
- 4 Samali B, Li J, Mayol E and Wu H, “System identification of a five storey benchmark model using modal analysis. *Proceedings of international conference on applications of modal analysis*, Gold Coast, Queensland, Australia, paper 12. 1999.

Examination of a Feeling of Pulse Control Method for Cruiser-type Motorcycle

Nobutaka Tsujichi, Takayuki Koizumi, Takuya Tonomura
Department of Engineering, Doshisha University,
1-3, Tataramiyakodani, Kyotanabe-city, Kyoto, 610-0321, Japan

• ABSTRACT

There is added value which is unique ride comfort called a feeling of pulse to the motorcycle of the cruiser type. To design the model with the feeling of pulse, it is necessary to understand the relationship between the rider's evaluation of the feeling of pulse and factors of physical quantity which originates the feeling of pulse.

From the memoir that was focused on the engine revolutionary order component of the seat vibration at the time of riding the motorcycle in this laboratory, it was known that the level of acceleration RMS value of 0.5th and 1st orders of vibration affects the feeling of pulse. It is necessary that I examine the engine region that generates the vibration, in order to match the optimum threshold of RMS value of acceleration amplitude on the seat vibration in the design of the motorcycle. Therefore I focus on the engine region in this study, as the factor of physical quantity which originates the feeling of pulse. I examine changes of the engine identity by changing the V-type engine setting angle, the ignition timing and the explosive power in the simulation of the engine model that I use.

1 INTRODUCTION

There are various models of motorcycles such as naked, off-road, motor scooter, racer replica, and cruiser type. In these models, there is added value which is unique ride comfort called a feeling of pulse to the motorcycle of the cruiser type. And there are a lot of riders in search of a model to feel the feeling of pulse. To design the model with the feeling of pulse, it is necessary to understand the relationship between the rider's evaluation of the feeling of pulse and factors of physical quantity which originates the feeling of pulse.

Two V type cylinder engines are equipped with in the large-sized two-wheeled vehicle of the cruiser type mainly, and as characteristics of the engine type, the explosion of the inequality interval and that changing bank angle of the engine can increase and decrease the vibration level and bring about original engine feeling. The vibration that occurred with an engine transmits it to a frame and communicates with the human body through a seat. Because the vibration is transmitted to the human body, riders feel the feeling of pulse. Main factors of physical quantity which originates the feeling of pulse in the equipment of the vehicle are the engine vibration, the transmission coefficient from the engine to the frame and the seat vibration.

From the memoir that was focused on the engine revolutionary order component of the seat vibration at the time of riding the motorcycle in this laboratory, it was known that the level of acceleration RMS value of 0.5th and 1st orders of vibration affects the feeling of pulse. However we don't examine the engine region that generates a vibration, it is necessary that I examine the engine identity that generates the vibration, in order to match the optimum threshold of RMS value of acceleration amplitude on the seat vibration in the design of the motorcycle. Therefore I focus on the engine region that generates the vibration in the equipment of the vehicle in this study, as the factor of physical quantity which originates the feeling of pulse. I focus on the ingredient of 0.5th and 1st in the engine region, and examine changes of the engine identity by changing the V-type engine setting angle, the ignition timing and the explosive power in the simulation of the engine model that I use.

The study the seat vibration characteristic

2 Vibration measure examination of the real motorcycle seat

I carried out a run examination to measure seat vibration at the time of the real motorcycle. I installed an examination motorcycle on a chassis dynamo and performed a sham run and measured seat vibration and the engine number of revolutions.

2.1 Measurement device and condition

I show the situation of the chassis examination in [figure. 1](#). I used a pulse meter for an electric charge type accelerometer, the measurement of the engine number of revolutions for a measurement of the seat vibration each. Possessed front and back, top and bottom and three courses of right and left for the progress direction of the vehicle, and the accelerometer measured sampling frequency as 1[kHz]. I show the state that installed an electric charge type accelerometer in the seat upper part in [figure. 2](#).

The test rider is professional rider of one person, the examination motorcycle model is cruiser type vehicles with V2 cylinders / 1600cc. The driving condition is the shift up acceleration run that felt that it was easy to be got a feeling of beating, and gear 1 from a speed to 5.



Fig.1 Actual vehicle test using chassis dynamo



Fig.2 Appearance of sensors attached to seat

2.2 Data analysis of the seat vibration

I show front and back that I measured and a result of the vibration acceleration of the top and bottom direction in figure. 3. In addition, I show the result of data in a career at the time of the engine number of revolutions that I measured in figure. 4.

I show the result that performed Fourier transform for vibration acceleration for a short time to watch a change in time of the frequency ingredient at the time of the shift up acceleration run in figure. 5. Figure. 5 (a) is front and back direction and figure. 5 (b) is results of the top and bottom direction. I define vibration to occur for one period by an engine 1 round per minute hit once here as a rotary primary ingredient. From a figure, I understand that the main vibration ingredient of the seat is 0.5th and 1st orders of the engine number of revolutions.

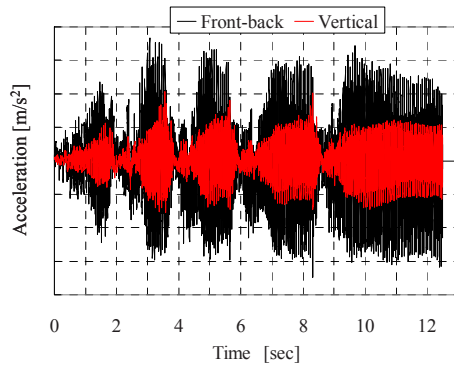


Fig.3 Acceleration response depend on engine rotation

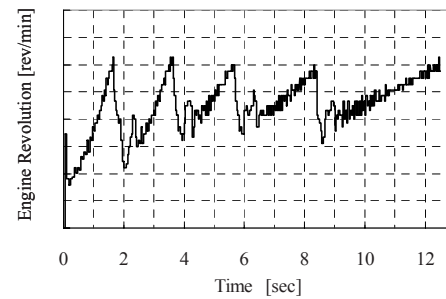


Fig.4 Time history of engine revolution

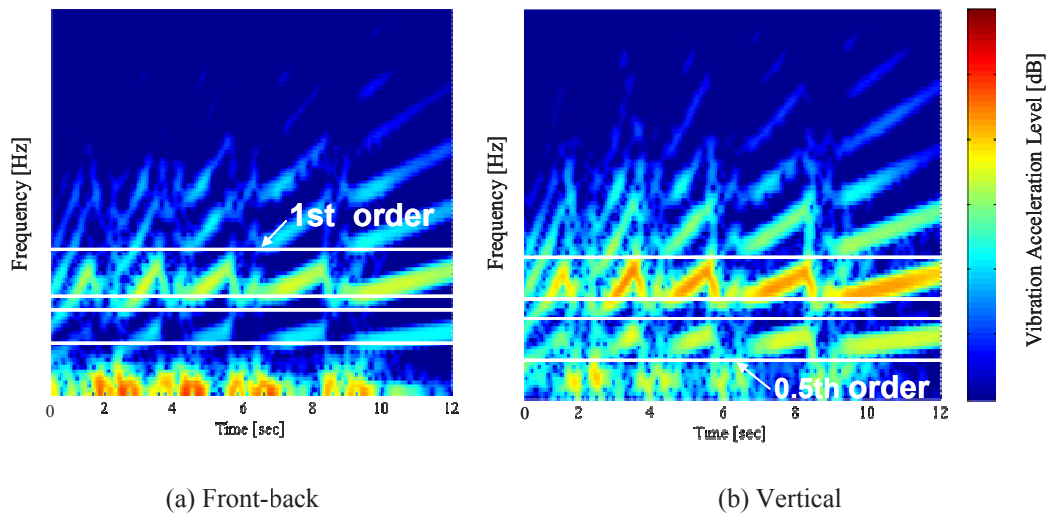


Fig.5 Result of analysis by STFT

The study which paid its attention to a change of the engine identity

3. The engine model of Adams-View

I perform the simulation analysis of the engine model that used Adams-View in this study and investigate a change of the engine identity. The engine model who uses it for analysis really

uses two V type cylinder engines equipped with for 1700 Balkan Voyager made by car model, Kawasaki to show in figure 6. I show an engine put on figure 7, table 1 and the main specifications required. Water cooled, four strokes, V type, two cylinders engine. A single overhead camshaft type (SOHC). The $\text{boa} \times \text{stroke}$ is $102 \times 104 \text{ mm}$. Engine displacement volume is $1,700 \text{ cm}^3$. In addition, I show an engine model to be able to employ in figure 8 on Adams-View simulation.



Fig.6 Kawasaki Vulcan 1700 Voyager



Fig.7 V type Engine

Table.1 Engine specifications

Engine type	Gasoline, V type, two cylinder, water cooled 4 stroke cycle, 1 camshaft (SOHC)
Bore \times Stroke [mm]	$\phi 102 \times 104$
Displacement [cm^3]	1700

3.1 Examination of the measurement point in the engine model and an evaluation method

I perform the simulation analysis that I used an engine model to show in figure 8 for in this study and evaluate the identity of the engine model.

In the model top, I do the measurement point on evaluating this engine identity with a crankcase part to show in figure 9. I investigate anti-power to act on in a rotary degree to depend on this crankcase part periodically and anti-torque and evaluate engine identity.

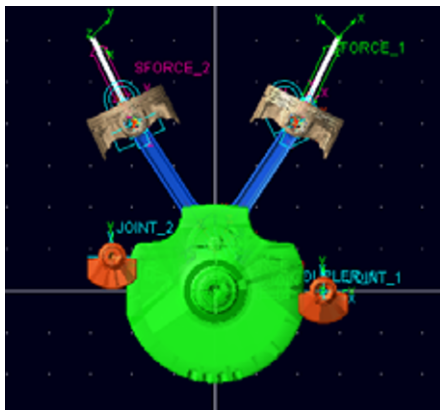


Fig.8 Engine model in Adams View

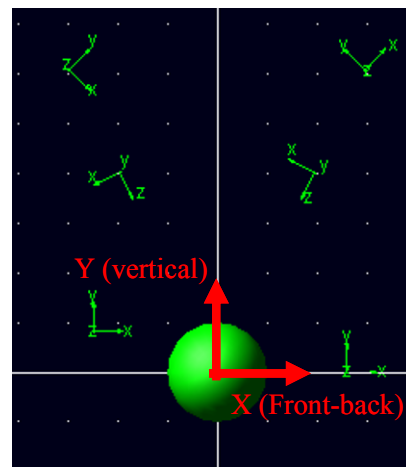


Fig.9 Crankcase in engine model

3.2 The setting of the ignition time / the pipe internal pressure in the engine model

I show in [figure 10](#) which an engine pipe internal pressures of the piston front side and rear side on the engine model. The crank angle [deg.CA] in engine 1 cycle and the pressure [N/mm²] are shown in the horizontal and vertical axes.

I am possible, and I plot pressure [N/mm²] every 0.5[deg] in crank angle 720[deg] in 1 cycle to show it in the figure, and the setting of the ignition time to be able to put it on an engine model sets it by changing this pressure setting. I can change it in this way in an

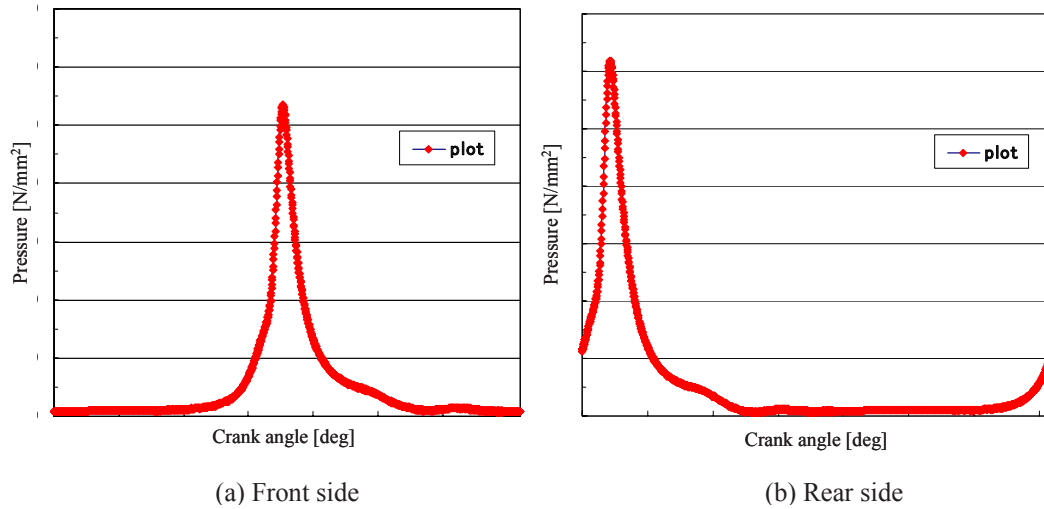


Fig.10 Settings of cylinder internal pressure and ignition timing in one cycle

3.3 Setting of the explosive power in the engine model

I show explosive power to be able to put on an engine model in [figure 11](#). It is defined in the next expression each in piston front side / the rear side.

$$F[N] = P[N/mm^2] \times S[mm^2]$$

Here, $F[N]$ is explosive power in the piston. $P[N/mm^2]$ is pressure in each crank angle [deg.CA]. $S[mm^2]$ show surface area in the piston section. Explosive power $F[N]$ which acts on a piston is calculated that multiply $P[N/mm^2]$ in each crank angle [deg.CA] by $S[mm^2]$ of surface area in the piston section. I show time order data of the explosive power to act on piston front side and rear side in [figure 12](#). The horizontal axel is time [sec], the vertical axis is power [N].

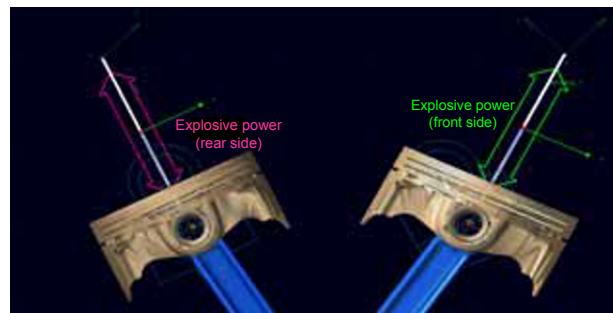


Fig.11 Explosive power in engine model (front & rear side)

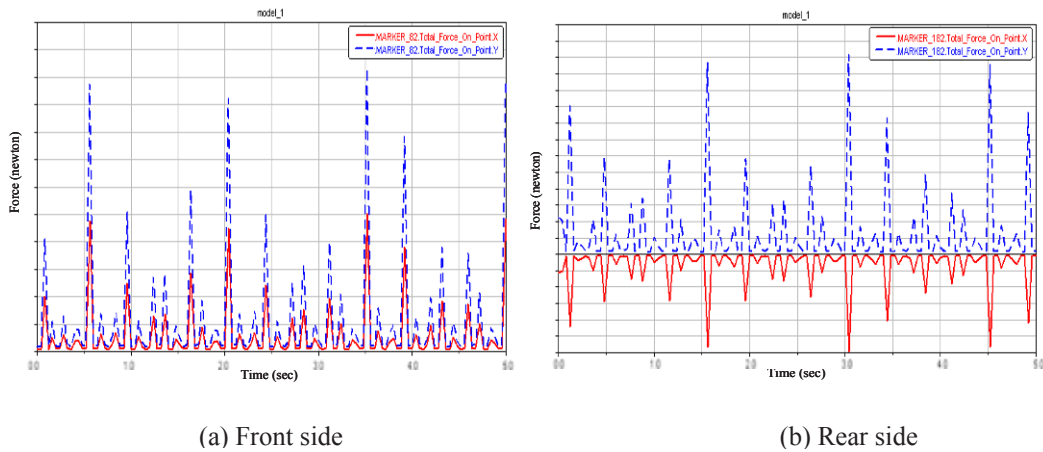


Fig.12 Explosive power in engine simulation

3.4 The grasp of the engine property in the measurement point

I show time order data the anti-power and the anti-torque of the front-back and vertical in the crankcase region which is a measurement point in [figure 13](#).

I make the color map which shows a vertical axis, anti-power in the frequency and size of the anti-torque in the cross axle based on the anti-power that I measured and anti-torque, an engine turn in time. I show the example in [figure 14](#).

The anti-power of each engine turn degree ingredient can measure anti-torque by using this analytical technique from a figure and can grasp the change of the engine characteristic.

Late; is similar, and make full use of this technique in the change of the explosive power in V-type engine setting an angle / the ignition time to pay its attention as the feeling of beating control method examination possibility factor that can change with an engine characteristic in this report, and investigate the change of the engine characteristic. In addition, I perform it at announcement about the investigation about these examination possibility factors in detail.

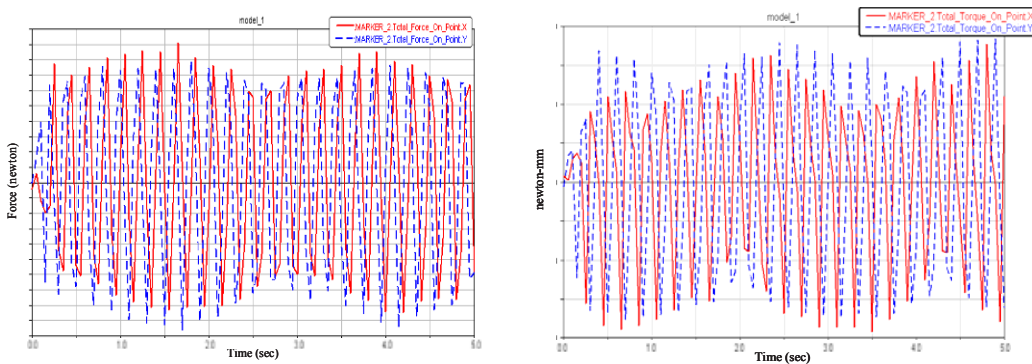


Fig.13 Anti-power and Anti-torque of the front-back and vertical in the crankcase region

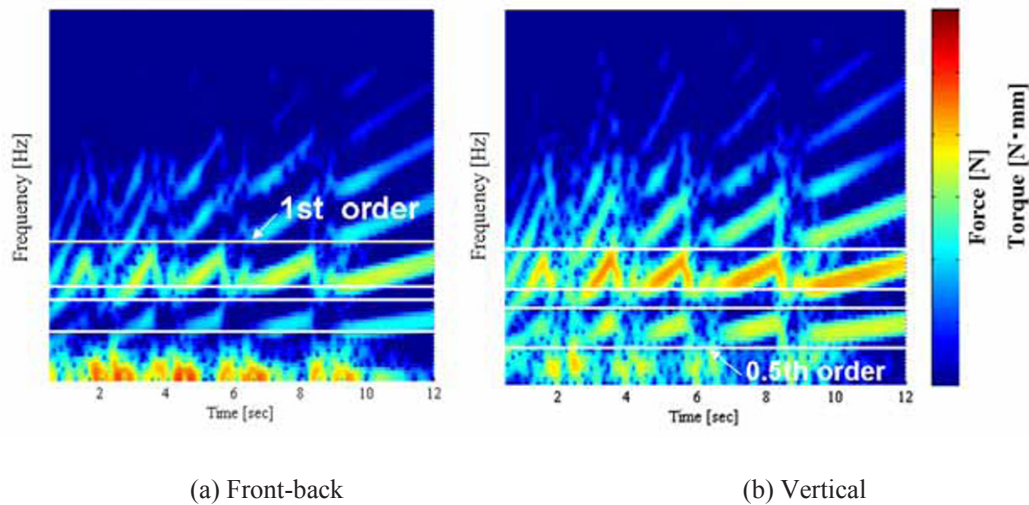


Fig.14 The color map of Force [N] & Torque [N • mm] level in the crankcase region

CONCLUSIONS

I understand that the main vibration ingredient of the seat is 0.5th and 1st orders of the engine number of revolutions.

In addition, I analyzed an engine property and I paid my attention about 0.5th and 1st orders from the engine part and established technique to examine evaluation.

In addition, I perform it at announcement about the investigation that is V-type engine setting an angle, ignition the time and explosive power, about these examination possibility factors in detail.

REFERENCES

- [1] Ichiro Kageyama, Koji Emoto, "Study about the shimmy to occur in the steering wheel system of the two-wheeled vehicle", Japan Society of Mechanical Engineers memoirs C, No 61-582, pp.227-232(1995)
- [2] Kan Utou, "Study of the machine", Vol.32, No 1, pp.227-231(1998)
- [3] Takeshi Nakajima, Hirohide Matsushima, "Improvement of the drive ability that utilized a measurement / control technology", Technical report of KHI, No. 162, pp.44-49 (2006)
- [4] Miyuki Morioka, "Application to the ride comfort evaluation - motorcycle of the many input vibration", JOURNAL OF INCE, Vol.31, No. 5, pp.378-383(2007)
- [5] Yasunori Suzuki, Keisuke Kamio, Hiroyuki Katsumata, Yasuo Oshinoya, Kazuhisa Ishibashi, Kouichi Ozaki, Hirohiko Ogino, "Active suspension of the compact car for two uses sheet (the examination of a factor influencing sensuality evaluation value) ", Tokai University bulletin department of engineering, Vol.45, No. 2, pp.79-84(2005)
- [6] Naoki Tsuchida, Kenichi Kajiware, "Feeling of acceleration improvement of the two-wheeled vehicle by the crank phase angle change", Preprints of Meeting on Automotive Engineers, No.963, , pp.85-88(1996.5)
- [7] Takahisa Onishi, Takayuki Koizumi, Nobutaka Tsuziuchi, "Evaluation of Feeling of Pulse for Cruiser-type Motorcycle" SETC, (2009)

Seeding Cracks Using a Fatigue Tester for Accelerated Gear Tooth Breaking

Nenadic Nenad G., Research Faculty, Golisano Institute for Sustainability, Rochester Institute of Technology, 133 Lomb Memorial Drive, Rochester, New York 14623, E-mail: nxnasp@rit.edu

Wodenscheck Joseph A., Senior Staff Engineer, Center for Integrated Manufacturing Studies, Rochester Institute of Technology, 133 Lomb Memorial Drive, Rochester, New York 14623, E-mail: jawasp@rit.edu

Thurston Michael G., Research Faculty, Golisano Institute for Sustainability, Rochester Institute of Technology, 133 Lomb Memorial Drive, Rochester, New York 14623, E-mail: mgtasp@rit.edu

Lewicki David G., Research Mechanical Engineer, NASA Glenn Research Center, Cleveland, Ohio 44135, E-mail: david.g.lewicki@nasa.gov

Abstract

This report describes fatigue-induced seeded cracks in spur gears and compares them to cracks created using a more traditional seeding method, viz. notching. Finite element analysis (FEA) compares the effective compliance of a cracked tooth to the effective compliance of a notched tooth where the crack and the notch are of the same depth. In this analysis, cracks are propagated to the desired depth using FRANC2D and effective compliances are computed in ANSYS. A compliance-based feature for detecting cracks on the fatigue tester is described. The initiated cracks are examined using both non-destructive and destructive methods. The destructive examination reveals variability in the shape of crack surfaces.

Background of the study

Of the four dominant modes of gear tooth failure (breakage, wear, pitting, and scoring), breakage is the most catastrophic and occurs precipitously, with no advanced warning. The present study is concerned with the breakage failure mode exclusively.

The work described here is a subset of a larger empirical study conducted on high-quality spur gears to evaluate performance of vibration-based features for detecting cracks and assessing crack depths. The features, also referred to as condition indicators (CIs), are summarized by [1-3].

In this larger study, the gears are first spun in a dynamometer-based fixture to obtain feature baselines. The cracks are then initiated using a fatigue tester to simulate overload conditions. Finally, the fatigue induced-cracks are propagated on the dynamometer-based fixture under different operating conditions, i.e., different levels of angular speed and torque, while the actual crack lengths on each gear face is measured using crack-propagation sensors. The main objective is to create a well-documented, statistically significant data for monitoring cracks from their inception to failure.

The complete service life of a gear has two phases: crack initiation and crack propagation [4]. A crack initiation phase is typically much longer than the subsequent crack propagation phase. In crack propagation studies the crack initiation phase is often accelerated by introducing a notch in a gear tooth. The present article describes an alternative approach to accelerate crack initiation where higher-than-normal loads are applied on a gear tooth using a fatigue tester.

Finite element analysis (FEA) of a cracked and a notched tooth

Before proceeding with accelerated crack initiation on a fatigue tester, it was of interest to compare the geometry of cracked and notched gear teeth. A gear with a notch was compared to a gear with a crack of the same length as the notch using FEA. The gear geometry was generated using a toolkit implemented in MATLAB for spur gear drawing and analysis, as shown in Fig. 1. The first version of the software was created by [5] and implemented by the Army Research Laboratory and NASA in Fortran. The present version is implemented by RIT, with added capabilities that include mesh generation and import and export capabilities.

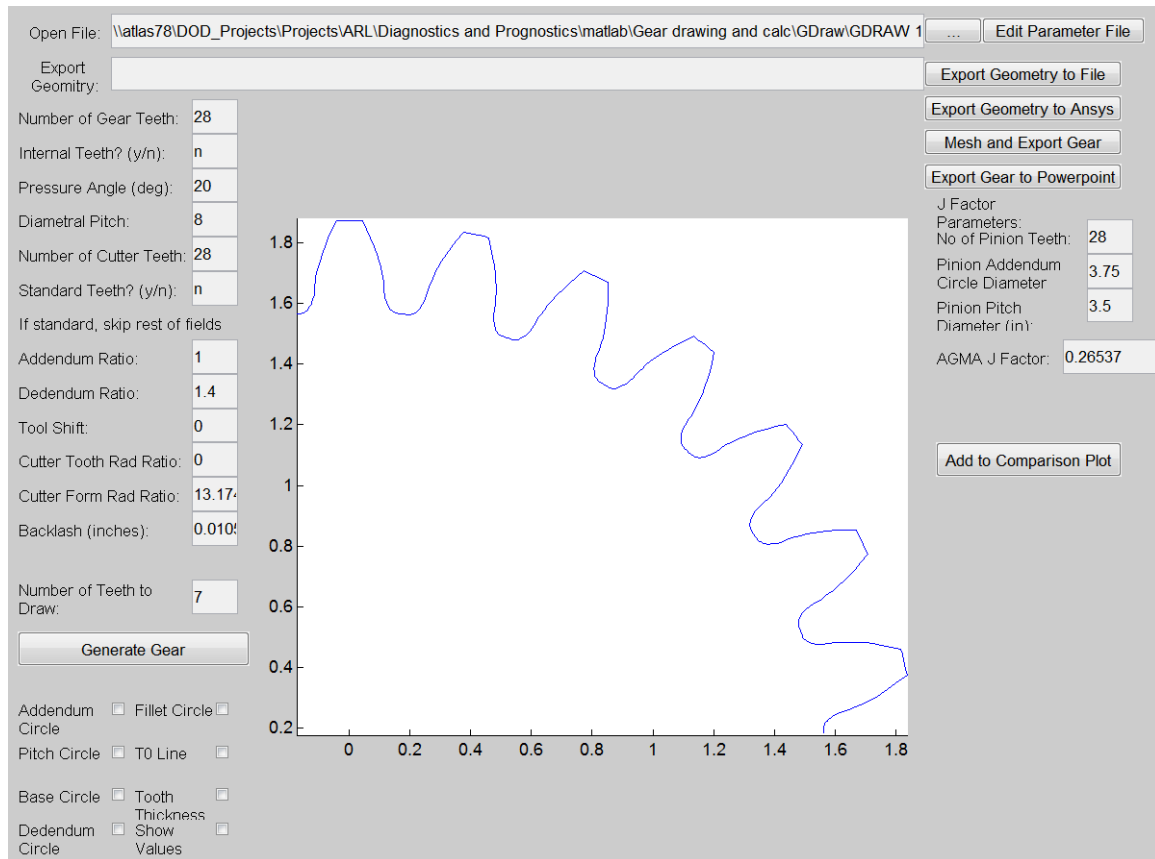


Fig. 1 Spur gear geometry generation

The toolkit is capable of generating the gear tooth geometry, creating a finite element mesh using linear triangular elements, and exporting the meshed geometry to two commercially available finite element programs, FRANC2D and ANSYS. The mesh generator employs the *distmesh* algorithm and implementation [6]. The implementation is tailored to generate finer mesh near the application of force and high stress areas. Fig. 2 shows the meshed geometry of a notched tooth, with non-uniform mesh density, generated entirely within the toolkit. The generation of the cracked tooth is a bit more involved. The uncracked tooth geometry is generated in the MATLAB toolkit. The geometry is then exported to FRANC2D, a program for simulation of crack growth [7] where the initial crack was formed and propagated to the desired length. The cracked geometry is then read and exported to ANSYS via the MATLAB toolkit.

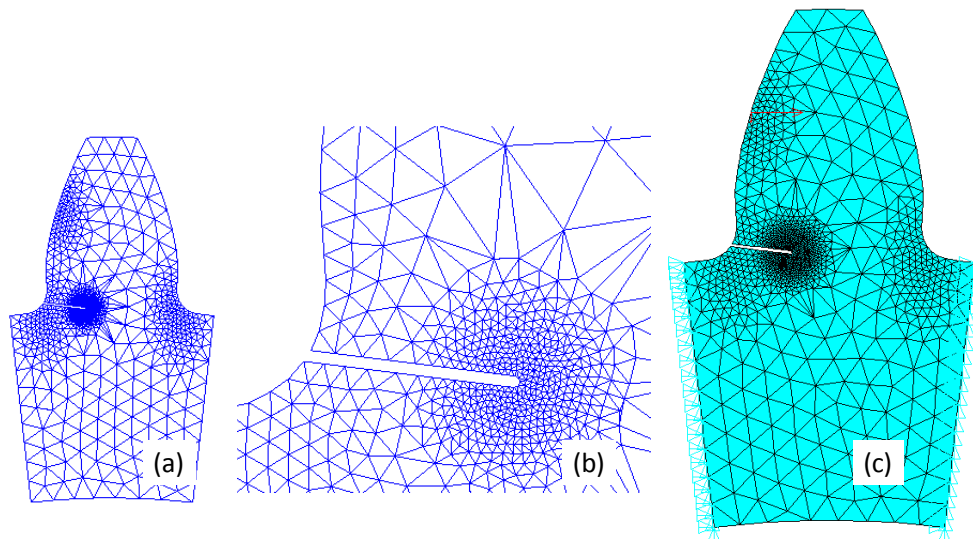


Fig. 2 A notched tooth generation within the MATLAB-based toolkit (a) Entire tooth geometry using MATLAB (b) Zoom into crack using MATLAB (c) Notch exported into ANSYS

Fig. 3 shows ANSYS static analysis of a gear with a notch, and the gear with the crack. The view is zoomed into the area of notch/crack. To minimize the difference in the crack length and the notch length, we generated the cracked geometry first, and then generated the notch later by aligning the tip of the notch to the tip of the crack.

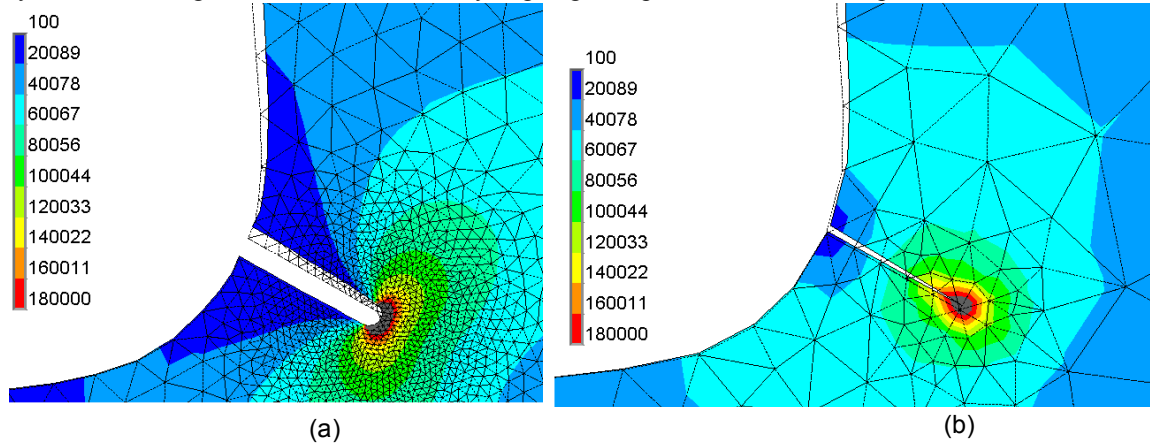


Fig. 3 Exaggerated deformations and contours of equivalent stress (psi) near (a) notch (b) crack

In the first analysis, a static force of 1000 lb was applied at the gear pitch radius, normal to the surface, and the magnitude of the displacement was measured at the tip of the outer radius, as depicted in Fig. 4a. The simulation was repeated for two crack/notch lengths: $\approx 1/8$ of the total gear thickness and $\approx 1/4$ of the total gear thickness. Two notch sizes were studied. One for a notch radius of $R=0.001$ ", and the other for a notch radius of $R=0.002$ ". The effect of mesh density on the result for the cracked tooth was also considered. Although we computed displacements, the results can be expressed also as effective compliances, since the force is held constant.

Table 1 FEM displacements (in) of cracked and notched gear teeth

Normalized crack length	Crack		Notch	
	Regular Mesh	Refined Mesh	R = 0.001"	R = 0.002"
0.125	1.33420E-03	1.33530E-03	1.33620E-03	1.33660E-03
0.25	1.87280E-03	1.87740E-03	1.97050E-03	2.00100E-03

The FEA results are summarized in Table 1 and in Fig. 4b. For the crack/notch length of $1/8$ of the gear thickness all the displacements are virtually indistinguishable, they are within less than 0.2 % of the mean. For a crack/notch length equal to $1/4$ of gear thickness, the notched gear exhibits larger displacements.

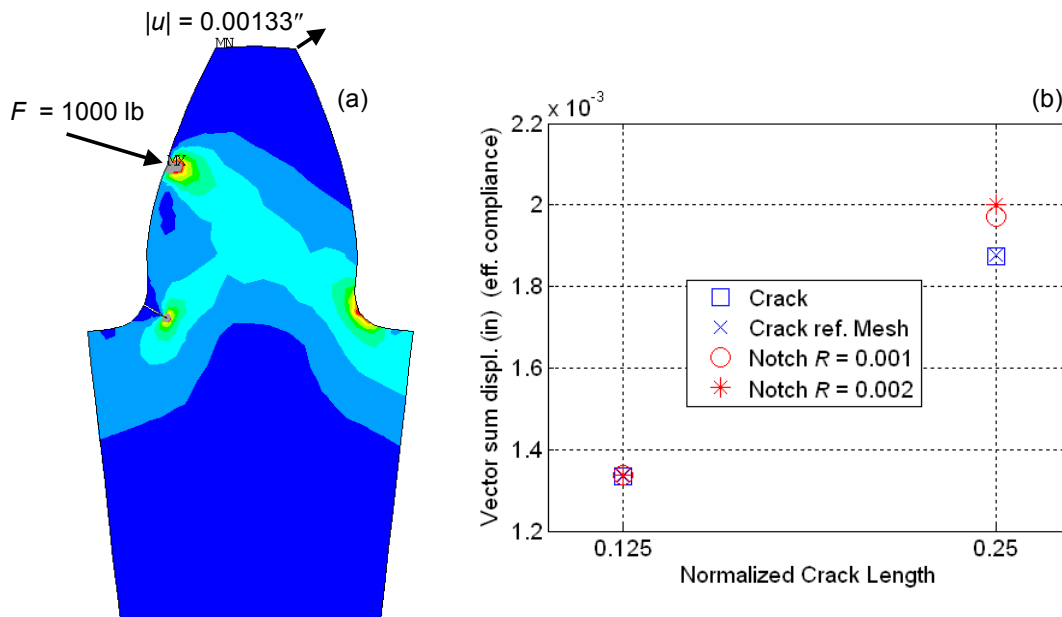


Fig. 4 Static analysis (a) Annotated contours of equivalent stress (b) Plot summary of displacements vs. crack length

An alternative metric for comparison of cracked and notched teeth is the fundamental natural frequency of a gear tooth. Fig. 5a shows the fundamental mode shape of the gear section of interest associated with the fundamental natural frequency. The fixed boundary conditions are indicated.

Table 2 and Fig. 5b summarize the FEA results of the modal analysis. Table 2 shows the actual frequencies, while Fig. 5b shows the frequency shifts from the baseline case, where the baseline is a healthy gear. The frequency decreases as the crack/notch grows. The notches give rise to the larger shifts, but the difference between the notched and cracked teeth is small.

Table 2 Fundamental frequency (Hz) of notched and cracked gear teeth.

Normalized crack length	Crack		Notch	
	Regular Mesh	Refined Mesh	R = 0.001"	R = 0.002"
0.125	3.02100E+03	3.02100E+03	3.00200E+03	2.98900E+03
0.25	2.56700E+03	2.56300E+03	2.54500E+03	2.52400E+03

Overall, the analysis shows that crack and notch of the same length agree very well. Although by a small amount, notched gears exhibit more change in effective compliance and frequency shifts than their cracked counterparts. Thus, it is expected that a vibration feature is slightly more sensitive to the notched tooth than to the cracked tooth.

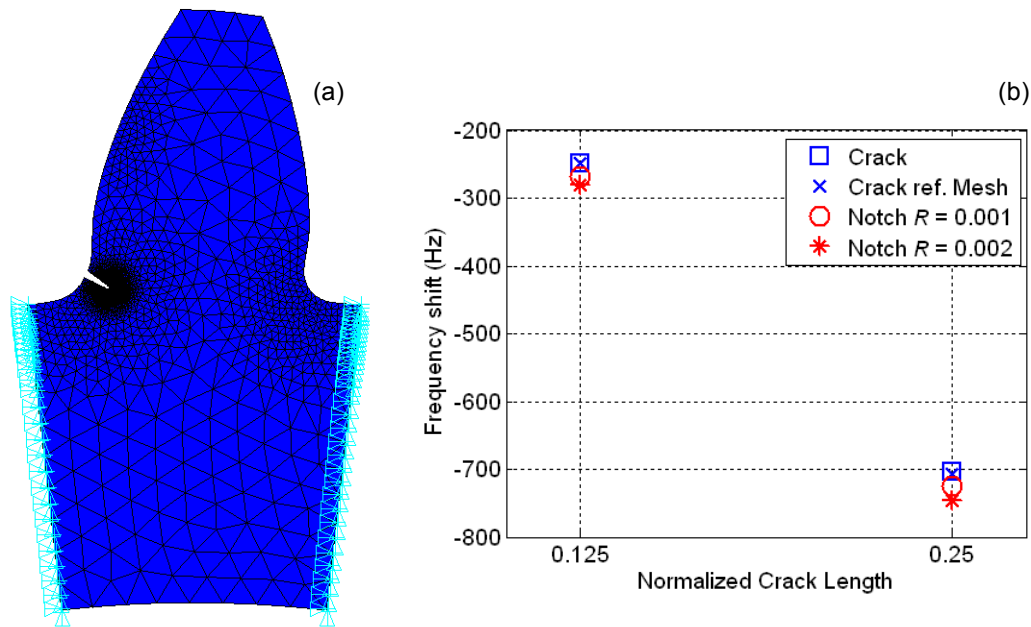


Fig. 5 Modal analysis (a) Fundamental mode shape (b) Summary of fundamental frequencies

Crack initiation fixture and crack initiation process

The cracks were initiated on a commercially available fatigue tester. A special fixture, shown in Fig. 6, was designed, developed, and built for this purpose. The fixture captures a single gear between two steel plates and uses an anvil to assert a load on to a single tooth. The gray anvil holder, shown in Fig. 6a, is inserted into the machine's lower ram and secured using a pin. The anvil is held within the anvil holder and captured with two set screws. The anvil width is greater than the gear tooth width and the anvil material is made of tool steel for strength. The anvil gear tooth interface is 5 degrees with respect to horizontal, similar to the ASME J1619 single tooth fatigue test fixture [8]. To provide the contact area near the high point of single tooth contact (HPSTC), the centerline of the gear tooth under test is located at 15.4 degrees with respect to the ground; see Fig. 6c. The gear is located between the 1 inch thick steel plates with a 1.181 inch diameter shaft locating the center of the gear. Keys were used to position the gear teeth with respect to polar angle. The primary device to react the input torque to the gear, however, was three internal gear teeth, shown in brown below, and three fasteners to provide clamping friction. Interfacing with several points within the fixture to transfer the input torque to the machine prevented damage to gear teeth not under test. The two side plate were fastened together and then bolted to a bottom subplate. This subplate was threaded and welded to a connecting rod, shown in red, that threaded into the load cell on the fatigue tester.

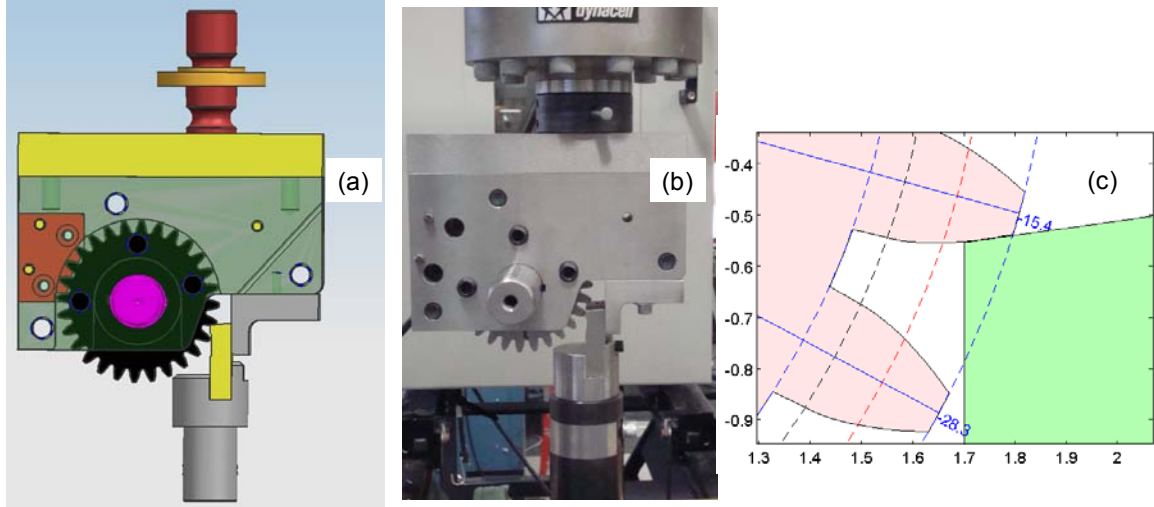


Fig. 6 The fixture for crack initiation (a) Computer aided design image (b) Photograph of the built fixture (c) Anvil angle detail.

The fatigue tester operated in load control mode with a cyclic compressive load between 100 and 3100lbs applied at a rate of 10Hz. The crack initiation region (tooth root) was always held in tension during the test.

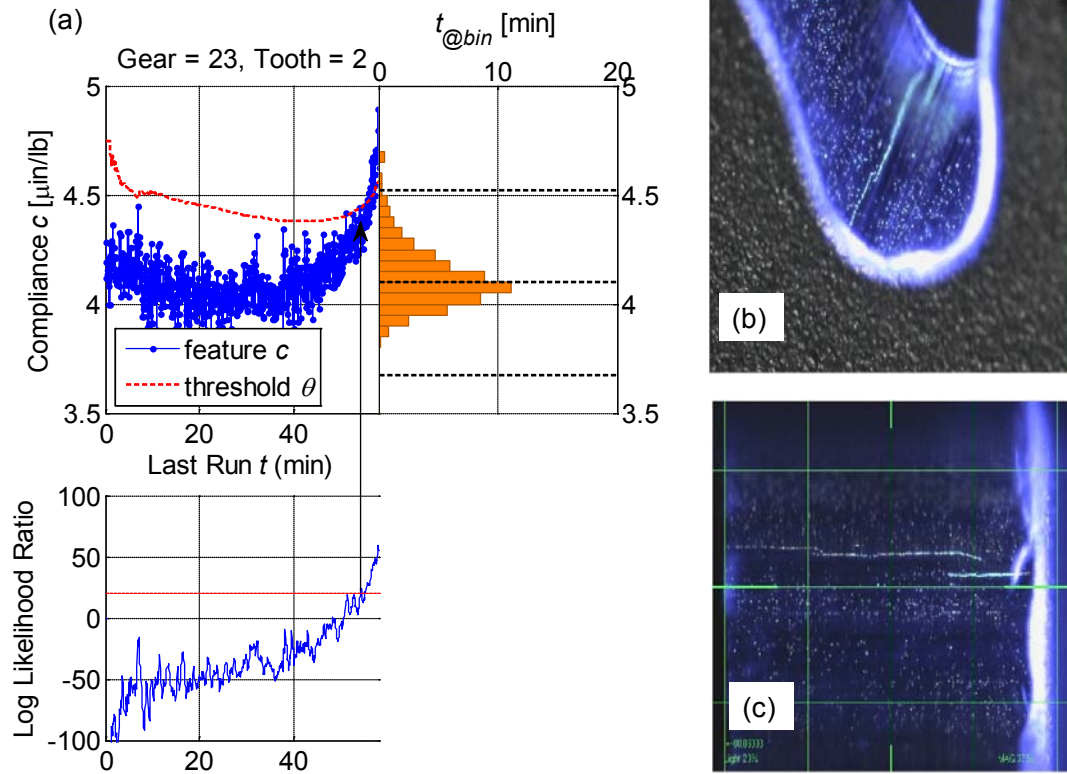


Fig. 7 Crack detection process (a) Characteristic signals (b) Angled view of a cracked tooth (c) 90 degree view of a cracked tooth

A compliance-based feature was developed for early detection of cracks, since the displacement-based feature did not have sufficient resolution. The crack detection is based on observation of N estimations of the feature. We compute the described feature in N points. The first $N-M$ points are used to establish the baseline distribution of the feature, and the last M points are used for determining if the crack occurred. The crack detection is then based on the likelihood ratio as follows

$$\Lambda = \prod_{k=N-M+1}^N \frac{\Pr[c_k | H_1]}{\Pr[c_k | H_o]} \quad (1)$$

where H_o is the null hypothesis that states that there is no crack, i.e., the feature is distributed according to the distribution of a healthy gear

$$H_o : c_k \sim \mathcal{N}(\mu_c, \sigma_c) \quad (2)$$

μ_c and σ_c are sample mean and standard deviation of the feature, excluding the last M points.

$$\mu_c = \frac{1}{N-M} \sum_{k=1}^{N-M} c_k \quad (3)$$

$$\sigma_c = \frac{1}{N-M-1} \sum_{k=1}^{N-M} (c_k - \mu_c)^2 \quad (4)$$

The alternative hypothesis states that the crack has occurred, viz. the feature c_k does not belong to the baseline distribution, but to a normal distribution centered around threshold θ

$$H_1 : c_k \sim \mathcal{N}(\theta, \sigma_c) \quad (5)$$

Fig. 7 depicts the process of crack detection. The compliance feature and the threshold are shown, as well as the distribution of the compliance feature. The threshold is set initially at a conservative, empirically determined, relatively high value. As more data becomes available, the threshold is adjusted to become a certain Mahalanobis distance from the distribution mean. The distance equals to $2.5\sigma_c$ for the example shown in Fig. 7a.

Crack verification using non-destructive methods

The non-destructive crack verification is based on the images taken using a commercially available high-resolution, optical video measuring system and custom fixture shown in Fig. 8. The custom fixture was designed and built to place the tooth under the test in tension of approximately 500 lb. Before the gear is being placed in the fixture, the tooth under inspection is covered with a layer of fluorescent iron powder. The tooth is then placed in strong magnetic field and observed under ultraviolet (UV) light. At the crack the magnetic lines are disturbed. The magnetic-particle-based inspection method is a standard technique for crack detection and it is described in fracture mechanics textbooks, e.g. [9]. Glowing particles indicate fracture site.

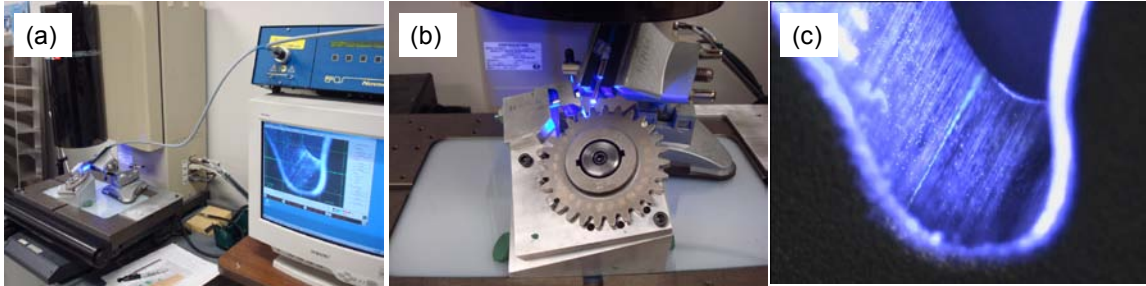


Fig. 8 Non-destructive method for crack verification (a) Imaging system (b) Custom gear fixture (c) Imaged tooth

Fig. 8 illustrates the non-destructive measurement process. Prior to imaging the tooth had been subjected to approximately 29 thousand cycles of load in the 100-3100 lb range. The final resulting threshold for the compliance feature was 4.40 $\mu\text{in/lb}$. The tooth was imaged $37.5\times$ magnification.

This non-destructive method was not completely successful in detecting gear tooth cracks. The gear face area was the only region where cracks could be observed. The gear flank surface was considerably rougher. Even after polishing, no cracks were detected on the gear flanks.

Crack characterization using destructive methods

The non-destructive inspection method was useful for confirmation of the crack initiation, but did not allow crack characterization, that is, determination of the actual crack depths. Two methods are described for measuring crack depth and characterization of the fracture surface: slicing and polishing (Method 1) and abruptly breaking teeth off after the initiation (Method2). Fig. 9 illustrates both methods. The cracks were initiated on several different teeth. The inspected using method are shown on top. The three teeth in lower left corner were subjected to the ramped load on the fatigue tester until they fractured.

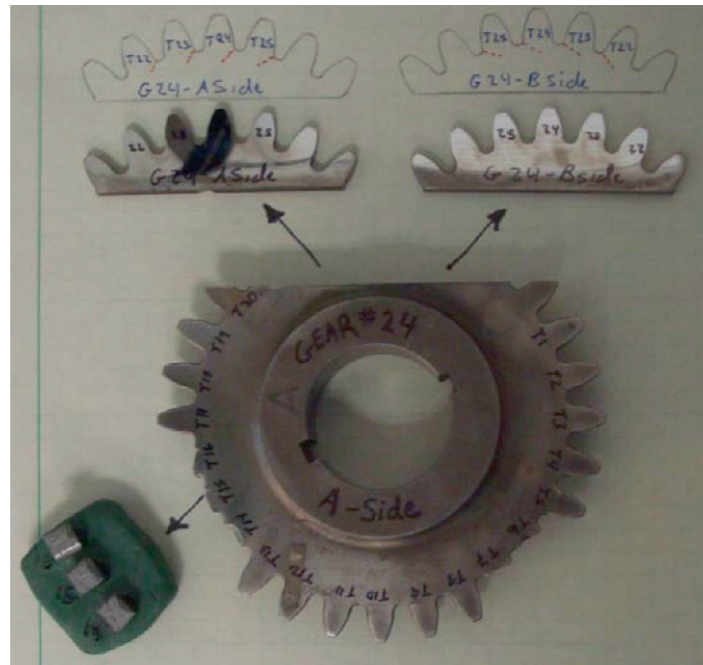


Fig. 9 Destructive inspection of gear tooth cracks

Method 1 employed a wire EDM to first section a number of previously tested teeth from the gear. The sectioned teeth were then sliced perpendicularly to the initial cut. The slices were polished, etched with an alcohol/nitric acid solution, and imaged with a standard metallographic microscope. Fig. 10 shows the gear slices as well as images of polished sections of a tooth demonstrating crack length differences throughout the tooth thickness. The depth of gear tooth crack propagation was 1-1.5 mm in this example.

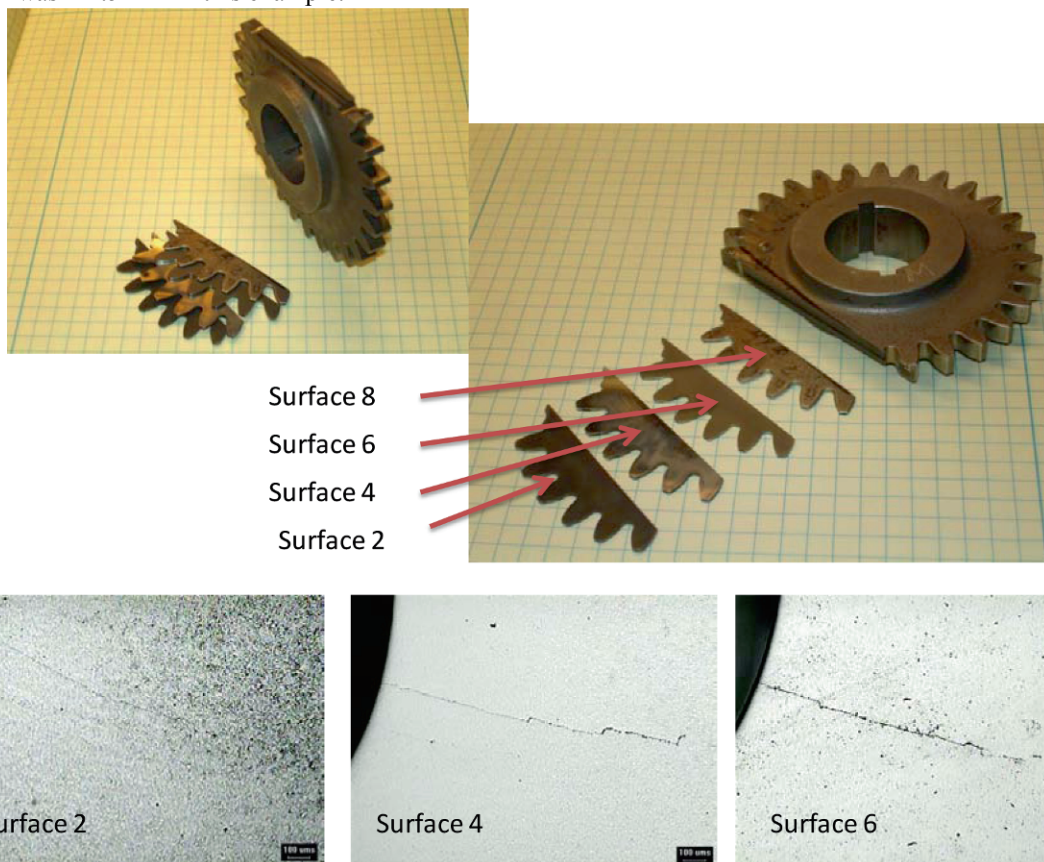


Fig. 10 Destructive inspection using Method 1

Method 2 was relatively straight forward. After crack initiation, the test tooth was imaged with the fluorescent iron powder, returned to the fatigue fixture, and the static load increased until fracture resulted. The fracture surfaces were then imaged with a stereo microscope at $24\times$ and $66\times$ magnification. Fig. 11 shows crack surfaces of four different teeth (all teeth imaged from the bottom). There is a clear, discernable boundary that separates the smooth surface of crack initiation from the rough surface of the abrupt breakage (see the annotation in Fig. 11b). For the various gear tests, the crack depths in the middle of the tooth were consistent with imaging obtained using Method 1 and shown in Fig. 10. However for some tests, the crack depths were virtually zero near the gear faces. It was clear that the crack profiles for these cases were significantly different than surfaces produced by notching, which have a uniform depth across the thickness of the gear. We have observed that generally as cracks propagate, the crack depth becomes more uniform across the gear thickness. Thus, for deeper cracks it is reasonable that the crack surface approaches an expected notch surface. This finding also suggests a larger variation than suggested in analysis results above in compliance change (from uncracked tooth) between real cracks compared to notched teeth, when the crack/notch depth is small. Method 2 was considerably more effective, far less labor intensive, and provided an immediate view of the entire crack surface as compared to Method 1. Method 1, in addition to being more laborious and requiring interpolation to visualize entire crack surface, suffered from a fundamental drawback: the wire EDM process affected cracks propagation to a certain unknown and difficult to quantify degree. The advantage of Method 2 was that it was able to show details of the crack shape in the direction of the propagation, as shown in Fig. 10.

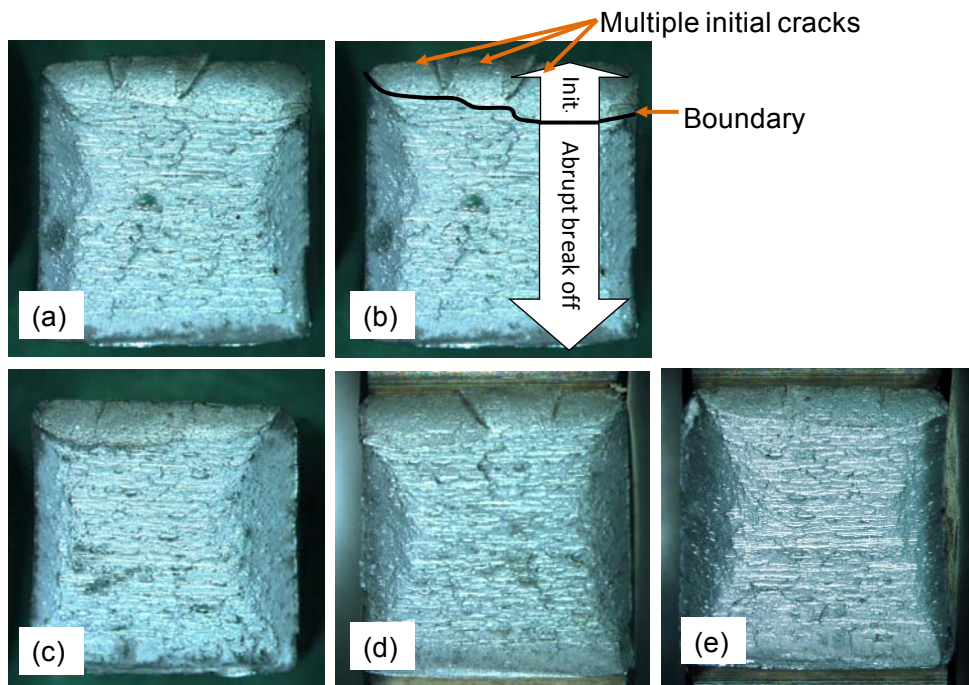


Fig. 11 Destructive inspection using Method 2

Summary

This paper describes an accelerated crack initiation where a selected tooth is subjected to cyclic bending on a fatigue tester. This method of seeding cracks is related to the traditional method (notching) using FEA. FEA compares effective compliance and change in fundamental natural frequencies between a cracked gear tooth and a notched gear tooth where the notch and the crack are of the same length and of uniform depth. Both metrics consistently show that their dependence on the length of the crack/notch is considerably higher than the dependence on the type of damage. The analysis suggests a plausible conclusion that a cracked and a notched tooth will exhibit very similar vibration features for a given length of crack/notch.

The fixture for crack initiation and the associated process are described, including a compliance based feature for crack detection. The induced cracks were verified using a non-destructive methods and characterized using the destructive methods. While the non-destructive methods indicates minimal damage to the tooth, closer (destructive) inspections shows that the crack surface is somewhat irregular initially and that the maximum depth of crack propagation can be appreciable at the point of detection by the suggested feature.

Acknowledgments

This work was made possible by Army Research Laboratory under Award No. W911NF-07-2-0080. We gratefully acknowledge the help of our colleagues from Rochester Institute of Technology: Dr. Michael Haselkorn, David Fister, Michael Leaty, and Dominic Maiola for their assistance in destructive crack assessment ; Mark Walluk and Michael Bradley for design of the crack initiation fixture; and Art Dee LabVIEW for implementation of the crack detection.

References

- [1] Zakrajsek, J. J., and Lewicki, D. G., 1998, "Detecting Gear Tooth Fatigue Cracks in Advance of Complete Fracture," *Tribotest*, 4(4), pp. 407-422.
- [2] Lebold, M., Mcclintic, K., Campbell, R., Byington, C., and Maynard, K., 2000, "Review of Vibration Analysis Methods for Gearbox Diagnostics and Prognostics," *Proc. 54th Meeting of the Society for Machinery Failure Prevention Technology*, Virginia Beach VA, pp. 623-634.
- [3] Samuel, P. D., and Pines, D. J., 2005, "A Review of Vibration-Based Techniques for Helicopter Transmission Diagnostics," *Journal of Sound and Vibration*, 282(1-2), pp. 475-508.
- [4] Glodez, S., Sraml, M., and Kramberger, J., 2002, "A Computational Model for Determination of Service Life of Gears," *International Journal of Fatigue*, 24(10), pp. 1013-1020.
- [5] Hefeng, B., Savage, M., and Knorr, R. J., 1985, "Computer Modeling of Rack-Generated Spur Gears," *Mechanism and Machine Theory*, 20(4), pp. 351-360.
- [6] Persson, P. O., and Strang, G., 2004, "A Simple Mesh Generator in Matlab," *SIAM review*, 46(2), pp. 329-345.
- [7] Wawrzynek, P. A., 1991, "Discrete Modeling of Crack Propagation : Theoretical Aspects and Implementation Issues in Two and Three Dimensions.", Ph.D. Dissertation, Cornell University, 1991.
- [8] Gasparini, G., Mariani, U., Gorla, C., Filippini, M., and Rosa, F., "Bending Fatigue Tests of Helicopter Case Carburized Gears: Influence of Material, Design and Manufacturing Parameters."
- [9] Broek, D., 1986, *Elementary Engineering Fracture Mechanics*, M. Nijhoff ;Distributors for the U.S. and Canada, Kluwer Academic, Dordrecht ; BostonHingham, Mass., U.S.A.

Operational Modal Analysis of a Rectangular Plate

Using Noncontact Acoustic Excitation

Y.F. Xu

Graduate Assistant

W.D. Zhu

Professor; Corresponding Author (Tel: 410-455-3394, Email: wzhu@umbc.edu)

Department of Mechanical Engineering

University of Maryland, Baltimore County

1000 Hilltop Circle

Baltimore, MD 21250

ABSTRACT

Output-only modal analysis has been extensively developed in the past decades and widely used especially when the input is unknown or difficult to measure. This paper presents a noncontact experimental technique for measuring the modal parameters of a rectangular aluminum plate using only the output data, with the intention to apply the technique to turbine blades. Operational modal analysis (OMA) is employed to analyze an aluminum plate with free boundaries in the frequency range from 0 to 15000 Hz, which can be an operation frequency range of a turbine blade, under acoustic excitation in the form of white noise in a direction of interest. A single-point laser vibrometer and a free-field microphone are used to simultaneously measure the responses of the plate in a noncontact manner, with the microphone measurement serving as the reference. A cross-power spectral density (CPSD) acquired using the microphone measurement as the reference is shown to be equivalent to that using a laser vibrometer measurement as the reference as long as the natural frequencies of the test structure that are of interest are sufficiently high but lower than a certain value. A measurement method for in-plane vibration modes is also proposed and applied by shining the laser from the vibrometer with a certain incident angle. The natural

frequencies and mode shapes of the out-of-plane and in-plane modes of the plate are measured. The experimental natural frequencies and mode shapes of the plate are compared with those calculated using commercial finite element software to demonstrate the validity of the experimental technique. Experimental modal analysis (EMA) is also performed on the plate using an impact hammer and the laser vibrometer to validate the experimental results from OMA. The maximum error between the measured and calculated natural frequencies of the plate is 1.53% for the first 18 elastic modes, including 16 out-of-plane modes and two in-plane modes. The Modal Assurance Criterion (MAC) values between the corresponding mode shapes of the plate are all above 93%.

1. Introduction

There are numerous cyclic excitations in the operation of a turbine that can excite the vibrations of its blades at certain frequencies. When the excitation frequencies are in the vicinity of some of the natural frequencies of the turbine, the blades can undergo large vibrations, which can result in large stresses. Most turbine blades fail due to high cycle fatigues that derive from cyclic stresses [1], and a turbine blade vibrating at or near one of its natural frequencies is more likely to fail due to high cycle fatigue. Modal analysis on this kind of structure is necessary since it can provide an accurate estimation of the modal parameters such as the natural frequencies and mode shapes. In addition, the experimental results can be used to validate a finite element model of a turbine blade and eventually improve the design of the turbine blade.

There are many types of modal analysis methods, and they can be classified as either Operational Modal Analysis (OMA) or Experimental Modal Analysis (EMA). OMA, an output-only modal analysis method, is a powerful technique for extracting modal parameters of a structure using only the response data of the structure; it can be used on a structure whose input is difficult or even unable to measure. The Natural Excitation Test (NExT) [2], where the input is assumed to be “natural” (i.e., white noise), was a kind of OMA. This technique requires multiple measurements of the responses due to white noise excitation, one of which serves as the reference, and the cross-correlations between the other measurements and the reference can be generated and used for modal parameter estimation. Besides NExT, there are other operational modal identification schemes that have been developed to extract the modal parameters [3]. These schemes are established in either the time domain or the frequency domain. The former schemes include the Auto-regression Moving Average (ARMA) model-based method [4], the Stochastic Realization-based method [5], and the Stochastic Subspace Identification technique [6], and the latter schemes include the Frequency Domain Decomposition (FDD) method [7] and the Least-square Complex Frequency-domain (LSCF) estimation [8]. EMA, unlike OMA, requires measurement of the input to obtain the Frequency Response Function (FRF) for modal parameter estimation [9]. In addition, EMA often requires a laboratory environment, while OMA does not and can be performed on site. Hence OMA is a more practical method than EMA, since it can be an in-situ test, and the dominating modes of a test structure in an operation environment can be observed, which gives more valuable information about the test structure.

EMA usually uses an impact hammer or a shaker to excite a test structure. There are four main drawbacks of this kind of excitation. First, the output quality can vary because an impact/driven point can happen to be a nodal point of a test structure and the output signal-to-noise ratio can be relatively low. Hence some tests need to be repeated several times with different excitation locations in order to completely understand the dynamic characteristics of the structure, and this can be tedious and time consuming. Second, a contact excitation force can damage a fragile test structure. Third, the input frequency bandwidth can be too low to fully excite the high frequency modes of a test structure. Fourth, the excitation force from an impact hammer is not fully controllable, the impact location can vary, and the signal-to-noise ratio can be low for a single impact. A shaker needs to be attached to a test structure and can introduce mass loading. The use of noncontact acoustic excitation can resolve these problems: the acoustic excitation can be widely distributed over a test structure, it can be easily repeated, and its bandwidth is controllable. However, the acoustic excitation cannot be easily measured; hence it cannot be used in EMA. Since OMA does not need the input measurement, the acoustic excitation can be used in OMA. At least two measurements of the responses are needed for OMA, one of which is used as the reference. While OMA does not need the input measurement, it requires the input to the test structure to be white noise, which can be easily generated using acoustic excitation. To avoid mass loading to a test structure, noncontact measurements using a laser vibrometer or a microphone are preferred.

In this work, OMA is performed on a small, rectangular aluminum plate using acoustic excitation in the form of white noise up to 15,000 Hz, which can be an operation frequency range of a turbine blade. Both the out-of-plane and in-plane modes of the plate within the frequency range are studied. While measuring the out-of-plane modes can be relatively easy, measuring the in-plane modes can be difficult. The in-plane vibration of an interior point of a plate was measured in Ref. [10] by attaching a side of an accelerometer to the plate surface, which can introduce measurement error. Such a contact measurement can also introduce mass loading to the plate, especially for a small and light plate. Only one single-point laser

vibrometer is available in this work to measure the vibrational velocities of various points on the plate using a roving sensor approach. A free-field microphone is used to measure the pressure near the reference point on the plate, which can be a point on the plate surface for an out-of-plane mode measurement and a point on a side of the plate for an in-plane mode measurement, and the measured pressure serves as the reference in OMA; the position and the orientation of the microphone remain unchanged in a whole test for an out-of-plane or in-plane mode measurement. The measured data are acquired and processed by an LMS spectrum analyzer, and the corresponding cross-power spectral densities (CPSDs), which are used in the modal parameter identification schemes, are calculated. These CPSDs are shown to be equivalent to the ones when two laser vibrometers are used to measure the velocities of the various points and the reference point as long as the natural frequencies of the test structure that are interest are sufficiently high but lower than a certain value. In addition, a method for accurately measuring the in-plane modes of the plate is developed; the laser beam from a laser vibrometer is shined at the various points on the plate with a certain incident angle, and the measured CPSDs are summed. The in-plane modes can be identified by comparing the resulting summed CPSD with that for the out-of-plane modes, which is obtained by shining the laser beam perpendicular to the plate surface. EMA using an impact hammer to excite the plate and a laser vibrometer to measure its responses is also performed to obtain the out-of-plane and in-plane modal parameters; a method similar to that for an in-plane mode measurement in OMA is used for an-plane mode measurement in EMA except that the FRFs, instead of the CPSDs, are measured and the summed FRF is used to identify the in-plane modes. The measured natural frequencies and mode shapes from OMA and EMA are compared with the calculated ones from commercial finite element (FE) software ABAQUS.

2. OMA Using a Microphone to Measure the Response of the Reference Point

In OMA, the cross-correlation functions between the responses of the various points and that of the reference point due to a single-point input in the form of white noise can be expressed as a sum of decaying sinusoids that involve modal parameters of the test structure [2]. In theory, the same type of measured responses (e.g., displacement, velocity, or acceleration) should be used. In this study, use of two laser vibrometers is preferred to measure the responses of the various points in a roving sensor approach and that of the reference point, since they can provide accurate non-contact measurements of the velocities of the test structure. However, usually only one laser vibrometer is available in a laboratory due to its relatively high cost. To perform OMA on a test structure, if only one laser vibrometer is available for measuring the velocities of the various points of the test structure in a roving sensor approach, the other measurement at the reference point should be directly related to the velocity in order to guarantee that the resulting cross-correlation functions between the two types of measured data can be used for modal parameter estimation. An OMA test method, in which a laser vibrometer and a free-field microphone are used to measure the velocities of the various points of the test structure in a roving sensor approach and the pressures near the reference point, and the resulting CPSDs between the measured velocities and pressures are obtained for modal parameter estimation, is discussed below.

In this method, a free-field microphone is placed closely above the reference point with a minimum distance d , but no contact between the microphone and the test structure, where the latter is excited to vibrate. The distance between the microphone and the reference point can be considered to be acoustically small if $kd \ll 1$, where k is the wave number of sound [11], defined by $k = \frac{\omega}{c}$, in which ω is the angular frequency of sound and c is the sound speed. Since the sound speed can be considered as a constant, the wave number depends only on the angular frequency of sound. For sound of frequency up to 15,000 Hz, the wave number in air varies from 0 to about 277 rad/m at 20°C ; the higher the frequency, the larger the wave number. In this work, d is set to be less than 0.001 m, i.e., $kd \leq 0.277$, and can be considered to be acoustically small. If a higher frequency is of interest, d should be smaller in order to make it acoustically small. Since d is so small, the pressure measured by the microphone mainly derives from the vibration of the reference point; the effect of other sound sources is negligible as a free-field microphone only measures the pressure perpendicular to its diaphragm [12].

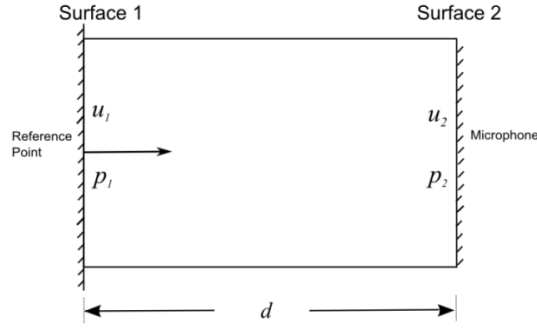


Fig. 1 The lumped acoustic element between the reference point and the microphone

For an acoustically small d , the air between the surface of the reference point (surface 1) and that of the diaphragm of the microphone (surface 2) can be treated as a lumped acoustic element with a uniform cross-section [11] (Fig. 1). The relations between the complex amplitudes of the particle velocity and the air pressure on surface 1, u_1 and p_1 , and those on surface 2, p_2 and u_2 , can be derived [11]. Note that the particle velocities on surfaces 1 and 2 are the vibrational velocities of the reference point and the diaphragm, respectively, and the air pressure on surface 2 is measured by the microphone.

For a lumped acoustic element, the ratio of the complex amplitude of the pressure difference $p_1 - p_2$ across the element to that of the mean particle velocity $\frac{u_1 + u_2}{2}$ can be expressed as [11]

$$\frac{2(p_1 - p_2)}{(u_1 + u_2)} \approx j\omega\rho_0 d \quad (1)$$

where ρ_0 is the density of air and $j = \sqrt{-1}$. The ratio of the complex amplitude of the mean pressure $\frac{p_1 + p_2}{2}$ to that of the particle velocity difference $u_1 - u_2$ across the element can be expressed as [11]

$$\frac{p_1 + p_2}{2(u_1 - u_2)} \approx -\frac{j\rho_0 c^2}{\omega d} \quad (2)$$

Since the microphone is fixed throughout the test, the complex amplitude of the velocity of the diaphragm vanishes, i.e. $u_2 = 0$. Rearranging Eq. (1) yields

$$p_1 = \frac{j\omega\rho_0 d u_1}{2} + p_2 \quad (3)$$

Substituting Eq. (3) in Eq. (2) yields

$$p_2 = -j \left(\frac{\rho_0 c^2}{\omega d} + \frac{\omega\rho_0 d}{4} \right) u_1 \quad (4)$$

It can be observed from Eq. (4) that the pressure measured by the microphone is related to the vibrational velocity of the reference point and the relation depends only on the vibration frequency ω , assuming that both the air density ρ_0 and the sound speed c remain constant. Further, for the case of air at 20°C , $\rho_0 = 1.2041 \text{ kg/m}^3$ and $c = 340 \text{ m/s}$. In the frequency range under investigation, $0 < \frac{\omega}{2\pi} \leq 15000$, even if $d = 0.001 \text{ m}$, $\frac{\rho_0 c^2}{\omega d} \gg \frac{\omega \rho_0 d}{4}$. Hence Eq. (4) can be approximated by

$$p_2 = -j \left(\frac{\rho_0 c^2}{\omega d} + \frac{\omega \rho_0 d}{4} \right) u_1 \approx -j \frac{\rho_0 c^2}{\omega d} u_1 = \frac{\rho_0 c^2}{j \omega d} u_1 = G(\omega) u_1 \quad (5)$$

where $G(\omega) = \frac{\rho_0 c^2}{j \omega d}$ can be considered as the ratio of the complex amplitude of the pressure measured by the microphone to that of the vibrational velocity of the reference point at frequency ω . More generally, the approximation in Eq. (5) can be made when $\omega \ll \frac{2c}{d}$; $\frac{2c}{d} = 680000$ here.

If a speaker is used to provide acoustic white noise to the test structure, the excitation can be considered as multiple inputs since it is distributed over an area of the test structure. The cross-correlation function between the responses of two points of the test structure, i and j , due to multiple white noise inputs can be expressed as [13]

$$c_{ij}(t) = \sum_{s=1}^N \frac{\phi_{si} A_{sj}}{m_s \omega_s^d} e^{-\omega_s \zeta_s t} \cos(\omega_s^d t + \theta_s) \quad (6)$$

where point i denotes a measurement point, point j denotes the reference point, t is time, ϕ_{si} is the i -th component of the s -th mode shape of the test structure, m_s is the s -th modal mass, ζ_s is the s -th modal damping ratio, ω_s is the s -th undamped natural frequency, ω_s^d is the s -th damped natural frequency, and θ_s is a phase angle, and A_{sj} is a constant associated with the response of the reference point. Note that classical damping [14] is assumed here for notational ease. Equation (6) can be written in the complex form

$$c_{ij}(t) = \sum_{s=1}^N \frac{\phi_{si} A_{sj}}{2m_s \omega_s^d} (e^{j\theta_s} e^{\sigma_s t} + \overline{e^{j\theta_s} e^{\sigma_s t}}) \quad (7)$$

where $\sigma_s = -\omega_s \zeta_s + j\omega_s^d$ and the overbar denotes complex conjugation. The Fourier transform of Eq. (7) gives the CPSD:

$$H_{ij}(\omega) = \sum_{s=1}^N \frac{\phi_{si} A_{sj}}{2m_s \omega_s^d} \left(\frac{e^{j\theta_s}}{j\omega - \sigma_s} + \frac{e^{-j\theta_s}}{j\omega - \overline{\sigma_s}} \right) \quad (8)$$

In this study, the Operational Polyreference Least-squares Complex Frequency-domain method, referred to as Operational PolyMax, is used to perform modal parameter estimation using CPSD data [15]. When the measurement and reference data are both velocity measurements, the CPSD can be expressed as [16]

$$H_{ij}(\omega) = U_i(\omega) \overline{U_j(\omega)} \quad (9)$$

where $U_i(\omega)$ and $U_j(\omega)$ are the Fourier transforms of the responses of the measurement point i and the reference point j , respectively. When a laser vibrometer is used to measure the velocity of the measurement point i and a microphone is used to measure the pressure near the reference point j , the CPSD between the two set of data can be expressed as

$$H'_{ij}(\omega) = U_i(\omega) \overline{P_j(\omega)} = U_i(\omega) \overline{U_j(\omega) G(\omega)} = H_{ij}(\omega) \overline{G(\omega)} \quad (10)$$

where Eqs. (5) and (9) have been used, $P_j(\omega)$ is the Fourier transform of the pressure near the reference point j , and $G(\omega)$ is the ratio of the complex amplitude of the pressure near the reference point j to that of the velocity of the reference point j . Using Eqs. (8) and (5) in Eq. (10) yields

$$\begin{aligned} H'_{ij}(\omega) &= \sum_{s=1}^N \frac{\phi_{si} A_{sj}}{2m_s \omega_s^d} \left(\frac{e^{j\theta_s}}{j\omega - \sigma_s} + \frac{e^{-j\theta_s}}{j\omega - \overline{\sigma_s}} \right) \overline{G(\omega)} = \sum_{s=1}^N \frac{\phi_{si} A_{sj}}{2m_s \omega_s^d} \left(\frac{e^{j\theta_s}}{j\omega - \sigma_s} + \frac{e^{-j\theta_s}}{j\omega - \overline{\sigma_s}} \right) \left(\frac{\rho_0 c^2}{-j\omega d} \right) \\ &= \sum_{s=1}^N -\frac{\phi_{si} \rho_0 c^2 A_{sj}}{2m_s \omega_s^d d} \left(\frac{e^{j\theta_s}}{(j\omega - \sigma_s)(j\omega)} + \frac{e^{-j\theta_s}}{(j\omega - \overline{\sigma_s})(j\omega)} \right) \end{aligned} \quad (11)$$

Since

$$\frac{e^{j\theta_s}}{(j\omega - \sigma_s)(j\omega)} = \frac{1}{\sigma_s} \left(\frac{e^{j\theta_s}}{j\omega - \sigma_s} - \frac{e^{j\theta_s}}{j\omega} \right), \quad \frac{e^{-j\theta_s}}{(j\omega - \overline{\sigma_s})(j\omega)} = \frac{1}{\overline{\sigma_s}} \left(\frac{e^{-j\theta_s}}{j\omega - \overline{\sigma_s}} - \frac{e^{-j\theta_s}}{j\omega} \right) \quad (12)$$

Eq. (12) can be written as

$$\frac{e^{j\theta_s}}{(j\omega - \sigma_s)(j\omega)} = \frac{1}{|\sigma_s|} \left(\frac{e^{j(\theta_s + \alpha_s)}}{j\omega - \sigma_s} - \frac{e^{j(\theta_s + \alpha_s)}}{j\omega} \right), \quad \frac{e^{-j\theta_s}}{(j\omega - \overline{\sigma_s})(j\omega)} = \frac{1}{|\sigma_s|} \left(\frac{e^{-j(\theta_s + \alpha_s)}}{j\omega - \overline{\sigma_s}} - \frac{e^{-j(\theta_s + \alpha_s)}}{j\omega} \right) \quad (13)$$

where $\frac{1}{\sigma_s} = \frac{1}{|\sigma_s|} e^{j\alpha_s}$ has been used. Let $\beta_s = \theta_s + \alpha_s$; substituting Eq. (13) into Eq. (11) yields

$$H'_{ij}(\omega) = \sum_{s=1}^N -\frac{\phi_{si} \rho_0 c^2 A_{sj}}{2m_s \omega_s^d d |\sigma_s|} \left(\frac{e^{j\beta_s}}{j\omega - \sigma_s} + \frac{e^{-j\beta_s}}{j\omega - \overline{\sigma_s}} - \frac{e^{j\beta_s}}{j\omega} - \frac{e^{-j\beta_s}}{j\omega} \right) \quad (14)$$

Let $\phi'_{si} = -\frac{\phi_{si} \rho_0 c^2}{d |\sigma_s|}$; it is obvious that the mode shapes, $\{\phi_s\}$ and $\{\phi'_s\}$, that are formed by ϕ_{si} and ϕ'_{si} are equivalent since

mode shapes can have an arbitrary multiplication factor. In addition, the last two terms $\frac{e^{j\beta_s}}{j\omega}$ and $\frac{e^{-j\beta_s}}{j\omega}$ in Eq. (14) are negligible when the natural frequencies of interest are sufficiently high, and Eq. (14) becomes

$$H'_{ij}(\omega) = \sum_{s=1}^N \frac{\phi'_{si} A_{sj}}{2m_s \omega_s^d} \left(\frac{e^{j\beta_s}}{j\omega - \sigma_s} + \frac{e^{-j\beta_s}}{j\omega - \overline{\sigma_s}} \right) \quad (15)$$

which is equivalent in form to the CPSD in Eq. (8). While the CPSDs in Eqs. (8) and (15) have different amplitudes and phases, they contain the same modal information. Hence a modal parameter estimation scheme developed for the CPSD in Eq. (8), such as Operational PolyMax [15], can be used for that in Eq. (15).

3. Method for Measuring In-plane Modes of a Rectangular Plate

A rectangular plate has out-of-plane and in-plane modes, which are orthogonal to each other. Measuring the out-of-plane modes can be relatively easy, and it is usually difficult to measure the in-plane modes. To measure the in-plane motion of the plate, the vibration of a side of the plate can be easily measured, but the in-plane vibration of an interior point of the plate cannot be easily measured. A non-contact method for measuring the in-plane modes of the plate using OMA is developed; a laser vibrometer is used to measure the vibrational velocities of the interior measurement points of the plate and a microphone is used to measure the pressure near the reference point, which is located on a side of the plate.

When the laser beam from the laser vibrometer is shined on the plate with an incident angle θ , as shown in Fig. 2, where the Z-axis corresponds to the out-of-plane vibration direction and the X-axis the in-plane vibration direction, the velocity measured by the vibrometer v_l is along the laser beam direction, and it contains the velocities of both the out-of-plane and in-plane motions. The velocity of the out-of-plane motion contained in the measured velocity along the laser beam v_l^z can be expressed as $v_l^z = v_z \cos \theta$, where v_z is the velocity of the out-of-plane motion (Fig. 2). The velocity of the in-plane motion measured by the laser vibrometer v_l^x can be expressed as $v_l^x = v_x \sin \theta$, where v_x is the velocity of the in-plane motion (Fig. 2). The velocity measured by the laser vibrometer can be expressed as $v_l = v_l^z + v_l^x$. It is obvious that the larger the incident angle, the more the in-plane motion and the less the out-of-plane motion that will be measured by the laser vibrometer, which is desirable for the measurement of the in-plane motion. However, the incident angle should not be too large in order to prevent the laser at the measurement point from being scattered, which can cause inaccurate measurement. Hence a proper incident angle should be selected, which can measure an adequate amount of the in-plane motion and does not affect the accuracy of the measurement at the same time.

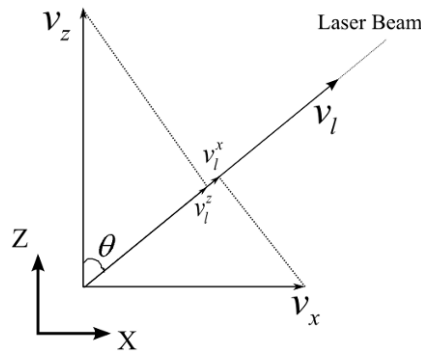


Fig. 2 Velocity measured by the laser beam v_l with an incident angle θ

Since only the modal parameters are of interest, the in-plane modes of the plate can be measured using OMA in an indirect way, as described as follows. First, the CPSDs for the out-of-plane modes are measured. The microphone is used to measure the pressure near the reference point, which can be any point on the plate surface, and the laser vibrometer shines the laser beam perpendicular to the plate surface to measure the velocities of the measurement points in a roving sensor approach. The measured CPSDs are summed and the resulting summed CPSD is referred to as the out-of-plane CPSD. Second, the microphone is used to measure the pressure in the X direction near the reference point on a side of the plate. The laser vibrometer shines the laser beam on the measurement points with a certain incident angle, which remains constant throughout a whole test. The measured CPSDs are then summed and the resulting summed is referred to as the mixed CPSD, where the word “mixed” is used since the measured CPSDs contain both the in-plane and out-of-plane vibrations of the plate. It is impossible to determine whether a mode belongs to an out-of-plane mode or an in-plane mode if only the mixed CPSD is used since the measured velocity contains the velocities of both the out-of-plane and in-plane vibrations. The in-plane modes,

however, can be identified by comparing the mixed CPSD with the out-of-plane CPSD, since both the out-of-plane modes and the in-plane modes would manifest themselves as peaks in the mixed CPSD, and only the peaks corresponding to the out-of-plane modes can be found in the out-of-plane CPSD; one can then easily conclude that those modes that can only be found in the mixed CPSD are the in-plane modes. Note that the summed CPSDs are used to distinguish the in-plane modes from the out-of-plane modes since they can show the overall characteristics of the measured CPSDs.

The method described above can be adapted for use in EMA to identify the in-plane modes of the plate. In EMA, an impact hammer is used to excite the plate by hitting a point on the plate surface, and the laser vibrometer shines the laser beam perpendicular to the plate to measure the velocities of the measurement points in a roving sensor approach; a series of FRFs are then obtained and summed. The resulting summed FRF is referred to as the out-of-plane FRF. The impact hammer is then used to hit a point on a side of the plate. The laser beam is shined with an incident angle on the measurement points of the plate in a roving sensor approach. The measured FRFs are summed, and the resulting summed FRF is referred to as the mixed FRF. The in-plane modes can be identified by comparing the mixed FRF with the out-of-plane FRF.

Since the out-of-plane and in-plane modes are orthogonal to each other, in the vicinity of one of the in-plane mode natural frequencies, the velocity measured by the laser beam with the incident angle θ mainly derives from the in-plane motion; the out-of-plane motion measured by the laser beam is negligible. Further, the velocity of the in-plane motion measured by the laser beam is equal to that of the in-plane motion of the measurement point multiplied by $\sin \theta$, which can be considered as a multiplier of the magnitudes of the estimated mode shapes and does not change the estimated mode shapes. Hence the measured CPSDs or FRFs using the laser beam with the incident angle θ can be used to perform modal parameter estimation for the in-plane modes of the plate.

4. Test Setup and Procedure

4.1 Test Specimen and Setup

The dimensions and material properties of the rectangular aluminum plate being studied are shown in Table 1. Figure 3 (a) shows the schematic of the experimental setup. The plate is laid on two slim elastic rubber bands, which simulate free boundaries of the plate (Fig. 3(b) and (c)). There are 42 measurement points on the plate surface, as shown in Fig. 4; a small reflective tape is attached to the plate surface at each measurement point to enhance the reflection of the laser beam. Two speakers (Fostex FT17H) are placed closely towards the plate in the direction of interest; the white noise signals are generated by the LMS spectrum analyzer and powered by an amplifier (QSC PLX-1802). The frequency range of the white noise signals is set to 0-15000 Hz. A free-field microphone is placed near the reference point in the direction of interest. Both the microphone and the laser vibrometer are connected to the LMS spectrum analyzer. Modal analysis is performed using LMS Test.Lab Rev. 9B modal analysis software. The directions in which the laser beam is shined on the plate surface, the directions towards which the speakers and the microphone are pointing, and the locations of the reference points for the out-of-plane and in-plane mode measurements using OMA are shown in Fig. 3 (b) and (c), respectively.

Table 1. Test Specimen Parameters

Parameter	Value
Length	0.18 m
Width	0.075 m
Thickness	0.006 m
Young's modulus	69 GN/m
Poisson's ratio	0.33
Density	2700 kg/m ³

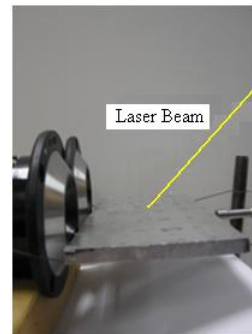
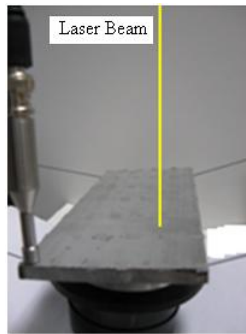
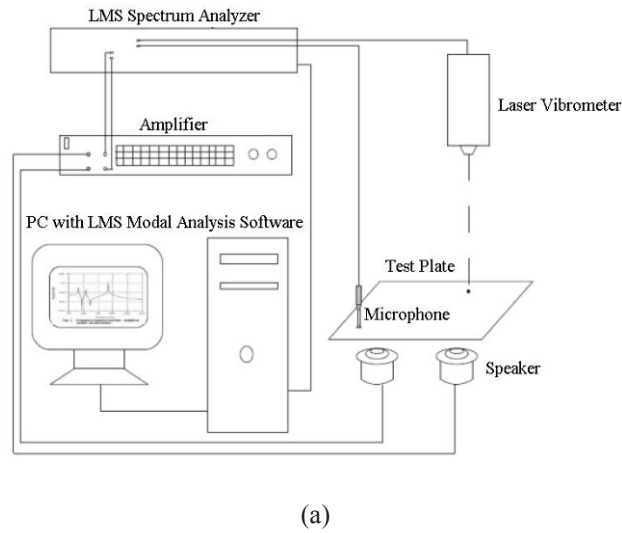


Fig. 3 Experimental setup for OMA: (a) schematic of the complete experimental setup; (b) excitation and measurement setups for the out-of-plane mode measurement; and (c) excitation and measurement setups for the in-plane mode measurement

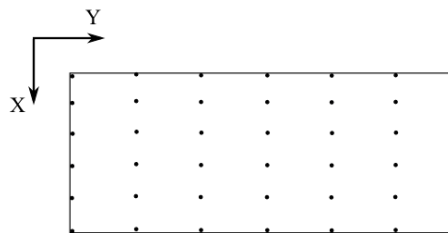


Fig. 4 Distribution of the 42 measurement points (shown as dots) on the plate; X- and Y-axes are two in-plane axes

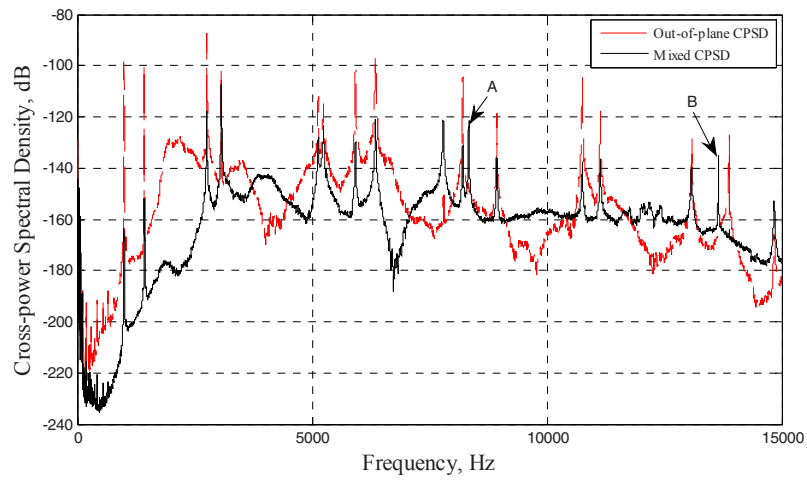
4.2 Test Procedure

For the out-of-plane mode measurement using OMA, the vibrometer shines the laser beam perpendicular to the measurement points on the plate. A measurement point on a corner of the plate is used as the reference point here since the distances between the measurement points are small and the microphone setup can be an obstacle for the laser beam if the reference

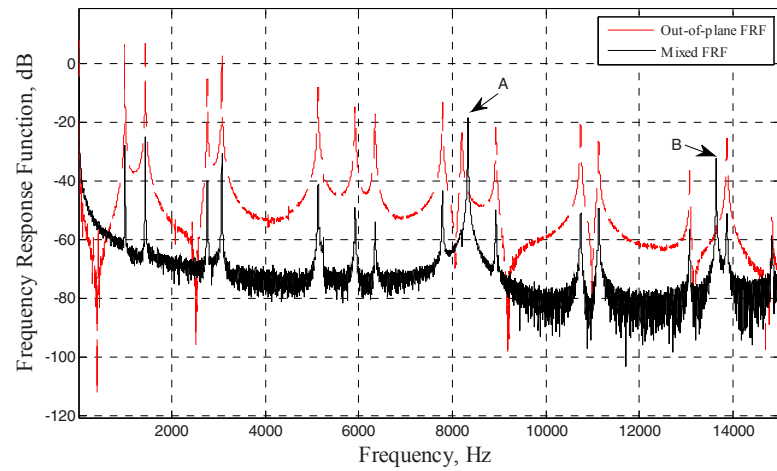
point is an interior point of the plate surface. The white noise acoustic excitation from the two speakers is triggered to excite the plate. The CPSD between the velocity measured by the laser vibrometer at a measurement point and the pressure measured by the microphone at the reference point is calculated by the LMS modal analysis software and averaged over 40 samples. A total of 41 averaged CPSDs are obtained for the 41 measurement points in a roving sensor approach; the resulting summed out-of-plane CPSD is shown in Fig. 5 (a).

For the in-plane mode measurement using OMA, the laser beam is shined to the measurement point with $\theta = 45^\circ$ and the reference point is on a side of the plate. In order to completely measure the in-plane modes, the in-plane vibrations in both the X and Y directions (Fig. 4) at each measurement point need to be measured. Hence there are two measured CPSDs at each measurement point; note that the position of the microphone remains unchanged throughout the test. A CPSD is averaged over 40 samples. Since there are 42 measurement points and two averaged CPSDs at each measurement point, a total of 84 averaged CPSDs are obtained in a roving sensor approach; the resulting summed mixed CPSD is shown in Fig. 5(a). The in-plane modes can then be identified by comparing the out-of-plane CPSD with the mixed CPSD. The two peaks labeled as A and B, which only appear in the mixed CPSD, correspond to the in-plane modes. Since the highest rigid body mode natural frequency in both the out-of-plane and in-plane mode measurements is lower than 10% of the first elastic mode natural frequency, the boundaries can be considered to be free [9]. Note that the 15th out-of-plane elastic mode cannot be found in the mixed CPSD possibly because it is not excited by the acoustic excitation used in the in-plane mode measurement. The modal parameters of the out-of-plane modes are then estimated using the 41 averaged CPSDs obtained in the out-of-plane mode measurement, and those of the in-plane modes are estimated using the 84 averaged CPSDs obtained in the in-plane mode measurement.

In addition, EMA is also performed to measure both the out-of-plane and in-plane modes. An impact hammer and the laser vibrometer are used to excite the plate and measure the response of the plate, respectively. For the out-of-plane mode measurement, the vibrometer shines the laser beam perpendicular to the plate surface and the hammer hits a point on the plate surface in the out-of-plane direction; the FRF is then measured and averaged over 40 samples. A total of 42 averaged FRFs are obtained in a roving sensor approach for the 42 measurement points; the resulting summed out-of-plane FRF is shown in Fig. 5(b). For the in-plane mode measurement, the vibrometer shines the laser beam with $\theta = 45^\circ$ and the hammer hits a point on a side of the plate in the in-plane direction. Similar to OMA, the FRFs in both the X and Y directions at each measurement point are measured and averaged over 40 samples; the position and direction of the impact by the hammer do not change throughout the test. A total of 84 averaged FRFs are obtained; the resulting summed, mixed FRF is shown in Fig. 5(b). The two peaks labeled as A and B, which only appear in the mixed FRF, correspond to the in-plane modes. The boundaries can be considered to be free since the highest rigid body mode natural frequency in both the out-of-plane and in-plane mode measurements are lower than 10% of the first elastic mode natural frequency [9]. Note that the 10th out-of-plane elastic mode cannot be found in the mixed FRF possibly because it is not excited by the impacts on the side of the plate in the in-plane mode measurement. The boundary can be considered as free in EMA, since the highest frequencies of the rigid body modes, both in the out-of-plane and in-plane mode measurements are lower than 10% of the frequency of the first elastic mode. The measured natural frequencies of the two in-plane modes from EMA are almost the same as those from OMA. Similar to OMA, the modal parameters of the out-of-plane modes are estimated using the 42 averaged FRFs obtained in the out-of-plane mode measurement, and those of the in-plane modes are estimated using the 84 averaged FRFs obtained in the in-plane mode measurement.



(a)



(b)

Fig. 5 Plots of (a) the out-of-plane and mixed CPSDs from OMA and (b) the out-of-plane and mixed FRFs from EMA

5. Experimental Results and Analysis

5.1 Finite Element Model Simulation

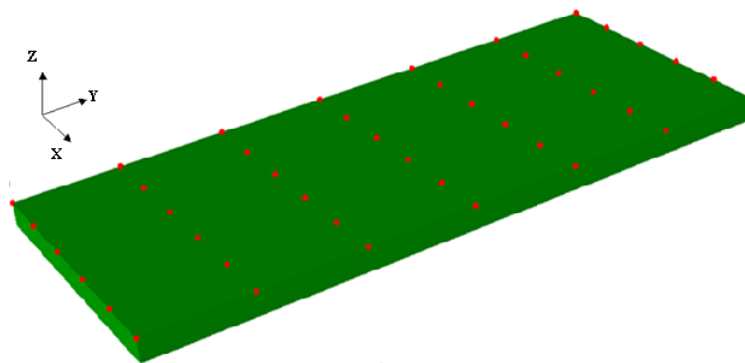


Fig. 6 The FE model of the plate, with the measurement points indicated

The FE simulation of the plate is carried for both the out-of-plane and in-plane modes out using commercial software ABAQUS. To accurately simulate the plate, the linear hexahedron solid elements (C3D8R) are used to construct the FE model (Fig. 6). The boundary conditions of the plate are set to be free. The natural frequencies and mode shapes of the first 16 out-of-plane and first two in-plane elastic modes are calculated and compared with the experimental results. The numerical mode shapes are extracted at the 42 measurement points.

5.2 Validation of Experimental Results

Table 2 shows the comparisons between the natural frequencies from the FE model and those from the experiments. The natural frequencies from the FE model, denoted by f_n , are compared with those obtained in OMA and EMA, denoted by f_e . The modal damping ratio of each mode ζ obtained in OMA and EMA is also shown in Table 2. The maximum errors of the measured natural frequencies from OMA and EMA, compared with those from the FE model, denoted by ε , are 1.53% and 1.52%, respectively, for the first 16 out-of-plane and first two in-plane elastic modes.

Table 2. Comparisons between the natural frequencies from the FE model and those from OMA and EMA (* denotes the in-plane modes); measured damping ratios from OMA and EMA are shown

Mode	Numerical f_n (Hz)	Experimental Results from OMA		Frequency Error ε (%)	Experimental Results from EMA		Frequency Error ε (%)
		f_e (Hz)	ζ (%)		f_e (Hz)	ζ (%)	
1	1000	999	0.01	-0.10	998	0.02	-0.20
2	1421	1431	0.03	0.70	1430	0.02	0.63
3	2756	2757	0.06	0.04	2756	0.05	0.00
4	3051	3068	0.01	0.56	3069	0.03	0.59
5	5103	5129	0.14	0.51	5127	0.08	0.47
6	5255	5241	0.13	-0.27	5238	0.11	-0.32
7	6007	5923	0.08	-1.41	5921	0.08	-1.43
8	6426	6346	0.11	-1.24	6347	0.08	-1.23
9	7746	7792	0.04	0.59	7790	0.06	0.57
10	8195	8204	0.04	0.11	8203	0.07	0.10
1*	8209	8335	0.01	1.53	8334	0.05	1.52
11	8885	8936	0.03	0.57	8936	0.01	0.57
12	10663	10748	0.04	0.80	10747	0.05	0.79
13	11053	11134	0.04	0.73	11133	0.05	0.72
14	12971	13080	0.02	0.84	13078	0.03	0.82
2*	13679	13650	0.01	-0.21	13648	0.01	-0.23
15	13726	13877	0.03	1.10	13875	0.04	1.09
16	14816	14838	0.03	0.15	14840	0.04	0.16

The Modal Assurance Criteria (MAC) values are employed to compare the measured mode shapes from OMA and EMA with those from the FE model. The MAC values between the measured out-of-plane and in-plane mode shapes from OMA and those from the FE model are shown in Table 3(a) and (b), respectively. Note that the measurement point used as the reference point in the out-of-plane mode measurement in OMA is not included in the measured out-of-plane mode shapes, and it is also excluded from the calculated out-of-plane mode shapes in calculating the MAC values. The MAC values between the measured out-of-plane and in-plane mode shapes from EMA and those from the FE model are shown in Table 4(a) and (b), respectively. The diagonal MAC values from OMA are all above 94%, and 93%, indicating that the measured and calculated mode shapes are in very good correlation; the off-diagonal MAC values are all below 30%, indicating that the mode shapes of different modes can be considered as orthogonal, the number of measurement points is adequate, and the distribution of their positions is proper [9]. The first 16 out-of-plane and first two in-plane elastic mode shapes measured from OMA are shown in Fig. 7.

Table 3. MAC values (in percentage) between the measured mode shapes from OMA and those from the FE model:
(a) out-of-plane modes, and (b) in-plane modes

EXP. NUM.	1	2	3	4	5	6	7	8	9	10	11	12	13	14	15	16
1	96.12	0.57	0.10	1.34	0.54	14.93	4.26	0.47	1.28	2.85	0.06	0.65	0.71	17.11	1.74	0.09
2	0.44	95.75	1.07	2.63	6.85	0.02	0.16	0.63	2.85	0.24	1.55	1.15	9.30	0.05	0.58	0.02
3	0.52	0.81	98.57	0.23	0.76	0.06	0.32	0.72	0.11	0.71	14.86	7.87	0.59	0.07	0.58	0.02
4	1.19	0.34	0.34	97.81	0.07	0.61	0.64	1.81	7.14	0.54	1.48	1.94	0.96	0.22	1.09	5.72
5	0.12	7.99	3.25	1.91	95.94	0.19	0.16	1.22	3.17	0.31	1.68	2.00	17.50	0.09	0.41	0.07
6	15.16	0.02	0.61	0.11	0.16	97.79	0.09	0.01	0.04	1.29	0.48	0.12	0.01	11.56	3.50	0.02
7	4.03	0.00	1.02	1.11	0.03	1.89	94.70	2.48	2.35	1.90	1.47	2.36	0.12	2.01	12.46	0.19
8	0.90	2.13	0.78	1.14	2.14	0.05	1.24	97.54	0.69	1.93	0.00	8.97	1.53	0.08	2.45	0.15
9	1.60	2.31	0.02	13.10	2.93	0.46	1.42	0.67	97.44	1.46	0.04	0.68	2.31	0.67	1.45	10.38
10	2.41	0.19	0.39	1.41	0.48	1.89	2.05	1.31	5.16	95.92	0.44	2.14	0.70	0.06	10.97	0.08
11	1.08	0.73	19.03	0.31	1.06	0.45	1.58	0.12	0.01	1.01	97.53	0.47	0.54	0.54	1.39	0.04
12	1.34	0.97	2.34	1.77	1.61	0.25	1.03	5.83	1.37	1.61	0.03	96.83	0.05	0.41	1.78	0.01
13	0.39	7.69	1.04	1.57	15.89	0.08	0.55	1.61	1.47	0.35	0.87	4.41	95.19	0.21	0.71	0.17
14	14.91	0.25	0.25	0.18	0.26	10.44	2.57	0.24	0.29	0.00	0.09	0.42	0.00	99.02	1.93	0.13
15	1.65	0.27	0.50	1.58	0.18	1.97	8.07	1.55	0.77	9.81	0.51	2.00	0.25	0.11	95.56	0.29
16	0.78	0.16	0.06	5.36	0.11	0.78	0.33	0.07	8.01	0.14	0.13	0.12	0.21	0.57	2.11	96.97

(a)

EXP. NUM.	1	2
1	97.46	0.03
2	0.27	96.56

(b)

Table 4. MAC values (in percentage) between the measured mode shapes from EMA and those from the FE model:
(a) out-of-plane modes, and (b) in-plane modes

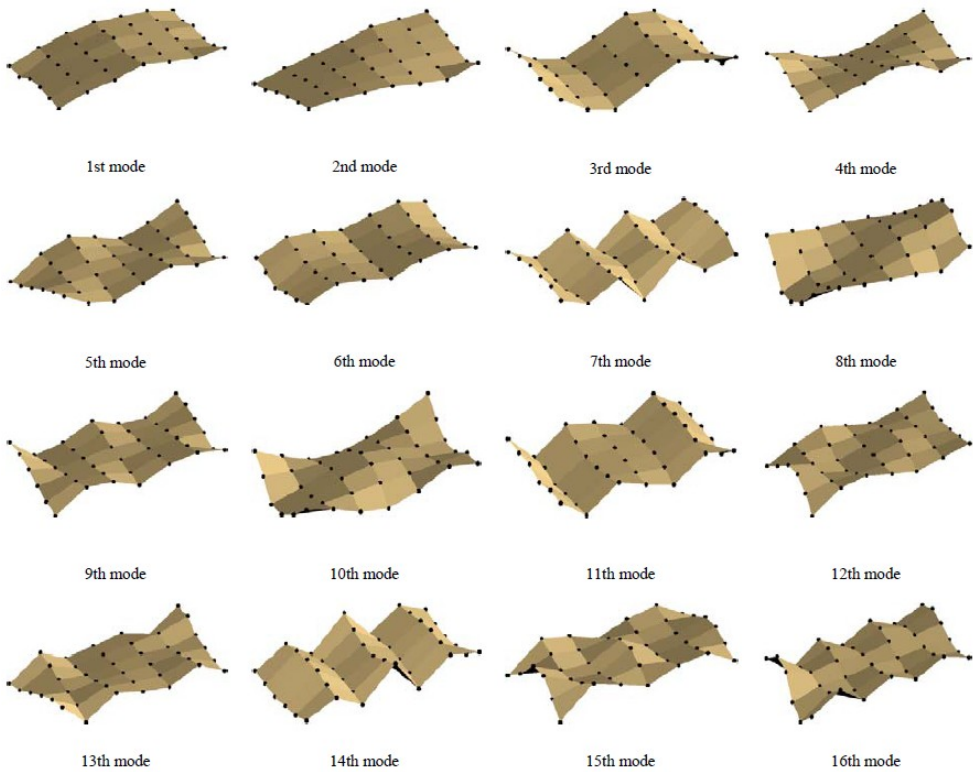
EXP. NUM.	1	2	3	4	5	6	7	8	9	10	11	12	13	14	15	16
1	99.81	0.74	0.37	0.79	0.59	14.12	3.42	0.74	0.84	5.97	0.38	0.91	0.34	17.93	3.70	0.07
2	0.43	99.33	0.47	1.39	7.12	0.02	0.95	1.56	1.14	0.67	0.59	1.84	7.66	0.14	0.77	0.07
3	0.47	0.48	99.69	0.63	0.75	0.03	0.49	0.49	0.25	0.61	18.39	7.65	0.69	0.19	0.77	0.00
4	0.35	2.11	0.50	99.41	2.15	0.04	1.36	0.98	12.22	1.72	0.49	0.99	1.33	0.11	2.17	7.01
5	0.66	7.31	0.19	2.54	98.88	0.06	0.69	1.73	1.80	1.50	0.65	1.97	17.16	0.03	0.70	0.35
6	13.30	0.13	0.03	0.01	0.50	98.63	0.05	0.02	0.26	0.90	0.04	0.01	0.04	10.88	4.48	0.15
7	4.22	0.84	1.01	1.22	0.63	1.55	97.09	2.09	1.05	2.13	1.10	2.28	0.32	2.15	12.76	0.03
8	2.30	0.36	1.30	0.36	0.75	0.08	3.01	95.73	0.15	2.42	0.08	6.60	0.62	0.47	2.34	0.06
9	0.50	1.23	0.41	11.45	1.88	0.00	0.96	0.70	98.80	3.07	0.09	0.98	1.25	0.08	2.62	12.05
10	1.82	0.65	1.85	0.28	0.71	1.86	1.09	2.55	0.20	95.72	1.50	3.37	0.20	0.16	8.49	0.00
11	0.41	0.54	19.26	0.41	0.81	0.23	0.92	0.16	0.59	0.82	99.22	0.64	0.74	0.04	1.33	0.00

12	2.10	1.94	2.48	0.78	1.44	0.48	1.87	7.19	0.21	3.08	0.00	95.35	3.83	0.66	2.99	0.00
13	0.64	7.51	0.14	1.42	17.24	0.14	1.16	0.34	2.49	1.20	0.14	0.10	98.53	0.02	1.43	0.11
14	16.59	0.10	0.17	0.42	0.13	11.57	3.56	0.18	0.24	0.03	0.13	0.31	0.41	98.74	2.86	0.26
15	1.36	0.50	2.11	1.74	0.76	1.79	7.79	1.78	1.16	9.95	2.10	3.56	0.27	0.05	96.43	0.41
16	0.00	0.00	0.32	5.17	0.03	0.01	0.11	0.02	12.84	0.02	0.30	0.13	0.01	0.03	0.01	96.74

(a)

EXP. NUM.	1	2
1	93.33	0.01
2	0.01	98.67

(b)



(a)



(b)

Fig. 7 Measured mode shapes from OMA: (a) out-of-plane modes, and (b) in-plane modes

6. Conclusion

A non-contact OMA test method is presented to measure the out-of-plane and in-plane modes of a rectangular plate, using acoustic white noise excitation in the frequency range from 0 to 15000 Hz. A single-point laser vibrometer is used to measure the velocities of the measurement points of the plate and a free-field microphone is used to measure the pressure near the reference point. It has been shown that the CPSDs between the velocities of the measurement points and the pressure near the reference point are equivalent to those between the velocities of the measurement points and the reference point if the natural frequencies of the test structure that are of interest are sufficiently high but lower than a certain value. The in-plane modes of the plate are identified by comparing the out-of-plane CPSD and the mixed CPSD. In addition, EMA is performed to measure the out-of-plane and in-plane modes of the plate. A FE model of the plate is created and the numerical results are compared with the experimental ones from OMA and EMA. The maximum error between the measured and calculated natural frequencies is 1.53% for the first 16 out-of-plane and first two in-plane elastic modes, and the corresponding MAC values are all above 93%.

7. Acknowledgement

This work was supported by Pratt & Whitney. The authors would like to thank Mr. Kun He for valuable discussion on the test setup.

8. References

- [1] Verhees, M., "Experimental Modal Analysis of a Turbine Blade," *Traineeship Report, Technische Universiteit Eindhoven*, Netherland, 2004.
- [2] James, G., Carne, T., Lauffer J., and Nord, A., "Modal Testing Using Natural Excitation," *Proceedings of the 10th IMAC*, San Diego, CA, USA, 1992.
- [3] Zhang, L., Brincker, R., and Andersen, P., "An Overview of Operational Modal Analysis: Major Developments and Issues," *Proceedings of the 1st IOMAC*, Copenhagen, Denmark, 2005.
- [4] Brincker, R., and Andersen, P., "ARMA Models in Modal Space," *Proceedings of the 17th IMAC*, Kissimmee, FL, USA, 1999.
- [5] Benveniste, A., and Fuche, J., "Single Sample Modal Identification of a Nonstationary Stochastic Process," *IEEE Transaction Automatic Control*, Vol. 30(1): 66-74, 1985.
- [6] Peeters, B., and De Roeck, G., "Stochastic System Identification for Operational Modal Analysis: A Review," *ASME Journal of Dynamic System, Measurement, and Control*, Vol. 123(4): 659-667, 2001.
- [7] Brincker, R., Zhang, L., and Anderson, P., "Modal Identification from Ambient Responses Using Frequency Domain Decomposition," *Proceedings of the 18th IMAC*, San Antonio, TX, USA, 2000.
- [8] Guillaume, P., Verboven, P., Vanlandiut, S., Van der Auwaerer, H., and Peeters, B., "A Poly-Reference Implementation of the Least-Squares Complex Frequency-Domain Estimator," *Proceedings of the 21st IMAC*, Kissimmee, FL, USA, 2003.
- [9] Ewins, D., *Modal Testing: Theory, Practice and Application, 2nd Edition*, Research Studies Press Ltd., Baldock, Hertfordshire, England, 1999.
- [10] Larsson, D., "In-plane Modal Testing of a Free Isotropic Rectangular Plate," *Experimental Mechanics*, Vol. 37(3): 339-343, 1997.
- [11] Fahy, F. *Foundations of Engineering Acoustics*, Elsevier Academic Press, London, England, 2001.
- [12] Valentino, M., *Microphone Handbook*, PCB Piezotronics, NY, USA.
- [13] Mohanty, P., "Operational Modal Analysis in the Presence of Harmonic Excitations," *Ph.D. Thesis*, Technische Universiteit Delft, Netherland, 2005.
- [14] Caughey, T., and O'Kelly, M., "Classical Normal Modes in Damped Linear Dynamic Systems," *ASME Journal of Applied Mechanics*, Vol. 32: 583-588, 1965.
- [15] Peeters, B., and Van der Auwaerer, H., "PolyMAX: a Revolution in Operational Modal Analysis," *Proceedings of the 1st IOMAC*, Copenhagen, Denmark, 2005.

[16] Heylen, W., Lammens, S., and Sas, P., *Modal Analysis Theory and Testing*, Katholieke Universiteit Leuven, Faculty of Engineering, Department of Mechanical Engineering, Division of Production Engineering, Machine Design and Automation, Belgium, 1998.

Algorithm hybridization for automated modal identification and structural health monitoring

C. Rainieri¹, G. Fabbrocino²

¹Ph.D., Research associate, Structural and Geotechnical Dynamics Laboratory *StreGa*, University of Molise, Via Duca degli Abruzzi – 86039Termoli, Italy

²Associate Professor, Structural and Geotechnical Dynamics Laboratory *StreGa*, University of Molise, Via Duca degli Abruzzi – 86039Termoli, Italy

Abstract

Modal-based damage detection algorithms are well-known techniques for structural health assessment. The development of several automated output-only modal identification techniques in the last few years is yielding an increasing interest towards modal-based damage detection. However, some aspects of automated modal identification need further developments. Robustness of the algorithm towards slightly non-stationary excitation, computational efforts and reliability of modal parameter and, in particular, damping estimates represent key issues for the development of reliable automated output-only modal identification techniques.

In the present paper, based on the results of sensitivity analyses to assess the performance of popular operational modal analysis techniques, an hybrid algorithm for automated output-only modal parameter estimation is proposed. The main advantages of the innovative approach consist of the control of the computational time and, in addition, the achievement of reliable damping estimates. Its performance will be assessed through application to a real record taken on a full scale civil structure.

Introduction

The modern issues in the field of management and maintenance of structures can find a solution in the installation, at least on strategic or heritage structures, of Structural Health Monitoring (SHM) systems. They can ensure a fast assessment of incipient damage conditions, follow their evolution and provide almost in real time information about the safety level of the structure itself. Reduction of inspection costs, seismic protection, possibility to develop post-earthquake scenarios and support rescue operations are some of the main advantages related to implementation of effective SHM systems.

SHM systems are based on the integration of a number of different sensors to monitor the physical quantities of interest to characterize the behavior and health state of the structure. SHM systems have been applied to different structural typologies, including civil engineering structures [1]. However, effective data processing procedures are required to extract information from the raw data. Among them, modal-based damage detection procedures are established and widely accepted methodologies for structural health assessment. The main issue is related to the availability of accurate and reliable automated procedure for modal parameter identification and monitoring.

A number of automated modal parameter identification and tracking procedures for modal based damage detection appeared in the literature in the last few years. A complete review can be found in [2]. The main drawbacks of existing automated modal identification methods can be summarized as follows:

- 1) Most of the methods use a threshold for peak or physical pole detection; as a consequence, a preliminary calibration phase is needed for its proper definition; moreover, the identified peaks or poles could not correspond to structural modes; performance of peak detection algorithms can also get worse in presence of measurement noise.
- 2) Identification of structural modes is based on a number of parameters so that a time consuming calibration process for each monitored structure is required; moreover, a static identification of thresholds and parameters may be inadequate to follow the natural changes in modal properties of structures due to damage or environmental effects.
- 3) Most of the algorithms are somehow sensitive to noise, and higher modes or even poorly excited modes are not always identified.

Some of the mentioned critical issues can be overcome through some objective criteria for the identification of mode bandwidth before modal parameter extrac-

tion, as described in [2]. However, even if the outlined procedure is effective in separating the different modes and extracting the modal parameters, it also suffers some drawbacks. They are mainly related to the need of long record durations and to the estimation of modal damping ratios.

In the present paper, based on the results of a large number of sensitivity analyses to assess the performance of popular operational modal analysis techniques, an hybrid algorithm for automated output-only modal parameter estimation is discussed. The main advantages of the innovative approach are represented by the control of the computational time and also the achievement of reliable damping estimates. Its performance will be assessed through application to a real case study.

The hybrid algorithm for automated modal identification

The proposed algorithm, called ARES (Automated modal paRameter Extraction System), is based on the combination of different steps from popular output-only modal identification procedures and a clustering approach to develop a new fully automated method for operational modal analysis. It takes advantage of the separation of modal contributions and noise operated by the Joint Approximate Diagonalization (JAD) [3] which is the basis of the Second Order Blind Identification (SOBI) [4]. The sources, including both modal and noise sources, are then passed, once a time, to the Stochastic Subspace Identification (SSI) [5, 6] based step for estimation of natural frequencies and damping ratios and identification of noise sources. This step of the algorithm takes advantage also of advanced clustering techniques [7, 8] to identify the physical poles. The source separation at the first step makes this identification easier and more reliable. In fact, one modal contribution is usually present in each source, eventually in combination with noise or minor contributions from other modes.

Thus, the physical mode parameters can be obtained by looking for the cluster with the largest number of elements. Cross checks between the results of different clustering techniques, namely hierarchical and subtractive clustering [7, 8], makes identification of noise sources possible, since they do not provide consistent results. Accuracy of natural frequency and damping estimates is ensured by sensitivity analyses of the results with respect to the number of block rows used in SSI, according to the procedure outlined in [9]. Finally, mode shape estimates are obtained, at the present stage of implementation, from Singular Value Decomposition (SVD) of the output Power Spectral Density (PSD) matrix at the previously estimated frequency of the mode [10]. The flowchart of the proposed algorithm is shown in [Figure 1](#).

The computational time can be controlled by properly setting the values of the number of time lags p and the threshold t in the JAD [3, 11]. Sensitivity analyses carried out on modal identification results provided by SOBI point out that the accuracy of estimates is basically insensitive to the value of the threshold if it is set equal or lower than $1\text{E-}4$. On the other hand, the accuracy in the natural frequency estimates improves for increasing values of p .

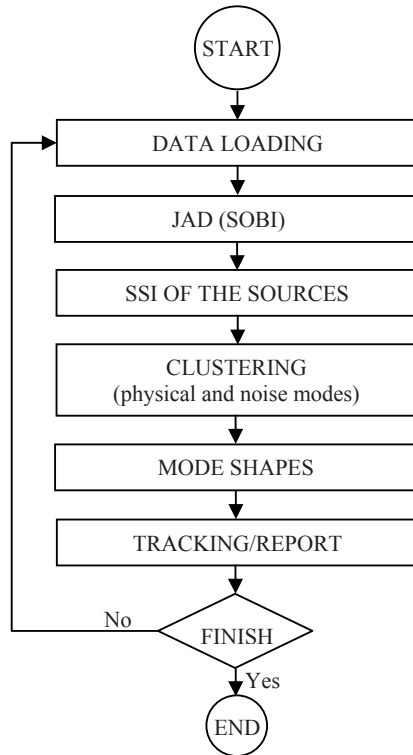


Fig. 1. ARES flowchart

However, after a certain value, the accuracy becomes basically stable, so that it is sufficient to choose a value of p large enough to obtain a high accuracy and a reasonable computational time [11]. For instance, if an estimate of the natural frequency and damping ratio of the fundamental mode is available, for instance using LEONIDA [2], an optimum value for p can be derived [11]. Based on such results, the computational time can be optimized by properly setting the values of t and p .

In the next section, the algorithm is applied to a real dataset. Results are compared with those provided by an accurate traditional (manual) modal identification process [9] and a preliminary performance assessment is carried out.

Results and discussion

An explanatory case is the analysis via ARES of a real record taken on a full scale civil structure. The latter is characterized by two closely coupled modes as fundamental modes. Attention is focused on both accuracy of estimates for the fundamental modes, which are commonly of interest for civil engineering structures in seismic areas due to the related large amount of participating mass ratios, and capability of identifying the higher modes, rejecting noise.

The total record length is 1200 sec at 100 Hz sampling frequency. The record has been decimated before processing, obtaining a final sampling frequency of 10 Hz. The structural response of the structure to ambient vibrations has been measured through 12 force balance accelerometers and a data acquisition hardware characterized by a 24 bit ADC.

The number of identifiable modes is limited by the number of measurement channels [4]. Thus, a maximum of 12 modes can be theoretically identified. Actually, among the 12 sources extracted from the JAD of the p correlation matrices [3, 4], some of them will be related to physical modes and some others to noise. For the present application, the values of p and t have been set equal to 500 and $1\text{E-}8$ respectively, since the sensitivity analyses carried out on modal parameters provided by SOBI show that optimum estimates are associated to this set of values for the analysis parameters. The assessment of the effect of p and t on the performance of the proposed algorithm is currently out of the scope of the paper and it will be the subject of future developments of the research.

The algorithm capability of identifying both the fundamental and higher modes and reject the noise sources has been checked at the first stage for a generic user-defined value of the number of block rows i [5, 6]. This value has assumed as constant during analysis of all sources.

Noise sources are identified by checking the consistency of the modal parameter estimates provided by hierarchical clustering, considering the cluster characterized by the maximum number of elements, and subtractive clustering. Then, the accuracy of the natural frequency and damping ratio estimates for the fundamental modes has been evaluated through a sensitivity analysis with respect to the number of block rows, as described in [9].

Results of automated modal identification via the proposed algorithm are shown in [Table 1](#), where results of manual identification and a description of the sources obtained from SOBI are also reported. Thus, the algorithm has been able to identify 7 structural modes, even in the case of sources slightly corrupted by noise or not very well separated, and reject 5 noise sources.

Table 1. ARES performance assessment

Source	Is mode? (ARES)	f [Hz] (ARES)	ξ [%] (ARES)	f [Hz] (manual)	Source description
I	Yes	1.30	0.65	1.30	Well separated mode
II	Yes	0.98	1.01	0.98	Well separated mode
III	Yes	0.92	1.29	0.92	Well separated mode
IV	Yes	3.38	1.82	3.40	Mode + noise (not well separated)
V	No	-	-	-	Noise
VI	No	-	-	-	Noise
VII	Yes	2.58	2.52	2.59	Mode + noise (not well separated)
VIII	No	-	-	-	Noise
IX	Yes	3.93	2.24	3.94	Well separated mode
X	Yes	4.21	1.61	4.20	Well separated mode
XI	No	-	-	-	Noise
XII	No	-	-	-	Noise

Table 2. ARES optimized estimates (“av” means average, “std” standard deviation)

Mode	i	f_{av} [Hz]	f_{std} [Hz]	ξ_{av} [%]	ξ_{std} [%]	ARES Best estimate	Ref. value (manual) – f [Hz]	Ref. value (manual) – ξ [%]
I	20	0.9206	0.0002	1.2911	0.0261	x	0.92	1.32
	30	0.9196	0.0006	1.3137	0.0590			
	40	0.9196	0.0002	1.2921	0.0440			
	50	0.9196	0.0002	1.2878	0.0179			
	80	0.9195	0.0001	1.2586	0.0080			
	100	0.9194	0.0001	1.2603	0.0114			
II	20	0.9844	0.0002	0.9857	0.0292	x	0.99	1.02
	30	0.9844	0.0001	1.0228	0.0157			
	40	0.9841	0.0003	1.0792	0.0352			
	50	0.9837	0.0030	1.1427	0.1083			
	80	0.9804	0.0110	0.9913	0.1900			
	100	0.9847	0.0005	1.2838	0.1939			
III	20	1.3033	0.0085	0.7628	0.5895	x	1.30	0.64
	30	1.2999	0.0001	0.6521	0.0051			
	40	1.2999	0.0001	0.6538	0.0030			
	50	1.2999	0.0001	0.6399	0.0099			
	80	1.2997	0.0001	0.6653	0.0194			
	100	1.2913	0.0124	0.0504	0.9142			

The accuracy of the fundamental mode natural frequency and damping ratio estimates for different values of the number of block rows i has been also evaluated, in analogy with the procedure described in [9]. In Table 2 the average value and the standard deviation of both natural frequency and damping ratio estimates of the mode of interest computed from the poles belonging to the largest cluster provided by hierarchical clustering are shown. The value of i which minimizes the overall variance of the poles in the cluster is also the one that ensures the best fit of the model to the data and the best modal parameter estimates [9]. It is worth noting that the optimal i value changes from one source to another. The obtained results seems to point out that the best fit depends not only on the natural frequency and damping ratio of the mode of interest and the sampling frequency of the data, but also on the signal-to-noise ratio in the data. However, more detailed analysis about this issue are in progress and will be the object of a future work.

Conclusions

In the present paper, based on the results of extensive sensitivity analyses to assess the performance of popular operational modal analysis techniques, an hybrid algorithm for automated output-only modal parameter estimation is proposed. It is based on the combination of different steps from popular output-only modal identification procedures and a clustering approach. In particular, it takes advantage of the separation of modal contributions and noise operated by SOBI to make easier and more reliable the modal parameter identification via repeated application of the SSI to the sources. In fact, the separated sources usually include only one physical mode and a certain amount of noise.

As a result, interpretation of the stabilization diagram through clustering is easier and it does not require the calibration of a threshold to separate physical from noise modes, since the largest cluster is that one containing the physical information (the one that better stabilizes). On the other hand, cross checks between the results of different clustering techniques, namely hierarchical and subtractive clustering, have been adopted to identify noise sources. Finally, sensitivity analyses of the results with respect to the number of block rows used in SSI lead to very accurate natural frequency and damping ratio estimates. The main advantages of the new technique are represented by the possibility to control the computational time and to obtain also reliable damping estimates in a fully automated way. Moreover, the algorithm can work on different structures without any manual tuning and initialization phase. The main drawback is, instead, the limit in the number of identifiable modes represented by the number of measurement channels. Its performance have been assessed through application to a real case study, obtaining promising results. The next steps of the present research consist of the analysis of the influence of the parameters p and t on the accuracy and reliability of estimates

and on the optimization of the computational time in view of integration of the algorithm into automated modal based SHM systems. Extensive checks of the algorithm performance for different datasets and structural typologies are also needed.

Acknowledgments

The present work is carried out within the activities of AT2 – LR 2 – Task 3 of the ReLuis-DPC Executive Project 2010-2013, rep. 823. Support of ReLuis Consortium is therefore gratefully acknowledged.

References

- [1] Doebling SW, Farrar CR, Prime MB, Shevitz DW (1996) Damage Identification and Health Monitoring of Structural and Mechanical Systems from Changes in their Vibration Characteristics: A Literature Review. Technical Report LA-13070-MS, UC-900, Los Alamos National Laboratory, New Mexico 87545, USA.
- [2] Rainieri C, Fabbrocino G (2010). Automated output-only dynamic identification of civil engineering structures. *Mechanical Systems and Signal Processing* 24: 678-695.
- [3] Belouchrani A, Abed-Meraim K, Cardoso JF, Moulines E (1997) A blind source separation technique using second-order statistics. *IEEE Transactions on Signal Processing* 45: 434-444.
- [4] Poncelet F, Kerschen G, Golinval JC, Verhelst D (2007) Output-only modal analysis using blind source separation techniques. *Mechanical Systems and Signal Processing* 21: 2335-2358.
- [5] Van Overschee P, De Moor B (1996) *Subspace Identification for Linear Systems: Theory – Implementation – Applications*. Kluwer Academic Publishers, Dordrecht, the Netherlands.
- [6] Peeters B (2000) *System Identification and Damage Detection in Civil Engineering*, Ph.D. Dissertation. Katholieke Universiteit Leuven, Leuven, Belgium.
- [7] Tan P-N, Steinbach M, Kumar V (2006) *Introduction to data mining*. Pearson Addison-Wesley, Reading, MA, USA.
- [8] Chiu S. (1994) Fuzzy Model Identification Based on Cluster Estimation. *Journal of Intelligent & Fuzzy Systems* 2: 267-278.
- [9] Rainieri C, Fabbrocino G, Cosenza E (2010) On damping experimental estimation. *The Tenth International Conference on Computational Structures Technology*, Valencia, Spain.
- [10] Brincker R, Zhang L, Andersen P (2000) Modal identification from ambient responses using frequency domain decomposition. *The 18th SEM International Modal Analysis Conference*, San Antonio, TX, USA.
- [11] Rainieri C, Fabbrocino G (2010) Performance assessment of Second Order Blind Identification for output-only modal analysis and vibration-based Structural Health Monitoring. Submitted for publication.

Fiber Optic Sensor Installation for Monitoring of 4 Span Model Bridge in UCF

Il-Bum Kwon¹, Masoud Malekzadeh, Qian Ma, Hasan Gokce, Thomas K. Terrell, Anton Fedotov,
F. Necati Catbas²

Department of Civil, Environmental and Construction Engineering
University of Central Florida, Orlando

¹ ibkwon7@gmail.com

² catbas@mail.ucf.edu

ABSTRACT

Fiber optic sensors can give us valuable data to assess the health of a structure, known as Structural Health Monitoring (SHM). Bridges, being critical structures, are monitored with different sensors such as strain measurements mostly at discrete locations with resistive based sensors. Fiber optic sensors can be used to sense the strain status by using one sensing optical fiber line. Recently, fiber optic Bragg grating sensors are a representative of point sensing technique, and also fiber optic BOTDR or BOTDA sensor is a unique measurement technique to sense fully distributed strain through the sensing optical fiber. Therefore, in this paper, fiber optic Bragg grating(FBG) sensor, fiber optic BOTDR(Brillouin optical time domain reflectometry) sensor, fiber optic BOTDA(Brillouin optical time domain analysis) sensor are installed on 4 span model bridge to study distributed sensing and data analysis to acquire some useful data to identify bridge condition assessment.

INTRODUCTION

Structural health monitoring is necessary for efficient maintenance and repair of structures. This technology is also one of interdisciplinary research works covered with sensing, communication, signal processing, data management, system identification, information technology, etc. It needs collaboration between many fields: civil, mechanical, electrical and computer engineering among others. The current challenges for bridge structural health monitoring are being recognized as distributed and embedded sensing, data management and storage, data mining and knowledge discovery, diagnostic methods, and presentation of useful and reliable information to bridge owners/managers for decision making on maintenance and management[1]. A benchmark structure, 4 span model bridge, was constructed in the University of Central Florida to simulate some representative bridge damages in order to explore the above challenges[2]. Therefore, in this article, the authors prepare fiber optic sensor instrumentation- fiber optic Bragg grating(FBG) sensor, fiber optic BOTDR(Brillouin optical time domain reflectometry) sensor, fiber optic BOTDA(Brillouin optical time domain analysis) sensor on the 4 span model bridge to study distributed sensing and data analysis to acquire some useful data to identify bridge damages.

FIBER OPTIC SENSORS

Fiber optic FBG sensor

Fiber Bragg grating (FBG) is a type of Bragg reflector that indexes in an optical fiber which reflects particular the Bragg wavelengths of light and transmits all others[3]. A conventional FBG sensor system is composed of a broadband light source, FBGs, a wavelength interrogator, and system software, as shown in Fig. 1. When broadband light is launched into an FBG, the reflection occurs at the FBG. Some light, of which wavelength satisfies Bragg condition of equation (1), is reflected, and the others passes the grating.

$$\lambda_B = 2n_e \Lambda \quad (1)$$

λ_B is the Bragg wavelength, n_e is the effective refractive index, and Λ is the grating period.

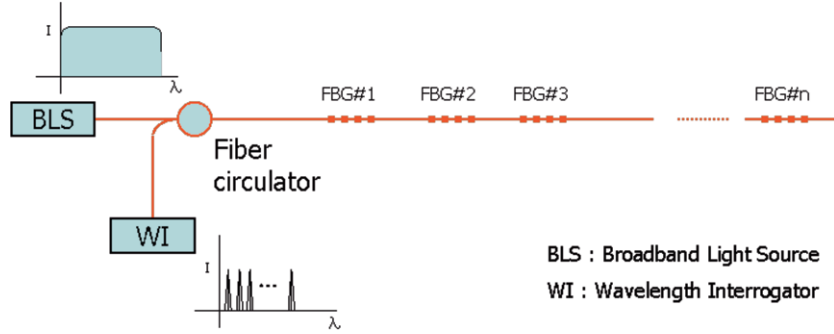


Figure 1. Schematic of fiber optic Bragg grating sensor

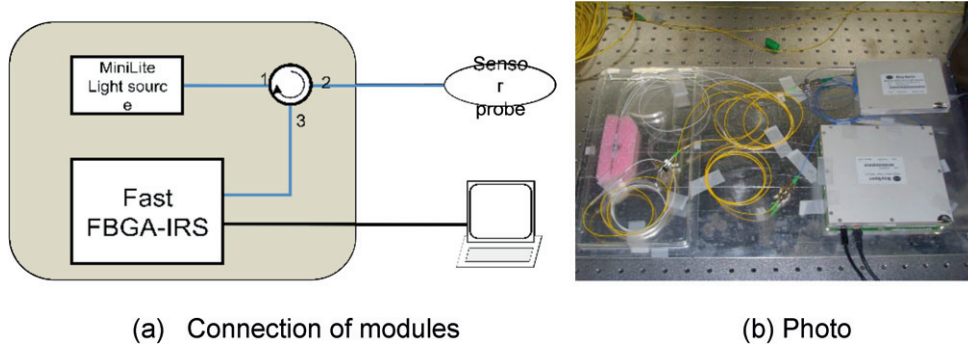


Figure 2. Construction of FBG sensor system

When strain is induced in an FBG, the Bragg wavelength is expected to have a proportional shift. The strain can be easily determined by analyzing the change of the wavelength. According to this principle, FBG sensors can sense the grating period change due to strain variation, and they can measure strain without the influence from noise and light intensity perturbation. The wavelength shift is proportional to strain, and absolute strain can be measured[4].

$$\frac{\Delta\lambda_B}{\lambda_B} = \left\{ 1 - \frac{n_e^2}{2} [p_{12} - \nu(p_{11} + p_{12})] \right\} \varepsilon \quad (2)$$

Where P_{ij} are the silica photo-elastic tensor components and ν is the Poisson's ratio.

In order to construct an FBG sensor system for applying 4 span model bridge, three major elements are needed, the power source, which has to have a voltage about 5V and 0.4-0.5 A to insure the optical light source is working fine; a minilite light source (ASE source) which has a wavelength range of 800-1650 nm, spectral width of 100 nm, output power : up to 30 mW and it is operating temperature between 10-70 °C. The most important part, the FBG interrogator has a wavelength range of 1525-1565 nm, resolution about 1 pm, operating frequency around 5 kHz and interface with USB 2.0 and it requires the operating temperature between 0-70 °C and the last one is the circulator, which is to making sure the reflect wavelength is going back to the FBG interrogator and the interrogator is going to send the data directly to the computer to do analysis (Figure 2).

Fiber Optic BOTDR/A sensor

When the power of optical signal which propagates along the single-mode optical fiber is larger than the Brillouin threshold power, the backward Brillouin scattering signal is generated. The backward Brillouin scattering signal can be described as a parametric interaction among the incident light, the Stokes light, and an acoustic wave. The Brillouin frequency shift λ_B of the backward scattering light of the propagating light in an optical fiber is given by

$$\nu_B = \frac{2n\nu_a}{\lambda_p} \quad (3)$$

where ν_a is the acoustic velocity, n the effective refractive index, and λ_p the pump wavelength[5]. In the first approximation, Brillouin frequency shift increases linearly with strain,

$$\nu_B = \nu_B(0)(1 + C\varepsilon) \quad (4)$$

where ε is strain and C the coefficient of strain, which is known to be 5 MHz per 0.01 for single mode optical fibers used at the 1.5 micro-meter wavelength range of the optical communication. If pulsed light is allowed to enter the optical fiber shown in the bellowing figure, frequency shift at each distance position of optical fiber is calculated from intensity data of Brillouin scattered light detected at the incident end, and strain on the optical fiber can be measured in a distributed manner.

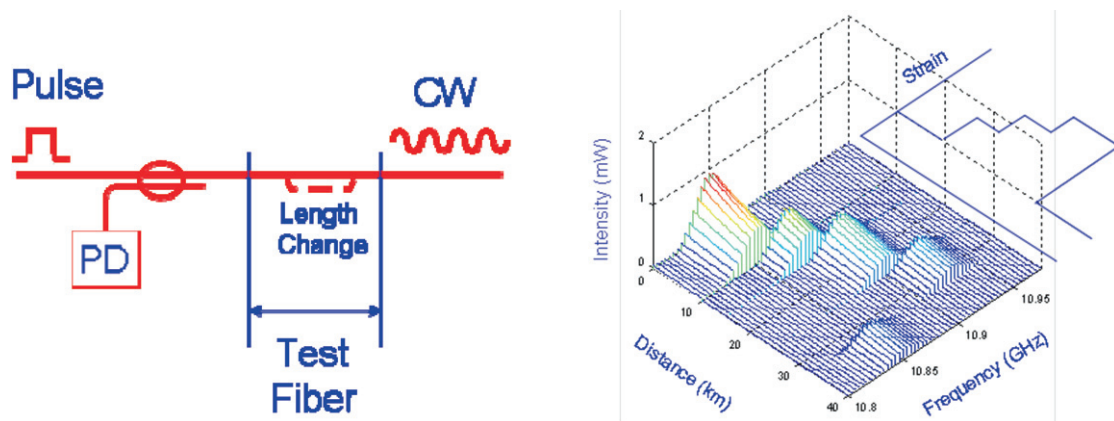


Figure 3. Brillouin scattering sensor and the output signal

Fiber optic BOTDR operate without continuous wave(CW) pumping light at the another end of the sensing fiber. However, BOTDA sensor should use the CW pumping light, and then, this sensor shows as a closed loop sensing optical fiber.

Comparison of various fiber optic sensors

In this work, three types of fiber optic sensors, FBG sensor, BOTDR sensor, and BOTDA sensor, are applied to sense the 4 span model bridge. FBG sensor can measure many points of strain with high operation time of 5 kHz. If it is necessary to measure other physical parameters, such as acceleration, pressure, and tilt, then these can be measured by the properly prepared probes. These FBG sensors are very useful for satisfying many point sensing needs by one optical fiber using multiplexing technique. However, if it is necessary to sense fully distributed manner, then BOTDR or BOTDA is a solution to apply for those needs. BOTDR, Advantest company, usually has the spatial resolution of 1 m, but BOTDA, recently developed by OZoptics company, can distinguish 0.1 m information through the sensing fiber measurement length range. These brillouin scattering sensors have an intrinsic drawback which is the long measurement time, about several minutes.

Table 1 Comparison of various fiber optic sensors

Sensors		Advantage and disadvantage	Measurement parameter	Specification
Fiber optic sensors	FBG sensor	Absolute mea. Multiplexing Fast mea.	Strain, Acceleration, Pressure, Tilt, Temperature	< 1 micro-strain 5k Hz
	BOTDR	Absolute mea. Distributed mea. Long mea. time	Strain, Temperature	< 1 micro-strain 1 m spatial resol. ~several minutes
	BOTDA	Absolute mea. Distributed mea. Long mea. time	Strain, Temperature	< 1 micro-strain 0.1 m spatial resol. ~several minutes

LAB STUDIES

Structural preparation (4 span model bridge)

A four span bridge, which has structural response characteristics of medium span bridge, is designed and constructed to demonstrate the new methodologies for damage identification (Figure 4). The setup consists of two approach spans (120 cm) and two main spans (305 cm) with a 3.2 mm thick, 120 cm wide steel deck supported by two high speed steel (HSS) 25x25x3 girders separated at 60 cm from each other. Moreover, special designed supports can be easily changed to roller, pin or fixed boundary conditions. These supports are sitting on top of the piers to simulate support settlement damage. In addition, girder and deck can be connected together by using bolts at different locations to modify the stiffness of the system and to simulate damage.



Figure 4: Four span bridge and vehicle

For this study, a two axle radio controlled vehicle which has 7 kg and 8 kg axle loads with a spacing of 45 cm is used (Figure 3). The vehicle moves around 50 seconds and the average vehicle speed is 0.5 m/s.

Installation of sensors

This 4 span model bridge is instrumented with various sensors such as FBG sensors(12), BOTDR/A sensor fiber(1 line), strain gages (20) accelerometers (16), tiltmeters (2) and a video camera (1) as shown in the instrumentation plan (Figure 5) concerning about the future study. The fiber optic BOTDR or BOTDA sensor uses just one sensing fiber. The signals of BOTDR are averaged with the data of 2^{14} . The sensing fiber is attached on the girders perfectly by using bonding epoxy. The FBG sensor system is operated as 1 kHz speed. A data acquisition system collects data while strain gages, accelerometers and tilt-meters are sampled at a rate of 1 kHz and are averaged every 100 points to minimize noise for an effective rate of 10 Hz. A total of 16 Model 603C01 ICP/PCB accelerometers are installed on the two girders, six on each of the inner spans.

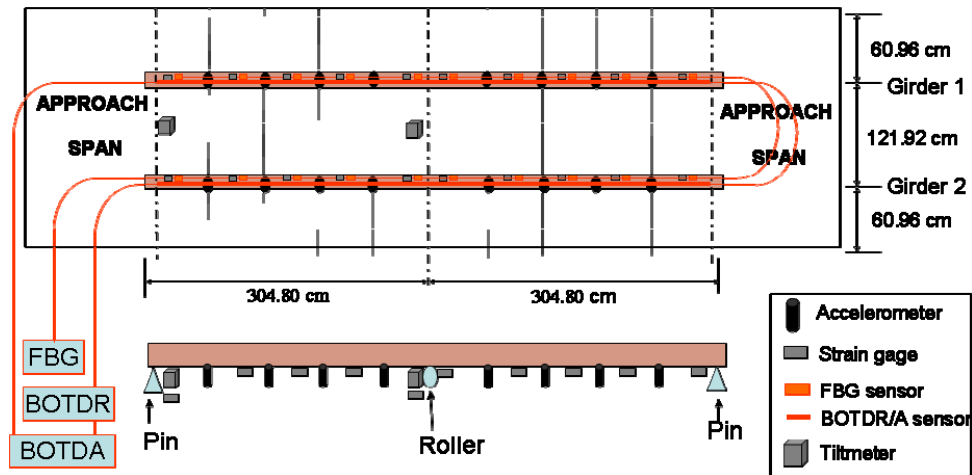


Figure 5: Four span bridge instrumentation plan

PRELIMINARY RESULTS

The dynamic strain acquired from FBG sensors are shown in Figure 6. The maximum strain (S1) can be obtained when the vehicle is located at the 1/4 point of the girder. Also, the strain (S2) is acquired from the FBG sensor located at the center of the bridge. The distributed static strains are acquired by BOTDR sensor shown in figure 7. The difference strains mean that the strains are generated by the loading on the 1/4 point of the girder by the weighting vehicle. However, the distributed strain can not show the loading effect on the strain change, because the spatial resolution of BOTDR is too wide (~1 meter). In future study, the authors will explore measuring with higher spatial resolution sensor with BOTDA sensor.

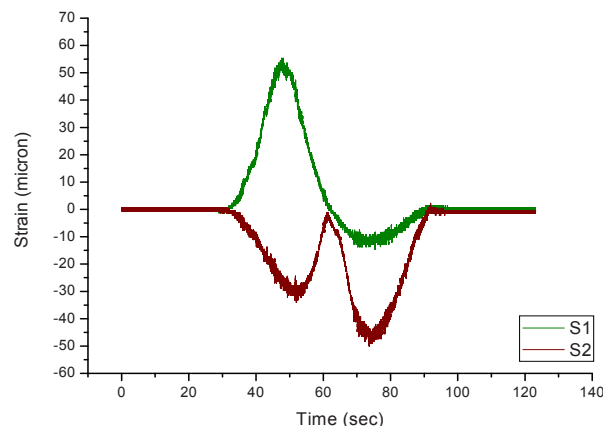


Figure 6. Dynamic point strains of 4 span model bridge measured by FBG sensors

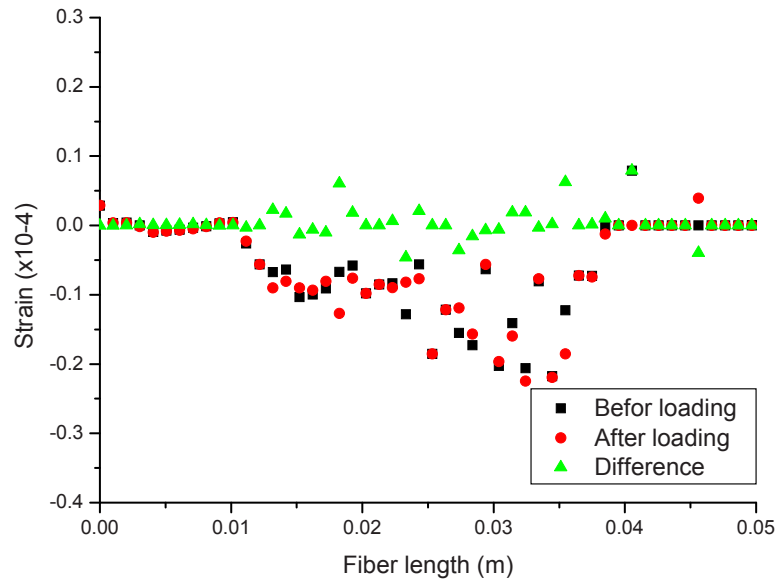


Figure 7. Static distributed strains of 4 span model bridge measured by BOTDR sensor

CONCLUSION

Fiber optic sensors including accelerometers, and strain gages, are installed on the 4 span model bridge to study various sensing technologies for assessing the structural behavior related to common bridge damage cases. FBG sensors can give us to measure point strain information by using one optical line instead of applying many cables of electrical strain gages and also without electrical noise. BOTDR sensor can sense the distributed strain data. Benchmark studies and detailed comparisons of different technologies will be conducted in a comparative manner. In future, it will be studied to show the characteristics of the distributed and point sensing of the bridge and the damage detection capability.

REFERENCES

1. J.M. Ko, and Y.Q. Ni, "Technology developments in structural health monitoring of large-scale bridges," *Engineering Structures*, 2009, 27: pp. 1715-1725.
2. Gul, M. and F.N. Catbas. *A Modified Time Series Analysis for Identification, Localization, and Quantification of Damage*. in *27th International Modal Analysis Conference (IMAC XXVII)*. 2009. Orlando, FL.
3. K.O. Hill, Y. Fuji, D.C. Johnson, B.S. Kawasaki, "Photosensitivity in optical fiber waveguides: application to reflection fiber fabrication," *Applied Physics Letters* 32, 1978: pp. 647.
4. M. Majumder, T.K. Gangopadhyay, A.K. Chakraborty, K. Dasgupta, D.K. Bhattacharya, "Review : Fibre Bragg gratings in structural health monitoring—Present status and applications," *Sensors and Actuators A*, 2008, 147: pp. 150-164.
5. I.B. Kwon, S.J. Baik, K. Im, and J.W. Yu, "Development of fiber optic BOTDA sensor for intrusion detection," *Sensors and Actuators A*, 2002, 101: pp. 77-84.

A Model of Uncertainty Quantification in the Estimation of Noise-Contaminated Transmissibility Measurements for System Identification

Zhu Mao, Michael Todd

Department of Structural Engineering, University of California San Diego, La Jolla CA 92093-0085;
Email: mdt@ucsd.edu

Abstract

System identification via techniques applied in the frequency domain is a very common activity across many applications in engineering. Among many forms of frequency domain system identification, transmissibility estimation has been regarded as one of the most practical tools for its clear physical interpretation, its compatibility with output-only data, and its sensitivity to structural parameters. Due to operational variability, estimation errors, and extraneous noise, the computation of transmissibility may contain significant uncertainty, and this will affect the system identification quality. In this paper, a probability density function for transmissibility estimates is derived analytically via a Chi-square bivariate approach, and validated with Monte Carlo simulation.

1. Introduction

System identification technologies are now widely applied to every branch of engineering, such as system design, control, behavior prediction, damage detection, etc. Mathematical approaches describing various input/output or output/output relationships have been applied in both the time and frequency domains in order to identify, characterize, or control aspects of global system behavior [1]. Frequency domain approaches, which typically involve estimation of the frequency response function (FRF) in a way that supports modal parameter estimation, are among the most common due to their clear physical interpretation and well-defined computational algorithms [2].

Any frequency domain approach that relies on FRF estimation, however, requires either direct measurement of or an assumption of the inputs to the system [3]. It is well-known that for some applications such measurements are impossible or difficult, and/or such assumptions would be poor or unavailable; for these situations, estimation of transmissibility is possible. Similar to a traditional input-output transfer function (such as the FRF), the transmissibility function is defined as the ratio between two outputs, and it describes the relative admittance between the two measurements. Devriendt et al interpret the transmissibility concept versus transfer function as the response data normalized by a reference response instead of by the input excitation [4]. As a parameter-change detector, the transmissibility function can outperform input-output transfer functions such as FRF under some circumstances, because it contains only the system zeros (anti-resonances) and not the system poles (resonances), which means that it is more sensitive to the local mechanical parameters [5]. This is one reason why transmissibility is getting more and more attention from the area of damage detection and structural health monitoring [6].

In any real application, it is well known the estimation of transmissibility from measurements is compromised by computational errors, noise, and other types of operational uncertainties. The objective of this paper is to develop a probability model for the estimation of noise-contaminated transmissibility. Most of the previous research in this area has been focused on modeling of FRF and input-output transfer functions, such as the uncertainty bounds derived by Bendat and Piersol with respect to coherence function and a Gaussian hypothesis [7-9]. In the same spirit, this paper considers a particular transmissibility estimator and derives an exact probability density function for uncertainties associated with its computation, and it includes the influence of corrupting external noise sources.

2. Transmissibility and estimation

Transmissibility, in the context of structural dynamics and identification, is generally defined as the frequency domain transfer function between the system responses of any two measured outputs. With arbitrary excitation, transmissibility essentially detects the relative magnitude and phase responses that occur between any pair of measurement degrees of freedom, including the degrees of freedom where the system is physically excited.

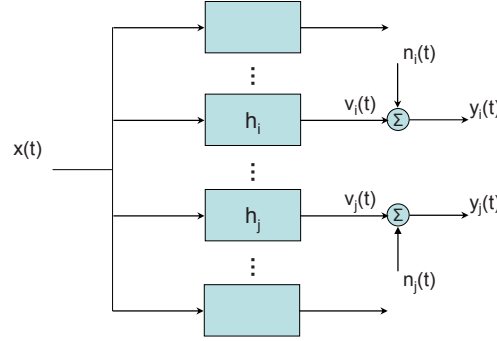


Fig. 1. A SIMO data flow model

Motivated by one of the most commonly-implemented vibration tests, this work will consider a single-input/multiple-output (SIMO) model, as shown in Figure 1. Although the outputs indicated may be any measurable quantity (strain, displacement, velocity, acceleration), the most common kinematic measurement in structural dynamics applications is acceleration, so we denote $v_i(t)$ and $v_j(t)$ as the noise-free acceleration response at any two arbitrary measurement locations i and j . The acceleration-based transmissibility may be expressed in the frequency domain as Equation (1), where capital letters represent Fourier-transformed quantities:

$$T_{ij}(\omega) = \frac{V_i(\omega)}{V_j(\omega)} \quad (1)$$

The magnitude of this form is equivalent to a more practical form involving the auto-power spectral density function G , shown in Equation (2) where “*” indicates the complex conjugate:

$$|T_{ij}| = \sqrt{\frac{V_i^* \cdot V_i}{V_j^* \cdot V_j}} = \sqrt{\frac{G_{v_i v_i}}{G_{v_j v_j}}} \quad (2)$$

$$\text{where } G_{vv} \in \mathbb{R}^+, \forall i \text{ or } j$$

In practice, we must resort to estimates of the transmissibility from finite, band-limited, sampled output records of v_i and v_j , which lead to raw estimations of power spectral densities (\tilde{G}), with an estimated quantity denoted with a tilde (\sim) over it. The accuracy of the estimates may be improved via Welch’s method, where we average multiple records or sub-segments of a single long record to obtain an improved, smooth estimate [10]. Equation (3) shows the smooth estimate of transmissibility magnitude, using n_d times of averages:

$$|\hat{T}_{ij}(\omega)| = \sqrt{\frac{\hat{V}_i^*(\omega) \cdot \hat{V}_i(\omega)}{\hat{V}_j^*(\omega) \cdot \hat{V}_j(\omega)}} = \sqrt{\frac{\frac{1}{n_d T} \sum_{k=1}^{n_d} \tilde{V}_{i,k}^*(\omega, T) \cdot \tilde{V}_{i,k}(\omega, T)}{\frac{1}{n_d T} \sum_{k=1}^{n_d} \tilde{V}_{j,k}^*(\omega, T) \cdot \tilde{V}_{j,k}(\omega, T)}} = \sqrt{\frac{\hat{G}_{v_i v_i}(\omega)}{\hat{G}_{v_j v_j}(\omega)}} \quad (3)$$

The estimation process shown in Equation (3) provides one source of uncertainty generation. Regardless of the specific estimator chosen, there is epistemic uncertainty present in the measured outputs due to a variety of external noise sources. Therefore, we must add noise terms to the measured outputs, as labeled in n_i and n_j in Figure 1, and only the noise-contaminated output measurements $y(t) = v(t) + n(t)$ are available.

This means that the transmissibility magnitude estimation in Equation (3) will have extra terms expressed as the form in Equation (4). If we assume that the noise additions to each channel are uncorrelated with each other and uncorrelated with each of the ideal outputs v_i and v_j , then the estimates on the transmissibility using the noise-contaminated measurements may be written as [7]:

$$|\hat{T}_{ij}| = \sqrt{\frac{\hat{G}_{y_i y_i}}{\hat{G}_{y_j y_j}}} = \sqrt{\frac{\hat{G}_{v_i v_i} + \hat{G}_{n_i n_i}}{\hat{G}_{v_j v_j} + \hat{G}_{n_j n_j}}} \quad (4)$$

3. Probability model for transmissibility uncertainty

Given the final form for noise-contaminated transmissibility estimation shown in Equation (4), we will now consider modeling the uncertainty associated with it from both estimator inaccuracy and noise effects, concluding with a proposed probability density function from which any order statistics may be computed.

3.1 Uncertainty of the power spectrum estimates

Broadband white noise is commonly used as an excitation source for frequency domain system identification, and the randomness of the input signal propagates to the output spectra; this leads to what we've called the "estimator inaccuracy". The other source of uncertainty is the additive noise on each channel. In this paper, the condition for both circumstances will be analyzed and modeled. For an excitation derived from a stationary Gaussian random process, the output power spectrum estimation \hat{G}_{vv} (without additive noise) will follow a Chi-square distribution [7,8], and thus $\chi_{2n_d}^2$ in Equation (5) represents a Chi-square distributed random variable with $2n_d$ degrees of freedom, where n_d is the number of averages in Welch's smoothed power spectrum estimation:

$$\hat{G}_{vv} = \frac{\chi_{2n_d}^2}{2n_d} G_{vv}, \text{ where } n_d \in \mathbb{N} \quad (5)$$

Therefore, the transmissibility estimate from Equation (3) is the square root of the ratio between two correlated Chi-square distributed random variables. Note that for the conditions under which the input is known, it might appear over-constrained to assume Gaussian noise excitation, but in real practice, the output is the convolution of the system with all sorts of operational random inputs. Under central limit assumptions, the output measurements will have a sufficient Gaussian characteristic in this regard.

For the situation where measurements are subject to extraneous noise, the auto power spectrum estimation is also Chi-square distributed with the assumption of independent Gaussian noise characteristics, as shown in Equation (6). Compared to Equation (5), there is a scaling factor with SNR involved:

$$\hat{G}_{yy} = \frac{\chi_{2n_d}^2}{2n_d} G_{yy} = \frac{\chi_{2n_d}^2}{2n_d} \left(1 + \frac{1}{SNR}\right) G_{vv} \quad (6)$$

3.2 An exact probability density function for the transmissibility estimation

The probability density function of a Chi-square distributed variable z with $2n_d$ -degrees of freedom may be expressed as:

$$p(z) = \frac{z^{2n_d-1} \cdot e^{-\frac{z}{2}}}{\Gamma(2n_d) \cdot 2^{2n_d}} \quad (7)$$

where $\Gamma(\cdot)$ is the regular Gamma function. In Ref. [11], the joint distribution of correlated bivariate Chi-square random variable is derived via a multivariate complex Wishart distribution, and the closed form for the bivariate joint distribution is shown in Equation (8), where $I_{n_d-1}(\cdot)$ denotes the modified Bessel function of the first kind.

$$p(I_X, I_Y) = \frac{\exp\left(-\frac{\sigma_Y^2 I_X + \sigma_X^2 I_Y}{2(\sigma_X^2 \sigma_Y^2 - c_{XY_A}^2 - c_{XY_C}^2)}\right) \cdot (I_X I_Y)^{\frac{n_d-1}{2}}}{2^{n_d+1} \cdot (\sigma_X^2 \sigma_Y^2 - c_{XY_A}^2 - c_{XY_C}^2) \cdot (c_{XY_A}^2 + c_{XY_C}^2)^{\frac{n_d-1}{2}} \cdot \Gamma(n_d)} \times I_{n_d-1}\left(\frac{\sqrt{(c_{XY_A}^2 + c_{XY_C}^2)} I_X I_Y}{\sigma_X^2 \sigma_Y^2 - c_{XY_A}^2 - c_{XY_C}^2}\right) \quad (8)$$

The symbols σ_X^2 , σ_Y^2 , $c_{XY_A}^2$ and $c_{XY_C}^2$ represent the variance and covariance (in the Wishart matrix, Equation (9)) of complex Gaussian random variables X and Y , where I_X and I_Y are the summation of the magnitude square of complex X and Y . Equation (10) gives X as an example to illustrate the relation between I_X and X .

$$\mathbf{C} = \begin{bmatrix} \sigma_X^2 & 0 & c_{XY_A}^2 & -c_{XY_C}^2 \\ 0 & \sigma_X^2 & c_{XY_C}^2 & c_{XY_A}^2 \\ c_{XY_A}^2 & c_{XY_C}^2 & \sigma_Y^2 & 0 \\ -c_{XY_C}^2 & c_{XY_A}^2 & 0 & \sigma_Y^2 \end{bmatrix} \quad (9)$$

$$I_X = \sum_{j=1}^{n_d} (\tilde{X}_{jR}^2 + \tilde{X}_{jI}^2) \quad (10)$$

$$\text{where } \tilde{X}_j = \tilde{X}_{jR} + i \tilde{X}_{jI} \in \mathbb{C} \text{ and } \tilde{X}_{jR} = \Re[\tilde{X}_j], \tilde{X}_{jI} = \Im[\tilde{X}_j].$$

Equation (11) is the general derivation of the distribution for ratio and square root of random variable(s), given the joint probability density function $p(\cdot, \cdot)$. We apply the joint probability density function of I_X and I_Y in Equation (8) onto Equation (11), and there will be the probability density function of the square root of ratio between correlated Chi-square random variables, which is exactly the transmissibility estimator described in Equation (3) and (4).

$$p_{ratio}(z) = \int_{-\infty}^{+\infty} |y| p(zy, y) dy$$

$$p_{SquareRoot}(u) = 2u \cdot p_{ratio}(u^2)$$
(11)

Equation (12) shows the final result we derived from the above mentioned process, after change of variables and normalization; the outcome is that we have obtained the probability density function of the normalized transmissibility estimation, which is the estimation divided by the true value, with respect to the variance from auto power spectrum estimations (σ_X^2 , σ_Y^2) and correlation coefficient (ρ) between any two measurement channels. It is necessary to make it more explicit that the transmissibility is a function of frequency, so the probability density function in Equation (12) should be evaluated at every frequency point, involved with the corresponding $\sigma_X^2(\omega)$, $\sigma_Y^2(\omega)$, and $\rho(\omega)$.

$$p_{\hat{T}/T}(t) = \frac{2^{2n_d} t^{(2n_d-1)} \left((1-\rho^2) \sigma_X^2 \sigma_Y^2 \right)^{n_d} \Gamma\left(n_d + \frac{1}{2}\right)}{\sqrt{\pi} \left(\sigma_X^2 + t^2 \sigma_Y^2 \right)^{\frac{3n_d-1}{2}} \left(1 - \frac{4t^2 \rho^2 \sigma_X^2 \sigma_Y^2}{(\sigma_X^2 + t^2 \sigma_Y^2)^2} \right)^{n_d + \frac{1}{2}} \Gamma(n_d)}$$

$$\text{where } \rho = \sqrt{\frac{c_{XY_A}^2 + c_{XY_C}^2}{\sigma_X^2 \sigma_Y^2}}$$
(12)

4. Probability model validation on sample system

A simply-supported beam test structure with proportional damping (shown in Figure 2) is considered for generating frequency response functions from which surrogate “experimental” data will be obtained in order to test the validity of Equation (12). The structure is excited with Gaussian white noise at a single location, and the responses at two arbitrary positions are considered as measured outputs. The frequency response function between input and output at any location can be approximated analytically by the superposition of first n mode shapes, as shown in Equation (13), where Ψ_{pk} and Ψ_{jk} are the k^{th} mode shape functions at input and output coordinate p and j , and Ω_k and ζ_k are the natural frequency and damping ratio for k^{th} mode respectively. For this analytical form of the transmissibility, as a benchmark for the statistical model, it is also equal to the ratio between the two input-output transfer functions (Equation (14)), where the two inputs will be cancelled and lead to the same form in Equation (1).



Fig. 2. Simply supported beam for model validation

$$H_j(\omega)_{(\text{accelerance})} = \frac{V_j}{X} = \sum_{k=1}^n \frac{\Psi_{jk} \Psi_{pk} \omega^2}{\Omega_k^2 - \omega^2 + 2i\zeta_k \Omega_k \omega} e^{i(\theta_k - \pi)} \quad (13)$$

$$\text{where } k = 1, 2, 3 \dots n \text{ and } \tan \theta_k = \frac{2\zeta_k \Omega_k \omega}{\omega^2 - \Omega_k^2}$$

$$T_{ij}(\omega) = \frac{V_i/X}{V_j/X} = \frac{\sum_{k=1}^n \frac{\Psi_{ik} \Psi_{pk}}{\Omega_k^2 - \omega^2 + 2i\zeta_k \Omega_k \omega} e^{i(\theta_k - \pi)}}{\sum_{k=1}^n \frac{\Psi_{jk} \Psi_{pk}}{\Omega_k^2 - \omega^2 + 2i\zeta_k \Omega_k \omega} e^{i(\theta_k - \pi)}} \quad (14)$$

The input and output positions are arbitrarily picked on the sample structure in Figure 2, and the two channels' frequency response functions are plotted in logarithm scale in Figure 3, with the first five modes taken into account.

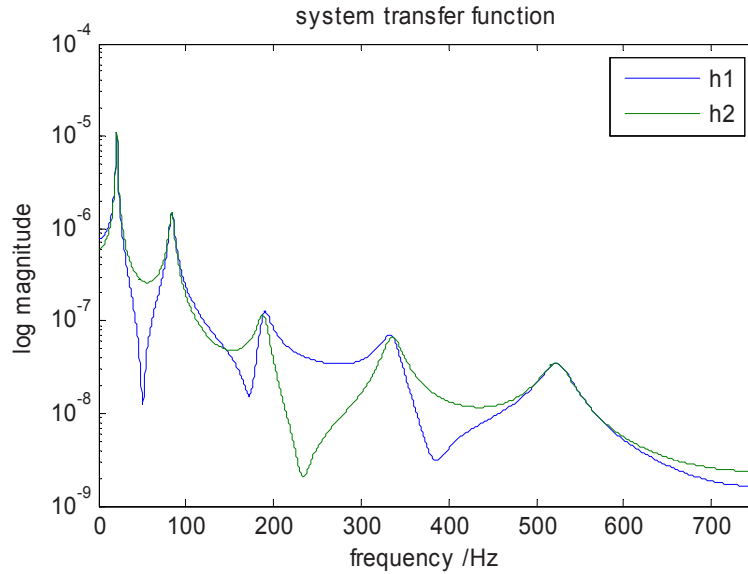


Fig. 3. Theoretical frequency response function for single channels

Case 1: No extraneous noise

Consider only the uncertainty from calculation of estimator, i.e., the case where no extraneous noise is present ($n_i = n_j = 0$, so $y_i = v_i$ and $y_j = v_j$). In Figure 4-a, one sample of the auto power spectrum estimations is plotted in green, with the 90% confidence bounds shown in red (calculated from Equation (7)), and the expectation value calculated from the distribution in blue. The same process is repeated for a large number of tests (n_t times), and the percentage of outliers beyond the 90% confidence bounds is shown in Figure 4-b. The results between predicted 90% confidence and measured 90% confidence are very consistent.

The same approach may then be applied on the transmissibility estimation, and the bounds and expectation calculated from Equation (12) are shown in Figure 5. The same observation is made from the Monte Carlo simulation, i.e., that of perfectly consistent model/measurement results.

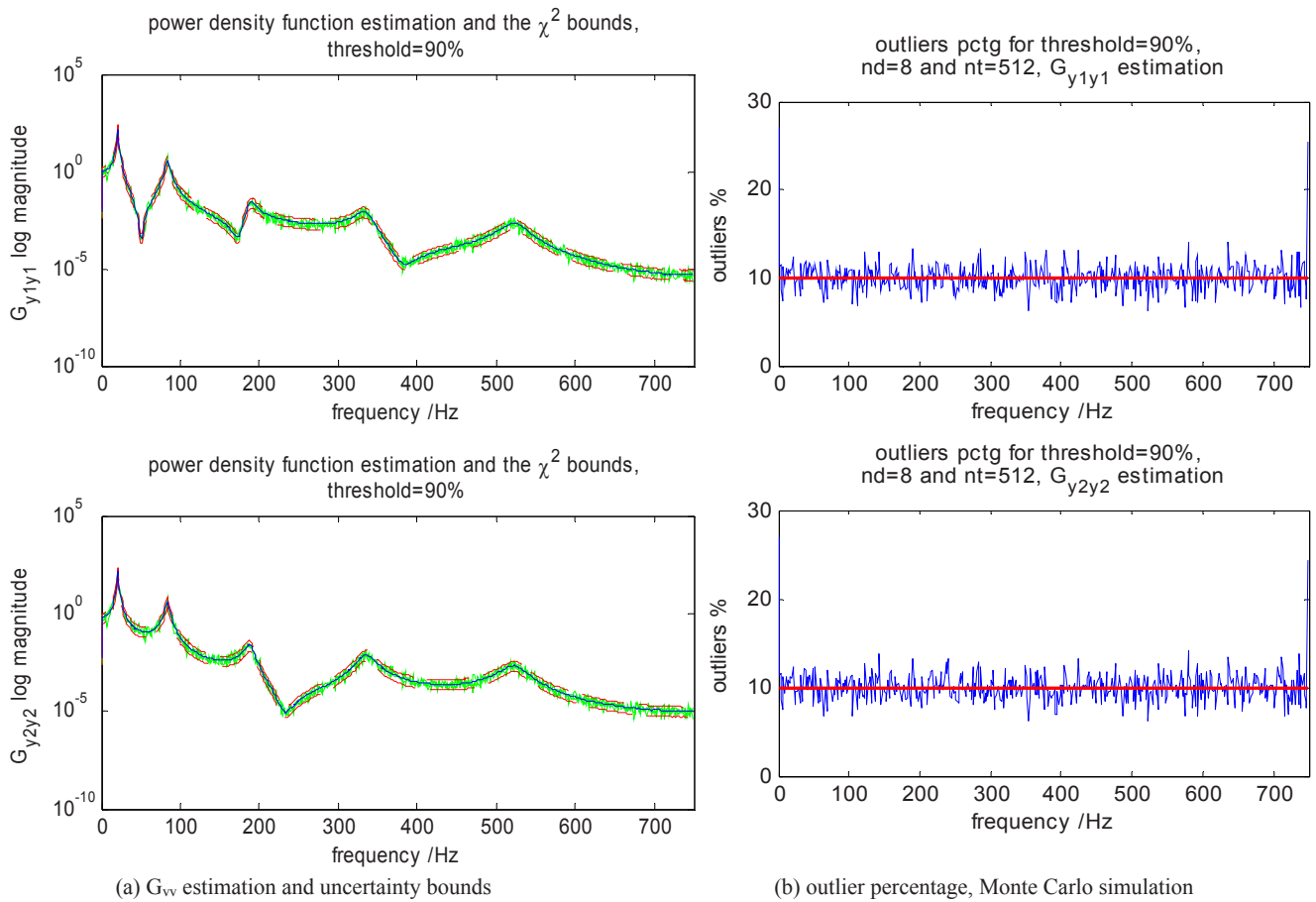


Fig. 4. Uncertainty of auto power spectrum at two arbitrary locations, noise free cases

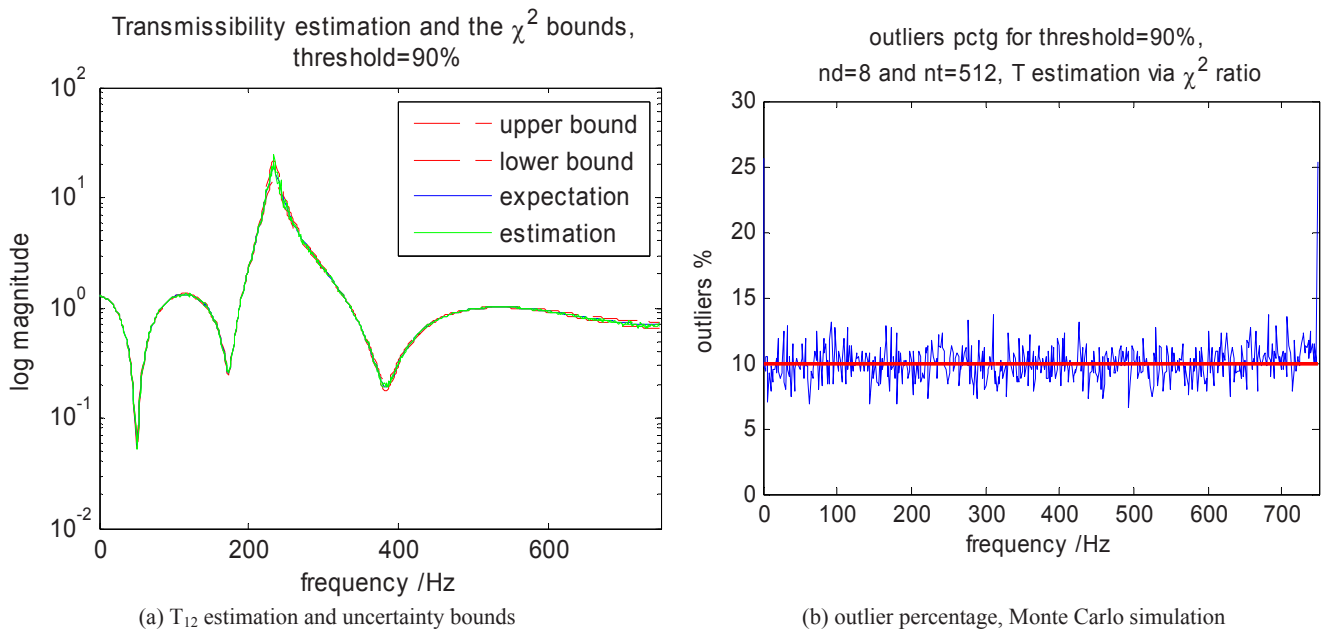


Fig. 5. Uncertainty in transmissibility with noise free measurements

Case 2: Noise-contaminated output measurements

The previous analysis considered only uncertainties from the estimation process, and this section will consider the influence of external noise contamination. Due to the inherent performance of any given channel, the output may be dominated by noise in some frequency regions where the SNR is not sufficiently high. Under this circumstance, there will be no useful power spectrum estimation or transmissibility estimation any more, and the estimator in Equation (4) will not work.

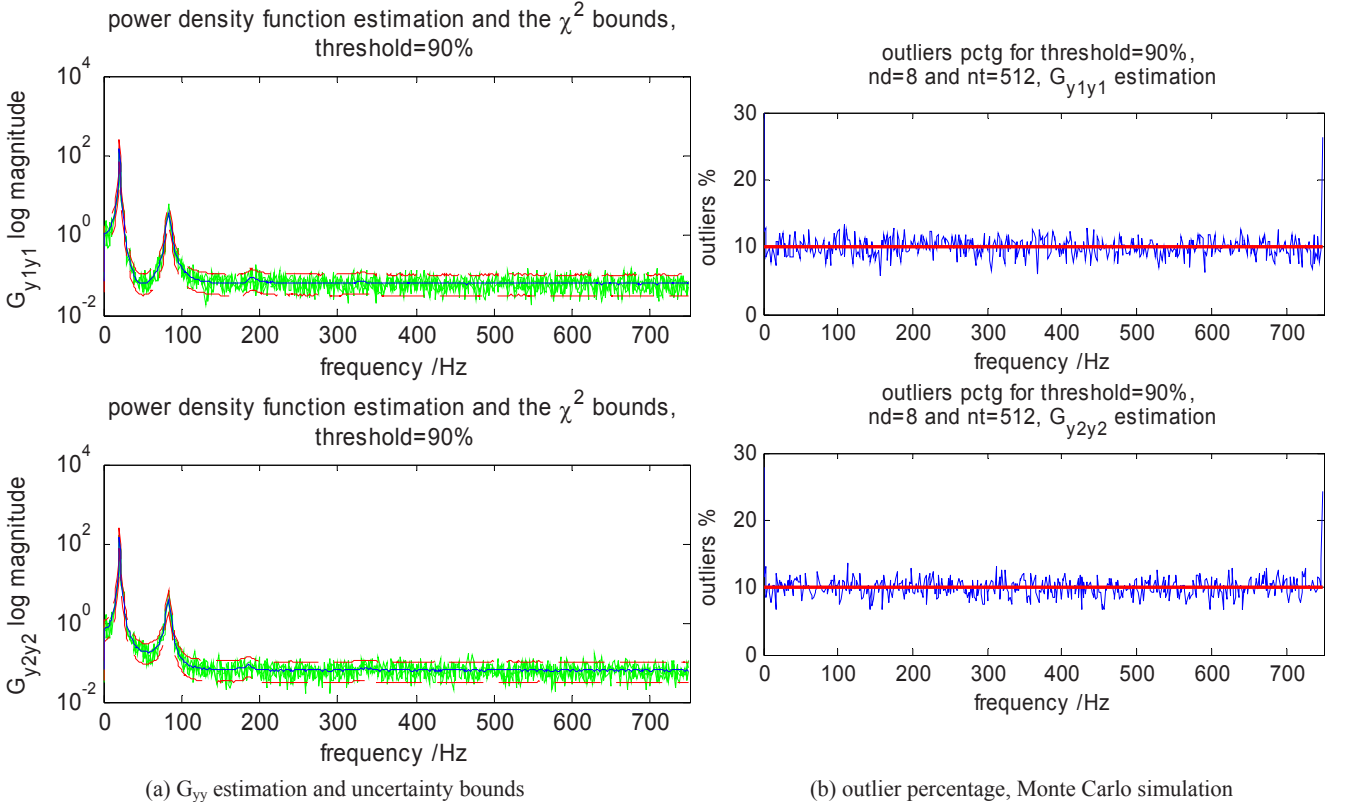


Fig. 6. Uncertainty of auto power spectrum at two arbitrary locations, noise contaminated

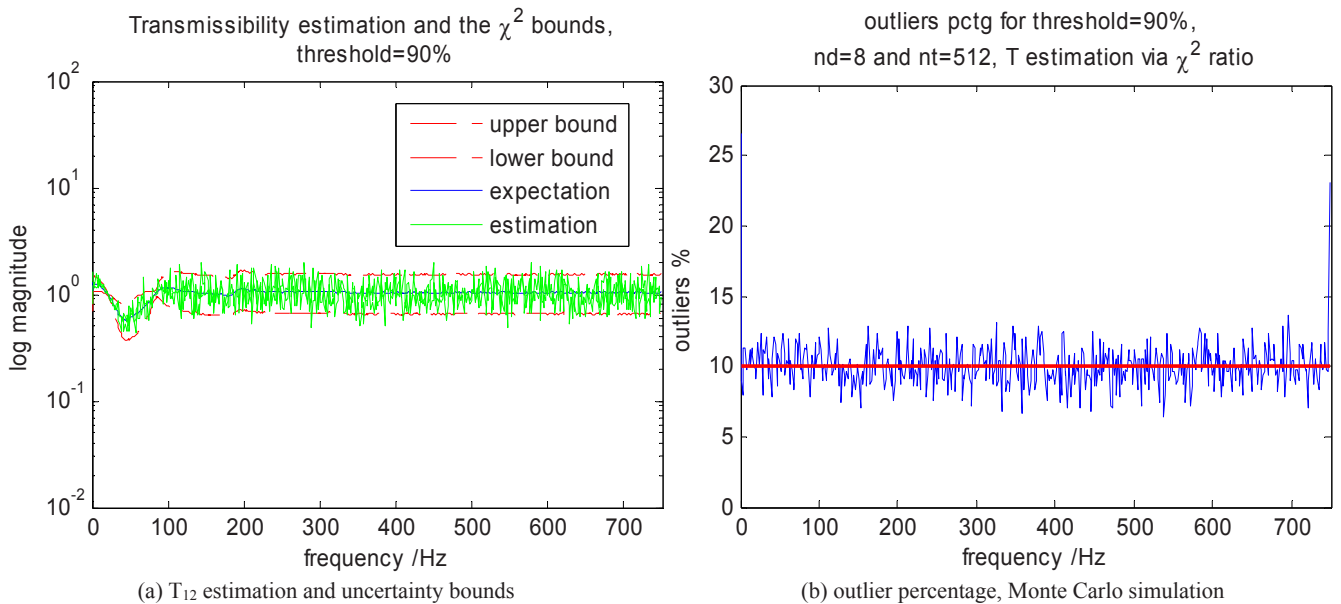


Fig. 7. Uncertainty of transmissibility with noise contaminated measurements

From Figure 6-a, where the case has an average 10% noise-to-signal ratio, we can see that the accurate auto power spectrum is dominated by the white noise when the gain factor of the channel is relatively small. When we verify the distribution model of the power density function and subsequent transmissibility estimation, the statistics model does not fail, but we can see only a flat noise floor with corresponding uncertainty bounds and consistent outlier percentage counts in Figure 6 and 7.

In both cases, we get a very consistent observation between the prediction and experiments, and this represents the first time such a predictive model has been verified. The model works for both noise-free cases and the cases with extraneous noise. The distribution of the estimation with noise is also accurate, but the estimation itself may be dominated by the noise.

5. Conclusion

For many system identification applications where measurement or assumption of the inputs is not possible, transmissibility is a very useful model to describe the dynamic system characteristics. In this paper, the uncertainty inherent in the noise-contaminated computation of a transmissibility estimator was modeled via a derived probability model. The derived model was validated with Monte Carlo simulation, with both noise-free and noise-contaminated conditions considered. A summary of key points is:

- The estimation of transmissibility is calculated from an estimator associated with the auto power spectral density of each measured output.
- A probability density function of this transmissibility estimator was derived, and it was validated with Monte Carlo simulation (via outlier percentage comparison to prediction), and the approach is very consistent for both noise-free and noise-contaminated situations.
- For the noise-contaminated case, the transmissibility estimator itself does not necessarily provide accurate estimates of the transmissibility if the measurement signal-to-noise ratio is poor (as expected). Nevertheless, the probability model continues to accurately describe the quantification of the uncertainty in those estimates (statistical moments), revealing the robustness of the proposed approach.

Relevant future work in this area will include further experimental confirmation and the propagation of predicted transmissibility uncertainties into the uncertainties associated with quantities derived from the transmissibility, which is useful in fields such as structural health monitoring.

Acknowledgments

This material is based on research sponsored by Air Force Research Laboratory, Space Vehicles Directorate under agreement number FA9453-09-1-0315. The U.S. Government is authorized to reproduce and distribute reprints for governmental purposes notwithstanding any copyright notation thereon. The views and conclusions contained herein are those of the authors and should not be interpreted as necessarily representing the official policies or endorsements, either expressed or implied, of Air Force Research Laboratory or the U.S. Government.

References

- [1] Ljung L, Aspects on the system identification problem. *Signal Processing* 4(1982):445-456
- [2] Doebeling SW, Farrar CR, Prime MB, A Summary Review of Vibration-Based Damage Identification Methods. *The Shock and Vibration Digest* 30(2)(1998):91-105
- [3] Brincker R, Zhang L, Andersen P, Modal identification of output-only systems using frequency domain decomposition. *Smart Materials and Structures* 10(2001):441-445
- [4] Devriendt C, Steenackers G, De Sitter G, Guillaume P, From operating deflection shapes towards mode shapes using transmissibility measurements. *Mechanical Systems and Signal Processing* 24(2010):665-677
- [5] Johnson TJ, Adams DE, Transmissibility as a Differential Indicator of Structural Damage. *Transactions of the ASME: Journal of Vibration and Acoustics* 124(2002):634-641
- [6] Worden K, Manson G, Fieller NRJ, Damage detection using outlier analysis. *Journal of Sound and Vibration* 229(3)(2000):647-667
- [7] Bendat JS, Piersol AG, *Random Data: Analysis and Measurement Procedures* (2nd Edition), John Wiley & Sons (New York), 1986
- [8] Bendat JS, Piersol AG, *Engineering Applications of Correlation and Spectral Analysis* (2nd Edition), John Wiley & Sons (New York), 1993

- [9] Bendat JS, Statistical Errors in Measurement of Coherence Function and Input/Output Quantities. *Journal of Sound and Vibration* 59(3) (1978):405-421
- [10] Welch PD, The Use of Fast Fourier Transform for the Estimation of Power Spectra: A Method Based on Time Averaging Over Short, Modified Periodograms. *IEEE Transactions on Audio and Electroacoustics* 15(1967):70-73
- [11] Hagedorn M, Smith PJ, Bones PJ, Millane RP, Pairman D, A trivariate Chi-squared distribution derived from the complex Wishart distribution. *Journal of Multivariate analysis* 97(2006):655-674

A Modified Whiteness Test for Damage Detection Using Kalman Filter Innovations

D.Bernal¹, Y. Bulut²

¹Northeastern University, Civil and Environmental Engineering Department, Center for Digital Signal Processing, Boston, MA 02192.

²Graduate Student, Northeastern University, Civil and Environmental Engineering Department.

ABSTRACT

Deviations from whiteness in the innovations of a Kalman filter indicate that the filter is not optimal for the given data. Accepting that the disturbances are stationary and white lack of optimality derives from the fact that the values of some parameters have changed between the time the filter was formulated and the present. The parameters that define the filter come from system properties and from the statistics of the disturbances. For the filter to perform effectively as a fault detector it is necessary to ensure that deviations from whiteness are not due to variations in the statistics of the noise. This paper examines the mathematical relation between the covariance function of the innovations and the changes in the disturbance statistics. It is shown that the effect of changes in the noise statistics on the discriminating metric can be minimized by shifting the range of lags for which the metric is evaluated. The fact that the modified whiteness test can retain adequate sensitivity to damage is illustrated numerically.

INTRODUCTION

Most approaches to the damage detection problem can be classified as parameter estimation techniques or residual based schemes [1]. In the parameter estimation strategy the changes in estimated model parameters are used to decide whether or not significant changes have taken place. In the residual approach the likelihood of changes is judged by inspecting differences between measurements and reference signals obtained from a reference model and the measurements. A residual based approach to detection contains the following components: 1) a model of the reference condition, 2) a scheme to generate a residual 3) a metric derived from the residuals and 4) criteria for deciding whether the metric indicates change or no change.

The classical residual detector uses a whiteness test on the innovations of a Kalman filter [2] and was introduced by Mehra and Peschon [3]. A particularly attractive feature of the Kalman filter whiteness test is the fact that the method can be used when all inputs that drive the system are stochastic. On the negative side, however, the filter is such that the detection algorithm identifies not only changes in the system properties but also changes in the statistics of the disturbances. As one gathers, if the contribution to the discriminating metric coming from fluctuations in the disturbances are significant when compared to those due to damage then the resolution of the detection task deteriorates. This paper examines the mathematical relation between changes in the noise statistics and the covariance function of the innovations. Based on the results obtained a modified whiteness test that is insensitive to variability of the disturbances but retains sensitivity to damage is formulated. The merit of the modified test is illustrated in the context of simulations.

ANALYTICAL FORMULATION

System Considered

It is assumed that the system considered has a description in sampled time given by

$$x(k+1) = Ax(k) + G\omega(k) \quad (1)$$

$$y(k) = Cx(k) + v(k) \quad (2)$$

where $A \in R^{N \times N}$ and $C \in R^{m \times N}$ are the system and the state to output matrices, $G \in R^{N \times r}$ specifies the distribution of the disturbances, $\omega \in R^{N \times 1}$ and $v \in R^{m \times 1}$ are the disturbances and the measurement noise, $y \in R^{m \times 1}$ is the output vector and $x \in R^{N \times 1}$ is the state vector. The integers, N , m and r are the system order, the number of outputs and the number of independent disturbances, respectively. It is assumed that ω and v are Gaussian zero mean and white with covariance matrices Q and R .

Innovations

Assuming that the system matrices in the reference state are known and that the (steady state) Kalman filter gain K has been computed (to be discussed subsequently) the innovations $e(k)$ are obtained from

$$\hat{x}^-(k+1) = A\hat{x}^+(k) \quad (3)$$

$$\hat{x}^+(k) = \hat{x}^-(k) + Ke(k) \quad (4)$$

$$e(k) = y(k) - C\hat{x}^-(k) \quad (5)$$

where e is the innovation sequence and the superscripts minus and plus indicate before and after the information from the measurement at the current time station is accounted for. The steady state Kalman gain is given by

$$K = APC^T [R + CPC^T]^{-1} \quad (6)$$

where P , the expected value of the state error, is the solution to the algebraic Riccati equation

$$P = APA^T - APC^T [R + CPC^T]^{-1} CPA^T + GQG^T \quad (7)$$

Data Driven Model

In the formulation outlined in Eqs3-7 the matrices $\{A, G, C, Q$ and $R\}$ have to be known. In practice the matrices Q and R are seldom known and it is appropriate, for detection purposes, to formulate the Kalman filter exclusively from measurements. A consequence of extracting the filter from the data is the fact that the physical significance of the state is lost. Nevertheless, for the purpose of computing the innovation sequence of Eq.5 this matter is immaterial. A data-driven Kalman filter model (for a second order MCK system) is a particular form of the ARMAX structure wherein the order of the autoregressive, exogenous and moving average terms are the same.

The Discriminating Metric

A test statistic that quantifies the “whiteness” of a signal can be defined in several ways [3]. Here we select the sum of the square of the covariance function of the signal (normalized to unit variance) for a preselected number of lags. The empirical estimate for the covariance of the normalized innovations \tilde{e} is given by

$$\tilde{e} = H^{-0.5}(e_j - \bar{e}) \quad (8)$$

where

$$H = \frac{1}{L} \sum_{j=1}^L (e_j - \bar{e})(e_j - \bar{e})^T \quad (9)$$

the length of the sequence is L and \bar{e} is the innovations mean. In Eq.8 the matrix square root is the unique non-negative option. The covariance function of the normalized innovations is, by definition

$$C_k = \frac{1}{L-k} \sum_{j=1}^{L-k} \tilde{e}_j \tilde{e}_{j+k}^T \quad (10)$$

for $k = 1, 2, \dots, p$, where p is the number of lags considered. On the premise that $L \gg k$ all C_k , under the null hypothesis (i.e., that the system is undamaged) are identically distributed random variables with variance $1/L$ [3]. Normalizing the distribution to unit variance one has

$$\tilde{C}_k = \sqrt{L} \cdot C_k \quad (11)$$

For any entry in the diagonal of Eq.11 one can compute the test statistic q_p as

$$q_p = \sum_{k=1}^p \tilde{C}_{k,j}^2 \quad (12)$$

which follows a χ^2 distribution with p degrees of freedom. The probability that the value from Eq.12 in any given realization is larger than any given number is readily obtained from the *cdf* of the χ^2 distribution for the appropriate # of DOF. For example, if one selects the probability of being exceeded at 5% and takes $p=20$ the cutoff value is 31.4. In practice the approach sets the damage or no damage classification as a hypothesis test. The null hypothesis is accepted if the test statistic is smaller than the selected threshold and rejected otherwise. It is worth noting, however, that this procedure is not without difficulty because all the information one actually has is conditional on the fact that the system is undamaged and it does not (in principle) allow for objective statements regarding the probability of identifying damaged. Nevertheless, if the test statistic has a probability distribution for the aggregate of all the possible damage scenarios of interest that is strongly shifted to the right relative to the reference then this standard operating mode is reasonable.

Effect of Fluctuations in the Noise Covariance Matrices

When the noise statistics change the Kalman filter formulated for the reference state becomes an arbitrary observer for which one has

$$C_0 = CPC^T + R \quad (13)$$

$$C_j = C\bar{A}^j PC^T - C\bar{A}^{(j-1)} AKR \quad (14)$$

where P is the solution of

$$P = \bar{A}P\bar{A}^T + GQG^T + AKRK^T A^T \quad (15)$$

with

$$\bar{A} = A(I - KC) \quad (16)$$

Eqs.14 and 15 can be combined to obtain

$$\text{vec}(C_j) = E_{QQ} \text{vec}(Q) + E_{RR} \text{vec}(R) \quad (17)$$

where

$$E_{QQ} = (C \otimes C\bar{A}^j) N^{-1} E_Q \quad (18)$$

$$E_{RR} = [(C \otimes C\bar{A}^j) N^{-1} E_R - (I \otimes C\bar{A}^{(j-1)} AK)] \quad (19)$$

with

$$E_Q = G \otimes G \quad (20)$$

$$E_R = (AK \otimes AK) \quad (21)$$

and

$$N = I - (\bar{A} \otimes \bar{A}) \quad (22)$$

Details of the derivations of Eqs.13-22 are not presented here due to space limitations but the theory from where they can be derived can be found in [4,5]. Eq.17 shows that the covariance function of the arbitrary observer is linearly related to the vectorized forms of Q and R. From this result one gathers that the manner in which the changes in the noise affect the covariance function is strongly dependent on the spatial distribution of the disturbance fluctuations. In particular, changes that in vectorized form have strong projections in the direction of the vectors associated with the higher singular values of E_{QQ} and E_{RR} induce large correlations while those that project on vectors associated with the smaller singular values behave opposite. The well-known fact that multiplying Q and R by the same scalar does not affect the Kalman filter gain is made evident by noting that if the covariance function is zero this operation does not change it.

Modified Whiteness Test

Inspection of Eqs.18 and 19 show that the matrices E_{QQ} and E_{RR} involve the matrix \bar{A} raised to powers that increase with the lag. Since this matrix has a spectral radius that is less than unity (i.e., the filter is stable) the entries decrease as the lags increase and one gathers that, for sufficiently large lags the changes in the disturbances will have no perceptible effect on the covariance function. A metric based on a modified Eq.12, namely

$$q_p = \sum_{k=p_1}^{p_2} \tilde{C}_{k,j}^2 \quad (23)$$

where the first lag is taken as p_1 instead of one, and $p = p_2 - p_1 + 1$, will have a χ^2 distribution that is essentially independent of the variations in the statistics of Q and R, provided p_1 is large enough. If the correlation introduced by damage persisted at all lags p_1 could be selected arbitrarily (provided it is small compared to L) but numerical results suggest that this is not the case. Namely, the sensitivity to damage of the metric of Eq.23 also decreases with lags, albeit at a different rate than that due to variations in Q and R. One way to choose p_1 is by inspecting the eigenvalues of the matrix in Eq.16 and selecting a value such that the largest eigenvalue in absolute value, raised to p_1 , is smaller than some pre-selected number (0.1 for example). Work on the optimal selection of p_1 and on the number of lags on which to base the test statistic is part of our present focus.

Effect of Damage in the Covariance Function

Ideally one would like to have an analytic expression that shows how damage affects the covariance of the innovations but derivation of such an expression has proven difficult because the innovations in the damaged condition cannot be viewed as sequences that would be obtained from a suboptimal filter connected to the reference system. One possibility that appears to hold some promise is to formulate the damage in terms of pseudo-forces but we have not at this point carried out this examination.

Numerical Examination

Consider a 5-DOF lumped-mass system with springs connecting mass #1 to #2, #2 to #3, etc, plus two additional springs (k_6 and k_7), connecting mass #1 to #3 and mass #2 to #4, respectively. All springs have a constant of 100 and the masses equal 0.05 in some consistent set of units. The damping distribution is classical with 2% damping in each of the 5 flexible modes and rigid body motion is restricted by grounding spring #1. To simplify the presentation we consider only one sensor consisting of an acceleration measurement on the 5th mass.

We take the disturbances as a realization from a covariance matrix that varies from one simulation to the next. The bounds that specify the entries in Q are selected assuming that the uncertainty on the spatial distribution is significantly less than that on the mean intensity. Specifically, we take the diagonal of Q in each simulation as a vector whose entries are realizations from a uniform distribution with limits of 0.75 and 1.50 and subsequently scale the complete diagonal matrix by a constant, also selected from a uniform distribution, but in this case with limits of 0.25 and 4. Damage is simulated as 10% loss of stiffness on spring #1. The results are presented in Fig.1 in the form of a Receiver Operating Characteristic, or ROC curve. The curve is derived using two hundred simulations of the healthy state and 200 hundred simulations of the damaged condition. The ROC curve illustrates the tradeoff that is made between false positives and false negatives when a discriminating threshold is selected. Although several formats are used the most common is the one used in Fig.1, wherein the horizontal axis is the false positive rate and the vertical is one minus the rate of false negatives which, of course, is the

rate of true positive detection. As can be seen, the lag shifted test displays has the potential of offering a reasonably good performance while in the standard test no threshold can lead to reasonable performance because the ROC curve deviates little from the case of no information given by a straight line that goes from the origin to $\{1,1\}$.

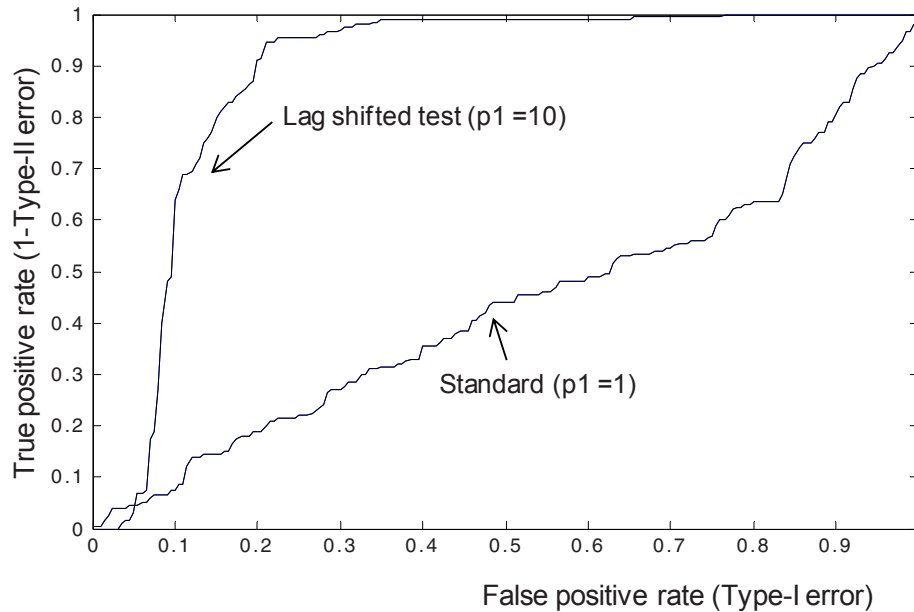


Figure 1. ROC curve illustrating the gains realized by the shifted whiteness test; damage considered is 10% loss of stiffness in spring #1.

The optimal threshold in any given case is a function of the ROC curve and of the relative cost of making a type-I or a type-II error. For illustration we assumed that the cost of a false negative (type-II error) is one unit and that of a type-I is β units and compute the total cost for $\beta = 0.5, 1$ and 2 . The results are plotted in Fig.2 and illustrate that the optimal threshold cut (for these cost ratios) is insensitive to β and is connected with a type-I error of around 0.2 (examination shows that the metric in this region is about 38).

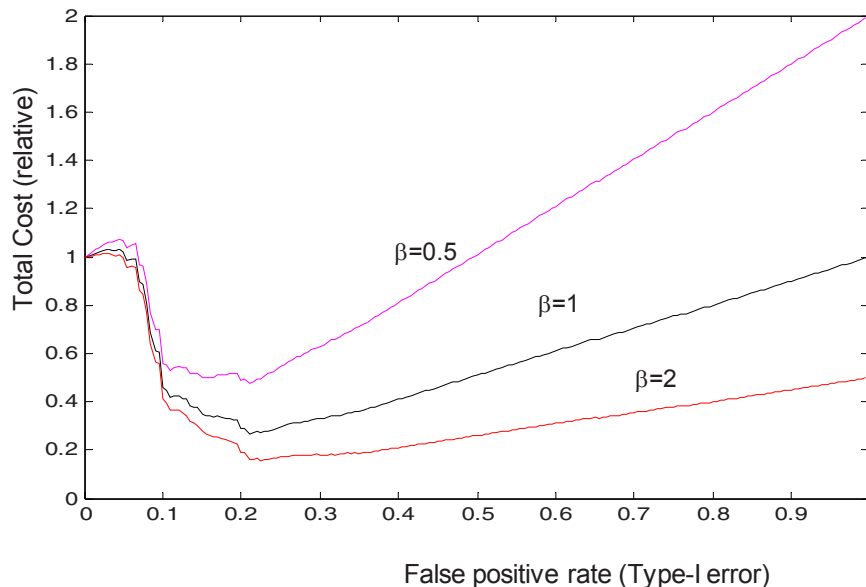


Figure 2. Total cost vs Type-I error rate for the ROC curve of Fig.1

It is opportune to note that in actual applications one typically does not have information about the damage scenarios and the metric threshold cut has to be selected based on information about the behavior of the type-I error.

CONCLUDING REMARKS

Use of a Kalman filter as a fault detector hinges on the fact that when the filter is operating optimally the innovation signals are white. In the real situation the whiteness property implies that the entries of the covariance function of the finite length innovations are realizations from a Gaussian distribution with zero mean and known variance and this allows one to cast the whiteness question as a hypothesis test at some selected level of confidence. The issue addressed in this paper is the fact that lack of optimality in the filter arises not only when the properties of the system change but also when the statistics of the disturbances vary. The basic contribution of the paper is the observation that the correlations resulting from changes in the noise model can be minimized by shifting the whiteness test to higher lags and that this can be done without removing the sensitivity of the correlations to damage.

REFERENCES

1. Patton, R. J., Frank P. M., and Clark R. N. *Issues of Fault Diagnosis for Dynamic Systems*. Springer. 2000.
2. Mehra, R. K., and Peschon, J. "An innovations approach to fault detection in dynamic systems." *Automatica*. 7 637–640. 1971.
3. Kalman R. E. "A new approach to linear filtering and prediction problems." *Journal of Basic Engineering*, Vol.82, 34-45. 1960.
4. H. Heffes, "The effect of erroneous models on the Kalman filter response," *IEEE Transactions on Automatic Control*, AC-11, July, 1966, pp. 541-543.
5. Mehra, R. K. "On the identification of variance and adaptive Kalman filtering", *IEEE Transactions on Automatic Control*, Vol. 15, No.2, 1970, pp. 175-184.

Vibration Reduction of an Atomic Force Microscope in the Point of the Mechanical Design

Chulsoo Kim, Jongkyu Jung, Jiseong Jeong, and Kyihwan Park

Abstract Vibration is one of most influential factors which need a great caution in designing the mechanical components for a high precision and high speed atomic force microscopy (AFM) since the scanned image can be contaminated by the AFM mechanical components' vibrations caused by the various external and internal vibration sources. It is required to design the mechanical components so that they have resonant frequencies higher than the external and internal vibration frequencies. In this work, the mechanical vibration in a conventional AFM system is analyzed by considering its mechanical components, and a vibration reduction is then achieved by reconfiguring the mechanical components.

1 Introduction

An atomic force microscope (AFM) is a device capable of investigating several physical characteristics of a material with sub-nanometer resolution using the interaction force between the cantilever tip and a sample surface [1][2][3]. There are many factors to be considered for designing the mechanical components for a high

Chulsoo Kim

Gwangju Institute of Science and Technology (GIST), 261 Cheomdan-gwagiro (Oryong-dong), Buk-gu, Gwangju, 500-712, Republic of Korea, e-mail: steelwat@gist.ac.kr

Jongkyu Jung

Gwangju Institute of Science and Technology (GIST), 261 Cheomdan-gwagiro (Oryong-dong), Buk-gu, Gwangju, 500-712, Republic of Korea e-mail: j1023@hanmail.net

Jiseong Jeong

Gwangju Institute of Science and Technology (GIST), 261 Cheomdan-gwagiro (Oryong-dong), Buk-gu, Gwangju, 500-712, Republic of Korea e-mail: stopstar@gist.ac.kr

Kyihwan Park

Gwangju Institute of Science and Technology (GIST), 261 Cheomdan-gwagiro (Oryong-dong), Buk-gu, Gwangju, 500-712, Republic of Korea e-mail: khpark@gist.ac.kr

speed and high precision AFM, though vibration is one of most influential factors since performance of the AFM can be degraded by vibration in the mechanical components caused by various external and internal vibration sources. As high speeds are required in the AFM, the vibrational influence on precision also significantly increases.

External vibration includes vibrations from operator footsteps, building vibration, seismic waves, and acoustic noise, whose frequencies are usually in a low frequency range, whereas internal vibration includes controller signals whose frequency ranges up to several hundred Hz . Therefore, mechanical components must be designed to have resonant frequencies higher than both the external and internal vibration frequencies. To this end, Thompson et al. [4], Chen et al. [5], and Kindt et al. [6] have reported that the mechanical loop between the tip and sample should be designed to have a high first resonant frequency to ensure that it is not affected by the external and internal vibration frequencies. In further attempts to increase the first resonant frequency of the scanning actuator, Schitter et al. [7] and Fantner et al. [8] proposed a method for enhancing the stiffness of the scanning actuator by adding an array of vertical blade springs to a flexure mechanism, and Fleming et al.

However, the Z-axis coarse motion actuator on which the XY-axis lateral scanning actuator is loaded lowers the first vibration frequency to a few hundred Hz due to the intrinsic features of the large mass and large volume of the Z-axis coarse motion actuator. In order to solve this problem, in this study the mechanical vibration is analyzed by considering all the mechanical components of the AFM including the Z-axis coarse motion actuator. As a result, vibration reduction is achieved through a reconfiguration of the mechanical components. To analyze the mechanical vibration, a schematic of the lumped model of the AFM system is derived and the vibration influences of the AFM components are experimentally examined. Based on this vibration analysis, a reconfigured AFM system is proposed and subsequently compared to a conventional system.

2 Mechanical vibration analysis of an AFM

Figure 1 shows a conventional AFM system configuration in which the Z-axis force regulating actuator is separated from the XY-axis lateral scanning actuator. The AFM is composed of a supporting frame, XY-axis lateral scanning actuator, Z-axis force regulating actuator, and an electric motor. The XY-axis lateral scanning actuator and Z-axis force regulating actuator are called fine motion actuators, whereas the electric motor is called a Z-axis coarse motion actuator based on its load capacity and working stroke. The Z-axis coarse motion actuator moves up the XY-axis lateral scanning actuator on which the sample is mounted to make contact with the cantilever tip; the cantilever is deflected by the force between the cantilever tip and the sample surface. This deflection can be conventionally measured using an optical sensor [11][12]. When the XY-axis lateral scanning actuator moves in the X and Y directions, the Z-axis force regulating actuator is controlled in the Z direc-

tion in order to maintain a constant deflection force. The topology of the sample is subsequently obtained from the controlled signal.

Figure 2 shows the overall schematic of the lumped model of a conventional AFM system, including the Z-axis coarse motion actuator. The Z-axis coarse motion actuator is comprised of a linear motion block, lead screw, electric motor, and linear motion guide. The torque of the electric motor is converted to the vertical force F_d , which acts at point D located at a distance l_d from point O . Here, the structure of the Z-axis coarse motion actuator is modeled using an equivalent mass m_c , and equivalent moment of inertia J_c with respect to point O , torsional spring k_θ , and torsional damper c_θ . The supporting frame and base plate are considered as rigid bodies, respectively, since they are designed to be very stiff. It is also assumed that the Z-axis force regulating actuator can be treated as a rigid body since it has a high stiffness; hence, the mass of the Z-axis force regulating actuator can be combined with the supporting frame. In addition, the spring coefficient of the cantilever is modeled as k_{can} since its mass is negligibly small. Furthermore, the XY-axis lateral scanning actuator is considered a rigid body having a mass m_s and a moment of inertia J_s with respect to point O ; its spring effect in the vertical direction is not considered since it also has a high stiffness compared to that of the lateral direction. And since the XY-axis lateral scanning actuator is mounted on the Z-axis coarse motion actuator, its mass can be simply added to m_c . Note that the centers of gravity

Fig. 1 Conventional AFM system configuration in which the Z-axis force regulating actuator is separated from the XY-axis lateral scanning actuator.

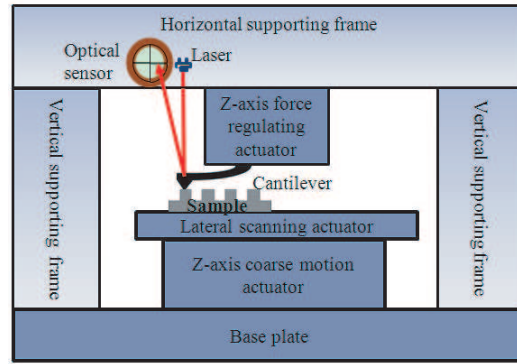
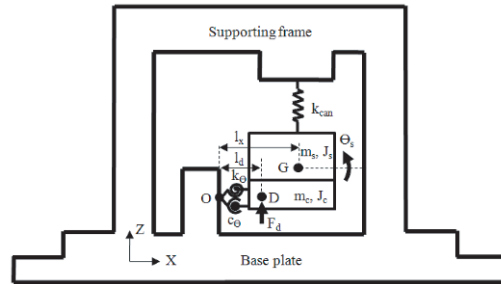


Fig. 2 Overall schematic lumped model of the conventional AFM system including the Z-axis coarse motion actuator.



of both m_c and m_s are located at point G , and the distance between points O and G is marked with l_x .

From the model obtained from the above assumptions, the moment equation of the AFM system at point O is represented as

$$(J_s + J_c) \ddot{\theta}_s = -k_\theta \theta_s - c_\theta \dot{\theta}_s + l_d \cdot F_d \quad (1)$$

where θ_s is the output angle with respect to point O . In addition, J_c and m_c are negligibly small compared to J_s and m_s , and J_s is represented as $K \cdot m_s$, where K is the geometrical constant of the XY-axis lateral scanning actuator. Therefore, the transfer function $\theta_s(s) / (l_d \cdot F_d(s))$ can be represented as

$$\frac{\theta_s(s)}{(l_d \cdot F_d(s))} = \frac{1 / (K \cdot m_s)}{s^2 + 2\zeta \omega_n s + \omega_n^2}. \quad (2)$$

Here, ω_n and ζ are the natural frequency and damping ratio of the AFM system, respectively, which can be represented as

$$\omega_n = \sqrt{\frac{k_\theta}{K m_s}}, \zeta = \frac{c_\theta}{2\sqrt{K m_s k_\theta}}. \quad (3)$$

As such, in order to reduce the vibration of θ_s , it is necessary to increase the natural frequency and the damping ratio of the AFM system. According to Eqs. (2) and (3), the natural frequency ω_n and damping ratio ζ of the AFM system depend on m_s , k_θ , and c_θ . Therefore, reduction of m_s can contribute to an increase of not only ω_n but also ζ .

In order to experimentally determine k_θ and c_θ , a modal analysis experiment was performed using a laser scanning vibrometer manufactured by Em4sys Co. Ltd. [13]. The first bending mode occurs at 136 Hz and the damping ratio ζ can be estimated as 0.0735 from the half-power bandwidth method [14]. The torsional spring constant ($k_\theta = (\omega_n)^2 \cdot J_s$) and damping constant ($c_\theta = 2\zeta \omega_n \cdot J_s$) are estimated as 5505.6 Nm/rad and 0.947 Nm/(rad/s), respectively.

From the parameter identification of k_θ and c_θ , the damped natural frequency ω_d and damping ratio ζ increase to 299 Hz and 0.16, respectively, when m_s is reduced by a factor of 5. This result confirms that a reduction in the payload of the Z-axis coarse motion actuator is very important to the vibration attenuation capability of a high speed and high precision AFM.

2.1 Reconfiguration of mechanical components for vibration reduction

In the previous section, it was suggested that m_s should be reduced to attenuate the vibration of θ_s . However, it is not easy to reduce m_s without affecting the design specifications of the XY-axis lateral scanning actuator/such as the working stroke

and overall size. Without changing the basic design of the XY-axis lateral scanning actuator, we instead propose a reconfiguration of the components in order to obtain a similar vibration attenuation performance.

Figure 3(a) and (b) show the structure and schematic of the lumped model of the reconfigured AFM system, respectively. In this model, the Z-axis coarse motion actuator is located beneath the horizontal supporting frame, and the XY-axis lateral scanning actuator is mounted on the base plate. Then, the Z-axis coarse motion actuator moves down the Z-axis force regulating actuator to make contact with the sample surface; different from the previous configuration in which it moves up the XY-axis lateral scanning actuator. In this new configuration, the Z-axis force regulating actuator, which has mass m_f and moment of inertia J_f with respect to point O , is only a payload for the Z-axis coarse motion actuator, in which m_f is approximately 1/5 of m_s . Note that the Z-axis force regulating actuator, XY-axis lateral scanning actuator, and supporting frames have high stiffness, and can therefore be treated as rigid bodies. Then, since the XY-axis lateral scanning actuator is mounted on the base plate, its mass m_s does not need to be considered.

For the vibration analysis of the reconfigured AFM system, its moment equation at point O can be represented as

$$(J_f + J_c) \ddot{\theta}_f = -k_\theta \theta_f - c_\theta \dot{\theta}_f + l_d \cdot F_e \quad (4)$$

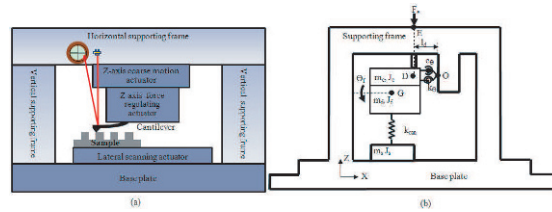
where θ_f is the output angle with respect to point O , and F_e is the applied force from the coarse motion actuator to point E , which is located on the supporting frame. The transfer function $\theta_f(s) / (l_d \cdot F_e(s))$ is then represented as

$$\frac{\theta_f(s)}{(l_d \cdot F_e(s))} = \frac{1 / (\tilde{K} \cdot m_f)}{s^2 + 2\tilde{\zeta} \tilde{\omega}_n s + \tilde{\omega}_n^2} \quad (5)$$

where \tilde{K} is a geometrical constant. In addition, $\tilde{\omega}_n$ and $\tilde{\zeta}$ are the natural frequency and damping ratio of the reconfigured AFM system, respectively, which can be represented as

$$\tilde{\omega}_n = \sqrt{\frac{k_\theta}{\tilde{K} m_f}}, \quad \tilde{\zeta} = \frac{c_\theta}{2\sqrt{\tilde{K} m_f k_\theta}}. \quad (6)$$

Fig. 3 (a)Structure and (b)schematic lumped model of the reconfigured AFM system.



The frequency response function (FRF) is then experimentally obtained (Fig. 4), in which the XY-axis lateral scanning actuator and cantilever are not considered since they do not affect the vibration characteristics of the reconfigured AFM system.

3 Experiments

Figure 5 presents real scanning images from the AFM for each configuration. The measured standard grid sample has a $3\ \mu\text{m}$ periodic square shape and $12\ \text{nm}$ height. Note that even though the XY-axis lateral scanning actuator is working in this experiment, it can be concluded that the reconfigured system has a higher performance in image accuracy due to its better vibration attenuation capability.

4 Conclusion

The importance of the Z-axis coarse motion actuator, the most dominant component affecting the accuracy of the AFM, was addressed in this paper. Since the mass mounted on the Z-axis coarse motion actuator was excessively high in the previous AFM system, the vibration characteristics became degraded. However, instead of designing a new lighter XY-axis lateral scanning actuator to be loaded on the Z-axis coarse motion actuator, vibration reduction was achieved by reconfiguring the mechanical components. The reconfigured AFM system helped to reduce the equivalent mass of the Z-axis coarse motion actuator, which subsequently contributed to

Fig. 4 Experimentally obtained FRF of the reconfigured AFM system.

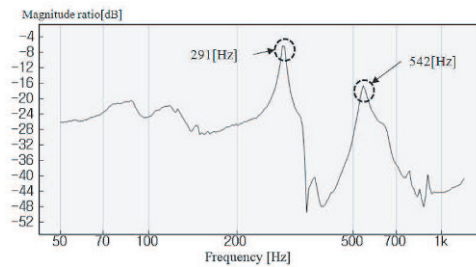
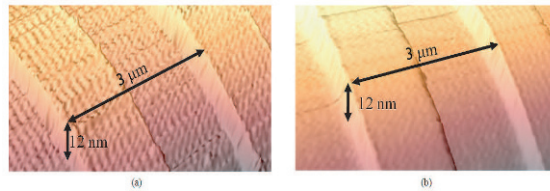


Fig. 5 Real scanning images of the (a)previous and (b)reconfigured AFM systems.



increasing the natural frequency and damping ratio of the AFM. Finally, by comparing the vibration of the cantilever of the reconfigured AFM system with that of the previous AFM system in each real scanning image, it was demonstrated that the vibration attenuation capability of the reconfigured AFM system was significantly improved.

Acknowledgements This work was supported by the Research Center for Bio-molecular Nanotechnology at the Gwangju Institute of Science and Technology, Republic of Korea (Grant No. K02035).

References

1. G. Binning, CH. Berber, E. Stoll, T. R. Alebrecht, and C. F. Quate, 1987, *Europhysics Letters*, Vol. 3, pp. 1281-1286.
2. K. Wildeer, C.F. Quate, B. Singh, and D.F. Kyser, 1998, *Journal of Vacuum Science and Technology B*, Vol. B16, pp. 3864-3873.
3. E. Betzig, J.K. Trautman, R. wolfe, E.M. Gyorgy, P.L. Finn, M.H. Kryder, and C.H. Cahang, 1992, *Applied Physics Letters*, Vol. 61, pp. 142-144.
4. J. B. Thomson, and B. Drake, J. H. Kindt, J. Hoskins, and P. K. Hansma, 2001, *Nanotechnology*, Vol. 12, pp. 394-397.
5. J. Chen, T. Guo, X. Hu, and X. Hu, 2009, *Journal of Vacuum Science and Technology B*, Vol. B27, pp. 1413-1417.
6. J. H. Kindt, G. E. Fantner, J. A. Cutroni, P. Hansma, 2004, *Ultramicroscopy*, Vol. 100, pp. 259-265.
7. G. Schitter, K. J. Astrom, B. E. DeMartini, P. J. Thurner, K. L. Turner, and P. K. Hansma, 2007, *IEEE Transactions on Control System Technology*, Vol. 15, No. 5, pp. 906-915.
8. G. E. Fantner, G. Schitter, J. H. Kindt, T. Ivanov, K. Ivanova, R. Patel, N. Holten-Anederson, J. Adams, P. J. Thurner, I. W. Rangelow, and P. K. Hansma, 2006, *Ultramicroscopy* Vol. 106, pp. 881-887.
9. A. J. Flemming, B. J. Kenton, K. K. Leang, 2010, *Ultramicroscopy*, Vol. 110, pp. 1205-1214.
10. G. K. Binning and D. Smith, 1986, *Review of Scientific Instruments*, Vol. 58, pp. 1688-1689.
11. C. A. J. Putman, B. G. De Grooth, N. F. Van Hulst, and J. Greve, 1992, *Journal of Applied Physics*, Vol. 72, pp. 6-12.
12. H. Butt, B. Cappella, and M. Kappl, 2005, *Surface Science Reports*, Vol. 59, pp.1-152.
13. <http://www.em4sys.com>.
14. A. F. Seybert, 1981, *Journal of Sound and Vibration*, Vol. 75, pp. 199-206.

Modal Analysis and SHM Investigation of CX-100 Wind Turbine Blade

Krystal Deines¹, Timothy Marinone², Ryan Schultz³, Kevin Farinholt⁴, Gyuhae Park⁴

1. Dept. of Aerospace Eng., New Mexico State University, Las Cruces, NM, 88003
2. Dept. of Mechanical Eng., University of Massachusetts Lowell, Lowell, MA 01854
3. Dept. of Mechanical Eng., Michigan Technological University, Houghton, MI 49931
4. The Engineering Institute, Los Alamos National Laboratory, Los Alamos, NM 87545

Abstract

This paper presents the dynamic characterization of a CX-100 wind turbine blade using modal testing. Obtaining a thorough dynamic characterization of turbine blades is important because they are complex structures, making them very difficult to accurately model without supplementing with experimental data. The results of this dynamic characterization can be used to validate a numerical model and understand the effect of structural damage on the performance of the blades. Also covered is an exploration into Structural Health Monitoring (SHM) techniques employed on the blade surface to detect changes in the blade dynamic properties. SHM design parameters such as traveling distance of the wave were examined. Results obtained during modal and SHM testing will provide a baseline for future work in blade damage detection and mitigation.

1.0 Introduction

1.1 Background

Wind energy in the United States is the fastest growing source of renewable domestic energy. A recent DOE technical report [1] proposed the potential for meeting 20% of the nation's energy needs through wind power by 2030. This significant investment in wind turbines is motivating manufacturers to produce more efficient and therefore larger and more complex wind turbines. The trend in wind energy is also toward larger, longer, yet lighter blades in order to generate more power. Significant effort is being expended in order to improve the design and manufacturability of the blades [2, 3, 4].

Maximizing the reliability of wind turbine design is a key to providing safe and cost effective operation. Monitoring the structural health of the turbine blades is particularly important as they account for 15-20% of the total turbine cost. In addition, blade damage is the most expensive type of damage to repair and can cause serious secondary damage to the wind turbine system due to rotating imbalance created during blade failure. Accurate assessment of blade structural health is critical financially as wind turbines are often in remote locations, and require substantial time, effort and cost to repair if failed [5]. If predictive maintenance can be employed, that could mean a substantial reduction in downtime which readily translates to significant cost savings for the wind farm operator.

1.2 Previous Work

Modal analysis of a CX-100 wind turbine blade in a free-free configuration and attached to a Micon 65/13 Wind Turbine by White et al. [6] determined that boundary condition supports affected the frequencies and mode shapes. Modal analysis of a Blade System Design Study (BSDS) blade by Griffith et al. [7] demonstrated a unique boundary condition approach by attaching the blade to a seismic mass and airbag assembly in a vertical orientation. Fatigue testing of a TX-100 blade with SHM by Rumsey et al. [8] determined that failure occurred at the out-board blade spar-cap termination point at 4.5 meters from the root.

A review of various SHM techniques was described by Ciang et al. [9], which compared the techniques for detecting localized vs. global damage along with the number of sensors needed and potential issues with each technique. Evaluation of three SHM techniques: Lamb wave, frequency response, and time series were performed by Light-Marquez et al. [10] showing the advantages and disadvantages of each technique.

1.3 Purpose

The purpose of this study is to characterize the dynamic response of the CX-100 wind blade and the design parameters of SHM techniques as they apply to the wind turbine blade. An examination of boundary conditions in both a free-free and fixed-free configuration will be investigated. This characterization will serve as a baseline for further work as well as validate developed dynamic models. Also explored is the usable frequency range for MFC patch sensors located on the spar at various span-wise locations along the length of the blade.

2.0 Experimental Procedure

2.1 Pre-Test Setup

A grid was created on the blade's high and low pressure surfaces for measurement location reference. This grid was aligned on the X, Y and Z axes of the CX-100 CAD model. As such, all measurement locations can be easily translated from a point on the complex surface of the blade to a point in the X, Y, and Z coordinate system of the model. The grid has points every 0.5 meters along the blade length and every 0.2 meters along the blade chord, [Figure 1](#).



Figure 1: Measurement location grid on CX-100

2.2 Free-Free Modal Test I

Due to data collection limitations, a roving hammer test was used, employing three shear accelerometers (PCB 352C22) and a modal impact hammer (PCB 086D20). Preliminary testing determined the required sensitivity and location of each accelerometer on the blade. The low-pressure surface was selected as the impacting and measuring surface as flap-wise modes were of primary interest. In addition, the low-pressure surface has less curvature than the high-pressure surface. Accelerometer locations are shown in [Figure 2](#). The impact hammer tip was selected to excite up to 150Hz which contains the first several modes.

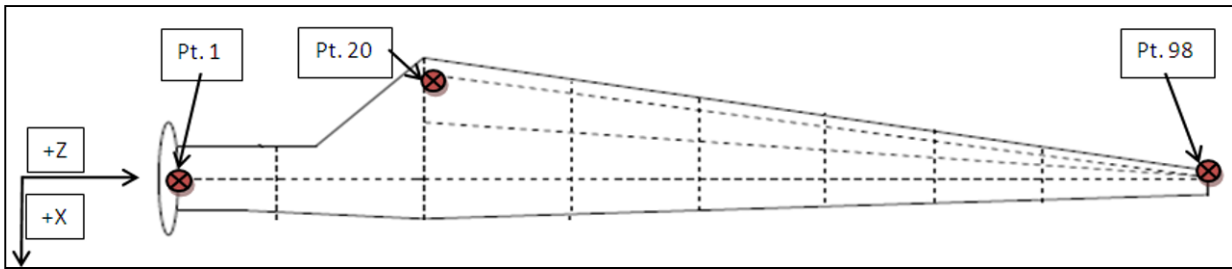


Figure 2: Accelerometer locations on blade low-pressure surface

The blade was suspended from metal frames by way of lifting sling support straps at two points. The tip-end support strap was placed at the node of the first flap-wise bending mode which was located during preliminary testing, Figure 3. In all tests, the response of the frames was characterized by instrumenting with accelerometers and impacting at various points to determine any coupling of frame and blade modes.

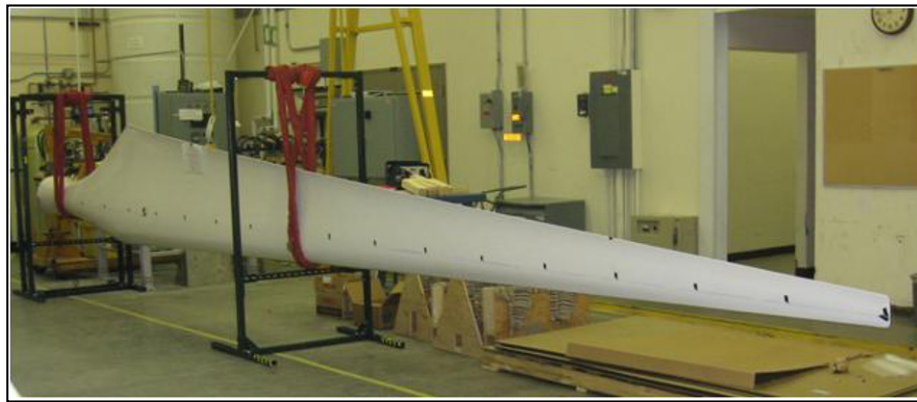


Figure 3: CX-100 in Free-Free I configuration

In order to minimize the effects of the boundary conditions (support straps) on the frequency and mode shape, the support strap was placed at the node of the first mode. The blade was impacted at several points along the length and chord of the blade in the flap-wise direction, taking care to measure and impact on the Y-Z plane. RT Dactron was used for collection of data which was output in UFF files, while ME'scope was used for curve-fitting and analysis. The data collection parameters used can be seen in Table 1.

Table 1: Modal Tests Data Collection Parameters

Sampling Frequency (Hz)	150
Number of Data Points	4096
Number of Averages	5
Sampling Time (s)	11
Type of Average	Linear
Window	None

2.2.1 Boundary Condition Study of Free-Free Modal Test I

To determine the effects of various boundary conditions on the blade response, a boundary condition study was performed. By changing one aspect of the blade boundary conditions at a time, measuring the response and comparing with a baseline measurement, the effects were quantified. Boundary conditions examined were the Z location of the support straps (both root and tip-ends), the angle of the blade in the support straps (rotating

about the length) which changes the contact of the straps with the blade surface, and the stiffness of the metal support frames. The blade was impacted and measured at the three drive points (1, 20 and 98), [Figure 2](#).

2.3 Free-Free Modal Test II

To create strain energy in the root of the blade that was absent in the first free-free test, a large mass was bolted to the root. This mass is the top of the fixture used in fixed-free testing (section 2.4) and weighs approximately 500lbf. To approach a free-free condition with this new setup, the fixture was set on wood blocks covered in carpet, leaving the root end with the fixture free to move. The tip-end was then supported with a support strap to keep the blade from tipping, [Figure 4](#). The same impact and measuring process as the Free-Free Modal Test I was used. As in Free-Free Modal Test I, a characterization of the fixture was performed.



Figure 4: Free-Free Modal Test II setup with fixture bolted to blade root

2.4 Fixed-Free Modal Test

Modal testing of the blade was also performed with a fixed-free condition by bolting the blade to a metal fixture in a cantilevered configuration. The blade was oriented with the chord at the tip vertical, as in the free-free tests.

Modal testing was performed using the same procedure as described in 2.2, using the same accelerometers and roving hammer technique to measure the flap-wise response. Next, accelerometers were placed on the trailing edge of the blade and oriented with the blade's X-axis to measure lead-lag modes. The blade was impacted along the leading edge with the same impact hammer to excite these lead-lag modes.

The fixture is not perfectly rigid and therefore not a truly fixed condition. To account for the effects of the fixture on the blade response, accelerometers were added to various locations on the fixture to characterize its response due to impacts on the blade and on the fixture.



Figure 5: Blade mounted to fixture for Fixed-Free Test

2.5 Structural Health Monitoring

An exploratory investigation into the application of structural health monitoring techniques on the full CX-100 blade was performed. The blade was bolted to the fixture as in the Fixed-Free Modal Test. The aim was to apply one large actuation macro-fiber composite (MFC) patch to the blade high-pressure surface and then detect the applied signals with several smaller sensor MFC patches placed along the length of the blade. The actuation patch is from www.smart-material.com, type 15B10-0211 and located on the X=0 centerline, which is also where the spar-cap is located, two meters from the root end (point three in Figure 6) below. The sensor patches are also from www.smart-material.com, type 20E10 and located per Figure 6.

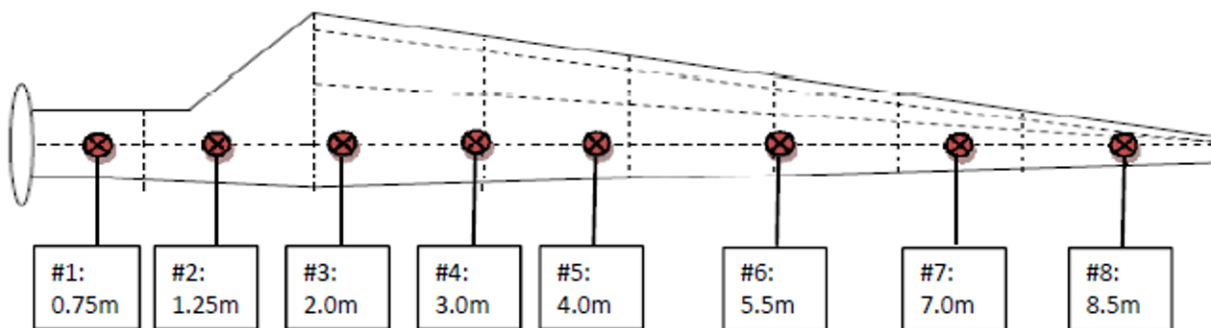


Figure 6: Sensor MFC patch locations on blade centerline

As can be seen in Figure 6, sensor patches were concentrated toward the root, because the transition region from structural to aerodynamic (near the root) is the region where failure typically occurs.

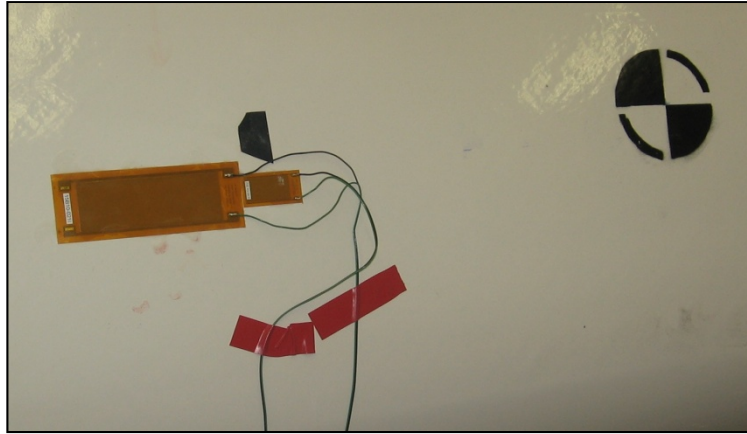


Figure 7: Large actuator MFC (left) and small sensing MFC (right) at point 3 near CG of CX-100

In this experiment, eight small MFC patches were used as sensing patches and one larger patch was used as an actuator. One sensing patch was placed immediately next to the actuating patch to read the strain output in the area close to the actuation patch, [Figure 7](#). Two excitation signals were used - sine chirp and burst random. A shear accelerometer (PCB 352C22, 100mV/g) was placed at the sensing MFC patch during each test for comparison of the observed signals in the frequency range of the accelerometer. An amplifier, AV Power Series 790, was used with the actuator patch to produce enough energy in the blade for the sensor patches to read.

3.0 Data Analysis

3.1 Free-Free Modal Test I

A modal test of the blade in a free-free configuration was performed as described in 2.2. Me'scope was used to curve fit the frequency response data and estimate natural frequencies, damping ratios, and mode shapes. The results are shown in [Table 2](#).

Table 2: Modal Results for CX-100 Rotor Blade with Free-Free I Boundary Condition

Mode	Frequency (Hz)	Damping (% critical)	Description
1	7.61	0.195	1 st Flap Bending
2	18.1	2.960	1 st Lag Bending
3	20.2	0.752	2 nd Flap Bending
4	32.2	0.353	3 rd Flap Bending
5	45.1	0.733	2 nd Lag Bending
6	50.5	0.630	4 th Flap Bending
7	63.9	0.740	1 st Torsion
8	70.1	0.568	3 rd Lag Bending

3.1.1 Boundary Condition Study of Free-Free Modal Test I

From previous literature [12], the boundary condition in a free-free configuration was found to have an effect on the natural frequencies and mode shapes observed. In order to determine the effect of the boundary conditions on the response, a boundary condition study was performed by varying the boundary condition and comparing the resultant FRFs.

[Table 3](#) is a summary of the different conditions tested with the average percent difference from the baseline for the first three flap-wise modes. The baseline test included a strap support at the root end and a strap support with standard metal frames at the node of the first flap-wise mode. The chord was oriented parallel to gravity. Details are in Appendix A.

Table 3: Summary of Boundary Condition Effects

Boundary Configuration	Percent Difference
Lifting the Blade	0.00
Rotation of the Blade	1.01
Attaching Angle Brackets to Unistrut Frame	1.67
Stiffened Frame Moved Out Toward Tip	8.20
Stiffened Frame Moved Slightly Inward	4.40
Stiffened Frame Moved to Center of Gravity	3.81
Percent of Support in Contact with Blade	2.87
Root Support Moved Slightly Outward	2.36

Overall, the boundary condition changes had an effect on the frequencies of the first mode. However, some boundary condition changes had greater effects on the first mode frequency than others, especially the shift of the tip-end support.

3.2 Free-Free Modal Test II

A modal test of the blade in the Free-Free II configuration was performed as described in 2.3. In order to ensure safety, an additional support needed to be located at the CG. Two configurations were examined: hanging the blade from Unistrut frame with a sling, and placing a cart with packing foam underneath, [Figure 8](#).

[Table 4](#) contains a comparison of the frequencies for both configurations.



Figure 8: Free-Free II configuration with cart and packing foam supporting blade

Table 4: Comparison of Natural Frequencies for Free-Free II

Mode	Unistrut Configuration (Hz)	Packing Foam Platform Configuration (Hz)	Percent Difference
1 st Flap-wise	3.29	2.93	10.94
2 nd Flap-wise	8.72	8.97	2.79
3 rd Flap-wise	17.60	17.40	1.14
4 th Flap-wise	30.70	30.00	2.28
5 th Flap-wise	45.00	42.30	6.00
1 st Torsion	50.90	54.90	7.29

As with Free-Free I, boundary conditions have an effect on the blade response, shown in

Table 4.

3.2.1 Nonlinear Study

A significant assumption during modal testing is system linearity, which allows the complete FRF matrix to be created from a subset of the data. In order to determine if the linearity assumption was valid for the blade and boundary condition system, two tests were performed on the system. The first test involved impacting the same location at different force amplitudes and comparing the resulting FRFs. The second test involved a reciprocity check by impacting and measuring at two points, and overlaying the FRFs. From the study, system nonlinearity was observed, but was found to have negligible effect on the resonant frequencies identified within a given input force range of interest. Thus, the linear assumption was deemed valid for the purpose of testing. Further details of the test can be found in Appendix B.

3.3 Fixed-Free Modal Test

A modal test of the blade in a Fixed-Free configuration was performed, as described in 2.4. The results are shown in [Table 5](#).

Table 5: Modal Results for CX-100 Rotor Blade with Free-Fixed Boundary Condition

Mode	Frequency (Hz)	Damping (% critical)	Description
1	3.22	0.203	1 st Flap Bending
2	4.15	0.250	1 st Lag Bending
3	8.81	0.245	2 nd Flap Bending
4	16.80	0.306	2 nd Lag Bending
5	19.20	0.345	3 rd Flap Bending
6	30.80	0.263	4 th Flap Bending
7	37.20	0.789	3 rd Lag Bending
8	43.90	0.499	1 st Torsion

Testing in the Fixed-Free configuration resulted in lower blade natural frequencies than either free-free test. In addition, the natural frequencies obtained from attaching the fixture to the blade in the free-free configuration are very similar to the natural frequencies obtained in the fixed-free configuration. This shows that the additional effect of the stiffness of the fixture attached to the frame is minimal compared to the effect of adding the fixture onto the blade.

3.4 Structural Health Monitoring

SHM tests of the blade were performed as described in 2.5. Examination of the responses at the 8 points showed an effective frequency range that is listed in [Table 6](#).

Table 6: Effective Frequency for Points on Blade

Point	1	2	3	4	5	6	7	8
Effective Frequency (kHz)	0-20	0-20	0-20	0-20	5-20	5-20	5-20	5-20

Locations in the structural region near the root exhibit noticeable responses across the entire frequency range, showing that SHM could be effective for the region. In contrast, locations in the aerodynamic region toward the tip exhibit a markedly decreased response across a smaller frequency range, indicating that SHM may not be as effective for that region. Further details of the test can be found in Appendix C.

4.0 Conclusions

Modal testing of a 9 meter CX-100 wind turbine blade was performed in both free-free and free-fixed configuration and the natural frequencies and mode shapes were obtained for the first several modes. A study of the effect of the boundary conditions on a free-free configuration was also performed, showing that the supports have a nontrivial effect on the blade response. MFC sensor patches were applied to the structure to determine the effective frequency range at various points along the blade. Greater signal attenuation existed in the aerodynamic region of the blade as compared to the structural region.

Modal analysis of the fixed-free configuration showed that the fixture and frame did not provide a perfectly fixed condition, which resulted in noticeable motion of the fixture and frame coupled with the blade.

Accordingly, another modal test of the blade should be performed with the blade attached to a large seismic mass with greater mass and inertia (like that at the National Renewable Energy Laboratory) in order to truly replicate a fixed boundary condition. Damage could not be induced in the blade due to need for further study of the blade in good condition. Accordingly, SHM testing of a blade with damage or simulated damage should be performed to determine the effectiveness in detecting damage in the structural region. The effect of the placement of the patches should also be studied to optimize their location.

5.0 Acknowledgements

All of this work was made possible by the Los Alamos National Laboratory Engineering Institute under the leadership of Dr. Chuck Farrar, which provided the blade and all the equipment used. Vibrant Technology Inc. graciously provided the license for ME'scope software which was used for all data analysis. ABAQUS graciously provided a license for their software which was used for analysis of the fixture support. Lastly, Dr. Peter Avitabile (University of Massachusetts Lowell) provided invaluable guidance over the course of this project.

6.0 References

1. U.S. Department of Energy. "20% Wind Energy by 2030." July 2008
2. TPI Composites, Inc., "Innovative Design Approaches for Large Wind Turbine Blades," Project Report for SNL, SAND2003-0723, March 2003.
3. TPI Composites, "Innovative Design Approaches for Large Wind Turbine Blades; Final Report", SAND2004-0074, Sandia National Laboratories, Albuquerque, NM
4. Ashwill, T.D., "Some Recent Trends & Activities in Turbines and Blades," Sandia National Laboratories 2nd Wind Turbine Blade Workshop, April 2006.
5. JÜNGERT, ANNE. "Damage Detection in Wind Turbine Blades using two Different Acoustic Techniques", 7th PhD Symposium in Stuttgart, Germany, September 11 – 13, 2008
6. White, J.R., Adams, D.E., Rumsey, M.A., "Modal Analysis of CX-100 Rotor Blade and Micon 65/13 Wind Turbine", Proceedings of the IMAC-XXVII, Feb. 1-4, 2010, Jacksonville, FL
7. Griffith, D.T., Carne, T.G., "Experimental Modal Analysis of 9-meter Research-sized Wind Turbine Blades", Proceedings of the IMAC-XXVII, Feb.1-4, 2010, Jacksonville, FL
8. Rumsey, M.A., Paquette, J.A., "Structural Health Monitoring of Wind Turbine Blades" , Sandia National Laboratories, Albuquerque, NM
9. Ciang, C.C., Lee, J.R., Bang, H.J., "Structural Health Monitoring for a Wind Turbine System: A review of Damage Detection Method," Meas. Sci. Technol. 19 (2008), 122001.
10. Light-Marquez, A., Sobin, A., Park, G., Farinholt, K., "Structural Damage Identification in Wind Turbine Blades using Piezoelectric Active-sensing," Proceedings of the IMAC XXVIII, Feb. 1-4, 2010, Jacksonville, FL.
11. Griffith, D.T., Carne, T.G., Paquette, J.A., "Modal Testing for Validation of Blade Models", Wind Engineering Vol. 32, No. 2, 2008, PP 91–102, Sandia National Laboratories, Albuquerque, New Mexico

Appendix A: Boundary Condition Study

In order to determine the effect of the boundary conditions on the free-free mode shapes and frequencies, testing of the blade was performed with several variations in the boundary conditions. A drive point measurement at the tip was used as a baseline FRF for comparison with the effect of the other conditions.

Test 1: Lifting of the Blade

Before going into any further study of the boundary conditions, there is a need to know if the measurement was repeatable without any boundary condition change. Accordingly, the tip end of the blade was lifted up out of the tip end support sling and set back down in the original position. The resulting FRF overlay is shown in [Figure 9](#), where the black trace is the baseline measurement, and the red trace is the measurement after lifting and returning the blade in the support sling.

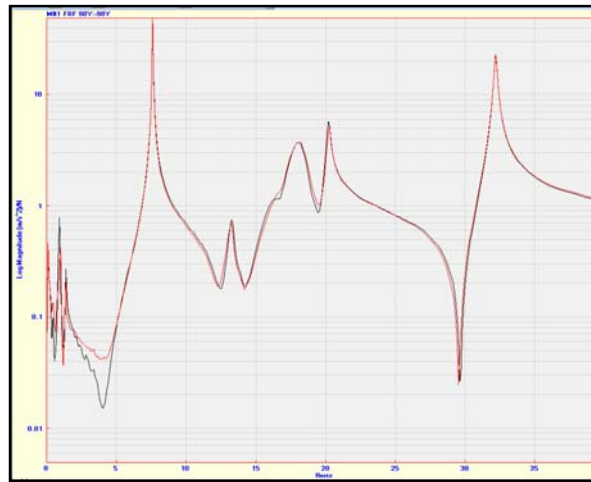


Figure 9: FRF comparison between baseline (black) and lifted (red) configurations

For the uses of this experiment, the frequency range of interest contains the first three flap-wise modes; zero to 40 Hz. Comparison of the two FRFs shows negligible difference between the two measurements in the frequency range of interest. In both frequency and amplitude, the FRFs are almost perfect replicas of each other, especially in the first three flap-wise modes. [Table 7](#) is a comparison of the frequencies for the first three flap-wise modes.

Table 7: Comparison of Natural Frequencies for the Baseline and Lifted Configuration

	Baseline Configuration (Hz)	Lifted Configuration (Hz)	Percent Difference
First Flap-wise	7.6	7.6	0
Second Flap-wise	20.2	20.2	0
Third Flap-wise	32.2	32.2	0

Test 2: Rotation of the Blade

The initial orientation of the blade was such that the chord at the tip was parallel to gravity in an attempt to maximize the response of the flap-wise modes. Since a true free-free configuration would produce the same modes regardless of the angle of orientation, the blade was rotated 12° clockwise to determine the effect of changing the contact areas of the tip end support sling, [Figure 10](#). The resulting FRF overlay is shown in [Figure 11](#), where the black trace is the baseline measurement, and the red trace is the measurement after rotating the blade.



Figure 10: Blade in baseline orientation (left) versus rotated 12° orientation (right)

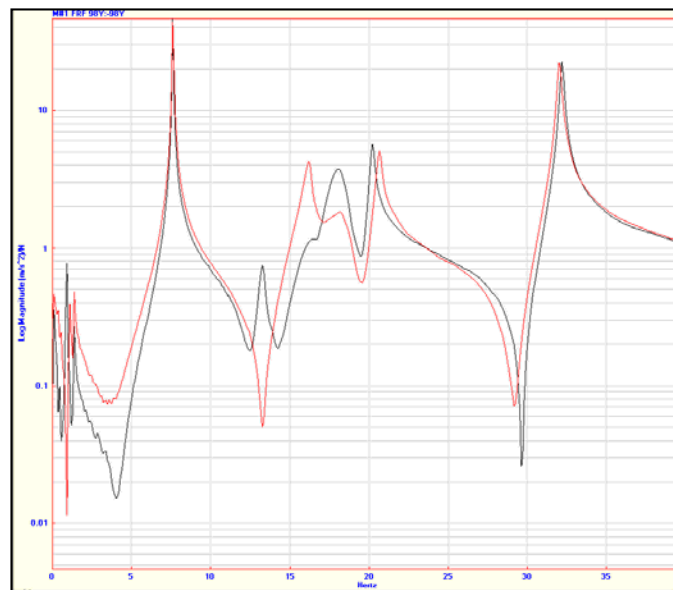


Figure 11: FRF comparison between baseline and rotated configurations

Comparison of the two FRFs shows minimal difference at the first and third flap-wise modes, but a noticeable difference at the second flap-wise mode. A possible explanation for this difference is a change in the interaction of the second flap-wise mode with the first lead-lag mode, which occurs at 18 Hz. Adjusting the rotation may cause the lead-lag mode to have a larger amplitude, affecting the frequency of the second flap-wise-mode. [Table 8](#) is a comparison of the frequencies for the first three flap-wise modes.

Table 8: Comparison of Natural Frequencies for the Baseline and Rotated Configurations

	Baseline Configuration (Hz)	Rotated Configuration (Hz)	Percent Difference
First Flap-wise	7.6	7.6	0
Second Flap-wise	20.2	20.7	2.42
Third Flap-wise	32.2	32.0	0.62

Test 3: Stiffening the Unistrut Frame

The original supports for the blade consisted of two Unistrut frames, one supporting the tip end and one supporting the root end. Testing of the tip end frame revealed a shearing mode at 8.1 Hz, close to the first natural frequency of the blade, 7.61 Hz. In order to determine if there was a coupling effect between the frame

and the blade, the frame stiffness was increased by adding angle brackets to the corners to shift the natural frequency out of the range of the blade's first flap-wise mode, [Figure 12](#). The resulting FRF overlay is shown in [Figure 13](#), where the black trace is the baseline measurement, and the red trace is the measurement after adding the angle brackets.



Figure 12: Frame in baseline configuration (left) versus the stiffened frame (right)

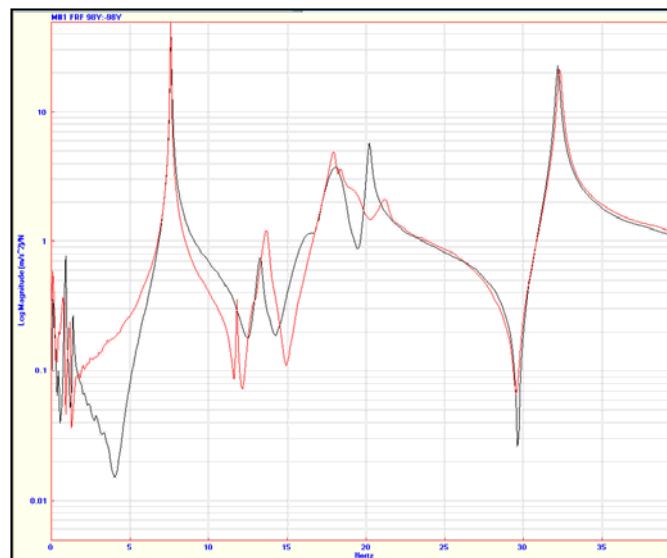


Figure 13: FRF Comparison between baseline (black) and stiffened frame Unistrut (red) configurations

Comparison of the two FRFs shows minimal difference at the first and third flap-wise modes, but a noticeable difference at the second flap-wise mode. A possible explanation for this difference is due to the change in frequency caused by the stiffened frames changing the interaction of the frame with the blade at that frequency. Modal analysis of the stiffened frame yielded a shearing mode at 18.1 Hz, which may couple with the second flap-wise blade mode and alter the measured frequency. [Table 9](#) is a comparison of the frequencies for the first three flap-wise modes.

Table 9: Comparison of Natural Frequencies for the Baseline and Stiffened Frame Configurations

	Baseline Configuration (Hz)	Stiffened Frame Configuration (Hz)	Percent Difference
First Flap-wise	7.6	7.6	0
Second Flap-wise	20.2	21.2	4.72
Third Flap-wise	32.2	32.3	0.31

Test 4: Stiffened Tip-End Frame Moved to 8 Meters from Root

Previous research had shown that the location of the supports had an effect on the natural frequencies obtained [11]. As such, the tip-end support was located at the node of the first flap-wise bending mode (6.518m from root) to minimize the effect of that support on that mode. To quantify the effect of support location on the frequencies and mode shapes, the tip-end support was moved outboard toward the tip (8m from root), [Figure 14](#). The resulting FRF overlay is shown in [Figure 15](#). All supports were stiffened with brackets.



Figure 14: Tip-end frame in baseline location 6.5m from root (left) versus moving the frame to 8m from root (right)

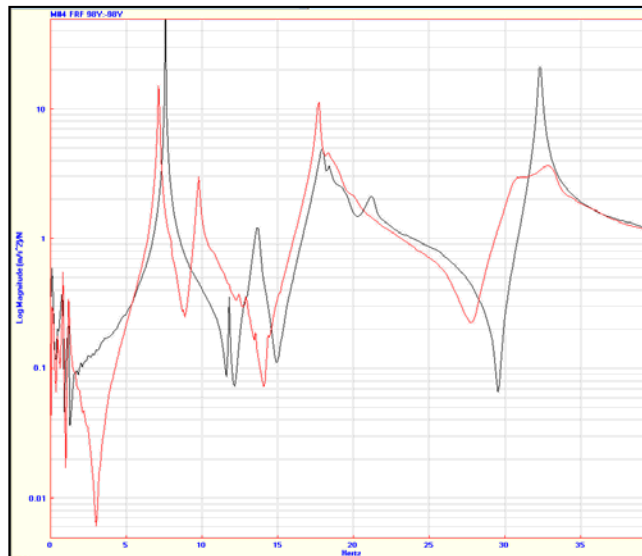


Figure 15: FRF comparison between stiffened baseline (black) and stiffened tip 8 meter (red) configurations

Comparison of the two FRFs shows noticeable difference at all three modes. This is due to relocating the added stiffness of the support (tip-end frame) to a new location on the blade that exhibits greater response, thereby magnifying the effect of the boundary condition. Changing the support location alters the system stiffness and

therefore changes the frequencies and mode shapes. [Table 10](#) is a comparison of the frequencies for the first three flap-wise modes.

Table 10: Comparison of Natural Frequencies for the Stiffened Baseline and Tip Support Configuration Stiffened 8 Meter Configurations

	Stiffened Baseline Configuration (Hz)	Stiffened 8 Meter Configuration (Hz)	Percent Difference
First Flap-wise	7.6	7.14	6.05
Second Flap-wise	21.2	17.7	16.51
Third Flap-wise	32.3	33.0	2.12

Test 5: Stiffened Tip End Frame Moved to 5 Meters from Root

Although moving the frame out to the tip showed significant change, that location would generally not be chosen for testing because the tip has the response with the greatest magnitude. To test the effect of locating a support near the node of the first flap-wise mode, the tip-end frame was placed 5 meters from the root end, [Figure 16](#). The resulting FRF overlay is shown in [Figure 17](#).



Figure 16: Tip-end frame in baseline location 6.5m from root (left) versus moving the frame to 5m from root (right)

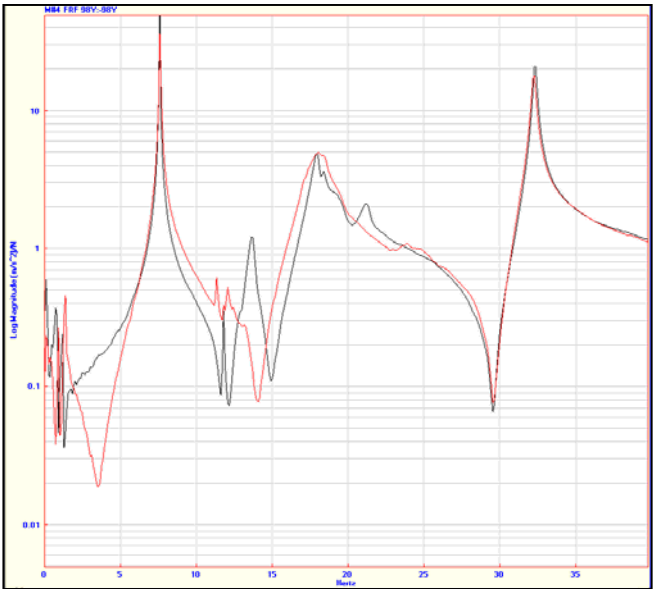


Figure 17: FRF comparison between stiffened baseline (black) and stiffened 5 meter (red) configurations

Comparison of the two FRFs shows minimal difference at the first and third flap-wise modes, but a noticeable difference at the second flap-wise mode. A possible explanation for this difference is the same as when moving the frame outboard; a change in the interaction of the lead-lag mode with the second flap-wise bending mode. [Table 11](#) is a comparison of the frequencies for the first three flap-wise modes.

Table 11: Comparison of Natural Frequencies for the Stiffened Baseline and Stiffened 5 Meter Configurations

	Stiffened Baseline Configuration (Hz)	Stiffened 5 Meter Configuration (Hz)	Percent Difference
First Flap-wise	7.6	7.6	0
Second Flap-wise	21.2	18.4	13.21
Third Flap-wise	32.3	32.3	0

Test 6: Stiffened Frame Moved to 3 Meters from Root

Although the best position for the supports would be at the node of a mode, a test to determine the effects of moving the tip-end support further inboard, near the center of gravity (CG) of the blade was performed. Accordingly, the frame was moved to 3 meters from the root, [Figure 18](#). Note that the strap contact area is significantly increased because of the much larger chord in this region of the blade, and the effects of strap contact are going to be greater for this configuration. In this test, the strap was in contact with the low-pressure (LP) side of the blade. The resulting FRF overlay is shown in [Figure 19](#).



Figure 18: Tip-end frame in baseline location 6.5m from root (left) versus moving the frame to 3m from root (right)

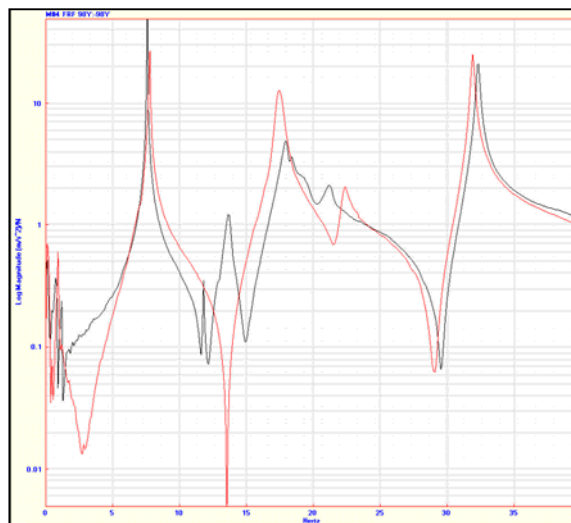


Figure 19: FRF comparison between stiffened baseline and stiffened 3 meter, LP-side contact configurations

Comparison of the two FRFs shows noticeable difference at all three modes. A possible explanation for this difference is due to the blade being substantially cantilevered in this configuration, which would change the frequencies. The extensive contact between the blade surface and the tip end support sling would have an effect on the frequencies and mode shapes as well. [Table 12](#) is a comparison of the frequencies for the first three flap-wise modes.

Table 12: Comparison of Natural Frequencies for the Stiffened Baseline and 3 Meter, LP-Side Contact Configurations

	Stiffened Baseline Configuration (Hz)	Stiffened 3 Meter, LP-Side Contact Configuration (Hz)	Percent Difference
First Flap-wise	7.6	8.15	6.75
Second Flap-wise	21.2	22.1	4.07
Third Flap-wise	32.3	32.1	0.62

Test 7: Changing Support Sling Contact with Blade Surface

With the tip end support located near the CG of the blade the sling has substantial contact with the blade surface. Rotating the blade drastically changes which surfaces (low-pressure or high-pressure) are in contact with the sling and the amount of contact. To test this effect, two measurements were taken, one with the blade rotated such that the sling was in contact with much of the low-pressure side and another where the blade was centered in the sling and the contact was roughly equal on both the low-pressure and high-pressure sides, [Figure 20](#). All support frames were stiffened. The resulting FRF overlay is shown in [Figure 21](#).



Figure 20: Blade with sling in contact with low-pressure surface (left) versus blade with sling contact equal on both sides (right)



Figure 21: FRF comparison between low-pressure side contact (black) and equal side contact (red) configurations

Comparison of the two FRFs shows noticeable difference at all three modes, particularly with the first and second modes. The difference is likely due to the drastic difference in surface contact scenarios changing the interaction between the blade and the tip-end support. [Table 13](#) is a comparison of the frequencies for the first three flap-wise modes.

Table 13: Comparison of Natural Frequencies for the Low-Pressure Side Contact and Equal Side Contact configurations

	Low-Pressure Side Contact Configuration (Hz)	Equal Side Contact Configuration (Hz)	Percent Difference
First Flap-wise	7.78	8.15	4.54
Second Flap-wise	22.4	22.1	1.35
Third Flap-wise	32.0	32.1	0.31

Test 8: Root Support Moved to 0.86 Meters

Although most of the testing was focused on the location of the tip end frame, the effect of the root support was also examined. The support was moved outboard to 0.86m from the root (originally at 0.57m), [Figure 22](#). The resulting FRF overlay is shown in [Figure 23](#), where the black trace is the baseline measurement with the stiffened frame with both the tip and root end supports at the original locations, and the red trace is the measurement after moving the root support outboard.



Figure 22: Root support in baseline location (left) versus moved to 0.86m from root (right)

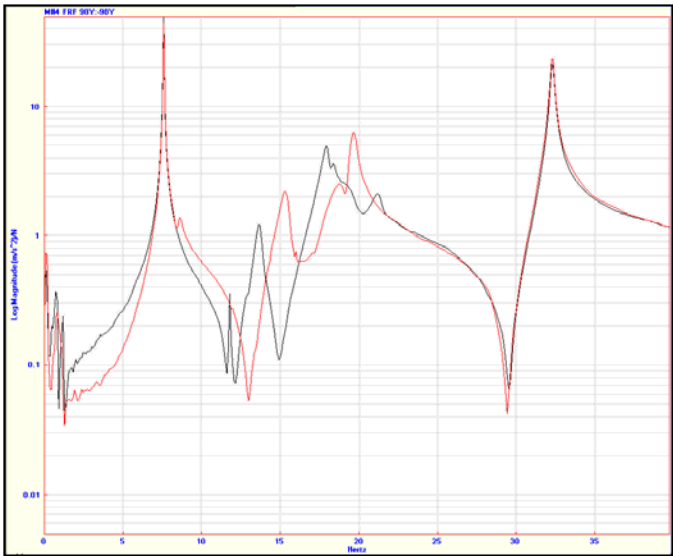


Figure 23: FRF comparison between stiffened baseline (black) and shifted root (red) configurations

Comparison of the two FRFs shows minimal difference at the first and third flap-wise modes, but a noticeable difference at the second flap-wise mode. [Table 14](#) is a comparison of the frequencies for the first three flap-wise modes.

Table 14: FRF Comparison of Natural Frequencies for the Stiffened Baseline and Shifted Root Configurations

	Stiffened Baseline Configuration (Hz)	Shifted Root Configuration (Hz)	Percent Difference
First Flap-wise	7.6	7.6	0
Second Flap-wise	21.2	19.7	7.08
Third Flap-wise	32.3	32.3	0

Appendix B: Nonlinear Study

B.1 Nonlinear Testing in Fixed-Free Configuration

In order to determine the existence of significant nonlinearities on the blade system, a nonlinear study was performed. The nonlinear study included a reciprocity check and a varied force impact test. The blade was in the Fixed-Free configuration for this testing.

B.1.1 Varied Impact Force Test

The FRF, $H(j\omega)$, is calculated by normalizing the autopower spectrum of the response by the input force spectrum. For a linear system, the FRF is independent of the impact force applied, and the same FRF is obtained regardless of the impact force.

To test if the system is linear and therefore independent of the force applied, drive point measurements at point 78 on the blade with varying impact forces were recorded. The FRFs were then compared to see if there was no difference, and therefore the system was linear, or if there were differences in magnitude or frequency, and therefore the system was nonlinear.

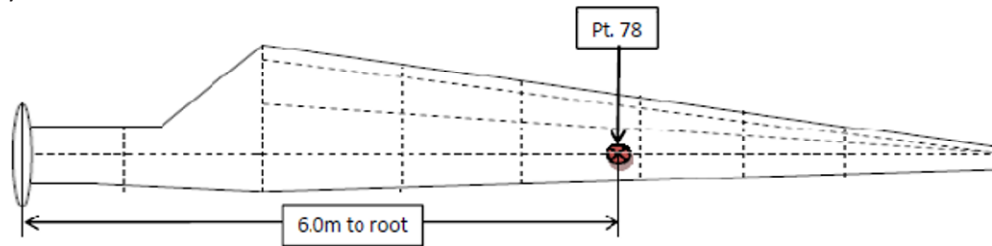


Figure 24: Layout of impact and measurement point on CX-100

Table 15: Frequencies and Magnitudes at First Six Modes

Impact Force (N)	1st Flap-wise		1st Lead-Lag		2nd Flap-wise	
	Freq (Hz)	Mag (m/s ²)	Freq (Hz)	Mag (m/s ²)	Freq (Hz)	Mag (m/s ²)
250	3.2	1.76	4.21	0.0692	8.79	0.893
330	3.2	1.38	4.21	0.0635	8.79	0.912
396	3.2	1.42	4.21	0.0642	8.79	0.942
438	3.2	1.59	4.21	0.0632	8.79	0.969
510	3.2	1.49	4.21	0.0604	8.79	0.986

Impact Force (N)	2nd Lead-Lag		3rd Flap-wise		4th Flap-wise	
	Freq (Hz)	Mag (m/s ²)	Freq (Hz)	Mag (m/s ²)	Freq (Hz)	Mag (m/s ²)
250	16.8	0.749	19.2	0.424	30.9	2.97
330	16.8	0.735	19.1	0.422	30.9	2.97
396	16.8	0.73	19.1	0.438	30.9	2.94
438	16.8	0.728	19.1	0.436	30.9	2.91
510	16.8	0.71	19.1	0.427	30.9	2.96

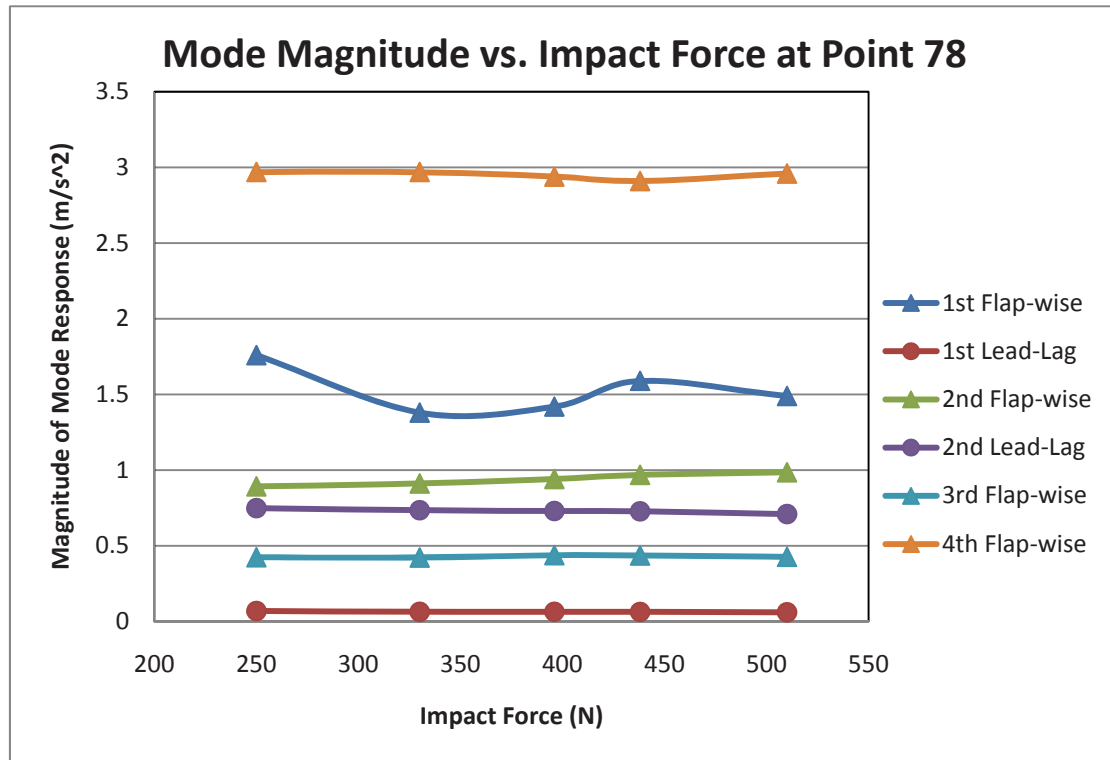


Figure 25: Change in magnitude of response at various low-order modes based on impact force

For each of the six modes analyzed, the frequencies did not change based on the impact force. However, the magnitudes of some modes varied depending on the impact force, with no deterministic patterns emerging. The first, second and fourth flap-wise modes, in particular, exhibit some change in the magnitude of response for different impact forces whereas the third flap-wise mode shows little change. The two lead-lag modes had little change in response magnitude for the changes in impact force. The existence of some fluctuation in the system response magnitude at differing impact forces may be indicative of nonlinearity in the system.

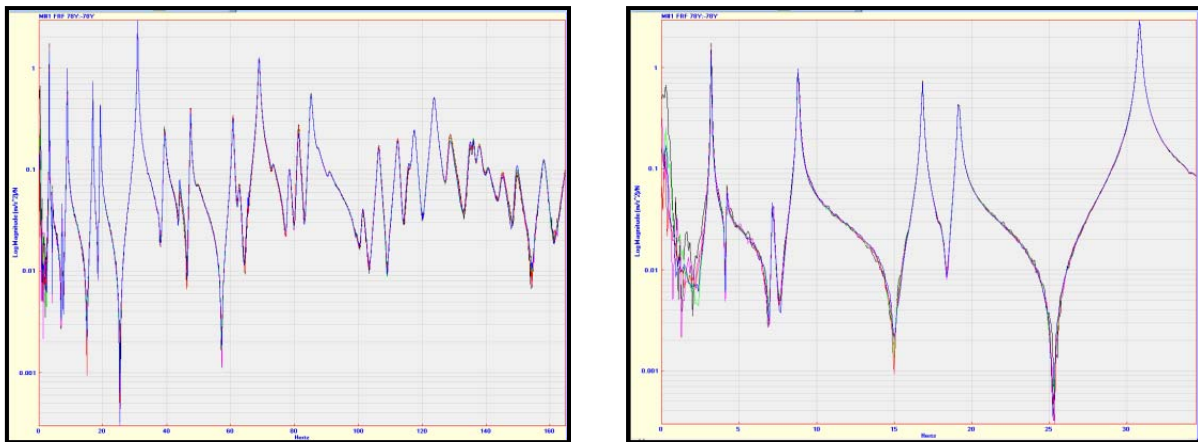


Figure 26: All impacts (250 to 510N) FRF overlay plot, showing a frequency range of zero to 160Hz (left) and zoom in of zero to 35Hz (right)

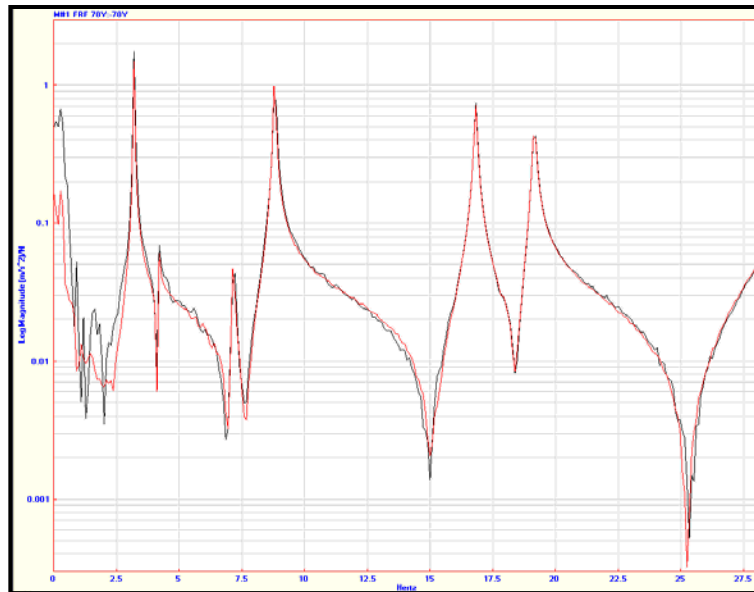


Figure 27: Lowest force impact (black) 250N, versus highest force impact (red) 510N, showing first five modes, zero to 28Hz

B.1.2 Reciprocity Test

The linear reciprocity assumption was tested by impacting at point 78 and measuring at point 91 versus impacting at 91 and measuring at 78. With a perfectly linear system, the FRF will be exactly the same for either scenario. If the system is nonlinear, the FRF from impacting at 91 and impacting at 78 may have different mode frequencies and/or magnitudes.

The same accelerometer was used to measure at both points and care was taken to measure and impact in the same spot for each point. Accelerometer used: PCB 352A24, S/N 39148. One impact and one measurement collected (no averaging). Impact at point 78 was force of 307N. Impact at point 91 was force of 220N

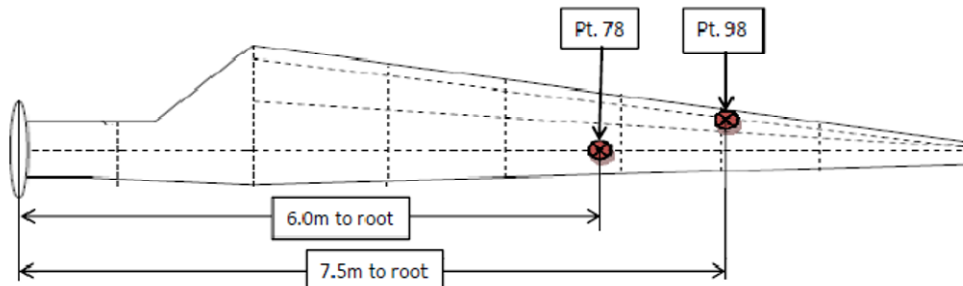


Figure 28: Layout of impact and measurement points on CX-100

Table 16: Frequencies and Magnitudes at First Six Modes, Comparing Impacting at Point 91 (Red) with Impacting at 78 (Blue)

Measure @:	Impact @:	Impact Force (N):	1st Flap-wise		1st Lead-Lag		2nd Flap-wise	
			Freq (Hz)	Mag (m/s ²)	Freq (Hz)	Mag (m/s ²)	Freq (Hz)	Mag (m/s ²)
78	91	220	3.2	2.45	4.21	0.156	8.79	0.731
91	78	307	3.2	2.22	4.21	0.112	8.79	0.798
% Diff. Measure @78 vs. Measure @91			0%	9%	0%	28%	0%	-9%
Measure @:	Impact @:	Impact Force (N):	2nd Lead-Lag		3rd Flap-wise		4th Flap-wise	
			Freq (Hz)	Mag (m/s ²)	Freq (Hz)	Mag (m/s ²)	Freq (Hz)	Mag (m/s ²)
78	91	220	16.8	1.11	19.1	1.21	30.9	4.32
91	78	307	16.8	1.25	19.2	1.15	30.9	4.46
% Diff. Measure @78 vs. Measure @91			0%	-13%	-1%	5%	0%	-3%

For the first several modes, there is no shift in frequency based on the impact or measurement location. The magnitudes at those frequencies are not perfectly consistent, with the lead-lag mode magnitudes having more variance between impacting at point 91 versus impacting at point 78. This greater difference is likely because impacts and measurements were only in the Y-axis, which is normal to the lead-lag direction and thereby not exciting or measuring the lead-lag modes. The flap-wise modes show less difference between impacting at one point versus the other. This difference may be negligible if multiple samples are taken and averaged, as only one impact for each measurement scenario was recorded.

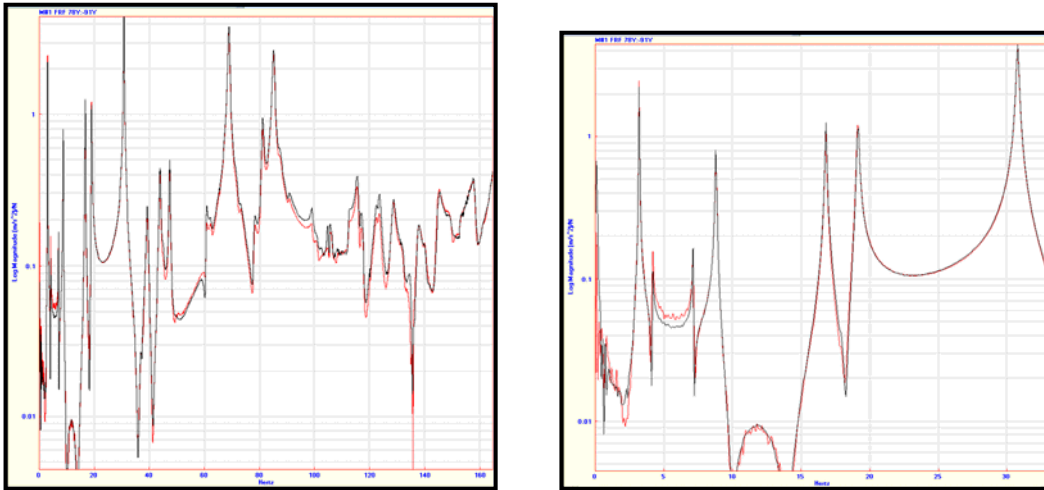


Figure 29: FRF overlay, impacting at point 91 (red) versus impacting at point 78 (black) from 0 to 160Hz and zoomed in from 0 to 30Hz

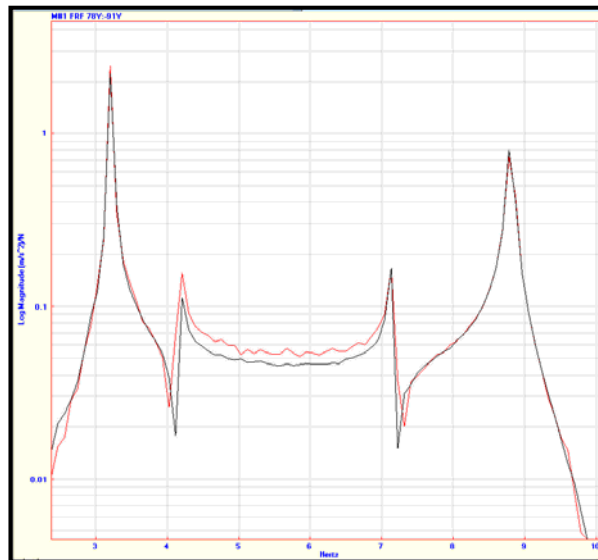


Figure 30: FRF overlay showing first 3 modes (3.2 Hz, 4.21 Hz, 8.79 Hz), impacting at 91 (red) versus impacting at 78 (black) from 0 to 10 Hz

After analyzing the data from the reciprocity check and the varied force impact test, nonlinearities were observed to be present in the system. In the future, further study may be needed to determine the nonlinear effects on the assumption of linearity for the purposes of modal testing.

Appendix C: Structural Health Monitoring Study

In order for SHM to be a viable method, variation should come from damage, rather than day-to-day conditions. Testing was done to determine the variation between tests on the same day, as well as between different days.

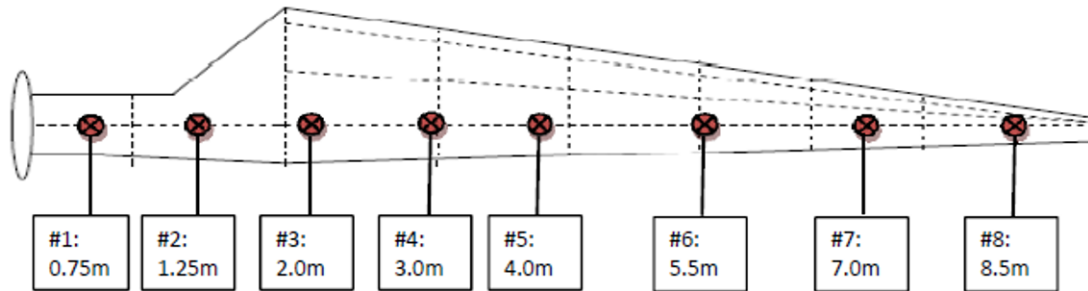


Figure 31: Sensor MFC patch locations on blade centerline

C.1 Same-Day Repeatability Test

Before studying any variations due to environment or loading, verification of repeatability between tests needed to be established. Accordingly, both the chirp and burst random excitations were applied twice for each measurement point. Figure 32 shows a FRF overlay of the chirp and burst random responses at point 1 with the first test in black and the second test in blue.

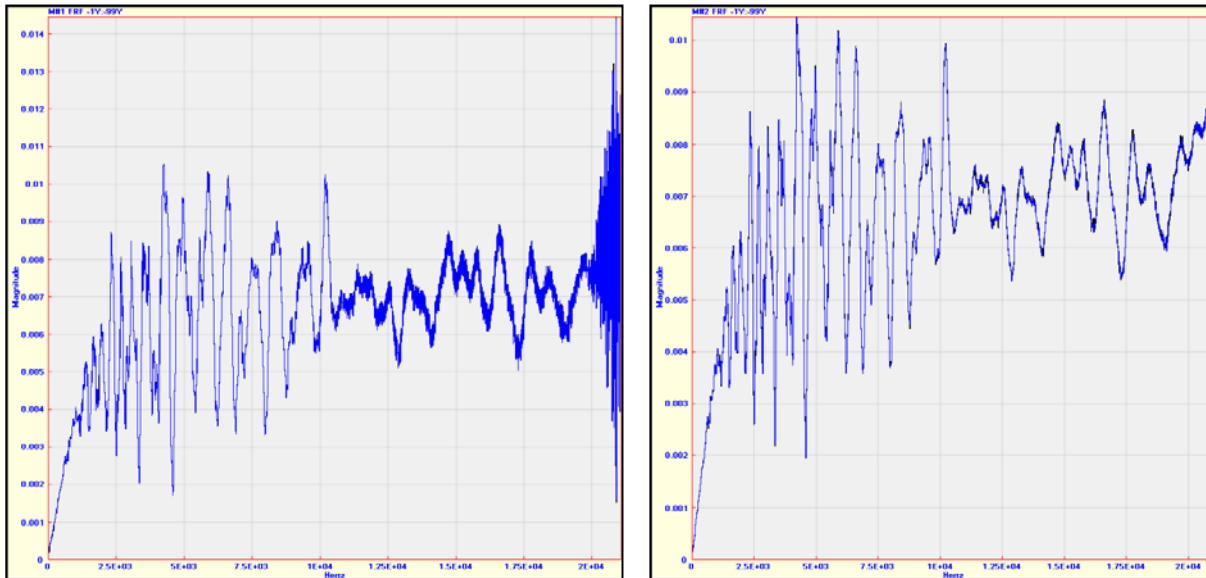


Figure 32: FRF overlay of sine chirp (left) and burst random (right) responses at point 1

The FRF overlay indicates that there is high repeatability between tests as the two traces are almost perfectly overlaid on top of each other. Accordingly, any variation in SHM results will not be due to the issue of repeatability with the same environmental and loading conditions. In addition, both excitation techniques experience the same repeatability, with identical responses up to 10 kHz.

C.2 Different Days Repeatability Test

Although important to establish repeatability between tests, equally important is the day to day repeatability. Since environmental conditions change frequently for wind turbines, there needs to be an awareness of the

effect of the environment on SHM results. Accordingly, the FRF at point 1 due to a burst random excitation is compared across four days of testing in Figure 33, where each color line corresponds to a temperature on a different day (Red = 78.7°F, Blue = 75.7°F, Green = 74.6°F, Purple = 75.5°F).

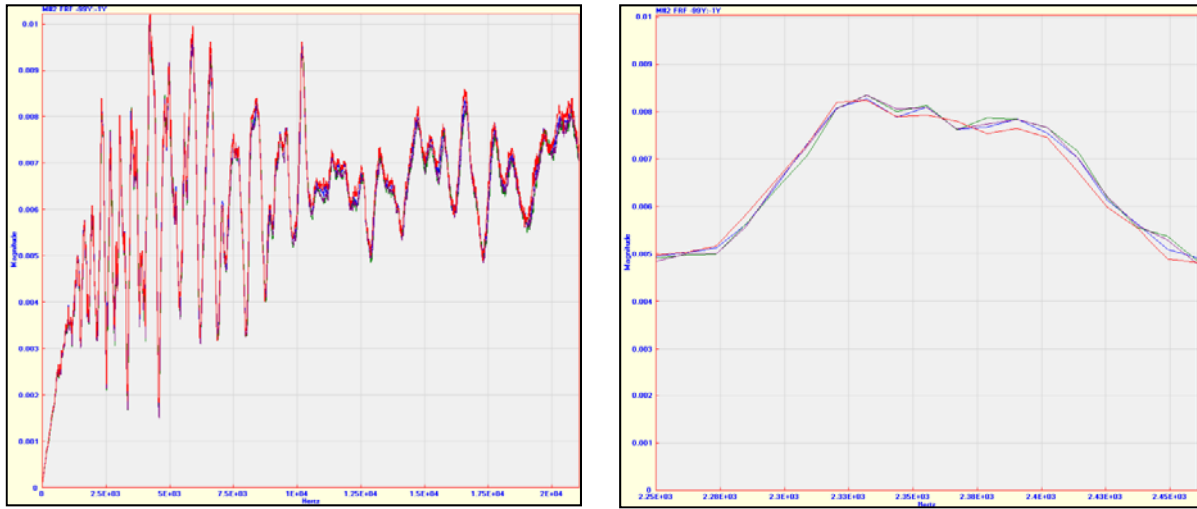


Figure 33: Comparison of temperature range over entire frequency range (left) and zoom in for one peak (right)

The FRF overlay indicates that there is high repeatability between tests as there is minimal variation. Further study may be needed to determine if the variation increases as the blade experiences a wider temperature range.

C.3 Effective Frequency Determination Test

Low frequency waves have a long wavelength, allowing them to travel substantially farther than high frequency waves. High frequency waves, however, are able to detect much smaller defects. Accordingly, for various sensor locations on the blade, there needs to be an awareness of the maximum frequency range at which a useable signal is measured. Figure 34 contains a comparison of the responses at points 4 and 8 with a burst random excitation where the black response is for point 4, and the blue response is for point 8.

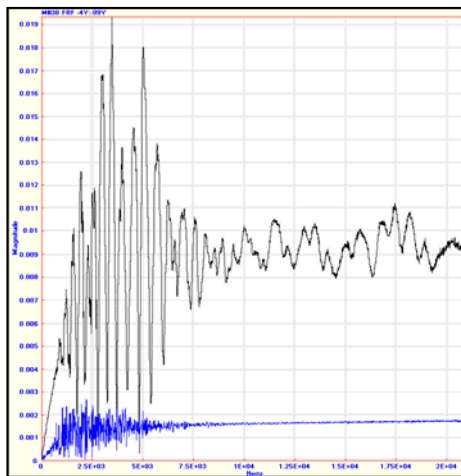


Figure 34: FRF overlay between points 4 and 8 for burst random excitation

While the response at point 4 contains a high signal to noise ratio across the entire frequency range, the response at point 8 contains noise at all frequencies. Comparing the responses at all 8 points yields [Table 17](#) which summarizes the effective frequency for each point.

Table 17: Effective Frequency for Points on Blade

Point	1	2	3	4	5	6	7	8
Effective Frequency (kHz)	0-20	0-20	0-20	0-20	5-20	5-20	5-20	5-20

The points located in the structural region have a measurable response across the entire frequency range. In comparison, the points located in the aerodynamic region experience a rapid drop in effective frequency as the distance from the actuator increases. In addition, the time signal also shows a drop off in amplitude due to the decreasing energy transferred to the sensor, as shown in [Figure 35](#), where red = point 3, black = point 4, orange = point 5 and green = point 6 for a burst random input.



Figure 35: Comparison of time signal responses for points 3, 4, 5, and 6

C.4 Preload Test

In addition to temperature variation, wind turbine blades experience significant variation in loads. Since SHM needs to distinguish damage from load variation, a study of the effect of loading on the blade was performed. With the blade in the fixed-free configuration, various displacements at the tip were applied upward in the vertical direction to simulate an operational load that might change the response. [Figure 36](#) is a FRF overlay for a random signal response at point 1, with the green line the baseline, the black line 1 inch, and the red line 1.5 inches of tip displacement, bending the blade in the lead-lag direction.

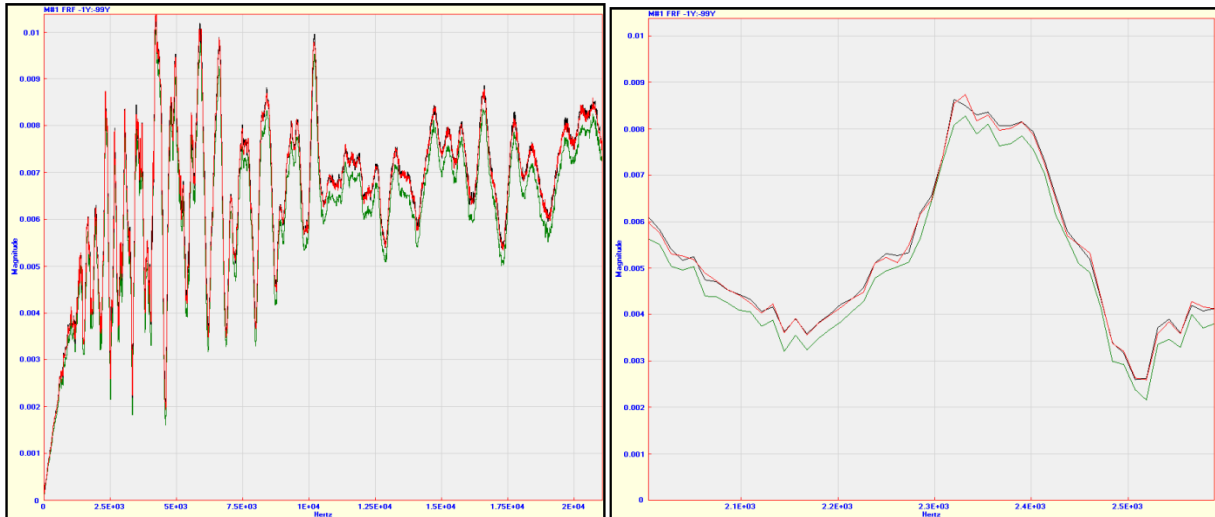


Figure 36: Comparison of preloads over entire frequency range (left) and zoom in for one peak (right)

As shown, the addition of the preload does not have an effect on the frequency peaks. The magnitude, however, is noticeably changed by the preload, and further study will be needed to determine a way to detect damage with the changing operational loads.

Model-Based Diagnostics and Fault Assessment of Induction Motors with Incipient Faults

Mohsen Nakhaeinejad¹, Jaewon Choi², Michael D. Bryant³

Department of Mechanical Engineering

The University of Texas at Austin, Texas 78712

¹mohsenn@mail.utexas.edu, ²jaewon.choi.eng@gmail.com, ³mbryant@mail.utexas.edu

ABSTRACT

Model-based diagnostics is relatively new for machine condition monitoring. Unlike signal-based approaches, health metrics are evaluated via physics-based models and sensor measurements. In this article, a framework of model-based fault diagnosis and severity assessment for induction motors is presented. A conventional symmetric induction motor model is suitable for simulation but cannot capture faulty behavior accurately. Induction motor is modeled in detail using vector bond graph technique. Staged faults are induced in simulation to emulate broken rotor bar, stator winding fault and bearing faults. Extended Kalman Filter (EKF) technique estimates and tunes parameters of the model to detect faults. Changes of the model parameters pinpoint degradation and faults of the actual system. Fault severity assessment is performed using Channel capacity technique, a novel health metric based on Shannon's information theory. Results suggest that stator winding faults and broken rotor bars can be detected with model-based diagnostics.

Keywords: Model-Based Diagnostics, Condition Monitoring, Induction Motor, Extended Kalman Filter, Health Assessment, Fault Isolation

1 Model Based Diagnostics

Machines break down due to wear, crack, lubricant issues, external impacts, faulty electronics, and so on. The economic losses often exceed the repair expenses itself [1]. Machine maintenance requires expertise, effort, time and most of all perseverance. Industry requires diagnostics packages, which might be constructed based on advanced diagnostics algorithm. But, they should be designed in such a way to be used by technicians.

Faults and degradation in machines are related to the change of states, parameters, or process. A model-based diagnostic system consisting of physics-based model, parameter tuning module, and decision making unit tracks changes of states and parameters to detect degradation and faults. Model Based Diagnostics (MBD) is based on fundamentals as tools for fault detection and isolation (FDI) [2]. Different from signal based approaches [3], MBD relies on constitutive laws of physics and

information theory. MBD is well suited for system level faults as well as component faults [4]. In MBD, models interpret signals and locate faults. Parameter tuning is for extracting health information from signals. Fault locations are isolated from parameter values. Health condition assessment via Shannon's theorem of information and signals [5] provides reliable diagnostics because it is based upon the principles that all telecommunication industry stands on. Figure 1 illustrates the framework of induction motor fault diagnosis as an example of the general model based diagnostic/prognostic approach. For other systems, such as pump, gear, turbine, and etc., sensors and model are changed, but the rest of approach is same. Prognosis of future health is performed by extracting parameter values and simulating performance.

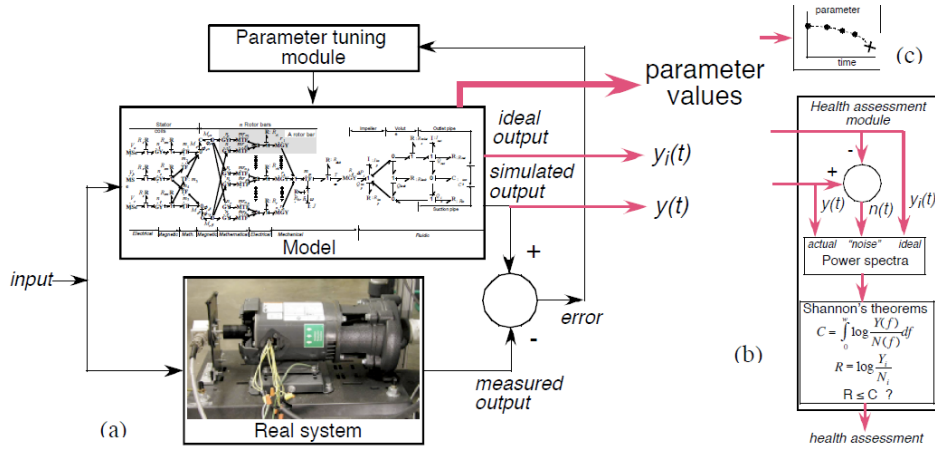


Fig. 1. Model-based diagnostics framework with health assessment unit

This article illustrates model-based diagnostics of induction motors. A detailed induction motor model is key to successful diagnostics. The detailed bond graph model and dynamic equations will be discussed in the next section. The principles of parameter tuning will be explained. Continuous-discrete extended Kalman Filter (EKF) is employed for parameter estimation. Shannon's information theory and channel capacity analogy for machine diagnostics will be illustrated for fault assessment. Sensor selection will be discussed in terms of observability analysis. Fault isolation is explained based on the simulation results. Finally, the general procedures of MBD are re-summarized.

2 Induction Motor Models

A detailed induction motor model is essential for successful diagnostics. Kim and Bryant developed a bond graph model [6,7] of induction motors. The model is reconstructed into the vector bond graph as shown Figure 2. The model is a universal model of induction motors with emphasis on correspondence to the physical details. Real induction motors may vary in size, shape, and parameters. But, the physics is the same and the proposed bond graph model is still valid.

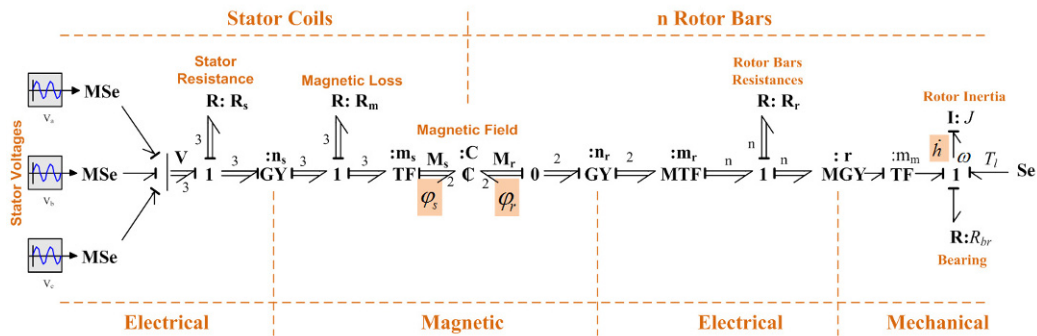


Fig. 2. Vector bond graph model of 3-phase induction motors

The vector bond graph clarifies the direction of power flow. A 3ph voltage source supplies power to the stator coils. The stator currents induce a rotating magnetic field (\mathbf{M}) and magnetic flux (ϕ) in the air gap. Equation (1) relates \mathbf{M} to ϕ of the rotor and stator windings.

$$\begin{bmatrix} \mathbf{M}_{s\alpha} \\ \mathbf{M}_{s\beta} \\ \mathbf{M}_{r\alpha} \\ \mathbf{M}_{r\beta} \end{bmatrix} = \begin{bmatrix} \mathbf{M}_s \\ \mathbf{M}_r \end{bmatrix} = \begin{bmatrix} a & 0 & b & 0 \\ 0 & a & 0 & b \\ b & 0 & c & 0 \\ 0 & b & 0 & c \end{bmatrix} \begin{bmatrix} \varphi_{s\alpha} \\ \varphi_{s\beta} \\ \varphi_{r\alpha} \\ \varphi_{r\beta} \end{bmatrix} = \begin{bmatrix} \mathbf{C}_a & \mathbf{C}_b \\ \mathbf{C}_b & \mathbf{C}_c \end{bmatrix} \begin{bmatrix} \varphi_s \\ \varphi_r \end{bmatrix} \quad (1)$$

where $a = \frac{n_s^2 L_r}{L_s L_r - L_m^2}$, $b = \frac{-n_s n_r L_m}{L_s L_r - L_m^2}$, $c = \frac{n_r^2 L_s}{L_s L_r - L_m^2}$ and $n_{r,s}$ is number of turns, $L_{r,s}$ is self-inductance, and L_m is mutual inductance.

The transformations between the electrical to the magnetic domains and the electrical to the mechanical domains are performed via matrix multiplication defined in the appendix. Energy loss (\mathbf{R}) is represented by electrical and magnetic resistances. The stator resistance matrices are 3 by 3 diagonal matrices, and the rotor resistance is represented by a n by n diagonal matrix. The input is a three phase voltage \mathbf{V} . The system of differential equations of the induction motor model is summarized in Equations (2-6). Equations (2-3) are the differential equations of stator and rotor fluxes. Equations (4-6) are the mechanical rotor dynamics equations.

$$\dot{\phi}_s = \mathbf{m}_s^T \mathbf{n}_s^{-1} [\mathbf{V} - \mathbf{R}_s \mathbf{n}_s^{-1} \mathbf{m}_s (\mathbf{C}_a \phi_s + \mathbf{C}_b \phi_r) - \mathbf{R}_m^{-1} \mathbf{n}_s \mathbf{R}_s^{-1} \mathbf{V} + \mathbf{R}_m^{-1} \mathbf{m}_s (\mathbf{C}_a \phi_s + \mathbf{C}_b \phi_r)] \quad (2)$$

$$\dot{\phi}_r = \mathbf{n}_r^{-1} \mathbf{m}_r \mathbf{R}_r \mathbf{m}_r^T (\mathbf{C}_b \phi_s + \mathbf{C}_c \phi_r) - \mathbf{n}_r^{-1} \mathbf{J}^{-1} \mathbf{m}_m^{-1} \mathbf{m}_r \mathbf{h} \quad (3)$$

$$\dot{\mathbf{h}} = -\mathbf{R}_{br} \mathbf{J}^{-1} \mathbf{h} - \mathbf{r}^T \mathbf{m}_r^T \mathbf{n}_r^{-1} (\mathbf{C}_b \phi_s + \mathbf{C}_c \phi_r) \quad (4)$$

Motor speed ω and shaft position θ can be obtained from

$$\dot{\theta} = \mathbf{J}^{-1} \mathbf{m}_m^{-1} \mathbf{h} \quad (5)$$

$$\omega = \mathbf{J}^{-1} \mathbf{h} \quad (6)$$

A detailed model with properly tuned parameters should be able to emulate measured signals accurately. For model validation, [Figure 3](#) compares simulated vs. experimental stator current I_1 , and motor speed ω . [Table 1](#) summarizes the motor specifications. The experiment was run with a 1/2 HP 3-phase induction motor at no load condition. Hall effect sensors and a rotary encoder measured currents and speed respectively. The encoder coupled via a long shaft, which was not part of the motor model, induced high frequency vibration. Beside those small errors, model simulations overlay measurements.

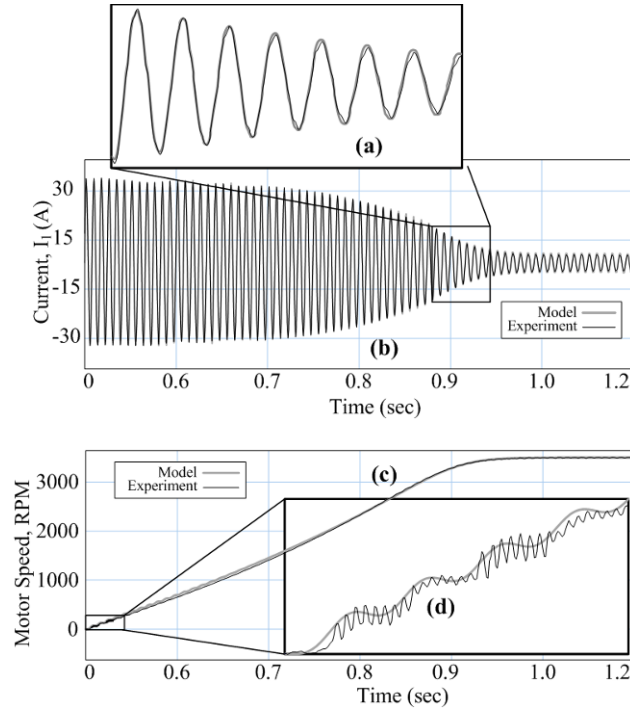


Fig. 3. Simulation vs. experiment: stator current (a,b) and motor speed (c,d)

Table 1. Induction Motor Model Parameters

Parameter	Value
Number of rotor coil turns, n_r	1
Number of stator slots, n_s	111
Number of rotor bars, n	34
Number of poles, p	2
Stator coil resistance, $R_{s1,s2,s3}$ [Ω]	2.1
Stator magnetic losses, $R_{m1,m2,m3}$ [$1/\Omega$]	0.03539
Rotor bar resistance, $R_{r1,r2, \dots, r34}$ [Ω]	0.8663
Stator inductance, L_s , [H]	1.02938
Rotor inductance, L_r , [H]	0.9834
Mutual inductance, L_m , [H]	1.00130
Bearing friction, R_{br} , [Ns/m]	0.0085
Moment of inertia, J , [kg m^2]	0.0115

3 Parameter Tuning

Parameter tuning is key to successful diagnostics. Parameter values represent the *internal physical condition* of a machine [2,4]. Those values can be measured from sensor signals, using the motor model of the previous section. The dynamic motor model provides the mathematical formulas necessary to link one measurement to the rest of measurements. Therefore, a system model is essential for parameter tuning because physical laws specify relations between measurements and parameters.

Measurements are inherently subject to additive noise. Kalman filter is necessary to eliminate noise and to obtain accurate estimates [8]. Parameters tuned accurately, the errors between measurements and simulated outputs should be negligible. A popular parameter tuning method for nonlinear systems is the extended Kalman filter (EKF) with parameters augmented as states. Here, the original states are augmented with new parameters to be tuned while the rest of parameters are intact. The augmentation often results in more nonlinearity in system equations because of the products of parameter states and original

states. Accuracy of parameter tuning generally depends on the quality of initial guess of parameters [9,10]. Initial guess can be obtained from operator's experience, design specifications and physical reasoning. Also global optimization techniques can be employed to obtain good initial guesses if the first methods fail.

Parameter tuning can be implemented in off-line or on-line forms [11,12]. In off-line approach, all measurements are processed to estimate parameters at a specific time, while the online algorithm processes one measurement at a time to produce best estimates at each time step. Online methods such as EKF are better suited for real-time applications. Here, real-time monitoring of parameter values is important. Hence, extended Kalman filter technique is employed for parameter tuning.

Kalman filtering is the *fully developed* and *field-proven* technique for parameter tuning [11-15]. Kalman filters first predict future states and correct them recursively based on Kalman gain and the error between simulations and measurements. Kalman gain is the analytical solution to the error minimization problem. EKF can be implemented in discrete time or/and continuous time. Most physics-based models are developed based on the first principles. This results in continuous time system models. Measurements are typically collected at discrete times by data acquisition system. A variant of EKFs suitable to this environment is called Continuous-Discrete EKF [14], where states are integrated with a fine time step and updated via Kalman gain and innovation at the time of new measurement's arrival. Interested readers refer to the appendix for the detailed algorithms. It is emphasized that this tuning methodology can be applied for other systems such as pumps, gears, turbines, etc. The difference is only in sensors and models.

4 Fault Assessments with Channel Capacity

Bryant et al.'s channel capacity assessment [16,17] is elegantly simple, but based upon the fundamentals of celebrated Claude Shannon's theory on information and communication. Machine operation is analogous to information transmission via communication channels. A faulty channel cannot transmit information at its full capacity. Likewise, a faulty component cannot perform a task originally prescribed by designers, which results in machine malfunction. Figure 4 compares the shaft speeds of health vs. faulty systems. The channel capacity is decreased logarithmically as fault severity increases.

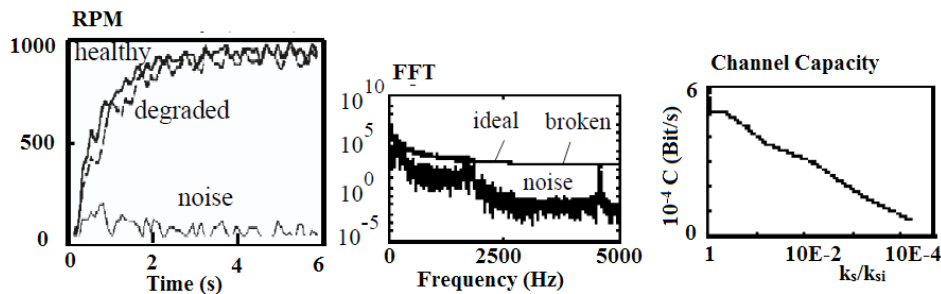


Fig. 4. Channel capacity of healthy vs. cracked shaft

Degradation of machine components becomes analogous to addition of noise to a communication channel. According to Shannon's theorem, the maximum capacity of a communication channel to transmit information in the presence of noise is defined as

$$C = \omega \log_2[(S_i + N)/N] \quad (7)$$

where S_i and N are the average power of signal and noise, and ω is the bandwidth of a communication channel.

The above equation is slightly modified for non-flat band channels as

$$C = \int_0^{\omega} \log_2[(S_i(f) + N(f))/N(f)] df \quad (8)$$

Channel capacity decreases as machine components degrade. The threshold capacity for fault detection can be defined based on Shannon's information entropy rate as

$$R = \omega \log_2(S_i/N_i) \quad (9)$$

where N_i is the maximum allowed noise power, set by the designer.

Figure 5 illustrates the changes of frequency spectra at different fault severities (from stage 0 to stage II) and the corresponding channel capacity values. The dashed line marks the threshold based on information entropy rate.

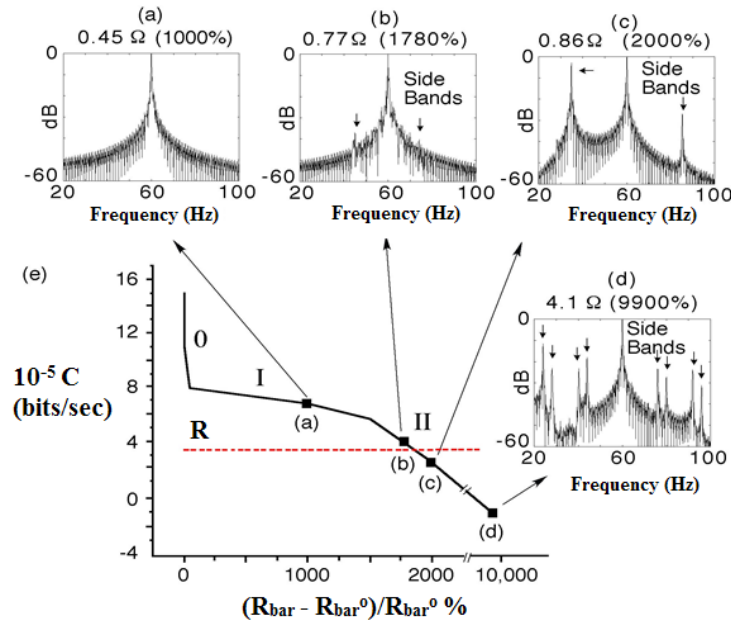


Fig. 5. Frequency spectra and channel capacity values at different fault stages [16]

Figure 6 shows the correlation between tuned rotor resistance and decreased channel capacity at different stages of broken rotor bar faults from simulation. The severity assessment is simple and reliable with channel capacity.

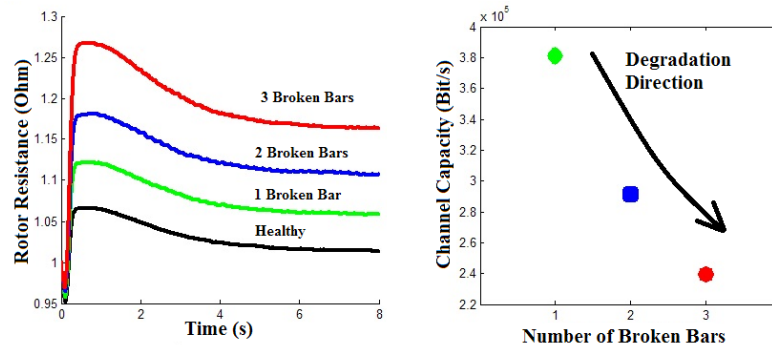


Fig. 6. Tuned rotor resistance for rotor fault and decreased channel capacity

5 Sensor Selections for System

One of the merits of model-based diagnostics is that it does not require exotic sensors. Commonly available sensing techniques are more than enough to ensure diagnosability. For motors, voltages, currents, run-outs, speed, vibration and temperature are typical measurements. Potential/current transformer, hall effect sensor, capacitive probe, encoder, accelerometer, thermocouple can be easily purchased and the corresponding sensing technologies are well documented in datasheets and manuals. The necessary devil lies in the selection of the right combination of sensors. This issue is closely related to fault observability. Observability definition is a measure for how well parameters can be inferred by information contained error signals of model outputs and measurements [15]. Figure 7 compares residuals from measurements I_1 , I_2 , I_3 and ω vs. I_1 , ω . Current residuals (a-c) and (e) look similar in amplitude while speed residual (f) is less noisy than (d). Though looked similar, the residuals (e) and (f) don't have enough information to prevent unbiased estimate happening.

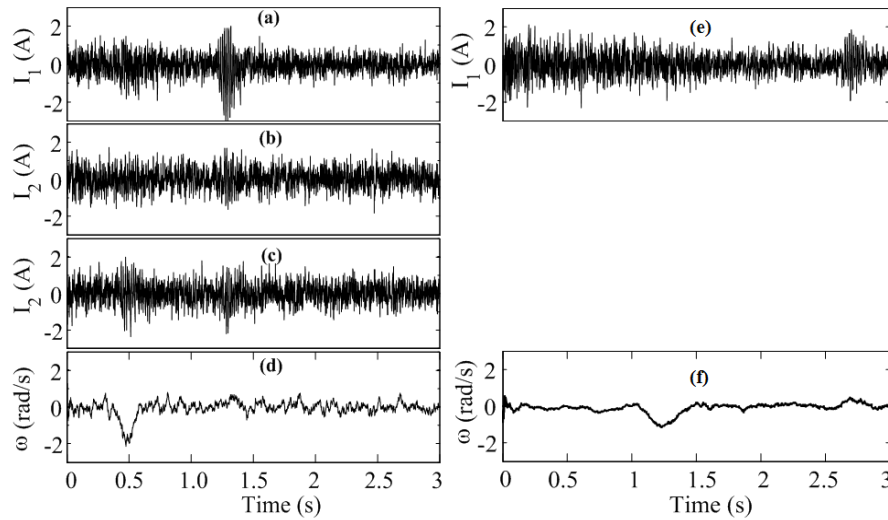


Fig. 7. Similar residuals of currents and speed signals when tuned from different measurements $I_{1,2,3}$, ω (a-d) vs. I_1 and ω (e,f)

Figure 8 compares the qualities of parameters turned from stator currents only vs. currents and speed. Lack of ω leads to biased estimation. Failed observability is manifested itself in the trip-off. This can cause a false alarm and make reliable fault detection difficult. Adding ω measurements can certainly improve accuracy. Observability analysis will define the best configuration of the sensors to provide enough information for an accurate diagnostics. The redundancy level of the sensors is also determined using the observability study.

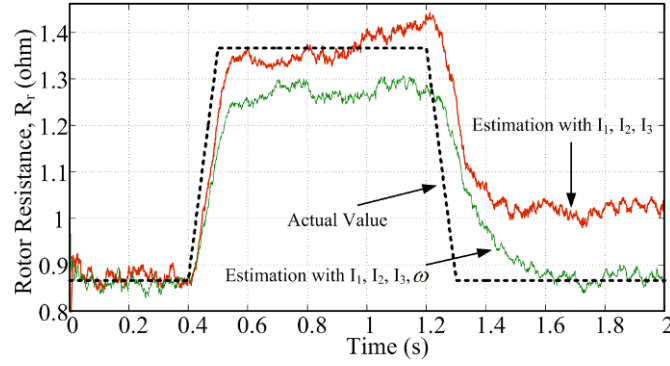


Fig. 8. Observability failed with only current measurements, observability restored by adding ω

6 Fault Isolation

Model based diagnostic simplifies fault isolation. The classification task becomes almost trivial. Table 2 shows how a suspected fault type can be isolated by simply checking the corresponding parameters. Fault isolation via classification table is a very general approach applicable to any systems. Here, this method is applied to isolate staged faults of the induction motors. Common faults of the induction motor are stator winding failure, broken rotor bar, inverter failure, bearing failure, bearing misalignment and shaft cracking [6]. Here, stator winding failure, broken rotor bar and bearing failures are tested. Stator winding fault is caused by insulation failure, manifested itself by increased stator and magnetic resistances R_{m1} and R_{s1} . Broken rotor bars limit rotor current passages and increase the rotor resistance R_r . Faulty bearings can be emulated by increased rotational damping R_{br} .

Faults can occur abruptly at any time. Such demanding conditions can show the true tracking performance of EKF employed to tune those parameters. To improve the tracking performance, EKF requires small adjustments of matrices \mathbf{Q} and \mathbf{R} [8,11,15].

Figure 9 shows the tracking results of estimated parameters, triggered by abrupt increases or decreases of the values. Two combinations of measurements are compared: unobservable I_1 and ω , vs. unobservable I_1, I_2, I_3 and ω . With observability hold, all the parameters were successfully estimated. For the sake of complete demonstration, the channel capacity of stator currents for stator faults at mild to medium fault stages is shown in Figure 10. This combined fault isolation and severity assessment can be a very powerful tool for machine diagnostics.

Table 2 Fault Classification Table

<i>Fault Type</i>	<i>Stator winding</i>	<i>Broken Rotor Bar</i>	<i>Bearing Damping</i>
R_s	Check	-	-
R_m	Check	-	-
R_r	-	Check	-
R_{br}	-	-	Check

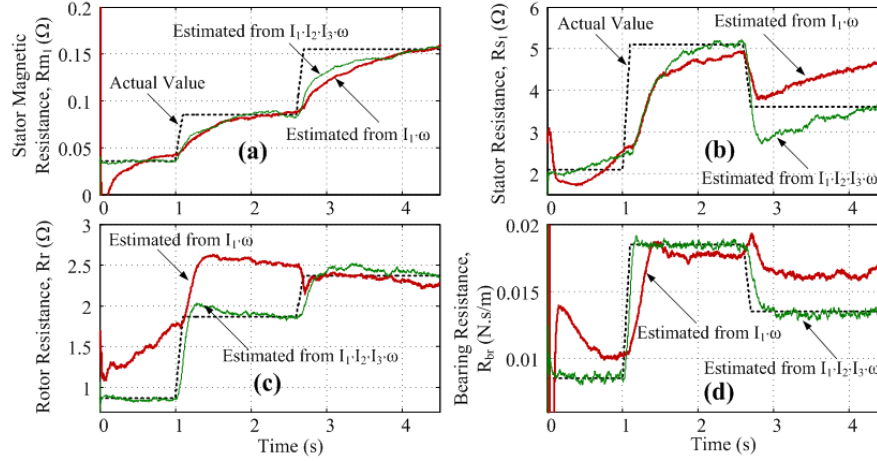


Fig. 9. Estimated parameters from two combinations of measurements: I_1, ω (unobservable) and I_1, I_2, I_3 and ω (observable). (a) magnetic resistance R_{m1} (b) stator winding resistance R_{s1} , (c) rotor resistance R_r , (d) bearings friction R_{br} .

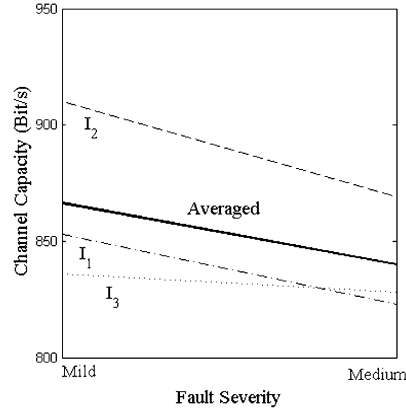


Fig. 10. Channel capacity of currents for the induction motor with mild to medium stator winding faults

7 Summary and Conclusion

General procedures of model-based diagnostics were presented with the example of the incipient faults of an induction motor. First, a detailed induction motor model was developed. An emphasis is generally put on the requirement of a physics based model with enough details so that simulation matches experiments within a marginal error. Parameter tuning was performed using extended Kalman filter (EKF). But, the general procedures do not mandate the use of EKF. Any tuning technique based on solid fundamentals of information theory will suffice. Channel capacity assessment was explained with a couple of real world examples. Though the formulas are simple, it is developed based on Shannon's ground work on communication channel. Sensor selection based on observability of the system was discussed. Such a software package that helps operators with a little background on machine diagnostics to choose right sensors will be promising. Fault isolation by checking parameters from classification table and assessing the severity via channel capacity was shown for the motor fault diag-

nostics. Results show that the model-based diagnostics can be an effective tool in detecting incipient faults of induction motors, gears, turbines, and etc.

References

- [1] Isermann, R.: Process Fault Detection Based on Modeling and Estimation Methods—A Survey. *Automatica*. 20, 387–404 (1984)
- [2] Isermann, R.: *Fault-Diagnosis Systems*. Springer, Berlin, Germany (2006)
- [3] El Hachemi Benbouzid, M.: A Review of Induction Motors Signature Analysis as a Medium for Faults Detection. *IEEE Trans. Ind. Electron.*, 47, 984–993 (2000)
- [4] Frank, P. M.: Fault Diagnosis in Dynamic Systems Using Analytical and Knowledge-Based Redundancy—A Survey and Some New Results. *Automatica*, 26, 459–474 (1990)
- [5] Shannon, C. E.: Communication in the presence of noise. *Proc. of the IEEE*, 72, 1192–1201 (1954)
- [6] Kim, J.: Bond Graph Models of a Squirrel-Cage Induction Motor and a Layshaft Gearbox for Degradation Analysis. M.S. thesis, The University of Texas—Austin, Austin, TX (1999)
- [7] Kim, J., and Bryant, M. D.: Bond Graph Model of a Squirrel Cage Induction Motor with Direct Physical Correspondence. *ASME J. Dyn. Syst., Meas., Control*, 122, 461–469 (2001)
- [8] Haykin, S. (ed.): *Kalman Filtering and Neural Networks*. John Wiley & Sons, Inc., NY (2001)
- [9] Li, P. Goodall, R. and Kadirkamanathan, V.: Estimation of Parameters in a Linear State Space Model using a Rao-Blackwellised Particle Filter. *Proc. of Control Theory Appl.*, 151, 727–738 (2004)
- [10] de Freitas, N.: Rao-Blackwellised particle filtering for fault diagnosis. *Proc. of Aerospace Conf.* 4, 767–1772 (2002).
- [11] Ljung, L.: *System Identification: Theory for Users*. Prentice Hall, Upper Saddle River, NJ (1999)
- [12] Tapley B. D., Schutz, B. E. and Born, G. H.: *Statistical Orbit Determination*. Elsevier Academic Press, Burlington, MA (2004)
- [13] Ansuji, S., Shokooch, F., and Schinzinger, R.: Parameter estimation for induction machines based on sensitivity analysis. *Ind. Appl.*, 25, 1035–1040 (1989)
- [14] Said, M. S. N., Benbouzid, M. E. H., and Benchaib, A.: Detection of broken bars in induction motors using an extended Kalman filter for rotor resistance sensorless estimation. *Energy Conv.*, 15, 66–70 (2000)
- [15] Gelb, A. (ed.): *Applied Optimal Estimation*. MIT Press, Cambridge MA (1974)
- [16] Bryant, M. D.: Application of Shannon's Communication Theory to Degradation Assessment of Systems. *Proc. ASME Congress*, New York, 72, 1192–1201 (1998)
- [17] Lee, S., Bryant, M. D. and Karlapalem, L.: Model-and Information Theory-Based Diagnostic Method for Induction Motors. *J. Dyn. Sys., Meas., and Control*, 128, 584–591 (2006)

Appendix 1: Transformation Matrices

Transformation matrices \mathbf{m}_s and \mathbf{m}_r are the moduli of transformers from the stator phases to the α - β phases, and from the rotor phases to the α - β phases, respectively. \mathbf{r} is the modulus of transformation from the electrical to the mechanical domain. The diagonal matrices \mathbf{n}_s and \mathbf{n}_r are the transformation moduli from the electrical to the magnetic domains. The diagonal entries are the numbers of turns of stator windings in the natural frame and rotor windings in α - β reference frame.

$$\mathbf{m}_s = \sqrt{\frac{2}{3}} \begin{bmatrix} \cos(0) & \cos(2\pi/3) & \cos(4\pi/3) \\ \sin(0) & \sin(2\pi/3) & \sin(4\pi/3) \end{bmatrix}$$

$$\mathbf{m}_{\mathbf{r}(2 \times n)} = \sqrt{\frac{2}{n}} \begin{bmatrix} \cos \theta & \cos(\theta + 2\pi/n) & \dots & \cos[\theta + 2(k-1)\pi/n] \\ \sin \theta & \sin(\theta + 2\pi/n) & \dots & \sin[\theta + 2(k-1)\pi/n] \end{bmatrix}$$

$$\mathbf{r}_{(1 \times n)} = \sqrt{\frac{2}{n}} \begin{bmatrix} \varphi_{r\alpha} & -\varphi_{r\beta} \end{bmatrix} \begin{bmatrix} \cos \theta & \cos(\theta + 2\pi/n) & \dots & \cos[\theta + 2(k-1)\pi/n] \\ \sin \theta & \sin(\theta + 2\pi/n) & \dots & \sin[\theta + 2(k-1)\pi/n] \end{bmatrix}$$

where $k = 1, 2, \dots, n$.

Appendix 2: Extended Kalman Filter Algorithm

Extended Kalman Filter consists of two recursive steps: prediction and innovation. First, states are numerically integrated from the previous observation time to the current time. It starts with initial guess of states and error covariance matrix of states. Since the best estimates are available at subsequent steps, the best estimates serve as new initial guesses for next steps.

$$\hat{\mathbf{X}}_{0|0} = E[\mathbf{X}(t_0)] \quad \text{and} \quad \hat{\mathbf{P}}_{0|0} = E[(\mathbf{X}(t_0) - \hat{\mathbf{X}}_{0|0})(\mathbf{X}(t_0) - \hat{\mathbf{X}}_{0|0})^T]$$

States and covariance matrix are propagated from the previous step ($k-1|k-1$) to the current step ($k|k-1$) via state differential equations and linearized covariance differential equations:

$$\begin{cases} \dot{\mathbf{X}}(t) = \mathbf{f}(\mathbf{X}(t), \mathbf{u}(t), t), & \text{with initial condition } \hat{\mathbf{X}}_{k-1|k-1} \\ \dot{\mathbf{P}}(t) = \mathbf{A}(t)\mathbf{P}(t) + \mathbf{P}(t)\mathbf{A}(t)^T + \mathbf{Q}(t), & \text{with initial condition } \hat{\mathbf{P}}_{k-1|k-1} \end{cases}$$

Note the linear covariance propagation because \mathbf{A} matrix is the Jacobian of nonlinear state differential equations, evaluated based on the predicted state at the current time step:

$$\mathbf{A}(t) = \left. \frac{\partial \mathbf{f}}{\partial \mathbf{X}} \right|_{k|k-1}$$

The update step corrects the predicted states and covariance matrix based on Kalman gain \mathbf{K}_k and innovation:

$$\mathbf{K}_k = \mathbf{P}_{k|k-1} \mathbf{H}_k^T (\mathbf{H}_k \mathbf{P}_{k|k-1} \mathbf{H}_k^T + \mathbf{R})^{-1}$$

$$\hat{\mathbf{X}}_{k|k} = \mathbf{X}_{k|k-1} + \mathbf{K}_k [\mathbf{Y}_k - \mathbf{h}(\mathbf{X}_{k|k-1}, t_k)]$$

$$\hat{\mathbf{P}}_{k|k} = (\mathbf{I} - \mathbf{K}_k \mathbf{H}_k) \mathbf{P}_{k|k-1}$$

$$\text{where } \mathbf{H}_k = \left. \frac{\partial \mathbf{h}}{\partial \mathbf{X}} \right|_{k|k-1}$$

These prediction and correction steps repeat until the final time.

Use of the cepstrum to remove selected discrete frequency components from a time signal

R.B. Randall, N. Sawalhi

School of Mechanical and Manufacturing Engineering, University of New South Wales, Sydney 2052

ABSTRACT

In machine diagnostics there are a number of tools for separating discrete frequency components from random and cyclostationary components. This is the basis of separating gear (deterministic) from bearing (second order cyclostationary) signals for example. Time synchronous averaging (TSA) requires a separate operation, including resampling, to be carried out for each periodic frequency, and the method cannot be used for discrete frequency sidebands, or partial bandwidth spectra. Self adaptive noise cancellation (SANC) and discrete/random separation (DRS) remove all discrete frequencies, whether harmonics or sidebands, and it is not possible to decide if some should be left. The method proposed here uses the cepstrum to localise discrete frequency components, which manifest themselves as harmonic or sideband families. Selected families can be removed in the cepstrum, leaving any it might be desirable to retain, and generating a notch filter that is flexible enough to allow for small speed fluctuations, or even narrow band noise peaks that sometimes result from slight random modulation of periodic signals. Normally, to edit the cepstrum and return to the time domain, it is necessary to use the complex cepstrum, but the latter requires the phase signal to be unwrapped. This is not possible for response signals containing discrete frequencies and noise, where the phase is not continuous. The procedure proposed here uses the real cepstrum to localise and edit the log amplitude of the original signal, removing the unwanted discrete frequency components, and then combines the edited amplitude with the original phase spectrum to return to the time domain. The paper shows how this technique can be used to remove discrete frequency components from signals measured on two machines with a faulty bearing, and then perform envelope analysis on the residual signal to diagnose the bearing fault. One is a gear test rig for which the discrete frequencies are harmonics of the shaft speed and gearmesh frequency, and the other a bladed disc test rig for which the discrete frequencies are harmonics of the shaft speed and blade-pass frequency. Envelope analysis can be done on both full bandwidth and partial (zoom) bandwidth signals, the latter to save on computation, and restrict the amount of discrete frequency components to be removed, since the signal envelope is independent of frequency shifts.

1. Introduction

Signal processing used for condition monitoring purposes is usually concerned with separating various signal components from each other, so as to identify changes in any one of them. This has to be done blind, since measured responses are a sum of components from a multitude of sources, and include deterministic (discrete frequency at constant speed), stationary random, and cyclostationary random components. The latter are typically produced by modulation of random signals by discrete frequencies, and are often produced by rotating and reciprocating machines.

A fundamental division is into discrete frequency and random components (both stationary and cyclostationary) for which a number of techniques have been developed over the years. This will normally separate gear from bearing signals, for example, since the former are deterministic and phase-locked to shaft speeds, whereas the latter can be treated as cyclostationary. As pointed out in [1], the signals generated by local faults in rolling element bearings are actually “pseudo-cyclostationary”, since the repetition frequency is affected by random slip, and is not known exactly in advance, but the signals can still be treated as cyclostationary for envelope analysis. The signals produced by bearings with extended spalls are truly cyclostationary if the discrete carriers (such as gearmesh harmonics) are modulated at a fixed cyclic frequency (shaft speed for an inner race fault), the roughness of the spall surface introducing randomness in the modulation, and allowing separation from deterministic gear faults.

Where the deterministic components are of primary interest, such as in gear diagnostics, the best separation method is undoubtedly time synchronous averaging (TSA) [2, 3], where a separate signal is obtained for each fundamental period over which the averaging is performed (typically a different result obtained for each individual gear in a complex gearbox). It can be used to obtain the residual signal after removal of all deterministic components [4], but is quite arduous since the signal has to be separately order tracked for each independent shaft speed (eg in a gas turbine engine) and in any case resampled to an integer number of samples per period for each periodicity even after order tracking (removal of small speed fluctuations by resampling at uniform increments in rotation angle rather than time). After removing all discrete components, the signal has to be converted back to a time axis by reverse mapping. This procedure does however result in the least disruption of the residual signal, though this is rarely necessary. It is limited to the removal of harmonics only, and will not for example remove modulation sidebands, unless these are also harmonics of one of the fundamental frequencies. The process also only works over the full frequency band, including zero frequency, and cannot be used for partial bands (eg from zoom).

Where the primary interest is in removing the discrete frequency components so as to obtain the random residual, often dominated by bearing signals in certain frequency bands, other methods have been developed which are based on the different correlation length of discrete frequency and random signals. The first is SANC (self adaptive noise cancellation) [5], which is a modification of ANC (adaptive noise cancellation). The latter procedure has two input signals, a primary signal containing a mixture of two components to be separated, and a reference signal containing only one. This does not have to be identical to the corresponding component in the primary signal, just coherent with it. An adaptive filter finds the linear transfer function between the two versions and subtracts the corresponding component from the primary signal, leaving the other in the residual. It has been used to separate gear and bearing signals in situations where the primary signal was measured on a faulty bearing in a gearbox, and the reference signal on another remote bearing with no fault signal present [6, 7]. In SANC, the reference signal is a delayed version of the primary signal, with a delay just longer than the correlation length of the random component, so that only the deterministic part is recognized by the adaptive filter. In Ref. [8], it was shown how the same effect could be achieved much more efficiently by the so-called “Discrete/Random Separation” (DRS) technique, using efficient FFT processing in the frequency domain. The transfer function between the primary signal and its delayed version (thus representing only the deterministic part) is calculated in the same way as the H_1 frequency response function (FRF). This thus has a value near one at discrete frequencies, and near zero at other frequencies. It is used to filter the whole signal by “fast convolution” in the frequency domain, and once again allows the deterministic part to be separated out and the random residual signal to be obtained by subtraction.

For both the SANC and DRS procedures, all discrete frequency components are removed, as long as they have a correlation length longer than the delay time. The correlation length of bearing signals is generally short in the vicinity of the high frequency resonances that are normally demodulated for diagnostic envelope analysis. For example, it is normal for the random slip in bearings to give about 1% variation in the characteristic fault frequencies. It is common for the resonance frequencies excited by the bearing faults to be two orders of magnitude higher than the repetition frequency, in which case the harmonic orders above about 50 will be smeared together, and this is the same as saying that the correlation length is shorter than the pulse spacing. If a bearing frequency is 100 Hz, but the demodulated resonance at about 10 kHz, the 1% variation will correspond to 100 Hz, and thus a correlation length of about 10 ms. The delay would then typically be set > 30 ms. DRS can operate on partial band signals obtained by selecting only the frequency band to be demodulated, using so-called Hilbert transform techniques, based on a one-sided frequency spectrum with positive frequencies only. It can easily be shown that the frequency shifting involved does not change the amplitude (envelope) of the demodulated signal, which can thus be used for diagnostics based on envelope analysis. It does however give a notch filter of fixed width, which can have detrimental effects at high and low frequencies. At low frequencies (eg low harmonics of the bearing frequencies if they exist) the bearing harmonics may still be within the bandwidth of the comb filter and they may be treated as discrete frequencies. At high frequencies, some random modulation of the discrete frequency components may be left in the form of a narrow band noise, and thus not completely removed. This can occur at harmonics of blade-pass frequencies in turbo-machines, because the transmission of the blade-pass signals to the casing is via a turbulent fluid rather than a mechanical connection.

The method proposed in the current paper gives some advantages compared with all the above-mentioned techniques. It can be used to remove selected discrete frequency components in one operation, without order tracking as long as the speed variation is limited, but can leave some periodic components if desired. It can operate on partial band (zoom) signals, at least in the same sense as the DRS technique, where it is only the envelope of the residual signal that is of interest. It is based on the cepstrum of the signal, which very efficiently collects spectral components that are uniformly spaced, ie both harmonics and modulation sidebands.

2. The cepstrum

The cepstrum has a number of versions and definitions, but all can be interpreted as a “spectrum of a log spectrum”. The original definition [9] was the “power spectrum of the log power spectrum”, but even though one of the authors (Tukey) was a co-author of the FFT algorithm, Ref. [9] pre-dated the latter, and was thus from the era before the FFT. The definition of the cepstrum was later revised (post FFT) [10] as the “inverse Fourier transform of the log spectrum”, this giving a number of advantages compared with the original definition. It can thus be represented as:

$$C(\tau) = \mathfrak{F}^{-1}[\log(X(f))] \quad (1)$$

where

$$X(f) = \mathfrak{F}[x(t)] = A(f)\exp(j\phi(f)) \quad (2)$$

in terms of its amplitude and phase

so that

$$\log(X(f)) = \ln(A(f)) + j\phi(f) \quad (3)$$

When $X(f)$ is complex, as in this case, the cepstrum of Equation (1) is known as the “complex cepstrum”, although since $\ln(A(f))$ is even and $\phi(f)$ is odd, the complex cepstrum is real-valued.

Note that by comparison, the autocorrelation function can be derived as the inverse transform of the power spectrum, or:

$$R_{xx}(\tau) = \mathfrak{F}^{-1}\left[|X(f)|^2\right] = \mathfrak{F}^{-1}\left[A^2(f)\right] \quad (4)$$

When the power spectrum is used to replace the spectrum $X(f)$ in Equations (1) and (4), the resulting cepstrum, known as the “power cepstrum” is given by:

$$C_{xx}(\tau) = \mathfrak{F}^{-1}\left[2 \ln(A(f))\right] \quad (5)$$

and is thus a scaled version of the complex cepstrum where the phase of the spectrum is set to zero. The term “real cepstrum” is sometimes used to mean the inverse transform of the log amplitude, thus not having the factor 2 in Equ. (5). It thus corresponds to the complex cepstrum obtained from Equ. (3) where the phase has been set to zero.

Note that before calculating the complex cepstrum, the phase function $\phi(f)$ must be unwrapped to a continuous function of frequency. This is often possible for frequency response functions, where the phase is continuous, and quite often related to the log amplitude (for minimum phase functions they are related by a Hilbert transform). However, it is not possible for response signals containing a mixture of discrete frequency components, for which the phase is undefined between components, and random signals for which the phase is discontinuous.

3. The Proposed Method

Editing in the real cepstrum has been used for some time to remove harmonics and/or sidebands from the spectrum, as illustrated in Fig. 1 [11]. Note that in this respect, periodic notches in the log spectrum also give components in the cepstrum, so there will be a tendency for the residual spectrum to be continuous at the former positions of discrete frequency components after removal.

In cases where it is desired to remove discrete frequency components, but leave a random residual signal with the same envelope (ie, no essential change in phase), it was realized that it would be possible to remove the discrete frequency components using the real cepstrum as in Fig. 1, but then generate the time signal of the random residual using the original phase spectrum. This would be in error only at the frequencies corresponding to the removed components, but these would be relatively few in number, and the corresponding amplitudes reduced to the same level as the adjacent random components. As mentioned, the act of setting cepstrum values to zero means that the residual log spectrum will tend to be continuous across the gap where the discrete frequencies have been removed, and for a random signal this gives the best estimate of the amplitude of the spectrum at those frequencies.

The proposed method is thus shown schematically in Figure 2.

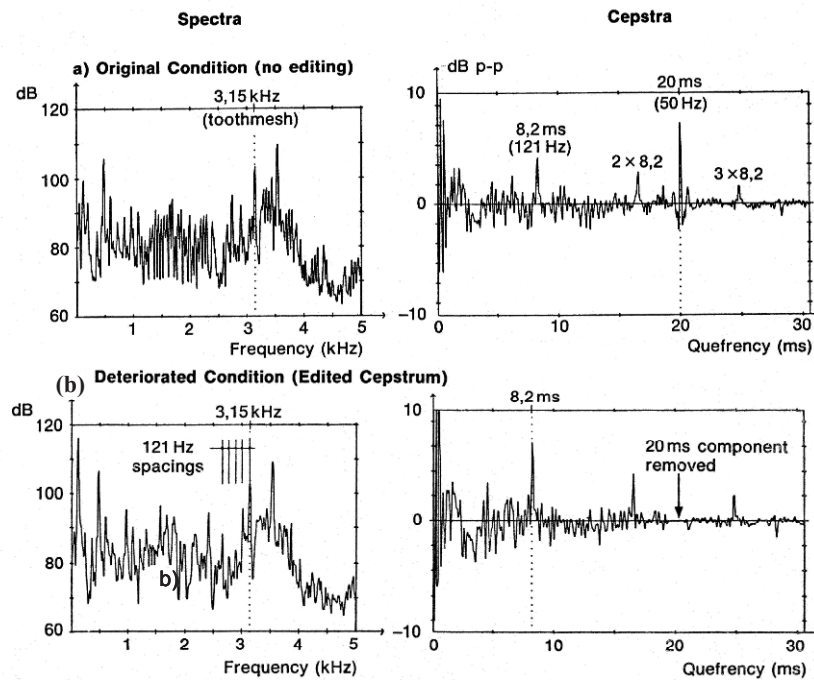


Figure 1 Editing in the cepstrum to remove a particular family of harmonics
 (a) Spectrum and cepstrum with two families of harmonics/sidebands
 (b) Spectrum with only one family retained, after editing the other family from the cepstrum

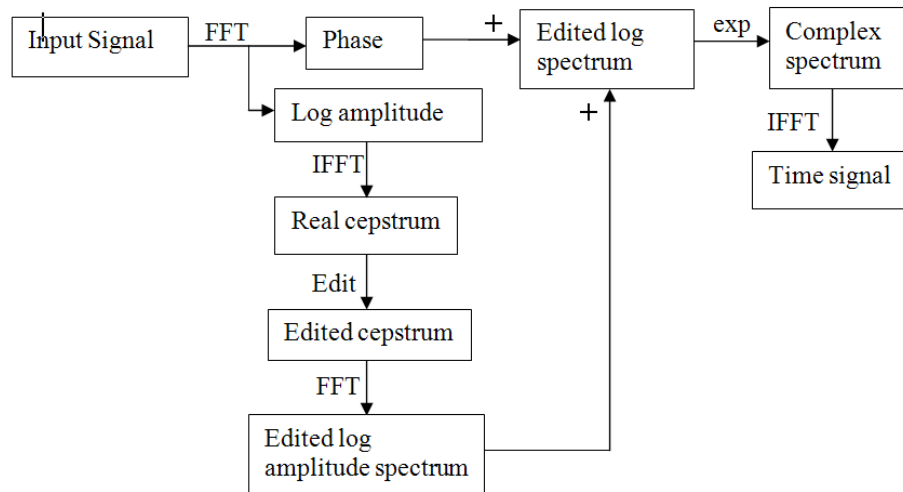


Figure 2: Schematic diagram of the cepstral method for removing selected families of harmonics and/or sidebands from time signals

Sections of the input signal are transformed to the frequency domain using the FFT algorithm. The phase is stored, while the log amplitude is processed using the IFFT (inverse fast Fourier transform) to obtain the real cepstrum. Families of “rahmonics” (uniformly spaced components in the cepstrum), corresponding to the families of harmonics and sidebands it is desired to remove from the signal, are set to zero as in Fig. 1, and the edited cepstrum transformed by a forward FFT to the edited log amplitude spectrum. This is then recombined with the original phase spectrum to form the complex log spectrum, which can be exponentiated to obtain it in rectangular (real and imaginary parts) rather than polar form

(log amplitude and phase). This complex spectrum can then be inverse transformed to obtain the time signal of the residual random part.

4. Results and Discussion

The new cepstral technique was applied to signals measured on two test rigs. One is the UNSW gear test rig illustrated in Figure 3. The rig is driven by a variable speed electric motor, but torque load can be increased using a circulating power loop involving a hydraulic pump supplying a hydraulic motor. For these tests, the motor was run at 10 Hz, with 50 Nm torque load, and two 32-tooth spur gears in mesh. A bearing with an inner race fault was inserted in the bottom right location in the diagram, and signals measured by an accelerometer on the casing immediately above it.

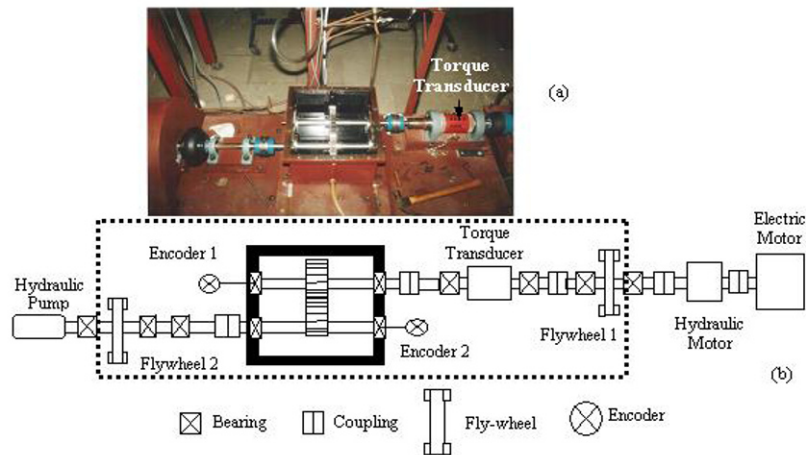


Figure 3: (a) spur gear test rig (b) schematic Diagram of the spur Gearbox Rig (Components of interest contained in dotted box)

Figure 4 compares the time signals for two separation methods, TSA and the new cepstral method, with the original signal. It is seen that removal of the gear signals reveals the hidden bearing signals, with a slightly better result achieved using TSA. It will be noted that even though this is an inner race fault, the expected modulation once per revolution (the rate at which the fault passes through the load zone) is not very strong in this case.

Figure 5 shows the corresponding power spectra up to 3 kHz (this being the band dominated by the gearmesh signal). Harmonics of the gearmesh frequency 320 Hz are indicated by a harmonic cursor in the spectrum of (a), and these can be seen to be surrounded by sidebands, which are spaced at shaft speed 10 Hz, the rotational speed of both gears. It can be seen that these discrete frequency components have been removed in both residual signals, for which the spectra are very similar.

Finally, Figure 6 shows the corresponding envelope spectra for the three signals. For the raw signal of Fig. 6(a) this is seen to be dominated by harmonics of shaft speed, including gearmesh frequency 320 Hz, even though some harmonics of BPFI (ballpass frequency, inner race) can be detected with some difficulty. Both residual signals give a clear diagnosis of the inner race bearing fault, though modulation sidebands spaced at shaft speed are more evident around the higher harmonics above about 350 Hz. This corresponds with the fact that the modulation is not very strong in the time signals.

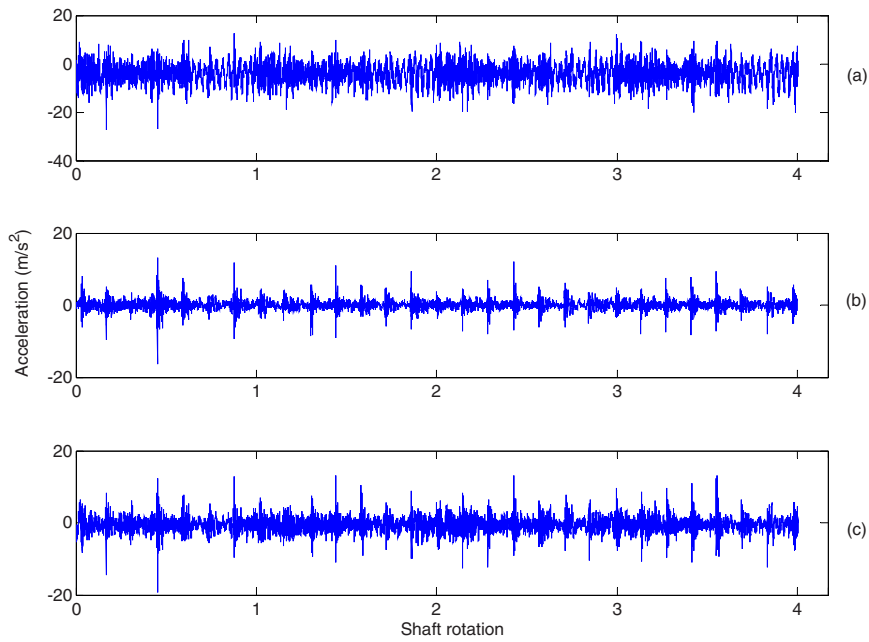


Figure 4: Time domain signals for gearbox test rig (a) Raw signal (b) Residual signal (after removing the synchronous average) (c) Residual signal after editing the Cepstrum to remove the shaft harmonics

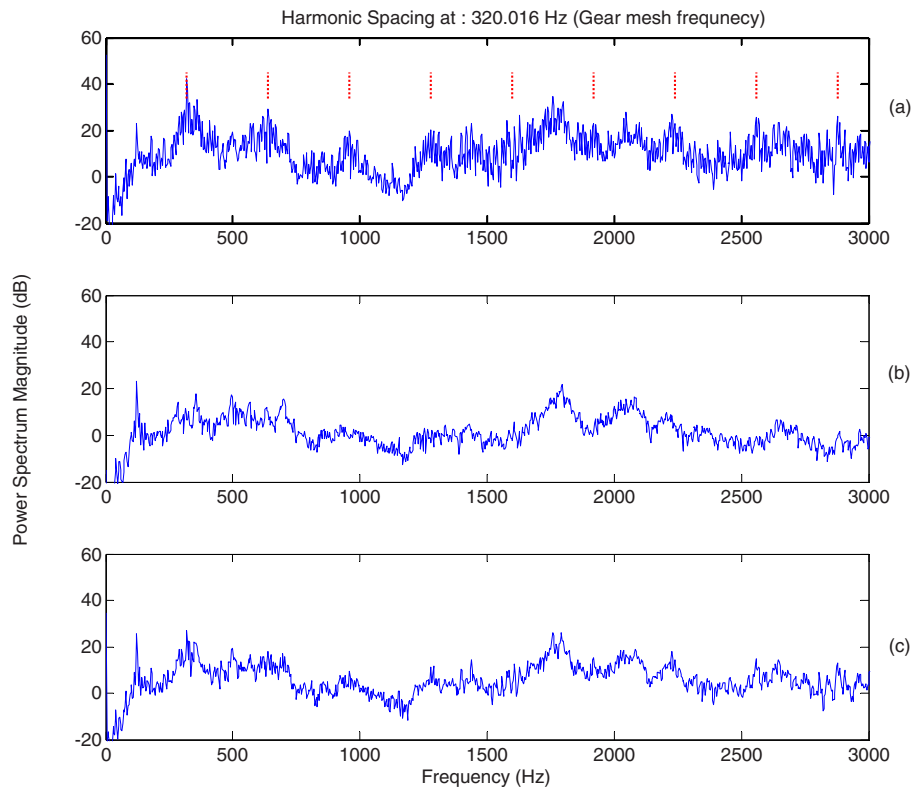


Figure 5: Power spectra for the time signals of Fig. 4 (a) Raw signal (b) Residual signal (after removing the synchronous average) (c) Residual signal after editing the Cepstrum to remove the shaft harmonics

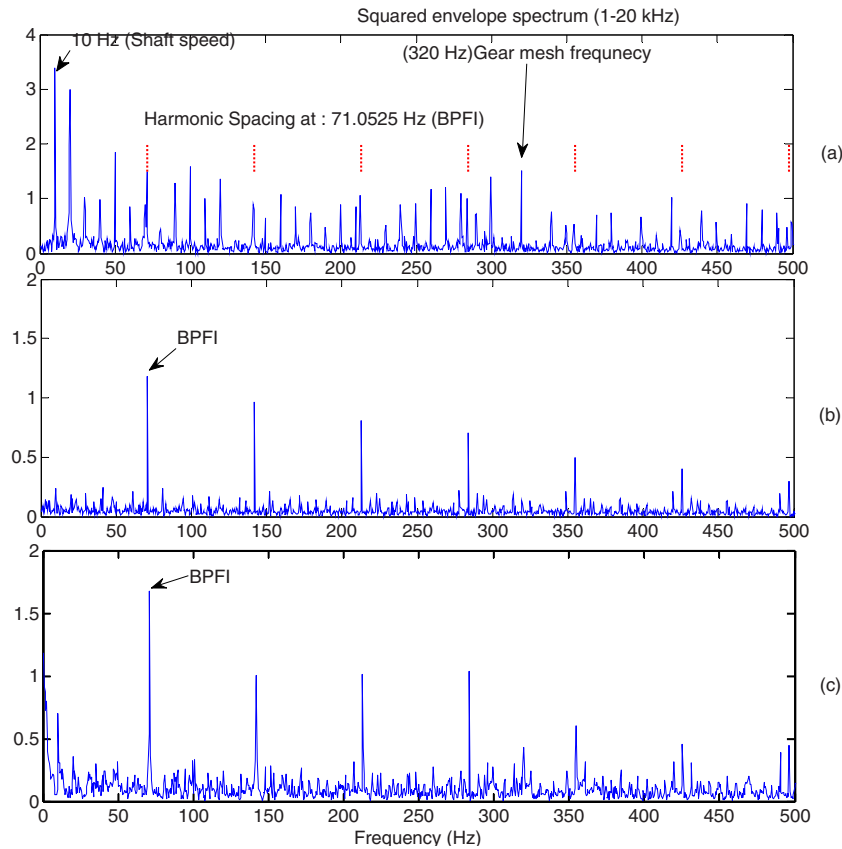


Figure 6: Squared envelope spectra (1-20 kHz) (a) raw signal (b) Residual signal (after removing the synchronous average) (c) Residual signal after editing the Cepstrum to remove the shaft harmonics

Measurements were also made on another test rig designed to study the signals from a rotating bladed disc, which can be run over a range of speeds. The shaft is supported by two self-aligning, double row ball bearings, in one of which an outer race fault was inserted, and on which acceleration measurements were made. The rotor has 19 flat blades, and because of its inefficiency as a fan, produces multiple harmonics of the bladepass frequency as well as sidebands around these spaced at shaft speed (these also being harmonics of shaft speed).

Analyses were made over a frequency range up to 30 kHz, but only results up to 10 kHz are shown here. The new cepstral method was compared primarily with TSA for the efficiency of removal of harmonics of shaft speed, including bladepass harmonics, but the DRS method was also tried.

Figure 7 compares spectra up to 5 kHz, and Figure 8 from 5-10 kHz. The order in both figures is the same, with the spectrum of the original signal at the top (a), the middle spectrum (b) representing the results after extraction of shaft speed harmonics using TSA, and the bottom spectrum (c) showing the results after extraction of shaft harmonics using the cepstral method. Figure 7(a) has two sets of harmonic cursors, showing the harmonics of shaft speed (39.8 Hz), and those of the bladepass frequency at 19X. Figure 7(b) shows the harmonics of BPFO (ballpass frequency, outer race), and these are seen to be the dominant components left after removal of the shaft speed harmonics. The cepstrum result in 7(c) appears to give similar results to the TSA.

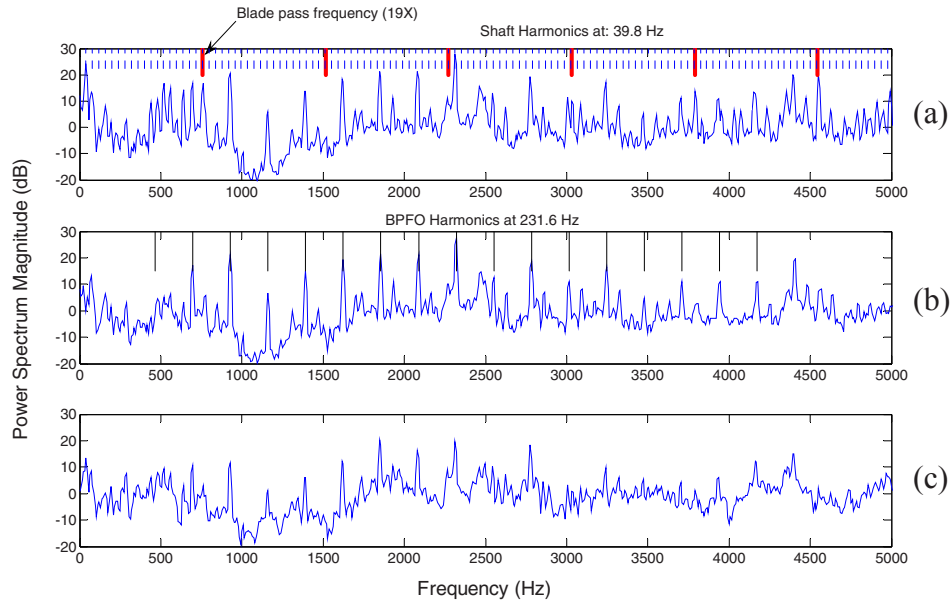


Figure 7: Comparison of spectra 0-5 kHz (a) Original signal
(b) residual after TSA (c) Residual after CEP

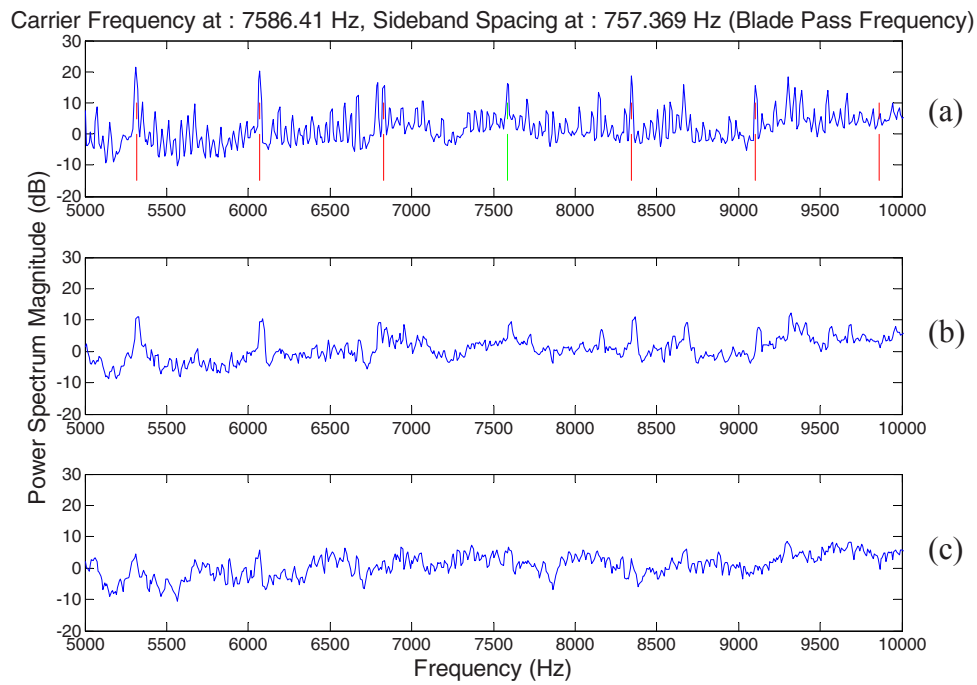


Figure 8: Comparison of spectra 5-10 kHz (a) Original signal
(b) residual after TSA (c) Residual after CEP

Figure 8(a) has a sideband cursor centred on the 10th harmonic of the blade pass frequency (approx. 7580 Hz), with sidebands spaced at the blade pass frequency. It is seen that in this frequency range, the TSA has left some components spaced at the blade pass frequency, though these are obviously not discrete frequency components. It is surmised that they are residual narrow band random sidebands around the blade pass harmonics, caused by the fact that the detection of blade passing on the casing is

via pressure pulsations transmitted through a turbulent fluid. Because this pattern is still periodic in the frequency domain, it has been removed by the cepstral method as seen in Figure 8(c).

Envelope analysis carried out on the residual signals shows even more clearly how the cepstral method removes all periodicity in the log spectrum, even that coming from uniformly spaced narrow band noise peaks. The envelope spectra in Figure 9 show periodic patterns in the signal envelopes. In the TSA result of Fig. 7(a), harmonics of BPFO can be found, but there is some disruption from residual harmonics corresponding to the shaft speed. These can possibly be explained by the same mechanism

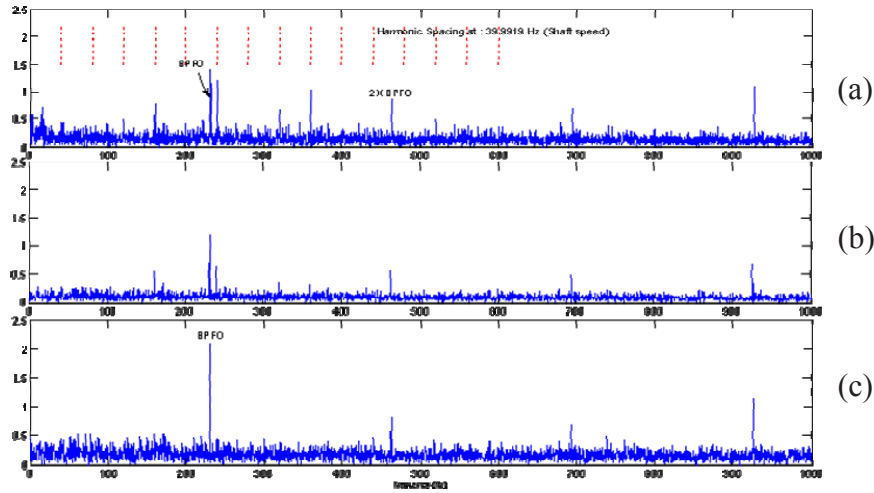


Figure 9: Envelope spectra obtained from the three residual signals
(a) TSA (b) DRS (c) CEP

as the residual bladepass pattern in Fig. 8(b), ie periodic narrow band noise peaks, but another possible explanation is that there are sidebands distributed throughout the spectrum caused by modulation of non-synchronous vibration components by the shaft speed. TSA removes only harmonics of the fundamental frequency, and not sidebands caused by modulation of non-synchronous components. Figure 9(c), using the cepstral method, shows only the harmonics of BPFO, all periodicity related to the shaft speed having been removed.

As a matter of interest, Figure 9(b) shows the results of applying the DRS technique. In principle this should remove all discrete frequency components, including sidebands, but it is seen that it also has some remnants related to shaft speed, although not as strongly as TSA. This is possibly because high order harmonics of shaft speed have been smeared sufficiently by minor speed variations (order tracking was not applied before the DRS) so as to be broader than the fixed width notch filter given by DRS.

8. Conclusions

A new method has been proposed for the separation of periodic and random components in a signal, such as those arising from bearings and gears. It is based on the cepstrum, which collects all periodicity in the log spectrum into a small number of components in the cepstrum, which can then be edited to remove selected families. This method has a number of advantages compared with alternative methods such as TSA and DRS. Unlike the former it can remove sidebands as well as harmonics, and also periodic narrow band noise peaks rather than just discrete frequency harmonics. It can also operate over limited band regions, where the TSA must include all harmonics down to zero frequency. Compared

with DRS, it can remove selected families, as opposed to all discrete frequency components, and is less sensitive to the bandwidth of the periodic spectral components. The cepstral method has got around the problem of regenerating time signals (formerly believed to require the use of the complex cepstrum), by removing the discrete frequency components in the real cepstrum, but then using the original phase spectrum together with the modified amplitude spectrum to regenerate the time signals.

Acknowledgements

This research was supported by the Defence Science and Technology Organisation (DSTO) through the Centre of Expertise in Helicopter Structures and Diagnostics at UNSW.

References

- [1] Antoni, J. and Randall R. B. (2002) "Differential Diagnosis of Gear and Bearing Faults", *ASME Journal of Vibration and Acoustics*, 124, pp. 165-171.
- [2] Braun, S. (1975) "The Extraction of Periodic Waveforms by Time Domain Averaging", *Acoustica*, 23(2), pp. 69-77.
- [3] McFadden, P.D. (1987), "A Revised Model for the Extraction of Periodic Waveforms by Time Domain Averaging", *Mechanical Systems and Signal Processing*, 1(1), pp 83-95.
- [4] Sawalhi, N. and Randall, R.B. (2008) "Localised fault diagnosis in rolling element bearings in gearboxes", *Fifth International Conference on Condition Monitoring and Machinery Failure Prevention Technologies (CM-MFPT)*, Edinburgh, 15-18 July.
- [5] Ho, D. and Randall, R.B. (2000) "Optimisation of Bearing Diagnostic Techniques Using Simulated and Actual Bearing Fault Signals", *Mechanical Systems and Signal Processing*, 14(5), pp.763-788.
- [6] Chaturvedi, G. K. and Thomas, D. W. (1982) "Bearing fault detection using adaptive noise cancelling", *Journal of Sound and Vibration* 104, pp.280-289.
- [7] Tan, C. C. and Dawson, B. (1987) "An adaptive noise cancellation approach for condition monitoring of gearbox bearings", *International Tribology Conference*, Melbourne.
- [8] Antoni, J. and Randall, R.B. (2004) "Unsupervised noise cancellation for vibration signals: part II—a novel frequency-domain algorithm", *Mechanical Systems and Signal Processing* 18, pp 103–117.
- [9] Bogert, B.P., Healy, M.J.R. and Tukey, J.W. in *Proc.of the Symp. on Time Series Analysis*, by M. Rosenblatt (Ed.), (1963) "The Quefrency Alanysis of Time series for Echoes: Cepstrum, Pseudo-Autocovariance, Cross-Cepstrum, and Saphe Cracking". Wiley, NY, pp 209-243.
- [10] Childers, D.G., Skinner, D.P. and Kemerait, R.C. (1977) "The Cepstrum: a Guide to Processing", *Proc. IEEE*, 65(10), pp1428-1443.
- [11] Randall, R.B. (2001) "Cepstrum Analysis", in *Encyclopedia of Vibration*, Eds. D. Ewins, S.S. Rao, S. Braun, Academic Press, London.

A Review of Signal Processing and Analysis Tools for Comprehensive Rotating Machinery Diagnostics

Thomas Reilly
Product Manager - DSP Systems
Data Physics Corporation
1741 Technology Drive, Suite 260
San Jose, CA 95110
USA

ABSTRACT

Rotating machinery diagnostics is an essential and often the most important function in industrial process and power generation applications. A variety of methods and tools have been employed by test personnel over the past several decades, from route based walk around methods with single and dual channel data collectors to permanently installed long term condition monitoring systems, but there does not appear to be a universally accepted set of practices that results in comprehensive diagnostic capabilities of the machinery under test. This paper examines the range of solutions available to analysts in the paper manufacturing and power generation industries with a closer look at important considerations for tachometer signal processing and the need for re-sampling of time domain data into the angle domain and presents a new paradigm for mobile and highly flexible testing of all machinery, regardless of size and complexity, with a single and customizable dynamic signal analyzer.

Basic RPM based Measurements and Order Analysis

A fundamental requirement for rotating machinery diagnostics is basic time and frequency domain measurement capabilities. Rotating machinery diagnostic analyzers must have the ability to measure RPM from either a single or multi-pulse per rev tachometer. The tachometer input measures the machine speed concurrently with the normal acquisition of measurement signals. The trigger input channels accept a periodic analog or TTL signal from a tachometer probe or shaft encoder monitoring the machine under test. In the example shown below, vibration data from a turbocharger run up and run down test is presented in a waterfall plot. The RPM axis shows the speed range for the test. Order cursors conveniently relate measured vibration frequencies to multiples of the turbocharger shaft rotational frequency.

Waterfall displays are commonly employed in studying the dynamic behavior of rotating machinery and mapping the time/frequency variations of signals. Several x,y,z graphic formats, including spectrogram, fine spectrogram, cascade, surface, standard waterfall and Campbell diagrams are used to dynamically map 3-D data. Also useful is the ability to view any constituent record or a slice across all records at a single frequency (or time) value. Waterfalls can be created from instantaneous or averaged spectra including single and dual-channel measurements. Waterfalls provide time/frequency/amplitude displays. The horizontal (x) axis is either frequency or time, the vertical axis (y) is amplitude and the inclined axis (z) represents time or machine speed.

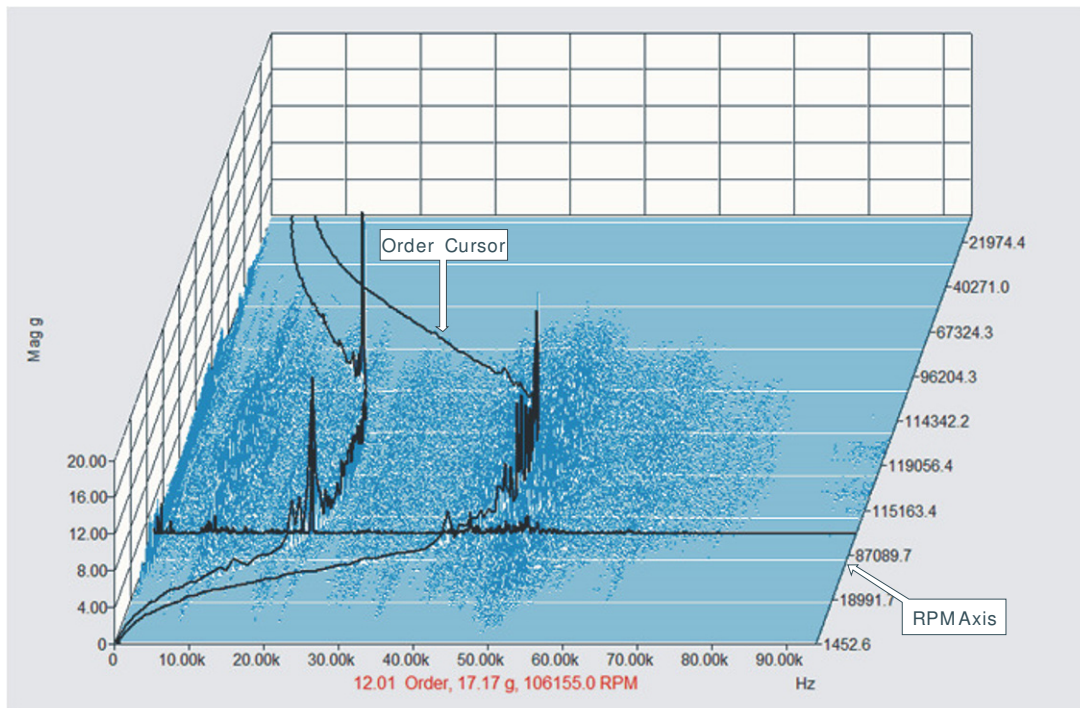


Figure 1. RPM based analysis

Advanced Order Tracking

Order analysis can be done either using high performance tracking filters or digital re-sampling of the measurement signal. In digital re-sampling, the signal analyzer synchronizes the sampling of input signals to the instantaneous angular position of the machine's shaft. The analyzer needs to measure a constant number of samples per revolution rather than sampling a constant number per period of time. Modern Dynamic signal analyzers use Sigma Delta ADCs for sampling that do not lend themselves to be driven by an external clock derived from a rotating machine. Therefore, in order to provide a sample stream at constant angular intervals of the shaft, modern analyzers use a digital re-sampling technique to convert samples delivered by the Sigma Delta ADCs. The digital re-sampling technique delivers more accurate samples than the old method using an external clock derived from the shaft speed with a phase locked loop.

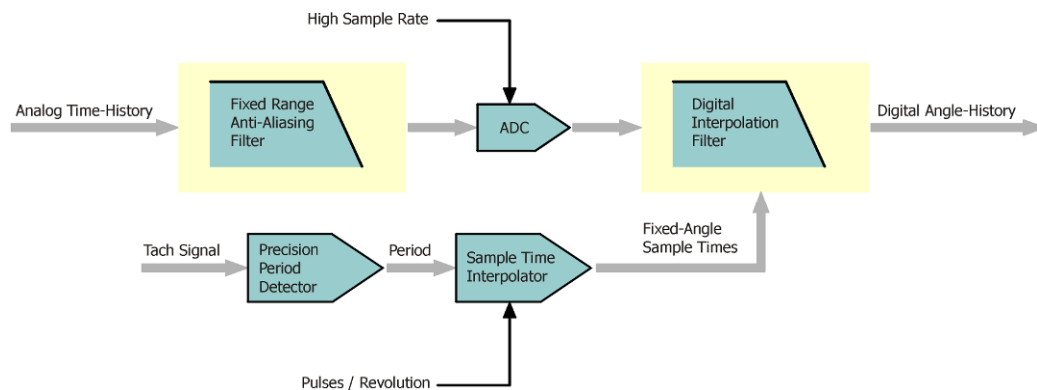


Figure 2. Digital re-sampling process

Figure 3 shows the same turbocharger run up and run down test data processed using digital re-sampling based order tracking; the results are presented in a color spectrogram with high resolution order spectra.

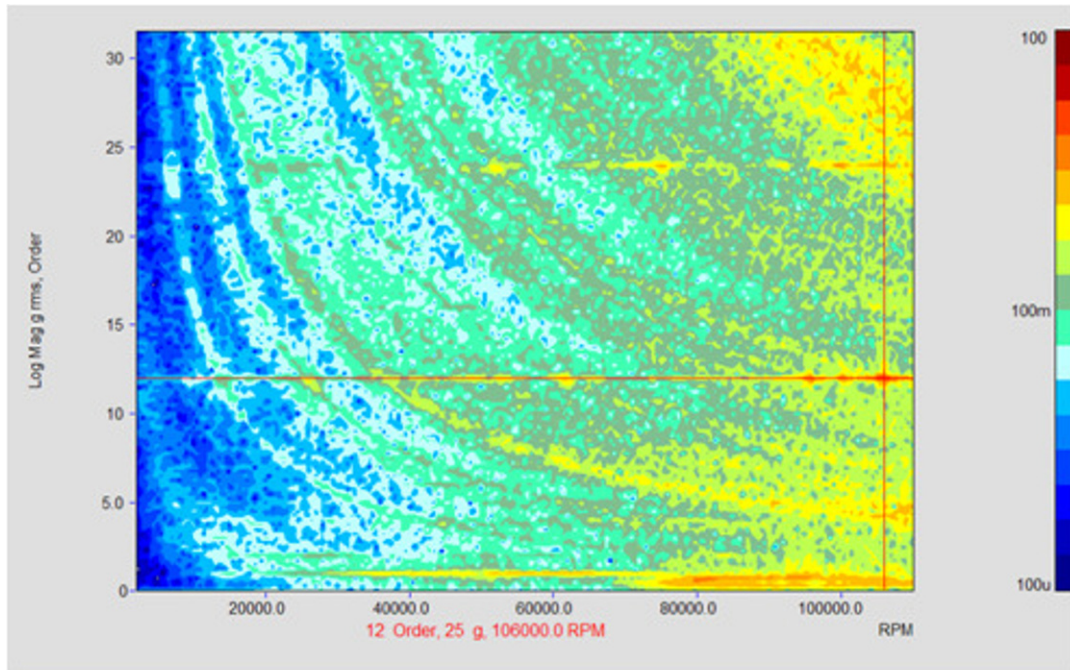


Figure 3. Order tracking results

Rotor Dynamics Analysis

In addition to accelerometers and velocity pickups commonly used to monitor vibration, turbo machinery, compressor, turbine and generator shaft systems with journal bearings (also known as sleeve or fluid film bearings) are also instrumented with proximity probes, which are displacement sensors. Movement of the shaft in the bearing is monitored very closely as that is an indication of problems with unbalance, misalignment, shaft rub, oil film, circumferential flow of the lubricant, etc. For any given journal bearing along the longitudinal axis of the turbine shaft, there are two proximity probes placed radially, 90 degrees to each other (usually at 45 degrees left and right). [Figure 4](#) shows a typical radial vibration measurement arrangement in journal bearings.

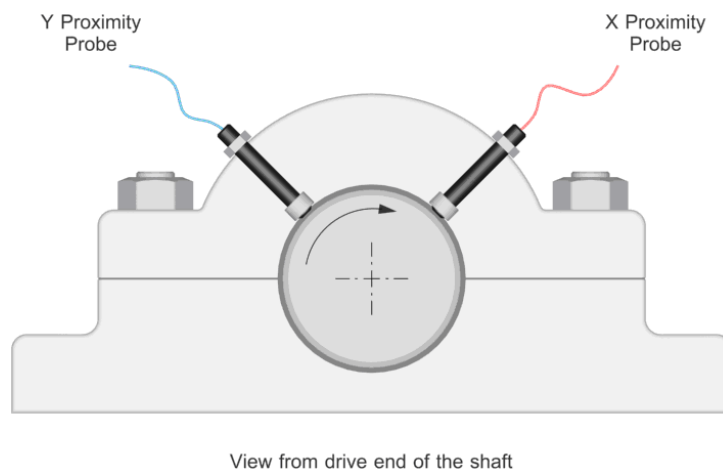


Figure 4. Proximity sensor arrangement

For comprehensive turbomachinery analysis, simultaneous asynchronous and synchronous sampling is used to obtain both vector and waveform samples. Sometimes data is also recorded to disk for optional post processing. Order detection is based on user selectable tracking filters which may be set up as fixed or proportional bandwidth filters, permitting users to optimize

accuracy for varying slew rates. Usually, 1x, 2x and a number of other orders, per measurement channel, are tracked and displayed.

Waveform based samples are used in the generation of orbit, time and spectrum plots, while Vector samples are used for the generation of filtered orbit, Bode and polar plots. DC measurements provide instantaneous gap voltage measurements and data required for the generation of shaft centerline plots.

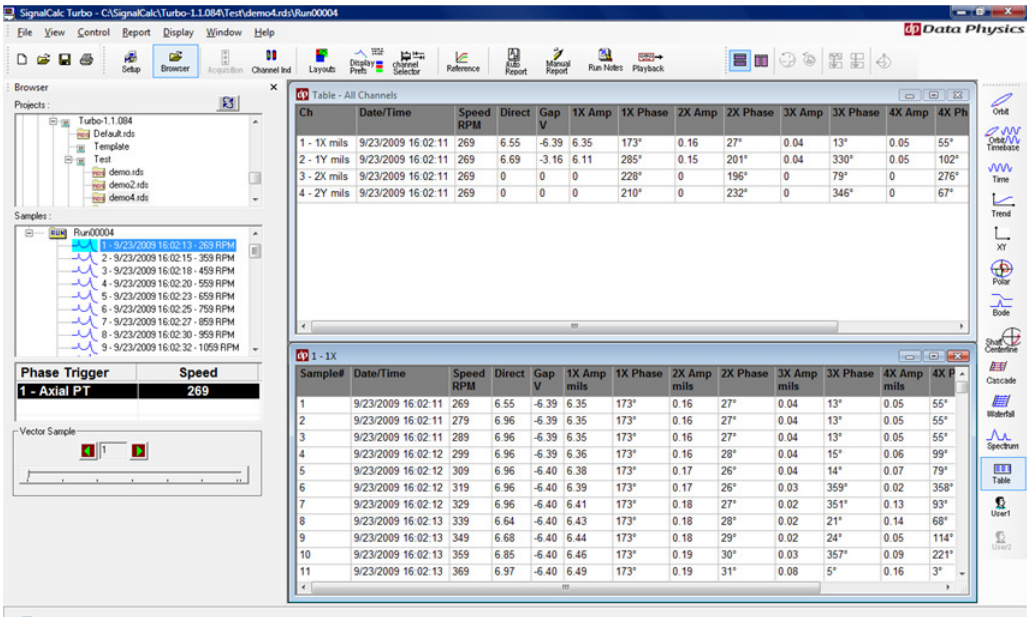


Figure 5. Table of Amplitudes vs. RPM

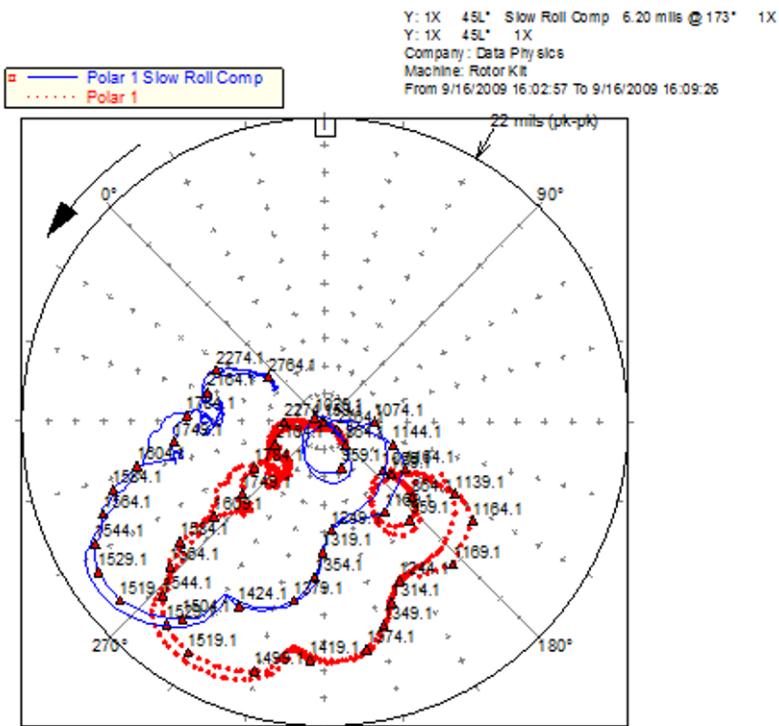


Figure 6. Polar Display

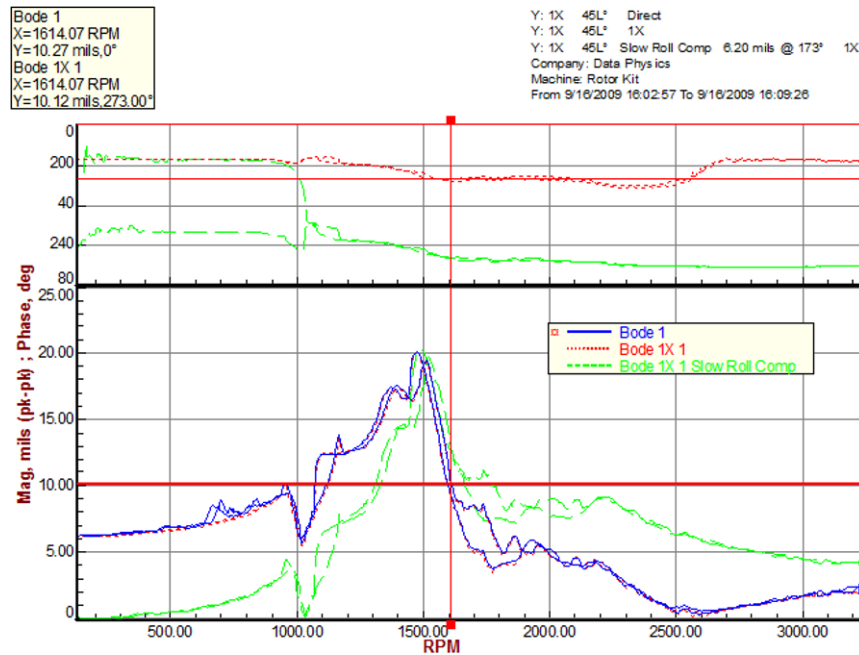


Figure 7. Bode Display

Synchronous Averaging

In synchronous averaging mode, a tachometer input is used to trigger an ensemble averaging process. This process removes the contribution of asynchronous vibration sources from a time or linear spectral average to isolate the contribution of synchronous rotating components. Non-synchronous components such as noise or structural resonances are de-emphasized by the averaging process.

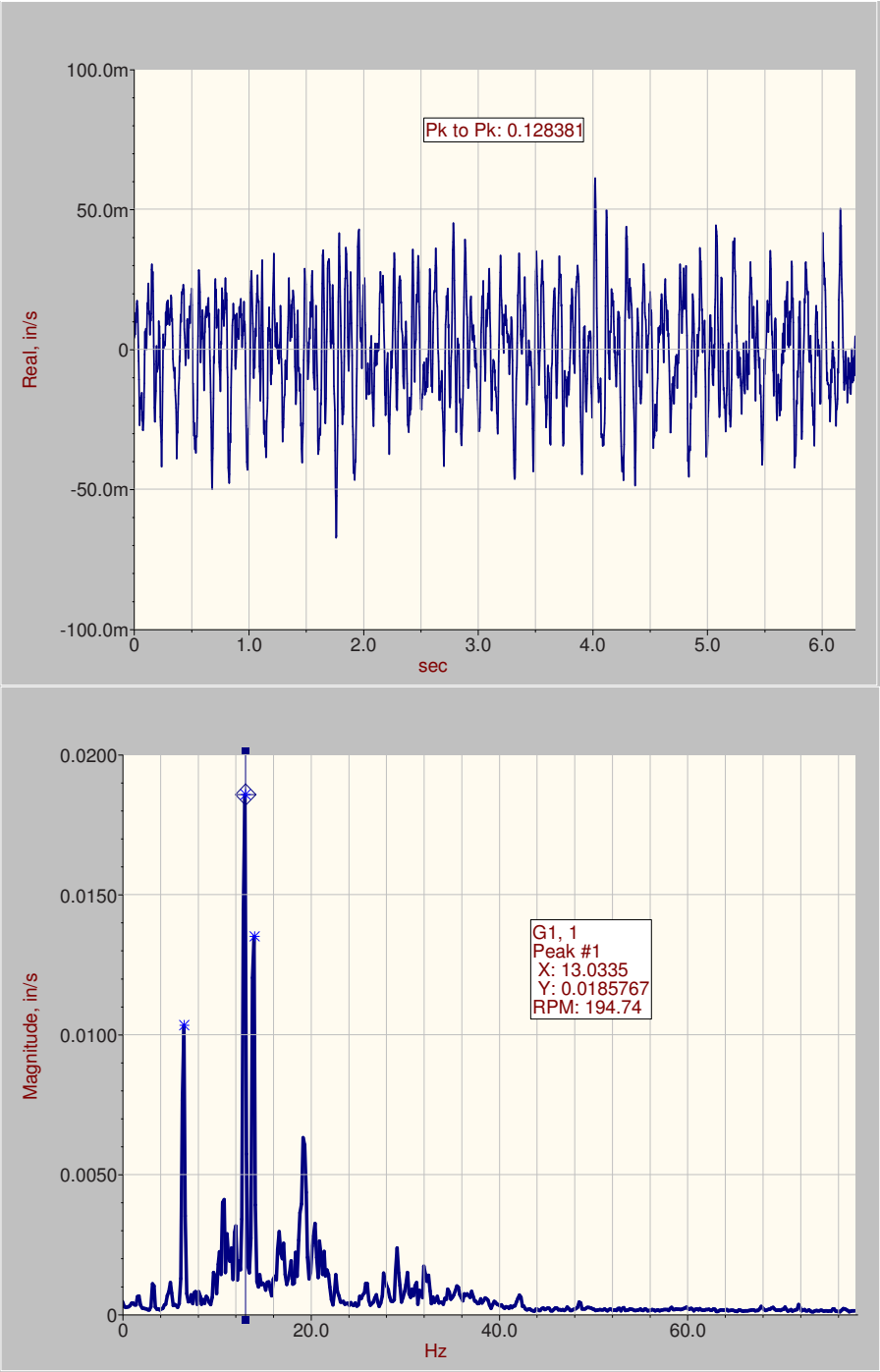


Figure 8. Overall vibration on paper machine press section

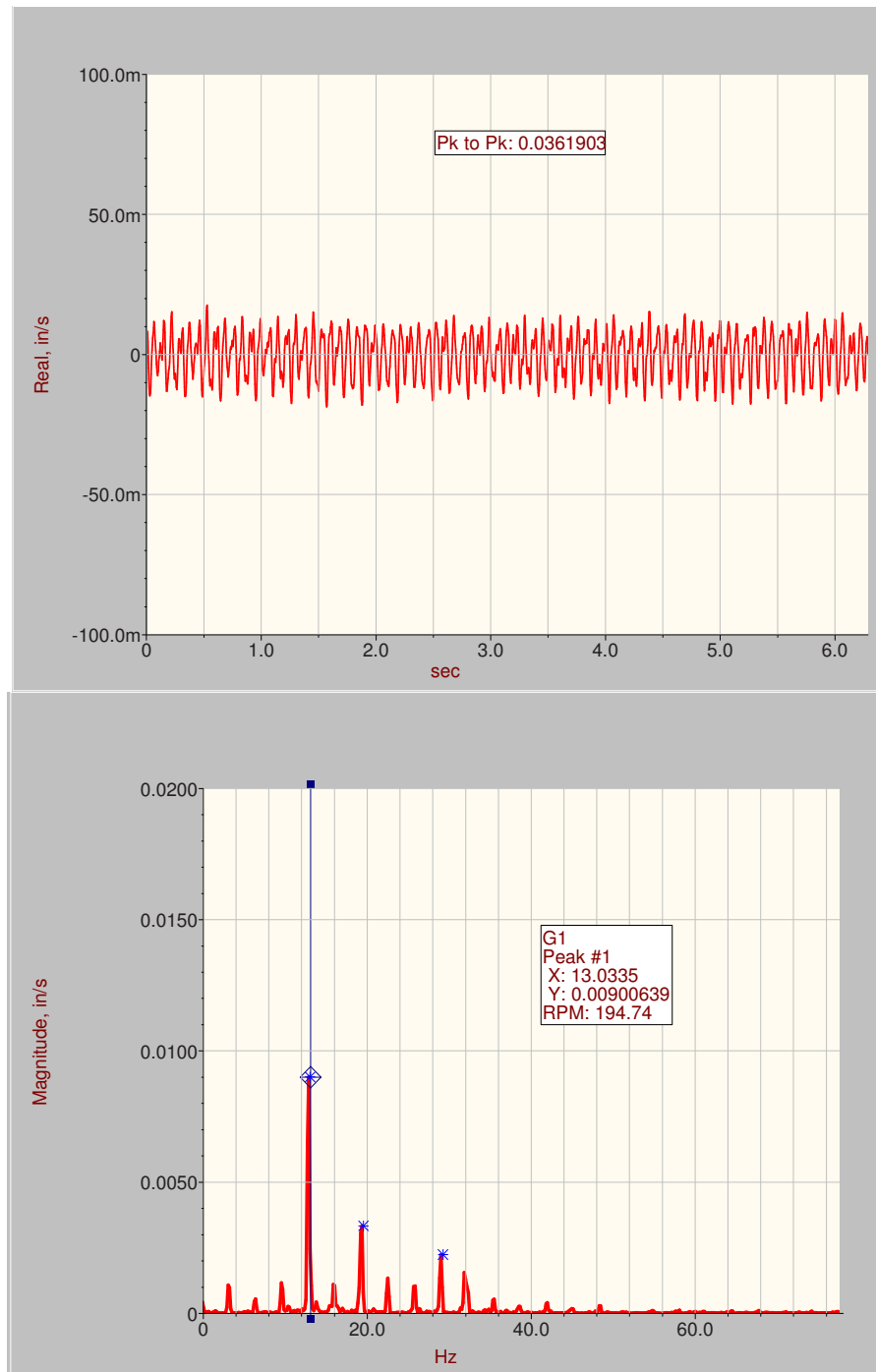


Figure 9. Synchronously averaged vibration on paper machine press section

Figures 10 and 11 show a unique method of presenting time synchronous average data: a polar runout plot, where the time average data for one shaft revolution is shown in a 0-360° circular format. The data resolution allows the user to see the contribution of the shaft coupling with the gear mesh frequency of the driving gear.

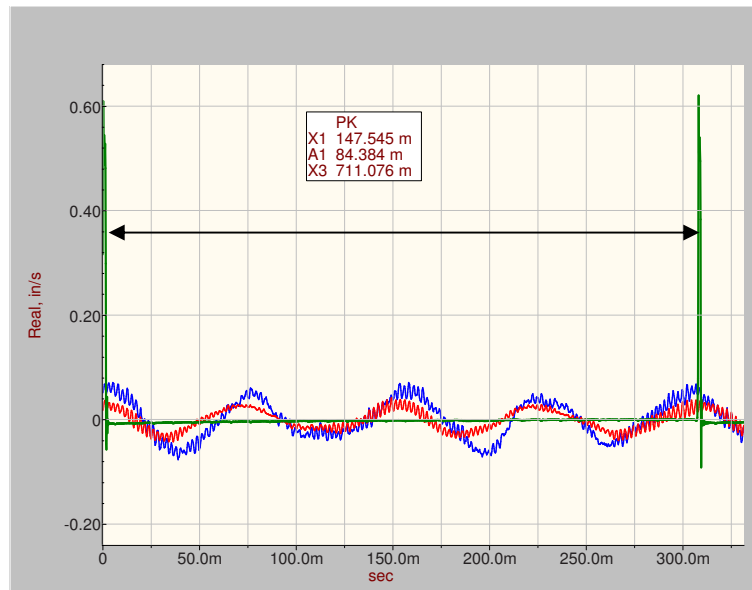


Figure 10. Duration corresponding to one revolution

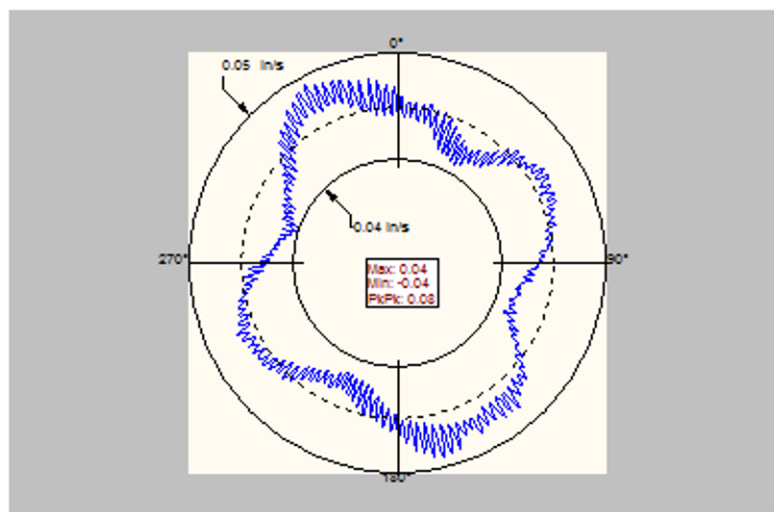


Figure 11. Polar runout display

Demodulation

Gear mesh vibration is a natural occurrence with most mechanical drives and geared transmissions. While the amplitude of gear mesh frequency (GMF) vibration is itself of importance, more important is the determination of the sources of increased GMF levels. This requires more sophisticated analysis. The root cause of the problem is usually one or more gears whose rotational frequency modulates the amplitude of the GMF energy.

Using auto power spectrum measurements, the bandwidth in the vicinity of the GMF vibration can be analyzed to show the modulating frequencies as sidebands. However, this analysis is useful when there is only amplitude modulation at play and then only if there is a single source of amplitude modulation. Traditional envelope analysis techniques are very useful in exposing the amplitude modulating frequencies, but such analysis does not reveal information about the phase or frequency modulating components in the signal.



Figure 12. Gear Mesh Vibration

Demodulation performed via the Hilbert Transform provides both amplitude and frequency/phase demodulation. Demodulation can be combined with zoom or synchronous averaging analysis in order to concentrate the analysis on the events of interest. The benefit of combining zoom analysis (band selectable Fourier analysis) with the Hilbert Transform is that the vibration at the primary rotational frequency (the carrier signal) is removed leaving only the modulation components in the result.

Underlying this analysis is the analytic signal, sometimes called the envelope. The analytic signal is composed of the original signal plus a 90-degree phase-shifted version of itself (the Hilbert transform), and the magnitude of the analytic signal is the envelope of the original signal, giving an outline of low-frequency events that modulate the main signal. Accelerometers situated around the drive train are connected to the analyzer and a baseband auto power spectrum measurement is first carried out to determine the general characteristics of the signals. Zoom analysis is then used to focus the measurement around the main rotational (carrier) frequency. The measurements may also be combined with synchronous averaging, with a once per rev tachometer providing a trigger for linear averaging. Synchronous averaging ties the analysis to a particular event such as the period of rotation of a shaft, and allows signal characteristics that happen at fixed times relative to the triggering event to reinforce each other in the average while non-synchronous events average out. The resultant amplitude modulation and phase modulation spectra allow analysis of the frequency and amplitude of the various modulating components in the signal.

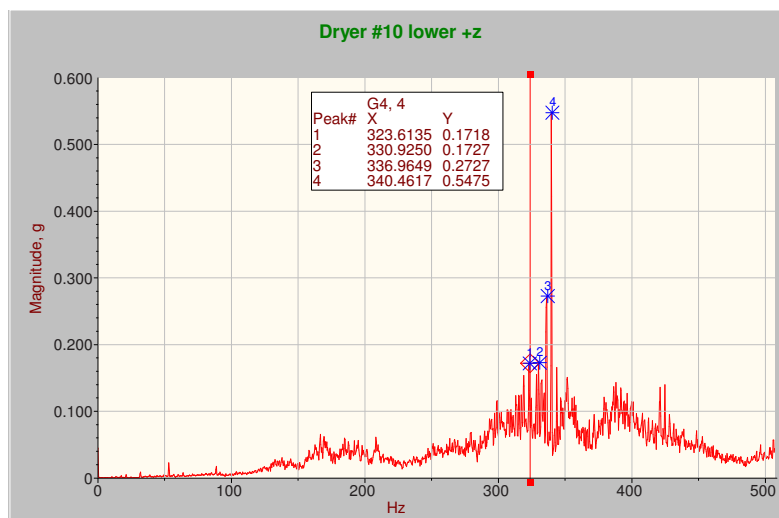


Figure 13. Autopower Spectrum

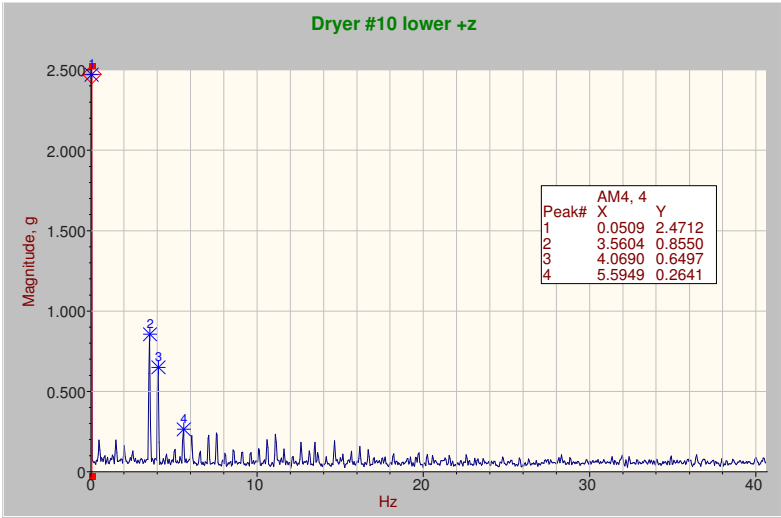


Figure 14. Amplitude Modulation Signal

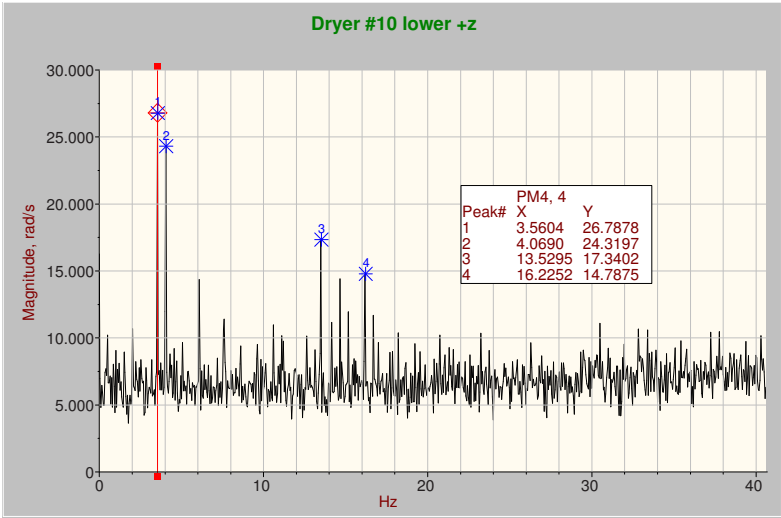


Figure 15. Phase Modulation Signal

Balancing

When the center of mass of a rotating element does not coincide with its axis of rotation a condition of unbalance exists. The force generated by this unbalance is proportional to the square of the rotational frequency. If the amount of unbalance exceeds permissible levels, even small increases in operating speeds of the rotor can lead to significant increases in vibration levels. This condition can only be corrected by accurately measuring the vibration response of the rotor at its fundamental frequency and following a series of steps designed to determine the amount of unbalance and adding (or subtracting) an appropriate amount of compensating mass at the necessary locations.

The first step in balancing is the definition of the number of balance planes, the maximum allowable vibration at each balance plane and the setup of vibration channels and tachometer input which is used to provide a measure of the rotor speed during balancing and also serve as a phase reference

Measurement of vibration channels may be defined in units of acceleration, velocity or displacement and the maximum allowable vibration limits for each balance plane may also be defined in any of these units. The tachometer has to be capable of jitter free triggering for the synchronous averaging of vibration required for accurate balancing runs.

The second step is to define the rotor geometry. Components making up the rotor being balanced can be defined as supports (usually bearing locations) along with rotors where the addition of correction masses occurs. The position of each component along the axis of rotation, a radius for each rotor and optionally, the number of pre-drilled holes available on the rotor for the addition of trial and correction masses which are used by the system for “weight splitting” must all be defined.

The final step is the balancing measurement. It is advantageous to view the measurements for all balancing planes in either the time or frequency domain along with the visualization of the addition of trial masses (see [Figure 18](#) below). The measurement concludes with a table of correction masses and locations for all the balance planes.

The screenshot shows the 'Data Physics Balancing Application' window with the 'Setup' tab selected. The interface is divided into several sections for configuring the balancing process.

Balance Type:

- No. of Balance Planes: 2
- Balance Quality Grade (ISO 1340): G1.6
- Maximum Machine Vibration: ☒ (selected)

Measurement:

- ☒ Nominal RPM: 1800
- Bandwidth (Hz): 156.25
- # Freq lines: 383
- # Averages: 16

Machine Info:

- Machine Type: mach type
- Machine ID: id
- Rotor Type: round
- Rotor ID: id
- Rotor Mass: 2 lbm
- Operator: me
- Rotation (Left hand rule): ☒ Clockwise, ☐ Counter-Clockwise

Tachometer:

- Tach: Tach 1
- Slope: Rising
- Level (V): 0.2
- Hysteresis (V): 0.05
- Hold off (s): 0
- Preset: 1
- PPR: 1
- Speed Ratio: 1
- Smoothing: 0

Input Channels:

Ch	Name	Plane	mV/EU	EU	Range (V)	Range (EU)	Coupling	Max Level
1		Plane 1	100	g	5	50	DC/DI	1
2		None	100	V	5	50	DC/DI	1
3		Plane 2	100	g	5	50	DC/DI	1

Figure 16. Balancing Setup

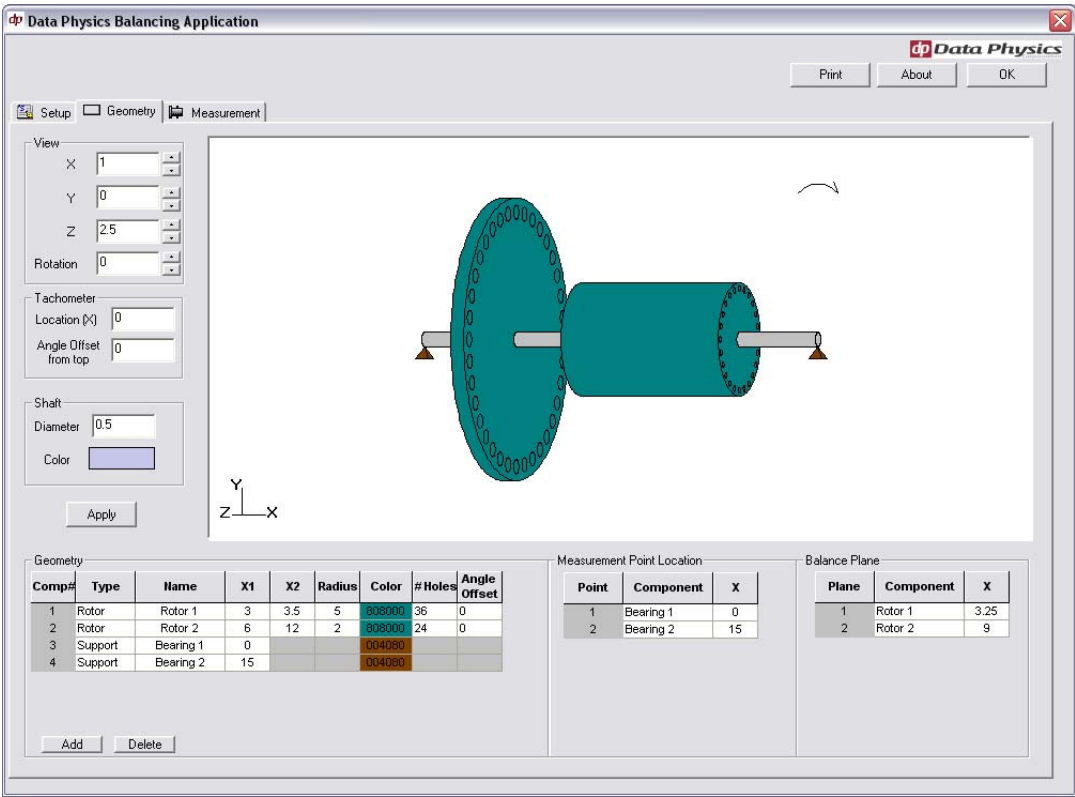


Figure 17. Balancing Geometry

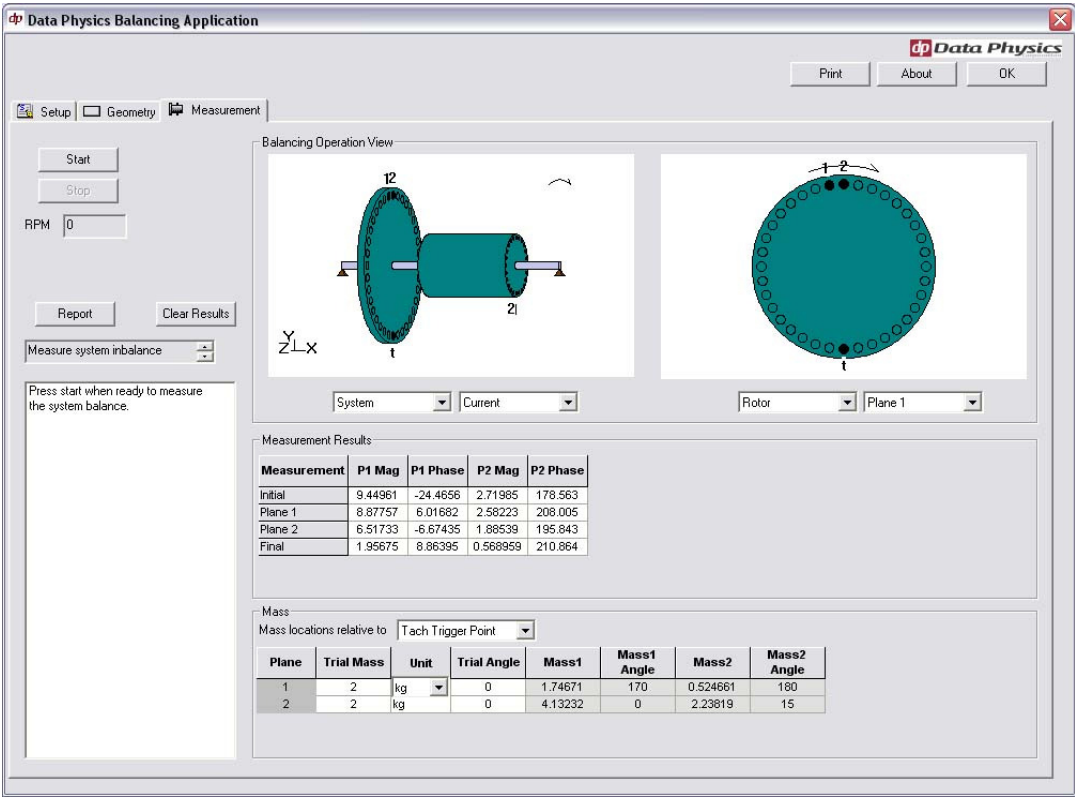


Figure 18. Balancing Measurement with Mass Locations

Correlation

Correlation analysis is useful in identification of sources and transmission paths of piping connected to rotating equipment. Cross correlation is a method of determining the degree to which two waveforms are correlated. Consider two sampled waveforms $x(i)$ and $y(i)$ where $i=0,1,2,\dots,N-1$. The cross correlation r for all delays (of one waveform with respect to the other) $d=0,1,2,\dots,N-1$ is defined as

$$r(d) = \frac{\sum_i [(x(i) - m_x) * (y(i-d) - m_y)]}{\sqrt{\sum_i (x(i) - m_x)^2} \sqrt{\sum_i (y(i-d) - m_y)^2}}$$

Where, m_x and m_y are the mean values of the x and y waveforms. This is illustrated by the following example that shows two waveforms x and y .

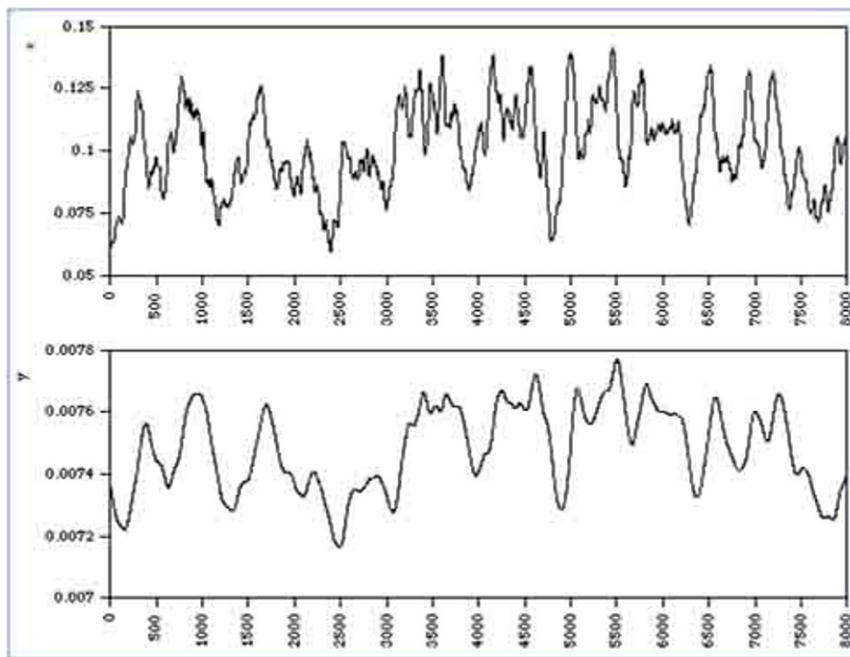


Figure 19. Two waveforms sampled

The cross correlation of these two waveforms with a maximum delay of 4000 is shown below. There is a strong correlation at a delay of about 40.

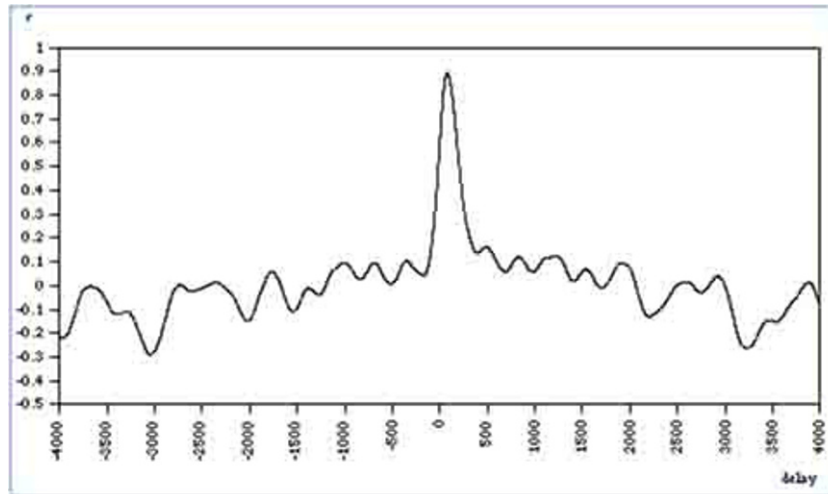


Figure 20. Correlation

Cross correlation is computed for two signals by calculating the cross power spectrum between the two signals and then taking the inverse Fourier transform of the result. Now let us look at a real example, comparing the signals from two pressure sensors shown in red below. The static pressure in the two lines is very different, one at approximately 18.5 psi and other at approximately 2.57 psi. Looking at the two signals, it is not visually clear that they are correlated at all.

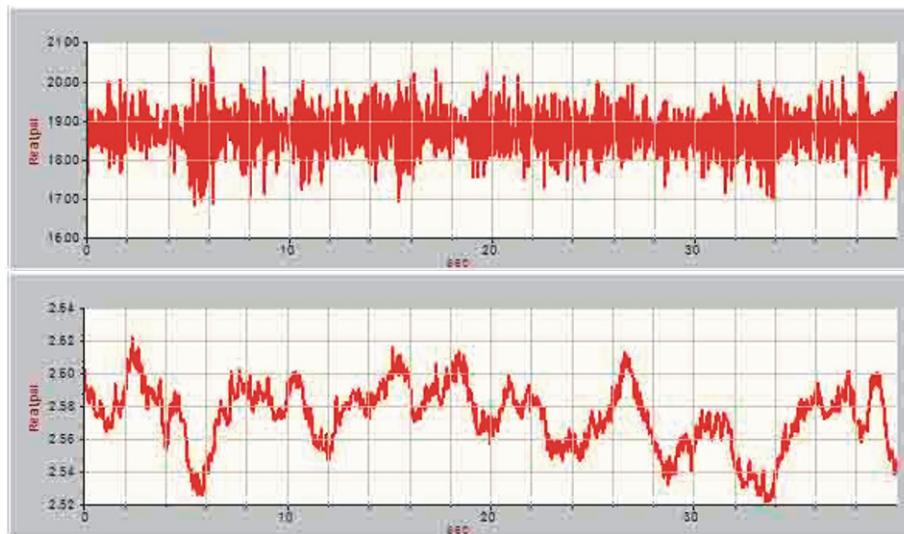


Figure 21. Signals from two pressure sensors

The cross correlation coefficient (1.0 indicates perfect correlation between two signals) seen between the above two signals is 0.1 for a 40 Hz FSpan and blocksize of 1024. The other significant piece of information available in the cross correlation result below is the lead/lag time between the two signals. A positive value of 0.39 between channels 6 and 7 indicates that channel 6 leads channel 7 by 0.39 seconds.

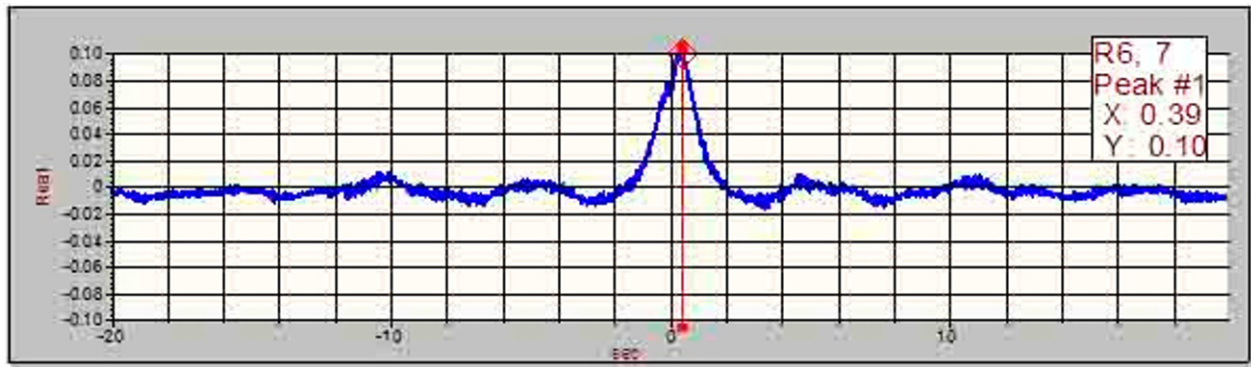


Figure 22. Correlation coefficient

Now consider the application of a low pass filter at 1 Hz to the signals. The use of the filter immediately shows a remarkable visual similarity between the two signals that in turn is supported by the correlation coefficient of 0.91.

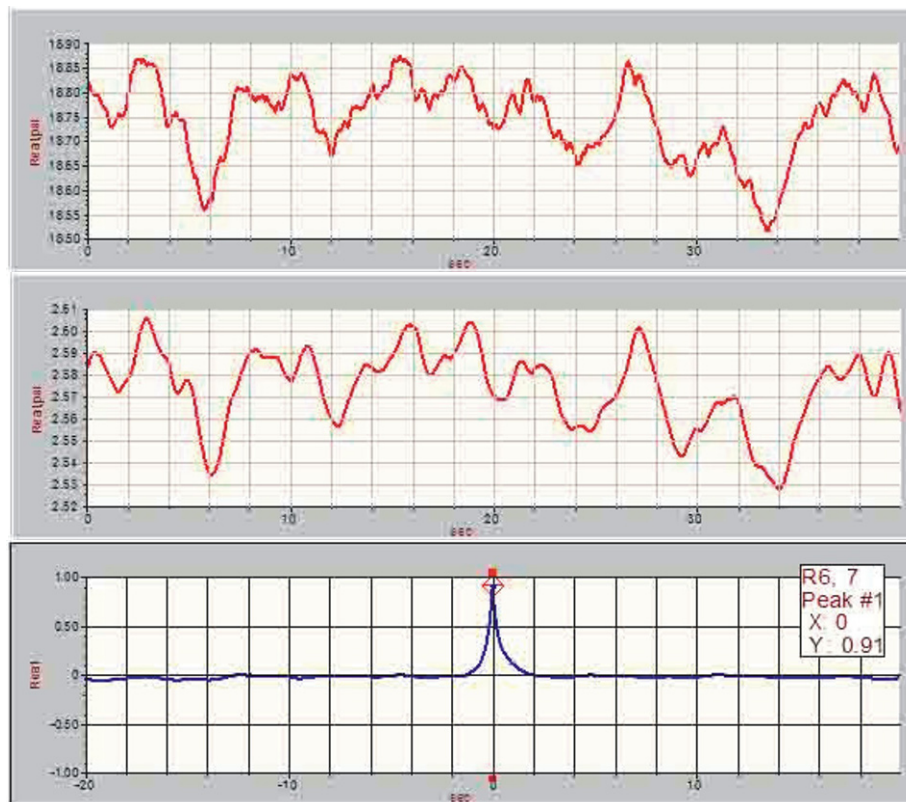


Figure 23. Signals and correlation after filter

Thus, in piping systems, the cross correlation function can be useful in characterizing the similarity between signals for selected frequency ranges, as well as provide a clear picture of the direction of transmission of disturbances and process upsets. Consequently, correlation measurements can be used to effectively diagnose rotating machine induced effects, such as irregularities of pulp thickness flowing in paper processing machines.

Operating Deflection Shape (ODS) Analysis and Modal Testing

An operating deflection shape analysis (ODS) consists of acquiring vibration data (under normal operating conditions) in three directions at various points on a structure or system. This is done by maintaining an accelerometer at a fixed, reference location on the structure and then roving tri-axial accelerometers around the structure. Obviously, having a large number of input channels in the data acquisition system greatly shortens the time required to acquire all the data. If the structure contains rotating machines the machine speed should be maintained as constant as possible during the data acquisition phase. This is typically not a problem for industrial machinery, although some preparation and planning is essential, if good measurements are to be expected. The fixed accelerometer measurement provides the reference for phase measurement between all measurement locations.

The frequency response functions used in ODS analysis are identical to those described above for transmissibility analysis and with the automated point number and direction tagging and export to UFF and ME'Scope formats, etc., users can generate complex ODS models for their systems under test effortlessly.

ODS analysis shows how a machine or structure moves in actual operation at specific frequencies of interest and helps determine the cause of the motion. Frequencies used in the analysis are usually multiples of running speed of the various rotating components in the system, such as rolls or gears etc.

If the data used in the ODS analysis is fit to natural frequencies of the system (identified in speed trials, etc.) then the resultant model will show mode shapes instead. Structural modification is made easier when the mode shapes can be visualized.

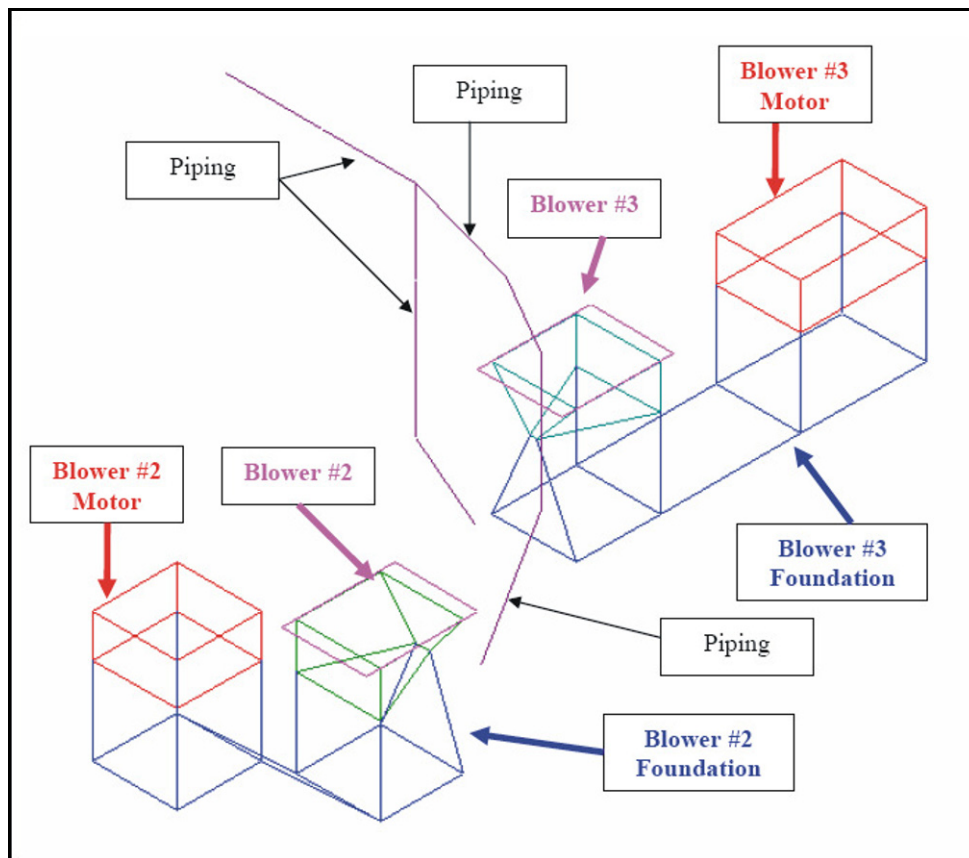


Figure 24. ODS Geometry

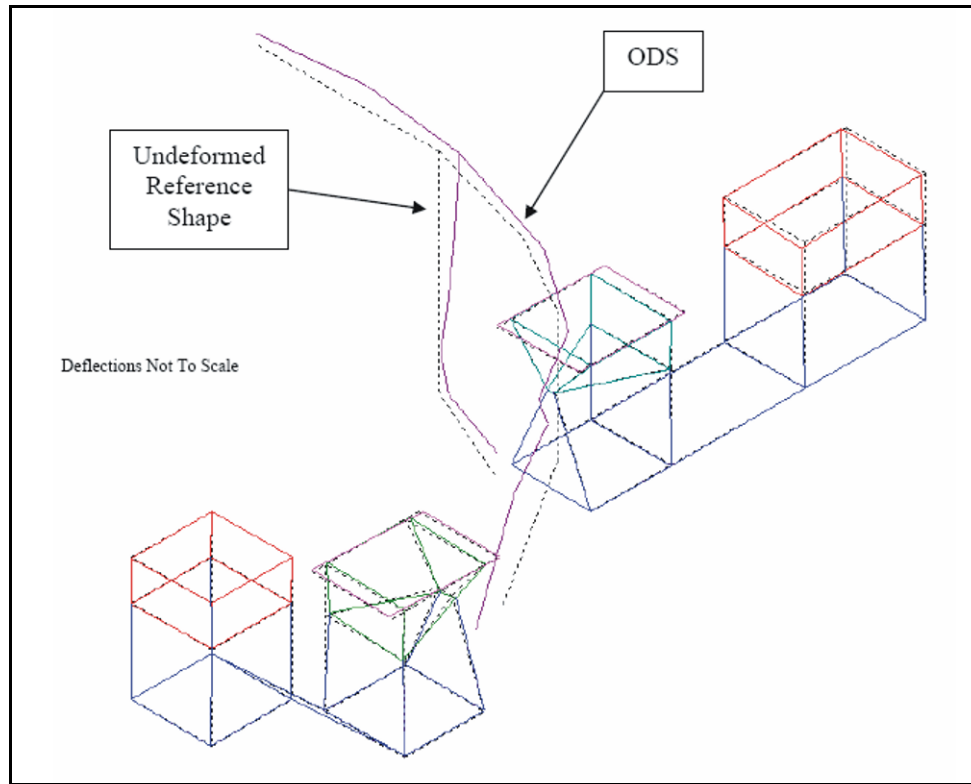


Figure 25. ODS Geometry and deformed shape

Summary

This paper describes a number of signal analysis techniques applicable to diagnostic measurements on or around rotating machines. All these techniques are based on the application of the Fast Fourier Transform to waveforms sampled in the time or angle domain. The results when transformed, is either in the Frequency domain or the Order Domain, both of which can reveal valuable information about the condition of the machine. With the evolution of DSP devices it has become possible to contain the entire range of measurements described here in a portable unit that can be used very effectively as a field test instrument. Where multiple instruments were required in the past, comprehensive testing of all machinery, regardless of size and complexity, may now be performed with a single mobile and highly flexible dynamic signal analyzer. Readers wishing to find out more may visit www.dataphysics.com.

Acknowledgement

References

- [1] **Data Physics Corp.**, *SignalCalc Dynamic Signal Analyzer Manual*, September. 2009.
- [2] **Vibrant Technology Inc.**, *ME'Scope VES 4.0 Operating Manual Volume 2 – Reference*, October 2003.
- [3] **Data Physics Corp.**, *SignalCalc Turbo Manual*, August, 2009.
- [4] **Donald E. Bently**, *Fundamental of Rotating Machinery Diagnostics*, 2002

Simple Tools for Simulating Structural Response to Underwater Explosions

Frederick A. Costanzo
Naval Surface Warfare Center Carderock Division, UERD
9500 MacArthur Boulevard
West Bethesda, MD 20817-5700
(301) 227-1650

ABSTRACT

Today, many underwater explosion (UNDEX) shock problems are solved using direct transient analysis methods applied to detailed finite element models. Solution methodologies are diverse and complex, and necessarily include detailed representations of both the dynamic loading and the structure. As a result of these computational complexities, it is imperative that all such solution strategies also employ simple tools to benchmark and “ground” the more complex solutions. This paper illustrates the use of simple bounding solutions in generating reliable estimates of the global dynamic response of surface ship and submarine structures subjected to underwater shock. Three well documented methodologies are presented, including the Taylor flat plate analogy for both air- and water-backed plates, the peak translational velocity (PTV) method, and the application of the conservation of momentum principle to estimating the vertical kickoff velocity of floating structures (spar buoy approach). Derivations of the governing equations associated with each of these solution strategies are presented, along with a description of the appropriate ranges of applicability. Finally, practical applications of these “bounding” methods are summarized.

INTRODUCTION

The field of underwater shock is complex and involves the consideration of many phenomena [1] in order to properly understand the influences of an UNDEX event on a given target. With advances made over the years in computational tools development as well as with computer resources, it is now possible to analyze detailed structures with a high degree of precision and within a timely manner. Current pre- and post-processing tools enable analysts to create large complex models and generate dynamic response solutions that lead to volumes of output results. The challenging aspect of this constantly growing simulation capability is to make proper sense of the solution and not get lost in all of the details associated with model development, dynamic load application including fluid-structure interaction analyses, and processing of the transient results. To achieve this goal, analysts must have at their disposal the means by which to benchmark or ground their solutions to ensure that both the analysis and the interpretation of the results are reasonable and within practical bounds.

Examples of the type of structures for which transient shock analyses are typically performed are presented in Fig. 1. In the top two photos, examples of a floating shock platform prior to and during an UNDEX test are shown. Below in the same figure are photos of an operational submarine and of a surface combatant ship undergoing a shock test. When analyzed for shock, each one of these typical examples usually results in a complex fluid-structure interaction simulation.

In Fig. 2, detailed transient shock analysis examples are presented. In the upper part of the figure, a full ship model of a decommissioned combatant was analyzed. The resulting simulated global velocity-time histories are shown for a number of longitudinal positions along the ship. In the lower part of Fig. 2, transient shock analysis of a model of the floating shock platform described above is presented, along with a comparison between the measured and computed vertical global velocity. These are just a couple of examples of the types of post-test analyses that analysts might perform upon completion of an UNDEX simulation.



Fig. 1 – Typical Structures Analyzed for UNDEX by Transient Shock Analysis

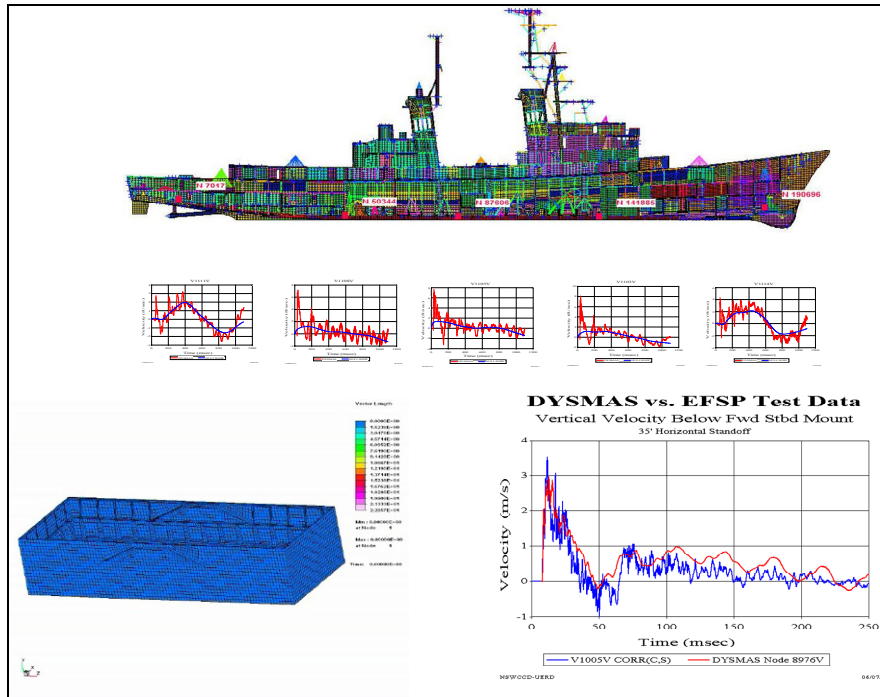


Fig. 2 – Detailed Transient Shock Analysis Examples

The objective of this paper is to present a few proven simple physics-based tools that can provide analysts who conduct transient UNDEX analyses a means to generate reliable estimates to bound their complex solutions. This will also enable analysts to perform quick sanity checks of their results and obtain a level of confidence in their results prior to continuing on with additional simulations.

TAYLOR FLAT PLATE ANALOGY

The first simple physics-based tool to be illustrated is the Taylor Flat Plate analogy [2]. The underlying assumptions associated with this approximation method are illustrated in Fig. 3. We begin with the assumption that the structure to be analyzed can be idealized as an infinite, unrestrained air-backed flat plate. Acoustic, planar shock wave propagation theory is assumed, where the incident and reflected shock wave pressures are related to the respective particle velocities by the relationship:

$$v = p / (\rho c), \quad (1)$$

where:

v is the particle velocity,

p is the pressure, and

ρc is the specific acoustic impedance of the fluid.

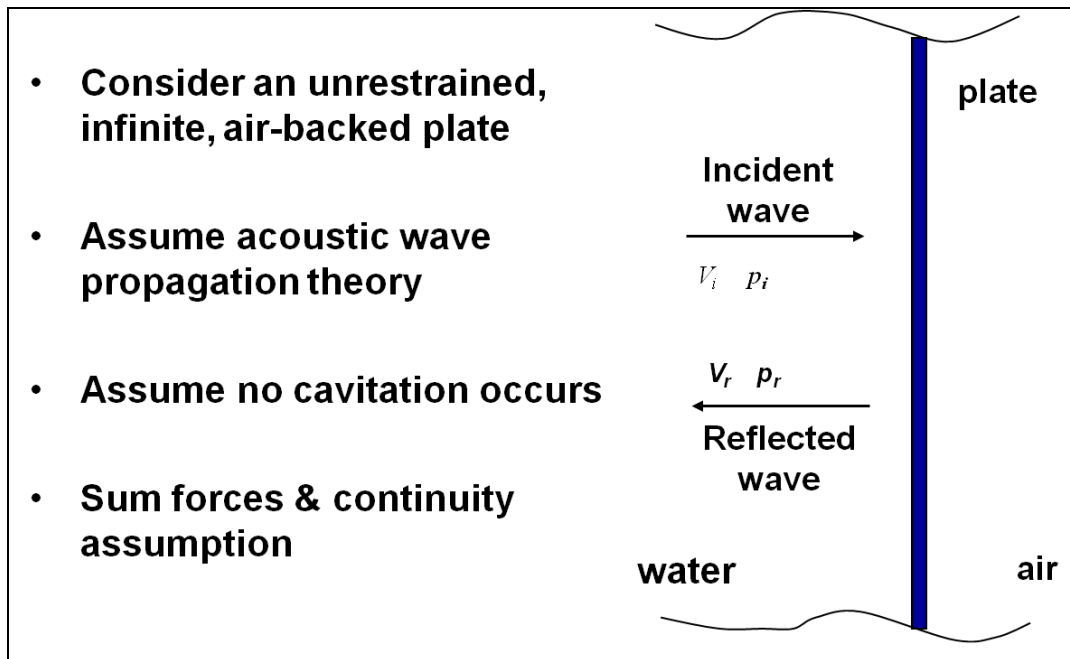


Fig. 3 – Taylor Flat Plate Analogy for Estimating Peak Vertical Global Motion

Also the assumption is made that no local cavitation occurs at the fluid-structure interface. With these assumptions, and the consideration of both the incident and reflected shock waves in Fig. 3, one can derive the governing differential equation of motion by first applying Newton's Second Law and summing the forces acting on the plate and equating them to the mass of the plate times its acceleration. Since the Taylor approximation deals with an infinite plate, the equation of motion is typically developed by considering pressures acting on a unit area of the plate. This results in Equation 1 in Fig. 4, where the m term represents the mass per unit area of the plate.

Next, a condition of continuity is applied where, as a result of the assumption of no cavitation, the vector sum of the incident and reflected shock wave pressures must equal the velocity of the infinite unrestrained flat plate. This condition is represented in Fig. 4 by Equation 2, and enforces the condition that there is no separation between the fluid and the plate at the interface.

Finally, to obtain the governing differential equation of motion, Equations 1 and 2 in Fig. 4 are added. This step results in a linear, second order ordinary differential equation in the plate displacement, x , which is non-homogeneous. This equation is usually rewritten as a linear, first order ordinary differential equation in the plate velocity, V , facilitating an easier solution.

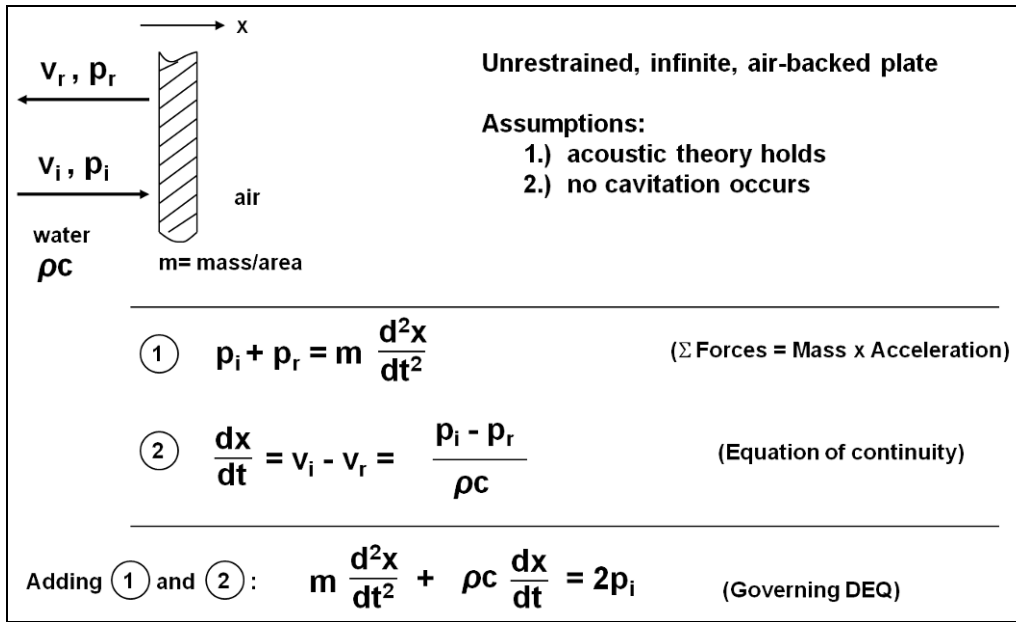


Fig. 4 – Taylor Flat Plate Theory - Derivation of the Equations of Motion

The forcing function on the right hand side of this equation, $2 \cdot p_i$, where p_i is the incident shock wave pressure and can be expressed as an exponentially decaying function:

$$p_i = p_o \cdot \exp(-t/\theta), \quad (2)$$

where:

p_o is the peak incident shock wave pressure,

t is the independent time variable, and

θ is the shock wave decay constant.

Next, this governing differential equation can be solved using integrating factor or a number of other solution techniques, and the solution is presented in Fig. 5. This solution has the form of a constant times the difference of two exponential functions. All of the terms in this solution have previously been defined except for the term, z , which is a non-dimensional quantity defined as:

$$z = m/(\rho c \theta). \quad (3)$$

Often times by expressing quantities in non-dimensional form like this, the solution takes on a much simpler and compact form. If we next revisit Equation 1 in Fig. 4, which represents the dynamic equilibrium equation, and substitute into this equation the solution for the plate velocity, dx/dt shown in Fig. 5, then we obtain the expression illustrated in the middle part of Fig. 5. When we examine the left hand side of this equation, we observe that the expression $p_i + p_r$ represents the total pressure loading the plate. When this expression becomes equal to zero, there is no more compressive shock loading on the plate and thus it is at this time that the plate will reach its maximum velocity. As a result, when we set the left hand side of this middle equation in Fig. 5 equal to zero, we can then solve for the value of time, t , at which the maximum plate velocity occurs. This time is referred to as t_{vm} and its solution is provided in the lower left hand expression in Fig. 5. When this expression is substituted into the solution for the plate velocity, dx/dt , the desired expression for the Taylor Flat Plate maximum kickoff velocity, V_m , is obtained. Finally, when this expression is divided by the time at which this maximum plate velocity occurs, t_{vm} , the average initial acceleration of the plate, \bar{a} , is obtained. The solutions for both V_m and \bar{a} are respectively presented as the lower right hand expressions in Fig. 5.

<p>Solution for $p_i = p_0 e^{-t/\theta}$:</p> <div style="border: 1px solid black; padding: 10px; margin: 10px auto; width: 80%; text-align: center;"> $\frac{dx}{dt} = \frac{2p_0}{\rho c(z-1)} \left[e^{-t/z\theta} - e^{-t/\theta} \right]$ </div> <p style="text-align: center;">(where $z = m/\rho c\theta$)</p>	
<p>From (1): $p_i + p_r = 2p_0 \frac{1}{(1-z)} \left[e^{-t/z\theta} - z e^{-t/\theta} \right]$</p> <p style="text-align: center;">($\frac{dx}{dt}$ reaches maximum when $p_i + p_r = 0$)</p>	
<div style="border: 1px solid black; padding: 10px; margin: 10px auto; width: 80%;"> $t_{vm} = \theta \frac{z}{(z-1)} \ln z$ </div> <p style="text-align: center;">Time to max. Velocity</p>	<div style="border: 1px solid black; padding: 10px; margin: 10px auto; width: 80%;"> $V_m = \frac{2p_0}{\rho c} z^{\frac{z}{(1-z)}}$ </div> <p style="text-align: center;">Max. Velocity</p> <div style="border: 1px solid black; padding: 10px; margin: 10px auto; width: 80%;"> $\bar{a} = V_m / t_{vm}$ </div> <p style="text-align: center;">Avg. Initial Acceleration</p>

Fig. 5 – Taylor Flat Plate Solution for Air-Backed Case

An example of a computed air-backed Taylor Flat Plate response is illustrated in Fig. 6. In this graph, the red curve represents the exponentially decaying incident pressure wave that loads the flat plate. The green curve is the total pressure at the fluid-plate interface. As the incident shock wave impinges upon the plate surface, it sees the plate as being initially rigid. As a result, the total pressure initially has an amplitude of twice the peak incident pressure. Shortly thereafter the plate begins to move away from the incident shock wave and thus the total pressure begins to decay very rapidly.

The blue curve represents the Taylor solution for the plate velocity. It initially starts at zero velocity and then accelerates as time progresses. The plate velocity continues to increase until the time at which the total pressure at the fluid-plate interface crosses zero. This is the point at which the fluid just begins to cavitate, and it is here that the flat plate has reached its maximum velocity, V_m . Beyond this point in time the Taylor solution is no longer valid as the assumption of no cavitation has now been violated. Continuing the linear solution at this point would place the fluid at the plate interface into a tension condition, which for most fluids, is not possible.

The associated average acceleration of the plate can now be determined by dividing the peak amplitude of the plate velocity by the time required for the plate to reach this peak starting from its at rest position. This average acceleration is depicted in Fig. 6 by the slope of the straight line drawn from the origin through the point of maximum plate velocity.

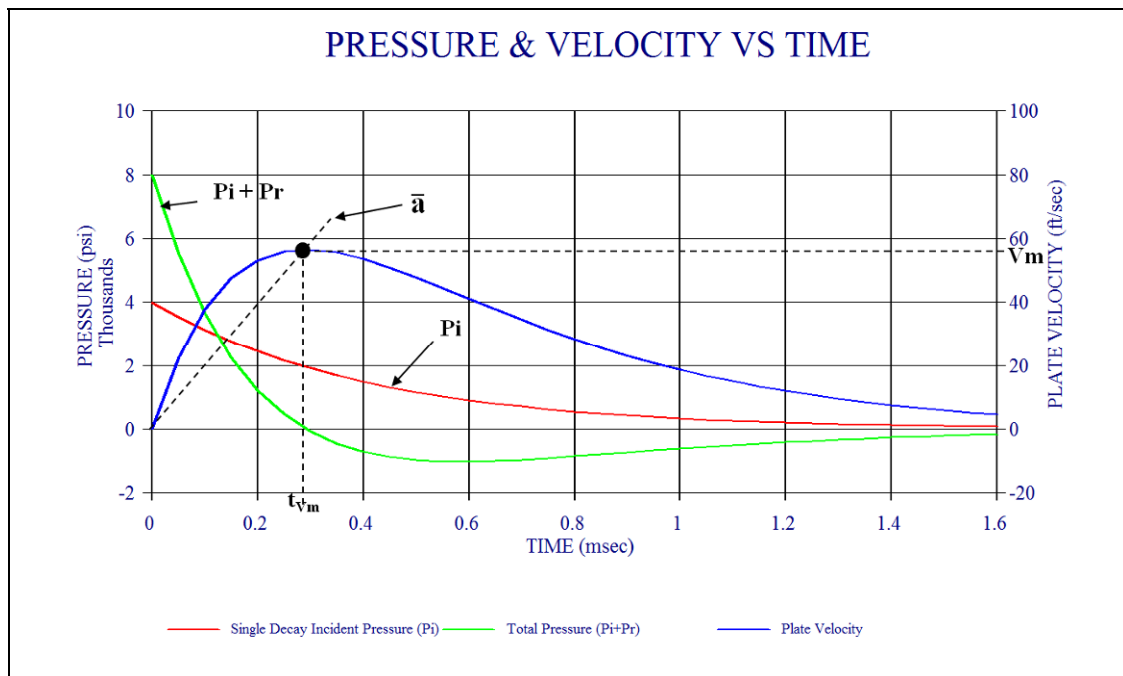


Fig. 6 – Example of Computed Taylor Flat Plate Response

Examples of typical responses of air-backed plates that are characterized using Taylor theory are provided in Fig. 7. The top curve shows the response of a lightly loaded shell. Here the characteristic rise to a peak velocity and subsequent deceleration phase are clearly evident. The straight line shown in the acceleration phase is what is actually being approximated by the Taylor calculation. A similar plot is shown in the lower part of Fig. 7, but this curve is taken from a more heavily loaded shell. Although the nature of these two responses is similar, the amplitudes of the resulting peak velocity and associated average acceleration and deceleration are significantly less, owing to the greater mass present.

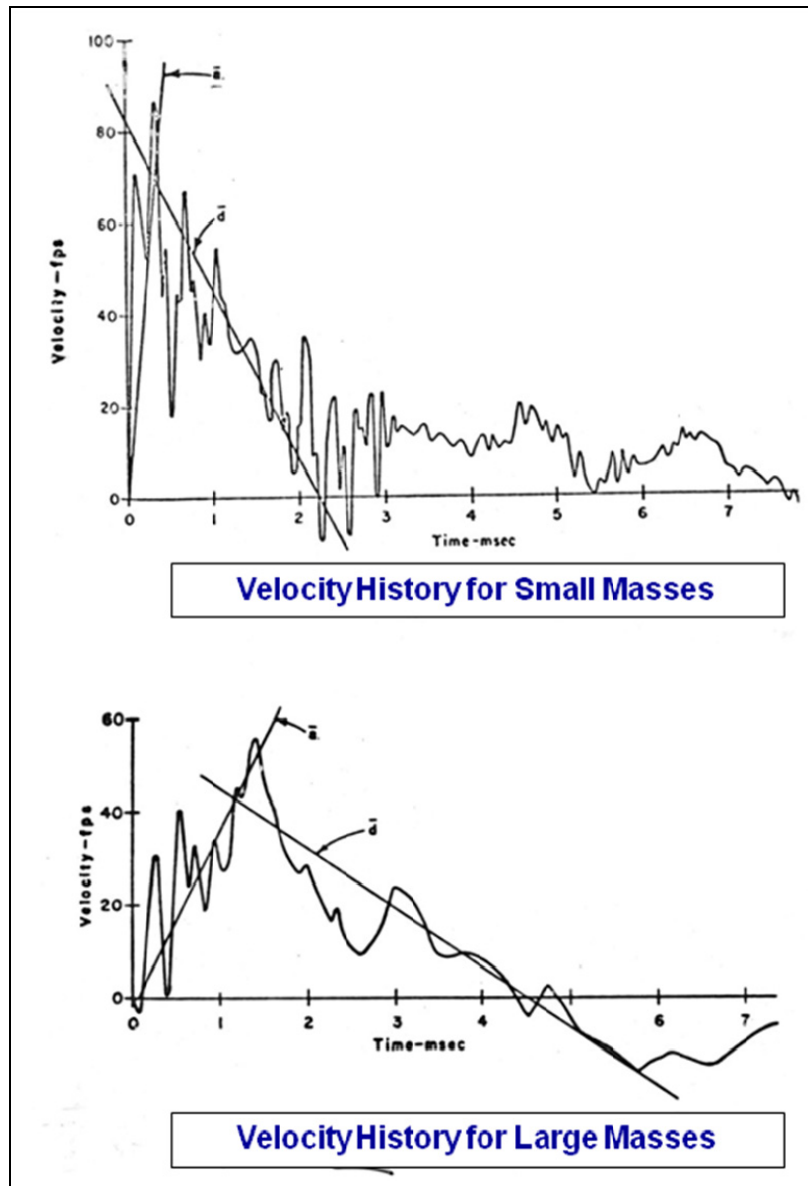


Fig. 7 – Typical Responses Characterized Using Taylor Theory

Correlations of Taylor Flat Plate estimates for a variety of cases with the associated experimental data are illustrated in Fig. 8. Here calculated maximum plate velocities are plotted vs. actual measured maximum plate velocities. The 45 degree diagonal line represents the line of perfect correlation. As can be seen in the figure, the data presented in general falls in a rather tight band around this line, indicating good correlation of Taylor theory with experiment for this air-backed case.

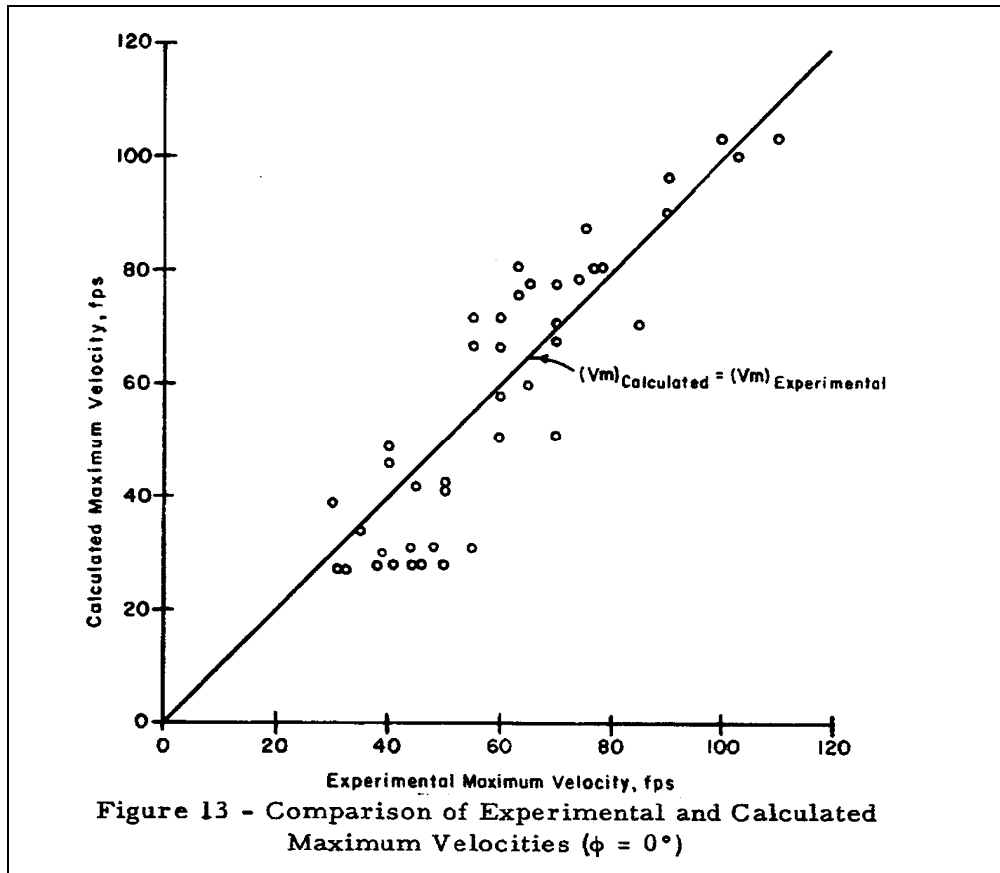


Fig. 8 – Correlations of Taylor Theory with Experimental Data

The application of the air-backed Taylor solution to estimate the peak vertical response of a floating structure will now be illustrated. In Fig. 9, the structure of interest is characterized as an infinite slab where the mass per unit area used is associated with the displaced mass and surface area of the ship section or zone. In applying the Taylor Flat Plate analogy, the infinite flat plate is rotated such that the incident shock wave from the UNDEX loads it directly from below. Thus, this condition represents an infinite unrestrained air-backed plate, the solution of which provides an estimate of the floating structure's peak vertical global kickoff velocity and associated average acceleration.

The Taylor solution for air-backed plates is repeated in Fig. 9 in terms of expressions for both the time to peak velocity and the magnitude of the peak velocity. As written, these expressions are valid if the floating structure were loaded directly from below by a shock wave at normal incidence. Since most UNDEX configurations involving a floating structure involve an incident shock wave traveling at oblique incidence, the Taylor solution must be modified to account for the angle of obliquity. From [2], to account for an oblique attack angle, the non-dimensional quantity, z , is modified by multiplying it by the cosine of this attack angle. This modified value, z' , is then used in the adjusted expression for V_m , as shown in the figure.

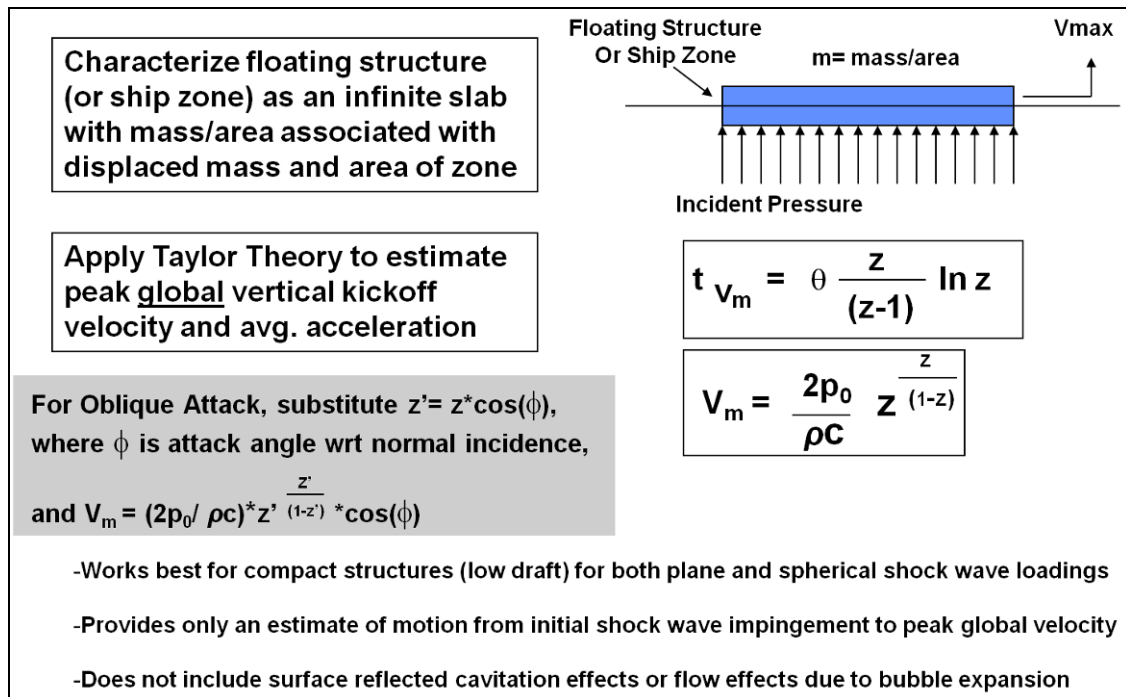


Fig. 9 – Application of the Taylor Analogy to a Floating Structure

This resulting expression represents a first order estimate for peak vertical kickoff velocity for a floating structure and can be used to perform a quick sanity check on more complex analyses. However, it is extremely important to understand the range of applicability of the underlying assumptions made with such an idealization with the Taylor method as presented here, as well as the associated limitations.

The method as presented works best for compact structures that have a relatively small draft. Test barges and small combatant craft fall into this category. Also, the method works well for both plane wave and spherical wave UNDEX scenarios. The method only provides an estimate of motion from the time of initial shock wave impingement until the peak velocity is reached. It does not compute the deceleration phase of global response, and does not include surface reflected cavitation effects or flow effects due to gas bubble expansion.

PEAK TRANSLATIONAL MOTION

This next simple tool will enable estimates of a floating structure's peak lateral motion to be made. It is adapted from Murray's Peak Translational Velocity (PTV) theory for estimating peak lateral global motion [3]. In the top portion of Fig. 10, a schematic of a fully submerged cylinder with a traversing planar shock wave is shown. In a manner somewhat similar to that developed in the previous section for Taylor theory, the equations of dynamic equilibrium are written, as shown in the figure. Here the first term, $f^{(1)}$ represents the forces exerted by the fluid on a fixed cylinder, while the second term, $f^{(2)}$ represents the forces exerted by the fluid due to cylinder motion. Since the structure (cylinder in this case) is assumed to be fully submerged, this condition becomes analogous to that of a fluid-backed Taylor Flat Plate. The application of this theory to estimate the lateral response of surfaced floating structures is illustrated in the lower part of Fig. 10.

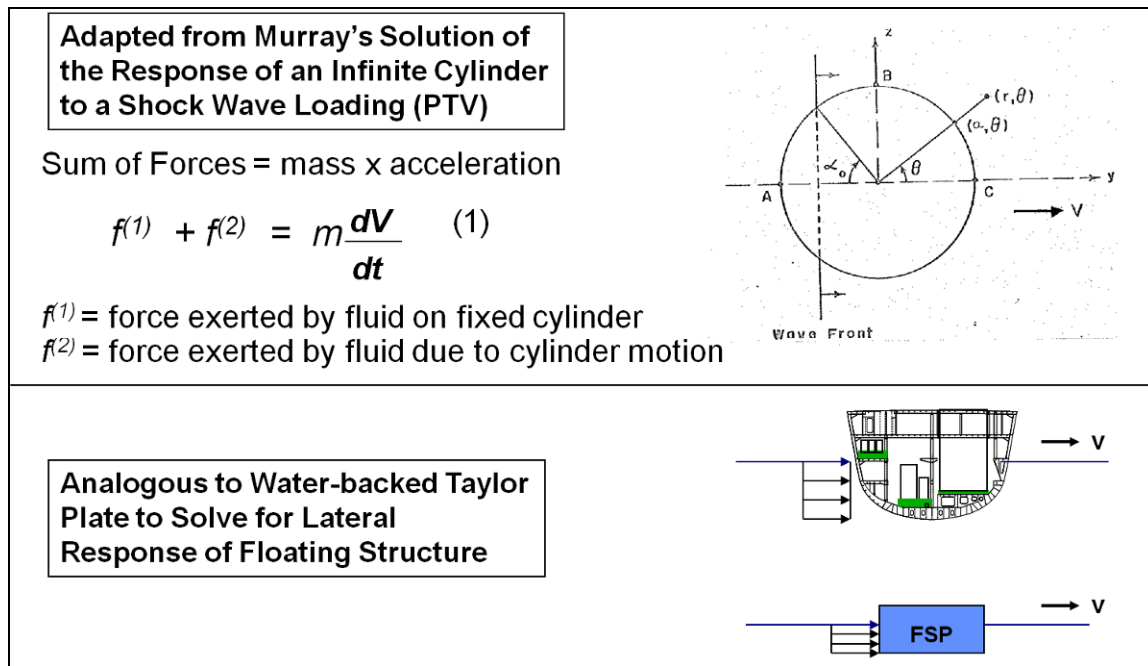


Fig. 10 – Application of Murray's PTV Theory for Estimating Peak Lateral Global Motion

With this adaptation in mind, the governing equations of motion for an infinite, unrestrained water-backed plate will be developed. In Fig. 11, a free-body diagram of such a plate is shown, along with the associated loads. This is very similar to that shown earlier in Fig. 4 for an air-backed plate, with the exception of the addition of a drag component of loading, p_d , due to the resistance of the fluid on the back side of the plate. The same assumptions of acoustic theory and no cavitation still apply as with the air-backed case. In addition, the drag force is related to the plate velocity by the expression,

$$p_d = \rho c * dx/dt. \quad (4)$$

The generation of the governing differential equation of motion for this Taylor water-backed condition, and its associated solution process, are similar to those followed for the air-backed case. The details are not presented here, but the resulting solution is summarized in the middle part of Fig. 11.

From these expressions, one can readily obtain first order estimates of both the peak lateral global velocity and average lateral acceleration of a floating structure. These results can then be used to perform a quick sanity check on more complex analyses. However, as with the first tool described earlier, it is extremely important to understand the range of applicability of the underlying assumptions made with such an idealization with the Taylor method as presented here, as well as the associated limitations.

The method as presented works best for structures that have near-rectangular cross sections. Test barges and combatant craft with relatively “boxy” hull forms fall into this category. Also, the method works well for plane wave UNDEX scenarios but begins to break down as the incident

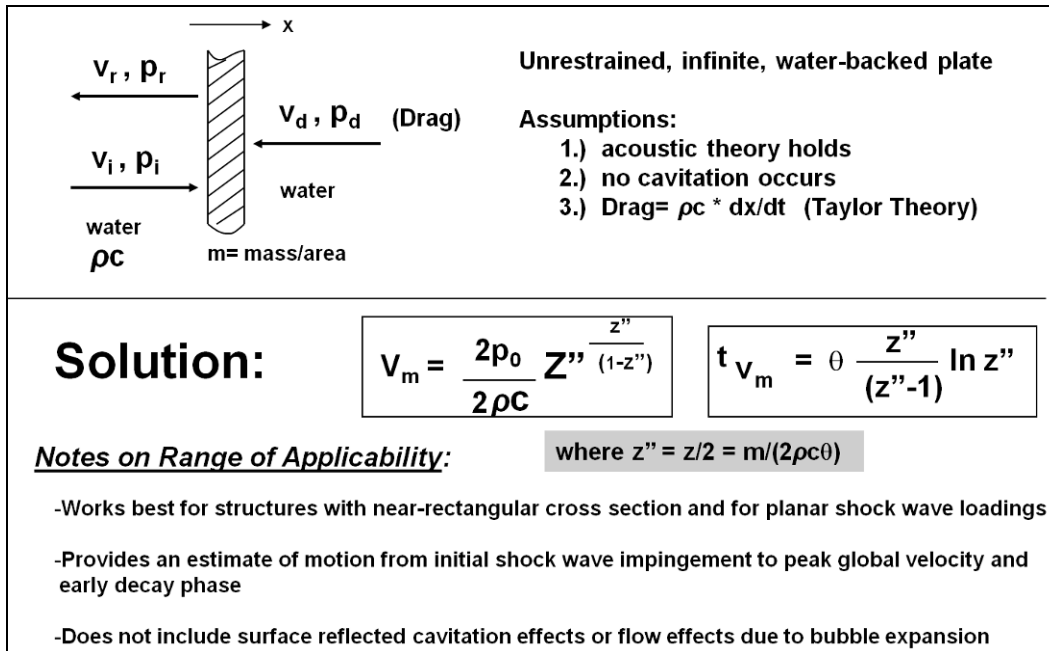


Fig. 11 – Taylor Flat Plate Solution for Water-Backed Case

shock waves become more spherical in nature. The method provides an estimate of motion from the time of initial shock wave impingement until the peak velocity is reached, and for the early part of the decay phase. It does not compute the complete deceleration phase of global response, and does not include surface reflected cavitation effects or flow effects due to gas bubble expansion.

IMPULSE-MOMENTUM APPROXIMATIONS

The first two simple tools used to provide bounding solutions for more complex analyses were based on Taylor Flat Plate and Murray PTV models. A third tool, which is also well known and is based on the Conservation of Momentum principle, will now be discussed. This method idealizes the floating structure as a column of water equal in depth to the ship's draft, d , as illustrated in Fig. 12. Here ρ is the mass density of the water and A is the cross sectional area of the water column. We now first investigate the effect of a shock wave approaching this column of water from directly below.

In the illustration of Fig. 13, an exponentially decaying shock wave is seen approaching the water column from below with a wave speed of c . At time equal to 0, the shock wave just begins to impinge upon the bottom of the water column. The shock wave then passes through the water column and reaches the surface at a time delay of d/c after first impingement. It then is reflected back into the water as a tensile wave and reaches the bottom of the water column at a time of $2d/c$ after initial impingement. This time of $2d/c$ represents the length of time that the shock wave is acting to accelerate the water column and thus forms the upper limit of the integral for the expression for applied impulse in the lower part of Fig. 13. This expression represents an impulse per unit area and is thus multiplied by the area, A , to give total impulse.

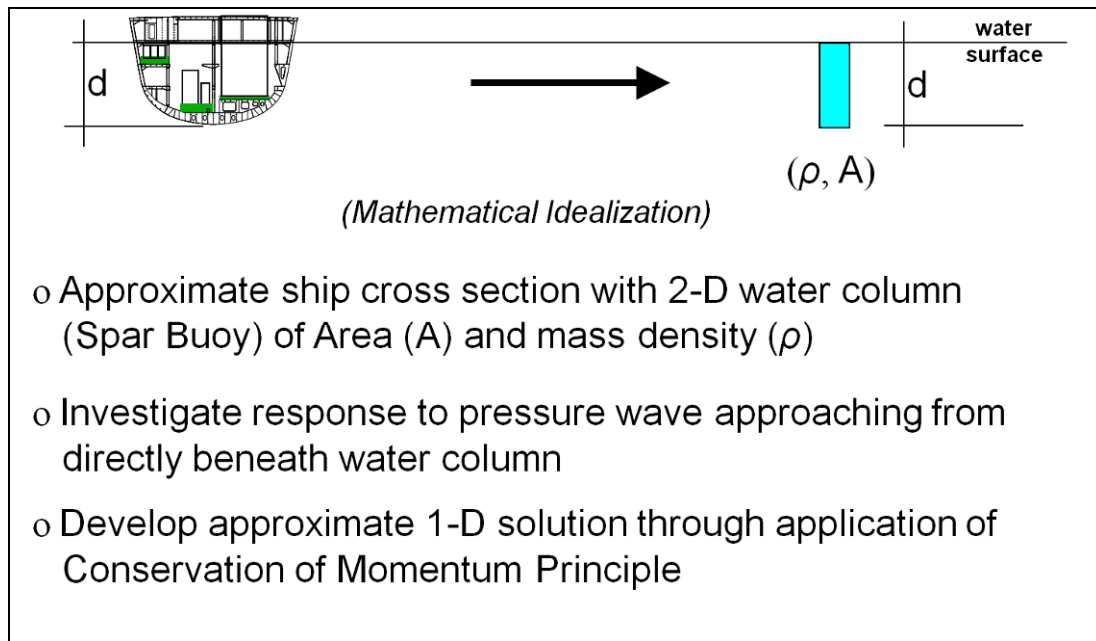


Fig. 12 – Impulse-Momentum Approximations for Estimating Peak Vertical Global Motion

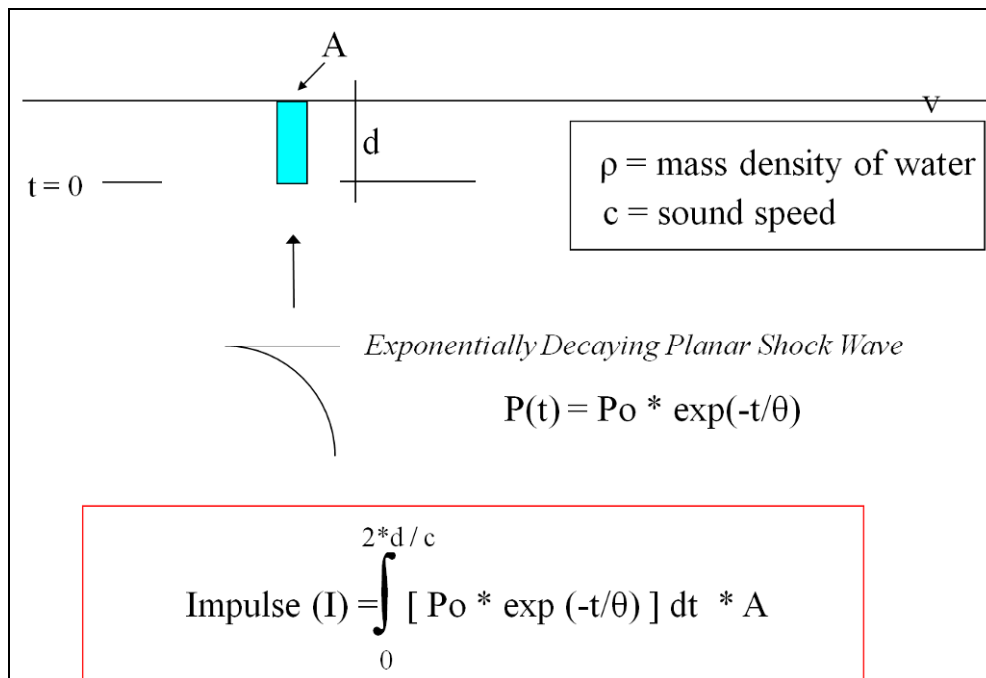


Fig. 13 – Derivation of the Spar Buoy Equation for Estimating Peak Vertical Global Motion

The next step is to then form the expression for the change in momentum of the column of water representing the ship section. This expression is developed by forming the product of the mass density of water times the volume of the water column. This expression is given in Fig. 14, where

Change in Momentum = $\rho * A * d * V_{sb}$

Impulse = Change in Momentum

$$\int_0^{2*d/c} [P_o * \exp(-t/\theta)] dt * A = \rho * A * d * V_{sb}$$

Solution:

$$V_{sb} = \frac{P_o * \theta}{\rho * d} * \left[1 - \exp(-2 * d / (c * \theta)) \right]$$

Fig. 14 – Application of Conservation of Momentum to Obtain Spar Buoy Solution for 1-D

V_{sb} is termed the “spar buoy” velocity, since the water column response is likened to the behavior of a very thin spar buoy.

Finally, the principle of the conservation of momentum is applied and the computed impulse is, equated to the change of momentum. In this equality, the area term, A , cancels out and when this equation is solved for V_{sb} , as in Fig. 14, we have the solution for the 1-D response of a ship section loaded directly from below.

This solution only has limited value, however, since most ship loading cases involve an oblique incidence of the incoming shock wave. As a result, a solution for the more general case of oblique loading will now be developed and thus the spar buoy solution will be extended to 2-D.

In Fig. 15, the direction of propagation of an oblique shock wave with respect to the vertical direction is illustrated. A planar shock wave is traveling at the speed of sound, c , along a path that is at an angle ϕ with respect to the vertical. The extension of the 1-D solution to 2-D is achieved by considering the effective propagation speed as the shock wave travels between points A and B along the oblique path. This distance, as can be seen in the figure, is represented by D . However, an observer at point B looking at point A perceives the shock wave as transiting the distance between these two points, which is the distance D' . If we let the time that the shock wave arrives at point A, $t_A=0$, and the time that the shock wave arrives at point B, $t_B=t_1$, then the distance that the shock wave travels, D , is also defined as the sound speed, c , multiplied by the transit time, t_1 , as shown in Fig. 15. Also seen in the figure is the relationship between the distances D and D' and the cosine of the angle ϕ . Since to an observer at point B the shock wave transit time between these two points is defined by the time t_1 , the apparent propagation sound speed is thus the distance that separates these two points, D' divided by this time t_1 . This is illustrated in Fig. 15, where the effective sound speed is seen to be equal to the nominal sound speed divided by the cosine of the oblique propagation angle ϕ .

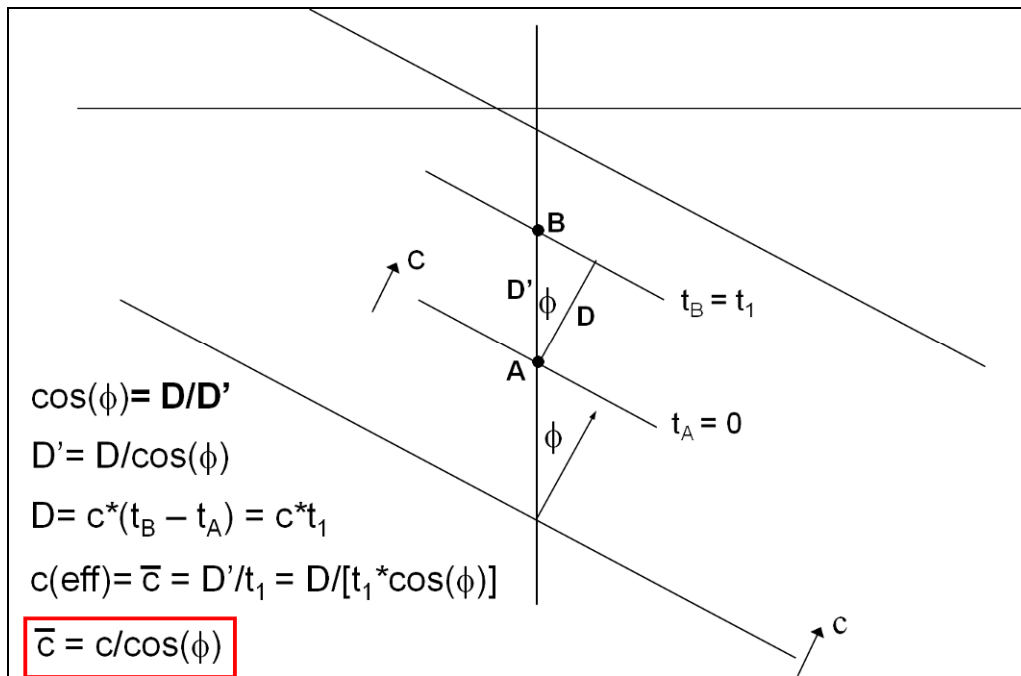


Fig. 15 – Extension of Spar Buoy Equation to 2-D

When this expression for the effective sound speed is substituted into the spar buoy velocity expression for 1-D shown in Fig. 14, the 2-D solution for the spar buoy velocity is obtained and is presented in Fig 16. This expression for V_{sb} represents an estimate for the peak vertical global kickoff velocity of a floating structure of draft d for a general oblique incident shock wave.

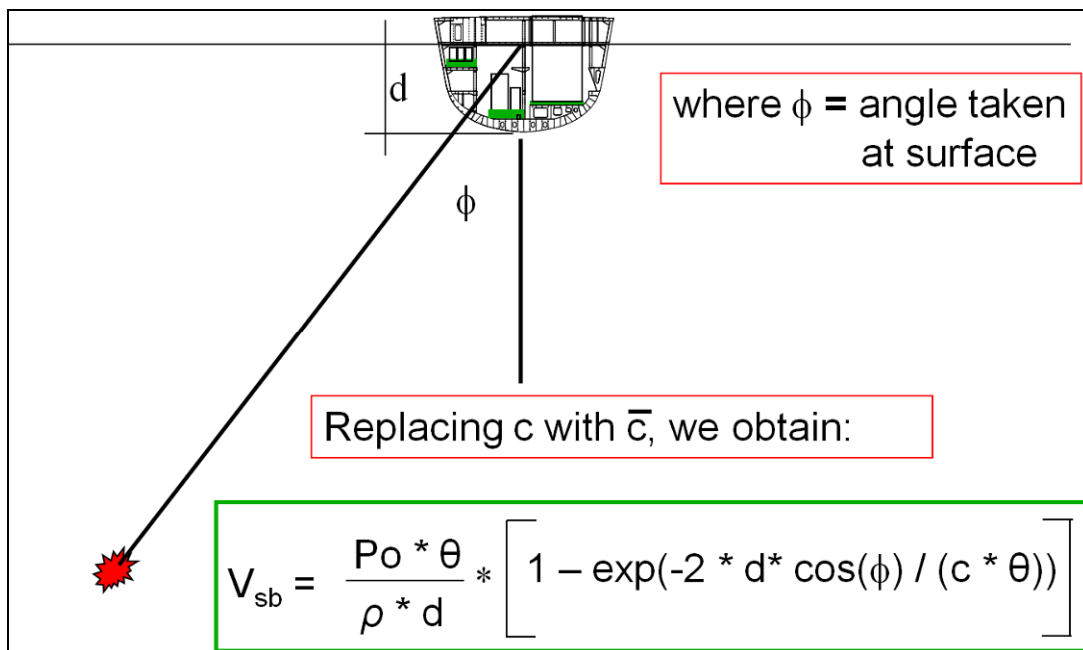


Fig. 16 – Two Dimensional Spar Buoy Solution for Estimating Peak Vertical Global Motion

With any approximate method it is extremely important to understand the ranges of applicability. For the spar buoy method presented above, the approximation is most accurate for scenarios involving large explosive charges at great distances (planar shock waves). Also, the method only approximates the peak shock wave-induced global kickoff velocity in the vertical direction. It does not include the flow effects associated with the expanding gas bubble. These ranges of applicability are summarized in Fig. 17.

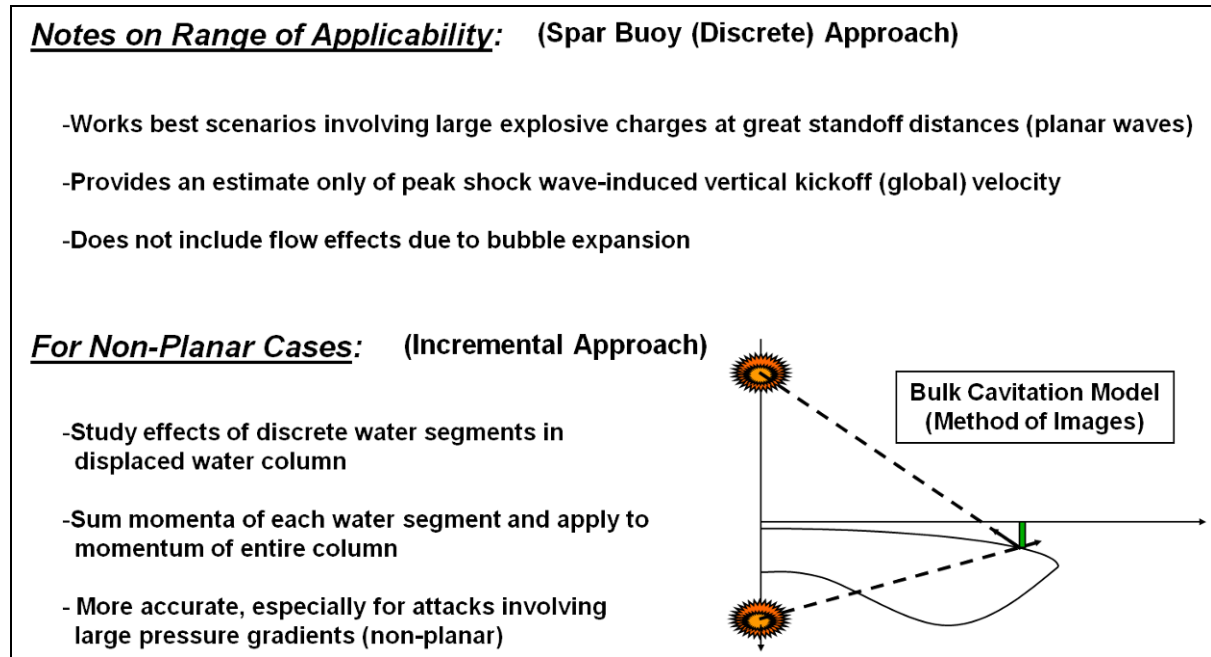


Fig. 17 – Extension of Impulse-Momentum Approximations to Non-Planar UNDEX Scenarios

For UNDEX scenarios involving non-planar loadings, an incremental approach can be substituted for the simpler spar buoy approximation to obtain a more accurate estimate of peak vertical global response. The concept associated with this approach is illustrated in the lower portion of Fig. 17. Here the method of images is applied in the evaluation of the total momentum imparted to the displaced water column. This approach was actually used in the development of the bulk cavitation closure model presented in [4]. For this approach, the effects of the incident and surface reflected shock waves are studied for each discrete water segment in the displaced column. The momenta imparted to each water segment is computed and summed for the entire water column. A more detailed illustration of this approach is shown in Fig. 18. From this total momentum a more accurate estimate of peak global vertical velocity is obtained, especially for UNDEX attacks involving large pressure gradients associated with non-planar attacks. Although this incremental approach requires a bit more computation than its spar buoy counterpart, it enables estimates to be made for vertical global velocity for a wide range of UNDEX scenarios.

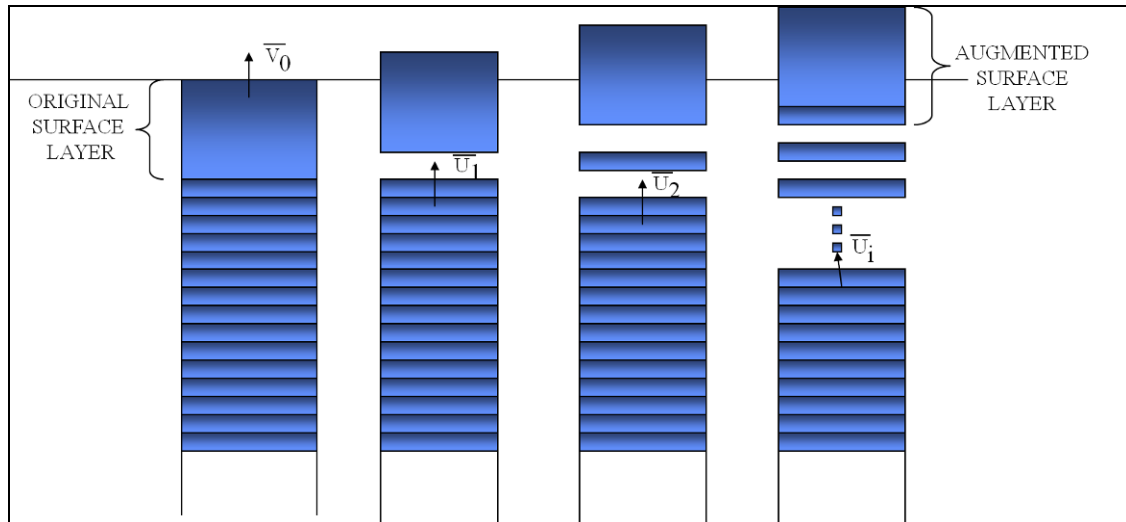


Fig. 18 – Incremental Method - Illustration of Surface Layer Motion and Accretion

To better illustrate the ranges of application of these approximate methods, the results from both the spar buoy and incremental approximations are contrasted in the curves presented in Fig 19. The ratio of the spar buoy result to the more accurate incremental result is plotted against charge weight. A family of curves is plotted for varying UNDEX severities, with the progression of severities increasing from the lower to upper curves. As can be seen for the lowest severity (indicated by the blue curve) the ratio does not change much throughout the entire range of charge weights. As the severity increases, however, the ratios of these two estimates begin to change significantly, especially for the smaller charge sizes, where the shock wave will be more spherical. It is for these ranges of charge weight and severity that the spar buoy approximation breaks down and the incremental method should be used.

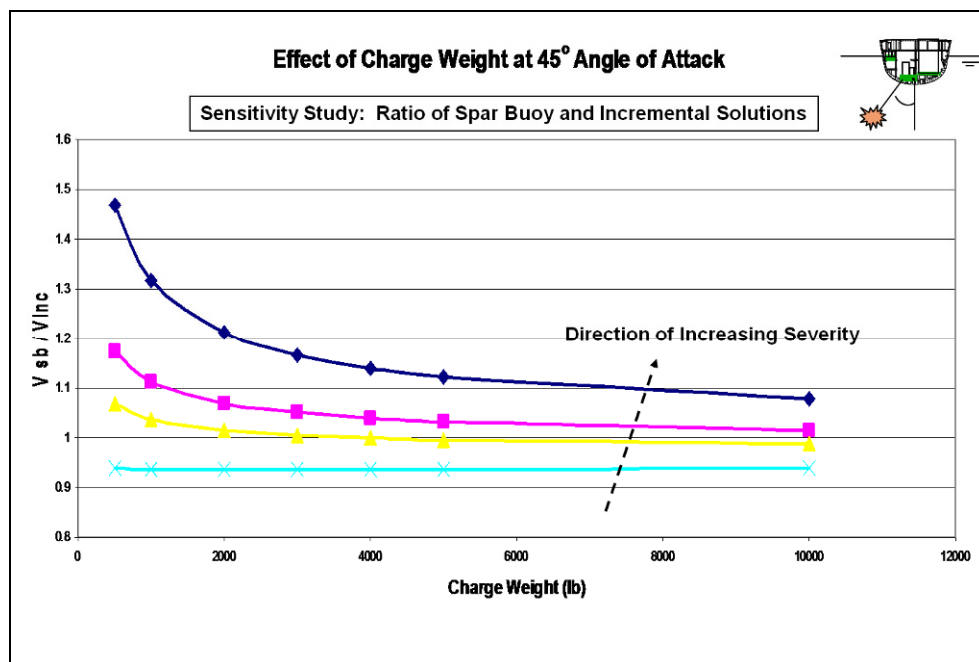


Fig. 19 – Contrast of Spar Buoy and Incremental Solutions with Increasing Charge Weight

SUMMARY

This paper described the need to benchmark and “ground” the solutions to underwater shock problems that are generated using detailed transient analyses. With solution methodologies becoming more diverse and complex, analysts can sometimes get caught up in the details and find it difficult to ascertain how good their results are in representing reality. As a result, simple physics-based analytical tools that provide reasonable first order approximations to the more complex problems can be a valuable asset to any analyst’s toolbox.

Presented in the discussions above were three well documented methodologies that enable the analyst to obtain quick, reliable estimates to bound their problems. The approximations that were presented will also enable analysts to perform quick sanity checks of their results and obtain a level of confidence in their results prior to continuing on with additional simulations. These methods include the Taylor flat plate analogy for both air-backed and water-backed plates, the peak translational velocity (PTV) method, and two variations of the conservation of momentum principle for estimating the vertical kickoff velocity of floating structures. Derivations of the governing equations associated with each of these solution strategies were provided, and the appropriate ranges of applicability were discussed. The simple approximations presented in this paper are very straightforward to apply. In addition to their value in enabling sanity checks for complex solutions to be made, they also can provide the analyst with increased insight into the physical problem and allow for quick and useful parametric studies to be conducted.

REFERENCES

1. Cole, Robert H., “Underwater Explosions,” Princeton University Press, 1st Edition, 1948.
2. Taylor, G. I., F.R.S., “The Pressure and Impulse of Submarine Explosion Waves on Plates,” Ministry of Home Security, R.C. 235, July 1941.
3. Murray, William W., “Interaction of Spherical Acoustic Wave With a Beam of Circular Cross Section,” Underwater Explosions Research Division, Portsmouth, VA., UERD-1-55, January 1955.
4. Costanzo, Frederick A., and John D. Gordon, “A Solution to the Axisymmetric Bulk Cavitation Problem,” 53rd Shock and Vibration Bulletin, Shock and Vibration Information Center, Naval Research Laboratory, Washington, D.C., May 1983.

Using Vibration Signatures Analysis to Detect Cavitation in Centrifugal Pumps

Surendra N. Ganeriwala (Suri)

Vetrivel Kanakasabai (Vetri)

SpectraQuest Inc.

8205 Hermitage Road

Richmond, VA 23228

(804)261-3300

www.spectraquest.com

Abstract

Timely detection of the occurrence of cavitation in pumps is very important as it can cause pitting, erosion, and loss of pump performance. Attempts to determine a unique signature of cavitation using vibration, acoustic emission [1] [2], audible-acoustics [3], and higher order non-linear modeling [4] techniques have been elusive. This paper presents the results of an experimental study undertaken first to understand the structure of cavitation and develop an effective means for on-line detection of it. Tests were performed to measure vibration, pressure, audible sound, motor current and the force due to cavitation of a centrifugal pump. A special force transducer capable of measuring fluctuating forces exerted by cavitation process on the pump casing was developed to understand the dynamics of cavitation phenomenon and signatures of a centrifugal pump operating under different cavitation conditions. Two of the abnormal operating conditions studied were the formation of tiny air bubbles (initiation of cavitation) and then fully developed cavitation. Experiments were also run with a transparent LEXAN cover using colored water to observe the cavitation. A Video was also taken for observing and developing an understanding of cavitation mechanism. Vibration, force, audible sound, and dynamic pressure were analyzed to detect cavitation. It was found that the pump has higher vibration amplitude in the axial direction than in the radial direction. This may be due to lower stiffness in the axial direction. From the experiments, it was also determined that significant amount of air bubbles will increase vibration component associated with the impeller vane pass frequency. Cavitation seems to excite high frequency structural resonances. Also, a fully developed cavitation may reduce the impeller vane pass frequency vibration amplitude. The force spectra did not provide any measurable information of cavitation.

1. Introduction

A pump is a mechanical device used to move liquids. Mechanical energy is transformed into hydraulic energy at the pump. Pumps can be classified into two categories: displacement pumps and centrifugal pumps. In this work, a centrifugal pump was tested and studied. Fig. 1 illustrates the single stage bronze centrifugal pump used in this work. This pump has a single rotating metal impeller. Liquid enters at the center and is thrown outward radially by centrifugal force. The five impeller vanes can be identified in Fig. 1 clearly.

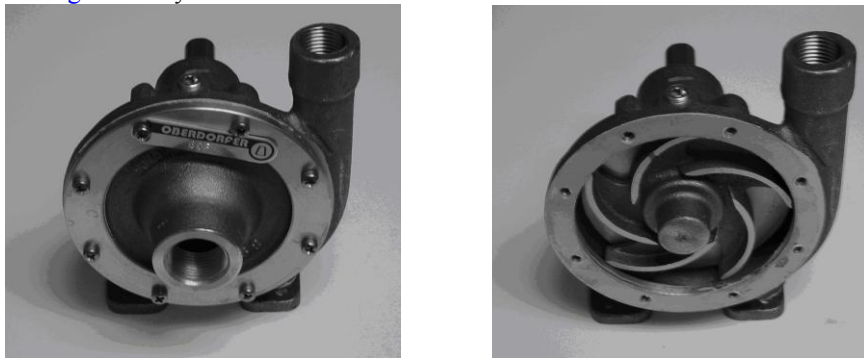


Figure 1a: Centrifugal Pump – Figure 1b: Impeller

One of the important, but damaging, phenomena in pumps is cavitation. Cavitation occurs when the pressure of the fluid drops below the vapor pressure for the temperature of the fluid. When this pressure drop occurs, whether it is a system pressure drop or a localized pressure drop, voids or cavities (bubbles) will form in the liquid. These bubbles implode or collapse when the fluid moves through impeller to the high pressure side of the pump, causing the impeller to erode. These implusions tear out tiny pieces of the metallic surface near which they implode. This can be very damaging and eventually the impeller will fail. Fig. 2 shows a schematic representation of the cavitation process.

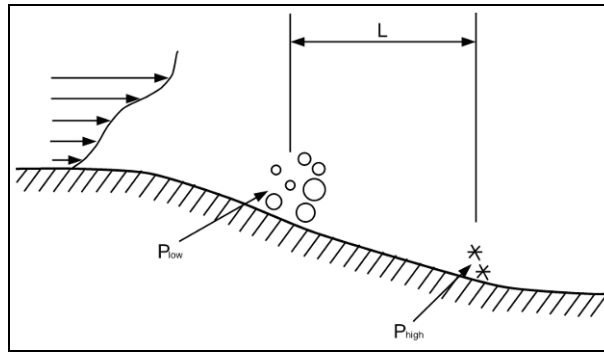


Figure 2: Cavitation

An essential concept in pump theory is net positive suction head (NPSH). NPSH is a measure of the difference between the total suction head and the fluid vapor pressure. The concept of NPSH is related with cavitation closely. For a specific pump, there are the required NPSH and available NPSH. The required NPSH is the factory suggested value which must be maintained to prevent cavitation. The available NPSH is the real pressure difference between the suction head and the fluid vapor pressure.

2. Experimental Setup

In this study, tests were performed on the SpectraQuest Machinery Fault Simulator equipped with pump kit as shown in [fig 3](#).

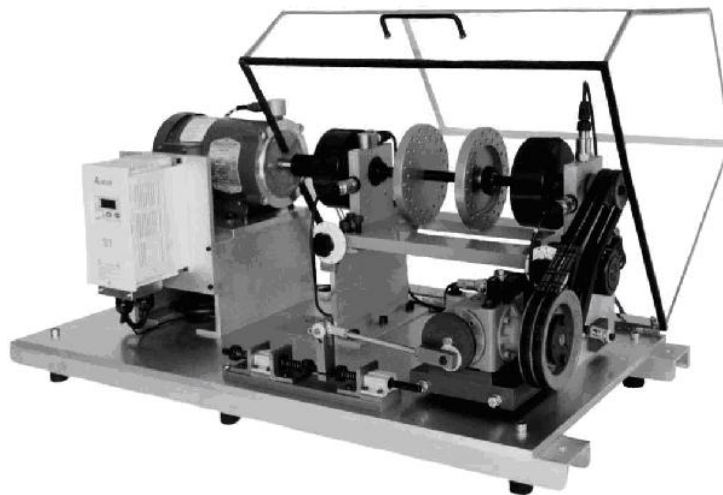


Figure 3: Machinery Fault Simulator (MFS)

In first arrangement the pump was directly connected to the motor. In the second arrangement the pump was mounted at the lower right hand corner of the MFS base plate and coupled to the rotor shaft by two drive belts. The transmission ratio of the belt drive is 1:1. Water was used as the liquid in the experiment. Both arrangements are shown on [figs. 4a](#) and [4b](#), respectively.

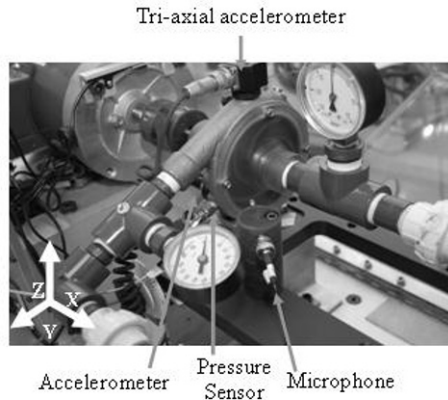


Figure 4a: Pump Direct Drive

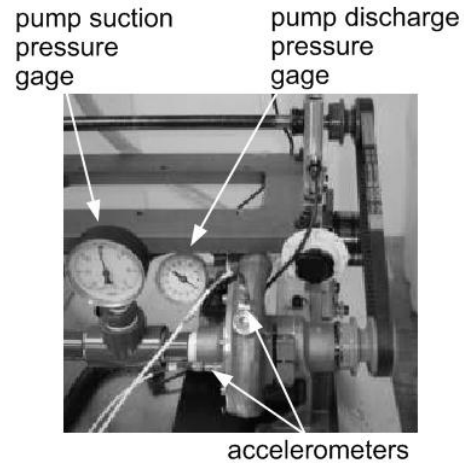


Figure 4b: Belt Drive

The pump and tank configurations during the experiment are illustrated in Figs. 4 and 5. The suction and discharge sides of the pump are fitted with pressure gauges. The pump discharge is directed through a manual modulating valve and then a flow meter back into the head tank. In the direct drive pump, a tri axial accelerometer over the pump, one single axis accelerometer in the axial direction, microphone and pressure sensor were installed. In the case of pump driven by belt, two single axis accelerometers were glued on the pump in the radial and axial directions respectively. The vibration, force, audible sound and motor current were measured using a SpectraQuest 16 channel, SpectraPad software/hardware system.

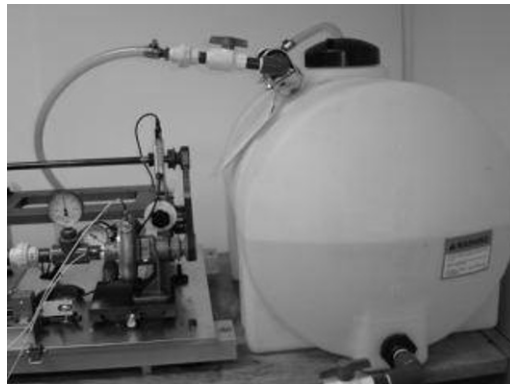
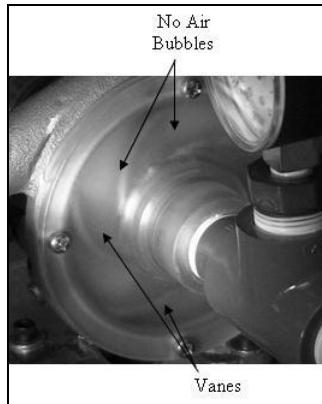


Figure 5: Tank

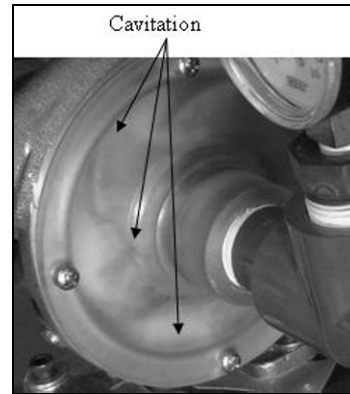
3. Experimental Procedure

The experiments are categorized into two groups. In the first group, the original brass pump was tested. In the second group, the original brass pump cover was replaced with a transparent plastic cover to observe the liquid motion inside the pump. Vibration, pressure, sound, motor current and force due to cavitation of the centrifugal pump were measured in this study.

First, the pump was running around 3600 rpm to check the integrity of the system. Through the transparent hose connected with the pump suction end, it was noticed that significant amount of air bubbles were sucked into the pump. By directing the water returning hose to the wall of the tank, the water would return to the tank smoothly without creating too many air bubbles. The data was collected for both the cases with and without air bubbles. The same experiments were performed by closing the suction valve to initiate and introduce different levels of cavitation. Tests were repeated at two lower speeds in order to understand the effects of speed on cavitation. The occurrence of cavitation is clearly seen when the pump is installed with a LEXAN cover instead of brass cover. The Figure 6a and 6b shows the vanes of the pump when there is no cavitation and when cavitation is occurring.



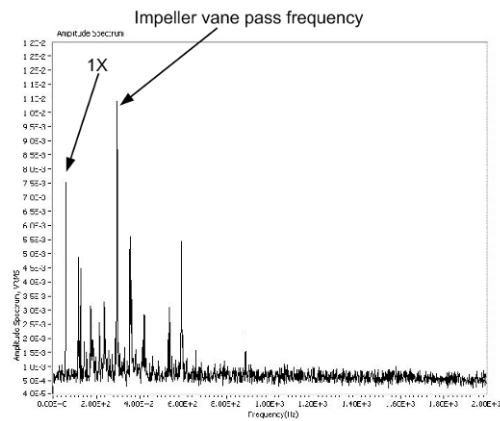
**Figure 6a: Cavitation in Centrifugal Pump:
No Cavitation**



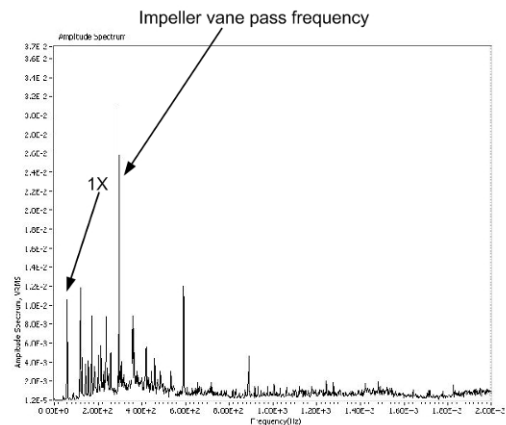
**Figure 6b: Cavitation in Centrifugal Pump:
Cavitation**

4. Experimental Observations and Results

The acceleration spectra are presented in Fig. 7 for pump speed of 3588 rpm without air bubble and cavitation. Figs. 7 (a) and (b) display the acceleration spectrum in the pump radial and axial directions respectively. The fundamental 1X component and its harmonics can be identified. The fifth harmonic which corresponds to the impeller vane pass frequency (Because there are five vanes on the impeller) has the highest amplitude. Moreover, two impeller vane pass frequency harmonics also have high amplitude. A comparison of the amplitude of Figs. 7 (a) and (b) indicates that the pump has higher vibration in the axial direction. This may be due to lower stiffness along the axial direction.



**Figure 7a: Vibration Spectrum for Pump
Speed 3588 RPM (Without air bubble and
extreme low suction head pressure): Radial
Acceleration**



**Figure 7b: Vibration Spectrum for Pump
Speed 3588 RPM (Without air bubble and
extreme low suction head pressure): Axial
Acceleration**

The same experiments were run both with direct couple and belt driven pumps. The data in the Figure 7 are belt driven configuration, but the results for the direct driven configuration were pretty much similar. Baseline data was also obtained for force transducer, pressure transducer and microphone. Spectral graphs for each transducer are shown in the Figure 8.

Figure 8 Baseline Data for (a) Force (b) Pressure (c) Motor Current and (d) Noise

As discussed earlier, the pump was running at different speeds. At each individual speed, the pump suction head and discharge pressures were read from the two pressure gauges connected with the pump for three

tank discharge valve position: 1) the valve is full open 2) the valve is closed somewhat until the appearance of cavitation 3) the valve is closed continuously until severe cavitation is observed. The pressures are shown in Table 1.

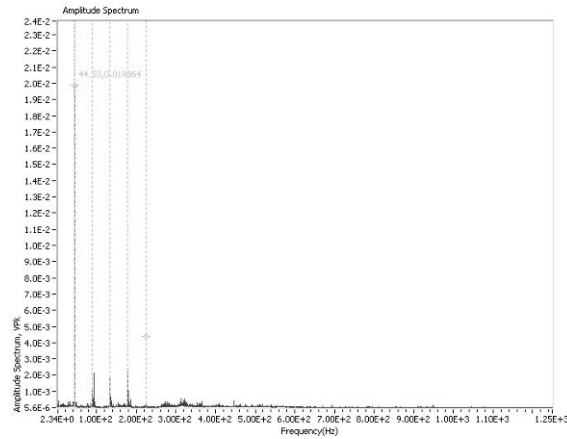


Figure 8a: Baseline Data for Force

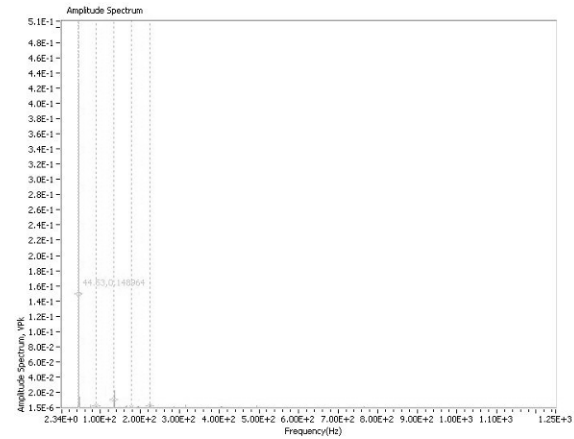


Figure 8c: Baseline Data for Motor Current

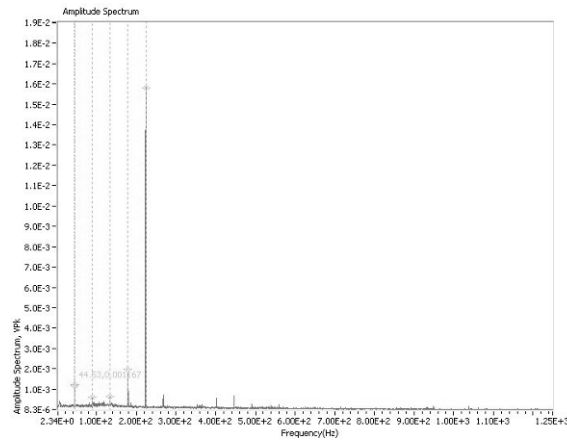


Figure 8b: Baseline Data for Pressure

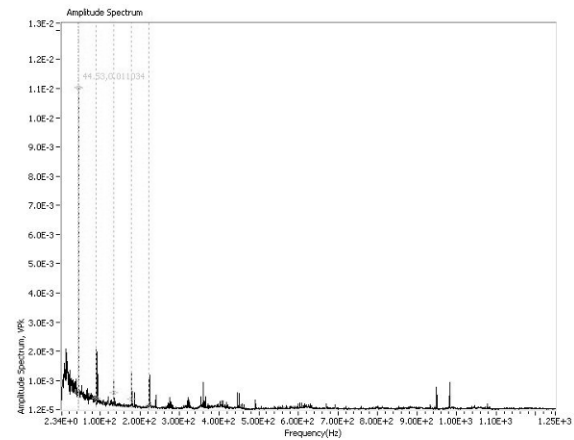


Figure 8d: Baseline Data for Noise

From Table 1, it can be found that the $NPSH_{available}$ and pump discharge pressure are all increasing with pump speed. Another observation from Table 1 and the experiments is that the NPSH range from the cavitation appearance to fully developed severe cavitation is also increasing with an increase in pump speed. For example, for pump speed 3600 rpm, the NPSH for cavitation appearance is -13 inHg. While the NPSH for severe cavitation is -20 inHg. It has a 7 inHg pressure difference. For pump speed of 3000 rpm, the NPSH for cavitation appearance is -20 inHg, the NPSH for severe cavitation is -21 inHg. The pressure difference is only 1 inHg. Moreover, for pump speed 2400 rpm, the cavitation appears at -18 inHg NPSH, and the cavitation develops into severe cavitation very quickly. This observation indicates that, although it is less likely for a slow speed pump to have the problem of cavitation, the cavitation will develop quickly into severe condition if it happens.

Pump RPM	Valve position	Pump Head Pressure (inHg)	Pump Discharge Pressure (psi)
3600	Full open	-5	14~15 (depends on air bubble)
	Cavitation appear	-13	13
	Severe cavitation	-20	9
3000	Full open	-4	11
	Cavitation appear	-20	5.5
	Severe cavitation	-21	3.5
2400	Full open	-2.5	8
	Cavitation appear	-18	3
	Further valve closing will cut water off		
1800	Full open	-1.5	5
	No cavitation can be generated		

Table 1: Pump Pressure

It can be seen from figures 9a-9d that as the cavitation starts the flow rate starts to decrease. This is another detrimental effect of cavitation beside erosion and loss of material. These results confirm that the cavitation must be detected and avoided.

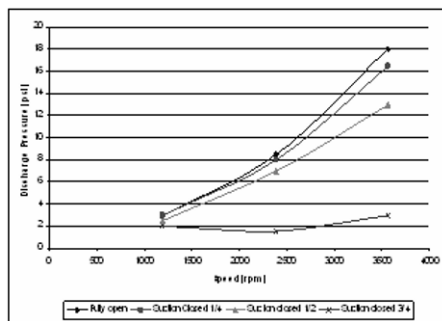


Figure 9a: Variation of Discharge Pressure with Speed

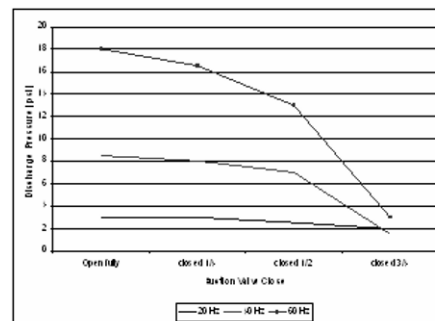


Figure 9b: Variation of Discharge Pressure with Suction Valve Closing

The acceleration in the radial and axial directions is presented in Fig. 10 for pump speed of 3590 rpm with significant amount of air bubble formed in the tank. A careful inspection of Fig. 7 (a) and Fig. 10 (a) indicates that with formation of air bubble, the vibration component associated with impeller vane pass frequency increase significantly. The vibration amplitudes of 1X and its other harmonics components do not change significantly. A comparison of Fig. 7 (b) and Fig. 10 (b) suggests similar trend. An examination of Figs 10 (a) and (b) indicates higher vibration level on the pump in the axial direction.

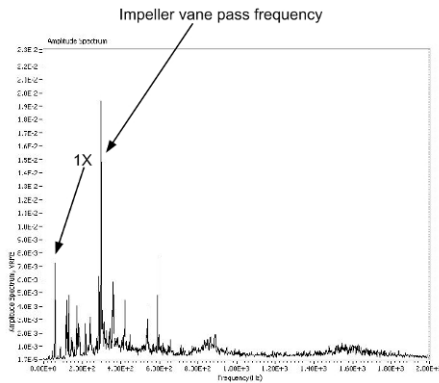


Figure 10a: Vibration Spectrum for Pump Speed 3590 RPM (With air bubble): Radial Acceleration

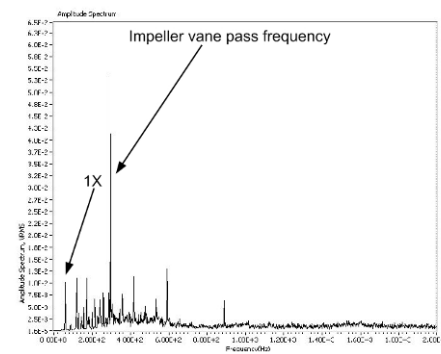


Figure 10b: Vibration Spectrum for Pump Speed 3590 RPM (With air bubble): Axial Acceleration

Figure 11 illustrates the vibration spectra in radial and axial directions respectively for pump speed 3617 rpm with severe cavitation. Figures 11 (a) and (b) present the spectrum of pump radial and axial vibration.

An inspection of Fig. 11 (a) indicates that the amplitude of the vibration component with impeller vane pass frequency (the fifth harmonic of 1X) has decreased significantly. However, this phenomenon does not appear for the pump axial vibration. The vane pass frequency vibration is still strong as illustrated in Fig. 11(b).

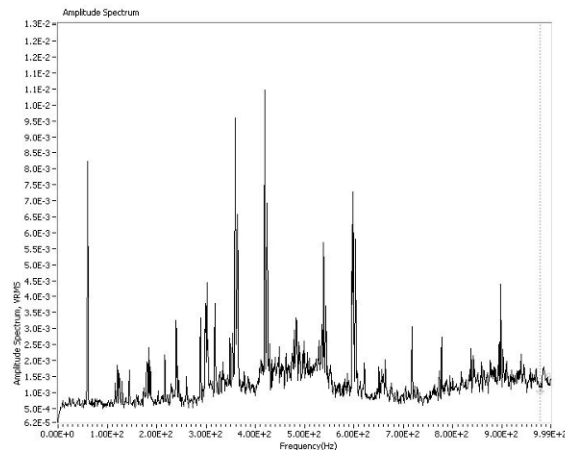


Figure 11a: Pump Vibration with Severe Cavitation: Radial Vibration

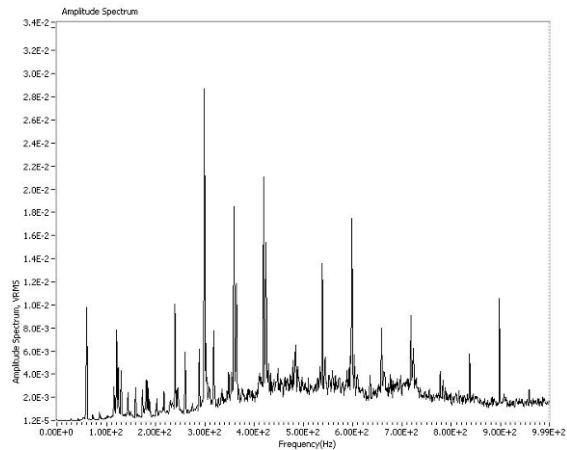


Figure 11b: Pump Vibration with Severe Cavitation: Axial Vibration

Fig. 12 shows the experimental data obtained when severe cavitation was observed in the pump. The comparison of vibration in the axial direction for baseline and severe cavitation shown in Figure 12(a) suggests that the vane pass frequency in the axial direction decreases when cavitation occurs. Fig. 12(b) shows the vibration comparison in the vertical direction of baseline and severe cavitation. The vane pass frequency in the vertical direction increases when cavitation occurs.

Fig. 12(c) and (d) indicate the amplitude spectrum of force along the axial and horizontal directions. Neither force along the axial nor horizontal directions change significantly when cavitation occurs. Fig. 12(e) shows the amplitude spectrum of pressure when the pump is experiencing severe cavitation. During cavitation the amplitude of pressure increases and indicates the occurrence of cavitation. Figures 12(f) and 12(e) show the amplitude spectrum of motor current and noise. The motor current and noise do not change notably when cavitation occurs.

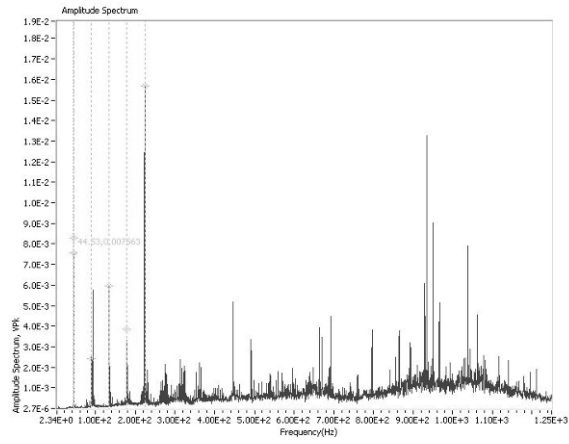


Figure 12a: Severe Cavitation: Axial Vibration

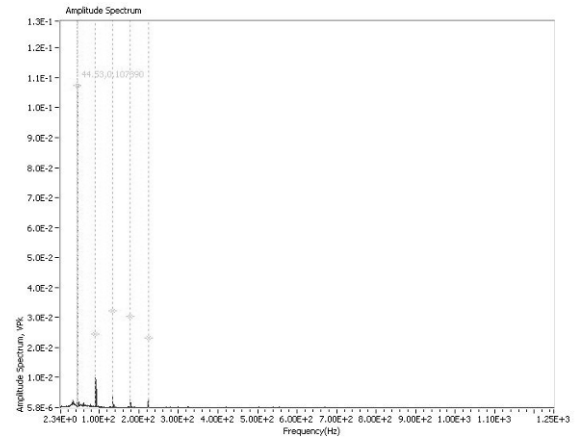


Figure 12d: Severe Cavitation: Horizontal Force

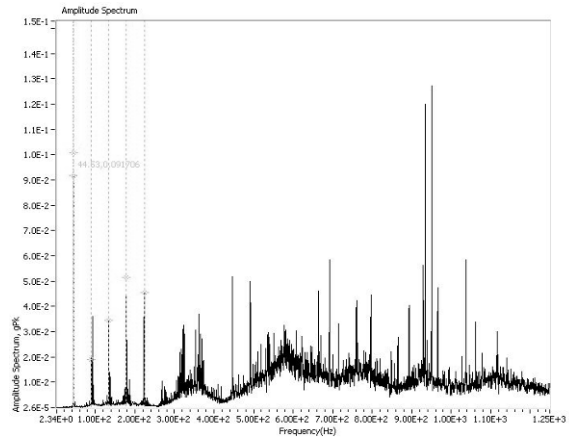


Figure 12b: Severe Cavitation: Vertical Vibration

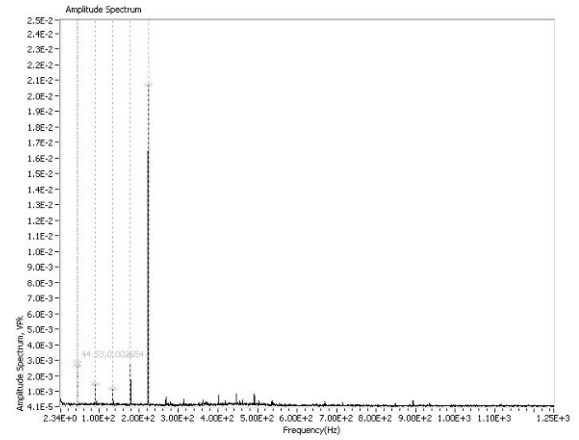


Figure 12e: Severe Cavitation: Pressure

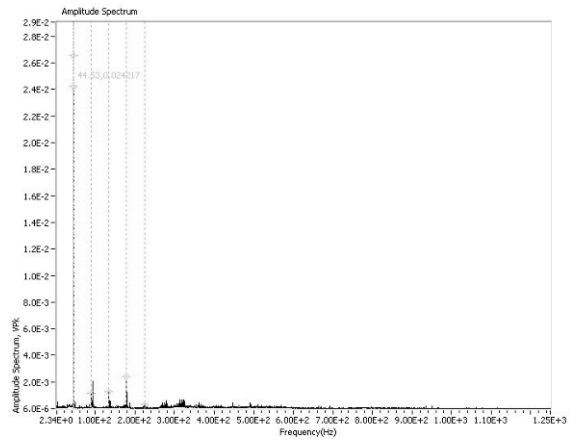


Figure 12c: Severe Cavitation: Axial Force

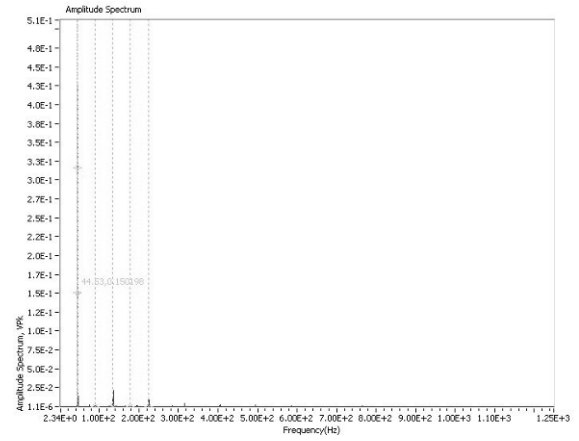


Figure 12f: Severe Cavitation: Motor Current

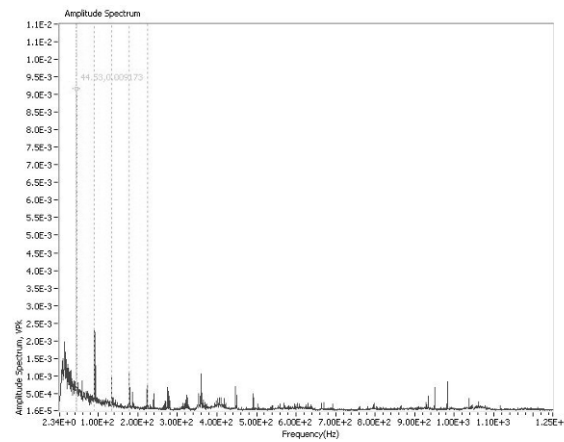


Figure 12g: Severe Cavitation: Noise

5. Summary

In this work, a single stage centrifugal pump was tested for its vibration signatures for different operational conditions. Pump vibration was measured in the radial and axial directions by accelerometers. The pump was running under three different speeds, 3600 rpm, 2400 rpm and 1200 rpm. Air bubble caused by the impacting of returning water with the water inside the tank was observed under pump speed of 3600 rpm. Cavitation was created intentionally by closing the tank discharge valve somewhat to drop the $NPSH_{available}$ below $NPSH_{required}$.

Several observations can be made tentatively based on the experiments.

1. Based on the vibration, pressure, force, noise, and motor current data, it is hard to see a unique signature associated with cavitation.
2. The centrifugal pump has higher vibration amplitude in the axial direction than in the radial direction.
3. Significant amount of air bubbles will increase vibration component associated with impeller vane pass frequency greatly.
4. Cavitation might decrease impeller vane pass frequency vibration.
5. While cavitation is less likely to happen in slow speed pump, it will develop very fast if it happens.
6. Force seems not to be affected by the cavitation.
7. Pressure seems to be a better indicator of cavitation – more correlated.
8. Motor current and noise do not change much with cavitation.
9. Cavitation seems to high frequency structural resonances.
10. Vibration appears to increase with the initiation of cavitation.
11. The centrifugal pump has higher vibration amplitude in the axial direction than in the radial direction.
12. More work needs to be done to determine the unique signature of cavitation.

6. Reference

1. L. Alfayez, D. Mba, G. Dyson, The Application of Acoustic Emission For Detecting Cavitation and the Best Efficiency Point of a 60kW Centrifugal Pump: Case Study, NDT & International, Vol 38, Issue 5, Pages 354-358, 2005
2. Seyed Farshid Chini, Hassan Rahimzadeh, Mohsen Bahrami, Cavitation Detection of a Centrifugal Pump Using Noise Spectrum, Proceedings of IDETC/CIE, DETC2005-84363, pages 13-19, 2005
3. M Dina, Detection of Cavitation Phenomenon in a Centrifugal Pump Using Audible Sound, Mechanical Systems and Signal Processing, Vol 17, Issue 6, pages 1335-1347, 2003
4. Lahdelma, Sulo, Juuso, Esko Kalevi, Vibration Analysis of Cavitation in Kaplan Water Turbines, World Congress, Vol 17, Part 1, 2008

Modes Indicate Cracks in Wind Turbine Blades

Surendra N. Ganeriwala (Suri)
Vetrivel Kanakasabai (Vetri)
Spectra Quest, Inc
8205 Hermitage Road
95066Richmond, VA 23228
suri@spectraquest.com
804-261-3300

Mark Richardson
Vibrant Technology, Inc
5 Erba Lane, Suite B
Scotts Valley, CA
mark.richardson@vibetech.com
831-430-9045

ABSTRACT

On-line surveillance of the structural integrity of wind turbines is a critical need in this currently fast growing industry. The structural integrity of the turbine blades themselves is critical to the continued operation of a wind turbine.

It is well known that the resonant or modal properties of a mechanical structure are directly influenced by its physical properties. Hence, any change in the physical properties of a structure should cause a change in its modal parameters. One question is always apparent though; *“Do structural faults cause significant changes in a structure’s modal parameters?”*

In this paper, we present test results from a wind turbine blade with different cracks induced in it. Each result shows that some of the modes of the blade are significantly affected by a crack, and that the modal parameters change more significantly with a more severe crack. Changes in modal frequency, damping, and mode shape are considered.

Using changes in modal parameters to indicate physical damage to turbine blades should be implemented in the on-line continuous monitoring of wind turbines. In such a system, differences between monitored modal parameters and their *base-line values* could be compared to both *absolute* and *percentage difference* warning levels. Comparing changes between operating and baseline modal parameters with warning levels will indicate when the blades of a wind turbine have undergone physical damage.

INTRODUCTION

It is well known that the elastic modes of a structure are strongly affected by its physical properties and boundary conditions. Its physical properties are summarized in its mass, stiffness and damping properties. Its boundary conditions are influenced by its geometric shape and its physical boundary conditions.

In this study, we tested a single wind turbine blade which was subjected to two types of material failures;

- 1) Cracks along one edge of the blade.
- 2) Cracks in the surface of the blade.

The blade was tested in a baseline condition with no cracks, and then with various cracks induced in it. The modal pa-

rameters of the blade without cracks were compared with those parameters from the blade with a crack. Modal frequencies, damping, and mode shape comparisons are presented.

MODAL TESTS

The blade test setup is shown in [Figure 1](#) below. Thirteen accelerometers were attached to the surface of the blade, and it was impacting with an instrumented hammer at each end and in the middle. The accelerometer locations are labeled in [Figure 2](#).

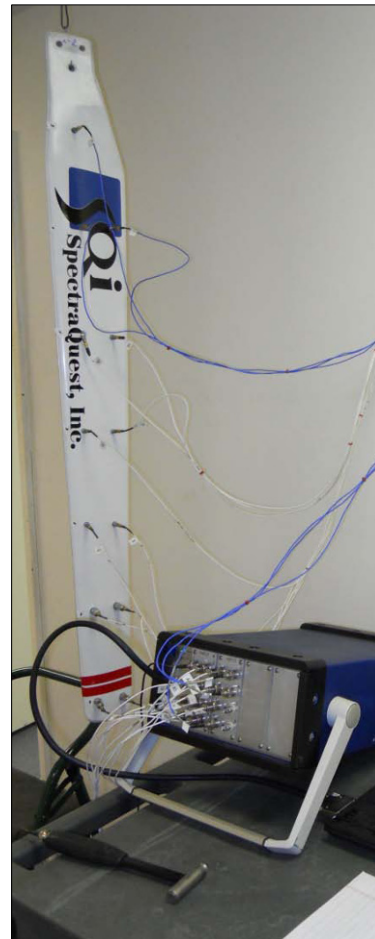


Figure 1 Blade Test Setup.

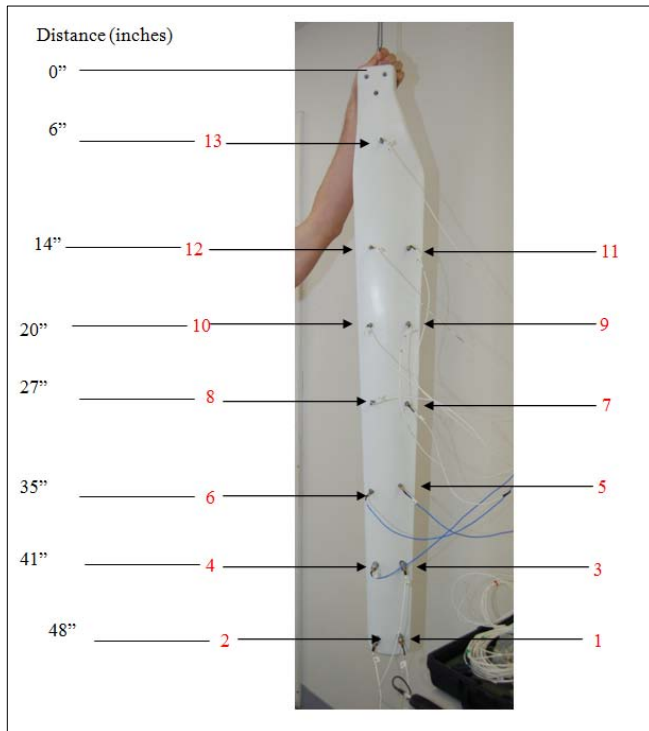


Figure 2 Accelerometer Locations.

During impact testing, time domain records of 64000 samples each were acquired from the impact hammer and 13 accelerometers. Each record contained data from 8 consecutive impacts. Three sets of data were taken by impacting in the middle and at each end of the blade. A typical set of the acquired time records (1 impact and 4 responses) is shown in Figure 3.

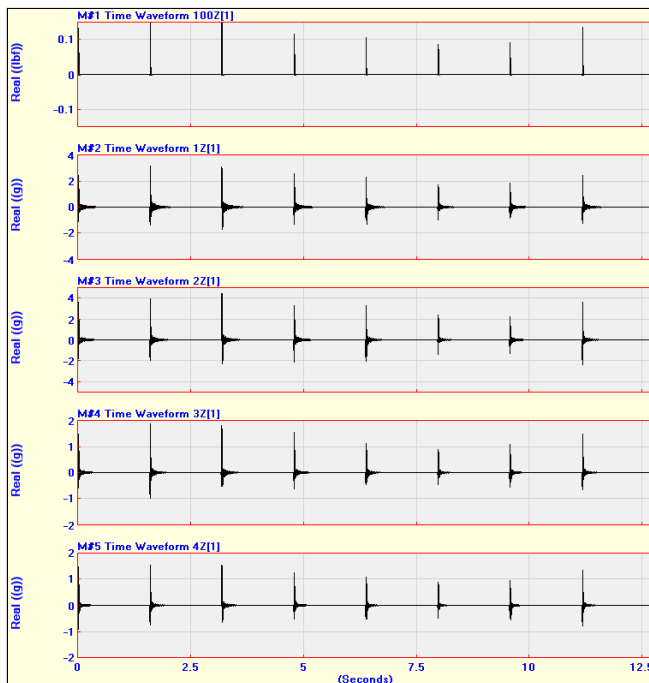


Figure 3 Typical Time Domain Records.

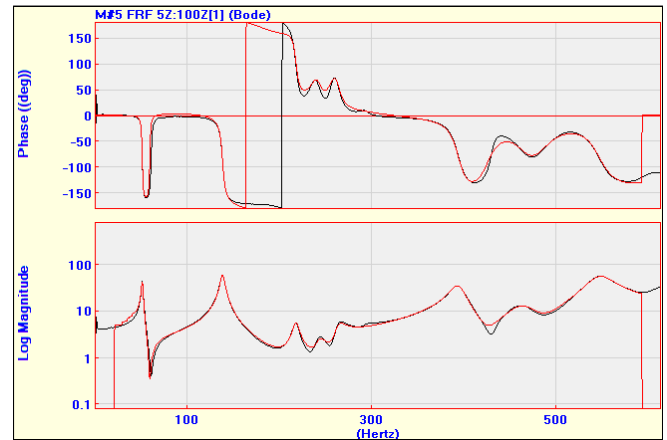


Figure 4 Typical FRF and Fit Function Overlaid.

The acquired time records were post-processed using tri-spectrum averaging (8 averages), with a pre-trigger delay to capture each impact signal and its corresponding responses. FRFs were then calculated from the Auto and Cross spectra. A typical FRF is shown in Figure 4. Each FRF contained 4000 samples of data, over a frequency span (0 to 2563.5 Hz) with frequency resolution of 0.64 Hz. The impact force Auto spectrum dropped off substantially above 800 Hz, so data was only used over the span (0 to 800 Hz).

Modal parameters (frequency, damping, mode shape) were obtained by *curve fitting* each set of FRFs. A **red curve fit** function is shown overlaid on the FRF data in Figure 4.

EDGE CRACK TESTS

The first kind of induced blade failure was a series of cracks along one edge of the blade, as shown in Figure 5. Four modal tests were performed so that the modal parameters of the blade with no crack could be compared with the parameters of the blade with edge cracks;

Test 1: No edge crack

Test 2: 5 inch edge crack

Test 3: 10 inch edge crack

Test 4: 20 inch edge crack

SURFACE CRACK TESTS

Following the first four tests, the blade was epoxy'd back together, and a second series of cracks were induced in the surface of the blade. A surface crack is shown in Figure 6. Four more modal tests were performed so that the modal parameters of the blade with no crack could be compared the parameters of the blade with surface cracks;

Test 5: No surface crack

Test 6: 1.3 inch surface crack

Test 7: 2.6 inch surface crack

Test 8: 3.9 inch surface crack



Figure 5 Edge Crack



Figure 6 Surface Crack

MODAL PARAMETERS FOR EDGE CRACKS

The modal frequencies obtained from the four edge crack tests are plotted in Figure 7. As expected, the frequencies trend downward with increased severity of the crack. This is because the edge cracks caused a decrease in the blade stiffness.

Modal damping for the four edge crack cases is shown in Figure 8. Most of the *damping changes from the baseline* are *negative*, except for modes 2 and 3 which are *positive*. A *negative change* means that the crack created *less damping* in the mode. A *positive change* means that the mode was *more heavily damped*.

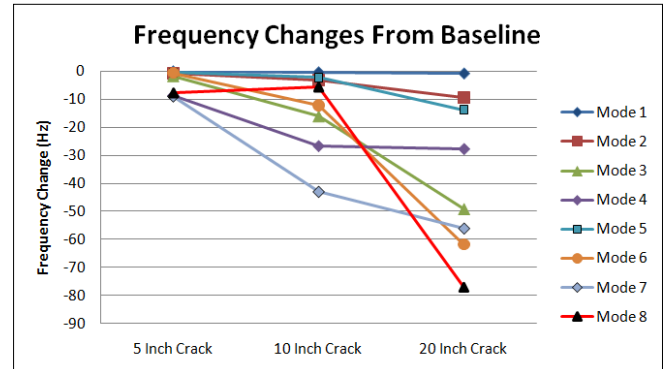
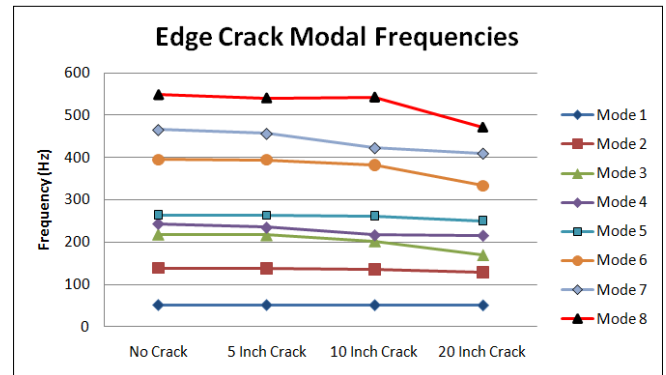


Figure 7

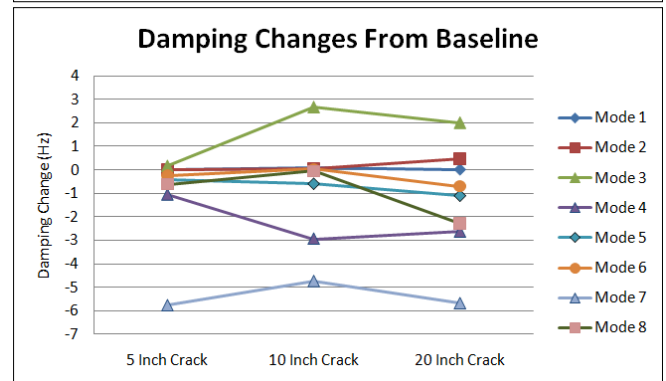
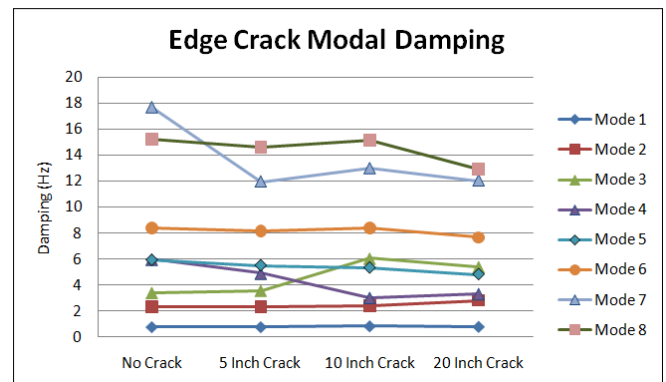
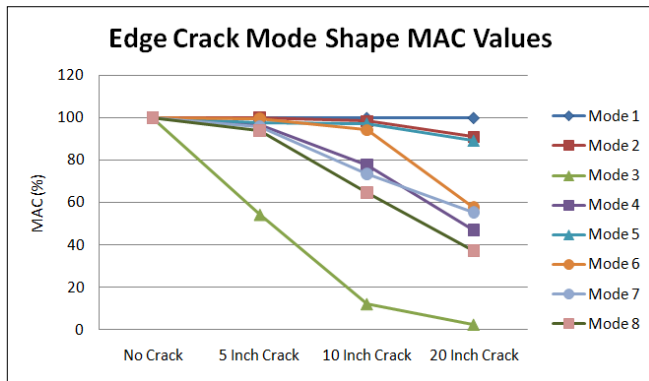


Figure 8



Mode shape MAC (Modal Assurance Criterion) [ref. 3] values for the four edge crack tests are shown in Figure 9. A MAC value of **100% indicates no change** in the mode shape.

The MAC values indicate **little significant change** due to the 5-inch crack, except for Mode 3. However, the 10-inch and 20-inch cracks caused **significant changes** in the mode shapes of several (but not all) modes.

MODAL PARAMETERS FOR SURFACE CRACKS

The modal frequencies obtained from the four surface crack tests are plotted in Figure 10. Most of the frequencies trend downward with increased crack severity, except Mode 4 which trended upward for the 2.6 inch crack. This upward trend was not expected.

Modal damping for the four surface crack cases is shown in Figure 11. All of the damping changes from the baseline are negative, meaning that the surface cracks created **less damping** in the blade.

Mode shape MAC values for the four surface crack tests are shown in Figure 12. All MAC values are **above 98.4%**. This means that all three surface cracks caused **very little change** in the mode shapes.

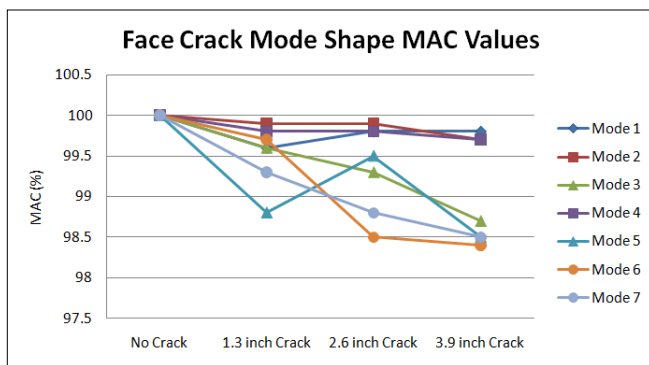


Figure 12

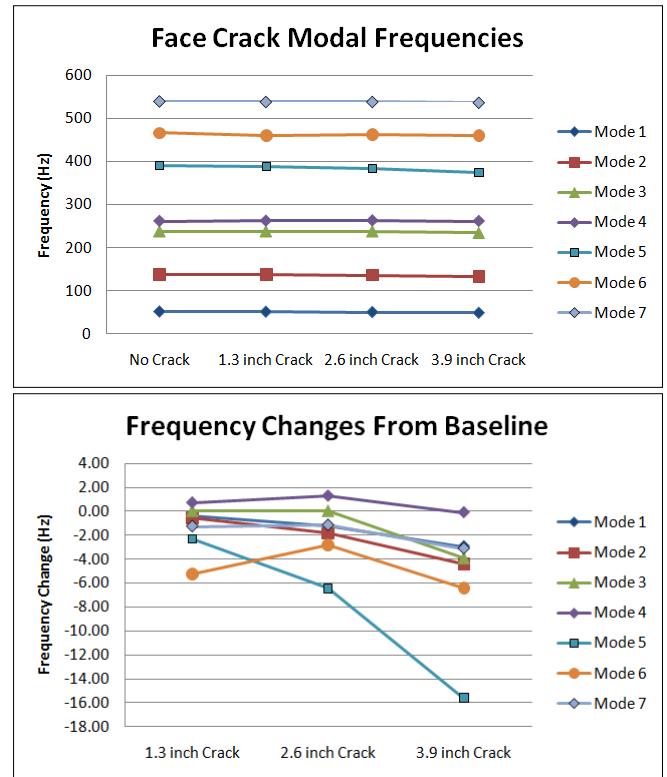


Figure 10

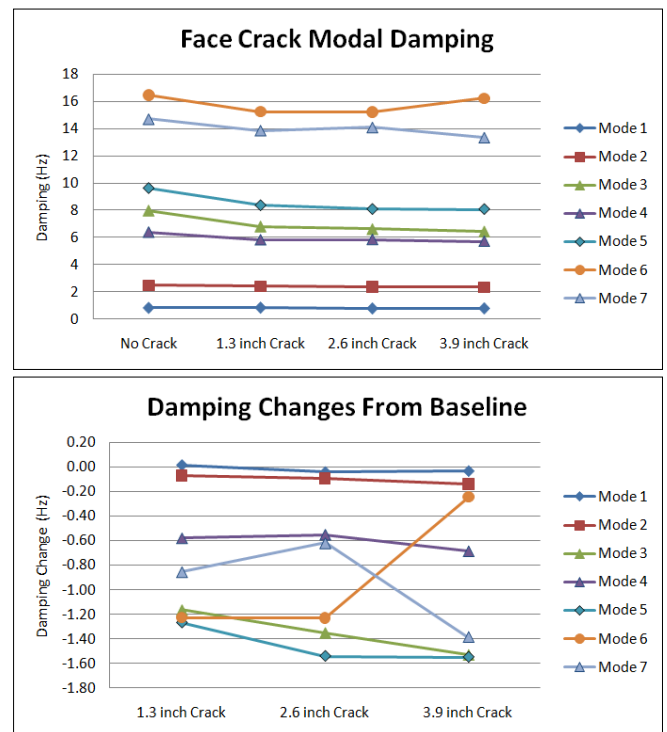


Figure 11

CONCLUSIONS

Eight different modal tests were performed on one of the blades of a wind turbine maintenance trainer and simulator. The blade was approximately 4 feet in length, and was made out of fiberglass. Two types of cracks were inducing into the blade, edge cracks and surface cracks. The purpose of the tests was to determine whether or not **significant changes** in the modal parameters of the blade would indicate the presence of a crack.

Thirteen accelerometers were mounted on the blade to obtain an adequate spatial sampling of its mode shapes. The blade was impacted with an instrumented hammer at its ends and its center. In other words, eight different **three reference** modal tests were performed on the blade. The acquired data was post-processed and 13 FRFs were calculated for each reference and each test case. Modal parameters (frequency, damping and mode shape) were obtained for the first 8 modes for the edge crack cases, and the first 7 modes for the surface crack cases.

The trend plots of the modal parameters indicated the following;

- The modal parameters of **modes 1 & 2** showed **no significant changes** due to any of the edge or surface cracks.
- The edge cracks caused **significant changes** in **all** of the modal parameters of **modes 3 through 8**.
- The surface cracks caused **significant changes** in the modal **frequency & damping** of **modes 3, 5, 6 & 7**. The parameters for modes 1, 2 & 4 showed little change.
- The surface cracks showed **no significant changes** in the **mode shapes** of the first 7 modes of the blade.

Several conclusions can be drawn from this study;

- **Changes in modal frequency** were the **most sensitive** indicators of the two types of blade cracks tested.
- **Higher frequency modes** are **stronger indicators** of localized blade cracks than are the lower frequency modes.
- **Changes in modal damping** are **less sensitive** than modal frequency, but damping did undergo **significant changes** in most of the test cases.
- **Mode shapes** were **significantly changed** by the edge cracks, but changed by less than 2% due to the surface cracks.

In conclusion, these tests showed that monitoring changes in the modal frequency of **the first seven modes** may be sufficient to indicate faults in wind turbine blades. Of course, each blade would have to be monitored separately in a wind turbine monitoring system to detect its faults. Moreover, output only Cross spectrum measurements (not FRFs) would have to curve fit, unless the blades were impact tested in the manner similar to the method used here.

Significant changes in modal damping and mode shape also indicated failures in many of these test cases. However, these parameters were less sensitive than modal frequency as indicators of the failures tested.

REFERENCES

1. Surendra N. Ganeriwala (Suri), Zhuang Li and Richardson, Mark "Using Operating Deflection Shapes to Detect Shaft Misalignment in Rotating Equipment" Proceedings of International Modal Analysis Conference (IMAC XXVI), February, 2008.
2. Surendra N. Ganeriwala (Suri, Schwarz, Brian and Richardson, Mark "Using Operating Deflection Shapes to Detect Unbalance in Rotating Equipment" Proceedings of International Modal Analysis Conference (IMAC XXVII), February, 2009.
3. R.J. Allemang, D.L. Brown "A Correlation Coefficient for Modal Vector Analysis", Proceedings of the International Modal Analysis Conference pp.110-116, 1982.
4. Wolff, T. and Richardson, M. "**Fault Detection in Structures from Changes in Their Modal Parameters**" Proceedings of the 7th International Modal Analysis Conference, Las Vegas, Nevada, SEM, Bethel, CT.
5. Richardson, M. and Mannan, M.A. "**Detection and Location of Structural Cracks Using FRF Measurements**" 8th International Modal Analysis Conference, Kissimmee Florida, Jan 29 - Feb 1, 1990, SEM, Bethel, CT.
6. Richardson, M. and Mannan, M.A. "**Remote Detection and Location of Structural Faults using Modal Parameters**" 10th IMAC Proceedings, San Diego, California, February 3-7, 1992.

Estimating Shock Severity

By Howard A. Gaberson, Ph.D., P.E.

Consultant

234 Corsicana Dr.; Oxnard, CA 93036; (805) 485-5307

hagaberson@att.net

ABSTRACT

The recently issued specification ANSI/ASA S2.62-2009, *Shock Test Requirements for Equipment in a Rugged Shock Environment*, specifies shock severity levels according to the plateau level on the PVSS plotted on 4CP, (pseudo velocity shock spectrum plotted on four coordinate paper). The levels run from 1 - 10 meters per second or 40 to 400 ips. These ANSI levels provide an example of how to identify shock severity. Examples are plotted of both PVSSs and SRSs divided by $2\pi f$, to form an acceleration PVSS or APVSS on 4CP. These show that the plateau of the APVSS is the same as the PVSS. Thus published SRSs can be evaluated with constant velocity lines drawn on the SRS which also show the severe frequency range. The paper shows severity levels of many SRSs. Several pyroshock references that refer to plateau severities of 50 ips as very mild, 100 ips as moderate, and 300 ips as very severe are examples.

INTRODUCTION

A shock is a violent transient motion delivered to the base of the equipment, and our concern is when it is severe enough to cause equipment failure. I'll say a shock is a violent velocity change. The Pseudo Velocity Shock Spectrum (PVSS) of a simple shock plotted on Four Coordinate Paper (4CP) looks like a flattened hill, as shown in Figure 1. The plateau or top of the hill of the PVSS plotted on 4CP shows the severe frequency range of the shock. The hill slopes down and to the right with an asymptote equal to the maximum acceleration. Maximum acceleration usually defines the high frequency extent of the

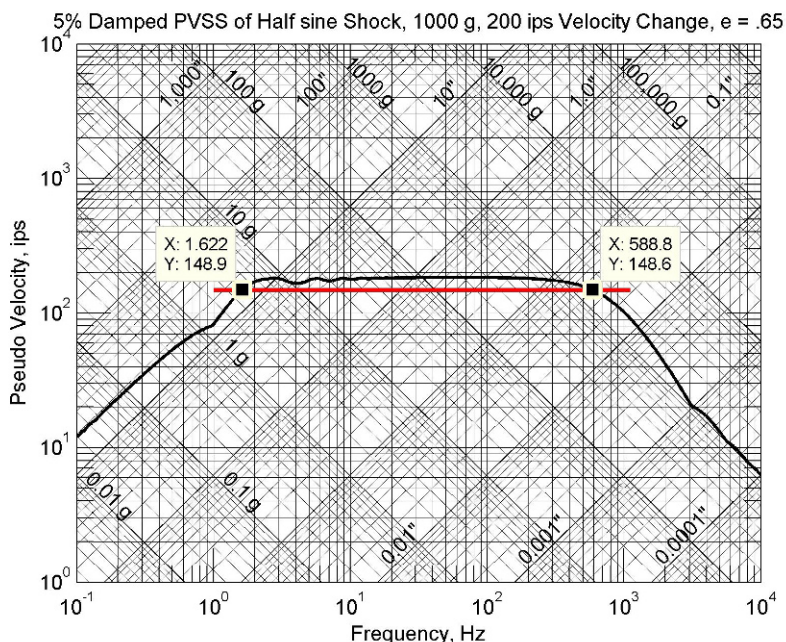


Figure 1. 5% damped PVSS on four coordinate paper (4CP) of the 1000 g, 200 ips half sine drop table shock.

plateau. The hill slopes down and to the left with an asymptote equal to the maximum displacement, and maximum

displacement defines the low frequency plateau limit.

The height of the plateau of the PVSS on 4CP is the severity of the shock. And the frequency range over which the plateau is at this high level is the range of equipment modal frequencies that can be excited to this velocity. Equipment and multi-degree of freedom systems accept shock energy only at their modal frequencies. Peak modal velocity is proportional to peak modal stress. Peak modal stress is proportional to PV [1, 2, 3, 4, 5].

Because we know the PVSS-4CP plateau is the severe shock region, we can classify the severity of a shock by the level of its plateau, and the frequency range over which the plateau is high. I'll be saying the severity of a shock as at 200 ips from 15 - 450 Hz. My job in this paper has two parts. Half is to show the SRS users how the PVSS plateau can be seen and measured on existing SRS plots, and the other half is to show some published SRSs along with their measured severities as examples.

The primary reason for defining the plateau level is that modal velocity is proportional stress. Since maximum stress limits severity it is natural that the velocity level that a shock can deliver to equipment is the severity level. Stress is proportional to modal velocity: $\sigma = K\rho cv$, where $1 \leq K \leq 10$; multi-degree of freedom systems, both lumped and continuous have modal responses given by the product of the participation factor and the modal PVSS value. [1, 2] In my training and course lectures [5] shock analysis for beams results in the maximum modal velocity of each mode equal to a participation factor times the PVSS value at the modal frequency. Severe velocities that cause yield point stresses in mild steel beams turn out to be about 115 ips. Thus 100 ips becomes a common floor for shock severity.

In 2009 ANSI issued ANSI/ASA S2.62-2009: *Shock Test Requirements for Equipment in a Rugged Shock Environment*. [8] This specification defines 10 severity levels in terms of velocity change at impact, Level 1 being a mild shock of 1 m/s velocity change and Level 10 a very severe shock of 10 m/s. Annex D defines the PVSS and links its plateau to the velocity change with its frequency limited by drop height and peak acceleration. Since 1 meter is approximately 40 inches, a level 2 shock has a plateau velocity of 80 ips. The specification does not specify a low frequency which I consider wrong. On a PVSS the impact velocity change is the plateau level, the peak acceleration and displacement range defines its frequency range.

STANAG 4559 [9] defines a shock level in terms of the PVSS on 4CP with 3 numbers: d_0 , v_0 , and a_0 which form the traditional flattened hill shaped simple shock PVSS on 4CP. [2] On May 18, 2008, NATO Standardized Agreement (STANAG) 4549: *Testing of Surface Ship Equipment on Shock Testing Machines* was adopted. The NATO standardized level notation is defined to take the form: NS LEVEL (m, m/s, m/s²). With this, the shock environment is completely defined in a compact notation.

Gaberson data of [6] indicated PV to be the best severity indicator with a PV of 150 ips as the failure level for the 6 fans he tested. Eubanks and Juskie [10], and Gaberson and Eubanks [11] defined equipment fragility as the highest PVSS on 4CP that the equipment is known to have survived.

Piersol [7] commented on shock severity in terms of velocities, and I'll quote his statement exactly. "Specifically, experience suggests that structural damage to equipment is rare when the equipment is exposed to a shock producing a peak modal velocity of less than 2.5 m/sec (100 in./sec), but is common when the peak modal velocity is more than 5 m/sec (200 in./sec)."

I recently discovered Morse's chart [12] and copied it here as [Figure 2](#). It was presented at an Aerospace Corporation conference in 2000. He clearly shows that the aerospace community understood the significance of shock spectrum velocities then and I was told that the ideas were known in the early seventies. Notice Morse is saying that 50 ips is a velocity below which failure seldom occurs, and 300 ips is a level of probable damage.

Some 4CP Details

I hate to bore you, so skip to Eq. (2g) if you already know it's true. For those who aren't sure, I'll present the details. Written with frequency as ω , in radians per second, a sine wave with maximum value, z_{\max} , and frequency, ω will be given by Eq (2a).

$$\omega = 2\pi f \quad (1)$$

$$z = z_{\max} \sin \omega t \quad (2a)$$

Differentiating to get velocity we have (One dot over the z represents velocity and two dots, acceleration.)

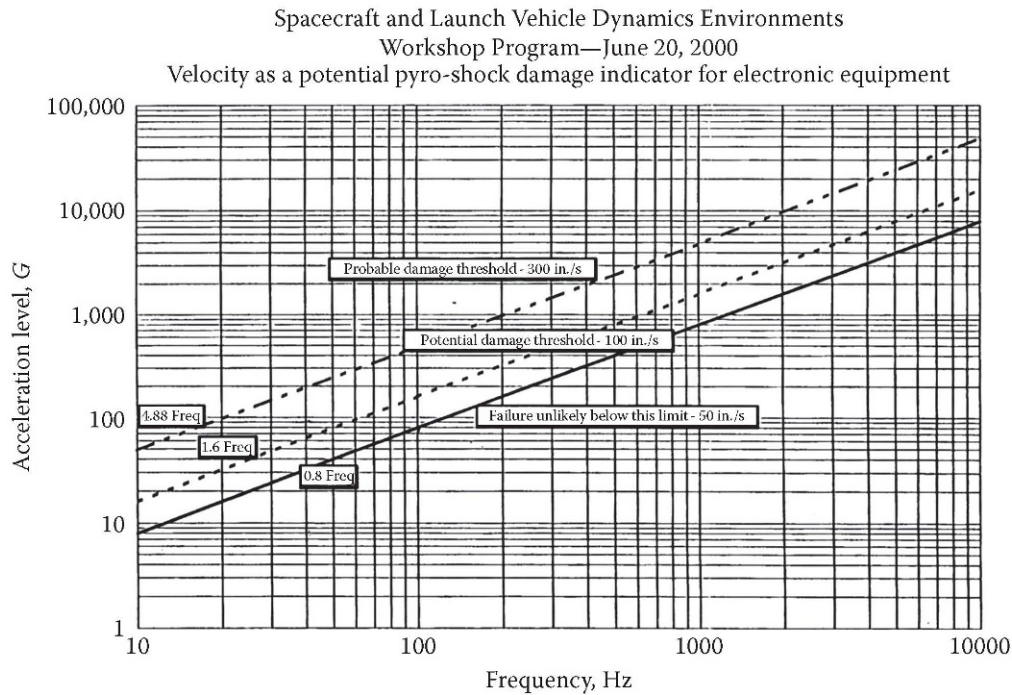


Figure 2. Morse's chart labeling velocity on an SRS as a "potential pyro-shock damage indicator for electronic equipment" [12]

$$\dot{z} = \omega z_{\max} \cos \omega t \quad (2b)$$

Differentiating to get acceleration gives Eq (2c)

$$\ddot{z} = -\omega^2 z_{\max} \sin \omega t \quad (2c)$$

Considering the maximum absolute values, we have from (2b)

$$\dot{z}_{\max} = \omega z_{\max} \quad (2d)$$

and from (2c)

$$\ddot{z}_{\max} = \omega^2 z_{\max} \quad (2e)$$

If we divide both sides of (2e) by ω , we get

$$\frac{\ddot{z}_{\max}}{\omega} = \omega z_{\max} \quad (2f)$$

If we compare (2f) to (2d), we get

$$\frac{\ddot{z}_{\max}}{\omega} = \dot{z}_{\max} \quad (2g)$$

I'll bring them all down here together to remember; they are:

$$\dot{z}_{\max} = \omega z_{\max} \quad (2d)$$

$$\omega z_{\max} = \frac{\ddot{z}_{\max}}{\omega} \quad (2f)$$

$$\dot{z}_{\max} = \frac{\ddot{z}_{\max}}{\omega} \quad (2g)$$

Four coordinate paper, 4CP, is a nomogram that shows these relations. At every point on the 4CP these relations relate the four coordinates.

Now a pseudo velocity shock spectrum, a PVSS, gives the peak value of the relative displacement of the single degree of freedom system (SDOF) at that frequency multiplied by the frequency (which gives it the units of velocity), and plotted on 4CP. If the maximum SDOF motion was a sine wave at that frequency, the relations would hold. I now define an APVSS, an acceleration pseudo velocity shock spectrum, as the maximum absolute acceleration of the SDOF mass divided by the frequency (which gives it the units of velocity) and plotted on 4CP.

The next section compares the PVSS and the APVSS for four very different shocks to show how well they agree and where they disagree.

Examples of Shock SRSs, PVSSs, and APVSSs to show how they relate to severity

This section of the paper carefully examines the differences and similarities between the PVSS and the SRS divided by $2\pi f$ to form an acceleration pseudo velocity shock spectrum (APVSS). They both are plotted on 4CP of four very different shocks. The reason this has to be done is because PV has been shown directly related (proportional) maximum modal velocity which in turn is proportional to maximum modal stress or shock severity. The APVSS provides a way to use the huge quantity of existing SRS data to approximate a PVSS and thereby show the severity of the SRS analyzed shocks.

I'll analyze four demonstration shocks: a drop table shock machine shock, a Navy explosive shock, a pyrotechnic explosive shock, and an earthquake shock. I want to show how the severe plateau on the PVSS shows up on the SRS, and the APVSS. I ultimately want show you that we can see the PVSS plateau on our SRSs, and that it's easy to draw severe velocity lines on an SRS to show the PVSS plateau. But first I think you should see how the PVSS and the APVSS compare.

Consider a 200 ips 1000 peak g half sine drop table shock. We'll have a coefficient of restitution $e = 0.65$. It is necessary to include the acceleration during the drop in order to understand the low frequency limits of the shock severity. [Figure 3](#) shows the acceleration time history and its integrals. On the top line I show an expanded view of the impact interval so you can see the half sine shape. [Figure 1](#) shows its 5% damped maximax PVSS on four coordinate paper (4CP). The flat top plateau occurs over a range of about 2 to 400 Hz, and it's at a level of 185 ips; thus its severity is 185 ips from 2 to 400 Hz. That is the frequency range for which the shock is severe, where it can induce the highest modal velocities. To more accurately show the range, I've drawn a red line at 80% of the plateau level of 185.34 ips. For 5% damping the simple shock plateau level is at 0.9267 of the undamped plateau [17] that is at the impact velocity change of 200 ips. 5% damping reduced it by

about 6%. The line intersects the plateau at about 1.62 and 589 Hz, which is determined by using Matlab's `datatip` function that can read the values on the curve. This is the frequency range where the shock can deliver 80% of its peak velocity into equipment modal responses.

This is going to get very instructive, at least it was to me. Let's now look at the SRS of the shock and compare it with the PVSS. This is going to demonstrate how to read the severity from the SRS, which is generally unknown. Figure 4 shows the SRS of our 1000g, 200 ips half sine. If you imagine the PVSS of Figure 1, tilted 45 degrees to the left, you can somewhat see the features on the SRS. What is interesting here is that the PVSS plateau shows clearly when it is marked. I've drawn a

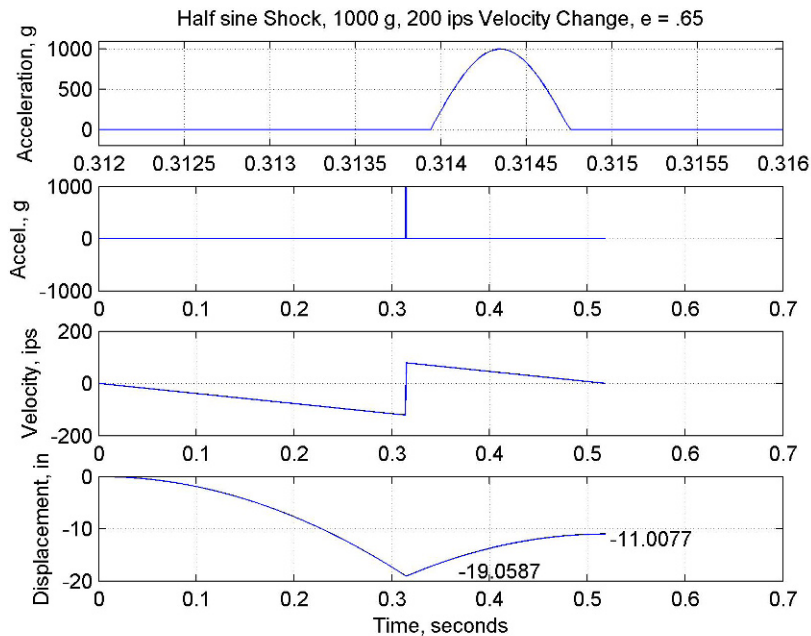


Figure 3. Time history and integrals for a drop table shock machine half sine shock with of 200 inches per second velocity change and 1000 g maximum acceleration.

straight red line from the same frequencies that were found on the PVSS. We identify the plateau from the same two frequencies we found on the PVSS.

In order to test the comparison of the APVSS (acceleration pseudo velocity shock spectrum, formed by dividing each SRS value by $2\pi f$) to the PVSS, Figure 5 shows the superposition of the two graphs with the APVSS shown in green. What I see is that the APVSS and the PVSS are the same from about 1 Hz on in this case. It's OK to draw in the velocity lines on SRSs, and it's OK to plot SRSs on 4CP by dividing by $2\pi f$. An SRS divided by $2\pi f$ and plotted on 4CP, will be exact accelerations on the 4CP, whereas the PVSS is exact displacements and PV on the 4CP.

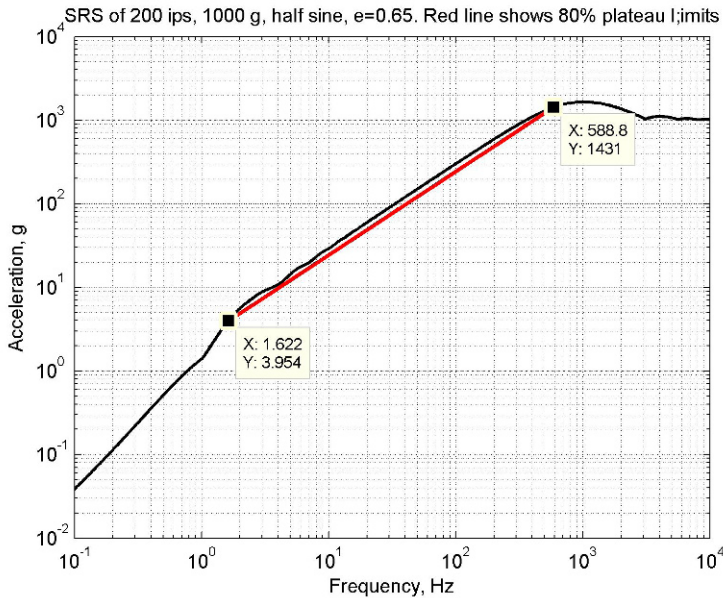


Figure 4. The SRS of our 200 ips, 1000g, half sine including the drop and rebound with a coefficient of restitution of 0.65. The red line runs from the same two frequencies as the 80% plateau line on the PVSS of Figure 1.

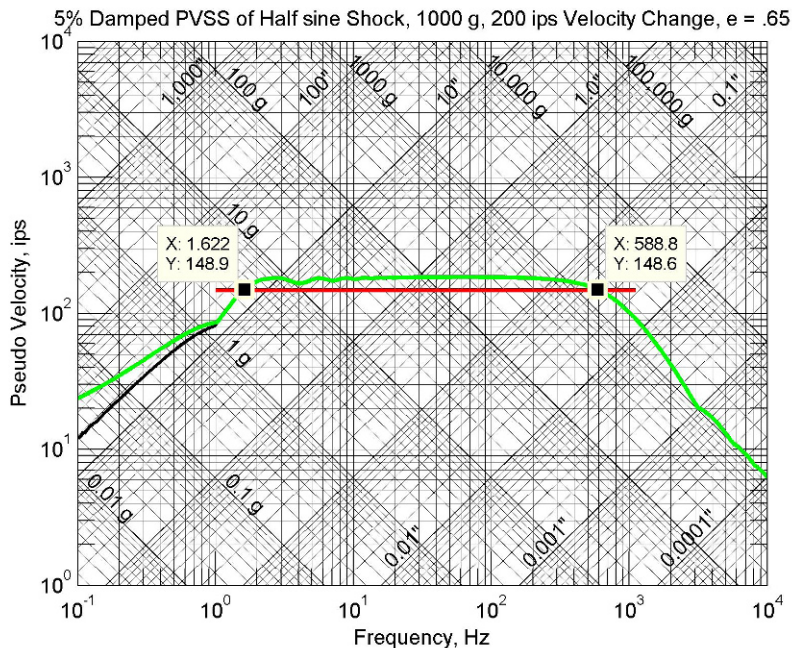


Figure 5. Superposition of the APVSS of our 1000 g 200 ips half sine on its PVSS on 4CP. The APVSS is green and the PVSS is black. In this case the two appear coincident until 1 Hz, at which time the APVSS wanders upward while the PVSS heads for its maximum displacement asymptote of 19 inches.

The APVSS is shown as a green line on top of the black PVSS line of Figure 5. It would be of no value, but we could also multiply the PV values by $2\pi f$ and plot them log log vs. frequency to form an approximate SRS. The lesson of this example is that if you have the calculated SRS values, you can divide them by $2\pi f$ and plot them on 4CP to read the shock severity.

Now let's do the same with an explosive test to show how the APVSS superimposed on the PVSS works out for another case. [Figure 6](#) shows the acceleration time history for a navy heavyweight floating shock platform carried on for about 2 seconds.

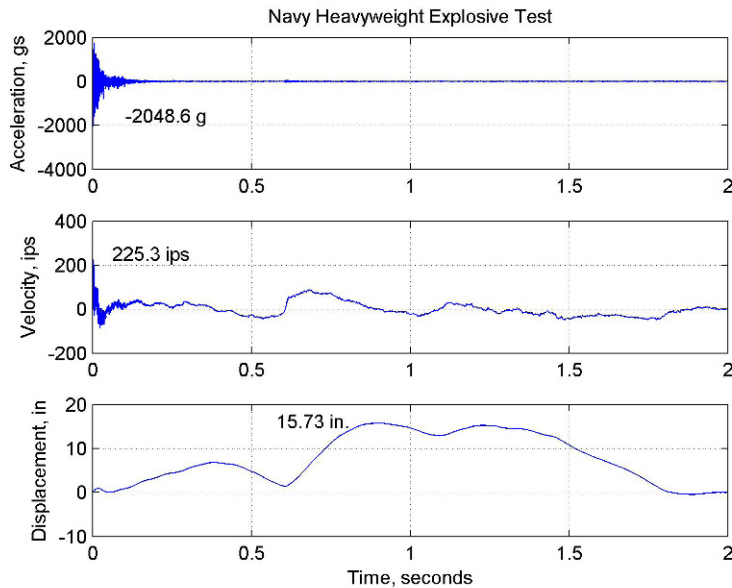


Figure 6. Explosive Navy shock test with a peak g level of 2049 and a peak velocity of 225 ips, with a maximum displacement of 15.7 inches.

Its rather lumpy plateau is shown in [Figure 7](#), where I have drawn in a plateau line at 150 ips, which is debatable. I calculated the SRS for this shock and plotted it in [Figure 8](#); this time I drew in the 150 ips line by calculating its ordinates at 0.1 and 10000 Hz from Eq (2g). This seems to work well and intersects the SRS at the same frequencies that it intersects the PVSS. I have plotted the APVSS for the shock on top of its PVSS in [Figure 9](#). Now we do see a slight discrepancy in the mid frequency region around 43 HZ., but you have to admit that the APVSS and the PVSS agree well in the plateau.

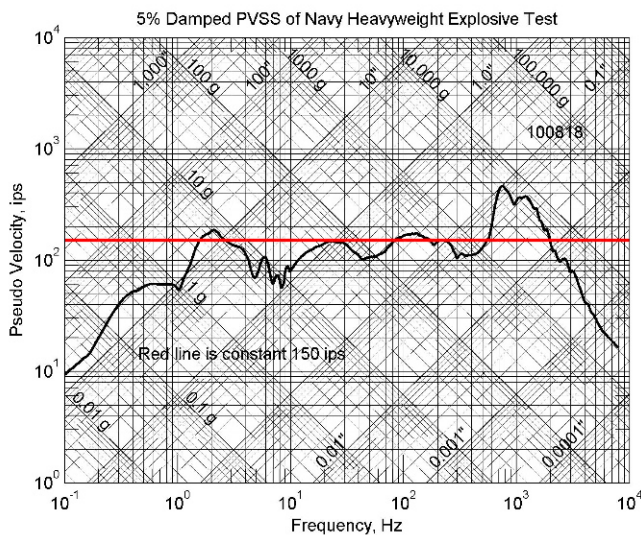


Figure 7. PVSS of explosive shock test

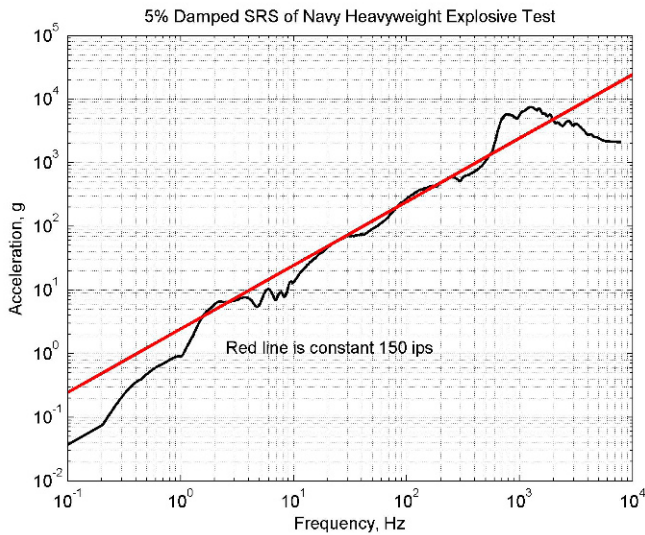


Figure 8 SRS of explosive shock test

Now let's take a look at a high frequency explosive pyroshock example, named Frapple 32. The time history is shown in [Figure 10](#). The maximum g levels are 17281 and -18659; peak velocities are 262 and -179 ips. The maximum displacement is 0.113 inches. The PVSS is shown in [Figure 11](#), and is very severe. The shock severity is 350 ips from 700 to 11,000 HZ. Notice I have had to shift the abscissa to one decade higher frequency to accommodate the higher frequency.

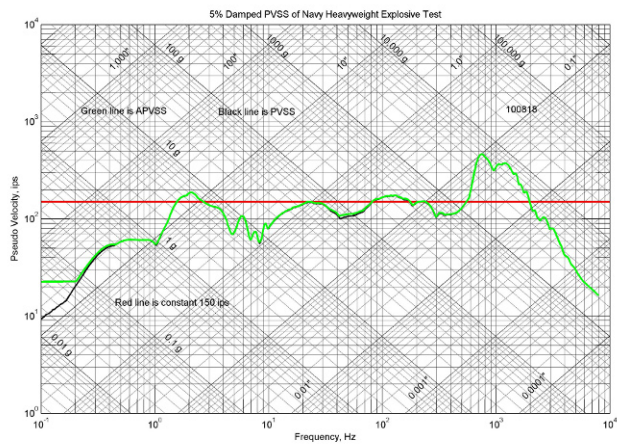


Figure 9 APVSS superimposed on PVSS.

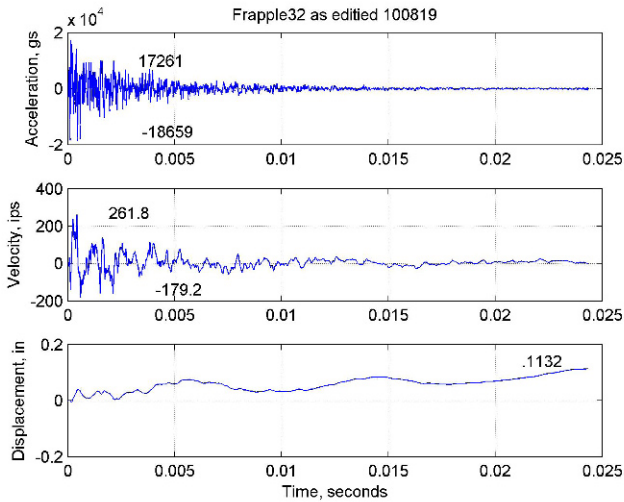


Figure 10. Frapple time history

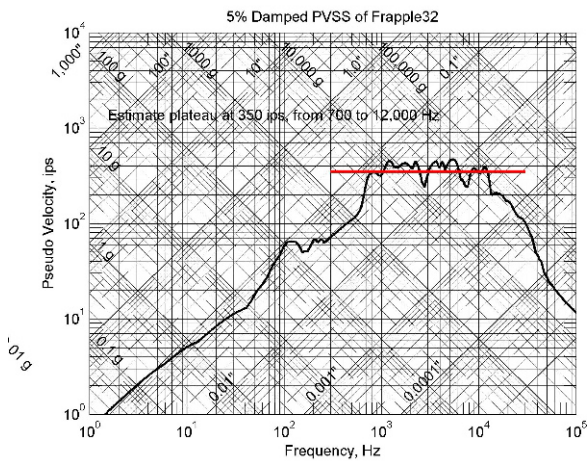


Figure 11 PVSS of the very severe Frapple 32 pyroshock with a plateau debatably drawn at 350 ips. (It could just as well have been placed at 400 or 450 ips.)

I calculated its SRS and drew in a 350 ips line from 10 to 100,000 Hz using ordinates calculated with Eq (2g). Notice that the velocity plateau line intersects the plateau at the same points as it does in the PVSS. Again I plotted the APVSS of Frapple 32 on its PVSS in [Figure 13](#). The low frequency discrepancy is surprising, but perhaps this is what we have to learn

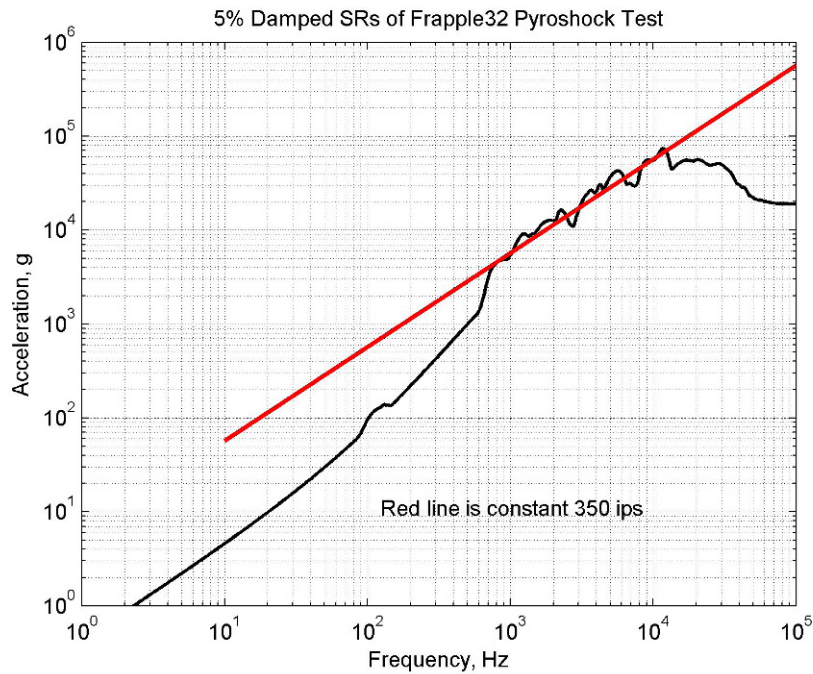


Figure 11 SRS of Frapple32 with the red line indicating the plateau

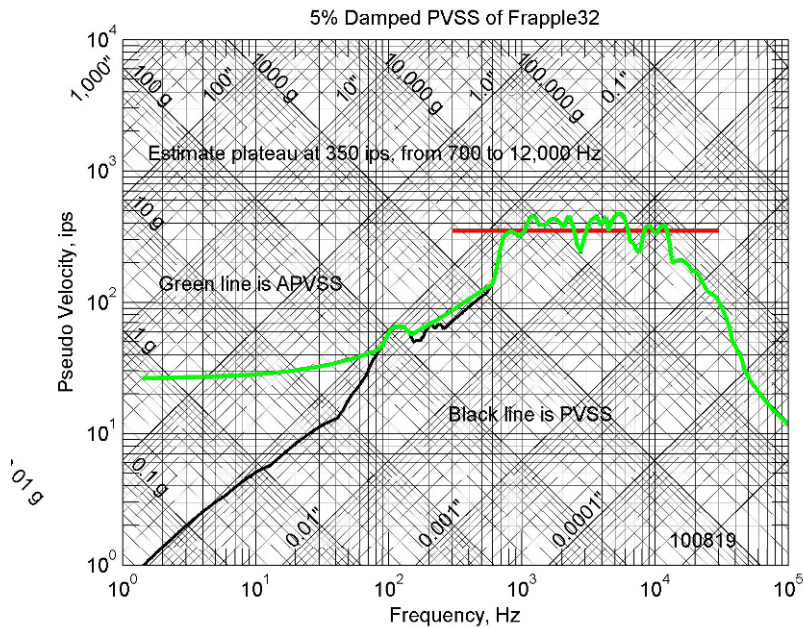


Figure 13. Superposition of APVSS on PVSS for Frapple32

to expect. I don't have much expectance in simultaneous plotting the PVSS and the APVSS, and so I will just have to accumulate experience as time goes on. I added the APVSS calculation to my SRS program and so its no trouble to accumulate plots like this and I will from now on. Maybe later it will make more sense to me and I can write something up on it.

Now finally a low frequency earthquake: I apologize for my lack of severe earthquake motion examples. I have not been able to manage my time to permit me to find a suitable example. But as a pittance representation of this great class of shocks,

I have only El Centro(IIA001 40.001.0 El Centro Site Imperial Valley Irrigation District, COMP S00 & 2688), which I am sure is not genuinely severe. It's a different motion and should add to the experience. Figure 14 shows the time history. Peak accelerations of about 0.3 g, peak velocities of 30 and -9 ips, with a maximum displacement of about 15 inches. Figure 15 shows its PVSS with a plateau drawn in at 30 ips. We could say the severity is 30 ips from about 0.4 to 2.0 Hz. Figure 16 shows the SRS with the plateau drawn in at 30 Hz. It seems to fit in place quite reasonably, and supports the idea that we can draw in a plateau on an SRS. Figure 17 shows the APVSS superimposed on the PVSS and again we see the low frequency discrepancy.

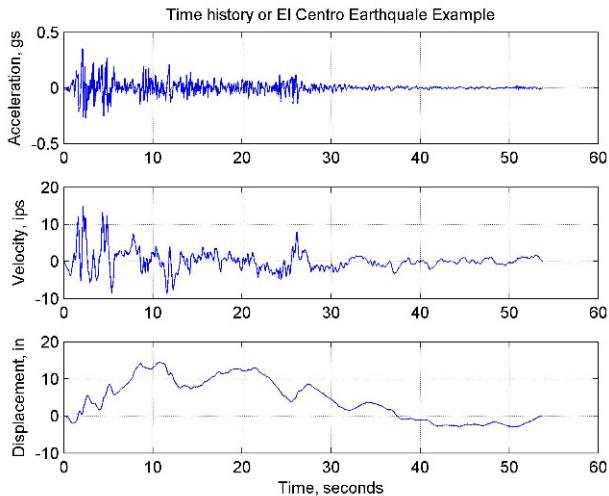


Figure 14 Earthquake Time history

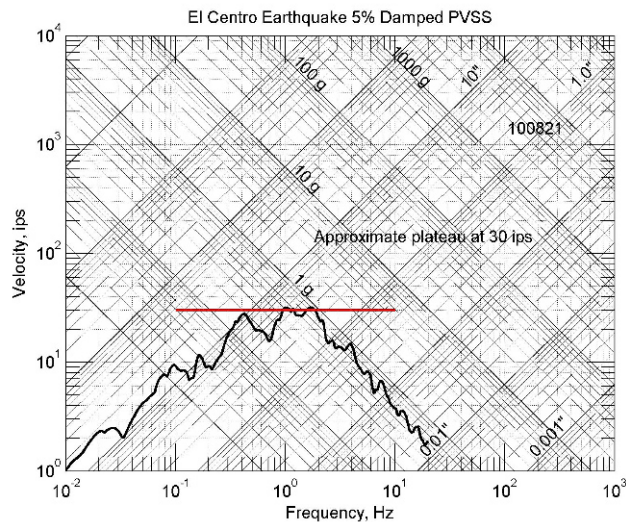


Figure 15 PVSS of example EQ

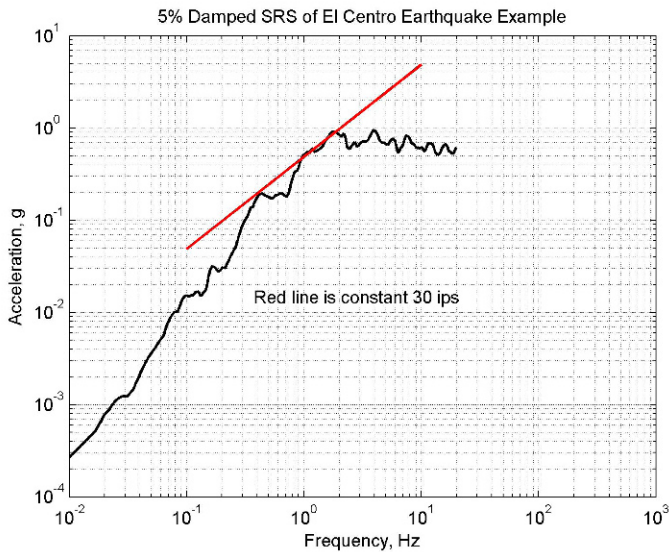


Figure 16 SRS of Earthquake

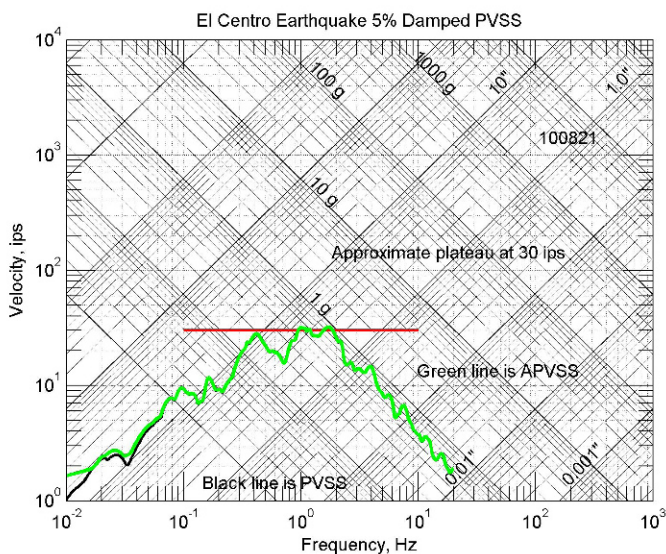


Figure 17 Superposition of APVSS on PVSS for the El Centro Earthquake

This completes the comparison. What you have seen is that in each case the PVSS and the APVSS agree excellently in the plateau and high frequency region. You have also seen that in all cases the low frequency limit of the plateau is shown by the APVSS as well as the PVSS, and this is important. I will show examples where the plateau limits do not show distinctly on many published SRSs. This is due to editing and to not assuring the final integrated velocity is zero. I have defined a collision and a kickoff shock [3, 4, 5] as a shock that begins at a high velocity and ends at zero velocity and a shock that begins at zero velocity and ends sailing off into space at a high velocity. In both of these cases the PVSS does not have a low frequency constant displacement asymptote, but has a low frequency asymptote at the constant velocity that collision began with or the kickoff ended with. That necessary editing detail only becomes apparent when studying the PVSS and is why the drop has to be included in simple shocks.

I also must call your attention to the fact that in all these four cases, the plateau was the furthest up and to the left of the SRS values or data. That's how it must be from the observation of the tipping of the PVSS counter clockwise to make an SRS. It is also true because these four shocks were edited to have a zero initial and final velocity. We will see cases where the low

frequency plateau limit does not exist; this is due to a final velocity. All real shocks begin and end with zero velocity; it may take longer than data was collected for the motion to stop but most shocks have a zero final velocity. The drop table shock machine shock starts at zero velocity prior to the drop, and the drop is normally not included in the data, so that integrating only the impact will not show the low frequency peak displacement asymptote. This must be drawn in at the drop height by the analyst on the 4CP to show the low frequency limit of the plateau.

Drawing Constant Velocity Lines on Existing SRSs

To visualize or draw constant velocity lines on the loglog SRS plots we have to do the following. I have shown you that in the plateau and the high frequency regions for the four example shocks the SRS divided by the frequency or the APVSS agrees well with the PVSS on 4CP. Its value is given by dividing by the frequency as shown in Eq (2g), repeated below.

$$\dot{z}_{\max} = \frac{\ddot{z}_{\max}}{\omega}. \quad (2g)$$

Let N_g mean the numerical value of the maximum acceleration expressed in g and let N_f be the numerical value of the frequency in Hz, (cps). Agreed upon values of the constants are: $g = 980.665 \text{ cm/sec}^2 = 386.087 \text{ in/sec}^2 = 32.18739 \text{ ft/sec}^2$ Chosen by international agreement per [18]. The values we use in Eq (2g) are in Eq (3).

$$\ddot{z} = N_g 386.087 \frac{\text{in}}{\text{sec}^2}, \text{ and } f = N_f \frac{1}{\text{sec}} \quad (3)$$

By substituting these values into (2g) we get (remember $\omega = 2\pi f$)

$$\begin{aligned} \dot{z} &= N_g \frac{386 \text{ in}}{\text{sec}^2} \frac{1}{N_f} \frac{\text{sec}}{2\pi} = \frac{N_g}{N_f} 61.4477 \text{ ips} \\ \dot{z}_K &= \frac{N_g}{N_f} 61.4477 \text{ ips} \end{aligned} \quad (3a)$$

Or in metric terms:

$$\ddot{z} = N_g 9.80665 \frac{\text{meters}}{\text{sec}^2} \quad (3b)$$

By substituting Eqs (3) and (3b) into (2g) we get

$$\begin{aligned} \dot{z} &= N_g \frac{9.80665 \text{ meters}}{\text{sec}^2} \frac{1}{N_f} \frac{\text{sec}}{2\pi} = \frac{N_g}{N_f} 1.5608 \text{ meters / sec} \\ \dot{z}_K &= \frac{N_g}{N_f} 1.5608 \text{ meters / sec} \end{aligned}$$

The line where $g = f$, is easy to draw in Power Point. Published SRSs can be scanned into .jpg or tiff files and inserted into a slide, where lines can drawn at $g = f$, and these are lines of constant 61.4 ips velocity. [Figure 18](#) is the first example. This mild shock only exceeds 61.4 ips from 800 to 1400 Hz. The PV content beyond 1400 Hz decreases steadily.

Figure 19 is the next example with four shock spectra. The general handling shock, the 30 g, 11 ms, half sine, of Figure 19 is interesting to discuss because I have a Matlab script that generates a half sine time history including the drop, given an acceleration and a duration. I have calculated the SRS of that and it is shown in Figure 20. Notice the similarity and

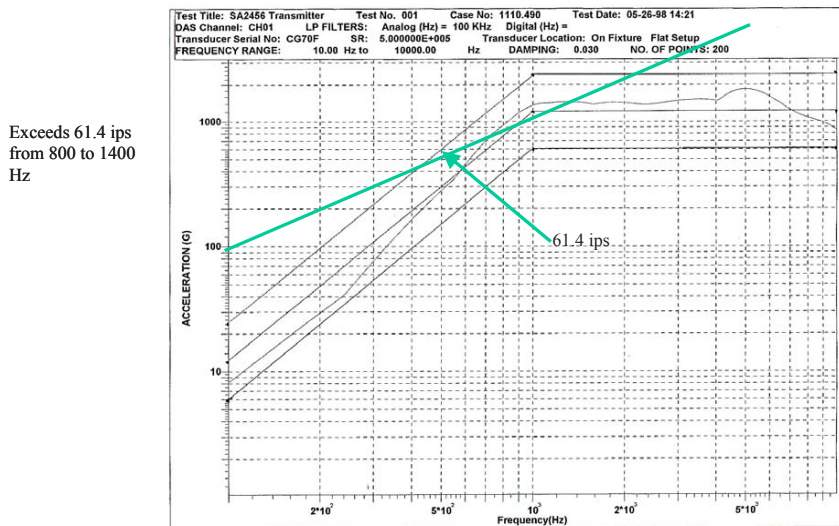


Figure 18. This is from Dr. Bateman's 79th (2008) Shock and Vibration Symposium paper [16]. In this case the grid was clearly drawn and was easy to use to draw the $g=f$ line.

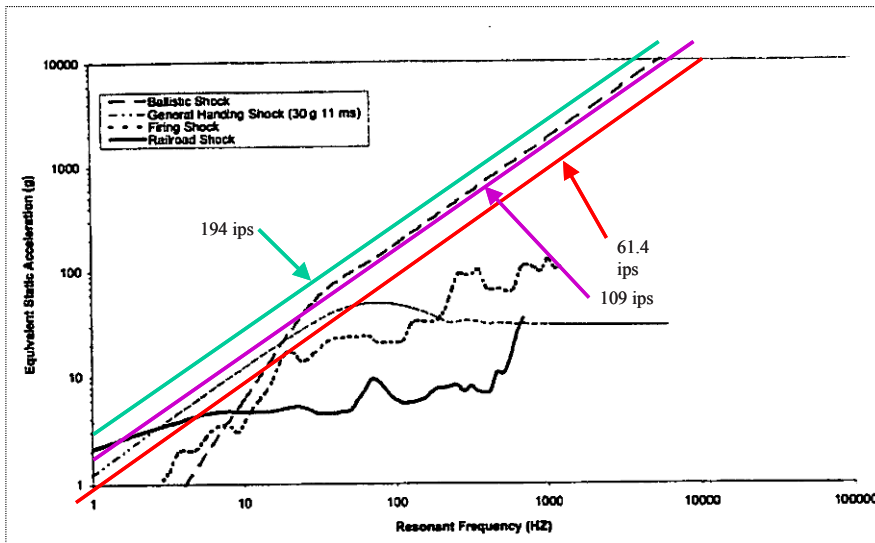


Figure 19. This is an interesting set of 4 shock spectra consisting of a ballistic shock, a general handling shock, a firing shock, and a railroad humping shock. [14]

difference between where the 61.4 ips line crosses both half sine shocks. The half sine of Figure 19 is a bare half sine with no drop included so it appears to have a plateau continuing on down to zero frequency. Including the drop terminates the plateau near 4 Hz which can be seen on Figure 20. However where the curved portion crosses the 61.4 kips line in both plots demonstrates that we have both calculated the same result. His ballistic shock looks like it is at a level of about 125 ips which is a moderately severe shock. However, all SRSs have a high frequency asymptote at the peak shock acceleration; his graph shows no horizontal acceleration asymptote and is indicating the peak acceleration is over 10,000 g, and that he only analyzed frequencies to about 10,000 Hz. That's unusual. His "firing" shock, perhaps gunfire, has an extremely low

frequency plateau; maybe 40 ips from 20 to 50 Hz. I would have expected it to be at higher frequencies. The railroad shock seems carelessly drawn; it doesn't show a peak acceleration asymptote, and appears to have extremely high content, over 200 ips at 1 Hz, which is unlikely.

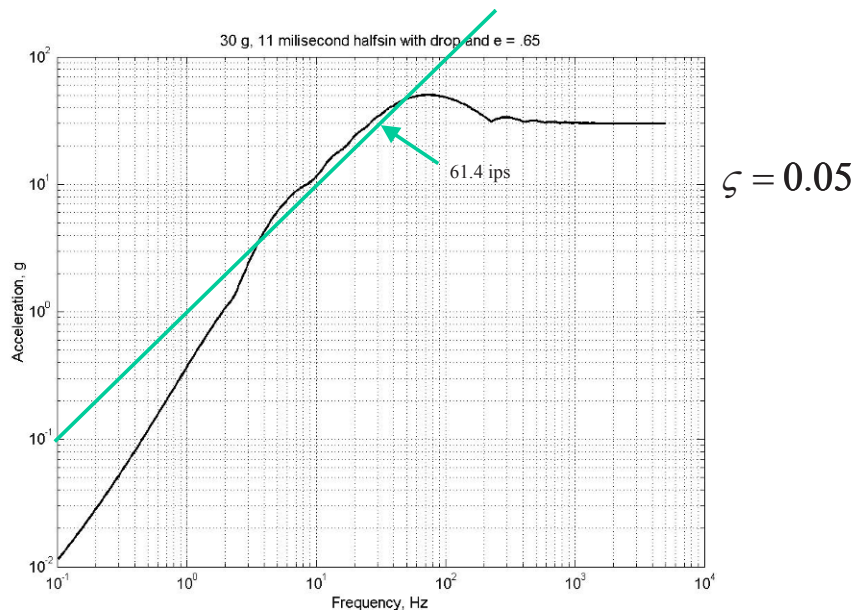


Figure 20. An SRS of a 30 g, 11 ms half sine with a drop and the 61.4 ips line drawn in green.

Figure 21 is also from [14] and is a good example of how the plateau should appear. The 61 ips line follows the SRSs of the 3 shocks well. All three have a severe region running from about 700 to 10,000 Hz; the plateau looks like about 120 ips, which is moderately severe.

Figure 22 certainly shows that pyro shock events can be high level shocks. The figure shows 7 shocks. The Super*Zip has a plateau well above 250 ips, but its low frequency region looks corrupted and ends at an unrealistic level. The trace probably had a zero shift that caused the low frequency problem. But it has a plateau above 250 ips from 250 to 3000 Hz. The Pin Puller is just under it also at the 250 ips level. The Release Nut has a shape that serves as a nice example. If you imagine the 100-10 to 10000-1000 line at 6.14 ips, you can see that the Bellow Actuator is not a shock, being below the 6 ips line. This is the important part of being able to estimate severity from an SRS. I have several shocks below 6 ips that are foolishly published because probably neither the author or the readers know what they are looking at. Picking off the velocity of any point on an SRS is done by using the acceleration and frequency in Eq (2g).

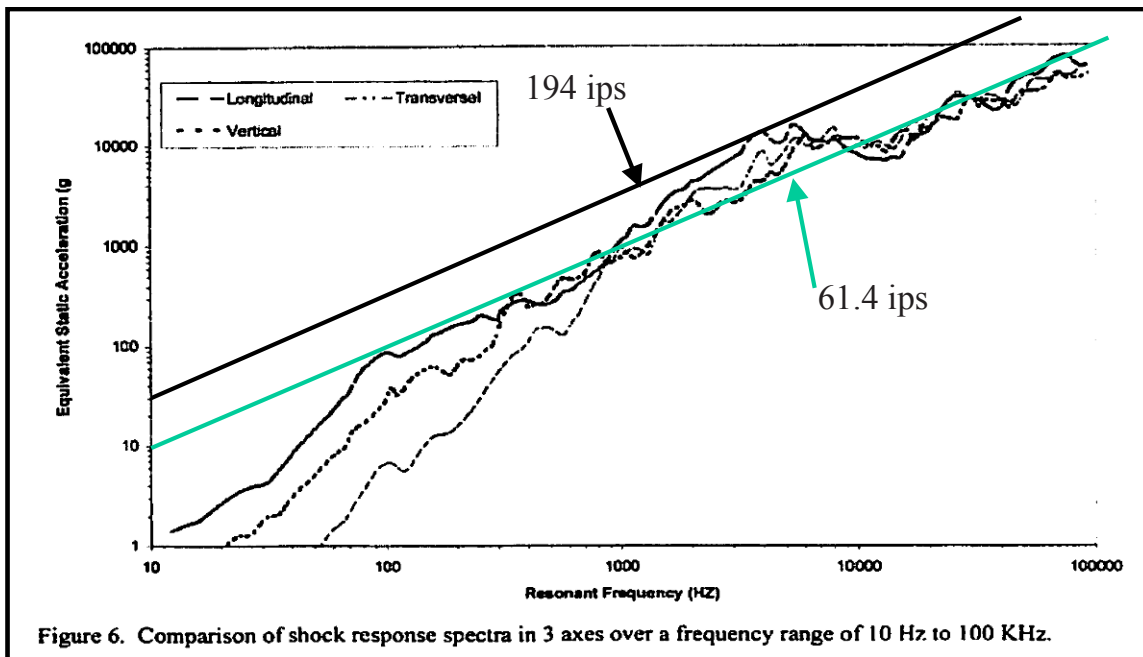


Figure 21. A good example of a plateau that shows up as it should from ref [14]. The three SRSs are labeled longitudinal, transverse, and vertical.

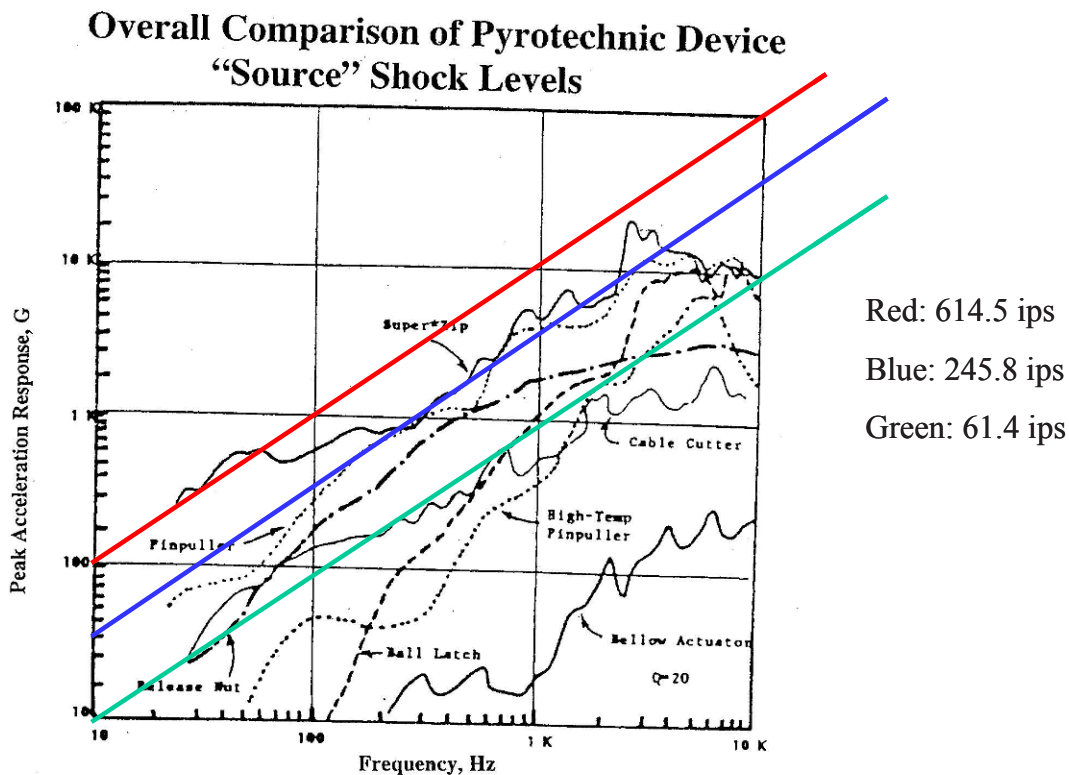


Figure 22 This is a busy very interesting SRS collection containing plots of 7 different pyrotechnic shock devices. The names of the SRSs in order of decreasing severity are: Super*Zip, Pin Puller, Release Nut, Ball Latch, High-Temp Pin Puller, Cable Cutter, and Bellow Actuator. [15]

Conclusions:

There is no question that velocity change during shock is the severity criterion. The PVSS calculates the plateau and its frequency range. I have demonstrated that much of that information can be read from an SRS. Eq (2g) tells you the velocity of any point on an SRS curve. Experts and I as well think that 100 ips is the severe shock threshold, and that 50 ips is a very mild shock. Plateaus at 200-300 ips plateaus are very severe. Damage at those levels is probable. I have copies of SRSs that have a plateau at 600 ips. Yet in one of my classes an experienced shock testing manager swore he has seen system failure at plateau levels below 50 ips. The levels are guidelines and there have to be exceptions.

The analysis requires significant calculation. I have learned to do it in Matlab and offer you my programs. There is a freeware calculating program called Octave. Students have told me it has run my programs, but for one reason or another, have not been able to teach me. Some of you have to learn it and teach the rest of us. The PVSS calculation solves the mystery of shock. Please send me your comments and suggestions.

References

1. Hunt, F. V. "Stress and Strain Limits on the Attainable Velocity in Mechanical Vibration;" J. Acoustical Soc. Am. Vol 32, no. 9, Sept 1960, pp 1123-1128.
2. Gaberson, H. A. and Chalmers, R. H., "Modal Velocity as a Criterion of Shock Severity," Shock and Vibration Bulletin 40, Part 2, Dec 1969, pp 31-49.
3. Gaberson, H. A., "Pseudo Velocity Shock Spectrum Rules for Analysis of Mechanical Shock"; IMAC XXV, Orlando, FL; Society of Experimental Mechanics; Bethel, CT, www.sem.org; Feb 2007; p 367
4. Gaberson, H. A. "Pseudo Velocity Shock Spectrum Rules and Concepts", Proceeding of the Annual Meeting of the Mechanical Failure Prevention Technology Society [[www,mfpt.org](http://www.mfpt.org)] Apr 07
5. Gaberson, H.A. SAVIAC Training lecture notes, Part 2, available on www.SAVIAC.org under Shock and Vibration Symposium, Training. 2008, 2007, etc.
6. Gaberson, H.A., D. Pal, and R.S. Chapler, "Shock Severity Measurement for Facilities Equipment" 69th Shock and Vibration Symposium, October 1998; published in the meeting proceedings spring of 1999.
- 7.. Piersol, Allan G., "Preliminary Design Procedures for Equipment Exposed to Random Vibration Environments", J. of the IEST, Winter 2001, pp 23-27
8. ANSI Equipment ruggedness specification ANSI/ASA S2.62-2009: *Shock Test Requirements for Equipment in a Rugged Shock Environment*.
9. STANAG 4549, NATO Standardization Agreement (STANAG) Testing of Surface Ship Equipment of Shock Testing Machines, 2008
- 10.. Eubanks, R.A. and Juskie, B.R., "Shock Hardening of Equipment," Shock and Vibration Bulletin 32, Part III, 1963, pp 23-73
11. Gaberson, H.A., and Eubanks, Ph.D., S.E.,R.A., "Simplified Shock Design for Equipment Installation," NCEL Technical Note, N-1622, March 1982 ADA AD114331.
12. Morse, Robert, presentation at Spacecraft & Launch Vehicle Dynamics Environments Workshop Program - June 20, 2000, Aerospace Corporation, El Segundo, CA
13. Walton, W. Scott; "Ballistic Shock Fundamentals"; Shock and Vibration Symposium; 2001

14. Kurng Y. Chang, "Pyrotechnic Devices, Shock Levels And Their Applications", Pyroshock Seminar, ICSV9 , July 8 - 11, 2002, Orlando, FL, Slide 18a
15. Bateman, Vesta I. "Are All Pyroshock Simulations with Resonant Fixtures the Same?", 79th Shock and Vibration Symposium, Oct 2008, Orlando, FL
- 16.. Gaberson, H. A, "Use of Damping in Pseudo Velocity Shock Analysis", IMAC XXVI, Orlando, FL; Society of Experimental Mechanics; Bethel, CT, www.sem.org; Feb 2008
17. "Harris' Shock and Vibration Handbook" 5th Ed. 2002, Ed by Cyril M. Harris and Allan G. Piersol, p 1.20

Progress in Shock and Vibration Technology Over 80 Symposia

Henry C. Pusey
SAVIAC Manager of Technical Services
1877 Rosser Lane
Winchester, VA 22601
Ph: 540-678-8678
E-Mail: hcpl@comcast.net

Abstract: The Shock and Vibration Symposia were chartered by the Navy in 1946. The Department of Defense has been a principal sponsor of this series of unique conferences since September 1949. This paper provides a brief history of the development of these symposia as they evolved over more than sixty years. The critical technology discussed in these symposia is an important mechanism for the interchange of technical information related to dynamic loads on structures, equipment and people. Progress in shock and vibration technology over eighty symposia is highlighted in selected areas. The paper will also discuss how the symposia continued without interruption even during transition from a DOD in-house information analysis center to an IAC operated by a contractor.

Introduction: This paper is an updated shortened version of a paper [1] that I presented at the 60th Symposium at the request of the ad hoc Technical Advisory Group for SVIC (TAG). When the TAG invited me to prepare and present that paper, I felt both honored and challenged. I am pleased to prepare this update on progress as reported in the shock and vibration symposia, partly because I have been closely associated with these meetings for more than 50 years, but mostly because it gives me the chance to mention the accomplishments of a few of the pioneers in this field that I have been privileged to know. I feel challenged because I recognize that it is not possible to describe three generations of progress in a 30 minute paper. At best, it can be only a partial story. I have often threatened to write a comprehensive history of shock and vibration technology "someday." This is not it. In this presentation, I will discuss how and why the symposia got started and why they have been successful. I will talk about technical progress, but mostly in general, rather than specific, terms and I will offer a partial list of nominees for a Shock and Vibration Hall of Fame.

Background: Although its origins go back more than 300 years [2], the general field of mechanical vibration and shock is a relatively new specialty. Lord Rayleigh (1842-1919) must be credited with publishing the first complete, formal and highly useful presentation on sound and vibration theory in 1877 [3]. But up to and including the Rayleigh era, sound and other vibration phenomena were treated together. Vibration engineering began to become as a specialty in the 1920s; the first college course was introduced around 1928. The first "modern" treatise on mechanical vibration was written by Timoshenko [4]. His book contributed significantly to the understanding of vibration, its elimination or isolation and its influence on fatigue life.

It is not certain when the term "shock" was first used to refer to mechanical disturbances, but developments in specific technological areas are usually driven by need. In the shock area, one of the most obvious driving forces was that military equipment had to be rugged and capable of withstanding the severe mechanical environments produced during warfare. During World War I, for example, the U.S. Navy developed a shock test machine to assess the capability of shipboard equipment to survive shock produced by the blast from the ships' own guns. It is almost certain that the Navy's World War II experience with shock generated by underwater explosions was a motivating force in the creation of a Centralizing Activity for Shock and Vibration and the inauguration of the shock and vibration symposia

In 1943, as a direct result of the serious shock damage to ships during World War II, a symposium [5] was organized by the Bureau of Ships to address the problem. An opening paper by LCDR Fluke and H. W. Hartzell of BuShips described in detail serious wartime shock damage to battleships, cruisers, destroyers, submarines and a minesweeper. At the same meeting, Charles E. Crede described field ship shock trials that had been conducted by both Great Britain and the United States. The immediate purpose of the field tests was to disclose shipboard equipment susceptible to shock; the long-range purpose was to obtain data as a basis for future design. W. P. Welch closed the 1943 meeting with a brief but useful paper on "Designing for Shock." His paper was expanded and later incorporated into what I consider the first comprehensive publication related to ship shock [6]. To my knowledge, the 1943 BuShips symposium was the first conference organized for the purpose of

exchanging information on shipboard shock effects. Approximately three and one half years later, the shock and vibration symposia began.

The Story of the Symposia: In January 2011 it was 64 years since the first Shock and Vibration Symposium was held. The world was then just emerging from the devastation of World War II. We were at the dawn of the nuclear age and had not yet seriously recognized the coming of the space age. During World War II, the armed services had been forced into a greater awareness of the damage caused by the explosive or vibratory forces acting on our vehicles, but there had been no time to attack the problem scientifically. Repairs had been made quickly and on the spot, and many ingenious "fixes" had been developed under the pressure of combat operations. When the war ended, whatever practical knowledge we had with respect to shock and vibration resided with a few isolated individuals and groups, primarily in the three military services and their laboratories. There was no mechanism for coordination or interchange of information. Shock and vibration was not widely recognized as a separate technology. Most solutions to shock and vibration problems were by "trial and error" methods. In this setting the idea for conducting a shock and vibration symposium was conceived.

The Navy Era: Dr. Elias Klein, a noted scientist at the Naval Research Laboratory, recognized that no coordinated plan was available to deal with the vulnerability of military equipment to shock and vibration loads and that a formal mechanism should be created for the interchange of scientific and technical information. He was instrumental in convincing the Navy that it could no longer afford to ignore the importance of shock and vibration technology. In a ten year progress report [7], Dr. Klein described the action taken by the Navy when they decided that the problem was real. "Early in 1946 the Chief of Naval Operations via ONR established at the Naval Research Laboratory one unit devoted to basic research in shock and vibration and another 'to act as a center for the collection, correlation and dissemination of all available information on this subject'." Thus the Centralizing Activity (CA) for Shock and Vibration was formally established by an ONR letter dated 20 December 1946. Dr. Klein was therefore able to celebrate the holidays with a feeling of satisfaction. He had achieved his objective. Dr. Klein wasted no time. On January 7, 1947, he arranged for an organizational meeting to be held at the Naval Research Laboratory. It came to pass that this was the first Shock and Vibration Symposium and that the minutes of that meeting were to become the first Shock and Vibration Bulletin. The first 12 symposia were sponsored solely by the Navy. Even so, participation by outside activities, such as NBS and the Army, began as early as the third symposium.

At the second symposium, the participants began the process of discussing shock and vibration terminology in order to agree upon acceptable definitions. They also heard presentations on the effects of blast, shock and vibration on humans. The third and fourth symposia highlighted shock and vibration test equipment, including instrumentation. Two of the early presentations were on the Lightweight High Impact Shock Machine, and complete descriptions of facilities at NOL (now gone) and DTMB (now NSWC, Carderock) were given. Between the second and third symposia, a Committee on Shock and Vibration Terminology and Standards was formed. This committee's minutes and other items of interest to the technical community are published in a section of the Bulletins labeled SAVIBULL (Shock and Vibration Information Bulletin).

The proceedings of both the third and fourth symposia were published in Shock and Vibration Bulletin No. 3. Thus Bulletins 4 through 11 contained the proceedings of symposia 5 through 12. This was corrected for the 13th symposium by labeling its proceedings as Shock and Vibration Bulletins 12 & 13. Shock and Vibration Bulletins 1 through 11, containing the proceedings of the first 12 symposia, were all published as NRL reports. Eight of the 12 conferences were at NRL; two were at NOL and two at DTMB. [Figure 1](#) is an illustration that appeared on all Navy bulletins.

[Figure 2](#) is a cartoon that appeared in Bulletin No.4. The words with the picture describe how information exchange should work. In my view, it is a superb illustration of the need for and the philosophy behind the Centralizing Activity and the shock and vibration symposia. The message must have gotten across. In less than two years, more than 60 significant technical papers were published. Many of these applied directly to pressing problems. The spectrum of participating organizations and activities widened rapidly. By the 12th Symposium, representatives from the Army, Air Force, various contractors and universities, the United Kingdom and special laboratories, such as Los Alamos, were listed among the attendees. This inevitably led to the next step in the process, operation of the symposia under the authority of the Department of Defense.

Tri-Service Sponsorship: Tri-Service participation was authorized under a Directive issued by the Research and Development Board of the Department of Defense. The 13th Shock and Vibration Symposium was held in Dayton, Ohio, in September 1949. Wright-Patterson AFB was the host for this first tri-service symposium. To guide the Centralizing Activity in its broader mission, an advisory council composed of representatives of the three military departments was established. This council was known as the Inter-service Technical Group for Shock and Vibration (ITG). It was my privilege to serve as

SHOCK AND VIBRATION BULLETIN

NO. 9

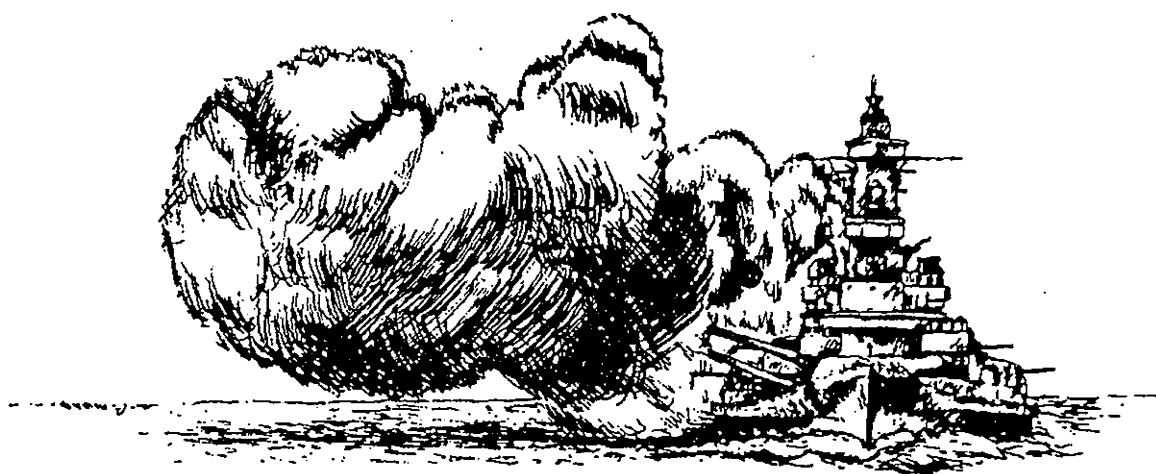


Fig. 1 Logo on Navy S & V Bulletins

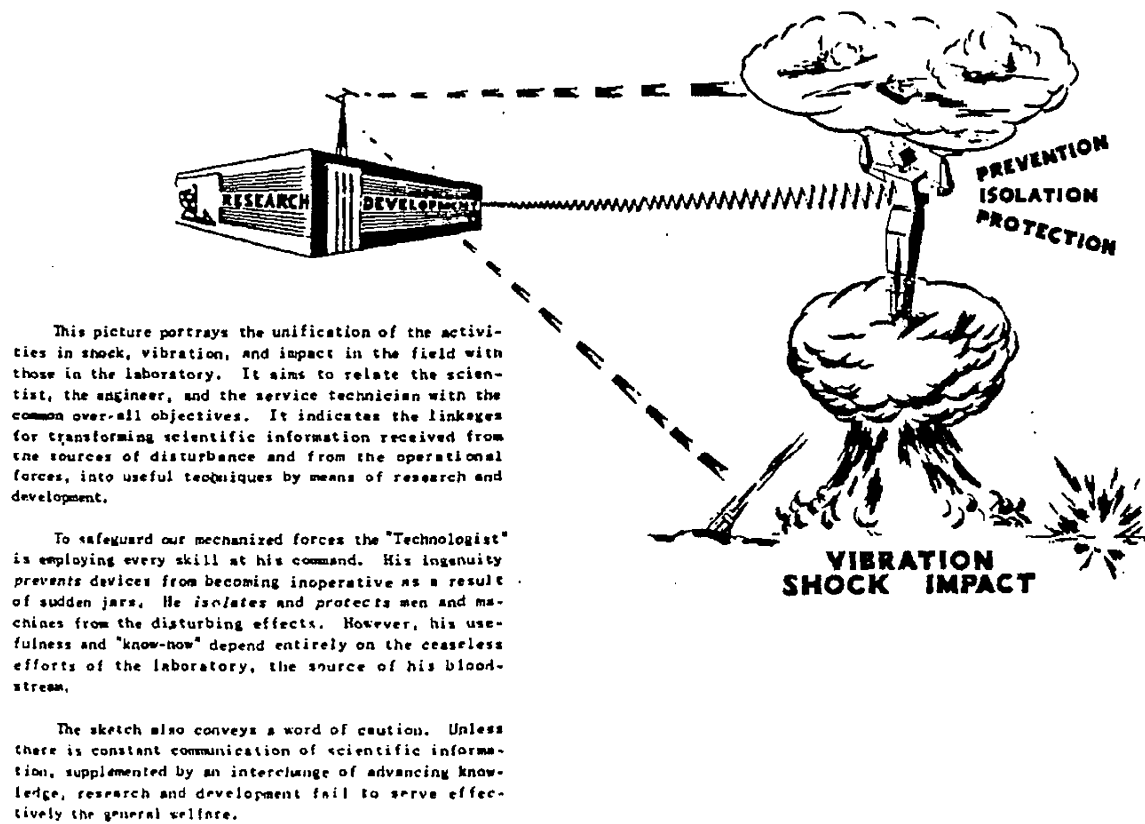


Fig. 2 Illustration of Information Interchange

an Army member of the ITG for several years prior to joining the staff of the Centralizing Activity.

From the 13th Symposium through the 57th (October 1986) when SVIC was disestablished, the Centralizing Activity/SVIC operated under the seal of the Department of Defense via one mechanism or another. In 1954, when the Research and Development Board disappeared, for example, the CA was placed under the control of the Assistant Secretary of Defense for Research and Development. Top level DOD management for the Center thereafter resided in the organizational successors of ASD/R&D).

In the early tri-service symposia, special artwork was frequently used on the covers of the bulletins or the technical program. The special covers illustrated the theme; occasionally they represented the host activity. [Figure 3](#) is the cover of the technical program for the 18th Symposium. The obvious theme was guided missile vibration problems. The cartoon was contributed by an artist from the Presidio of San Francisco, the Army host for the 18th Symposium.

NASA Joins the Team: Although the Centralizing Activity continued to operate under DOD management, an increasing number of government agencies participated in the symposia and were able to benefit from the information services provided. In the early 1960s, the National Aeronautics and Space Administration (NASA) formally became the fourth sponsor. In 1965, the Marshall Space Flight Center was the first NASA host for a shock and vibration symposium. Coincidentally, this 35th Symposium was the only four-day conference in the series. The 35th Bulletin contained 152 technical papers.

NASA's active participation in this well-established shock and vibration institution proved to be of great benefit, both to NASA and to the other members of the team. The interchange of technical information rose to an unprecedented level. Newly developed technology was made widely available, so that it could be applied to programs totally unrelated to the source from which it came.

The CA Becomes SVIC: In 1964, the Department of Defense issued an Instruction [8] establishing policy and procedures for creating, operating and administering information analysis centers (IACs). DOD directed that the Centralizing Activity was to operate thereafter in accordance with this instruction. At the same time, the name of the Activity was changed to the Shock and Vibration Information Center (SVIC) and the ITG became the Technical Advisory Group (TAG). As a result of this action, SVIC became an official DOD Information Analysis Center (IAC) operated in-house by the Naval Research Laboratory and administered through the Office of Naval Research. Over the next 22 years, this change was to prove both a blessing and a curse.

As a DOD IAC, SVIC operated with a strong mandate. Its mission was clearly defined and its activities were structured. SVIC was now authorized to continue with all its previous activities and to add some new products and services that would prove to benefit the user community. On the negative side, as the only in-house IAC operated by the Navy, SVIC was subject to DOD policy directives as interpreted by Navy technical information managers. At times the Navy implementation of DOD policy, especially with respect to requirements for recovery of user charges, made it difficult for SVIC to operate effectively. The problem was that the Center was being directed to operate like a small business and, at the same time, abide by all the rules and regulations of a Navy laboratory. The difficulties that arise in such a situation are obvious. However, even under these constraints, SVIC was able to operate effectively as a DOD IAC.

Of course, the last and most serious blow came in 1986 when a procedure from DOD Instruction 5100.45 was invoked to disestablish SVIC. As a result, the organization that officially sponsored these symposia ceased to exist on October 31, 1986.

Post SVIC Action: The Interagency Technical Advisory Group and a large number of SVIC users and symposium participants were unhappy about the loss of SVIC and the potential loss of the series of symposia. Using interagency funds, a study [9] was sponsored and completed to examine options for establishing a new information resource. While awaiting the outcome of the study, there was unanimous support for continuing the symposia without interruption, and there was no shortage of volunteer hosts to make this happen. The hosts for the 58th, 59th, 60th and 61st symposia were: 58 – NASA Marshall Space Flight Center & Army Missile Command; 59 – Sandia National Laboratories & Kirtland AFB; 60 – NSRDC Carderock; and 61 – Jet Propulsion Laboratory. It should be noted that the 58th Symposium was Interagency funded; there was no registration fee. The 59th, 60th and 61st symposia were funded mostly from registration fees, with Interagency support taking up the slack.



Fig. 3 Symposium Program Cover Illustration

SAVIAC Begins: In October 1990 a contract was awarded by NSWC White Oak Laboratory to Booz, Allen and Hamilton (BAH) to manage and operate the Shock and Vibration Information Analysis Center (SAVIAC). In October 1991 BAH held the 62nd Symposium in Springfield, Virginia. BAH managed SAVIAC through the 72nd Symposium after which the SAVIAC contract was awarded to HI-TEST Laboratories who organized and held the 73rd Symposium in Newport, Rhode Island in 2002. HI-TEST held the most recent 81st Symposium under the leadership of Program Manager Drew Perkins in October 2010 in Orlando, Florida.

Growth and Trends: A few salient facts about the early Navy symposia have already been presented. However, I will describe some additional activities during the first two years that reveal the care with which Dr. Klein and his constituents approached the tasks at hand. For example, consider the Committee on Definition and Standards that was mentioned earlier. In Bulletin No.4, the committee published proposed definitions and a chart to show how definitions are tied together.

At the sixth symposium, comments to the Editor were sought and received and then published in Bulletin No.5. Of course, many comments praised the usefulness of the symposia and the Bulletins, but there were also a number of constructive suggestions. Dr. Klein profitably used a number of these ideas for future symposia.

In the SAVIBULL section of Bulletin No.6, the CA published its first comprehensive review of technical conferences. The two symposia conducted by the Society for Experimental Stress Analysis (now the Society for Experimental Mechanics) in 1948 were specifically considered. A total of 18 papers of special interest to the shock and vibration community were reviewed. Among the authors of these papers were R. D. Mindlin, R. O. Fehr, I. Vigness, N. M. Newmark and C. E. Crede. All are now recognized as pioneers in our field. The purpose of the reviews was to make the reader aware of results from related technical meetings that might have a bearing on their work. Meeting reviews were also featured in the Shock and Vibration Digest, a current-awareness journal established by SVIC then published by the Vibration Institute and now by Sage Press.

Over a 40 year history, the CA and its successor SVIC worked very hard to be aware of the needs of the technical community. As a result the Center was able to carry out its mission efficiently by responding to those needs through the symposia, special publications and other mechanisms. An excellent description of how this was done is aptly given by Kennard [10]. His progress report includes some excellent examples of technical information services that were provided during the first quarter century.

It is interesting to note the distribution of the number of published papers over the history of the symposia. There was an irregular but persistent growth, with some exceptional lows and highs. The 32nd Symposium had a special theme of narrow scope, with only 36 papers published. As mentioned earlier, the 35th Symposium was the longest meeting and therefore contains the most papers in the SVIC proceedings. Some of the recent SAVIAC may have exceeded that high point. If we assume an average of 50 papers per symposium, which is probably low, approximately 4000 published technical papers have resulted from 80 symposia. This is an extraordinary body of literature for any specific discipline. It is perhaps even more significant when one considers that a high percentage of this technical material is applicable to problems related to real systems.

Attendance at the symposia increased to a peak of nearly 1000 in 1956 and has gradually decreased to an average of about 400 over the last several years of the SVIC era. This trend can be attributed to ever-increasing travel costs coupled with tighter restrictions on travel budgets. However, during the same time, the number of organizations represented by the attendees rose to about 300 and has remained near that level. Obviously, more organizations are being represented by fewer people. To derive maximum benefit, each participant must share with his colleagues the information he has learned as well as the published material he has received. All of the above apply to the SAVIAC symposia as well.

Klein [7] pointed out that the goal in planning the symposia was to have a maximum number of participants leave the meeting with a sense of profit and a feeling of time well spent. An Air Force survey of their contractors at that time (ca 1956) showed that 86 percent of symposia attendees received definable benefits from the meetings. In a more recent survey, the value of the series of symposia was highly rated by an overwhelming majority of the respondents. Over 55 percent rated participation in the symposia as "extremely useful." On the basis of this and other evidence, there is little doubt about the continuing value of this forum. This value is further confirmed by a modern record-breaking attendance at the 80th symposium while attendance at several other conferences was reduced.

Shock and Vibration Snapshots: As was stated earlier, the Center's principal goal was to meet the technical information needs of the user community. Thus, the shock and vibration symposia were often organized to highlight special technical

areas. Scientists and engineers were frequently "persuaded" to write and present papers on solutions to particularly pressing problems or on new methods and techniques destined to have a major impact on the advancement of our technology. I have selected three examples to illustrate what I mean.

The Shock Spectrum: In my view, the development and application of the concept of the shock spectrum is among the most significant contributions to naval shock measurement, analysis and design and almost certainly, to earthquake engineering as well. Remmers [11] provided an excellent description of how the use of this technique evolved from the original concept developed by Maurice Biot. As a result of the work of Biot, a mechanical device to record the shock spectrum of a transient motion directly was eloped in 1942 at DTMB. The instrument, called a reed gage, was first described in Bulletin No.6. It is interesting that the word "spectrum" was not mentioned in that paper. The Navy's Dynamic Design Analysis Method (DDAM), based on the use of shock design spectra and the normal mode method, was introduced in 1959 by Belsheim and O'Hara at the 28th Symposium. Under procedures specified by the Navy, DDAM is now used to qualify shipboard equipment that is too heavy to be qualified by test. However, a word of caution is necessary.

Although the shock spectrum idea has served us well, there is still considerable controversy over the use of this concept. In fact, there was an excellent session at the 60th Symposium where the debate continued. Over the years there have been many papers and much discussion about the Shock Response Spectrum (SRS) as a tool for shock analysis in the frequency domain. The controversy has been mostly about the choice of the spectrum parameter used in shock analysis. The aerospace industry over time has tended to favor the acceleration SRS, while the Navy has recognized the relevance of velocity spectra for the analysis of ship shock. In the last few years, Dr. Howard Gaberson has published and presented convincing arguments that the pseudo velocity shock spectrum is the best indicator of damage potential from shock loads. It is most useful to plot shock spectra on four coordinate paper (often called tripartite paper). It is a nomograph on which may be plotted frequency, displacement, velocity and acceleration; if one knows two of these parameters, the other two may be determined instantly. Gaberson continues to make the case for pseudo velocity; he gave training presentations at the 81st symposium. More and more aerospace engineers are now convinced that his approach is correct.

Transportation and Packaging: In the early stages of the Korean conflict, extensive damage to military shipments was occurring due in large part to shock and vibration effects. In response to this critical problem, two symposia (15th and 16th) on lading damage were held in 1950. The prevailing deficiencies in packaging, handling and transportation were identified, and recommendations on how to improve safety in transit were made. As a result, a cooperative effort between government and the common carriers ultimately led to a significant reduction in damage during shipments.

As guided missile advancements produced more complex and sensitive guidance and control systems, improved methods of packaging these missiles for shipment were required. The 21st Symposium addressed this issue in 1953. Recommendations coming out of that conference led to the publication by the CA of a guidance document [12] that was for a number of years to remain the authoritative publication on the design of shipping devices for guided missiles and other sensitive equipment. I was one of many contributors to this useful reference. In many of the symposia that followed a number of papers were published that advanced our capability in this field.

Vibration Testing: Until the mid 1950s, vibration testing involved the use of sinusoidal inputs for the qualification of equipment. A landmark paper by Morrow and Muchmore [13] questioned the realism of this approach and suggested random vibration as a solution. This set off a controversy on sinusoidal versus random vibration that was to last many years. Today, of course, random vibration tests are routinely specified and random vibration test equipment is prominent in most test laboratories.

At the 25th Symposium, Hansen [14] introduced the oil film "slip table" to the test arena. His paper presented a novel test technique and, at the same time, highlighted the potential importance of improved fixture design in the test laboratory. As a direct result, more than a dozen definitive papers were presented at the 27th Symposium on the design of vibration test fixtures and on variations in slip table design for horizontal testing. Two years after Hansen's paper most test laboratories had acquired this capability.

During the SAVIAC era a number of papers pursued the idea of true three-dimensional vibration testing. I believe one of the early advocates for 3-D testing was Ami Frydman of the Army Research Laboratory. Because of a rather remarkable research and development effort, this test capability now exists in several laboratories.

Perspectives: It has been said that the more things change, the more they remain the same. There is an element of truth in this ambivalence. There is no doubt that we have made significant progress in our ability to handle most shock and vibration problems. Yet, as we develop new methodology to solve the old problems, new problems continue to surface as new and more complex systems and ever-increasing performance requirements evolve. Furthermore, there are always old problems that defy solution. Let us examine two specific areas.

Measurement and Data: Over the past three generations, we have made quantum leaps in our ability to measure and analyze dynamic data. Sixty years ago, many of our instruments were crude, massive and inaccurate. Signals were recorded on oscillographs, and data was reduced by hand. Today we have highly accurate transducers and sophisticated computerized on-line data analysis capabilities. Yet we have continued to hear, at almost every one of the 81 symposia, a demand that realistic field data be used as a basis for design and test criteria. This demand has been met only in a limited way, largely because it would be a massive and very expensive task to develop data banks with valid input data for every major system. There is little doubt that technology is available to solve all of our requirements for valid data. The question is whether we can do it at a cost that we can afford.

Analysis Versus Test: Sixty years ago some form of qualification testing was the only acceptable proof of design. Analysis was a useful tool but was not considered very practical for design evaluation. Today we have the capability of powerful computers and dynamic analysis codes that provide quite reliable estimates of the response of structures. Many finite element computations can now be done on microcomputers. This capability, coupled with our ability to verify mathematical models using modal tests, brings the analysts and the experimentalists a lot closer together. Over the last two decades the shock and vibration community has significantly advanced our capability to analyze response to dynamic loads. This has spurred some to advocate the elimination of qualification by test. In my opinion this will never happen. Analysis will play an increasingly important role, but it will never replace testing.

Six Men: In my paper [1] twenty years ago, I had lifted the title from a book by Alistair Cooke in which he wrote about six men who impressed him for very special reasons. In a similar way, I listed six men who have made outstanding contributions to these symposia and to our technology. I was privileged to know all of them personally and have benefited by their counsel. In fact, all of these talented, but humble, men stood ready to respond to any young engineer seeking advice. In alphabetical order they are: Robert O. Belsheim, Charles E. Crede, Elias Klein, Robert M. Mains, Charles T. Morrow and Irwin Vigness. If there were a Shock and Vibration Hall of Fame, these men would be among those that I would nominate. Many other engineers and scientists are outstanding contributors in our field. Their work is sure to be discussed in any comprehensive history of dynamics; a number of them would also be Hall of Fame candidates.

Let us consider briefly the men I have named. Belsheim, along with George O'Hara, created DDAM and made many other significant contributions to shock analysis. Crede is best known for his book on isolation and as co-editor of the Shock and Vibration Handbook. Klein, of course, is responsible for these symposia. Mains, a dynamicist with great insight, is a strong advocate for practical analysis and design. Morrow's pioneer efforts related to random vibration are well known. Vigness is recognized as a leader in shock and vibration measurement and testing.

It should be noted that at the time I first wrote the preceding material, SAVIAC did not yet exist. At about the 50th anniversary of the symposia SAVIAC published two new monographs [15,16] in the series initiated by SVIC. The first book was about pioneers in shock and vibration; the second was a 50 year history of the technology. My six men and other notables in the field are evident in these publications. In recent years SAVIAC has presented a number of Lifetime Achievement Awards to persons who went above and beyond in their contributions to our technology. I am honored to be one of the award recipients. The most recent awardees were Harry Himelblau and William Yancey at the 81st symposium.

The Legacy and the Hope: Figure 4 is the sketch of Dr. Elias Klein that appeared on the cover of a monograph written in celebration of his 80th birthday. In 1957, Klein gave his views [7] on the real function of an effective information agency in research and development and how it can best accomplish its mission. He based his opinion on his experience with 24 symposia in shock and vibration, a technology that impinges on all military and most civilian systems.

"The rate at which the application of science is being made in weapons programs today demands that engineers and scientists have ready access to current developments relating to their work. Hence the channeling of pertinent and new knowledge to the working scientist becomes of vital importance to the defense program. The information disseminated must be live and relevant; it must be communicated with directness and dispatch. Thus, to achieve tomorrow's effective weapon developments,



ELIAS KLEIN
THE FIRST EIGHTY YEARS
January 1968

Fig. 4 Cover of Dr. Klein's Career Summary

it is imperative to supply the working engineer and scientist with the best available technical information of today."

Dr. Klein founded the shock and vibration symposia as a part of the scheme to meet this information need. In doing so he left us a valuable legacy that has been perpetuated through the 81st Symposium. His statement of the need probably applies even more today than it did in 1957, since tomorrow's military and space systems will present ever greater challenges in dynamics. We can only hope that these symposia will continue to operate as an effective forum for the interchange of shock and vibration technology.

REFERENCES

1. Pusey, H.C., "Two Generations of Shock and Vibration Technology – Progress Over Sixty Symposia", Proceedings of Shock and Vibration Symposium No. 60, November 1989
2. Zand, S. J., "Three Hundred Years of Vibration Engineering,," Shock and Vibration Bulletin No. 13, September, 1949
3. Baron Rayleigh(John William Strutt), Theory of Sound, First American Edition, Dover Publications, 1945
4. Timoshenko, S, Vibration Problems in Engineering, D. Van Nostrand Company, Princeton, NJ, 1937
5. BuShips Electrical Equipment Shock Committee, Proceedings of a Symposium on the Effect of Shock on Electrical Equipment, Navy Department, Washington, DC, October 30, 1943
6. Welch, W. P., Mechanical Shock on Naval Vessels, NAVSHIPS Report 250-660.26, 1946
7. Klein, Elias "Progress in Shock and Vibration During the Last Decade -Correlation and Dissemination," Proc. ONR Tenth Anniversary Symposium, Naval Research Laboratory, 1957
8. Department of Defense Instruction 51005.45, Centers for Analysis of Scientific and Technical Information, July 28, 1964
9. Pusey, Henry C. Information Resource Support on Shock and Vibration, NSWC TR88-138, Apr. 4, 1988
10. Kennard, Dwight C., "A Quarter Century of Progress," Shock and Vibration Bulletin 43. Part 1, June, 1973
11. Remmers, Gene, The Maurice Biot 50th Anniversary Lecture, "The Evolution of Spectral Techniques in Navy Shock Design," Shock and Vibration Bulletin No 53. Part 1, May, 1983
12. Klein, Elias, Ayre, R. S. and Vigness, Irwin, Editors, Fundamentals of Guided Missile Packaging -Shock and Vibration Design Factors, Department of Defense, RD 219/3, July 1955
13. Morrow, C. T. and Muchmore, R. B. "Shortcomings of Present Methods of Measuring and Simulating Vibration," Shock and Vibration Bulletin 21, November 1953
14. Hansen, W. O., "A Novel High-and Low-Temperature Horizontal Vibration Test Fixture," Shock and Vibration Bulletin 25. Part II, December, 1957
15. Freeman, M. T., Pioneers of Shock and Vibration, SVM 14, SAVIAC, Arvonion, VA
16. Pusey, H. C., Editor., 50 Years of Shock and Vibration Technology, SVM 15, SAVIAC, Arvonion, VA

Rationale for Navy Shipboard Shock & Vibration (S&V) Requirements

(To be presented by James E. Howell, III P.E. of NSWCCD)

A presentation titled "Rationale for Navy Shipboard Shock & Vibration (S&V) Requirements" will be given to provide a brief overview of the origins and history of the Navy's underwater explosion (UNDEX) shock and shipboard vibration testing requirements found in test specifications and standards. These requirements originated during World War II (WW II) and eventually evolved into MIL-S-901 for UNDEX shock testing and MIL-STD-167 for shipboard vibration testing.

The presentation begins with a brief introduction and background followed by a brief review of definitions for mechanical shock and vibration including an illustration of these excitation sources. The presentation will then expound on the origins of shock and vibration requirements that go back to the early years of WWII based on experiences by the United Kingdom, Japan and the United States of America (US). More detailed information will be presented on documented US experiences throughout WWII and later including results from those experiences. Short videos will be shown to highlight some of those experiences. Following the origins discussion, a historical review of S&V test specifications and standards as they evolved throughout the years will be briefly discussed starting from WWII through the present day. Rationale for various aspects of the S&V test specifications and standards will be discussed at various points throughout the presentation. Finally, the presentation will conclude by summarizing the main points of the presentation.

Deformation and Vibration Measurement and Data Evaluation on Large Structures Employing Optical Measurement Techniques

Hagen Berger, Markus Klein, Theodor Möller
GOM Gesellschaft für Optische Messtechnik mbH
Mittelweg 7-8, 38106 Braunschweig, Germany

Abstract

Deformation and vibration measurements and frequency analysis are part of complex product development cycles, typically performed during component development and testing phases. Optical measuring systems have become important tools in industrial testing processes, reducing the time frame for preparation, testing and evaluation of components and structures. Optical measuring systems rapidly deliver comprehensive operator-independent results and contribute to development and testing time optimization for deformation and vibration measurement procedures. This paper focuses on one recent trend in the field of optical measurements, application to large areas from 3-4 meters up to more than 100 meters. Point tracking videogrammetry systems measure the 3D coordinates and derive measurement results for 3D displacements, velocities and accelerations of a large amount of applied point targets at the same time and replaces the time consuming application of displacement sensors (LVDT's) and accelerometers. By transforming the measurement results into the frequency domain, an easy and fast evaluation of the frequency response of structures and components under various excitation load conditions, even for large measuring areas and small amplitudes, is enabled.

With the full-field digital image correlation system, 3D coordinates are measured and 3D displacements, velocities and also strain distributions for thousands of points on the surface of the test object are derived. Therefore shape information is intrinsically obtained, and the application of strain gauges can be replaced.

Measurement examples that are presented for large structures include single wind turbine blades, complete full scale wind turbines, and airplane wings. Detailed evaluation of the measurement results provides a better understanding of the deformation and vibration response of standard test specimens, components and structures.

1. Introduction

Since the industrialization the demand of electrical energy is constantly increasing, especially since the industries of former third world countries are rapidly developing. To satisfy the huge energy demand all over the world nuclear and coal-fired power plants were built. Recent studies have shown that this former way of energy production highly pollutes the environment and potentially causes diseases e.g. cancer. Even more threatening is the fact that these ways of producing energy are also the biggest producers of green house gases, especially CO_2 . It is a well known although controversially discussed fact that the green house gas CO_2 causes global warming. Therefore new ways of energy production were developed and have proven their potential such as solar power plants and wind turbines. Not to mention the oldest and greenest way to turn natural power into consumable energy are water power plants.

This paper will focus on wind turbines. For wind turbines the operational reliability and safety depends on the mechanical design of the blades and the tower and of course the operational conditions. The operational conditions can be limited to certain wind speeds, but they can't be changed. The even bigger problem is, that these conditions are not stable at all, which turns a decent blade design into a very challenging job. To better understand the operational behavior of wind turbines and therefore support the designers and engineers the measurement of the operational deflection shapes (ODS) is of high interest.

The problem with available measuring techniques is the size of full scale wind turbines and to measure the real behavior of. Due to the unpredictable wind conditions around a wind turbine in operation it is not easy to simulate these conditions. Therefore reliable and accurate measuring techniques are demanded. Laser vibrometers and accelerometers are so far the only methods to gather vibration data of real wind turbines. The problem with accelerometers is the amount of time that is needed to prepare a measurement. The accelerometers have to be mounted on the blade and calibrated. This is a very time consuming and therefore cost-producing process of an already very expensive procedure. A slight influence of these accelerometers on the blades is also not negotiable, although it is an advantage that a large number of measurement points can be placed on the blades. For rotating objects the cabling for strain gauges or accelerometers has to be solved by sliding contacts which limits the amount of measurement points and accuracy anyhow. The problem with laser vibrometry is that the laser beam will always change its position on the blade and will therefore lead to unreliable results for the measurement point. It is also a problem that every single measurement point has to be measured individually which also influences the entire results because results were captured at different wind load conditions.

Optical point tracking techniques were used to measure the operating deflections shapes of wind turbines in the past [1],[2], [3]. The following chapters will explain the principle of these optical 3D point measurements and show a new approach of measuring the deflections and calculating a fast fourier transformation (FFT) in real time.

2. Principle of the 3D measurement technique

The optical point tracking system PONTOS developed by GOM mbH, Germany uses a stereo camera setup that synchronously records images from any object under test. For the image processing and evaluation it is important that both cameras capture the images synchronized. This is assured by an integrated control device which relays a trigger signal synchronously to both cameras.

To be able to evaluate 3D coordinates with high accuracy in a stereo camera setup a calibration of the camera system must be performed. Considering that measurement points shall be evaluated in 3D space a 3D measuring volume needs to be set-up and defined, too (s. [figure 1](#)). The 3D measuring volume setup is done by choosing lenses with an appropriate focal length suitable for the object size, setting the right aperture and focus, aligning the correct camera base distance and positioning the sensor in the correct measuring distance.

By this procedure the measurement system can be adapted to a wide range of object sizes from $10 \times 10 \text{ mm}^2$ to $100 \times 100 \text{ m}^2$.

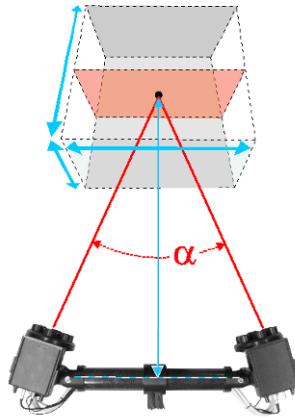


Figure 1: Measuring volume definition of the PONTOS system.

The calibration of the sensor setup is carried out by recording multiple pairs of images from a calibration object, in this case a calibration cross. The calibration object is hereby positioned in different distances and orientation to the camera system to retrieve a good definition of the needed 3D measuring volume.

During the calibration calculation the relative camera positions to each other and the lens distortion parameters are calculated and automatically corrected numerically.

With a photogrammetric evaluation strategy digital images from an object under load are used to obtain 3D coordinates of previously applied measurement points. White targets with black surrounding are used as measurement point markers. The grayscale deviation between the white dot in the middle and the black surrounding

allows the PONTOS software to accurately determine 2D point coordinates in each camera image. Once the software recognizes a measurement points in a pair of captured images, its position in three dimensional space is determined using spatial triangulation (s. [figure 2](#)).

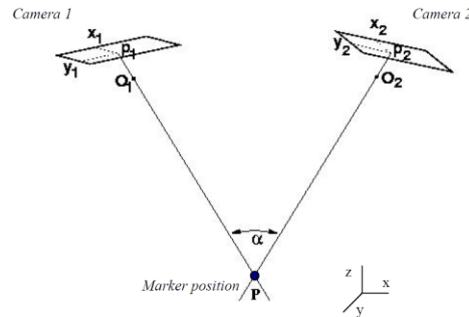


Figure 2: Measurement principle to determine the object coordinates using two known image points [3].

The 3D coordinates of all object points are calculated from the intersection point arisen from the center point rays from the two observation image points. The main measurement results are 3D coordinates of an unlimited number of measurement point markers. These results are typically used in motion tracking and deformation or vibration applications [4].

The PONTOS system offers two options for 3D measurements, post-processing and real-time image evaluation. In the post-processing mode recorded images are stored and evaluated after the test is already over. In the real-time evaluation mode just the 3D coordinates of the evaluated 3D points are stored or transferred to third party evaluation software packages or systems. The images in the real-time mode are not stored. Both measurement strategies were used during the further described measurements.

3. Real-time measurement

PONTOS has the capability of measuring point coordinates on a vibrating object from a live video stream with up to several 100 images per second. Additionally the data can be stored for post processing or sent out to a live data stream. This data stream uses the TCP/IP protocol and can therefore be sent to any computer available and be implemented easily to any software package providing live stream data processing for advanced real time evaluation. By employing the third party software LabVIEW the real time FFT can be calculated by using standard LabVIEW functions for TCP/IP communication, data handling and frequency analysis.

The frontend of such a VI is shown in [figure 3](#). It shows the coordinates of several points measured on a video stream with image rates of e.g. 200Hz. These signals can be used for a FFT and further signal analysis. With this evaluation you get di-

rect feedback during the test from several synchronously measured points in all coordinate directions. Usually accelerations are used in fast fourier transformations to transfer the measurement data from the time domain into the frequency domain, but this is due to the reason that normally accelerometers are used to gather the deflection data. The PONTOS system is measuring coordinates and calculates displacements without any losses in the data; therefore the FFT was customized to better support the measurement data.

This measurement technique can be combined with other measurement devices. The trigger signal for the live video stream can be sent/received to/from other devices and analog voltage signals (e.g. from a load measurement cell or a single vibrometer) can be measured synchronized to the images (e.g. for transfer function or comparison) or measured values can be sent out by analog voltage signals.

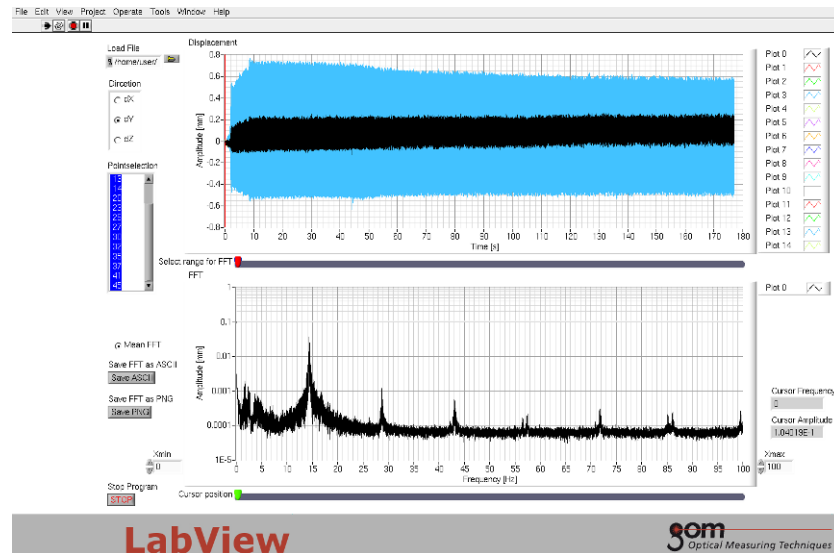


Figure 3: VI frontend

4. Postprocessing employing vibration analysis software

To completely postprocess the data in terms of vibrational analysis the in real time gathered data has to be transferred to third party analysis software. Already in the late sixties of the last century the Structural Dynamics Research Corporation (SDRC) developed the universal file format (UFF) to simplify the data exchange between computer aided design (CAD), computer aided testing (CAT) and computer aided engineering (CAE). UFF is not a single file format, it rather consists of multiple small formats to exchange evaluation specific data such as point positions, coordinate system definition, measurement for every single point and the cross-linking between the points. Vibration analysis software usually provides the capability of importing this exchange format.

In a first step of the postprocessing the imported data which was gathered in the time domain is used to illustrate the operating deflection shapes of the rotor blades (see [figure 4](#)). The ODS shows the deformation behavior of the blades due to the wind load. The maximum displacements can be evaluated in the time domain.

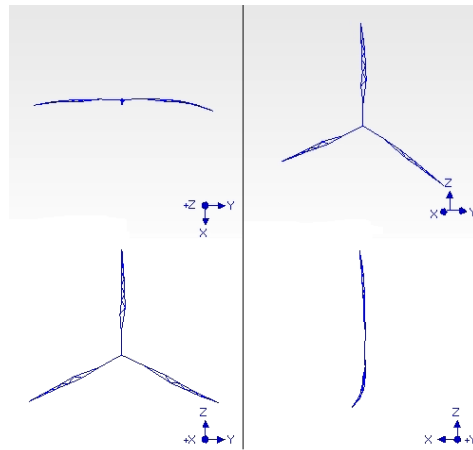


Figure 4: Time domain results

In a next step the data is analyzed with respect to the frequencies the modal shape consists of. Therefore a FFT analysis is conducted again by using the capabilities of the vibration analysis software. The analysis software provides of course more options with respect to the FFT, e.g. cascaded display of FFT of all measurement points. It is also possible to apply filter on the measurement data. The results of the FFT are the frequencies the modal shape in the time domain consists of.

Figure 5 shows the modal shape of the wind turbine blades at different frequencies. These are the frequencies that were obtained from the translation of the results from the time domain into the frequency domain. They represent the mode shapes of the wind turbine (from left to right first mode to third mode).

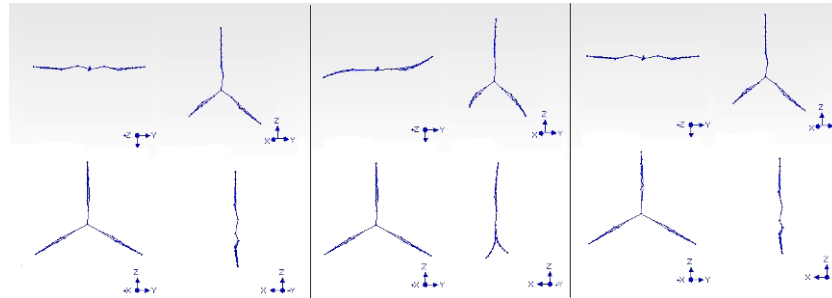


Figure 5: Modal shapes at different frequencies

5. Conclusions

The results show that optical measuring techniques are capable of gathering the data for vibration analysis on large objects. In combination with third party vibration analysis software full evaluations on operating deflection shapes and modal analysis can be performed.

The big advantage compared to conventional vibration measurement techniques is the isochronous measurement of all measurement points applied to the object.

6. References

- [1] Schmidt-Paulsen, U.; et.al., Modal Analysis on a 500 kW Wind Turbine with Stereo Camera Technique. SEM Paper, 2009
- [2] Schmidt-Paulsen, U.; et.al., Wind Turbine Operational and Emergency Stop Measurements Using Point Tracking Videogrammetry, SEM Conference and Exposition, Albuquerque, NM, June 3, 2009
- [3] Berger, H., Klein, M., Lambert, F., Levadoux, B., Optical Vibration Measurement and Frequency Response Analysis on Large Structures under Multiple Excitation Load Conditions, Proceedings of ISMA Conference, 2010

- [4] Gölling, B.; Erne, O., Experimental Investigation on Periodic Rolling of a Delta Wing Flow at Transonic Mach Numbers, Notes on Numerical Fluid Mechanics and Multidisciplinary Design, Volume 92/2006, pp. 112-119, 2006
- [5] Berger, H., Optische Messtechnik als Instrument zur Schwingungsmessung, Diploma Thesis, Technical University of Braunschweig, Institut für Dynamik und Schwingungen, Braunschweig, 2009